CODEN: JASMAN

The Journal of the Acoustical Society of America

ISSN: 0001-4966

Vol. 115, No. 3 March 2004

(Continued)

THE JOURNAL OF THE ACOUSTICAL SOCIETY OF AMERICA VOL. 115, NO. 3, MARCH 2004

CONTENTS—*Continued from preceding page*

(Continued)

THE JOURNAL OF THE ACOUSTICAL SOCIETY OF AMERICA VOL. 115, NO. 3, MARCH 2004

CONTENTS—*Continued from preceding page*

ACOUSTICAL NEWS—USA

Elaine Moran
Acoustical Society of America, Suite 1NO1, 2 Huntington Quadrangle, Melville, NY 11747-4502

Editor's Note: *Readers of this Journal are encouraged to submit news items on awards, appointments, and other activities about themselves or their colleagues. Deadline dates for news items and notices are 2 months prior to publication.*

Gaylon Hollis selected recipient of the ASA 2003 Minority Fellowship

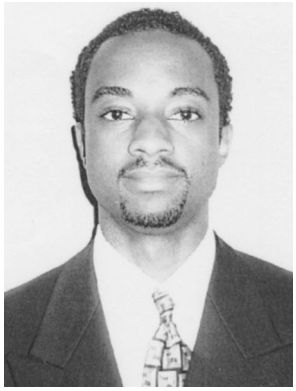

ASA member Gaylon Hollis has been selected the recipient of the Acoustical Society of America's 2003–04 Minority Fellowship. Mr. Hollis is a graduate student in the George Woodruff School of Mechanical Engineering at the Georgia Institute of Technology in Atlanta, Georgia. He received a B.S. in Mathematics at Morehouse College and a B.S. in Mechanical Engineering at the Georgia Institute of Technology. His research interests are in bioacoustics and acoustic emissions. The Minority Fellowship was established in 1992 with the goal of supporting minority students in their pursuit of graduate level degrees in acoustics. The Fellowship includes a $13 000 stipend for one academic year plus $1000 in travel support to attend an ASA meeting. Past recipients have been Brian Scott (1993), J. Sean Allen (1997), Guillermo E. Aldana (1994), Vernecia Sharaé McKay (2001), and David T. Bradley (2002). The next award will be available for the 2005–06 academic year. The fellowship may be renewed for one additional year.

For further information about the Fellowship, please contact the Acoustical Society of America, Suite 1NO1, 2 Huntington Quadrangle, Melville, NY 11747-4052, Tel.: 516-576-2360; Fax: 516-576-2377; E-mail: asa@aip.org; Web: http://asa.aip.org. Application information may also be found on the ASA home page at ⟨http://asa.aip.org/fellowships.html⟩.

Regional Chapter News

Greater Boston Chapter

We had a very successful 2002–2003 season!! We even had some months with two meetings! We are continuing to strive to broaden our audience further by hosting joint meetings with other local societies and organizations. We are preparing another exciting schedule for the next year of events and meetings for the Greater Boston Chapter of the Acoustical Society of America. This year we have more formally acknowledged local student chapters in order to foster growth and sharing of ideas with those students and faculty liaisons.

This year's officers are:

Chairman: Matthew Moore mmoore@cavtocci.com
Secretary: Rose Mary Su rsu@cavtocci.com or gbcasa@gbcasa.org
Treasurer: Ben Davenney bdavenny@acentech.com
National Liaison: Tim Foulkes tfoulkes@cavtocci.com

As many of you know, the Greater Boston Chapter and its events are supported on a volunteer basis. The intent is to reach a broad spectrum of people with a common interest in acoustics who gather about once a month to discuss topics in the field. Our goal is to offer perspectives on current issues in acoustics to those with an interest in acoustics. Please be aware that it is not necessary to be a Member of ASA national to join our local chapter, and guests are welcome to all events.

Be sure to check the chapter's website at http://www.gbcasa.org/ and download the latest chapter information, including meeting notices. We encourage you to join the electronic mailing list in order to receive meeting notices and updates right away. You can sign up instantly by accessing http://www.gbcasa.org/ and browsing down to the Groups Signup.

2002–2003 Year... a year in the life of GBC-ASA

Each year in June or July the Officers, members of the Executive Committee and any other chapter members interested in helping plan the next year's activities and meetings gather for dinner at some convenient centrally located restaurant for a creative ''think tank'' session. Those who suggest a meeting topic and possible presenter, as well as those not in attendance who may be ''volunteered'' by others, usually end up as organizers for a meeting or two responsible for contacting the presenter(s) and getting a title and short abstract for the meeting. For the next month or so the Chapter Chair chases the meeting organizers to firm up the commitments for presenters and meeting places so that with the meeting notice for the first scheduled meeting, usually in September, the Chair can include a ''Save the Dates'' tentative schedule for the full meeting year.

If all goes well, the Greater Boston Chapter ends up with generally successful, highly diverse, well attended and always very interesting meetings. We meet on the average of one meeting each month for the period, September through June, as we did for the 2002–2003 meeting year just completed. Always particularly satisfying for the membership are ''field trip'' meetings to see to-be-completed, and sometimes under construction, projects in which Chapter members may have provided consulting services or have been principals in some research effort. A notable example of this type of field meeting has been the Boston Central Artery/Third Harbor Tunnel Project, also known as the ''Big Dig.'' Each year, usually in late Spring, Mary Newman, wife of the late Prof. Robert Newman of MIT, Harvard, and Bolt Beranek and Newman fame, hosts along with the Chapter a benefit concert-meeting at her home in Lincoln, MA with the proceeds going to the Newman Student Award Fund now administered by the Society through the Technical Committee on Architectural Acoustics. The Chapter has had anniversary banquet meetings, book signing meetings featuring authors of acoustics texts, lecture meetings by distinguished faculty including one by recent ASA past President Bill Hartmann while he was on sabbatical at Boston University, and others.

The recently completed 2002–2003 season reflects the above diversity and is outlined below for the benefit of our colleagues in other ASA regional chapters. (Most of the presenters are willing to make presentations as long as their travel costs can be reimbursed.)

GBC/ASA 2002-2003 MEETINGS

24 September 2002

Active vibration control using complex "SEA." Richard Lyon, RH Lyon Corp President and 2003 ASA Gold Medal Recipient

The meeting on Tuesday, 24 September 2002, was a discussion of Active Vibration Control. Richard Lyon discussed how this applies to work completed for the Air Force.

23 October 2002

Joint meeting with Acoustical Society at Berklee College of Music

Spatial hearing and acoustics in ordinary rooms, Barbara Shinn-Cunningham, Department of Cognitive & Neural Systems and Biomedical Engineering, Boston University

This talk explored how the echoes and reverberations in small rooms influence acoustic cues and listener perception. Behavior on psychophysical tasks ranging from sound localization to understanding speech in noise (performed in both real rooms and ''virtual auditory space'') were reviewed.

28 October 2002

Joint meeting with INCE

Who wants a national noise policy? William W. Lang, Past President of INCE/USA and International INCE

Many engineers and technologists are convinced that America needs a national noise policy to replace the failed policy of the 1970s. But the need for, or lack of, a noise policy for the nation is neither universally recognized

 0001-4966/2004/115(3)/933/3/$20.00

nor accepted. A lively discussion on the pros and cons of a new National Policy followed a brief presentation by Dr. Lang.

20 November 2002

Do you hear what I hear? Robert Redden, Professor of Audiology, Northeastern University; Sandra Cleveland, Director of Audiology Clinical Services, Northeastern University; Mary Florentine and Søren Buus, Past GBC-ASA Chairs, Northeastern University

Have you ever been curious about your hearing? Have you ever wondered how hearing is clinically evaluated, or how hearing loss is determined? Or perhaps you want to know how to protect your hearing. This presentation addressed these issues, and a Q&A session was held relating to hearing health and rehabilitation. The chapter also toured the state-of-the-art Hearing, Speech and Language Center in the new Behrakis Health Sciences Center at Northeastern University.

17 December 2002

The soundscape of modernity—Architectural acoustics and the culture of listening in America, 1900–1933. Emily Thompson, Senior Fellow of Dibner Institute for the History of Science and Technology, MIT

In this meeting Emily Thompson discussed her new book, *The Soundscape of Modernity—Architectural Acoustics and the Culture of Listening in America, 1900–1933*, and the research involved.

14 January 2003

Joint meeting with Narragansett Chapter

Bisonar approach to synthetic aperture imaging. James A. Simmons, Department of Neuroscience, Brown University, Providence, RI

The January meeting was a presentation by James A. Simmons, Ph.D., of the Department of Neuroscience at Brown University. Dr Simmons showed how the bat's auditory system develops a cascade of representations for the broadcast and echoes that together solve several design problems in sonar in a way that is not mutually exclusive.

26 February 2003

The ANSI standard for classroom acoustics—What does it say and how will it influence future classroom design? Panel discussion with Lincoln Berry, Cavanaugh Tocci Associates; Pip Lewis, AIA—HMFH; Klaus Kleinschmidt, Cambridge Acoustics; and Steve Mahler, Ellenzweig

In summer 2002, ANSI approved Standard S12.60-2002, which is titled *Acoustical Performance Criteria, Design Requirements, and Guidelines for Schools*. This standard sets new expectations for classrooms and requires low background noise levels, noise isolation from sources outside the classrooms, and low reverberation times. These criteria will impact the selection and design of mechanical systems, building constructions, and classroom finishes. This meeting began with a discussion of the specific criteria of the standard from two acousticians who have studied it. Two local architects who have applied these types of performance goals on their projects presented a discussion of the impacts resulting from these criteria. A question and discussion period followed the panel presentations.

18 March 2003

Sabine's influence on the acoustical design of Boston's Gaiety Theatre. Steve Landrigan & The Friends of the Gaiety Theatre; David Griesinger, Lexicon

The meeting began with a brief presentation by Steve Landrigan and colleagues from *The Friends of the Gaiety Theatre* group as well as a technical presentation by Dave Griesinger, Chief Scientist for Lexicon, who did a feasibility study for the group. Dave's study speculates that Wallace Sabine's fingerprints are likely on the design of the theater since he worked with the architect Clarance Blackall in the early 1900s on several Boston theaters being built at that time. The Boston Landmarks was in the process of a final review and will be holding public hearings and reporting to Mayor Menino on whether to grant this theater landmark status.

22 April 2003

Joint meeting with Communications & Digital Signal Processing Center, and Northeastern Speech & Hearing Club

When sound effects are better than the real thing. Laurie Heller, Brown University

Dr. Heller discussed experiments that examine the perception of Foley sound effects. Sound effect technicians, known as ''Foley artist,'' have long known that two physically different events can produce similar sounds. For example, the sound of footsteps in the snow can be imitated by squeezing a box of cornstarch. This raises interesting questions for auditory psychology: Why do sound effects work? If two sounds do not have to be acoustically identical for them to represent the same event, what similarities are necessary? What differences are unimportant? And what does that tell us about the mental representation (and memory) of sounds? It has been claimed that sound effects can benefit from ''exaggerating'' aspects of the sound, but this assumption has not been explicitly tested.

9 May 2003

Orchestra pit and sound system design for the Boston Ballet Company's home: **The Wang Center for the Performing Arts**. Jonathan McPhee, Music Director Boston Ballet Company; John F. Allen, President, High Performance Stereo

Attendees had a great opportunity to experience a performance of *Romeo and Juliet* by the Boston Ballet at the Wang Center. Immediately following the dinner there were short presentations by Jonathon McPhee, the music director for the Boston Ballet, and John Allen, the resident sound designer for the Ballet, as well as by the Boston Ballet Company director Mikko Nissen. A backstage tour following the performance.

21 May 2003

The Robert Bradford Newman Student Award Fund Annual Benefit Concert at the residence of Mary Shaw Newman in Lincoln, MA. Virginia Eskin, one of New England's best loved concert pianists, ''A Piano Recital to Remember''

Following the concert, the Greater Boston Chapter presented a Certificate of Honor to Richard H. Lyon, recipient of the 2003 Gold Medal of the Acoustical Society of America.

14 June 2003

A late spring extra... informal weekend visit to Fisk Organ Open Shop, Gloucester, MA.

A visit was made to the OPEN SHOP for OPUS 121, a three-manual forty-two stop organ for Furman University in Greenville, SC, at the Fisk Organ Company in Gloucester, MA where the organ is undergoing its final construction and pre-installation adjustments before shipment to Furman University. Built for the Charles Ezra Daniel Chapel, an attractive contemporary building on the Furman campus, the specification, with both Positive and Swell divisions under expression, will be especially versatile in accompanying choir and orchestra, as well as playing a wide range of the organ repertory.

MATTHEW J. MOORE AND ROSE MARY SU

USA Meetings Calendar

Listed below is a summary of meetings related to acoustics to be held in the U.S. in the near future. The month/year notation refers to the issue in which a complete meeting announcement appeared.

2004

24–28 May	75th Anniversary Meeting (147th Meeting) of the Acoustical Society of America, New York, NY [Acoustical Society of America, Suite 1NO1, 2 Huntington Quadrangle, Melville, NY 11747-4502; Tel.: 516-576-2360; Fax: 516-576-2377; E-mail: asa@aip.org; WWW: http://asa.aip.org].
12–14 July	Noise-Con 2004, Baltimore, MD [Institute of Noise Control Engineering of the USA, Inc., INCE/USA Business Office, 212 Marston Hall, Iowa State Univ., Ames, IA 50011-2153; Tel.: 515-294-6142; Fax: 515-294-3528; E-mail: ibo@inceusa.org; WWW: http://www.inceusa.org/NoiseCon04call.pdf]
3–7 Aug.	8th International Conference of Music Perception and Cognition, Evanston, IL [School of Music, Northwestern Univ., Evanston, IL 60201; WWW: www.icmpc.org/conferences.html].
20–24 Sept.	ACTIVE 2004—The 2004 International Symposium on Active Control of Sound and Vibration, Williamsburg,

VA [INCE Business Office, Iowa State Univ., 212 Marston Hall, IA 50011-2153; Fax: 515-294-3528; E-mail:ibo@ince.org; WWW: inceusa.org]

15–19 Nov. 148th Meeting of the Acoustical Society of America, San Diego, CA [Acoustical Society of America, Suite 1NO1, 2 Huntington Quadrangle, Melville, NY 11747-4502; Tel.: 516-576-2360; Fax: 516-576-2377; E-mail: asa@aip.org; WWW: http://asa.aip.org].

Cumulative Indexes to the *Journal of the Acoustical Society of America*

Ordering information: Orders must be paid by check or money order in U.S. funds drawn on a U.S. bank or by Mastercard, Visa, or American Express credit cards. Send orders to Circulation and Fulfillment Division, American Institute of Physics, Suite 1NO1, 2 Huntington Quadrangle, Melville, NY 11747-4502; Tel.: 516-576-2270. Non-U.S. orders add $11 per index.

Some indexes are out of print as noted below.

Volumes 1–10, 1929–1938: JASA and Contemporary Literature, 1937–1939. Classified by subject and indexed by author. Pp. 131. Price: ASA members $5; Nonmembers $10.

Volumes 11–20, 1939–1948: JASA, Contemporary Literature, and Patents. Classified by subject and indexed by author and inventor. Pp. 395. Out of Print.

Volumes 21–30, 1949–1958: JASA, Contemporary Literature, and Patents. Classified by subject and indexed by author and inventor. Pp. 952. Price: ASA members $20; Nonmembers $75.

Volumes 31–35, 1959–1963: JASA, Contemporary Literature, and Patents. Classified by subject and indexed by author and inventor. Pp. 1140. Price: ASA members $20; Nonmembers $90.

Volumes 36–44, 1964–1968: JASA and Patents. Classified by subject and indexed by author and inventor. Pp. 485. Out of Print.

Volumes 36–44, 1964–1968: Contemporary Literature. Classified by subject and indexed by author. Pp. 1060. Out of Print.

Volumes 45–54, 1969–1973: JASA and Patents. Classified by subject and indexed by author and inventor. Pp. 540. Price: $20 (paperbound); ASA members $25 (clothbound); Nonmembers $60 (clothbound).

Volumes 55–64, 1974–1978: JASA and Patents. Classified by subject and indexed by author and inventor. Pp. 816. Price: $20 (paperbound); ASA members $25 (clothbound); Nonmembers $60 (clothbound).

Volumes 65–74, 1979–1983: JASA and Patents. Classified by subject and indexed by author and inventor. Pp. 624. Price: ASA members $25 (paperbound); Nonmembers $75 (clothbound).

Volumes 75–84, 1984–1988: JASA and Patents. Classified by subject and indexed by author and inventor. Pp. 625. Price: ASA members $30 (paperbound); Nonmembers $80 (clothbound).

Volumes 85–94, 1989–1993: JASA and Patents. Classified by subject and indexed by author and inventor. Pp. 736. Price: ASA members $30 (paperbound); Nonmembers $80 (clothbound).

Volumes 95–104, 1994–1998: JASA and Patents. Classified by subject and indexed by author and inventor. Pp. 632. Price: ASA members $40 (paperbound); Nonmembers $90 (clothbound).

BOOK REVIEWS

P. L. Marston
Physics Department, Washington State University, Pullman, Washington 99164

These reviews of books and other forms of information express the opinions of the individual reviewers and are not necessarily endorsed by the Editorial Board of this Journal.

Editorial Policy: *If there is a negative review, the author of the book will be given a chance to respond to the review in this section of the Journal and the reviewer will be allowed to respond to the author's comments. [See "Book Reviews Editor's Note," J. Acoust. Soc. Am.* ***81****, 1651 (May 1987).]*

Random Vibration, Vol. 3 of Mechanical Vibration & Shock

Christian Lalanne

Taylor & Francis, New York, 2002.
xvii+346 pp. Price: $150 hardcover ISBN: 1560329882.

Christian Lalanne's third volume in the *Mechanical Vibration and Shock* series delivers the same accumulation of practical experience apparent in the other four volumes, some of which have been reviewed here. Lalanne has successfully catalogued a career in research and engineering, providing the academic or the engineer with an indexed resource of analysis and decision-making tools, most with complete theoretical development.

Random Vibration covers a breadth of methods for analysis, modeling, and probabilistic interpretation of random vibration signals. Chapter 1 outlines methods of statistical modeling and study of random vibration. Pertinent terms and basic methods are mathematically defined, including correlation, covariance, and ergodicity. The flowchart of analysis approaches and the table of statistical definitions are both valuable references.

Chapter 2 introduces the study of random vibration in the frequency domain. Power spectral density is derived and explained in detail. Lalanne explicitly defines coherence and provides significant insight on the application and understanding of frequency response analysis. Chapter 3 continues in the frequency domain, defining root-mean-square values of random vibration using power spectral density with several pertinent example cases. Chapter 4 concludes the frequency-domain approach with more advanced topics in windowing methods for discrete Fourier transforms and fast Fourier transforms, along with associated errors and confidence intervals. Lalanne provides further guidance with detailed discussions of overlapping methods, bandwidth filters, and direction for using these tools to minimize statistical errors in practical cases.

Chapter 5 introduces methods for random vibration analysis in the time domain, including statistical properties of instantaneous values, derivatives, correlation, and moments of the power spectral density. Several cases for varying dimensional scales are provided. Chapter 6 extends this analysis to probability densities of vibration maxima. Extensive practical examples in fatigue analysis are provided. This chapter also explains irregularity factors and other tools for predicting frequency and severity of peak vibrations. Chapter 7 concludes the main text with statistics of extreme values. Probability density of highest values and asymptotic laws are explained. Lalanne provides a wealth of advice for selection of appropriate statistical analysis measures, particularly in the calculation of fatigue damage without direct peak counting. Finally, a 40-page Appendix thoroughly presents, in context, the laws of probability, octave analysis, spectrum conversion to power spectral density, and other appropriate mathematical functions. The book contains a vast bibliography and a short but useful index.

Though some minor typographical errors, relatively poor figure quality, and weak diction may detract from the overall experience of the reader, this text will be a valuable resource of practical knowledge for the vibration analyst.

JONATHAN D. KEMP
Acentech, Incorporated
33 Moulton Street
Cambridge, Massachusetts 02138-0118

Formulas of Acoustics

F. P. Mechel (Editor)

Springer, New York, 2002
1175 pp. Price: $199.00 (hardcover) ISBN: 3540425489.

This lengthy book clearly represents a considerable labor by its editor, Professor Dr. Fridolin P. Mechel, who has contributed the vast majority of the material in the book. He is joined by a number of distinguished contributors for some chapters. The aim of the book, as its title suggests, is to present formulas found in classical acoustics problems. As noted by the editor, it is not intended as a textbook, and complete derivations of the formulas are rarely given. However, the ''source'' of the result is provided for the interested reader. This review cannot attempt to summarize all the material covered in this book; instead, a few examples are provided and some comments are given on how the book could prove useful to both scientists and engineers engaged in problems in acoustics.

Following an introductory section on notation and conventions, there are 18 chapters covering topics from: linear to nonlinear acoustics; sound reflection and scattering; sound radiation, transmission and absorption; duct acoustics and mufflers; capsules, cabins and room acoustics; and flow acoustics. Numerical and variational methods in acoustics are also considered, as are elasto-dynamics and ultrasound absorption in solids.

Each section is self-contained, with its own set of references. In addition, the index is also divided by chapter titles, making for relatively easy searching if the reader knows something of the context of their interest. However, though the editor has taken some care to cross-reference the different chapters to avoid repetition, some of the supporting material from other chapters that would be useful to the reader is unreferenced. An example is the use of Mathieu functions in the chapter on acoustic scattering. Some useful material on these functions is contained in the preceding chapter on the reflection of sound, but it is left to the reader to track this down.

To give some sense of the material covered by the book, two chapters are discussed here in more detail. The chapter on acoustic scattering begins with definitions of the incident, scattered, and interior fields, including the plane-wave expansions in terms of Bessel functions. The surface boundary conditions for matching of pressure and radial particle velocity are also given. Definitions of scattering, absorption, extinction, and backscattering cross sections are then provided. General formulas for plane-wave scattering from cylinders and spheres are then tabulated. Some numerical examples and figures are then shown to provide the reader with a sense of the quantities and relations given in the tables. This is followed by scattering problems from more complex geometry bodies such as corners surrounded by a cylinder and various screens and dams. Scattering in random media is then covered and this is followed by formulas for scattering by deformable objects and absorbing bodies. Though this brief chapter review is not comprehensive, it hopefully gives some idea of the breadth of coverage within a given topic. Each subtopic contains a short introduction with definitions. This is followed by solutions for the different configurations, sometimes in the form of tables. The model problems solved in this section, as well as in other sections of the book, offer a wealth of benchmark problems for com-

 0001-4966/2004/115(3)/941/2/$20.00

putational acoustics. They include some problems with complex geometries and mixed boundary conditions, including both reflecting as well as absorbing surfaces.

The difficult topic of flow acoustics is tackled in another chapter. This topic differs from most of the others in that it deals with sound radiation from unsteady fluid motion. Since this motion is usually turbulent, no closed-form predictions are available. However, perhaps in the spirit of the book, this chapter does provide a comprehensive survey of the various formulations that have been developed in the study of aerodynamic noise. The relevant forms of the equations of motion and their simplifications for different applications are provided. The acoustic analogy in several forms is given. These include Lighthill's original formulation, extensions for the presence of solid boundaries, and extensions to account for mean-flow acoustic interaction effects. In the presentation of Lighthill's acoustic analogy, no attempt is made to address the nature of the equivalent source: that is, it is based on instantaneous fluctuations in density and velocity rather than fluctuations in these values. Of course, this difficulty is overcome with the introduction of the Lilley equation and Ribner's reformulation of Lighthill's analogy: but, these finer points are not represented by the formulas or equations alone. No attempt is made to provide the range of applicability or limitations of the various formulations.

One measure of the value of a book of this type is the ease with which the reader can find formulas on a given topic. As a test I chose two problems: the radiation of sound from a tube termination (given by Morse and Feshbach, Sec. 11.3), and the reflection of sound from a point monopole above a locally reacting plane. The latter problem is a useful case for computational acoustics to test numerical accuracy in either time- or frequency-domain calculations. I had no problem finding both exact and approximate solutions to this problem in the chapter on the reflection of sound. However, I could find no reference to the former problem, even though I scanned the sections on sound radiation and duct acoustics.

It is hard to find too much fault with this book, given the considerable effort clearly expended by the authors, especially the editor. However, in an attempt to be as comprehensive as possible, some sections are weaker than others. For example, the nonlinear acoustics section is very brief and without references. It also contains no discussion of acoustic streaming. Also, in some cases, particularly in the flow acoustics section, the statement of the flow equations in their various forms alone obscures some important issues in aerodynamic noise modeling. A short introduction to this section, noting that the provision of an equation is far from the provision of a prediction, would have been helpful. However, this a minor point and doesn't apply to the book as a whole, where the problems are well posed and the solutions exact. Overall, this is a valuable and helpful book. I expect that it will find its way onto many researchers' bookshelves next to other oft-referenced works such as Abramowitz and Stegun, Gradshteyn and Ryzhik, and, of course, Morse and Feshbach.

PHILIP J. MORRIS
Penn State University
Department of Aerospace Engineering
University Park, Pennsylvania 16802-1401

OBITUARIES

Govindappa Krishnappa • 1936–2003

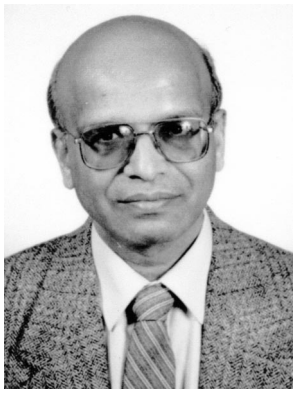

Dr. Krishnappa, who was known as Krish to his colleagues and who was a Fellow of this Society, died on 18 September 2003 in Ottawa, Canada. He was born in India in 1936, and he attended the University of Mysore from 1954 to 1958, where he received a bachelor's degree in engineering. After a brief period of employment with the Mysore Public Works, he attended the Indian Institute of Science (from 1961 to 1963) and obtained the Master of Science degree. He subsequently undertook advanced graduate work in mechanical engineering at the University of Waterloo in Canada, where he received a Ph.D. in 1967.

After completion of his doctoral work, Dr. Krishnappa joined the Division of Mechanical Engineering of the National Research Council (NRC) in Ottawa. This was a long and distinuished association which led to many significant accomplishments in acoustics. His early research at NRC was applied to gas turbine noise, jet noise, turbomachinery noise, and vibration control. Later he became involved with research issues in sound intensity measurements, in the determination of sound power from noise sources, and in the monitoring of the condition of machinery. His work at NRC was well regarded, and he was promoted to Senior Research Officer in 1981. Then, in 1994, he was promoted to the position of Principal Research Officer, this being the highest scientific rank at NRC. In subsequent years he was associated with the NRC's Manufacturing Technology Institute in Vancouver, from which he retired in 1999 after 31.5 years of service with the NRC. After his formal retirement, he continued in his professional activities and was associated with the Institute for Aerospace Research (IAR) in Ottawa as a Guest Worker. At the invitation of the NRC, which had a new project that needed Dr. Krishnappa's unique expertise, he left his retirement in 2001 to manage this project.

Over his years at NRC, Krish was influential in helping his younger colleagues, and he was widely regarded as a good mentor. He was active in collegial activities at NRC; his activities in this regard included a long service as Secretary of the NRC Associate Committee on Noise from 1980 to 1989.

Dr. Krishnappa joined the ASA in 1975 and was awarded the honor of being elected a Fellow in 1984. He served as a member of the ASA Noise Technical Committee from 1987 to 1993. He was chairman of the Acoustical Society's working group that developed the standard for sound intensity measurement. [The working group carried the designation S1-WG12, and the standard that was developed was the American National Standard ANSI S1.9-1996 (R 2001).] He was also active in other professional societies, and was recognized by the USA's branch of the Institute of Noise Control Engineering with the title of Distinguished International Member. He was also a member of the Canadian Acoustical Association and of the International Institute of Acoustics and Vibration (IIAV), and he was Chairman of the latter organization's Awards, Honors, and Membership Committee. His activities in the development of standards were extensive, and he had a long association with the International Standards Organization (ISO) that dated back to 1984, and he was on many occasions the Head of the Canadian Delegation to international standards meetings.

Dr. Krishnappa is survived by his wife, Nimmi, his son, Ninni Krishnappa, and his daughter, Chitty Berger.

GEORGE S. K. WONG

 0001-4966/2004/115(3)/943/1/$20.00

REVIEWS OF ACOUSTICAL PATENTS

Lloyd Rice
11222 Flatiron Drive, Lafayette, Colorado 80026

The purpose of these acoustical patent reviews is to provide enough information for a Journal reader to decide whether to seek more information from the patent itself. Any opinions expressed here are those of reviewers as individuals and are not legal opinions. Printed copies of United States Patents may be ordered at $3.00 each from the Commissioner of Patents and Trademarks, Washington, DC 20231. Patents are available via the Internet at http://www.uspto.gov.

Reviewers for this issue:

GEORGE L. AUGSPURGER, *Perception, Incorporated, Box 39536, Los Angeles, California 90039*
MARK KAHRS, *Department of Electrical Engineering, University of Pittsburgh, Pittsburgh, Pennsylvania 15261*
HASSAN NAMARVAR, *Department of BioMed Engineering, University of Southern California, Los Angeles, California 90089*
DAVID PREVES, *Starkey Laboratories, 6600 Washington Ave. S., Eden Prarie, Minnesota 55344*
DANIEL R. RAICHEL, *2727 Moore Lane, Fort Collins, Colorado 80526*
CARL J. ROSENBERG, *Acentech Incorporated, 33 Moulton Street, Cambridge, Massachusetts 02138*
WILLIAM THOMPSON, JR., *Pennsylvania State University, University Park, Pennsylvania 16802*
ERIC E. UNGAR, *Acentech, Incorporated, 33 Moulton Street, Cambridge, Massachusetts 02138*
ROBERT C. WAAG, *Univ. of Rochester, Department of Electrical and Computer Engineering, Rochester, New York 14627*

6,617,765

43.30.Yj UNDERWATER BROADBAND ACOUSTIC TRANSDUCER

Yves Lagier *et al.*, assignors to Thales Underwater Systems S.A.S.
9 September 2003 (Class 310/330); filed in France 22 October 1999

An underwater transducer comprises a single plate of piezoceramic **101** bonded to the underside of the bottom of a free-flooding cuplike vessel **105** which is welded along its periphery at **109** to a housing assembly that also creates air cavity **108** at the other face of the piezoceramic. The plate of piezoceramic and the base of the vessel **107** comprise a bender (a unimorph) whose vibrations excite the entrained column of water. Two distinct resonances are observed, that of the bender plus a quarter-wavelength resonance

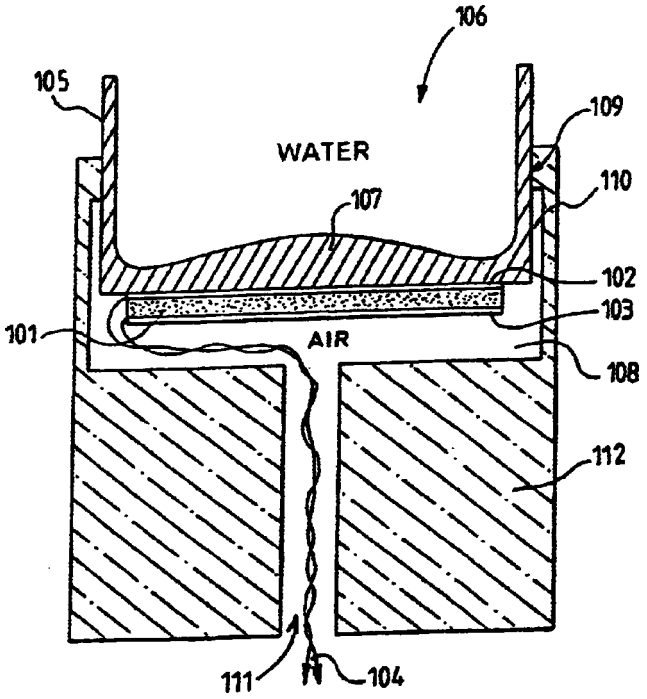

associated with the column of water. Assuming these two resonances are in reasonably close frequency juxtaposition, a broad bandwidth transmitting response is realized. The thickness of the base of the vessel **107** is not constant so as to mitigate deflection of the piezoceramic under the hydrostatic load. The cavity of the vessel can also be partially filled with material in an attempt to further modify the transmitting response characteristics. In an alternate embodiment, two such units are mounted back-to-back and driven so as to produce a dipole radiation pattern.—WT

6,614,724

43.30.Yj HYDROPHONE ARRAY WITH INDIVIDUALLY SWITCHABLE HYDROPHONE SENSORS

William H. Behrens and Jim Nash, assignors to Input/Output, Incorporated
2 September 2003 (Class 367/154); filed 8 November 2001

Hydrophone streamers often have pressure sensitive disabling switches wired in parallel with the several hydrophones in the streamer. These switches close at a preselected depth in the ocean thus shorting out all the hydrophones that are wired in parallel with that switch. Premature failure of the switch can thus disable the whole set of hydrophones. In the present patent, pressure sensitive switches that open, instead, at a preselected depth are wired in series with each hydrophone with the result that a switch failure only disables a single hydrophone.—WT

6,628,451

43.35.Sx ACOUSTO-OPTIC REFLECTION-ACTIVE IMAGING

Jaswinder S. Sandhu, Buffalo Grove and Honghui Wang, Palatine, both of Illinois
30 September 2003 (Class 359/285); filed 14 February 2002

Advantage is taken of the fact that acousto-optic reflection-active media have an optical reflectivity that varies with changes in the interacting acoustic energy intensity. This fact helps to form images of the detectable defects in samples because defects reflect acoustic energy differently from known acoustically reflecting parts of the samples.—DRR

 0001-4966/2004/115(3)/947/19/$20.00

6,636,201

43.35.Ty ACOUSTIC TOUCHSCREEN HAVING WAVEGUIDED REFLECTOR ARRAYS

Paulo Irulegui Gomes *et al.*, assignors to ELO TouchSystems, Incorporated
21 October 2003 (Class 345/173); filed 26 May 2000

This acoustic touchscreen contains transmitting transducers for generating acoustic signals that are deflected across a touch-sensitive area by an array of partially acoustically reflective elements. A touch on the touch-sensitive area causes a perturbation in the acoustic signals. After traversing the touch-sensitive area, these acoustic signals are redirected by another array of partially acoustically reflective elements toward receiving transducers, where the signals (and, thus, any perturbations) are sensed. In order to accommodate touchscreens having narrow border regions, the acoustic signals are propagated across the border regions through wave guides. The wave guides confine the acoustic signals to traveling along a narrow path, but yet allow them to be deflected across the touch-sensitive area. This allows transducers and reflective elements to be of narrower construction and to fit within narrow border regions.—DRR

6,626,837

43.35.Wa ULTRASONOGRAPH

Hiroyuki Muramatsu *et al.*, assignors to Seiko Instruments Incorporated
30 September 2003 (Class 600/459); filed in Japan 27 November 2000

One embodiment of this device involves a sensor portion incorporating an ultrasound generator for sending signals to a body region to be diagnosed and an ultrasound-receiving unit to accept waves reflected from the diagnosed region. A support unit holds the sensor portion from its back side

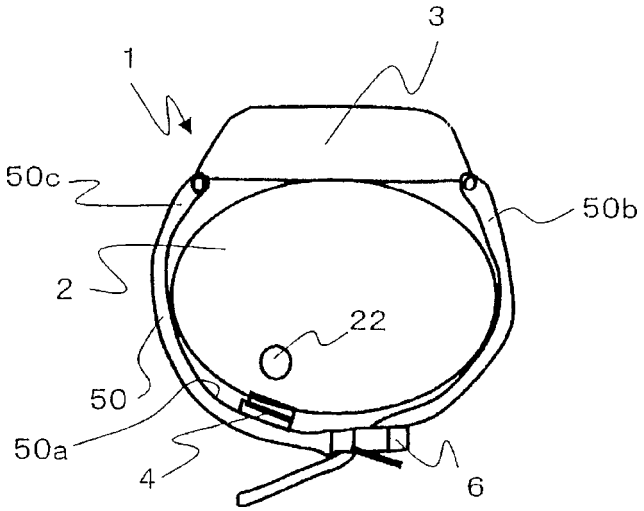

relative to the diagnosed region and an information acquisition unit obtains information based on the reflected waves received by the ultrasound-receiving unit. An ultrasound attenuator may be interposed between the sensor portion and the support unit.—DRR

6,633,774

43.35.Wa THERMOACOUSTIC TISSUE SCANNER

Robert A. Kruger, assignor to Optosonics, Incorporated
14 October 2003 (Class 600/407); filed 15 November 2002

This thermoacoustic scanner is based on the fact that imaging properties of tissues depend on differential absorption of electromagnetic waves in differing tissue types. The thermoacoustic imaging system includes an electromagnetic radiation source for irradiating tissue to evoke a thermoacoustic response and an acoustic sensor array, to which the response is acoustically coupled. The array consists of sensors arranged on a surface which swivels about an axis to position the sensors into any number of positions for detecting thermoacoustic response. The source of electromagnetic waves for irradiating the tissue is a set of sources arranged about the tissue and producing synchronized electromagnetic radiation in varying polarizations or phases.—DRR

6,612,991

43.35.Yb VIDEO-ASSISTANCE FOR ULTRASOUND GUIDED NEEDLE BIOPSY

Frank Sauer and Ali Khamene, assignors to Siemens Corporate Research, Incorporated
2 September 2003 (Class 600/461); filed 16 August 2002

This patent describes a system to assist in performing a biopsy of a patient using an ultrasound-guided needle. A transducer lead is used to obtain an ultrasound image of the patient in an ultrasound imaging plane. A video camera mounted on the transducer is held in such a manner that the ultrasound imaging plane corresponds to a line in the video image. A body surface video image of the patient is obtained in the area in which the ultrasound imaging plane surface intersects the body surface. Graphic markers overlayed onto the video image help to indicate the ultrasound imaging plane as a line of possible entry points for the needle biopsy.—DRR

6,612,992

43.35.Yb MEDICAL DIAGNOSTIC ULTRASOUND CATHETER AND METHOD FOR POSITION DETERMINATION

John A. Hossack *et al.*, assignors to Acuson Corporation
2 September 2003 (Class 600/467); filed 2 March 2000

This patent relates to a method for determining the position of a catheter within the cardiovascular system. Local bending and twisting are measured at multiple locations along the catheter. By integrating the measurements, the position and orientation of the catheter are established. The

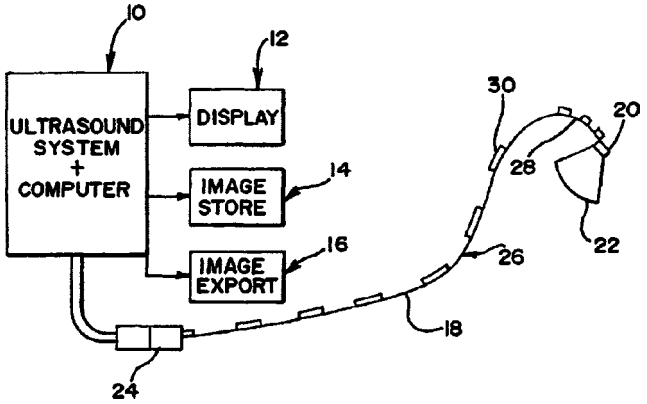

location and orientation of an ultrasonic transducer array connected to the catheter are based on the catheter position information. Information on the imaging array position and orientation can help a physician to determine the tissue structure or fluid being scanned and/or assist in the precise generation of three-dimensional representations.—DRR

6,613,005

43.35.Yb SYSTEMS AND METHODS FOR STEERING A FOCUSED ULTRASOUND ARRAY

Zvi Friedman and Dov Maor, assignors to InSightec–TxSonics, Limited
2 September 2003 (Class 601/2); filed 28 November 2000

This is another method of providing focused ultrasound in which a mechanical controller is coupled to a transducer array consisting of subarrays, each subarray of transducer elements defining an acoustic emission surface. The subarrays include actuators for adjusting the orientation of the acoustic emission surfaces to facilitate steering of the acoustic energy emitted by these transducer elements toward a target tissue region. Drive circuitry drives the transducer elements so as to emit sufficient acoustic energy from their respective emission surfaces to ablate the target region (such as a tumor).—DRR

6,616,611

43.35.Yb DOPPLER ULTRASOUND METHOD AND APPARATUS FOR MONITORING BLOOD FLOW

Mark A. Moehring, assignor to Spentech, Incorporated
9 September 2003 (Class 600/454); filed 16 June 2000

This patent relates to a pulse Doppler ultrasound system and associated methods for monitoring blood flow. A graphic information display simultaneously presents depth-mode and spectrogram displays. The depth-mode display indicates the various positions along the ultrasound beam axis at which the blood flow is discerned. These positions are represented as one or more colored regions, with each color indicating the direction of the blood flow and varying in intensity as a function of detected Doppler ultrasound signal amplitude or detected blood flow velocity. The depth-mode display also provides a pointer whose position may be selected by the operator. A spectrogram is displayed corresponding to the location identified by the pointer. Embolus detection and characterization are also included.—DRR

6,629,929

43.35.Yb METHOD AND APPARATUS FOR AUTOMATICALLY SETTING THE TRANSMIT APERTURE AND APODIZATION OF AN ULTRASOUND TRANSDUCER ARRAY

James Jago and David Rust, assignors to Koninklijke Philips Electronics N.V.
7 October 2003 (Class 600/447); filed 8 November 2002

The object of this device is to provide adaptive control of the focal zone or focal zones of an ultrasonic transducer array in response to user input defining a range of interest. The depth range for each focal zone and the transmit apodization are automatically defined. A system controller sets a focus zone on the point of interest and adjusts the aperture and apodization for the range of interest. If the range of interest can not be covered by one focal zone, additional focal zones are added.—DRR

6,632,178

43.35.Yb FABRICATION OF CAPACITIVE MICROMACHINED ULTRASONIC TRANSDUCERS BY MICRO-STEREOLITHOGRAPHY

John Douglas Fraser, assignor to Koninklijke Philips Electronics N.V.
14 October 2003 (Class 600/459); filed 27 October 2000

Recent developments have led to the prospect that medical ultrasound transducers can be manufactured by the same processes used to make semiconductors. These developments have produced capacitive micro-machined ultrasonic transducers or cMUTs. Such transducers are tiny diaphragmlike devices with electrodes that convert the sound vibration of a received ultrasound signal into a modulated capacitance. For transmission, the capacitive charge is modulated to vibrate the diaphragm of the device to transmit a sound wave. Because they are manufactured by semi-conductor processes, these devices have dimensions in the 10–200 micron range. Also, many such devices can be grouped together and operated in unison as a single transducer element. The cMUT cells can be fabricated by conventional semiconductor processes to be integrated with ancillary transducer circuitry such as a bias charge regulator. The cMUT cells can also be fabricated by micro-lithography wherein the cells can be formed using a variety of polymers and other materials.—DRR

6,632,179

43.35.Yb ACOUSTIC IMAGING SYSTEM WITH NON-FOCUSING LENS

Martha Grewe Wilson and Wojtek Sudol, assignors to Koninklijke Philips Electronics N.V.
14 October 2003 (Class 600/460); filed 31 July 2001

In a preferred embodiment, this acoustic imaging system includes a transducer lens configured to mate with a transducer body. The transducer lens is formed, at least partially, from an acoustic matching material that manifests acoustic properties corresponding to the acoustic properties of a body to be imaged. In this configuration, acoustic energy emitted from the transducer into the body can be substantially nonfocusing until modified by electronic focusing techniques.—DRR

6,609,609

43.35.Zc OBJECT LEVITATING APPARATUS AND METHOD FOR CONTROLLING THE SAME

Masaki Takasan *et al.*, assignors to Kabushiki Kaisha Toyota Jidoshokki
26 August 2003 (Class 198/630); filed in Japan 20 September 2000

An object in the shape of a small rectangular plate is levitated via air pressure generated by sound waves produced by a series of transducers. Each transducer is actuated by an oscillator, and each oscillator is controlled in accordance with the transducer's measured impedance, which depends on the location and proximity of the levitated object relative to the transducer.—EEU

6,612,156

43.35.Zc ACOUSTIC MIXING AND MEASUREMENT SYSTEM AND METHOD

Mustafa Hakimuddin, assignor to Halliburton Energy Services, Incorporated
2 September 2003 (Class 73/61.75); filed 25 October 2001

This system, intended primarily for the analysis of drilling fluid, consists of a sample cell that includes two ultrasonic devices. One of these is intended to promote mixing of the liquid and solid elements, the other functions to measure the mixture's acoustic properties, such as its sound speed.—EEU

6,629,928

43.38.Hz MODULAR TRANSDUCER CONNECTION SYSTEM

David P. Dolan and Richard H. Jundanian, assignors to Koninklijke Philips Electronics N.V.
7 October 2003 (Class 600/437); filed 8 November 2002

This is a system for accommodating multiple interchangeable transducer connector modules (TCMs). Each TCM contains an ultrasound connector, a switching circuit, a pluggable interface, and an ultrasound control unit. The ultrasound control unit itself contains a number of bays, each of which allows a TCM to be plugged into the distribution bus of the ultrasound control unit. A system controller selects a combination of TCMs and activates the switching circuit of the selected TCMs.—DRR

6,607,051

43.38.Ja YOKE STRUCTURE OF A SPEAKER DIAPHRAGM

Jack Peng, assignor to Meiloon Industrial Company, Limited
19 August 2003 (Class 181/171); filed 6 October 2000

The accordian edge speaker suspension was patented by Olson *et al.* in

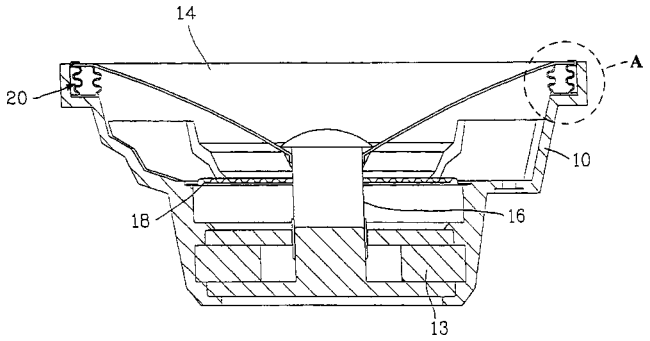

1949. In this version, a double bellows **20** provides additional stability and ease of assembly.—GLA

6,611,606

43.38.Ja COMPACT HIGH PERFORMANCE SPEAKER

Godehard A. Guenther, San Francisco, California
26 August 2003 (Class 381/421); filed 27 June 2001

In the loudspeaker shown, the magnetic circuit consists of two conventional ring magnets **1** and **2** plus metal plates **3**, **4**, and **5**. This arrange-

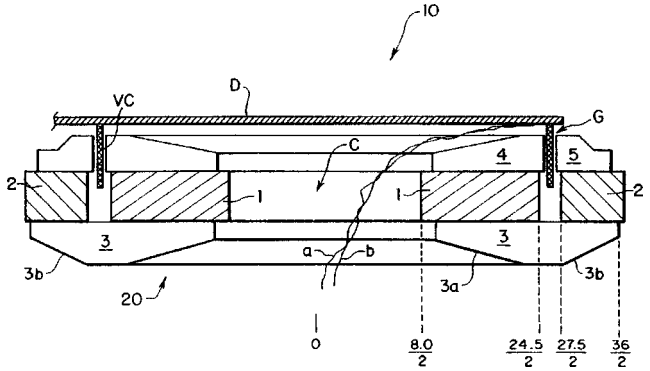

ment is said to concentrate magnetic flux more efficiently than conventional designs.—GLA

6,611,604

43.38.Ja ULTRA LOW FREQUENCY TRANSDUCER AND LOUD SPEAKER COMPRISING SAME

Steven M. Irby and William O. Doering, assignors to Stillwater Designs & Audio, Incorporated
26 August 2003 (Class 381/398); filed 5 July 2000

Almost all electrodynamic loudspeakers use round coils to drive round cones, however commercial speakers have been designed with square cones driven by square coils. Obviously, opportunities exist for enterprising inven-

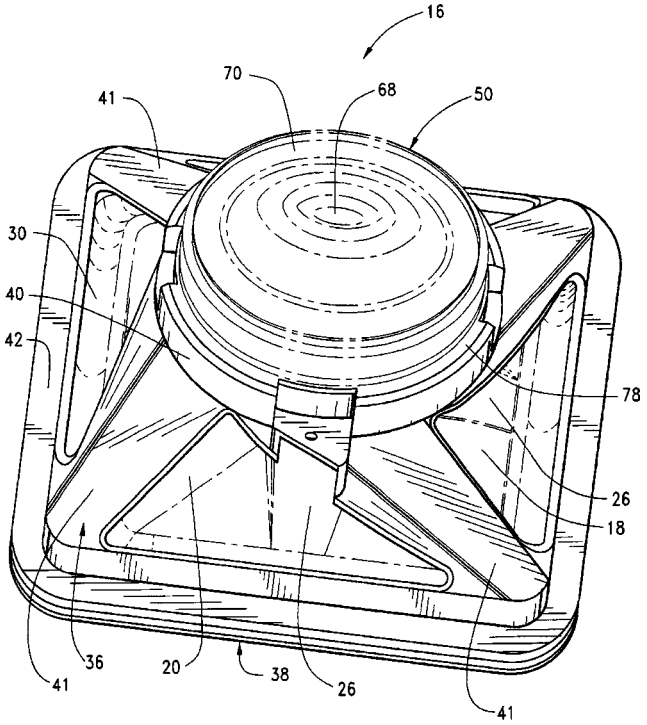

tors to design round cones driven by square coils and square cones driven by round coils. The latter option has now been covered by this short patent that consists mostly of four illustrations and 70 claims.—GLA

6,621,909

43.38.Ja HORN LOUDSPEAKER AND LOUDSPEAKER SYSTEMS

William Webb *et al.*, assignors to Martin Audio Limited
16 September 2003 (Class 381/342); filed in the United Kindgom 28 November 1997

The invention is an active horn mouth. If loudspeakers **32** are mounted at suitable locations around the bell of a conventional horn **22**, their outputs

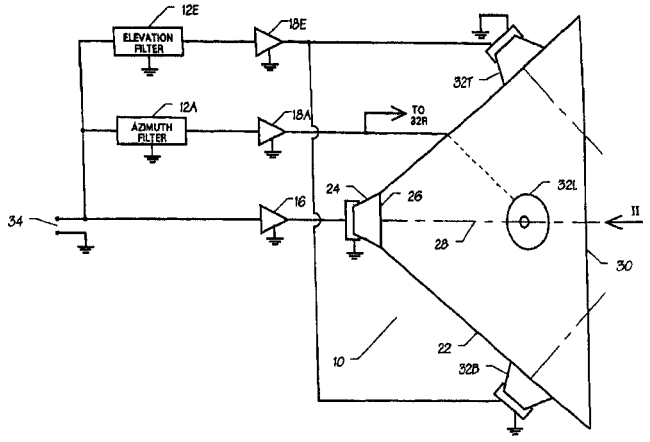

can be combined with that from the main driver 24 to modify the far-field coverage pattern. Although not shown in the diagram, the signal to the main driver may also be filtered.—GLA

6,618,488

43.38.JA SPEAKER SYSTEM

Takeshi Nakamura, assignor to Murata Manufacturing Company, Limited
9 September 2003 (Class 381/349); filed in Japan 28 December 1999

In this loudspeaker design, vent duct **16** is located directly behind speaker **14**. A second duct **20** partially overlaps the vent duct. The arrangement is said to allow the use of a shorter vent duct for a given resonance

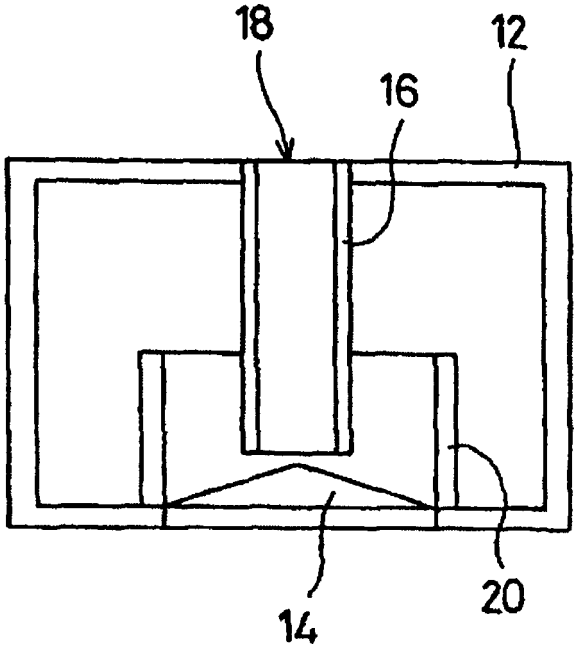

frequency. If the geometry is unwrapped, it can be seen that instead of driving the air chamber directly, the rear of the loudspeaker drives a relatively long stepped vent at roughly one-third its length. Novel and interesting.—GLA

6,621,911

43.38.Ja MULTIFUNCTION ACOUSTIC DEVICE

Takashi Kobayashi and Akira Nikaido, assignors to Citizen Electronics Company, Limited
16 September 2003 (Class 381/396); filed in Japan 19 December 2000

This beeper/vibrator includes a diaphragm **14** driven by voice coil **15** for sound reproduction. To minimize interaction with the sound transducer, a

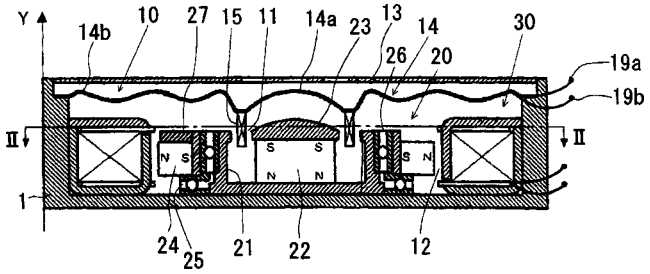

separate rotary motor **24**, **25**, **26**, **27** is used to supply the vibrator function.—GLA

6,611,196

43.38.Md SYSTEM AND METHOD FOR PROVIDING AUDIO AUGMENTATION OF A PHYSICAL ENVIRONMENT

Elizabeth D. Mynatt *et al.*, assignors to Xerox Corporation
26 August 2003 (Class 340/5.8); filed 20 March 1998

For those corporations seeking to provide employees with a ''...palpable sense of their work group's activity,'' Xerox has the answer. Everyone wears a wireless earphone that transmits information about its wearer's location to a central computer which responds with an appropriate informational soundscape. A secretary approaching his or her office may hear sea gull calls indicating a medium volume of E-mail, along with a ship whistle, indicating E-mail from the boss. I am not making this up.—GLA

6,614,365

43.38.Md CODING DEVICE AND METHOD, DECODING DEVICE AND METHOD, AND RECORDING MEDIUM

Shiro Suzuki *et al.*, assignors to Sony Corporation
2 September 2003 (Class 341/50); filed in Japan 14 December 2000

The patent is concerned with low-bit-rate encoding of audio signals using known MS or IS stereo coding formats. In prior art systems, the selection of MS, IS, or dual coding is dynamically performed for optimum efficiency, but only after the two coding processes are actually performed. Moreover, sound quality variations with time can be appreciable. The patent

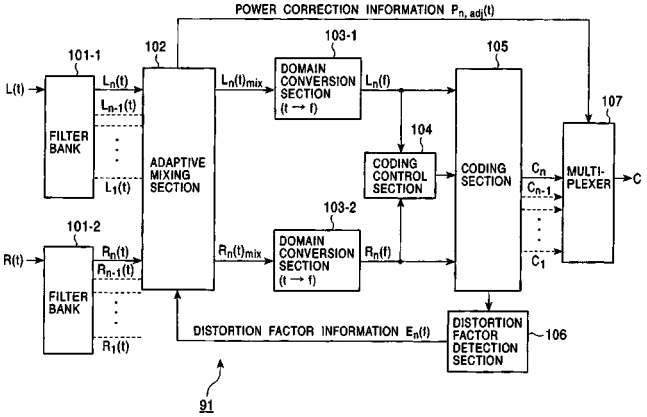

describes a new method in considerable detail. An adaptive mixing section mixes filter bank outputs based on distortion information and controls the operation time of MS or IS coding as selected by a separate coding control section. ''Coding is made possible with higher efficiency while the listener is prevented from feeling a sense of incongruity.''—GLA

6,614,729

43.38.Md SYSTEM AND METHOD OF CREATING DIGITAL RECORDINGS OF LIVE PERFORMANCES

David D. Griner, Austin Texas and James C. Griner, Woodinville, Washington
2 September 2003 (Class 369/1); filed 26 September 2001

This patent seems to argue that having different stages of capturing, editing, and recording live music is new and novel. Since this was filed in 2001, it's hard to see how this got through the patent office so fast. As expected, the disclosure of prior art (one reference) is underwhelming.—MK

6,619,594

43.38.Md CONTROL, SOUND, AND OPERATING SYSTEM FOR MODEL TRAINS

Michael Paul Wolf *et al.*, assignors to Mike's Train House, Incorporated
16 September 2003 (Class 246/187 A); filed 9 September 2002

In the interest of increasingly realistic model train operation, computers have been introduced to control the locomotive speed and track switching. Now, by using the track as a transmission medium for encoded commands, the locomotive can offer new capabilities including emitting new sounds depending on engine speed.—MK

6,621,768

43.38.Md COMPACT DISC RECORDER

Peter J. Keller and Michael J. Kelley, assignors to Advanced Audio Devices, LLC
16 September 2003 (Class 369/30.05); filed 17 August 2000

Filed in 2000, this patent describes a Compact Disk (audio) recorder. It is pointed out that editing is possible if the tracks are stored in memory first. There is absolutely nothing that was not obvious to those ''skilled in the art.'' It doesn't help that all the prior art was supplied by the examiner.—MK

6,626,704

43.38.Ne ACOUSTIC ADAPTER DEVICE

Daniel Pikel, West Chicago, Illinois
30 September 2003 (Class 439/638); filed 25 April 2002

The device constitutes an adaptor for connecting an integrated microphone plus another device (e.g., a second microphone) to the line input of a laptop computer. The device consists of a body **17** that incorporates a stan-

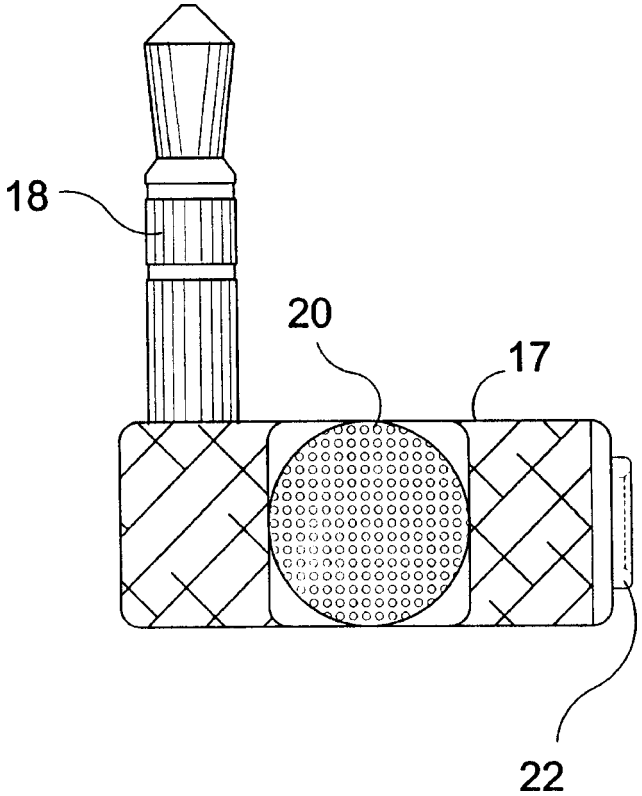

dard 3.5-mm stereo male connector **18** with an integral microphone **20** and a 3.5-mm stereo female connector input **22**. This combination allows the user to plug the adaptor into the line input of a laptop computer and also to connect another device through the female connector **22**.—DRR

6,608,903

43.38.Vk SOUND FIELD REPRODUCING METHOD AND APPARATUS FOR THE SAME

Hideo Miyazaki and Yasushi Shimizu, assignors to Yamaha Corporation
19 August 2003 (Class 381/17); filed in Japan 17 August 1999

A number of inventors have played with the idea of surrounding a performance space with an array of microphones and then reproducing the signals through a corresponding array of loudspeakers. Yamaha has refined

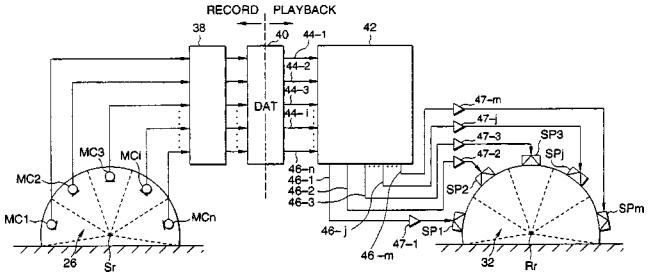

the concept by including impulse responses. ''The pickup signals are respectively subjected to a convolution operation with impulse responses which are obtained for each of the sound source element regions in corresponding directions.''—GLA

6,611,603

43.38.Vk STEERING OF MONAURAL SOURCES OF SOUND USING HEAD RELATED TRANSFER FUNCTIONS

John Norris and Timo Kissel, assignors to Harman International Industries, Incorporated
26 August 2003 (Class 381/309); filed 19 August 1999

The patent provides a succinct description of the invention: ''...an efficient system whereby any number of monaural sound sources can be steered in real time to any desired spatial locations. The system incorporates

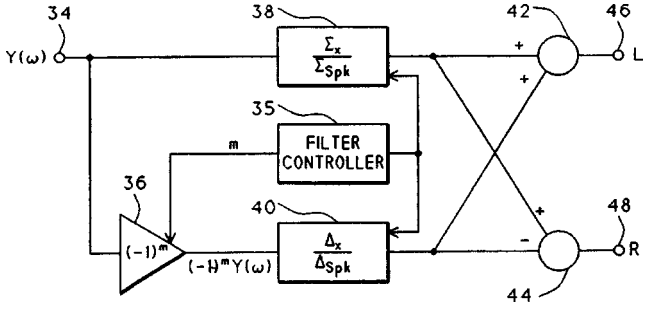

compensation of the loudspeaker feed signals to cancel crosstalk, and a new technique for interpolation between measured HRTFs for known sound source locations in order to generate appropriate HRTFs for sound sources in intermediate locations.''—GLA

6,614,910

43.38.Vk STEREO SOUND EXPANDER

Richard David Clemow and Alastair Sibbald, assignors to Central Research Laboratories Limited
2 September 2003 (Class 381/1); filed in the United Kingdom 1 November 1996

According to the patent abstract, ''By not modifying a Head Related Transfer Function (HRTF) for one signal and equalizing the HRTF for the

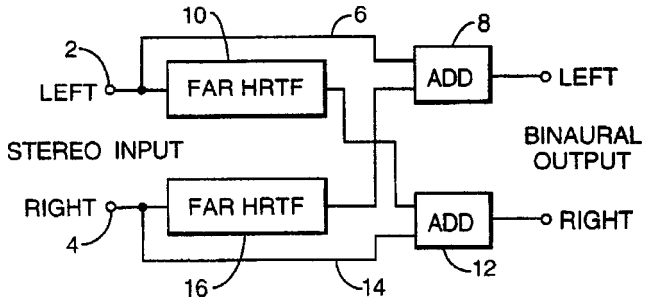

other signal, a flattened frequency response is produced with no tonal changes, but with a high degree of spatial accuracy.'' The patent is short, interesting, and easy to understand.—GLA

6,615,143

43.38.Vk METHOD AND APPARATUS FOR RECONSTRUCTING AND ACOUSTIC FIELD

Sean F. Wu, assignor to Wayne State University
2 September 2003 (Class 702/39); filed 1 March 2001

Suppose we want to identify and analyze individual sources contributing to the overall noise from automobile engine **30**. Known prior art includes several methods that can be used to analyze vibrating surfaces in three dimensions, but they all suffer from various practical drawbacks. The

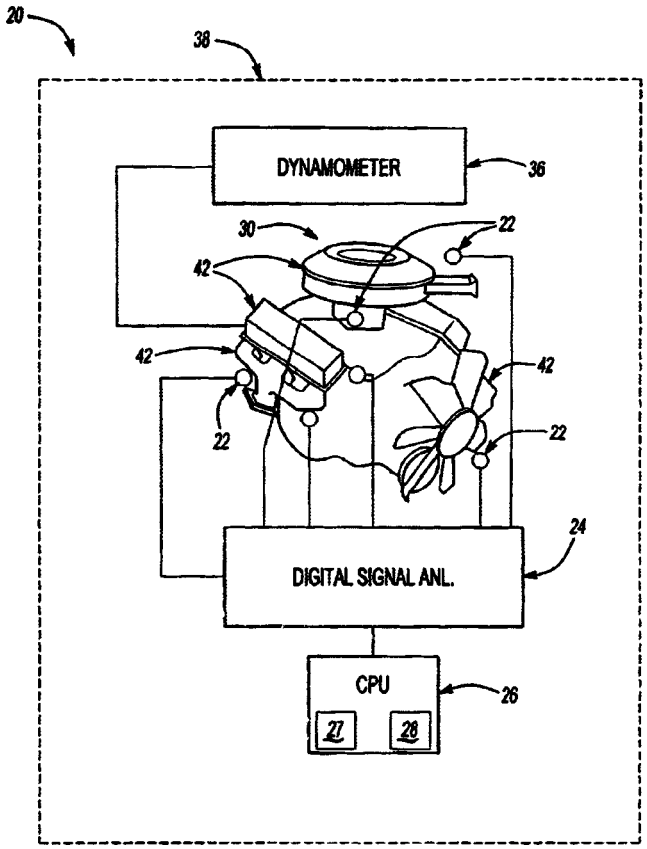

patent discloses a new algorithm, ''CRAFT,'' that can be used to reconstruct acoustic radiation from a plurality of sources or from a single source surrounded by reflecting surfaces. It does not require prior knowledge of source geometry or dimensions.—GLA

6,621,906

43.38.Vk SOUND FIELD GENERATION SYSTEM

Hiromi Fukuchi and Yoshiki Ohta, assignors to Pioneer Corporation
16 September 2003 (Class 381/17); filed in Japan 28 April 2000

Japanese inventors love to simulate concert hall acoustics in home and automotive playback systems. The method described here includes measuring the interaural correlation coefficient of a listener in a given concert hall and then generating a target sound field during reproduction that matches the spatial impression of the recording venue. Some fairly complex digital processing is involved.—GLA

6,625,084

43.40.Dx SYSTEM FOR ACOUSTICALLY PASSING ELECTRICAL SIGNALS THROUGH A HULL

Robert M. Payton, assignor to The United States of America as represented by the Secretary of the Navy
23 September 2003 (Class 367/134); filed 20 August 2002

A system is discussed that allows the passage of electrical signals across a rigid boundary such as the pressure hull of a submarine. This is accomplished without making any holes in the rigid boundary. The system comprises a set of transmitting electroacoustic transducers that are mounted on one face of the boundary and a set of receiving transducers, each in alignment with a respective transmitter, mounted on the opposite face of the boundary. Appropriate buffers, modulators, power amplifiers, and demodulators, plus a source of the signal to be transmitted across the boundary, are associated with the various transducers.—WT

6,631,799

43.40.Hb VIBRATORY FEEDING SYSTEM

Bruce L. Samson, assignor to Moore Push-Pin Company
14 October 2003 (Class 198/771); filed 16 May 2001

This vibratory feeding system, used to ''feed'' components in the course of manufacturing processes, consists of a hopper, a tray, and a vibrator. The hopper is suspended above the tray so that components can flow from the hopper into the tray. The vibrator is attached to the tray so that the tray can be vibrated to move components along its surface.—DRR

6,629,058

43.40.Le FAULT DIAGNOSIS METHOD AND APPARATUS

Hidemichi Komura *et al.*, assignors to Rion Company, Limited
30 September 2003 (Class 702/183); filed in Japan 20 April 2000

This relates to a method and apparatus for diagnosing a machinery fault arising from frictional wear which generates vibrations at a high frequency, a failure in a rotating metallic machine element (such as bearings or gears), or belt slippage in a rotating machine. The apparatus includes a vibration sensor for detecting vibration waveforms, a computing device for obtaining a cumulative frequency distribution curve of the absolute value of the vibration waveforms, a maximum detection device for detecting the maximum value of the waveforms, a peak ratio computing device, and a fault-detecting device for diagnosing the degree of fault of machinery or equipment on the basis of the computed peak ratio.—DRR

6,609,681

43.40.Tm METHOD AND APPARATUS FOR DAMPING VIBRATION

Daniel A. Buder, assignor to The Boeing Company
26 August 2003 (Class 244/54); filed 5 July 2001

An isolator that can attach a payload to a launch vehicle securely consists of a pair of metal rings. These rings are provided with recesses, enabling them to be bolted together, one atop the other, with the inclusion of elastomeric elements.—EEU

6,612,279

43.40.Tm VIBRATION REDUCING SYSTEM FOR INTERNAL COMBUSTION ENGINE

Yasuyuki Asahara, assignor to Nissan Motor Company, Limited
2 September 2003 (Class 123/192.1); filed in Japan 28 March 2000

In order to reduce the roll vibrations of an engine, there is provided an anti-resonant arrangement. This arrangement, which is tuned to the engine's roll vibration frequency, makes use of the inertia of the engine's alternator and of a resilient element in the alternator pulley, which is connected to the engine shaft via a belt.—EEU

6,619,165

43.40.Tm TUNABLE TOOLHOLDER

Randy M. Perkowski, assignor to Kennametal Incorporated
16 September 2003 (Class 82/160); filed 1 February 2002

This holder for machining tools includes a dynamic absorber that can be tuned so as to suppress vibrations in a certain frequency range. The dynamic absorber consists of an essentially cylindrical mass that is located in an oversized cylindrical cavity and that is supported on elastomeric elements on its two ends. A support plate on one of these ends can be moved axially via a screw arrangement, thus changing the compression of the elastomeric elements and thereby their stiffness.—EEU

6,619,445

43.40.Tm TELESCOPIC VIBRATION DAMPER

Andreas Förster, assignor to ZF Sachs AG
16 September 2003 (Class 188/315); filed in Germany 12 January 2001

This damper, intended for use in automobile suspensions and the like, consists of a telescoping arrangement of liquid-filled tubes. A piston rod is arranged to move axially in a pressure tube, with the piston dividing the volume in that tube into two chambers that are interconnected only via valves in the piston. The pressure tube is located within an intermediate tube and has a piston section at its end, outside of the pressure tube, forming an annular chamber between the walls of the pressure tube and the intermediate tube. At the base of the pressure tube, a second piston seals off a gas-filled volume at the bottom of the intermediate tube. The intermediate tube is contained within an outer tube and the various volumes formed by all of these tubes, except the aforementioned one, are filled with an incompressible fluid and interconnected with various valves.—EEU

6,619,523

43.40.Tm BACKPACK INCLUDING INTEGRAL VIBRATION DAMPER

David G. Duckworth, Laguna Beach, California
16 September 2003 (Class 224/634); filed 20 March 2002

In order to reduce the bouncing of a heavy backpack that its wearer experiences as he/she strides along rhythmically, the pack's shell is connected to its frame via ''dampers.'' Each such damper consists of a spring in a cylindrical housing, with one end of the spring resting on a piston. The housing is provided with an adjustable valve, so that the wearer can adjust the damping resulting from air being forced through the valve. The dampers are intended to act predominantly in the vertical direction. The springs are selected to accommodate predetermined loads and the dampers contain no provisions for changing the frequency of the spring/payload system.—EEU

6,619,611

43.40.Tm PNEUMATIC VIBRATION ISOLATOR UTILIZING AN ELASTOMERIC ELEMENT FOR ISOLATION AND ATTENUATION OF HORIZONTAL VIBRATION

Vyacheslav Ryaboy *et al.*, assignors to Newport Corporation
16 September 2003 (Class 248/631); filed 2 July 2001

This isolator is intended primarily for use in ''air legs'' employed to support isolation tables. It includes a stable elastomeric element atop a vertical piston/cylinder air-spring arrangement. The elastomeric element permits horizontal motion, whereas the air-spring provides vertical motion; thus the combination can provide vibration isolation in the horizontal and the vertical directions.—EEU

6,619,887

43.40.Tm METHOD AND APPARATUS FOR REDUCING DRAG AND SUPPRESSING VORTEX-INDUCED VIBRATION

Albin A. Szewczyk, South Bend, Indiana *et al.*
16 September 2003 (Class 405/211); filed 21 November 2001

The shedding of large correlated vortexes from cylindrical elements, such as pipes, across which fluid flows in a given direction is reduced by giving the cylindrical elements a wavy form, as seen in a plane parallel to the flow.—EEU

6,621,694

43.40.Tm VIBRATION TOLERANT ELECTRONIC ASSEMBLY AND RELATED METHODS

Ying-Ming Lee and Frank Daneshgar, assignors to Harris Corporation
16 September 2003 (Class 361/685); filed 7 September 2001

This patent relates to the support of electronic assemblies, such as disc drives, that need to be protected from severe dynamic environments. An apparatus according to this patent consists of a base and one or more isolation stages. A first stage consists of a linear bearing coupling that constrains movement of a first frame along a given axis, plus a means for damping this movement. A second stage is configured similarly to address motion along a second axis.—EEU

6,611,081

43.40.Yq VIBRATION ACTUATOR WITH TWO VIBRATION MODES

Mitsuhiro Okazaki *et al.*, assignors to Nikon Corporation
26 August 2003 (Class 310/323.16); filed in Japan 10 September 1999

The device is a vibration element that actuates both a radial symmetric expansion vibration mode in which it expands and contracts in the radial direction and also a nonaxisymmetric planar vibration mode whereby it bends to and fro in a nonasymmetric fashion within a single plane. The actuator drives a relative movement member and a base member to which the vibration element is affixed. The vibration element consists of at least one superimposed layer structure that includes a pair of electrical-to-mechanical energy conversion elements and an elastic member sandwiched between the pair of these conversion elements.—DRR

6,629,464

43.40.Yq LASER SHOCK PEENING QUALITY ASSURANCE BY ACOUSTIC ANALYSIS

Ui Won Suh and James Douglas Risbeck, both of Cincinnati, Ohio
7 October 2003 (Class 73/602); filed 3 October 2001

Laser shock peening is a process for producing a region of deep compressive residual stresses by laser peening the surface area of a workpiece. This method typically uses multiple radiation pulses from high power pulsed lasers to produce shock waves at the surface of a workpiece for the purpose of increasing its fatigue strength. A method is provided here for quality control monitoring of the peening process by acoustic means. An acoustic signal from each laser beam pulse is monitored during the period of time corresponding to the duration of each plasma pulse, and an acoustic energy parametric value for each of the acoustic signals is calculated. A statistical function, such as the average of the acoustic energy of the laser beam pulses, is compared to a pass or fail criteria for accepting or rejecting the workpiece.—DRR

6,616,337

43.50.Gf NOISE-REDUCING MACHINE COMPONENT

Bevan V. Smith, assignor to The Timken Company
9 September 2003 (Class 384/476); filed 28 February 2002

A machine component, such as the race **12** of an antifriction bearing, contains a pocket bordered by reflecting surfaces that intersect at alternating peaks and valleys. Longitudinal noise propagating through the machine component, upon encountering the reflecting surfaces at the pocket, is partially converted into transverse waves, which are more easily attenuated in the material of the component. It is argued that the pockets reduce noise in the machine component.—DRR

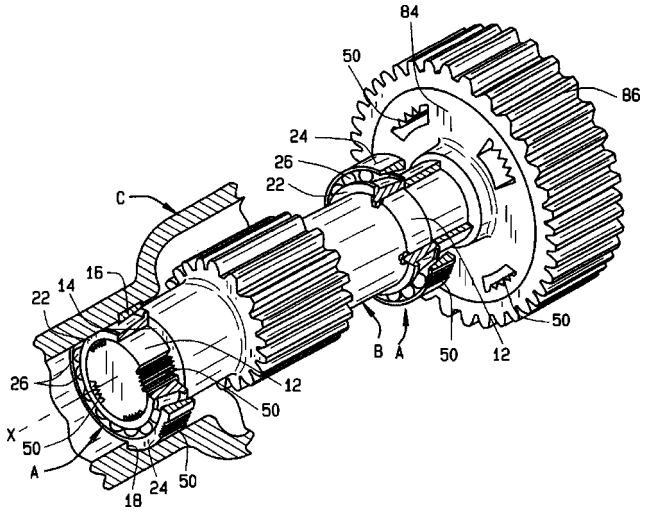

6,622,818

43.50.Gf SOUND ATTENUATING DEVICE

Peter Lee Jenvey, assignor to HRL Technology Pty Limited
23 September 2003 (Class 181/224); filed in Australia 11 September 1997

Intended for use in a gas duct, this sound attenuating device consists of a core of acoustically absorptive material that is enclosed by an impervious film. The film prevents direct contact between the gas flowing through the duct and the absorptive material. Perforated plates on either side of the absorptive material provide rigidity to the ensemble.—DRR

6,630,222

43.55.Ev ACOUSTIC MEDIA

Ralph Michael Fay and Lawrence J. Gelin, assignors to Johns Manville International, Incorporated
7 October 2003 (Class 428/118); filed 16 June 2000

Two continuous fabric curtains are pleated together to make elongated tubular sections. Drawing the collapsible sections together (like raising a shade) can retract the curtains. When extended, the two layers of the curtain, with their airflow resistance properties, provide sound absorption within a room.—CJR

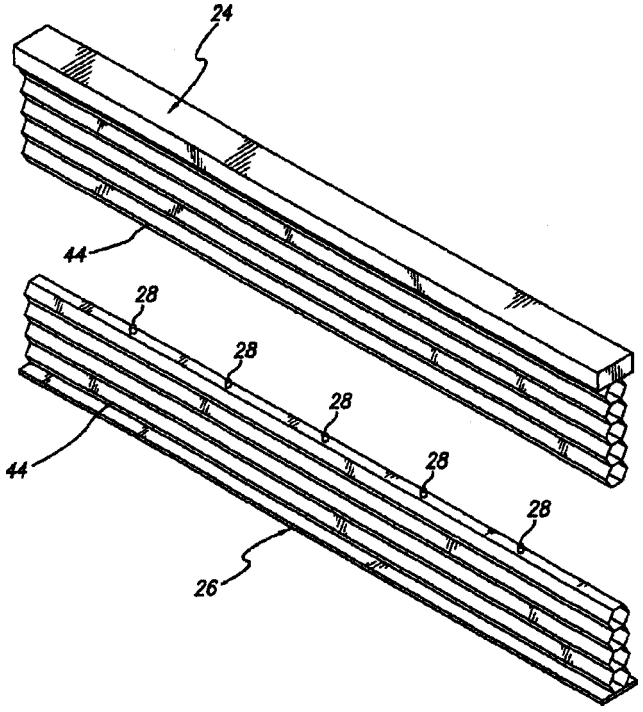

6,615,950

43.55.Ti SANDWICH ACOUSTIC PANEL

Alain Porte and Jacques Lalane, assignors to Airbus France
9 September 2003 (Class 181/292); filed in France 8 December 2000

This acoustic sound barrier panel is designed to allow multiple degrees of freedom of movement between different layers of compartmentalized structures without problems of misalignment. For example, this panel could

be used for the walls of turbojet casings. The panel contains a barrier layer with a porous separator between the adjacent compartmentalized layers, and then a reflector forming the back face of the panel. There are guides on each face of the porous separator, and these surfaces makes it possible for the compartments to be continuous between the inner surface and the reflector. Because of these guides, there are no risks of local misalignment and nonhomogeneity.—CJR

6,634,458

43.55.Ti SOUNDPROOFING SYSTEM

Dennis R. Adamson, Scottsdale, Arizona
21 October 2003 (Class 181/285); filed 20 March 2002

The patent covers a laminate material which embodies uncured rubber and a fabric mesh in a floor system to reduce sound and impact energy transfer.—CJR

6,621,658

43.55.Vj VIBRATION DAMPING LAMINATE WITH VIBRATION ISOLATING CUT THEREIN

Ahid Nashif, assignor to Material Sciences Corporation
16 September 2003 (Class 360/97.02); filed 13 July 2000

This vibration damping laminate has two metal skins separated by a viscoelastic damping layer. Each of the metal skins has a separate series of circular cuts that isolate the area where the laminate is connected to another body (i.e., where there is a bolt). The cuts extend through each of the metal skins up to the damping layer. This technique improves vibration damping for computer disk drive assemblies, automotive body panels, etc.—CJR

6,628,570

43.58.Dj LASER VELOCIMETRY DETECTION OF UNDERWATER SOUND

Anthony A. Ruffa, assignor to The United States of America as represented by the Secretary of the Navy
30 September 2003 (Class 367/149); filed 20 August 2001

An apparatus is described for measuring the velocity of sound waves in a liquid medium. A laser transmits a light pulse that interacts with the sound wave. The backscattered light, which is enhanced because of the entrained air bubbles in the liquid that have been set in motion by the sound wave, is processed so as to determine a distance traveled and the time of travel and hence the velocity of the sound wave.—WT

6,609,943

43.58.Wc ELECTRONIC TALKING TOY AND DOLL COMBINATION

Albert Wai Tai Chan, assignor to Thinking Technology, Incorporated
26 August 2003 (Class 446/297); filed 5 February 2002

Using the ubiquitous sound chip, we can now replace the virtual

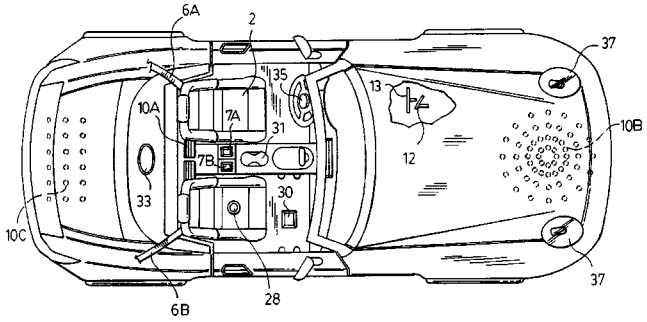

sounds of children driving a car with the stored engine sounds on-chip.—MK

6,612,897

43.58.Wc MUSICAL TOY WITH A MOTOR DRIVEN DISPLAY

Michael Greenberg, assignor to Shelcore Incorporated
2 September 2003 (Class 446/408); filed 30 January 2002

Combine a child's jack-in-the-box with a popper and a piano style

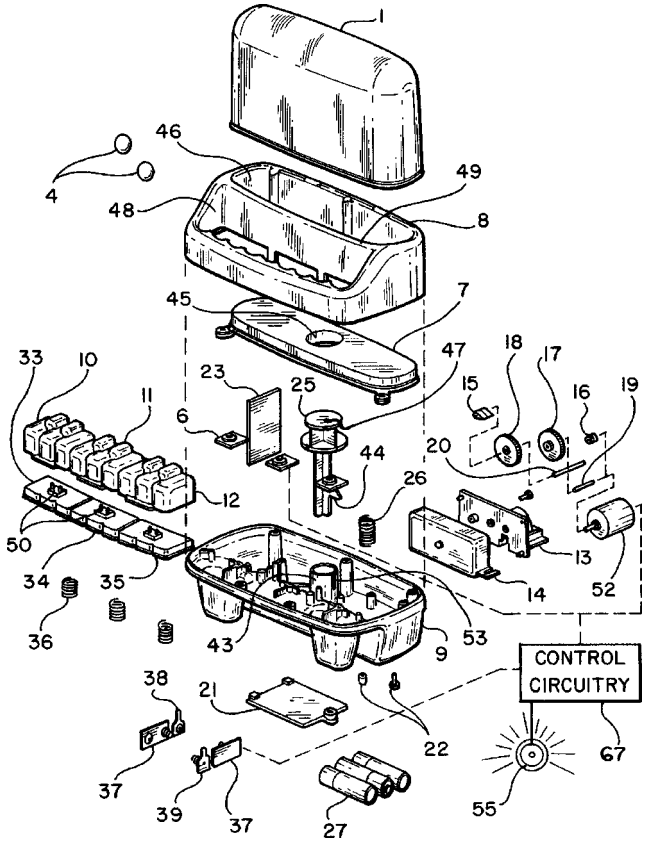

keyboard, all driven by a motor, and you have the ultimate child amusement toy. Unfortunately, the music is provided by electronic means.—MK

6,609,944

43.58.Wc ANIMAL BALL TOY

Charles A. Viola, Fairfield, Iowa
26 August 2003 (Class 446/409); filed 24 May 2002

Entertainment and amusement toys are appreciated by many large

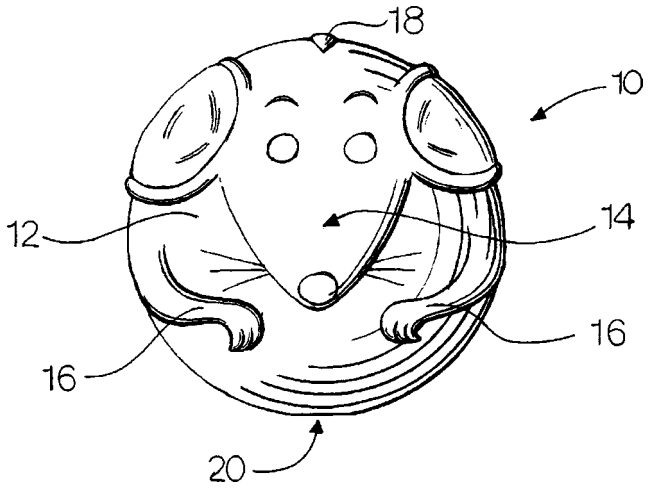

mammals. Here, a spherical surface with a squeaker **20** can roll and squeak, reminding house cats of small furry mice.—MK

6,619,225

43.58.Wc WHISTLE FOR MULTI-IMPLEMENT FOLDING KNIFE

Alexander Presniakov, San Francisco, California and George M. Davison III, Pittsburgh, Pennsylvania
16 September 2003 (Class 116/137 R); filed 19 September 2000

The venerable ''Swiss Army knife'' has been missing a whistle. So, the authors propose adding a cover **38** on the whistle structure **40**. The user

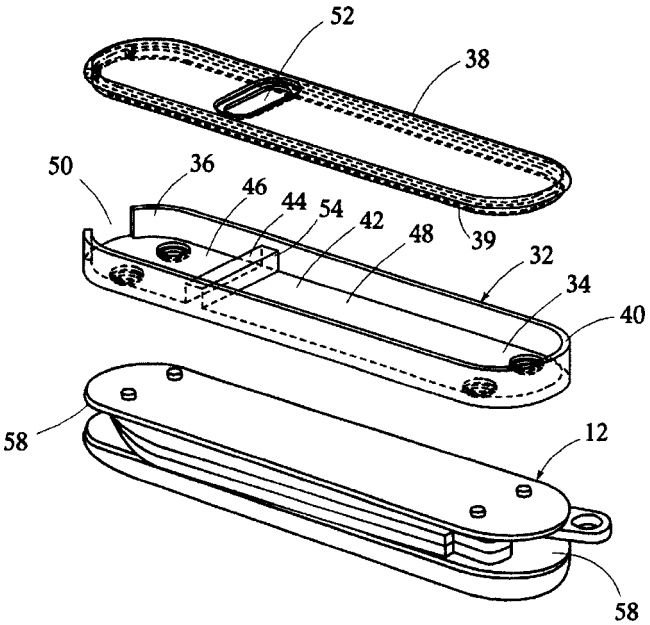

blows through slot **50** and the breath exits though slot **52**. Will reeds and a harmonica be next?—MK

6,610,014

43.60.Rw ULTRASONIC TOMOGRAPH WHICH SETS DOPPLER SAMPLE POINT FROM BLOOD FLOW INFORMATION, AND DOPPLER SAMPLE POINT SETTING METHOD

Masa Yamamoto and Masaru Suemune, assignors to Hitachi Medical Corporation
26 August 2003 (Class 600/453); filed in Japan 26 May 1997

In a conventional ultrasonic tomograph, the Doppler sample point for the bloodstream is controlled by manually moving the Doppler point setting indicator using a pointer, such as a track ball, to the position of interest in the bloodstream, on the basis of the color information displayed in superposition with the ultrasonic tomogram. It is the object of the present device to provide an automatic tomograph capable of automatically or semi-

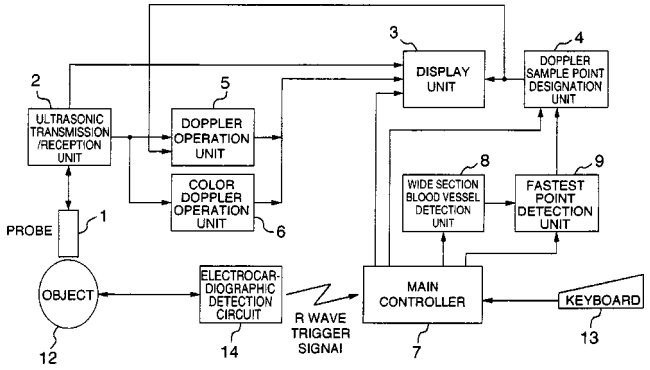

automatically setting the Doppler sample point to the bloodstream portion of the tomographic image. A signal-processing unit activates the probe to transmit ultrasonic waves and processes the reflected echo to produce an ultrasonic sonogram and bloodstream image and information. A control unit automatically sets the position of the Doppler sample point on the basis of the bloodstream information.—DRR

6,620,100

43.64.Ri HEARING EVALUATION DEVICE WITH NOISE-WEIGHTING CAPABILITIES

Matthijs P. Smits and Aaron R. Thornton, assignors to Natus Medical Incorporated
16 September 2003 (Class 600/300); filed 17 October 2001

This is an apparatus that uses electroencephalographic responses to auditory stimuli to evaluate the hearing of a subject and weight the response based upon an analysis with normative data. The device uses evoked audi-

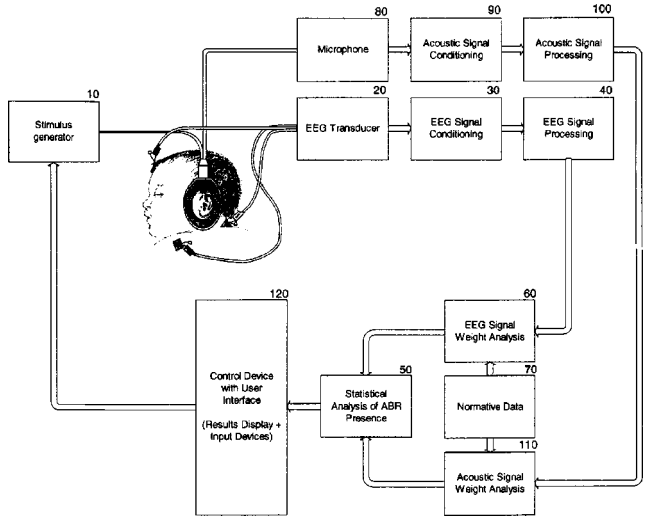

tory brainstem responses to determine if the subject is able to hear repeatedly administered click stimuli. In order to optimize evaluation, the device uses normative data to weight the auditory responses, so as to permit an evaluation under different or changing noise conditions.—DRR

6,610,019

43.66.Lj METHOD AND APPARATUS FOR TREATMENT OF MONOFREQUENCY TINNITUS UTILIZING SOUND WAVE CANCELLATION TECHNIQUES

Daniel S. J. Choy, assignor to Daniel S. J. Choy
26 August 2003 (Class 600/559); filed 1 March 2002

Tinnitus, defined as the sound heard by an individual in the absence of external auditory stimulus, afflicts more than 50 million Americans. In an effort to treat tinnitus of the monofrequency sort, this patent describes a phase cancellation method. An externally generated sound is subjectively selected by the tinnitus patient to match the tinnitus sound in both tone and loudness. This generated sound wave is either sequentially phase shifted through steps totaling at least 180 degrees or is directly phase-shifted in a single step into a 180-degree out-of-phase reciprocal. This cancels the patient-determined tinnitus tone.—DRR

6,611,600

43.66.Ts CIRCUIT AND METHOD FOR THE ADAPTIVE SUPPRESSION OF AN ACOUSTIC FEEDBACK

Remo Leber and Arthur Schaub, assignors to Bernafon AG
26 August 2003 (Class 381/66); filed in Switzerland 14 January 1998

To reduce acoustic feedback problems in hearing aid fittings, a system models the feedback path and tracks changes adaptively. Two adaptive decorrelation filters employ lattice filter structures which are said to provide rapid convergence with minimum distortion and added signal delay. The feedback signal components are continuously subtracted from the input signal, thus providing a greater amount of stable gain.—DAP

6,611,718

43.66.Ts HYBRID MIDDLE EAR/COCHLEA IMPLANT SYSTEM

Yitzhak Zilberman and Joseph H. Schulman, assignors to Yitzhak Zilberman; Joseph Schulman
26 August 2003 (Class 607/57); filed 15 June 2001

A hearing enhancement system consists of both middle ear and cochlear implants. Information in the frequency range up to approximately 4 kHz is routed to the middle ear implant and signals at higher frequencies are sent to the cochlear implant which stimulates the basal portion of the cochlea. A rf receiver in the microphone module receives programming and

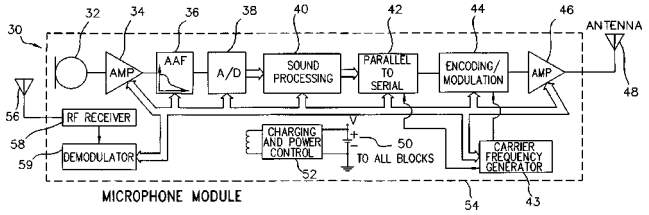

parameter tuning information from a fitting system based on monitored performance transmitted back to the clinician. After processing, audio signals are transmitted from the microphone module via modulated rf carrier to a second implant module which contains output drivers for the middle ear and cochlear implants.—DAP

6,618,704

43.66.Ts SYSTEM AND METHOD OF TELECONFERENCING WITH THE DEAF OR HEARING-IMPAIRED

Dimitri Kanevsky *et al.*, assignors to IBM Corporation
9 September 2003 (Class 704/271); filed 1 December 2000

This is a system for allowing a deaf or hearing-impaired person to participate in a teleconference by providing a platform that allows various automatic speech recognition (ASR) systems to communicate over various chat message systems so that the hearing-impaired person may receive a transcribed text of the teleconference. In one embodiment of the system each participant has an ASR system and a chat service system such as AOL Instant Messenger®. Each participant may have a different type of ASR system and a different chat service system and the hearing-impaired person need not have an ASR system. The patent discusses the general problem of instant message communication due to the variety of different formats in use.—DRR

6,631,295

43.66.Ts SYSTEM AND METHOD FOR DIAGNOSING AND/OR REDUCING TINNITUS

Jay T. Rubinstein *et al.*, assignors to University of Iowa Research Foundation
7 October 2003 (Class 607/55); filed 25 September 2001

This patent relates to an apparatus and method for providing stochastic independent neural stimulation and, in particular, a neural stimulation system for identifying candidates for intervention and treatment of tinnitus by initiating pseudo-spontaneous activity in the auditory nerve. High rate pulse trains, e.g., can generate random spike patterns in auditory nerve fibers that are statistically similar to those produced by spontaneous activity in the normal ear, i.e., pseudo-spontaneous activity is produced. Varying rates of pseudo-spontaneous activity can be produced by varying the intensity of a fixed amplitude, high-pulse-rate stimulus (e.g., 5000 pps). The patent asserts that monitored patient response to the generated pseudo-spontaneous activity in the auditory nerve, even if temporary, can produce successful reduction or elimination of perceived tinnitus by subsequent treatment.—DRR

6,611,798

43.72.Gy PERCEPTUALLY IMPROVED ENCODING OF ACOUSTIC SIGNALS

Stefan Bruhn and Susanne Olvenstam, assignors to Telefonaktiebolaget LM Ericsson
26 August 2003 (Class 704/219); filed in the European Patent Office 20 October 2000

To transmit and reproduce with natural sound quality audio frequency components above 4 kHz, the signal from an acoustic source is encoded to represent the perceptually significant characteristics of the acoustic signal.

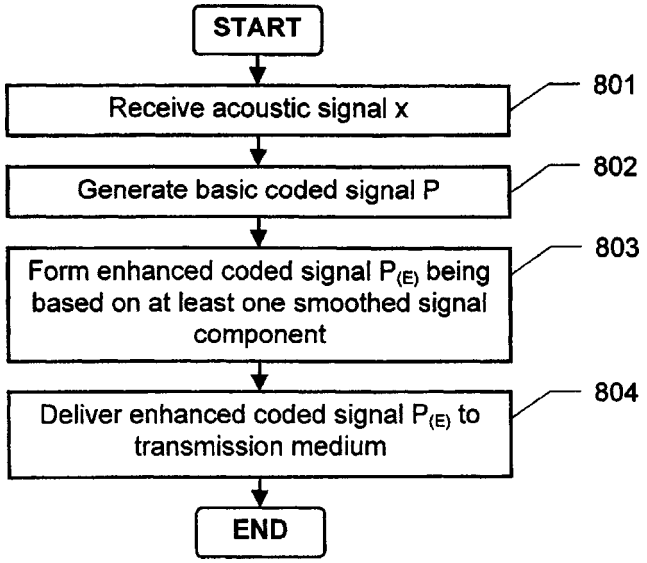

The encoder in the transmitter or receiver spectrally smooths the components by reducing the variation in the coefficient values representing frequency information above a threshold value.—DAP

6,629,071

43.72.Ne SPEECH RECOGNITION SYSTEM

Robert James Mann, assignor to International Business Machines Corporation
30 September 2003 (Class 704/251); filed in the United Kingdom 4 September 1999

This large-vocabulary speech recognition system recognizes spoken letters in alphabetic or alphanumeric sequences by processing spelled-out speech in the form of ''letter for word,'' e.g., ''A for Apple.'' The large recognition vocabulary allows an arbitrary word to be spoken with each letter.—HHN

6,629,073

43.72.Ne SPEECH RECOGNITION METHOD AND APPARATUS UTILIZING MULTI-UNIT MODELS

Hsiao-Wuen Hon and Kuansan Wang, assignors to Microsoft Corporation
30 September 2003 (Class 704/256); filed 27 April 2000

A speech recognition system mixes different types of acoustic models for both a large acoustic unit, such as a word, and subunits, such as phonemes or senones.—HHN

6,631,348

43.72.Ne DYNAMIC SPEECH RECOGNITION PATTERN SWITCHING FOR ENHANCED SPEECH RECOGNITION ACCURACY

Ben S. Wymore, assignor to Intel Corporation
7 October 2003 (Class 704/233); filed 8 August 2000

A dynamic speech recognition system generates separate reference models at different environmental noise levels based on training information. The system includes a sensor to detect the environment noise level. In response to a received speech signal, the system switches to an appropriate stored model for noisy speech based on the level of measured noise.—HHN

6,633,842

43.72.Ne SPEECH RECOGNITION FRONT-END FEATURE EXTRACTION FOR NOISY SPEECH

Yifan Gong, assignor to Texas Instruments Incorporated
14 October 2003 (Class 704/233); filed 21 September 2000

To estimate the feature vector, i.e., Mel-frequency cepstral coefficients of clear speech from noisy speech, the proposed method uses the conditional

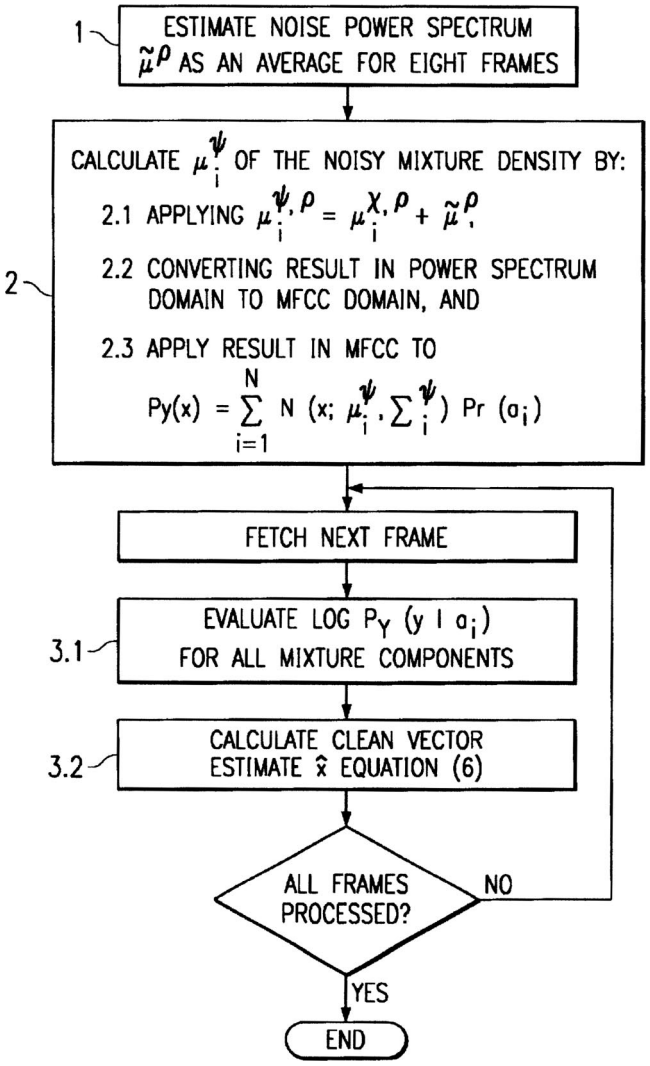

expectancy of a clean signal given an observed noisy vector. The method uses two Gaussian mixtures, one for the clean signal and a second one derived from the first using some noisy samples.—HHN

6,633,843

43.72.Ne LOG-SPECTRAL COMPENSATION OF PMC GAUSSIAN MEAN VECTORS FOR NOISY SPEECH RECOGNITION USING LOG-MAX ASSUMPTION

Yifan Gong, assignor to Texas Instruments Incorporated
14 October 2003 (Class 704/233); filed 27 April 2001

HMMs are first trained for clean speech. Parallel model combination (PMC), as described here, then uses the noise distribution to estimate noise

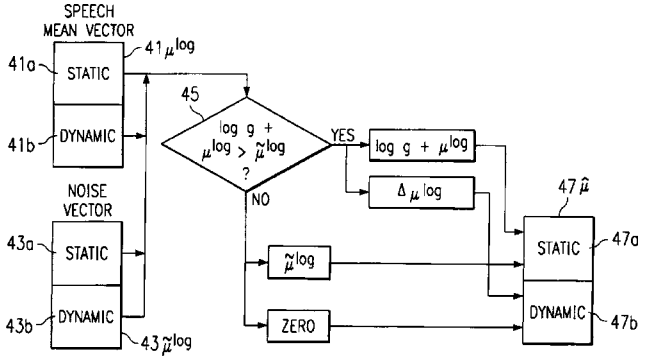

HMMs. The system takes the mean vector **41** of speech and noise vector **43** and then applies decision rule **45** for log-spectral compensation of Gaussian mean vector **47**.—HHN

6,610,915

43.75.De SOUNDBOARD OF COMPOSITE FIBRE MATERIAL CONSTRUCTION

Martin Schleske, Munich, Germany
26 August 2003 (Class 84/291); filed in Germany 23 August 2000

Here, the author presents an analysis of his attempt to construct a composite sound board (plate) for stringed instruments. He defines the ''Quality Quotient,'' $Qm = c/\rho$, where c is the speed of sound in the longitudinal direction and ρ is the density of the material. Because the higher Qm in the composite material affects the modal distribution, the patent proposes an increase in area to compensate for the change in material. Unfortunately, the final design or performance is not disclosed, so we are left hanging.—MK

6,613,970

43.75.Kk PROCESS OF MAKING ACOUSTIC DEVICES

Maurice P. Davies, Ashford Middlesex, the United Kingdom
2 September 2003 (Class 84/402); filed 2 August 2001

The inventor extends his earlier patent on the ''Belleplate'' hand bell

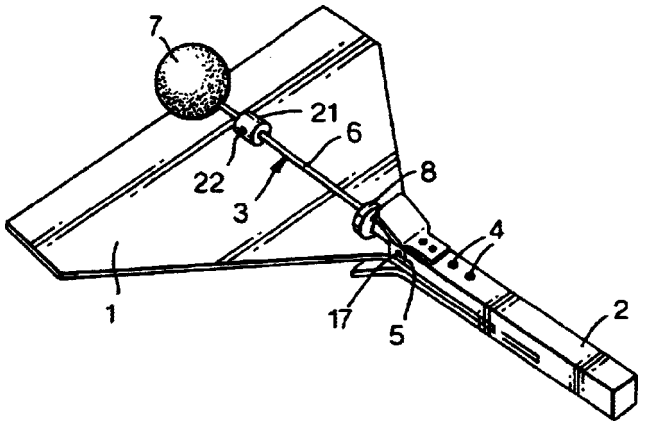

(United States Patent 5,177,310) to facilitate fabrication with CNC machines.—MK

6,617,501

43.75.Kk CYMBAL SYSTEM

Otto Kaufmann, assignor to Roland Meinl Musikinstrumente GmbH & Company
9 September 2003 (Class 84/422.3); filed in Germany 2 December 2000

To change the timbre of a cymbal in a pal controlled drum set, the

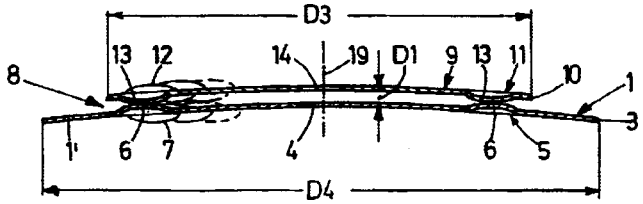

inventors propose adding an indented ring on both surfaces thereby creating an air cushion.—MK

6,620,991

43.75.Kk PERCUSSION INSTRUMENT

Houlton Honiball, Etobicoke, Canada
16 September 2003 (Class 84/402); filed 6 March 2002

Each cylinder **34** is filled with rattle beads and can be shaken much

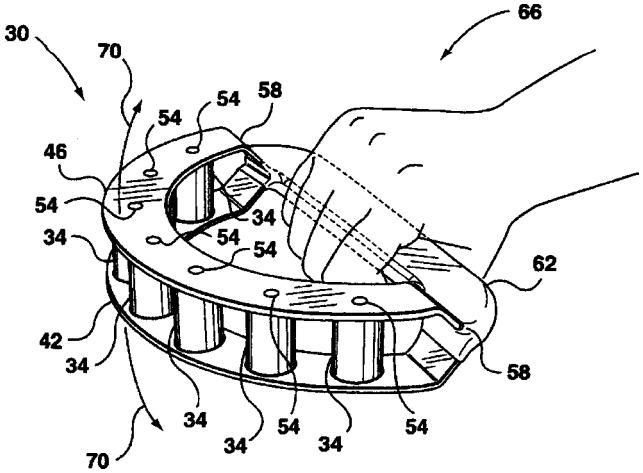

like a tambourine. Should be easy to make and manufacture.—MK

6,612,894

43.75.Pq METHOD OF CALLING GAME USING A DIAPHRAGM GAME CALL HAVING AN INTEGRAL RESONANCE CHAMBER

L. Wayne Carlton, assignor to Hunter's Specialties, Incorporated
2 September 2003 (Class 446/202); filed 19 February 2002

This patent proposes a new replaceable diaphragm **215** for a turkey

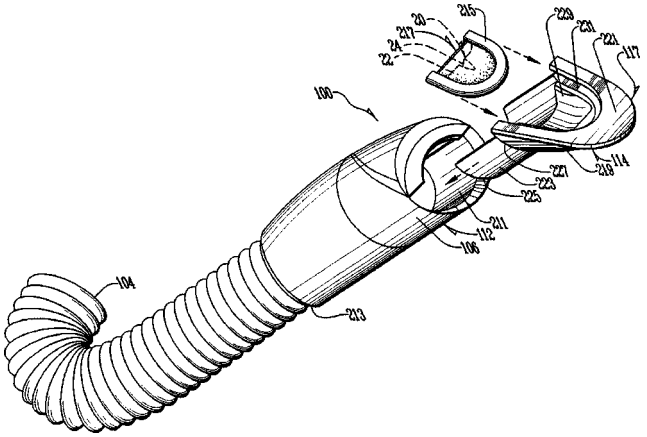

caller. This uses an external resonant chamber **213** instead of the hunter's mouth. Other useful properties are cited in the claims.—MK

6,615,249

43.75.Wx METHOD FOR COMPARING AND SYNCHRONIZING DATA FROM DIFFERENT DATA SOURCES

Regina Schulte Am Hülse, Hamburg, Germany
2 September 2003 (Class 709/217); filed in Germany 14 January 2000

The basic idea is that a data source (a musical signal) is located a large distance from the data sink; an accompaniment can be created and transmitted back to the source for recording on a ''data carrier.'' There is nothing new or novel in any of these proposals.—MK

6,618,336

43.75.Wx REPRODUCING APPARATUS

Kohei Kanou *et al.*, assignors to Sony Corporation
9 September 2003 (Class 369/53.34); filed in Japan 26 January 1998

In this automated accompaniment machine, the acoustic input is divided into four different bands, a simple analog envelope detector digitizes

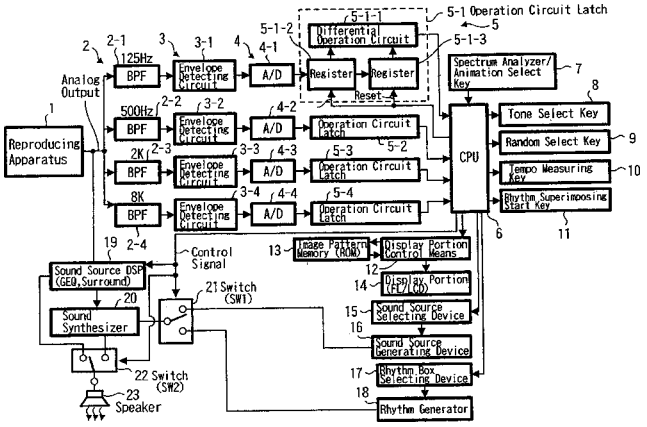

the signal and gives it to a CPU. The processor detects rhythm from the input and generates the very simple accompaniment.—MK

6,616,618

43.80.Qf METHOD OF AND DEVICE FOR VISUALIZING THE ORIENTATION OF THERAPEUTIC SOUND WAVES ONTO AN AREA TO BE TREATED OR PROCESSED

Ulrich Hagelauer, assignor to Storz Medical AG
9 September 2003 (Class 600/587); filed in Germany 14 September 1998

This device provides a method of visualizing the orientation of therapeutic sound waves onto an area undergoing treatment. The orientation of the therapeutic sound waves is symbolically displayed on the screen of a display unit. The operational principle is based on the three-dimensional approach of computer-aided design (CAD) and the application of virtual reality techniques.—DRR

6,618,493

43.80.Qf METHOD AND APPARATUS FOR VISUALIZATION OF MOTION IN ULTRASOUND FLOW IMAGING USING PACKET DATA ACQUISITION

Hans Garmann Torp and Steinar Bjaerum, assignors to GE Medical Systems Global Technology Company, LLC
9 September 2003 (Class 382/131); filed 26 November 1999

In ultrasound imaging, the returned echoes are processed coherently. There are variations in the intensity of the images due to constructive and destructive interference of the sound wave scattered back from a large number of scatterers. These intensity variations constitute the ''speckle pattern.'' When there is a slight displacement of the scatterers (viz. red blood cells) there will be a corresponding displacement of the speckle pattern. By enhancing the speckle pattern from moving scatterers and displaying a stream of such images, an intuitive display of the blood flow is obtained. Based on this principle, a method and an apparatus are described for imaging blood motion by displaying an enhanced image of the fluctuating speckle pattern. The first step is high-pass filtering of the signal vector from each range gate. Next, a speckle signal is formed and a nonlinear scale conversion is applied. The resulting speckle signal is displayed as the desired blood flow image concurrently with a corresponding tissue image.—DRR

6,626,838

43.80.Qf BLOOD FLOW METER APPARATUS AND METHOD OF USE

Gregory P. Doten and Brian P. Brockway, assignors to Transoma Medical, Incorporated
30 September 2003 (Class 600/465); filed 8 August 2001

This patent covers a device and method for estimating blood flow or blood flow velocity in a blood vessel over a period of time. In this method, at least part of the measurement circuits used to estimate blood flow are activated automatically only during the time an estimate is being obtained. At least part of the measurement circuits are automatically deactivated during the time an estimate is not being obtained. These steps are performed in sequence to establish a sequence of blood flow estimates to yield a waveform indicative of the blood flow. Measurement techniques include continuous wave Doppler flow measurement, pulsed Doppler flow measurement, laser Doppler flow measurement, transit time flow measurement, thermal dilation flow measurement, electromagnetic flow measurement or other suitable flow measurement techniques. In several embodiments, a base-banded Doppler-shifted signal provides the blood flow estimate. In this manner, the device provides a strobed blood flow meter, such as an implantable strobed ultrasonic Doppler blood flow meter, having reduced average power consumption, advantageous for minimizing battery size, extending battery life, and improving signal-to-noise ratio.—DRR

6,626,842

43.80.Qf HEART-SOUND ANALYZING APPARATUS

Tohru Oka, assignor to Colin Corporation
30 September 2003 (Class 600/528); filed in Japan 9 August 2000

The purpose of this heart-sound apparatus is to determine, on an iterative basis, the timing when the aortic valve closes. The components of the apparatus are a heart-sound microphone adapted to be worn by a subject for the purpose of iteratively detecting heart sound, a respiration-synchronous signal detecting device, and an inspiration–expiration judging device, based on each of the iteratively detected respiration-synchronous signals.—DRR

6,629,937

43.80.Qf SYSTEM FOR PROCESSING AUDIO, VIDEO AND OTHER DATA FOR MEDICAL DIAGNOSIS AND OTHER APPLICATIONS

Raymond L. Watrous, assignor to Siemens Corporate Research, Incorporated
7 October 2003 (Class 600/586); filed 2 January 2001

This current application is a continuation-in-part of United States Patent 6,572,560. It involves a system that provides diagnostic decision support for auditory evaluation of anatomical systems. The system processes an acoustical signal by acquiring acoustic data representative of an acoustic

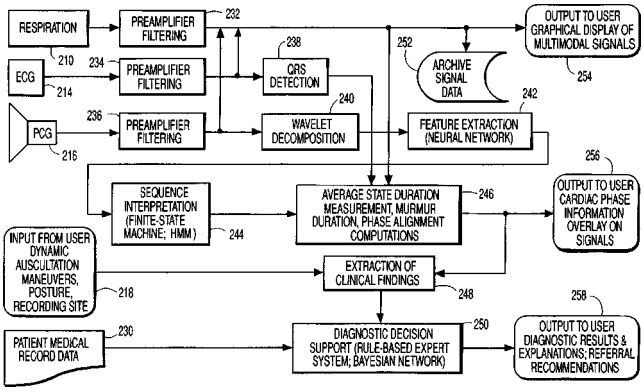

signal associated with an anatomical function. The acquired acoustic data is stored in a patient's medical record file. The acquired data and medical record information are automatically analyzed in order to establish physiologically significant features useful in medical diagnosis.—DRR

6,635,018

43.80.Qf ULTRASONIC DIAGNOSIS APPARATUS

Tetsuya Kawagishi *et al.*, assignors to Kabushiki Kaisha Toshiba
21 October 2003 (Class 600/447); filed in Japan 22 May 2000

This is an ultrasonic diagnosis apparatus in which ultrasonic beams scan a living body, thereby setting optimal transmission conditions for each scanning line in order to yield a uniform image quality over an image and providing information for analysis of an application site. To achieve this effect, the apparatus is equipped with a transmission coefficient controller configured to set transmission conditions that differ with scanning directions

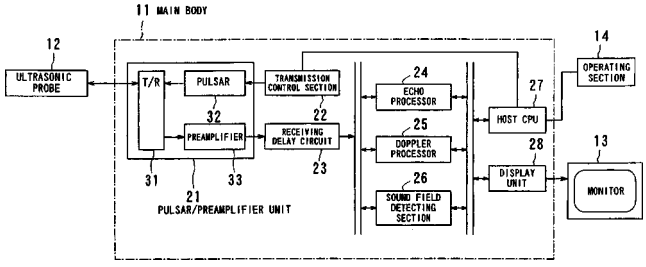

of ultrasonic beams so as to correct for nonuniformity of the transmission sound field for each scanning region. An ultrasonic transmitter is configured to transmit the ultrasonic beams to a subject under the transmission conditions established by the controller. An image generator is configured to obtain an ultrasonic image of the subject from the ultrasonic echo signals reflected from the subject.—DRR

6,612,988

43.80.Sh ULTRASOUND THERAPY

Dov Maor *et al.*, assignors to Brigham and Women's Hospital, Incorporated; InSightec–Image Guided Treatment Limited
2 September 2003 (Class 600/439); filed 15 December 2000

This method of delivering ultrasound signals includes providing an image of at least a portion of a target subject between the sources of the ultrasound signals and a target region for receiving focused ultrasound signals, identifying from the image physical characteristics of different layers

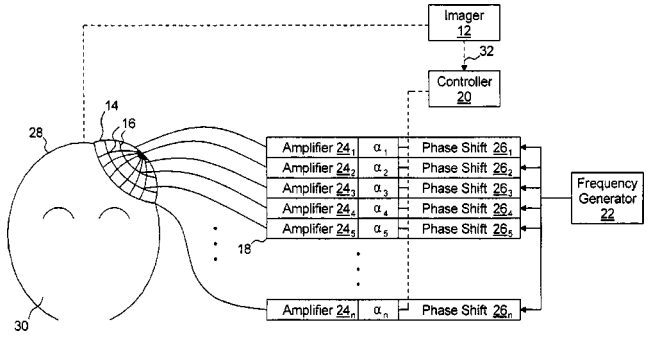

of material between the sources and the target, and determining phase and/or amplitude corrections for the sources depending on the respective thickness of portions of each of the layers positioned between each source and target.—DRR

6,613,004

43.80.Sh SYSTEMS AND METHODS FOR CREATING LONGER NECROSED VOLUMES USING A PHASED ARRAY FOCUSED ULTRASOUND SYSTEM

Shuki Vitek and Dov Maor, assignors to InSightec–TxSonics, Limited
2 September 2003 (Class 601/2); filed 21 April 2000

The aim of the methods described here is to perform noninvasive surgical procedures through the use of focused ultrasound, in particular, to create long necrosed volumes through the use of a focused ultrasound transducer array. The system includes multiple transducer elements and a controller coupled to drive circuitry. Each of the sets of transducer elements is driven for a predetermined duration during sonification, while generally continuously focusing ultrasonic energy onto a desired focal zone. The controller also controls a phase component of the respective drive signals to provide a desired size, shape, and/or location of the focal zone, and thereby necrose a target tissue region at the focal zone.—DRR

6,623,430

43.80.Sh METHOD AND APPARATUS FOR SAFETY DELIVERING MEDICANTS TO A REGION OF TISSUE USING IMAGING, THERAPY AND TEMPERATURE MONITORING ULTRASONIC SYSTEM

Michael H. Slayton *et al.*, assignors to Guided Therapy Systems, Incorporated
23 September 2003 (Class 600/439); filed 10 February 2000

This noninvasive therapeutic ultrasound system is capable of acoustically imaging and heating a specific region to be treated. The system also carries the capability of monitoring the temperature of the region. Thermosensitive liposomes containing medicants are delivered to the region of interest, which is targeted through imaging and then heated ultrasonically. When the desired temperature is reached and the liposomes are melted, thereby releasing the medicants, the treatment stops. If necessary, the application of ultrasound therapy and ultrasound imaging are alternated until the desired threshold temperature is reached.—DRR

6,623,444

43.80.Sh ULTRASONIC CATHETER DRUG DELIVERY METHOD AND DEVICE

Eliaz Babaev, assignor to Advanced Medical Applications, Incorporated
23 September 2003 (Class 604/22); filed 21 March 2001

This ultrasonic catheter drug delivery device consists of an ultrasonic transducer that is mechanically attached to a catheter body or chamber. The transducer features a distal tip with a distal radiation surface. When a therapeutic agent from a fluid source is directed to the catheter body or chamber, the radiation surface generates ultrasonic pressure and delivers the fluid and ultrasonic energy to a patient's vascularity or a selected body lumen.—DRR

6,626,854

43.80.Sh SYSTEMS AND METHODS FOR ULTRASOUND ASSISTED LIPOLYSIS

Zvi Friedman *et al.*, assignors to Insightec–Txsonics Limited
30 September 2003 (Class 601/2); filed 27 December 2000

This relates to systems and methods for destroying tissue by focusing ultrasound from an external source toward subcutaneous tissues, such as adipose tissue, to aid in body contouring. The transducer emits acoustic energy that is focused on a linear focal zone within the tissue region, the acoustic energy having sufficient energy to rupture cells within the focal zone without overheating. The transducer may include one or more transducer elements possessing a partial cylindrical shape, a single planar transducer element coupled to an acoustic lens, or a plurality of linear transducer elements positioned adjacent to each other in an arcuate or planar configuration. A frame may be provided for controlling movement of the transducer along the patient's skin.—DRR

6,626,855

43.80.Sh CONTROLLED HIGH EFFICIENCY LESION FORMATION USING HIGH INTENSITY ULTRASOUND

Lee Weng *et al.*, assignors to Therus Corporation
30 September 2003 (Class 601/3); filed 22 November 2000

This ultrasound system, used for both imaging and delivering high-intensity therapeutic ultrasound beams, has an ultrasound transducer array deployed at the distal end of a relatively thin, elongated shaft. In one embodiment, the transducer array is deployed within a liquid-filled elastomeric material that more effectively couples ultrasound energy into a tumor. With the device functioning in a continuous wave mode, a necrotic zone of tissue having a desired size and shape (e.g., a necrotic volume selected to interrupt a blood supply to a tumor) can be created by controlling at least one or more of the following: focal length, duration, intensity, and direction of the ultrasound administered. It is said that this method speeds the therapy and avoids continuous pausing to enable intervening normal tissue to cool.—DRR

6,635,017

43.80.Sh METHOD AND APPARATUS COMBINING DIAGNOSTIC ULTRASOUND WITH THERAPEUTIC ULTRASOUND TO ENHANCE THROMBOLYSIS

Mark A. Moehring *et al.*, assignors to Spentech, Incorporated
21 October 2003 (Class 600/439); filed 9 February 2000

This apparatus combines therapeutic pulsed or continuous-wave ultrasound with diagnostic pulsed ultrasound. For both therapeutic and diagnostic modes, the ultrasound is administered from a single probe to a patient suffering from thrombosis. The ultrasound can have constant or varying frequency ranges in both of these modes. The pulsed or continuous-wave

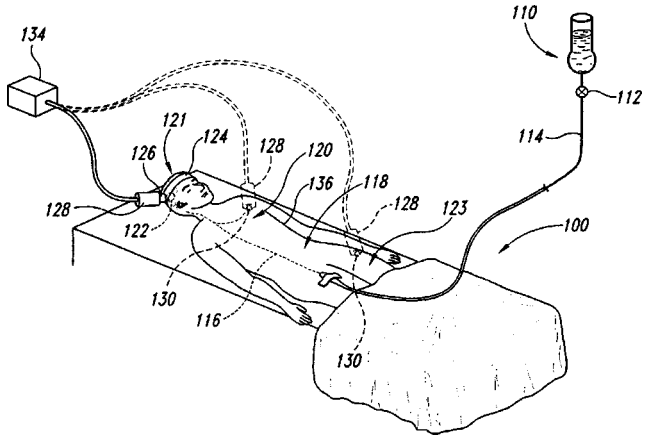

ultrasound in the therapeutic modes may increase the lysing effect of a thrombolytic agent. The pulsed ultrasound in the diagnostic mode allows monitoring of blood flow to locate the thrombus, to determine an optimal window to administer the therapeutic pulsed ultrasound, and to detect when recanalization has occurred. A graphic display is available to display an image representative of the blood flow.—DRR

6,610,016

43.80.Vj ECHOGENIC COATINGS

Michael R. Violante *et al.*, assignors to STS Biopolymers, Incorporated
26 August 2003 (Class 600/458); filed 4 August 1999

These coatings are comprised of a polymer matrix that includes gas in bubbles, surface channels, or cavities. Methods to prepare and apply these coatings are described. The methods include formation of bubbles by a chemical reaction during the coating process.—RCW

6,612,989

43.80.Vj SYSTEM AND METHOD FOR SYNCHRONIZED PERSISTENCE WITH CONTRAST AGENT IMAGING

George Brock-Fisher, assignor to Koninklijke Philips Electronics N.V.
2 September 2003 (Class 600/447); filed 18 June 2002

An ultrasonic imaging instrument is described with a frame memory, a frame processor, and a frame processing controller. Frame-to-frame temporal filtering is disabled during transmissions that destroy the contrast agent. The filtering is re-enabled to observe tissue reperfusion.—RCW

6,620,103

43.80.Vj ULTRASONIC DIAGNOSTIC IMAGING SYSTEM FOR LOW FLOW RATE CONTRAST AGENTS

Matthew Bruce and David Hope Simpson, assignors to Koninklijke Philips Electronics N.V.
16 September 2003 (Class 600/458); filed 11 June 2002

Pairs of differently modulated pulses are transmitted in a number of beam directions to acquire echoes that are combined to separate harmonic frequencies by using pulse inversion. The pairs of pulses are transmitted in rapid succession to minimize motion artifacts. Transmission in different directions is interleaved in time so that each beam direction is sampled over a long period for detection of low flow rates.—RCW

6,620,404

43.80.Vj GASEOUS ULTRASOUND CONTRAST MEDIA AND METHOD FOR SELECTING GASES FOR USE AS ULTRASOUND CONTRAST MEDIA

Steven C. Quay, assignor to Amersham Health A/S
16 September 2003 (Class 424/9.52); filed 28 September 2000

These agents are microbubbles composed of specially selected gases. The microbubbles are small enough to pass through the lungs and have a long life span in solution. The gases are selected using calculations that estimate from gas properties the time for microbubbles containing the gas to dissolve.—RCW

6,621,341

43.80.Vj DIAGNOSTIC MEDICAL ULTRASOUND SYSTEMS HAVING A METHOD AND CIRCUITRY FOR FRONT-END GAIN CONTROL

Lazar A. Shifrin, assignor to Acuson Corporation
16 September 2003 (Class 330/174); filed 22 May 2000

Received echoes are amplified to compensate for increasing attenuation with depth by using a time-varied gain that is proportional to an electronically variable capacitive load.—RCW

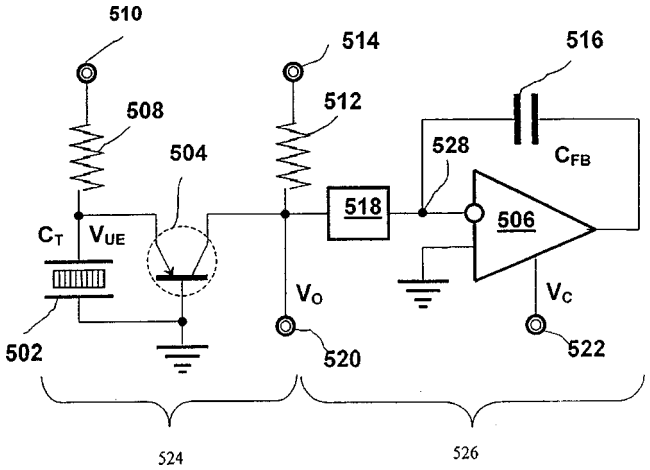

6,623,431

43.80.Vj EXAMINATION METHOD OF VASCULAR ENDOTHELIUM FUNCTION

Ichiro Sakuma *et al.*, assignors to Ichiro Sakuma
23 September 2003 (Class 600/443); filed in Japan 25 February 2002

This method uses a sequence of steps with an ultrasonic imaging system probe attached to a positioning assembly to obtain images from which the diameter of a blood vessel is found in a series of positions along the axis of the vessel before and after dilation.—RCW

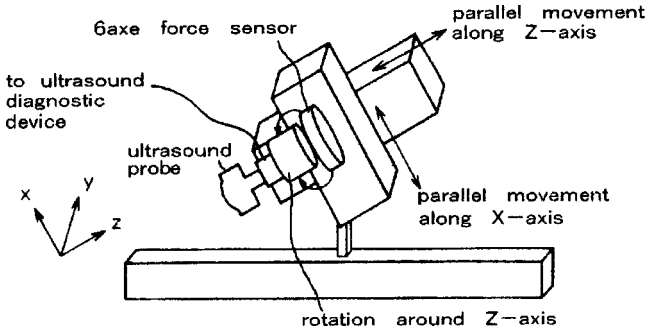

6,623,433

43.80.Vj AUTOMATED LONGITUDINAL POSITION TRANSLATOR FOR ULTRASONIC IMAGING PROBES, AND METHODS OF USING SAME

William E. Webler and Mark S. Buhr, assignors to SciMed Life Systems, Incorporated
23 September 2003 (Class 600/467); filed 3 May 2002

An ultrasound transducer probe at the distal end of a catheter is translated at a constant rate along the axis of a blood vessel to obtain cross-sectional images that are uniformly positioned for reconstruction into three-dimensional or other two-dimensional representations of the region scanned from the vessel.—RCW

6,626,831

43.80.Vj GATED ULTRASOUND IMAGING APPARATUS AND METHOD

Gregory L. Holley *et al.*, assignors to Acuson Corporation
30 September 2003 (Class 600/437); filed 22 January 2001

Ultrasonic image frames with image quality optimized to show the presence of a contrast agent are acquired at a selected phase of the heart cycle. So-called locator image frames are also acquired at additional times with instrument settings optimized for reduced degradation of the contrast agent. The two sets of frames are displayed to provide the user with essentially continuous transducer location information with reduced destruction of contrast agent between frames.—RCW

6,626,836

43.80.Vj ADAPTIVE SIGNAL PROCESSING SCHEME FOR CONTRAST AGENT IMAGING

Zuhua Mao *et al.*, assignors to Siemens Medical Solutions USA, Incorporated
30 September 2003 (Class 600/455); filed 4 April 2001

Echos are processed to determine whether they arise from a tissue region or a contrast region. Processing is used that depends on which region produces the echos. Echos from tissue regions can be processed with a harmonic filter while echoes from contrast regions can be processed using a harmonic filter and a fundamental filter.—RCW

6,628,989

43.80.Vj ACOUSTIC SWITCH AND APPARATUS AND METHODS FOR USING ACOUSTIC SWITCHES WITHIN A BODY

Avi Penner and Eyal Doron, assignors to Remon Medical Technologies, Limited
30 September 2003 (Class 607/59); filed 16 October 2000

This device, to be implanted within a patient's body, can activate, deactivate, and control implants located within the body to monitor physiological conditions and/or provide therapeutic functions. The device includes an electrical circuit for performing one or more commands when the implant is activated, a battery (or some other energy source), and a switch. An acoustic transducer is coupled to the switch, activated upon acoustic excitation by an external acoustic energy source. One or more commands include measuring a physiological parameter with a biosensor coupled to the electrical circuit. The therapeutic device or biosensor may be activated for a predetermined time or until the switch is opened in response to an acoustic excitation of the acoustic transducer.—DRR

6,632,177

43.80.Vj DUAL PROCESS ULTRASOUND CONTRAST AGENT IMAGING

Patrick J. Phillips and Ismayil M. Guracar, assignors to Acuson Corporation
14 October 2003 (Class 600/458); filed 1 May 2002

Dual detection paths are employed to identify differences between different sized vessels throughout a period of contrast enhancement without depleting the available contrast agent. One path is used to detect nonlinear response. Another path is used to detect differences between responses to two or more pulses.—RCW

6,635,019

43.80.Vj SCANHEAD ASSEMBLY FOR ULTRASONIC IMAGING HAVING AN INTEGRAL BEAMFORMER AND DEMOUNTABLE ARRAY

Richard Edward Davidsen, assignor to Koninklijke Philips Electronics N.V.
21 October 2003 (Class 600/459); filed 14 August 2001

This scanhead consists of a transducer assembly and a beamformer

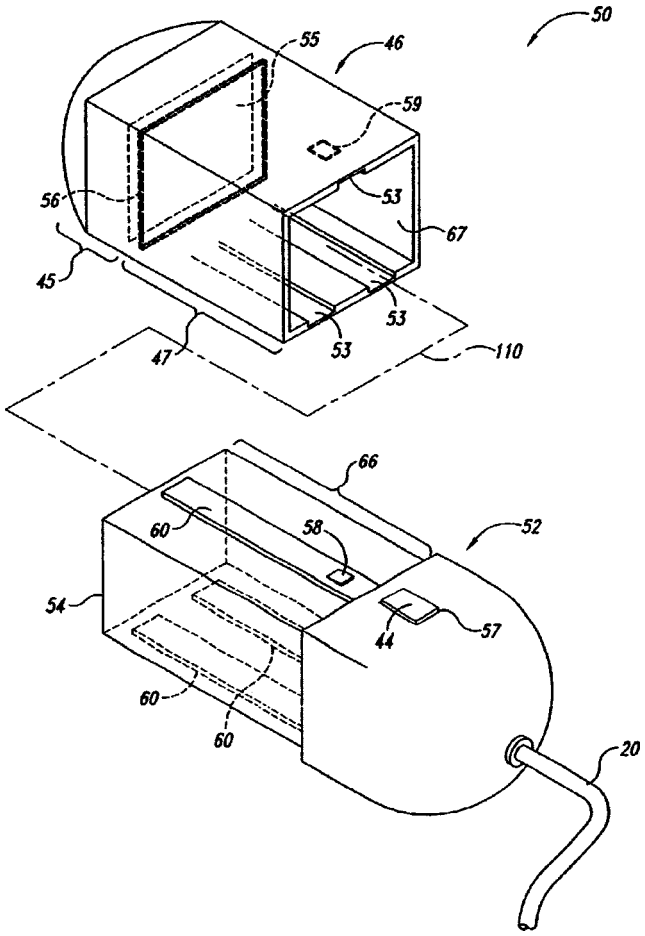

assembly that may be separated.—RCW

LETTERS TO THE EDITOR

This Letters section is for publishing (a) brief acoustical research or applied acoustical reports, (b) comments on articles or letters previously published in this Journal, and (c) a reply by the article author to criticism by the Letter author in (b). Extensive reports should be submitted as articles, not in a letter series. Letters are peer-reviewed on the same basis as articles, but usually require less review time before acceptance. Letters cannot exceed four printed pages (approximately 3000–4000 words) including figures, tables, references, and a required abstract of about 100 words.

Hawkins and Stevens revisited with insert earphones (L)

Adrianus J. M. Houtsma[a)]
U.S. Army Aeromedical Research Laboratory, Fort Rucker, AL 36362-0577

(Received 24 July 2003; revised 22 November 2003; accepted 1 December 2003)

The classical experiment on masking of pure tones by white noise by Hawkins and Stevens [J. Acoust. Soc. Am. **22**, 6–13 (1950)] has left two general notions about broadband masking that are still being echoed in present-day textbooks on hearing. One is that broadband masking is linear (i.e., if the noise power level increases, the signal threshold level increases by exactly the same amount). The other is the existence of a nonmonotonic function of frequency, the critical ratio (CR) which, unlike the critical band (CB) or equivalent rectangular bandwidth (ERB) functions, shows a distinct upturn below 300 Hz. Exploring the possibility that Hawkins and Stevens' measurements may have been adversely affected by acoustic leakage at the headphones at low frequencies, the experiment was repeated with insert earphones. The resulting critical ratio function shows a monotonic dependence on frequency down to 90 Hz, similar to CB and ERB functions. Moreover, the CR function appears to closely approximate the ERB function when the dependence of each filter's detection efficiency on masker energy uncertainty is incorporated. Masking appears to be linear below 1000 Hz, but thresholds, expressed as S/N_0 ratios, were found to increase systematically with increasing masker intensity at higher frequencies. [DOI: 10.1121/1.1645246]

PACS numbers: 43.66.Dc [GDK] Pages: 967–970

I. INTRODUCTION

The most quoted data on masking of pure tones by broadband noise were collected by Hawkins and Stevens (1950). Using an adjustment method, they measured detection thresholds for a continuous pure tone between 100 and 9000 Hz against a background of white noise, using spectral density (N_0) values between −10 and 60 dB.[1] A still frequently cited property of their data is that masking appears to be linear with noise intensity, that is, signal threshold levels appear to rise by the same amount as the spectral density level of the masker (Rossing, 1990; Gelfand, 1997; Hartmann, 1997). It enabled Hawkins and Stevens to combine several masking contours to compute estimates of the width of the auditory filter as a function of frequency. Following Fletcher (1940), the underlying assumption was that, for detection, the signal power had to be a given fixed fraction of the total effective noise power. If the auditory filter is idealized to have unit gain, and a rectangular passband, this assumption can in its simplest form be stated as

$$S_{\mathrm{tr}} = kN_0W, \tag{1}$$

where S_{tr} is the signal power at threshold, N_0 is the spectral density of the masking noise, W the auditory filter's bandwidth, and k a constant that is inversely related to the detection efficiency of the channel. Hawkins and Stevens assumed k to be unity. The result was a nonmonotonic, U-shaped function with a minimum around 300 Hz, with bandwidth roughly proportional to center frequency from 1000 Hz upwards, but with a distinct upturn below 300 Hz. This function became known as the *critical ratio* (CR) function.

The main reason for undertaking the present study was the shape inconsistency of the CR function compared with other estimates of the auditory frequency resolution like the *critical band* (CB) function (Zwicker, Flottorp, and Stevens, 1957) and the *equivalent rectangular bandwidth* (ERB) function (Glasberg and Moore, 1990). These functions, although different from each other, both increase monotonically between 100 and 10 000 Hz, and do not show the upturn at low frequencies observed in the CR function. Particularly, the shape difference between the CR and the ERB functions is bothersome because, unlike many methods that were used to

[a)]Experimental work was performed while the author was at the Institute for Perception Research, Eindhoven University of Technology, The Netherlands. Parts of this study were reported at the 103rd meeting of the ASA in Seattle (1998). Opinions, interpretations, and conclusions contained in this letter are those of the author and are not necessarily endorsed by the U.S. Army and/or the Department of Defense.

measure the CB, both the CR's broadband masking paradigm and the ERB's notched-noise procedure substantially reduce the possibility of so-called ''off-frequency listening.''

Explanations for the upturn of the CR function at low frequencies have focused on (a) the additional difficulty of detecting a tone in noise that has an unsteady temporal envelope due to the narrow auditory bandwidth at low frequencies (Zwicker *et al.*, 1957), and (b) the possible frequency dependence of the factor *k*. Fidell *et al.* (1983) presented evidence for a frequency dependence of *k*, and showed how CR and CB results could be made to agree with one another if $k(f)$ was given a U-shaped form with a minimum around 500 Hz. More recent notched-noise experiments by Glasberg and Moore (2000) also suggest a U-shaped $k(f)$.

There might, however, be a simple acoustic cause for the low-frequency upturn of the CR. The supra-aural headphones used by Hawkins and Stevens provide poor acoustic coupling to the ear canal at low frequencies. This also holds for the earphones used by Green *et al.* (1959) and Reed and Bilger (1973), who obtained results similar to Hawkins and Stevens. Although acoustic losses can be measured and in principle be compensated for, compensation will fail if both the effective signal and noise levels become comparable to the level of internal noise in the auditory system. This could easily happen at low frequencies where acoustic losses are augmented with substantial attenuation in the middle ear and cochlear mechanical short-circuiting effects at the helicotrema. Therefore, it was thought worthwhile to repeat the measurements of Hawkins and Stevens with insert earphones that assure effective acoustic coupling with the eardrum, even at very low frequencies. Moreover, a recent increase in military use of insert earphones, for noise protection and effective communication in noisy conditions (Murphy and Mozo, 1999), is an additional practical reason to re-evaluate the effect of such devices on fundamental properties of human hearing.

II. EXPERIMENTS

Two broadband masking experiments were performed. In both cases, the masker was diotic continuous spectrally flat white noise, low-pass filtered at 10 kHz. The signal to be detected was a diotic tone burst, with frequencies between 30 and 8000 Hz in $\frac{1}{2}$-octave steps. Presentation was through Etymotic ER-2 insert earphones, which have an essentially flat frequency response between 0 and 10 000 Hz. The two experimental methods were as follows.

(a) A tracking procedure using 60 signal bursts of 200-ms duration, including 10 ms on and off ramps, presented at every test frequency. Pressing or releasing a button on a response box either made the test tone decrease or increase by 1 dB with every burst. Subjects were instructed to keep the test tone at such a level that it was barely audible. Thresholds were computed by averaging the sound-pressure levels of the last 30 bursts. Two traces were measured on four subjects (three young normal-hearing adults and the author), against a continuous background of quiet and of noise at spectral density levels between 0 and 50 dB in 10-dB steps. A 60-dB contour was measured only on the author.[2] Subjects were seated in a sound-insulated chamber. Signals were generated by analog Tucker Davis Technologies System-II equipment.

(b) A 2-interval forced-choice adaptive 2-down, 1-up procedure, with only the author as subject.[2] Observation intervals were marked with lights, where the masker was continuous and the test tone could be present in either the first or the second observation interval. Tone bursts were 300 ms, including 10-ms on and off ramps. Feedback was provided after each response. The step size was 1 dB, runs were terminated after 12 reversals, and thresholds were computed by averaging the levels of the last 10 reversals. Each set of half-octave threshold points took about 45 min to measure. Two sets were measured at each noise level, including a quiet background. The set with the highest noise level was done in segments to avoid too-long exposures to high-intensity noise.

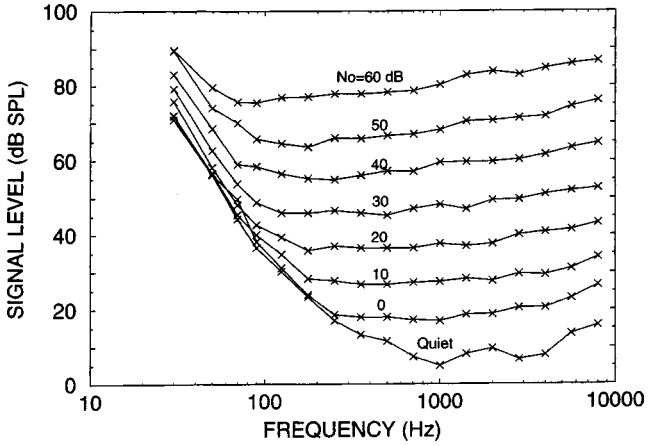

FIG. 1. Threshold sound-pressure levels for sinusoidal tones in broadband noise as a function of signal frequency for eight noise conditions. Thresholds are averages of four subjects and were obtained with a tracking method.

III. RESULTS

The raw results of the tracking experiment, plotted the same way as Hawkins and Stevens, looked sufficiently similar for each of the four subjects that averaging appeared justified, with the exception that for the author data, at 8 kHz below N_0, values of 20 dB were not included in the group average. The results are shown in Fig. 1. The adaptive forced-choice results looked very similar to the results of Fig. 1, except that, on average, all contours were 1.5 dB lower than their tracking equivalents. This is not surprising since forced-choice procedures typically yield lower thresholds than adjustment or tracking procedures (Reed and Bilger, 1973).

IV. DISCUSSION

A. Critical ratio function

Using Eq. (1), a critical ratio function $W(f)$ was computed from the tracking data of Fig. 1, following the same procedure used by Hawkins and Stevens. The constant *k* was

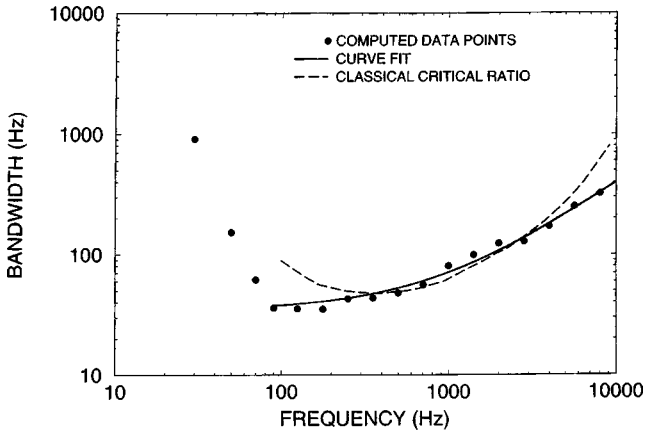

FIG. 2. Critical ratio values computed from averaged tracking results (solid dots), best linear fit to these values between 90 and 1000 Hz (solid line), and critical ratio function determined by Hawkins and Stevens, 1950 (dashed line). For all results, k was assumed to be unity.

assumed to be unity, and linear growth of masking was assumed to hold over the entire frequency range for N_0 levels of 30 dB and higher. Values for W were computed from the average S/N_0 values of the four upper contours at each test frequency, except that at 30 Hz only the upper contour, at 50, 70, and 90 Hz only the upper two contours, and at 125 Hz only the upper three contours were used to avoid data points that might be too close to absolute threshold and might cause a ''bottom'' effect.

The results are shown in Fig. 2 as filled circles. A linear fit to these data points at frequencies between 90 and 8000 Hz, following the general formulas of Greenwood (1961, 1990) and of Glasberg and Moore (1990), resulted in the relationship

$$W(f) = 36.43f + 34.41, \tag{2}$$

($r^2 = 0.99$), with f given in kHz. It is shown as a solid function in Fig. 2. Below 90 Hz, data points begin to deviate strongly from this linear relationship. The reason is that the model used to compute the CR breaks down. Similar observations were made by Fidell *et al.* (1983). Potential reasons for the model breakdown at very low frequencies are (a) the increasing dominance of absolute over masked thresholds (seen in Fig. 1 as a convergence of contours below 90 Hz); (b) a decrease in mechanical coupling between cochlear fluid and basilar membrane when the active region approaches the helicotrema; and (c) an increasing asymmetry in the cochlear filter as cochlear activity approaches the apex (Greenwood, 1961). Figure 2 also shows the original CR function computed by Hawkins and Stevens. Deviations of our data from theirs between 90 and 300 Hz are obvious. Since Reed and Bilger (1973) obtained the same function shape as Hawkins and Stevens did, using pulsed tones in combination with a 4-interval forced-choice adaptive method and supra-aural headphones, it is unlikely that the different low-frequency behavior of our results can be attributed to differences in signal configuration or measurement method. This leaves our use of insert earphones as the main contributor to observed differences in CR at low frequencies

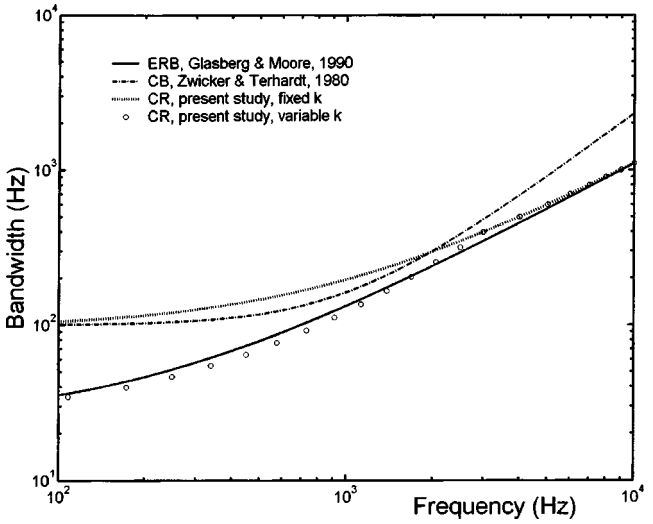

FIG. 3. Equivalent rectangular bandwidth (Glasberg and Moore, 1990), critical bandwidth (Zwicker and Terhardt, 1980), and the critical ratio function of this study with a constant, frequency-independent k of 0.4. Open circles represent a correction to this CR function using a frequency-dependent k below 3 kHz, based on independent evidence.

A comparison of our present CR results with the classical *critical band* (Zwicker and Terhardt, 1980) and the *equivalent rectangular bandwidth* (Glasberg and Moore, 1990) are shown in Fig. 3, where the value k of Eq. (1) was considered frequency independent and empirically set to 0.4 for the best comparison. This simply shifts the entire CR function upwards without altering its shape, as can be seen by comparing it with Fig. 2. The CR function derived in the present experiment appears to approximate the classical CB function at low, and the ERB function at high frequencies.

A likely explanation for the increasing discrepancy between the CR and the ERB function at frequencies below 1000 Hz is the frequency dependence of k. Measurements of masked thresholds for pure tones in narrow-band noise as a function of noise bandwidth by van de Par and Kohlrausch (1999) have shown that, if the bandwidth of masking noise is increased within the range of the critical band involved, k decreases at a rate of 1.5 dB per doubling of the bandwidth. This suggests that detection efficiency is primarily determined by the variability of the masker energy. For the broadband masking used in this study, the variability in masker energy is determined by the bandwidth of the internal filter, so that k is expected to increase by 1.5 dB every time this bandwidth is reduced by a factor of 2.

This potential explanation was tested by a correction to the experimental CR function below a 3000-Hz cutoff frequency. Every time the critical bandwidth appeared reduced by a factor of 2 as indicated by the ERB function, k was increased by 1.5 dB. The result is the function formed by the open circles shown in Fig. 3. The ERB and both the uncorrected and corrected CR functions were all made to coincide exactly at 10 000 Hz. The correction in the CR function, which is based on an independent data-supported model, makes the critical ratio function match the ERB function almost perfectly. The only free, empirically determined parameter of the correction procedure was the cutoff frequency below which k begins to change.

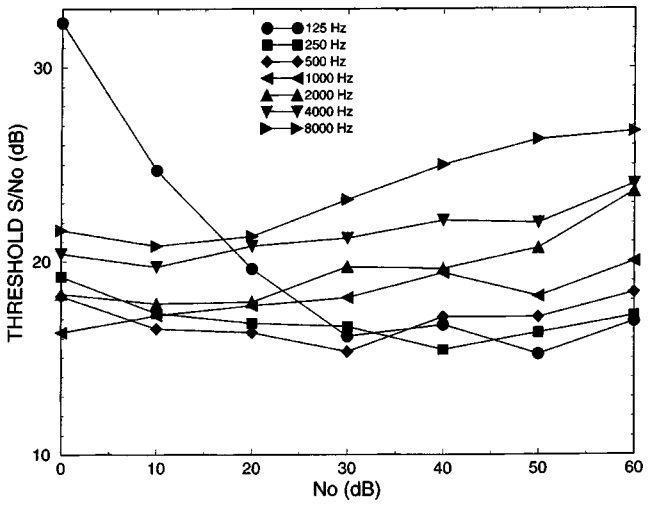

FIG. 4. Pooled data from both experiments, plotted as S/N_0 thresholds against N_0 values, with signal frequency as parameter. Data produced by the author at 8 kHz and N_0 levels of 0 and 10 dB were not included.

B. Linearity of broadband masking

Masking results as shown in Fig. 1 can be replotted to test the degree of linearity in broadband masking. Figure 4 shows S/N_0 levels as a function of N_0, with signal frequency as parameter. For this purpose the data of the tracking and the adaptive procedures were pooled, after all adaptive threshold data were increased by 1.5 dB to correct for the difference in procedure. Adaptive data at 8 kHz for N_0 values below 30 dB were discarded.[2]

If broadband masking behaved linearly, all replotted contours should have zero slopes. This appears to be true for contours corresponding to frequencies below 1000 Hz, with the exception of the 250-Hz contour which steeply increases at low noise levels (absolute threshold ''bottom'' effect). All contours for signal frequencies above 1000 Hz, however, show a positive slope, at least within an N_0 range of 20 to 60 dB. A linear regression on the contours of 2000, 4000, and 8000 Hz yielded an average slope of 0.12 dB/dB. This finding appears consistent with the results of Reed and Bilger (1973), who found flat contours for signal frequencies of 250 and 500 Hz, and positive slopes between 0.07 and 0.14 dB/dB for frequencies between 1000 and 8000 Hz. There is, however, recent evidence from notched-noise masking (Baker, Rosen, and Darling (1998); Glasberg and Moore (2000) and pulsation threshold measurements (Plack and Oxenham, 2000) that basilar-membrane nonlinearity extends to frequencies well below 1000 Hz. This apparent discrepancy deserves further investigation.

V. CONCLUSIONS

The following conclusions can be drawn from the results of this study.

(a) Discrepancies between estimates of auditory frequency resolution using critical ratios and those using critical band or ERB measures can be accounted for by a lack of sufficient acoustic coupling at low frequencies in several of the classical critical ratio experiments.

(b) The concept of linearity of broadband masking holds for frequencies below 1000 Hz, but not for frequencies beyond. Aural frequency resolution can not, therefore, in principle, be accurately represented by a single intensity-independent CR function. Intensity dependencies of S/N_0 thresholds (or, equivalently, CRs) above 1000 Hz are in the order 1 dB for every 10-dB increase in background noise power.

ACKNOWLEDGMENTS

The author is indebted to the Institute for Perception Research for providing the funds for this research, to three dedicated colleagues who served as subjects, and to Richard Baker, Bertram Scharf, and an anonymous reviewer for helping improve the manuscript.

[1]The spectral density of while noise is the sound intensity per Hz. On a decibel scale, it is the intensity level (in dB) of a certain test band of width W, in this case 10 kHz, minus $10 \log_{10} W$.

[2]The author was 59 years old at the time the measurements were made. His absolute threshold showed elevations of 5 dB at 3000 Hz, increasing to 20 dB at 8000 Hz, compared with averages of the other subjects. Masked threshold contours for noise of 0-dB and 10-dB spectral density were normal up to 6000 Hz. All other masked threshold contours were normal up to 8000 Hz.

Baker, R. J., Rosen, S., and Darling, A. M. (**1998**). ''An efficient characterization of human auditory filtering across level and frequency that is also physiologically reasonable,'' in *Psychophysical and Physiological Advances in Hearing*, edited by A. R. Palmer, A. Rees, A. Q. Summerfield, and R. Meddis (Whurr, London), pp. 81–87.

Fidell, S., Horonjeff, R., Teffeteller, S., and Green, D. M. (**1983**). ''Effective masking bandwidth at low frequencies,'' J. Acoust. Soc. Am. **73**, 628–638.

Fletcher, H. (**1940**). ''Auditory patterns,'' Rev. Mod. Phys. **12**, 47–65.

Gelfand, S. A. (**1997**). *Essentials of Audiology* (Thieme, New York).

Glasberg, B. R., and Moore, B. C. J. (**1990**). ''Derivation of auditory filter shapes from notched-noise data,'' Hear. Res. **47**, 103–138.

Glasberg, B. R., and Moore, B. C. J. (**2000**). ''Frequency selectivity as a function of level and frequency, measured with uniformlty exciting notched noise,'' J. Acoust. Soc. Am. **108**, 2318–2328.

Greenwood, D. D. (**1961**). ''Critical bandwidth and the frequency coordinates of the basilar membrane,'' J. Acoust. Soc. Am. **33**, 1344–1356.

Greenwood, D. D. (**1990**). ''A cochlear frequency-position function for several species—29 years later,'' J. Acoust. Soc. Am. **87**, 2592–2605.

Green, D. M., McKey, M., and Licklider, J. (**1959**). ''Detection of a pulsed sinusoid in noise as a function of frequency,'' J. Acoust. Soc. Am. **31**, 1446–1452.

Hartmann, W. M. (**1997**). *Signal, Sound, and Sensation* (AIP, Woodbury, NY).

Hawkins, J. E., and Stevens, S. S. (**1950**). ''The masking of pure tones and speech by white noise,'' J. Acoust. Soc. Am. **22**, 6–13.

Murphy, B. A., and Mozo, B. T. (**1999**). ''Flight evaluation of the Communications EarPlug in the OH-58D helicopter,'' USAARL Report 2000-4/5 (Parts 1 and 2).

van de Par, S., and Kohlrausch, A. (**1999**). ''Dependence of binaural masking level difference on center frequency, masker bandwidth, and interaural parameters,'' J. Acoust. Soc. Am. **106**, 1940–1947.

Plack, C. J., and Oxenham, A. J. (**2000**). ''Basilar-membrane nonlinearity estimated by pulsation threshold,'' J. Acoust. Soc. Am. **107**, 501–507.

Reed, C. M., and Bilger, R. C. (**1973**). ''A comparative study of S/N_0 and E/N_0,'' J. Acoust. Soc. Am. **53**, 1039–1044.

Rossing, T. D. (**1990**). *The Science of Sound* (Addison-Wesley, Reading MA).

Zwicker, E., and Terhardt, E. (**1980**). ''Analytical expressions for critical-band rate and critical bandwidth as a function of frequency,'' J. Acoust. Soc. Am. **68**, 1523–1525.

Zwicker, E., Flottorp, G., and Stevens, S. S. (**1957**). ''Critical band width in loudness summation,'' J. Acoust. Soc. Am. **29**, 548–557.

Comment on "Acoustical losses in wet instrument bores" [J. Acoust. Soc. Am. 114, 1221 (2003)] (L)

William V. Slaton
Department of Physics and Astronomy, University of Mississippi, University, Mississippi 38677

(Received 6 November 2003; revised 9 December 2003; accepted 15 December 2003)

This letter is a comment on Coltman's [J. Acoust. Soc. Am. **114**, 1221 (2003)] letter describing increased acoustic losses for a water-saturated air mixture in a tube. Recent publications are referenced which supply the necessary theoretical background to calculate the attenuation of sound in an inert gas–vapor mixture enclosed in a wet-walled tube. It is shown that these references are sufficient to analyze the results presented by Coltman. © *2004 Acoustical Society of America.*
[DOI: 10.1121/1.1645612]

PACS numbers: 43.20.Hq, 43.35.Ud, 43.75.Fg [NHF] Pages: 971–972

This Comment provides references of which Coltman[1] was unaware, but which provide a theoretical complement to his experimental results. Extensive theoretical analysis has been published that allows detailed prediction of the attenuation of sound in a vapor-saturated inert gas mixture enclosed in a wet-walled tube. This theoretical analysis is little more complicated than predictions of attenuation of sound in a dry gas enclosed in a tube. Predicted increases in attenuation due to the presence of water-saturated air agree very well with those presented by Coltman.

Coltman describes the internal physical environment of a wind instrument as water-saturated air with liquid water coating the instrument walls. He correctly surmises that an evaporation–condensation process can occur during the acoustic cycle at the interface between the saturated mixture and the liquid layer lining the tube wall. When the acoustic wave causes a rarefaction of the mixture, the partial pressure of vapor within the mixture drops below the vapor pressure at the wet wall, thus causing vapor molecules to evaporate from the liquid layer and diffuse into the mixture. When the acoustic wave causes a compression of the mixture, the partial pressure of the vapor within the mixture rises above the vapor pressure at the wet wall, thus causing vapor molecules to diffuse through the mixture to condense on the wet wall. The act of molecular diffusion is a loss mechanism and will result in an increased attenuation of the sound wave within the tube.

The experimental setup described by Coltman consists of a 93-cm-long copper pipe with a smooth inside diameter of 19 mm. This pipe is closed at one end with a piston driver and at the other by a microphone. The pipe was cleaned and the air inside dried using a desiccant. The first two resonance modes of this system filled with dry air at atmospheric pressure and a room temperature of 24 °C were measured to be 186 and 374 Hz. Measurement of the Q of these resonances yield attenuation coefficients for dry air of 0.0463 Np/m for 186 Hz and 0.0637 Np/m for 374 Hz. The system was then wetted by either breathing into the pipe or by the use of an atomizer, both of which result in a saturated mixture and a thin layer of liquid coating the pipe wall. This thin liquid layer will act as a site for evaporation–condensation during the acoustic cycle. Coltman then measures the Qs for the same resonance frequencies and calculates the changed attenuation coefficients. These new attenuation coefficients for water-saturated air were larger by 3.5% for the first mode and 4.6% for the second mode.

The most important type of attenuation that must be considered when analyzing this problem is the attenuation caused by viscous, thermal, and diffusive energy transport from the gas mixture to the tube wall. A recent series of papers addressing the effect of evaporation–condensation on sound propagation in wet-walled tubes is applicable.[2–4] The calculations have also been extended to predict sound attenuation in wet tubes for application to soils and thermoacoustic refrigeration. Of most interest for comparing to the measurements of Coltman is Ref. 2, which derives an expression for the complex wave number squared for an inert-gas–vapor mixture in a wet-walled tube, Eq. (44), with no temperature gradient along the tube wall. Equation (44) from Ref. 2 may be simplified for an air–water vapor mixture by noting that the thermal diffusion ratio, k_T, is very small and may be ignored. This simplification results in an expression for the wave number squared which is dependent on the viscous, thermal, and diffusive energy transport processes for the given geometry and gas properties and is reproduced here

$$k^2=\frac{\gamma}{F(\lambda_\mu)}\frac{\omega^2}{c^2}\left[1+\frac{n_2}{n_1}-\frac{\gamma-1}{\gamma}F(\lambda_T)-\frac{n_2}{n_1}F(\lambda_D)\right], \quad (1)$$

where $\lambda_\mu=R\sqrt{\rho\omega/\mu}$ is the dimensionless shear wave number, $\lambda_T=R\sqrt{\rho\omega c_p/\kappa}$ is the dimensionless thermal wave number, and $\lambda_D=R\sqrt{\omega/D_{12}}$ is the dimensionless diffusion wave number with R given by the tube radius. The pore geometry is characterized by the porous media dissipation function $F(\lambda_j)=1-(2/\sqrt{i}\lambda_j)[J_1(\sqrt{i}\lambda_j)]/[J_0(\sqrt{i}\lambda_j)]$ for cylindrical tubes with $j=\mu,T,D$ and the Js denoting Bessel functions of the zeroth- and first order. Thermodynamic properties of the gas mixture include the ratio of specific heats, γ, the ambient speed of sound, c, the angular frequency, ω, the mixture density, ρ, the mixture viscosity, μ, the mixture heat capacity, c_p, the mixture thermal conductivity, κ, the mixture diffusion coefficient, D_{12}, and the number density of the gas and vapor, n_1 and n_2, respectively. The mixture properties for a saturated air and water vapor mixture at a total pressure of 1 atmosphere and a temperature

TABLE I. Attenuation in dry and water saturated air with predicted percent increase for one atmosphere of total pressure and 24 °C in a 19-mm-diameter tube.

Frequency (Hz)	$\alpha_{\text{Dry wall}}$ (Np/m)	$\alpha_{\text{Wet wall}}$ (Np/m)	Percent increase
186	0.0423	0.0433	2.4%
374	0.0597	0.0611	2.3%

of 24 °C may be calculated as indicated in Ref. 2. Note that the equation above allows for calculation of the saturated-air attenuation coefficient as well as the dry-air attenuation coefficient. In the dry-air case, the terms that arise due to molecular diffusion are removed by noting that the number density of vapor goes to zero for dry air. Bulk attenuation within the gas mixture due to acoustic energy transport to the vibration and rotational modes of the nitrogen and oxygen molecules is negligible for this situation and is only mentioned for completeness.[5,6]

Using these references it is possible to predict the attenuation for a water vapor-saturated air mixture at one atmosphere total pressure at 24 °C in a 19-mm-diameter pipe. Table I contains the calculated attenuations and compares the values for the wet-walled case to the dry-walled case. It is found that the total attenuation due to viscous, thermal, diffusive, and bulk energy transport is indeed larger than the attenuation found for the dry air at the same frequencies. The table displays the frequencies examined in column 1, attenuation due to energy transport at the tube wall for dry air in column 2, the attenuation due to energy transport at the tube wall for saturated air in column 3. Column 4 contains the predicted percent increase in attenuation at the given frequency due to the presence of water-saturated air. This theory from Refs. 2–4 accurately predicts an increased attenuation that is of the same size as presented by Coltman for the given frequencies.

In conclusion, relevant references have been given for the theoretical modeling of an inert gas–vapor mixture in a tube. These references accurately describe the measured increase in attenuation for a water-saturated air mixture as measured by Coltman. These references indicate that the complex wave number squared for sound propagation in a wet-walled tube housing a vapor-saturated gas mixture is little more complicated than similar expressions for a dry-gas mixture with both wet and dry expressions being easy to calculate and compare to experimental results.

[1] J. W. Coltman, "Acoustical losses in wet instrument bores," J. Acoust. Soc. Am. **114**, 1221 (2003).

[2] R. Raspet, C. J. Hickey, and J. Sabatier, "The effect of evaporation–condensation on sound propagation in cylindrical tubes using the low reduced frequency approximation," J. Acoust. Soc. Am. **105**, 65–73 (1999).

[3] C. J. Hickey, R. Raspet, and W. V. Slaton, "Effects of thermal diffusion on sound attenuation in evaporating and condensing gas–vapor mixtures in tubes," J. Acoust. Soc. Am. **107**, 1126–1130 (2000).

[4] W. V. Slaton, R. Raspet, and C. J. Hickey, "The effect of the physical properties of the tube wall on the attenuation of sound in evaporating and condensing gas–vapor mixtures," J. Acoust. Soc. Am. **108**, 2120–2124 (2000).

[5] H. E. Bass, L. C. Sutherland, A. J. Zuckerwar, D. T. Blackstock, and D. M. Hester, "Atmospheric absorption of sound: Further developments," J. Acoust. Soc. Am. **97**, 680–683 (1995).

[6] H. E. Bass, L. C. Sutherland, A. J. Zuckerwar, D. T. Blackstock, and D. M. Hester, "Erratum: Atmospheric absorption of sound: Further developments," J. Acoust. Soc. Am. **99**, 1259(E) (1996).

Comment on "Adaptive tuning of an electrodynamically driven thermoacoustic cooler" [J. Acoust. Soc. Am. 111(3), 1251–1258 (2002)] (L)

Robert W. M. Smith[a)]
Penn State University Applied Research Laboratory, State College, Pennsylvania 16804-0030

(Received 19 August 2003; revised 15 December 2003; accepted 16 December 2003)

Corrections for equations contained in a recent paper [Li *et al.*, J. Acoust. Soc. Am. **111**(3), 1251–1258 (2002)] are provided and unclear items are discussed. Comments are provided on some of the observations and conclusions of this paper. © *2004 Acoustical Society of America.*
[DOI: 10.1121/1.1647511]

PACS numbers: 43.35.Ud, 43.58.Wc, 43.38.Dv [RR] Pages: 973–975

In a recent paper, Li *et al.* [J. Acoust. Soc. Am. **111**(3), 1251–1258 (2002)] developed a model for electro-acoustic conversion efficiency for an electrically driven thermoacoustic refrigerator. In the model they employed a transfer function formulation, shown in their Fig. 5. From this formulation, the authors obtain several relations, primarily aimed at obtaining the electro-acoustic conversion efficiency.

First, some corrections are appropriate. In the paper, Eqs. (8) and (10) are missing a factor of K in the numerator. Equation (9) is missing a factor of $K\cdot(Bl)$ in the numerator. In the development of subsequent equations, interpretation of the paper becomes more difficult because of what appear to be two definitions of the variable $U_c(s)$. $U_c(s)$ is first defined in the text, and explicitly in Fig. 5 to be "...the voltage on the output side of the amplifier..." Later, in the text immediately leading Eq. (11), which is the first mathematical expression containing $U_c(s)$, the authors appear to establish a second definition, such that this quantity represents "coil voltage."

Assuming the first definition of $U_c(s)$, Eq. (11) in the Li paper is observed to be in error, since this equation must simply reduce to the factor K for the case when one chooses $H(s)=0$. For this case the correct form of the equation is given by

$$\frac{U_c(s)}{U(s)}=\frac{K\{(LCs^2+RCs+1)(1+G_m(s)AG_{PV}(s))+Bl^2G_m(s)Cs\}}{(LCs^2+RCs+1)(1+G_m(s)AG_{PV}(s))+Bl(Bl+KH(s))G_m(s)Cs}. \tag{1}$$

Assuming the second possible definition of $U_c(s)$, and here this second definition shall be renamed as $U_{\text{coil}}(s)$, then Eq. (11) in the Li paper is also in error. This is most readily observed again in the limiting case where $H(s)$ is zero. For such a case, the equivalent electrical impedance of the postamplifier system is

$$Z_{\text{eq}}=\frac{1}{G_e(s)}+Bl^2\left(\frac{G_m(s)}{1+G_m(s)AG_{PV}(s)}\right). \tag{2}$$

Then, the ratio of the postamplifier voltage to the coil voltage can be equivalently expressed as the ratio of the impedance with and without the series capacitance. Since $U_c(s)=KU(s)$, when $H(s)=0$ this results in a form closest to Eq. (11) in the Li paper in

$$\left.\frac{U_{\text{coil}}(s)}{U_c(s)}\right|_{H(s)=0}=\frac{U_{\text{coil}}(s)}{KU(s)}=\frac{Cs\{(Ls+R)(1+G_m(s)AG_{PV}(s))+Bl^2G_m(s)\}}{(LCs^2+RCs+1)(1+G_m(s)AG_{PV}(s))+Bl^2G_m(s)Cs}. \tag{3}$$

One may see in Eq. (11) of the Li paper that K appears only in products of $H(s)$. Using only the transfer function formulation presented in the Li paper, it is does not appear straightforward to formulate a full corrected version of Eq. (11) for this second possible definition.

The equations referenced are combined to produce their result for efficiency shown in Eq. (13), which may be recognized to be in error since the second term in the denominator is dimensionally incompatible. If we define here a new quantity, $\Phi_{Up-a,I}$, to be the phase angle between the *postamplifier* voltage and the current, a correct replacement for the Eq. (13) by Li *et al.* is given here in Eq. (4), after some further discussion.

a)Electronic mail: rws100@psu.edu

With Φ_{UcI} defined as the phase between *coil* voltage and current, as described in the Li paper, Eq. (13) in the Li paper can be corrected with the addition of a factor of $G_m(s)$ in the second term of the denominator if the series capacitor is omitted, since this case collapses to our Eq. (4). With this correction it is believed that this equation also produces the correct solution when a capacitor *is* present, because one does not expect a series electrical nondissipative element to have any effect on the efficiency, and one expects the impact on efficiency of $H(s)$ to be tantamount to varying the input voltage on an assumed linear system.

About their result in Eq. (13), the authors of the paper observe that "...the capacitance C does not appear in Eq. (13). This shows that the addition of a capacitor in series with the coil does not affect the efficiency." This observation is in concert with established theory.[1,2] However, the emphasis on the capacitance, and lack of mention of the role of the machine inductance, could be misleading, since it too has no impact on the efficiency. In fact, it is not necessary, as appears to have been the goal in formulating the equations, to try isolate the capacitance C. Using $U_c(s)$ and the other variables as defined in the paper, and $\Phi_{Up-a,I}$, which as a reminder is the phase between the postamplifier voltage $U_c(s)$ and the current, the following equation for efficiency results:

$$\eta(s)=\frac{A|G_{PV}(s)|(Bl)^2|G_m(s)|^2\cos(\Phi_{PV})}{|[1+AG_{PV}(s)G_m(s)]||(Ls+R+1/Cs)[1+AG_{PV}(s)G_m(s)]+(Bl)^2G_m(s)|\cos(\Phi_{Up-a,I})}. \tag{4}$$

In this case, while L and C appear explicitly in the equation, they also appear implicitly in $\cos(\Phi_{Up-a,I})$, as is true for L in $\cos(\Phi_{UcI})$ in the Li paper, in such a manner as to cancel any impact on efficiency. An alternate form for the efficiency shows this more explicitly. Again, using the block variables from the Li paper, and defining for convenience the quantity which appears in a block in Fig. 5(b)

$$G_B(s)=\frac{G_m(s)}{[1+AG_{PV}(s)G_m(s)]}, \tag{5}$$

the efficiency is

$$\eta(s)=\frac{\mathrm{Re}(A\cdot G_{PV}(s))}{\mathrm{Re}\left(\frac{1}{G_B(s)}\right)+\left(\frac{1}{(Bl)^2|G_B(s)|^2}\right)\mathrm{Re}\left(\frac{1}{G_E(s)}\right)}, \tag{6}$$

where G_E represents the blocked electrical admittance of the transducer and a series capacitor, as defined in their paper. Since only the real part of $(1/G_E(s))$ enters this equation, the series electrical impedance associated with the coil inductance and the capacitor are explicitly seen to have no impact on the efficiency.

In Fig. 6 of the Li paper, the authors compare predicted and measured efficiency using their model. Assuming the authors have correctly calculated the efficiency, the result shows a notable difference between the frequency (approximately 1.3 Hz or $\sim$1%) and predicted magnitudes (16% relative error) for the location and magnitude of the efficiency, although the two curves are not identified in the plot. It is also not clear how G_{PV} was obtained for the model, to compare the model and the measurement. The differences apparent in Fig. 6 might be attributed to nonlinearity or frequency dependence in the motor parameters, but the authors make no comment on the origin of the discrepancy.

This same model is also exercised to predict the optimum efficiency for an electrodynamic source that drives a thermoacoustic resonator having a resonance frequency that is roughly twice the expected *in vacuo* mechanical resonance frequency of the source. Their model predicts a maximum electro-acoustic conversion efficiency of 27.4%. Theory predicts that 70 percent is possible, based on the source parameters given in their Table I, for a properly coupled source. They state that a "mere 0.8-Hz change in frequency" from the optimum efficiency point to the acoustic resonance results in a factor-of-4 reduction in efficiency, to 7.4%.

The conclusion that the authors reach, based in part on their model predictions, is that "...the acoustic resonance frequency does not match the frequency for optimal efficiency..." This is undoubtedly true. In practical systems, however, the magnitude of the impact is substantially smaller than this model might suggest and is often negligible. Our experience[3] indicates that for practical systems (i.e., systems with optimum achievable efficiencies very near the theoretically achievable electro-acoustic conversion efficiency, based on the driver parameters), that the "indirect efficiency control" employed by Hofler[4] and others[5,6] can work very well (i.e., tracking and operation at the acoustic resonance) and can produce efficiencies often reaching within measurement error (a fraction of a percent) of the predicted optimum achievable efficiency. In general, this optimum will occur at some frequency slightly different than the acoustic resonance for the case when the source mechanical and acoustic resonance frequencies are close but not exactly the same. Given the relative simplicity of tracking the acoustic resonance, and the fact that the penalty is negligible for not directly detecting the maximum efficiency, tracking the acoustic resonance is an effective and practical engineering strategy.

In observing that the acoustic resonance does not correspond to the optimum efficiency, and the substantial degradation in efficiency for their modeled system corresponding to operating at acoustic resonance, Li *et al.* cite Hunt[2] in support to say "*While it is customary to assume that the maximum in efficiency always occurs at 'resonance,' a closer examination of Eqs. (4.19) and (4.20) reveals that a still higher efficiency can be obtained for some other value of frequency or reactance than the one for which* $p=0=X_M$

$+X_L$.'' In fact, Hunt points out that this higher efficiency is only available for transducers that have complex (as opposed to purely real) transduction coefficients. An imaginary component in the transduction coefficient does not appear to be modeled by Li *et al.*, per the parameters in their Table I, or elsewhere in the paper. Our measurements of transducers of similar design from the same supplier exhibit a negligible complex component in the transduction coefficient.[7] For transducers with real transduction coefficients, any nonzero combined acousto-mechanical reactance experienced by the source reduces the efficiency from what theoretically could have been achieved.

ACKNOWLEGMENTS

I would like to thank Steven Garrett for guidance and Thomas Gabrielson for helpful discussions and corrections. I would also like to thank the Penn State University Applied Research Laboratory, the Office of Naval Research, and Ben and Jerry's Homemade for their continued support of thermoacoustic research.

[1] R. S. Wakeland, ''Use of electrodynamic drivers in thermoacoustic refrigerators,'' J. Acoust. Soc. Am. **107**(2), 827–832 (2000).
[2] F. V. Hunt, *Electroacoustics: The Analysis of Transduction, and its Historical Background* (Acoustical Society of America, 1984).
[3] T. L. Shearer, ''Thermoacoustic refrigeration using a linear actuator without pressure and displacement transducers,'' Master's thesis, Penn State Dept. of Electrical Engineering (May 2002).
[4] T. J. Hofler, ''Accurate acoustic power measurements with a high-intensity driver,'' J. Acoust. Soc. Am. **83**(2), 777–786 (1988).
[5] S. L Garrett, J. A. Adeff, and T. J. Hofler, ''Thermoacoustic refrigerator for space applications,'' J. Thermophys. Heat Transfer **7**(4), 595–599 (1993).
[6] R. B. Byrnes, ''Electronics for autonomous measurement and control of a thermoacoustic refrigerator in a space environment,'' DTIC Report No. AD B141 388 (1989).
[7] R. W. Smith, ''High efficiency two kilowatt acoustic source for a thermoacoustic refrigerator,'' Master's thesis, Penn State Dept. of Engineering Science and Mechanics (Dec. 2000).

Reply to "Comment on 'Adaptive tuning of an electrodynamically driven thermoacoustic cooler' " [J. Acoust. Soc. Am. 111, 1251–1258 (2002)] (L)

Yaoyu Li,[a] In-Su Paek, George T.-C. Chiu, Luc G. Mongeau, and James E. Braun
Ray W. Herrick Laboratories, 140 South Intramural Drive, West Lafayette, Indiana 47907-2031

(Received 4 November 2003; accepted for publication 8 November 2003)

This Letter is a response to the comments by Smith on the paper published by Li *et al.* entitled "Adaptive tuning of an electrodynamically driven thermoacoustic cooler." Some editorial errors in the original paper are corrected. Some confusing notations are clarified and an additional discussion is provided. Questions about the generality of the results are clarified by the author's comments.
 [DOI: 10.1121/1.1647512]

PACS numbers: 43.35.Ud, 43.58.Fm, 43.38.Dv [RR] Pages: 976–979

The author's comments on the paper published by Li *et al.*, entitled "Adaptive tuning of an electrodynamically driven thermoacoustic cooler,"[1] are gratefully acknowledged. These comments[2] outline editorial errors in the original paper, and offer additional insight on the impact of tuning the system to operate at the acoustic resonance frequency as opposed to the frequency at which the system reaches maximum efficiency. Questions about the generality of the results are clarified by the author's comments. Corrections and additional discussion are provided in the following reply.

Flaws in the notation and editorial errors in the equations were indeed present, as correctly pointed out in Ref. 2. These errors, however, did not affect the accuracy of the results. The main conclusions and contributions of Ref. 1 are thus not invalidated by the mistakes. The notation $U_c(s)$ is indeed misleading based on Fig. 1 and Fig. 5 as they appeared in Ref. 1. A transformer was used to enhance the current output of the audio power amplifier shown in Fig. 1 of Ref. 1. The combination of the audio amplifier and the transformer is considered as the power amplification unit for the driver. Considering the voltage output of the audio amplifier alone is unnecessary. So the gain K in Fig. 5 should be the gain for the concatenation of the audio amplifier and the transformer. The output of the K block is therefore not the coil voltage, but the voltage across both the capacitor and the coil. The coil voltage is not explicitly shown in the original block diagram. Therefore, the output of the K block should have been labeled as $U_{\text{out}}(s)$ in place of $U_c(s)$ in Fig. 5 of Ref. 1, as correctly pointed out in Ref. 2. A corrected version of Figs. 1 and 5 of Ref. 1 are shown in Figs. 1 and 2 in this Letter. Note that $U_c(s)$ was taken as the coil voltage in the efficiency derivation.

There were indeed errors in Eqs. (8)–(13) of Ref. 1, as pointed out in Ref. 2. The correct expressions, however, were used in the calculations. In the simulation program used for efficiency modeling, the gain K was not explicitly included in the equations because it cancels out anyway. This omission was unfortunately carried over in the write-up, which explains why the gain K was wrongly omitted in Eqs. (8)–(11). In the program, the variables were calculated in a sequential manner instead of using closed form equations. The quantity $V(s)$ was calculated first, and then $P(s) = G_{pv}(s)*V(s)$ was calculated. Equation numbers refer to the numbering in the original paper, Ref. 1.

There was indeed a missing (Bl) term in Eq. (9). The corrected transfer function between the input voltage $U(s)$ and the output voltage of the combined power amplifier is

$$\frac{U_{\text{out}}(s)}{U(s)} = \frac{K\{(LCs^2+RCs+1)[1+AG_{PV}(s)G_m(s)]+(Bl)^2G_m(s)Cs\}}{(LCs^2+RCs+1)[1+AG_{PV}(s)G_m(s)]+(Bl)[Bl+KH(s)]G_m(s)Cs}. \tag{9}$$

The transfer function for the coil voltage was calculated using $U_c(s)/U(s) = U_{\text{out}}(s)/U(s) - [I(s)/U(s)](1/Cs)$.

Equation (11) should be corrected as follows:

$$\frac{U_c(s)}{U(s)} = \frac{KCs\{(Ls+R)[1+AG_{PV}(s)G_m(s)]+(Bl)^2G_m(s)\}}{(LCs^2+RCs+1)[1+AG_{PV}(s)G_m(s)]+(Bl)[Bl+KH(s)]G_m(s)Cs}, \tag{11}$$

with an additional term in the numerator. The insertion of a $KH(s)$ term in the numerator of the original Eq. (11) was again a mistake, possibly the result of copying variable blocks in the Equation Editor. Based on the above corrections, Eq. (12) should be

[a]Electronic mail: liyaoyu@ecn.purdue.edu

$$\eta(\omega)=\frac{A|G_{PV}(s)|(Bl)^2|G_m(s)|^2\cos(\Phi_{PV})}{|1+AG_{PV}(s)G_m(s)||[Ls+R][1+AG_{PV}(s)G_m(s)]+(Bl)^2G_m(s)|\cos(\Phi_{UcI})}. \tag{12}$$

The effects of capacitance on efficiency may be conveniently highlighted based on the following expression for the transfer function between the coil voltage and the coil current:

$$\frac{U_c(s)}{I(s)}=\frac{(Ls+R)[1+AG_{PV}(s)G_m(s)]+(Bl)^2G_m(s)}{1+AG_{PV}(s)G_m(s)},$$

based on the corrected Eq. (11) and Eq. (10). The term $\cos(\Phi_{UcI})$ should not be affected by C, the capacitance. The electrical power is obtained from $U_c(s)$ and $I(s)$. Since the capacitor does not consume any electrical power, using $U_{\text{out}}(s)$ in the place of $U_c(s)$ yields the same electrical power and thus the same efficiency.

The capacitance C was introduced to tune the electrical resonance closer to the operating frequency of the system. The benefit was the amplifier input needed was smaller, and input saturation could be avoided. This naturally brought up the question of whether varying capacitance would also change the driver efficiency. The expression for efficiency, Eq. (13) in Ref. 1, is a convenient way of showing that it cannot. The author's observation that inductors do not consume energy either is of course correct, and fairly obvious (and not too misleading). Inductors and capacitors are both energy storage components, so neither of them should affect electric power in the efficiency calculation. However, the choice of voltage in the power computation can help isolate the effect of capacitor and inductor in the resulting efficiency expression. The analysis in Ref. 1 used the voltage across the coil, i.e., the voltage across the inductor and the resistor of the coil including the back-emf. This quantity is directly measurable, and allows the isolation of the effect of the capacitor. If the voltage across the resistor alone including the back-emf is selected, as in Ref. 2, neither L nor C appear in the efficiency expression. Furthermore this voltage cannot be measured physically.

About the discrepancies between model predictions and experimental data. In Fig. 6 of Ref. 1, the dashed line was the measured curve while the solid was the predicted curve. The legend was omitted by the printer (a legend was provided in the typescript). G_{pv} was obtained by measuring the pressure-to-velocity ratio at the driver within the vessel of the thermoacoustic cooler prototype. Commercially available piezoelectric accelerometers and pressure transducers were used. There are many factors that can contribute to the discrepancies between prediction and measurement, including non-linearity and frequency-dependence as mentioned in Ref. 2, and also the inaccuracy of model parameters. A temporal drift in parameter values was omnipresent, due to mechanical relaxation under load and the deformation of certain components like the springs.

It is important to note that the motivation for the model was not to provide accurate predictions, but to emphasize the following points: (1) the application of a straightforward acoustical feedback scheme based on readily measured pressure, velocity, coil current and voltage alone cannot successfully improve the efficiency of the system in the configuration used in the experiments, as shown by the analysis; (2) the use of a capacitor to alter the input electrical resonance frequency and reduce the required input level from the audio amplifier does not adversely impact efficiency; and (3) the frequency dependency of the driver efficiency peaks sharply, and thus a nontrivial loss of efficiency is possible due to parameter variations, at least for the system used. An in-depth discussion of Fig. 6 was omitted to emphasize the main result of the paper, i.e., the active control study. Consequently, more emphasis was placed on the comparison between the time–domain and the frequency–domain methods of calculating efficiency, as shown in Fig. 4, because of the need for accurate on-line efficiency computations. If analytical models could provide very consistent and accurate predictions of the system behavior, there would be no reason to do feedback control. High fidelity predictions were not expected nor needed for the purposes of the study reported in Ref. 1.

About the importance of tuning for maximum efficiency

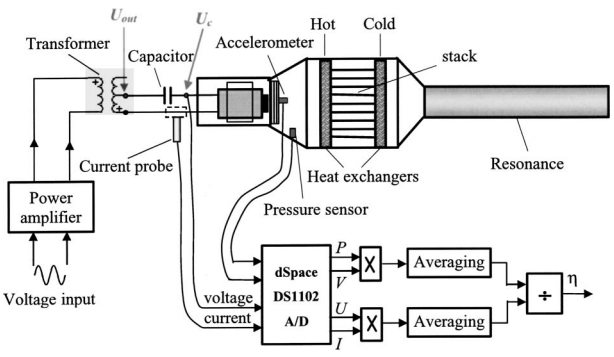

FIG. 1. Modified version of Fig. 1 in Ref. 1 clarifying the definitions of U_c and U_{out}.

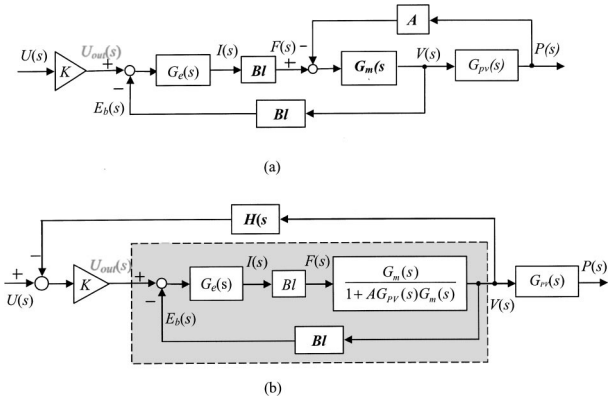

FIG. 2. The modified version of Fig. 5 in Ref. 1. (a) Acoustic driver; and (b) acoustic driver with velocity feedback.

rather than to main acoustic resonance. The emphasis of the research in Ref. 1 was not to find the best spring to maximize driver efficiency. The problem of interest was the following: given a certain driver and a duct (so the setup is frozen), how can the best possible efficiency be maintained. To demonstrate that, it does not matter if the driver is working in an optimized configuration or not. In general, the best achievable efficiency is neither the one that can be obtained after optimizing the duct length for a given driver, nor the one that can be obtained after optimizing the driver stiffness for a given vessel.

Wakeland's equation indeed predicts around 70% optimal efficiency:

$$\eta_{\max}=\frac{\sqrt{\frac{Bl^2}{R_eR_m}+1}-1}{\sqrt{\frac{Bl^2}{R_eR_m}+1}-1}=\frac{\sqrt{\frac{9^2}{0.11\times 25}+1}-1}{\sqrt{\frac{9^2}{0.11\times 25}+1}+1}$$

$$=0.693.$$

The driver's linear parameters, shown in Table 1 of Ref. 1, were measured for the unsprung driver (this can be checked by calculating the undamped natural frequency of the driver, which is about 34 Hz). The measured driver parameters are appropriate only in the vicinity of the driving frequency (34 Hz), and for similar coil displacement amplitude. The electrical resistance increases with the operating frequency due to eddy currents. The parameters R_m and Bl in Table 1 were obtained for much larger piston displacements than for the measurements reported in Ref. 1. After the resonator was assembled with the additional leaf springs, it became clear that the 70% efficiency could not be achieved around the operating frequency.

The term "optimum efficiency" in Ref. 1 therefore refers to the best driver efficiency, 27%, achievable for given driver parameters without optimization. It is much lower than the best achievable efficiency, 70%, because the piston area was too large. A driver efficiency closer to the best achievable efficiency, per the optimization method of Wakeland,[2] would require the piston area to be changed (a major redesign). The objective of the paper, again, was not to optimize the driver parameters to achieve 70% of efficiency but to develop a tool to estimate the driver efficiency online, estimate the equivalent driver parameters, and maintain the best possible efficiency with the hardware available.

It is true that the efficiency bandwidth when the mechanical resonance frequency and the acoustic resonance frequency are very close to each other (i.e., the piston diameter is properly chosen for the target optimal frequency) is relatively broader than when in the situation reported in the study of Ref. 1. The maximum efficiency still occurs slightly off resonance, but the difference between operating at resonance and off resonance could be relatively smaller compared to the situation reported in Ref. 1. This is supported by Fig. 5.8 in Ref. 3, and Fig. 8.2 in Ref. 4. The same trends were also made apparent in our own optimization studies using DeltaE. Note, however, that linear models, nevertheless, predict some performance degradation away from the tuned frequency, and it is reasonable to assume that some adaptive tuning is needed in many circumstances anyway. The case reported in Ref. 1 may represent a "worse case scenario," exacerbating the need for active tuning.

The issue of phase-lock loop versus direct efficiency measurement was discussed. In Ref. 1, the simulation was done for a spring stiffness of 300 kN/m, about four times the nominal stiffness shown in Table I. Using the nominal stiffness did not cause the results to be much different from the results shown in the paper. It would be interesting to find out under what conditions, or for what kind of parameter combination, this discrepancy is significant, and to what extent. It is mentioned that Hofler and other studies have shown an excellent match. This is most likely due to the very good match between driver and duct resonance frequencies. It seems moreso, considering the discussion on the transduction coefficients in the next paragraph. Their transducers were well tuned to have transduction coefficients with a negligible complex component, and the consequence was that their maximum achievable efficiency was very close to the theoretical maximum. The resonance frequency matched that corresponding to the maximum efficiency very well.

The author of the comments is correct in observing that the citation of the following sentence; "*While it is customary to assume that the maximum in efficiency always occurs at 'resonance' a closer examination of Eqs. (4.19) and (4.20) reveals that a still higher efficiency can be obtained for some other value of frequency or reactance than the one for which* $p=0=X_M+X_L$" from Hunt's book[5] is not really appropriate to explain why the maximum efficiency for a certain combination of driver parameters is not at the acoustic resonance frequency. The $X_M+X_L=0$ condition is possible when both X_M and X_L are zero. This occurs when the mechanical and the acoustical resonance frequencies are matched, and the driver is operated at the resonance frequency. The $X_M+X_L=0$ condition is also achieved when $-X_M=X_L$, and at this condition, the driving frequency is neither at the mechanical resonance frequency nor at the acoustic resonance frequency. For both cases, the $p=0=X_M+X_L$ condition is satisfied. The Li *et al.* case corresponds to the condition $-X_M\approx X_L$. This is because the driver parameters are not optimized, and the $-X_M=X_L$ condition cannot be satisfied.

The cited sentence means that the efficiency can be greater when $X_M+X_L=-R_{em}X_{em}/R_e$.

This equation was obtained by setting the derivative of the denominator of the efficiency equation in Hunt's book [Eq. (4.19) or from Eq. (4.20)] to zero. R_{em} and X_{em} in the equation represent the real part and the imaginary part of the force constant, Bl, respectively. This condition is only possible when Bl is complex, as mentioned in Ref. 5.

In summary, the results presented in Ref. 1 are correct despite some unfortunate errors in the equations. Some of the conclusions reached in the same study may not necessarily be generalized to other systems that have been tuned to achieve a greater efficiency. The discussion provided by the author of Ref. 2 helps clarify these points. As the authors of Ref. 2 pointed out that with careful design and matching parameters, one can come very close to the theoretical maxi-

mum efficiency. However, the fact that very careful design and precise parameter matching is needed imply that the maximum efficiency is very sensitive to these system parameters. In actual commercialization of the device, manufacturing tolerance, variations in operating conditions, and component aging will inevitably cause a sub-optimal result. The cost of custom manufacturing custom parts or custom tuning of each device will significantly increase the cost of such a device. We want to stress that the tuning technique presented in Ref. 1 was not developed to replace careful and hardcore understanding and modeling of the process. The tuning technique is to provide options to complement the continuing development of the technology by demonstrating that there are methods to handle variability and uncertainties that are unavoidable in the deployment of such technology.

[1] Y. Li, B. L. Minner, G. T. C. Chiu, L. Mongeau, and J. E. Braun, ''Adaptive tuning of an electrodynamically driven thermoacoustic cooler,'' J. Acoust. Soc. Am. **111**, 1251–1258 (2002).
[2] R. W. Smith, ''Comments on: Adaptive tuning of an electrodynamically driven thermoacoustic cooler,'' submitted to J. Acoust. Soc. Am., 2003.
[3] R. W. Smith, ''High efficiency two kilowatt acoustic source for a thermoacoustic refrigerator,'' Master's thesis, The Pennsylvania State University, 2000.
[4] M. E. H., Tijani, ''Loudspeaker-driven thermo-acoustic refrigeration,'' Ph.D. dissertation, Technische Universiteit Eindhoven, 2001.
[5] F. V. Hunt, *Electroacoustics* (Harvard University Press, Cambridge, MA, 1954).

Sound wave channelling in near-critical sulfur hexafluoride (SF_6)

Stefan Schlamp[a] and Thomas Rösgen
ETH Zürich, Institute of Fluid Dynamics, Switzerland

(Received 13 February 2003; revised 10 December 2003; accepted 23 December 2003)

Strong density and speed of sound gradients exist in fluids near their liquid-vapor critical point under gravity. The speed of sound has an increasingly sharp minimum and acoustic waves are channelled within a layer of fluid. Geometrical acoustic calculations are presented for different isothermal fluid columns of sulfur hexafluoride (SF_6) under gravity using a semiempirical crossover equation of state. More than 40% of the emitted acoustic energy is channelled within a 20 mm high duct at 1 mK above the critical temperature. It is shown how, by changes in temperature, frequency, and gravitational strength, the governing length scales (wavelength, radius of ray curvature, and correlation length of the critical density fluctuations) can be varied. Near-critical fluids allow table-top sound channel experiments. © *2004 Acoustical Society of America.*
[DOI: 10.1121/1.1648319]

PACS numbers: 43.20.Dk, 43.20.Mv, 64.60Fr [RR] Pages: 980–985

NOMENCLATURE

Fluid and equation of state parameters

a	speed of sound
A	Helmholtz free energy
$\tilde{A}_j$	parameters for analytic background of Helmholtz free energy ($j=0,...,4$); see Table I
c, c_ρ, c_t, d_1	scaling field coefficients; see Table I
C_v, C_p	specific heats at constant volume and pressure
M	densitylike order parameter; defined by Eq. (6)
p	pressure
t	temperaturelike order parameter; defined by Eq. (5)
T	Temperature
u	crossover parameter; see Table I
u^*	universal fixed-point coupling constant; see Table I
V	volume
Y	crossover function; defined by Eqs. (9) and (10)
T_c, ρ_c, p_c	temperature, density, and pressure at liquid-vapor critical point; see Table I
χ	susceptibility
κ	proportional to fluctuation-induced portion of the inverse correlation length; defined by Eq. (10)
μ	specific chemical potential
ξ	correlation length of critical density fluctuations
ρ	density
Λ	dimensionless cutoff wave number; see Table I
α_c, ν_c, γ_c, η_c	critical exponents; see Table I
a_05, a_06, a_14, a_22	parameters from classical mean-field theory; see Table I
Δ_S, Δ_A	critical exponents of symmetric and asymmetric correction terms; see Table I
$\tilde{\mu}_j$	parameters for analytic background of chemical potential ($j=0,...,4$); see Table I
$\mathcal{T}$, $\mathcal{D}$, $\mathcal{U}$, $\mathcal{V}$, $\mathcal{K}$	rescaling functions, defined by Eq. (8)

Acoustics parameters

f	frequency of acoustic source
g	constant of gravity ($=9.81$ m/s^2)
h	height of duct ($=20$ mm)
$\hat{\mathbf{n}}$	unit vector perpendicular to wavefront
R, R^+, R^-	range of loop, range of upper/lower cycle section
r	radius of curvature of rays
$r_{\min}$	defined by Eq. (16)
$\mathbf{s}=(s_x,s_y,s_z)$	wave slowness vector ($=\hat{\mathbf{n}}/a$ for fluid at rest)
t	time
$\mathbf{x}=(x,y,z)$	coordinate vector
Y	crossover function; defined by Eqs. (9) and (10)
η	waveguide efficiency
λ	wavelength of acoustic waves ($=a/f$)
τ, τ^+, τ^-	propagation times associated with R, R^+, and R^-

[a]Author to whom correspondence should be addressed; Electronic mail: schlamp@ifd.mavt.ethz.ch

I. INTRODUCTION

Bending of waves occurs when the gradient of the propagation speed in the direction perpendicular to the direction of propagation is nonzero. In this case, the wave bends in the direction of smaller propagation speeds. This is observed at interfaces as well as for smooth gradients. Consider, for example, optical lenses made from glass of smoothly varying index of refraction or the phenomenon of sound shadows after big explosions.[1] Assuming that the speed of wave propagation only varies in one direction and that it has a local minimum, rays can be channelled within a finite material layer. If no such minimum exists, but if the propagation speed decreases towards an interface (e.g., water surface) then the waves are reflected at the interface and channelling is possible, where the interface represents one boundary of the wave channel. Wave channelling purely by means of reflection (e.g., in an optical fiber) is also possible. Waveguides involving the reflection from an interface are not considered as wave channelling devices for the purpose of this work. Interest in sound wave channelling has mostly focused on underwater sound propagation in the context of long-range communication,[2–5] submarine detection and detection avoidance, and global temperature sounding.[6] Pedersen *et al.*[7,8] examine a range of sound speed profiles, both generic and from measured data in the Pacific.

Critical phenomena in fluids, i.e., the behavior of fluids in the vicinity of the vapor-liquid critical point, have gained a lot of interest in physics and thermodynamics. Near the critical point, many thermodynamic properties, such as the isothermal compressibility, diverge. At the same time, the correlation length of the density fluctuations, which normally is microscopic, becomes macroscopic, causing the phenomenon of critical opalescence when the correlation length becomes comparable to the wavelength of visible light. Since the isothermal compressibility tends to infinity when approaching the critical point, the fluid collapses under its own weight in the presence of gravity. Very steep density gradients over short vertical distances (10% over 1 mm; also see Fig. 1) result. Along with the density profile goes a variation of the speed of sound. An increasingly sharp minimum is observed near the point where the density equals the critical density as one approaches the critical temperature [Fig. 2(a)].

In the present work, numerical results are presented for SF_6. This choice is motivated by several factors: First, by the availability of a suitable equation of state, second, by the experimentally convenient location of the critical point (see Table I), and last by the availability of SF_6 in good purities due to its applications in the semiconductor industry. Xenon and CO_2 are similarly popular for experiments with near-critical fluids, but adequate equations of state for these fluids are not available to date.

II. SETUP AND PROCEDURE

A. Setup

A duct of height $h=20\,\mathrm{mm}\,(z=-10\ldots+10\,\mathrm{mm})$ is considered, which is filled with near-critical, isothermal, pure sulfur hexafluoride (SF_6). Due to gravity and the large compressibility, a density and consequently a speed of sound profile develops in the duct. By choosing the average density in the duct such that $a(+10\,\mathrm{mm})=a(-10\,\mathrm{mm})$ and by placing the acoustic point source at the sound speed minimum, the waveguide efficiency is maximized. The walls of the test duct are assumed to be perfectly absorbing, i.e., wave reflections are neglected.

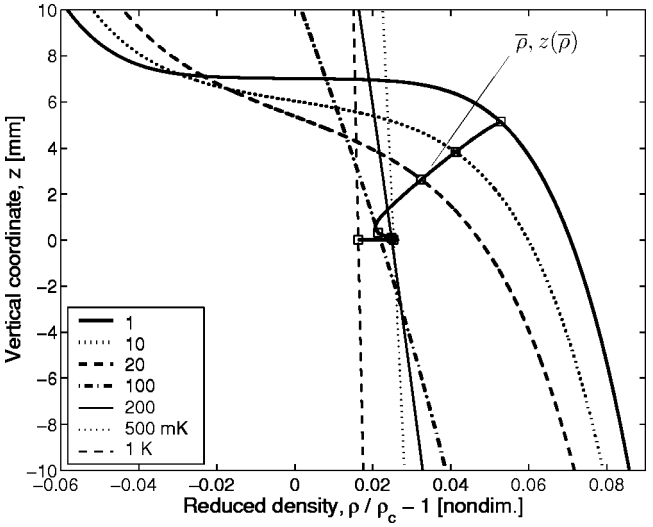

FIG. 1. Density profiles in isothermal fluid columns of near-critical SF_6 under gravity for different temperatures above T_c. The average density is chosen such that $a(-10\,\mathrm{mm})=a(+10\,\mathrm{mm})$ [see Fig. 2(a)]. The symbols mark the average density in the duct and the location at which it is equal to the local density.

B. Equation of state

Critical phenomena are not captured by analytical equations of state. Wyczalkowska *et al.*[9] propose a semiempirical equation of state for SF_6, which shows the correct singular behavior near the critical point (including the correct critical exponents) and crosses over smoothly to regular thermody-

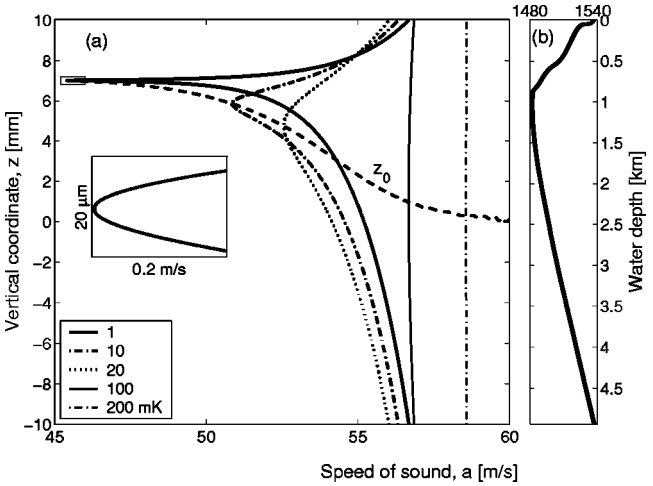

FIG. 2. (a) Left, speed of sound profiles in isothermal fluid columns of near-critical SF_6 under gravity for different temperatures above T_c. The dashed line labeled z_0 connects the sound speed minima. The inset shows a magnification of the minimum for $T-T_c=1\,\mathrm{mK}$ in the range $z=\pm 20\,\mu\mathrm{m}$; (b) right, Sound speed profile in the Pacific ocean after Pedersen *et al.* (Ref. 8). The two panels are drawn such that the relative scales for the speed of sound match (with respect to the sound speed at the panel centers).

TABLE I. Parameters for equation of state (adopted from Wyczalkowska *et al.*[9]). The first two caloric background coefficients only influence the zero of energy and entropy.

Critical point		T_c	318.717	K
		ρ_c	742	kg/m^3
		p_c	3.7545	MPa
Crossover parameters			$\overline{u}$	0.500 43
			Λ	0.806 21
Scaling field parameters			c_t	1.737 90
			c_ρ	2.400 61
			c	−0.069 04
			d_1	−0.792 71
Classical parameters			a_{05}	0.168 38
			a_{06}	0.732 51
			a_{14}	0.550 23
			a_{22}	1.226 24
Critical exponents				
ν_c	α_c	γ_c	Δ_S	Δ_A	u^*
0.630	0.110	1.239	0.51	1.32	0.472
Equation of state and caloric background parameters					
j	0	1	2	3	4
$\tilde{A}_j$	−1	−6.064 33	7.715 01	−3.085 01	6.700 90
$\tilde{\mu}_0$	N/A	N/A	−34.212 10	0.373 34	−59.998 10

namic behavior away from the critical point. Results as they are relevant for the present work are summarized here. For a more detailed derivation, the reader is referred to Ref. 9.

Nondimensionalize the density, temperature, chemical potential μ, Helmholtz free energy A, the heat capacities C_p and C_v, and the susceptibility χ by

$$\tilde{\rho}=\rho/\rho_c, \quad \tilde{T}=-T_c/T,$$
$$\tilde{\mu}=\frac{\rho_c T_c}{p_c}\frac{\mu}{T}, \quad \tilde{A}=\frac{T_c}{p_c}\frac{A}{VT}, \tag{1}$$
$$\tilde{C}_{p,v}=\frac{T_c}{p_c}\frac{C_{p,v}}{V}, \quad \tilde{\chi}=\frac{\partial\tilde{\rho}}{\partial\tilde{\mu}}\bigg|_T.$$

The Helmholtz free energy and the chemical potential are expressed in terms of an analytic background $\tilde{A}_0$ and $\tilde{\mu}_0$, respectively, and a critical part $\Delta\tilde{A}$ and $\Delta\tilde{\mu}$, respectively,

$$\tilde{A}=\Delta\tilde{A}+\tilde{\rho}\tilde{\mu}_0(\Delta\tilde{T})+\underbrace{\sum_{j=0}^{4}\tilde{A}_j(\Delta\tilde{T})^j}_{\tilde{A}_0(\Delta\tilde{T})}, \tag{2}$$

$$\tilde{\mu}=\underbrace{\frac{\partial\Delta\tilde{A}}{\partial\Delta\tilde{\rho}}\bigg|_{\Delta\tilde{T}}}_{\Delta\tilde{\mu}}+\underbrace{\sum_{j=0}^{4}\tilde{\mu}_j(\Delta\tilde{T})^j}_{\tilde{\mu}_0(\Delta\tilde{T})}, \tag{3}$$

where $\Delta\tilde{\rho}=\tilde{\rho}-1$ and $\Delta\tilde{T}=\tilde{T}+1$. The constants $\tilde{A}_j$ and $\tilde{\mu}_j$ are obtained from a fit to experimental data. They are given in Table I, which also contains the parameters which will be introduced subsequently.

The critical part of the Helmholtz free energy is given by

$$\Delta\tilde{A}=\Delta\tilde{A}_x-c\frac{\partial\Delta\tilde{A}_x}{\partial M}\bigg|_t\frac{\partial\Delta\tilde{A}_x}{\partial t}\bigg|_M, \tag{4}$$

where

$$t=c_t\Delta\tilde{T}+c\frac{\partial\Delta\tilde{A}_x}{\partial M}\bigg|_t, \tag{5}$$

$$M=c_\rho(\Delta\tilde{\rho}-d_1\Delta\tilde{T})+c\frac{\partial\Delta\tilde{A}_x}{\partial t}\bigg|_M, \tag{6}$$

are temperaturelike and densitylike order parameters and

$$\Delta\tilde{A}_x=\frac{1}{2}tM^2\mathcal{T}\mathcal{D}+\frac{u^*\overline{u}\Lambda}{24}M^4\mathcal{D}^2\mathcal{U}+\frac{1}{60}a_{05}M^5\mathcal{D}^{5/2}\mathcal{V}\mathcal{U}$$
$$+\frac{1}{360}a_{06}M^6\mathcal{D}^3\mathcal{U}^{3/2}+\frac{1}{24}a_{14}tM^4\mathcal{T}\mathcal{D}^2\mathcal{U}^{1/2}$$
$$+\frac{1}{4}a_{22}t^2M^2\mathcal{T}^2\mathcal{D}\mathcal{U}^{-1/2}-\frac{1}{2}t^2\mathcal{K}. \tag{7}$$

$\mathcal{T}$, $\mathcal{D}$, $\mathcal{U}$, $\mathcal{V}$, and $\mathcal{K}$ are rescaling functions defined as

$$\mathcal{T}=Y^{(2\nu_c-1)/\Delta_S}, \quad \mathcal{D}=Y^{-\eta_c\nu_c/\Delta_S}, \quad \mathcal{U}=Y^{\nu_c/\Delta_S},$$
$$\mathcal{V}=Y^{(\Delta_A-\nu_c/2)/\Delta_S}, \quad \mathcal{K}=\frac{\nu}{\alpha_c\overline{u}\Lambda}(Y^{-\alpha_c/\Delta_S}-1). \tag{8}$$

η_c is related to the other critical exponents (see Table I) by $\eta_c=2-\gamma_c/\nu_c$. Y is the crossover function, which is found by solving the coupled algebraic equations

$$1-(1-\overline{u})Y=\overline{u}Y^{\nu_c/\Delta_S}\left(1+\left(\frac{\Lambda}{\kappa}\right)^2\right)^{1/2}, \tag{9}$$

$$\kappa^2=t\mathcal{T}+\frac{u^*\overline{u}\Lambda}{2}M^2\mathcal{D}\mathcal{U}+\frac{1}{6}a_{05}M^3\mathcal{D}^{3/2}\mathcal{V}\mathcal{U}$$
$$+\frac{1}{24}a_{06}M^4\mathcal{D}^2\mathcal{U}^{3/2}+\frac{1}{2}a_{14}tM^2\mathcal{T}\mathcal{D}\mathcal{U}^{1/2}$$
$$+\frac{1}{2}a_{22}t^2\mathcal{T}^2\mathcal{U}^{-1/2}. \tag{10}$$

The pressure and the speed of sound are related to the chemical potential and the Helmholtz free energy by

$$\tilde{p}=\tilde{\rho}\tilde{\mu}-\tilde{A}, \tag{11}$$

$$\tilde{a}=\left(\frac{\tilde{\rho}}{\tilde{\chi}}\frac{\tilde{C}_p}{\tilde{C}_v}\right)^{1/2}, \tag{12}$$

with

$$\frac{\tilde{C}_v}{\tilde{T}^2}=-\frac{d^2\tilde{A}_0(\tilde{T})}{d\tilde{T}^2}-\tilde{\rho}\frac{d^2\tilde{\mu}_0(\tilde{T})}{d\tilde{T}^2}-\frac{\partial^2\Delta\tilde{A}}{\partial\Delta\tilde{T}^2}\bigg|_{\Delta\tilde{\rho}}, \tag{13}$$

$$\tilde{C}_p=\tilde{C}_v+\frac{\tilde{\chi}}{\tilde{\rho}^2}\left(\tilde{p}-\tilde{T}\frac{\partial\tilde{p}}{\partial\tilde{T}}\bigg|_{\tilde{\rho}}\right)^2. \tag{14}$$

For the purpose of this work, only the relationships $p(\rho,T)$ and $a(\rho,T)$ are used. The relationship $\rho(p,T)$ is implemented by iteratively solving $p(\rho,T)$.

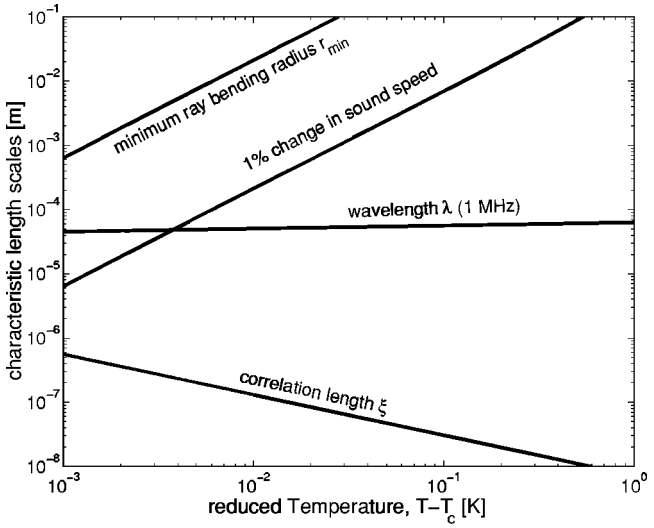

FIG. 3. Relevant characteristic length scales for an acoustic source with $f=1$ MHz located in an isothermal fluid column (height $h=20$ mm) of near-critical SF_6 at the sound speed minimum. The acoustic wavelength is at least two orders of magnitude larger than the correlation length of the critical fluctuations and at least one order smaller than the minimum ray bending radius. For reference, the minimum vertical distance over which the speed of sound changes by 1% is shown.

C. Geometrical acoustics

Geometrical acoustics assumes that the radius of curvature of rays is much larger than the wavelength and that the amplitude does not change significantly over the same length scale. These assumptions simplify the general solution of the wave equation. For rays in an inhomogeneous medium at rest, one finds[1]

$$\frac{d\mathbf{s}}{dt}=-\frac{1}{a}\nabla a \quad \text{and} \quad \frac{d\mathbf{x}}{dt}=a^2\mathbf{s}, \tag{15}$$

where $\mathbf{s}=(s_x,s_y,s_z)=\hat{\mathbf{n}}/a$ denotes the wave slowness and a is the local speed of sound.

For a given temperature, the smallest possible radius of curvature of a ray is

$$r_{\min}=\min_{|z|\leqslant 10\ \mathrm{mm}}\left\{\frac{a}{da/dz}\right\}, \tag{16}$$

which is observed for a ray perpendicular to the sound speed gradient. In order for the geometrical limit to be applicable, this length scale has to be much larger than the wavelength of the acoustic waves, $r_{\min}\gg\lambda$. The correlation length of the critical density fluctuations on the critical isochore is[9]

$$\xi=\xi_0^+\left|\frac{T}{T_c}-1\right|^{-\nu_c}, \quad \rho=\rho_c, \quad T>T_c \tag{17}$$

with $\xi_0^+=0.19$ nm and $\nu_c=0.630$. This neglects the limiting effect of gravity. When $\lambda\gg\xi$, then the diffraction of the acoustic waves at the critical fluctuations is negligible. The wavelength can be adjusted by varying the driving frequency of the transducer. Figure 3 shows the characteristic length scales for the case $f=1$ MHz. The wavelength satisfies both conditions, namely $\lambda\gg\xi$ and $\lambda\ll r_{\min}$. Mueller *et al.*[10] and examine ultrasonic attenuation in near-critical xenon. Kogan *et al.*[11] present experimental results on critical attenuation and dispersion in He-3 and He-4. No such data exists for sulfur hexafluoride. Onuki[12] reviews some theoretical concepts of critical sound attenuation. It is assumed that attenuation does not invalidate the assumption of ray acoustics.

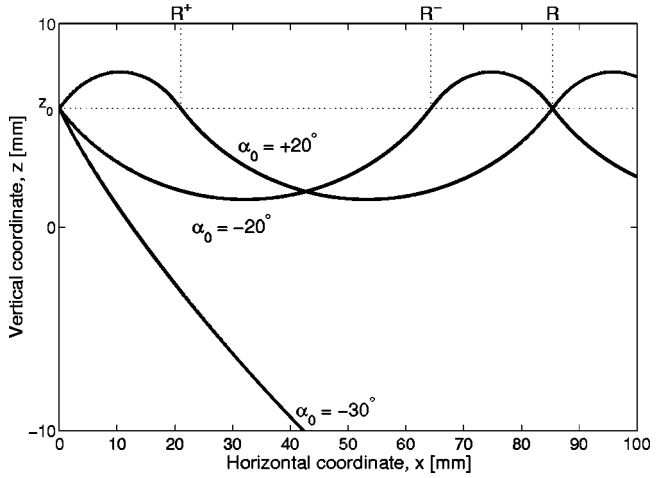

FIG. 4. Rays emanating with different initial ray angles from an acoustic point source located at the sound speed minimum in isothermal, near-critical SF_6 at $T-T_c=10$ mK under gravity. Reflections from the duct boundaries are not considered.

D. Numerical integration of the ray equations

Density profiles are calculated iteratively for a range of temperatures. Initially, they span a range of z values, which is much larger than the duct height. A uniform density is used as starting value, from which a vertical pressure distribution is obtained by integration in z direction. An improved density profile then follows from the equation of state. This procedure converges after a few iterations. The sound speeds corresponding to the density profile are calculated subsequently from the equation of state. Finally, a 20 mm section of the profile is extracted, for which $a(-10\,\mathrm{mm})=a(+10\,\mathrm{mm})$. Integrating the densities over this section yields the average density $\overline{\rho}$.

Given speed of sound profiles, the ray equations (15) are integrated numerically using a fifth order Runge–Kutta scheme (Dormand–Prince pair).[13] Initial conditions

$$\mathbf{x_0}=(0,0,z_0) \quad \text{and} \quad \mathbf{s_0}=(\cos\alpha_0/a(z_0),0,\sin\alpha_0/a(z_0)) \tag{18}$$

are used to calculate rays originating at different initial ray angles α_0 from a source at z_0, the location of the sound speed minimum. Figure 4 shows a few representative rays for the case $T-T_c=10$ mK.

III. RESULTS

Figure 1 depicts the calculated density profiles for isothermal sulfur hexafluoride under gravity ($g=9.81\,\mathrm{m/s^2}$). For temperatures away from the critical point, the density varies linearly with the vertical coordinate. When the temperature approaches T_c, the range of densities increases and the profile becomes nonlinear. The total density variation over 20 mm increases from 0.24% for $T-T_c=1$ K to 14.4% for $T-T_c=1$ mK, where an increasing fraction of the

total density variation is limited to an increasingly narrow region. For $T-T_c=1$ mK, for example, the density varies by 10% over 1 mm.

Given a temperature, the vertical shift of the density profiles in Fig. 1 is controlled by the average density $\overline{\rho}$ in the duct. It is found from the condition that $a(-10\,\mathrm{mm})=a(+10\,\mathrm{mm})$. The symbols in Fig. 1 mark the results for $\overline{\rho}$ and the location where $\overline{\rho}=\rho$. In an experiment one would fill the test section with the appropriate average density and then equilibrate the duct at the desired temperature, which can take hours or even days, depending on the temperature and the size of the fluid volume.

The sound speed profiles, which provide the vertical reference for the density profiles, are shown in Fig. 2(a) for a selection of temperatures. The sound speeds generally increase with increasing temperature and an increasingly sharp minimum develops as one approaches the critical temperature from above. As required, the speeds of sound at the top and bottom of the duct are identical. Due to the global properties of the sound speed profile (no local maxima), this places the local sound speed minimum within the duct. The dashed line connects the location of the sound speed minima. Since the acoustic point source is located at the sound speed minimum, its location is used as one of the initial conditions for Eqs. (15) and is therefore denoted by z_0. The sound speed profiles are not symmetric with respect to the minima, which are thus off center. For $T-T_c=1$ mK, for example, the sound speed minimum is located at $z=+7$ mm. For larger reduced temperatures, the location of the minimum approaches the center line. The inset in Fig. 2(a) shows a magnification of the sound speed minimum for $T-T_c=1$ mK. The minimum is not a cusp, but smooth and numerically well resolved. Figure 2(b) shows the speed of sound variation vs depth below MSL at a point in the Pacific Ocean for comparison.[8] The horizontal scales and panel sizes in Figs. 2(a) and (b) are chosen such that the relative variation of the speed of sound is preserved. The total variation is approximately 4% over 4700 m. The same variation is achieved over 20 mm in near-critical SF_6 at a temperature of $T-T_c=31$ mK.

Figure 3 shows plots of the relevant length scales. The acoustic wavelength (assuming a frequency of 1 MHz) increases by 40% between $T-T_c=1$ K and 1 mK. The correlation length of the critical density fluctuation ξ and the minimum ray bending radius $r_{\min}$ depend more strongly on the temperature. ξ increases by almost two orders of magnitude as one approaches T_c. Over the same range of temperatures, $r_{\min}$ decreases by more than six orders of magnitude. For all temperatures under consideration, the requirements for geometrical acoustics to be applicable, $\xi \ll \lambda$ and $r_{\min} \gg \lambda$, is satisfied. Also plotted in Fig. 3 is the minimum vertical distance over which the speed of sound varies by 1%.

Some example results of the numerically integrated ray equations are shown in Fig. 4. The temperature is $T-T_c=10$ mK. For initial angles $\alpha_{0,\min} \leqslant \alpha_0 \leqslant \alpha_{0,\max}$, rays can propagate within $|z| \leqslant 10$ mm. Because $a(10\,\mathrm{mm})=a(-10\,\mathrm{mm})$, $\alpha_{0,\max}=-\alpha_{0,\min}$ by construction. Rays with $|\alpha_0|>\alpha_{0,\max}$ hit the upper or lower duct boundary as shown in Fig. 4 for the ray with $\alpha_0=-30°$. For channelled rays,

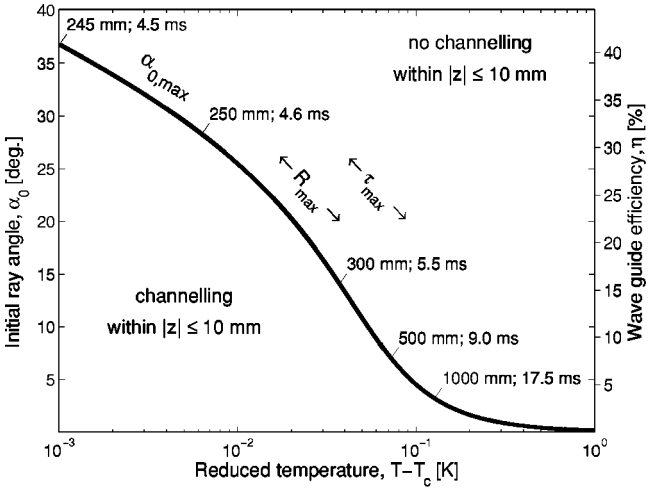

FIG. 5. Maximum initial ray angle $\alpha_{0,\max}=-\alpha_{0,\min}$ for ray channelling to occur in 20 mm of isothermal, near-critical SF_6 under gravity. The numerical values represent ranges and corresponding loop times for $\alpha_0=\alpha_{0,\max}$. The scale on the right shows the corresponding channelling efficiency.

the length of a ray loop is referred to as range $R=R^+ +R^-$,[8] where R^+ and R^- are the ranges of the ray loop above and below z_0, respectively. The propagation times over one loop is denoted by τ. Like the sound speed profiles, the waves are not symmetric with respect to $z=z_0$. By construction, however, the range is independent of the sign of α_0.

Snell's law applied to the current example is[7]

$$\cos \alpha_{0,\max}=\frac{a_{\min}}{a_{\max}}=\frac{a(z_0)}{a(10\ \mathrm{mm})}. \tag{19}$$

The maximum initial ray angles as function of the temperature are plotted in Fig. 5. The fraction of acoustic energy channelled within the duct out of the total emitted energy is the waveguide efficiency η. It is

$$\eta=\frac{2\alpha_{0,\max}}{180°}. \tag{20}$$

The scale for the waveguide efficiency is plotted in the secondary vertical axis on the right of Fig. 5. $\alpha_{0,\max}$ does not seem to level off as one approaches T_c. At a reduced temperature of 1 mK, $\alpha_{0,\max}=36.8°$. This value drops to 25.5° and 4.55° for $T-T_c=10$ mK and 100 mK, respectively. Corresponding to $\alpha_{0,\max}(T)$ is a range $R_{\max}$ and a run time of the acoustic waves over one loop $\tau_{\max}$. Some typical values are given in Fig. 5. Initially the range $R_{\max}$ increases very slowly with increasing reduced temperature. It only doubles (from 245 mm to 500 mm) over almost two orders of magnitude in $T-T_c$ (1 mK to 70 mK), but doubles again between 70 mK and 110 mK.

IV. CONCLUSIONS

The effect of dispersion, which is observed near the critical point,[14–18] has been neglected in the present analysis. The definition of the speed of sound is the limit for zero frequency, which is the speed of sound given by the equation of state. The sound speed profiles for higher frequencies might therefore be different from those shown in Fig. 2. Dy-

TABLE II. The three characteristic length scales (wavelength λ, radius of curvature r, and correlation length ξ) are influenced by the reduced temperature $T-T_c$, the frequency f, and the level of gravity g.

			Wavelength λ	Radius of curvature r	Correlation length ξ
Reduced temperature	$T-T_c$	↑	↑	↑	↓
Frequency	f	↑	↓	?	—
Gravity	g	↑	—	↑	↑

namic critical phenomena are an active area of research and an equation of state providing the speed of sound as function of the thermodynamic variables as well as frequency is not yet available. Likewise, and for the same reason, attenuation has not been considered. The results presented should therefore only be taken as qualitative rather than quantitative. The form of the variations in density and the sound speed along isotherms near the critical point is universal. Other fluids will show the same qualitative behavior. Intramolecular vibrations strongly influence the dispersion relationship such that the speed of sound profiles at a given frequency is fluid dependant.

From Fig. 3 one sees that the three characteristic length scales (wavelength, correlation length, and ray bending radius) become comparable for even smaller reduced temperatures. Interactions between acoustic waves and the critical density fluctuation become significant for $\lambda/\xi=\mathcal{O}(1)$. A smooth transition away from geometrical acoustics can be observed for $r/\lambda=\mathcal{O}(1)$. The length scales can be controlled by the temperature, gravity, and frequency. These effects are summarized qualitatively in Table II. Increasing the temperature, for example, and leaving all other parameters unchanged results (a) in a larger wavelength, because the speed of sound increases with increasing temperature, (b) in a larger radius of curvature through smaller speed of sound gradients, and (c) in a reduced correlation length by being further away from the critical point. The frequency, on the other hand, primarily only impacts the wavelength. Its influence on r by means of dispersion (frequency-dependent sound speed profiles) is not clear. The formation of the density gradients is driven by gravity. In a reduced-gravity environment, these profiles are more uniform and the radius of curvature of the rays is thus larger. Furthermore, very close to the critical point gravity limits the correlation length to approximately 2 μm on earth,[19] but much larger values can be achieved in low-g experiments.

The combination of the two areas of research, wave channelling and critical phenomena, makes it possible to study the former using table-top facilities. Acoustics, on the other hand, can be used to study critical phenomena. While not discussed here, it can be shown that caustics exist for the sound speed profiles shown in Fig. 2. Acoustics could thus be used to introduce local energy disturbances into near-critical fluids. Another application is to use acoustic wave propagation to study the statistics of the critical density and sound speed fluctuations, e.g., as outlined by Ostashev for fluids with random inhomogeneities.[20] Analogous to other tomographic techniques, an experimental setup with several ultrasonic transducers and receivers could yield the sound speed profile within a test section by means of an appropriate reconstruction algorithm.

[1] A. D. Pierce, *Acoustics—An Introduction to Its Physical Principles and Applications* (McGraw-Hill, New York, 1981).
[2] A. G. Bessios and F. M. Caimi, "High-rate wireless data communications: An underwater acoustic communications framework at the physical layer," Math. Problems Eng. **2**, 449–485 (1996).
[3] D. N. Dutt, "Ray transmission in coastal sea using nonlinear velocity profiles," J. Sound Vib. **157**, 538–544 (1992).
[4] D. E. Weston and P. B. Rowlands, "Guided acoustic waves in the ocean," Rep. Prog. Phys. **42**, 347–387 (1979).
[5] W. H. Munk, "Sound channel in an exponentially stratified ocean, with application to SOFAR," J. Acoust. Soc. Am. **55**, 220–226 (1974).
[6] J. A. Schröder, E. R. Westwater, P. T. May, and L. M. McMillin, "Prospects for temperature sounding with satellite and ground-based RASS measurements," J. Atmos. Ocean. Technol. **8**, 506–513 (1991).
[7] M. A. Pedersen, "Ray theory applied to a wide class of velocity functions," J. Acoust. Soc. Am. **43**, 619–634 (1968).
[8] M. A. Pedersen and D. White, "Ray theory for sources and receivers on an axis of minimum velocity," J. Acoust. Soc. Am. **48**, 1219–1248 (1970).
[9] A. K. Wyczalkowska and J. V. Sengers, "Thermodynamic properties of sulfur hexafluoride in the critical region," J. Chem. Phys. **111**, 1551–1560 (1999).
[10] P. E. Mueller, R. C. Williams, D. Eden, and C. W. Garland, "Ultrasonic attenuation and dispersion in xenon near its critical point," Phys. Rev. A **6**, 2272 (1972).
[11] A. B. Kogan and H. Meyer, "Sound propagation in He-3 and He-4 above the liquid-vapor critical point," J. Low Temp. Phys. **110**, 899–918 (1998).
[12] A. Onuki, "Dynamic equations and bulk viscosity near the gas-liquid critical point," Phys. Rev. E **55**, 403–420 (1997).
[13] J. R. Dormand and P. J. Prince, "A family of embedded Runge–Kutta formulae," J. Comput. Appl. Math. **6**, 19–26 (1980).
[14] H. Z. Cummins and H. L. Swinney, "Dispersion of the velocity of sound in xenon in the critical region," Phys. Rev. Lett. **25**, 1165–1169 (1970).
[15] D. Eden, C. W. Garland, and J. Thoen, "Sound absorption and dispersion along the critical isochore in xenon," Phys. Rev. Lett. **28**, 726–729 (1972).
[16] J. Thoen and C. W. Garland, "Sound absorption and dispersion as a function of density near the critical point of xenon," Phys. Rev. A **10**, 1311–1327 (1974).
[17] R. Span, E. W. Lemmon, R. T. Jacobsen, W. Wagner, and A. Yokozeki, "A reference equation of state for the thermodynamic properties of nitrogen for temperatures from 63.151 to 1000 K and pressures to 2200 MPa," J. Phys. Chem. Ref. Data **29**, 1361–1433 (2000).
[18] M. F. C. Gomez and J. P. M. Trusler, "The speed of sound in nitrogen at temperatures between $T=250$ K and $T=350$ K and at pressures up to 30 MPa," J. Chem. Thermodyn. **30**, 527–534 (1998).
[19] M. Moldover, J. Sengers, R. Gammon, and R. Hocken, "Gravity effects in fluids near the gas-liquid critical point," Rev. Mod. Phys. **51**, 79–99 (1979).
[20] V. E. Ostashev, "Sound-propagation and scattering in media with random inhomogeneities of sound speed, density and medium velocity," Waves Random Media **4**, 403–428 (1994).

Multiple scattering in single scatterers

Liang-Wu Cai[a)]
Department of Mechanical and Nuclear Engineering, 331 Rathbone Hall, Kansas State University, Manhattan, Kansas 66506

(Received 26 March 2003; revised 7 November 2003; accepted 1 December 2003)

Scattering by a multilayered scatterer is analyzed via a novel multiple-scattering approach. Based on the recognition that multiple scattering occurs within single scatterers having internal interfaces, the solution procedure follows the physical process, and yields analytically exact solutions. A simple two-layered scatterer subjected to SH incident waves is used to illustrate the detailed solution procedure. The solution is then verified by a two-layered circular cylindrical scatterer, whose exact analytical solution has previously been obtained by the author [J. Acoust. Soc. Am. (2004)]. The proposed approach opens new ways for analyzing scatterers of more complicated geometrical and physical compositions. © *2004 Acoustical Society of America.* [DOI: 10.1121]

PACS numbers: 43.20.Gp, 43.20.Fn, 43.40.Fz [GCG] Pages: 986–995

I. INTRODUCTION

Scattering of elastic waves by single scatterers has been one of the major topics of study in wave motions since it holds a key to understanding various wave propagation phenomena in solid materials and structures. Analyses of scattering by single scatterers of simple shapes have been classical examples in many textbooks and monographs (see, e.g., Pao and Mow, 1971; Graff, 1975). Many approximation methods and techniques have been developed for analyzing geometrically more complicated scatterers. They include Waterman's *T*-matrix method, boundary element method, Sommerfeld-Watson transformation method, Born approximation method, resonant scattering theory, etc. Interested readers are referred to an excellent review by Datta (1978) and a more recent review by Hackman (1993).

Scattering by single scatterers is also the basis for analyses of scattering by multiple scatterers, which is often referred to as multiple scattering. For example, one of the assumptions in the multiple-scattering theory of Cai and Williams (1999a) is that the solutions to single-scatterer problems for all scatterers are assumed to be known. A single-scatterer problem is defined as a single scatterer embedded in the same infinite medium as in the multiple-scatterer problem. The importance of the solutions to single-scatterer problems is further demonstrated by the so-called *scatterer polymerization methodology* (Cai and Williams, 1999a) in which an assemblage of scatterers is mathematically transformed into a single abstract scatterer. This transformation paves the way for analyzing multiple-scattering problems involving large numbers of scatterers (Cai and Williams, 1999b).

Multiple scattering usually occurs in settings in which multiple scatterers are present in the field. However, in a strict sense, multiple scattering refers to a process in which a scattered wave is further scattered. The scatterer that causes the further scattering can be the same scatterer that causes the initial scattering. In such a scenario, multiple scattering also occurs in problems involving only one single scatterer. Figure 1 schematically illustrates the multiple scattering that occurs within a scatterer having an internal delineative interface, which is often referred to as a multilayered scatterer.

Scattering by single multilayered scatterers has been studied extensively for the past few decades. Most of the solved problems involved simple geometric shapes. The separation of variables method, also known as normal mode expansion method, has been used by Akay (1991), Sinclair and Addison (1993), Mal and Yang (1994), Bogen and Hinders (1994), Huang *et al.* (1995), Yim and Williams (1995), Nozaki and Shindo (1998), and Cai (2004) for various multilayered concentric circular cylindrical scatterers and by Gerard (1983), Schmidt (1993), Sato and Shindo (2003), and Videen (2003) for multilayered spherical shells. Among them, Huang *et al.* (1995) proposed using a transfer matrix that relates the displacements on two surfaces across a layer as an iteration mechanism to treat scatterers of arbitrary number of layers. Shindo and Niwa (1996) proposed a recursive process based on directly solving the boundary conditions. Videen (2003) solved a scattering of spherical scatterer, along with a source, eccentrically located inside another sphere.

For scatterer shapes that are unsolvable via the separation of variables method, the surface integral equation method usually serves as a starting point, and various approximations are made in the process of evaluating individual integrals. Using this approach, DeSanto (1980) obtained a formalism for a three-layered cylindrical scatterer of an arbitrary cross-section; Peterson and Ström (1975), Pillai *et al.* (1983), and Olsson *et al.* (1990) obtained formalisms in the framework of Waterman's *T*-matrix method for two-layered cylindrical scatterers of arbitrary cross-sections, and obtained numerical results for simpler shapes such as spheres or elliptic cylinders. In particular, Peterson and Ström (1975) used the multiple scattering mechanism to interpret some terms that appeared in their formulation.

In this paper, a novel method for analyzing the scattering by single scatterers having internal delineative interfaces is proposed, based on the recognition that multiple scattering

a)Electronic mail: cai@ksu.edu

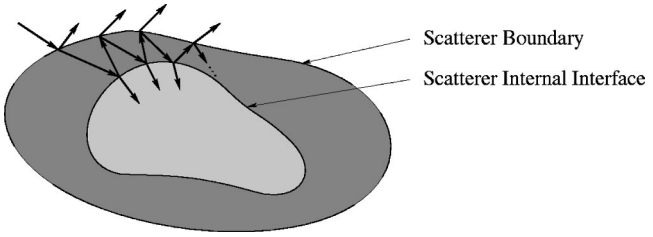

FIG. 1. Schematic of multiple scattering process in single scatterer.

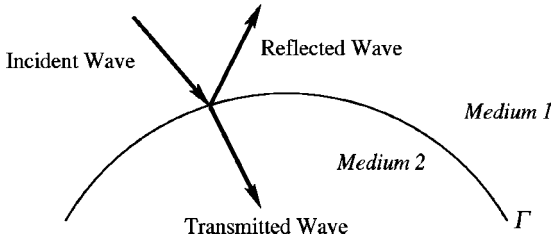

FIG. 2. First canonical problem.

occurs within such single scatterers. Following the physical process, the solution procedure is illustrated by an example of a two-layered cylindrical scatterer in two-dimensional space. The proposed method yields analytically exact solutions, and, in the mean time, has provisions to accommodate approximations when necessary. Numerical results for a two-layered concentric circular cylindrical scatterer, whose exact analytical solution has been obtained previously by the author (Cai, 2004), show that such multiple scattering does indeed physically exist in single scatterers and the associated mathematical description is exact.

II. TWO CANONICAL PROBLEMS

Without loss of generality, consider a two-dimensional problem configuration in which a cylindrical scatterer is embedded in an unbounded medium. Consideration is restricted to the so-called anti-plane strain problems, also known as SH wave problems, in which the scatterer is perpendicular to the plane in which the waves propagate. Assume the unbounded medium is homogeneous and linearly elastic, and the scatterer is either homogeneous and linearly elastic, rigid, or void such that the problem is linear. The only nontrivial displacement component is the out-of-plane displacement, denoted as w.

The scattering of an incident SH wave by such a multilayered scatterer is analyzed with the aids of two canonical problems. The canonical problems serve as mathematical descriptions of essential wave-interface interactions in the multiple scattering process that occurs in a multilayered scatterer.

Each canonical problem involves one incident wave and two homogeneous media that are separated by a closed interface Γ. The medium outside the enclosure of Γ is denoted as *medium 1*, and the medium enclosed by Γ is denoted as *medium 2*. Mathematical description of each canonical problem is facilitated by a polar coordinate system (r,θ), whose origin is located within the enclosure of Γ.

In the steady state, the displacement in either medium can be written as

$$w(r,\theta,t)=\phi(r,\theta)\mathrm{e}^{-\hat{i}\omega t}, \tag{1}$$

where $\hat{i}=\sqrt{-1}$, ω is the circular frequency, ϕ is the complex amplitude of the displacement that satisfies the following Helmholtz equation

$$\nabla^2\phi+k^2\phi=0, \tag{2}$$

and k is the wave number in the medium in question.

In the polar coordinate system (r,θ), the general solution for the Helmholtz equation is the so-called cylindrical wave functions, which consist of Bessel functions as the spatial factor and simple harmonics as the angular factor (Pao and Mow, 1971).

The following forms of cylindrical wave functions are often used: $J_n(kr)\mathrm{e}^{\hat{i}n\theta}$ can be used in any problem domain since the Bessel function of the first kind $J_n(\cdot)$ is nonsingular throughout the plane; $Y_n(kr)\mathrm{e}^{\hat{i}n\theta}$ is only suitable for describing waves in regions that exclude the origin, since the Bessel function of the second kind $Y_n(\cdot)$ is singular at the origin. Alternatively, Hankel functions, which are combinations of Bessel functions of both kinds, can be used in place of Bessel functions. Waves represented by $H_n^{(1)}(kr)\mathrm{e}^{\hat{i}n\theta}$ are often called the outgoing waves, and waves represented by $H_n^{(2)}(kr)\mathrm{e}^{\hat{i}n\theta}$ are often called the incoming waves, where $H_n^{(1)}(\cdot)$ and $H_n^{(2)}(\cdot)$ are Hankel functions of the first and second kinds, respectively.

A. First canonical problem: Inward problem

In this problem, the incident wave is a regular wave in medium 1 and is traveling inward towards medium 2. Upon encountering with the interface Γ by the incident wave, two waves are generated: a reflected wave in medium 1 and a transmitted wave in medium 2, as depicted in Fig. 2.

The incident wave is specified in the following form:

$$\phi^{\mathrm{I}}=\sum_{n=-\infty}^{\infty}A_nJ_n(k_1r)\mathrm{e}^{\hat{i}n\theta}=\{\mathbf{A}\}^T\{\mathbf{J}_1(r,\theta)\}. \tag{3}$$

The reflected and transmitted waves are expressible as

$$\phi^{\mathrm{R}}=\sum_{n=-\infty}^{\infty}B_nH_n^{(1)}(k_1r)\mathrm{e}^{\hat{i}n\theta}=\{\mathbf{B}\}^T\{\mathbf{H}_1(r,\theta)\}, \tag{4}$$

$$\phi^{\mathrm{T}}=\sum_{n=-\infty}^{\infty}C_nJ_n(k_2r)\mathrm{e}^{\hat{i}n\theta}=\{\mathbf{C}\}^T\{\mathbf{J}_2(r,\theta)\}, \tag{5}$$

where superscripts I, R, and T signify the incident, reflected, and transmitted waves, respectively. In the above equations, the second equality in each equation represents the matrix notation adopted for this paper: a bold-faced symbol enclosed by flower brackets denotes a column matrix whose row index runs from $-\infty$ to ∞. Column matrices $\{\mathbf{A}\}$, $\{\mathbf{B}\}$, and $\{\mathbf{C}\}$ are called the *wave expansion coefficient matrices* for the respective waves. Column matrices $\{\mathbf{J}_j(r,\theta)\}$ and $\{\mathbf{H}_j(r,\theta)\}$ are called the *regular wave expansion basis* and the *singular wave expansion basis*, respectively, for medium j. Entries for the wave expansion bases at the nth row are

$$\{J_j(r,\theta)\}_n = J_n(k_j r)e^{\hat{i}n\theta}, \tag{6}$$

$$\{H_j(r,\theta)\}_n = H_n^{(1)}(k_j r)e^{\hat{i}n\theta}. \tag{7}$$

Additionally, because all waves in the field have the same circular frequency, wave numbers k_j for different media are related by the following relation:

$$\frac{k_1}{k_2} = \sqrt{\frac{\rho_1\mu_2}{\rho_2\mu_1}}, \tag{8}$$

where ρ_j and μ_j are the mass density and Lamé constant, respectively, of medium j.

The canonical problem can be viewed as an input–output system in which the incident wave is the input and the resulting waves are the output. For a linear system, the input and output can be related by a linear transformation. In analogy, for the linear canonical problem at hand, the wave expansion coefficient matrices of the resulting waves, $\{\mathbf{B}\}$ and $\{\mathbf{C}\}$, can be related to the wave expansion coefficient matrix of the incident wave, $\{\mathbf{A}\}$, by linear transformations. In matrix form, these input–output relations can be formally written as

$$\{\mathbf{B}\} = [\mathbf{R}_{12}]\{\mathbf{A}\} \tag{9}$$

$$\{\mathbf{C}\} = [\mathbf{T}_{12}]\{\mathbf{A}\}, \tag{10}$$

where the subscripts "12" signify a canonical problem in which the incident wave propagates from medium 1 towards medium 2—the case of the first canonical problem.

Matrices $[\mathbf{R}_{12}]$ and $[\mathbf{T}_{12}]$ are the *reflection matrix* and the *transmission matrix*, respectively, of the first canonical problem. Such matrices are properties of the interface geometry and the materials on both sides of the interface. It is noted that different waves in the field, in Eqs. (3)–(5), are expressed in different wave expansion bases.

Specific expressions for the transformation matrices $[\mathbf{R}_{12}]$ and $[\mathbf{T}_{12}]$ can be found by the interface conditions at Γ for a specific problem. In general, the conditions at the interface Γ are that the displacement and the surface traction must be continuous. For the two-dimensional problem under consideration, such interface conditions can be written as

$$(\phi^{\mathrm{I}} + \phi^{R})|_{\Gamma} = (\phi^{\mathrm{T}})|_{\Gamma}, \tag{11}$$

$$\mu_1\left(\frac{\partial\phi^{\mathrm{I}}}{\partial r} + \frac{\partial\phi^{\mathrm{R}}}{\partial r}\right)\bigg|_{\Gamma} = \mu_2\left(\frac{\partial\phi^{\mathrm{T}}}{\partial r}\right)\bigg|_{\Gamma}. \tag{12}$$

The interface conditions for a specific problem can also be written in the form of integral equations. Interested readers are referred to the monograph by Krupradze (1963) on the general theory of integral equations for elastodynamic problems. One particularly fitting method for solving the canonical problem using the integral equation method is the *T*-matrix method, originally conceived by Waterman (1969). Subsequent developments in *T*-matrix method are presented in Varadan and Varadan (1980).

B. Second canonical problem: Outward problem

In this problem, the incident wave is a singular wave propagating from within medium 2 towards medium 1. Upon encountering with the interface Γ by the incident wave, two waves are generated: a reflected wave in medium 2 and a transmitted wave in medium 1, as depicted in Fig. 3

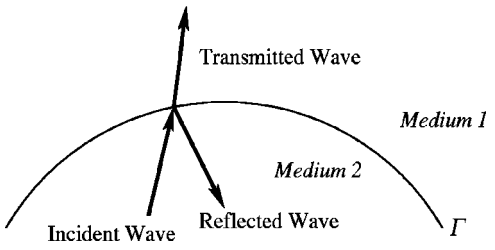

FIG. 3. Second canonical problem.

The incident wave is specified in the following form:

$$\phi^{\mathrm{I}} = \sum_{n=-\infty}^{\infty} A_n H_n^{(1)}(k_2 r)e^{\hat{i}n\theta} = \{\mathbf{A}\}^T\{\mathbf{H}_2\}. \tag{13}$$

Other waves in the field are expressible as

$$\phi^{\mathrm{R}} = \sum_{n=-\infty}^{\infty} B_n J_n(k_2 r)e^{\hat{i}n\theta} = \{\mathbf{B}\}^T\{\mathbf{J}_2\}, \tag{14}$$

$$\phi^{\mathrm{T}} = \sum_{n=-\infty}^{\infty} C_n H_n^{(1)}(k_1 r)e^{\hat{i}n\theta} = \{\mathbf{C}\}^T\{\mathbf{H}_1\}. \tag{15}$$

Similar to the first canonical problem, for a linear system, wave expansion coefficient matrices for the resulting waves, $\{\mathbf{B}\}$ and $\{\mathbf{C}\}$, can be related to the wave expansion coefficient matrix of the incident wave, $\{\mathbf{A}\}$, by linear transformations. In matrix form,

$$\{\mathbf{B}\} = [\mathbf{R}_{21}]\{\mathbf{A}\}, \tag{16}$$

$$\{\mathbf{C}\} = [\mathbf{T}_{21}]\{\mathbf{A}\}, \tag{17}$$

where the subscripts "21" signify a canonical problem in which the incident wave propagates from medium 2 towards medium 1—the case of the second canonical problem.

Interface conditions for specific problems at the interface Γ can be used to obtain specific expressions for the matrix entries. For the two-dimensional problem under consideration, the displacement and surface traction continuity conditions at Γ can be written as

$$(\phi^{\mathrm{I}} + \phi^{\mathrm{R}})|_{\Gamma} = (\phi^{\mathrm{T}})|_{\Gamma}, \tag{18}$$

$$\mu_2\left(\frac{\partial\phi^{\mathrm{I}}}{\partial r} + \frac{\partial\phi^{\mathrm{R}}}{\partial r}\right)\bigg|_{\Gamma} = \mu_1\left(\frac{\partial\phi^{\mathrm{T}}}{\partial r}\right)\bigg|_{\Gamma}. \tag{19}$$

III. FORMALISM FOR TWO-LAYER SCATTERER

In this section, a formal solution for a general two-layered scatterer is sought, following the multiple scattering process depicted in Fig. 1.

The outermost medium is denoted as medium 1, the innermost medium is denoted as medium 3, and the region between media 1 and 3 is denoted as medium 2. The interface that separates media 1 and 2 is denoted as Γ_1, and the interface that separates media 2 and 3 is denoted at Γ_2. To

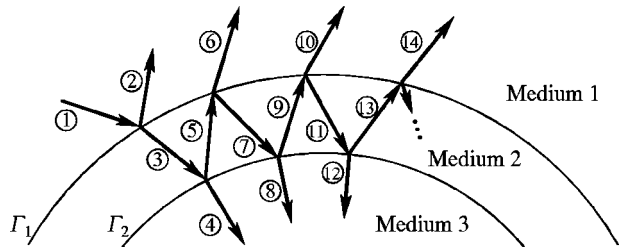

FIG. 4. Schematics depicting multiple scattering process in two-layered scatterer, with waves labeled by numbers.

facilitate the discussion, different waves in the multiple scattering process are identified by numbers, as depicted in Fig. 4.

Wave interactions can be tracked as follow: Wave ① is the incident wave with known wave expansion coefficients $\{\mathbf{A}\}$. The incident wave impinges onto medium 2, producing waves ② and ③. This process is described by the first canonical problem at Γ_1. Hence,

$$\phi^{②}=([\mathbf{R}_{12}]\{\mathbf{A}\})^T\{\mathbf{H}_1(r,\theta)\}, \tag{20}$$

$$\phi^{③}=([\mathbf{T}_{12}]\{\mathbf{A}\})^T\{\mathbf{J}_2(r,\theta)\}. \tag{21}$$

When wave ③ impinges onto medium 3, producing waves ④ and ⑤, the process is described by the first canonical problem at Γ_2, with wave ③ being the incident wave. Subsequently, when wave ⑤ impinges onto medium 1, producing waves ⑥ and ⑦, the process is described by a second canonical problem at Γ_1, with wave ⑤ being the incident wave.

The process continues in the like manner. Assuming the polar coordinate systems used in all canonical problems coincide, expressions for the wave expansion coefficients of various resulting waves are summarized in Table I.

In Table I, wave expansion coefficient matrices are expressed as successive matrix multiplications. Each matrix in the chain represents a particular scattering sequence. The entire chain can be used to track, in inverse chronicle order, the multiple-scattering process tracing eventually back to the incident wave. The subscripts for each matrix can be interpreted as follows: if the first subscript is smaller than the second subscript, the scattering process is a first canonical problem (inward problem) at the interface that separates the two media identified by the subscripts; otherwise the scattering process is a second canonical problem (outward problem).

TABLE I. Expressions for waves obtained from two canonical problems.

Wave	Incident	Canonical problem	Wave expansion coefficient
②	①	First	$[\mathbf{R}_{12}]\{\mathbf{A}\}$
③	①	First	$[\mathbf{T}_{12}]\{\mathbf{A}\}$
④	③	First	$[\mathbf{T}_{23}][\mathbf{T}_{12}]\{\mathbf{A}\}$
⑤	③	First	$[\mathbf{R}_{23}][\mathbf{T}_{12}]\{\mathbf{A}\}$
⑥	⑤	Second	$[\mathbf{T}_{21}][\mathbf{R}_{23}][\mathbf{T}_{12}]\{\mathbf{A}\}$
⑦	⑤	Second	$[\mathbf{R}_{21}][\mathbf{R}_{23}][\mathbf{T}_{12}]\{\mathbf{A}\}$
⑧	⑦	First	$[\mathbf{T}_{23}][\mathbf{R}_{21}][\mathbf{R}_{23}][\mathbf{T}_{12}]\{\mathbf{A}\}$
⑨	⑦	First	$[\mathbf{R}_{23}][\mathbf{R}_{21}][\mathbf{R}_{23}][\mathbf{T}_{12}]\{\mathbf{A}\}$
⑩	⑨	Second	$[\mathbf{T}_{21}][\mathbf{R}_{23}][\mathbf{R}_{21}][\mathbf{R}_{23}][\mathbf{T}_{12}]\{\mathbf{A}\}$
⑪	⑨	Second	$[\mathbf{R}_{21}][\mathbf{R}_{23}][\mathbf{R}_{21}][\mathbf{R}_{23}][\mathbf{T}_{12}]\{\mathbf{A}\}$
⑫	⑪	First	$[\mathbf{T}_{23}][\mathbf{R}_{21}][\mathbf{R}_{23}][\mathbf{R}_{21}][\mathbf{R}_{23}][\mathbf{T}_{12}]\{\mathbf{A}\}$
⑬	⑪	First	$[\mathbf{R}_{23}][\mathbf{R}_{21}][\mathbf{R}_{23}][\mathbf{R}_{21}][\mathbf{R}_{23}][\mathbf{T}_{12}]\{\mathbf{A}\}$
⑭	⑬	Second	$[\mathbf{T}_{21}][\mathbf{R}_{23}][\mathbf{R}_{21}][\mathbf{R}_{23}][\mathbf{R}_{21}][\mathbf{R}_{23}][\mathbf{T}_{12}]\{\mathbf{A}\}$
⋯	⋯	⋯	⋯

Take wave ⑩ as an example. The incident wave is first transmitted into medium 2 ($[\mathbf{T}_{12}]$) as a first canonical problem at Γ_1. It is then reflected at the interface between media 2 and 3 ($[\mathbf{R}_{23}]$) as another first canonical problem at Γ_2. It is then reflected at the interface between media 1 and 2 ($[\mathbf{R}_{21}]$) as a second canonical problem at Γ_1. Subsequently it is reflected again at the interface between media 2 and 3 ($[\mathbf{R}_{23}]$) as a first canonical problem at Γ_2. Finally, it is transmitted into medium 1 from medium 2 ($[\mathbf{T}_{21}]$) as a second canonical problem at Γ_1.

Expressions for individual waves can be obtained by combining the wave expansion coefficient matrix given in Table I with an appropriate wave expansion basis. The wave expansion basis depends on the final medium, which is indicated by the second subscript in the first matrix in the chain, and the direction, which is indicated by the propagation type (the symbolic designation of the matrix—*T* for transmission and *R* for reflection). For wave ⑩, for instance, the first matrix in the chain $[\mathbf{T}_{21}]$ indicates that it exists in medium 1, and it is a transmitted wave in the first canonical problem at Γ_1. Hence wave ⑩ is expressed in the wave expansion basis $\{\mathbf{H}_1(r,\theta)\}$; that is,

$$\phi^{⑩}=([\mathbf{T}_{21}][\mathbf{R}_{23}][\mathbf{R}_{21}][\mathbf{R}_{23}][\mathbf{T}_{12}]\{\mathbf{A}\})^T\{\mathbf{H}_1(r,\theta)\}. \tag{22}$$

The total wave in each of the three media is the summation of all waves that appear in the medium.

For medium 1, the total wave consists of the incident wave ϕ^{inc} and the total scattered wave. The total scattered wave consists of waves ②, ⑥, ⑩, ⑭, and subsequent waves, all of which are expressed in the wave expansion basis $\{\mathbf{H}_1(r,\theta)\}$. Thus, the total scattered wave can be written as

$$\begin{aligned}\phi_s=&[([\mathbf{R}_{12}]+[\mathbf{T}_{21}][\mathbf{R}_{23}][\mathbf{T}_{12}]+[\mathbf{T}_{21}][\mathbf{R}_{23}][\mathbf{R}_{21}][\mathbf{R}_{23}][\mathbf{T}_{12}]\\&+[\mathbf{T}_{21}][\mathbf{R}_{23}][\mathbf{R}_{21}][\mathbf{R}_{23}][\mathbf{R}_{21}][\mathbf{R}_{23}][\mathbf{T}_{12}]+\cdots)\\&\times\{\mathbf{A}\}]^T\{\mathbf{H}_1(r,\theta)\}.\end{aligned} \tag{23}$$

Define

$$[\mathbf{E}]=[\mathbf{I}]+[\mathbf{R}_{21}][\mathbf{R}_{23}]+[\mathbf{R}_{21}][\mathbf{R}_{23}][\mathbf{R}_{21}][\mathbf{R}_{23}]+\cdots, \tag{24}$$

and recall the following Taylor expansion

$$(1-x)^{-1}=1+x+x^2+\cdots. \tag{25}$$

In analogy, Eq. (24) can be written as

$$[\mathbf{E}]=([\mathbf{I}]-[\mathbf{R}_{21}][\mathbf{R}_{23}])^{-1}. \tag{26}$$

Furthermore, define

$$[\mathbf{S}]=[\mathbf{E}][\mathbf{T}_{12}]. \tag{27}$$

Then Eq. (23) can be written as

$$\phi_s=[([\mathbf{R}_{12}]+[\mathbf{T}_{21}][\mathbf{R}_{23}][\mathbf{S}])\{\mathbf{A}\}]^T\{\mathbf{H}_1(r,\theta)\}. \tag{28}$$

Finally, the total wave in medium 1 can be written as

$$\phi_1=\phi^{\text{inc}}+[([\mathbf{R}_{12}]+[\mathbf{T}_{21}][\mathbf{R}_{23}][\mathbf{S}])\{\mathbf{A}\}]^T\{\mathbf{H}_1(r,\theta)\}, \tag{29}$$

where, when necessary, the incident wave can be written as

$$\phi^{\text{inc}}=\{\mathbf{A}\}^T\{\mathbf{J}_1(r,\theta)\}. \tag{30}$$

Following the same manner, waves in media 2 and 3 can be summed to give

$$\phi_2=([\mathbf{S}]\{\mathbf{A}\})^T\{\mathbf{J}_2(r,\theta)\}+([\mathbf{R}_{23}][\mathbf{S}]\{\mathbf{A}\})^T\{\mathbf{H}_2(r,\theta)\}, \tag{31}$$

$$\phi_3=([\mathbf{T}_{23}][\mathbf{S}]\{\mathbf{A}\})^T\{\mathbf{J}_3(r,\theta)\}. \tag{32}$$

Using matrix notation, sometimes it is advantageous to define each wave by a single transformation matrix that linearly relates the resulting wave to the incident wave, in analogy to those in Eqs. (9) and (10). Hence the following matrices are defined:

$$[\mathbf{R}]=[\mathbf{R}_{12}]+[\mathbf{T}_{21}][\mathbf{R}_{23}][\mathbf{S}], \tag{33}$$

$$[\mathbf{F}]=[\mathbf{R}_{23}][\mathbf{S}], \tag{34}$$

$$[\mathbf{T}]=[\mathbf{T}_{23}][\mathbf{S}]. \tag{35}$$

Subsequently, the total waves in all three media can be written as

$$\phi_1=\phi^{\text{inc}}+([\mathbf{R}]\{\mathbf{A}\})^T\{\mathbf{H}_1(r,\theta)\}, \tag{36}$$

$$\phi_2=([\mathbf{S}]\{\mathbf{A}\})^T\{\mathbf{J}_2(r,\theta)\}+([\mathbf{F}]\{\mathbf{A}\})^T\{\mathbf{H}_2(r,\theta)\}, \tag{37}$$

$$\phi_3=([\mathbf{T}]\{\mathbf{A}\})^T\{\mathbf{J}_3(r,\theta)\}. \tag{38}$$

In Eqs. (36)–(38), $[\mathbf{R}]$ is called the *reflection matrix* that represents the reflected (scattered) wave, $[\mathbf{T}]$ is called the *transmission matrix* that represents the wave transmitted into the core of the scatterer; $[\mathbf{S}]$ and $[\mathbf{F}]$ together represent the wave in the intermediate layer of the scatterer, in which $[\mathbf{S}]$ represents the portion of standing wave, while $[\mathbf{F}]$ represents the portion of outgoing wave emanating from the scatterer core.

IV. APPLICATION TO LAYERED CIRCULAR CYLINDRICAL SCATTERER

Consider a two-layered circular cylindrical scatterer whose inner and outer radii are a and b $(b>a)$, respectively, as shown in Fig. 5. This model has been widely used in modeling the micro-mechanics of fiber-reinforced composite materials. The exact analytical solution for the scattering of SH waves by this scatterer has been studied by the author (Cai, 2004). Here, the terminologies for composite materials are adopted: the medium outside the scatterer is called the matrix; the medium at the outer layer of the scatterer is called the interphase; and the inner portion of the scatterer is the fiber. Material properties for the three media are denoted by subscripts *m*, *i*, and *f*, respectively. They correspond to media 1, 2, and 3 for the general two-layered scatterer in Sec. III.

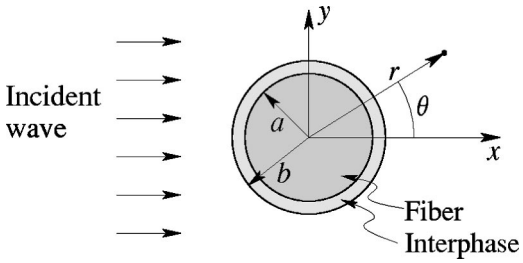

FIG. 5. Configuration for two-layered circular cylindrical scatterer.

A. First canonical problem

The first canonical problem for this case is a classic problem of wave scattering by a circular cylindrical elastic scatterer, whose solution can be found in many textbooks on elastic waves, such as Pao and Mow (1971). For the problem under consideration, there are two first canonical problems.

For the first canonical problem at the interface $r=b$, involving media 1 and 2 (the matrix and the interphase), the interface conditions corresponding to Eqs. (11) and (12) are

$$\begin{bmatrix} H_n^{(1)}(k_mb) & -J_n(k_ib) \\ k_m\mu_mH_n^{(1)\prime}(k_mb) & -k_i\mu_iJ_n'(k_ib) \end{bmatrix}\begin{Bmatrix} B_n \\ C_n \end{Bmatrix} = \begin{Bmatrix} -J_n(k_mb)A_n \\ -k_m\mu_mJ_n'(k_mb)A_n \end{Bmatrix}. \tag{39}$$

Following the definitions in Eqs. (9) and (10), matrices $[\mathbf{R}_{12}]$, and $[\mathbf{T}_{12}]$ are found to be diagonal matrices with entries

$$[R_{12}]_{nn}=\frac{B_n}{A_n}=-\frac{\mu_ik_iJ_n'(k_ib)J_n(k_mb)-\mu_mk_mJ_n(k_ib)J_n'(k_mb)}{\mu_ik_iJ_n'(k_ib)H_n^{(1)}(k_mb)-\mu_mk_mJ_n(k_ib)H_n^{(1)\prime}(k_mb)}, \tag{40}$$

$$[T_{12}]_{nn}=\frac{C_n}{A_n}=-\frac{2\hat{i}}{\pi b}\frac{\mu_m}{\mu_ik_iJ_n'(k_ib)H_n^{(1)}(k_mb)-\mu_mk_mJ_n(k_ib)H_n^{(1)\prime}(k_mb)}. \tag{41}$$

Similar interface conditions can be written for the first canonical problem at the interface $r=a$, involving media 2 and 3, leading to the following matrices:

$$[R_{23}]_{nn}=-\frac{\mu_fk_fJ_n'(k_fa)J_n(k_ia)-\mu_ik_iJ_n(k_fa)J_n'(k_ia)}{\mu_fk_fJ_n'(k_fa)H_n^{(1)}(k_ia)-\mu_ik_iJ_n(k_fa)H_n^{(1)\prime}(k_ia)}, \tag{42}$$

$$[T_{23}]_{nn}=-\frac{2\hat{i}}{\pi a}\frac{\mu_i}{\mu_fk_fJ_n'(k_fa)H_n^{(1)}(k_ia)-\mu_ik_iJ_n(k_fa)H_n^{(1)\prime}(k_ia)}. \tag{43}$$

B. Second canonical problem

For the second canonical problem at the interface $r=b$, involving media 1 and 2 (matrix and interphase), the interface conditions corresponding to Eqs. (18) and (19) are

$$\begin{bmatrix} J_n(k_ib) & -H_n^{(1)}(k_mb) \\ k_i\mu_iJ_n'(k_ib) & -k_m\mu_mH_n^{(1)'}(k_mb) \end{bmatrix} \begin{Bmatrix} B_n \\ C_n \end{Bmatrix} = \begin{Bmatrix} -H_n(k_ib)A_n \\ -k_i\mu_iH_n^{(1)'}(k_ib)A_n \end{Bmatrix}. \tag{44}$$

Again, both $[\mathbf{R}_{21}]$ and $[\mathbf{T}_{21}]$ are found to be diagonal matrices, with matrix entries

$$[T_{21}]_{nn} = -\frac{\mu_ik_iH_n^{(1)'}(k_ib)H_n^{(1)}(k_mb) - \mu_mk_mH_n^{(1)}(k_ib)H_n^{(1)'}(k_mb)}{\mu_kk_iJ_n'(k_ib)H_n^{(1)}(k_mb) - \mu_mk_mJ_n(k_ib)H_n^{(1)'}(k_mb)}, \tag{45}$$

$$[R_{21}]_{nn} = -\frac{2\hat{i}}{\pi b}\frac{\mu_i}{\mu_ik_iJ_n'(k_ib)H_n^{(1)}(k_mb) - \mu_mk_mJ_n(k_ib)H_n^{(1)'}(k_mb)}. \tag{46}$$

It is noted that the solution process outlined in Sec. III does not require the second canonical problem at the interface $r=a$.

C. Multiple-scattering solution

The multiple scattering solution for the two-layered circular cylindrical scatterer includes the following: Eqs. (36)–(38) give expressions for waves in all three media, with definitions for various matrices given in Eqs. (33)–(35) and Eqs. (26) and (27). Detailed expressions for matrices $[\mathbf{R}_{ij}]$ and $[\mathbf{T}_{ij}]$ $(i,j=1,2,3)$ are given in Eqs. (40)–(43) and Eqs. (45) and (46).

D. Verification via exact analytical solution

The exact analytical solution for the two-layered circular cylindrical scatterer (Cai, 2004) is used to verify that the proposed multiple-scattering solution procedure indeed gives analytically exact solutions for problems in which the canonical problems are solved analytically.

Using the matrix notation in this paper, the exact analytical solution for the waves in the three media can be re-expressed as

$$\phi_m = \phi^{\text{inc}} + ([\hat{\mathbf{R}}]\{\mathbf{A}\})^T\{\mathbf{H}_m(r,\theta)\}, \tag{47}$$

$$\phi_i = ([\hat{\mathbf{S}}_1]\{\mathbf{A}\})^T\{\mathbf{H}_i^{(1)}(r,\theta)\} + ([\hat{\mathbf{S}}_2]\{\mathbf{A}\})^T\{\mathbf{H}_i^{(2)}(r,\theta)\}, \tag{48}$$

$$\phi_f = ([\hat{\mathbf{T}}]\{\mathbf{A}\})^T\{\mathbf{J}_f(r,\theta)\}, \tag{49}$$

where $[\hat{\mathbf{R}}]$, $[\hat{\mathbf{S}}_1]$, $[\hat{\mathbf{S}}_2]$, and $[\hat{\mathbf{T}}]$ are diagonal matrices with entries

$$[\hat{R}]_{nn} = -\frac{\mu_mk_mM_1J_n'(k_mb) - \mu_ik_iM_2J_n(k_mb)}{\mu_mk_mM_1H_n^{(1)'}(k_mb) - \mu_ik_iM_2H_n^{(1)}(k_mb)}, \tag{50}$$

$$[\hat{T}]_{nn} = -\frac{4\hat{i}}{\pi^2ab}\frac{\mu_i\mu_m}{\mu_mk_mM_1H_n^{(1)'}(k_mb) - \mu_ik_iM_2H_n^{(1)}(k_mb)}, \tag{51}$$

$$[\hat{S}_1]_{nn} = -\frac{\mu_m}{\pi b}\frac{\mu_fk_fJ_n'(k_fa)H_n^{(2)}(k_ia) - \mu_ik_iJ_n(k_fa)H_n^{(2)'}(k_ia)}{\mu_mk_mM_1H_n^{(1)'}(k_mb) - \mu_ik_iM_2H_n^{(1)}(k_mb)}, \tag{52}$$

$$[\hat{S}_2]_{nn} = \frac{\mu_m}{\pi b}\frac{\mu_fk_fJ_n'(k_fa)H_n^{(1)}(k_ia) - \mu_ik_iJ_n(k_fa)H_n^{(1)'}(k_ia)}{\mu_mk_mM_1H_n^{(1)'}(k_mb) - \mu_ik_iM_2H_n^{(1)}(k_mb)}, \tag{53}$$

and

$$M_1 = \Delta_2J_n(k_ib) - \Delta_1Y_n(k_ib), \tag{54}$$

$$M_2 = \Delta_2J_n'(k_ib) - \Delta_1Y_n'(k_ib), \tag{55}$$

$$\Delta_1 = \mu_fk_fJ_n'(k_fa)J_n(k_ia) - \mu_ik_iJ_n(k_fa)J_n'(k_ia), \tag{56}$$

$$\Delta_2 = \mu_fk_fJ_n'(k_fa)Y_n(k_ia) - \mu_ik_iJ_n(k_fa)Y_n'(k_ia). \tag{57}$$

In the exact analytical solution, the wave in the interphase, Eq. (48), is expanded over a pair of wave expansion bases that is different from that in the multiple-scattering solution in Eq. (37), with

TABLE II. Constituent material properties for metal-matrix ceramic-fiber composite system (after Yim and Williams, 1995).

Property	Matrix (AA520 Aluminum)	Fiber (Alumina, Al_2O_3)	Interphase (Zirconia, ZrO_2)
Density (kg/m^3)	2600	3700	6300
Young's modulus (GPa)	66	360	97
Poisson's ratio	0.31	0.25	0.33
Lamé constant λ (GPa)	41	144	71
Lamé constant μ (GPa)	25	144	37
P wave speed (m/s)	5930	10 800	4780
S wave speed (m/s)	3110	6240	2400

$$\{H_i^{(1)}(r,\theta)\}_n = H_n^{(1)}(k_i r)e^{\hat{i}n\theta} \quad \text{and}$$

$$\{H_i^{(2)}(r,\theta)\}_n = H_n^{(2)}(k_i r)e^{\hat{i}n\theta}. \tag{58}$$

Recall the relations between Hankel functions and Bessel functions,

$$H_n^{(1)}(\cdot) = J_n(\cdot) + \hat{i}Y_n(\cdot) \quad \text{and} \quad H_n^{(2)} = J_n(\cdot) - \hat{i}Y_n(\cdot). \tag{59}$$

It can be readily shown that for any coefficients α and β,

$$\alpha H_n^{(1)}(\cdot) + \beta H_n^{(2)}(\cdot) = 2\beta J_n(\cdot) + (\alpha - \beta)H_n^{(1)}(\cdot). \tag{60}$$

Since the two solutions are for the same physical problem, if the following relationships are satisfied,

$$[\mathbf{R}] = [\hat{\mathbf{R}}], \tag{61}$$

$$[\mathbf{S}] = 2[\hat{\mathbf{S}}_2], \tag{62}$$

$$[\mathbf{F}] = [\hat{\mathbf{S}}_1] - [\hat{\mathbf{S}}_2], \tag{63}$$

$$[\mathbf{T}] = [\hat{\mathbf{T}}], \tag{64}$$

then the two solutions are identical. Equations (61)–(64) serve as a verification for the correctness of the multiple-scattering solution.

A metal-matrix ceramic-fiber composite system is used as the example for numerical verification. Constituents' material properties, after Yim and Williams (1995), are listed in Table II. Computations using both multiple-scattering solution (MSS) and the exact analytical single-scatterer solution (SSS) are performed at two arbitrarily chosen frequencies $k_m a = 2$ and $k_m a = 10$. The computer used for the computation typically furnishes 14–15 significant figures for double-precision data type, and the high-accuracy Bessel and Hankel functions used in the computation have been shown (Cai, 1998) to have 11–15 significant figures in general. Results for the first ten terms in each pair of matrices in Eqs. (61)–(64) are listed and compared in Tables III–VI.

In Tables III–VI, results computed according to the left- and right-hand sides of Eqs. (61)–(64) are shown for the first 14 significant figures. A short line segment is used to identify the complex value of a matrix entry in the single-scatterer solution is either entirely or partly identical to that of the multiple-scattering solution for all the 14 significant figures shown.

Results in Tables III–VI show that for all results except $[\mathbf{F}]$ matrix at $k_m a = 2$, there are only occasional cases in which the results using the multiple-scattering solution and

TABLE III. Comparison of matrix $[\mathbf{R}]$ as computed using multiple scattering solution (MSS) and single scatterer solution (SSS).

n	$[R]_{nn}$ via MSS	$[\hat{R}]_{nn}$ vis SSS
	(a) $k_m a = 2$	
0	$-0.045\,027\,017\,665\,097 - 0.207\,363\,413\,709\,57\hat{i}$	———
1	$-0.708\,508\,177\,089\,91 - 0.454\,449\,491\,238\,180\hat{i}$	———
2	$-0.177\,750\,755\,276\,19 - 0.382\,302\,791\,351\,22\hat{i}$	———
3	$-0.009\,902\,046\,573\,239\,9 - 0.099\,015\,130\,393\,80\hat{i}$	———
4	$-0.000\,130\,190\,412\,831\,62 - 0.011\,409\,358\,583\,55\hat{i}$	———
5	$-5.102\,832\,621\,674\,9\times10^{-7} - 0.000\,714\,340\,956\,251\,63\hat{i}$	———
6	$-8.097\,340\,386\,423\,2\times10^{-10} - 2.845\,582\,608\,160\,7\times10^{-5}\hat{i}$	———
7	$-6.328\,125\,065\,342\,4\times10^{-13} - 7.954\,951\,329\,416\,4\times10^{-7}\hat{i}$	———
8	$-2.747\,543\,585\,705\,7\times10^{-16} - 1.657\,571\,592\,935\,2\times10^{-8}\hat{i}$	———
9	$-7.201\,790\,785\,099\,0\times10^{-20} - 2.683\,615\,245\,354\,5\times10^{-10}\hat{i}$	$-7.201\,790\,785\,099\,1\times10^{-20} - \text{———}\hat{i}$
10	$-1.212\,032\,521\,662\,7\times10^{-23} - 3.481\,425\,744\,810\,2\times10^{-12}\hat{i}$	———
	(b) $k_m a = 10$	
0	$-0.969\,871\,912\,684\,18 + 0.170\,939\,713\,555\,71\hat{i}$	———
1	$-0.952\,582\,464\,326\,36 - 0.212\,530\,263\,690\,31\hat{i}$	———
2	$-0.995\,133\,907\,715\,04 + 0.069\,587\,451\,676\,505\hat{i}$	$\text{———} + 0.069\,587\,451\,676\,504\hat{i}$
3	$-0.753\,269\,981\,423\,88 - 0.431\,108\,242\,219\,46\hat{i}$	———
4	$-0.079\,508\,452\,060\,749 - 0.270\,530\,697\,170\,68\hat{i}$	———
5	$-0.178\,909\,116\,012\,30 + 0.383\,276\,198\,347\,87\hat{i}$	———
6	$-0.778\,554\,692\,082\,12 + 0.415\,219\,560\,617\,07\hat{i}$	———
7	$-0.995\,116\,791\,791\,11 - 0.069\,709\,127\,712\,758\hat{i}$	$-0.995\,116\,791\,791\,12 - \text{———}\hat{i}$
8	$-0.732\,211\,513\,367\,04 - 0.442\,806\,744\,596\,09\hat{i}$	———
9	$-0.359\,606\,344\,535\,90 - 0.479\,885\,008\,627\,51\hat{i}$	———
10	$-0.121\,313\,262\,444\,30 - 0.326\,490\,972\,002\,94\hat{i}$	———

TABLE IV. Comparison of matrix [**T**] as computed using multiple scattering solution (MSS) and single scatterer solution (SSS).

n	$[T]_{nn}$ via MSS	$[\hat{T}]_{nn}$ via SSS
	(a) $k_m a = 2$	
0	$0.365\,538\,523\,764\,03 - 0.079\,373\,257\,183\,397\hat{i}$	———
1	$0.298\,188\,051\,458\,11 - 0.464\,889\,227\,167\,93\hat{i}$	———
2	$0.668\,065\,715\,256\,40 - 0.310\,615\,533\,413\,30\hat{i}$	———
3	$1.677\,443\,797\,6830 - 0.167\,753\,418\,518\,84\hat{i}$	———
4	$3.977\,093\,848\,457\,8 - 0.045\,381\,998\,138\,559\hat{i}$	———
5	$8.728\,894\,509\,056\,2 - 0.006\,235\,410\,032\,444\,2\hat{i}$	———
6	$18.421\,538\,073\,574 - 0.000\,524\,200\,084\,001\,78\hat{i}$	$——— - 0.000\,524\,200\,084\,001\,79\hat{i}$
7	$38.226\,572\,785\,601 - 3.040\,905\,260\,000\,4\times10^{-5}\hat{i}$	———
8	$78.626\,618\,151\,407 - 1.303\,292\,486\,963\,4\times10^{-6}\hat{i}$	$——— - 1.303\,292\,486\,963\,3\times10^{-6}\hat{i}$
9	$160.848\,514\,831\,62 - 4.316\,555\,265\,947\,7\times10^{-8}\hat{i}$	$——— - 4.316\,555\,265\,947\,8\times10^{-8}\hat{i}$
10	$327.852\,052\,696\,19 - 1.141\,392\,576\,745\,4\times10^{-9}\hat{i}$	———
	(b) $k_m a = 10$	
0	$0.060\,846\,391\,306\,199 + 0.345\,228\,178\,335\,76\hat{i}$	———
1	$-0.097\,885\,024\,383\,617 + 0.438\,730\,730\,056\,69\hat{i}$	———
2	$0.028\,335\,813\,135\,339 + 0.405\,215\,707\,348\,19\hat{i}$	———
3	$-0.154\,713\,604\,675\,74 + 0.270\,329\,125\,511\,80\hat{i}$	———
4	$-0.365\,749\,242\,860\,57 + 0.107\,492\,999\,67200\hat{i}$	———
5	$-0.556\,232\,709\,634\,22 - 0.259\,643\,314\,160\,25\hat{i}$	———
6	$-0.552\,721\,430\,208\,44 - 1.036\,376\,663\,622\,5\hat{i}$	———
7	$0.176\,870\,853\,412\,15 - 2.524\,879\,624\,575\,2\hat{i}$	———
8	$3.080\,050\,778\,013\,3 - 5.093\,076\,537\,200\,4\hat{i}$	———
9	$11.944\,660\,303\,218 - 8.950\,843\,537\,805\,4\hat{i}$	———
10	$36.531\,966\,882\,862 - 13.574\,072\,382\,091\hat{i}$	———

TABLE V. Comparison of matrix [**S**] as computed using multiple scattering solution (MSS) and single scatterer solution (SSS).

n	$[S]_{nn}$ via MSS	$2[\hat{S}_2]_{nn}$ via SSS
	(a) $k_m a = 2$	
0	$0.416\,718\,276\,789\,89 + 0.557\,654\,036\,350\,83\hat{i}$	———
1	$0.782\,730\,958\,484\,30 + 0.238\,199\,742\,632\,20\hat{i}$	———
2	$0.600\,064\,210\,06800 + 0.143\,281\,450\,086\,16\hat{i}$	———
3	$0.486\,445\,612\,934\,51 + 0.057\,209\,130\,290\,916\hat{i}$	———
4	$0.362\,734\,809\,901\,29 + 0.010\,177\,646\,010\,434\hat{i}$	———
5	$0.268\,381\,783\,282\,91 + 0.000\,866\,601\,563\,413\,09\hat{i}$	———
6	$0.203\,539\,782\,616\,15 + 4.358\,266\,921\,0060\times10^{-5}\hat{i}$	———
7	$0.156\,449\,769\,388\,61 + 1.477\,086\,762\,042\,5\times10^{-6}\hat{i}$	———
8	$0.120\,979\,201\,834\,84 + 3.634\,908\,553\,499\,1\times10^{-8}\hat{i}$	———
9	$0.093\,844\,276\,686\,001 + 6.819\,104\,062\,932\,1\times10^{-10}\hat{i}$	———
10	$0.072\,930\,341\,239\,853 + 1.009\,974\,451\,062\,6\times10^{-11}\hat{i}$	———
	(b) $k_m a = 10$	
0	$-0.758\,303\,875\,286\,76 + 0.294\,473\,850\,332\,58\hat{i}$	———
1	$-0.742\,286\,306\,482\,58 - 0.181\,507\,819\,637\,34\hat{i}$	$——— - 0.181\,507\,819\,637\,35\hat{i}$
2	$-0.896\,068\,161\,355\,60 + 0.350\,435\,976\,740\,35\hat{i}$	———
3	$-0.586\,528\,866\,179\,43 + 0.165\,698\,602\,445\,75\hat{i}$	———
4	$-0.672\,897\,313\,934\,33 - 0.029\,900\,295\,352\,699\hat{i}$	———
5	$-0.907\,191\,162\,465\,96 - 0.008\,413\,003\,059\,521\,4\hat{i}$	$——— - 0.008\,413\,003\,059\,521\,5\hat{i}$
6	$-1.073\,645\,351\,788\,5 + 0.261\,941\,863\,300\,94\hat{i}$	———
7	$-1.001\,833\,538\,707\,3 + 0.651\,353\,179\,874\,65\hat{i}$	———
8	$-0.677\,618\,570\,207\,55 + 0.951\,093\,558\,42900\hat{i}$	———
9	$-0.235\,640\,774\,140\,77 + 1.019\,638\,345\,591\,4\hat{i}$	———
10	$0.146\,961\,011\,692\,48 + 0.851\,948\,988\,333\,37\hat{i}$	———

TABLE VI. Comparison of matrix $[\mathbf{F}]$ as computed using multiple scattering solution (MSS) and single scatterer solution (SSS).

n	$[F]_{nn}$ via MSS	$([\hat{S}_1]_{nn}-[\hat{S}_2]_{nn})$ via SSS
	(a) $k_m a=2$	
0	$-0.134\,400\,625\,857\,01-0.618\,956\,662\,635\,36\hat{i}$	———
1	$-0.662\,821\,036\,399\,82-0.425\,144\,963\,056\,13\hat{i}$	———
2	$-0.161\,438\,764\,870\,59-0.347\,219\,286\,615\,24\hat{i}$	———
3	$-0.010\,481\,376\,610\,097-0.104\,808\,118\,612\,56\hat{i}$	———
4	$-0.000\,163\,345\,007\,518\,93-0.014\,314\,892\,495\,398\hat{i}$	$-0.000\,163\,345\,007\,518\,91-$———$\hat{i}$
5	$-7.559\,997\,213\,775\,9\times10^{-7}-0.001\,058\,317\,220\,911\,6\hat{i}$	$-7.559\,997\,213\,801\,9\times10^{-7}-$———$\hat{i}$
6	$-1.404\,993\,945\,415\,8\times10^{-9}-4.937\,456\,182\,958\,3\times10^{-5}\hat{i}$	$-1.404\,993\,940\,634\,6\times10^{-9}-$———$\hat{i}$
7	$-1.274\,018\,700\,850\,8\times10^{-12}-1.601\,541\,792\,1400\times10^{-6}\hat{i}$	$-1.274\,036\,431\,908\,6\times10^{-12}-$———$\hat{i}$
8	$-6.357\,516\,791\,202\,3\times10^{-16}-3.835\,440\,241\,796\,5\times10^{-8}\hat{i}$	$-6.314\,393\,452\,555\,6\times10^{-16}-$———$\hat{i}$
9	$-1.897\,569\,847\,001\,5\times10^{-19}-7.070\,945\,994\,535\,9\times10^{-10}\hat{i}$	$0-$———$\hat{i}$
10	$-3.604\,545\,000\,928\,4\times10^{-23}-1.035\,364\,607\,819\,6\times10^{-11}\hat{i}$	$0-$———$\hat{i}$
	(b) $k_m a=10$	
0	$0.785\,794\,905\,545\,70-0.138\,496\,181\,104\,75\hat{i}$	———$-0.138\,496\,181\,104\,74\hat{i}$
1	$0.745\,664\,823\,834\,27+0.166\,364\,957\,963\,15\hat{i}$	———
2	$0.916\,093\,757\,585\,97-0.064\,060\,353\,679\,975\hat{i}$	$0.916\,093\,757\,585\,96-0.064\,060\,353\,679\,974\hat{i}$
3	$0.370\,380\,554\,892\,94+0.211\,974\,609\,250\,11\hat{i}$	———
4	$0.061\,589\,971\,574\,129+0.209\,562\,348\,615\,98\hat{i}$	———
5	$0.159\,080\,265\,101\,61-0.340\,796\,939\,805\,61\hat{i}$	———
6	$0.944\,655\,011\,654\,15-0.503\,804\,347\,803\,45\hat{i}$	———
7	$0.951\,536\,114\,945\,12+0.066\,656\,248\,901\,822\hat{i}$	———$+0.066\,656\,248\,901\,821\hat{i}$
8	$0.075\,009\,476\,363\,028+0.045\,362\,168\,493\,409\hat{i}$	———
9	$-0.404\,571\,238\,858\,70-0.539\,889\,452\,453\,1\hat{i}$	———
10	$-0.295\,981\,973\,078\,41-0.796\,577\,720\,676\,54\hat{i}$	———

the single-scatterer solution differ; and in all such cases the differences only occur at the 14th significant figure.

For $[\mathbf{F}]$ matrix at $k_m a=2$ (Table VI), the number of significant figures apparently decreases as n increases. The errors are primarily due to the so-called cancellation errors. Results for the single-scatterer solution are computed according to the right-hand side of Eq. (63). A major loss of significant figures occurs when two numbers are subtracted to produce a significantly smaller number. This occurs for the real parts of the right-hand side of Eq. (63). Using $[F]_{77}=([\hat{S}_1]_{77}-[\hat{S}_2]_{77})$ as an example, the value of the real part of $[\hat{S}_2]_{77}$ before the substraction, half of that of $[S]_{77}$ in Table V according to Eq. (62), is 0.078 224 884 684 31; the result after the subtraction is in the order of 10^{-12}. During the subtraction, 9–10 significant figures have been lost. For a computer with 14–15 significant figures, this means that the result has no more than 5 significant figures. Indeed, the SSS result for the real part of $([\hat{S}_1]_{77}-[\hat{S}_2]_{77})$ in Table VI has exactly 5 significant figures that are identical to those in the MSS result.

From the results in Tables III–VI, it can be concluded that the two solutions give identical results, and the errors are purely the computation system's.

V. DISCUSSIONS

In the multiple-scattering formalism for general two-layered scatterers in Sec. III, solving the canonical problems is not a part of the formalism. As discussed earlier, different methods can be used to solve the canonical problems, which, mathematically, are boundary value problems. For this reason, computational aspects of the solution procedure, such as convergence behaviors and truncation criteria, are not discussed in this paper. They are more appropriately discussed in conjunction with a specific method used for a specific canonical problem.

The multiple-scattering formalism for the two-layered scatterer is analytically exact, as no approximations have been introduced in the process. A simple example is used for the verification because of the existence of its exact analytical solution. Such a verification verifies that both the formalism and the computational implementation of the multiple-scattering solution are correct. More importantly, such a verification validates the use of the multiple scattering formalism for analyzing scatterers of more complicated geometrical and physical compositions.

The solution procedure places an emphasis on the physical process of multiple scattering, which is often overlooked for individual single scatterers. Furthermore, since the multiple-scattering solution follows the physical process of wave propagation, it would be possible to incorporate some phenomenological approximations such as material attenuation effects into the consideration.

The formalism presented in Sec. III assumes that the coordinate systems for both canonical problems coincide. This is not a requirement. When the coordinate systems do not coincide, a coordinate translation can be performed to transform the wave expansion bases in one coordinate system into another. Coordinate transformations for wave expansion bases would be similar to those used in the multiple-scattering theory of Cai and Williams (1999a). In such case,

eccentrically layered scatterers can be analyzed in the same manner, giving analytically exact solutions.

An extension of current solution procedure to analyzing multilayered scatterers of an arbitrary number of layers is rather straightforward. The analysis may start from the innermost two layers, using the formalism in Sec. III. Then, these two layers can be considered as a single core. This abstract core and its adjacent layer form another two-layered scatterer, subsequently analyzed by using the formalism in Sec. III again. Similar process is continued, one layer at a time, until all layers have been incorporated into a core. In essence, the two-layered scatterer becomes another canonical problem whose solution has been given by the formalism in Sec. III. It can be further envisioned that scatterers having continuously varying cross-sectional profiles of physical properties can be analyzed when each layer in the general multilayered scatterer becomes a differential layer. Combined with the allowance for eccentricity of the layers, it would be possible to analyze some geometrically and physically fairly complicated scatterers.

Another possible application of the present method is for analyzing multi-core scatterers. The geometrical configuration of such scatterers resembles that of a multiconductor cable. Such multi-core scatterers are a common configuration in many engineering applications and among many biological tissues and structures. In such cases, the multiple cores can be analyzed first by using the scatterer polymerization methodology developed by the author (Cai and Williams, 1999a). After scatterer polymerization, the cores become one single abstract scatterer whose reflection matrix is known. This matrix corresponds to matrix $[\mathbf{R}_{23}]$ in the first canonical problem at the inner interface in the two-layered formalism.

In summary, the significance of the multiple scattering formalism for multilayered scatterers in the present paper is that it opens new ways of analyzing the scattering by single scatterers that have complicated physical or geometrical compositions.

VI. CONCLUSIONS

A novel solution procedure is proposed for analyzing the scattering by multilayered scatterers. The solution is based on the observation that multiple scattering process occurs in single scatterers having delineative internal structures. A formalism was presented for a general two-layered cylindrical scatterer subjected to SH waves. Numerical computations are performed for a two-layered concentric circular cylindrical scatterer whose exact analytical solution is known. The multiple-scattering procedure yields an analytically exact solution when the canonical problems can be solved analytically. The solution procedure opens new ways for analyzing scatterers with complicated internal structure.

Akay, A. (**1991**). ''Scattering of sound from concentric cylindrical shells,'' J. Acoust. Soc. Am. **89**, 1572–1578.

Bogen, S. D., and Hinders, M. K. (**1994**). *Interface Effects in Elastic Wave Scattering* (Springer-Verlag, Berlin).

Cai, L.-W. (**1998**). ''Full-Scale Simulation of Multiple Scattering of Elastic Waves in Fiber Reinforced Composite,'' Sc. D. thesis, Massachusetts Institute of Technology, Cambridge, MA.

Cai, L.-W. (**2004**). ''Scattering of anti-plane shear waves by layered circular elastic cylinder,'' to appear in J. Acoust. Soc. Am. **115**, 515–522.

Cai, L.-W., and Williams, J. H. (**1999a**). ''Large-scale multiple-scattering problems,'' Ultrasonics **37**, 453–462.

Cai, L.-W., and Williams, J. H. (**1999b**). ''Full-scale simulation of elastic wave scattering in fiber reinforced composite,'' Ultrasonics **37**, 463–482.

Datta, S. K. (**1978**). ''Scattering of elastic waves,'' in Mechanics Today, edited by S. Nemat Nasser (Pergamon, New York), Vol. 4, pp. 149–208.

DeSanto, J. A. (**1980**). ''Theory of scattering from multilayered bodies of arbitrary shape,'' Wave Motion **2**, 63–73.

Gerard, A. (**1983**). ''Scattering by spherical elastic layers: exact solution and interpretation for a scalar field,'' J. Acoust. Soc. Am. **73**, 13–18.

Graff, K. F. (**1975**). *Wave Motion in Elastic Solids* (Dover, New York).

Hackman, R. H. (**1993**). ''Acoustic scattering from elastic solids,'' in *Physical Acoustics*, (Academic, New York), Vol. XXII, pp. 1–193.

Huang, W., Rokhlin, S. I., and Wang, Y. J. (**1995**). ''Effect of fiber-matrix interphase of wave propagation along, and scattering from, multilayered fibers in composite. Transfer matrix approach,'' Ultrasonics **33**, 365–375.

Krupradze, V. D. (**1963**). ''Dynamical problems in elasticity,'' in *Progress in Solid Mechanics, Volumn III*, edited by I. N. Snedden and R. Hill (North-Holand, Amsterdam).

Mal, A. K., and Yang, R.-B. (**1994**). ''The influence of the fiber-matrix interfacial layer properties on wave characteristics in metal matrix composites,'' in *Review of Progress in Quantitative Nondestructive Evaluation*, edited by D. O. Thompson, D. E. Chimenti (Plenum, New York), Vol. 13B, pp. 1453–1460.

Nozaki, H., and Shindo, Y. (**1998**). ''Effect of interface layers on elastic wave propagation in a fiber-reinforced metal-matrix composite,'' Int. J. Eng. Sci. **36**, 383–394.

Olsson, P., Datta, S. K., and Bostrom, A. (**1990**). ''Elastodynamic scattering from inclusions surrounded by thin interface layers,'' J. Appl. Mech. **57**, 672–676.

Pao, Y.-H., and Mow, C.-C. (**1971**). *Diffraction of Elastic Waves and Dynamic Stress Concentrations* (Crane Russak, New York).

Peterson, B., and Ström, S. (**1975**). ''Matrix formulation of acoustic scattering from multi-layered scatterers,'' J. Acoust. Soc. Am. **57**, 2–13.

Pillai, T. A. K., Varadan, V. K., and Varadan, V. V. (**1983**). ''Acoustic wave scattering by elastic cylindrical shells in water,'' J. Acoust. Soc. Am. **74**, 619–624.

Sato, H., and Shindo, Y. (**2003**). ''Multiple scattering of plane elastic waves in particle-reinforced-composite medium with graded interfacial layers,'' Mech. Mater. **35**, 83–106.

Schmidt, H. (**1993**). ''Numerically stable global matrix approach to radiation and scattering from spherically stratified shells,'' J. Acoust. Soc. Am. **94**, 2420–2430.

Shindo, Y., and Niwa, N. (**1996**). ''Scattering of antiplane shear wave in a fiber-reinforced composite medium with interfacial layers,'' Acta Mech. **117**, 181–190.

Sinclair, A. N., and Addison, R. C. Jr., (**1993**). ''Acoustic diffraction spectrum of a SiC fiber in a solid elastic medium,'' J. Acoust. Soc. Am. **94**, 1126–1135.

Varadan, V. K., and Varadan, V. V. (eds.) (**1980**). *Acoustic, Electromagnetic and Elastic Wave Scattering—Focus on the T-Matrix Approach*, (Pergamon, New York).

Videen, G. (**2003**). ''Seismic scattering from a spherical inclusion eccentrically located within a homogeneous, spherical host: theoretical derivation,'' Waves Random Media **13**, 177–190.

Waterman, P. C. (**1969**). ''New formulation for acoustic scattering,'' J. Acoust. Soc. Am. **45**, 1417–1429.

Yim, H., and Williams, J. H. Jr., (**1995**). ''Database generation and parametric study for ultrasonic non-destructive characterization of a single fiber composite interphase,'' Ultrasonics **33**, 389–401.

Mode-exciting method for Lamb wave-scattering analysis

Arief Gunawan and Sohichi Hirose
Department of Mechanical and Environmental Informatics, Tokyo Institute of Technology, 2-12-1 O-okayama, Meguro-ku, Tokyo 152-8552, Japan

(Received 15 December 2002; revised 8 October 2003; accepted 29 October 2003)

This paper presents an innovative method, called the mode-exciting method, to solve Lamb wave-scattering problems in an infinite plate. In this method, a set of Lamb wave modes is excited by appropriate boundary conditions given on the virtual edges of a finite plate. After solving numerically the elastodynamic problem defined in the finite domain, the numerical solution is decomposed into Lamb wave modes. The Lamb wave modes constitute a system of equations, which can be used to determine the scattering coefficients of Lamb waves for the original problem in an infinite plate. The advantage of the mode-exciting method is that a well-developed numerical method such as finite-element (FEM) or boundary element (BEM) can be used in the elastodynamic analysis for the finite region without any modification like coupling with other numerical techniques. In numerical examples, first the error estimation of the mode-exciting method is discussed by considering three types of error indicators. It is shown that among them, the power ratio of nonpropagating modes to propagating modes is the most suitable for the error estimation. Numerical results are then shown for scattering coefficients as a function of nondimensional frequency for edge reflection and crack scattering problems. [DOI: 10.1121/1.1639330]

PACS numbers: 43.20.Gp, 43.20.Mv [DEC] Pages: 996–1005

I. INTRODUCTION

Lamb wave ultrasonic method is usually applied in nondestructive evaluation to detect a defect in a thin plate.[1] This method is very useful because it can scan a wide range of the plate without moving a transducer during inspection. Therefore, the Lamb wave method is suitable to *in situ* inspection. Scattering characteristics of Lamb waves are, however, very complicated, because the interaction between Lamb waves and scatterers causes mode conversions which involve not only propagating modes but also an infinite number of nonpropagating modes. Therefore, a Lamb wave-scattering analysis is hard to carry out analytically.

Some researchers have carried out the Lamb wave-scattering analysis semianalytically.[2–5] However, the problems solved by the semianalytical analysis have been restricted to simple examples. Moreover, the semianalytical method still needs specific numerical calculation that has the possibility to cause instability or divergency in the solution.

On the other hand, numerical analyses have great potential to solve a variety of problems. Koshiba *et al.*[6] and Al-Nassar *et al.*[7] have applied a finite-element method (FEM) combined with a normal-mode expansion to Lamb wave-scattering analysis. Cho and Rose[8,9] have developed a hybrid method of the boundary element method (BEM) and a normal-mode expansion technique to solve scattering and edge reflection of Lamb waves. However, because FEM and BEM are coupled to the other numerical technique, the FEM and BEM have to be modified properly before their application to Lamb wave-scattering analysis. This modification always needs supplemental knowledge about the FEM and BEM, and tends to reduce the ability of the FEM and BEM themselves.

In this paper, we develop an innovative method, called the mode-exciting method, to calculate scattering coefficients of Lamb waves generated by the interaction of an incident Lamb wave with scatterers in an infinite plate. In all previous studies mentioned above, the scattering coefficients subjected to an incident Lamb wave of the specified mode and the unit amplitude were directly determined by using an FEM or a BEM in conjunction with a normal-mode expansion. In the mode-exciting method, however, all Lamb wave modes are simultaneously excited by appropriate boundary conditions given on both ends of a finite plate. The excited Lamb wave modes constitute a system of equations which is solved to determine the scattering coefficients for all Lamb modes.

The advantage of the mode-exciting method is that the wave analysis is carried out for the finite domain bounded by the upper and lower plate surfaces and the virtual edges, even though the original problem deals with the infinite plate. Therefore, in the wave analysis we can use a well-developed numerical method such as an FEM or a BEM with no modification and no coupling scheme to other methods.

In Sec. II, the basic theories of Lamb wave modes are summarized and in Sec. III, then, the formulation of mode-exciting method is presented with some remarks. Some numerical examples for the problems of edge reflection and crack scattering are shown in Sec. IV, which is followed by the conclusions in Sec. V.

II. BASIC THEORY OF LAMB WAVE MODES

Before presenting the mode-exciting method for Lamb wave-scattering analysis, some fundamental properties of Lamb wave modes are summarized in this section.

A. Fundamental relationships

Let us consider a homogeneous, isotropic, and linearly elastic plate with the thickness $2h$. We take the x_1 axis in the longitudinal direction, the x_2 axis in the thickness direction, and the x_3 axis in the antiplane direction of the plate. On the assumption that traction-free conditions are given on the upper and lower surfaces and the wave field in the plate is time harmonic and in a plane strain state, it is known that there exist Lamb wave modes[1,10,11] with the dispersive relations

$$\frac{\tan(qh)}{\tan(ph)}+\frac{4k^2pq}{(q^2-k^2)^2}=0, \tag{1}$$

for symmetric modes and

$$\frac{\tan(qh)}{\tan(ph)}+\frac{(q^2-k^2)^2}{4k^2pq}=0, \tag{2}$$

for antisymmetric modes, where k and ω denote the wave number and the frequency, respectively. In Eqs. (1) and (2)

$$p^2=\frac{\omega^2}{c_L^2}-k^2, \quad q^2=\frac{\omega^2}{c_T^2}-k^2, \tag{3}$$

c_L and c_T are the velocities of longitudinal and transverse waves, respectively. As a numerical example, the dispersion curves for the steel with $c_L=5940$ m/s and $c_T=3200$ m/s are shown in Fig. 1. Detailed discussion on dispersion of Lamb waves can be found in many books, e.g., see the textbook authored by Achenbach.[10]

The displacement of the Lamb wave modes can be expressed as

$$u_1=iAk\left\{\frac{\cos(px_2)}{\sin(ph)}+\frac{2pq}{k^2-q^2}\frac{\cos(qx_2)}{\sin(qh)}\right\}e^{i(kx_1-\omega t)},$$

$$u_2=-Ap\left\{\frac{\sin(px_2)}{\sin(ph)}-\frac{2k^2}{k^2-q^2}\frac{\sin(qx_2)}{\sin(qh)}\right\}e^{i(kx_1-\omega t)}, \tag{4}$$

for symmetric modes and

$$u_1=iAk\left\{\frac{\sin(px_2)}{\cos(ph)}+\frac{2pq}{k^2-q^2}\frac{\sin(qx_2)}{\cos(qh)}\right\}e^{i(kx_1-\omega t)},$$

$$u_2=Ap\left\{\frac{\cos(px_2)}{\cos(ph)}-\frac{2k^2}{k^2-q^2}\frac{\cos(qx_2)}{\cos(qh)}\right\}e^{i(kx_1-\omega t)}, \tag{5}$$

for antisymmetric modes, where A is an arbitrary constant.

The stress components can be evaluated by substituting Eqs. (4) and (5) into the stress—displacement relation

$$\tau_{ij}=\rho(c_L^2-2c_T^2)u_{k,k}\delta_{ij}+\rho c_T^2(u_{i,j}+u_{j,i}), \tag{6}$$

where ρ is the density and δ_{ij} is the Kronecker delta.

B. Orthogonality of Lamb wave modes

Let $\mathcal{L}_1,\mathcal{L}_2,\ldots$ be the Lamb wave modes without distinguishing symmetric and antisymmetric modes. These modes are assumed to have different wave numbers from each other.

We now consider two modes $\mathcal{L}_m$ and $\mathcal{L}_n$ with the wave numbers k_m and k_n that have the displacement and tensor fields $[\mathbf{u},\boldsymbol{\tau}]$ and $[\mathbf{v},\boldsymbol{\sigma}]$, respectively, where

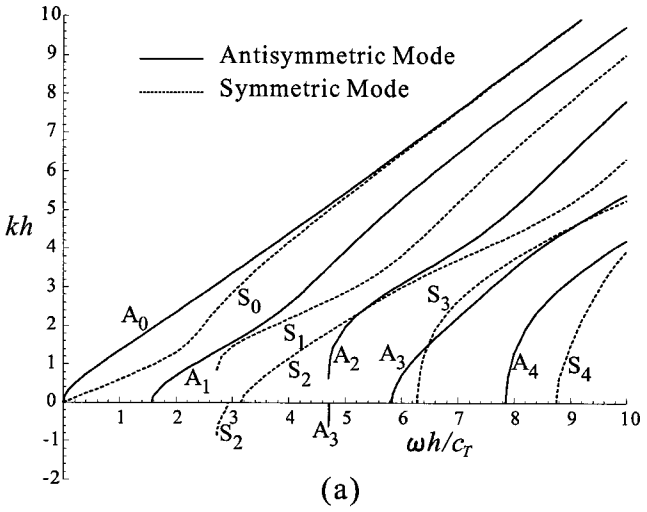

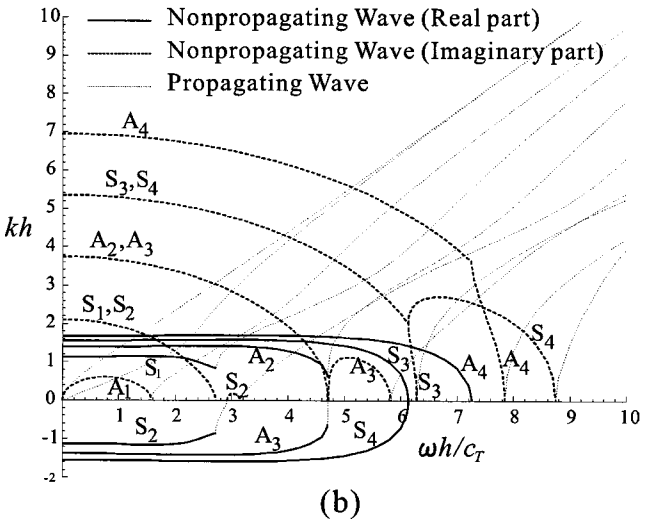

FIG. 1. Dispersion curves for (a) propagating Lamb waves and (b) nonpropagating Lamb waves.

$$\mathbf{u}=\tilde{\mathbf{u}}e^{-i\omega t}=\hat{\mathbf{u}}e^{i(k_mx_1-\omega t)}, \quad \boldsymbol{\tau}=\tilde{\boldsymbol{\tau}}e^{-i\omega t}=\hat{\boldsymbol{\tau}}e^{i(k_mx_1-\omega t)},$$

$$\mathbf{v}=\tilde{\mathbf{v}}e^{-i\omega t}=\hat{\mathbf{v}}e^{i(k_nx_1-\omega t)}, \quad \boldsymbol{\sigma}=\tilde{\boldsymbol{\sigma}}e^{-i\omega t}=\hat{\boldsymbol{\sigma}}e^{i(k_nx_1-\omega t)}. \tag{7}$$

Then, it has been proved by Auld[11] that

$$(k_m-k_n^*)P_{mn}=0, \tag{8}$$

where

$$P_{mn}=\frac{i\omega}{4}\int_{-h}^{h}(\hat{u}_i\hat{\sigma}_{1i}^*-\hat{v}_i^*\hat{\tau}_{1i})dx_2. \tag{9}$$

We will now further discuss the physical meaning of P_{mn}. For two modes $\mathcal{L}_m$ and $\mathcal{L}_n$ defined in Eq. (7), the powers passing through a vertical section of the plate are calculated by

$$\mathcal{P}[\mathcal{L}_m]=\Re\int_{-h}^{h}-\frac{i\omega}{2}\tilde{u}_i^*\tilde{\tau}_{1i}dx_2, \tag{10}$$

$$\mathcal{P}[\mathcal{L}_n]=\Re\int_{-h}^{h}-\frac{i\omega}{2}\tilde{v}_i^*\tilde{\sigma}_{1i}dx_2, \tag{11}$$

where $\Re$ denotes the real part of the integral. In the sequel, we will omit the symbol $\Re$ for simplicity.

According to the linearity of elastodynamic field, the displacement and stress of the superposition of $\mathcal{L}_m$ and $\mathcal{L}_n$ can be written as $[\mathbf{u}+\mathbf{v}, \boldsymbol{\tau}+\boldsymbol{\sigma}]$, and then the power becomes

$$\mathcal{P}[\mathcal{L}_m+\mathcal{L}_n]=\int_{-h}^{h}-\frac{i\omega}{2}(\tilde{u}_i^*+\tilde{v}_i^*)(\tilde{\tau}_{1i}+\tilde{\sigma}_{1i})dx_2$$

$$=\mathcal{P}[\mathcal{L}_m]+\mathcal{P}[\mathcal{L}_n]-\frac{\omega}{2}\int_{-h}^{h}(i\tilde{u}_i^*\tilde{\sigma}_{1i}+i\tilde{v}_i^*\tilde{\tau}_{1i})dx_2.$$

Because only the real part of power is considered, we can replace $i\tilde{u}_i^*\tilde{\sigma}_{1i}$ with its conjugate $-i\tilde{u}_i\tilde{\sigma}_{1i}^*$ to have

$$\mathcal{P}[\mathcal{L}_m+\mathcal{L}_n]=\mathcal{P}[\mathcal{L}_m]+\mathcal{P}[\mathcal{L}_n]-\frac{i\omega}{2}\int_{-h}^{h}(-\tilde{u}_i\tilde{\sigma}_{1i}^*+\tilde{v}_i^*\tilde{\tau}_{1i})dx_2. \quad (12)$$

Using Eq. (7), Eq. (12) can be written as

$$\mathcal{P}[\mathcal{L}_m+\mathcal{L}_n]=\mathcal{P}[\mathcal{L}_m]+\mathcal{P}[\mathcal{L}_n]+\frac{i\omega}{2}\int_{-h}^{h}(\hat{u}_i\hat{\sigma}_{1i}^*-\hat{v}_i^*\hat{\tau}_{1i})e^{i(k_m-k_n^*)x_1}dx_2$$

$$=\mathcal{P}[\mathcal{L}_m]+\mathcal{P}[\mathcal{L}_n]+2e^{i(k_m-k_n^*)x_1}P_{mn}. \quad (13)$$

Let us consider the third term on the right-hand side of Eq. (13). When $P_{mn}=0$, it is obvious that $2e^{i(k_m-k_n^*)x_1}P_{mn}=2P_{mn}$. Even for $P_{mn}\neq 0$, we also have $2e^{i(k_m-k_n^*)x_1}P_{mn}=2P_{mn}$, since $k_m-k_n^*=0$ from Eq. (8). Hence, Eq. (13) can be rewritten as

$$\mathcal{P}[\mathcal{L}_m+\mathcal{L}_n]=\mathcal{P}[\mathcal{L}_m]+\mathcal{P}[\mathcal{L}_n]+2P_{mn}. \quad (14)$$

From Eq. (14), it is clear that the real part of P_{mn} represents the difference between the sum of the powers of two modes and the power of their superposition. If $P_{mn}=0$, then the power of the sum of two modes is equal to the sum of the powers of each mode.

Next, we consider the special case of $m=n$. From Eq. (14), we can easily find that P_{mm} is equal to the power of $\mathcal{L}_m$, i.e.,

$$P_{mm}=\mathcal{P}[\mathcal{L}_m]. \quad (15)$$

If the Lamb wave mode $\mathcal{L}_m$ is a nonpropagating mode, the wave number k_m is not a pure real value, i.e., $k_m-k_m^*\neq 0$. Then, we obtain

$$\mathcal{P}[\mathcal{L}_m]=P_{mm}=0, \quad (16)$$

from Eqs. (8) and (15). It can, therefore, be said that the nonpropagating mode has no power flow.

Taking the same procedure as in the case of two modes, we can also extend Eq. (14) to the case of three or more modes. The result for a set of K modes $\mathcal{L}_{m_1},\mathcal{L}_{m_2},\ldots,\mathcal{L}_{m_K}$ can be expressed as

$$\mathcal{P}\left[\sum_{i=1}^{K}\mathcal{L}_{m_i}\right]=\sum_{i=1}^{K}\mathcal{P}[\mathcal{L}_{m_i}]+\sum_{i=1}^{K-1}\sum_{j=i+1}^{K}2P_{m_im_j}. \quad (17)$$

It is noted that $m_1,m_2,\ldots,m_K$ need not differ from each other.

Furthermore, if a set of Lamb wave modes $\mathcal{L}_{m_i}$ $(i=1,\ldots,K)$ with the wave numbers k_{m_i} has the property that any two Lamb wave modes $\mathcal{L}_{m_i}$ and $\mathcal{L}_{m_j}$ $(1\leqslant i<j\leqslant K)$ are different from each other in the sense of $k_{m_i}-k_{mj}^*\neq 0$, then Eq. (8) yields $P_{m_im_j}=0$, and hence we have

$$\mathcal{P}\left[\sum_{i=1}^{K}\mathcal{L}_{m_i}\right]=\sum_{i=1}^{K}\mathcal{P}[\mathcal{L}_{m_i}]. \quad (18)$$

In this paper, we say that a set of Lamb wave modes satisfying Eq. (18) has the property of *orthogonality of power distribution*.

Next, we consider in detail the cases of $k_m=k_n^*$, where the orthogonality of power distribution is not guaranteed. The condition of $k_m=k_n^*$ is satisfied in the case of

(i) $k_m=k_n$ and k_m has no imaginary part;
(ii) $k_m=-k_n$ and k_m has no real part; and
(iii) $k_m=k_n^*$ and k_m has both real and imaginary parts.

In the first case, both Lamb wave modes $\mathcal{L}_m$ and $\mathcal{L}_n$ are propagating modes with the same wave numbers, which have apparently no orthogonality of power distribution. In the latter two cases, $\mathcal{L}_m$ and $\mathcal{L}_n$ are nonpropagating modes with the opposite signs in the imaginary parts of the wave numbers, which have no orthogonality of power distribution. Hereafter, we call a pair of these modes *conjugate nonpropagating modes*. It is of interest that a single nonpropagating mode cannot carry power as shown in Eq. (16), but the conjugate nonpropagating modes can.[11] From Eqs. (14) and (16), the power of conjugate nonpropagating modes $\mathcal{L}_m$ and $\mathcal{L}_n$ can be found as

$$\mathcal{P}[\mathcal{L}_m+\mathcal{L}_n]=2P_{mn}. \quad (19)$$

C. Normalized Lamb wave modes

The expressions of Lamb wave modes in Eqs. (4) and (5) contain an arbitrary factor A in the amplitude. We now introduce a power-based normalized Lamb wave mode to relate the magnitude of the amplitude directly to the power.

The normalized displacement $\overline{\mathbf{u}}$ of a propagating Lamb wave mode $\mathcal{L}_m$ is defined as

$$\overline{\mathbf{u}}=\frac{\mathbf{u}}{\sqrt{|\mathcal{P}[\mathcal{L}_m]|}}, \quad (20)$$

where $\mathbf{u}$ is the displacement of mode $\mathcal{L}_m$. According to the above definition, it is clear that $|\mathcal{P}[\overline{\mathcal{L}_m}]|=1$ for a normalized propagating mode $\overline{\mathcal{L}_m}$.

In the normalization of a nonpropagating Lamb wave mode, we need to use the power of the superposition of conjugate nonpropagating modes, since a single nonpropagating mode has no power. If $\mathbf{u}$ and $\mathbf{v}$ are displacements of conjugate nonpropagating Lamb wave modes $\mathcal{L}_m$ and $\mathcal{L}_n$, respectively, the normalized displacements $\overline{\mathbf{u}}$ and $\overline{\mathbf{v}}$ are defined as

$$\overline{\mathbf{u}}=\frac{\mathbf{u}}{\sqrt{|P_{mn}|}},\quad \overline{\mathbf{v}}=\frac{\mathbf{v}}{\sqrt{|P_{mn}|}},\tag{21}$$

where P_{mn} is defined in Eq. (9). From the definition of $\overline{\mathbf{u}}$ and $\overline{\mathbf{v}}$, it is clear that $|\mathcal{P}[\overline{\mathcal{L}_m}+\overline{\mathcal{L}_n}]|\leqslant 2$.

It can easily be shown that the power of normalized propagating mode is evaluated as

$$|\mathcal{P}[A_m\overline{\mathcal{L}_m}]|=|A_m|^2,\tag{22}$$

where A_m is the amplitude of the mode $\overline{\mathcal{L}_m}$. Also, the power of the superposition of normalized conjugate nonpropagating modes is evaluated as

$$|\mathcal{P}[A_m\overline{\mathcal{L}_m}+A_n\overline{\mathcal{L}_n}]|=2\Re(A_mA_n^*\overline{P}_{mn})\leqslant 2|A_mA_n|,\tag{23}$$

where $\overline{P}_{mn}$ is defined for the normalized modes $\overline{\mathcal{L}_m}$ and $\overline{\mathcal{L}_n}$.

Hereafter, we use the symbol $\mathcal{L}_n$ for the normalized Lamb wave mode without the upper bar in $\overline{\mathcal{L}_n}$.

D. Mode decomposition

Here, we present a mode decomposition method for a time-harmonic elastodynamic field $\mathcal{E}=[\tilde{\mathbf{u}}e^{-i\omega t},\tilde{\boldsymbol{\tau}}e^{-i\omega t}]$ in a plate which satisfies the traction-free boundary condition on the top and bottom surfaces. To simplify the notation, we introduce a new operator "$\odot$" that relates two time-harmonic elastodynamic fields $\mathcal{E}$ and $\mathcal{E}'$ to a scalar value as follows:

$$\mathcal{E}\odot\mathcal{E}'\equiv\frac{i\omega}{4}\int_{-h}^{h}(\tilde{u}_i\tilde{\sigma}_{1i}^*-\tilde{v}_i^*\tilde{\tau}_{1i})dx_2,\tag{24}$$

where $\mathcal{E}=[\tilde{\mathbf{u}}e^{-i\omega t},\tilde{\boldsymbol{\tau}}e^{-i\omega t}]$ and $\mathcal{E}'=[\tilde{\mathbf{v}}e^{-i\omega t},\tilde{\boldsymbol{\sigma}}e^{-i\omega t}]$. From Eqs. (7)–(9), it is obvious that $\mathcal{L}_m\odot\mathcal{L}_n$ is equal to P_{mn}.

Suppose that a general elastodynamic field $\mathcal{E}$ is expressed by the superposition of the Lamb wave modes as follows:

$$\mathcal{E}=\sum_{n=1}^{\infty}A_n\mathcal{L}_n.\tag{25}$$

Note that the right-hand side of Eq. (25) contains all of the propagating modes and the nonpropagating modes. If we apply $\odot\mathcal{L}_m$ to both sides of Eq. (25), then we have

$$\mathcal{E}\odot\mathcal{L}_m=\sum_{n=1}^{\infty}A_n\mathcal{L}_n\odot\mathcal{L}_m=\sum_{n=1}^{\infty}A_nP_{nm}.\tag{26}$$

From Eq. (8), P_{mn} is not zero only if $k_n=k_m^*$. Then, we find that

$$A_m=\frac{\mathcal{E}\odot\mathcal{L}_{\tilde{m}}}{P_{m\tilde{m}}},\tag{27}$$

where

$$\tilde{m}=\begin{cases}m, \text{if } \mathcal{L}_m \text{ is a propagating mode,}\\ n \text{ satisfying } k_n=k_m^*, \text{if } \mathcal{L}_m \text{ is a}\\ \quad\text{nonpropagating mode.}\end{cases}$$

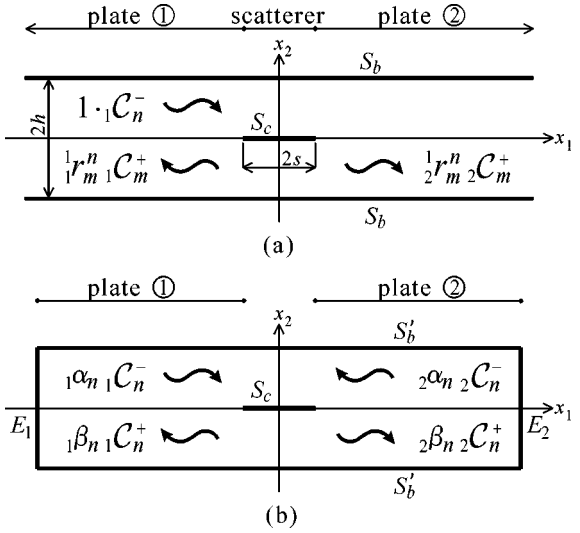

FIG. 2. (a) Scattering problem by a horizontal crack in an infinite plate and (b) the boundary value problem for a finite plate considered in the mode exciting method.

III. MODE-EXCITING METHOD

A. Statement of the problem

The scattering problem in an infinite plate with a horizontal crack as shown in Fig. 2(a) is considered here to explain the mode-exciting method. The plate is composed of two plain plates ① and ② with semi-infinite lengths, connected by a central part including a crack as a scatterer. Application of the mode-exciting method to problems with more complicated geometries will be shown later.

When an incident wave hits the scatterer, scattered waves are generated so that the superposition of the incident and scattered waves, i.e., the total wave, satisfies the boundary condition on the surface of the scatterer as well as the boundary condition on the top and bottom surfaces of the plates. Generally, the scattered waves include not only propagating modes, but also nonpropagating modes. However, because the receiving transducer is normally located far from the scatterer in Lamb wave ultrasonic testing, scattered nonpropagating modes decay before reaching the receiver. On the other hand, propagating modes can travel without attenuation in a plate. In the Lamb wave-scattering analysis, therefore, the scattered nonpropagating modes are neglected and only the scattered propagating modes are taken into account.

Now, we introduce the symbol ${}_i\mathcal{C}_n^{\pm}$ for the *propagating* Lamb wave mode of nth order in the plate ⓘ. Here, the superscripts $^-$ and $^+$ in ${}_i\mathcal{C}_n^{\pm}$ denote the incident wave propagating toward the scatterer and the scattered wave traveling away from the scatterer, respectively. As shown in Fig. 2(a), suppose that the Lamb wave ${}_1\mathcal{C}_n^-$ of the nth propagating mode in the plate ① is incident to the scatterer and the scattered waves of all Lamb modes are generated in both plates ① and ②. Note that the incident wave has a unit amplitude. In the far field where all scattered nonpropagating modes vanish, then the scattering process can be written in the form

$$1 \cdot {}_i\mathcal{C}_n^- \rightarrow \sum_{j=1}^{2} \sum_{m=1}^{\mathcal{N}_j} {}_j^i r_m^n \, {}_j\mathcal{C}_m^+ \quad (i=1), \tag{28}$$

where ${}_j^i r_m^n$ is the amplitude of the scattered Lamb wave ${}_j\mathcal{C}_m^+$ of the mth propagating mode in the plate ⓙ due to the incident Lamb wave ${}_i\mathcal{C}_n^-$ of the nth propagating mode in the plate ⓘ, and $\mathcal{N}_j$ is the number of propagating modes in the plate ⓙ, which depends on the frequency times the thickness of the plate as shown in Fig. 1(a). The arrow in Eq. (28) means the scattering process in which the incident wave ${}_i\mathcal{C}_n^-$ is transformed into the scattered waves ${}_j\mathcal{C}_m^+$ ($j=1,2, m=1,...,\mathcal{N}_j$). The problem in Lamb wave-scattering analysis is to determine ${}_j^i r_m^n$, which are called *scattering coefficients*. The coefficients ${}_j^i r_m^n$ are complex variables, and their square absolute values and arguments represent the powers and the phase shifts, respectively.

Note that $\mathcal{N}_1=\mathcal{N}_2$ for the problem shown in Fig. 2(a), because the plates ① and ② have the same thickness and material. In general, however, $\mathcal{N}_1$ and $\mathcal{N}_2$ may take different values. For general description of the mode-exciting method, therefore, we still keep using the subscripts in $\mathcal{N}_1$ and $\mathcal{N}_2$ in the following.

B. Formulation of mode-exciting method

As stated in the previous subsection, the original problem in Lamb wave-scattering analysis is related to the plate with infinite length. The wave problem in an infinite plate, however, is relatively troublesome to be solved by using a normal numerical method such as an FEM or BEM. In the mode-exciting method, Lamb waves in the plate with finite length are analyzed to obtain the scattering coefficients of Lamb waves in an infinite plate. Thus, a usual numerical method can be applied to the wave analysis in a finite domain without any modification.

As shown in Fig. 2(b), let us consider the time-harmonic boundary value problem defined in the interior domain D enclosed by the plate surfaces S_b', the crack surface S_c, and the virtual edges E_1 and E_2. Since S_b' and S_c are traction free, the boundary conditions on these surfaces are given by $\tau_{21}=\tau_{22}=0$. Unlike S_b' and S_c, however, the boundary conditions on E_1 and E_2 cannot be specified *a priori* so as to produce the same wave field as that in Fig. 2(a). Nevertheless, we set some boundary conditions, called *exciters*, on the virtual edges E_1 and E_2. Here, the exciters can be chosen arbitrarily, and the wave field excited by the exciters is generally different from that in the original problem in Fig. 2(a). In the mode-exciting method, the wave field excited by the exciters is used to constitute a system of equations to determine the scattering coefficients ${}_j^i r_m^n$ as described in the sequel. Also given later are details on where the virtual edges E_1 and E_2 should be taken and how the exciters given on E_1 and E_2 are selected. After all boundary conditions are specified for the interior domain D, the boundary value problem becomes a well-posed problem, which can be solved easily by using a usual numerical tool.

For a preliminary procedure in making a system of equations in the mode-exciting method, we consider here the Lamb wave modes in a finite plate as shown in Fig. 2(b). Suppose that the solution of the boundary value problem yields a time-harmonic elastodynamic field ${}_i\mathcal{E}$ in the plate ⓘ in Fig. 2(b). Because ${}_i\mathcal{E}$ satisfies the traction free boundary condition on the surfaces of the plate ⓘ, ${}_i\mathcal{E}$ can be decomposed into the superposition of Lamb wave modes by virtue of the mode decomposition technique stated in Sec. II D, i.e.,

$${}_i\mathcal{E}=\sum_{n=1}^{\infty} {}_iA_n \, {}_i\mathcal{L}_n, \tag{29}$$

where ${}_i\mathcal{L}_n$ is the nth Lamb wave mode in the plate ⓘ and ${}_iA_n$ is the amplitude of ${}_i\mathcal{L}_n$. Generally, the Lamb wave modes ${}_i\mathcal{L}_n$ in Eq. (29) contain both propagating modes and nonpropagating modes. As shown before, the propagating modes can be divided into two types, ${}_i\mathcal{C}_n^-$ and ${}_i\mathcal{C}_n^+$, depending on the propagation direction. Similarly, the nonpropagating modes can also be divided into two types depending on the evanescing directions. Let ${}_i\mathcal{D}_n^-$ and ${}_i\mathcal{D}_n^+$ be the *nonpropagating* Lamb wave modes of nth order in plate ⓘ which decay in the directions toward the scatterer and toward the virtual edge, respectively. Hence, the elastodynamic field ${}_i\mathcal{E}$ can be separated into four types of Lamb wave modes as follows:

$${}_i\mathcal{E}=\sum_{n=1}^{\mathcal{N}_i} ({}_i\alpha_n \, {}_i\mathcal{C}_n^- + {}_i\beta_n \, {}_i\mathcal{C}_n^+) + \sum_{n=1}^{\infty} ({}_i\gamma_n \, {}_i\mathcal{D}_n^- + {}_i\delta_n \, {}_i\mathcal{D}_n^+), \tag{30}$$

where ${}_i\alpha_n$, ${}_i\beta_n$, ${}_i\gamma_n$, and ${}_i\delta_n$ are the amplitudes of the Lamb wave modes ${}_i\mathcal{C}_n^-$, ${}_i\mathcal{C}_n^+$, ${}_i\mathcal{D}_n^-$, and ${}_i\mathcal{D}_n^+$, respectively. Note that there are a finite number of modes in propagating Lamb waves, whereas nonpropagating Lamb waves have an infinite number of modes.

Now, we discuss the wave field near the scatterer in more detail. Since ${}_i\alpha_n \, {}_i\mathcal{C}_n^-$ and ${}_i\gamma_n \, {}_i\mathcal{D}_n^-$ are considered as incident waves, and ${}_i\beta_n \, {}_i\mathcal{C}_n^+$ and ${}_i\delta_n \, {}_i\mathcal{D}_n^+$ are taken as scattered waves, the scattering process in the vicinity of the scatterer can be written as follows:

$$\sum_{i=1}^{2} \left(\sum_{n=1}^{\mathcal{N}_i} {}_i\alpha_n \, {}_i\mathcal{C}_n^- + \sum_{n=1}^{\infty} {}_i\gamma_n \, {}_i\mathcal{D}_n^- \right) \rightarrow \sum_{j=1}^{2} \left(\sum_{m=1}^{\mathcal{N}_j} {}_j\beta_m \, {}_j\mathcal{C}_m^+ + \sum_{m=1}^{\infty} {}_j\delta_m \, {}_j\mathcal{D}_m^+ \right). \tag{31}$$

In the above equation, the Lamb wave modes $\Sigma_i \Sigma_n \, {}_i\gamma_n \, {}_i\mathcal{D}_n^-$ are nonpropagating incident wave generated by the exciters. If the distance between the virtual edge and the scatterer is taken large enough, however, the displacements of these modes will become quite small when these modes reach the scatterer, because of exponentially evanescing property of the nonpropagating modes. Thus, ${}_i\gamma_n \, {}_i\mathcal{D}_n^-$ can be neglected in Eq. (31), and hence we have

$$\sum_{i=1}^{2} \sum_{n=1}^{\mathcal{N}_i} {}_i\alpha_n \, {}_i\mathcal{C}_n^- \rightarrow \sum_{j=1}^{2} \left(\sum_{m=1}^{\mathcal{N}_j} {}_j\beta_m \, {}_j\mathcal{C}_m^+ + \sum_{m=1}^{\infty} {}_j\delta_m \, {}_j\mathcal{D}_m^+ \right). \tag{32}$$

In this equation, the incident wave consists of only propagating modes that can travel with constant amplitudes in a plain plate. It means that Eq. (32) expresses the scattering process equivalent to that in an *infinite* plate subjected to the incident wave of propagating modes $\Sigma_i \Sigma_n {}_i\alpha_n {}_i\mathcal{C}_n^-$. Note that the scattering wave near the scatterer includes propagating modes as well as nonpropagating modes, which are indispensable to satisfy the boundary condition on the scatterer. However, because the nonpropagating scattered wave evanesces exponentially, the scattering process in the far field can be written as follows:

$$\sum_{i=1}^{2} \sum_{n=1}^{\mathcal{N}_i} {}_i\alpha_n {}_i\mathcal{C}_n^- \rightarrow \sum_{j=1}^{2} \sum_{m=1}^{\mathcal{N}_j} {}_j\beta_m {}_j\mathcal{C}_m^+ . \tag{33}$$

In the following, we show how to constitute a system of equations to determine the scattering coefficients ${}_j^i r_m^n$ in the original problem. Multiplying both sides of Eq. (28) by ${}_i\alpha_n$ and taking the summation for all modes in all plates leads to the following relation:

$$\sum_{i=1}^{2} \sum_{n=1}^{\mathcal{N}_i} {}_i\alpha_n {}_i\mathcal{C}_n^- \rightarrow \sum_{j=1}^{2} \sum_{m=1}^{\mathcal{N}_j} \sum_{i=1}^{2} \sum_{n=1}^{\mathcal{N}_i} {}_i\alpha_n {}_j^i r_m^n {}_j\mathcal{C}_m^+ . \tag{34}$$

Comparison between Eqs. (33) and (34) yields a set of equations with ${}_j^i r_m^n$ as unknown variables

$$\sum_{i=1}^{2} \sum_{n=1}^{\mathcal{N}_i} {}_i\alpha_n {}_j^i r_m^n = {}_j\beta_m \quad (m=1,...,\mathcal{N}_j, \quad j=1,2). \tag{35}$$

Note that ${}_i\alpha_n$ and ${}_j\beta_m$ are known coefficients, which are obtained by the mode decomposition of the wave field in a plate with finite length.

In Eq. (35) the number of equations is $\mathcal{N}_T$, where $\mathcal{N}_T = \mathcal{N}_1 + \mathcal{N}_2$, while the number of unknown variables ${}_j^i r_m^n$ is $\mathcal{N}_T^2$. Therefore, the number of equations in Eq. (35) is not sufficient to determine ${}_j^i r_m^n$. Additional equations can be obtained easily, however. It is clear that the values of ${}_i\alpha_n$ and ${}_j\beta_m$ depend on the exciters applied on the virtual edges. If another set of exciters is applied on the virtual edges, then another set of ${}_i\alpha_n$ and ${}_j\beta_m$ can be obtained. Using $\mathcal{N}_T$ different sets of exciters, therefore, $\mathcal{N}_T$ different sets of ${}_i\alpha_n$ and ${}_j\beta_m$ are obtained, and hence the number of equations becomes $\mathcal{N}_T^2$, compatible with the number of unknowns ${}_j^i r_m^n$. Note that since ${}_i\alpha_n$ and ${}_j\beta_m$ are complex values, the scattering coefficients ${}_j^i r_m^n$ are obtained as complex numbers.

C. Remarks on the mode exciting method

1. How to select the exciters

As stated in the last subsection, $\mathcal{N}_T$ different sets of exciters are necessary to determine the scattering coefficients ${}_j^i r_m^n$ in the mode-exciting method. The problem is how we should select $\mathcal{N}_T$ sets of exciters so that we can obtain a solution.

The scattering coefficients ${}_j^i r_m^n$ are solutions of the system of linear equations (35) with the Lamb wave amplitudes ${}_i\alpha_n$ in coefficients. Obviously, the necessary and sufficient condition for the existence of the solution for Eq. (35) is that the amplitudes ${}_i\alpha_n$ of the incident propagating modes are linearly independent for all sets of exciters given on the virtual edges E_1 and E_2.

It is, however, quite difficult to derive the explicit relation between the amplitudes of incident propagating modes ${}_i\alpha_n$ and the exciters given on E_1 and E_2. Since linear dependence in sets of exciters obviously causes linear dependence in sets of amplitudes of incident propagating modes, it can be said that linear independence in sets of exciters is a necessary condition for the existence of the solution. Linear independence in the sets of exciters is not, however, a sufficient condition for the existence of the solution, as shown in the following. Consider two sets of exciters on virtual edges which are different from each other only by displacement distribution of a certain nonpropagating mode. If the virtual edges are set far enough from the scatterer, nonpropagating displacement components in exciters have no effect on the scattering process near the scatterer. These two sets of exciters may, therefore, generate incident propagating modes with the same amplitudes, which violate the existence of the solution.

Although only the necessary condition is known as mentioned above, linear independence in exciters is usually sufficient in practice unless the displacement distributions of nonpropagating modes are used intentionally as an exciter. Linearly independent $\mathcal{N}_T$ sets of exciters can be easily constructed, for example, by using the displacement distribution of propagating modes as an exciter. An example is given in Sec. IV A.

2. Computational time

In the mode-exciting method, the boundary value problems have to be solved for $\mathcal{N}_T$ different sets of exciters even if only one mode of Lamb wave is of interest as incident wave in the scattering analysis. Since most of computational time is spent for solving the boundary value problem by a numerical method such as FEM or BEM, the computational time of the whole of the mode-exciting method is ordinarily proportional to $\mathcal{N}_T$. Therefore, the mode-exciting method may be considered to be inefficient for a large $\mathcal{N}_T$. However, because the domain in the boundary value problem is unchanged for different sets of exciters, the stiffness matrix is also unchanged. Therefore, the matrix inverse calculation, which is the most time-consuming part in the numerical calculation, is necessary to be carried out only once. Considering this computational aspect, the computational time of the mode-exciting method is nearly independent of $\mathcal{N}_T$. Moreover, since the mode-exciting method obtains all of the scattering coefficients simultaneously, the mode-exciting method becomes a powerful method when the scattering coefficients of more than one incident wave are to be found.

3. Error estimation

In the mode-exciting method, the system of equations (35) is constituted by the Lamb wave decomposition of the numerical solutions, which are obtained by using a numerical method such as FEM or BEM. It is, therefore, clear that the accuracy of the mode-exciting method depends largely on

that of the numerical solutions. In this section, however, we do not further discuss the accuracy of the numerical solutions, and our focus is given only on the error caused by the mode-exciting method itself.

As stated in Sec. III B, we neglect the nonpropagating incident wave of $\Sigma_i \Sigma_{n\,i} \gamma_{n\,i} \mathcal{D}_n^-$ assuming that the nonpropagating modes decay enough during the travel from the virtual edges to the scatterer. If the distances between the virtual edges and the scatterer are not large enough, however, then the scattering process may be affected by the nonpropagating incident wave, which can be the source of the error in the mode-exciting method. Since conjugate nonpropagating modes carry the power, the error may be estimated by taking the ratio of the power of nonpropagating modes to that of propagating modes.

Let ϵ be the error bound for the scattering coefficients. Under the assumption of $\epsilon \ll 1$, the error of the scattering coefficients has the same order as the error of the power. Therefore, we have the following relation:

$$\frac{\mathcal{P}_D}{\mathcal{P}_C} < \epsilon, \tag{36}$$

where $\mathcal{P}_C$ is the total power of all the propagating modes given by $\mathcal{P}_C = \Sigma |A_m|^2$, and $\mathcal{P}_D$ denotes the maximum total power of all conjugate nonpropagating modes given by $\mathcal{P}_D = \Sigma 2|A_m A_n|$. Here, A_m is the amplitude of Lamb wave mode $\mathcal{L}_m$ and A_n is the amplitude of the conjugate nonpropagating mode $\mathcal{L}_n$ corresponding to the mode $\mathcal{L}_m$.

Generally, the power ratio $\mathcal{P}_D/\mathcal{P}_C$ becomes smaller as we take larger distances between the virtual edges E_i and the scatterer. Thus, Eq. (36) can be used as a criterion to determine the locations of the virtual edges E_i. Note that in the calculation of $\mathcal{P}_D$, although there are an infinite number of nonpropagating modes, from our experience it is sufficient to consider only the conjugate nonpropagating modes with the smallest imaginary part in wave number.

D. Procedure of mode-exciting method

We summarize the calculation procedure of the mode exciting method as follows.

(1) Set the virtual edges at appropriate locations in the infinite plates.
(2) Choose linearly independent $\mathcal{N}_T$ sets of exciters as boundary conditions on the virtual edges.
(3) Apply a set of exciters to the virtual edges and solve numerically the boundary value problem defined in a finite domain bounded by the virtual edges and the traction-free surfaces.
(4) Decompose the numerical solution of the boundary value problem into Lamb wave modes by using Eq. (27) and obtain the amplitudes of Lamb waves, ${}_i\alpha_n$, ${}_j\beta_m$, ${}_i\gamma_n$, and ${}_j\delta_m$.
(5) Check whether the decomposed Lamb waves satisfy the power ratio given by Eq. (36) or not. If not, increase the distances between virtual edges and scatterer, and go back to step 3.
(6) Repeat steps 3 to 5 for $\mathcal{N}_T$ sets of exciters to have $\mathcal{N}_T$ sets of ${}_i\alpha_n$ and ${}_j\beta_m$.

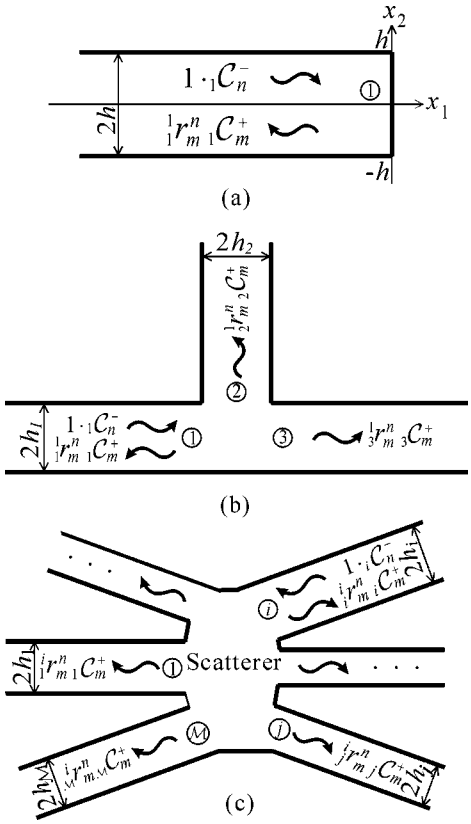

FIG. 3. (a) Reflection of Lamb waves by an edge. (b) Scattering of Lamb waves in *T*-shaped connected plates. (c) Scattering of Lamb waves in multiconnected plates.

(7) Substitute $\mathcal{N}_T$ sets of ${}_i\alpha_n$ and ${}_j\beta_m$ into Eq. (35) and solve the system of equations to obtain the scattering coefficients ${}_j^ir_m^n$.

For simplicity, so far, the formulation of the mode-exciting method is presented for the scattering problem by a crack in an infinite plate as shown in Fig. 2(a). As shown in Fig. 3, however, the mode-exciting method can also be applied to other types of scattering problems such as reflection by a plate edge, scattering by a T-shaped connection of plates, and scattering in multiconnected plates. For the problem with $\mathcal{M}$ plates' connection as shown in Fig. 3(c), $\mathcal{N}_T$ is defined by $\mathcal{N}_T = \mathcal{N}_1 + \mathcal{N}_2 + \cdots + \mathcal{N}_\mathcal{M}$ in the mode-exciting method.

IV. NUMERICAL EXAMPLES

This section presents numerical implementation of the mode-exciting method and shows numerical results for the problems of the edge reflection and the crack scattering. The plate is a steel one, for which the Rayleigh–Lamb frequency spectrum is shown in Fig. 1.

A. Numerical implementation of mode exciting method

As shown in Sec. III C 3, the accuracy of the mode-exciting method is affected by the distances between the virtual edges and the scatterer. So, we have to choose the locations of the virtual edges cautiously, taking account of the error estimation. Figure 4 shows three types of errors as a

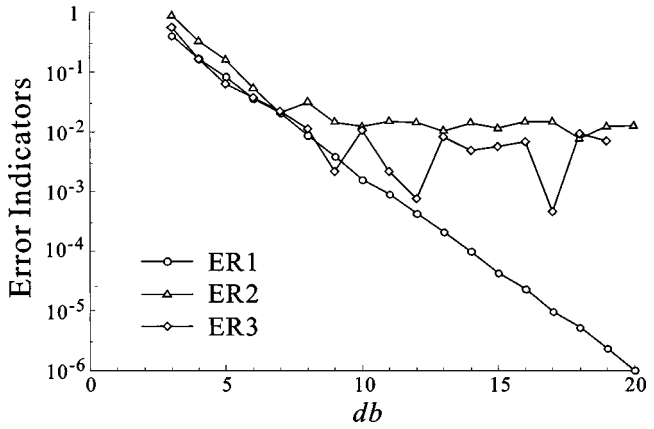

FIG. 4. Errors $ER1$, $ER2$, and $ER3$ as a function of the distance d between the virtual edge and the scatterer.

function of the distance d between the virtual edge and the end of the plate for the edge reflection problem as shown in Fig. 3(a) with the nondimensional frequency $\omega h/c_T=3.4$, The abscissa denotes the distance d, which is normalized by the smallest absolute value b among the imaginary parts of the wave numbers of nonpropagating modes. Here, b is used for the normalization because the imaginary part of the wave number of nonpropagating mode has a close relation to the attenuation of that mode.

In Fig. 4, $ER1$ shows the power ratio $\mathcal{P}_D/\mathcal{P}_C$ as defined in Eq. (36). $ER2$ denotes the maximum error in the power balance expressed by Eq. (B3) in Appendix B. $ER3$ represents the error of the specific scattering coefficient ${}_1^1r_1^1$, which is evaluated by taking the difference between ${}_1^1r_1^1$ and a reference value. Here, we use ${}_1^1r_1^1$ at $db=20$ as the reference value. From Fig. 4, it can be seen that the power ratio $ER1$ decreases as db increases. For $db<10$, $ER2$ and $ER3$ also decrease as $ER1$ does. For $db>10$, however, $ER2$ and $ER3$ do not decrease any more while $ER1$ continues to decrease. This is because $ER2$ and $ER3$ are directly influenced by the limit of the precision of the BEM solutions. Since $ER1$ is not affected by the error of numerical calculation, the power ratio $\mathcal{P}_D/\mathcal{P}_C$ is taken as the most proper indicator for the error of the mode-exciting method. For all examples shown in the following, we use $db=8.0$.

Given here is an example showing how to set linearly independent exciters on the virtual edges E_i. Consider the scattering problem by a crack shown in Fig. 2(a). If the frequency $\omega h/c_T$ is less than $\pi/2$, there exist only two propagating Lamb wave modes, A_0 and S_0, as shown in Fig. 1(a). So, we have $\mathcal{N}_1=\mathcal{N}_2=2$ and $\mathcal{N}_T=\mathcal{N}_1+\mathcal{N}_2=4$ for $\omega h/c_T<\pi/2$. Therefore, four sets of linearly independent boundary conditions are required as exciters to solve the problem by the mode exciting method. As shown in Table I, four sets of displacement boundary conditions on E_1 and E_2 are chosen as exciters. In each set of exciters, the displacement of a propagating mode, A_0 or S_0, is specified on one edge, while null displacement is given on the other edge. Note that the traction components on the edges are unknown terms in the boundary value problem. Thus, we can construct linearly independent $\mathcal{N}_T$ sets of exciters to solve the mixed boundary value problems, where the displacement conditions in Table I and the traction-free condition are given on the virtual edges and the other boundaries, respectively.

TABLE I. Four sets of exciters given on the virtual edges E_1 and E_2. $\mathbf{u}_{A_0}(x_1,x_2)$ and $\mathbf{u}_{S_0}(x_1,x_2)$ are the displacements of A_0 and S_0 modes expressed in Eqs. (4) and (5) which are normalized by Eq. (20), and $-a$ and a are the x_1 coordinates of E_1 and E_2, respectively.

	E_1	E_2
Exciters 1	$\mathbf{u}(x_2)=\mathbf{u}_{A_0}(-a,x_2)$	$\mathbf{u}(x_2)=\mathbf{0}$
Exciters 2	$\mathbf{u}(x_2)=\mathbf{u}_{S_0}(-a,x_2)$	$\mathbf{u}(x_2)=\mathbf{0}$
Exciters 3	$\mathbf{u}(x_2)=\mathbf{0}$	$\mathbf{u}(x_2)=\mathbf{u}_{A_0}(a,x_2)$
Exciters 4	$\mathbf{u}(x_2)=\mathbf{0}$	$\mathbf{u}(x_2)=\mathbf{u}_{S_0}(a,x_2)$

In this paper, the mixed boundary value problems are solved by using the BEM with quadratic elements. The boundaries are discretized as follows. The virtual edges, the free edge in the edge reflection problem and the crack surface of the crack scattering problem are divided into 5 elements, 5 elements, and 10 elements, respectively. The top and bottom surfaces of the plates are discretized into the elements with the length less than one-fifth of the smallest wavelength of propagating mode.

B. Numerical results

In Figs. 5(a) and (b), the absolute values of scattering coefficients for the edge reflection problem illustrated in Fig. 3(a) are shown for A_0 incidence and S_0 incidence, respec-

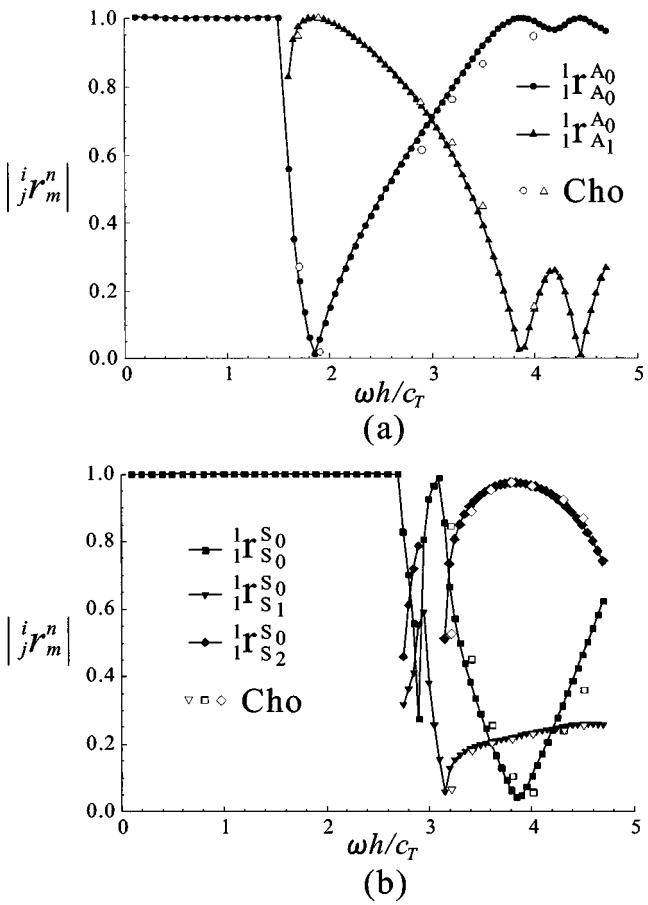

FIG. 5. Scattering coefficients for the edge reflection due to (a) A_0 incidence and (b) S_0 incidence.

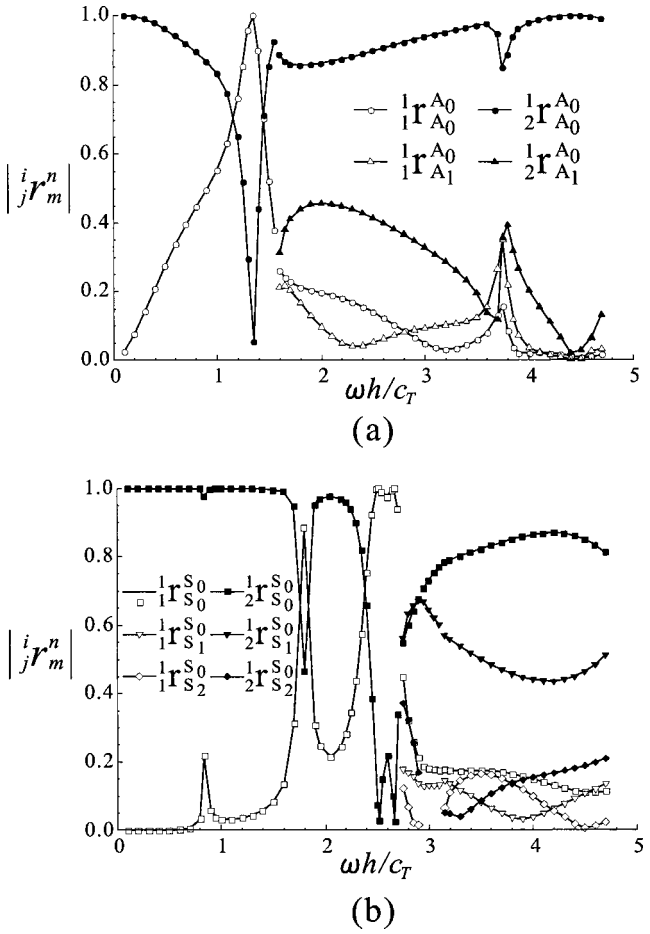

FIG. 6. Scattering coefficients by a horizontal crack located in the middle plane of the plate subjected to (a) A_0 incidence and (b) S_0 incidence.

tively. Since the scatterer is vertically symmetric, the symmetric and antisymmetric modes are uncoupled each other. As seen in Figs. 5(a) and (b), the scattering coefficients ${}_1^1r_{A_0}^{A_0}$ and ${}_1^1r_{S_0}^{S_0}$ have the unit absolute values in the frequency range below the cutoff frequencies of A_1 mode ($\omega h/c_T=\pi/2$) and S_1 mode ($\omega h/c_T=2.715$), respectively, where only single mode exists. For comparison, the results of the HBEM obtained by Cho and Rose[8] are plotted by the blank symbols in Fig. 5. Fairly good agreement is obtained between both results. Although only a small difference is observed at high frequencies, our results seem to be more accurate as far as the power balance is verified.

Figures 6(a) and (b) show the absolute values of scattering coefficients by the horizontal crack illustrated in Fig. 2(a) with length of $2s=2h$ subjected to A_0 and S_0 incident Lamb waves, respectively. Since the crack is located at the middle plane of the plate, the symmetric and antisymmetric modes are uncoupled. Furthermore, the scatterer is also symmetric with respect to the x_2 axis; therefore, we have the relations of ${}_1^1r_m^n={}_2^2r_m^n$ and ${}_2^1r_m^n={}_1^2r_m^n$. Hence, only ${}_1^1r_m^n$ and ${}_2^1r_m^n$ are shown in Fig. 6. For both incident modes of A_0 and S_0, we can see some peaks where the reflection power becomes nearly unity, i.e., no power passes through the crack. These resonance phenomena were also observed by Rokhlin.[2,12] The investigation of these resonance phenomena will be carried out in more detail in future.

V. CONCLUSIONS

The conclusions obtained in this paper are summarized below.

(1) The mode-exciting method has been successfully developed to solve any types of Lamb wave-scattering problems.
(2) The error of the mode-exciting method has been estimated quantitatively by evaluating the proportion of the power of nonpropagating modes to the power of propagating modes.
(3) This method has been applied to the problems of the edge reflection and the crack scattering. Comparison between the results obtained by our method and the HBEM has shown a good agreement.
(4) It is remarked that the basic idea of this method can be extended to the scattering analyses of any other guided waves in pipes and layered media.

APPENDIX A: UNIQUENESS OF THE SCATTERING COEFFICIENTS

The uniqueness of the scattering coefficients ${}_j^ir_m^n$ is shown as follows. Suppose that there are two solutions of the scattering coefficients ${}_j^ir_m^n$ and ${}_j^iR_m^n$ for the incident mode ${}_i\mathcal{C}_n^-$. Then, we have the relations

$$1\cdot {}_i\mathcal{C}_n^- \rightarrow \sum_{j=1}^{\mathcal{M}}\sum_{m=1}^{\mathcal{N}_j} {}_j^ir_m^n\,{}_j\mathcal{C}_m^+, \tag{A1}$$

$$1\cdot {}_i\mathcal{C}_n^- \rightarrow \sum_{j=1}^{\mathcal{M}}\sum_{m=1}^{\mathcal{N}_j} {}_j^iR_m^n\,{}_j\mathcal{C}_m^+. \tag{A2}$$

Subtraction of Eq. (A1) by Eq. (A2) yields

$$0\rightarrow \sum_{j=1}^{\mathcal{M}}\sum_{m=1}^{\mathcal{N}_j} ({}_j^ir_m^n-{}_j^iR_m^n)\,{}_j\mathcal{C}_m^+. \tag{A3}$$

Here, we have no propagating mode toward the scatterer, as shown on the left-hand side in Eq. (A3). From the conservation of power, the total power of Lamb modes on the right-hand side of Eq. (A3) must be 0. Since the set of propagating modes satisfies the orthogonality of power distribution [see Eq. (18)] and all Lamb modes ${}_j\mathcal{C}_m^+$ have powers in the outgoing direction, then ${}_j^ir_m^n-{}_j^iR_m^n$ must be 0. According to the uniqueness of the scattering coefficients, the values of the scattering coefficients obtained from different sets of exciters should be equal within a tolerance of the error.

APPENDIX B: ORTHOGONALITY IN THE SCATTERING COEFFICIENT

The scattering coefficients in Lamb wave-scattering problem have orthogonal property as follows. Let us consider the definition of the scattering coefficients ${}_j^ir_m^n$ as shown in Eq. (28). For the incident Lamb wave ${}_i\mathcal{C}_n^-$ with the unit power, the total power of the scattered Lamb waves should be equal to unity from the power balance. Since the set of scattered propagating modes in Eq. (28) has the orthogonality of power distribution as discussed in Sec. II B, the total

scattered power is equal to the sum of the squares of the absolute amplitudes of all scattered propagating modes as shown in Eq. (18), namely

$$\sum_{j=1}^{\mathcal{M}} \sum_{m=1}^{\mathcal{N}_j} |{}_j^i r_m^n|^2 = 1,$$

or

$$\sum_{j=1}^{\mathcal{M}} \sum_{m=1}^{\mathcal{N}_j} {}_j^i r_m^n ({}_j^i r_m^n)^* = 1. \tag{B1}$$

Next, let us consider two different incident modes with the difference θ in phase

$${}_{i1}\mathcal{C}_{n_1}^- + e^{i\theta}\, {}_{i_2}\mathcal{C}_{n_2}^- \rightarrow \sum_{j=1}^{\mathcal{M}} \sum_{m=1}^{\mathcal{N}_j} ({}_j^{i_1} r_m^{n_1} + {}_j^{i_2} r_m^{n_2} e^{i\theta})\, {}_j\mathcal{C}_m^+ ,$$

where $i_1 \neq i_2$ or $n_1 \neq n_2$. The power relation then becomes

$$2 = \sum_{j=1}^{\mathcal{M}} \sum_{m=1}^{\mathcal{N}_j} ({}_j^{i_1} r_m^{n_1} + {}_j^{i_2} r_m^{n_2} e^{i\theta})({}_j^{i_1} r_m^{n_1} + {}_j^{i_2} r_m^{n_2} e^{i\theta})^*.$$

Using Eq. (B1) and taking into account that θ can take an arbitrary value, we can derive the following relation:

$$\sum_{j=1}^{\mathcal{M}} \sum_{m=1}^{\mathcal{N}_j} {}_j^{i_1} r_m^{n_1} ({}_j^{i_2} r_m^{n_2})^* = 0. \tag{B2}$$

Equations (B1) and (B2) are summarized as follows:

$$\sum_{j=1}^{\mathcal{M}} \sum_{m=1}^{\mathcal{N}_j} {}_j^{i_1} r_m^{n_1} ({}_j^{i_2} r_m^{n_2})^* = \begin{cases} 1 & \text{for } i_1 = i_2, n_1 = n_2, \\ 0 & \text{otherwise.} \end{cases} \tag{B3}$$

This relation expresses the power balance that can be used to verify the validity of the scattering coefficients as shown in Fig. 4.

[1] I. A. Viktorov, *Rayleigh and Lamb Waves: Physical Theory and Application* (Plenum, New York, 1967).
[2] S. Rokhlin, "Diffraction of Lamb waves by a finite crack in an elastic layer," J. Acoust. Soc. Am. **67**, 1157–1165 (1980).
[3] R. D. Gregory and I. Gladwell, "The reflection of symmetric Rayleigh–Lamb wave at the fixed or free edge of a plate," J. Elast. **13**, 185–206 (1983).
[4] W. M. Karunasena, A. H. Shah, and S. K. Datta, "Reflection of plane strain waves at the free edge of a laminated composite plate," Int. J. Solids Struct. **27**, No. (8) 949–964 (1991).
[5] L. J. Crane, M. D. Gilchrist, and J. J. H. Miller, "Analysis of Rayleigh–Lamb wave scattering by a crack in an elastic plate," Comput. Mech. **19**, 533–537 (1997).
[6] M. Koshiba, S. Karakida, and M. Suzuki, "Finite-element analysis of Lamb waves scattering in an elastic plate waveguide," IEEE Trans. Sonics Ultrason. **31**, 18–25 (1984).
[7] Y. N. Al-Nassar, S. K. Datta, and A. H. Shah, "Scattering of Lamb waves by a normal rectangular strip weldment," Ultrasonics **29**, 125–132 (1991).
[8] Y. H. Cho and J. L. Rose, "A boundary element solution for a mode conversion study on the edge reflection of Lamb waves," J. Acoust. Soc. Am. **99**, 2097–2109 (1996).
[9] Y. H. Cho and J. L. Rose, "Lamb wave scattering analysis for reflector characterization," IEEE Trans. Ultrason. Ferroelectr. Freq. Control **44**, 44–52 (1997).
[10] J. D. Achenbach, *Wave Propagation in Elastic Solids* (North-Holland, Amsterdam, 1973).
[11] B. A. Auld, *Acoustic Fields and Waves in Solids* (Wiley, New York, 1973).
[12] S. I. Rokhlin, "Resonance phenomena of Lamb waves scattering by a finite crack in a solid layer," J. Acoust. Soc. Am. **69**, 922–928 (1981).

Analysis of strong scattering at the micro-scale

Kasper van Wijk
Physical Acoustics Laboratory, Department of Geophysics, Colorado School of Mines, Golden, Colorado 80401, USA

Dimitri Komatitsch
Seismological Laboratory, 1200 E. California Boulevard, Mail Code 252-21, Pasadena, California 91125, USA

John A. Scales
Physical Acoustics Laboratory, Department of Geophysics, Colorado School of Mines, Golden, Colorado 80401, USA

Jeroen Tromp
Seismological Laboratory, 1200 E. California Boulevard, Mail Code 252-21, Pasadena, California 91125, USA

(Received 23 August 2003; revised 17 December 2003; accepted 22 December 2003)

Exploiting the fine structure of strongly scattered waves could provide a wealth of new information in seismology, ultrasonics, acoustics, and other fields that study wave propagation in heterogeneous media. Therefore, noncontacting laser-based measurements of ultrasonic surface waves propagating in a strongly disordered medium are performed in which the ratio of the dominant surface wavelength to the size of a scatterer is large, and waves that propagate through many scatterers are recorded. This allows analysis of scattering-induced dispersion and attenuation, as well as the transition from ballistic to diffusive propagation. Despite the relatively small size of the scatterers, multiple scattering strikingly amplifies small perturbations, making changes even in a single scatterer visible in the later-arriving waveforms. To understand the complexity of the measured waveforms, elastic spectral-element numerical simulations are performed. The multiple-scattering sensitivity requires precise gridding of the actual model, but once this has been accomplished, we obtain good agreement between the measured and simulated waveforms. In fact, the simulations are invaluable in analyzing subtle effects in the data such as weak precursory body-wave diffractions. The flexibility of the spectral-element method in handling media with sharp boundaries makes it a powerful tool to study surface-wave propagation in the multiple-scattering regime. [DOI: 10.1121/1.1647480]

PACS numbers: 43.20.Gp, 43.20.Jr, 43.35.Cg, 43.35.Pt [YHB] Pages: 1006–1011

I. INTRODUCTION

Indications of multiple scattering in seismic waves have been observed,[1,2] but questions remain how to characterize media in which energy is multiply scattered (e.g., Ref. 3) Exciting advances have been made in using the later-arriving arrivals—or coda—of multiply scattered waves to detect minute changes in disordered media (e.g., Refs. 4–6), and the cross correlation of equipartitioned waves has been exploited to retrieve the Green's function between two detectors.[7–10]

In previous work we have described a tunable multiple scattering system, consisting of a block of aluminum with a disordered pattern of grooves cut in it.[11,12] Surface waves propagating parallel to the grooves are not scattered, but as we increase the angle between the scatterers and the direction of surface-wave propagation, scattering increases. Bulk properties of the propagation—including attenuation and dispersion—were studied to describe scattering on the *macroscopic* scale,[11] and we used a radiative transfer model to study the *mesoscopic* scale of the medium in terms of scattering and absorption mean-free paths.[13,13b] Here, we introduce two-dimensional (2D) numerical simulations of the physical system, based on the spectral-element method (SEM) (e.g., Ref. 14) to model this ultrasonic experiment with sharp topographic features, and investigate subtle details in the laboratory data on the scale of the individual scatterer, i.e., the *microscopic* scale.

Henceforth, we refer to the vertical component of the particle velocity measured in laboratory experiments as *data* and to the numerical results as *simulations*.

II. PHYSICAL EXPERIMENT

The setup of the experiment is shown in Fig. 1. A 200 V repetitive pulse is used to excite an angle-beam transducer mounted on the surface of an aluminum block of dimensions $x=232\ \text{mm}\times y=215\ \text{mm}\times z=280\ \text{mm}$. The transducer wedge has a footprint of $x=70\ \text{mm}\times y=42\ \text{mm}$. The angle of the transducer is such that its output in the aluminum block is mainly a broadband surface (Rayleigh) wave, effectively planar in the transverse (y) direction, with a dominant wavelength around 6 mm.

The wave field is detected along the x direction by a scanning laser vibrometer that measures absolute particle velocity on the surface of the sample via the Doppler shift (e.g.,

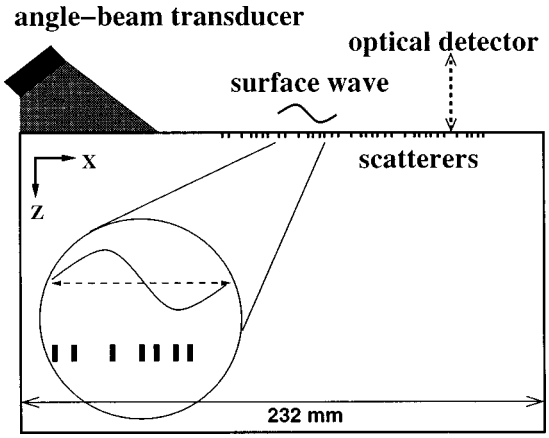

FIG. 1. Schematic setup of the experiment. The angle-beam transducer generates a Rayleigh wave that is multiply scattered by the grooves cut across one face of the aluminum block in the *y* direction. Vertical particle velocity is recorded by the laser Doppler vibrometer.

Refs. 11, 15). The signal is digitized at 14-bit resolution using a digital oscilloscope card, while the entire setup is positioned on a vibration isolation table to reduce background noise.

The aluminum block has a Fibonacci pattern of aligned linear grooves machined into one face. This sequence is quasiperiodic, but increases in complexity as it gets longer.[16] Theoretical and experimental results for transmission through Fibonacci multilayers have been published in Ref. 17. These authors show that minima in the transmission coefficient (as a function of wave number) become deeper as the number of layers in the Fibonacci multilayer increases, asymptotically leading to true band gaps. Analytic solutions for the Fibonacci scattering problem exist,[18] although they were not used in this article.

The grooves are nominally 1 mm wide (*x* direction), 2.75 mm deep (*z* direction), and 1 or 2 mm apart, but to represent the actual groove pattern more accurately in the numerical model, we scanned the surface at 2400 dots per inch (90 dots per mm), allowing us to include variations—coming from mechanical machining—in the average width of the grooves and the surface between grooves, which we call a nongroove.

III. NUMERICAL MODELING

The SEM is a high-order variational numerical technique[19,20] that combines the flexibility of the finite-element method with the accuracy of global pseudospectral techniques. Widely used in seismology,[14,21–23] here the SEM is used to simulate wave propagation at ultrasonic frequencies in a model that contains a large number of sharp grooves. The simulations can be compared to measurements at every surface location, because the optical detector can record at any location on the surface of the block (Fig. 1). The source in the simulations is the analytic solution to a Rayleigh wave,[24] and detectors are located in a line directly in front of the source. Intrinsic losses (i.e., anelastic effects) are so weak in aluminum[11] that attenuation is negligible.

The block is modeled by a mesh with cells whose size is on the order of a scatterer (i.e., a groove). The total number

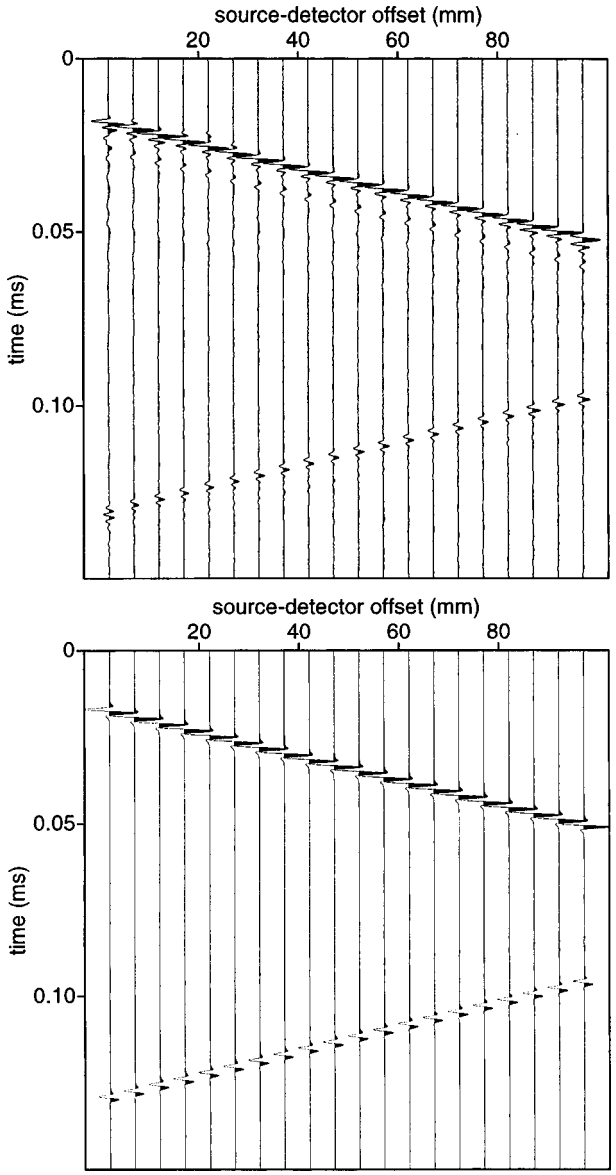

FIG. 2. Data (top) and simulations (bottom) for wave paths on the smooth side of the model.

of cells (spectral elements) is $232\,(x)\times 202\,(y)=46\,864$. In a classical finite-element method, the wave field is interpolated on these cell points. In the SEM, we use Lagrange polynomials of degree $N=4$ to interpolate the wave field in each quadrangular cell; the total number of grid points is 751 561. The time step Δt in the explicit integration scheme is 10 ns and we propagate the signal for 0.2 ms. Besides modeling the rapid topographic variations of the grooves, reflections off all boundaries of the block are included via free-surface boundary conditions, which are naturally taken into account by the SEM.

IV. COMPARING DATA AND SIMULATIONS

We compare data and simulations at 20 detector locations at 5-mm increments on the smooth face of the model, and on the first 42 nongrooves along a line perpendicular to the grooves (strong scattering). In both experiments, the source–detector distance (offset) for the first trace is 2 mm.

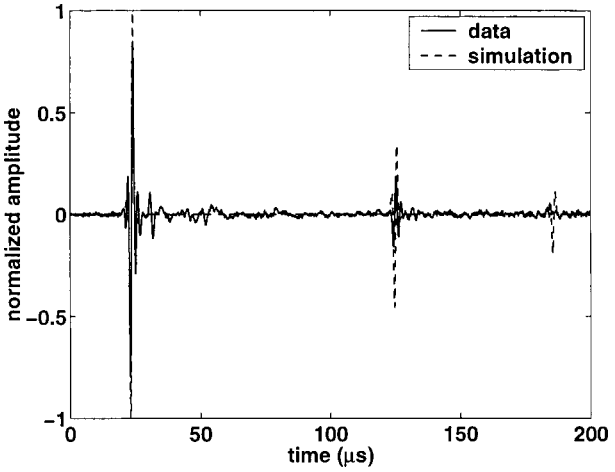

FIG. 3. Comparison between data and simulations for detector 1 on the smooth side of the model.

The data and simulations on the smooth aluminum surface are shown in Fig. 2. Both panels show a large direct surface-wave arrival, followed by a reflection from the far end of the aluminum block. The wavelet in the data has some energy after the main pulse caused by ringing in the transducer. This energy is not included in the source term of the simulations and will therefore limit our ability to fit the data. The data show little intrinsic losses and no evidence of reflections from the sides of the block, which means that the source energy emitted has little geometrical spreading, justifying 2D elastic simulations.

Also, we observe that the source wedge acts as an additional scatterer in the model, causing the maximum correlation on the smooth side of the aluminum to be smallest for detector 1. This near-field effect can be seen in the differences in amplitude and phase in the direct arrival and more clearly in the reflected event (Fig. 3), when compared to the other traces in Fig. 2. The second reflection from the edge of the block near the source is almost undetected in the data, because it requires the Rayleigh wave to travel along the surface between the bottom of the source wedge and the aluminum block. This is not an obstacle in the simulations, because the source is modeled by an analytically incident Rayleigh wave. This becomes even clearer from the simulated event at 190 μs. This is the surface wave that reflected once more from the side of the block near the source. The presence of the source wedge suppressed this event entirely in the laboratory measurements.

Figure 4 shows the data (top) and simulations (bottom) for waveforms in the strong scattering case. At each groove, energy is partially reflected, causing the direct arrival to be attenuated and the group velocity to be lowered compared to the unscattered wave propagation. The strongest events are interfering surface waves, which look qualitatively similar in the two panels. These strong events show coherence in the sense that a single phase can be tracked from one detector location to the next, whereas for late times, scattering causes arrivals to be incoherent from trace to trace.

Next, we compute the normalized cross correlation between simulations and data in 10-μs windows along the trace. If the wave fields are identical in the time window, a value of unity is assigned to the center of that window. Figure 5 contains the windowed, normalized cross correlation as a function of time, averaged over all source–detector distances. A correlation of unity is unlikely, because, for instance, the numerical simulations lack the random noise of the laboratory measurements, the ringing of the source, and the damping by the presence of the wedge observed in Fig. 3.

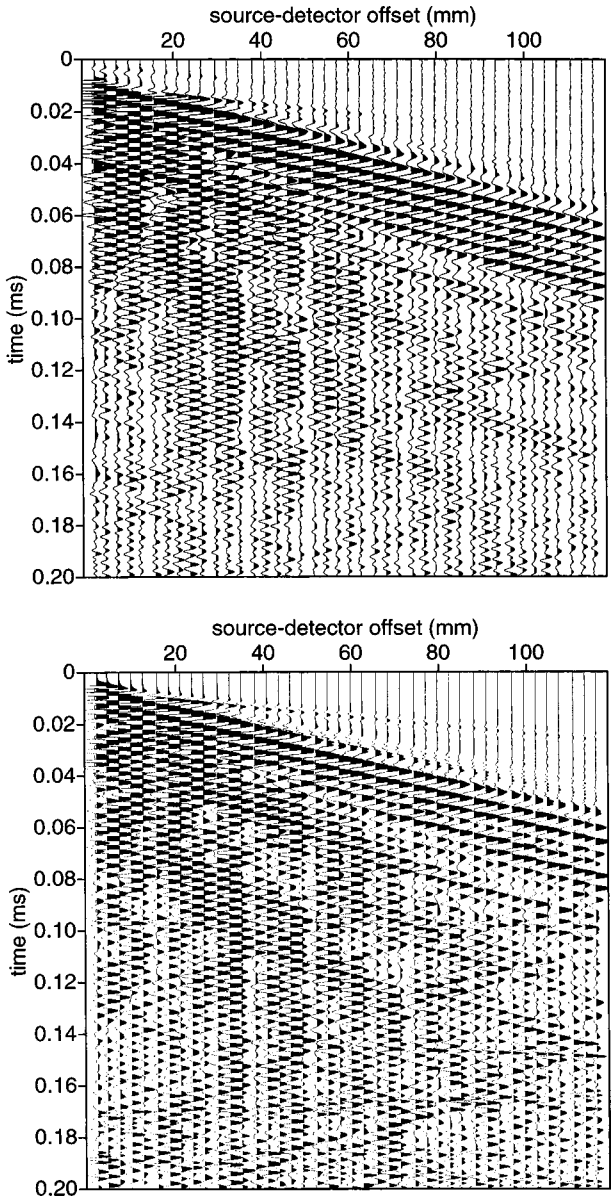

FIG. 4. Data (top) and simulations (bottom) for wave paths traveling perpendicular to the grooves (i.e., in the x direction). The main energy consists of surface waves bouncing between grooves, but the small-amplitude, faster events are body waves diffracted at the grooves.

The correlation between data and simulations on the smooth side of the model is visibly large for the direct wave and the reflection for all detectors. The average correlation for all 42 detectors on the grooved side first increases with time, as the coherent wave reaches the receivers at greater distance from the source. After the coherent energy has passed all receivers ($t > 0.1$ ms), the average correlation decreases. This shows that small discrepancies between the physical and numerical models on the order of a fraction of

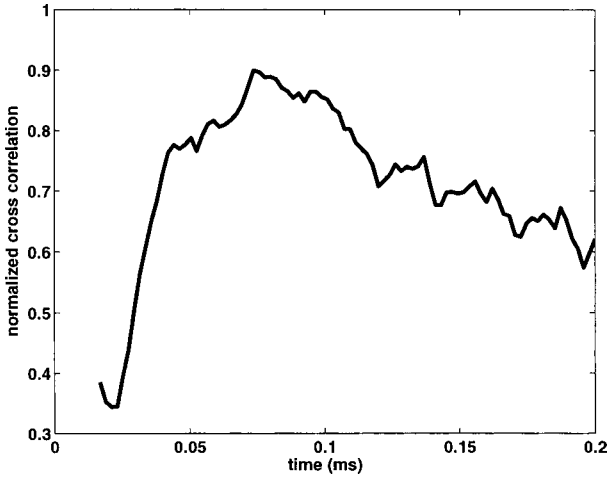

FIG. 5. Average normalized correlation between data and simulations for the 42 detectors as a function of time, on the grooved side of the model. Time windows of identical traces would have a correlation of 1.

the size of a single scatterer consistently decrease the accuracy of the simulations with time. The same effect is seen in coda wave interferometry[4] and diffusing wave spectroscopy;[5] these techniques derive their great sensitivity to small changes in a medium from the repeated sampling of the change by waves that bounce back and forth many times.

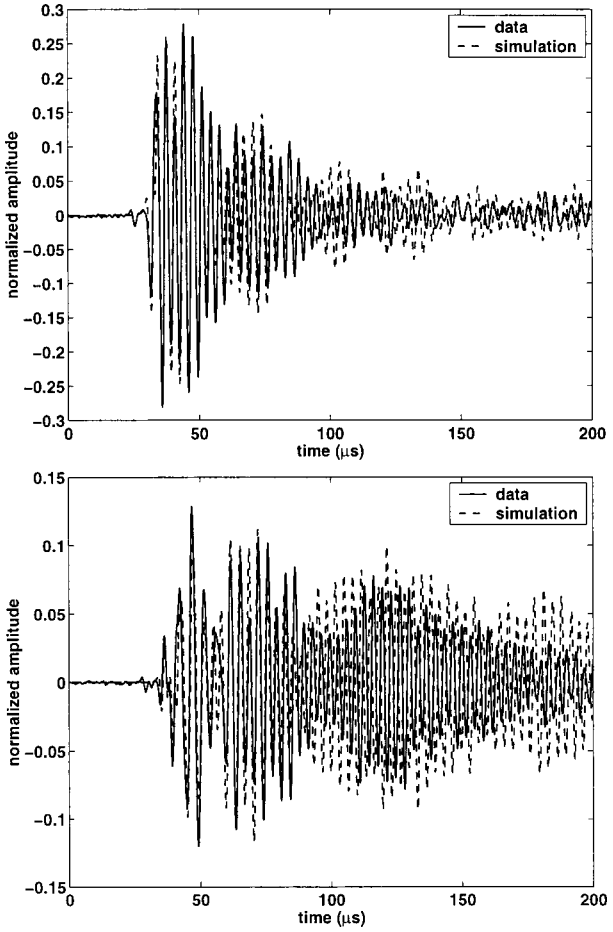

FIG. 6. Comparison between data and simulations on a thick (top) and a thin nongroove (bottom). Note the relatively stronger amplitudes at later times in the right panel.

In addition, both data and simulations on a nongroove with the size on the order of 1 mm show considerably more energy at later times than do traces on the thicker nongrooves. An example of this is detector 12, compared to detector 4 (Fig. 6): the relatively thin ridge of aluminum under detector 12 is excited in a 300-kHz resonance. While this mode is too low in frequency to represent multiple scattering of energy in the nongroove, it is possible that this resonance is a flexural mode of the thin nongrooves.[25] The power in the simulations of the thin nongrooves is visibly enhanced relative to the measurements (Fig. 7). We believe this is because the machined grooves are not perfectly rectangular, while the numerical mesh includes only fixed rectangular shapes whose dimensions are the average width and depth from the scan. In effect, imperfections in the machining reduce the Q of these resonances. This effect—plus the absence of the damping wedge in the simulations—results in the fact that the simulations have overall higher power than the measurements (Fig. 4).

V. DISCUSSION

In the strong-scattering case, relatively lower-amplitude and faster events arrive before the main surface-wave energy; Fig. 4 shows two coherent events with the *P*-wave velocity of aluminum. The first, starting at $t=0$, is caused by the angle-beam transducer producing some *P* waves in addition to surface-wave energy. This event is not present in the simulations, because the source is a pure Rayleigh wave. The second event with a *P*-wave velocity cannot be seen until the 6th or 7th trace at 0.01 ms, but is confirmed by the simulations.

To support the existence of these body-wave precursors to the surface-wave energy, we conducted a second experiment, in which the source is mounted on the face of the aluminum model with a single groove. In this case, the source is driven by a 5-cycle tone burst, centered around the resonant frequency of 500 kHz of the source transducer, as opposed to the broader-band signal used before. The particle velocity before and past a single groove is depicted in the top

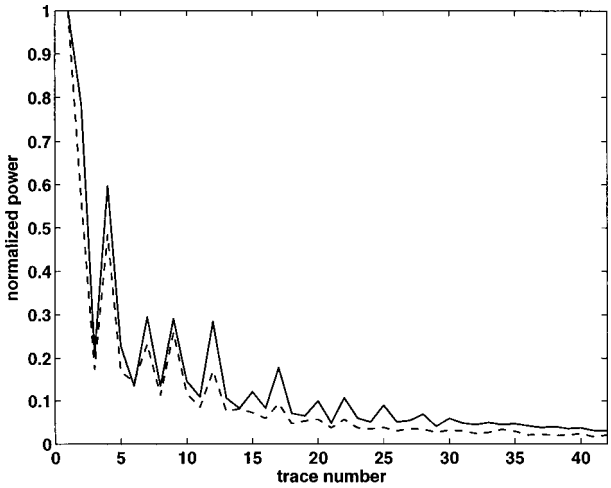

FIG. 7. Comparison between the normalized power in data and simulations. Especially for the detectors on thin non-grooves (detectors 4, 7, 9, 12, 15, 17, etc.), the simulations show more power.

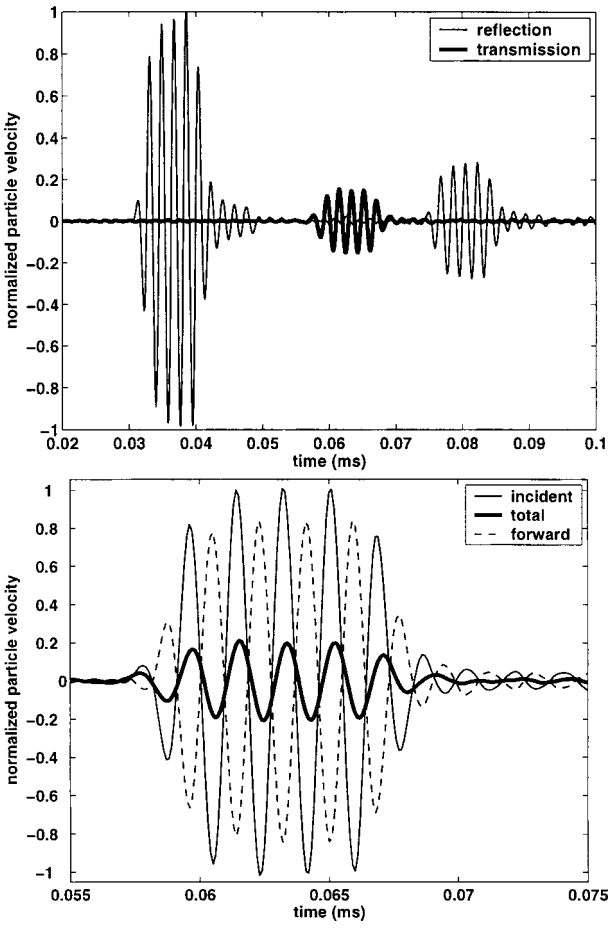

FIG. 8. Top: particle velocity measured before and after a single groove. The thinner line shows first the arrival of the incident field, followed by the backscattered signal from the groove. The thicker line is the total field past the scatterer, consisting of the incident plus the forward-scattered field. Bottom: decomposition of the total field (thick solid) past the groove into an incident (thin solid) and forward scattered component (dashed).

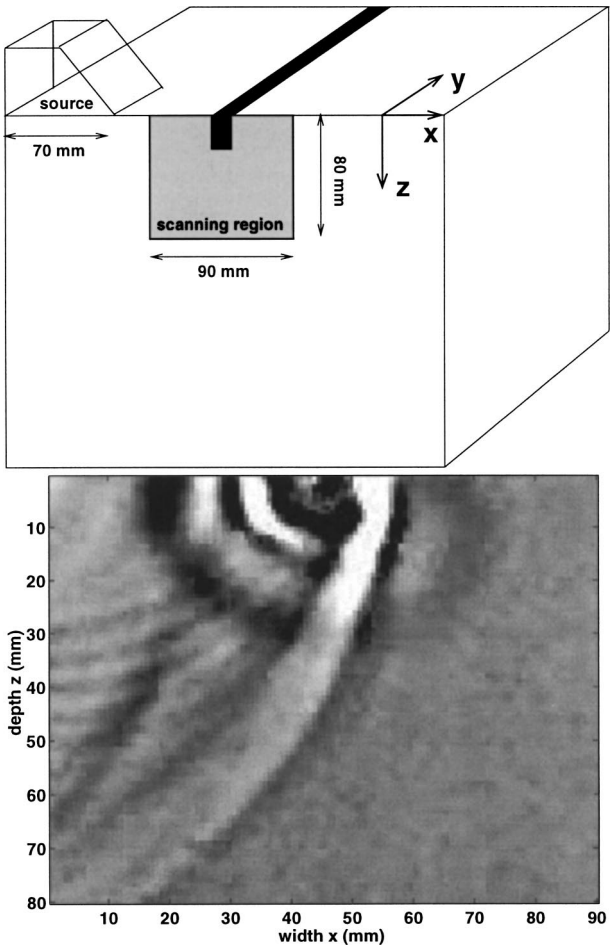

FIG. 9. Top: experimental configuration, where the source is perpendicular to a single groove on the top of the block, while the detector scans part of the (x,z) plane. Bottom: snapshot at $t=0.06$ ms of particle motion in the scanned region after the incident field scattered off a single groove. A movie of this experiment can be viewed at ⟨http://acoustics.mines.edu/onedee.html⟩.

panel of Fig. 8. The transmitted and reflected total intensity (the square of the particle velocity) is on the order of 0.04 and 0.06 times the incident field, respectively. This means that roughly 90 percent of the energy at this particular frequency is diffracted by a single scatterer. Lower frequencies are less influenced by the groove. This is why in the data with many grooves the dominant frequency after a few grooves drops from approximately 500 kHz to roughly 250 kHz.

The total transmitted field can be decomposed in the incident field and the forward-scattered field. By measuring the incident field at the same source–detector distance on the smooth side of the aluminum, we are able to estimate the forward-scattered field directly. Note that the forward-scattered field estimated in the bottom panel of Fig. 8 is 180 deg out of phase with the incident field, with a scattering strength of 0.8, making our scattering anisotropic. This strong out-of-phase forward scattering is known as the extinction paradox, observed in the shadow zone directly behind scatterers.[26]

The measurement is repeated with the detector scanning the side of the model (top panel of Fig. 9). The bottom panel of Fig. 9 shows a snapshot of particle motion, measured shortly after the incident wave interacted with the single groove. The side of the aluminum block breaks the symmetry of the Rayleigh-wave motion purely in the *x*- and *z* direction, creating particle motion in the *y* direction. Higher frequencies in the upper left part are due to ringing of the source, and the incident field is the strong event extending from top to bottom. The circular events are body waves scattered off the single groove. Scattering to body waves is stronger in the backward direction, but significant *P*-wave energy travels ahead of the surface wave, causing the precursors observed in Fig. 4. These spherical body-wave fronts diffracted at the individual grooves arrive before the Rayleigh waves and may be analogous to precursors to the seismic phase PKKP in global seismology[27] that some authors believe to be caused by scattering at the rough boundary between the Earth's outer core and mantle.[28,29]

VI. CONCLUSIONS

Laser ultrasonics provides a powerful tool for studying the fine structure of multiply scattered waves. Being able to place the detector, in effect, inside the scattering medium for surface waves allows one to directly visualize diffraction,

scattering, and mode conversion. However, the resulting waveforms in strong scattering media become increasingly complicated with time. Thus, it is useful to have the ability to make precise elastic simulations. In this study we have applied the numerical spectral-element method to simulate surface-wave multiple scattering in a grooved block of aluminum. Comparing the simulations to the data allowed us to analyze subtle imperfections in the physical model as well as precursory body-wave diffractions and flexural resonances of the grooves. The ability to handle complex boundaries with sharp edges makes the spectral-element method an ideal tool for laboratory ultrasonics.

ACKNOWLEDGMENTS

This work was supported by the Consortium Project on Seismic Inverse Methods for Complex Structures at the Center for Wave Phenomena, the National Science Foundation (EAR-0111804 and EAR-0003761), and the Army Research Office (DAAG55-98-1-0277 and DAAD19-03-1-0292). We thank Francisco José Sánchez-Sesma for the use of his Rayleigh wave code and Roel Snieder, Ken Larner, and Matt Haney for stimulating discussions. Finally, we are thankful for the many useful suggestions of the two anonymous reviewers. This is contribution No. 8928 of the Division of Geological and Planetary Sciences of the California Institute of Technology.

[1] K. Aki and B. Chouet, ''Origin of coda waves: Source, attenuation, and scattering effects,'' J. Geophys. Res. **80**, 3322–3342 (1975).
[2] R. Hennino, N. Trégourès, N. M. Shapiro, L. L. Margerin, M. Campillo, B. A. van Tiggelen, and R. L. Weaver, ''Observation of equipartition of seismic waves,'' Phys. Rev. Lett. **86**(15), 3447–3450 (2001).
[3] R. Benites, P. Roberts, K. Yomogida, and M. Fehler, ''Scattering of elastic waves in 2-D composite media. I. Theory and test,'' Phys. Earth Planet. Inter. **104**, 161–173 (1997).
[4] R. Snieder, A. Grêt, H. Douma, and J. A. Scales, ''Coda wave interferometry for estimating nonlinear behavior in seismic velocity,'' Science **295**, 2253–2255 (2002).
[5] M. L. Cowan, I. P. Jones, J. H. Page, and D. A. Weitz, ''Diffusing acoustic wave spectroscopy,'' Phys. Rev. E **65**, 066605 (2002).
[6] G. Poupinet, W. Ellsworth, and J. Frechet, ''Monitoring velocity variations in the crust using earthquake doublets—An application to the Calaveris fault, California,'' J. Geophys. Res. **89**, 5719–5731 (1984).
[7] M. Campillo and A. Paul, ''Long-range correlations in the diffuse seismic coda,'' Science **299**, 547–549 (2003).
[8] O. I. Lobkis and R. L. Weaver, ''Ultrasonics without a source: Thermal fluctuation correlations at MHz frequencies,'' Phys. Rev. Lett. **87**(13), 134301 (2001).
[9] R. L. Weaver and O. I. Lobkis, ''On the emergence of the Green's function in the correlations of a diffuse field,'' J. Acoust. Soc. Am. **110**, 3011–3017 (2001).
[10] A. Malcolm, J. A. Scales, and B. A. van Tiggelen (submitted).
[11] J. A. Scales and K. van Wijk, ''Multiple scattering attenuation and anisotropy of ultrasonic surface waves,'' Appl. Phys. Lett. **74**, 3899–3901 (1999).
[12] J. A. Scales and K. van Wijk, ''Tunable multiple-scattering system,'' Appl. Phys. Lett. **79**, 2294–2296 (2001).
[13] K. van Wijk, ''Multiple scattering of surface waves,'' Ph.D. thesis, Colorado School of Mines, 2003; K. van Wijk, M. Maney and J. A. Scales, ''1D energy transport in a stongly scattering laboratory model,'' Phys Rev. E (to be published).
[14] D. Komatitsch and J. Tromp, ''Introduction to the spectral-element method for 3-D seismic wave propagation,'' Geophys. J. Int. **139**, 806–822 (1999).
[15] O. Nishizawa, T. Satoh, X. Lei, and Y. Kuwahara, ''Laboratory studies of seismic wave propagation in inhomogeneous media using a laser Doppler vibrometer,'' Bull. Seismol. Soc. Am. **87**(4), 809–823 (1997).
[16] P. Carpena, V. Gasparian, and M. Ortuño, ''Energy spectra and level statistics of Fibonacci and Thue–Morse chains,'' Phys. Rev. B **51**(18), 12813–12816 (1995).
[17] W. Gellermann, M. Kohmoto, B. Sutherland, and P. C. Taylor, ''Localization of light waves in Fibonacci dielectric multilayers,'' Phys. Rev. Lett. **72**, 633 (1994).
[18] L. Dal Negro, C. J. Oton, Z. Gaburro, L. Pavesi, P. Johnson, A. Lagendijk, R. Righini, M. Colocci, and D. S. Wiersma, ''Light transport through the band-edge states of Fibonacci quasicrystals,'' Phys. Rev. Lett. **90**(5), 055501 (2003).
[19] E. Priolo, J. M. Carcione, and G. Seriani, ''Numerical simulations of interface waves by high-order spectral modeling techniques,'' J. Acoust. Soc. Am. **95**, 681–693 (1994).
[20] E. Faccioli, F. Maggio, R. Paolucci, and A. Quarteroni, ''2D and 3D elastic wave propagation by a pseudo-spectral domain decomposition method,'' J. Seismol. **1**, 237–251 (1997).
[21] D. Komatitsch and J. P. Vilotte, ''The spectral-element method: An efficient tool to simulate the seismic response of 2D and 3D geological structures,'' Bull. Seismol. Soc. Am. **88**, 368–392 (1998).
[22] D. Komatitsch and J. Tromp, ''Spectral-element simulations of global seismic wave propagation. I. Validation,'' Geophys. J. Int. **150**, 390–412 (2002).
[23] D. Komatitsch, J. Ritsema, and J. Tromp, ''The spectral-element method, Beowulf computing, and global seismology,'' Science **298**, 1737–1742 (2002).
[24] D. Komatitsch, J. P. Vilotte, R. Vai, J. M. Castillo-Covarrubias, and F. J. Sánchez-Sesma, ''The spectral element method for elastic wave equations—Application to 2-D and 3-D seismic problems,'' Int. J. Numer. Methods Eng. **45**, 1139–1164 (1999).
[25] T. D. Rossing and N. H. Fletcher, *Principles of Vibration and Sound* (Springer, New York, 1995).
[26] H. C. van de Hulst, *Light Scattering by Small Particles* (Wiley, New York, 1957).
[27] A. C. Chang and J. R. Cleary, ''Precursors to PKKP,'' Bull. Seismol. Soc. Am. **68**(4), 1059–1078 (1978).
[28] P. S. Earle and P. M. Shearer, ''Observations of PKKP precursors used to estimate small-scale topography on the core–mantle boundary,'' Science **277**, 667–670 (1997).
[29] A. C. Chang and J. R. Cleary, ''Scattered PKKP: Further evidence for scattering at a rough core–mantle boundary,'' Phys. Earth Planet. Inter. **24**, 15–29 (1981).

Atmospheric absorption in the atmosphere up to 160 km

Louis C. Sutherland[a)]
Consultant in Acoustics, 27803 Longhill Drive, Rancho Palos Verdes, California 90275-3908

Henry E. Bass
National Center for Physical Acoustics, The University of Mississippi, University, Mississippi 38677

(Received 14 March 2002; accepted for publication 20 October 2003)

This paper describes new algorithms, not previously available, for predicting atmospheric absorption of sound at high altitudes. A basis for estimating atmospheric absorption up to 160 km is described. The estimated values at altitudes above 90 km must be considered as only approximate due to uncertainties about the composition of the atmosphere above 90 km and simplifying assumptions. At high altitudes, classical and rotational relaxation absorption are dominant, as opposed to absorption by molecular vibrational relaxation that is the principle atmospheric absorption loss mechanism for primary sonic booms propagating downward from a cruising supersonic aircraft. Classical and rotational relaxation absorption varies inversely with atmospheric pressure, thus increasing in magnitude at high altitudes as atmospheric pressure falls. However, classical and rotational losses also relax at the high values of frequency/pressure reached at high altitudes and thus, for audio and infrasonic frequencies, begin to decrease at altitudes in the range of 80–160 km. This paper includes: (1) modifications to the existing algorithms in the ISO/ANSI standards for atmospheric absorption at high altitudes, and (2) algorithms for definition of mean atmospheric conditions, including humidity content at high altitude conditions. Also included are suitable values for the temperature-dependent physical parameters of the atmosphere, viscosity, and the specific heat ratio, involved in defining atmospheric absorption at temperatures found at high altitudes. It has been found that carbon dioxide plays a major role in the relaxation of O_2 and N_2 at high altitudes due to the absence of H_2O. Molecular relaxation by CO_2, not covered by the current ANSI or ISO standards, is the dominant source of molecular relaxation absorption at altitudes above 60 km at frequencies of 1 Hz and above 10 km at a frequency of 10 kHz. However, at such high altitudes, classical plus rotational losses dominate reaching maximum values at 80–160 km, depending on frequency. In this regime, vibrational relaxation is less important. More accurate predictions of absorption at altitudes above 90 km would require more sophisticated models for the variation in atmospheric viscosity and specific heat ratio above such altitudes. [DOI: 10.1121/1.1631937]

PACS numbers: 43.20.Hq, 43.28.Bj, 43.28.Fp [RAR] Pages: 1012–1032

I. INTRODUCTION

A long range sound propagation topic which has received recent attention is the propagation of sounds through the atmosphere at high altitudes.[1] Altitudes of concern include the thermosphere up to about 160 km. Secondary sonic booms from proposed supersonic transports, a source of potentially annoying low frequency sounds on the ground,[2] can propagate initially upward before being refracted down to the ground. Sounds generated by atmospheric explosions can also travel along a path that goes up to the thermosphere giving rise to shadow zones on the ground spaced by thousands of miles. For purposes of monitoring nuclear explosions or supersonic aircraft, waves that travel upward to the thermosphere and then turn back to the ground are very important—often that is the only arrival. Absorption of sound at such altitudes involves atmospheric conditions very different from those normally encountered near, or on, the ground. These conditions are not covered by current ISO or ANSI standards[3] on atmospheric absorption of sound.

New algorithms, not previously available for predicting atmospheric absorption of sound at high altitudes (up to about 160 km) have been developed. At such high altitudes, classical and rotational relaxation absorption are dominant, as opposed to absorption by molecular vibrational relaxation that is the primary atmospheric absorption loss mechanism for primary sonic booms propagating directly down from a supersonic aircraft to the ground. Classical and rotational relaxation absorption varies inversely with atmospheric pressure, thus increasing in magnitude at high altitudes. For the latter, the relaxation frequencies vary directly with atmospheric pressure and depend on moisture content which rapidly decreases at high altitudes. However, classical and rotational motion also relax at the high values of frequency/pressure reached at high altitudes and thus, for audio and infrasonic frequencies, absorption due to these mechanisms begins to decrease at altitudes above 90 km.

The next three sections define modifications, some of them major, to existing algorithms in ISO/ANSI standards for atmospheric absorption at high altitudes for classical and rotational loss (Sec. II), diffusion loss (Sec. III) and molecu-

a)Electronic mail: lou-sutherland@juno.com

 0001-4966/2004/115(3)/1012/21/$20.00

lar vibration relaxation loss (Sec. IV). Section V provides algorithms for definition of mean atmospheric conditions, including estimates of humidity content up to and above 90 km. Also included are algorithms for viscosity and specific heat ratio as a function of temperature since these parameters are involved in defining atmospheric absorption for the temperatures encountered at high altitudes.

The analysis of atmospheric absorption of sound at high altitudes treats the variation in the mole ratios of the atmospheric constituents in two ways. For molecular relaxation, this variation has a primary effect and it is considered explicitly using polynomial fits to published data to define the variation in mole ratios (or mole fractions) as a function of altitude. This includes, for the first time, consideration of the added effects of molecular relaxation loss by carbon dioxide and ozone. The algorithms also include, for all four of these gases, an accurate assessment of temperature effects on their molecular vibration relaxation frequencies.[4] For evaluation of classical plus rotational relaxation loss, the effect of this high altitude variation in the proportion of atmospheric constituents on viscosity and specific heat ratio at high altitudes is assumed to be of second order and is not considered in this paper. While methods are available to take such effects into account,[5] they are complex and their application should not lend further insight into the first-order effects. Furthermore, the authors are not aware of data that would validate the application of these complex methods to predict viscosity at altitudes above the stratosphere.

It should be noted that standard values[6] are not available in the 1962 US Standard Atmosphere for atmospheric parameters, such as viscosity, at altitudes above 90 km. Thus, as stated earlier, the viscosity-dependent values for classical and rotational relaxation losses at altitudes above 90 km must be considered only as best estimates. Nevertheless, these estimates do account accurately for the dominant effect of temperature on viscosity assuming a constant atmospheric composition. One atmospheric attenuation effect that was not considered due to its negligible contribution is thermal radiation.[7]

II. CLASSICAL AND ROTATIONAL LOSS

Sound propagating through the atmosphere is subject to two forms of energy loss,[7] classical and relaxation. The former is associated with energy transfer from the organized kinetic energy of molecules due to passage of a sound wave to equivalent random kinetic energy of translation of the molecules. The relaxation form of energy loss is associated with redistribution of translational or internal energy of the molecules. Relaxation losses break down into rotational and vibrational relaxation losses—the former generally being more significant at high values of the frequency/pressure ratio (100 kHz/atm and above).

The total attenuation coefficient, α_t, in Np/m due to atmospheric absorption can be defined in a general form by the summation[7]

$$\alpha_t = \alpha_{\mathrm{cr}} + \alpha_{\mathrm{diff}} + \Sigma_i \{[A_{\max,i}/c] \times [(2f^2/f_{\mathrm{vib}})/(1+(f/f_{\mathrm{vib},i})^2)]\}, \quad (1)$$

where α_{cr} is the combined attenuation coefficient for classical plus rotational relaxation losses, α_{diff} is the attenuation coefficient for diffusion loss, and $A_{\max,i}$ is the maximum loss per wavelength for the ith molecular vibration relaxation component with a relaxation frequency $f_{\mathrm{vib},i}$, f is the frequency, and c is the speed of sound.

The rigorous presentation of the theoretical background involved in these processes is given in Ref. 7. However, the revised expressions developed in this paper for classical and rotational relaxation losses are based primarily on theoretical[8,9] and experimental[9] work by Greenspan. The expressions employed from Greenspan's theory can be summarized as follows. The complex propagation constant, k_{cr}, for the combined classical (translational) and rotational losses is

$$k_{\mathrm{cr}} = -\mathrm{i}k_1 k_2, \quad (2)$$

where k_1 and k_2 are the complex propagation constants for translational and rotational energies, respectively, each normalized by the low frequency phase constant, β_0, and having the general form:

$$k_i = [\alpha_i + i\beta_i]/\beta_0, \quad (3)$$

where $\beta_0 = (2\pi f/c_0)$, associated with the speed of sound, c_0, for low frequencies below the lowest relaxation frequency. Inserting Eq. (3) into Eq. (2), it can be shown that the real part of the product $k_{\mathrm{cr}}\beta_0$ is the attenuation coefficient, α_{cr}, given by

$$\alpha_{\mathrm{cr}} = \alpha_1\beta_2/\beta_0 + \alpha_2\beta_1/\beta_0. \quad (4)$$

At low ratios of frequency/pressure (below about 250 MHz/atm), the normalized phase constants, β_1/β_0 and $\beta_2/\beta_0 \cong 1.0$ so Eq. (4) reduces to $\alpha_{\mathrm{cr}} \cong \alpha_1 + \alpha_2$. However, Eq. (4) will be used throughout without making this approximation and will be used in most of the following (except for the discussion on dispersion).

In his earlier paper,[8] Greenspan gives a simplified version of k_1 as

$$k_1^2 = -1/[1+\mathrm{i}\nu], \quad (5)$$

where $\nu = 8\pi f\mu/3P$, a nondimensional frequency. This more convenient variable is employed here in place of Greenspan's $r = (4/3)/\nu$. For this variable, f is the frequency, in Hz, μ is the viscosity in $\mathrm{kg\,m^{-1}\,s^{-1}}$, and P is the atmospheric pressure in pascals. Applying Eq. (3) with the index, $i=1$, k_1 is given by

$$k_1 = [\alpha_1/\beta_0] + \mathrm{i}[\beta_1/\beta_0] \quad (6)$$

and using Eq. (5), it can be shown that α_1/β_0 and β_1/β_0 can be given by

$$\alpha_1/\beta_0 = \{1/2[(1+\nu^2)^{1/2} - 1]/(1+\nu^2)\}^{1/2}, \quad (7)$$

$$\beta_1/\beta_0 = \{1/2[1+\nu^2)^{1/2} + 1]/(1+\nu^2)\}^{1/2}. \quad (8)$$

For low frequencies, ($\nu \ll 1$), Eq. (6) reduces to

$$k_1 \cong [2\pi^2 f^2 \mu/\gamma c_0 P][(4\gamma/3)/\beta_0] + \mathrm{i}1, \quad (9)$$

where γ=the specific heat ratio, C_p/C_ν and c_0=the ambient speed of sound (the speed of sound at frequencies well below the lowest relaxation frequency)=$[\gamma R_0 T/M]$, m/s. (Note that c_0 is the ambient speed of sound in the absence of dis-

persion. It is not the true sound speed as discussed later), R_0=the universal gas constant=8314.48 J/kmol K, M=molecular weight=28.964 kg/kmol for altitudes below 90 km, and T is the absolute temperature in kelvin. Above 90 km, as we shall discuss later, M decreases slightly; this minor adjustment for the value for M is used in this paper for altitudes above 90 km.

The unity imaginary term shows, as required, that there is no dispersion at low frequencies. For γ=7/5 (for air), the value of the second bracketed term in the real part is 1.867, just 0.5% below the value of 1.876 in Eq. (18) from Ref. 7 for the low frequency attenuation coefficient due to classical losses. In fact, if the Eucken relationship between viscosity and the ratio of thermal conductivity to the specific heat for constant pressure is employed, the real part of this equation can be expressed in exactly the same form as in Eq. (11) of Ref. 7. It should be noted that the theoretical expression employed here for the value of k_2 can be given as

$$k_2=[\alpha_2/\beta_0]+i[\beta_2/\beta_0] \tag{10}$$

and Greenspan shows that the real and imaginary parts are given by

$$\alpha_2/\beta_0=(\sigma/2-1/2\sigma)(x)/[(1+x^2)(1+(\sigma x)^2)]^{1/2} \tag{11}$$

and

$$\beta_2/\beta_0=[(1+x^2)/(1+(\sigma x)^2)]^{1/2}, \tag{12}$$

where $x=3n\nu/4$ is a modified nondimensional frequency, $n=4/5[(C_p^\infty C_\nu^\infty)/(C_p^0 C_\nu^0)]^{1/2}Z_{\rm rot}$, $\sigma=c_\infty/c_0=[\gamma_\infty/\gamma_0]^{1/2}=[(C_p^\infty/C_\nu^\infty)/(C_p^0/C_\nu^0)]^{1/2}$, and $Z_{\rm rot}$ is the rotational collision number for air.[10] The subscripts and superscripts ∞ and 0 applied to c and γ or to the specific heats at constant pressure, C_p, and constant volume, C_ν, denote conditions at frequencies well above or below the rotational relaxation frequency (i.e., $\nu\gg1$ or $\ll1$). We can write $C_p=C_\nu+R$, and, for diatomic molecules, $C_\nu^\infty\equiv3R/2$, so $C_p^\infty\equiv5R/2$. At low frequencies, well below the rotational relaxation peak and for moderate temperatures (<400 K), $C_\nu^0=5R/2+\Sigma C'_{\nu i}\approx5R/2$, where $C'_{\nu i}$ are the vibrational relaxation specific heats and their sum is much less than $5R/2$. Thus $C_p^0\approx7R/2$ and it is readily found that $n\approx(4/5)(3/7)^{1/2}Z_{\rm rot}$ and $\sigma\approx5/\sqrt{21}$. Thus, as $f/P^*\to\infty.$, ν and $x\to\infty$ and $\beta_2/\beta_0\to1/\sigma\approx0.9165$.

Anticipating the need to allow for changes in the mixture ratio of oxygen and nitrogen in air at altitudes above the stratosphere, $Z_{\rm rot}$ is given in a more general form by[10]

$$Z_{\rm rot}=1/[(X_{\rm N_2}/Z_{{\rm rot},{\rm N_2}})+(X_{\rm O_2}/Z_{{\rm rot},{\rm O_2}})], \tag{13}$$

where $Z_{{\rm rot},{\rm N_2}}=63.3\exp[-16.7(T^{-1/3})]$, the collision number for N_2, T=absolute temperature in K, $Z_{{\rm rot},{\rm O_2}}=54.1\exp[-17.3(T^{-1/3})]$, the collision number for O_2, and $X_{\rm N_2}$ and $X_{\rm O_2}$ are the mole fractions of N_2 and O_2.

For low frequencies ($\nu\ll1$), Eq. (10) reduces to

$$(\alpha_2+i\beta_2)/\beta_0\approx[2\pi^2f^2\mu/\gamma cP][16\gamma/175]Z_{\rm rot}/\beta_0+i. \tag{14}$$

For air, γ=7/5 and the second bracketed term is 0.128, exactly the same as in Eq. (29) of Ref. 7.

Equations (4), (6), and (10) can now be combined to give the attenuation coefficient $\alpha_{\rm cr}$ for the combined classical plus rotational loss in Np/m at a frequency, f, in the more familiar form

$$\alpha_{\rm cr}=\alpha_{\rm cl}+\alpha_{\rm rot}, \tag{15}$$

where $\alpha_{\rm cl}$ and $\alpha_{\rm rot}$ are the complete attenuation coefficients. However, as will be shown, these terms exhibit a relaxation-type behavior at values of f/P^* of the order of 200 to 1000 MHz/atm where P^* is the pressure in atmospheres. An empirical adjustment, explained later, is included for the value of the parameter x in both the numerator and denominator of the phase term, β_2/β_0 in Eq. (12). Then, using $\beta_0=2\pi f/c_0$, the first term in Eq. (15), which is the classical loss attenuation coefficient, $\alpha_{\rm cl}$, can be expressed as

$$\alpha_{\rm cl}=\alpha_1(\beta_2/\beta_0)=(2\pi/c_0)\left[\frac{1/2[(1+\nu^2)^{1/2}-1][1+(x')^2]}{[1+\nu^2][1+(\sigma x')^2}\right]^{1/2}, \tag{16}$$

where ν is a nondimensional frequency=$8\pi f\mu/3P$, $\sigma\approx5/(21)^{1/2}$, $x'=2.36x$ (2.36 is an empirical adjustment factor explained later), $x=3n\nu/4$, $n\approx(4/5)(3/7)^{1/2}Z_{\rm rot}$, and $Z_{\rm rot}$ is the rotational collision number for air as before.

The viscosity, μ, is given by a modified version of the Sutherland equation[9] (see Sec. V C 3) as

$$\mu/\mu_0=(T/T_0)^{1/2}[1+S/T_0]/[1+S/T], \tag{17}$$

where μ_0=the reference viscosity at T_0=18.192 $\times10^{-6}$ kg m^{-1} s^{-1}, T_0=293.15 K (20 °C), and S=117 K. The classical attenuation coefficient, $\alpha_{\rm cl}$, exhibits a relaxation-type behavior with a maximum value for the α_1 term at $\nu_{\max}=8\pi f_{\max}\mu/3P=\sqrt{3}$ or $f_{\max}/(P/P_0)=(3\sqrt{3})P_0/(8\pi\mu)\approx10^9$ Hz/atm. At an altitude of 140 km, P/P_0 is of the order of 10^{-8} and ignoring the temperature effects on μ, the "relaxation" peak frequency, $f_{\max}$, would occur at about 10 Hz. It can be shown that Eq. (16) for $\alpha_{\rm cl}$ reduces to the usual form showing a dependency with f^2 at low frequencies well below the rotational relaxation frequency.

The second term in Eq. (14) is the attenuation coefficient, $\alpha_{\rm rot}$, for rotational loss. One basic change and one empirical adjustment are required for this expression. However, these would not be needed for evaluation of atmospheric absorption by rotational relaxation at low altitudes and at frequencies below 1000 MHz. The change is that the term must be multiplied by the sum of the mole fractions for molecular oxygen and nitrogen, $(X_{\rm O_2}+X_{\rm N_2})$, normalized by its sea level value of 0.9903. The quantity $\alpha_{\rm rot}$ defines the rotational loss for the diatomic molecules, O_2 and N_2, and does not apply for atomic oxygen and nitrogen which do not exhibit rotational relaxation. While this correction is essentially unity at altitudes below about 85 km, this normalized mole fraction sum begins to fall significantly below 1.0 at higher altitudes. For example, at an altitude of 125 km, it falls to a value of about 0.75.

The adjustment is the same empirical adjustment to the parameter, x (i.e., using $x'=2.36x$), but only for the x terms

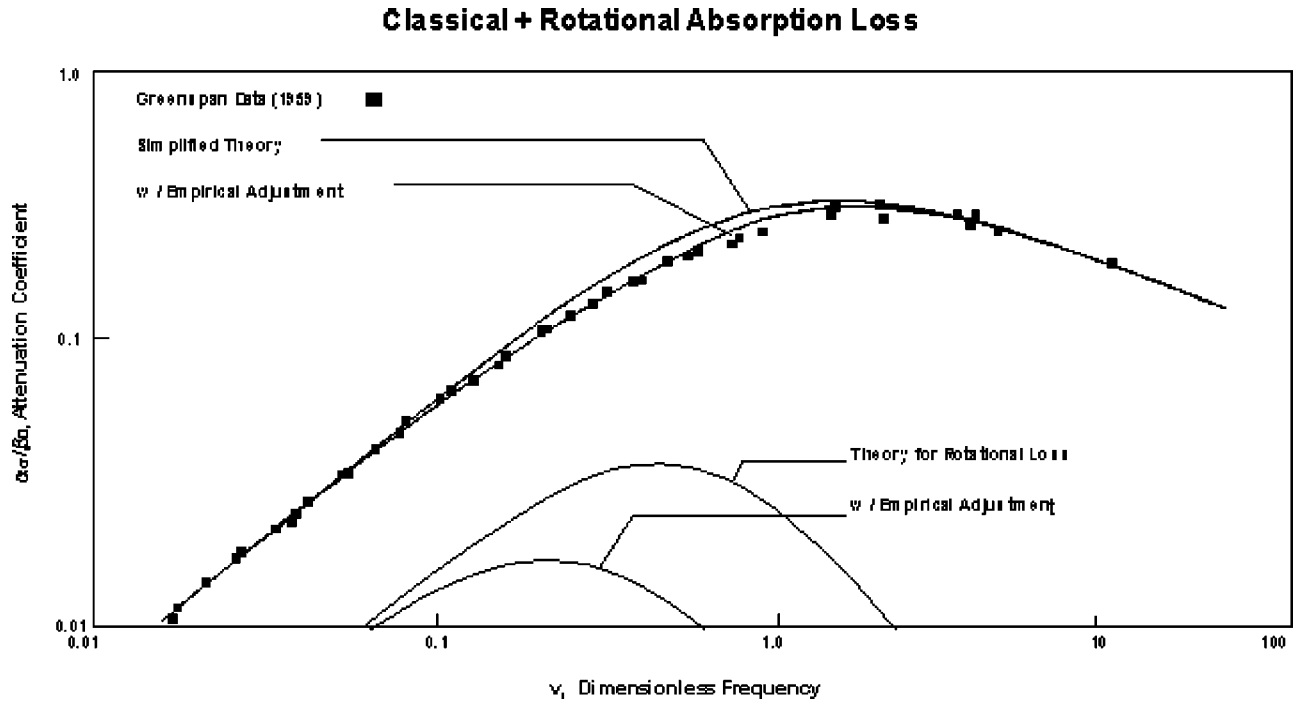

FIG. 1. Classical plus rotational absorption loss: Greenspan theory and data. The simplified theory and adjustments are explained in the text.

in the denominator of Eq. (10). With these two changes, the attenuation coefficient, α_{rot} for the rotational vibration loss, in Np/m, is given by

$$\alpha_{\text{rot}} = \alpha_2(\beta_1/\beta_0) = (2\pi f/c_0)X_{\text{ON}}\left[\frac{(\sigma^2-1)x}{2\sigma}\right]\left[\frac{1/2[(1+\nu^2)^{1/2}+1]}{[1+\nu^2][1+(x')^2]}\right]^{1/2}, \tag{18}$$

where $X_{\text{ON}} = (X_{\text{O}_2}+X_{\text{N}_2})/(X_{\text{O}_2,0}+X_{\text{N}_2,0})$, $(X_{\text{O}_2}+X_{\text{N}_2})$ = the sum of the mole fractions for oxygen and nitrogen at any altitude, $(X_{\text{O}_2,0}+X_{\text{N}_2,0})$ = the sea level value, 0.9903 (for dry air), and the remaining parameters, ν, x, x' and σ are the same as for Eq. (16).

As mentioned earlier, the prediction model for α_{cr} gives exactly the same low frequency values as in Ref. 7 for α_{rot} and within 0%–0.5% for α_{cr} depending on how the latter is expressed. Figure 1 compares the predicted values computed from Eq. (15) using Eqs. (16) and (18) with Greenspan's data for air.[9] The data and theory are plotted as nondimensional values of α_{cr}/β_0 versus the nondimensional frequency $\nu = 8\pi f\mu/3P$ where $\beta_0 = (2\pi f/c_0)$ is the low frequency phase constant at the reference temperature, T_0. The uppermost line in Fig. 1 is the theoretical result computed with Eq. (15) using Eqs. (16) and (18) but without any empirical adjustment, i.e., with $x' = x$. The line closest to the data is the theory with the empirical adjustment using $x' = 2.36x$ as explained earlier. This adjustment reduces the effect of the rotational relaxation peak and adjusts the "theory" line to provide better agreement with Greenspan's measured data. This purely empirical adjustment is considered a reasonable artifice to allow use of practical computational algorithms. When $\nu \geqslant 1$, the wavelength is comparable to the mean free path. In this regime, the simple Navier–Stokes equation is not strictly valid. There are more general solutions of the resulting gas dynamic equations in this regime. We have chosen to use an empirical correction since it allows us to maintain an analytical solution over the entire f/P^* range allowing good physical insight into the meaning of each of the terms. Moreover, this empirical modification does not change the low frequency value of α_{rot} since the second bracketed term in Eq. (18) approaches 1.0 as the frequency f, and ν, x, and x' approach zero. The theoretical and empirically adjusted value for α_{rot} predicted by Eq. (18), without and with the empirical adjustment (i.e., with $x' = 1.0$ or 2.36 times x), is shown by the lower two lines in Fig. 1.

In summary, Eqs. (16) and (18) are the basic expressions employed in this paper to compute classical plus rotational loss in the atmosphere. Equation (17) is employed to compute viscosity as a function of temperature. One other temperature-dependent parameter is also required in Eqs. (16) and (18)—the ambient speed of sound, c_0, in the absence of dispersion. The method used to compute c_0 as a function of altitude is considered later. To complete the picture, it is also desirable to define the true speed of sound at high altitudes by including the effect of dispersion.

Dispersion from classical and rotational losses

Since the primary concern for this study is sound propagation at high altitudes, it is appropriate to include the necessary equations for the frequency-dependent change in speed of sound, or dispersion, associated with the classical and rotational losses which are dominant at these altitudes. The basic expressions are already available from the previous results by simply evaluating the imaginary part of the

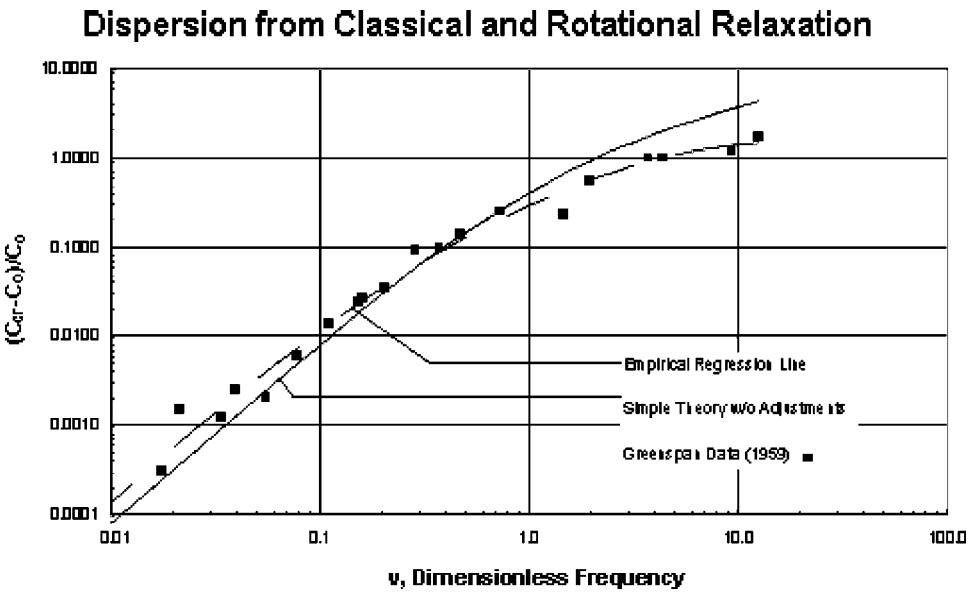

FIG. 2. Computed and measured velocity dispersion including classical and rotational relaxation losses. The dimensionless frequency, v, is defined following Eq. (5).

normalized complex propagation constant, k_{cr}, defined by Eq. (2). The resulting normalized phase constant, β_{cr}/β_0, is given by[9]

$$\beta_{cr}/\beta_0=(\beta_1/\beta_0)(\beta_2/\beta_0)-(\alpha_1/\beta_0)(\alpha_2/\beta_0), \tag{19}$$

where $\beta_{cr}=(2\pi f/c_{cr})$, $\beta_0=(2\pi f/c_0)$, and c_{cr} and c_0 are the sound speeds in the presence and absence of dispersion, respectively. The two terms in Eq. (19) are

$$(\beta_1/\beta_0)(\beta_2/\beta_0)=\left[\frac{\frac{1}{2}[(1+\nu^2)^{1/2}+1][1+(x)^2]}{[1+\nu^2][1+(\sigma x)^2]}\right] \tag{20}$$

and

$$(\alpha_1/\beta_0)(\alpha_2/\beta_0)=\left[\frac{\frac{1}{2}[(1+\nu^2)^{1/2}-1][(\sigma/2)-(1/2\sigma)]x}{[1+\nu^2][1+x^2][1+(\sigma x)^2]}\right]^{1/2} \tag{21}$$

and the variables, ν, x, and σ are the same as for Eqs. (16) and (18). Note, however, that x remains the exact, unadjusted value ($=3n\nu/4$) in these equations for the dispersion effect. That choice allows us to make the equations simple with a clear indication of how each factor affects the result. The dispersion model defined here is actually a simplified version from Greenspan's theory.[9] This employs Greenspan's simplified version[8] for the propagation constant for (classical) translational loss and thus avoids having to compute the roots of a sixth-order complex equation required in his later paper.[9] Using different corrections to get simplified but accurate values for absorption and dispersion means that they do not satisfy the Kramers–Kronig relation when $1.0<\nu<0.1$. Care should be taken if the equations are to be used in an integral transform.

The dispersion effect can be defined more clearly by an expression for the relative change in the speed of sound, δc, given by

$$\delta c=(c_{cr}-c_0)/c_0=[(1/\beta_{cr})-(1/\beta_0)]/(1/\beta_0)$$
$$=(\beta_{cr}/\beta_0)^{-1}-1. \tag{22}$$

As shown in Fig. 2, the resulting theoretical prediction from Eq. (22) provides a reasonable fit to Greenspan's experimental data[9] at low frequencies (low values of ν) but fails at higher values. An alternative to Eq. (22) is provided by the following simple empirical polynomial which defines the data in Fig. 2 more accurately. Using this approach, the speed of sound, c_{cr}, can be given by

$$c_{cr}=(\delta c+1)c_0, \tag{23}$$

where $\delta c=10^Z$, and $Z=A_0+A_1\mathrm{Lg}(\nu)+A_2[\mathrm{Lg}(\nu)]^2+A_3[\mathrm{Lg}(\nu)]^3$, $A_0=-0.536$, $A_1=1.082$, $A_2=-0.366$ and $A_3=-0.037$.

As can be seen in Fig. 2, this simple model, shown by the dashed line, fits the data quite well over the entire range of ν evaluated by Greenspan but is not reliable for values of $\nu>10$. In all cases, the reference speed of sound, c_0, would be the temperature-dependent ambient speed at altitude in the absence of dispersion.

III. DIFFUSION LOSS

A small addition to classical plus rotational relaxation loss, generally too small to be apparent in measured data, is provided by a mass and thermal diffusion loss. The attenuation coefficient, α_{diff}, in Np/m for this diffusion loss is defined by[7]

$$\alpha_{diff}\approx\frac{2\pi^2 f^2\gamma X_1 X_2 D_{12}}{c_0^3}\left[\frac{(M_2-M_1)}{M_{12}}+\frac{(\gamma-1)K_T}{\gamma D_{12}X_1X_2}\right]^2, \tag{24}$$

where D_{12}, the mass diffusion coefficient[11] for a mixture of O_2 and N_2, is equal to $2.05\times10^{-5}(T/T_0)^{7/4}(P_0/P)$ m^2/s, P_0=the reference value of pressure, 101 325 Pa, K_T=the thermal diffusion coefficient in m^2/s, and X_1, X_2, M_1, and M_2 are the mole fractions and molecular weights of the two major components, N_2 and O_2, respectively. M_{12} is equal to $X_1M_1+X_2M_2$. Reference (sea level) values for these four parameters are:[6]

$$X_{N_2}=0.78084, \quad M_{N_2}=28.0134 \text{ kg/kmol},$$

$$X_{O_2} = 0.20948, \quad M_{O_2} = 31.9988 \text{ kg/kmol}.$$

The temperature variation in D_{12} is based on published recommendations[11] and limited experimental data on the temperature variation in the diffusion constant for rare gases.[12] The dependence on pressure is inherent in the parameter.[11]

The thermal diffusion term in Eq. (24)—the second term inside the brackets—is estimated to be only 10% of the mass diffusion term for the primary constituent gases of air, molecular oxygen, and nitrogen.[5] In the first approximation,[5] the ratio K_T/D_{12} is proportional to X_1X_2, and is independent of pressure. A higher value of the order of 30% for the thermal diffusion relative to the mass diffusion term is estimated by Rind for atomic oxygen and molecular nitrogen.[13] Nevertheless, the thermal diffusion part is neglected for this study since the entire diffusion term is believed to be very small relative to the classical absorption term based on measurements near standard atmospheric conditions.[9]

Adding the remaining mass diffusion loss to the total classical plus rotational relaxation loss predicted by Eqs. (16) and (18) results in excellent agreement with experimental data in air under conditions and for frequencies where the only significant losses are classical, rotational, and diffusion losses. The predicted low frequency value for $\alpha_{cr}+\alpha_{diff}$ from the sum of Eqs. (16), (18), and (24) (with K_T assumed$=0$) is $1.84\times10^{-11}f^2$ Np/m at the reference temperature and pressure, T_0 and P_0. This predicted value agrees within 0.5% (well within experimental error) with the average from an extensive evaluation of experimental data.[14]

While this validation would seem to justify incorporation of this small diffusion loss as specified by Eq. (24) without further modification except to assume that $K_T=0$, this equation does not predict any of the relaxation behavior at high values of f/P^* that is shown by the classical loss according to Eq. (12). Referring to Eq. (24), the diffusion loss depends upon γ, which in turn depends upon the specific heat of the gas. Relaxation makes the specific heats frequency dependent, which will introduce a small additional frequency dependence in Eq. (24). For the calculations reported here, this frequency correction is effectively included in the following way. It is assumed that the diffusion loss remains equal to its predicted low frequency value relative to the value of the classical absorption loss at all frequencies. Thus, with $\alpha_{diff}=0.3\%$ of α_{cl} for low frequencies, it is assumed that α_{diff} is given at all frequencies by

$$\alpha_{diff} \approx 0.003 \ \alpha_{cl}, \tag{25}$$

where α_{cl} is given by Eq. (16).

IV. VIBRATIONAL RELAXATION LOSS

This section first defines the algorithms for the maximum loss per wavelength at the relaxation peak frequencies for each of the four primary gas components in air, O_2, N_2, CO_2, and O_3. This is followed by definitions of the relaxation frequencies at which this maximum relaxation loss occurs for each of these primary components.

TABLE I. Parameters used to define the maximum absorption loss per wavelength for the four major constituents of air.

Molecule	C_ν^∞/R[a]	C_p^∞/R[a]	θ_i (K)	X_i (sea level)
Diatomic, O_2	5/2	7/2	2239.1	0.20948
N_2	5/2	7/2	3352	0.78084
Triatomic, CO_2[b]	3	4	915	2×0.000314[c]
O_3[d]	3	4	1037	$<10^{-19}$[e]

[a]For frequencies below the rotational relaxation frequency.
[b]Known to be a linear molecule.
[c]For CO_2, X_{CO_2}, is multiplied by 2 to account for the double degeneracy of its two orthogonal vibration modes.
[d]O_3 may not be a linear molecule in which case, C_v^∞/R would be$=3$ 1/2 and C_p^∞/R would be 4 1/2. (This would introduce a negligible change in the total atmospheric loss.)
[e]X_{O_3} reaches a maximum of about 7.6×10^{-6} at an altitude of 33 km.

A. Maximum loss per wavelength

The maximum loss per wavelength, $A_{max,i}$ from vibrational relaxation for each of the four dominate constituent gases in air considered in this paper is defined by[7]

$$A_{max,i} = X_i(\pi/2)(C_i'/R)/[(C_p^\infty/R)(C_\nu^\infty/R + C_i'/R)], \tag{26}$$

where X_i=the mole fraction of the ith constituent gas. (Note that since the bending vibrational mode of CO_2 is doubly degenerate, its mole fraction is multiplied by 2 for computation of its vibrational relaxation strength.) The relaxing specific heat C_i' for the gas, normalized by the universal gas constant, R, is given by the Planck–Einstein equation in terms of its characteristic temperature, θ_i, and the atmospheric temperature, T, as

$$C_i'/R = (\theta_i/T)^2 \exp(-\theta_i/T)/[1-\exp(-\theta_i/T)]^2. \tag{27}$$

The parameters C_p^∞/R and C_ν^∞/R are defined for Eq. (12). These normalized parameters, values for θ_i and sea level values for the mole fractions, X_i, are summarized in Table I. The temperature dependence of C'/R for different constituents, i, is shown in Fig. 3. When it is assumed that $(C_i'/R) \ll 1$, Eq. (26) reduces to a simpler form more commonly employed.[7] However, the general form of Eq. (26) is retained here to ensure accuracy for the higher temperature range encountered at high altitudes where (C_i'/R) can approach values of the order of 0.3 (i.e., not $\ll 1$).

It is desirable, at this point, to anticipate one aspect of the final results by showing how the relaxation strength, C_i/R, varies with temperature for the four gases identified in Table I. Applying Eq. (27), the value of C_i/R, relative to its value at the sea level temperature is shown in Fig. 3 for these four gases. Note that at the highest temperature which will occur at the highest altitudes, the relaxation strength is markedly higher (by a value of about 400) than its sea level value. This behavior, attributable to the higher characteristic temperature, θ_i of nitrogen will be apparent later when examining the variation in the molecular relaxation loss for each of the four gases.

B. Vibrational relaxation frequencies

Based on values in the current ANSI/ISO Standards,[3] on other published data,[4] and estimates by the authors where data were not available, the following expressions have been

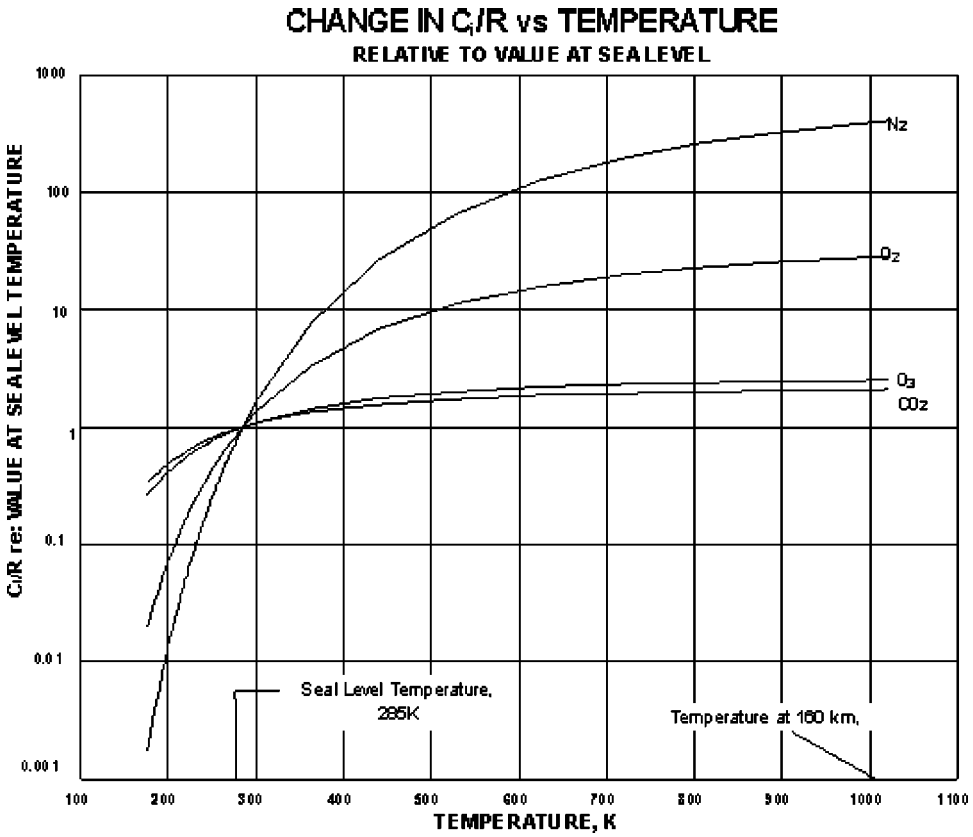

FIG. 3. Change in molecular vibration relaxation strength, C/R, with temperature. The contributions from different constituents are identified.

developed to define the molecular vibration relaxation frequencies which can account for the unusual atmospheric composition and temperature conditions at high altitudes. Note that while the experimental relaxation rate data in Ref. 4 do not extend to the full temperature range encountered up to the altitude of 160 km considered herein, the data do extend up to about 500 K, well beyond the maximum temperature (about 300 K) at the lower altitudes where molecular relaxation is significant. Thus, the data in Ref. 4 provide a valid experimental data base for nearly all the new vibrational relaxation contributing gases and temperature correction effects included herein for vibrational relaxation frequencies which are not already well documented for the existing standards.[3] In the few cases where no data are available to support the new relaxation frequency parameters, conservative, physically reasonable estimates were made. As pointed out later, changing these estimated parameters by a factor of 2 changed the total attenuation coefficient by less than 0.2% for the worst case.

1. Oxygen

In a variation on the ANSI standard, the molecular vibration relaxation frequency for oxygen, f_{vib,O_2}, in Hz, is estimated to be given by[3,4]

$$f_{\mathrm{vib},O_2}=(P/P_0)(\mu_0/\mu)[A_1+A_2+Bh'(C+h')\times(D+h')], \tag{28}$$

where $A_1=(X_{O_2}+X_{N_2})24\exp(-9.16\,T_r)$, Hz; $A_2=(X_O+X_N)2400$, Hz; $B=40\,400\exp(+10.0\,T_r)$, Hz/%; $C=0.02\exp(-11.2\,T_r)$, %; $D=0.391\exp(+8.41\,T_r)$; $T_r=[(T/T_0)^{(-1/3)}-1]$; $T_0=293.15$ K, and $h'=100[(X_{H_2O})+X_{O_3}]$, the mole concentration, in %, of water vapor plus ozone. (Note the distinction between the mole concentration, h', in percent for water vapor and the corresponding mole fraction, X_{H_2O}.) The various mole fractions, X_i, where i corresponds to O_2, N_2, O_3, O, N, and H_2O, are their fractional parts, by volume, in the mixture of moist air.

The A_2 term in the above-given expression is an estimated correction for the presence of atomic oxygen and nitrogen. As will be shown later, the mole fraction of the former exceeds that for O_2 at altitudes above about 95 km. The term, $(P/P_0)(\mu_0/\mu)$ accounts for the inherent effect of the pressure- and viscosity-dependent molecular collision frequency, $f_{\mathrm{col}}=1.25\,P/\mu$, on all vibrational relaxation frequencies.[7]

The temperature correction factors in Eq. (28) are defined in terms of the relative temperature variable, T_r, which is zero at the reference temperature, T_0, resulting in a temperature correction factor of unity at this temperature. For each component, the exponents are based on the experimental data reviewed in Ref. 4.

2. Nitrogen

The relaxation frequency for nitrogen, f_{vib,N_2}, is also modified from the ANSI/ISO Standards[3] to account for the atypical conditions at high altitudes. The resulting new expression is

$$f_{\mathrm{vib},N_2}=(P/P_0)(\mu_0/\mu)[E+FX_{O_3}+GX_{H_2O}], \tag{29}$$

where $E=9\exp(-19.9\,T_r)$. This includes a temperature correction[4] for the low humidity term believed to represent relaxation of N_2 by CO_2. $F=60\,000$ Hz is an estimate to account for relaxation of N_2 by ozone. $G=28\,000\exp(-4.17\,T_r)$ and is the same term as in the ANSI/ISO Standards to account for relaxation of N_2 by water vapor. There are no available data for relaxation of N_2 by O_3 so we assumed that since O_3 and H_2O both have large dipole moments, their effect on the relaxation of N_2 should be similar. This estimate can easily be off by a factor of 2. However, it is found later that the results are not sensitive to F. (A change in F by a factor of 2 only changes the total attenuation coefficient by 0.13% at 1 Hz and by much less at higher frequencies.)

3. Carbon dioxide

For carbon dioxide, based on experimental relaxation rates[4] for CO_2 in mixtures with O_2, N_2, H_2O and on rough estimates for O, N, and O_3, the relaxation frequency, $f_{\mathrm{vib,CO_2}}$ is estimated to be given by the following:

$$f_{\mathrm{vib,CO_2}}=(P/P_0)(\mu_0/\mu)Z, \tag{30}$$

where $Z=[HX_{\mathrm{CO_2}}+I(X_{\mathrm{O_2}}+0.5X_{\mathrm{O}})+J(X_{\mathrm{N_2}}+0.5X_{\mathrm{N}})+K(X_{\mathrm{H_2O}}+X_{\mathrm{O_3}})]$ and $H=22\,000\exp(-7.68\,T_r)$, Hz; $I=15\,100\exp(-10.4\,T_r)$, Hz; $J=11\,500\exp(-9.17\,T_r)$, Hz, and $K=8.48\times10^8\exp(+9.17\,T_r)$, Hz. Data are available[4] to support the temperature correction factors in the above-noted expression for the molecular species (i.e., O_2 and N_2) but there are no similar experimental data for vibrational relaxation of CO_2 by the atomic species, O and N. In Eq. (30), we have effectively assumed that the atoms are 0.5 times as effective as the molecules O_2 and N_2 if relaxing CO_2. This might seem strange since free atoms are often very efficient as energy transfer catalysts. But the molecules transfer energy via vibrational to vibrational energy transfer reactions that are typically more effective than collisions that require vibrational to translational energy transfer. Again, sensitivity to this assumption of a correction by 0.5 for effective mole fraction of either atomic O or N is not critical. A change in this correction by a factor of 2 changed the total atmospheric attenuation coefficient, for the worst case (at 1 Hz), by less than 0.0007% so that this adjustment for the contribution of O and N could, after the fact, have been ignored.

4. Ozone

Finally, the relaxation frequency, $f_{\mathrm{vib,O_3}}$ for ozone, based on limited data,[4] is estimated to be

$$f_{\mathrm{vib,O_3}}=(P/P_0)(\mu_0/\mu)(1.2\times10^5)L, \tag{31}$$

where $L=\exp(-7.72T_r)$. For Eqs. (29)–(31), T_r is the same as defined for Eq. (28).

The expressions developed up to this point can now be applied to the computation of atmospheric absorption as a function of altitude given a model, or models, for the atmospheric pressure, temperature, and composition. These models are defined in Sec. V. The above-outlined expressions for atmospheric absorption differ substantially from those employed in the ANSI/ISO Standards and are intended only for application at altitudes above the approximate upper bound of 20 km covered by these standards.[3]

V. ATMOSPHERIC CONDITIONS

The primary model given in this section to define reference values for atmospheric pressure and temperature up to 160 km was developed by NASA for application at Cape Kennedy.[15] The profile of water vapor as a function of altitude was based on the data in Ref. 16. Although the data only extended to 100 km, it was possible to extrapolate values to 160 km with considerable confidence since: (1) a linear decrease in the log of mole fraction of water vapor as a function of altitude was clearly indicated by the data in Ref. 16 for altitudes from 50 to 100 km and (2) water vapor plays little or no role in atmospheric absorption beyond an altitude of about 80 km and only then for very low frequencies. The model used to define the chemical composition (in terms of mole fractions) of the significant constituent gases considered in Sec. IV (i.e., N_2, O_2, N, O, CO_2, O_3, and H_2O) is also based on information from Ref. 16. The latter defined the mole fractions for most of these constituent gases to an altitude of 240 km. For CO_2, extension of $X_{\mathrm{CO_2}}$ values to such an altitude necessarily involves extrapolation to altitudes well above those for which data were available. However, information on mole fractions is only applied up to 160 km in this paper. Although more recent data on atmospheric conditions are available, the values employed for this paper are considered reasonable and based on authoritative sources for purposes of illustrating the changes in atmospheric absorption at high altitudes. The reader is free to apply the above-given algorithms to any other atmospheric composition data. However, the basic trends illustrated herein are unlikely to change significantly.

A. Reference values for atmospheric pressure, temperature, and humidity

Atmospheric pressure and temperature are defined, for the default model, by the following two types of polynomial equations (up to fifth order) with geometric altitude, Y, in km, as the independent variable. However, each equation—one for atmospheric pressure and one for temperature—utilizes different sets of polynomial coefficients to cover seven different altitude ranges or legs. These coefficients and the corresponding equations are specified in Table II. In all cases, at any one interface between two legs, either set of coefficients may be used with negligible error in the resulting value for pressure or temperature.

1. Atmospheric pressure

The atmospheric pressure, P, in pascals, is given as a function of the geometric altitude, Y, in km, from 0 to 160 km, by

$$P=10^5\exp(A_0+A_1Y+A_2Y^2+A_3Y^3+A_4Y^4+A_5Y^5), \tag{32}$$

where the coefficients A_i are found in Table II for seven different altitude ranges. (For convenience, the three different equation forms used in Ref. 15 to define atmospheric

TABLE II. Coefficients for polynomial expressions for atmospheric pressure and temperature versus altitude.

Altitude range (km)			Use with	Coefficients					
Lower	Upper	Leg	Eq. No.	A_0	A_1	A_2	A_3	A_4	A_5
Pressure									
0	11	I	(32)	$1.68716E-02$	$-1.14252E-01$	$-1.36123E-03$	$7.36241E-05$	$-1.08003E-05$	$3.30464E-07$
11	18	II	(32)	$-7.99108E-02$	$-8.10464E-02$	$-5.55224E-03$	$3.11170E-04$	$-1.66878E-05$	$3.83200E-07$
18	28	III	(32)	$9.84143E-01$	$-2.69769E-01$	$8.52275E-03$	$-3.96203E-04$	$1.01465E-05$	$-1.02643E-07$
28	50	IV	(32)	$2.18198E+00$	$-4.11497E-01$	$1.33665E-02$	$-3.59519E-04$	$5.10097E-06$	$-2.89056E-08$
50	83	V	(32)	$7.63380E+00$	$-2.58298E-01$	$3.76139E-03$	$-4.20887E-05$	$1.60200E-07$	$-1.92509E-10$
83	90	VI	(32)	$-1.12790E+01$	$3.19820E-01$	$-5.80930E-03$	$2.23310E-05$	0	0
90	160	VII	(32)	$-1.09914E+02$	$4.71430E+00$	$-8.21230E-02$	$6.62200E-04$	$-2.55930E-06$	$3.84825E-09$
Temperature									
0	11	I	(33)	$2.85000E+02$	$-5.07619E+00$	$1.97780E-01$	$-5.61320E-02$	$1.46360E-03$	$1.42000E-04$
11	18	II	(33)	$1.25350E+03$	$-3.28270E+02$	$4.18980E+01$	$-2.67240E+00$	$8.44850E-02$	$-1.05260E-03$
18	28	III	(33)	$2.12120E+03$	$-4.19180E+02$	$3.64740E+01$	$-1.57300E+00$	$3.36670E-02$	$-2.85790E-04$
28	50	IV	(33)	$-9.01040E+02$	$1.58750E+02$	$-8.92550E+00$	$2.46170E-01$	$-3.28070E-03$	$1.68830E-05$
50	83	V	(33)	$-5.03980E+02$	$3.92140E+01$	$-4.95180E-01$	$-3.26220E-03$	$9.66650E-05$	$-4.78800E-07$
83	90	VI	(33)	$1.75740E+02$	0	0	0	0	0
90	160	VII	(33)	$-6.84520E+04$	$2.82794E+03$	$-4.57421E+01$	$3.62065E-01$	$-1.39987E-03$	$2.12100E-06$

pressure as a function of altitude have been reduced to one common form.) Values of P as a function of altitude are given in Fig. 4. Note that at an altitude of 120 km, the pressure is more than seven orders of magnitude less than at sea level.

2. Temperature

The absolute temperature, T of the atmosphere, in kelvin, is given as a function of the geometric altitude, Y in km, by

$$T=A_0+A_1Y+A_2Y^2+A_3Y^3+A_4Y^4+A_5Y^5. \quad (33)$$

The above equations and Table II are used to define the profiles for mean atmospheric pressure and temperature shown in Figs. 4 and 5, respectively. Also shown in the figures are the mean values for the atmospheric pressure and temperature from other sources for model atmospheres.[6,17,18] As expected, there is very little disagreement between the various models for atmospheric pressure as a function of altitude. The NASA model[15] was preferred, in this case, since the polynomial coefficients had already been developed.

The temperature profile prediction model, shown by the solid line in Fig. 5, is in reasonable agreement with data from the alternative models. Note, for example, that the predicted temperature profile follows the US Standard atmosphere model fairly well. However, as expected, temperature profiles show considerably more variation than do pressure profiles. Furthermore, at altitudes above about 110 km (i.e., in the thermosphere), the temperature can vary widely with time of day,[18] a detail not reflected in the other models which only provide long-time average values.

It must be emphasized that the weather profiles presented in this paper, especially those for temperature, only scratch the surface of this highly complex topic with a very rich literature base. However, based on comparisons shown

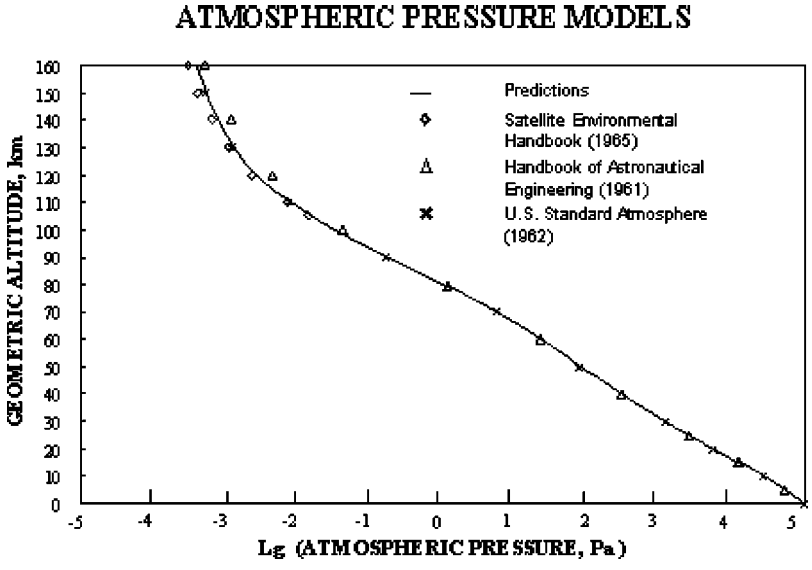

FIG. 4. The $\log_{10}$ of the atmospheric pressure vs altitude. The solid line, used in this study up to 160 km, is a fit to different atmospheric pressure models.

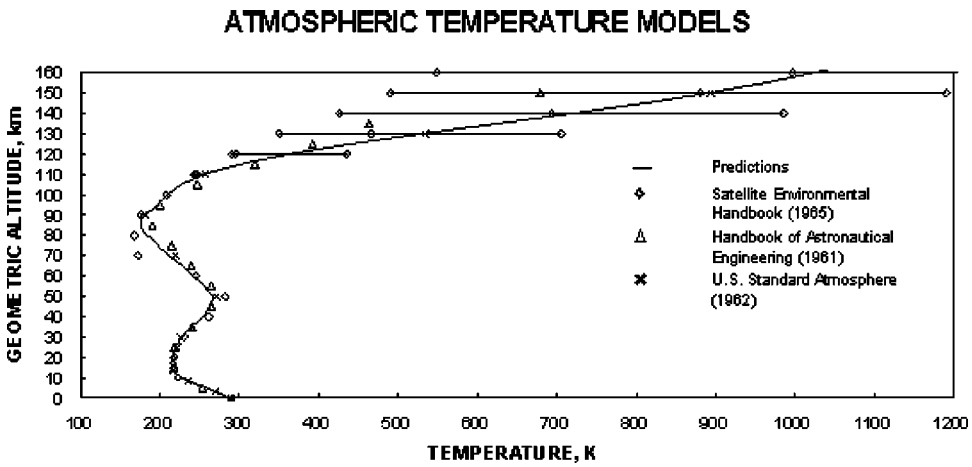

FIG. 5. Atmospheric temperature vs altitude. The solid line represents a fit to different models for atmospheric temperature and was used in the calculations in this paper.

in Figs. 4 and 5 with the data from the numerous alternative models, the default prediction models do appear to provide representative values suitable for evaluation of sound propagation at high altitudes.

3. Humidity profiles

Although properly a part of the next section on composition of the atmosphere, it is convenient to treat the profile of humidity content in this section. As stated earlier, the humidity profile was based on plotted data in Ref. 16. Three regression equations were developed to define this water vapor profile in terms of the mole fraction of water vapor, X_{H_2O}, as a function of altitude. The first two equations fitted the data from 0 to 30 km and from 30 to 100 km and the third expression was a linear extrapolation above 100 km. The results are shown in Fig. 6 along with comparison with humidity data from other sources.[3,15]

B. Reference values for composition of the atmosphere

Knowledge of the mole fraction profile for the major constituents of the atmosphere considered in this paper is essential in order to be able to apply the algorithms in Sec. IV, especially for prediction of relaxation frequencies. Reference 16 was employed to define this composition profile. It contained a plot of the density of molecules or atoms of the atmospheric constituents as a function of altitude. Careful reconstruction of this plot by reading values from the published figure provided the profile of composition density shown in Fig. 7. The values employed here for Fig. 7 are believed accurate within better than $\pm 2\%$. Although the atmospheric composition is believed to provide reasonable approximations of these average values, some of the constituents considered, such as water vapor, can be expected to have significant variations with location and time which would have a major effect on atmospheric absorption by molecular relaxation at low altitudes—outside the primary focus of this paper.

Furthermore, no attempt is made here to develop the very complex pattern of spatial and temporal variation in ozone content[19] since it turns out to be the least significant of the sources of molecular relaxation loss at high altitudes. The maximum value of the contribution of molecular relaxation loss from ozone is about 2.7% of the total molecular vibration relaxation loss (at 400 Hz at 30 km) but it only reaches a maximum of about 0.1% of the total atmospheric absorption loss (at 120 Hz at 32 km). Clearly, further refinement of ozone mole fraction data is not required for these calculations.

From this atmospheric composition density profile, mole

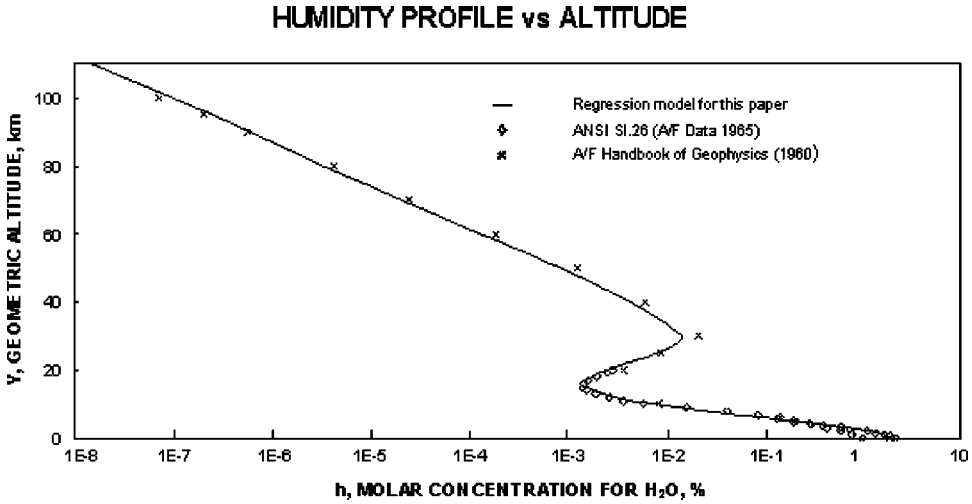

FIG. 6. Humidity vs altitude. The solid line, used in the calculations in this paper, represents a fit to the atmospheric humidity models for altitudes up to 100 km. As explained in Sec. V A 3, values above 100 km were extrapolated on the basis of the linear trend above 80 km.

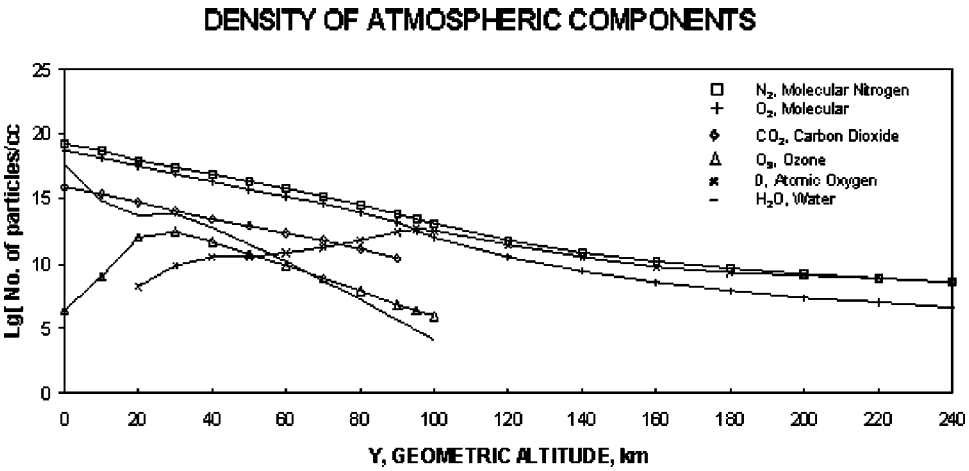

FIG. 7. Density of atmospheric components as a function of altitude. Here and for Figs. 8 and 10, while values are shown up to an altitude of 240 km to help illustrate the variations in the atmospheric constituents at these high altitudes, atmospheric absorption is only computed up to 160 km for this paper.

fraction values were computed for dry air. That is, the water vapor content was initially assumed equal to zero in order to establish the basic mole fraction profile of the remaining constituents which is assumed to remain essentially invariant with time. (One exception to this ''fixed-in-time'' assumption is the long time variation in CO_2 content discussed in the following.) Least-squares polynomial regression equations were then developed from these computed dry-air mole fraction profiles and the results are shown in Fig. 8(a) for molecular oxygen, O_2; in Fig. 8(b) for molecular nitrogen, N_2; in Fig. 8(c) for atomic oxygen, O, and nitrogen, N, and in Fig. 8(d) for ozone, O_3. These polynomial expressions are defined later.

1. Carbon dioxide content

For carbon dioxide, the situation is different. First, it will be shown that the atmospheric absorption loss from CO_2 molecular vibration relaxation is the dominant relaxation absorption component at moderate altitudes. This dominance occurs at an altitude of about 65 km at a frequency of 1 Hz decreasing to an altitude of about 10 km at a frequency of 10 000 Hz. Second, it is known that the amount of carbon dioxide in the atmosphere has been slowly increasing for many years above its oft-cited level of 314 ppm.[6] Thus it was considered desirable to estimate a mole fraction for this constituent that would correspond to an expected value by the year 2010—an arbitrary future target year for purposes of this paper. Measurements of carbon dioxide content in the atmosphere have been monitored by Charles Keeling of the Scripps Institute of Oceanography since 1958 at a 3500 m high observatory on the Mauna Loa volcano in Hawaii.[20] The historical trend in the average annual CO_2 levels observed at this site are shown in Fig. 9 from data published in Ref. 21. Also shown are projections of possible increasing levels.[22] A growth rate for the mole fraction, X_{CO_2} of CO_2 was estimated by the following regression line through the measured data:

$$X_{CO_2} \approx 6.9049\times 10^{-2} - 7.0781\times 10^{-5}(\mathrm{yr}) + 1.8222 \times 10^{-8}(\mathrm{yr})^2, \tag{34}$$

where yr is the calendar year.

For the year 2010, Eq. (34) predicts a mole fraction for CO_2 corresponding to about 400 ppm equivalent to a value of X_{CO_2} of 4×10^{-4}. As shown in Fig. 7, the particle density for CO_2 decreases initially at approximately the same rate as for O_2 and N_2. Thus, the mole fraction of CO_2 does not appear to vary significantly with altitude up to at least 90 km. The actual value of the mole fraction for CO_2 derived from the 1960-vintage data in Fig. 7 varied by less than $\pm 10\%$ about a mean value close to the expected nominal value at that time of about 314 ppm. This tendency for an approximately constant mole ratio with altitude is consistent with the observation by Keeling[20] that ''the mixing ratio of CO_2 is fairly stable up to the stratosphere.''

In the absence of more definitive data, it was assumed, therefore, that the mole ratio of CO_2 would be constant with altitude up to the upper limit of 160 km considered in this study. Furthermore, since the data in Fig. 7 supports an approximately constant mole fraction up to about 90 km and this exceeds the altitude of 70 km noted earlier where molecular relaxation by CO_2 dominates this form of atmospheric absorption loss, the actual CO_2 content above 90 km is not expected to have any real significance for atmospheric absorption of sound.

2. Computation of mole fractions

A generic equation, given in the following, is used with the corresponding coefficients in Table III to define the mole fraction, X_i (not the % concentration) of the ith constituent as a function of altitude. From one to three sets of coefficients, depending on the constituent gas, are required for different altitude ranges. The total mole fraction over all constituents considered, except water vapor, was very nearly equal to the theoretical value of about 0.99 for dry air. Argon and other trace constituents make up the remaining 1%. Therefore, to provide the correct sum in mole fractions, argon was added at a constant ratio of 1.2% of the mole fraction of nitrogen. This proportion was derived from the data in Fig. 7 and remained nearly constant up to about 90 km dropping off slightly at higher altitudes. With this addition of argon, the

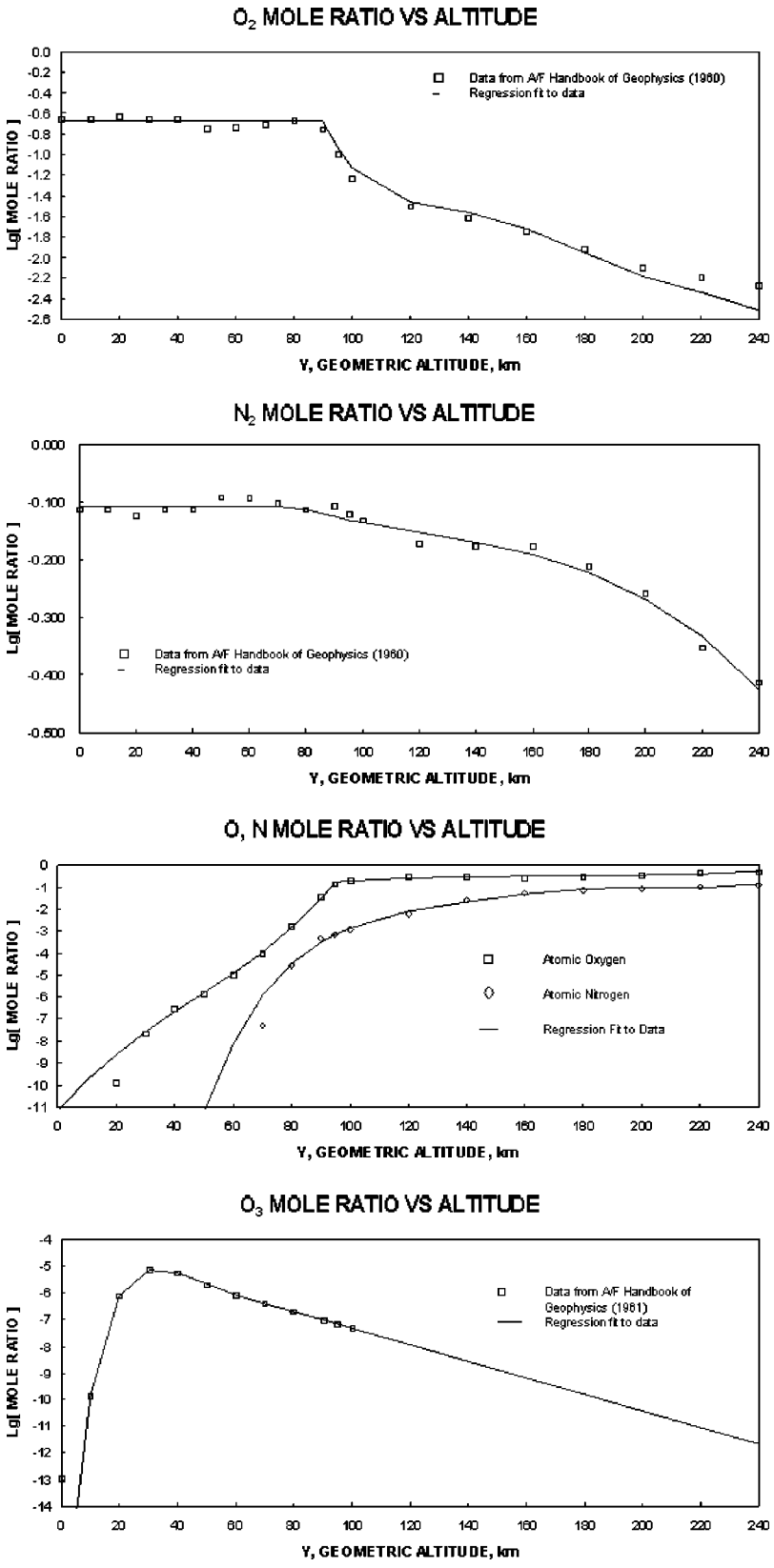

FIG. 8. Mole ratio of atmospheric constituents vs altitude for major atmospheric constituents (a) O_2; (b) N_2; (c) O, N; (d) O_3. The extrapolation for O_3 beyond the limit of data above 100 km is not critical since it is shown later that its contribution to the total absorption is completely negligible above about 60 km.

sum of the mole ratios for dry air was within 1% of a theoretical value of 1.0 at all altitudes below 90 km and deviated by less than 3% at higher altitudes.

The mole fraction of water vapor, X_{H_2O}, was also computed from three different polynomial expressions derived from analysis of the data in Fig. 7 covering the range of 0–160 km as explained in Sec. V A 3. As shown previously in Fig. 6, the resulting prediction model agrees reasonably well with other humidity profile data.

Thus, for the *i*th component, the mole fraction, X_i is given by the following generic expression where the number of terms involved varies from 1 to 5 with from one to three

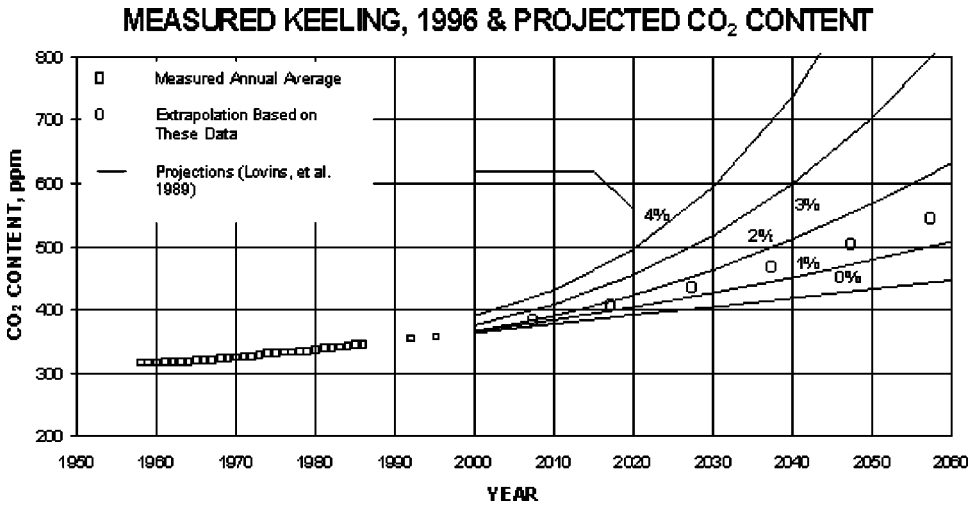

FIG. 9. CO_2 content measured by Keeling at an altitude of 3.5 km [Lashof and Tirpak (1989), Projections for future years by Levins *et al.*, (1989) and extrapolation used for this paper].

sets of coefficients required, as defined by Table III, to cover the entire altitude range for Y from 0 to 240 km,

$$X_i = 10^B, \tag{35}$$

where $B = A_0 + A_1 Y + A_2 Y^2 + A_3 Y^3 + A_4 Y^4 + A_5 Y^5$. The mole fraction profiles versus altitude for the constituents, using Eq. (35) and the appropriate coefficients from Table III, are shown by the solid lines in Figs. 8(a)–(d). The symbols correspond to the values computed from the data of Ref. 16 shown earlier in Fig. 7.

3. Computed molecular weight

A further test of the accuracy of the mole fraction model is provided by a comparison of the molecular weight for air as a function of altitude computed by the following expression [with the help of Eq. (35) and Table III] to tabulated values from the literature (i.e., Refs. 6, 17, 18, and 23). When making this computation of molecular weight, it is necessary to normalize the mole fractions of all the constituents, including water vapor, so that their sum is again equal to 1.0. Without this correction, the molecular weight for moist air would be higher than the true value and the resulting value for the speed of sound would be erroneous. However, the error realized if this normalization was not made would only be significant below about 6 km where the mole concentration for water vapor can be of the order of 1%–5%.

Based on the above-noted approach, the molecular weight of air, M, at any altitude was computed by

$$M = \sum_i^n [X_i M_i] \Big/ \sum_i^n X_i, \tag{36}$$

where X_i are the unnormalized mole fraction values, (i.e., for dry air) computed with Eq. (35) and Table III and M_i are the mole molecular weight values for the ith component as specified in the following:

TABLE III. Coefficients for polynomial expressions for atmospheric composition.

Component	O_2	N_2	CO_2	O_3	O	N	H_2O
Alt (km)	0–90	0–76	0–240	0–80	0–95	0–240	0–30
A_0	−0.67887	−0.10744	−3.3979	$-1.9027E+01$	$-1.1195E+01$	$-5.3746E+01$	$-1.7491E+00$
A_1				$1.3093E+00$	$1.5408E-01$	$1.5439E+00$	$4.4986E-02$
A_2				$-4.6496E-02$	$-1.4348E-03$	$-1.8824E-02$	$-6.8549E-02$
A_3				$7.8543E-04$	$1.0166E-05$	$1.1587E-04$	$5.4639E-03$
A_4				$-6.5169E-06$		$-3.5399E-07$	$-1.5539E-04$
A_5				$2.1343E-08$		$4.2609E-10$	$1.5063E-06$
Alt (km)	90–240	76–240		80–240	95–240		30–100
A_0	$4.9296E+01$	$1.3972E-01$		$-4.2340E+00$	$-3.2456E+00$		$-4.2563E+00$
A_1	$-1.5524E+00$	$-5.6269E-03$		$-3.0975E-02$	$4.6642E-02$		$7.6245E-02$
A_2	$1.8714E-02$	$3.9407E-05$			$-2.6894E-04$		$-2.1824E-03$
A_3	$-1.1069E-04$	$-1.0737E-07$			$5.2640E-07$		$-2.3010E-06$
A_4	$3.1990E-07$						$2.4265E-07$
A_5	$-3.6211E-10$						$-1.2500E-09$
Alt (km)							100–240
A_0							$-6.2534E-01$
A_1							$-8.3665E-02$

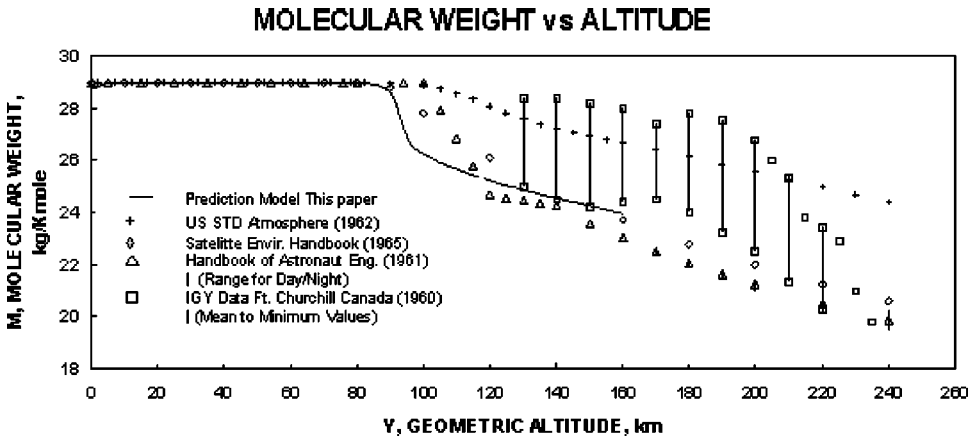

FIG. 10. Molecular weight vs altitude. Solid line comes from Eq. (36).

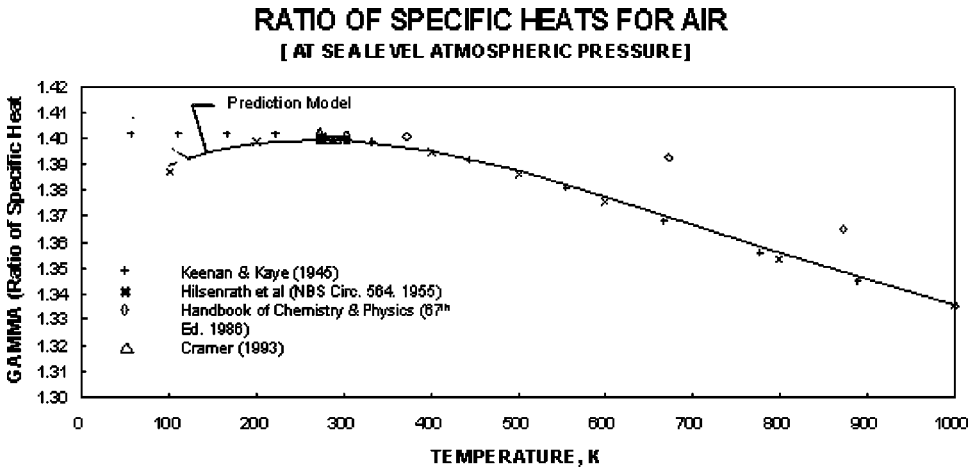

FIG. 11. Ratio of specific hearts at different temperatures for air at sea level atmospheric pressure. Different models are given by the symbols. The solid line is from Eq. (38).

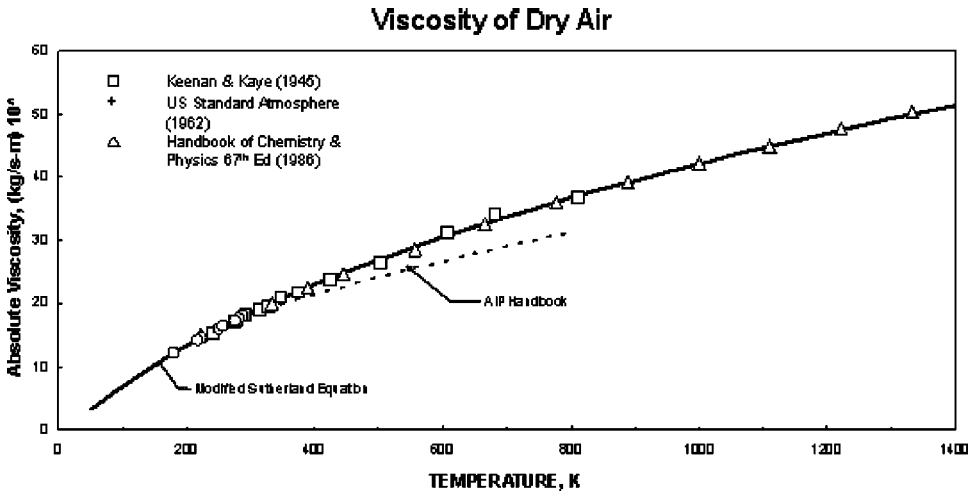

FIG. 12. Viscosity of dry air as a function of temperature. We use a modified Sutherland equation described by Eq. 17.

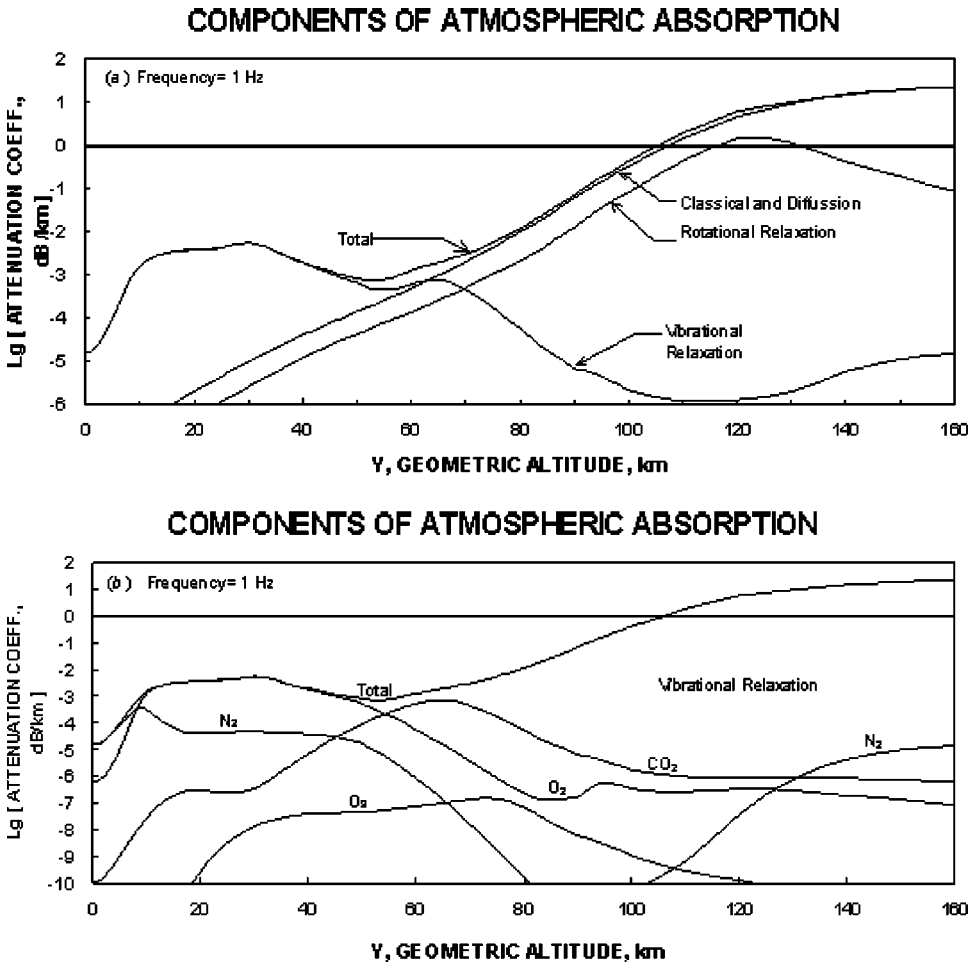

FIG. 13. Components of atmospheric absorption as a function of altitude. At a frequency of 1 Hz. (a) Contributions from different mechanisms; (b) molecular vibrational relaxation contributions for each molecule.

*i*th component	M_i (kg/kmol)
Nitrogen	28.0134
Oxygen	31.9988
Carbon dioxide	44.0095
Ozone	47.9982
Atomic nitrogen	14.0067
Atomic oxygen	15.9994
Water vapor (H_2O)	18.0153
Argon ($X_i = 0.012\, X_{N_2}$)	39.948

The values of molecular weight computed in this manner are compared in Fig. 10 with published values from several sources[6,17,18] including one actual measurement at high altitudes obtained during the extensive studies carried out during the International Geophysical Year (IGY) program in the late 1950s.[23] Below 90 km, i.e., within the stratosphere, the computed molecular weight agrees, as expected, with the standard value for dry air of 28.964 kg/kmol. However, above that altitude, the mole fractions of the constituents of air, especially molecular and atomic oxygen, change markedly and the agreement between prediction and published or measured values is less satisfactory. Nevertheless, the computed values based on the atmospheric model of this paper, which in turn is very dependent on the plotted data from Ref. 16, are not inconsistent with a lower bound for the reported[17,18] and measured[23] values for the molecular weight of air at high altitudes. This result has a small effect on the computed value for the ambient speed of sound, c_0, which enters into all of the expressions for atmospheric absorption of sound.

C. Temperature-dependent parameters

The following briefly summarizes the background data and prediction models employed to define the three basic temperature-dependent parameters that are needed for evaluation of atmospheric absorption of sound at high altitudes. These are: (1) the ambient speed of sound, c_0, (2) the specific heat ratio, γ, needed to define c_0, and (3) finally, viscosity, μ, so basic for classical plus rotational relaxation loss.

1. Ambient speed of sound

Using the standard expression for the speed of sound, c_0, for an ideal gas,[7] the low frequency speed of sound in air, in m/s, in the absence of dispersion, is given by

$$c_0 = [\gamma R_0 T/M]^{1/2}, \tag{37}$$

where γ=the ratio of specific heats, C_p/C_v; R_0=the universal gas constant, 8314.48 J/kmol K; T=absolute temperature, K; M=molecular weight, kg/kmol [from Eq. (36)].

2. Specific heat ratio

Ideally, the value of the specific heat ratio at altitudes above 90 km should be computed from a weighted average based on the values for the specific heat at constant pressure for each constituent weighted by the product of their molecu-

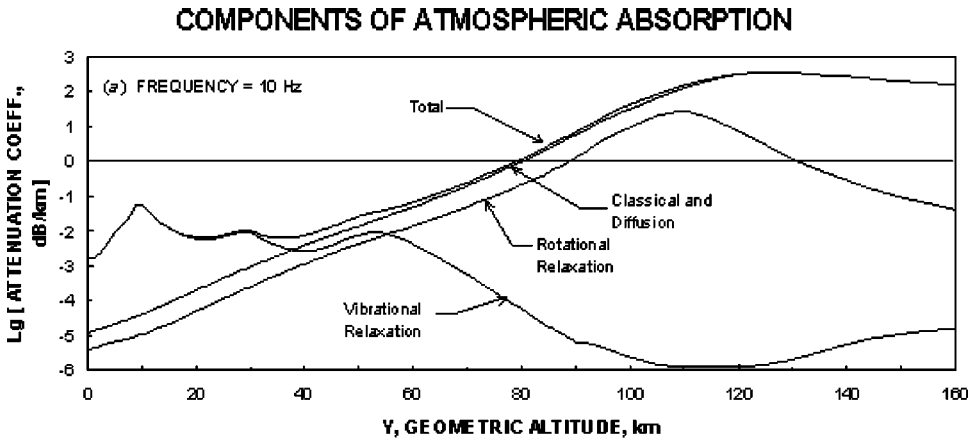

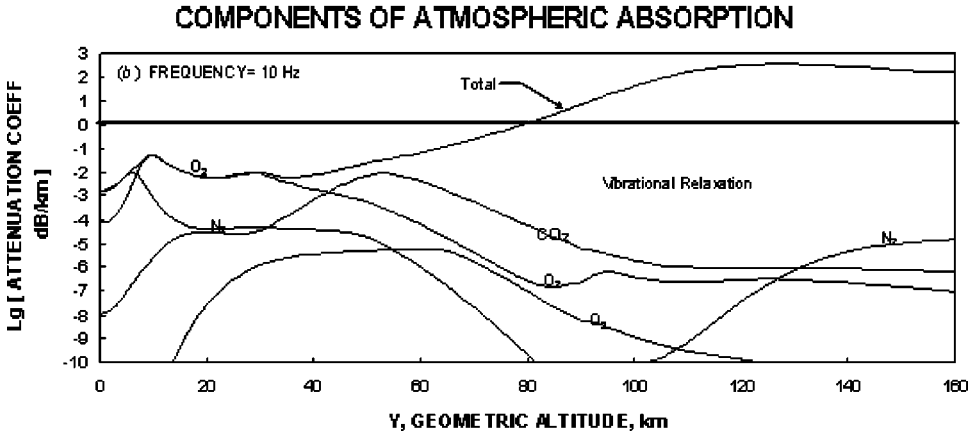

FIG. 14. Components of atmospheric absorption as a function of altitude at a frequency of 10 Hz. (a) Contributions from different mechanisms; (b) molecular vibrational relaxation contributions for each molecule.

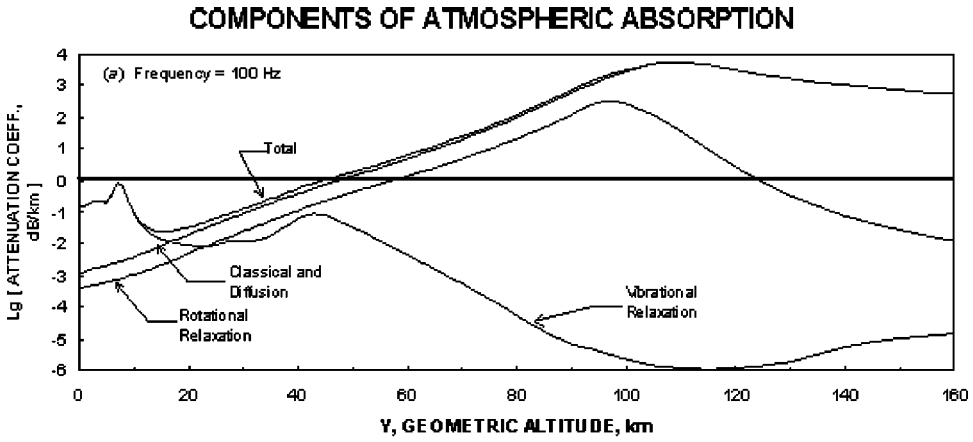

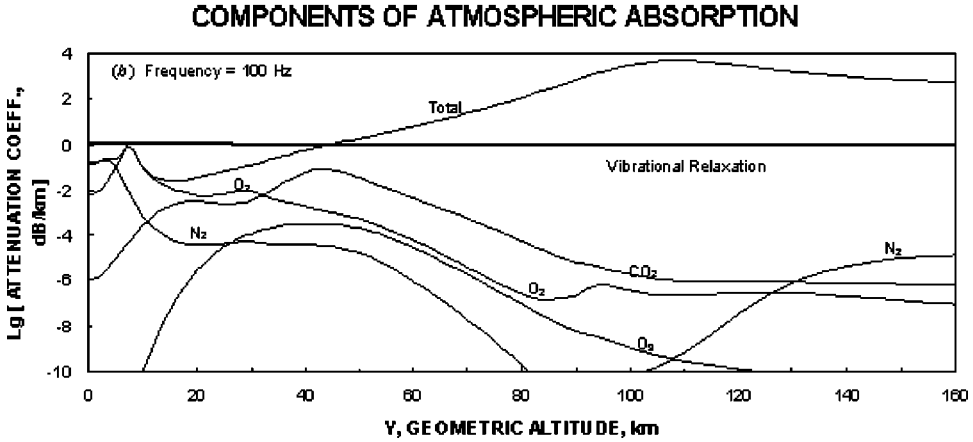

FIG. 15. Components of atmospheric absorption as a function of altitude at a frequency of 100 Hz. (a) Contributions from different mechanisms; (b) molecular vibrational relaxation contributions for each molecule.

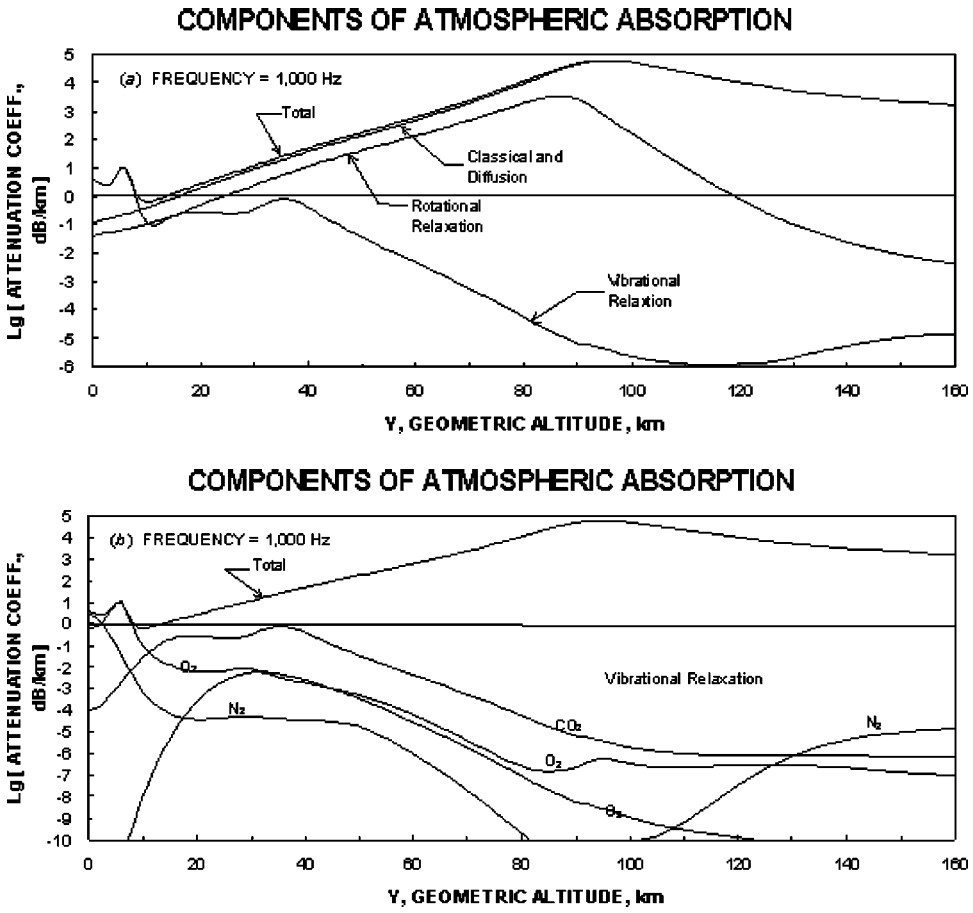

FIG. 16. Components of atmospheric absorption as a function of altitude at a frequency of 1000 Hz. (a) Contributions from different mechanisms; (b) molecular vibrational relaxation contributions for each molecule.

lar weight and mole fraction.[24] However, this refinement has not been employed here for the same reason that the predicted viscosity of air assumed a constant mole fraction profile of the atmosphere at all altitudes. The actual variation in mole fractions is considered to have only a second-order effect on viscosity and the specific heat ratio and thus, second order on atmospheric absorption. However, the first-order effects of temperature on the specific heat ratio are included just as they were for viscosity. Based on a review of published values for γ as a function of temperature,[24–28] shown in Fig. 11, the following empirical expression is defined for estimating the variation in the specific heat ratio, γ with temperature, T in kelvin. (The small increase in γ with increasing pressure[28] can be ignored for this paper since only atmospheric pressures equal to or less than one atmosphere are of concern)

$$\gamma = A_0 + A_1 T + A_2 T^2 + A_3 T^3 + A_4 T^4 + A_5 T^5, \tag{38}$$

where $A_0 = 1.371$, $A_1 = 2.460E-04$, $A_2 = -6.436E-07$, $A_3 = 5.200E-10$, $A_4 = -1.796E-13$, and $A_5 = 2.182E-17$.

This expression was developed by a least-squares regression fit to what is believed to be the most credible data[24,26,28] illustrated in Fig. 11. The NBS data from Hilsenrath *et al.*[26] were considered the most important part of these data providing an authoritative set covering the temperature range from 50 to over 1000 K.

3. Viscosity

As mentioned in Sec. II, a slightly modified version of the Sutherland equation[9] was employed to define viscosity, μ, as a function of temperature. This equation, Eq. (17), provides a slightly better fit to tabulated data for viscosity at high temperatures than the usual form used, for example, in the ICAO 1964 Standard atmosphere[29] where $T_0 = 300\,\mathrm{K}$, $S = 110.4\,\mathrm{K}$, and $\mu_0 = 18.46 \times 10^{-6}\,\mathrm{kg\,m^{-1}\,s^{-1}}$. Viscosity values predicted by Eq. (17) are compared in Fig. 12 with values reported from several sources.[18,25,27] It is satisfying to find such excellent agreement between the various published data for this fundamental atmospheric parameter in contrast to the variance in a few of the published values for the specific heat ratio shown in Fig. 11. Note, however, that Fig. 12 also identifies another prediction model[30] (theory-based) which does not appear to accurately predict the trend in viscosity at high temperatures. The small, readily developed, modification made for this paper to the Sutherland equation should probably be verified by comparison with more recent data sources although its general accuracy for application in this study is considered reasonable. As stated earlier, however, this must be qualified by recognizing the second-order effect not accounted for in the viscosity model which assumes that the constituent mixture is the same at all altitudes. While there are no values for viscosity presented in the 1962 U.S. Standard Atmosphere above an altitude of 90 km,[6] the temperature variation in viscosity up to 160 km is indicated by the data in Figs. 5 and 12.

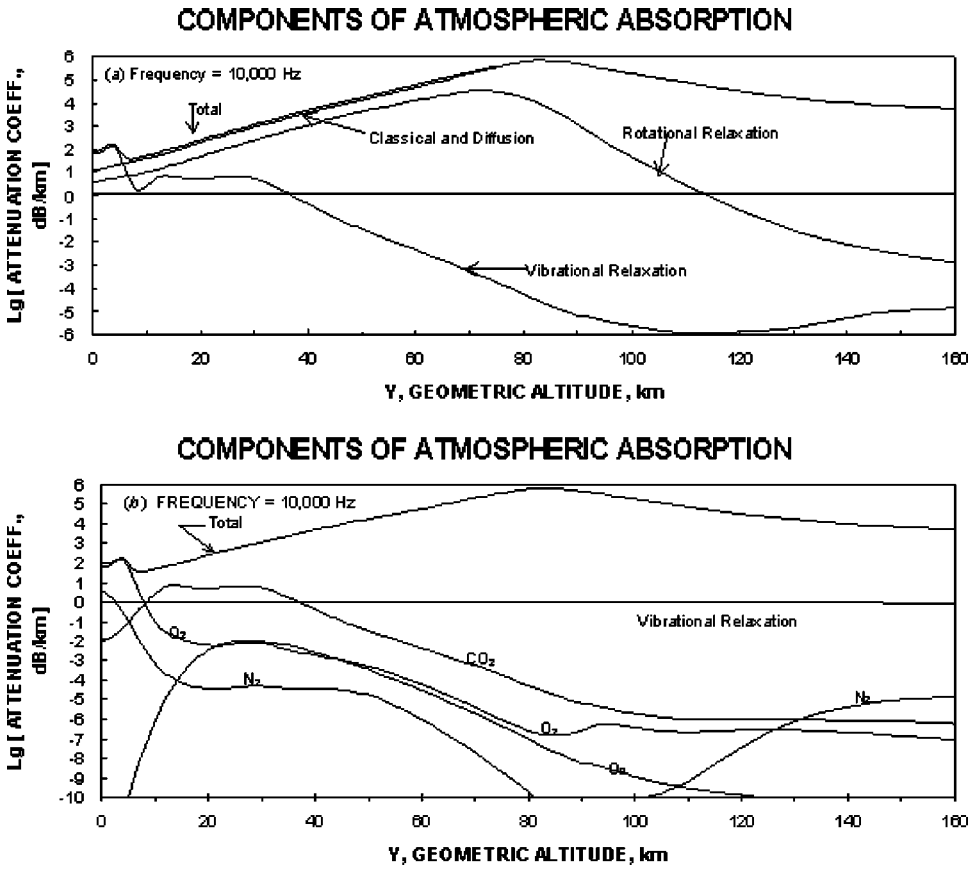

FIG. 17. Components of atmospheric absorption as a function of altitude at a frequency of 10 000 Hz. (a) Contributions from different mechanisms; (b) molecular vibrational relaxation contributions for each molecule.

VI. ATMOSPHERIC ABSORPTION TO 160 km

The atmospheric absorption algorithms in Secs. II–IV and the atmosphere models in Sec. V are now combined to compute values for the absorption coefficients as a function of altitude. (To convert the absorption coefficients computed with the equations in Secs. II, III, and IV from Np/m to dB/km, the values in Np/m are multiplied by 8685.9) The results are shown in Figs. 13–17 in terms of the attenuation coefficient in dB/km as a function of altitude from 0 to 160 km for frequencies of 1, 10, 100, 1000, and 10 000 Hz, respectively.

Part (a) of each figure shows the classical loss (including the added 0.3% for the diffusion loss), rotational relaxation loss, and total molecular vibration relaxation losses and the resultant total attenuation coefficient. Part (b) of each figure shows the molecular vibration relaxation components and the resulting total attenuation coefficient.

There are a number of features of these figures that should be noted. First consider Fig. 13, which shows absorption at 1 Hz. Under conditions typical for the lower atmosphere, atmospheric absorption can generally be neglected. It is nominally less that 0.01 dB/km so even for path lengths on the order of one-tenth the radius of the earth (or about 830 km), absorption would be less than 10 dB. Referring to the same figure, the absorption at 160 km altitude is more than 10 dB/km. The earth's thermosphere lies above about 80 km so for acoustic waves launched upward from lower altitudes, this is the last refractive layer to turn the waves back toward the earth. With an absorption of 10 dB/km, waves at a frequency of 1 Hz would not make it to the thermosphere and then back down to earth.

Some other observations based upon examination of Figs. 13–17 can be summarized as follows.

(a) Classical plus rotational losses predominate over molecular vibration losses at altitudes which decrease from about 60 km at 1 Hz to about 10 km at 10 000 Hz. This means that any errors introduced by the various assumptions employed for vibrational relaxation by O and N are not so important because by the time the concentration of these atoms become large, absorption is dominated by classical plus rotational loses.

(b) For evaluation of propagation of ''over-the-top'' sonic booms, or high altitude blasts, it is likely, that classical plus rotational absorption attenuation will be the most important. These over-the-top booms or blast waves will lose high frequency content though some high frequency energy might be restored by nonlinear effects not considered here.

(c) Estimated molecular absorption by CO_2, which has not been explicitly included in the existing ANSI and ISO standards, dominates molecular vibration losses at altitudes just above the point where classical plus rotational relaxation losses begin to control the total absorption loss. Over a very small range of altitudes it might be dominant.

(d) Although not important for the total attenuation at high altitudes, it is interesting to note how molecular vibration by nitrogen reappears as the dominant part of this form of loss at altitudes above about 130 km. This is due to the large increase in relaxation strength for nitrogen at the high temperatures involved at these altitudes (see Fig. 3).

TABLE IV. Attenuation coefficient (dB/km) for atmospheric absorption.

Y (km)	Frequency (Hz)												
	2	4	8	16	31.5	63	125	250	500	1000	2000	4000	8000
0	6.53E−5	2.61E−4	1.04E−3	4.18E−3	1.61E−2	6.38E−2	2.40E−1	8.22E−1	2.11E+0	3.87E+0	6.96E+0	1.74E+1	5.82E+1
2	8.43E−5	3.37E−4	1.35E−3	5.38E−3	2.07E−2	7.97E−2	2.76E−1	7.56E−1	1.45E+0	2.57E+0	6.13E+0	2.00E+1	7.34E+1
4	2.17E−4	8.67E−4	3.44E−3	1.33E−2	4.65E−2	1.33E−1	2.72E−1	5.12E−1	1.28E+0	4.25E+0	1.55E+1	5.25E+1	1.36E+2
6	7.21E−4	2.77E−3	9.66E−3	2.68E−2	6.11E−2	1.62E−1	5.29E−1	1.85E+0	5.46E+0	1.10E+1	1.54E+1	2.03E+1	3.55E+1
8	2.27E−3	7.18E−3	2.21E−2	7.35E−2	2.22E−1	4.94E−1	7.19E−1	8.30E−1	9.32E−1	1.24E+0	2.43E+0	7.20E+0	2.63E+1
10	5.31E−3	1.72E−2	4.39E−2	7.33E−2	8.82E−2	9.46E−2	1.02E−1	1.27E−1	2.27E−1	6.24E−1	2.21E+0	8.56E+0	3.39E+1
12	7.59E−3	1.71E−2	2.51E−2	2.86E−2	3.01E−2	3.26E−2	4.13E−2	7.61E−2	2.15E−1	7.71E−1	2.99E+0	1.18E+1	4.68E+1
14	7.62E−3	1.24E−2	1.48E−2	1.57E−2	1.67E−2	1.99E−2	3.23E−2	8.22E−2	2.82E−1	1.08E+0	4.25E+0	1.67E+1	6.39E+1
16	6.61E−3	8.78E−3	9.63E−3	1.01E−2	1.13E−2	1.58E−2	3.33E−2	1.04E−1	3.85E−1	1.50E+0	5.91E+0	2.28E+1	8.60E+1
18	5.72E−3	6.80E−3	7.22E−3	7.71E−3	9.25E−3	1.54E−2	3.94E−2	1.36E−1	5.22E−1	2.06E+0	8.07E+0	3.10E+1	1.18E+2
20	5.21E−3	5.88E−3	6.19E−3	6.77E−3	8.81E−3	1.70E−2	4.92E−2	1.79E−1	6.95E−1	2.75E+0	1.09E+1	4.20E+1	1.62E+2
22	5.14E−3	5.69E−3	6.01E−3	6.76E−3	9.47E−3	2.04E−2	6.33E−2	2.35E−1	9.24E−1	3.67E+0	1.46E+1	5.71E+1	2.22E+2
24	5.62E−3	6.27E−3	6.67E−3	7.66E−3	1.13E−2	2.59E−2	8.31E−2	3.13E−1	1.23E+0	4.91E+0	1.95E+1	7.73E+1	3.04E+2
26	6.62E−3	7.56E−3	8.12E−3	9.46E−3	1.43E−2	3.40E−2	1.11E−1	4.20E−1	1.66E+0	6.60E+0	2.63E+1	1.04E+2	4.13E+2
28	7.56E−3	8.73E−3	9.48E−3	1.13E−2	1.79E−2	4.44E−2	1.48E−1	5.66E−1	2.24E+0	8.92E+0	3.55E+1	1.41E+2	5.59E+2
30	7.66E−3	8.62E−3	9.43E−3	1.18E−2	2.07E−2	5.67E−2	1.98E−1	7.64E−1	3.03E+0	1.21E+1	4.81E+1	1.91E+2	7.56E+2
32	5.77E−3	6.19E−3	7.04E−3	1.02E−2	2.23E−2	7.13E−2	2.63E−1	1.03E+0	4.11E+0	1.64E+1	6.48E+1	2.56E+2	1.02E+3
34	4.26E−3	4.60E−3	5.68E−3	9.98E−3	2.64E−2	9.30E−2	3.54E−1	1.40E+0	5.56E+0	2.20E+1	8.65E+1	3.42E+2	1.36E+3
36	3.24E−3	3.62E−3	5.09E−3	1.09E−2	3.33E−2	1.24E−1	4.78E−1	1.89E+0	7.47E+0	2.92E+1	1.15E+2	4.56E+2	1.82E+3
38	2.56E−3	3.07E−3	5.06E−3	1.30E−2	4.36E−2	1.67E−1	6.46E−1	2.54E+0	9.85E+0	3.84E+1	1.52E+2	6.05E+2	2.42E+3
40	2.12E−3	2.80E−3	5.53E−3	1.64E−2	5.81E−2	2.25E−1	8.66E−1	3.33E+0	1.28E+1	5.02E+1	2.00E+2	7.98E+2	3.19E+3
42	1.83E−3	2.76E−3	6.49E−3	2.14E−2	7.80E−2	3.02E−1	1.13E+0	4.27E+0	1.66E+1	6.56E+1	2.62E+2	1.05E+3	4.18E+3
44	1.64E−3	2.92E−3	8.03E−3	2.83E−2	1.04E−1	3.92E−1	1.43E+0	5.45E+0	2.14E+1	8.52E+1	3.40E+2	1.36E+3	5.44E+3
46	1.54E−3	3.30E−3	1.03E−2	3.75E−2	1.35E−1	4.91E−1	1.79E+0	6.96E+0	2.76E+1	1.10E+2	4.40E+2	1.76E+3	7.04E+3
48	1.54E−3	3.92E−3	1.33E−2	4.87E−2	1.69E−1	6.06E−1	2.26E+0	8.89E+0	3.54E+1	1.41E+2	5.66E+2	2.26E+3	9.04E+3
50	1.64E−3	4.86E−3	1.72E−2	6.08E−2	2.05E−1	7.51E−1	2.86E+0	1.14E+1	4.53E+1	1.81E+2	7.24E+2	2.90E+3	1.16E+4
52	1.84E−3	6.07E−3	2.15E−2	7.32E−2	2.49E−1	9.38E−1	3.63E+0	1.44E+1	5.77E+1	2.31E+2	9.23E+2	3.69E+3	1.47E+0
54	2.20E−3	7.62E−3	2.60E−2	8.72E−2	3.07E−1	1.18E+0	4.62E+0	1.84E+1	7.37E+1	2.95E+2	1.18E+3	4.71E+3	1.88E+4
56	2.72E−3	9.38E−3	3.08E−2	1.06E−1	3.84E−1	1.51E+0	5.91E+0	2.36E+1	9.44E+1	3.78E+2	1.51E+3	6.04E+3	2.41E+4
58	3.39E−3	1.12E−2	3.65E−2	1.31E−1	4.88E−1	1.93E+0	7.59E+0	3.04E+1	1.21E+2	4.85E+2	1.94E+3	7.76E+3	3.09E+4
60	4.12E−3	1.31E−2	4.41E−2	1.65E−1	6.27E−1	2.49E+0	9.80E+0	3.92E+1	1.57E+2	6.27E+2	2.51E+3	1.00E+4	3.97E+4
62	4.87E−3	1.55E−2	5.49E−2	2.11E−1	8.11E−1	3.23E+0	1.27E+1	5.09E+1	2.04E+2	8.14E+2	3.25E+3	1.30E+4	5.13E+4
64	5.65E−3	1.88E−2	7.00E−2	2.74E−1	1.06E+0	4.22E+0	1.66E+1	6.65E+1	2.66E+2	1.06E+3	4.25E+3	1.69E+4	6.64E+4
66	6.68E−3	2.36E−2	9.08E−2	3.59E−1	1.39E+0	5.55E+0	2.18E+1	8.74E+1	3.49E+2	1.40E+3	5.58E+3	2.21E+4	8.61E+4
68	8.18E−3	3.04E−2	1.19E−1	4.75E−1	1.84E+0	7.35E+0	2.89E+1	1.16E+2	4.63E+2	1.85E+3	7.38E+3	2.91E+4	1.12E+5
70	1.04E−2	4.01E−2	1.59E−1	6.33E−1	2.45E+0	9.81E+0	3.86E+1	1.54E+2	6.17E+2	2.47E+3	9.82E+3	3.85E+4	1.45E+5
72	1.36E−2	5.35E−2	2.13E−1	8.51E−1	3.30E+0	1.32E+1	5.19E+1	2.08E+2	8.30E+2	3.31E+3	1.31E+4	5.10E+4	1.86E+5
74	1.83E−2	7.24E−2	2.89E−1	1.15E+0	4.47E+0	1.79E+1	7.05E+1	2.82E+2	1.13E+3	4.49E+3	1.77E+4	6.74E+4	2.38E+5
76	2.48E−2	9.89E−2	3.95E−1	1.58E+0	6.12E+0	2.45E+1	9.64E+1	3.85E+2	1.54E+3	6.12E+3	2.39E+4	8.87E+4	3.00E+5
78	3.41E−2	1.36E−1	5.45E−1	2.18E+0	8.44E+0	3.38E+1	1.33E+2	5.31E+2	2.12E+3	8.38E+3	3.22E+4	1.16E+5	3.72E+5
80	4.74E−2	1.89E−1	7.58E−1	3.03E+0	1.17E+1	4.70E+1	1.85E+2	7.39E+2	2.94E+3	1.15E+4	4.33E+4	1.49E+5	4.47E+5
82	6.64E−2	2.66E−1	1.06E+0	4.25E+0	1.65E+1	6.59E+1	2.59E+2	1.03E+3	4.10E+3	1.59E+4	5.76E+4	1.87E+5	5.10E+5
84	9.49E−2	3.79E−1	1.52E+0	6.07E+0	2.35E+1	9.41E+1	3.70E+2	1.47E+3	5.79E+3	2.18E+4	7.55E+4	2.28E+5	5.42E+5
86	1.37E−1	5.47E−1	2.19E+0	8.75E+0	3.39E+1	1.36E+2	5.33E+2	2.11E+3	8.16E+3	2.96E+4	9.59E+4	2.58E+5	5.31E+5
88	1.97E−1	7.90E−1	3.16E+0	1.26E+1	4.89E+1	1.96E+2	7.66E+2	3.01E+3	1.13E+4	3.88E+4	1.16E+5	2.71E+5	4.91E+5
90	2.85E−1	1.14E+0	4.55E+0	1.82E+1	7.05E+1	2.81E+2	1.10E+3	4.22E+3	1.52E+4	4.88E+4	1.30E+5	2.63E+5	4.36E+5
92	4.14E−1	1.66E+0	6.62E+0	2.65E+1	1.02E+2	4.07E+2	1.56E+3	5.75E+3	1.94E+4	5.69E+4	1.29E+5	2.30E+5	3.59E+5
94	5.93E−1	2.37E+0	9.48E+0	3.79E+1	1.46E+2	5.74E+2	2.13E+3	7.43E+3	2.35E+4	6.09E+4	1.20E+5	1.96E+5	2.94E+5
96	8.40E−1	3.36E+0	1.34E+1	5.35E+1	2.05E+2	7.87E+2	2.79E+3	9.29E+3	2.71E+4	6.05E+4	1.06E+5	1.65E+5	2.43E+5
98	1.18E+0	4.71E+0	1.88E+1	7.48E+1	2.83E+2	1.05E+3	3.58E+3	1.13E+4	2.92E+4	5.71E+4	9.29E+4	1.40E+5	2.03E+5
100	1.64E+0	6.55E+0	2.61E+1	1.03E+2	3.81E+2	1.36E+3	4.47E+3	1.31E+4	2.93E+4	5.16E+4	8.01E+4	1.18E+5	1.70E+5
105	3.57E+0	1.42E+1	5.57E+1	2.08E+2	7.07E+2	2.33E+3	6.50E+3	1.39E+4	2.38E+4	3.64E+4	5.34E+4	7.68E+4	1.09E+5
110	7.29E+0	2.82E+1	1.03E+2	3.55E+2	1.13E+3	3.13E+3	6.46E+3	1.09E+4	1.65E+4	2.42E+4	3.47E+4	4.95E+4	7.02E+4
115	1.33E+1	4.75E+1	1.62E+2	5.33E+2	1.44E+3	2.97E+3	4.96E+3	7.55E+3	1.10E+4	1.58E+4	2.26E+4	3.20E+4	4.53E+4
120	2.03E+1	6.89E+1	2.30E+2	6.51E+2	1.36E+3	2.31E+3	3.52E+3	5.15E+3	7.40E+3	1.06E+4	1.50E+4	2.12E+4	3.00E+4
125	2.74E+1	9.33E+1	2.79E+2	6.30E+2	1.10E+3	1.70E+3	2.50E+3	3.60E+3	5.14E+3	7.31E+3	1.04E+4	1.47E+4	2.07E+4
130	3.54E+1	1.14E+2	2.85E+2	5.38E+2	8.53E+2	1.27E+3	1.84E+3	2.63E+3	3.74E+3	5.31E+3	7.51E+3	1.06E+4	1.50E+4
135	4.32E+1	1.23E+2	2.62E+2	4.44E+2	6.73E+2	9.85E+2	1.41E+3	2.01E+3	2.85E+3	4.04E+3	5.72E+3	8.10E+3	1.15E+4
140	4.90E+1	1.22E+2	2.31E+2	3.69E+2	5.45E+2	7.90E+2	1.13E+3	1.60E+3	2.27E+3	3.21E+3	4.55E+3	6.44E+3	9.10E+3
145	5.23E+1	1.16E+2	2.02E+2	3.12E+2	4.54E+2	6.54E+2	9.30E+2	1.32E+3	1.87E+3	2.65E+3	3.75E+3	5.30E+3	7.50E+3
150	5.34E+1	1.08E+2	1.78E+2	2.69E+2	3.88E+2	5.56E+2	7.89E+2	1.12E+3	1.59E+3	2.24E+3	3.18E+3	4.49E+3	6.35E+3
155	5.30E+1	9.91E+1	1.58E+2	2.35E+2	3.38E+2	4.83E+2	6.84E+2	9.70E+2	1.37E+3	1.94E+3	2.75E+3	3.89E+3	5.50E+3
160	5.16E+1	9.11E+1	1.41E+2	2.08E+2	2.98E+2	4.25E+2	6.02E+2	8.53E+2	1.21E+3	1.71E+3	2.42E+3	3.42E+3	4.84E+3

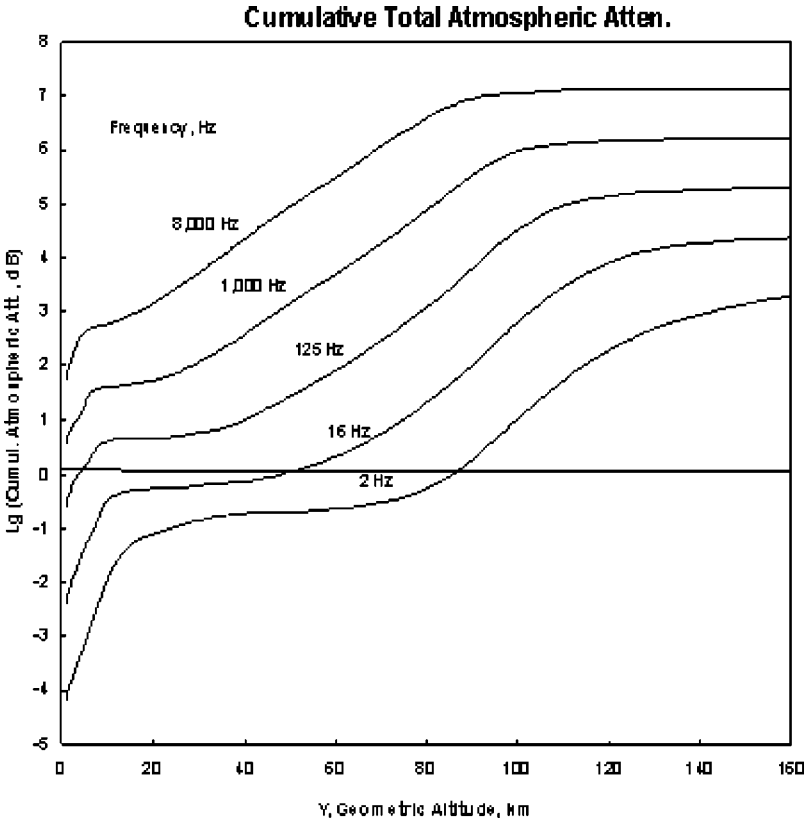

FIG. 18. Cumulative total attenuation by atmospheric absorption for a wave propagating vertically up or down as a function of altitude.

A more complete presentation of the attenuation coefficients is provided by Table IV which provides a tabulation of their values as a function of altitude from 0 to 160 km and for pure tone signals with the exact frequencies specified from 2 to 8000 Hz in octave frequency intervals.

Another assessment of the overall trend in total attenuation from any source at high altitudes down to the ground is provided by carrying out a numerical integration of the cumulative total attenuation using the same algorithms which generated the attenuation coefficients given in Table IV. The results are shown in Fig. 18 for frequencies of 2, 16, 125, 1000, and 8000 Hz. This shows the interesting trend of two semi-plateaus in cumulative attenuation that correspond to: (a) the frequency/altitude range where molecular vibration loss is falling off but classical plus rotational relaxation loss has not yet overtaken the former and (b) the latter loss has reached its relaxation peak and is beginning to fall off.

VII. CONCLUSIONS

Algorithms are provided for estimating atmospheric absorption at altitudes up to 160 km covering atmospheric conditions well beyond the range of applicability of the existing ANSI and ISO Standards for computing atmospheric absorption of sound. The algorithms are based on well-founded, but simplified, theoretical models for classical plus rotational relaxation loss with a small empirical adjustment to the latter to improve agreement with measured data. An important aspect of the model for these dominant sources of atmospheric absorption at high altitude is to show that they undergo relaxation due to the very high values of frequency/pressure encountered at high altitudes.

The algorithms for classical and rotational loss do not attempt, at this time, to account for what are considered second-order effects due to changes in viscosity and specific heat ratio with deviations in the composition of the atmosphere at altitudes above about 90 km. However, methods are available to account for such changes and it is recommended that these improved models be considered if it appears necessary from application of the methods provided in this paper. Such an effort should also be based on better information, if available, on the composition of the atmosphere at these high altitudes.

Existing algorithms for molecular vibration relaxation loss included in the ANSI/ISO Standards are modified and substantially augmented in an effort to estimate the latter form of atmospheric absorption for conditions encountered at high altitudes. The major significance of molecular relaxation in the atmosphere by CO_2 is explicitly developed for the first time although at its peak, this part of the total atmospheric absorption is still substantially overcome by classical plus rotational relaxation loss.

ACKNOWLEDGMENTS

The authors wish to express their appreciation to Robert G. Rackl of The Boeing Company for his guidance and support during preparation of an earlier report by the authors upon which this paper is largely based, to Leick D. Robinson of Science Applications Incorporated for his assistance in reviewing portions of the prior report, and to the authors of Ref. 1, Christine Besset and Elisabeth Blanc, for helping to stimulate the authors' pursuit of the topic of this paper.

[1] C. Besset and E. Blanc, ''Propagation of vertical shock waves in the atmosphere,'' J. Acoust. Soc. Am. **95**, 1830–1839 (1994).
[2] H. Poling, L. Robinson, and L. C. Sutherland, ''Secondary boom of supersonic transports,'' AIAA Pap. 97-1659 (1997).
[3] American National Standard, ''Method for calculation of the absorption of sound by the atmosphere,'' ANSI S1-26-1995 (ASA 13-1995), July, 1995. (See, also, International Organization for Standards, ''Acoustics-Attenuation of sound during propagation outdoors, Part I: Method of atmospheric absorption.'' ISO 9613-1, 1993.)
[4] H. E. Bass, ''Absorption of sound by air: High temperature predictions,'' J. Acoust. Soc. Am. **69**, 124–138 (1981).
[5] J. O. Hirschfelder, C. F. Curtiss, and R. B. Bird, *Molecular Theory of Gases and Liquids* (Wiley, New York, 1954).
[6] *U.S. Standard Atmosphere, 1962* (US GPO, Washington, DC, 1962).
[7] H. E. Bass, L. C. Sutherland, J. Piercy, and L. Evans, ''Absorption of sound by the atmosphere,'' *Physical Acoustics*, edited by W. P. Mason and R. N. Thurston (Academic, New York, 1984), Vol. XVII, Chap. 3.
[8] M. Greenspan, ''Combined translational and relaxational dispersion of sound in gases,'' J. Acoust. Soc. Am. **26**, 70–73 (1954).
[9] M. Greenspan, ''Rotational relaxation in nitrogen, oxygen and air,'' J. Acoust. Soc. Am. **31**, 155–160 (1959).
[10] H. E. Bass and L. C. Sutherland, ''On the rotational collision number for air at elevated temperatures,'' J. Acoust. Soc. Am. **59**, 1317–1318 (1976).
[11] R. C. Roberts, ''Molecular diffusion of Gases,'' *American Institute of Physics Handbook*, edited by D. E. Gray (McGraw–Hill, New York, 1972), Chap. 2s.
[12] A. Law, N. Koronaios, and R. B. Lindsay, ''Effect of diffusion on ultrasonic attenuation in mixtures of the rare gases,'' J. Acoust. Soc. Am. **41**, 93–99 (1967).
[13] D. Rind, ''Heating of the lower thermosphere by the dissipation of acoustic waves,'' J. Atmos. Terr. Phys. **39**, 445–456 (1977).
[14] L. C. Sutherland, ''Review of experimental data in support of a proposed new method for computing atmospheric absorption loss,'' U.S. Dept. of Transportation Report No. TST-75-87, 1975.
[15] O. E. Smith and D. K. Weidner, ''A Reference atmosphere for Patrick AFB, Florida, Annual (1963 Revision),'' NASA Tech. Memo. **X-53139**, (1964).
[16] Air Force Geophysics Directorate, *Handbook of Geophysics* (Macmillan, New York, 1960).
[17] *Handbook of Astronautical Engineering*, edited by H. H. Koelle (McGraw–Hill, New York, 1961).
[18] F. S. Johnson, (ed), *Satellite Environment Handbook*, 2nd ed. (Stanford University Press, Stanford, 1965).
[19] R. T. Watson *et al.*, ''Present state of knowledge of the upper atmosphere 1990: An assessment report,'' Report to Congress, NASA Ref. Publication 1242 (1990).
[20] C. Keeling, Director, Carbon Dioxide Research Group, Scripps Institute of Oceanography, La Jolla, CA. (private personal communication, 1996).
[21] *Policy Options for Stabilizing Global Climate*, edited by D. A. Lashof and D. A. Tirpak (U.S. Environmental Protection Agency, Washington, DC, 1989).
[22] A. B. Lovins *et al.*, ''Least-cost energy: Solving the CO_2 problem,'' Rocky Mountain Institute, Snowmass, CO, 1989.
[23] ''A second compilation of US IGY Rocket Program results,'' IGY Rocket Report No. 6, edited by J. P. T. Pearman and I. Guttmacher, National Academy of Sciences, 1960.
[24] G. S. K. Wong and T. F. W. Embleton, ''Variation of specific heats and of specific heat ratio in air with humidity,'' J. Acoust. Soc. Am. **76**, 555–559 (1984).
[25] J. H. Keenan and J. Kaye, *Gas Tables, Thermodynamic Properties of Air* (Wiley, New York, 1945).
[26] J. Hilsenrath *et al.*, ''Tables of thermal properties of gases,'' National Bureau of Standards Circular 564, U.S. Dept. of Commerce, Washington, DC (1955). [See also J. Hilsenrath *et al.*, *Tables of Thermodynamic and Transport Properties of Air, etc.* (Pergamon, Oxford, 1960)].
[27] *Handbook of Chemistry and Physics*, 67th Ed. (Chemical Rubber Co., Cleveland, OH, 1986).
[28] O. Cramer, ''The variation of the specific heat ratio and the speed of sound in air with temperature, pressure, humidity and CO_2 concentration,'' J. Acoust. Soc. Am. **93**, 2510–2516 (1993).
[29] International Civil Aviation Organization, ''Manual of the ICAO Standard Atmosphere, extended to 32 kilometres,'' 2nd ed., Doc. 7488/2, 1964.
[30] J. Kestin and R. DiPippo, ''Viscosity of Gases,'' *American Institute of Physics Handbook*, 3rd ed., edited by D. E. Gray (McGraw–Hill, New York, 1972), Chap. 2r.

Boundary element modeling of the external human auditory system

Timothy Walsh
Sandia National Laboratories, P.O. Box 5800, MS 0835, Albuquerque, New Mexico 87185

Leszek Demkowicz[a)]
Texas Institute for Computational and Applied Mathematics, The University of Texas at Austin, ACES 6.332, Austin, Texas 78712

Richard Charles
Sulzer Carbomedics, 1300 E. Anderson Lane, Austin, Texas 78752

(Received 20 February 2002; revised 22 November 2003; accepted 1 December 2003)

In this paper the response of the external auditory system to acoustical waves of varying frequencies and angles of incidence is computed using a boundary element method. The resonance patterns of both the ear canal and the concha are computed and compared with experimental data. Specialized numerical algorithms are developed that allow for the efficient computation of the eardrum pressures. In contrast to previous results in the literature that consider only the ''blocked meatus'' configuration, in this work the simulations are conducted on a boundary element mesh that includes both the external head/ear geometry, as well as the ear canal and eardrum. The simulation technology developed in this work is intended to demonstrate the utility of numerical analysis in studying physical phenomena related to the external auditory system. Later work could extend this towards simulating *in situ* hearing aids, and possibly using the simulations as a tool for optimizing hearing aid technologies for particular individuals. © *2004 Acoustical Society of America.* [DOI: 10.1121/1.1643360]

PACS numbers: 43.20.Fn, 43.64.Ha [LLT] Pages: 1033–1043

I. INTRODUCTION

The external human auditory system consists of the head, the pinna, the ear canal, and the eardrum, which collect the sound waves from the exterior domain, filter the spectral properties, and provide an input signal to the middle and inner ears through oscillations of the eardrum.

In this work numerical simulations, augmented with the capabilities of parallel computing, are used as tools to study the overall functionality of the outer ear. By comparing the results to experimental data from the literature, it is demonstrated that the simulations are capable of capturing the essential physics of the external auditory system. This suggests that such simulations could be used to assist in the development of relevant technologies, such as hearing aids, hearing protection devices, and virtual acoustic simulators.

In the context of the external auditory system, an important parameter is the head-related transfer function (HRTF), which measures the pressure at the eardrum as a function of the frequency and angle of incidence of the incident acoustical wave. It gives a measure of the filtering characteristics of the outer ear, as well as the directional dependence, which is critical for localization ability.

The directionality information provided by an HRTF is useful in localization research [Katz (1998)], and in virtual acoustic simulators [Moller (1996), Takeuchi (1998), Kahana (1999)]. The HRTF also provides information on the frequency dependence of the sound amplification, as well as the resonance frequencies of the ear canal, and this can be useful for hearing aid designs [Sandlin (1995)]. The ability to compute this quantity could alleviate the need for experimental generation, and provide a tool to be used by all of the technologies above for phenomenological studies.

Although the need for careful, accurate laboratory measurements will never be replaced, numerical simulations provide a useful alternative in cases when the experimental procedures are time-consuming or expensive, or when parametric studies are necessary which would require many repeated measurements. The measurement of an HRTF is an illustrative example. The eardrum pressures must be measured in an anechoic chamber at varying frequencies and angles of incidence, for each individual of interest. The determination of ear-canal resonances is another example. In this paper, numerical computations of both quantities are presented.

There have been some results reported in the literature regarding numerical simulations of the external auditory system. The literature is very limited, and this is part of the motivation for the current paper.

Ciskowski (1991) studied both the plug and the earmuff-type hearing protection devices (HPD) in an attempt to characterize the best possible design for attenuating strong pulses in the ear canal. He modeled the plugged ear canal as a structure/acoustic cavity that coupled an elastodynamic finite-element model for the plug to a pressure boundary element model for the cavity. The resonances of the acoustic cavity were reproduced and compared with experimental measurements.

[a)]Author to whom correspondence should be addressed.

Katz (1998) computed the HRTF of real subjects using a boundary element method applied to the Helmholtz integral equation. In this study the finite impedance of the skin and hair was experimentally measured and incorporated into the numerical models. The frequency range of the simulations was 1–5 kHz. Only linear triangulations were used, and a decimation scheme was employed to provide appropriate mesh densities for the desired range of frequencies.

Kahana (1999) used a boundary element method to compute the HRTF up to a maximum frequency of 15 kHz. The principle of reciprocity was used to deal with sources at variable locations, simply by locating the source at the blocked meatus position, and computing the response at the original locations of the sources. A drawback to this approach was that the source could not be located directly on the surface, and had to be lifted off of the surface a small amount. This introduced an additional error in the approximation. An alternative approach would be to construct an adaptive mesh that is well-resolved for all incident waves, and then solve the linear system with multiple right-hand sides. This is certainly a more general approach, and would be useful for problems in which the principle of reciprocity is not applicable. Such an approach is taken in this paper.

The two previous references [Katz (1998), Kahana (1999)] use the ''blocked meatus'' configuration in the simulations, meaning that the ear canal is not included in the mesh. Conversely, the first reference [Ciskowski (1991)] involves modeling the ear canal, but the external head/ear geometry is not included. This eliminates the directional dependence imparted by the head and external ear. Also, in this reference the canal is modeled using simplified geometries, instead of actual canal data.

In the current study a mesh of an actual ear canal is extracted from the literature [Stinton (1989)], and connected to a separate mesh of the head and pinna. This allows for simulations on the entire external auditory system, and with more realistic geometries. For completeness, simulations are also conducted on the original blocked meatus configuration, so that they can be compared to those with ear canal.

Although in this paper the internal parts of the hearing system are not included in the model, it is recognized that a long-term goal of this research is to model the entire auditory system, including the middle and inner ears. A full auditory simulation would involve coupling the external boundary element model with finite-element models for both the middle and inner ear. Some attempts have been made to model separately the inner parts of the auditory system. Ladak (1996) used the finite-element method to study the middle ear of the cat. Wada (1992) did a similar study, but on the human middle ear. Several new investigations have been undertaken to simulate the main structure of the inner ear, the cochlea: Parthasarathi (2000), Kolston (1996), Duncan (1997). The latter reference models to the level of the hair bundles on the cochlea, using a micromechanical model. Models of this type are the first step towards understanding hearing system damage on a particular individual, since in many cases the cause of hearing impairment can be traced to the cochlea.

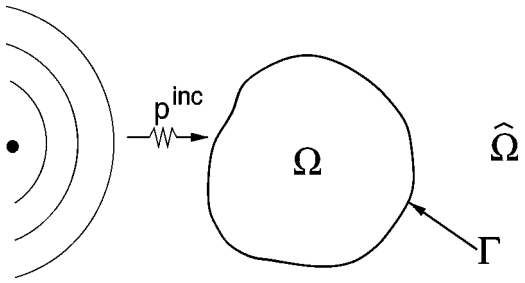

FIG. 1. The model scattering problem in $\mathbb{R}^3$.

II. THE BOUNDARY ELEMENT TECHNOLOGIES

In this section we give brief remarks regarding the various simulation technologies used in this work. These remarks are not intended to be complete descriptions, but instead only introductions that give the reader the main ideas of the approaches taken. Complete details on the numerical formulation and implementation can be found in Walsh (2003).

A. BEM for scattering problems in acoustics

The boundary element method (BEM) is a very attractive technique for modeling acoustic scattering/radiation problems, and in particular the external auditory system. By reducing the exterior boundary value problem to a boundary integral equation, it eliminates the need for a volume grid, and the problems associated with discretizing the unbounded domain. The Galerkin approach is taken in this work, since it has the following advantages over collocation.

(i) The collocation approach can simply be viewed as an underintegrated Galerkin method, and so pursing the Galerkin method is the most general approach one can take.
(ii) Unlike collocation, the Galerkin method comes with a complete mathematical convergence theory.
(iii) The Galerkin method allows for an ''integration by parts'' of the hypersingular part of the Burton–Miller formulation, thus eliminating the need for Hadamard finite part integration.

B. Burton–Miller formulation for BEM

For exterior acoustic scattering problems, the two widely used classical formulations are the Helmholtz and hypersingular integral formulations. However, neither one is fully equivalent to the original Helmholtz differential equation with Sommerfeld radiation condition, over the entire range of frequencies. Both exhibit the so-called fictitious frequencies, where the integral formulations contain spurious modes. Burton (1971) presents a new formulation that consists of a complex combination of the Helmholtz and hypersingular integral equations, and proved that this is equivalent to the original problem. For this reason it is chosen as the formulation for the work in this paper.

The problem of interest is shown schematically in Fig. 1. Given an incident wave p^{inc} with wave number k, and a bounded domain Ω with a boundary Γ (in our case Ω would

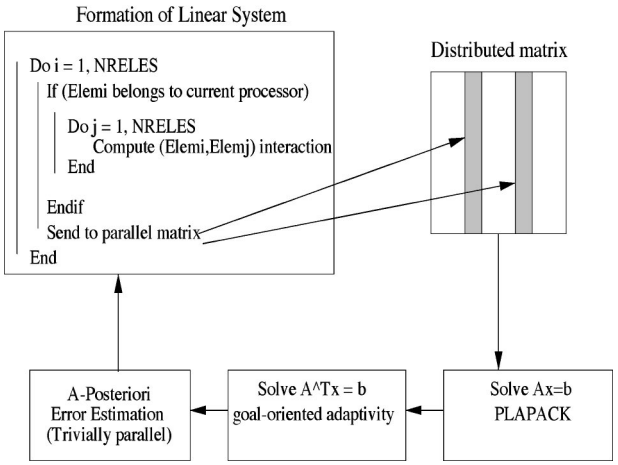

FIG. 2. The parallelization of the boundary element method.

be the human head, with or without the ear canal) the goal is to find a scattered pressure p^s satisfying the Helmholtz differential equation

$$\Delta p^s + k^2 p^s = 0 \quad \text{in} \quad \hat{\Omega} = \mathbb{R}^3 - \Omega, \tag{1}$$

Sommerfeld radiation condition

$$\left| \frac{\partial p^s}{\partial R} - ikp^s \right| = O\left(\frac{1}{R^2} \right) \quad \text{for} \quad R \to \infty, \tag{2}$$

and rigid boundary condition on Γ

$$\frac{\partial (p^s + p^{\text{inc}})}{\partial n} = 0 \quad \text{on} \quad \Gamma. \tag{3}$$

The rigid condition can be replaced by a finite impedance condition, which would produce more accurate results, especially in the vicinity of the eardrum. However, the results presented in this paper only model rigid scattering. The exterior boundary-value problem is next replaced with the Burton–Miller integral formulation, a weak formulation is constructed, and a boundary element discretization is applied. More details are given in Walsh (2003).

C. *hp* boundary element discretizations

The present work is a continuation of earlier work on *hp*-adaptive boundary elements for the solution of exterior and structure–fluid interaction problems in underwater acoustics; see Demkowicz (1991, 1992), Chang (1999), and Geng (1996). The present boundary element code is implemented within a new FORTRAN 90 implementation of a two-dimensional *hp*-adaptive package described in Demkowicz (1998), allowing for full *hp* adaptivity.

D. Parallel computations

The parallelization of the *hp* boundary element method involves three separate tasks: formation of the linear system, dense solve, and error estimation. Figure 2 shows a schematic of the adaptive process in the parallel environment. Both the formation and the factorization of the (dense) linear system utilize the PLAPACK software of van de Geijn (1997). The computation of the elementwise residuals for the purpose of error estimation is trivially parallelizable and thus is simply distributed across the processors. All computations are performed on the CRAY T3E distributed memory parallel architecture using between 4 and 64 processors, depending on the frequency.

E. Goal-oriented error estimation and mesh adaptivity

It is always desirable to have an estimate of the discretization error involved in numerical computations. Without such an estimate, it would be difficult to separate errors due to other sources, such as geometrical representation. Following the results derived in Walsh (2003), a local, or goal-oriented error estimation and mesh adaptivity scheme is used in this work, rather than a classical scheme based on a global energy norm. Details on the formulation and implementation can be found in this reference, as well as an exposition on various error estimation and adaptivity techniques. These techniques allow the pressure on the eardrum to be computed with high accuracy.

III. NUMERICAL COMPUTATION RESULTS

This section presents the results of the acoustical simulations. Using the boundary element technology described in the previous section, the simulation results are generated and compared to experimental data from the literature. All of the numerical results in this section involve rigid scatterers, with infinite impedance. This is, of course, an additional simulation error, but its consequences are somewhat obvious in the results and are pointed out when appropriate. Due to its simple geometry and well-known exact solution, results are first presented on a sphere.

A. Sphere

The simplest model one can consider for the head is a sphere with a small microphone on either side. Since the exact solution is known for this case, the transfer function can be computed exactly. This model, though very simplified compared with the head, can be used to gain intuition for the types of responses that can be expected in more complicated simulations.

For the case of normal incidence, Fig. 3 shows the exact transfer function (obtained from the exact solution for scattering of a plane wave on a rigid sphere). The abscissa is ka, the wave number k multiplied by the sphere radius a, and the ordinate is $\text{dB} = 20 \log(p/p_0)$, where p_0 is the magnitude of the pressure of the incident wave, and p is the pressure at the detection point. The asymptotic limits on the transfer function in Fig. 3 have very simple physical explanations, which are useful when interpreting the results for the head. We consider the case where the sphere has a fixed radius, and the wavelength of the incident field is allowed to vary. When the wavelength becomes large relative to the radius of the sphere, the interference that the sphere has on the incident field becomes less and less significant. In the limit, the amplitude of the scattered pressure is negligible compared to the that of the incident field. At the point of normal incidence

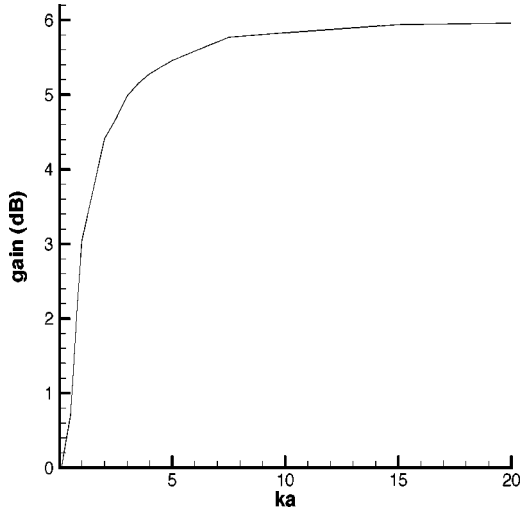

FIG. 3. Exact solution for scattering on a rigid sphere at the point of normal incidence.

$$\text{gain(dB)} = 20\log\left(\frac{p}{p_0}\right) = 20\log(1) = 0, \tag{4}$$

where $p = p^s + p_0$ is the total pressure field, and p^s and p_0 are the scattered and incident pressure fields, respectively. Thus, when $ka \to 0$ the limit in Fig. 3 is zero.

On the other hand, when the wavelength becomes small relative to the radius of the sphere, the local surface curvature at the point of normal incidence effectively disappears. In the limit, the solution at the point of normal incidence should be the same as for scattering of a plane wave on a planar, rigid surface. The well-known solution to this problem requires that the scattered pressure be equal to the incident pressure. Thus

$$\text{gain(dB)} = 20\left(\frac{p}{p_0}\right) = 20\log(2) \approx 6, \tag{5}$$

which is the upper limit in Fig. 3. A much more extensive discussion of the scattering of sound from a sphere is given by Duda (1998).

The results presented for the sphere provide a starting point for the understanding of the acoustics of the head/ear. In the case when the wavelength is large relative to the size of the pinna and canal, these structures do not contribute significantly to the acoustical gain, and the transfer function resembles that of a head without pinna, which one would expect to have a very similar transfer function as the sphere. This is especially true for normal incidence at very low frequencies, where the pinna has little effect on the pressure at the blocked meatus position.

In the case when the wavelength is on the order of or smaller than the pinna/ear canal, however, the situation is markedly different. Here, the pinna, concha, and ear canal dramatically change the attainable gain as well as the directional dependence of the pressure field. This is a result of the structure of the pinna and ear canal, which are cavities that resonate within certain frequency ranges, and in the process amplify the incident waves more than was possible with just a convex surface. More detail on the frequency response of the head/ear is given in the next section.

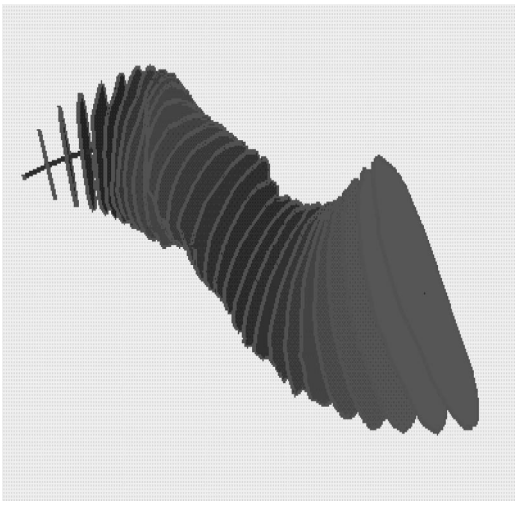

FIG. 4. Cross-sectional slices of the ear canal, before connection.

B. Computational mesh of the ear canal

Before presenting results of the acoustical simulations, a word is needed on the procedure for constructing the mesh of the ear canal and joining it to the head mesh. The starting point is a mesh of the human head with blocked meatus configuration from the Center for Computational Visualization at the University of Texas at Austin. This mesh is constructed from a CT scan. Second, a mesh of an actual ear canal is reconstructed from the detailed experimental measurements given in the paper by Stinton (1989). This consists of joining several cross-sectional slices, as shown in Fig. 4. Next, this mesh is scaled, rotated, and joined to the original head mesh by cutting a small opening on the ear, attaching the canal, and redefining the local connectivities. Figure 5 shows images of the ear mesh with the ear canal included.

C. Comparisons of numerical results with experimental data

In order to isolate the influence of the ear canal and other parts of the external auditory system, the simulations are conducted on meshes of the human head with and without (blocked meatus) the ear canal, so that the two could later be distinguished and the overall function of the canal could be isolated.

An initial word is needed on the level of agreement that can be expected. Of course, the ideal procedure would be to perform the necessary acoustical measurements in a laboratory on a fixed geometry, scan that same geometry, and construct a corresponding boundary element mesh on which the simulations would be conducted. In this study, however, the numerical simulations are made using a fixed representation of the human head. Thus, there is some difference between this geometry and those drawn from the literature for comparison, and this introduces some uncertainty in the comparisons. Even if the geometries were the same, exact agreement between the numerical and the experimentatal data sets could not be expected, and thus even more so in this case. However, reasonably good agreement has been obtained with regard to the main features of the response, and this is the intended goal of this work.

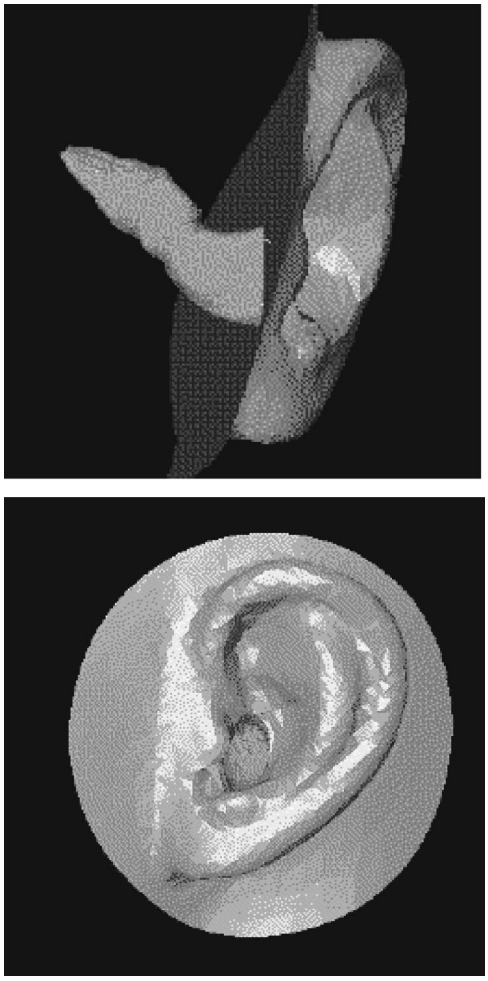

FIG. 5. Views of the ear canal connected to the ear mesh.

Also, a word is needed on terminology. Figure 6 shows the horizontal plane around the head divided into three sectors: frontal (−60° to 60°), lateral (60° to 135°), and posterior (135° to −150°) [terminology taken from Sandlin (1995)]. Note that the angles are measured from the midfrontal position. Also note that the view in this figure is from the top of the head, and that only the horizontal plane is considered.

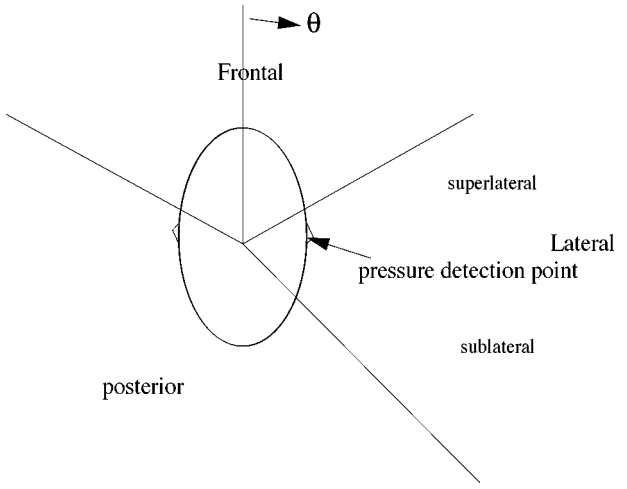

FIG. 6. Terminology used in describing HRTF data for the human head.

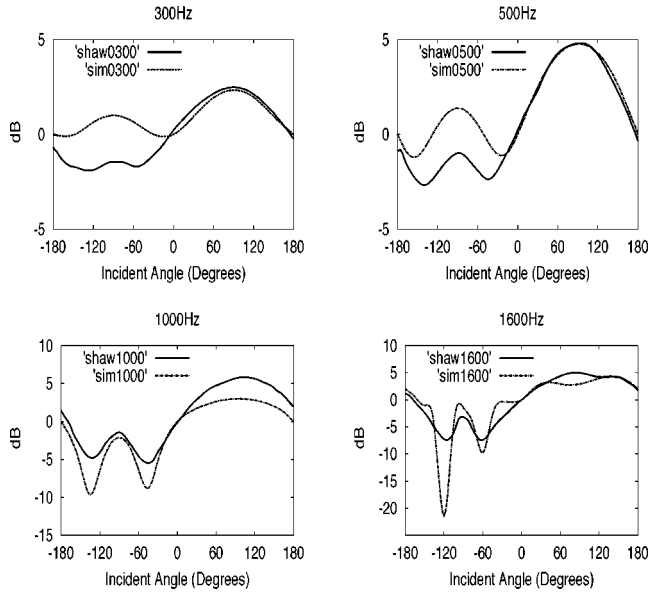

FIG. 7. Comparison of experimental data from Shaw (1974) and numerical simulations showing the variation of sound-pressure level at the eardrum for various frequencies, angles of incidence.

Finally, the term ''resonance'' is frequently used with different intended meanings, and it would be wise to clarify this point. Since the simulations in this paper are formulated with respect to the *exterior* problem, the domain is unbounded from the standpoint of the boundary element simulations (i.e., the domain includes both the ear canal as well as the infinite space surrounding the head). Standing waves can only exist in a bounded domain, and thus the term resonance is a bit unclear in this case. However, the response of the ear canal is highly frequency dependent, and in this paper the peak amplitude responses are denoted as resonances, simply to be consistent with most of the literature on the subject.

1. Directional dependence

The first set of experimental data that is considered is that of Shaw (1974). This work presents the response of a generic head/ear by combining data from 12 separate studies. These data and the corresponding computational results are presented in Figs. 7 and 8, with the angle of incidence as the abscissa, and normalized so that the gain at frontal incidence is zero. That is, the ordinate is computed as dB $=20\log(p/p_0)$, where the denominator $p_0=p^{\mathrm{inc}}+p_0^s$ is the total pressure generated at the eardrum by a plane wave impinging from the front (0° according to the definitions in Fig. 6). Also, the numerator is $p=p^{\mathrm{inc}}+p^s$, which implies that at 0° the ratio is unity and thus the gain is zero. This is the same format that was used in the original paper by Shaw (1974), and has the advantage that the gain at 0° is zero, which facilitates interpretation of the results.

The experimental data are available in graphical format. In order to plot these data simultaneously with the numerical simulation results, it is necessary to extract this data from the graphs presented in Shaw (1974). This is accomplished using graphical extraction software. The data is sampled at approximately every 2°, giving a total of 180 points for the entire range of interest (−180° to 180°).

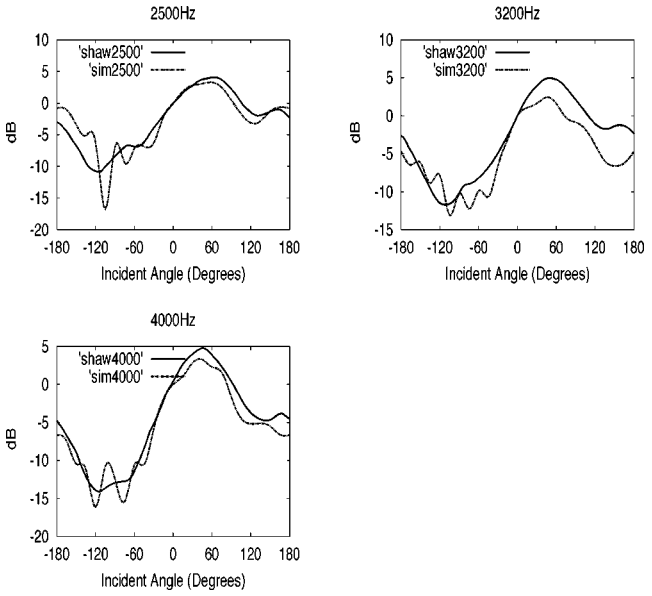

FIG. 8. Comparison of experimental data from Shaw (1974) and numerical simulations showing the variation of sound-pressure level at the eardrum for various frequencies, angles of incidence.

The numerical simulation results presented in Figs. 7 and 8 are generated using the boundary element procedure described earlier. For each curve, 24 right-hand sides are used, at increments of 15°, so that the entire 360° is spanned. These data are normalized in the same way as the experimental data (described above).

Reasonably good agreement is seen between the experimental and numerically generated data sets. At 300 and 500 Hz, two minimums and one maximum at negative angles of incidence are apparent, and one maximum at positive angles. At 1 and 1.6 KHz, there is a similar response, only that the peaks are more pronounced. Remarkably, the pronounced peak and valleys at 500 Hz and 1 KHz for negative angles of incidence are reproduced almost identically by the numerics.

A point of interest in the comparisons shown in Figs. 7 and 8 is that for 2500, 3200, and 4000 Hz, and at negative angles of incidence, the numerical results show small oscillations that are not present in the data of Shaw. This is likely due to the fact that Shaw's data were obtained by averaging the results from several studies. Any slight shifting of these peaks from one subject to another could cause an artificial cancellation effect. For example, the data of Mehrgardt (1977) also show oscillations at 2500, 3200, and 4000 Hz, and at negative angles of incidence, which makes artificial cancellation in Shaw's data seem more likely.

Also at these higher frequencies, and at positive angles, the maximum occurs earlier than at the lower frequencies, and is followed by a sharp downturn between 90° and 120°. The numerics reproduce this feature remarkably well.

Views of the pressure field on the blocked meatus configuration at 30° increments and the frequency of 500 Hz are shown in Fig. 9. In general, the pressure is higher on the receiving side of the wave than in the shadow zone, as expected. However, a small pressure peak around the ear at −90° is seen, and this is identified as the "bright spot," which occurs when the incident wave is directed along the contralateral direction. This is also evident in the curves in Fig. 7 at 500 Hz, 1 kHz, and 1.6 kHz at −90°, where a local maximum in pressure occurs, in between two local minima. The bright spot is contrary to intuition which would predict the shadow zone to receive the lowest pressure in a scattering situation. It may be partially explained in the case of a sphere, however, by considering the constructive interference between the waves that travel around the sphere and meet on the other side. The bright spot effectively results in a peak in pressure on the opposite side. In the case of a sphere, the bright spot is well-documented by Duda (1998). In the case of the human head, the paths around either side are not identical, but presumably the same phenomenon is responsible for the peak at −90°.

The same numerical experiments that are conducted on the head mesh with ear canal are also conducted on the mesh with blocked meatus. In the latter case, the results are normalized as $\mathrm{dB}=20(p/p_0)$, where p_0 is the pressure generated at the entrance to the (blocked) ear canal, instead of at the eardrum, again by a plane wave impinging from the front. This is the same normalization procedure that was used for Figs. 7 and 8, only that the reference is taken at the blocked meatus position rather than at the eardrum. Thus, this allows for a *relative* comparison of the angular dependence with and without the ear canal. Using this consistent normalization, Figs. 10 and 11 show a direct comparison of the computational results with and without the ear canal. The comparison reveals that the directional dependence is indistinguishable. Thus, as eluded to earlier, the presence of the canal does not appear to influence the directional dependence of the pressures, and this is consistent with the experimental data of Hammershoi (1996).

When normalized with the same denominator, an *absolute* comparison of the cases with and without the canal is obtained. The results are shown in Figs. 12 and 13, where the ordinate is $\mathrm{dB}=20(p/p^{\mathrm{inc}})$. That is, in this case the denominator is the same with and without the ear canal. The comparison of the cases with and without the ear canal on an *absolute* basis (Figs. 12 and 13) reveals that the eardrum pressures are only slightly higher than those at the blocked meatus for low frequencies, but near the resonance frequency of the canal (2.5 kHz), the gain is higher at the eardrum. This difference between the eardrum pressure and blocked meatus pressure near the resonance of the canal is also documented in the experimental data of Shaw (1968).

When compared on an absolute basis (Figs. 12 and 13), the eardrum pressure at 2.5 kHz is much higher than the blocked meatus pressure at this same frequency, even though at lower frequencies the difference between the two configurations is less dramatic. As mentioned in the previous paragraph, this can be attributed to the fact that the first resonance mode of the canal is around 2.5 kHz, whereas the first mode of the concha (which would be the mode of interest in the blocked meatus case) peaks around 5 kHz, as shown in Shaw (1968). At resonance the canal amplifies the sound-pressure level significantly, whereas at 2.5 kHz the concha has not achieved full resonance. This accounts for the difference seen at 2.5 kHz in Fig. 13.

The fact that the ear canal does not influence the direc-

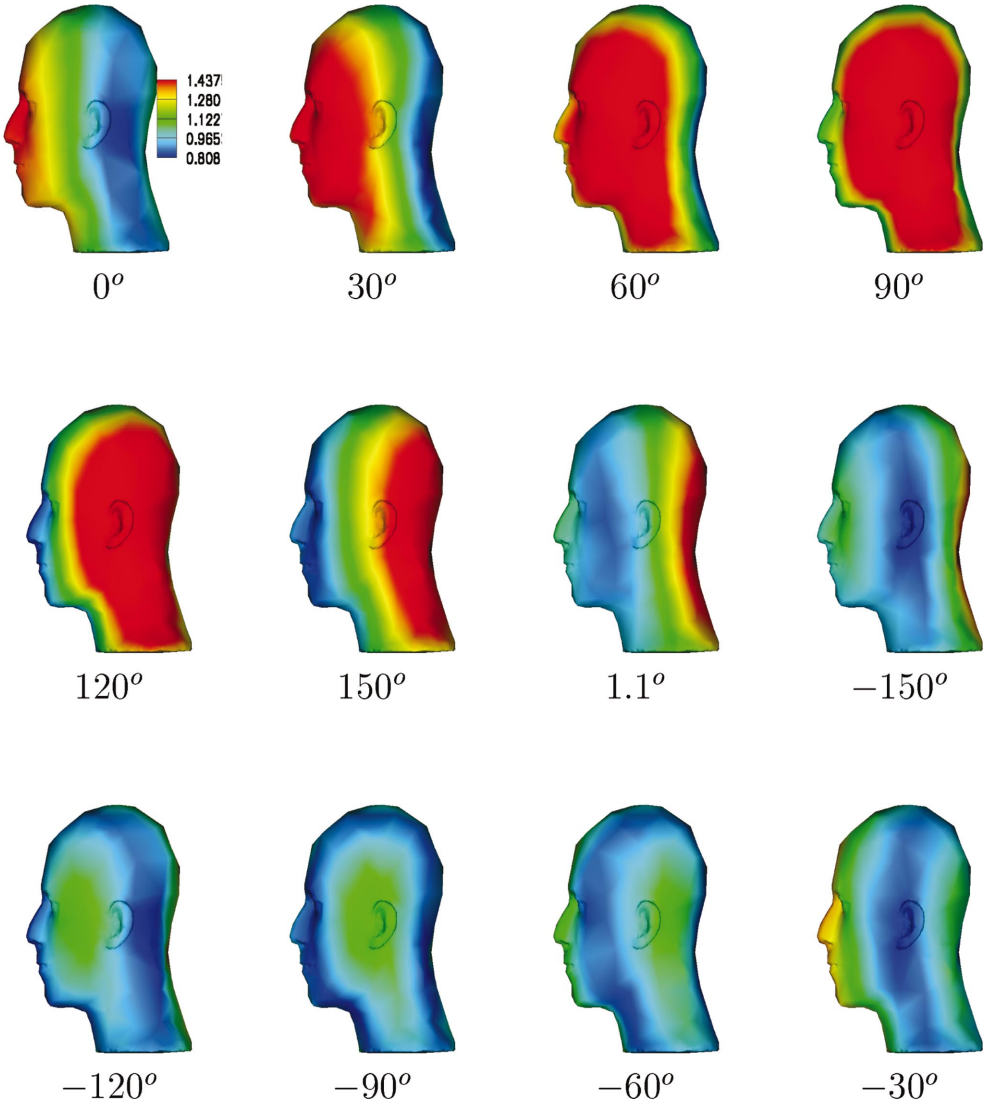

FIG. 9. Magnitude of surface pressure resulting from plane waves at various inclinations at 500 Hz. The legend in the first figure is the same for the remaining figures, showing red as maximum pressure and blue as minimum.

tionality of the acoustic signal that reaches the eardrum (as demonstrated in Figs. 10 and 11) appears to imply that simplified models of the ear canal could be used if directional information is of interest. The simplest such model would be a cylindrical tube, and thus would imply neglecting the distinctive kinks that real ear canals have along their length. At high enough frequency this simplification would certainly break down, though it would be interesting to see how high into the frequency range such a model could be used.

2. Frequency dependence and resonance modes

Figure 14 shows the computed pressure at the entrance to the ear canal for the blocked meatus configuration, along with the exact solution for the sphere, which was given in Fig. 3. In this case, the abscissa is the wave number multiplied by the radius of the scatterer. For low wave numbers, the responses are similar, but significantly higher gain is observed for the head at higher wave numbers, and this behavior deserves an explanation.

In Fig. 15, the pressure field is examined in the vicinity of the ear for the case of normal incidence, again for the

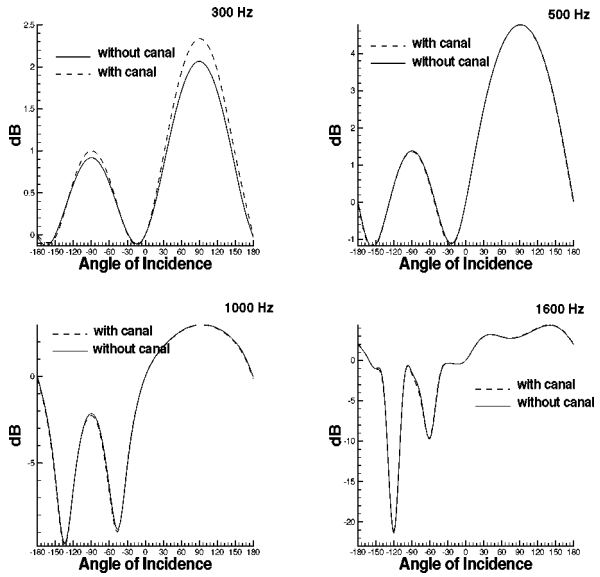

FIG. 10. Numerical computation of the pressure at the eardrum vs that at the blocked meatus position. Ordinate is $\mathrm{dB}=20\log(p/p_0)$, where p_0 is the eardrum (with ear canal) or blocked meatus (without ear canal) pressure induced by frontal incidence.

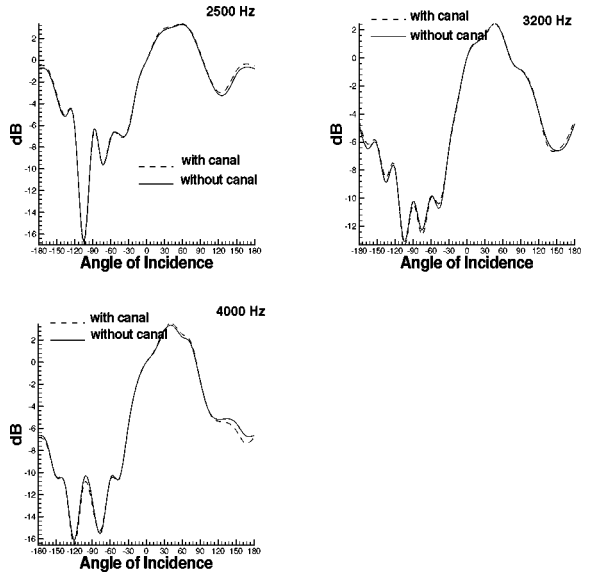

FIG. 11. Numerical computation of the pressure at the eardrum vs that at the blocked meatus position. Ordinate is $\mathrm{dB}=20\log(p/p_0)$, where p_0 is the eardrum (with ear canal) or blocked meatus (without ear canal) pressure induced by frontal incidence.

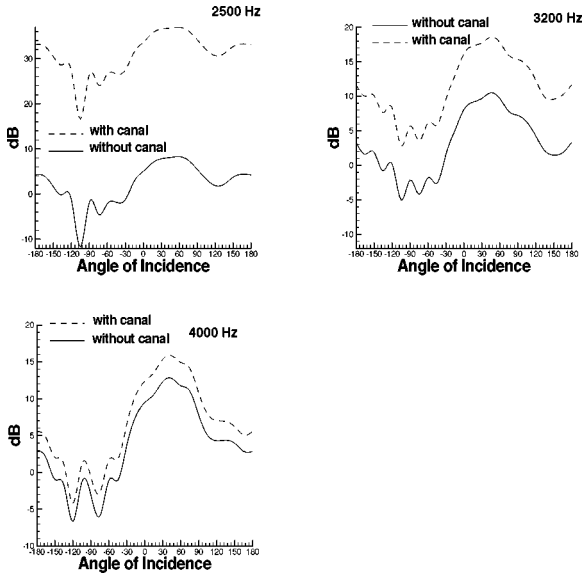

FIG. 13. Numerical computation of the pressure at the eardrum vs that at the blocked meatus position. In both cases the ordinate is $\mathrm{dB}=20\log(p/p^{\mathrm{inc}})$, where p^{inc} is the incident pressure.

blocked meatus configuration. Note that for this configuration the ear canal is not present. For low frequencies the wave is not sensitive to the presence of the ear, and a very uniform pressure field is observed in its vicinity of the ear. The second frequency (5.0 kHz) shows a marked change. In this case the pressure is greatest at the base of the cavity (concha), and decreases near the entrance of the cavity. As suggested from the experimental measurements of Sandlin (1995) and Crocker (1995), this pressure pattern fits the description of the first resonant frequency of the concha, which is a quarter-wave ''depth'' resonance, with maximum value at the bottom. Thus, both experimentation and numerics show that the broad resonance seen in the blocked meatus case around 5 kHz is directly attributable to the first mode of the concha, and this explains the fact that a much higher gain is obtained with the head/ear than in the case of a sphere.

Figure 16 shows the numerical computations of the gain versus frequency for the case with ear canal. In this case, the location of the resonance frequency (2.5 kHz) is much lower than in the blocked meatus configuration, and this is consistent with experimental measurements of the first resonance of the ear canal [Shaw (1974)]. However, the overall gain is much higher in the numerical computations than in typical experimental data [see, e.g., Shaw (1974)], and the resonance mode is much more narrow. This is actually expected since in this simulation the entire head, along with the ear canal and eardrum, is considered to be rigid, i.e., of infinite impedance. This assumption is most erroneous at the flexible eardrum, where the pressures are actually measured. The nu-

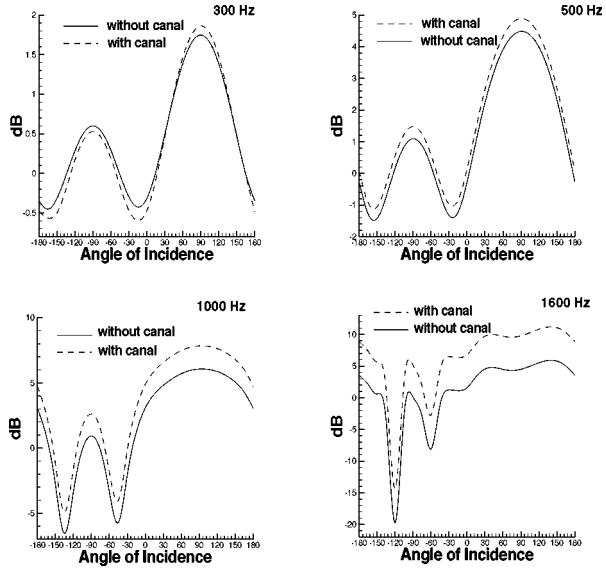

FIG. 12. Numerical computation of the pressure at the eardrum vs that at the blocked meatus position. In both cases the ordinate is $\mathrm{dB}=20\log(p/p^{\mathrm{inc}})$, where p^{inc} is the incident pressure.

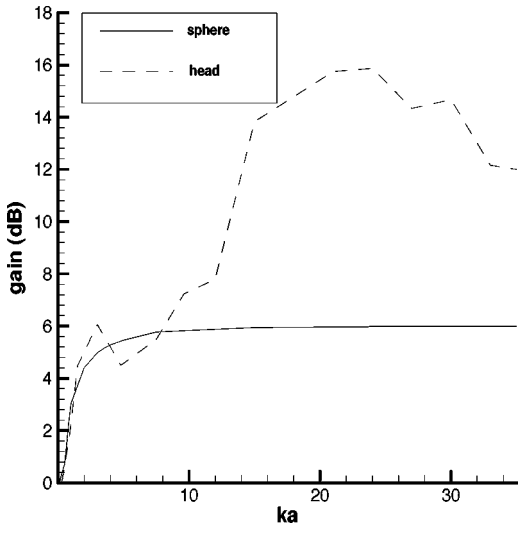

FIG. 14. A comparison of the sound-pressure level for a sphere and the human head at the blocked meatus position for normal incidence. Of significance is the dramatically higher gain experienced by the head, as a result of concha resonance.

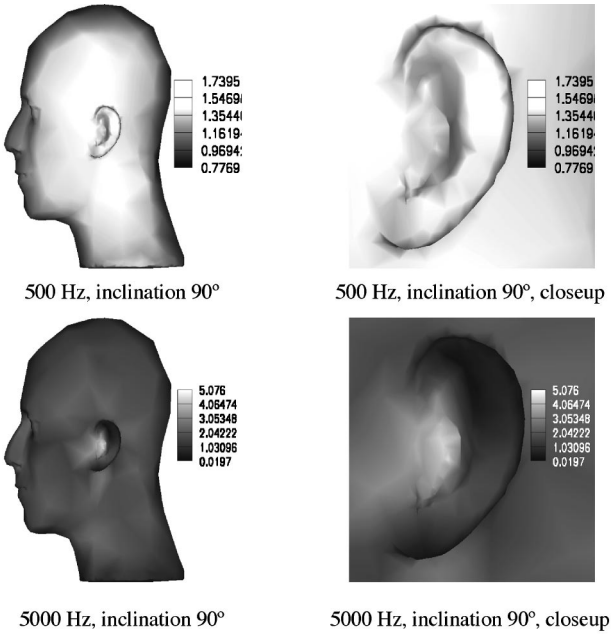

FIG. 15. The variation of pressure near the blocked meatus position for increasing frequency, at normal incidence. The final figure shows the first (quarter-wave) resonance mode of the concha.

merical roundoff error is also likely to increase as one approaches the approximate resonance condition of the ear canal, which will further decrease the accuracy of the computations. A finite impedance condition would help alleviate the roundoff problem, and help to model the actual physics more accurately. This would decrease the amplitude of the curve in Fig. 16, and thus would bring the results into better agreement with the experiments. Indeed, the data of Shaw (1968) show an almost 10-dB reduction in maximum gain when going from the rigid eardrum to the case of a typical eardrum impedance, and a significant broadening of the region of resonance.

Figures 17 and 18 show images of the magnitude of the

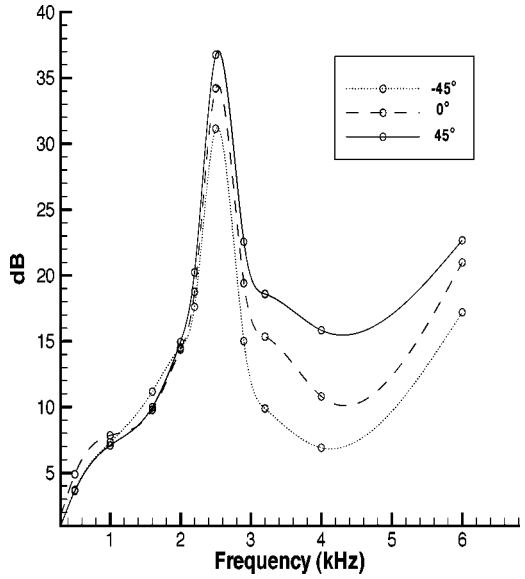

FIG. 16. Numerical computations showing the variation of sound-pressure level at the eardrum for various frequencies, angles of incidence.

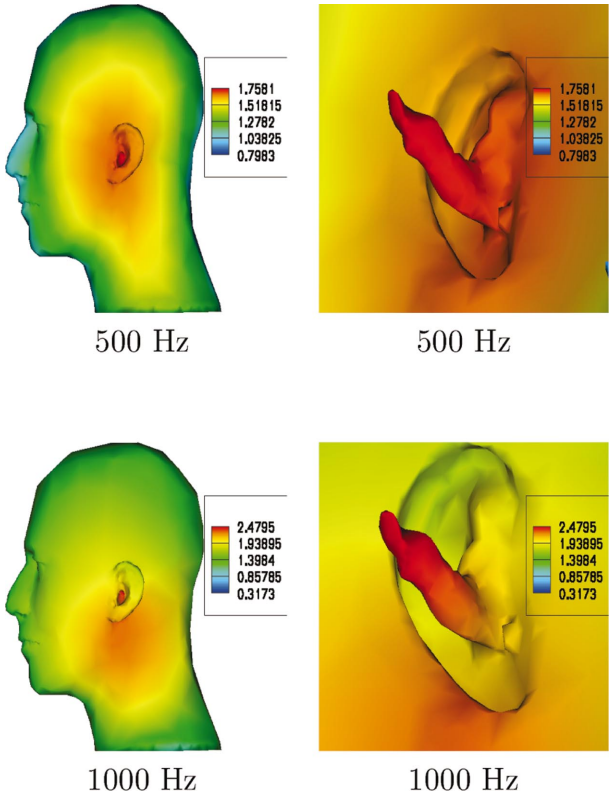

FIG. 17. Magnitude of surface pressure on the human head and within ear canal resulting from plane waves at normal incidence on head mesh with ear canal.

total pressure on the head mesh with ear canal, corresponding to a sequence of increasing frequencies. For each frequency two images are shown, the one on the left showing the pressure distribution on the impact zone on the head, and the one on the right showing the pressure distribution within the ear canal. The legends are the same in the two cases. Note that the images of the ear canal are taken from inside the head so that the canal is clearly visible, but that from this viewpoint the pinnas appear inverted.

As frequency increases, the areas of highest pressure become more and more localized within the ear canal, in a consistent manner as was seen in Fig. 15. However, a dramatic change is seen at a much lower frequency (2.9 kHz) than in the blocked meatus case, since this is the first resonant mode for the canal. In the 2.9-kHz case the pressure around the head is small compared with that at the eardrum, and Fig. 18 shows a distinctive quarter-wave resonant mode within the ear canal, as expected. The legends also show significant increases of the maximum pressure as the frequency approaches 2900 Hz.

IV. CONCLUSIONS

This paper presents computations of the head-related transfer function (HRTF) and typical resonance behaviors of a typical human subject with and without the ear canal. The computations are compared with various sets of experimental data and showed reasonable agreement. The resonance frequencies are deduced from the numerical computations, and the graphical display of the pressure distributions in these

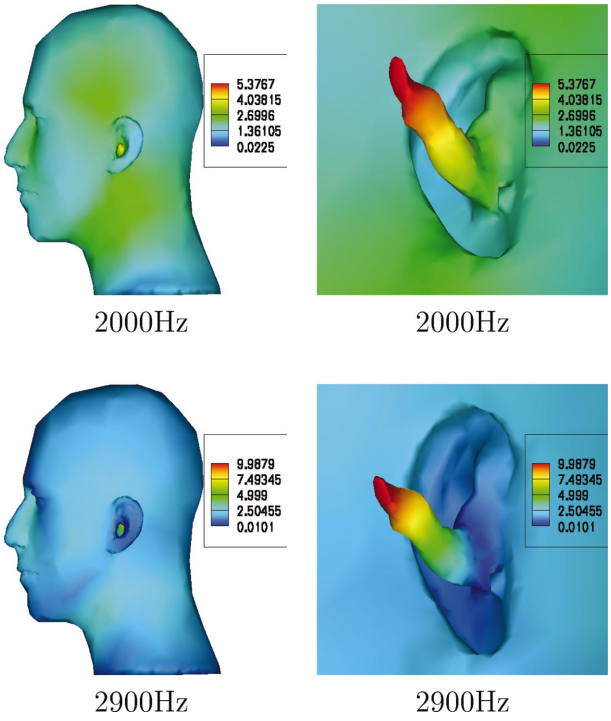

FIG. 18. Magnitude of surface pressure on the human head and within ear canal resulting from plane waves at normal incidence on head mesh with ear canal.

cases shows the same quarter-wave patterns that are reported in the literature. While the absolute pressure at the eardrum is generally greater than that at the blocked meatus position, the *relative* response with respect to the angle of incidence in both cases is shown to be the same. This is consistent with experimental data and confirms that, up to a certain frequency, the ear canal does not influence spatial cues.

There are several possibilities for the use of numerical simulations for the design of individualized hearing aids. A few such possibilities are described here.

(i) As shown in this paper, an approximate resonance frequency of the ear canal can be computed simply by sweeping through discrete frequencies and computing the maximum eardrum amplification. Such a technology could be used to match the resonance frequencies of a hearing aid to those of the ear canal of the particular individual. We note that such a calculation should probably be done on the closed canal cavity only.

(ii) Currently, canal bores have several possible designs, including single diameter, multiple diameter, tapered, etc. In most cases, a trial and error process is used to select the best design for a given individual. An additional variable is the depth of insertion of the bore into the canal. The resonant frequency of the canal is affected by the position of the bore, and the internal canal acoustics will be affected by the shape of insertion device. Numerical simulations could be used to study the acoustical affects of different bore geometries, and optimal insertion depths (for a given geometry). This would result in better overall designs for hearing aids, as well as greater comfort for the listener.

(iii) Undesirable feedback is common in behind the ear (BTE) hearing aids, especially when the hearing mold bore does not completely seal the ear canal. Numerical simulations could be used to simulate the feedback phenomena, which could help to understand and to control the phenomena.

It is believed that these results demonstrate that numerical computations can capture the essential physics involved in the external auditory system. Consequently, the use of such simulations in helping to advance technologies for the hearing impaired seems to be an exciting next step.

ACKNOWLEDGMENTS

The authors are grateful for funding for this project through the National Partnership for Advanced Computational Infrastructure (NPACI). Also, the authors thank Professor Chandra Bajaj and Dr. Guoliang Xu of the Center for Computational Visualization at the University of Texas for the mesh of the human head, along with assistance in graphical visualization of the results.

Burton, A., and Miller, G. (**1971**). "The application of integral equation methods to the numerical solution of some exterior boundary-value problems," Proc. R. Soc. London, Ser. A **323**, 201–210.

Chang, Y., and Demkowicz, L. (**1999**). "Solution of viscoelastic scattering problems in linear acoustics using *hp* boundary/finite element method," Int. J. Numer. Methods Eng. **44**(12), 1885–1907.

Ciskowski, R. (**1991**). "Applications in bioacoustics," in *Boundary Element Method in Acoustics*, edited by R. Ciskowski and C. Brebbia (Computational Mechanics, Southhampton).

Crocker, M. (**1995**). (Editor), *Handbook of Acoustics* (Wiley, New York).

Demkowicz, L., Oden, J., Ainsworth, M., and Geng, P. (**1991**). "Solution of elastic scattering problems in linear acoustics using *hp* boundary element methods," J. Comput. Appl. Math. **36**, 29–63.

Demkowicz, L., Karafiat, A., and Oden, J. T. (**1992**). "Solution of elastic scattering problems in linear acoustics using *hp* boundary element method," Comput. Methods Appl. Mech. Eng. **101**, 251–282.

Demkowicz, L., Gerdes, K., Schwab, C., Bajer, A., and Walsh, T. (**1998**). "HP90: A general and flexible FORTRAN 90 *hp*-FE code," Comput. Vis. Sci. **1**, 145–163.

Duda, R. O., and Martens, W. L. (**1998**). "Range dependence of the response of a spherical head model," J. Acoust. Soc. Am. **104**(5), 3048–3058.

Duncan, R. K., and Grant, J. W. (**1997**). "A finite-element model of the inner ear hair bundle micromechanics," Hear. Res. **107**, 15–26.

Geng, P., Oden, J. T., and Demkowicz, L. (**1996**). "Solution of exterior acoustic problems by the boundary element method at high wave number, error estimation, and parallel computation," J. Acoust. Soc. Am. **100**(1), 335–345.

Hammershoi, D., and Moller, H. (**1996**). "Sound transmission to and within the human ear canal," J. Acoust. Soc. Am. **100**(1), 408–427.

Kahana, Y., Nelson, P., Petyt, M., and Choi, S. (**1999**). "Numerical modeling of the transfer functions of a dummy-head and of the external ear," AES 16th International Conference on Spatial Sound Rep., Finland.

Katz, B. (**1998**). "Measurement and calculation of individual head related transfer functions using a boundary element model including the measurement and effect of skin and hair impedance," Doctoral dissertation, The Pennsylvania State University.

Kolston, P. J., and Ashmore, J. F. (**1996**). "Finite element micromechanical modeling of the cochlea in three dimensions," J. Acoust. Soc. Am. **99**(1), 455–465.

Ladak, H. M., and Funnell, W. R. J. (**1996**). "Finite-element modeling of the

normal and surgically repaired cat middle ear,'' J. Acoust. Soc. Am. **100**(2), 933–944.
Mehrgardt, S., and Mellert, V. (**1977**). ''Transformation characteristics of the external human ear,'' J. Acoust. Soc. Am. **61**(6), 1567–1576.
Moller, H., Sorenson, M. F., Jenson, C. B., and Hammershoi, D. (**1996**). ''Binaural technique: Do we need individual recordings?,'' J. Audio Eng. Soc. **44**(6), 451–469.
Parthasarathi, A. A., Grosh, K., and Nuttall, A. L. (**2000**). ''Three-dimensional numerical modeling for global cochlear dynamics,'' J. Acoust. Soc. Am. **107**(1), 474–485.
Sandlin, R. (**1995**). *Handbook of Hearing Aid Amplification* (Singular Publishing, San Diego), Vol. 1.
Shaw, E. A. G. (**1974**). ''Transformation of sound pressure level from the free field to the eardrum in the horizontal plane,'' J. Acoust. Soc. Am. **56**(6), 1848–1861.
Shaw, E. A. G., and Teranishi, R. (**1968**). ''Sound pressure generated in an external ear replica and real human ears by a nearby point source,'' J. Acoust. Soc. Am. **44**(1), 240–249.
Stinton, M. R., and Lawton, B. W. (**1989**). ''Specification of the geometry of the human ear canal for the prediction of sound-pressure level distribution,'' J. Acoust. Soc. Am. **85**(6), 2492–2503.
Takeuchi, T., Nelson, P. A., Kirkeby, O., and Hamada, H. (**1998**). ''Influence of individual head-related transfer functions on the performance of virtual acoustic imaging,'' Audio Eng. Soc. 104th Convention, preprint 4700.
van de Geijn, R. A. (**1997**). *Using* PLAPACK (The MIT Press, Cambridge, MA).
Wada, H., Metoki, T., and Kobayashi, T. (**1992**). ''Analysis of dynamic behavior of human middle ear using a finite element method,'' J. Acoust. Soc. Am. **92**(6), 3157–3168.
Walsh, T. F., and Demkowicz, L. (**2003**). ''hp boundary element modeling of the external human auditory system—Goal oriented adaptivity with multiple load vectors,'' Comput. Methods Appl. Mech. Eng. **192**(1–2), 125–146.

Frequency dependence of dynamic hysteresis in the interaction of acoustic wave with interface

Vitalyi Gusev[a)]
Université du Maine, 72085, Le Mans Cedex 9, France

(Received 22 May 2003; accepted for publication 11 December 2003)

The motion of an interface in acoustic field is modeled as a nonlinear relaxator driven by sound wave. The nonlinearity is due to nonlinear dependence of an interaction force between the surfaces composing the interface on their separation distance. The theory describes hysteresis in the response of the interface to continuously varying acoustic loading: with increasing acoustic field a strongly unharmonic variation of a characteristic interface width starts under some circumstances at higher amplitudes of external action than those at which it later stops with decreasing acoustic field. This dynamic hysteresis phenomenon is found to be dispersive in a sense that it depends on the relative values of the acoustic frequency and characteristic relaxation frequencies of the interface. These theoretical predictions might be also relevant to some recent experimental observations of hysteresis phenomena in the interaction of powerful ultrasonic fields with cracks. © *2004 Acoustical Society of America.* [DOI: 10.1121/1.1646398]

PACS numbers: 43.25.Dc, 43.25.Ts [MFH] Pages: 1044–1048

I. INTRODUCTION

Recently experimental observations of hysteresis in the interaction of the acoustic field with an individual crack have been reported.[1,2] The transition from quasiharmonic motion of the crack to nonlinear motion (presumably with clapping) takes place with increasing acoustic wave amplitude at higher field amplitudes than the inverse transition, which takes place with decreasing acoustic wave amplitude. Both transitions are identified by an abrupt variation in the level of the higher harmonics emitted by the crack[1,2] and in the level of the fundamental frequency wave transmitted through the crack.[2] One possible mechanism for the observed hysteresis might be the influence on the crack of the thermoelastic stresses caused by crack heating in the acoustic field.[1] Clearly the thermoelastic stresses could modify the threshold acoustic loading necessary to initiate clapping of the crack lips (or clapping of some intermediate contacts between the crack lips[2]). Another possible mechanism, which is not related to such a relatively slow (at the scale of acoustic period) process as heating, has been proposed in Refs. 2 and 3. It has been demonstrated that the observed hysteresis phenomena might be due to intrinsic nonlinearity of the interaction force between the crack lips (or between the intermediate contacts). In particular, in Ref. 3 (devoted to sound interaction with the interfaces) it has been demonstrated that dynamic hysteresis might exist if either the interaction force admits two different possible equilibrium separation distances between the surfaces composing the interface (bistable interface) or the interaction force is hysteretic itself (hysteretic interface). The latter might be possible if the adhesion hysteresis[4] is important.

However the analysis in Refs. 2 and 3 has been restricted to low or high frequency regimes where acoustic frequency ω is, respectively, significantly lower or significantly higher than all the characteristic relaxation frequencies of the system. In particular the theory[3] predicts the existence of the dynamic hysteresis in the high frequency (HF) regime and its absence in the low frequency (LF) regime. This indicates that the phenomenon is dispersive. In the present publication the dependence of the dynamic hysteresis on acoustic frequency is studied. It is demonstrated that the considered hysteresis phenomenon might exist at intermediate acoustic frequencies as well.

II. NONLINEAR BISTABLE RELAXATOR AS A MODEL FOR INTERFACE MOTION IN ACOUSTIC FIELD

In Ref. 3 it has been demonstrated that in many realistic situations the motion of interface caused by normally incident plane longitudinal acoustic wave is described by the equation of the forced relaxator. For example, in the case, where contributions of all the acoustic waves reflected from the sample boundaries are negligible [Fig. 1(a)], the variation of the interface width y is controlled by the following equation:[3]

$$\frac{\partial y}{\partial t}-\frac{2}{\rho c}F_{\mathrm{eff}}(y)=-2\frac{\partial u_i(t)}{\partial t}. \tag{1}$$

Here $u_i(t)$ is the mechanical displacement in the incident acoustic wave, $F_{\mathrm{eff}}(y)$ is the effective interaction force (per unit area) between the surfaces composing the interface, ρ is the material density, and c is the sound velocity. Mathematically the interface width can be associated with the difference in the mechanical displacements u of the surfaces composing the interface $[y=u(x=0+0)-u(x=0-0)]$. Here $x=0\pm0$ are the coordinates of the surfaces [Fig. 1(b)]. It is straightforward to verify Eq. (1) when there is a single wave incident on the interface [denoted by u_i in Fig. 1(a)] and there are only two additional waves (reflected u_r and trans-

a)Electronic mail: vitali.goussev@univ-lemans.fr

 0001-4966/2004/115(3)/1044/5/$20.00

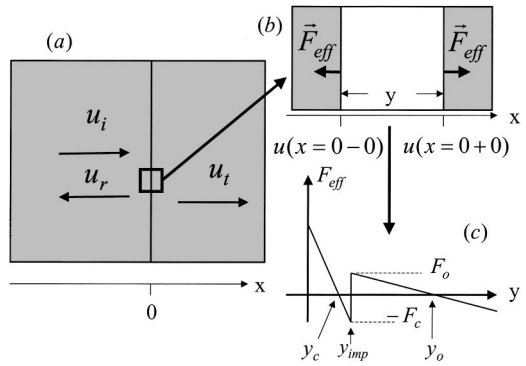

FIG. 1. (a) Schematic presentation of the incident (u_i), reflected (u_r), and transmitted (u_t) acoustic waves interacting with plane interface located in $x=0$. (b) Graphic illustration of the interface width y definition. (c) Piecewise linear model for the effective force $F_{\text{eff}}(y)$ admitting two equilibrium values (y_o and y_c) for the interface width. Abrupt variation of the effective force takes place when the interface width y is equal to the impact width y_{imp}.

mitted u_t) to be included in the total acoustic field [see Fig. 1(a)]. In the case of the nonlinear dependence of F_{eff} on y the relaxator described by Eq. (1) is nonlinear. It is worth mentioning here that the equation of a forced nonlinear relaxator appears also in the theory of a pulse response of a nonlinear layer, when the layer is acoustically thin.[5]

The effective force $F_{\text{eff}}(y)$ in Eq. (1) describes all possible interactions[4] including loading of the interface by external static stresses (see, for example, the experimental configurations in Refs. 6 and 7). In Ref. 3 it is demonstrated that the effective force can admit the existence of two positions of equilibrium for the interface. In Fig. 1(c) a piecewise linear modeling of this type of $F_{\text{eff}}(y)$ is presented. The equilibrium width y_o is attributed to an ''open'' state of the interface and the equilibrium width y_c is attributed to a ''closed'' state of the interface. From a physics point of view the region of $F_{\text{eff}}(y)$ near $y \approx y_o$ corresponds to the interaction between the surfaces through the elasticity of the contacts between the interfaces. The contribution to negative $F_{\text{eff}}(y)$ in the region $y_c \leqslant y \leqslant y_{\text{imp}}$ is predominantly provided by intermolecular attractive forces and other forces participating in adhesion, which might become important at short separation distances between the surfaces composing the interface. Finally, a positive $F_{\text{eff}}(y)$ in the region $0 \leqslant y \leqslant y_c$ models the repulsion, which should be sufficient to avoid mutual penetration of the surfaces (to avoid $y<0$). For more detailed discussion see Refs. 3, 4, and references therein.

For the quantitative mathematical analysis of the response of a bistable relaxator to the action of an acoustic field we introduce the following parametrization of the effective force in Eq. (1) [Fig. 1(c)],

$$F_{\text{eff}} = \begin{cases} -k_o(y-y_o), & y_{\text{imp}} < y, \\ -k_c(y-y_c), & y < y_{\text{imp}}. \end{cases} \tag{2}$$

Here $k_{o,c}$ denote the interface (crack) rigidity per unit area in the open (''o'' index) and closed (''c'' index) states, respectively. We will call the impact width (y_{imp}) the separation distance between the surfaces, where the force abruptly changes from repulsive to attractive (see Fig. 1). We will assume that the product $k_c y_c$ is sufficiently large to avoid mutual penetration of the interacting surfaces $x=0+0$ and $x=0-0$. With the use of Eq. (2) we rewrite Eq. (1) for the sinusoidal incident acoustic wave with the amplitude u_{ac} and frequency ω [$u_i = u_{ac}\sin(\omega t)$] in the form valid in both regions (i.e., for $y > y_{\text{imp}}$ and $y < y_{\text{imp}}$),

$$\frac{\partial}{\partial t}(y-y_{o,c}) + \omega_{o,c}(y-y_{o,c}) = -2u_{ac}\omega\cos(\omega t). \tag{3}$$

Here $\omega_{o,c} = 2k_{o,c}/(\rho c)$ are the characteristic relaxation frequencies of the interface (crack) in two states of equilibrium. It is convenient to introduce for the analysis of Eq. (3) the nondimensional time variable $\theta = \omega t$ and the nondimensional relaxation parameters $R_{o,c} = \omega_{o,c}/\omega$,

$$\frac{\partial}{\partial \theta}(y-y_{o,c}) + R_{o,c}(y-y_{o,c}) = -2u_{ac}\cos\theta. \tag{4}$$

In Ref. 3 the solutions of Eq. (4) in the LF regime ($R_{o,c} \gg 1$, $R_{o,c} \to \infty$) and in the HF regime ($R_{o,c} \ll 1$, $R_{o,c} \to 0$) have been obtained and analyzed. Here we investigate the regime of the intermediate acoustic frequencies.

III. INTERFACE WIDTH VARIATION UNDER SINUSOIDAL ACOUSTIC ACTION OF ARBITRARY FREQUENCY

For an arbitrary magnitude of the acoustic frequency ω relative to the relaxation frequencies $\omega_{o,c}$ the following general solutions of Eq. (4) should be used to describe a periodic motion of the interface:

$$y = y_{o,c} + c_{o,c}e^{-R_{o,c}\theta} - \frac{2u_{\text{ac}}R_{o,c}}{1+R_{o,c}^2}\left(\cos\theta + \frac{\sin\theta}{R_{o,c}}\right)$$

$$= y_{o,c} + c_{o,c}e^{-R_{o,c}\theta} - \frac{2u_{\text{ac}}}{\sqrt{1+R_{o,c}^2}}\cos(\theta - \phi_{o,c}), \tag{5}$$

where $\phi_{o,c} = \arctan(1/R_{o,c})$. If the clapping is absent (i.e., $y \neq y_{\text{imp}}$ during complete acoustic period) then from the periodicity condition it follows that the integration constants $c_{o,c}$ in Eq. (5) are equal to zero,

$$y = y_{o,c} - \frac{2u_{\text{ac}}}{\sqrt{1+R_{o,c}^2}}\cos(\theta - \phi_{o,c}). \tag{6}$$

The critical acoustic amplitude $u_{o,c}$ to start the clapping by the action on the initially open (closed) interface can be found by using Eq. (6) and the impact condition $y = y_{\text{imp}}$,

$$u_{o,c}=\pm(\sqrt{1+R_{o,c}^2}/2)(y_{o,c}-y_{\mathrm{imp}}). \tag{7}$$

These critical amplitudes are [in accordance with Eq. (7)] frequency dependent.

In the clapping regime the exponential terms in Eq. (5) should be taken into account. The impacts persistently introduce a component of eigenrelaxations of the system (the solution of the homogeneous differential equations) into motion, which together with the component due to forced relaxation (the particular solution of the equation of motion) cause ambiguity of the response of a mechanical system with impacts to periodic excitation.[8] If the transition from the open region to closed region takes place at time $\theta=\theta_1$ and the system returns back to the open region at $\theta=\theta_2=\theta_1+\Delta\theta$, then the next transition from open to closed region will take place at $\theta=\theta_1+2\pi$. The conditions for the impacts over a single acoustic period can be written as

$$\begin{aligned}
&y_{\mathrm{imp}}=y_c+c_c e^{-R_c\theta_1}-(y_{\mathrm{imp}}-y_c)\frac{u_{\mathrm{ac}}}{u_c}\cos(\theta_1-\phi_c),\\
&y_{\mathrm{imp}}=y_c+c_c e^{-R_c(\theta_1+\Delta\theta)}\\
&\qquad -(y_{\mathrm{imp}}-y_c)\frac{u_{\mathrm{ac}}}{u_c}\cos(\theta_1+\Delta\theta-\phi_c),\\
&y_{\mathrm{imp}}=y_o+c_o e^{-R_o(\theta_1+\Delta\theta)}\\
&\qquad -(y_o-y_{\mathrm{imp}})\frac{u_{\mathrm{ac}}}{u_o}\cos(\theta_1+\Delta\theta-\phi_o),\\
&y_{\mathrm{imp}}=y_o+c_o e^{-R_o(\theta_1+2\pi)}-(y_o-y_{\mathrm{imp}})\frac{u_{\mathrm{ac}}}{u_o}\cos(\theta_1-\phi_o).
\end{aligned} \tag{8}$$

These are four equations for the unknowns c_c, c_o, θ_1, and $\Delta\theta$. First the integration constants $c_{o,c}$ are excluded and the system of the remaining two equations is written in the matrix form

$$\begin{pmatrix} [1-\cos(\Delta\theta)e^{R_c\Delta\theta}] & \sin(\Delta\theta)e^{R_c\Delta\theta} \\ [\cos(\Delta\phi)-\cos(\Delta\theta+\Delta\phi)e^{R_o(\Delta\theta-2\pi)}] & [\sin(\Delta\theta+\Delta\phi)e^{R_o(\Delta\theta-2\pi)}-\sin(\Delta\phi)] \end{pmatrix}\begin{pmatrix}\cos\theta_1'\\ \sin\theta_1'\end{pmatrix}=\begin{pmatrix}\frac{u_c}{u_{\mathrm{ac}}}[e^{R_c\Delta\theta}-1]\\ \frac{u_o}{u_{\mathrm{ac}}}[1-e^{R_o(\Delta\theta-2\pi)}]\end{pmatrix}, \tag{9}$$

where $\Delta\phi=\phi_c-\phi_o$ and $\theta_1'=\theta_1-\phi_c$. Second the system (9) for the unknowns $\cos\theta_1'$ and $\sin\theta_1'$ is solved. Then the substitution of this solution into the trigonometric identity $(\cos\theta_1')^2+(\sin\theta_1')^2=1$ leads to the final relation between the time $\Delta\theta$ spent by the relaxator in the closed region ($y<y_{\mathrm{imp}}$) and the acoustic amplitude u_{ac}

$$\begin{aligned}
&u_{\mathrm{ac}}^2=N/D,\\
&N=u_c^2(e^{R_c\Delta\theta}-1)^2[e^{2R_o(\Delta\theta-2\pi)}-2\cos(\Delta\theta)e^{R_o(\Delta\theta-2\pi)}+1]+u_o^2(1-e^{R_o(\Delta\theta-2\pi)})^2[e^{2R_c\Delta\theta}-2\cos(\Delta\theta)e^{R_c\Delta\theta}+1]\\
&\quad +2u_cu_o(e^{R_c\Delta\theta}-1)(1-e^{R_o(\Delta\theta-2\pi)})[\cos(\Delta\phi+\Delta\theta)e^{R_o(\Delta\theta-2\pi)}+\cos(\Delta\phi-\Delta\theta)e^{R_c\Delta\theta}\\
&\quad -\cos(\Delta\phi)(e^{R_c\Delta\theta+R_o(\Delta\theta-2\pi)}+1)].\\
&D=[\sin(\Delta\phi+\Delta\theta)e^{R_o(\Delta\theta-2\pi)}+\sin(\Delta\phi-\Delta\theta)e^{R_c\Delta\theta}-\sin(\Delta\phi)(e^{R_c\Delta\theta+R_o(\Delta\theta-2\pi)}+1)]^2.
\end{aligned} \tag{10}$$

The average interface width could be evaluated directly using its definition $\langle y\rangle=(1/2\pi)\int_{\theta_1}^{\theta_1+2\pi}y\,d\theta$ and the solution (5). The result would have the form $\langle y\rangle=\langle y\rangle(c_o,c_c,\theta_1,\Delta\theta,u_{\mathrm{ac}})$. The constants $c_{o,c}$ could be eliminated with the help of the relations in Eq. (8) and then θ_1 could be eliminated using the solution of the system (9). This would result in the dependence of $\langle y\rangle$ on $\Delta\theta$ and u_{ac} only, $\langle y\rangle=\langle y\rangle(\Delta\theta,u_{\mathrm{ac}})$. With the help of Eq. (10) we could finally get the dependence of the interface width on the amplitude of the acoustic oscillations in the parametric form

$$\langle y\rangle=\langle y\rangle(\Delta\theta,u_{\mathrm{ac}}(\Delta\theta)),\quad u_{\mathrm{ac}}=u_{\mathrm{ac}}(\Delta\theta). \tag{11}$$

Here the parameter is $\Delta\theta$. However we will not present here either the results of Eq. (11) evaluation, or even the exact form of Eq. (11). It is clear that the hysteresis phenomena in the dependence of $\langle y\rangle$ on u_{ac} are reflected in the dependence of $\Delta\theta$ on u_{ac}. Because of this we evaluate here the solution (10) for the time $\Delta\theta$ spent by the relaxator in the closed region.

From a nonlinear vibrations theory point of view Eq. (8) provides a possible presentation of the Poincaré map (return map) of the system. The point of discontinuity in stiffness is a natural place to slice the space (y,t).[9] Starting from Eq. (8) we are studying not the complete motion but only the time instants when the system crosses the Poincaré session. In fact Eq. (8) are also the recursion relations providing opportunity to predict the next impact if the information on the previous impact is available. One can evaluate the periodicity (stability in time) of the impacts rather than to follow the complete motion. The idea of studying dynamical systems using recursion relations, or maps, has its foundations in the works of Poincaré.[10] It is important that the stability of periodic points of return map is the same as the stability of the corresponding orbits of the system, and bifurcations of these orbits may

be studied by considering the periodic points of the return map.[9]

In Refs. 2 and 3 the hysteresis phenomenon of interest here have been predicted in the HF limiting case $R_{o,c}\to 0$, where the acoustic frequency ω is significantly higher than both relaxation frequencies $\omega_{o,c}$. In this regime $R_{o,c}\ll 1$ in Eq. (4) and in the leading approximation the variation in the crack width follows the displacement in the acoustic field: $y\cong c'-2u_i(\theta)$. Clearly for the periodic acoustic action the integration constant c' in the above solution has a meaning of the average interface width

$$y\cong\langle y\rangle-2u_i(\theta). \tag{12}$$

It is the average interface width $\langle y\rangle$ that contains in the HF regime the information on the interaction between the surfaces $x=0-0$ and $x=0+0$ composing the interface. In this regime the periodic acoustic action on the interface manifests itself in the variation of the average interface width. In other words, the nonlinearity of the interface acts as a diode (or a rectifier). The similar high-frequency regime in the atomic force microscopy (AFM) (when the interaction between the tip and the surface is modulated by an ultrasonic wave incident on the surface or by HF vibrations of the canteliever) is known as the ultrasonic force mode (UFM).[11–13] It is worth mentioning that the effect of rectification (demodulation) was experimentally observed not only in the UFM of AFM[11–13] but in the interaction of the acoustic waves with the unbonded interfaces as well.[14,15]

In the high frequency regime ($R_{o,c}\to 0$) the average interface width $\langle y\rangle$ can be found from the condition that the average effective force should be equal to zero,

$$\langle F_{\text{eff}}(y)\rangle=\langle F_{\text{eff}}(\langle y\rangle-2u_i(\theta))\rangle=0, \tag{13}$$

that follows from the averaging of Eq. (1) over an acoustic period. Consequently the dependence of the average interface width $\langle y\rangle$ on the amplitude of the acoustic wave can be evaluated in the HF regime by substituting the solution (12) in the condition (13) for a particular model of the effective force. This is precisely the mathematical method that has been used in Ref. 3 to predict the hysteresis in the variation of $\langle y\rangle$ in response to acoustic loading of first increasing and then decreasing amplitude when the interface is initially in the open state. However it has not been verified in Ref. 3 if the predicted phenomenon exists at high ($\omega\gg\omega_{o,c}$) but not infinitely high ($\omega\neq\infty$) acoustic frequencies.

Here numerical evaluation of the analytical solution in Eq. (10) is used to answer this question. In Fig. 2 the dependence of the time $\Delta\theta$ spent by the interface in the closed region on the normalized acoustic amplitude u_{ac}/u_o is presented in a particular case (where $k=k_c/k_o=100$ and $F=F_c/F_o=10$). The increasing index of the curve [from (1)–(5)] corresponds to decrease in acoustic frequency [$R_o=10^{-3}$ (1), 10^{-2} (2), 5×10^{-2} (3), 10^{-1} (4), 1 (5)]. Note that due to the normalization the first impact of the interface with increasing acoustic amplitude takes place always in the same point [$\ln(u_{\text{ac}}/u_o)=0$, $\Delta\theta=0$] of Fig. 2. In Fig. 3 the part $-5/2\leqslant\ln(u_{\text{ac}}/u_o)\leqslant 9/2$, $0\leqslant\Delta\theta\leqslant 2\pi/5$ of the curve (2) for $R_o=10^{-2}$ is zoomed. The hysteresis phenomenon manifests itself as follows. When the acoustic amplitude u_{ac} reaches the critical value u_o the impact leads to abrupt increase of the time spent by the interface in the closed region (the trajectory $A\to B$ in Fig. 3). The subsequent increase of u_{ac} leads to continuous increase in $\Delta\theta$ (the trajectory $B\to C$). When later the acoustic amplitude starts to diminish the clapping motion does not stop at critical amplitude $u_{\text{ac}}=u_o$ but persists at lower amplitudes. Along the trajectory $C\to B\to D$ (Fig. 3) the time $\Delta\theta$ is continuously diminishing with diminishing acoustic field. The clapping stops by the transition $D\to E$ at lower acoustic amplitude than one necessary to initiate clapping. As has been pointed out above this hysteresis in the dependence of $\Delta\theta$ on u_{ac} corresponds to hysteresis in the dependence of the interface width $\langle y\rangle$ on the acoustic wave amplitude. The results presented in Fig. 2 demonstrate that theoretically predicted dynamic hysteresis do exist in the regime of high but finite acoustic frequencies [the curve (1) in Fig. 2 corresponds to $R_o=10^{-3}$, $R_c=kR_o=10^{-1}$ both significantly less than 1 but finite]. Moreover from Fig. 2 it follows that hysteresis exists when the acoustic frequency ω is higher than the relaxation frequency ω_o of the interface in the open state but lower than the relaxation frequency ω_c of the interface in the closed state [the curve (3) in Fig. 2 corresponds to $R_o=5\times10^{-2}<1$ but $R_c=kR_o=5>1$]. The hysteresis in Fig. 2 disappears when $R_o\geqslant 10^{-1}$,

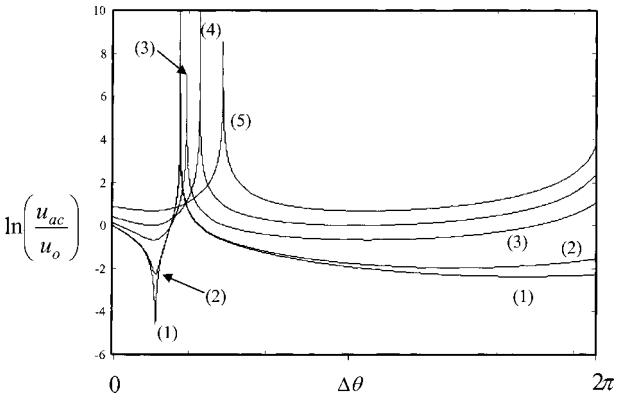

FIG. 2. The dependence of the time $\Delta\theta$ spent by the interface in the closed region ($y\leqslant y_{\text{imp}}$) on the logarithm of the normalized acoustic amplitude u_{ac}/u_o for $k=k_c/k_o=100$, $F=F_c/F_o=10$ and different values of the relaxation parameter $R_o=10^{-3}$ (1), 10^{-2} (2), 5×10^{-2} (3), 10^{-1} (4), 1 (5).

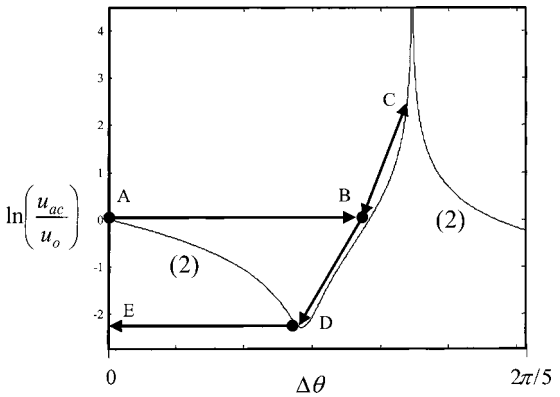

FIG. 3. The part $-5/2\leqslant\ln(u_{\text{ac}}/u_o)\leqslant 9/2$, $0\leqslant\Delta\theta\leqslant 2\pi/5$ of Fig. 2 zoomed for $R_o=10^{-2}$ [curve (2)]. The arrowheads indicate the trajectory $A\to B\to C\to B\to D\to E$ of the nonlinear bistable relaxator in response to first increasing and then decreasing in amplitude sinusoidal acoustic loading.

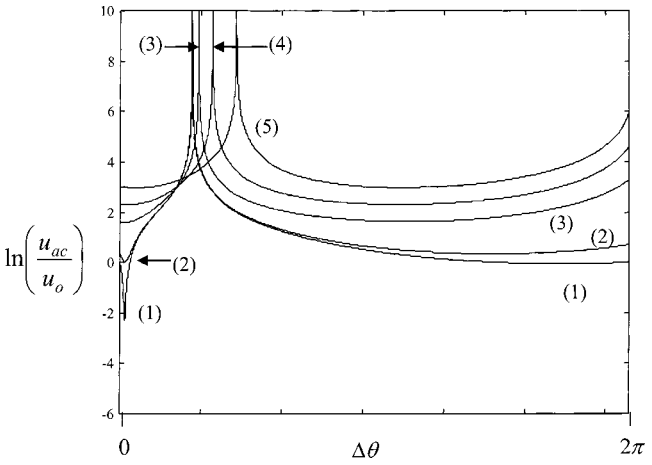

FIG. 4. The dependence of the time $\Delta\theta$ spent by the interface in the closed region ($y \leqslant y_{\text{imp}}$) on the logarithm of the normalized acoustic amplitude u_{ac}/u_o for $k=k_c/k_o=100$, $F=F_c/F_o=100$ and different values of the relaxation parameter $R_o=10^{-3}$ (1), 10^{-2} (2), 5×10^{-2} (3), 10^{-1} (4), 1 (5).

$R_c=kR_o \geqslant 10 \gg 1$. For $R_o \geqslant 10^{-1}$ the first impact is accompanied by the jump of the interface from harmonic motion around open equilibrium position to harmonic motion around closed equilibrium position. This transition is similar to one predicted for LF (quasistatic) regime in Ref. 3. The transition to clapping from the harmonic motion around the closed state starts with increasing u_{ac} at higher acoustic amplitudes (when $u_c > u_o$).

In Fig. 4 the curves (1)–(5) correspond to the same values of the relaxation parameter [$R_o=10^{-3}$ (1), 10^{-2} (2), 5×10^{-2} (3), 10^{-1} (4), 1 (5)] and the same relative stiffness ($k=100$) as in Fig. 2, but for higher attractive force ($F=100$). Comparison between Fig. 4 and Fig. 2 demonstrates that for higher relative attractive forces, when the acoustic frequency is diminishing the hysteresis disappears and the interface switches from the harmonic motion around y_o to harmonic motion around y_c earlier (i.e., at higher frequencies). This prediction is in accordance with physical intuition.

IV. CONCLUSIONS

The analytical solution for the interface width variation induced by sinusoidal acoustic field (in the case where the interface is characterized by two possible positions of static equilibrium) is obtained. The numerical analysis of the particular situations demonstrates that the predicted earlier[2,3] effect of dynamic hysteresis persists at intermediate acoustic frequencies. The transition from sinusoidal interface motion to clapping regime takes place at higher acoustic amplitudes than the inverse transition at acoustic frequencies ω that are higher than the relaxation frequency ω_o of the open interface and lower than the relaxation frequency ω_c of the closed interface. Because the regimes $\omega \gg \omega_c \gg \omega_o$ and $\omega_c \gg \omega_o \gg \omega$ have been analyzed earlier,[3] the prediction obtained here for the intermediate regime $\omega_c \gg \omega \gg \omega_o$ completes a qualitative picture of the behavior of the forced bistable relaxator as a function of driving frequency.

ACKNOWLEDGMENT

This work was supported by DGA (Contract No. 00.34.026.00.470.75.65).

[1] I. Yu. Solodov and B. A. Korshak, "Instability, chaos, and "memory" in acoustic-wave-crack interaction," Phys. Rev. Lett. **88**, 014303 (2002).
[2] A. Moussatov, V. Gusev, and B. Castagnede, "Self-induced hysteresis for nonlinear acoustic wave in cracked material," Phys. Rev. Lett. **90**, 124301 (2003).
[3] V. Gusev, B. Castagnède, and A. Moussatov, "Hysteresis in response of nonlinear bistable interface to continuously varying acoustic loading," Ultrasonics **41**, 643–654 (2003).
[4] N. A. Burnham and A. J. Kulik, "Surface forces and adhesion," in *Handbook of Micro/Nano Tribology*, edited by B. Bhushan (CRC Press, Boca Raton, 1999), Chapter 5, 247–272.
[5] C. M. Hedberg and O. V. Rudenko, "Pulse response of a nonlinear layer," J. Acoust. Soc. Am. **110**, 2340–2350 (2001).
[6] O. Buck, W. L. Morris, and J. M. Richardson, "Acoustic harmonic generation at unbonded interfaces and fatigue cracks," Appl. Phys. Lett. **33**, 371–373 (1978).
[7] I. Yu. Solodov and Chin An Vu, "Popping nonlinearity and chaos in vibrations of a contact interface between solids," Akust. Zh. **39**, 904–910 (1993) [English transl.: Acoust. Phys. **39**, 476–479 (1993)].
[8] F. Peterka and J. Vacik, "Transition to chaotic motion in mechanical systems with impacts," J. Sound Vib. **154**, 956115 (1992).
[9] S. W. Shaw and P. J. Holmes, "A periodic forced piecewise linear oscillator," J. Sound Vib. **90**, 129–155 (1983).
[10] H. Poincaré, *Les Méthodes Nouvelles de la Mécanique Céleste* (Gauthier-Villars, Paris, 1899), 3 volumes.
[11] O. Kolosov and K. Yamanaka, "Nonlinear detection of ultrasonic vibrations in an atomic force microscope," Jpn. J. Appl. Phys., Part 2 **32**, L1095–L1098 (1993).
[12] K. Yamanaka, H. Ogiso, and O. Kolosov, "Analysis of subsurface imaging and effect of contact elasticity in the ultrasonic force microscopy," Jpn. J. Appl. Phys., Part 1 **33**, 3197–3203 (1994).
[13] K. Iganaki, O. Matsuda, and O. B. Wright, "Hysteresis of the canteliever shift in ultrasonic force microscopy," Appl. Phys. Lett. **80**, 2368–2389 (2002).
[14] F. M. Severin and I. Yu. Solodov, "Experimental observation of acoustic demodulation in reflection from a solid-solid interface," Akust. Zh. **35**, 764–765 (1989) [English transl.: Sov. Phys. Acoust. **35**, 447–448 (1989)].
[15] B. A. Korshak, I. Yu. Solodov, and E. M. Ballad, "DC effects, subharmonics, stochasticity and "memory" for contact acoustic nonlinearity," Ultrasonics **40**, 707–713 (2002).

Dynamics and noise emission of laser induced cavitation bubbles in a vortical flow field

Ghanem F. Oweis, Jaehyug Choi, and Steven L. Ceccio
Mechanical Engineering Department, University of Michigan, Ann Arbor, Michigan 48109

(Received 30 March 2003; revised 22 November 2003; accepted 11 December 2003)

The sound produced by the collapse of discrete cavitation bubbles was examined. Laser-generated cavitation bubbles were produced in both a quiescent and a vortical flow. The sound produced by the collapse of the cavitation bubbles was recorded, and its spectral content was determined. It was found that the risetime of the sound pulse produced by the collapse of single, spherical cavitation bubbles in quiescent fluid exceeded that of the slew rate of the hydrophone, which is consistent with previously published results. It was found that, as collapsing bubbles were deformed by the vortical flow, the acoustic impulse of the bubbles was reduced. Collapsing nonspherical bubbles often created a sound pulse with a risetime that exceeded that of the hydrophone slew rate, although the acoustic impulse created by the bubbles was influenced largely by the degree to which the bubbles became nonspherical before collapse. The noise produced by the slow growth of cavitation bubbles in the vortex core was not detectable. These results have implications for the interpretation of hydrodynamic cavitation noise produced by vortex cavitation. [DOI: 10.1121/1.1646402]

PACS numbers: 43.25.Yw, 43.30.Nb, 43.25.Vt [AJS] Pages: 1049–1058

I. INTRODUCTION

The sound associated with the growth and collapse of single cavitation bubbles has been a topic of interest for some time.[1–4] Discrete cavitation events are often the source of significant cavitation noise in underwater flows and within turbomachinery. Over time, researchers have undertaken to understand how cavitation bubbles create noise and how that noise can be scaled with changes in cavitation and Reynolds number.

A widely used scaling method for hydrodynamic cavitation noise was proposed by Fitzpatrick and Strasberg[5] in 1957. They used spherical bubble dynamics to analyze the volume growth and collapse of a single cavitation bubble in an infinite fluid. Fourier analysis of the volume acceleration was then used to determine the spectral content of the noise emitted by the bubble. A time scale of the problem is the Rayleigh collapse time, t_C,

$$t_C = 0.915 R_M \sqrt{\rho/\Delta P}, \tag{1}$$

where R_M is the maximum radius of the bubble [sometimes taken as the cubic root of the maximum bubble volume], $|\Delta P|$ is the pressure difference between the external fluid and the bubble contents, and ρ is the liquid density. With monopole sound generation, the acoustic pressure generated by the bubble will scale with the volume acceleration, an estimate of which can also be derived from Rayleigh's analysis. The sound pressure produced by the growth and collapse of the bubble is then given by

$$S(r,\omega) = \frac{\rho^2}{8\pi r^2} |\ddot{V}(\omega)|^2, \tag{2}$$

where r is the distance between the bubble and the sound pressure measurement.[6]

The Fitzpatrick and Strasberg model predicts that the sound spectrum generated by single bubble collapse should scale as $(\omega t_C)^4$ for $\omega t_C < 1$. The peak of the spectrum is near $\omega t_C = 1$, and higher frequencies will roll off as $(\omega t_C)^{-2}$. Mellen's[7] measurements of bubble cavitation noise spectra resulting from a bubble cloud formed at the end of a rotating rod exhibit these spectral features and has been used to support the validity of this analysis. Corrections to this analysis have included the effect of liquid compressibility and the introduction of noncondensable gas within the cavity.[8,9] These processes tend to limit the predicted energy emitted at frequencies greater than $10 \cdot (\omega t_C)$.

If the external bubble pressure greatly exceeds the pressure of the noncondensable bubble contents at the time of the bubble maximum volume, the bubble wall velocity can approach the local liquid sound speed, leading to the formation of a pressure shock wave during the rapid volume accelerations near the point of minimum bubble volume. Baiter[10] has shown that such a shock wave can exhibit a pressure pulse of the form

$$P_a(r,t) = P_S e^{-t/\theta}. \tag{3}$$

The peak pressure is $P_S(r) = f_1(r, R_M, R_m, P_G, \rho c^2)$, and the pulse width is $\theta(r) = f_2(r, R_M, R_m, P_G, \rho c^2)$. R_M, and R_m and maximum and minimum bubble radii, P_G, is the noncondensable gas pressure of the bubble at its maximum volume, and c is the liquid sound speed. The spectrum associated with the sound pulse is:

$$S(r,\omega) = \frac{(P_S \theta)^2}{1 + (\omega\theta)^2} \tag{4}$$

which is flat until the cutoff frequency $1/(\omega\theta)$. The cutoff frequency is strongly affected by the amount of noncondensable gas present in the collapsing cavity. The noncondensable gas may have existed within the original gas nucleus,

and diffusion to or from the liquid may either increase or reduce the total mass of noncondensable gas, depending on the pressure/volume history of the bubble and saturation level of the surrounding liquid prior to bubble collapse.

Measurement of noise spectra from discrete hydrodynamic cavitation has been reported. Typically, the noise produced by traveling bubble cavitation has been examined.[11–15] The pressure pulse created by a collapsing cavitation bubble can be characterized by the acoustic impulse, I,

$$I = \int_{\theta} P_a \, dt, \tag{5}$$

where θ is the pulse width. However, shearing and fission of the bubble can significantly reduce the total emitted sound.[16] The presence of nearby bubbles can also lead to significantly reduced acoustic emission.[17]

Measurements of the spectral content of discrete hydrodynamic cavitation events have not been consistent. Reverberations in confined flow facilities and the limitations of the fidelity and bandwidth of the measurement equipment can contaminate the measured spectrum. Much of the spectral data presented consists of the average spectra produced by many cavitation events. Beside the data reported by Mellen, there is little evidence that the spectral content of single cavitation bubble noise will scale as predicted by incompressible bubble dynamics. Spectra measured from traveling bubble and vortex cavitation are not consistent.[12–15] Some spectra are reported to exhibit the features predicted by Fitzpatrick and Strasberg (i.e., low Mach number bubble collapse), while others are reported to be broadband. Moreover, the relative noise contribution due to the growth and collapse phases of hydrodynamic bubble cavitation are often considered comparable, although most researchers report experimental noise measurements principally from the bubble collapse. Further complications arise from the generally complex and nonspherical shape of hydrodynamic cavitation bubbles.

Capture of the true acoustic transients created by collapsing cavitation bubbles usually requires the construction of a high frequency response transducer, typically made from a thin film of polyvinylide fluoride (PVDF). The pressures measured with these devices have been compared to the optically measured volume change of the bubble, and it has been shown that, by far, the strongest noise is emitted when the bubble reaches a minima of volume.[18,19] Sound is produced as a shock wave that radiates away from the bubble, and the risetime of the shock wave is on the order of 5 nanoseconds, the maximum peak pressures on the order of hundreds of atmospheres near the bubble, and the pulse width is on the order of 10 to 100 ns. The collapse of nonspherical bubbles can produce less noise. Bubbles collapsing near a solid boundary can be deformed, and the lack of spherical focusing can significantly reduce the emitted noise.[18] The sharp risetime high pressures observed in these studies indicate that the spectrum of the emitted sound is dominated by the collapse processes and is, largely, broadband.

In the present work, we will measure the noise pulse and spectra associated with single cavitation bubble events using techniques that are often employed in the study of hydrodynamic cavitation. Bubbles will be produced in the vicinity of a low-pressure vortex core. We will show that the noise emitted by the focused collapse of distorted bubbles is broadband and does not exhibit significant spectral content, even for highly distorted bubbles. The noise produced by highly distorted cavitation bubbles is still scaled by the dynamics of spherically collapsing bubbles. Last, we will show that the magnitude of the noise produced during bubble growth is significantly smaller than the noise produced upon collapse.

II. EXPERIMENT

Single cavitation bubbles were created in both a quiescent liquid and in a vortical flow. Figure 1(a) shows the schematic diagram of the quiescent cavitation bubble experiment. A small cubical Lucite water tank (205 mm side) was created with an optical glass window (100 mm diameter) for the introduction of laser light. The infrared light pulse (1064 nm wavelength, ~10 ns pulse duration, 280 mJ/pulse, maximum) was produced by a *Q*-switched Nd:YAG laser (Spectra Physics PRO 250). Through a set of spherical lenses, the beam was expanded to a diameter of 100 mm and then focused to a waist within the tank. The cone angle was 19.4° in air. The space over the liquid in the tank could be evacuated, and the gas pressure was recorded with an Omega PX203 pressure transducer. Distilled water was placed within the tank. In order to increase the repeatability of bubble production, a small amount of drinking tap water was added to the tank. The tap water contained enough micron sized contaminants that led to the regular absorption of the laser light in the location of the beam waist and the production of a single cavitation bubble, although intermittent production of multiple bubbles was also observed. Variation in the static pressure above the tank and the energy of the light pulse resulted in variation of the maximum bubble volume and collapse time of the cavitation bubble.

Images of the bubble were observed with a Cooke Corporation ''FlashCam'' digital camera. This camera has an effective resolution of 752×240 pixels, and it is capable of recording up to 10 consecutive exposures on the same image frame, with varying integration times and delays between each exposure. A pulse delay generator (Stanford Research Systems model DG535) was used to trigger the camera at varying delays from the laser *Q*-switch pulse. These images were then recorded digitally. The acoustic center of a Brüel and Kjær type 8103 hydrophone was placed 30 mm from the location of the beam waist, and the resulting sound emission was conditioned with a Brüel and Kjær type 2635 charge amplifier and digitally acquired using a TekTronix TDS430A 2-Channel storage oscilloscope. The sampling rate was 2.5 million samples/second.

Figure 1(b) shows the setup for the creation of single cavitation bubbles in a vortical flow. The water tunnel has a circular contraction downstream of a series of flow management screens with area contraction ratio 6.4:1. The test section has a 22.9 cm (9 in.) diameter round inlet that is then faired into a rectangular test section with widely rounded corners. Four acrylic windows ($93.9\ \text{cm} \times 10.0\ \text{cm}$ viewing area) permit optical access to the test section flow. The flow

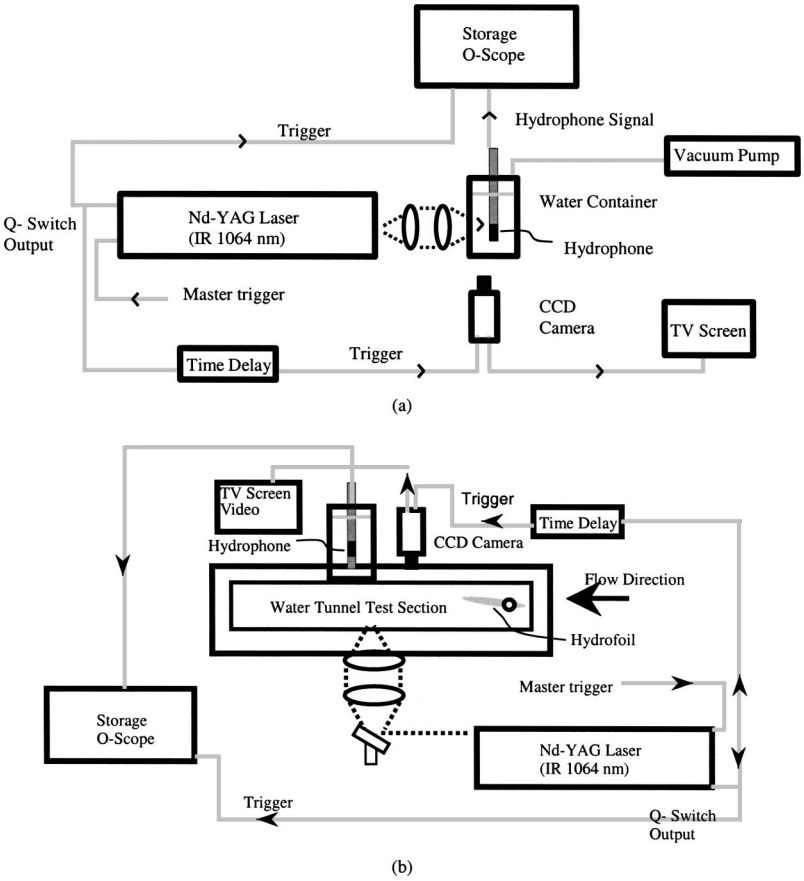

FIG. 1. (a) Schematic diagram of the quiescent cavitation bubble experiment; (b) the bubble–vortex interaction experiment. A single laser pulse is used to create a cavitation bubble in the bulk of the fluid. Images of the bubble are captured with a multiexposure digital camera, and the acoustic emission of the bubble is captured with a hydrophone.

in the test section can be operated at pressures from vapor pressure to approximately 200 kPa (30 Psia). The average velocity in the test section is variable up to 18 m/s (59.05 ft/s). A deaeration system can be used to vary the dissolved gas content of the flow, and the inlet water is filtered to 1 microns.

A vortical flow was created using a cambered hydrofoil mounted to one window of the test section. The hydrofoil has a rectangular planform of 9.5 cm span and 16.8 cm chord, and the tip of the hydrofoil was truncated with sharp edges. The hydrofoil mount allows continuous changes of the incident flow angle. A series of tip and trailing edge vortices will be shed near the tip, and these vortices will merge to form a single vortex within one-half chord length downstream of the hydrofoil trailing edge. The tip vortex produced by the hydrofoil can be visualized with developed cavitation, as shown in Fig. 2. Measurements of the bubble/vortex interactions were conducted using a free-stream velocity of 10 m/s and a variety of pressures. The dissolved oxygen content was measured with an Orion Model 810 dissolved oxygen meter. In order to reduce the number of free-stream nuclei, the free-stream gas content was reduced to below 1.5 ppm during the measurements.

Planar particle imaging velocimetry (PIV) was used to measure the vortical flow field at a station 9.0 cm downstream of the trailing edge. A double-pulsed light sheet 9 mm thick was created perpendicular to the mean flow direction using two pulsed Nd:YAG lasers (Spectra Physics model Pro-250 Series). 15-micron average diameter silver coated glass spheres (from Potters Industries) were used to seed the flow. An acrylic prism was optically mounted to a window of the test section for viewing of the light sheet with reduced optical distortion. The light sheet was imaged with a PIV image capture system produced by LaVision Inc. Double-pulsed images of the light sheet were acquired with a digital camera with 1280×1024 pixels. Optical distortion of the planar light sheet image was corrected through a calibration procedure that employed the imaging of a regular grid in the location of the light sheet plane. Velocity vectors were produced from the double-pulsed images using the LaVision im-

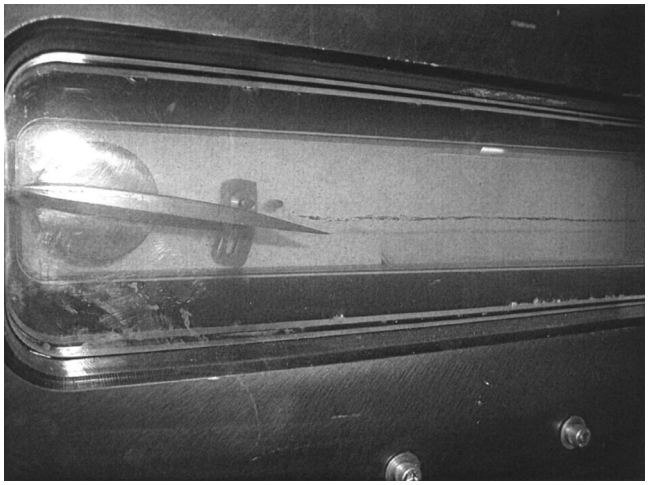

FIG. 2. Photograph of the hydrofoil in the water tunnel test section with developed tip-vortex cavitation with $U_\infty=10$ m/s, and $\sigma_\infty=1.4$. Flow is from left to right.

age analysis software DaVis6.0.4. Multipass processing with a final window size of 32×32 pixels was used with 12% window overlap in the final pass to produce 41×27 in-plane velocity vectors at 0.62 mm spacing. Since the camera-imaging plane was not parallel to the light sheet and it had an angular shift of 45° with the horizontal direction, this velocity component was corrected by knowledge of the camera angle and the tunnel free stream velocity.

Optically stimulated vortex-cavitation bubbles were created at the vortex centerline. As the cavitation number was reduced, discrete cavitation events occurred in the vortex core due to the capture of free-stream nuclei. This cavitation occurred at various locations along the vortex axis downstream of the location of vortex roll-up. However, at such low air contents, the event rate of this cavitation was quite low (<1 event per second). Vortex cavitation could then be stimulated by the introduction of a nucleus through a focused pulse of IR laser light near the axis of the vortex. By varying the free-stream pressure and laser energy, the initial size of the laser-induced bubble could be controlled. Images of the bubble's growth and collapse were captured with the pulse-synchronized digital camera after an appropriate delay, as described above. A small cast acrylic tank of water was placed in a pool of water on the top window of the test section, and in this tank the hydrophone was mounted. This produced an acoustic path between the cavitation event and the hydrophone of relatively matched impedance, although acoustic impedance mismatches between the acrylic and the water led to some attenuation and internal reflections.

III. RESULTS—CAVITATION IN QUIESCENT FLUID

As discussed in the introduction, several researchers have examined in detail the noise emitted by single cavitation events in quiescent fluid. They have shown that the amplitude and frequency content of the noise emission often greatly exceeds the capabilities of standard high-frequency hydrophones. In the present work, we first recreated the basic elements of these experiments to characterize our process of bubble formation and noise measurement by examining spherical and near-spherical bubbles created in the small tank. The effect of buoyancy can be characterized by the dimensionless quantity

$$\delta=\left(\frac{\rho g R_M}{\Delta P}\right)^{1/2}, \tag{6}$$

where g is the gravitational acceleration.[20] For sufficiently small values of δ, the effect of buoyancy can be neglected. Spherical bubbles corresponding to $\delta\approx0.01$ were created to characterize the hydrophone's ability to record the noise pulse produced by a single vaporous cavitation event.

Figure 3(a) shows multiple images of a near spherical bubble created with a laser light pulse. The acoustic pressure signal produced by the collapse of the spherical bubble is shown in Fig. 3(b). Two distinct sound pulses are detected. The first occurs during the rapid growth of the bubble volume when the bubble is created. Between the pulses, a slow reduction and increase in pressure is seen that corresponds to the relatively slow volume acceleration around the point of maximum bubble volume. The second pulse corresponds to the first collapse of the bubble. Figure 3(c) shows a time-expanded pressure trace recorded for the collapse of the bubble. The response is that of a damped harmonic oscillator. Also plotted is the response of a damped harmonic oscillator excited with a narrow pulse where the natural frequency and damping of the oscillator were chosen to best fit the measured voltage trace. The natural frequency of the oscillator, ϖ_n, was calculated to be 105 kHz, and the damping coefficient, ζ, was 0.18. The natural frequency is in good agree-

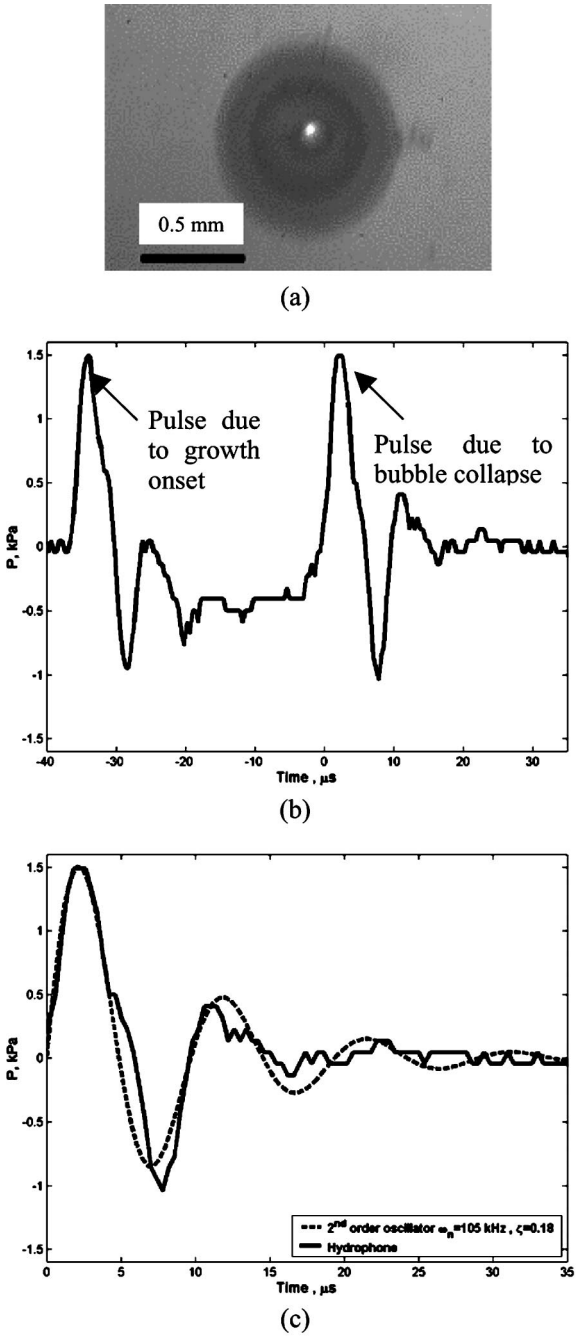

FIG. 3. (a) Five superposed exposures of a laser produced spherical cavitation bubble taken every 6 μs in a quiescent water container; (b) the resulting acoustic pressure trace recorded from the hydrophone; (c) the expanded hydrophone pressure trace produced upon bubble collapse (solid line) along with the second-order response of a damped harmonic oscillator to a Dirac-delta input with system $\omega_n=105$ kHz and damping ratio, $\zeta=0.18$ (dashed line).

ment with the specifications of the hydrophone, which reported a resonance frequency of nearly 109 kHz. Variation in laser input power changed the maximum bubble volume and the corresponding maximum pulse amplitude. However, the shape of the measured signal did not change. This was also true for bubbles undergoing nonspherical collapse as well. Rebounding bubbles and bubbles collapsing near a wall could sometimes produce two discernable pulses, due to bubble fission or the interaction of jet impingement with the wall. But, the temporal response of the hydrophone was always that of a damped harmonic oscillator responding to an impulsive pressure input.

The measurement illustrates that the high-frequency limit of the measured sound spectrum is limited by the hydrophone response, even though the hydrophone would be considered ''broadband'' relative to other commercially available hydrophones that are normally used in the hydrodynamic and marine engineering communities for measuring cavitation noise in test facilities. The pressure pulse created by the bubble may be approximated as $P_a(r,t)=P_S e^{-t/\theta}$ as discussed above. Pulse widths measured with optical and piezoelectric transducers are on the order of 10 to 100 ns.[18,19] An oscillator will respond to such a pulse with an underdamped response like that of Fig. 3(c). The peak amplitude of the response will be proportional to P_S, and the initial pulse width will be proportional to $1/\varpi_n$, the natural frequency of the hydrophone, if $1/\varpi_n \gg \theta$. The measured pulse widths were typically $10\pm 2\ \mu s \approx 1/\varpi_n$, which is consistent with the reported hydrophone natural frequency.

The actual acoustic impulse will be approximately $I(r_H)\approx P_S(r_H)\theta(r_H)$ at the location of the hydrophone, r_H. The *measured* acoustic impulse, I_m, will scale as

$$I_m(r_H)\approx \frac{P_S(r_H)}{\varpi_n}\theta(r_H)\varpi_n \approx P_S(r_H)\theta(r_H) \tag{7}$$

based on the dynamic impulse response function of the hydrophone. However, the measured peak pressure and the pulse duration will be approximated by $P_S(r_H)\theta(r_H)\varpi_n$ and $1/\varpi_n$, respectively. The maximum bubble volume accelerations achieved and the resulting amplitude and time scale of the emitted pressure wave is affected by the amount of noncondensable gas in the cavity, the collapsing pressure, and the topology of the collapsing bubble.

A scaling for the acoustic impulse can be derived from spherical bubble dynamics and energy conservation.[10] However, for highly deformed bubbles, it may be more appropriate to scale the impulse based on the initial energy of the collapsing bubble, E_M,

$$E_M=\tfrac{4}{3}\pi R_M^3 \Delta P. \tag{8}$$

The energy radiated away from the bubble after the collapse and rebound, E_R, is given by

$$E_R(r)=\eta_R \frac{4\pi r^2}{\rho c}\int_0^\infty P_a^2\, dt, \tag{9}$$

where η_R is the proportion of mechanical potential energy that is converted into acoustic energy. Vogel and Lauterborn[18] have shown that up to 90% of a bubble's mechanical energy can be converted to acoustic energy during the first collapse of spherical laser-produced cavitation bubbles, but the percentage can be reduced substantially if the collapsing bubble is nonspherical.

The measured peak shock pressure, P_S, is expected to scale with the maximum potential energy,

$$P_S \sim \frac{1}{2r_H}\left(\frac{\rho c E_R}{\pi\theta}\right)^{1/2} \sim \frac{1}{2r_H}\left(\frac{\eta_R \rho c E_M}{\pi\theta}\right)^{1/2}. \tag{10}$$

The acoustic impulse would then scale as

$$I_m(r_H)\sim \frac{1}{2r_H}\left(\frac{\eta_R \rho c E_M \theta}{\pi}\right)^{1/2} \sim \frac{1}{r_H}\left(\frac{1}{3}\eta_R \rho c \Delta P R_M^3 \theta\right)^{1/2}. \tag{11}$$

The functional relationship between θ and the other parameters of the flow is not straightforward, especially in the case of nonspherical collapse. The amount of noncondensable gas within the laser-produced bubble will vary due to variation in the process of bubble creation. Moreover, the amount of noncondensable gas at collapse will increase with increased maximum bubble volume, due to gas diffusion, and the minimum bubble volume and shape during the last phases of collapse will also vary. Consequently, variability of the measured impulse was observed given nominally constant laser-energy pulse input. However, the relationship between the impulse and the maximum bubble volume can be discerned.

IV. RESULTS—VORTEX CAVITATION

Next, the growth and collapse of nonspherical hydrodynamic cavitation is considered. Cavitation bubbles were produced in the vicinity of a strong line vortex. The free-stream velocity was fixed at 10 m/s. Figure 4(a) shows a vector map of the average planar vortical flow field measure perpendicular to the vortex axis produced after averaging 100 instantaneous flow fields. Figure 4(b) plots the average tangential velocity, $u_\theta(r)$, as a function of the distance from the vortex center, r, along with a fitted curve for a Gaussian vortex,

$$u_\theta(r)=\frac{\Gamma_0}{2\pi r}(1-e^{-\alpha(r/r_C)^2}). \tag{12}$$

Here, $\alpha\approx 1.255$ which makes r_C the ''core radius'' defined as the radius where the tangential velocity is maximum,

$$u_\theta(r_C)=\beta\frac{\Gamma_0}{2\pi r_C}, \tag{13}$$

where $\beta=0.715$. For the measured vortex, the fitted core radius was 5.6 mm and the strength Γ_0 was 0.290 m^2/s. Examination of the instantaneous images indicated that the vortex core did not wander significantly. The amplitude of wandering was consistently less than 15% of the core radius. Consequently, no correction for vortex wandering was needed.[21]

The pressure depression due to the vortex is given by

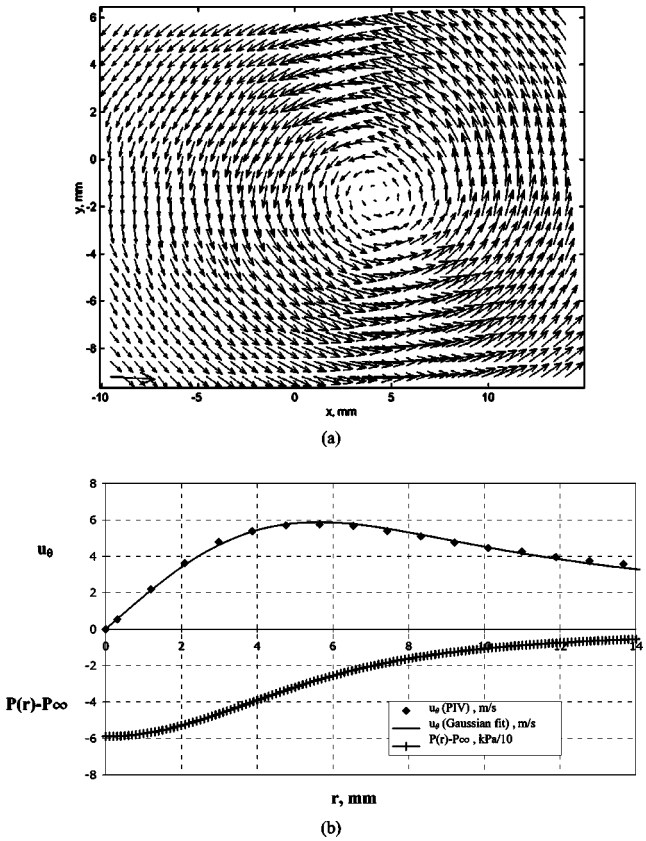

FIG. 4. (a) The average vector map of the flow perpendicular to the vortex axis 90 mm downstream of the tailing edge for $U_\infty = 10$ m/s; (b) the measured tangential velocity, $u_\theta(r)$, along with the velocity distribution for the Gaussian vortex with $r_C = 5.6$ mm and $\Gamma_0 = 0.290\ \mathrm{m^2/s}$ and the resulting calculated pressure depression, $P(r) - P_\infty$.

$$P(r) - P_\infty = \int_\infty^0 -\frac{\rho u_\theta^2(r)}{r}\,dr$$

$$= -\rho\left(\frac{\Gamma_0}{2\pi r_C}\right)^2\left(\frac{1}{2(r/r_C)^2}\right)$$

$$\times\begin{bmatrix} -1 + 2e^{-\alpha(r/r_C)^2} - e^{-2\alpha(r/r_C)^2} \\ -2\alpha(r/r_C)^2 Ei(\alpha(r/r_C)^2) \\ +2\alpha(r/r_C)^2 Ei(2\alpha(r/r_C)^2) \end{bmatrix}, \quad (14)$$

where $Ei(x)$ is the exponential integral function. The calculated radial pressure distribution for the vortex is also shown in Fig. 4(b). Here we are assuming that $\partial u_z/\partial r \approx 0$, where z corresponds to the direction along the vortex axis. Images of the bubbles in the vortex core indicate an axial velocity within 95% of the free-stream speed. The pressure at the axis of the vortex, $r = 0$, is given by

$$P_C = P_\infty - \eta\rho\left(\frac{\Gamma_0}{2\pi r_C}\right)^2, \quad (15)$$

where $\eta = 0.870$.

Bubbles captured by the vortex can cavitate if the core pressure is at or below vapor pressure. The free-stream cavitation number is defined as $\sigma_\infty = (P_\infty - P_V)/\frac{1}{2}\rho U_\infty^2$, where U_∞ is the free-stream velocity. Captured bubbles can grow if $P_C \leqslant P_V$, making the cavitation number at inception, $\sigma_{\infty,i}$,

$$\sigma_{\infty,i} \leqslant \frac{\eta}{2}\left(\frac{\Gamma_0}{\pi r_C U_\infty}\right)^2. \quad (16)$$

For the measured vortex, this corresponds to a free-stream cavitation number of 1.18.

Before creating bubbles within the vortex, near-spherical bubbles were created in the test section but without any flow. Figure 5(a) shows 10 superimposed images of the laser produced bubble taken with a time interval $\Delta t = 40\ \mu$s, and Fig. 5(b) shows the resulting acoustic pulse. The test-section static pressure was 31.1 kPa. Again, when the laser pulse initiates the bubble, an acoustic pulse is created. The bubble passes through its maximum volume and collapses, creating a second pulse of sound. The sound pulse created upon collapse is still limited by the response of the hydrophone. Numerous bubbles were created with fixed static pressure. The maximum size of the bubbles varied with the amount of laser-light energy deposited in the liquid. The laser pulse energy could be varied manually, but the actual amount of light absorbed by the liquid varied with the size and density of small particulates that were present in the focal volume of the laser during the pulse. This is the principal cause for the variability of the laser-induced bubbles.

The acoustic pulse created during the collapse of the bubble was recorded, and the acoustic impulse was calculated by time integration of the pressure pulse using the trapezoidal rule. The maximum bubble diameter was recorded with the digital camera. Figure 5(c) shows the variation of the acoustic impulse with the maximum bubble radius. While there is significant scatter, the data indicate that the impulse increases with the bubble volume, as expected. The spectrum analyzer was triggered to capture the noise signal produced by the collapse, although the residual echo from the initiation pulse was also present. To calculate the impulse, the average reverberant pattern was subtracted from the individual noise traces, and then the collapse pulse was identified and measured. This reverberant pattern from the bubble initiation pulse was highly repeatable when the bubble and hydrophone locations were fixed.

Figures 6, 7, and 8 present similar series of data for bubbles induced in the center of the vortex. Bubbles were created with three free-stream cavitation numbers, $\sigma_\infty = 2.15$, 1.73, and 1.49. With $\sigma_\infty = 2.15$, the bubbles collapse immediately after they are created, with $\sigma_\infty = 1.73$, the bubbles slowly collapse after growing along the vortex axis, and with $\sigma_\infty = 1.49$, the bubbles do not collapse but continue to grow along the axis.

The normalized acoustic impulse, $\hat{I}$, is defined as

$$\hat{I} = I\frac{r_H}{(\frac{1}{3}\eta_R\rho c\Delta P R_M^3\theta)^{1/2}}. \quad (17)$$

While the values of η_R and θ are unknown, the pulse width, θ, is expected to be on the order of 10 ns, for the case of spherical collapse.[18,19] The energy conversion efficiency, η_R, can vary with the collapse geometry of the bubble,[18] but is expected to be >60% for the bubbles under consideration. Figure 9 shows a plot of the normalized $\hat{I}$ against the bubble maximum radius with $\eta_R = 1$ and $\theta = 10$ ns for all the cases

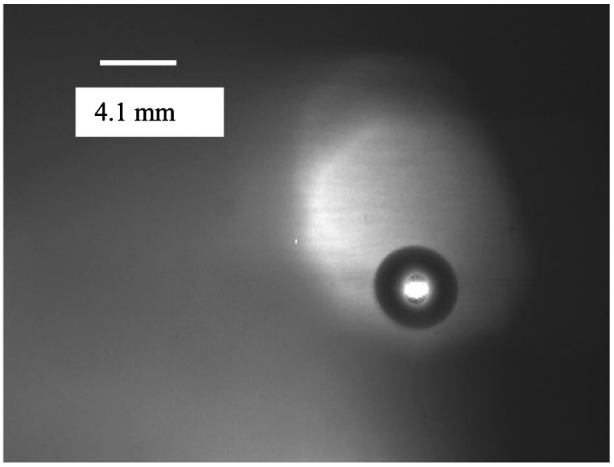

(a)

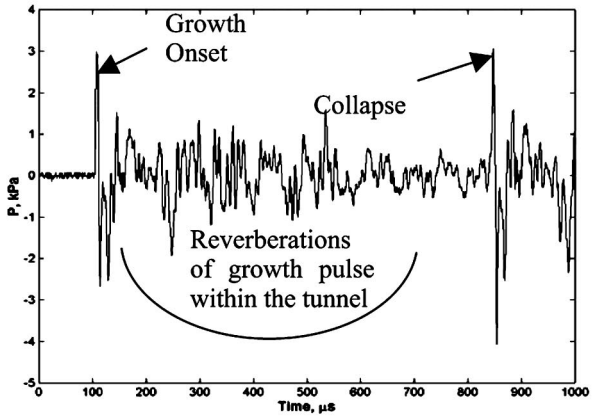

(b)

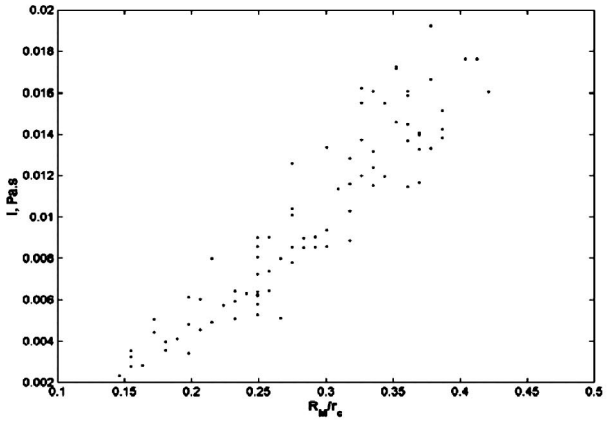

(c)

FIG. 5. (a) Ten images of a laser produced bubble taken 40 μs apart in the water tunnel test section without flow with $P_\infty = 31$ kPa; image dimensions (V 23.1 × H 31.9 mm); (b) the pressure–time trace recorded by the hydrophone; (c) the acoustic impulse created during bubble collapse versus the maximum bubble radius.

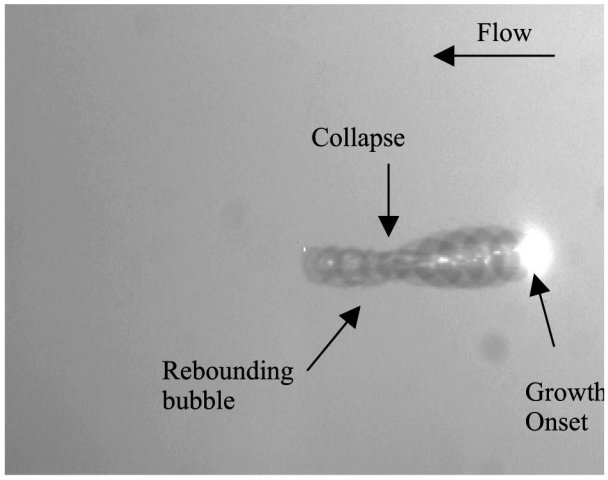

(a)

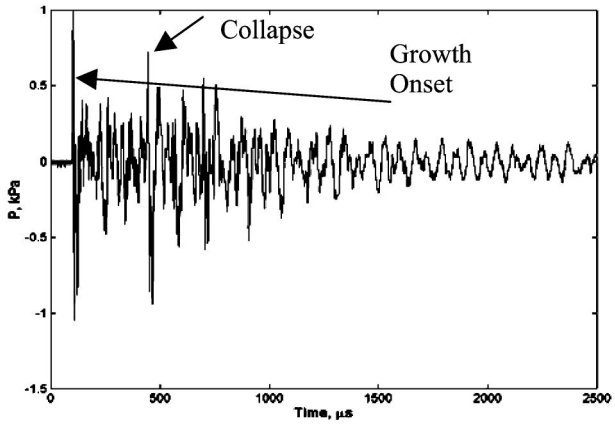

(b)

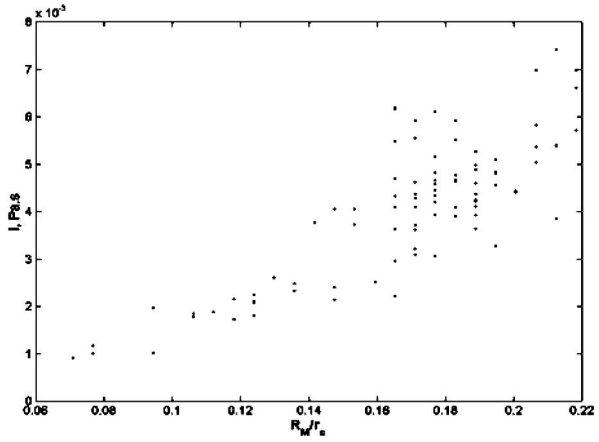

(c)

FIG. 6. (a) Ten exposures of a laser produced bubble created in the vortex taken 54 μs apart with $\sigma_\infty = 2.15$, $U_\infty = 10$ m/s; the bright region on the right results from pixel saturation from the original laser pulse; image dimensions (V 15.9 × H 21.0 mm); (b) the pressure–time trace recorded by the hydrophone; (c) the acoustic impulse created during bubble collapse versus the normalized maximum bubble radius (normalized by the vortex core radius).

studied. The normalized acoustic impulse of bubbles imploding in quiescent fluid as well as bubbles that are not greatly deformed by the vortex field ($\sigma_\infty = 2.82$ and $\sigma_\infty = 2.15$) are independent of the bubble maximum radius, as expected from a proper scaling. The deformed bubbles ($\sigma_\infty = 1.73$) have a normalized impulse that is clearly lower than the spherical and less deformed bubbles. If it is assumed here that the collapse pressure pulse width does not change with the bubble collapse geometry. The results then imply that highly deformed bubbles are less efficient (have lower η_R) in converting their mechanical energy into radiated acoustic pressure in comparison to the slightly deformed and spheri-

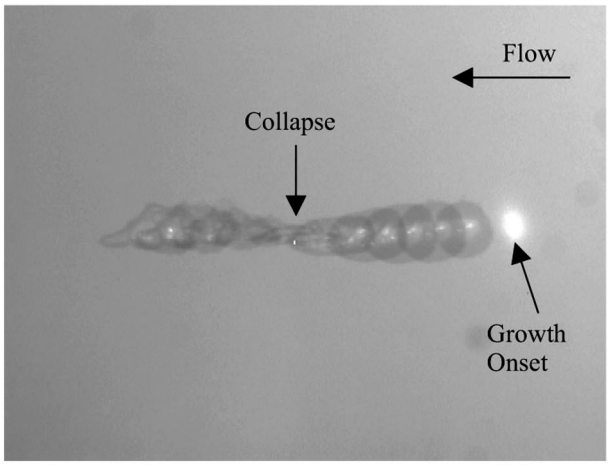

(a)

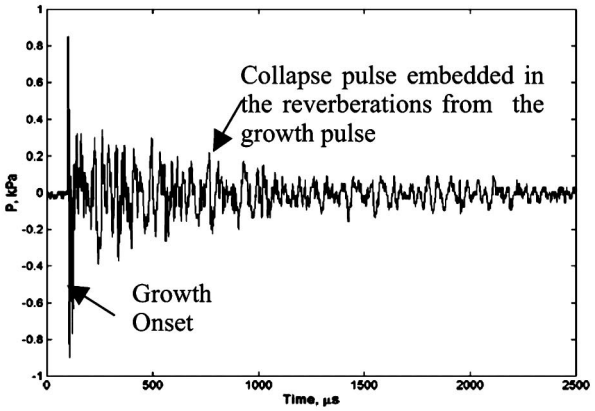

(b)

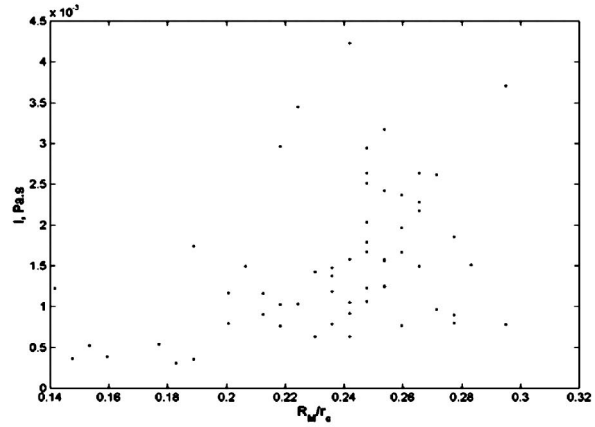

(c)

FIG. 7. (a) Ten exposures of a laser produced bubble created in the vortex taken 94 μs apart with $\sigma_\infty = 1.73$, $U_\infty = 10$ m/s; the bright region on the right results from pixel saturation from the original laser pulse; image dimensions (V 15.9$\times H$ 21.0 mm); (b) the pressure–time trace recorded by the hydrophone; (c) the acoustic impulse created during bubble collapse versus the normalized maximum bubble radius (normalized by the vortex core radius).

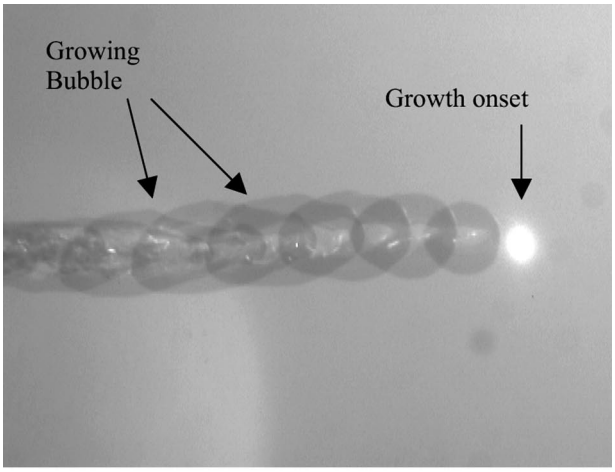

(a)

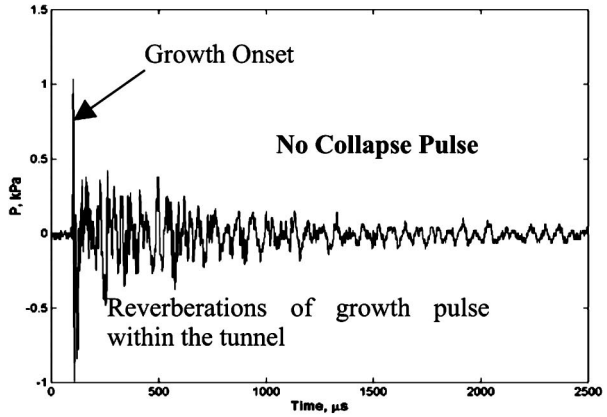

(b)

FIG. 8. (a) Ten exposures (last two exposures outside the frame) of a laser produced bubble created in the vortex taken 154 μs apart with $\sigma_\infty = 1.49$, $U_\infty = 10$ m/s; the bright region on the right results from pixel saturation from the original laser pulse; image dimensions (V 15.9$\times H$ 21.0 mm); (b) the pressure–time trace recorded by the hydrophone. At this cavitation number, the bubble continues to grow along the vortex axis after initiation with the laser.

cally imploding bubbles. Still in all of these highly deformed as well as spherical bubbles, resolution of the collapse pressure pulse is limited by the hydrophone response. The measured bubble collapse time (time from maximum volume to minimum volume) relative to the Rayleigh collapse is plotted in Fig. 10. This figure shows that highly deformed bubbles ($\sigma_\infty = 1.73$) have a longer collapse time than the more acoustic-efficient spherical bubbles, but the collapse time is on the same order.

A second case was considered where the bubbles did not collapse but continued to grow at $\sigma_\infty = 1.19$, and this is shown in Fig. 11. Here, the laser energy was greatly reduced, created only a small bubble that grew slowly under the influence of the low pressure in the vortex core. In this case, the nucleus grew slowly and no noise was detectable. The magnitude of the volume acceleration during the natural bubble growth is much smaller that the acceleration during the last stages of bubble collapse. As the bubble grows under the influence of the low vortex core pressure, $\dot{R} \sim \sqrt{-\Delta P/\rho}$, and $\ddot{R} \sim 0$. Consequently, the minimal amount of noise produced during the slow process of bubble growth was not detectable over the background noise created by the water tunnel flow.

Last, the pressure spectra recorded by the hydrophone for many bubble collapses was collected for the cases described above. The sound traces for 1000 events were col-

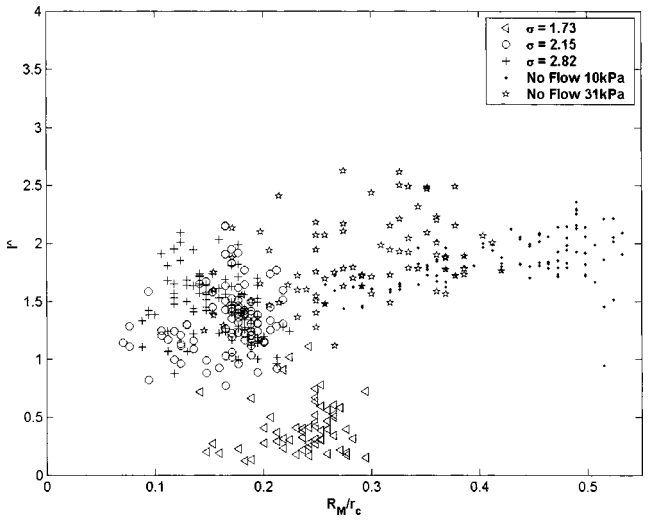

FIG. 9. The dimensionless acoustic impulse, $\hat{I}=I\ r_H/(\frac{1}{3}\eta_R\rho c\Delta P R_M^3\theta)^{1/2}$ versus the dimensionless maximum bubble radius, $\hat{R}_M=R_M/r_C$, for $P_\infty=10$ kPa without flow (●), $P_\infty=31$ kPa without flow (*), $\sigma_\infty=2.82$ (+), $\sigma_\infty=2.15$ (○), and $\sigma_\infty=1.73$ (◁). For this plot the acoustic conversion efficiency η_R was chosen to be 100%, and the collapse pulse width $\theta=10$ nanoseconds.

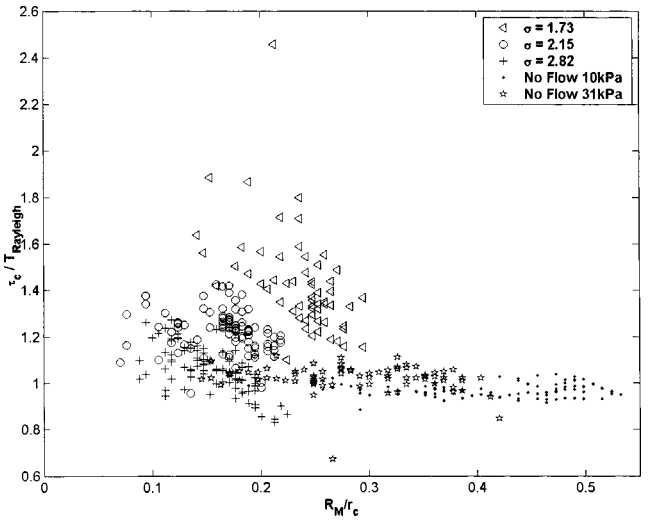

FIG. 10. The dimensionless collapse time $\tau_c/T_{\text{Rayleigh}}$ versus the dimensionless maximum radius, $\hat{R}_M=R_M/r_C$, for $P_\infty=10$ kPa without flow (●), $P_\infty=31$ kPa without flow (*), $\sigma_\infty=2.82$ (+), $\sigma_\infty=2.15$ (○), and $\sigma_\infty=1.73$ (◁).

lected. These are shown in Fig. 12. These spectra do not include the noise pulse produced by the initial bubble growth, but do include some of the reverberation resulting from bubble production. The case of the small bubble (sb) production corresponds to the background noise of the tunnel operating at 10 m/s. The spectral features below 30 kHz correspond to reverberant modes of the facility. As the impulse of the bubbles increases, the energy in the reverberations increases as well. Also, the energy in frequencies greater than 30 kHz increases, but the spectra is flat until 100 kHz. This is consistent with the input of a sharp impulse into the bandwidth-limited hydrophone.

V. DISCUSSION AND CONCLUSIONS

Acoustic transients by discrete hydrodynamic cavitation events were examined in both a quiescent and a vortical flow, and the following conclusions were found.

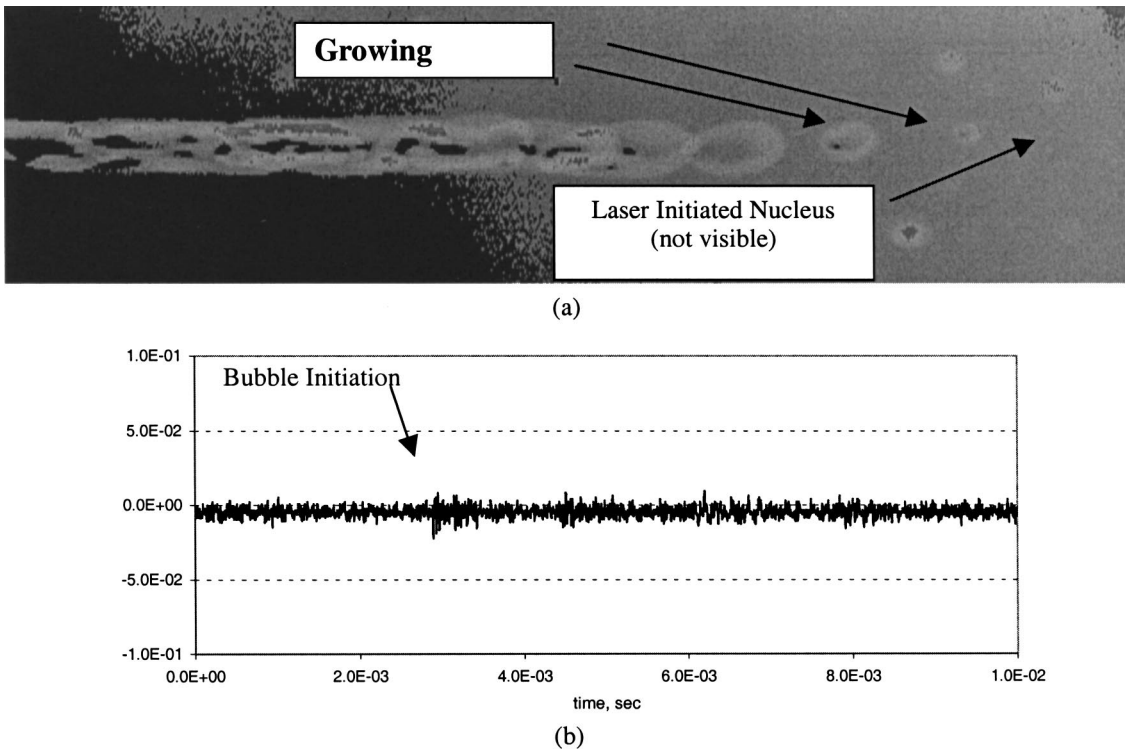

FIG. 11. (a) Ten exposures of a bubble created by a low energy laser pulse in the vortex taken 300 μs apart with $\sigma_\infty=1.19$; the initial nucleus is small and not visualized in the image; flow is from right to left; (b) the pressure–time series recorded by the hydrophone, which is equivalent to the baseline hydrophone signal before inception.

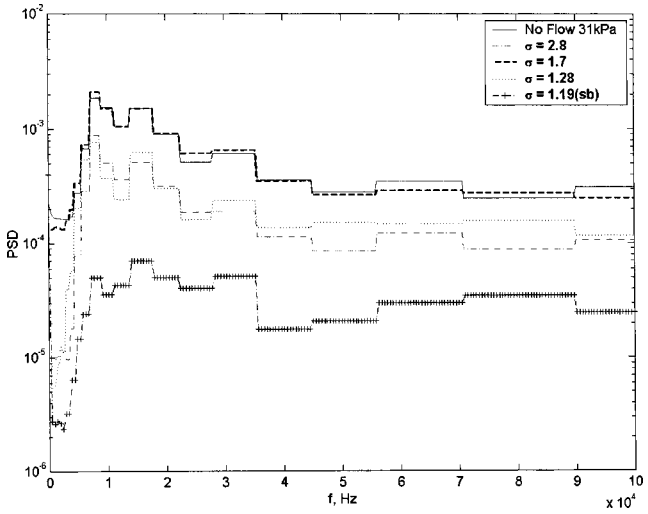

FIG. 12. Average power spectral density of the hydrophone signal for the five different cases corresponding to macroscopic bubbles created without test-section flow, and in the vortex for $\sigma_\infty = 2.8$, 1.70, 1.28. The spectrum of the noise recorded when the microscopic bubbles (sb) were created at $\sigma_\infty = 1.19$ is also included, and this is equivalent to the baseline spectrum without cavitation. The spectrum analyzer was triggered to analyze the noise signal produced due to the bubble collapse only, and the spectra from 1000 acoustic events were averaged.

(1) The hydrophone used was not capable of resolving the dynamics of the pressure pulse produced upon the collapse of a spherical cavitation bubble.
(2) The acoustic impulse produced by a collapsing bubble scales with the collapse pressure and the maximum volume, even for nonspherical collapse. The noise pulse produced by deformed collapsing bubbles is often sufficiently narrow to be unresolved by the hydrophone.
(3) The normalized impulse created by the collapse of spherical bubbles represents the most efficient collapse, converting potential mechanical energy into acoustic energy. Deformed bubbles collapse with less transfer efficiency.
(4) The noise produced by the natural bubble growth in the vortex is not measurable.

Vortex cavitation occurs when naturally occurring nuclei are captured by a concentrated vortex, and they grow and collapse. The results of this study suggest that significant noise is created only when the bubbles collapse, even if they are highly distorted. The noise produced is broadband, with a high-frequency cutoff beyond the bandwidth of most conventional hydrophones. However, the impulse created by the collapsing bubbles can be scaled with spherical bubble dynamics. Such scaling will provide the upper bound on the noise that a bubble of a given maximum volume can create when collapsing under a given pressure difference.

Finally, an unsteady pressure in the vortex core is required for a single nucleus to experience both rapid growth and collapse. The vortical flow employed in the present study is steady, and natural cavitation occurred only when the core pressure dropped below vapor pressure. At this point, captured nuclei continued to grow and ultimately filled the vortex core as the bubble convected downstream. The case of growth without collapse can be contrasted with cavitation accompanying more complicated vortical flows. In these flows variation in the local mean pressure, vortex–vortex interactions, and other flow unsteadiness can result in rapid growth and collapse of bubbles in the vortex core. Such cavitation occurs in turbulent shear flows and in the wake vortex system of complex turbomachinery. However, the results of this study suggest that spherical bubble dynamics can be used to scale the upper bound of the noise impulse produced by discrete cavitation events, even when the bubbles are quite deformed.

ACKNOWLEDGMENTS

This work was supported by a grant from the Office of Naval Research under Contract No. N00014-99-1-0307, Dr. K.-H. Kim, technical monitor.

[1] L. Rayleigh, "On the pressure developed in a liquid during the collapse of a spherical cavity," Philos. Mag. **34**, 94 (1917).
[2] R. Coles, *Underwater Explosions* (Princeton University Press, Princeton, NJ, 1948).
[3] M. Harrison, "An experimental study of single bubble cavitation noise," D.T.M.B. Rep. No. 815 DTNSRDC, Washington, DC, 1952.
[4] R. T. Knapp and A. Hollander, "Laboratory investigations of the mechanism of cavitation," Trans. ASME **70**, 419 (1948).
[5] H. M. Fitzpatrick and M. Strasberg, "Hydrodynamic sources of sound," Proceedings of the 1st Symposium on Naval Hydrodynamics, Washington, DC, 1956.
[6] W. K. Blake, *Mechanics of Flow-Induced Sound and Vibration* (Academic, New York, 1986), Vol. 2.
[7] R. H. Mellen, "Ultrasonic spectrum of cavitation noise in water," J. Acoust. Soc. Am. **26**, 356–360 (1954).
[8] F. R. Gilmore, "The growth and collapse of a spherical bubble in a viscous compressible liquid," Hydrodynamics Laboratory Report 26-4. California Institute of Technology, 1952.
[9] B. E. Noltingk and E. A. Neppiras, "Cavitation produced by ultrasonics," Proc. Phys. Soc. London, Sect. B **63**, 674–685 (1950).
[10] H. J. Baiter, "Aspects of cavitation noise," *Proceedings of the Symposium on High Powered Propulsion of Ships* (Wageningen, The Netherlands, 1974).
[11] W. K. Blake, M. J. Wolpert, and F. E. Geib, "Cavitation noise and inception as influenced by boundary-layer development on a hydrofoil," J. Fluid Mech. **80**, 617–640 (1977).
[12] M. F. Hamilton, D. E. Thompson, and M. L. Billet, "An experimental study of traveling bubble cavitation noise," J. Fluids Eng. Trans. ASME **108**, 241–247 (1986).
[13] S. L. Ceccio and C. E. Brennen, "Observation of the dynamics and acoustics of traveling bubble cavitation," J. Fluid Mech. **233**, 633–660 (1991).
[14] S. Kumar and C. E. Brennen, "A study of pressure pulse generated by traveling bubble cavitation," J. Fluid Mech. **255**, 541–564 (1993).
[15] C. I. Li and S. L. Ceccio, "Interaction of single traveling bubbles with the boundary layer and attached cavitation," J. Fluid Mech. **322**, 329–353 (1996).
[16] C. E. Brennen, "Fission of collapsing cavitation bubbles," J. Fluid Mech. **472**, 153–166 (2002).
[17] V. H. Arakeri and V. Shanmuganathan, "On the evidence of the effect of bubble interference on cavitation noise," J. Fluid Mech. **159**, 131–150 (1985).
[18] A. Vogel and W. Lauterborn, "Acoustic transient generation by laser-produced cavitation bubbles near solid boundaries," J. Acoust. Soc. Am. **84**, 719–731 (1988).
[19] T. J. Matula, I. M. Hallaj, R. O. Cleveland, L. A. Crum, W. C. Moss, and R. A. Roy, "The acoustic emissions from single-bubble sonoluminescence," J. Acoust. Soc. Am. **103**, 1377–1382 (1998).
[20] J. R. Blake and D. C. Gibson, "Cavitation bubbles near boundaries," Annu. Rev. Fluid Mech. **19**, 99–123 (1987).
[21] O. Boulon, M. Callenaere, J.-P. Franc, and J.-M. Michel, "An experimental insight into the effect of confinement on tip vortex cavitation of an elliptical hydrofoil," J. Fluid Mech. **390**, 1–24 (1999).

A high-resolution algorithm for wave number estimation using holographic array processing

Philippe Roux
Marine Physical Laboratory, Scripps Institute of Oceanography, La Jolla, California, and UC San Diego, San Diego, California

Didier Cassereau
Laboratoire Ondes et acoustique, ESPCI, Université Paris 7, France

André Roux
Laboratoire MMAS, CNRS FRE 2344, Université de Metz, France

(Received 17 October 2002; revised 4 September 2003; accepted 22 December 2003)

This paper presents an original way to perform wave number inversion from simulated data obtained in a noisy shallow-water environment. In the studied configuration an acoustic source is horizontally towed with respect to a vertical hydrophone array. The inversion is achieved from the combination of three ingredients. First, a modified version of the Prony algorithm is presented and numerical comparison is made to another high-resolution wave number inversion algorithm based on the matrix-pencil technique. Second, knowing that these high-resolution algorithms are classically sensitive to noise, the use of a holographic array processing enables improvement of the signal-to-noise ratio before the inversion is performed. Last, particular care is taken in the representations of the solutions in the wave number space to improve resolution without suffering from aliasing. The dependence of this wave number inversion algorithm on the relevant parameters of the problem is discussed. © *2004 Acoustical Society of America.* [DOI: 10.1121/1.1648321]

PACS numbers: 43.30.Bp, 43.30.Pc, 43.60.Pt [RAS] Pages: 1059–1067

I. INTRODUCTION

In underwater acoustics, the shallow-water zone is classically described as a waveguide. In a waveguide, the pressure field P_ω at a frequency is decomposed under the propagating modes as follows:

$$P_\omega(R) = \sum_{m=1}^{M} a_m \exp(ik_m R), \tag{1}$$

where M is the number of propagating modes, R is the source–receiver range, k_m is the wave number associated with mode number m, and a_m takes into account the amplitude dependence of the field at the source and receiver depths with respect to mode m. Even if the amplitude variable a_m depends on the distance R, we assume here that it varies much more slowly with R than the phase terms given in Eq. (1). For sake of simplicity, we consider that the attenuation in the waveguide is negligible, even though it could be simply introduced in the formalism as an exponential decreasing term $\exp(-\alpha_m R)$ for every mode m. Thus, the wave numbers k_m considered here are real. Furthermore, in the case of real data, we are also to take into account some frequency and range-dependent additive noise $N_\omega(R)$. Once again, to simplify the developments leading to the mathematical formulation of our inversion algorithm, we prefer not to include noise in Eq. (1), even though noisy data will be considered in the numerical simulations performed in Secs. III and IV.

The goal of our work is to determine the wave numbers k_m of a waveguide in the configuration described in Fig. 1. An acoustic source is horizontally towed with respect to a vertical hydrophone array. The towed source and the hydrophone array are coplanar. Many experiments have been performed in shallow-water environments in such a configuration in order to localize acoustic sources[1,2] or in the field of ocean-acoustic tomography.[3] In this paper, we restrict our goal to the estimation of the wave numbers. This means that we intend to determine k_m from the measurement of $P_\omega(R)$ on the hydrophone array, where the distance R between the source and the array varies from $R=R_0$ to $R=R_0+L$. No *a priori* knowledge of the waveguide characteristics is required.

Our inversion algorithm relies on the combination of three ingredients. First, we present a modified version of the Prony method.[4] The classical Prony inversion is based on an autoregressive algorithm which is replaced in our approach by a linear inversion. Second, knowing that this high-resolution technique is sensitive to noise, we improve the signal-to-noise ratio by coherently cumulating the acoustic field on the hydrophone array using holographic array processing. Last, we solve the classical ambiguity between resolution and aliasing by representing all multivalued solutions of the inversion in a histogram.

This paper is divided into three parts. The theoretical aspects of our inversion method are presented in Sec. II. We describe successively our modified version of the Prony algorithm, the use of holographic array processing, and the representation of the solutions in the wave number space. Section III deals with the application of this algorithm to a shallow-water waveguide using simulated data obtained from a horizontal synthetic aperture. In Sec. IV, the performance of the inversion algorithm is discussed with respect to the parameters of the problem.

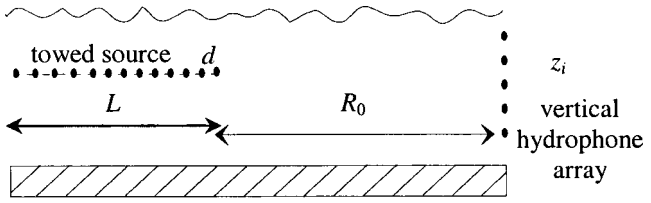

FIG. 1. Schematic of the waveguide. z_i is one element of the vertical hydrophone array. The source is towed from range R_0 to R_0+L, d is the elementary distance between two points as defined in the inversion algorithm.

II. THEORETICAL APPROACH

Wave number inversion finds many applications in underwater acoustics. For example, searching for the wave numbers of propagating modes in shallow water is an important step toward the determination of ocean-bottom properties. Beyond underwater acoustics, extracting k_m from Eq. (1) is a classical problem that can be generalized as a complex spectrum search. Thus, wave number inversion in a waveguide is formally equivalent to the determination of discrete frequencies in a multitone audible signal. Many theoretical, numerical, and experimental works have been performed in this area and it is beyond the task of this paper to make an overview of all these techniques. Focusing solely on underwater acoustics, wave number inversion was extensively investigated in the eighties using the classical Fourier and Hankel transforms[5–7] or correlation techniques.[8] Later on, high-resolution methods were developed such as the MUltiple SIgnal Classification technique,[9–12] the Prony method,[13] and the more sophisticated ESPRIT algorithm.[14,15] This latter is similar to the more general matrix-pencil method.[16,17] We would like also to mention the use of a global search technique such as simulated annealing as an efficient tool to obtain wave numbers in a waveguide.[18]

A. Inversion algorithm

In most high-resolution techniques, the aperture L on which the moving source is towed is decomposed into equally spaced points $R=R_0+nd$, which leads to the following decomposition of the field $P_\omega(R)$ received on any element of the array:

$$P_\omega(n)=\sum_{m=1}^{M}\tilde{a}_m[\exp(ik_md)]^n=\sum_{m=1}^{M}\tilde{a}_m z_m^n. \tag{2}$$

Taking $2N+1$ points (with $N>M$) in the aperture L, Eq. (2) can be written under a matrix form in which the variables $\tilde{a}_m$ and z_m are separated. We have

$$P_\omega=\begin{bmatrix} P_\omega(0) & P_\omega(1) & \cdots & P_\omega(N) \\ P_\omega(1) & P_\omega(2) & \cdots & P_\omega(N+1) \\ \cdots & \cdots & \cdots & \cdots \\ P_\omega(N) & P_\omega(N+1) & \cdots & P_\omega(2N+1) \end{bmatrix} = S_N A S_N^T, \tag{3}$$

with

$$S_N=\begin{bmatrix} 1 & 1 & \cdots & 1 \\ z_1 & z_2 & \cdots & z_M \\ \cdots & \cdots & \cdots & \cdots \\ z_1^N & z_2^N & \cdots & z_M^N \end{bmatrix} \quad \text{and} \quad A=\begin{bmatrix} \tilde{a}_1 & 0 & 0 \\ 0 & \cdots & 0 \\ 0 & 0 & \tilde{a}_M \end{bmatrix}. \tag{4}$$

It is then possible to apply a matrix-pencil method to P_ω, leading to the determination of z_m. This numerical technique is accurate but expensive in terms of computation time. Indeed, starting from a matrix representation of the data P_ω, it classically requires a generalized eigenvalue decomposition of P_ω.[16] One of the latest algorithms based on this approach is an eigenmatrix-pencil technique.[19] In the following, we will use this latest inversion algorithm as a comparison to our inversion technique.

Our inversion is based on a new formulation of the Prony algorithm.[4] Basically, starting from Eq. (2), we have to calculate M amplitudes $\tilde{a}_m$ and M phases z_m. Consequently, we need at least $2M$ equations to solve the problem, meaning that we need $2M$ points in the aperture L

$$\begin{cases} P_\omega(0)=\tilde{a}_1+\tilde{a}_2+\cdots+\tilde{a}_M \\ P_\omega(1)=\tilde{a}_1z_1+\tilde{a}_2z_2+\cdots+\tilde{a}_Mz_M \\ \cdots \\ P_\omega(M-1)=\tilde{a}_1z_1^{M-1}+\tilde{a}_2z_2^{M-1}+\cdots+\tilde{a}_Mz_M^{M-1} \\ \cdots \\ P_\omega(2M-1)=\tilde{a}_1z_1^{2M-1}+\tilde{a}_2z_2^{2M-1}+\cdots+\tilde{a}_Mz_M^{2M-1} \end{cases}. \tag{5}$$

Using a matrix representation of this system, it follows that

$$P_\omega=S_{2M-1}\tilde{A} \tag{6}$$

where S_{2M-1} is defined as in Eq. (4), and

$$P_\omega=\begin{bmatrix} P_\omega(0) \\ \cdots \\ P_\omega(2M-1) \end{bmatrix} \quad \text{and} \quad \tilde{A}=\begin{bmatrix} \tilde{a}_1 \\ \cdots \\ \tilde{a}_M \end{bmatrix}. \tag{7}$$

The Prony algorithm intends to solve Eq. (6). In itself, Eq. (6) is simpler than Eq. (3), from which the matrix-pencil method is derived, because the data are now written using a vector format instead of a matrix format. We now describe the classical Prony inversion method. First, we observe that the $2M$ equations in Eq. (5) are linear with respect to the unknowns $\tilde{a}_1,\ldots,\tilde{a}_M$. In the first step of the inversion, the system made of the first M equations is symbolically inverted (using Cramer's rule, for example) in order to obtain $\tilde{a}_1,\ldots,\tilde{a}_M$ as a function of the data $P_\omega(0),\ldots,P_\omega(M-1)$ and the phases $z_1,\ldots,z_M$. The next step consists of replacing $\tilde{a}_1,\ldots,\tilde{a}_M$ by their expressions in the last M equations. This leads to a new system of M relationships between the variables $z_1,\ldots,z_M$ and the data $P_\omega(0),\ldots,P_\omega(2M-1)$. This system has a strongly nonlinear behavior with respect to $z_1,\ldots,z_M$ and cannot be inverted directly with classical linear techniques. Among the various methods that can be addressed to solve this problem, there exists the extended Prony method.[20] According to this processing method, the z_m coefficients are proved to be the zeros of a polynomial, whose coefficients are calculated using an autoregressive procedure based on the data vector $P_\omega(0),\ldots,P_\omega(2M-1)$.

In Ref. 13, this step is based on a Burg algorithm,[21] coupled to a minimization method devoted to the determination of the appropriate order of the method.

In this paper, we propose an alternate description of the calculation steps. Although the main idea is still based on the Prony method, we give an interpretation of the coefficients of the polynomial in terms of a linear system that can be inverted using a large variety of numerical algorithms. Indeed, we show that the above M-equation system that is strongly nonlinear with respect to the variables $z_1,\ldots,z_M$ is linear with respect to the elementary symmetric polynomials (ESP) $E_1,\ldots,E_M$ of the unknowns $z_1,\ldots,z_M$. The ESPs are classically defined as[22]

$$E_1=\sum_{i=1}^{M} z_i, E_2=\sum_{i=1}^{M}\sum_{j=i+1}^{M} z_i z_j,\ldots,E_M=\prod_{i=1}^{M} z_i. \tag{8}$$

Using the ESP as unknowns, the last M equations of Eq. (5) can be rewritten as (see the Appendix for more details)

$$\begin{cases} P_\omega(M)=P_\omega(M-1)E_1-P_\omega(M-2)E_2 \\ \qquad +\cdots+(-1)^{M-1}P_\omega(0)E_M \\ P_\omega(M+1)=P_\omega(M)E_1-P_\omega(M-1)E_2 \\ \qquad +\cdots+(-1)^{M-1}P_\omega(1)E_M \\ \cdots \\ P_\omega(2M-1)=P_\omega(2M-2)E_1-P_\omega(2M-3)E_2 \\ \qquad +\cdots+(-1)^{M-1}P_\omega(M-1)E_M \end{cases}. \tag{9}$$

The ESP $E_1,\ldots,E_M$ are then easily found from (9) using Cramer's rule or any other inversion algorithm of linear systems. This linear inversion is simpler to implement than the autoregressive technique usually used in the extended Prony method. From there, it is well known that the solutions $z_1,\ldots,z_M$ are the roots of a polynomial of degree M whose coefficients are $E_1,\ldots,E_M$. Thus, as in the Prony method, the last step of the inversion consists of finding the roots of this polynomial, which has been addressed by various numerical algorithms. Whatever the technique used, though, finding the root of a polynomial is always a nonlinear process, which means that a small error on the polynomial coefficients (due to noisy data, for example) leads to a large error on the polynomial roots.

Once the solutions $z_1,\ldots,z_M$ are found, we also note that the inversion provides the amplitudes $\tilde{a}_1,\ldots,\tilde{a}_M$ from which the depth of the towed source can be determined [see Eq. (12)]. In this work, we restrict our analysis to the measurement of the phase variables $z_1,\ldots,z_M$ that are related to the wave numbers of the waveguide.

B. Holographic array processing

As every nonlinear inversion technique, the Prony algorithm is known to be highly sensitive to the signal-to-noise ratio.[13,20] In order to improve the quality of the inversion in the presence of noise, our ambition is to develop a coherent processing of the data by using a holographic approach of the acoustic field. Holographic array processing consists of cross-correlating the field coming from an unknown source to the field coming from a reference source.[23–25] Applying this principle to the vertical array shown in Fig. 1, we define a new variable $H_\omega(\Delta R)$ such that

$$H_\omega(\Delta R)=\sum_i P_\omega(z_i,R)^* P_\omega(z_i,R+\Delta R), \tag{10}$$

where the sum is performed on all the hydrophones of the vertical array. We assume now that the hydrophone array covers the whole water column. We also invoke the orthonormality relation between modes that leads to

$$\sum_i a_m(z_i)a_n(z_i)\propto\delta_{mn}, \tag{11}$$

where δ_{mn} is the Kronecker symbol classically defined by $\delta_{mn}=0$ if $m\neq n$ and $\delta_{mm}=1$ otherwise. This relationship is only an approximation here because the hydrophone array does not completely sample the field in the bottom of the waveguide. From Eqs. (1), (10), and (11), we obtain

$$H_\omega(\Delta R)\approx\sum_{m=1}^{M} b_m\exp(ik_m\Delta R), \quad \text{and} \quad b_m\approx\frac{u_m^2(z_s)}{k_m R}, \tag{12}$$

which is formally equivalent to Eq. (1). In Eq. (12), $u_m(z_s)$ is the amplitude of mode m at the source depth z_s. The advantage of using the new variable $H_\omega(\Delta R)$ based on holographic array processing is that it cumulates coherently all the information obtained from the towed source on the hydrophone array. This leads to an increase of the signal-to-noise ratio, which is a major issue when working with nonlinear inversion technique. The coherent gain (in dB) on the signal-to-noise ratio that results from holographic array processing is on the order of $10\log_{10}(K)$, where K is the number of hydrophones in the vertical array. We note also that, even in the case of a vertical hydrophone array that does not cover the water column, Eq. (12) is still valid but the amplitude coefficients b_m have a more complicated form.

As previously, the inversion is based on the decomposition of the aperture ΔR into n equally spaced points ($\Delta R=nd$), leading to

$$H_\omega(n)=\sum_{m=1}^{M} b_m\exp(ik_m d)^n=\sum_{m=1}^{M} b_m z_m^n. \tag{13}$$

Equation (13) is then formally equivalent to Eq. (2), on which the Prony inversion is performed as described in Sec. II A.

C. Representation of the multivalued solutions

The combination of our modified Prony algorithm and the holographic array processing results in an original way to obtain the phase variables $z_m=\exp(ik_m d)$ from $2M$-equally spaced points in a waveguide. However, the determination of the corresponding values of k_m is not straightforward, even if the distance d is known. The reason is that the phase of a complex number is classically multivalued, and we have

$$k_m=\frac{\text{phase}(z_m)}{d}\,\text{modulo}\left[\frac{2\pi}{d}\right]. \tag{14}$$

This means that an infinite number of potential solutions exist for every wave number k_m, even if only one is effectively acceptable. Wave number inversion has then to face the following trade-off. When large values of d are used to

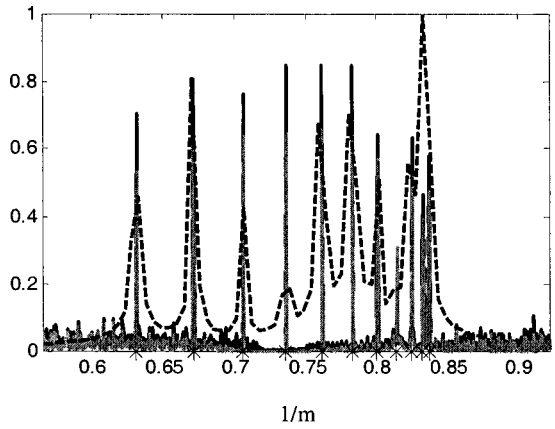

FIG. 2. Histogram of the solutions obtained with our inversion technique (black curve) and the matrix pencil method (gray curve). The source is towed on an aperture $L=1200$ m. The hydrophone array is made of $K=19$ equally spaced elements. The signal-to-noise ratio on every hydrophone of the array is 100 dB. The dashed curve corresponds to the incoherently averaged and normalized spatial Fourier transform of the field received from the source on the hydrophone array. The black stars on the x axis are the exact wave numbers.

perform the inversion, the large synthetic horizontal aperture enables one to resolve the wave numbers that are close together. However, large values of d lead to aliasing, which means that, according to Eq. (14), there are multiple potential values of k_m in the interval $[\min(k_m),\max(k_m)]$. On the other hand, aliasing is avoided if

$$d \leqslant \frac{2\pi}{(\max(k_m)-\min(k_m))}, \tag{15}$$

but the resolution provided by the synthetic horizontal aperture in this case may not allow separation of close wave numbers.

In order to solve this aliasing-resolution trade-off and find out the exact wave numbers, we have developed the following algorithm:

(i) we choose a small distance d and $2M$ equally spaced points in the horizontal aperture L covered by the towed source such that $(2M-1)d<L$;
(ii) we calculate $H(n)$ for $n=0,...,2M-1$ as in Eq. (13), and run the modified Prony inversion described in Sec. II A;
(iii) we obtain $z_1,\ldots,z_M$, from which we deduce the multivalued wave numbers $k_m=(\text{phase}(z_m)+2p\pi)/d$, where p is an integer;
(iv) steps (i)–(iii) are run again for larger values of d until $(2M-1)d=L$ and we represent a histogram of all solutions obtained for the wave numbers.

The idea of step (iv) of this algorithm is to cumulate the multivalued wave numbers obtained for a wide range of d's into a histogram. All the multivalued solutions of a given k_m follow Eq. (14), meaning that they are incommensurate with respect to d. For two different d's that are not multiple of each other, the only two same multivalued solutions correspond to the good value of k_m. As a consequence, the histogram of all possible multivalued solutions should exhibit some strong peaks only for the true values of the wave numbers (Fig. 2).

III. APPLICATION TO A SHALLOW-WATER ENVIRONMENT

In the following, the acoustic field is simulated at 200 Hz in a 60-m deep Pekeris waveguide using the Kraken normal-mode code. The bottom sound speed, density, and attenuation are 2000 m/s, 2000 kg/m^3, and 0.05 dB/λ, respectively. The source is towed on an aperture L from a range $R_0=5000$ m at a 15-m depth. The hydrophone array covers the whole water column and is made of K equally spaced elements. Uncorrelated white noise is added on the array. The acoustic field received from the source is sampled every 1 m on the source track L. Though unrealistic, the Doppler shift associated with the source motion is not considered here.

After wave number inversion performed as described in Sec. II, one typical histogram of the solutions is plotted in Fig. 2 in the case of a high signal-to-noise ratio. There are $M=11$ propagating modes in the waveguide, and the algorithm has been run between $d=20$ m and $d=57$ m. If the histogram reaches the value of 1, the corresponding wave number has been found as a suitable solution for all possible values of d and sets of $2M$ points. The bin between two spatial frequencies in the histogram is $(k_{\max}-k_{\min})/300$, where $k_{\max}$ and $k_{\min}$ are the larger and the smaller wave numbers. The sharp peaks visible in Fig. 2 correspond to the exact wave numbers. The residual noise around the peaks comes from the multivalued solutions issued from z_m.

In Fig. 2, we compare the results provided by our inversion technique to those obtained by the eigenmatrix-pencil method following the steps described in Secs. II B and II C. We also represent the results obtained by a spatial Fourier transform of the field emitted from the aperture L and received on the hydrophone array. We observe that the two high-resolution methods give similar results that are much more accurate than those obtained with the linear spatial Fourier transform. More particularly, our inversion technique is able to distinguish the wave numbers that correspond to modes 1–3 even though they are much closer in the k space than the resolution cell $2\pi/L$ given by the aperture L. Moreover, despite the fact that the source depth is close to a zero of mode 4, we note that the corresponding wave number is found with the two high-resolution methods in Fig. 2.

In order to understand the way our algorithm works, we have plotted in Fig. 3 the histogram of the solutions for different values of the elementary distance d. As expected from Sec. II C, results are quite different from one value of d to another. For a small d, the aperture $(2M-1)d$ is much smaller than the total aperture L, which means that a lot of sets of $2M$ points are available for the inversion. Moreover, the modulo $2\pi/d$ is larger, and less incorrect multivalued solutions are found, i.e., the inversion does not suffer from aliasing. On the other hand, it is obvious that a larger horizontal aperture $(2M-1)d$ provides a better inversion for the wave numbers related to the lower-order modes. This analysis is confirmed in Figs. 3(a) to (d). If $18\text{ m}<d<22$ m [Fig. 3(a)], the histogram exhibits sharp peaks for the higher-order

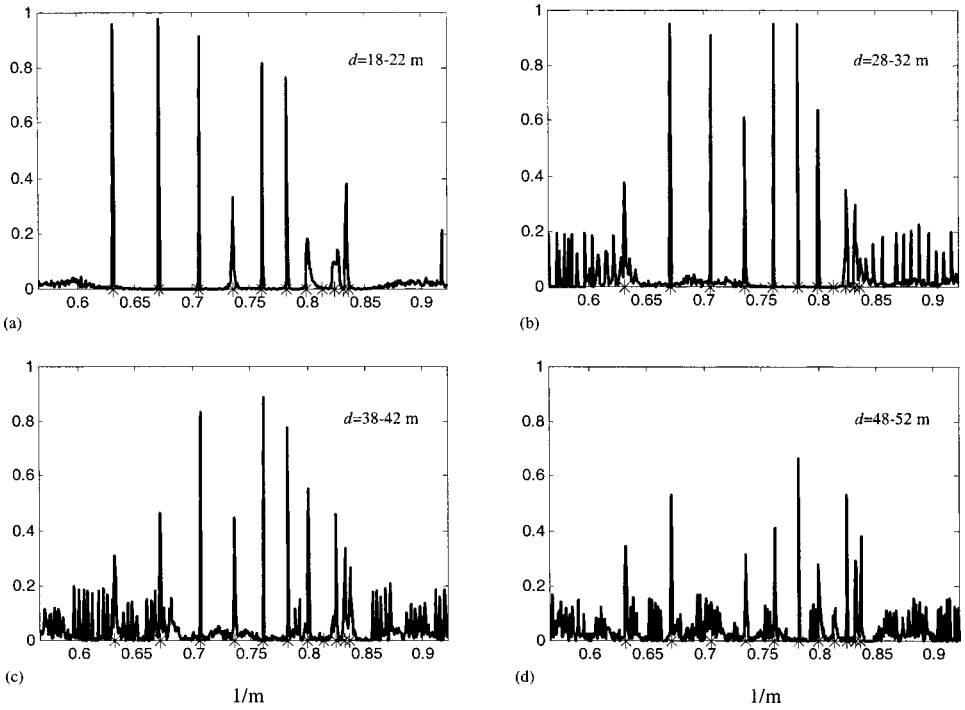

FIG. 3. Histograms of the solutions obtained with our inversion technique for different intervals of elementary distance d: (a) $18\,\mathrm{m}<d<22\,\mathrm{m}$; (b) $28\,\mathrm{m}<d<32\,\mathrm{m}$; (c) $38\,\mathrm{m}<d<42\,\mathrm{m}$; (d) $48\,\mathrm{m}<d<52\,\mathrm{m}$. The waveguide is the same as in Fig. 2. The source is towed at a 15-m depth on an aperture $L=1200\,\mathrm{m}$. The hydrophone array covers the whole water column and is made of 19 equally spaced elements. The signal-to-noise ratio on every hydrophone of the array is 30 dB. The black stars on the x axis are the exact wave numbers.

modes and a low noise, but the inversion is not able to distinguish mode 1 from mode 2. If $48\,\mathrm{m}<d<52\,\mathrm{m}$ [Fig. 3(d)], the histogram is more noisy but the lower-order modes are well defined. By running the algorithm on a large interval for d, as in Fig. 2 where $20\,\mathrm{m}<d<57\,\mathrm{m}$, the goal is to make a satisfactory trade-off between the histogram noise and the determination of every wave number.

We now investigate the computation time that is required for the inversion. Here, the choice of the inversion algorithm is of importance. Indeed, starting from $2M$ points among the raw data P_ω, the inversion has to be performed many times using different elementary distances d in order to provide the wave numbers as described in Sec. II C. In Fig. 2 and later in Fig. 4, we see that our modified Prony method and the eigenmatrix pencil roughly lead to the same results in terms of accuracy and noise sensitivity. However, the structure of these two algorithms is different. The matrix-pencil technique requires a generalized eigenvalue decomposition, while our modified Prony method only needs a linear inversion and a rooting procedure. Moreover, there exists some fast algorithm to solve nonsymmetric Hankel systems as Eq. (9),[20] whereas it does not appear to be anything similar for speeding up the matrix-pencil. Roughly speaking, if our Prony algorithm made use of a fast algorithm of order $O((2M)^2)$ operations while the matrix-pencil required order $O((2M)^3)$ operations, this would appear as a clear advantage.

IV. DISCUSSION

The aim of this section is to study the sensitivity of our wave number inversion to the relevant parameters of the problem. Because our technique relies on the finding of the roots of a polynomial, it is strongly nonlinear. Nonlinear inversions are more accurate than linear ones, as seen in Fig. 2, but they are also more sensitive to the signal-to-noise ratio (SNR). The quality of the inversion globally depends then on the signal-to-noise ratio on each receiver, on the number of hydrophones K in the array, and on the length of the aperture L. We define the accuracy of the inversion by two criteria. First, the histogram exhibits sharp peaks for the higher-order modes that correspond to the exact wave numbers. Second, the inversion is able to separate the wave numbers for the lower-order modes.

In Fig. 4, we present histograms obtained for different values of the aperture length L, the number of hydrophones K, and the SNR. In every studied case, the wave numbers that correspond to the higher-order modes are found with an excellent accuracy. On the other hand, it appears difficult to separate the wave numbers related to modes 1–2 without a high SNR [SNR=30 dB in Fig. 4(a)] or a large aperture [$L=1500\,\mathrm{m}$ in Fig. 4(e)]. Comparing Figs. 2 and 4(a), we note that a very high SNR is needed to obtain the fourth wave number, which is hardly excited by the source. From Figs. 4(a) and (c), we show that the results are improved when the number of hydrophones on the array is increased. This confirms the gain in terms of SNR provided by the holographic array processing performed on the hydrophone array. For an SNR=15 dB and only one hydrophone on the array, the results are clearly degraded, as shown in Fig. 4(d), i.e., the peaks are lower and two wave numbers are not found. Finally, we see in Figs. 4(e) and (f) that increasing/decreasing the aperture L plays the same role as increasing/decreasing the SNR.

Up to now, two parameters are needed to run the inversion algorithm: first, the number of propagating modes M in the waveguide in order to derive the system of $2M$ equations to be solved [Eq. (9)]. Second, the elementary distance d is required to obtain the wave numbers k_m from the phase z_m [Eq. (14)]. What happens if M and d are unknown?

In Fig. 5, we present histograms of solutions obtained in

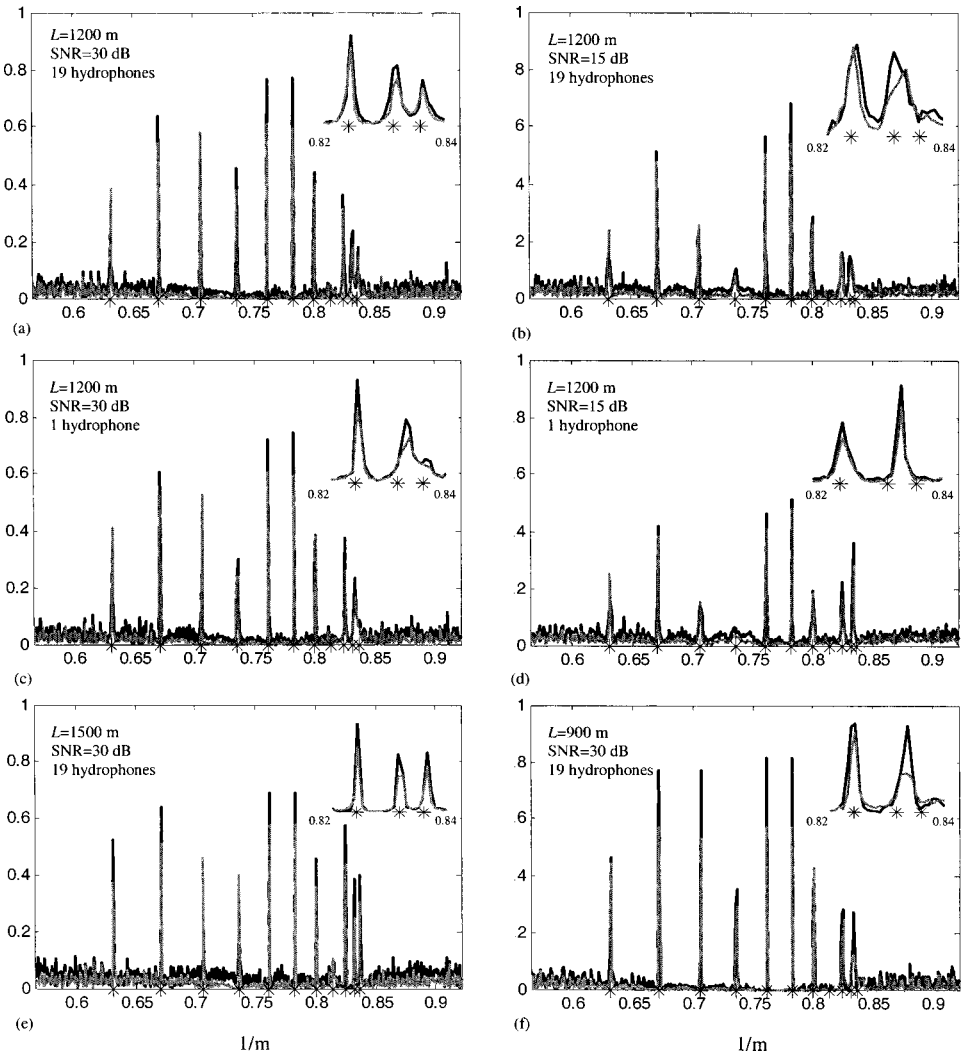

FIG. 4. Histogram of the solutions obtained with our inversion technique (black curve) and the matrix pencil method (gray curve): (a) SNR=30 dB, $L=1200$ m, $K=19$ hydrophones; (b) SNR=15 dB, $L=1200$ m, $K=19$ hydrophones; (c) SNR=30 dB, $L=1200$ m, $K=1$ hydrophone; (d) SNR=15 dB, $L=1200$ m, $K=1$ hydrophone; (e) SNR=30 dB, $L=1500$ m, $K=19$ hydrophones; (f) SNR=30 dB, $L=900$ m, $K=19$ hydrophones. A zoom between $k=0.82\ \mathrm{m}^{-1}$ and $k=0.84\ \mathrm{m}^{-1}$ is plotted in the upper-right corner of each figure. The black stars on the x axis are the exact wave numbers.

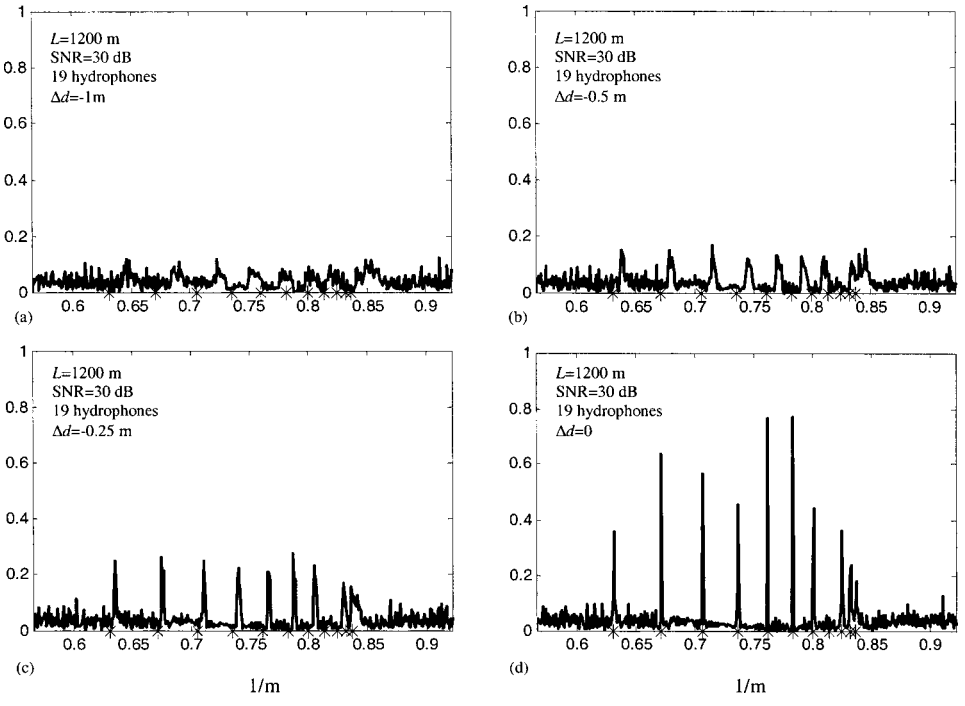

FIG. 5. Histogram of the solutions obtained with our inversion technique in the case of a mismatch Δd on the elementary distance d. The inversion is performed with $20\ \mathrm{m}<\tilde{d}<57\ \mathrm{m}$ and (a) $\Delta d=-1$ m; (b) $\Delta d=-0.5$ m; (c) $\Delta d=-0.25$ m; (d) $\Delta d=0$. The waveguide is the same as in Fig. 2. The source is towed at a 15-m depth on an aperture $L=1200$ m. The hydrophone array is made of $K=19$ equally spaced elements. The SNR on every hydrophone of the array is 30 dB. The black stars on the x axis are the exact wave numbers.

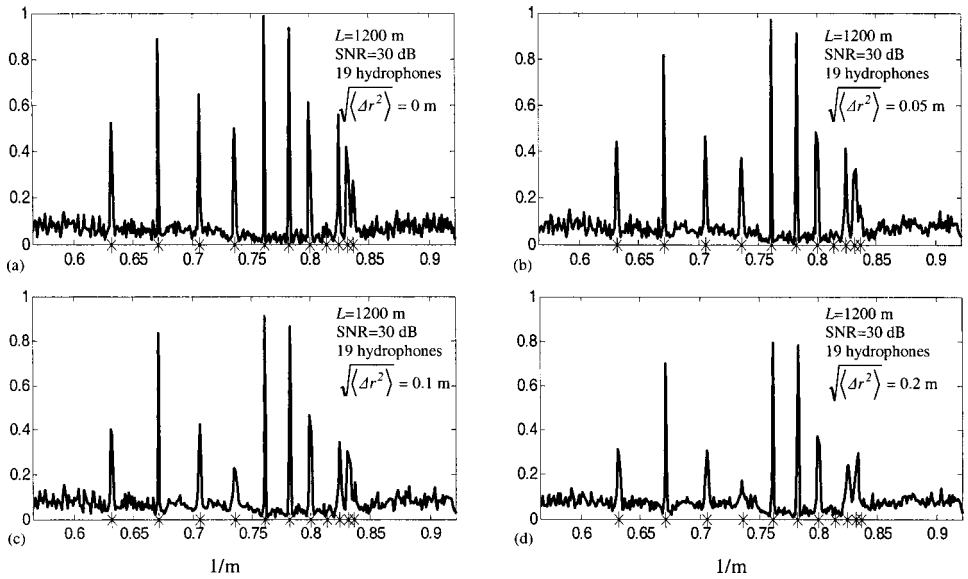

FIG. 6. Histogram of the solutions obtained with our inversion technique in the case of a fluctuating velocity v. A random Gaussian-distributed distance Δr is added every meter on the source track of distance L. The standard deviation $\sqrt{\langle \Delta r^2 \rangle}$ is, respectively (a) 0 m; (b) 0.05 m; (c) 0.1 m; and (d) 0.2 m. The waveguide is the same as in Fig. 2. The source is towed at a 15-m depth on an aperture $L=1200$ m. The hydrophone array is made of $K=19$ equally spaced elements. The SNR on every hydrophone of the array is 30 dB. The black stars on the x axis are the exact wave numbers.

the case of a mismatch on the distance d. This means that the value of $\tilde{d}$ used during stage (iii) of the inversion algorithm is not the correct value d issued from the computation of the acoustic field. We define the mismatch as $\Delta d=\tilde{d}-d$. Practically speaking, this problem will be encountered when the acoustic data are continuously recorded from a moving source whose speed is constant but unknown. Indeed, during a time interval δt in the acoustic data record, the elementary distance covered by the source is $d=v\,\delta t$. An incorrect estimation of the source speed v leads then to a mismatch Δd. Histograms in Figs. 5(a) to (c) show that the inversion is very sensitive to a small error Δd. The sharp peaks that correspond to the exact wave numbers when $\Delta d=0$ in Fig. 5(d) rapidly disappear even for a small perturbation $\Delta d/d$. There are two ways to look at these results. This inversion algorithm may be described as an accurate way to measure the speed of a moving source in a shallow-water environment. On the other hand, this sensitivity may also cause the inversion to be completely impractical.

However, the simulation showing how wave number inversion is impacted by the error Δd may be too pessimistic. Assuming a consistent wrong velocity produces an accumulating error in the position of the source. In Fig. 6, inversion results are presented when the source velocity is simulated to fluctuate around the mean velocity v. To do so, a random Gaussian-distributed distance Δr is introduced at every point of the source track, $P_\omega(z_i,R)$ now being replaced by $P_\omega(z_i,R+\Delta r)$. This means that the synthetic aperture created by the moving source is now irregularly sampled.[21] Interestingly enough, we observe in Fig. 6 that our inversion algorithm is quite robust to such error.

In Fig. 7, we present histograms of the solutions when the number of modes in the waveguide is unknown. The idea is then to perform the four stages (i)–(iv) of the inversion

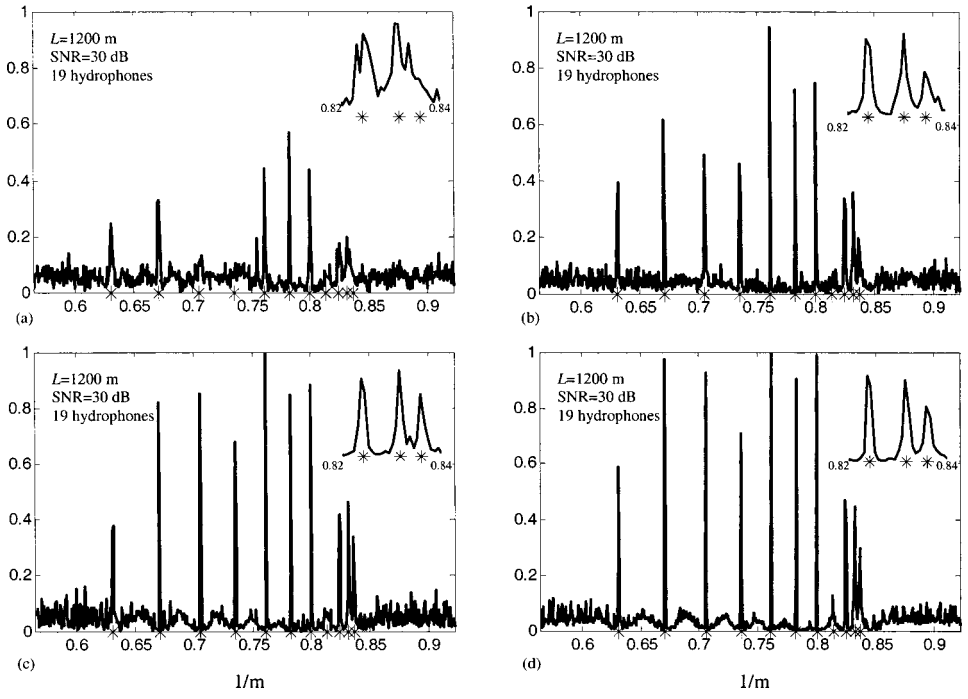

FIG. 7. Histogram of the solutions obtained with our inversion technique if the number of modes in the waveguide is *a priori* unknown. The inversion is performed with (a) $M=7$ modes and $60\text{ m}<d<92$ m; (b) $M=11$ modes and $30\text{ m}<d<57$ m; (c) $M=15$ modes and $25\text{ m}<d<41$ m; (d) $M=19$ modes and $15\text{ m}<d<32$ m. The waveguide is the same as in Fig. 2. The source is towed at a 15-m depth on an aperture $L=1200$ m. The hydrophone array is made of $K=19$ equally spaced elements. The SNR on every hydrophone of the array is 30 dB. A zoom between $k=0.82\text{ m}^{-1}$ and $k=0.84\text{ m}^{-1}$ is plotted in the upper-right corner of each figure. The black stars on the x axis are the exact wave numbers.

algorithm using a guess M for the number of modes. In this paper, the acoustic field is computed in a waveguide with 11 propagating modes. As expected, the inversion gets poor results when only $M=7$ modes are used [Fig. 7(a)]. The peak's amplitude is low and some wave numbers are not found. However, it is surprising to see that the results significantly improve when the inversion is performed with more modes than the actual number of modes in the guide, as shown in Figs. 7(c) and (d). With $M=19$ modes, the peaks are sharper, the wave numbers related to the low-order modes are well separated, and even the fourth wave number is obtained. Actually, working with M larger than the correct number of modes leads to the use of more equations than unknowns in Eq. (5). The fact that some equations are redundant tends to reduce the noise on the determination of the ESP $E_1,\ldots,E_M$ of the phase unknowns $z_1,\ldots,z_M$. This induces an effective increase of the SNR before running the nonlinear part of the inversion which is the search of the roots of a degree-M polynomial. The price to pay when working with a larger M is obviously an increase of the computational time. The upper limit for the number of modes M to be used in the inversion is reached when a too-small number of elementary distances d is available in the aperture L. Even if the inversion is still accurate, the histogram then becomes noisy as in Fig. 3(d) because of the multivalued solutions of the wave numbers.

V. CONCLUSION

The ambition of this work was threefold. First, we have presented in a classical configuration an original technique to perform wave number estimation based on the Prony method and the use of the elementary symmetric polynomials. Second, knowing that this high-resolution technique is classically sensitive, we improved the signal-to-noise ratio by using holographic array processing on the hydrophone array. Last, we solved the classical trade-off between resolution and aliasing by representing all the multivalued solutions of the inversion in a histogram. We then practically performed wave number estimation from the recording of the acoustic field on an aperture L. We studied the performance of this algorithm with respect to the important parameters of the problem: the horizontal aperture on which the array is towed, the SNR, and the number of hydrophones in the vertical array.

APPENDIX: USE OF ESPS

The goal of our modified Prony algorithm is to solve the system of $2M$ equations (5) where the M principal unknowns are the z_m and the M auxiliary unknowns are the $\tilde{a}_m$.

$$\begin{cases} P_\omega(0)=\tilde{a}_1+\tilde{a}_2+\cdots+\tilde{a}_M \\ P_\omega(1)=\tilde{a}_1 z_1+\tilde{a}_2 z_2+\cdots+\tilde{a}_M z_M \\ \cdots \\ P_\omega(M-1)=\tilde{a}_1 z_1^{M-1}+\tilde{a}_2 z_2^{M-1}+\cdots+\tilde{a}_M z_M^{M-1} \\ \cdots \\ P_\omega(2M-1)=\tilde{a}_1 z_1^{2M-1}+\tilde{a}_2 z_2^{2M-1}+\cdots+\tilde{a}_M z_M^{2M-1} \end{cases} . \quad (5')$$

The principal unknowns are the ones we want to extract. Each equation is linear with respect to the auxiliary unknowns $\tilde{a}_m$.

The inversion technique is divided into three steps.

(1) We write symbolically the $\tilde{a}_m$ as a function of the z_m and $P_\omega(0),\ldots,P_\omega(M-1)$ using the first M equations of (5).
(2) By replacing the expression of the $\tilde{a}_m$ into the last M equations of (A1), we obtain M linear equations (9) between the elementary symmetric polynomials (ESP) $E_1,\ldots,E_M$ of the unknowns $z_1,\ldots,z_M$

$$\begin{cases} P_\omega(M)=P_\omega(M-1)E_1-P_\omega(M-2)E_2 \\ \qquad +\cdots+(-1)^{M-1}P_\omega(0)E_M \\ P_\omega(M+1)=P_\omega(M)E_1-P_\omega(M-1)E_2 \\ \qquad +\cdots+(-1)^{M-1}P_\omega(1)E_M \\ \cdots \\ P_\omega(2M-1)=P_\omega(2M-2)E_1-P_\omega(2M-3)E_2 \\ \qquad +\cdots+(-1)^{M-1}P_\omega(M-1)E_M \end{cases} . \quad (9')$$

This system is solved using linear inversion techniques in order to obtain $E_1,\ldots,E_M$ as a function of the data $P_\omega(0),\ldots,P_\omega(2M-1)$.

(3) The z_m are then the roots of a polynomial of degree M whose coefficients are the ESP $E_1,\ldots,E_M$.

The difficult part in the mathematical development of this inversion technique is to obtain the linear system (9) at stage 2. The calculation steps are long and tedious as soon as $M>2$. As an example, we describe in more details below the case $M=2$.

Case $M=2$

In this case, we obviously suppose $z_1\neq 0$, $z_2\neq 0$, and $z_1\neq z_2$ (otherwise it follows $M=0$ or $M=1$). Using Cramer's rule in stage 1, we obtain $\tilde{a}_1$ and $\tilde{a}_2$ as a function of z_1, z_2 and $P_\omega(0)$, $P_\omega(1)$:

$$\tilde{a}_1=\frac{\begin{vmatrix} P_\omega(0) & 1 \\ P_\omega(1) & z_2 \end{vmatrix}}{\begin{vmatrix} 1 & 1 \\ z_1 & z_2 \end{vmatrix}}=\frac{z_2P_\omega(0)-P_\omega(1)}{z_2-z_1} \quad \text{and} \quad \tilde{a}_2$$
$$=\frac{\begin{vmatrix} 1 & P_\omega(0) \\ z_1 & P_\omega(1) \end{vmatrix}}{\begin{vmatrix} 1 & 1 \\ z_1 & z_2 \end{vmatrix}}=\frac{P_\omega(1)-z_1P_\omega(0)}{z_2-z_1}. \quad (A1)$$

We then replace $\tilde{a}_1$ and $\tilde{a}_2$ in the last two equations of (5), which leads to

$$\begin{cases} P_\omega(2)=P_\omega(1)(z_1+z_2)-P_\omega(0)z_1z_2 \\ P_\omega(3)=P_\omega(0)(z_1+z_2)-P_\omega(1)z_1z_2 \end{cases}. \quad (A2)$$

The new variables are now the two ESP of z_1 and z_2, $E_1=z_1+z_2$ and $E_2=z_1z_2$. The system (A2) is linear with respect to E_1 and E_2. A Cramer-type inversion gives

$$E_1=\frac{(P_\omega(2))^2-P_\omega(1)P_\omega(3)}{(P_\omega(1))^2-P_\omega(0)P_\omega(2)} \quad \text{and} \quad E_2$$

$$=\frac{P_\omega(1)P_\omega(2)-P_\omega(0)P_\omega(4)}{(P_\omega(1))^2-P_\omega(0)P_\omega(2)}. \tag{A3}$$

Note that we must have $(P_\omega(1))^2-P_\omega(0)P_\omega(2)\neq 0$ because of the initial statement $z_1\neq 0$, $z_2\neq 0$, and $z_1\neq z_2$.

Finally, Eq. (A3) determines z_1 and z_2 as the solutions of the polynomial of degree two

$$[(P_\omega(1))^2-P_\omega(0)P_\omega(2)]X^2-[P_\omega(1)P_\omega(2)$$
$$-P_\omega(0)P_\omega(4)]X+(P_\omega(2))^2-P_\omega(1)P_\omega(3)=0. \tag{A4}$$

[1] A. B. Baggeroer, W. A. Kuperman, and H. Schmidt, "Matched field processing: Source localization in correlated noise as an optimum parameter estimation problem," J. Acoust. Soc. Am. **83**, 571–587 (1988).

[2] H. Y. Chen and I.-T. Lu, "Matched mode processing schemes of a moving point source," J. Acoust. Soc. Am. **92**, 2039–2050 (1992).

[3] A. Tolstoy, O. Diachok, and L. N. Frazer, "Acoustic tomography via matched field processing," J. Acoust. Soc. Am. **89**, 1119–1162 (1991).

[4] S. M. Kay and S. L. Marple, "Spectrum analysis—A modern perspective," Proc. IEEE **69**, 1380 (1981).

[5] G. V. Frisk and J. F. Lynch, "Shallow water waveguide characterization using the Hankel transform," J. Acoust. Soc. Am. **76**(1), 205–216 (1984).

[6] S. D. Rajan, J. F. Lynch, and G. V. Frisk, "Perturbative inversion methods for obtaining bottom geoacoustic parameters in shallow water," J. Acoust. Soc. Am. **82**(3), 998–1017 (1987).

[7] J. F. Lynch, S. D. Rajanand, and G. V. Frisk, "A comparison of broadband and narrow-band modal inversions for bottom geoacoustic properties at a site near Corpus Christi, Texas," J. Acoust. Soc. Am. **89**(2), 648–665 (1991).

[8] S. Stergiopoulos and E. J. Sullivan, "Extended towed array processing by an overlap correlator," J. Acoust. Soc. Am. **86**(1), 158–171 (1989).

[9] S. D. Rajan and S. D. Bhatta, "Evaluation of high-resolution frequency estimation methods for determining frequencies of eigenmodes in shallow water acoustic field," J. Acoust. Soc. Am. **93**(1), 378–389 (1993).

[10] J. V. Candy and E. J. Sullivan, "Model-based passive ranging," J. Acoust. Soc. Am. **85**, 2472–2480 (1989).

[11] H. M. Chouhan and G. V. Anand, "Normal mode wave-number estimation using towed array," J. Acoust. Soc. Am. **93**, 1807–1814 (1993).

[12] L. G. Krasny and S. P. Antonyuk, "Wave-number estimation in an ocean waveguide," J. Acoust. Soc. Am. **102**(5), 2697–2704 (1997).

[13] E. C. Shang, Y. P. Wang, and Z. Y. Huang, "Waveguide characterization and source localization in shallow water waveguides using the Prony method," J. Acoust. Soc. Am. **83**, 103–108 (1988).

[14] R. Roy, A. Paulraj, and T. Kailath, "ESPRIT—A subspace rotation approach to estimation of parameters of cissoids in noise," IEEE Trans. Acoust., Speech, Signal Process. **34**(10), 1340–1342 (1986).

[15] R. Roy and T. Kailath, "ESPRIT—Estimation of signal parameters via rotational invariance techniques," IEEE Trans. Acoust., Speech, Signal Process. **37**(7), 984–995 (1989).

[16] Y. Hua and T. K. Sarkar, "Matrix pencil method for estimating parameters of exponentially damped/undamped sinusoids in noise," IEEE Trans. Acoust., Speech, Signal Process. **38**(5), 892–900 (1990).

[17] J. Laroche, "The use of the matrix pencil method for the spectrum analysis of musical signals," J. Acoust. Soc. Am. **94**(4), 1958–1965 (1993).

[18] M. D. Collins and W. A. Kuperman, "Nonlinear inversion for ocean-bottom properties," J. Acoust. Soc. Am. **92**(5), 2770–2783 (1992).

[19] I.-T. Lu, R. C. Qiu, and J. Kwak, "A high-resolution algorithm for complex spectrum search," J. Acoust. Soc. Am. **104**(1), 288–299 (1998).

[20] L. L. Scharf, *Statistical Signal Processing: Detection, Estimation, and Time Series Analysis* (Addison-Wesley, Reading, MA, 1991), pp. 483–513.

[21] R. Bos, S. de Waele, and P. M. Broersen, "Autoregressive spectral estimation by application of the Burg algorithm to irregularly sampled data," IEEE Trans. Instrum. Meas. **51**(6), 1289–1294 (2002).

[22] P. Samuel and O. Zariski, *Commutative Algebra* (Springer, New York, 1997), Vol. II.

[23] P. D. Mourad, D. Rouseff, R. P. Porter, and A. Al-Kurd, "Source localization using a reference wave to correct for oceanic variability," J. Acoust. Soc. Am. **92**(2), 1031–1039 (1992).

[24] A. Al-Kurd and R. P. Porter, "Performance analysis of the holographic array processing algorithm," J. Acoust. Soc. Am. **97**(3), 1747–1763 (1995).

[25] M. Siderius, D. R. Jackson, D. Rouseff, and R. P. Porter, "Multipath compensation in shallow water environments using a virtual receiver," J. Acoust. Soc. Am. **102**(6), 3439–3449 (1997).

Travel time stability in weakly range-dependent sound channels

Francisco J. Beron-Vera[a] and Michael G. Brown
RSMAS/AMP, University of Miami, Miami, Florida 33149

(Received 1 July 2003; revised 10 December 2003; accepted 22 December 2003)

Travel time stability is investigated in environments consisting of a range-independent background sound-speed profile on which a highly structured range-dependent perturbation is superimposed. The stability of both unconstrained and constrained (eigenray) travel times is considered. Both general theoretical arguments and analytical estimates of time spreads suggest that travel time stability is largely controlled by a property ω' of the background sound-speed profile. Here, $2\pi/\omega(I)$ is the range of a ray double loop and I is the ray action variable. Numerical results for both volume scattering by internal waves in deep-ocean environments and rough surface scattering in upward-refracting environments are shown to confirm the expectation that travel time stability is largely controlled by ω'. © *2004 Acoustical Society of America.* [DOI: 10.1121/1.1648320]

PACS numbers: 43.30.Cq, 43.30.Ft, 43.30.Pc [RAS] Pages: 1068–1077

I. INTRODUCTION

Measurements made during the Slice89 propagation experiment,[1,2] performed in the eastern North Pacific Ocean, suggested that in that environment the near-axial energy is more strongly scattered than the energy corresponding to the steeper rays. Similar behavior was subsequently observed in measurements made during the AET experiment,[3,4] also performed in the eastern North Pacific Ocean. Motivated in large part by these observations, several studies[5–8] have been carried out to investigate the dependence of ray stability on environmental parameters. All of these studies have focused on ray stability in either physical space (depth, range) or phase space (depth, angle). The present study extends the earlier work by considering the sensitivity of ray travel times to environmental parameters. Our focus on travel times is more closely linked to the Slice89 and AET observations than the earlier sensitivity studies inasmuch as both sets of measurements were made in depth and time at a fixed range.

In this study we consider ray motion in environments consisting of a range-independent background on which a range-dependent perturbation, such as that produced by internal waves in deep-ocean environments, is superimposed. We consider the influence of the background sound-speed structure on both unconstrained and constrained (eigenray) measures of travel time spreads. Surprisingly, the conclusion of this work is that travel time stability is largely controlled by the same property[8] of the background sound-speed structure that controls ray trajectory stability. Although this work was motivated by the deep-ocean measurements mentioned above, the results presented apply to a much larger class of problems. To illustrate this generality, we include numerical simulations of ray scattering by a rough surface in upward-refracting environments.

The remainder of the paper is organized as follows. In Sec. II the equations on which our analysis is based are presented. These are the coupled ray/travel time equations written in terms of both the usual phase-space variables and action–angle variables. In Sec. III two simple expressions for unconstrained travel time spreads in terms of action–angle variables are derived (trivially) and shown to be in good agreement with numerical simulations. In Sec. IV an expression for constrained (eigenray) time spreads is derived, again using action–angle variables, and shown to be in good agreement with numerical simulations. The same result was recently derived using a different argument by Virovlyansky.[9] The combination of the results presented in Secs. III and IV provides strong evidence that, quite generally, travel time spreads are largely controlled by the same property $\omega' = \mathrm{d}\omega/\mathrm{d}I$ of the background sound-speed structure. Here, $2\pi/\omega(I)$ is the range of a ray double loop and I is the ray action variable. In Sec. V our results are summarized and discussed. Two explanations for why ω' controls travel time spreads are given.

II. BACKGROUND

A. Theory

This paper is concerned with the scattering of sound, in the geometric limit, by weak inhomogeneities. Consistent with these assumptions, our analysis is based on the one-way form (cf., e.g., Ref. 10 and references therein) of the *ray equations*

$$\frac{\mathrm{d}p}{\mathrm{d}r} = -\frac{\partial h}{\partial z}, \quad \frac{\mathrm{d}z}{\mathrm{d}r} = \frac{\partial h}{\partial p}, \tag{1a}$$

and *travel time equation*

$$\frac{\mathrm{d}T}{\mathrm{d}r} = p\frac{\mathrm{d}z}{\mathrm{d}r} - h, \tag{1b}$$

where

$$h(p,z,r) = -\sqrt{c^{-2}(z,r) - p^2}. \tag{2}$$

Here, r, which is the independent variable, denotes range; z is depth; p is vertical ray slowness; T is travel time; and $c(z,r)$ is sound speed. Equations (1) constitute a canonical Hamiltonian system with h the Hamiltonian; (z,p) the generalized coordinate–conjugate momentum pair; and T play-

[a]Author to whom correspondence should be addressed. Electronic mail: fberon@rsmas.miami.edu

ing the role of the mechanical action. It follows from Eqs. (1a) and $dz/dr=\tan\varphi$, where the ray angle φ is measured relative to the horizontal, that $cp=\sin\varphi$. We shall assume that the sound speed is the sum of a range-independent background component, $C(z)$, and a (weak) range-dependent perturbation, $\delta c(z,r)$. This allows us to write the Hamiltonian as the sum of a range-independent (integrable) component, $H(p,z)=-\sqrt{C^{-2}(z)-p^2}$, plus a range-dependent (nonintegrable) perturbation, $\delta h(p,z,r)\approx-\delta c(z,r)/[C^3(z)H(p,z)]$.

In the background environment, i.e., when $\delta c=0$, the ray motion is naturally described using *action–angle variables* (I,ϑ). The transformed ray equations maintain their Hamiltonian structure with Hamiltonian $\bar{H}(I)=H(p(I,\vartheta),z(I,\vartheta))$, namely

$$\frac{dI}{dr}=-\frac{\partial\bar{H}}{\partial\vartheta}=0,\quad \frac{d\vartheta}{dr}=\frac{\partial\bar{H}}{\partial I}=\omega(I). \tag{3a}$$

The travel time equation, in turn, reads

$$\frac{dT}{dr}=I\omega-\bar{H}+\frac{d}{dr}(G-I\vartheta). \tag{3b}$$

Here

$$G(z,I)=\pi I\pm\int_{z_-}^{z}d\xi\sqrt{C^{-2}(\xi)-H^2(I)}, \tag{4}$$

where the $\pm$ sign applies to $\pm p$, is the (multiply valued) generating function of the *canonical transformation* that relates implicitly the new variables (I,ϑ) to the original variables (p,z) through

$$p=\frac{\partial G}{\partial z},\quad \vartheta=\frac{\partial G}{\partial I}. \tag{5}$$

The action variable is defined by

$$I=\frac{1}{2\pi}\oint dz\,p=\frac{1}{\pi}\int_{z_-}^{z_+}dz\sqrt{C^{-2}(z)-H^2}, \tag{6}$$

where the loop integral is taken along an isoline of H and thus $z_\pm$ corresponds to the ray upper $(+)$ and lower $(-)$ turning depths.

Equations (3a) show that in the background environment each ray trajectory forms a closed loop in (p,z) space, or phase space, on which I is a constant. The line integral in Eq. (6) can also be expressed as an integral over the enclosed area in phase space. It follows from Eq. (6) that $I=0$ for the axial ray and that I increases monotonically as axial ray angle increases. For rays making multiple loops, G advances by $2\pi I$ and ϑ advances by 2π each time a loop is completed. Following a ray, the difference $G-I\vartheta$ makes small oscillations about zero. The term $d(G-I\vartheta)/dr$ in (3b) gives small endpoint contributions to T. The fractional contributions from this term to T are non-negligible only at very short range. The contribution from this term to several of the analytical travel time-spread estimates presented below is zero. In those cases where this contribution is not identically zero, it is very small.

In range-dependent environments, i.e., with $\delta c\neq0$, action–angle variables can be defined using the same relations as in the unperturbed environment.[11] This is in fact possible because the range-independent canonical transformation $(p,z)\mapsto(I,\vartheta)$ depends solely on the geometry of phase space, characterized by the symplectic two-form $dp\wedge dz$, which is the same with $\delta c=0$ or $\delta c\neq0$; it does *not* depend on the Hamiltonian itself (cf., e.g., Ref. 12). It is important to realize, however, that in the presence of a range-dependent perturbation δc, the action variable I as defined in Eq. (6) is *not* constant anymore because H is *not* a first integral of (1). The Hamiltonian in the new variables takes the form $\bar{H}(I)+\delta\bar{h}(I,\vartheta,r)$, where $\bar{H}(I)=H(p(I,\vartheta),z(I,\vartheta))$ and $\delta\bar{h}(I,\vartheta,r)=\delta h(p(I,\vartheta),z(I,\vartheta),r)$. The ray and travel time equations then read

$$\frac{dI}{dr}=-\frac{\partial\delta\bar{h}}{\partial\vartheta},\quad \frac{d\vartheta}{dr}=\omega+\frac{\partial\delta\bar{h}}{\partial I}, \tag{7a}$$

and

$$\frac{dT}{dr}=I\frac{d\vartheta}{dr}-\bar{H}-\delta\bar{h}+\frac{d}{dr}(G-I\vartheta). \tag{7b}$$

In realistic ocean environments Eqs. (7) are difficult to apply because in such environments the dependence of δh on I and ϑ is not known explicitly. Because of this, most of the results presented below assume that the environment is piecewise range independent. These results follow from piecewise application of Eqs. (3). This procedure eliminates difficulties associated with the lack of availability of an explicit expression for $\delta\bar{h}(I,\vartheta,r)$. The endpoint correction term $d(G-I\vartheta)/dr$ in (3b) will be neglected throughout the remainder of this paper.

The reason for introducing action–angle variables is that these variables provide the most succinct description of the underlying ray dynamics. The equations presented in the next three sections that make use of action–angle variables can also be written in terms of the original phase space variables (p,z), but the (p,z) form of the equations are more complicated and obscure the important role, described below, played by ω' in controlling travel time spreads.

B. Some qualitative features of scattered ray travel time distributions

Some basic features of ray travel times in deep-ocean environments without and with internal-wave-induced scattering are shown in Fig. 1. Travel time and ray depth are plotted at $r=2$ Mm for rays emitted from an axial source in each of the two sound channels shown in Fig. 2. The nonscattered ray travel times plotted in Fig. 1 correspond to rays with launch angles φ_0 confined to 4° bands. The scattered ray travel times plotted in Fig. 1 correspond to an ensemble of 200 rays with a fixed launch angle, each in the same background sound-speed structure but with an independent realization of the internal-wave-induced perturbation superimposed. (Independent realizations were generated using the same internal wave field by staggering the initial range at which rays were launched with $\Delta r=5$ km; the vertical derivative of internal-wave-induced sound-speed perturbations has a horizontal correlation length shorter than 5 km,[13] so

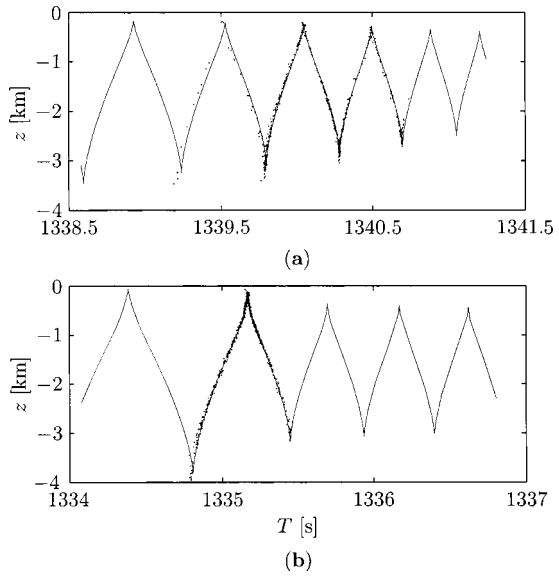

FIG. 1. (a) Ray travel time and depth at $r=2$ Mm in the C0 sound channel (cf. Fig. 2) without (solid curve) and with (dots) internal-wave-induced sound-speed perturbations superimposed. The source is on the sound channel axis in both cases. In the absence of internal-wave-induced perturbations $8° \leqslant \varphi_0 \leqslant 12°$, where φ_0 is ray launch angle. In the presence of internal-wave-induced perturbations $\varphi_0 = 10°$ in each of 200 realizations of the internal wave field. (b) Same as (a) except that the C14 sound speed was used with $10° \leqslant \varphi_0 \leqslant 14°$ without internal-wave-induced perturbations, and $\varphi_0 = 12°$ with internal-wave-induced perturbations.

this simple procedure ensures statistical independence.) Figure 1 shows two examples of a portion of what is commonly referred to as a *timefront*, consisting of many smooth branches that meet at cusps.

The internal-wave-induced sound-speed perturbation used to produce Fig. 1—and all subsequent numerical calculations shown in this paper that include internal-wave-induced sound-speed perturbations—was computed using Eq. (19) of Ref. 14. In that expression y and t were set to zero, i.e., a frozen vertical slice of an internal wave field was assumed. The range-averaged buoyancy frequency profile measured during the AET experiment was used. The dimensionless strength parameters E and μ were taken to be 6.3×10^{-5} and 17.3, respectively. Horizontal wave number and vertical mode number cutoffs of 2π km^{-1} and 30, respectively, were used. The resulting sound-speed perturbation field is highly structured and fairly realistically describes a typical deep-ocean midlatitude internal-wave-induced sound-speed perturbation.

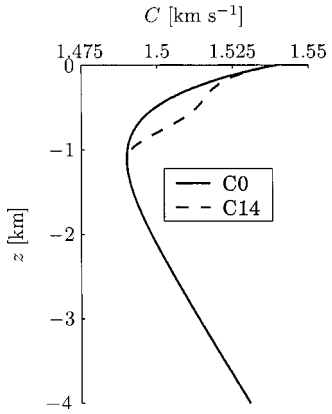

FIG. 2. Background sound-speed profiles used in the numerical work presented in Figs. 1, 3, 4, 8, 9, and 10.

Figure 1 shows that internal-wave-induced scattering is predominantly along the background timefront. Internal-wave-induced scattering also causes a broadening of individual branches of the timefront. This broadening occurs even for a single realization of the sound-speed perturbation field if rays with a dense set of launch angles are plotted. In the two sections that follow, simple analytic expressions that describe time spreads are derived and compared to numerical simulations. These expressions describe: (i) the relatively large scattering-induced travel time spreads along the timefront seen in Fig. 1 as a function of range, without regard to the depth or timefront branch on which a scattered ray falls; (ii) the relatively large scattering-induced travel time spreads of rays whose turning history and final depth are fixed, but whose final range is not; and (iii) the relatively small scattering-induced broadening of an individual branch of the timefront at a fixed depth and range as a function of range or ray double loops. We refer to (i) and (ii) as *unconstrained travel time spreads* and (iii) as a *constrained travel time spread*. The latter is constrained by the imposition of an eigenray constraint. Both unconstrained and constrained measures of time spreads will be shown below to be largely controlled by $\omega'(I)$.

It is not surprising that time spreads in the presence of sound-speed perturbations are largely controlled by ω' inasmuch as travel time dispersion in the absence of perturbations is controlled by ω'. Equation (3b), with the term $\mathrm{d}(G - I\vartheta)/\mathrm{d}r$ neglected, can be integrated immediately to give

$$T(I;r) = [I\omega(I) - \overline{H}(I)]r, \tag{8}$$

where, from the first of Eqs. (3a), I is constant following a ray. It follows that

$$\mathrm{d}T/\mathrm{d}I = I\omega' r, \tag{9}$$

where the second of Eqs. (3a) has been used. This simple expression succinctly describes the travel time dispersion seen in Fig. 1. In both environments ω' is negative for all nonaxial rays; because I is a non-negative monotonically increasing function of $|\varphi_0|$ for an axial source, (9) describes the decrease in travel time with increasing $|\varphi_0|$ that is shown in Fig. 1.

For one of the rays used to produce Fig. 1(a), the Hamiltonian h (whose numerical value is identical to that of $\overline{H} + \delta\overline{h}$, although they depend on different variables) as a function of range is shown in Fig. 3. It is seen that h vs r consists of a sequence of approximately piecewise-constant segments, separated by fairly narrow transition regions. The transition regions coincide with each of the ray's upper turning points. A useful and widely used approximation, the *apex approximation*, assumes that the width of each transition region is negligibly small. In the action–angle description of ray motion that makes use of the apex approximation, I is piecewise constant following a ray, making jumps ΔI of negligibly small width $\Delta\vartheta$ at each upper turning depth of the ray; between such jumps ϑ advances by 2π. A slightly relaxed form of the apex approximation in which $\Delta\vartheta$ is treated

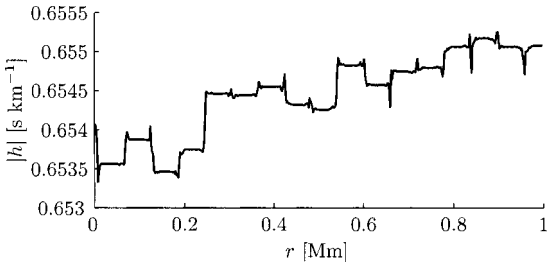

FIG. 3. Hamiltonian h vs range for one of the scattered rays shown in Fig. 1(a) in the presence of an internal-wave-induced sound-speed perturbation field.

as a small parameter will be described in Sec. IV. Generally, the apex approximation works fairly well in typical midlatitude deep-ocean environments for rays with axial angles greater than about 10°; it is usually a poor approximation for rays with axial angles less than approximately 5°. More generally, the apex approximation can be thought of as a special case of a scattering model in which I is piecewise constant on a sequence of range intervals of variable extent. Such a model is used in Secs. III and IV. Although the apex approximation is a special case, it is useful to focus on this special case when considering constrained spreads because it is often the case[1,3,4] that only the steep ray travel time spreads can be measured experimentally.

III. UNCONSTRAINED TIME SPREADS

A. Spreading along the timefront

In this section we imagine launching rays from a fixed source location with a fixed launch angle in an ensemble of oceans, each with the same background sound-speed structure, but with an independent realization of the internal-wave-induced perturbation field superimposed. At a fixed range we consider the resulting distribution of ray travel time perturbations without regard to the final ray depth or the ray turning point history. Such a distribution is seen in Fig. 1.

With the assumption that I is piecewise constant following a ray, it follows from Eqs. (3), neglecting $\mathrm{d}(G-I\vartheta)/\mathrm{d}r$, that

$$\Delta T=\int_0^r \mathrm{d}\xi\, I(\xi)\omega'(I(\xi))\Delta I(\xi). \tag{10}$$

Here, $\Delta T=T-T_0$, where $T_0(r)$ is the travel time of the unperturbed ray whose initial action is I_0; $\Delta I=I-I_0$; and I and ω' are understood to be piecewise-constant functions of r. If the product $I\omega'\approx I_0\omega'(I_0)$ over the domain of I values assumed by the ray between ranges 0 and r, then (10) can be approximated by

$$\Delta T\approx I_0\omega'(I_0)\int_0^r \mathrm{d}\xi\,\Delta I(\xi). \tag{11}$$

Successive upper turns are typically separated by about 50 km, which is large compared to the horizontal correlation length of internal-wave-induced sound-speed fluctuations, so each perturbation to I is independent. This leads to $\langle(\Delta I)^2\rangle^{1/2}\sim r^{1/2}$, where $\langle\cdot\rangle$ indicates ensemble average, and, in turn, to $\langle(\Delta T)^2\rangle^{1/2}\sim r^{3/2}$. This $r^{3/2}$ dependence was previously derived by Henyey and Colosi (personal communication, 2002), who also found that this dependence is in good agreement with simulations. [Our simulations also indicate that when (11) is valid, then $\langle(\Delta T)^2\rangle^{1/2}\sim r^{3/2}$; our focus, however, is on the dependence of (10) and (7) on the background sound-speed structure, via $I\omega'$. We note, in addition, that if $\langle(\Delta I)^2\rangle^{1/2}$ is computed using an ensemble of rays with the same launch angle then the r dependence of this quantity is characterized by oscillations in r superimposed on the $r^{3/2}$ trend. The oscillations are caused by the cycling between relatively small time spreads when distributions are centered near the cusps where neighboring timefront branches join and relatively large time spreads when distributions are centered near the midpoint of timefront branches. At long range when scattered ray distributions are very broad, this effect is greatly diminished.] At long range the contributions to (10) or (11) from ray partial loops near the source and receiver are unimportant. Then, because $2\pi/\omega$ is the range of a ray double loop, for a ray that has undergone N apex scattering events and has N complete double loops, (11) can be further approximated

$$\Delta T\approx 2\pi\frac{I_0\omega'(I_0)}{\omega(I_0)}\sum_{i=1}^{N}(I_i-I_0). \tag{12}$$

Equation (12) provides an explanation for the observation (recall Fig. 1) that $\varphi_0=10°$ rays in the C0 environment are more strongly scattered than $\varphi_0=12°$ rays in the C14 environment; the same internal wave field was used to generate the ensemble of scattered rays, so the difference between these figures is due to the difference in the background sound-speed profiles. The $\varphi_0=12°$ rays in the C14 environment have a $|\omega'(I_0)|$ value that is approximately one-fourth that of the $\varphi_0=10°$ rays in the C0 environment, and this scattering-induced time spread is seen to be reduced by a nearly commensurate amount, consistent with Eq. (12). According to that equation, travel time perturbations are the product of the amplification factor $I\omega'/\omega$ and a term that depends on the history of the scattering-induced perturbations to the ray action variable.

It is convenient to introduce the *stability parameter*[7,8,11]

$$\boxed{\alpha=I\omega'/\omega,} \tag{13}$$

which, in addition to appearing in Eq. (12), is a natural nondimensional measure of ω'. Figure 4 compares numerically simulated time spreads $\langle(\Delta T)^2\rangle^{1/2}$ as a function of launch angle φ_0 for a source on the sound channel axis at $r=2$ Mm to α in the two different background environments shown in Fig. 2 on which identical internal-wave-induced sound speed perturbation fields were superimposed. In the Fig. 4 plots, dependence on I_0 is replaced by dependence on the more familiar variable φ_0; for an axial source this constitutes a simple stretching of the horizontal axis. Ensembles of ΔT for rays with the same launch angle were generated using the same technique that was used to generate Fig. 1.

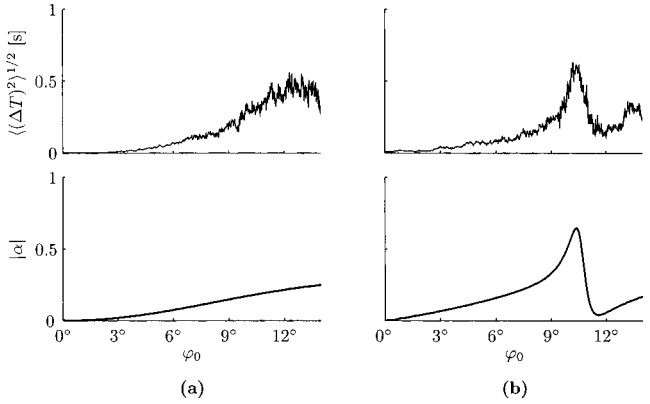

FIG. 4. Estimates of unconstrained travel time spreads (upper panels) and the stability parameter α (lower panels) as a function of launch angle in background sound channels C0 (a) and C14 (b) (cf. Fig. 2). To generate the upper plots, ray simulations based on Eqs. (1) were performed by launching rays from a source located at the sound channel axis with a fixed launch angle in an ensemble of 50 oceans, each with the same background sound-speed structure, but with an independent realization of the internal-wave-induced perturbation field superimposed.

Figure 4 shows that in both environments almost all of the structure seen in $\langle(\Delta T)^2\rangle^{1/2}$ can be attributed to the stability parameter α. This is because in the environments considered Eq. (12) is generally a good approximation to Eq. (10). Also, the dependence of $\Sigma_{i=1}^{N}(I_i-I_0)$ on axial ray angle is somewhat weaker than the dependence of α on axial ray angle. We conclude from Fig. 4 that travel time spreads along the timefront are largely controlled by the background sound-speed structure via α, and that, provided $\alpha(I)$ does not have too much structure, the dependence of ΔT on α in Eq. (10) can be taken outside the integral.

B. Spreading of rays with fixed turning history and final depth

We now consider a different measure of unconstrained travel time spread. To illustrate the generality of the results presented, we consider rays in upward-refracting environments (Fig. 5) in the presence of rough surface scattering. In such environments the action–angle form of the ray equations is unchanged. The action I is defined as in (6) with the upper turning depth $z_+=0$ for all rays. It follows from Eqs.

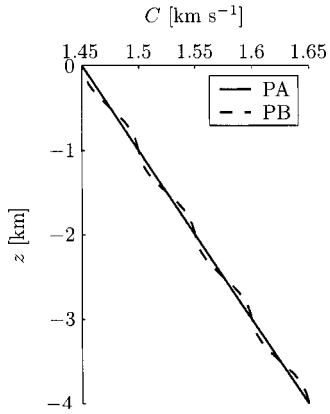

FIG. 5. Background sound-speed profiles used to construct the curves in Fig. 6.

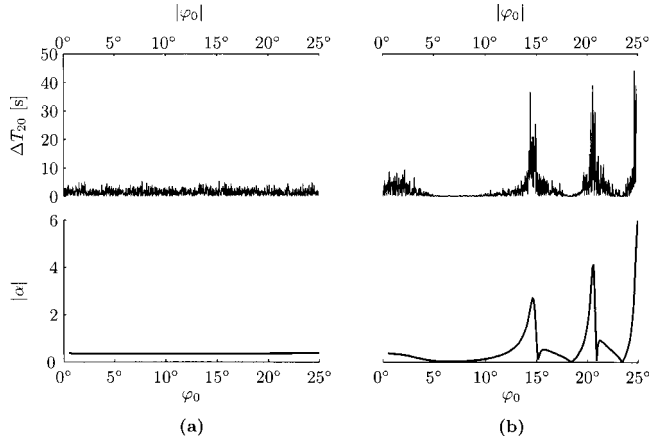

FIG. 6. Upper panels: absolute value of the difference between perturbed (rough surface) and unperturbed (flat surface) ray travel time after 20 surface reflections as a function of initial ray angle at the surface for sound-speed profiles PA (a) and PB (b) shown in Fig. 5. Lower panels: stability parameter as a function of ray angle in each of the two environments.

(3) that the travel time for one ray cycle is $T(I)=2\pi[I-\bar{H}(I)/\omega(I)]$. At each reflection from the rough surface the ray action gets modified. After N surface reflections and $N+1$ ray cycles, the travel time perturbation to the ray is

$$\Delta T_N \approx 2\pi \frac{\bar{H}(I_0)\omega'(I_0)}{[\omega(I_0)]^2}\sum_{i=1}^{N}(I_i-I_0), \tag{14}$$

where I_0 is the initial action of the ray, and the first of Eqs. (3a) has been used. Note that Eq. (14) constrains the ray geometry and final ray depth but not the final range of the scattered rays.

Figure 6 shows plots of ΔT_{20}, defined in (14), vs launch angle φ_0 for a source at the surface [so, again, $\varphi_0(I_0)$ is a simple stretching] in the environments shown in Fig. 5. The rough surface was a single frozen realization of a surface gravity wave field with a $k^{-7/2}$ surface elevation wave number spectrum with $0.02\,\mathrm{rad\,m^{-1}}\leqslant k\leqslant 0.16\,\mathrm{rad\,m^{-1}}$, $\Delta k=10^{-3}\,\mathrm{rad\,m^{-1}}$, and an rms slope of 4×10^{-3}. Ray reflections from this surface were specular, but with a linearized boundary condition; the surface elevation was neglected, but the nonzero slope was not approximated. The same environment was used in Ref. 8.

Consistent with Eq. (14), Fig. 6 shows that travel time perturbations are largely controlled by the background sound-speed structure via α, rather than details of the rough surface.

IV. CONSTRAINED TIME SPREAD

In this section we focus on deep-ocean conditions and consider the scattering-induced broadening of an individual branch of the timefront. Note that this broadening is much smaller than the scattering-induced spreading along the timefront that was considered in Sec. III A. We refer to the broadening of an individual branch of the timefront as a constrained time spread because to calculate this broadening two constraints must be incorporated into the calculation. First, the rays contributing to the spread must have the same fixed endpoints in the (z,r) plane. Second, the rays contributing to

the spread must have the same turning point history, i.e., the same ray inclination (positive or negative) at the source, and the same number of turning points M (upper and lower) between source and receiver. Note, however, that these constraints do not fix the values of the ray angle at either the source or receiver.

The approach taken here to compute appropriately constrained travel time spreads is based on a perturbation expansion that exploits the assumed smallness of the sound-speed perturbation δc. The method by which the constraints are incorporated into the travel time perturbation estimates presented below is different than the method that was used in Ref. 15; that result will be discussed below.

The expression for travel time perturbation that is presented below consists of a sum of two contributions. One contribution comes from a scattering model in which I following a scattered ray is piecewise constant in the background environment. The other contribution comes from the perturbation Hamiltonian δh. To compute the piecewise constant I contribution, Eqs. (3) are applied piecewise, with I making a jump at each scattering event. To impose the eigenray constraint, the total range of each scattered ray must be constrained to be equal to the range of the unperturbed ray. In addition, the turning point history, starting depth, and ending depth of the scattered ray must be the same as those of the unperturbed ray. This is accomplished by constraining the total change in ϑ following the scattered ray to be equal to that of the unperturbed ray. For some choices of the source–receiver geometry this procedure exactly enforces the eigenray constraint. In general, however, small endpoint corrections must be applied. For simplicity, these small endpoint corrections will be neglected.

We assume that between source and receiver the environment can be approximated as n piecewise range-independent segments. Let I_i denote the action of a scattered ray in the ith segment whose horizontal extent is $\Delta r_i = \Delta\vartheta_i/\omega(I_i)$, and let $\tilde{I}$ denote the action of the unperturbed ray. The eigenray constraint requires the perturbed ray total range, r, to be equal to the unperturbed ray total range. This condition reads

$$r=\sum_{i=1}^{n}\frac{\Delta\vartheta_i}{\omega(I_i)}=\frac{1}{\omega(\tilde{I})}\sum_{i=1}^{n}\Delta\vartheta_i, \tag{15}$$

which, for sufficiently small $\Delta I_i = I_i - \tilde{I}$, can be approximated by

$$\frac{\omega'(\tilde{I})}{[\omega(\tilde{I})]^2}\sum_{i=1}^{n}\Delta I_i\Delta\vartheta_i=\frac{1}{2}\frac{\mathrm{d}^2}{\mathrm{d}I^2}\bigg|_{I=\tilde{I}}\left(\frac{1}{\omega}\right)\sum_{i=1}^{n}(\Delta I_i)^2\Delta\vartheta_i. \tag{16}$$

The right-hand side term of (16) is almost always negligible compared to the left-hand side term in deep-ocean environments, even at ranges comparable to basin scales. Then, because $\Delta\vartheta_i=\omega(I_i)\Delta r_i\approx\omega(\tilde{I})\Delta r_i$, the eigenray constraint reduces approximately to a statement that the range-weighted average of the perturbed action is equal to the unperturbed action, i.e.,

$$\tilde{I}\approx r^{-1}\sum_{i=1}^{n} I_i\Delta r_i. \tag{17}$$

This equation constrains the action history of scattered eigenrays.

The difference between the perturbed and unperturbed ray travel times is

$$\begin{aligned}\Delta T_2&=\sum_{i=1}^{n}\left[I_i-\frac{\overline{H}(I_i)}{\omega(I_i)}\right]\Delta\vartheta_i-\left[\tilde{I}-\frac{\overline{H}(\tilde{I})}{\omega(\tilde{I})}\right]\sum_{i=1}^{n}\Delta\vartheta_i\\&\approx\frac{\omega'(\tilde{I})\overline{H}(\tilde{I})}{[\omega(\tilde{I})]^2}\sum_{i=1}^{n}\Delta I_i\Delta\vartheta_i\\&\quad-\frac{1}{2}\frac{\mathrm{d}^2}{\mathrm{d}I^2}\bigg|_{I=\tilde{I}}\left(\frac{\overline{H}}{\omega}\right)\sum_{i=1}^{n}(\Delta I_i)^2\Delta\vartheta_i\\&=\frac{1}{2}\frac{\omega'(\tilde{I})}{\omega(\tilde{I})}\sum_{i=1}^{n}(\Delta I_i)^2\Delta\vartheta_i,\end{aligned} \tag{18}$$

where the eigenray constraint (16) has been used. The reason for introducing the subscript 2 will be clear below. Virovlyansky[9] recently provided an alternate derivation of Eq. (18) [written as an integral over r using $\Delta\vartheta_i = \omega(I_i)\Delta r_i$]. We will discuss his result in more detail below. The apex approximation is a special case of the analysis leading to Eqs. (15)–(18). If the contributions to ΔT_2 from the incomplete ray cycles at the beginning and end of the ray path are neglected, Eq. (18) applies with $\Delta\vartheta_i = 2\pi$ and $n = N$, the number of complete ray cycles. (For large N the neglected incomplete ray cycle contributions to ΔT_2 constitute small corrections to the sum of the retained contributions.)

In the derivation of (18) it was assumed that, following a scattered ray, the action I is piecewise constant in the unperturbed environment. Relaxing that assumption leads immediately to a simple nonzero first-order estimate of an eigenray travel time perturbation: $T=\int \mathrm{d}s/c$, where s is arc length along an unperturbed eigenray path $z(r)$, so $\delta T = -\int \mathrm{d}s\,\delta c/c^2 = -\int \mathrm{d}r\,\delta c/(c^2\cos\vartheta)$. In terms of $H(p,z)$ and $\delta h(p,z,r)$, introduced earlier

$$\begin{aligned}\Delta T_1&=\int_0^r \mathrm{d}\xi\frac{\delta c(z(\xi),\xi)}{C^3(z(\xi))H(p(\xi),z(\xi))}\\&\approx-\int_0^r \mathrm{d}\xi\,\delta h(p(\xi),z(\xi),\xi)\\&\approx-c_0^{-1}\int_0^r \mathrm{d}\xi\,\delta c(z(\xi),\xi),\end{aligned} \tag{19}$$

where c_0 is a (constant) reference sound speed.

Because ΔT_2 is derived from the background Hamiltonian H while ΔT_1 is linked to the perturbation Hamiltonian δh, their contributions to the travel time perturbation are additive

$$\Delta T=\Delta T_1+\Delta T_2, \tag{20}$$

where ΔT_1 and ΔT_2 are defined in (19) and (18), respectively. Expression (20) differs from Virovlyansky's[9] estimate

of ΔT in that his expression included an additional term which, like (18), is second order in small quantities, but which is expected to grow more slowly in range than (18). Virovlyansky[9] argued that the term not included in (20) can be neglected. Note that the same symbol ΔT is being used to denote a constrained (eigenray) travel time perturbation that was used in the previous section to denote an unconstrained travel time perturbation. This choice was made to keep the notation simple. Also, for the same reason, we make no notational distinction between a theoretical estimate of ΔT and a numerically computed ΔT.

In Ref. 15 an alternative [to Eq. (19)] first-order expression for an eigenray travel time perturbation was derived. That analysis was restricted to steep rays for which the apex approximation is approximately valid. It was shown that while a strict application of the apex approximation gives no contribution to ΔT to first order in ΔI_i [as in the derivation of (18)], a relaxed form of the apex approximation, in which $I(\vartheta)$ is continuous in the transition region, gives a nonvanishing first-order contribution to ΔT. In that analysis the jump $\Delta I_{\mathrm{T}}=I_i-I_{i-1}$ had a transition width $\Delta\vartheta_{\mathrm{T}}$, which is assumed here to be small, $\Delta\vartheta_{\mathrm{T}}\ll 2\pi$. In the transition region a particular form $h(I-\vartheta\Delta I_{\mathrm{T}}/\Delta\vartheta_{\mathrm{T}})$ of the Hamiltonian was assumed. This finite width transition region was shown to contribute a travel time perturbation $\frac{1}{2}\Delta I_{\mathrm{T}}\Delta\vartheta_{\mathrm{T}}$ for a single scattering event. After N scattering events, assuming the transition width $\Delta\vartheta_{\mathrm{T}}$ of each is the same, this gives a contribution

$$\Delta T_1^{\mathrm{A}}=\tfrac{1}{2}(I_N-I_0)\Delta\vartheta_{\mathrm{T}}, \tag{21}$$

to ΔT. This expression will be discussed below as a possible alternative to ΔT_1 in (20). It should be emphasized, however, that, unlike (19), formula (21) is expected to be approximately valid only for steep rays.

Under typical deep-ocean conditions ΔT_1 dominates ΔT_2 at short range. For steep rays δc is negligible everywhere except near a ray's upper turning points, which are separated horizontally by a distance (approximately 50 km) that is greater than the horizontal correlation length (approximately 10 km) of the sound-speed perturbation field. Because successive apex scattering events are independent, ΔT_1 grows diffusively, approximately like $0.7\,\mathrm{ms}\times[r/(50\,\mathrm{km})]^{1/2}$ in our simulations. The alternate expression ΔT_1^{A} with $\Delta\vartheta_{\mathrm{T}}/(2\pi)\approx 0.04$ and $\Delta I_{\mathrm{rms}}\approx 3$ ms gives a similar estimate. For steep rays ΔT_2, with $n=N$, $\Delta\vartheta_i=2\pi$, and $\omega'/\omega=\alpha/I\approx 0.2/(0.08\,\mathrm{s})$, grows approximately like $0.13\,\mathrm{ms}\times r/(50\,\mathrm{km})$. Although this term is negligible at short range, it dominates ΔT_1 at ranges greater than approximately 3 Mm. Note that when ΔT_2 dominates ΔT_1, this equation predicts a scattering-induced travel time bias in the direction of $\mathrm{sgn}\,\omega'$.

These observations are consistent with the simulations shown in Fig. 7. There, scattered and unperturbed ($\delta c=0$) ray travel times are shown in the vicinity of two branches of the timefront at $r=1$ Mm ($N=18$) and $r=3$ Mm ($N=54$). At both ranges the source was on the sound channel axis in the C0 environment shown in Fig. 2; launch angles for the rays shown are near 10° at both ranges. In that environment $\mathrm{sgn}\,\omega'=-1$. It is seen in this figure that there is no indication

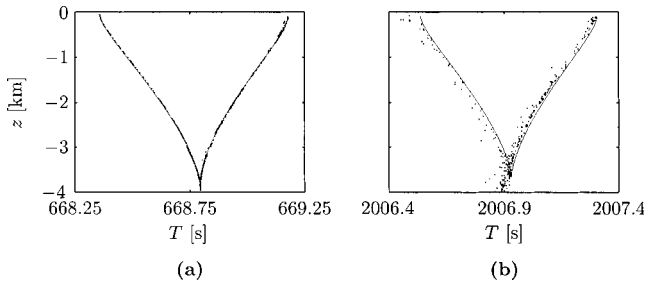

FIG. 7. (a) Ray travel time and depth of rays with positive launch angles and which have $N=18$ upper turning points at $r=1$ Mm in the C0 environment shown in Fig. 2. The solid curve corresponds to rays in the absence of internal-wave-induced scattering. Dots correspond to rays scattered by internal waves. (b) Same as the left panel except that $r=3$ Mm and $N=54$.

of a negative travel time bias at 1 Mm, while there is a clear negative bias at 3 Mm, consistent with Eq. (20). At ranges sufficiently short that ΔT_1 dominates, travel time perturbations of either sign can be expected as ΔT_1 can be of either sign. Because ΔT_1 is a continuous function of launch angle, the sign of the travel time perturbation should have a nonzero correlation scale along the timefront. These features are readily evident in our simulations in the presence of realistic internal-wave-induced sound-speed perturbations.

Quantitative tests of the correctness of Eq. (20) are shown in Fig. 8. There, numerically computed travel time differences ΔT are compared separately to ΔT_1 and ΔT_2 under conditions in which one of the two terms dominates the other. The constrained travel time difference ΔT was computed using a single realization of an internal-wave-induced sound-speed perturbation as the travel time difference between perturbed and unperturbed rays whose turning history, range, and final depth are the same. In Fig. 8 attention is restricted to rays that are sufficiently steep that the apex approximation is approximately valid, but not so steep that rays reflect off the surface.

In Fig. 8(a) numerically simulated travel time differences ΔT are compared to numerical estimates of ΔT_1 at $r=100\,\mathrm{km}$; for the rays used to construct this plot the mean value of ΔT_2 is approximately -0.25 ms, which is seen to account for most of the difference between ΔT and ΔT_1. Apart from this small offset, simulated travel time differences ΔT are seen to be accurately predicted by ΔT_1. In Fig. 8(b) simulated travel time differences ΔT are compared to

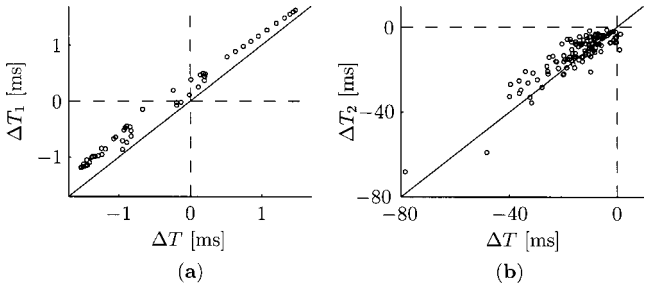

FIG. 8. (a) Constrained travel time perturbation (ΔT) vs Eq. (19) (ΔT_1) at $r=100$ km for rays with axial launch angles $0.5°\leqslant\varphi_0\leqslant 14°$ in the C0 environment with an internal-wave-induced sound-speed perturbation superimposed. (b) As in (a) but vs Eq. (18) (ΔT_2) at $r=3$ Mm and for rays with $11°\leqslant\varphi_0\leqslant 13.5°$.

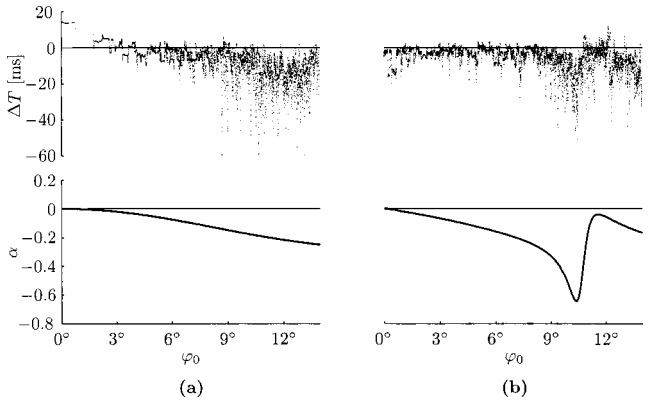

FIG. 9. Travel time difference $\Delta T = T_{\mathrm{IW}} - T_0$ at $r = 3$ Mm vs ray launch angle φ_0 for an axial source, and stability parameter α vs φ_0, in each of the environments C0 (a) and C14 (b) shown in Fig. 2. Here, T_{IW} is the travel time of a ray in the presence of an internal-wave-induced sound-speed perturbation field, and T_0 is the travel of a ray in the same background environment, but without the sound-speed perturbation field superimposed, whose turning point history and final depth are the same as those of the T_{IW} ray.

ΔT_2 (with $n = N$ and $\Delta \vartheta_i = 2\pi$) at $r = 3$ Mm; for the rays used to construct this plot the rms value of ΔT_1 is approximately 5 ms, which is seen to represent a small but not negligible correction, on average, to ΔT_2. The agreement between ΔT and ΔT_2 in this plot is seen to be very good, indicating that for the rays used to construct this plot ΔT_2 is a very good predictor of ΔT. Overall, for steep rays we have found very good quantitative agreement at short range between ΔT and ΔT_1, and very good quantitative agreement at long range between ΔT and ΔT_2.

At intermediate ranges one would hope that the sum $\Delta T_1 + \Delta T_2$ would be a good predictor of ΔT. In our simulations this was true only for ranges of approximately 500 km or less. Our interpretation of this observation is that at ranges greater than this approximate limit, the first-order term ΔT_1 starts to fail as a deterministic predictor of the difference between ΔT and ΔT_2; Eq. (19) fails when the spatial separation between perturbed and unperturbed eigenrays exceeds the local correlation length of δc. Our simulations indicate, however, that at ranges between 0.5 and 3 Mm $\Delta T_1 + \Delta T_2$ remained a good statistical predictor for ΔT. Similarly, our simulations indicate that for steep rays with a least one upper turn $\Delta T_1^{\mathrm{A}} + \Delta T_2$ is a good statistical predictor of ΔT. Unlike ΔT_1, however, ΔT_1^{A} was not found to be a good deterministic predictor for ΔT at short range. The failure of ΔT_1^{A} as a deterministic predictor of ΔT, we believe, is attributable to the overly idealized form of the Hamiltonian in the apex transition region that was used to derive Eq. (21).

Figure 9 shows plots of ΔT vs launch angle and α vs launch angle at $r = 3$ Mm in each of the two background sound-speed profiles shown in Fig. 2. Again, the constrained travel time spread ΔT was computed using a single realization of an internal-wave-induced sound-speed perturbation as the difference between the perturbed ray travel time and the travel time of the unperturbed ray with the same turning history and the same final depth as the perturbed ray. The small gaps in the plot correspond to perturbed rays whose final depth lies outside the bounds of the portion of the timefront which has the same turning history as the perturbed ray. In Fig. 9 ray angles are not limited to the band for which the apex approximation is expected to be valid. Because (18) remains valid across the entire band, however, the trend in $\alpha(\varphi_0)$ should be approximately reproduced in the $\Delta T(\varphi_0)$ points plotted. This is seen to be the case; variations in ΔT are caused by variations in $\Sigma_{i=1}^{n} (\Delta I_i)^2 \Delta \vartheta_i$. The probable cause of the positive values of ΔT for near-axial rays in the C0 environment seen in Fig. 9 will be discussed below. Even after fitting a smooth curve through the fluctuations seen in the Fig. 9 ΔT plot for the C14 environment, the peak in $|\Delta T|$ is seen to be less pronounced than the peak in $|\alpha|$. This is expected because the scattering process leads to a local average over a band of adjacent α values. With these minor caveats, Fig. 9 shows that constrained travel time spreads at long range are largely controlled by the background sound-speed structure via the stability parameter α. The same conclusion can be drawn from Fig. 8(b).

The probable cause of the positive computed values of ΔT for near-axial rays seen in Fig. 9 in the C0 environment is not the failure of Eq. (18); rather, it is the failure of our ray labeling scheme for near axial rays. We have implicitly assumed that the ray identifier $\pm M$ uniquely identifies each timefront branch. This assumption fails for near-axial rays. (The assumption also fails for steep rays in the vicinity of the cusps where adjacent timefront branches join, and whenever ω' has isolated zeros. We have intentionally avoided the latter situation.) The correct way to identify timefront branches is by the Maslov index[10] μ which, for waves in two space dimensions, advances by one unit each time a caustic is touched. For near-axial rays the portion of the timefront corresponding to a constant value of the ray identifier consists of two adjacent partial branches joined at a cusp. For these rays a ray-identifier-based definition of ΔT can lead to either undefined or nonuniquely defined ΔT values.

In addition to the recent work of Virovlyansky,[9] the results reported in this section are closely related to recent work by Godin *et al.*[16] Those authors derived an expression for an eigenray travel time perturbation consisting of ΔT_1 plus three second-order correction terms. We note, in particular, that one of the second-order terms that was derived is due to scattering out of the (z,r) propagation plane, an effect not considered here or in Ref. 9. It was shown in Ref. 16 that out-of-plane scattering results in a negative travel time bias which is small at short range but grows like r^2. The numerical simulations presented in Ref. 16 using an internal-wave-induced sound-speed perturbation suggest that the contribution to the total travel time perturbation due to the out-of-plane scattering should dominate the contribution from our ΔT_2 (18) at ranges in excess of approximately 2 Mm.

V. DISCUSSION AND CONCLUSIONS

In this paper we have investigated three measures of travel time spreads for sound propagation in environments consisting of a range-independent background on which a range-dependent perturbation is superimposed: (i) unconstrained spread of ray travel time along the timefront; (ii) unconstrained spread of rays whose turning history and final

depth are fixed but whose final range is not; and (iii) scattering-induced broadening of an individual branch of the timefront at a fixed location. All three measures of time spreads were shown to be largely controlled by a property ω' of the background sound-speed profile. Surprisingly, this is the same property that controls ray spreading and, hence, ray amplitudes.[8] We now present two arguments that provide some insight into why travel time spreads should be controlled by the same property of the background sound-speed profile that controls ray spreading.

The variational equations that describe how small perturbations $(\delta I, \delta\vartheta, \delta T)$ evolve in the extended phase space (I, ϑ, T) are given by

$$\frac{\mathrm{d}}{\mathrm{d}r}\begin{pmatrix} \delta I \\ \delta\vartheta \\ \delta T \end{pmatrix} = \begin{bmatrix} 0 & 0 & 0 \\ \omega' & 0 & 0 \\ I\omega' & 0 & 0 \end{bmatrix}\begin{pmatrix} \delta I \\ \delta\vartheta \\ \delta T \end{pmatrix} + \begin{bmatrix} -\partial_{I\vartheta}\overline{\delta h} & \partial_{\vartheta\vartheta}\overline{\delta h} & 0 \\ \partial_{II}\overline{\delta h} & \partial_{I\vartheta}\overline{\delta h} & 0 \\ I\partial_{II}\overline{\delta h} & I\partial_{I\vartheta}\overline{\delta h} - \partial_{\vartheta}\overline{\delta h} & 0 \end{bmatrix}\begin{pmatrix} \delta I \\ \delta\vartheta \\ \delta T \end{pmatrix}, \tag{22}$$

where a shorthand notation for partial differentiation has been introduced. In general, Eqs. (22) and (7) constitute a set of six coupled differential equations. For the special case $\overline{\delta h} = 0$, I and ω' are constant following trajectories and (22), like (7), have a simple analytical solution. For the class of problems treated in this paper the nonzero sound-speed perturbation terms in the second matrix on the right-hand side of (22) are generally much smaller than the ω' and $I\omega'$ terms in the first matrix, corresponding to contributions from the background sound-speed profile. Thus, one expects that generically the dominant cause of the growth of $(\delta I, \delta\vartheta, \delta T)$ is the background sound-speed structure via ω', rather than the small sound-speed perturbation terms. Loosely speaking, the perturbation terms provide a seed for the growth of $(\delta I, \delta\vartheta, \delta T)$, while subsequently growth of these quantities is largely controlled by ω'.

Additional insight into the role played by ω' is obtained by making a fluid mechanical analogy. Equations (1) define a flow in the three-dimensional space (p, z, T) with velocity components $\mathrm{d}(p, z, T)/\mathrm{d}r$. (Recall that r plays the role of the independent or time-like variable in the one-way ray equations.) Alternatively, the flow in this three-dimensional space can be described using action–angle variables (I, ϑ, T). The coordinates (I, ϑ, T) behave qualitatively like cylindrical coordinates (ρ, θ, ζ), say. If we neglect the contributions from the sound-speed perturbation term $\overline{\delta h}$, then the velocity components of the background flow in these coordinates are $u_I = \mathrm{d}I/\mathrm{d}r = 0$, $u_\vartheta = (\mathrm{d}\vartheta/\mathrm{d}r)I = \omega I$, and $u_T = \mathrm{d}T/\mathrm{d}r = I\omega - H$. The strain rate tensor, which in cylindrical coordinates is[17]

$$\mathbf{S} = \begin{bmatrix} \partial_\rho u_\rho & \frac{1}{2}[\rho^{-1}\partial_\theta u_\rho + \rho\partial_\rho(\rho^{-1}u_\theta)] & \frac{1}{2}(\partial_\zeta u_\rho + \partial_\rho u_\zeta) \\ \frac{1}{2}[\rho^{-1}\partial_\theta u_\rho + \rho\partial_\rho(\rho^{-1}u_\theta)] & \rho^{-1}(u_\rho + \partial_\theta u_\theta) & \frac{1}{2}(\partial_\zeta u_\theta + \rho^{-1}\partial_\theta u_\zeta) \\ \frac{1}{2}(\partial_\zeta u_\rho + \partial_\rho u_\zeta) & \frac{1}{2}(\partial_\zeta u_\theta + \rho^{-1}\partial_\theta u_\zeta) & \partial_\zeta u_\zeta \end{bmatrix}, \tag{23}$$

describes how small elements of fluid are deformed by the flow. With the identification $(I, \vartheta, T) \leftrightarrow (\rho, \theta, \zeta)$ and with the velocity field (u_I, u_ϑ, u_T) defined above, the strain rate tensor is

$$\mathbf{S} = \begin{bmatrix} 0 & \frac{1}{2}I\omega' & \frac{1}{2}I\omega' \\ \frac{1}{2}I\omega' & 0 & 0 \\ \frac{1}{2}I\omega' & 0 & 0 \end{bmatrix}. \tag{24}$$

Although (24) is only qualitatively correct [because of the qualitative connection between (I, ϑ, T) and (ρ, θ, ζ)], the conclusion to be drawn from this tensor is extremely important: deformation of small elements of the extended phase space (I, ϑ, T) by the background sound-speed structure is caused entirely by shear (off-diagonal elements of $\mathbf{S}$) and is quantified by the product $I\omega'$. This behavior is consistent with the discussion above concerning Eq. (22) and the growth of small perturbations in the extended phase space (I, ϑ, T).

Arguments similar to those given above relating to Eqs. (22) and (24) were given in Ref. 8; in that study, however, attention was confined to ray spreading in (p, z) or, equivalently, (I, ϑ). That problem is described by the first two of Eqs. (1) or (7), the upper 2×2 system in Eqs. (22) and (24), etc. In that study it was shown that ray spreading is largely controlled by ω'. The surprising result of the present study is that travel time spreads are also largely controlled by ω'. This is evident from the unconstrained and constrained travel time spread estimates, (10), (14), (18), and (20), and the more heuristic arguments associated with Eqs. (22) and (24).

Inasmuch as the AET experimental observations[3,4] provided much of the motivation for the present work, it is noteworthy that the results presented here are consistent with

the ray-based analysis of those observations presented in Ref. 15. Two points relating to the results in Ref. 15 deserve further comment. First, it was argued in Ref. 15 that, for moderately steep rays, constrained travel time spreads could be approximately estimated using ΔT_1^{A}, Eq. (21). This is moderately surprising in that the AET range was 3.25 Mm, which is large enough that one would expect that the second term on the right-hand side of (20) should be important. The neglected term, however, is proportional to α, which is unusually small (cf. Ref. 15) in that environment for the relevant band of launch angles. Thus, the estimated travel time spread reported in Ref. 15 is close to what one obtains using both terms on the right-hand side of Eq. (20). Second, it was noted in Ref. 15, without explanation, that in the AET environment constrained travel time spreads are much larger for near-axial rays than for steeper rays. This behavior is consistent with Eq. (20) and the observation[15] that in the AET environment $|\alpha|$ is very large for the near-axial rays.

The results presented in this paper, coupled with those presented in Refs. 8 and 9, represent an important step toward the development of a theory of wave propagation in random inhomogeneous media (WPRIM). These studies have shown that both ray amplitude statistics and ray travel time statistics are largely controlled by the background sound-speed profile, via ω'. It follows that finite frequency wave field intensity statistics should also be largely controlled by the background sound-speed profile via ω'. This is different from the classical treatment of the problem of wave propagation in random media (WPRM), which assumes that the background sound-speed structure is homogeneous—for which $\omega'=0$. Ideally, one would like to develop a uniformly valid theory of WPRIM that reduces to known WPRM results in the limit $\omega'\to 0$. A more modest goal is to develop an approximate theory of WPRIM, appropriate for long-range underwater sound propagation, that treats the case where the wave field intensity statistics are largely controlled by ω'. To develop such a theory the results presented here and in Refs. 8 and 9 have to be combined and extended. Necessary extensions are the inclusion of finite frequency effects (interference and diffraction) and a more accurate treatment of the link between sound-speed perturbations and perturbations to I and ϑ. These topics will be explored in future work.

ACKNOWLEDGMENTS

We thank O. Godin, A. Virovlyansky, J. Colosi, S. Tomsovic, M. Wolfson, G. Zaslavsky, F. Henyey, and W. Munk for the benefit of discussions on ray dynamics. We note, in particular, that A. Virovlyansky independently derived Eq. (18); S. Tomsovic independently derived Eqs. (14) and (21); W. Munk, J. Colosi, and F. Henyey independently derived Eq. (18), although not in the action–angle form given here; and F. Henyey and J. Colosi independently derived Eq. (11), but not in the action–angle form given here. Also, the technique of staggering the starting range in a single realization of an internal wave field to generate effectively independent realizations was pointed out to us by F. Henyey. This research was supported by Code 321OA of the Office of Naval Research.

[1] T. F. Duda, S. M. Flatté, J. A. Colosi, B. D. Cornuelle, J. A. Hildebrand, W. S. Hodgkiss, P. F. Worcester, B. M. Howe, J. A. Mercer, and R. C. Spindel, "Measured wavefront fluctuations in 1000-km pulse propagation in the Pacific Ocean," J. Acoust. Soc. Am. **92**, 939–955 (1992).

[2] P. F. Worcester, B. D. Cornuelle, J. A. Hildebrand, W. S. Hodgkiss, T. F. Duda, J. Boyd, B. M. Howe, J. A. Mercer, and R. C. Spindel, "A comparison of measured and predicted broadband acoustic arrival patterns in travel time-depth coordinates at 1000-km range," J. Acoust. Soc. Am. **95**, 3118–3128 (1994).

[3] P. F. Worcester, B. D. Cornuelle, M. A. Dzieciuch, W. H. Munk, J. A. Colosi, B. M. Howe, J. A. Mercer, A. B. Baggeroer, and K. Metzger, "A test of basin-scale acoustic thermometry using a large-aperture vertical array at 3250-km range in the eastern North Pacific Ocean," J. Acoust. Soc. Am. **105**, 3185–3201 (1999).

[4] J. A. Colosi, E. K. Scheer, S. M. Flatté, B. D. Cornuelle, M. A. Dzieciuch, W. H. Munk, P. F. Worcester, B. M. Howe, J. A. Mercer, R. C. Spindel, K. Metzger, and T. Birdsall, "Comparison of measured and predicted acoustic fluctuations for a 3250-km propagation experiment in the eastern North Pacific Ocean," J. Acoust. Soc. Am. **105**, 3202–3218 (1999).

[5] T. F. Duda and J. B. Bowlin, "Ray-acoustic caustic formation and timing effects from ocean sound-speed relative curvature," J. Acoust. Soc. Am. **96**, 1033–1046 (1994).

[6] J. Simmen, S. M. Flatté, and G. Yu-Wang, "Wavefront folding, chaos and diffraction for sound propagation through ocean internal waves," J. Acoust. Soc. Am. **102**, 239–255 (1997).

[7] I. P. Smirnov, A. L. Virovlyansky, and G. M. Zaslavsky, "Theory and application of ray chaos to underwater acoustics," Phys. Rev. E **64**, 036221, 1–20 (2001).

[8] F. J. Beron-Vera and M. G. Brown, "Ray stability in weakly range-dependent sound channels," J. Acoust. Soc. Am. **144**, 123–130 (2003).

[9] A. L. Virovlyansky, "Ray travel times at long range in acoustic waveguides," J. Acoust. Soc. Am. **113**, 2523–2532 (2003).

[10] M. G. Brown, J. A. Colosi, S. Tomsovic, A. L. Virovlyansky, M. Wolfson, and G. M. Zaslavsky, "Ray dynamics in long-range deep ocean sound propagation," J. Acoust. Soc. Am. **113**, 2533–2547 (2003).

[11] S. S. Abdullaev and G. M. Zaslavsky, "Classical nonlinear dynamics and chaos of rays in problems of wave propagation in inhomogeneous media," Usp. Fiz. Nauk **161**, 1–43 (1991).

[12] V. I. Arnold, *Mathematical Methods of Classical Mechanics*, 2nd ed. (Springer, New York, 1989).

[13] M. G. Brown and J. Viechnicki, "Stochastic ray theory for long-range sound propagation in deep ocean environments," J. Acoust. Soc. Am. **104**, 2090–2104 (1998).

[14] J. A. Colosi and M. G. Brown, "Efficient numerical simulation of stochastic internal-wave-induced sound-speed perturbation fields," J. Acoust. Soc. Am. **103**, 2232–2235 (1998).

[15] F. J. Beron-Vera, M. G. Brown, J. A. Colosi, S. Tomsovic, A. L. Virovlyansky, M. A. Wolfson, and G. M. Zaslavsky, "Ray dynamics in a long-range acoustic propagation experiment," J. Acoust. Soc. Am. **114**, 1226–1242 (2003).

[16] O. A. Godin, A. G. Voronovich, and V. U. Zavorotny, "Coherent scattering of underwater sound and its implications for ocean remote sensing," Tenth Intl. Conf. on Sound and Vibration, Stockholm, 2593–2546 (2003).

[17] G. K. Batchelor, *An Introduction to Fluid Dynamics* (Cambridge University, Cambridge, 1964).

Geoacoustic inversion in range-dependent ocean environments using a plane wave reflection coefficient approach

S. A. Stotts, D. P. Knobles, R. A. Koch, D. E. Grant, K. C. Focke, and A. J. Cook
Applied Research Laboratories, The University of Texas at Austin, P.O. Box 8029, Austin, Texas 78713-8029

(Received 11 July 2003; accepted for publication 15 December 2003)

A new, efficient, versatile ray-based model is presented that performs geoacoustic inversions in range-dependent ocean waveguides faster than alternative forward models for which the computation time becomes extremely long, especially for broadband inversions. The water propagation is approximately separated from the seabed interaction using predetermined bathymetry and a possibly range-dependent water sound speed profile. The geometrical optics approximation is used to calculate eigenrays between sources and receivers, including bottom reflecting paths. Modeled broadband pressure fields are obtained by computing the plane wave reflection coefficient at specific angles and frequencies and by then linking this result with the bottom reflected eigenrays. Each perturbation of the seabed requires a recalculation of the plane wave reflection coefficient, but not a recalculation of the eigenrays, resulting in a highly efficient method. Range-independent problems are treated as a limiting case of the approach. The method is first described and then demonstrated with a few simple range-independent theoretical models. The versatility of addressing range-dependence in the bottom seabed is demonstrated with a simulated data set. Finally, the new model is applied to inversion from a measured data set, taken with impulsive sources, for both range-independent and range-dependent continental shelf environments. [DOI: 10.1121/1.1646405]

PACS numbers: 43.30.Cq, 43.30.Ma, 43.30.Pc [AIT] Pages: 1078–1102

I. INTRODUCTION

Geoacoustic inversion techniques have a long history in both land and ocean environments. Seismology, natural resource exploration, earthquake studies, and moving vehicle detections—all benefit from having an accurate environmental description. The last 10 or more years have seen a dramatic increase of interest in shallow water environments and littoral regions, the characteristics of which typically involve range dependence. Shallow water and shelf regions have been a primary focus of geoacoustic inversion studies from their inception.

Similarly, sound propagation predictions in ocean environments rely on accurate knowledge of the area under consideration. Water sound speed profiles, bathymetry, and the underlying bottom structure are important physical properties that influence sound propagation, and all are possibly functions of depth and range. In addition, frequency bands of interest often range from a few Hz up to tens of kHz. However, obtaining the complete parameter description required for these calculations by such methods as sediment coring is costly. Thus, the ability to infer parameter values from a limited amount of experimental acoustic data is an attractive alternative in many regions of interest.

Current inversion methods are based on combining an accurate optimization method, which varies selected geoacoustic parameters, with a forward propagation model. At each call to the forward model, a cost function is evaluated and stored. Finding the global minimum of this cost function results in the best solution of the bottom parameters for the assumed seabed representation, acoustic data, and propagation model adopted for the inversion. Forward model choices may include, but are not limited to, normal modes, parabolic approximation (PE) models, and geometric approximations (ray theory). For range-dependent environments, adiabatic-mode, coupled-mode, PE, or ray trace models could be used. In principle, a full-wave approach with any of these models could be developed for both types of environments, but the computation time could be excessive for practical applications involving many forward calls.

Improving efficiency and accuracy of the optimization algorithm is an ongoing topic of research. Recent workshops[1,2] have demonstrated several techniques for optimization, including simulated annealing,[3–6] genetic algorithms,[7] and least squares.[8] Collins and Fishman introduced a rotated coordinate approach to improve the efficiency of simulated annealing.[9] Recent developments of this rotated coordinate approach involve ordering the inversion parameters based on their perturbative sensitivities and uncovering any couplings that exist between the parameters.[10] Another advance involves hybrid methods, which combine a gradient method with a global method to increase efficiency,[11–13] one example being a method combining simulated annealing with a Levenberg–Marquardt gradient approach.[14] This technique quickly improves the estimate of the current minimum's location at each temperature reduction by applying the gradient calculation. A recent application of the simulated annealing approach to a range-independent data set is given in Ref. 15.

The technique presented in this paper is intended to simplify and accelerate the inversion process by using a ray-based approach. The forward model is constructed by first calculating the propagation paths in the water column from a range-dependent ray model. The ray paths are linked to bottom interaction effects by the plane wave reflection coeffi-

cient at the ray-path bottom angles. Range-independent environment calculations are simplified because each bottom interaction of a given ray path has the same grazing angle, whereas for variable bathymetry, the range at which each bottom interaction occurs must be stored along with the corresponding grazing angle.

One of the techniques presented here is that of separating the water column propagation from the bottom interaction, which allows any plane wave reflection coefficient model to be used for the bottom interaction description. Thus, the method is adaptable to future advances in bottom loss measurements and/or theory, but can also be used with previous models. The measurement of bottom loss or reflection coefficients has a long history in ocean acoustics.[16–18] Signals from explosive charges in deep-water regions were analyzed with ray theory to arrive at reflection loss as a function of angle and frequency.[19,20] Many theoretical models have been developed to describe reflection coefficients from stratified layers.[21]

For the analysis presented here with real data, an order of magnitude gain in the inversion time was achieved by use of the plane wave reflection coefficient (PWRC) method rather than a normal mode forward model for a range-independent example. Inversions in range-independent or range-dependent environments requires approximately the same run time for the PWRC method, whereas an inversion with a broadband PE model would be slower by at least an order of magnitude.

The efficiency of the PWRC method is due in part to the water-borne eigenray paths being calculated once prior to invoking the inversion procedure. The frequency dependence of the pressure field occurs in the phase associated with the ray path travel time and in the reflection coefficients. Beam displacement at the water–sediment interface would depend on frequency and grazing angle, which would then require a recalculation of the water-borne eigenrays at each inversion step. This would reduce the efficiency of the inversion procedure and is not performed in the PWRC method. The field contribution from the bottom interactions does, however, partially include beam displacement effects associated with internally reflected or refracted returns from the sediment since the complex bottom reflection coefficients are obtained from a full wave solution.

The propagation formalism is developed in Sec. II, with progressively more complicated examples showing the accuracy of a plane wave reflection coefficient approach. One of the goals of this study was to understand the low frequency limits of the PWRC method since beam displacement at the water–sediment interface is not included in the model. Frequencies 25–200 Hz are examined in the PWRC method examination presented in Sec. II. A brief discussion of the inversion technique, including the range-dependent ray model, is presented in Sec. III. Results of the application of the method to both simulated and measured data are presented in Sec. IV. The simulated data in Sec. IV A demonstrate two main points. First, the PWRC method has the capability of resolving thin-layer environments. Second, this method is also easily adapted to possible range dependence in the seabed by storing the ranges of each interaction and dividing the waveguide into range segments. Finally, the inversion of a measured data set is presented in Sec. IV B, and the resulting inversion demonstrates that a geometrical approach in shallow water environments can yield accurate and timely geoacoustic inversion results for both range-independent and range-dependent data. The range-independent data are analyzed first. Next, the resulting inverted parameters are used to assess the accuracy of the range-dependent inversions. The importance of having reliable sound speed profile data is revealed for the range-dependent analysis. A brief summary is presented in Sec. V.

II. REFLECTION COEFFICIENT FORMALISM

This section describes the theoretical development of the PWRC approach to geoacoustic inversion. The pressure field is modeled approximately by separating ocean propagation ray paths from the layered bottom interaction. The bottom interaction is included by using a full wave description, making the PWRC method a hybrid model. This is in contrast to a full ray theory approach, which traces rays into the bottom layers. The equations which describe the PWRC model are first presented and then compared to full ray theory.

The general form of the equation that describes the PWRC process is given by

$$P_m = \sum_{j=1}^{n_r} \prod_{n'=i}^{n_{t,j}} [R_S(\theta_{n',j})]^i \prod_{n=k}^{n_{b,j}} [R_B(\theta_{n,j})]^k G_j e^{i\omega\tau_j}, \quad (1)$$

where R_S and R_B are the surface and layered-bottom plane wave reflection coefficients, respectively, and are derived from wave theory. The frequency is $f=\omega/2\pi$, τ_j is the water-borne ray travel time, and the geometric spreading loss, G_j, for the water-borne ray path j is given by

$$G_j = \sqrt{\frac{\cos\psi_{s,j}}{r(dr/d\psi_{s,j})\sin\psi_{r,j}}}, \quad (2)$$

with $\psi_{s,j}$ and $\psi_{r,j}$ being corresponding ray angles at the source and receiver, respectively, for the jth ray when the source-to-receiver range is r.

In Eq. (1), the index k is defined to be

$$k = \begin{cases} 1 & \text{for range-dependent environments,} \\ n_{b,j} & \text{for range-independent environments.} \end{cases} \quad (3)$$

Similarly, for the surface reflections, $i=n_{t,j}(1)$ for range-independent (dependent) environments, while n_r is the total number of ray paths included at receiver m, and $n_{t,j}$ and $n_{b,j}$ are the total number of top and bottom interactions for ray path j, at corresponding angles $\theta_{n',j}$ and $\theta_{n,j}$, respectively. Here $\theta_{n',j}$ is the nth top bounce for the jth ray, and $\theta_{n,j}$ is the grazing angle for the nth bottom bounce. $R_B(\theta_{n,j})$ includes the effect of all orders of internal reflections in the sediment. For surface reflections $R_S=-1$ is assumed to hold for all the examples and analyses presented here.

It is important to distinguish the PWRC model from ray theory. The ray approximation within a single, constant

sound speed, range-independent water layer, written in terms of individual bounces and ignoring any losses, is given by[22,23]

$$P=\sum_{j=0}^{N_{\text{ray}}} G_j \overline{R}_j(\overline{\theta}_{w,j}) e^{i\omega\overline{\tau}_j}, \tag{4}$$

where $j=0$ corresponds to the direct path with $\overline{R}_0(\overline{\theta}_{w,j=0})=1$. The angle index w refers to the incident grazing angle for each ray at the water-layer interface, $\overline{\theta}_{w,j}$ is the bottom grazing angle for the jth eigenray, and N_{ray} is the total number of rays included in the pressure field, P. The ray reflection coefficient $\overline{R}_j(\overline{\theta}_{w,j})$ is the combined reflection-transmission coefficient for each ray, with $j=1$ corresponding to reflection from the layer without penetration, $j=2$ corresponding to one layer traversal, etc., i.e., multiple reflections within each layer, as well as refraction within a layer. The notation, $\overline{R}$, is used to distinguish the ray reflection coefficients from the PWRC reflection coefficients throughout this paper.

To properly include the contribution from higher order layer traversals, different eigenray grazing angles are required. The ray travel time is given by $\overline{\tau}_j$, and the geometric spreading loss for fixed source-to-receiver depth and range is given by Eq. (2).

To examine the accuracy of the PWRC model and to understand its differences from ray theory, it is helpful to present the transmission loss (TL) calculated from the complex pressure field for several examples. First, the field from the interaction with an interface between two fluid half-spaces is examined. This is followed by a discussion of the Pekeris waveguide. Then the reflection from a single fluid–sediment layer is analyzed. For the case of reflection from a single layer, the relationships among the full wave model, ray theory with layer-penetrating paths, and the PWRC model will be illustrated. These scenarios are represented in Fig. 1. As another benchmark, comparisons to the normal mode solution are also presented for some of these examples.

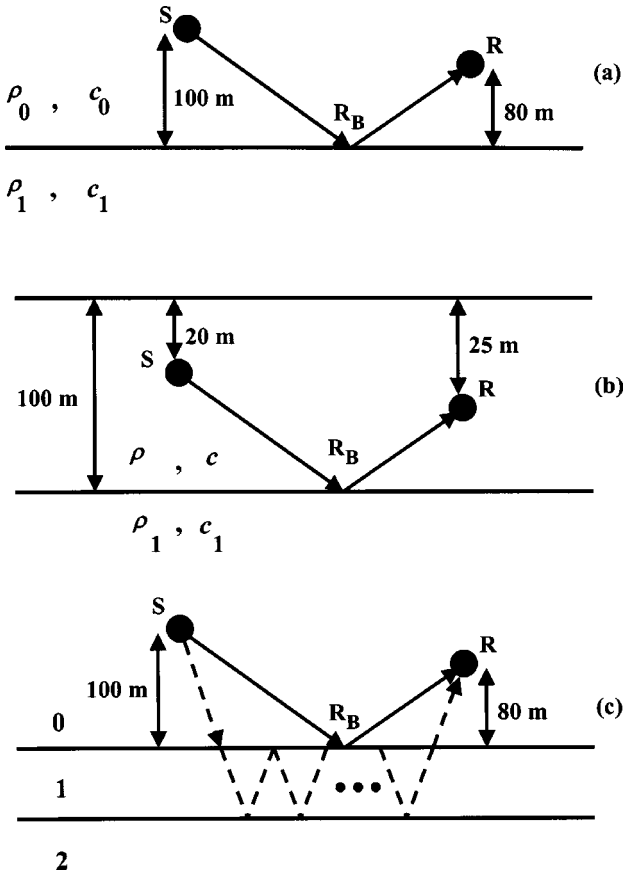

FIG. 1. Sketches of the reflection from the fluid-over-fluid half-space (a), Pekeris waveguide (b), and a single layer between two half-spaces (c). The solid lines represent the PWRC method, whereas the dashed lines in (c) represent ray paths with multiple layer traversals. The source, receiver, bottom reflection coefficient, density, and sound speed are identified by S, R, R_B, ρ, and c, respectively.

A. Two fluid half-spaces

For a point source located at z_s above the interface between two fluid half-spaces, the total pressure field at a receiver located within the same half-space as the source can be written as

$$\Phi(r,z,z_s)=\frac{S_\omega}{2\pi}\int_0^\infty G(k,z,z_s)J_0(kr)k\,dk, \tag{5}$$

where $z_<=\min(z,z_s)$, $z_>=\max(z,z_s)$, and S_ω is the source term which does not need specification since TL comparisons between the models will be discussed below and are calculated relative to the intensity at 1 m from the source.

The Green's function is derived from the continuity of the potential and the depth derivative of the potential across the interface between layers and from the discontinuity of the depth derivative of the potential at the source. The result is[24]

$$\Phi(r,z,z_s)=\frac{S_\omega}{2\pi}\int_0^\infty\left[\frac{\alpha_0(\rho_1/\rho_0)\cosh\alpha_0 z_< + \alpha_1\sinh\alpha_0 z_<}{\alpha_0(\alpha_0(\rho_1/\rho_0)+\alpha_1)}\right]e^{-\alpha_0 z_>}J_0(kr)k\,dk, \tag{6}$$

where $\alpha_j=\sqrt{k^2-k_j^2}$ with $k_j=\omega/c_j$, $j=0,1$. Here, c_0 is the sound speed in the upper half-space fluid, typically water, which contains the source and receiver. The lower half-space exhibits a higher sound speed c_1. Figure 1(a) depicts the reflection from this fluid–fluid interface.

The reflection coefficient obtained from Eq. (6) by separating the upgoing and downgoing fields is

$$R_{hs}=\frac{(\alpha_0\rho_1-\alpha_1\rho_0)}{(\alpha_0\rho_1+\alpha_1\rho_0)}, \tag{7}$$

where ρ_j is the density of layer j. This is the reflection coefficient used in the PWRC method and is equivalent to the ray reflection coefficient given by[25]

$$V=\frac{(m\cos\theta_0-n\cos\theta_1)}{(m\cos\theta_0+n\cos\theta_1)}, \tag{8}$$

where $m=\rho_1/\rho_0$, $n=c_0/c_1$, $k=k_j\cos\theta_j$, with θ_j, $j=0,1$, corresponding to the angles from the normal of the incident and transmitted rays. The boundary conditions are continuity of pressure and of the normal derivative of the pressure at the interface between half-spaces. This result shows that, for reflection in a water half-space from a higher speed fluid half-space, the PWRC method will approach the ray solution for all frequencies, if the eigenray angles are used to evaluate the reflection coefficient. This result ignores any corrections that account for interface wave phenomenon.

Figure 2 shows three TL model solutions for a source and receiver depth located 100 m and 80 m from the interface between the half-spaces, respectively. The three solutions plotted in Fig. 2(a) are the analytic, normal mode, and ray approximation, at a frequency of 100 Hz. The PWRC method is equivalent to the ray approximation for this problem, as stated above. The normal mode solution was obtained using the propagation model ORCA,[26] using the complex horizontal wave number normal modes. The upper half-spaces containing the source and receivers had a sound speed $c_0=1500$ m/s and a density $\rho_0=1.0$ g/cm^3, with a slight density change to $\rho_0=1.1$ g/cm^3 at a depth of 5000 m from the interface, while the lower half space, assumed to be homogeneous, had a sound speed $c_1=2000$ m/s and a density $\rho_1=1.5$ g/cm^3. To obtain the analytic solution, the right-hand side of Eq. (6) was calculated numerically.[27] This solution was shown in Ref. 27 to be equivalent to the solution obtained from the full wave model, OASES.[28] The wave-number integration scheme used in OASES was used for the analytic solutions presented here; namely, minimum and maximum phase speed are initially specified along with a number of integration points, and from these the maximum wave number included in the integral is calculated. The phase speed bounds are chosen such that the integrand is negligible outside $[c_{\min},c_{\max}]$. Typically, $c_{\max}=10^{20}$, and $c_{\min}=10\%$ of the minimum sound speed in the problem. The analytic solution is presented here to provide insight into detailed comparisons with both the ray and PWRC solutions, as discussed below.

For this example and at 100 Hz (or greater), the PWRC method is comparable in accuracy to the normal mode and analytic solutions. At frequencies below 50 Hz, however, the ray approximation loses accuracy at ranges exceeding 150 m, where the interference of the direct and bottom-reflected paths produces a shift in the nulls of the TL compared to the normal mode and analytic solutions, as demonstrated in Fig. 2(b). This shows that, for the half-space example, the PWRC method is limited by the ray theory approximation of the complex pressure field.

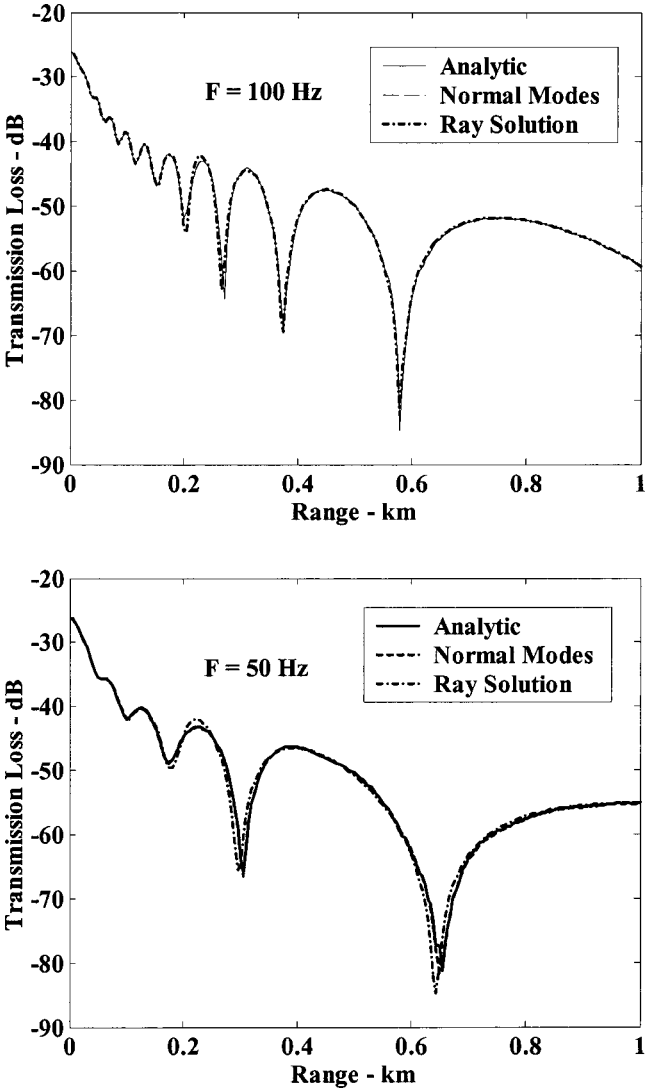

FIG. 2. Transmission loss for a source and receiver located 100 m and 80 m, respectively, above the interface, between two fluid half-spaces.

B. Pekeris waveguide

The second example illustrating the lower frequency limits of the PWRC method for waveguide-type problems is the Pekeris waveguide with a vacuum above the upper interface and a lower half-space with a sound speed greater than that of the water layer. Using a source and receiver inside the 100 m thick water layer, as depicted in Fig. 1(b), reflection from the lower half-space was examined. The surface reflection coefficients are given by $R_S=-1$ for all $\theta_{n',j}$, as stated previously; R_B is given by Eq. (8). A comparison of the ray model solution and the PWRC calculation shows exact agreement, neglecting any interface wave effects, since the reflection coefficients are equivalent. Convergence of the field is achieved after five traversals of the waveguide for the PWRC and ray solutions; however, three times this number of traversals were included for the results presented here to assure convergence at these ranges.

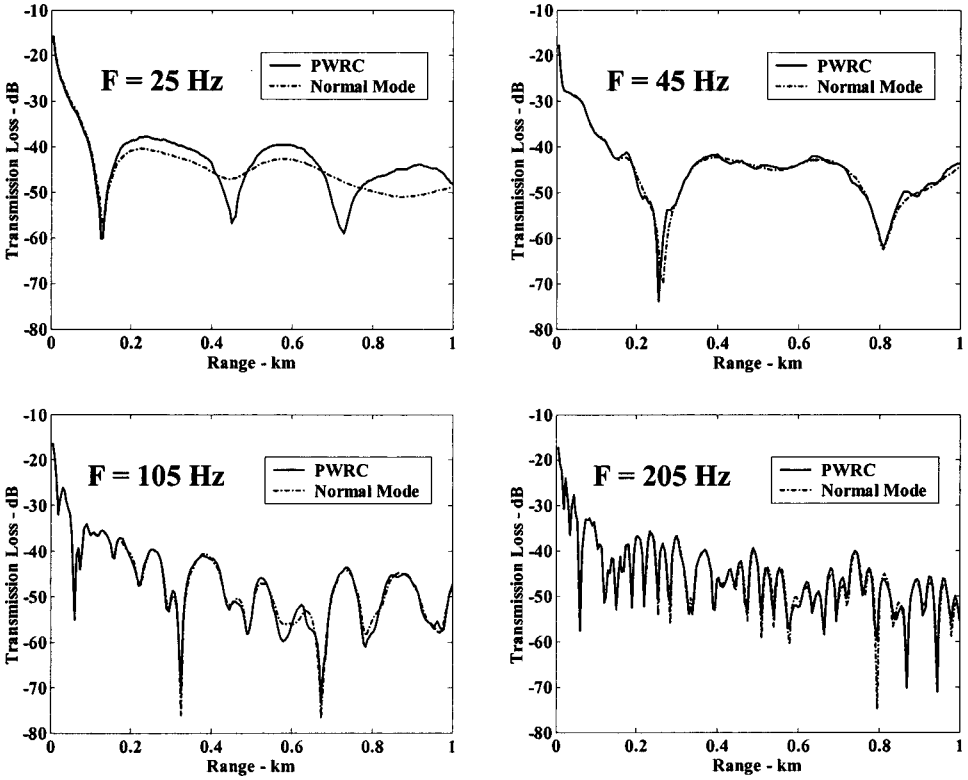

FIG. 3. Transmission loss for a 100 m deep ocean waveguide ($c=1500$ m/s, $\rho=1.0$ g/cm^3) overlying a substrate ($c_1=2000$ m/s, $\rho_1=1.5$ g/cm^3). The source and receiver depths are 20 m and 25 m, respectively.

TL at 25, 45, 105, and 205 Hz is shown in Fig. 3 for the normal mode and PWRC solutions. The source depth was $z_s=20$ m, the receiver depth was $z_r=25$ m, $c=1500$ m/s, $\rho=1.0$ g/cm^3, and the underlying substrate had a sound speed $c_1=2000$ m/s and a density $\rho_1=1.5$ g/cm^3. The comparisons to the normal mode model solution (calculated in the complex horizontal wave-number plane) illustrate the accuracy of the PWRC method as a function of frequency. The PWRC model at 25 Hz produces destructive interference (Lloyd's mirror) that is too strong at ranges where bottom reflections contribute. For these examples, ray theory solutions, ignoring beam displacement, are equivalent to the PWRC method since the reflection is from a half-space. The agreement between ray theory and the normal mode solution could be improved by accounting for beam displacement; however, the point is to illustrate the low frequency limit of the PWRC method when these effects are excluded. As expected, the PWRC solutions improve with increasing frequency. For frequencies above 50 Hz, i.e., wavelengths less than 0.3 water depths, good agreement is seen between the normal mode and PWRC solutions. This approximate lower frequency limit of 50 Hz was also substantiated with the ONR Inversion Techniques (IT) workshop synthetic data, test cases I and II (Ref. 29).

C. Penetrable layer between two fluid half-spaces

The next comparison was made with a fluid layer of thickness L, inserted between two half-spaces, with the upper half-space representing the ocean and the lower half-space, a penetrable substrate. The sound speed in the layer is greater than that in the ocean, but less than in the penetrable substrate. The source and receiver are located in the ocean, and reflection from the fluid layer was considered. Comparisons between the analytic solution and the ray model were made to determine the number of layer traversals necessary to reproduce the analytic solution, whereas comparisons between the analytic, ray, and PWRC methods are presented here to illustrate the deviation of the PWRC method from ray theory.

The exact solution for the pressure field in the ocean half-space above the layer is given by

$$\Phi(r,z,z_s)=\frac{S_\omega}{4\pi}\int_0^\infty\left[\frac{e^{-\alpha_0 z_>}}{\alpha_0}+\frac{e^{\alpha_0(z_>-2H)}}{\alpha_0}\times\left(\frac{r_{01}+r_{12}e^{-2\alpha_1 L}}{r_{01}r_{12}e^{-2\alpha_1 L}+1}\right)\right]e^{\alpha_0 z_<}J_0(kr)k\,dk, \tag{9}$$

where the reflection coefficients are defined as

$$r_{ij}=\frac{\rho_j\alpha_i-\rho_i\alpha_j}{\rho_j\alpha_i+\rho_i\alpha_j}, \tag{10}$$

with $i=0$, 1 and $j=1,2$, $i\neq j$.

The denominator in the second term of the integrand can be expanded by noting that $r_{01}=-r_{10}$. Each term in the expansion can be associated with a given number of traversals within the fluid layer, and by expanding each term, a direct comparison to the ray approximation can be made. For $|r_{10}r_{12}|<1$, the denominator is

$$\frac{1}{1-r_{10}r_{12}e^{-2\alpha_1 L}}=1+r_{10}r_{12}e^{-2\alpha_1 L}+(r_{10}r_{12}e^{-2\alpha_1 L})^2+\cdots. \tag{11}$$

Substituting this expansion in the integrand and then regrouping the multiple reflection terms gives

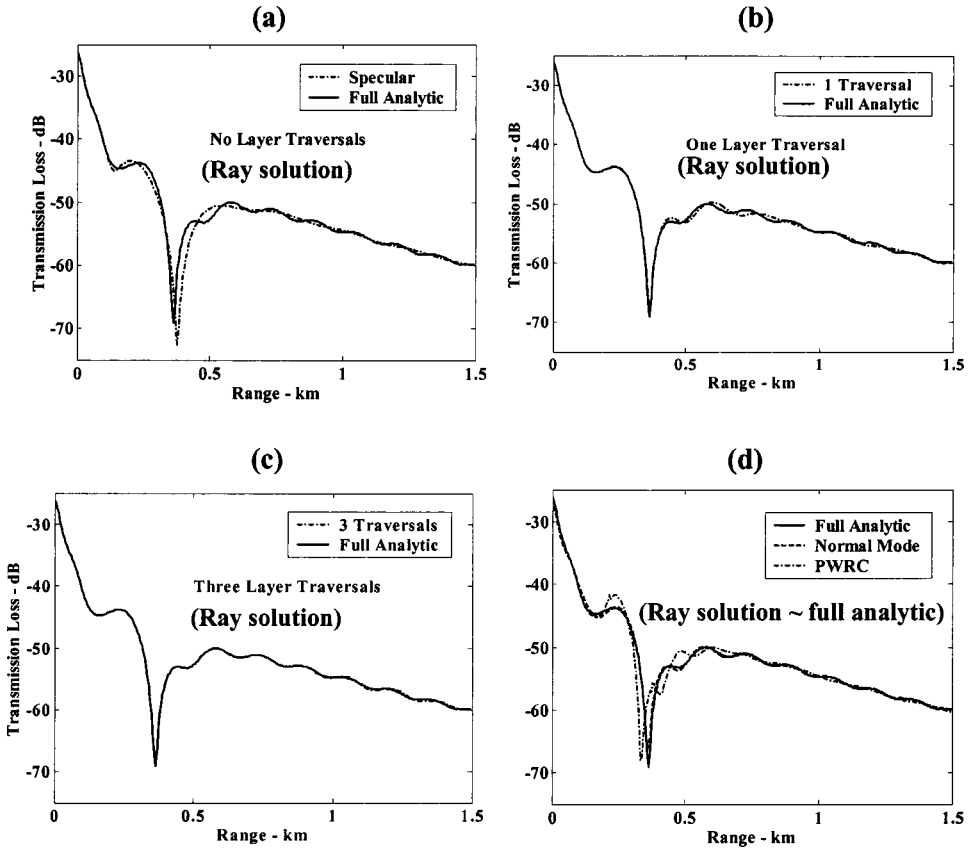

FIG. 4. Reflection at 25 Hz from a fluid layer overlying a penetrable half-space from a term by term expansion of the field including (a) specular reflection, (b) one layer traversal, (c) three layer traversals, and (d) the full analytic solution. The source and receiver are 100 m and 80 m, respectively, above the water-layer interface and the layer thickness is 30 m. Sound speeds in the water/fluid/half-space are 1500/2000/2500 m/s and the corresponding densities are 1.0/1.5/1.5 g/cm^3.

$$r_{01}+r_{12}e^{-2\alpha_1 L}(1+r_{10}r_{01})+r_{12}e^{-2\alpha_1 L}(1+r_{10}r_{01}) \times r_{10}r_{12}e^{-2\alpha_1 L}+\cdots. \tag{12}$$

The quantity in the parentheses can be factored to give

$$(1+r_{01}r_{10})=(1+r_{01})(1-r_{01})=t_{01}t_{10}, \tag{13}$$

where $t_{01}\equiv 1+r_{01}$ is the transmission coefficient from the water to the sediment layer. Similarly, t_{10} is the transmission from the sediment layer to the water. Thus, each wave term resulting from the substitution of Eq. (12) into Eq. (9) can be compared to terms for individual ray paths in Eq. (4). The result for the analytic pressure field is

$$\Phi(r,z)=\frac{S_\omega}{4\pi}\int_0^\infty\left\{\frac{e^{-\alpha_0 z_>}}{\alpha_0}+\frac{e^{\alpha_0(z_>-2H)}}{\alpha_0}[r_{01}+t_{01}r_{12}t_{10}e^{-2\alpha_1 L}+t_{01}r_{12}t_{10}e^{-2\alpha_1 L}r_{10}r_{12}e^{-2\alpha_1 L}\cdots]\right\}e^{\alpha_0 z_<}J_0(kr)k\,dk, \tag{14}$$

corresponding to the incident field, reflected field off the upper layer interface, reflected field off the lower layer interface, etc. The total reflection coefficient is given by[25]

$$V=r_{01}+t_{01}t_{10}r_{12}e^{-2\alpha_1 L}\times\sum_{n=0}^{\infty}(r_{10}r_{12}e^{-2\alpha_1 L})^n. \tag{15}$$

The ray reflection coefficients are defined by

$$\begin{aligned}\overline{R}_1&=r_{01},\\ \overline{R}_2&=t_{01}r_{12}t_{10},\\ \overline{R}_j&=t_{01}r_{12}t_{10}(r_{10}r_{12})^{j-2},\end{aligned} \tag{16}$$

where the right-hand side coefficients correspond to the reflection and transmission coefficients used in Eqs. (9)–(15).

The analytic reflection coefficients are related to the ray reflection coefficients by

$$R_j=\overline{R}_j(e^{-2\alpha_1\theta(k)L})^{j-1}, \tag{17}$$

where the wave number index k is defined in Eq. (9).

The TL at 25 Hz in the half-space above a finite fluid layer overlying a penetrable half-space is shown in Fig. 4. The source and receiver are located 100 m and 80 m, respectively, above the water-sediment interface, and the layer thickness is $L=30$ m. The PWRC and ray theory paths are sketched in Fig. 1(c). The ray solution gives almost exact agreement to the analytic TL to a range of 1.5 km using three or fewer traversals inside the sediment layer as shown in Figs. 4(a)–(c). Additional traversals must be included to maintain the agreement at greater ranges. The comparison in Fig. 4(d) of the PWRC solution with the ray and analytic

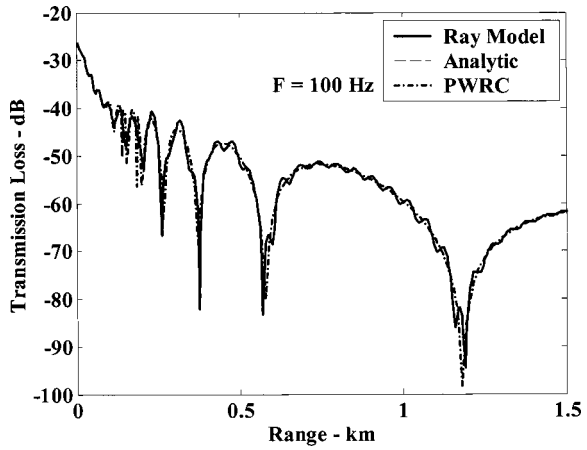

FIG. 5. Comparison of the analytic and ray solutions to the PWRC method for reflection off a layer overlying a penetrable half-space at a frequency of 100 Hz.

solutions, represented by the full analytic curve, demonstrates that for reflection from a layer at 25 Hz, the PWRC solution differs slightly from the ray theory solution. The normal mode solution in Fig. 4(d) gives good agreement to the analytic and ray solutions, as expected.

The PWRC accuracy increases with increasing frequency, as shown in Fig. 5 for a frequency of 100 Hz. The ray, analytic, and PWRC solutions in Fig. 5 agree although the PWRC does not reproduce some of the small-scale structure of the TL.

Several factors may contribute to the deviation of the ray theory results from those obtained with the PWRC method. In the ray theory solution, individual eigenrays are traced for each layer traversal class; however, in the PWRC method, the grazing angle of one incident eigenray (the specularly reflected ray) is used to evaluate the effect of all the internal layer traversal paths. The reflection coefficient for each bottom interaction contains an infinite sum of bottom traversals within the layer.[30] The use of the same grazing angle for all traversals in the PWRC method smooths the interference between the individual paths, which accounts for the mismatched result in Fig. 5.

D. Range-dependent propagation

1. Tank wedge experiment

Another demonstration of the accuracy of the PWRC method when applied to a range-dependent calculation is the down-slope propagation problem shown in Fig. 6(a). The source for the TL measurement was at a depth of 47 m, and the receiver was at a depth of 30 m. This is a scaled version of a tank experiment.[31] The water sound speed is constant at 1490 m/s; the bottom consists of a 200 m thick layer with sound speed $c_1 = 1784$ m/s, density $\rho_1 = 1.97$ g/cm^3, and attenuation $\alpha_1 = 0.547$ dB/(m kHz). The half-space parameters are $c_{\text{sub}} = 5790.0$ m/s, $\rho_{\text{sub}} = 9.8$ g/cm^3, and $\alpha_{\text{sub}} = 0.0173$ dB/(m kHz). The bottom slope is 3°. In this comparison, there is better agreement between the ray and PWRC models than in the previous example. The improved agreement may be due to the attenuation and thickness of the sediment layer.

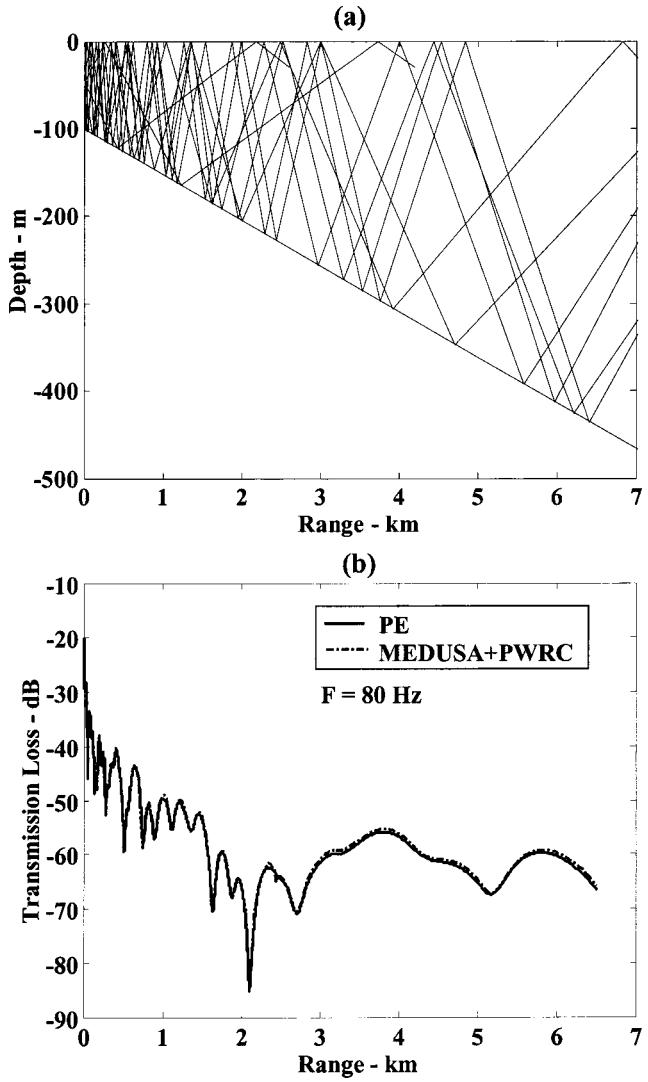

FIG. 6. (a) Ray trace and (b) TL at 80 Hz for a down-slope waveguide, comparing the PE and PWRC models. The water depth, 100 m at the source, increases to approximately 624 m at a range of 10 km.

Excellent agreement between the PWRC and PE models is shown in Fig. 7 for up-slope propagation in the same environment as used in Fig. 6, but with a slightly different geometry. The TL was calculated at 80 Hz to a range of approximately 3500 m. The bottom slope is similar to the measured bathymetry discussed in Sec. IV B.

2. Shallow water ocean environment

A final example compares a range-dependent environment simulated using two measured sound speed profiles (SSP) and bathymetry obtained from the data set discussed in Sec. IV B and depicted in Fig. 8(a). The source depth is 30 m, and the receiver depth is 228.7 m.

Initially, a substrate below the water–sediment interface was used in the TL calculation. The SSP was linearly interpolated with respect to range for the PE calculation, according to the interpolation method used in MEDUSA.[32] The substrate sound speed, density, and attenuation was 1827.4 m/s, 1.88 g/cm^3, and 0.79 dB/(m kHz), respectively. Excel-

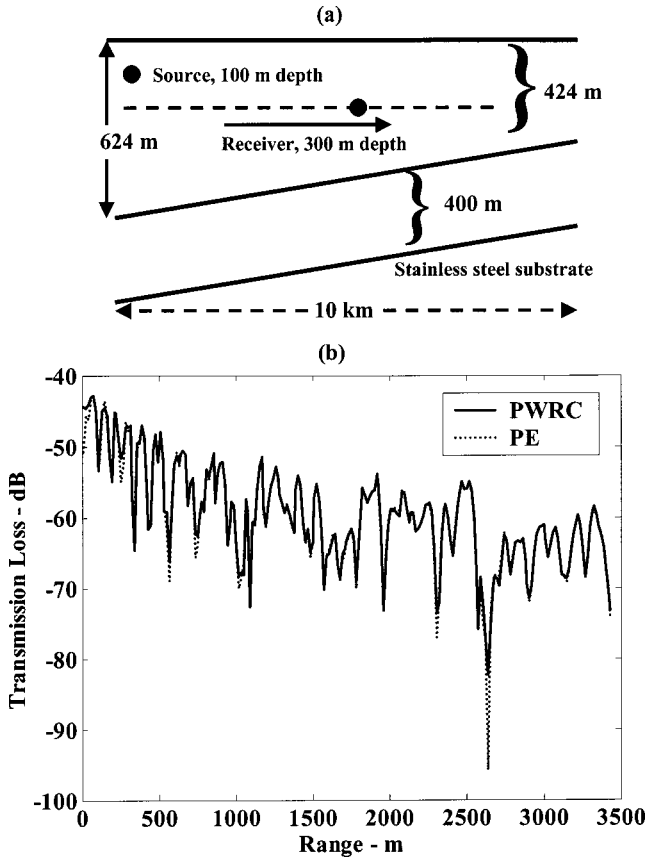

FIG. 7. Geometry and TL at 80 Hz for an up-slope waveguide, comparing the PE and PWRC models. The water depth, 624 m at the source, decreases to 424 m at a range of 10 km. The source and receiver depths are 100 and 300 m, respectively.

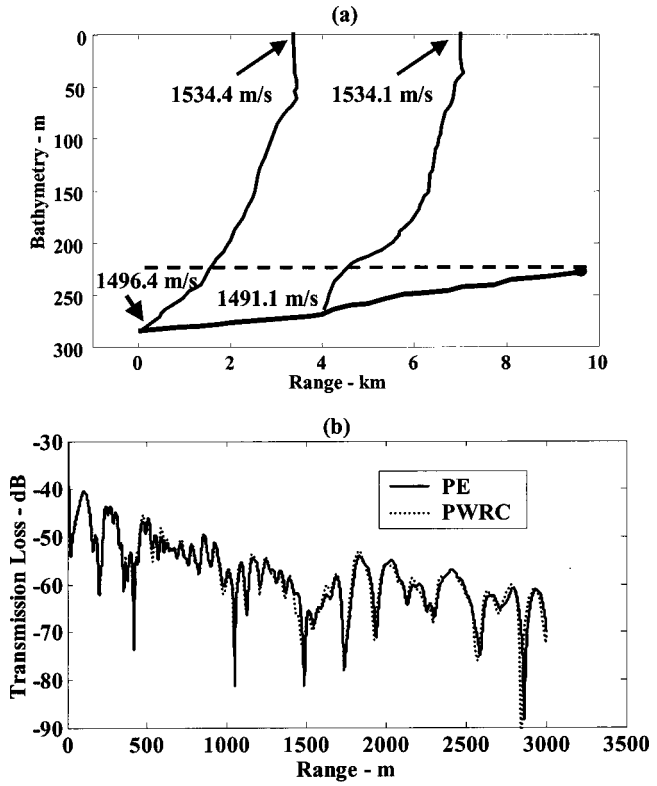

FIG. 8. (a) Simulated SSPs, bathymetry, and bottom layers. (b) TL at 100 Hz for the up-slope waveguide, comparing the PE and PWRC models.

lent agreement between the PWRC and PE models for the TL at 100 Hz was obtained, similar to the agreement exhibited in Fig. 7(b).

Next, a 10 m thick sediment layer was inserted below the water–sediment interface but above the same substrate. The sound speed at the top and bottom of the sediment layer was $c_t = 1526.3$ m/s and $c_b = 1548.0$ m/s, respectively, the sediment density was 1.74 g/cm^3, and the sediment attenuation was 0.18 dB/(m kHz). The bottom was divided into five 2 meter thick layers with continuous interfaces to approximate a linear profile with respect to depth, since ORCA forces a $1/c^2$ linear depth dependence in each layer. The TL from the PWRC and PE models at 100 Hz for the single sediment layer environment is shown in Fig. 8(b). The two models agree except for some small scale structure. A similar environment will be addressed in the range-dependent inversions presented in Sec. IV B 1.

E. Summary

In this section, the PWRC method, applying full wave reflection coefficients to the bottom interactions along the water-borne propagation paths, has been shown to give a good approximation to analytic solutions. This was demonstrated for increasingly complicated environments, concluding with range-dependent, two-dimensional wedges and with simulations to approximate the measured fields in Sec. IV B. The PWRC method was compared to ray theory, normal modes, analytic solutions, and PE for these examples.

III. RANGE-DEPENDENT PWRC MODEL AND INVERSION TECHNIQUES

The preceding section demonstrated the accuracy and limitations of the PWRC hybrid model. In this section, details of the inversion procedure that uses the PWRC forward model will be presented. The cost function used in the applications is also given here.

For the current work, MEDUSA[32] was chosen for the ray trace model because of its modularity, the robustness of the approach, and its familiarity. MEDUSA incorporates range-dependent sound speed and bathymetry profiles, providing a modified cubic spline interpolation for both. A two-dimensional sound speed field is constructed using linear range interpolation between the modified profiles. Initially, a fan of rays are launched from a specified source depth, and the path history for each ray to the specified receivers is recorded. Rays of similar path history bracketing a given receiver range are identified, and the nonlinear ray equations are solved numerically to calculate corresponding eigenrays.

For the inversion forward model, eigenrays are calculated for a fixed waveguide geometry and fixed source and receiver depths. The frequency independent eigenray characteristics are stored, including each ray's travel time, bottom grazing angles, and geometric spreading loss. In addition, for range-dependent environments, the range for a given bottom interaction for each eigenray is recorded, since each bottom interaction will occur at a different grazing angle along a single ray path. These characteristics are calculated only

once and then are stored on a file for subsequent access. Although the bottom loss is not included at this stage, it is part of the forward model in the PWRC. Clearly, the method is equally applicable for range-dependent and range-independent environments.

The plane wave reflection coefficients were obtained using ORCA, which can incorporate depth gradients in sound speed, density, and attenuation. Again, the versatility of the PWRC approach allows any reflection coefficient model to be incorporated. Current or future advances in experimental and theoretical bottom descriptions, such as a Biot–Stoll-type description,[33–37] or with geoacoustic models describing unconsolidated sediments,[38] could be substituted for the ORCA model to obtain a more detailed description of the seabed physics.

The reflection coefficients for specified grazing angles are stored to improve the efficiency of the model. A linear interpolation of both the magnitude and phase of the reflection coefficient at each eigenray grazing angle is performed. Several sample computations, 50–500 Hz, were made to optimize speed and accuracy of this interpolation. The result was that approximately 1° increments in the grazing angles provide accurate interpolations and still achieve rapid field evaluations. For the phase interpolation, multiple cycles are incremented successively by 2π to make the phase function monotonic. For many of the examples considered, about 15 increments of 2π are required to reconstruct the phase function up to approximately 500 Hz. More may be needed for higher frequencies. A simple combined threshold and zero crossing detector method was incorporated to search for these phase cycles.

The inversion program was based on simulated annealing.[5] Modeled complex pressure fields are compared to simulated data by a Bartlett-type cost function.[15] This cost function can be written as

$$\Phi = \frac{1}{N}\sum_{i=1}^{N} \phi_i , \tag{18}$$

where N is the number of receivers used in the inversion. The contribution for each receiver is

$$\phi_i = \min_k \left\{ 1 - \frac{|\Sigma_j M_{i,j} D_{i,j}^* e^{i\omega_j \delta\tau_{i,k}}|}{\sqrt{M_i \times D_i}} \right\}, \tag{19}$$

where $M_{i,j}$ is the model value at the ith receiver and the jth frequency ω_j. $D_{i,j}$ is the corresponding data value. Note that this cost function is a coherent sum in frequency since the sum over j is inside the absolute value. The absolute value implies an incoherent sum over receivers is calculated. The average over all the receivers yields the cost function in Eq. (18). This incoherent average over receivers translates into an incoherent cost function average with respect to range for these discrete sources and is similar to a more traditional matched field calculation where averaging over data values for a given receiver is applied to moving sources.

The phase term containing $\delta\tau_{i,k}$ corresponds to the kth bin of a delay time window introduced because absolute arrival times were not recorded in the data. To begin, the $\delta\tau_{i,k}$ that gives the maximum value (such that ϕ_i is a minimum) is determined. The delay time window spans the entire τ_i search space during the first iteration for each receiver to determine an initial minimum independently for each receiver. Subsequent calls to the forward model use a reduced search space, $\delta\tau_i$, centered on the location of this initial minimum for use in subsequent calls. Limiting the reduced window to approximately 200 τ_i values maintains the efficiency of the inversion, although fewer values may be acceptable for even faster calculations. For the simulated data, exact travel times are known, so the delay term $\delta\tau_i = 0$ for all i.

In the model norm

$$M_i = \sum_j |M_{i,j} M_{i,j}^*|, \tag{20}$$

with a similar expression for the data norm, D_i.

The global minimum of this cost function occurs for the highest correlation between model and data for a coherent sum over frequencies, j, and for an incoherent average over the hydrophones, i. In this definition of the cost function, $M_{i,j}$ is a product of the source spectrum and the impulse response field, which can be written as

$$M_{i,j} = S_j R_{i,j}, \tag{21}$$

where the source term for the simulated data, S_j, is unity for all frequencies. However, for real data, the actual frequency-dependent source spectrum was measured independently to provide as complete a representation of the field as possible.

Several points are made concerning the inversions with this cost function. First, for the applications presented in Sec. IV, the bathymetry and sound speed field are assumed known (for the data that were measured). Thus, no geometric parameters corresponding to the SSP or water depth are included in the inversion. This limitation facilitates the efficiency of the PWRC method, but the result may produce some inversion artifacts to compensate for possible errors in the field. However, time series analysis of the data and model will substantiate the geometric values used in Sec. IV. Nevertheless, the model could easily be expanded to allow variations in the geometric field by calculating and storing eigenray characteristics for several geometries. Minimizing the cost function given in Eq. (18) with respect to the stored geometries may result in more accurate inversions.

IV. APPLICATIONS

In this section, the PWRC method is applied to the inversion of both simulated and measured data. The simulated data set discussed in Sec. IV A demonstrates the versatility of the PWRC method in accounting for possible range dependence in real seabeds. For the data, an experiment was designed to record sufficient information to perform geoacoustic inversions. Data from impulsive sources were recorded for both range-independent and range-dependent environments and are analyzed in Sec. IV B. The approach taken with these data was to first invert the range-independent data for geoacoustic values and then use these values as a starting point for inverting the range-dependent data recorded nearby.

Comparisons of overall data and model time series structure obtained from a final set of inverted parameters will be presented along with validations.

A. Inversion techniques workshop simulated data

Simulated data from the recent Inversion Techniques Workshop, May 2001,[2] were inverted using the PWRC method. The three test cases (I–III) contain some common environmental parameters and data specifications. For the simulated data, the source depth was 20 m, and for the simulated data the frequency was sampled in 1 Hz steps for 25–199 Hz and in 5 Hz steps for 200–500 Hz. The ranges 5–5000 m were sampled in 5 m steps at depths of 25 m and 85 m. The water column was a downwardly refracting profile with a linear gradient, $c_w(z)=(1495-0.04z)$ m/s. The benchmark fields were produced using a parabolic equation (PE) model.[39,40] Reference 29 gives another solution set to this data with a PE-forward model and obtained concurrently with, but independently of, the PWRC method.

In the PWRC solution, good results[29] were obtained for the top layers for test cases I and II, using a realistic set of array data ranges, 100–3000 m in 100 m increments, and frequencies, 50–500 Hz in either 10 or 20 Hz increments. All the results reported for the PWRC method used the 25 m depth horizontal array data.[41] The initial results were obtained prior to workshop presentations. Note that, in test case III, there is a range-independent thin top layer and that an intrusion is introduced, but only involves layers below the first layer. However, all that was known initially was that an intrusion was present in the seabed. Thus, various models of the seabed were attempted to model the intrusion and are briefly discussed here.

1. Seabed models—test case III

Various models of the intrusion in the seabed were attempted, but only two types will be discussed here. The first seabed model is a linear range-dependent solution for either one or two layers, with the slope determined by allowing the end points to be varied. The second seabed model represents the intrusion by a nonlinear model given by

$$h(r)=h_t+T_0(1-e^{-((r-r_c)/\sigma)^2}), \tag{22}$$

where σ is the width of the intrusion, h_t is the minimum layer thickness located at range r_c, and T_0 is a scaling factor. Both one- and two-layer inversions were performed using this function. For the single layer case, r_c, T_0, and σ were allowed to vary. For the two-layer model, separate values for the T_0 and σ parameters were used for each layer; however, the center point, r_c, was fixed at 2500 m. Several attempts were made with this model, including using data up to 2500 m in range, as well as the full 5000 m data.

The range dependence of the bottom was accounted for by dividing the ranges into segments of 100–500 m. For the linear models, 100 m range segments were used and for the nonlinear models, 250 m range segments were used when the total inversion range was 2500 m, whereas 500 m range segments were used for the 5000 m nonlinear model. For each iteration, the reflection coefficients were evaluated for all the range segments before the model field was calculated. For each eigenray, the range location of the bottom interaction was stored in addition to the corresponding grazing angle. This information determined which range segment was used to evaluate the reflection coefficient at a particular bottom interaction. A linear range interpolation of the reflection coefficient was performed to evaluate the reflection coefficient at a given range within the range segment.

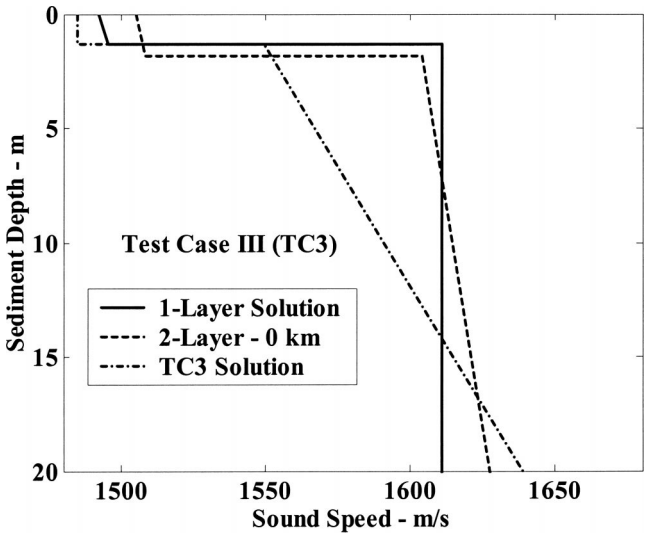

FIG. 9. Test case III solutions for the linear one-layer and two-layer models, as compared to the actual TC3 solution.

2. PWRC inversion results—test case III

In the one-layer linear model, a 1 km maximum range was used, and the environment was divided into 100 m range segments. The single-layer model result matched very closely the first layer of the correct solution. For instance, the thickness at a range of 100 m was 2.39 m and decreased to 1.36 m at a range of 2500 m. The correct answer was 1.30 m. The inversion result is shown as a function of depth in Fig. 9. The correct density for the top layer, 1.49 g/cm^3, is slightly underpredicted by the single layer model solution (1.38 g/cm^3), whereas the attenuation is overpredicted by almost a factor of 2.

The two-layer linear solution was extended to 2500 m with 250 m range segments. The final solutions for this linear model also tended toward a thin first layer with little range variation, i.e., the slope was approximately zero, and the first layer thickness approximated the correct result. The first layer thickness was 1.82 m at a range of 100 m and decreased to 1.67 m at a range of 2500 m. The correct thickness is 1.3 m. The two-layer linear solution is also shown in Fig. 9. The solutions at 0 m and 2500 m are almost identical to each other except for the layer thicknesses, so that only the 0 km solution is shown for the model results, along with the actual solutions in the 0–1100 m range.

The second layer sound speeds are overpredicted at the top of the layer by approximately 70 m/s; however, the two-layer solution has a lower gradient, so that this second layer solution lies between the actual sound speeds at the top and bottom of the layer. A similar result was found for the one-layer linear solution for the substrate sound speed as shown

TABLE I. Results of single-layer nonlinear model inversion for test case III (TC3) of IT workshop data, prior to conference. Thickness values at 0.0 and 2.5 km shown for PWRC solutions. Parameters for TC3 values shown for both top (t) and bottom (b) of the layer.

Parameter	H_1 m	C_1 m/s	ρ_1 g/cm^3	α_1 dB/(m kHz)
TC3 data	1.30	1485.0	1.49	0.210
PWRC	0.0 km–1.48	t 1490.2	1.44	0.305
	2.5 km–1.09	b 1491.8		
Parameter	H_2 m	C_2 m/s	ρ_2 g/cm^3	α_2 dB/(m kHz)
TC3 data	20.2	t 1549.4	t 1.81	t 0.550
		b 1646.2	b 1.83	b 0.330
PWRC	∞	1601.4	1.61	0.398

in Fig. 9. For the two-layer linear solution, the second layer thickness was overpredicted by a factor of almost 2, and the attenuations in both layers were 0.34 dB/(m kHz), as compared to 0.21 dB/(m kHz) for the correct solution. Also, the densities in the layers for the two-layer linear solution were 1.63 g/cm^3 and 1.86 g/cm^3 for layers one and two, respectively, as compared to 1.49 g/cm^3 for layer one and 1.81 g/cm^3 at the top of layer two for the correct solution.

The above results were consistent with solutions obtained from an inversion with a single layer range-independent model using the PWRC method. For this run, the data, ranging from 100 m to 5000 m in 200 m increments were used over the frequency range of 60–500 Hz, in steps of 10 Hz. The resulting layer thickness was 1.33 m, with a sound speed of 1492 m/s, a density of 1.38 g/cm^3, and an attenuation of 0.46 dB/(m kHz).

Table I shows a summary of the parameters obtained for the first 2500 m for the single-layer nonlinear intrusion given by Eq. (22), along with the correct solution for the range intervals of 0–1100 m and 2900–5000 m. The result of assuming the single layer model was that the σ value tended to be very large, resulting in an almost range-independent result, converging to the first layer of the actual solution, as shown in Table I.

The simulated-data models do not, however, correctly describe the discontinuity of the actual intrusion at the ranges 1100 and 2900 m. Between these ranges the sound speeds greatly increase below the first layer. Nevertheless, the resulting TL curves from the linear two-layer result show good agreement with the actual TL. Figure 10 shows the comparison for 200 and 500 Hz, corresponding to the depth dependent solution given in Fig. 9, obtained over the range of 0–2500 m for the 25 m horizontal array. The model TL curves were generated using the PWRC inversion solution in a PE model. Good agreement, even over the inclusion region 1100–2900 m, suggests a difficulty in choosing the proper sensor configuration necessary to identify a given buried inclusion. A closer examination of the TL curves near the boundary ranges of 1100 and 2900 m does show more model-data discrepancies than at other places, but there is no sharp contrast at these specific points. The differences decrease again at the farther ranges. The results for this example show that an average fit of the sound speed over the entire range of data does a decent job of modeling the TL.

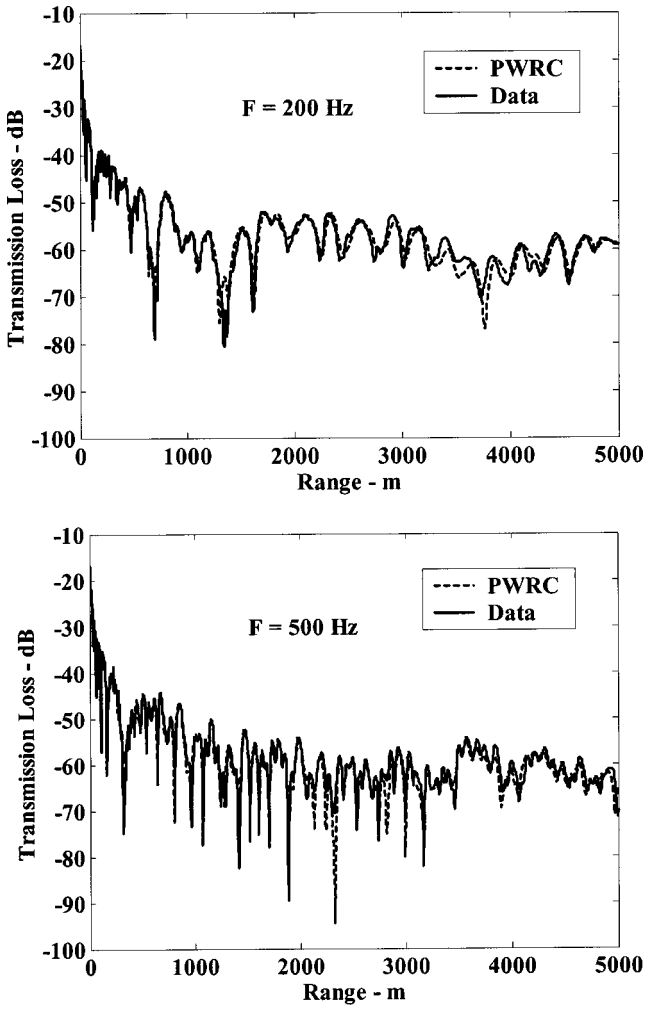

FIG. 10. Transmission loss comparisons to TC3 simulated TL, using parameters determined with the PWRC model prior to the IT workshop, at frequencies of 200 Hz and 500 Hz, respectively.

The PWRC method was also applied to a seabed model with the correct structure for the case III example. The range-dependent bottom layers were modeled with three range segments. The first (0–1100 m) and third (2900–5000 m) segments were described with 15 parameters, corresponding to a two layer model as listed in Table II, because these two range segments had the same geoacoustic properties. Sound speed and attenuation ratios at layer interfaces were used in the inversion, and the solution values listed for these ratios were calculated from the sound speeds and thicknesses of the solutions. Note that the density gradient in layer two of the first and third range segment was not included in the inversions. Subsequent calculations at several frequencies showed this omission to have a negligible effect on the TL. Also, the first layer in Table II and the first layer of the single layer solution (Table I) correspond to the first layer of the case III solution, and the second layer modeled corresponds to the seven layers below the first, which are continuous in sound speeds and attenuations. The middle segment (1100–2900 m) was modeled with an additional but independent set of 15 parameters. To apply the PWRC method, the range and grazing angle of each bottom interaction for each ray was

TABLE II. Two-layer solutions for TC3, including parameter bounds, with range-dependent bottom layer inversions using three range segments. The parameters for ranges 2900–5000 m are the same as 0–1100 m.

Parameter	Solution	PWRC	Lower bound	Upper bound
Range m	0–1100 m			
C_{t1} m/s	1485.0	1485.3	1480.0	1490.0
H_1 m	1.3	1.3	0.5	2.0
C_{g1} 1/s	0.0	0.854	0.0	1.0
ρ_1 g/cm^3	1.49	1.45	1.4	1.6
C_{t2}/C_{b1}	1.043	1.056	1.0	1.2
α_{t1} dB/(m kHz)	0.21	0.25	0.1	0.3
α_{g1} dB/(m^2 kHz)	0.0	-4.0×10^{-3}	-0.01	0.01
H_2 m	20.2	22.7	15.0	25.0
C_{g2} 1/s	4.792	3.895	3.5	5.0
ρ_{t2} g/cm^3	1.81	1.80	1.7	2.0
C_{sub}/C_{b2}	1.109	1.097	1.0	1.5
α_{t2} dB/(m kHz)	0.55	0.45	0.1	0.7
α_{g2} dB/(m^2 kHz)	1.09×10^{-2}	2.53×10^{-2}	-0.03	0.03
α_{sub} dB/(m kHz)	0.02	0.10	0.0	0.3
ρ_{sub} g/cm^3	1.98	1.90	1.8	2.2
Range m	1100–2900 m			
C_{t1} m/s	1485.0	1486.8	1480.0	1490.00
H_1 m	1.3	1.56	0.5	2.0
C_{g1} 1/s	0.0	0.32	0.0	1.0
ρ_1 g/cm^3	1.49	1.58	1.4	1.6
C_{t2}/C_{b1}	1.207	1.237	1.0	1.27
α_{t1} dB/(m kHz)	0.21	0.36	0.1	0.4
α_{g1} dB/(m^2 kHz)	0.0	-5.06×10^{-4}	-0.01	0.01
H_2 m	20.2	23.8	15.0	25.0
C_{g2} 1/s	1.683	1.539	1.0	2.0
ρ_2 g/cm^3	1.98	1.93	1.85	2.2
C_{sub}/C_{b2}	1.0	1.138	0.95	1.2
α_{t2} dB/(m kHz)	0.02	0.017	0.0	0.1
α_{g2} dB/(m^2 kHz)	0.0	2.48×10^{-3}	-0.005	0.005
α_{sub} dB/(m kHz)	0.02	0.139	0.0	0.3
ρ_{sub} g/cm^3	1.98	1.81	1.8	2.1

stored prior to the inversion. A separate set of reflection coefficients was calculated for each range segment, and the ray range location at each interaction was used to access the appropriate set of reflection coefficients. Range interpolations between the segments were not performed, although this could be easily incorporated in the model for a smoother transition between the segments.

The model was able to determine several of the important parameters for all three segments in layers one and two from a limited frequency and range sampling of the data. Frequencies in the band 60–500 Hz in 10 Hz increments, and receiver ranges of 100–3000 m in 50 m increments were used in the inversions. The last few data ranges were just beyond the intrusion at 2900 m, although more could have been used. Table II gives the inversion results compared to the actual solutions. The upper and lower bounds of the parameters are listed in Table II. The inversion was initialized with the correct solution, and the resulting cost function was $\approx$0.016. After approximately 26 000 iterations, the final parameter values (listed in Table II) gave a cost function of $\approx$0.011. Good comparisons to the correct solution were obtained for most of the parameters, although the intrusion sound speed was somewhat overpredicted.

Cost function distribution plots of the most sensitive parameters are listed in Fig. 11 for the first two range segments. Discernable minima for the parameters are obtained, although the cost function envelopes shown in Fig. 11 were somewhat flattened in the region of the actual solution for several of these parameters, resulting in the deviations from the actual solutions seen in Table II.

The receiver at 85 m may yield a closer fit to the actual solution due to the depth separation between the 20 m deep source and the receiver. For the 25 m receiver, the eigenray launch angles approach horizontal for increasing ranges. The result is that at farther ranges, some of the bottom interacting paths (1 or 2 bounces) are difficult to locate. This result is not unique to MEDUSA, but points to a difficulty of ray theory in shallow environments in producing an accurate field description of the water-borne propagation at long ranges.

The TL shown in Fig. 12 at 200 and 500 Hz is obtained from the ray model MEDUSA in conjunction with the range-dependent bottom reflection coefficients. The actual solution and the inversion solution were used to generate the TL, and both are compared to the synthetic data for the case III example. For ranges less than 4000 m a good fit to the data TL was obtained. Some differences are seen, however, and are due to the near horizontal launch angle of the eigenrays as mentioned above. For ranges 1000–4000 m these discrepancies correspond to the disappearance of the direct and surface reflected paths. For ranges beyond 4000 m, as seen from the comparison of the ray TL from the TC3 data and the actual solution in Fig. 12, the bottom interacting paths (with 1 or 2 bounces) are also difficult for the ray model to obtain, which results in excess energy loss at these farther ranges. In the inversion, the effect of the inaccuracy in the water column propagation is to adjust the bottom parameters to compensate for the loss. This resulted in the slightly better fit to the TL at these ranges and thus a slightly improved cost function minimum in the solution.

To summarize, the PWRC method was able to resolve a thin upper layer on the order of 1 m thick and obtain good TL predictions, even though the wavelengths are greater than the layer thickness.[42] This point will be important to the data analysis given in Sec. IV B. The main emphasis here is on the successful application of the PWRC method to a range-dependent bottom environment.

B. Measured data analysis

The preceding sections motivate the use of the PWRC method as a tool for inverting actual geoacoustic data. The goal is to obtain parameters sufficient to describe propagation. Direct measurement of some of the quantities necessary to predict the propagation reduces the inversion parameter search space and can result in a more efficient inversion method.

An experiment was executed in the spring of 2001 in a southeastern location off the Florida coast, on and along the continental shelf. The experiment was performed in conjunction with the Harbor Branch Oceanographic Institute's crew and vessel, the R/V Seward Johnson.[43] The objectives were to collect sufficient experimental data to characterize a shallow water environment using an inversion methodology de-

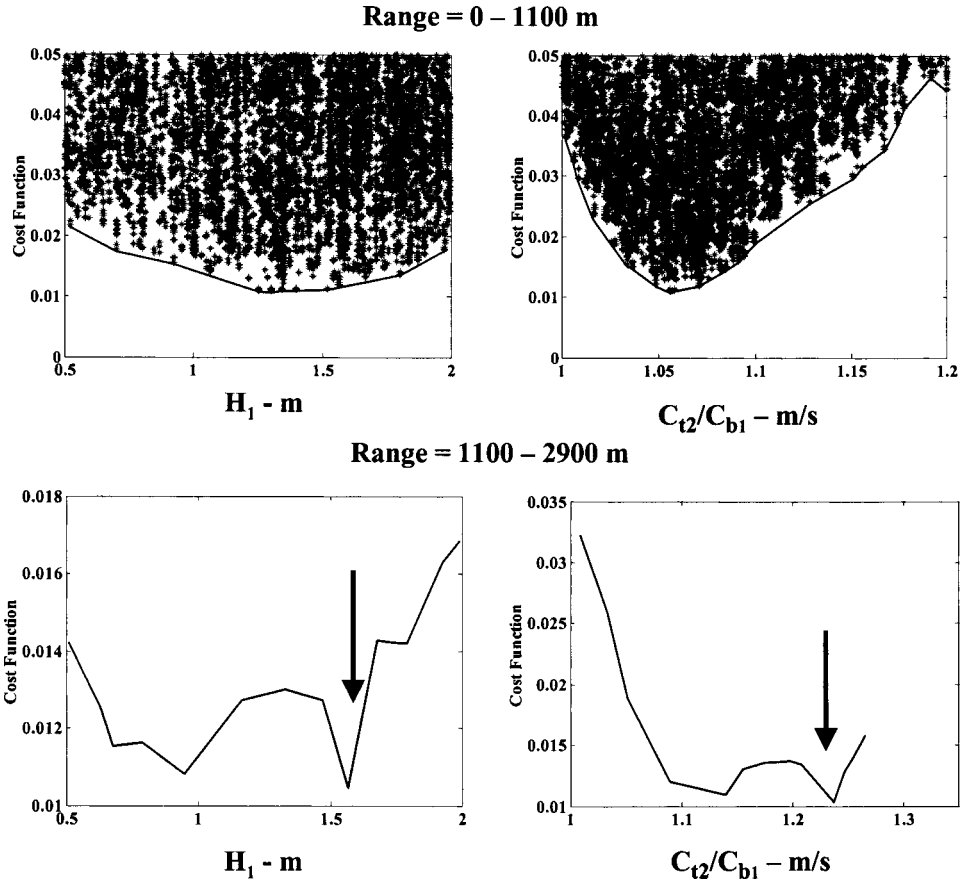

FIG. 11. Cost function distributions using the PWRC model for the inversion analysis performed after knowing the actual solutions. The distribution plots are for the first layer thickness, and ratio of sound speed from the first to the second layer at range intervals before the inclusion and within the inclusion.

veloped at ARL:UT.[15] The collected data provided a unique opportunity to test inversion models by providing both range-independent and range-dependent data from impulsive broadband light bulb sources. The light bulbs were imploded at a few hundred meters from a bottom mounted array to about 10 km in range at intervals of approximately 1 km. In addition, expendable bathythermograph (XBT) measurements and conductivity-temperature-depth (CTD) data were collected at various locations in the experiment field.

Acoustic data were collected on the Shallow Water Acoustic Measurement Instrumentation[15] (SWAMI) array located on the bottom. It was approximately 350 m long and was center tapered. The axis of the array was located along a bathymetric contour and was positioned at two different sites in the experiment.[44] Site I was approximately 129 m deep. Site II was approximately 45 m deep. At both sites data were collected along tracks parallel to the array (range independent) and tracks cross slope (range dependent), passing over the array as shown in the plan view in Fig. 13 for site I. (Only the results of the site I analysis will be reported here.)

The array location was the same for both the range-independent and range-dependent source tracks, and the same cost function given in Eq. (18) was used for both data sets. Therefore, the cost function for the range-independent data corresponds to a coherent frequency average and an incoherent range average. For the range-dependent data the source to receiver range was approximately the same for each receiver, i.e., perpendicular to the array axis. Therefore, the cost function for the range-dependent source track corresponds to a coherent frequency average and includes an average over the receivers used in calculating the cost function, although the ranges are approximately constant for each receiver. Approximately half as many receivers were used for the range-dependent inversions as for the range-independent inversions although, as discussed below, the inversion results were essentially independent of the number of receivers used. The cost function value increases, however, as more data are included in the calculation, as expected.

Sound speed profile data were calculated from measured XBTs dropped at each source location and at the end points of each experiment run. In addition, CTD data were recorded at these end points, with an additional CTD taken just to the west of leg B–C. The CTD collection was invaluable since both temperature and salinity were recorded. The recorded CTD salinity values were used to calibrate the SSP from the XBT data. Agreement within a few tenths of m/s for all measured depths between the two types of SSPs that were collocated at each end point of the runs were obtained thereby.

Figure 14 shows the XBT SSPs, along with the location of several bulb implosions recorded during the range-independent run, leg B–C. The bottom of each profile marks the approximate range to the first receiver for that XBT. The differences suggest a range- or time-dependent SSP environment, or both, although the differences between the profiles decrease going from point B to point C. In the range-independent analysis results presented, an SSP approximately 3.1 km from the first receiver was used. This SSP was nearly identical to the one nearest the receiver. An analysis of the effects of using the range dependence of the SSP field

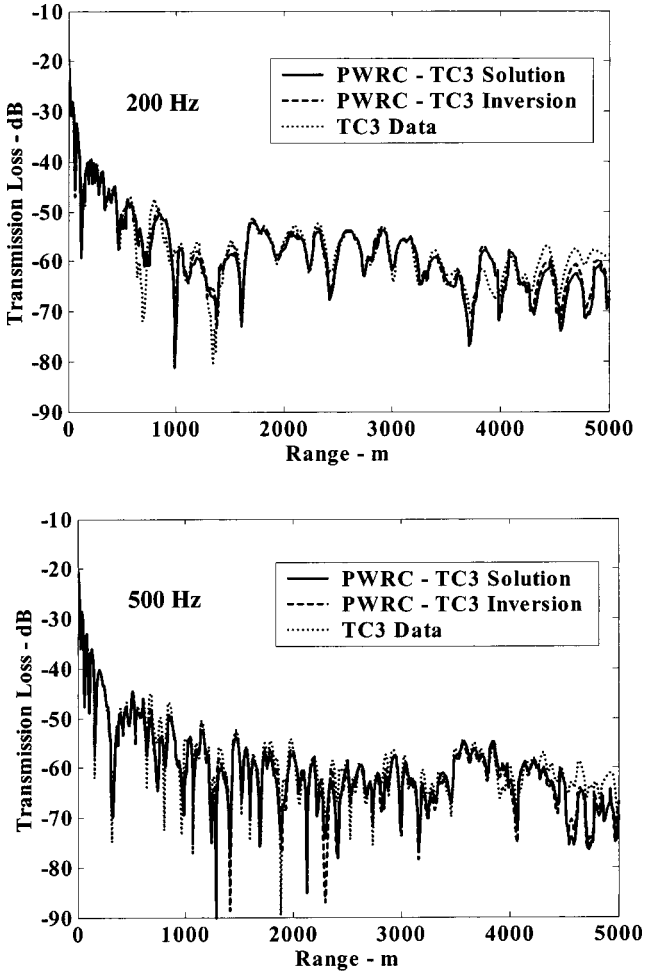

FIG. 12. Transmission loss comparisons to TC3 simulated TL, using parameters determined with the PWRC model after the IT workshop, at frequencies of 200 Hz and 500 Hz, respectively.

will be presented for both the range-independent and range-dependent data.

During the experiment, grab samples were collected using a 3 in. diameter gravity core; these samples suggested a very hard layer overlying the bottom over much of the range-independent run. The consistency of these samples was similar to hard asphalt, such as that in a paved parking lot, and was so hard that a coring device made no penetration into the bottom and was dented. An examination of the samples revealed holes, as much as several mm in diameter, and voids permeating the material, possibly due to percolation during the rock formation. Such crusted material is believed to be partially caused by the Gulf Stream activity which produced an upwelling in the area, resulting in the formation of phosphorite sheets. These sheets were further recemented with carbonate debris, and as a result hard manganese pavements were formed.[45]

1. Inversion results—range-independent data

The inversion approach for the range-independent data is discussed first, along with the analysis of the inversion results. Several bulbs at various ranges were used to determine different parameters. Generally, longer range sources yielded more information about the upper layers, and shorter

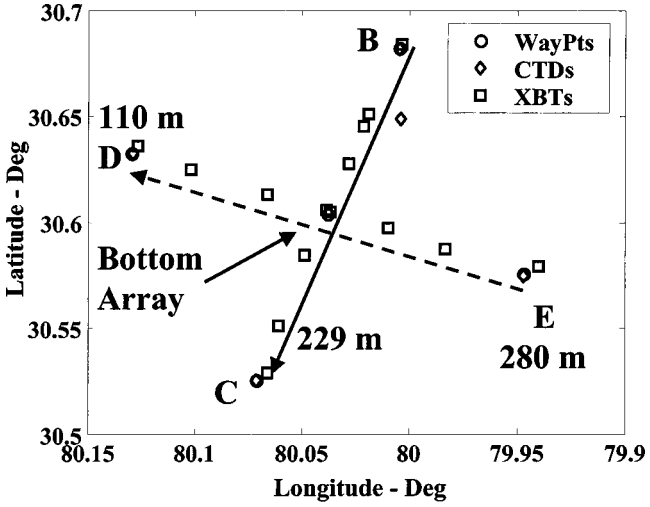

FIG. 13. Plan view showing the locations of the array, CTD and XBT collection, and tracks of the range-independent (leg B–C, solid line) and range-dependent (leg D–E, dashed line) runs. Source implosions and XBTs are collocated.

range data gave more information about underlying layers. Time series comparisons between the data and model at several ranges are also presented, using a single set of inverted parameters.

Examples of spectra from several ranges revealed the peak energy to be in the 200–400 Hz band, although frequencies up to 500 Hz had suitable signal-to-noise ratio (SNR) for performing inversions and were used for the longest range sources. For all of these range-independent solutions, 19 receivers and 354 frequencies, with a frequency spacing of 0.6 Hz, were used in calculating the cost function. Other combinations of receivers and frequencies gave similar results. Broad constraints were placed on the inversion parameters. Consistent with the IT data analysis, the PWRC method demonstrates the ability to resolve upper layer properties.

a. Inversion results. A light bulb implosion at $r = 4.12$ km was used to obtain an inversion for the compressional speed in the sediment at the water–sediment interface.

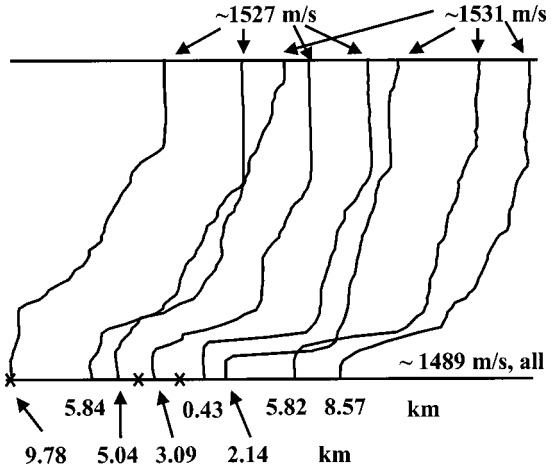

FIG. 14. Range dependence of SSPs for the constant bathymetry (range-independent) runs. The approximate location of the XBT with respect to the array is indicated at the bottom of the profile.

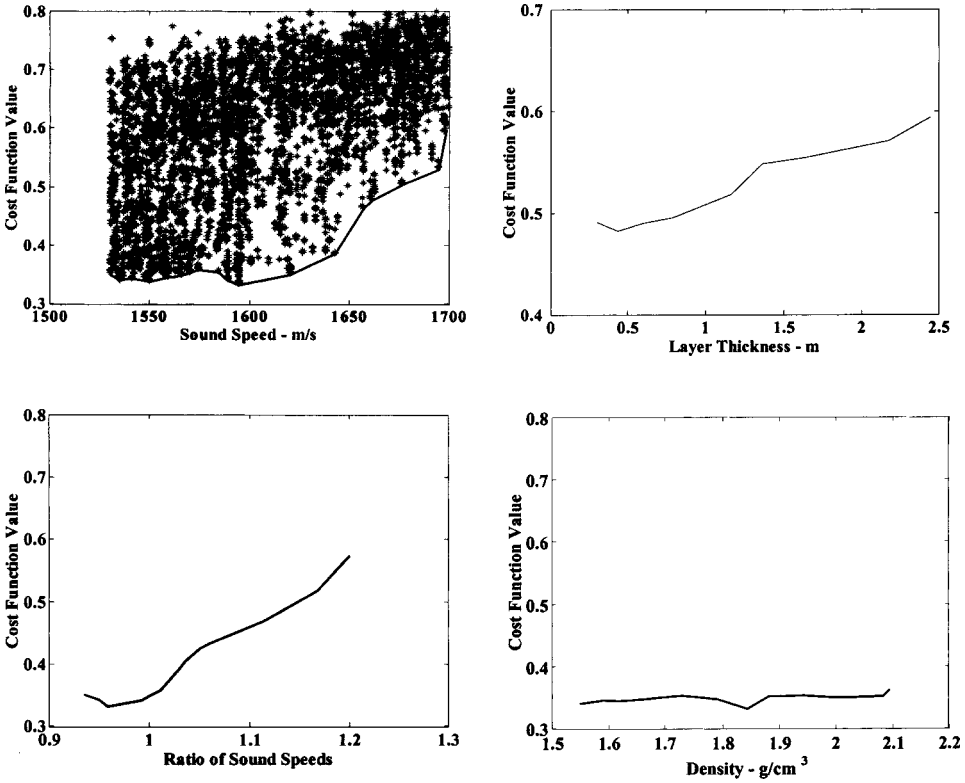

FIG. 15. Cost function distribution plot showing the top sound speed in the first layer. Envelopes of the distribution are shown for the first layer thickness, the sound speed ratio, c_{t2}/c_{b1}, and the first layer density.

The result was a sound speed of $c_{t1}=1594.5$ m/s with a layer thickness $h_1=0.64$ m. Here, ranges to the closest receiver of the array are used to designate the range-independent bulb sources used in the inversion. This result is consistent with that from the farthest bulb at 9.78 km, where frequencies greater than 300 Hz were used for the inversion to help resolve the thin upper layer. The inversion using this bulb gave a solution of $c_{t1}=1593.8$ m/s and $h_1=0.43$ m. The cost function distribution for c_{t1} is shown in Fig. 15 for the 4.12 km bulb. The envelope of the cost function distribution for h_1 for the 9.78 km bulb is also shown in Fig. 15. Well-determined minima in the distribution of the cost function values are seen for these parameters. All the distribution plots shown in Fig. 15 and the following were obtained by varying all the parameters used in the inversion, i.e., none were held fixed in generating the distributions.

The longest range light bulbs did not yield as much information about the other parameters within the first layer as did the 4.12 km bulb. Vertical components that contribute to the received field from the 9.78 km bulb were below the critical grazing angle corresponding to the water–sediment interface and did not penetrate well into the sediment.

To estimate the geoacoustic parameters within the first layer, the bulb at 4.12 km was used. The remaining range-independent inversions were performed in the 200–400 Hz band to maximize the SNR, although it was found that similar results were obtained using shifted frequency bands but with higher cost function values because of lower SNR. Accurate determinations were made for the ratio of the compressional sound speed at the top of the second layer to the speed at the bottom of the first layer, i.e., $\text{ratio}_1=c_{t2}/c_{b1}=0.959$. The corresponding envelopes of the cost function distributions shown in Fig. 15 again demonstrate that minima are well defined for the sound speed ratio. However, the density is not as well determined since the distribution is almost flat. Note that changing the layer thickness value to $h_1=0.43$ m (result from the bulb at 9.78 km) produced no appreciable change, 0.335 to 0.34, in the cost function value.

Also, from the $r=4.12$ km bulb, the first layer density was determined to be $\rho_1=1.88$ g/cm^3, and the attenuation at the top of the layer was 0.5 dB/(m kHz), although the cost distribution for the latter parameter was flat. The values for attenuation in the first layer spanned 0.3–0.5 dB/(m kHz) for the various sources used in the inversion. The cost function distribution in Fig. 15 reveals a minimum in the density that is discernable but not as well defined as those of the other parameters.

Acoustic data generated by a light bulb implosion at a range of $r=1.6$ km did not give information about the first layer. This is due to the transparency of the layer for rays above the critical grazing angle, at the peak frequencies between 200–400 Hz, whose corresponding wavelengths are at least 10 times the layer thickness. From the $r=1.6$ km bulb, the second-layer sound speed was determined, giving a result of 1531.7 m/s. Using this value with the first layer results from the bulb at 4.12 km yields a ratio of $c_{t2}/c_{b1}=0.960$. This value compares well with the ratio 0.957, obtained independently from the $r=4.12$ km inversion.

The remaining second-layer parameters, as well as the substrate values, were obtained from the 4.12 km bulb and are listed in Table III. These values were used to model the range-independent time series and were also used to model the time series for the range-dependent bulbs to be discussed in Sec. IV B 2.

A range dependence of the first layer was not assumed. An underlying slower sound speed substance was revealed in

TABLE III. Two-layer solutions for PWRC method, including parameter bounds, for range-independent inversions.

Parameter	PWRC	Lower bound	Upper bound
C_{t1} m/s	1594.49	1530.00	1900.00
H_1 m	0.64	0.30	2.50
C_{g1} 1/s	0.531	0.000	3.000
ρ_1 g/cm^3	1.883	1.550	2.100
C_{t2}/C_{b1}	0.957	0.935	1.200
α_{t1} dB/(m kHz)	0.506	0.100	0.800
α_{g1} dB/(m^2 kHz)	-2.78×10^{-3}	-0.01	0.01
H_2 m	34.70	5.00	40.00
C_{g2} 1/s	2.170	0.000	4.000
ρ_2 g/cm^3	1.741	1.600	2.100
C_{sub}/C_{b2}	1.141	0.950	2.000
α_{t2} dB/(m kHz)	0.179	0.100	0.900
α_{g2} dB/(m^2 kHz)	1.57×10^{-5}	-0.02	0.02
α_{sub} dB/(m kHz)	0.792	0.100	0.900
ρ_{sub} g/cm^3	1.878	1.600	2.200

the inversion. This was found to be consistent with other findings for this region.[45] In addition, the results may indicate an effective sound speed for this combination of hard, extremely porous material. The parameter bounds, as well as the final solutions are summarized in Table III.

To determine the attenuation consistency with respect to range an inversion was performed for the attenuations and attenuation gradients, holding constant the sound speeds and densities. The first two receivers were used for sources with ranges from 9.78 km to 3.1 km. The result was that the first layer attenuation was consistent with the results given in Table III, although no discernable minimum was seen, possibly due to the thinness of this layer. The attenuation at the top of the second layer was, however, easily determined from the cost function distribution, giving a value of 0.27 dB/(m kHz), as shown in Fig. 16.

b. Time series analysis. Recorded time series from several ranges for 10 of the receivers are plotted in Fig. 17. These plots were obtained by first applying a filter that excludes the data below 5 Hz (where high wind-noise was seen), normalizing the peak arrival amplitude to unity for each corresponding receiver, and then plotting the resulting

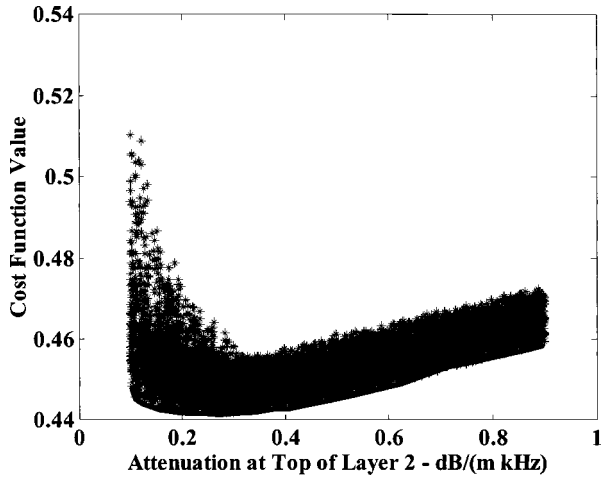

FIG. 16. Cost function distribution for the attenuation at the top of the second layer.

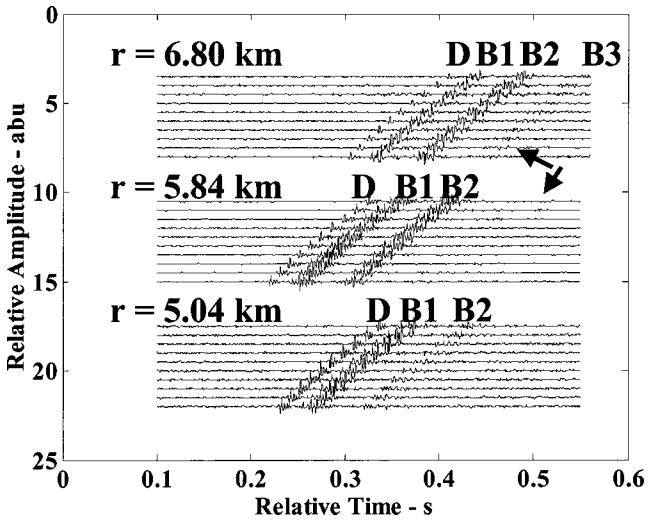

FIG. 17. Time series from range-independent data, $r=6.8$ km (top), $r=5.84$ km (middle), and $r=5.04$ km (bottom) set of curves for receivers 1–10. The arrow indicates the disappearing third bottom interaction. The amplitudes are in arbitrary units (abu), and the ranges indicate the distance to the first receiver of the array.

traces with vertical offsets. The array spacing produces the travel time variation with receiver. These plots reveal the gross arrival structure, where the individual bottom interactions are designated at the top of each arrival set. The direct path is designated by the symbol D and includes the ray that just grazes the bottom at the receiver, the surface reflected path, and the surface reflected path that grazes the bottom at the receiver. The next group of arrivals are designated as B1 and again includes four paths: the arrival with one bottom interaction, the arrival with one bottom interaction which also grazes the bottom at the receiver, the surface reflected arrival, and the arrival with one surface reflection which also grazes the bottom at the receiver. Higher order bounces similarly include four arrivals. This notation is useful since the corresponding pairs which arrive at the receivers with similar paths, one directly and one just grazing the bottom, are indistinguishable for a bottom mounted array. Therefore, time series arrivals are compared using the leading edge arrivals for the model and data.

The disappearance of a given bottom arrival as the range decreases can be used to determine the critical angle of the water–sediment interface. Knowing the water sound speed at the bottom then yields the sediment sound speed. Here, an approximate determination is made, since the sources were only deployed at approximately 1000 m intervals in range from the array. The disappearance of the third bottom interaction occurs at an approximate range of 5.8 km. The water sound speed at the receiver is approximately 1489.7 m/s. A list of eigenray arrival angles was constructed from a range-independent ray model,[22,23] using the measured water sound speed profile. The bottom grazing angle for this range is approximately 18.67° and corresponds to a sound speed $c_{t1}=1572.4$ m/s. The second bottom arrival has vanished at an angle of 19.48° at approximately 3.9 km in range and gives a sound speed of $c_{t1}=1580.2$ m/s. Both values, although slightly lower, are consistent with the inversion results obtained at ranges near these observations. These two bottom

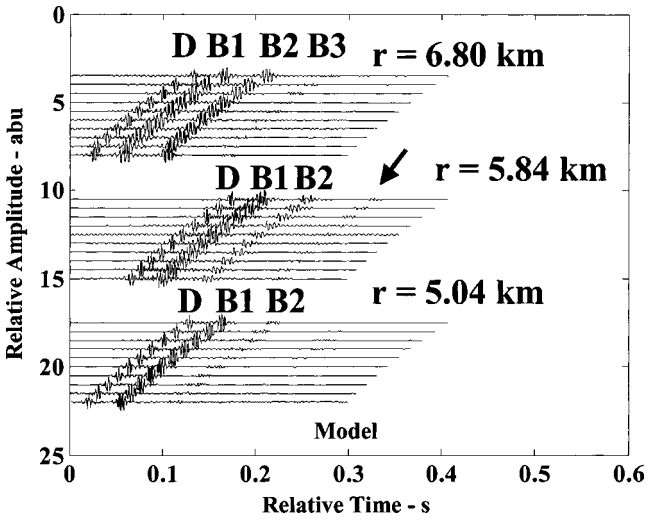

FIG. 18. Model time series from range-independent inversion, $r=6.8$ km, $r=5.84$ km, and $r=5.04$ km for data filtered in the 200–400 Hz frequency band.

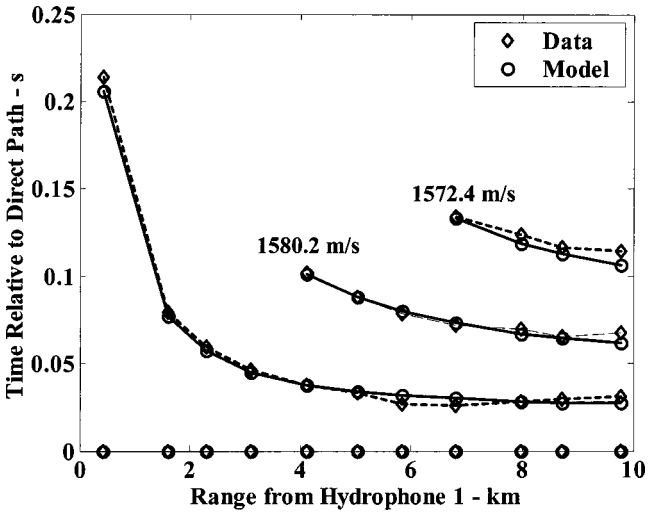

FIG. 20. Range-independent arrival structure comparing model to data, with time being relative to the first arrival, D. The sound speeds corresponding to the respective critical angles are also designated.

sound speed determinations were used only as a validity check for the upper layer inversion sound speed value listed in Table III and not as ground truth parameter estimates.

The modeled time series were obtained using, in the frequency band of 200–400 Hz, the determined parameters. Figure 18 shows the resulting model time series arranged in vertical sequential order. The overall structure is consistent with that of the data. This is demonstrated by the detailed comparison of modeled and measured data in Fig. 19 for receiver 1, using an example source range of 6.80 km.

A key point about the comparison is that eigenrays with up to six bottom interactions were stored as possible contributors to the overall field; however, the inversion process, via the reflection coefficient, correctly reduced by absorptive losses, the number of interactions in agreement with the data.

For comparison to the time series in Fig. 17, the sound speed at the water–sediment interface was varied, keeping the other parameters constant at the values given in Table III. The minimum cost function value was obtained at approximately 1594 m/s, consistent with Table III. In contrast, modeling the time series for the 4.12 km bulb, using a much higher sound speed value of 1800 m/s, produced many more arrivals than in either the data (Fig. 17) or in the Table III solution (Fig. 18) and gives further evidence of the accuracy of the inversion result presented here.

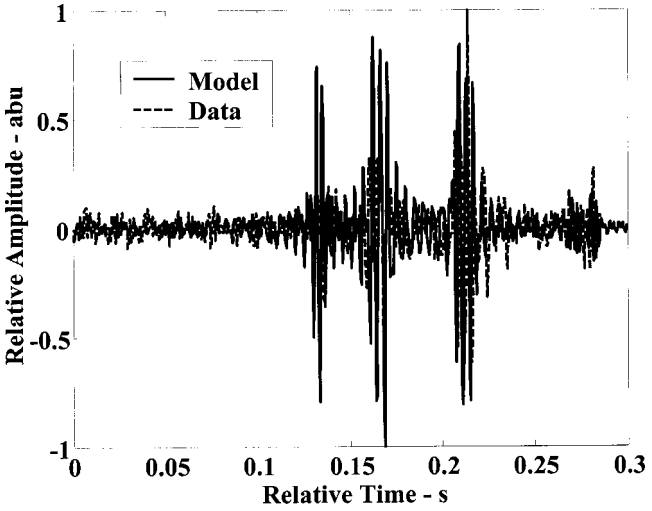

FIG. 19. Example time series for model and data from receiver 1 with $r=6.8$ km. Data was filtered in peak energy band of 200–400 Hz.

The overall geometric structure of the propagation is demonstrated by comparing the model and data arrival times of each bottom interaction. The initial arrivals from each bottom interaction, as designated by the letters D, B1,..., are identified and matched to the corresponding eigenray arrival times. These arrival times were referenced to the first arrival, since absolute travel times were not recorded for the data, and are shown in Fig. 20. The third and second bounces disappear at approximate ranges of 7 and 4 km, respectively, for both model and data. Slight differences between the model and data arrival delays could arise because the data arrivals were identified by examination of the time series. Figure 20 demonstrates that the propagation in this relatively shallow environment can be understood in terms of a ray description. The sound speed at the water–sediment interface, determined using the model bottom grazing angle, and the data ranges are designated in the figure for the bottom interactions B2 and B3.

c. Dependence on SSPs. An examination of the dependence of the inversion results on the sound speed profile was also made. The previous results were obtained using the profile taken 2.8 km from the array, except for the bulb for which $r=1.6$ km, where the SSP at 1.6 km was used since it was closest to both the receiver and the source. The results of using the SSP closest to each bulb were examined. No appreciable difference in the range-independent results were obtained, whether the source or the receiver SSPs were used. The sound speed profile nearest the farthest range bulbs, at position B, had a difference of a few meters per second from the other profiles at the same depths, as shown in Fig. 14; however, this was not significant enough to alter the inversion results obtained for the range-independent data. There-

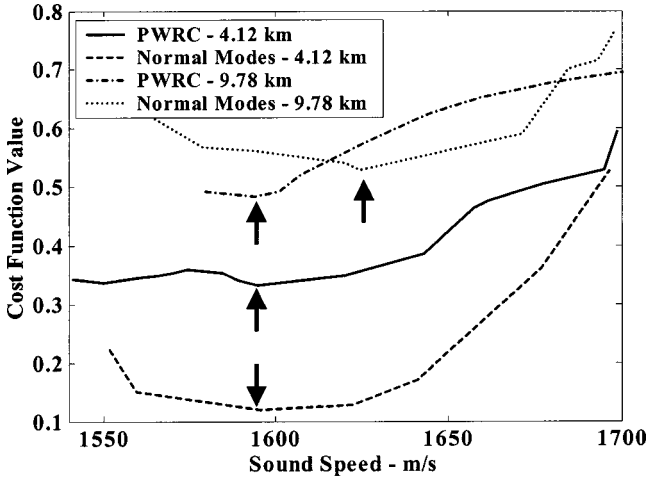

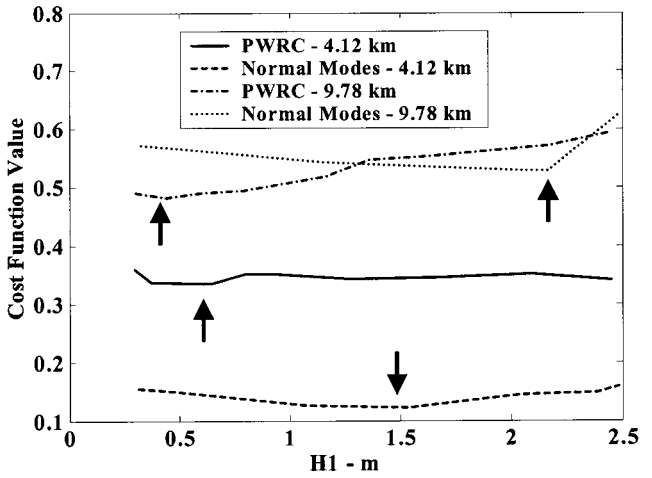

FIG. 21. Cost function distribution envelopes for the two-layer normal mode model, compared to the PWRC curves shown in Fig. 15 for the sound speed at the top of the first layer, C_{t1}, and the first layer thickness, H_1.

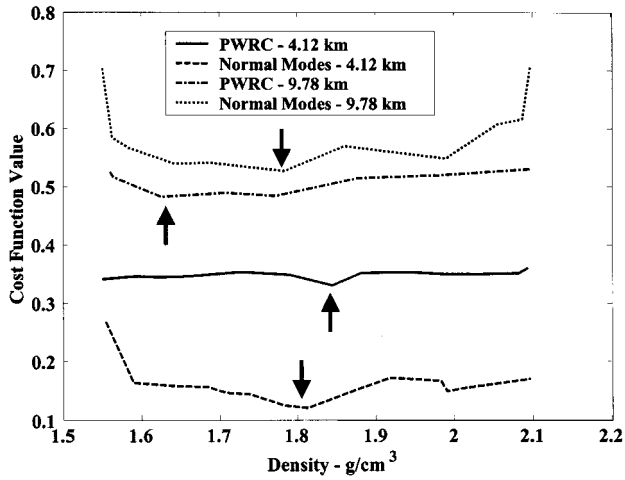

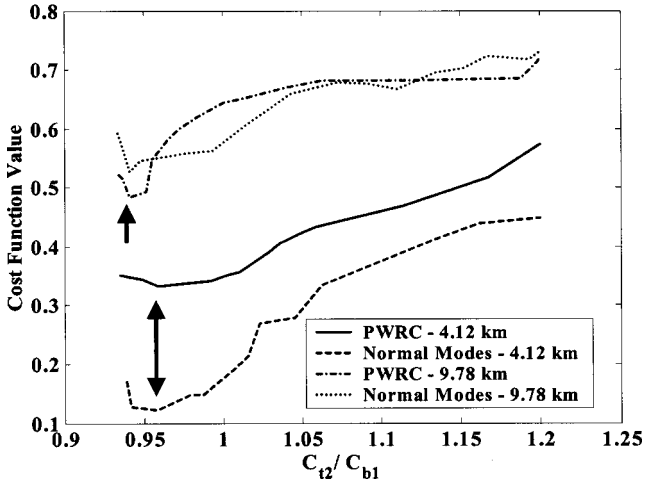

FIG. 22. Cost function distribution envelopes for the two-layer normal mode model, compared to the PWRC curves shown in Fig. 15 for the density, ρ_1, and the ratio of the sound speed at the top of the second layer to the sound speed at the bottom of layer 1, C_{t2}/C_{b1}.

fore, no further range analysis of the SSPs were performed along the track.

d. Normal mode forward model. The results obtained in Table III were compared to those obtained by repeating the inversion using the normal mode model, ORCA, as the forward model. A single layer sediment description was initially chosen for the normal mode forward model, prior to accounting for the thin upper layer substance described above, using ORCA. Both the PWRC and normal mode forward models gave similar results with a single layer above a half-space for all the bulbs used in the comparison. For example, similar to the PWRC forward model, the normal mode solution with the bulb for which $r=4.12$ km gave a sound speed of 1536.3 m/s, which compares well with the PWRC second-layer solution of 1526.3 m/s, as calculated from the parameters listed in Table III.

Next, the two-layer model obtained from the PWRC model was tested using ORCA. Consistent results were obtained here as well, although as stated previously, the PWRC method was faster than the normal mode model by a factor of approximately 10. Figures 21 and 22 show the envelopes of the uncertainty plots for the normal mode inversions corresponding to those in Fig. 15 for the PWRC model. Normal mode solutions at two different ranges are included. The cost function values from the normal mode inversion are lower than the PWRC inversion for the source at 4.12 km and lower than the normal mode solutions from the farthest range bulb at 9.78 km. The water–sediment sound speed and the first-layer thickness for the PWRC method were obtained with the 9.78 km bulb; however, for comparison the PWRC solution at 4.12 km is also included in Fig. 21. A slightly thicker first layer was obtained from the normal mode model for sources at both 4.12 km and 9.78 km; however, the cost function value was shown to be almost insensitive to the first layer thickness values 0.4–2.2 m, as observed by the flatness of the distributions for this parameter. For the last two parameters shown in Fig. 22, the source range was 4.12 km for the PWRC method. For the PWRC model the longest range sources were used to determine the first layer parameters and the shortest range sources were used to obtain the second layer parameters, due to deeper energy penetration at the short ranges.

The PWRC and normal mode forward models produced similar results for the sound speed ratio between the first and second layers and for the density of the first layer, as shown in Fig. 22 for the source at 4.12 km. These parameter values were listed in Table III for the PWRC method. The cost

TABLE IV. Two-layer solutions for PWRC and normal mode inversion methods, for range-independent inversions. The last four entries are calculated with the parameters obtained from the inversion. The last column gives a normal mode solution near minima for the 9.78 km source.

Parameter	PWRC	NM 4.12 km	NM 9.78 km	NM2 9.78 km
C_{t1} m/s	1594.49	1594.51	1624.64	1595.56
H_1 m	0.64	1.53	2.17	1.93
C_{g1} 1/s	0.531	1.920	1.303	2.043
ρ_1 g/cm^3	1.883	1.814	1.783	2.054
C_{t2}/C_{b1}	0.957	0.959	0.942	0.961
α_{t1} dB/(m kHz)	0.506	0.432	0.281	0.439
α_{g1} dB/(m^2 kHz)	-2.78×10^{-3}	5.92×10^{-3}	-1.37×10^{-3}	4.68×10^{-3}
H_2 m	34.70	36.05	27.10	35.50
C_{g2} 1/s	2.170	2.109	0.991	3.109
ρ_2 g/cm^3	1.741	1.649	1.852	1.803
C_{sub}/C_{b2}	1.141	1.100	1.348	1.083
α_{t2} dB/(m kHz)	0.179	0.112	0.198	0.312
α_{g2} dB/(m^2 kHz)	1.57×10^{-5}	0.016	-0.019	2.83×10^{-3}
α_{sub} dB/(m kHz)	0.792	0.392	0.418	0.508
ρ_{sub} g/cm^2	1.878	1.726	1.867	1.964
C_{b1} m/s	1594.83	1597.45	1627.46	1599.50
C_{t2} m/s	1526.25	1532.02	1533.05	1537.66
C_{b2} m/s	1601.55	1608.07	1559.91	1648.03
C_{sub} m/s	1827.37	1768.63	2102.64	1785.09

function values were lower for the normal mode model at the 4.12 km range but larger for the normal mode model at 9.78 km. The density in the first layer at the 9.78 km range for the normal mode model is slightly lower than that obtained for the PWRC model; however, the normal mode distribution is flatter than the PWRC distribution. The sound speed ratios are consistent between the models at a given range, as seen in Fig. 22.

The parameters for the normal mode model are included in Table IV for three normal mode solutions, one for the 4.12 km source and two solutions for the 9.78 km source, along with the PWRC results repeated from Table III. The second normal mode solution from the 9.78 km source, referred to here as NM2, was near the minima, but had a slightly greater cost function than the solution labeled NM and is more consistent with the normal mode solution at 4.12 km, and the PWRC results. Note, that all the parameters from the four solutions are consistent for several of the more sensitive upper layer parameters including the sound speed at the water–sediment interface, the layer thickness, the density, and the ratio of the sound speed at the top of the second layer to the sound speed at the bottom of the first layer. The attenuations in the first layer are not as well determined for either forward model and are less sensitive to the inversion. The values for all the examples listed in Table IV are from 0.28–0.51 db/(m kHz) for the attenuations.

The layer thicknesses are within approximately 1.5 m for all the solutions. The top layer thickness could be slightly range dependent, due to variable deposition of the substances forming the top layer. A more precise determination of the top layer thickness was not made. Given the correct determination of the upper 1.3 m layer for the case III example in Sec. IV A by the PWRC method, the lower thickness value obtained in Fig. 21 is plausible.

Also, the lower sound speed ratio from the first to the second layer from the normal mode inversion for the source at 9.78 km, column four, compensates for the slightly thicker layer and higher sound speed gradient in the first layer, to produce a comparable sound speed at the top of the second layer, as listed at the bottom of Table IV. Another possibility for the slight inconsistency for the farthest range bulb with the normal mode model may also be slight errors in the bathymetry. A comparison of the sensitivity for the normal mode and PWRC models to bathymetry errors was not investigated in this study.

The thickness of the second layer for both forward models was also less sensitive, but gave some consistent values near 35 m, except for the normal mode solution, NM. The second layer parameters from the 4.12 km source were consistent with those from the PWRC method, since these were also obtained from the 4.12 km source. Attenuation gradients are less consistent between the models and between the same model for different sources, although they are very small for most of the inversion results.

The cost function values for the 9.78 km source are greater than for the 4.12 km source for both models. This is due to the decrease in the SNR as the range increases, independent of which forward model used. The SNR would define an upper limit on the cost function values that would reveal determinable parameters. However, since discernable minima are seen for the farthest range bulbs at 9.78 km for both models for some of the parameters shown in Fig. 21, this limit was not reached for the experimental data presented here for either the PWRC or the normal mode models.

The attenuations in the first layer were comparable between the two forward models, as was the layer thicknesses. Finally, for the normal mode model, lowering the sound speed at the water–sediment interface by several meters per second only changed the cost function value from 0.530 to 0.538, showing the insensitivity to the exact determination of the parameters for the 9.78 km source with the normal mode model.

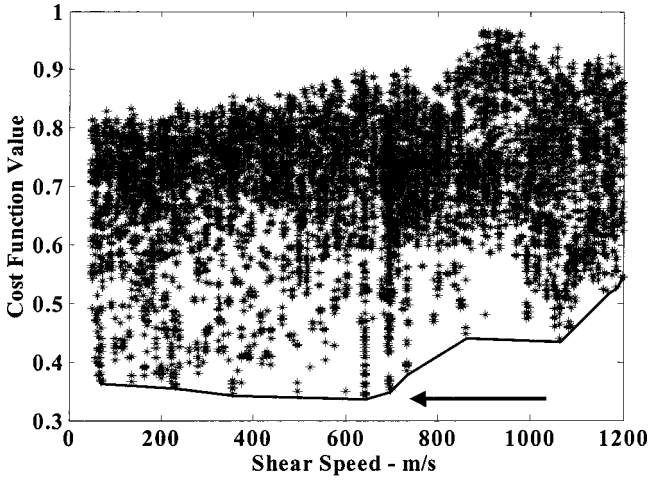

FIG. 23. Cost function distribution envelope of the shear speed in the first layer, showing a minimum corresponding to a shear speed of approximately 642 m/s.

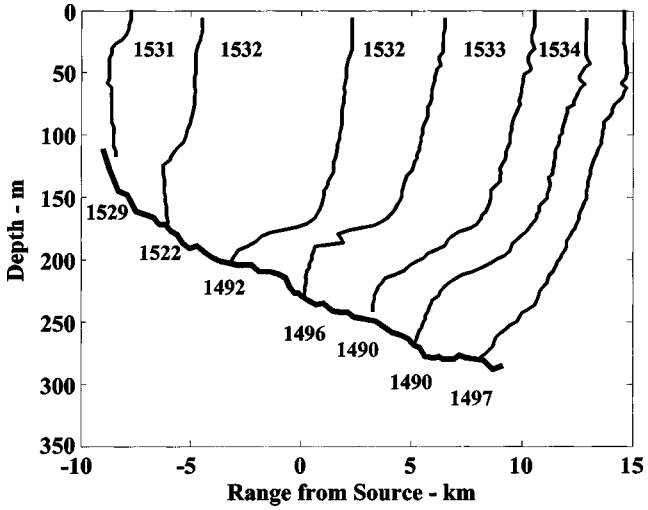

FIG. 24. Bathymetry plot taken along the range-dependent track run from point D to point E, and the sound speed profiles taken along the track. The approximate location of the XBT with respect to the array is indicated at the bottom of the profile.

e. Shear speed determinations. The effects of adding shear wave contributions to the reflection coefficients were also examined for the phosphorite material of the first layer. One possible effect could be an adjustment of the attenuation values, since the conversion of energy into shear waves might be manifested in the increased loss seen for this environment. The PWRC program was easily adapted to include these terms since the ORCA reflection coefficient model could account for shear wave effects. Figure 23 shows the uncertainty for the shear speed associated with the hard layer. The minimum value is determined to be approximately 642.4 m/s. The two-layer model was used to obtain this value, with the result that a similar compressional sound speed was found for the first layer of the 4.12 km range bulb. The compressional attenuations increased to 0.742 dB/(m kHz); however, the uncertainty plot did not reveal very clear minima, and the previous value of 0.342 dB/(m kHz), obtained with the fluid model, was also near this same minimum cost function value. The shear attenuations were not well determined either, but the minimum at 0.42 dB/(m kHz) was consistent with the compressional attenuations. For this data set, there was no appreciable effect from adding shear contributions for the upper layer. In other words, a fluid model description is adequate to describe the propagation for this environment, which may be consistent with the large voids seen in the samples of the overlying crusted layer obtained here. This example does demonstrate, however, that a more complete physical reflection coefficient model is easily incorporated into the PWRC model.

2. Range-dependent data

The results obtained from the range-independent site I data were a starting point for the analysis of the site I range-dependent data. The range-independent bottom parameter results were used to predict the data time series for the range-dependent propagation. Finally, these results were compared to actual inversions of the range-dependent data.

Range-dependent data were taken perpendicular to the array along the track from D to E as shown in Fig. 13. The bathymetry was determined from 38 kHz data recorded using four sensors mounted underneath the ship. The location of the bottom as revealed by the XBTs are roughly consistent with the 38 kHz data. The bathymetry is shown in Fig. 24, where negative ranges are used for sources up-slope from the receiver array.

a. Range dependence of SSPs. The range-varying sound speed profiles for the eigenray calculations appear in Fig. 24, where the sound speed at the bottom of each profile is located in the figure at the approximate range where the corresponding XBT was dropped. This variability in the water sound speed with respect to range was found to be important for range-dependent data, in contrast to the range-independent data results.

Ray plots for both the up-slope and down-slope propagation reveal details of the propagation behavior that are consistent with the range dependence of the SSPs in Fig. 24. Propagation paths starting from the longest range source up slope from the array are shown in Fig. 25. The region of the sound speed profiles below approximately 100 m in depth creates a channel that traps energy below this depth for source-to-receiver ranges beyond approximately 6 km. The refraction of the paths down slope in this channel results in a caustic region, as seen by correlating the ray path structures in Fig. 25 to the SSP at the corresponding range in Fig. 24.

The up-slope propagation paths also reflect the range dependence in the SSP structure. Starting from the longest range source down slope from the array, an upper channel is apparent initially near the surface at depths less than approximately 50 m. This channel persists to approximately 6 km in range, as shown by the paths in Fig. 26 which refract upwards and reflect off the surface, but then refract downwards to the bottom after this range. Correlating this channel with the upper depths of the last three profiles in Fig. 24 reveals an upper channel that diminishes as the receiver range is approached.

b. Time series analysis. Good agreement was obtained by using the range-independent results to predict the time

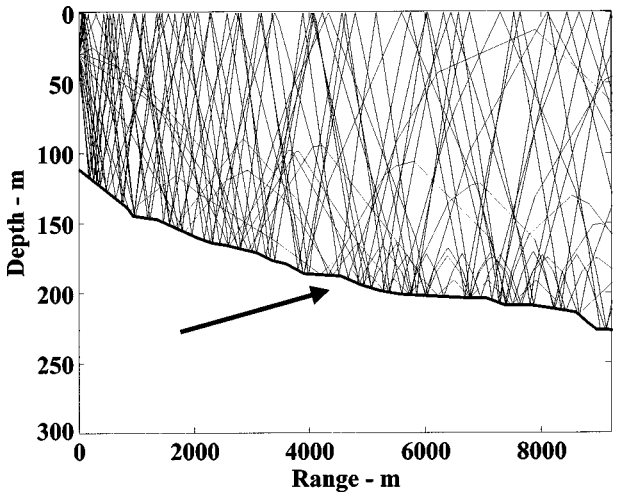

FIG. 25. Ray trace plot starting from the farthest source and propagating down slope to the receiver array. The arrow indicates the downward refracting channel that results in a caustic region.

series of the range-dependent data. Data time series for the first 10 receivers are shown in Fig. 27 for two of the sources, using the range-independent results. Similar to the range-independent runs, approximately two to three bottom-interacting arrivals are seen at each range. The model time series for these same sources are also shown in Fig. 27. Notice that the first arrival group's decreasing amplitude with increasing range is correctly predicted by the model time series.

Similar to the range-independent path determinations, the initial arrival from each interaction at the first receiver for each range was determined from the data. These were compared to the identified eigenray arrivals from the model output. The decreasing SNR at the farther ranges limits the usefulness of the data beyond approximately 6 km, except for coarse determinations of arrival structure. Data recorded from sources located within approximately 1 km overloaded the hydrophones and was not used for inversion analysis. However, the initial arrival of each bottom interaction was still discernable.

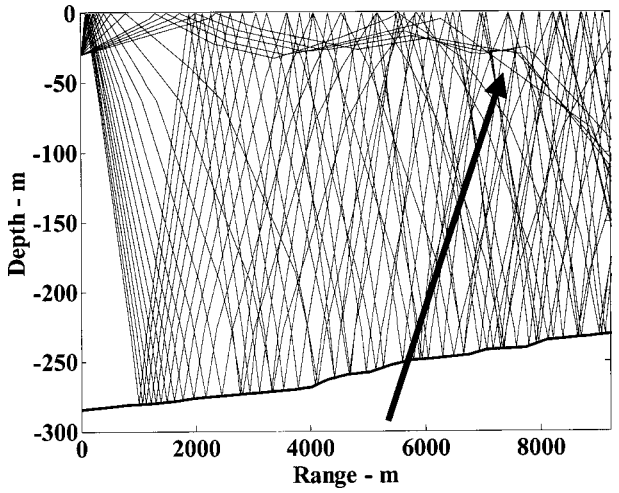

FIG. 26. Ray trace plot starting from the farthest source and propagating up slope to the receiver array. The arrow designates the upper channel that diminishes with range from the source.

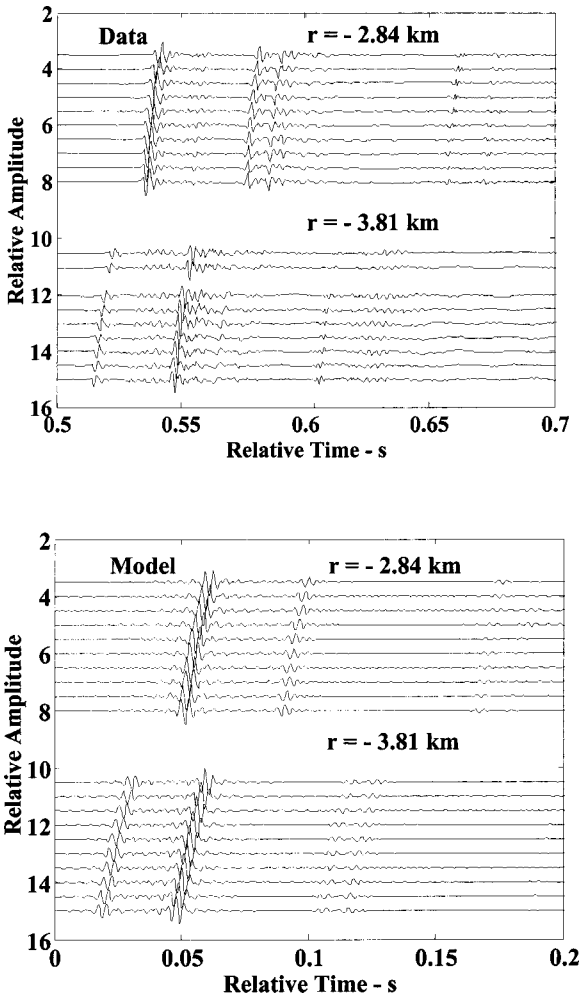

FIG. 27. Time series of range-dependent data for receivers 1–10, excluding receiver 3, up slope from the array at ranges of $r=-2.84$ km and $r=-3.81$ km. Corresponding model time series generated from the range-independent inversion are also shown.

The comparison of the model and data results shown in Fig. 28 indicate that the ray paths are correctly identified, showing the usefulness of a geometric model even for a shallow-water range-dependent environment. Small differ-

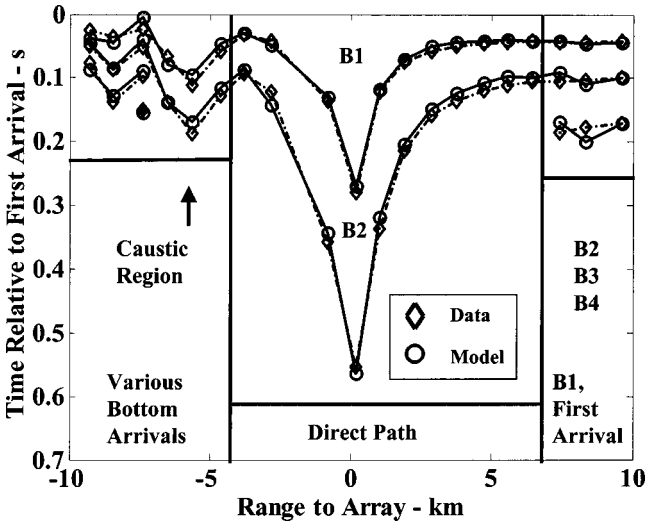

FIG. 28. Range-dependent arrival time structure. Times are shown relative to the first arrival.

ences in the arrivals may be caused by the use of a specific ray path travel time as compared to using the generated model time series and picking off the arrivals, as was done with the data. Also, errors in the bathymetry because of sampling and measurement may contribute small differences. Nonetheless, it is clear that the arrival structure can be understood in terms of geometrical optics, and that information can be obtained by examining the bottom interacting angles determined by the model. To the left of the array, beyond the 4.63 km source, the caustic region was identified in the ray model and corresponded to locations where the first bottom interactions did not contribute to the field. This results in the discontinuity in the arrivals from the data beyond this range, up to about 7 km up slope from the array. Down slope, the direct path persists to a range of approximately 7 km, as designated by the vertical line in Fig. 28. Beyond this, the first bottom interaction is used as the reference arrival.

The water-borne eigenray paths were constructed taking into account the range-dependent SSPs and bathymetry to facilitate the range-dependent inversions to be discussed in Sec. IV B 2 *c*. MEDUSA was used to calculate the range-dependent eigenrays to the receiver array for the first 10 receivers (excluding hydrophone 3 because of a malfunction in this receiver). The cost function values obtained by using the parameters from the range-independent inversion were similar to the range-independent results at corresponding ranges to the array, but were slightly lower for sources at the shallower water depths because data from fewer receivers were used. For instance, for a source 2.86 km up slope from the array, the cost function value was 0.286 for the final solution from the range-dependent inversion. The cost function minimum increased with increasing range as the SNR decreased. The source at 3.81 km towards end point E gave a minimum cost function value of 0.36. More discussion of the range-dependent inversions are given in Sec. IV B 2 *c*.

Using the range-independent parameters listed in Table III gave cost function values that were similar to the minimum values of the range-independent inversions. This similarity suggests that much of the analysis of the range-dependent data can be simplified by using the range-independent parameters. For example, the importance of including the range-varying SSPs and bathymetry was also examined by using the range-independent parameters. The SSP analysis was done by assuming a constant SSP taken at the receiver, similar to the range-independent inversions. The result was that the direct path did not propagate to ranges distant enough as compared to the data. Also, the caustic region up slope from the array was not reproduced. This result is shown in Fig. 29, where the disappearance of the direct path is designated and is shown to occur at a much shorter range than in Fig. 28.

The importance of using the experimentally determined bathymetry was shown by comparing the data arrival structure to the model results obtained by assuming the bathymetry was constant at the receiver depth of 228.7 m. The result, presented in Fig. 30, shows that it is not possible to explain the arrival structure unless the actual bathymetry is included. The direct path for a constant bathymetry persists to all source ranges, in contrast to the recorded arrival structure. Also, bottom interacting paths accumulate an increasing arrival time error for each bottom reflection because of a path difference error resulting from the assumption of constant bathymetry as compared to an increasing bottom depth with range from the measurement. On the up-slope side of the array, the caustic region is not realized in the model, due to using the SSP near the receiver instead of the SSP farther up the slope where the caustic region is generated.

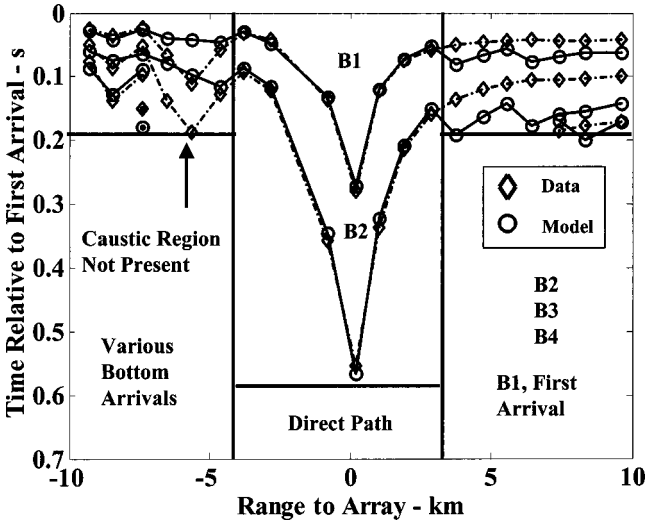

FIG. 29. Arrival structure assuming the SSP at the receiver along with the measured bathymetry.

c. Range-dependent inversions. The inversions for the range-dependent data were performed with several sources both up slope and down slope to the array. The results were very close to the range-independent solutions, again used as the starting values. Table V shows the inversion results obtained for two sources up slope from the array and one source down slope. The resulting cost function values are seen to be very close to the initial cost value for a given source. Several thousand iterations were taken to obtain these minimum values; the number of iterations required are listed in the third row of Table V. Note that the lack of

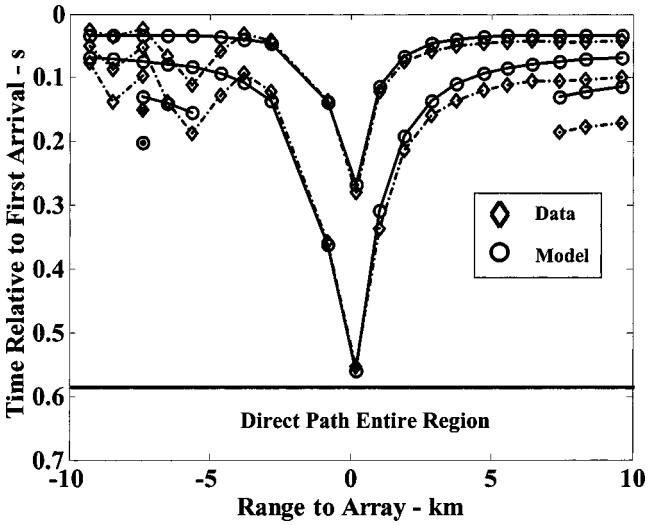

FIG. 30. Arrival structure assuming a flat bathymetry at receiver depth and using the SSP taken at the receiver.

TABLE V. Two-layer solutions for PWRC method range-dependent inversion. The units are sound speed, m/s; layer thickness, m; sound speed gradient, 1/s, density, g/cm^3; attenuation, dB/(m kHz); and attenuation gradient, dB/(m^2 kHz).

Parameter	Source 4.65 km Up slope	Source 3.81 km Up slope	Source 6.42 km Down slope
Init. cost	0.464	0.368	0.295
Min. cost	0.462	0.360	0.248
Iteration No.	3003	10	343
C_{t1}	1594.49	1595.30	1588.40
H_1	0.44	0.51	0.43
C_{g1}	0.531	1.476	2.077
ρ_1	1.883	1.895	2.039
C_{t2}/C_{b1}	0.957	0.957	0.965
α_{t1}	0.506	0.441	0.640
α_{g1}	-2.78×10^{-3}	4.45×10^{-2}	-8.53×10^{-3}
H_2	34.70	34.35	31.82
C_{g2}	2.170	2.587	2.975
ρ_2	1.741	1.741	1.932
C_{sub}/C_{b2}	1.141	1.141	1.290
α_{t2}	0.179	0.179	0.125
α_{g2}	1.57×10^{-5}	1.57×10^{-5}	7.15×10^{-3}
α_{sub}	0.792	0.792	0.592
ρ_{sub}	1.878	1.878	2.176

variation of some the parameters is because of their weak dependence in the received data. The range-dependent bathymetry and SSPs were used to construct the water-borne paths for these inversion results.

The range-dependent solution from the source at 4.65 km only differs from the range-independent solution in the first layer thickness of 0.44 m. Recall that a similar value was obtained for the farthest source range of 9.78 km in the range-independent inversion. Similar range-dependent inversion results were also obtained for the source at 3.81 km, although the first layer parameters have some slight differences. Down-slope from the array, the source at 6.42 km produced a slightly lower sound speed but higher density in the first layer. However, the cost function value only changed from 0.295 to 0.248 for this source. The thickness of the first layer was similar to those at the two up-slope sources, producing a value of 0.43 m for the inversion. The sound speed ratio, c_{t2}/c_{b1}, was 0.965 for this down-slope source, slightly larger than for the two up-slope sources which both match the range-independent result. The down-slope source produced smaller cost function values than either the range-independent source or the up-slope sources at similar ranges.

Cost function distributions were generated for the range-dependent parameters from the source at 3.81 km and were shown to be very similar in shape to the range-independent inversion distributions. Cost function distribution envelopes for all three sources listed in Table V are shown in Fig. 31, where the minimum values can be seen by inspection. Despite the range of cost function values, due to the decrease in SNR with range, all three envelopes have very similar shapes and minima location. The difference in cost function values, at a given range, as compared to the range-independent results at a similar range is because only nine receivers were used for the range-dependent inversions as compared to 19 for the range-independent data. Since the array was approximately perpendicular to the range-dependent sources, further averaging in the cost function was pointless.

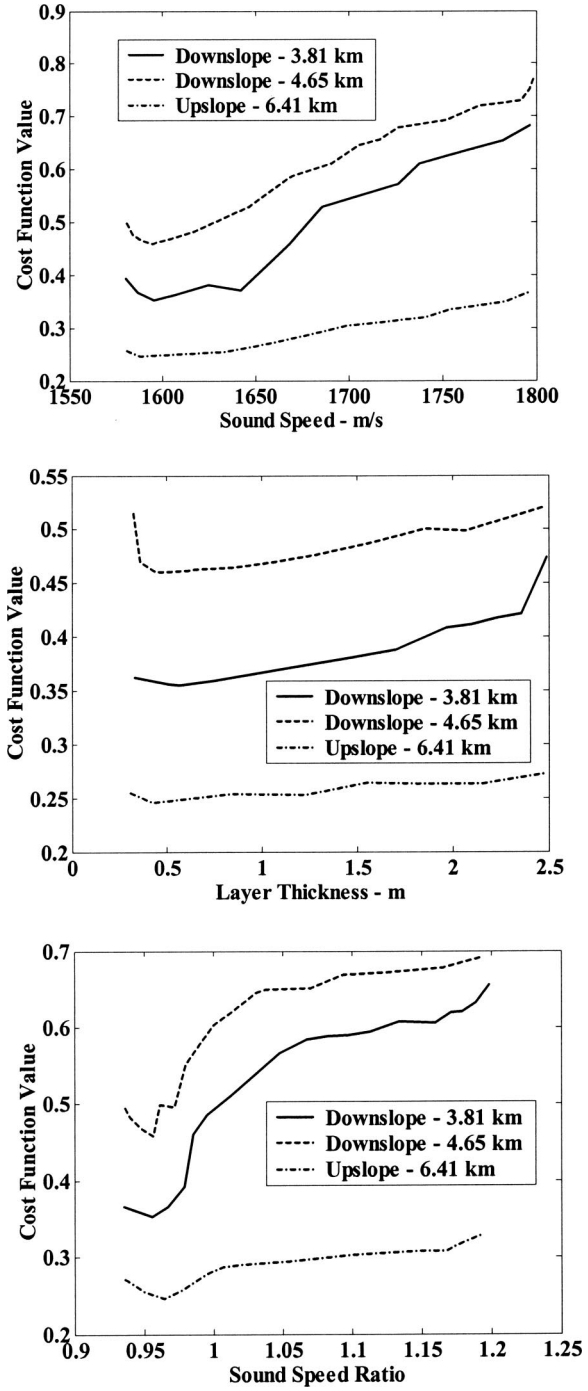

FIG. 31. Cost function distribution envelopes for several of the range-dependent inversion parameters for the sources listed in Table III.

Several other sources show inversion results similar to those in Table V and are not included here. The excellent agreement between the range-independent and range-dependent data inversions averts the need for a range-dependent seabed analysis of this data. More exact measurements would have to be performed to necessitate a range-dependent seabed model but are beyond the scope of this work.

As a final confirmation, two of the inversions were repeated using initial parameter values different from those of

TABLE VI. Two-layer solutions for PWRC method range-dependent inversion starting away from range-independent results. The units are sound speed, m/s; layer thickness, m; sound speed gradient, 1/s; density, g/cm^3; attenuation, dB/(m kHz), and attenuation gradient, dB/(m^2 kHz).

Parameter	3.81 km Up slope	3.81 km Up slope	6.42 km Down slope	6.42 km Down slope	6.42 km Down slope
Results	*Initial*	*Final*	*Initial*	*Final*	*Final*
Total iterations	1	16600	1	22900	24500
Min. cost	0.385	0.354	0.300	0.246	0.237
C_{t1}	1575.30	1594.03	1625.30	1594.870	1615.10
H_1	0.800	0.667	0.900	0.356	0.356
C_{g1}	1.076	2.602	1.076	0.212	1.464
ρ_1	1.995	2.069	1.775	1.811	1.970
C_{t2}/C_{b1}	0.967	0.952	0.987	0.956	0.945
α_{t1}	0.451	0.183	0.251	0.269	0.142
α_{g1}	3.45×10^{-3}	-5.27×10^{-3}	3.45×10^{-3}	-2.17×10^{-3}	5.35×10^{-3}
H_2	34.35	29.44	39.05	10.26	37.66
C_{g2}	2.687	3.684	1.687	3.658	3.618
ρ_2	1.941	1.703	1.641	1.855	1.881
C_{sub}/C_{b2}	1.241	1.277	1.041	1.047	1.136
α_{t2}	0.279	0.115	0.579	0.113	0.101
α_{g2}	1.57×10^{-3}	1.33×10^{-2}	1.57×10^{-3}	8.72×10^{-3}	-4.19×10^{-3}
α_{sub}	0.582	0.299	0.282	0.130	0.379
ρ_{sub}	2.078	1.787	1.978	1.674	1.614

the range-independent solution in Table III. The results were consistent with those in Table V for sources 3.81 km up slope and 6.42 km down-slope from the array. Table VI shows the results of these inversions, including the initial values. The total number of iterations that were performed are in Table VI. Although, slightly different, the values are again close to the range-independent results. This analysis was performed as a consistency check of the results in Table V, where some of the second layer and substrate parameters did not change from the range-independent results. The last column of Table VI was obtained after 24 500 iterations and gives a slightly better cost function than that in column five. However, the ratio of the second layer sound speed to the first layer sound speed is also lower in column six and is consistent with the results for the sound speed in layer two from the range-independent inversions.

V. CONCLUSION

A plane wave reflection coefficient approach to geoacoustic inversions was presented. Range-independent and range-dependent environments each are treated by separating the water column propagation from the interaction with the seabed. A detailed analysis of this propagation method was given, and results were compared to analytic solutions for some simple environments. Good results from the application of the PWRC method to the recent IT workshop test case III problem were presented. All three test cases reported here and in Ref. 41 validate the PWRC method for rapidly determining multilayer geoacoustic parameters in range-independent environments. In test case III, the range-independent first layer was determined. Test case III also showed that by generalizing the PWRC method to account for range segments a range dependence in the geoacoustics of the bottom layers could be modeled.

Geoacoustic parameters obtained from the inversion of both a range-independent and a range-dependent shallow-water environment were presented. A two-layer analysis of the range-independent environment was first discussed, resulting in a single parameter set to describe the time series for all the sources. The range dependence of the sound speed profiles was then examined. For this environment, consistent results were obtained using either the source or the receiver water sound speed profile for the range-independent data. However, analysis of the range-dependent data showed the importance of taking into consideration the range-dependent water sound speed profiles to properly account for the propagation and to obtain accurate inversion results. Finally, the determined range-independent parameter values were used to predict the range-dependent data. These parameters values compared well to the parameter values obtained by direct inversions of the range-dependent data. Time series comparisons were made between the model solutions and the actual data to demonstrate the accuracy of the inversion results. The propagation in this environment is represented well by a geometric theory.

ACKNOWLEDGMENTS

The authors appreciate the data collection efforts of the ESL/ARL:UT engineering team for the experimental setup and data collection, including Lewis Thompson, Paul Eisman, and other members of their staff. Special thanks also to James Piper of ESL/ARL:UT for his help in collecting the acoustic data and the bottom core samples, and for many helpful discussions.

[1] A. Tolstoy, N. R. Chapman, and G. Brooke, "Workshop '97: Benchmarking for geoacoustic inversion in shallow water," J. Comput. Acoust. **6**, 1–28 (1998).
[2] ONR Inversion Techniques Workshop, Gulfport, Mississippi, May 2001.
[3] N. Metropolis *et al.*, "Equation of state calculations by fast computing machines," J. Chem. Phys. **21**, 1087–1092 (1953).
[4] S. Kirkpatrick, C. D. Gelatt, Jr., and M. P. Vecchi, "Optimization by simulated annealing," Science **220**, 671–680 (1983).
[5] W. L. Goffe, G. D. Ferrier, and J. Rogers, "Global optimization of statis-

tical functions with simulated annealing,'' J. Econometr. **60**, 65–99 (1994).
[6] H. Szu and R. Hartley, ''Fast simulated annealing,'' Phys. Lett. A **122**, 157–162 (1987).
[7] P. Gerstoft, ''Inversion of seismoacoustic data using genetic algorithms and *a posteriori* probability distributions,'' J. Acoust. Soc. Am. **95**, 770–782 (1994).
[8] D. P. Knobles, R. A. Koch, E. K. Westwood, and T. Udagawa, ''The inversion of ocean waveguide parameters using a nonlinear least squares approach,'' J. Comput. Acoust. **6**, 83–97 (1998).
[9] M. D. Collins and L. Fishman, ''Efficient navigation of parameter landscapes,'' J. Acoust. Soc. Am. **98**, 1637–1644 (1995).
[10] T. B. Neilsen, ''An iterative implementation of rotated coordinates for inverse problems,'' J. Acoust. Soc. Am. **113**, 2574–2586 (2003).
[11] P. Gerstoft, ''Inversion of acoustic data using a combination of genetic algorithms and the Gauss–Newton approach,'' J. Acoust. Soc. Am. **97**, 2181–2190 (1995).
[12] M. R. Fallat and S. E. Dosso, ''Geoacoustic inversion via local, global, and hybrid algorithms,'' J. Acoust. Soc. Am. **105**, 3219–3230 (1999).
[13] M. R. Fallat, P. L. Nielsen, and S. E. Dosso, ''Hybrid geoacoustic inversion of broadband Mediterranean Sea data,'' J. Acoust. Soc. Am. **107**, 1967–1977 (2000).
[14] M. Haire, ''Geoacoustic inversion using a hybrid optimization algorithm,'' M. Sc. thesis, The University of Texas at Austin, 2001.
[15] D. P. Knobles, R. A. Koch, L. A. Thompson, and P. E. Eisman, ''Broadband sound propagation in shallow water and geoacoustic inversion,'' J. Acoust. Soc. Am. **113**, 205–222 (2003).
[16] S. R. Rutherford and K. E. Hawker, ''The effects of density gradients on bottom reflection loss for a class of marine sediments,'' J. Acoust. Soc. Am. **63**, 750–757 (1978).
[17] K. E. Hawker, A. L. Anderson, K. C. Focke, and T. L. Foreman, ''Initial phase of a study of bottom interaction of low frequency underwater sound,'' ARL Technical Report No. 76-14 (ARL-TR-76-14), Appl. Res. Lab., The Univ. of Texas at Austin, 1976.
[18] K. E. Hawker, K. C. Focke, and A. L. Anderson, ''A sensitivity study of underwater sound propagation loss and bottom loss,'' ARL Technical Report No. 77-17 (ARL-TR-77-17), Appl. Res. Lab., The Univ. of Texas at Austin, 1977.
[19] J. Hanna, ''The design of transmission loss experiments,'' *Proceedings of the International Workshop on Low-Frequency Propagation and Noise* (Maury Cent. Ocean Sci., U.S. Navy, Washington, DC, 1977), Vol. 1.
[20] L. Hampton, S. K. Mitchell, and R. R. Gardner, ''Acoustic bottom loss measurement using multipath resolution,'' IEEE, 235–251, 1978.
[21] K. E. Hawker and T. L. Foreman, ''A plane wave reflection loss model based on numerical integration,'' J. Acoust. Soc. Am. **64**, 1470–1477 (1978), and references cited therein.
[22] E. K. Westwood and P. J. Vidmar, ''Eigenray finding and time series simulation in a layered-bottom ocean,'' J. Acoust. Soc. Am. **81**, 912–924 (1987).
[23] E. K. Westwood and C. T. Tindle, ''Shallow water time-series simulation using ray theory,'' J. Acoust. Soc. Am. **81**, 1752–1761 (1987).
[24] E. A. Kraut, *Fundamentals of Mathematical Physics* (McGraw-Hill, New York, 1967), Chap. 7.
[25] L. M. Brekhovskikh, *Waves in Layered Media*, 2nd ed. (Academic, New York, 1980).
[26] E. K. Westwood, C. T. Tindle, and N. R. Chapman, ''A normal mode model for acousto-elastic ocean environments,'' J. Acoust. Soc. Am. **100**, 3631–3645 (1996).
[27] S. A. Stotts, R. A. Koch, and N. R. Bedford, ''Development of an arctic ray model,'' J. Acoust. Soc. Am. **95**, 1281–1298 (1994).
[28] H. Schmidt, ''SAFARI: Seismo-acoustic fast field algorithm for range independent environments: User's guide,'' Technical Report SR 113, SACLANT ASW Research Centre, La Spezia, Italy, 1987. (See also ''OASES User's Guide, Version 1.7 Applications and Upgrade Notes,'' available from H. Schmidt, Dept. of Ocean Engineering, Massachusetts Institute of Technology.)
[29] D. P. Knobles, R. A. Koch, S. A. Stotts, and T. B. Neilsen, ''Numerical study of geoacoustic inversion in range-dependent ocean environments,'' IEEE J. Ocean. Eng. **28**, 355–369 (2003).
[30] S. K. Mitchell and J. J. Lemmon, ''A ray theory model of acoustic interaction with the ocean bottom,'' J. Acoust. Soc. Am. **66**, 855–861 (1979).
[31] C. T. Tindle and Z. Y. Zhang, ''Continuous modes and shallow water sound propagation,'' *OCEANS '93: Engineering in Harmony with the Ocean, Proceedings I, 18–21 October*, Victoria, British Columbia, Canada (IEEE, New York, 1993), pp. 81–86.
[32] T. L. Foreman, ''Ray modeling methods for range dependent ocean environments,'' Applied Research Laboratories, The University of Texas, ARL:UT Technical Report, ARL-TR-83-41, 1983.
[33] M. A. Biot, ''Theory of propagation of elastic waves in a fluid-saturated porous solid: I. Low-frequency range,'' J. Acoust. Soc. Am. **28**, 168–178 (1956).
[34] M. A. Biot, ''Theory of propagation of elastic waves in a fluid-saturated porous solid: II. Higher frequency range,'' J. Acoust. Soc. Am. **28**, 179–191 (1956).
[35] M. A. Biot, ''Mechanics of deformation and acoustic propagation in porous media,'' J. Appl. Phys. **33**, 1482–1498 (1962).
[36] R. D. Stoll, *Sediment Acoustics*, *Lecture Notes on Earth Sciences* (Springer-Verlag, Berlin, 1989).
[37] N. P. Chotiros, ''Biot model of sound propagation in water-saturated sand,'' J. Acoust. Soc. Am. **97**, 199–214 (1995).
[38] M. J. Buckingham, ''Theory of acoustic attenuations, dispersion, and pulse propagation in unconsolidated granular materials including marine sediments,'' J. Acoust. Soc. Am. **102**, 2579–2596 (1997).
[39] F. D. Tappert, ''The parabolic equation method,'' in *Wave Propagation and Underwater Acoustics*, edited by J. B. Keller and J. S. Papadakis (Springer, New York, 1977).
[40] M. D. Collins, ''A split-step Padé solution for the parabolic equation method,'' J. Acoust. Soc. Am. **93**, 1736–1742 (1993).
[41] S. A. Stotts and D. P. Knobles, ''Geoacoustic inversion in range-dependent environments: A plane wave reflection coefficient approach,'' J. Acoust. Soc. Am. **109**, 2334 (2001).
[42] D. P. Knobles and R. A. Koch, ''A time series analysis of sound propagation in a strongly multipath shallow water environment with an adiabatic normal mode approach,'' IEEE J. Ocean. Eng. **21**, 1–13 (1996).
[43] Harbor Branch Oceanographic Institute, 5600 US 1 North, Ft. Pierce, FL, 34946.
[44] D. E. Grant, ''East Coast SWAMI Test Plan,'' Applied Research Laboratories, The University of Texas, ARL:UT Technical Report, ARL-TL-EV-01-12, 2001.
[45] K. O. Emery and E. Uchupi, *The Geology of the Atlantic Ocean* (Springer-Verlag, New York, 1984), pp. 440–441.

Criteria for discretization of seafloor bathymetry when using a stairstep approximation: Application to computation of T-phase seismograms

Catherine de Groot-Hedlin[a)]
Scripps Institution of Oceanography, UCSD, 8795 Biological Grade, La Jolla, California 92093-0225

(Received 11 March 2003; revised 21 November 2003; accepted 1 December 2003)

Acoustic solutions for numerical models in which an overly coarse discretization of a stairstep boundary is employed to simulate smoothly varying bathymetry are degraded in a way that simulates scattering. Geometrical optics approximations are used to derive discretization criteria for simulating a smoothly sloping interface for the case of a source embedded in either an acoustic or an elastic seafloor, and applied to modeling T-phases. A finite difference time-domain modeling approach is used to synthesize T-phases for both smoothly sloping and rough seafloor boundaries. It is shown that scattering at a rough seafloor boundary yields ocean-borne acoustic phases with velocities near those of observed T-phase, while smooth seafloor models yield T-phases with slower horizontal velocities. The long duration of the computed T-phases for both the rough acoustic and elastic models is consistent with energy being scattered into the sound channel both as it transits the ocean/crust boundary, as well as at several subsequent seafloor reflections. However, comparison between the elastic and acoustic modeling solutions indicates that the T-phase wavetrain duration decreases with decreasing impedence contrast between the ocean and seafloor. [DOI: 10.1121/1.1643361]

PACS numbers: 43.30.Hw, 43.30.Cq, 43.30.Ma, 43.20.Gp [RAS] Pages: 1103–1113

I. INTRODUCTION

In many computational methods, a series of flat surfaces, or stairsteps, is used to represent a smooth, sloping boundary. Jensen (1998) demonstrated that the representation of sloping seafloor bathymetry by overly coarse stairsteps in ocean acoustic models leads to acoustic field solutions that include significant sidelobe diffractions. These numerical artifacts arise because each step acts as a point scatterer. If the spacing between stairsteps is a significant fraction of the incident wavelength for a source in the ocean column, the reflected phase consists of both a specularly reflected phase corresponding to the result for a smooth seafloor, and diffracted sidelobes resulting from coherent interference between waves diffracted from the array of point scatterers (Jensen, 1998). For sufficiently small spacing between the steps, the solution for the faceted boundary approximation approaches that for the smooth boundary.

This paper addresses the question of how finely seafloor bathymetry must be discretized to accurately model T-phase excitation. T-phases are seismically excited acoustic waves that propagate in the oceanic low-velocity sound channel, known as the SOFAR channel. Ray theory predicts that, because of the high velocity constrast between the oceanic crust and the ocean, *P* waves excited by a source within the crust or upper mantle are refracted into acoustic waves that propagate nearly vertically within the ocean column. Two mechanisms, or some combination thereof (Park *et al.*, 2001), are commonly invoked to explain how crustal sources excite nearly horizontally propagating acoustic phases trapped within the SOFAR channel. These are downslope propagation (Tolstoy and Ewing, 1950; Talandier and Okal, 1998), which predicts that repeated interactions with a sloping seafloor result in an almost horizontally propagating acoustic phase, and scattering from a rough seafloor (de Groot-Hedlin and Orcutt, 1999, 2001), which predicts that acoustic phases are excited in proportion to the acoustic model amplitude at the seafloor depth.

In order to develop the modeling capability to distinguish between these competing hypotheses, it is vital to eliminate numerical artifacts associated with an overly coarse discretization of the seafloor and thus ensure that only physically realistic acoustic phases are synthesized. In this paper, the stairstep spacing necessary to avoid diffracted sidelobes is examined for sources embedded within the oceanic crust. The results for a fluid–fluid interface, that is, neglecting shear (*S*) velocities in the crust, and for a fluid–elastic boundary, with nonzero shear velocities within the crust, are considered separately. The results are applied to the computation of T-phases to determine which of the two competing excitation mechanisms is dominant in their excitation.

II. DIFFRACTIONS AT A STAIRSTEP INTERFACE

A. Fluid–fluid boundary

If each stairstep acts as an omnidirectional scatterer, then diffraction lobes are generated by constructive interference between waves radiated from neighboring scatterers. The direction in which the sidelobes propagate can be deduced from physical and geometrical considerations, as in Jensen (1998). In the following, sidelobe propagation angles are derived for a plane wave incident from below on a sloping fluid–fluid interface represented by a series of stairsteps. Although the focus of this investigation is on the excitation

a)Electronic mail: chedlin@ucsd.edu

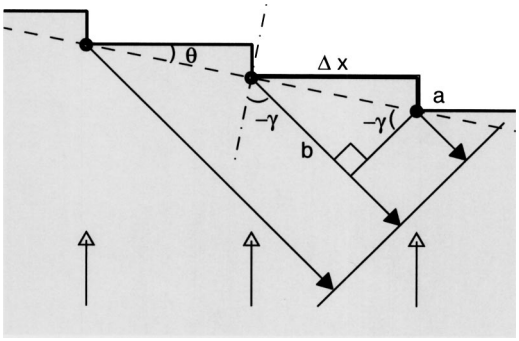

FIG. 1. Diagram showing the geometry for computing the propagation angle of forward-reflected diffractions at a sloping boundary represented by stairsteps, for a plane wave incident directly from below. Coherent reflections occur when the stairstep spacing Δx is large enough that the difference in path length $(a+b)$ is an integral number of wavelengths. Diffraction angles are defined as positive clockwise from the normal to the interface.

of acoustic energy within the ocean, it is important to avoid creating reflected diffraction sidelobes within the seafloor, since reverberations within oceanic sediments or crustal layers can leak acoustic energy back into the seafloor. Therefore, discretization levels required to accurately model both seismic energy reflected back into the crust, and acoustic energy transmitted into the ocean column, are considered.

1. Reflected diffraction lobes

Consider a vertically propagating acoustic phase incident directly from below on an interface inclined downward to the right at an angle θ, represented by a series of stairsteps of height a located at intervals of Δx. The lower medium represents oceanic crust and sediments and the upper medium represents the ocean column. The angles at which forward-scattered diffraction lobes are reflected into the crust can be derived from the geometry shown in Fig. 1 (where forward is defined as the downslope direction). Constructive interference occurs at angles γ, for which the path difference $(a+b)$ is an integral number of wavelengths. Referring to Fig. 1, one obtains

$$\sin(-\gamma_n)=\frac{n\lambda_{\text{seis}}}{\Delta x}\cos(\theta)-\sin(\theta), \quad n=0,1,2,..., \tag{1}$$

where γ_n is defined as positive clockwise with respect to the normal to the interface, and λ_{seis} is the wavelength of the incident seismic wave. For $n=0$, this reduces to $\gamma_0=\theta$, i.e., the angle of reflection is equal to the angle of incidence at a smooth interface. Thus, for a smooth interface modeled as a stairstep boundary, only the solution for $n=0$ is physically realistic and higher-order diffraction lobes are numerical artifacts.

The stairstep spacing necessary to eliminate these forward-reflected sidelobes may be derived from Eq. (1) as

$$\Delta x<\frac{\lambda_{\text{seis}}\cos(\theta)}{1+\sin(\theta)}. \tag{2}$$

Similarly, the angles at which backward-reflected diffraction lobes are generated can be derived as indicated in Fig. 2. This time, constructive interference occurs when the path length difference $(b-a)$ is an integral numbers of

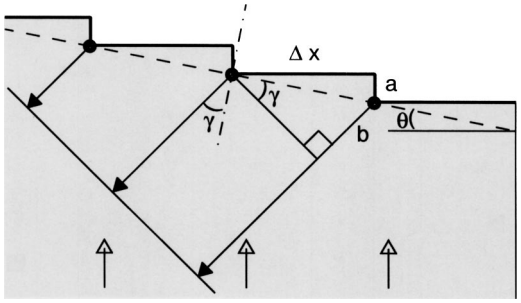

FIG. 2. Geometry for computing the propagation angle of upslope-reflected diffractions. Coherent reflections occur when the path length difference $(b-a)$ is an integral number of wavelengths. The solution for $b=a$ corresponds to specular reflection, and yields the physically realistic solution for a smooth boundary.

wavelengths. Thus, diffraction lobes are generated at angles

$$\sin(\gamma_n)=\frac{n\lambda_{\text{seis}}}{\Delta x}\cos(\theta)+\sin(\theta), \quad n=0,1,2,.... \tag{3}$$

The solution for $n=0$ in Eq. (3) is identical to that of Eq. (1). The criterion for eliminating backscattered sidelobes is

$$\Delta x<\frac{\lambda_{\text{seis}}\cos(\theta)}{1-\sin(\theta)}. \tag{4}$$

Comparing Eqs. (2) and (4), it can be seen that the criterion for eliminating forward-reflected sidelobes is slightly more stringent than that for eliminating backscattered reflections. For the small-slope angles typical of the seafloor, the stairstep spacing need only be slightly smaller than the seismic wavelength.

2. Transmitted diffraction lobes

Derivation of the angles at which diffraction lobes are transmitted into the overlying medium is complicated by the fact that the wavelength of the acoustic phase excited in the ocean differs from that in the oceanic crust. As indicated in Fig. 3, these diffraction lobes are scattered forward at angles such that the path length difference $(a+b)$ is an integral number of wavelengths. Taking into account the difference in velocity, and hence wavelengths, between the crust and ocean, each path length may be written in terms of the fractional number of wavelengths, i.e., $a=\alpha\lambda_{\text{seis}}$ and $b=\beta\lambda_{\text{oc}}$,

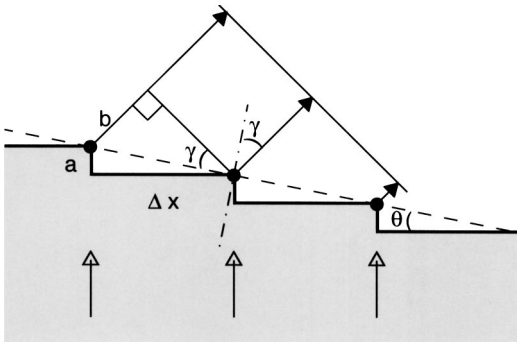

FIG. 3. Geometry for computing the propagation angle of diffractions transmitted into the ocean column in the downslope direction. Coherent reflections occur when the path length difference $(a+b)$ is an integral number of wavelengths.

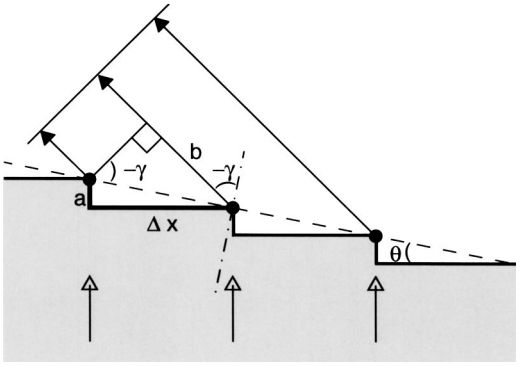

FIG. 4. Geometry for computing the propagation angle of diffractions transmitted into the ocean column in the upslope direction. Coherent reflections occur when the path length difference $(b-a)$ is an integral number of wavelengths. The solution for $b=a$ yields Snell's law, and corresponds to the physically realistic solution for a smooth boundary.

where λ_{oc} is the acoustic wavelength within the ocean. Constructive interference occurs at angles such that $\alpha+\beta=n$, i.e.,

$$a+b=\alpha\lambda_{seis}+(n-\alpha)\lambda_{oc}. \tag{5}$$

Referring to the geometry of Fig. 3, one derives, after some algebraic manipulation

$$\sin(\gamma_n)=\frac{n\lambda_{oc}}{\Delta x}\cos(\theta)-\frac{v_{oc}}{v_{seis}}\sin(\theta), \quad n=0,1,2,..., \tag{6}$$

where v denotes velocity, and γ_n is the angle at which sidelobes are transmitted in the downslope direction, defined as positive clockwise with respect to the normal to the interface.

The solution for the fundamental lobe $n=0$ is just a statement of Snell's law (since γ_n is defined as positive clockwise from the normal to the interface) and is thus the physical solution for a smooth boundary. For $\theta=0$, Eq. (6) reduces to the equation for a diffraction grating (Halliday and Resnick, 1974); thus, higher-order lobes are numerical artifacts associated with overly coarse discretization of the boundary. From Eq. (6), it can be seen that a physically realistic solution is achieved given stairstep spacings of

$$\Delta x<\frac{\lambda_{oc}\cos(\theta)}{1+(v_{oc}/v_{seis})\sin(\theta)}. \tag{7}$$

Finally, diffraction lobes can be transmitted upslope into the overlying medium as shown in Fig. 4. Constructive interference occurs at angles for which the path length $(b-a)$ is an integer number of wavelengths. These angles are given by

$$\sin(-\gamma_n)=\frac{n\lambda_{oc}}{\Delta x}\cos(\theta)+\frac{v_{oc}}{v_{seis}}\sin(\theta), \quad n=0,1,2,..., \tag{8}$$

and sidelobe diffractions transmitted in the upslope direction are eliminated for

$$\Delta x<\frac{\lambda_{oc}\cos(\theta)}{1-(v_{oc}/v_{seis})\sin(\theta)}. \tag{9}$$

Given that acoustic velocities within the ocean column are usually lower than those of the crust, the criteria for avoiding numerical artifacts associated with the stairstep approximation are not especially limiting. These criteria, given by Eqs. (2), (4), (7), and (9), indicate that for shallow slopes, the stairstep spacing must be slightly smaller than the smallest wavelength within the environmental model. For a typical ocean acoustic model, the ocean sound speed is less than that of the seafloor, so that Eq. (7) provides the limiting criterion for accurate solutions. As will be shown next, the introduction of shear velocities within the oceanic crust imposes stricter criteria on the stairstep spacing for a fluid–elastic boundary.

B. Fluid–elastic boundary

A multiplicity of phases can be excited at a fluid–elastic boundary. Compressional (P) waves incident on a smooth boundary can be reflected both as P- and S waves, and transmitted into the ocean as acoustic energy. Conversely, incident S waves give rise to reflected P- and S waves, as well as transmitted acoustic waves. For a stairstep boundary, each reflected and transmitted phase is potentially associated with diffracted lobes arising from an overly coarse discretization of the slope.

The criteria for ensuring that physically unrealistic sidelobes are not excited in the ocean column by a vertically propagating S wave incident on the solid–fluid interface are given by Eqs. (7) and (9), where v_{seis} is the S-wave velocity. Equations (2) and (4) hold for either P- to P-wave reflections or S- to S-wave reflections, where λ_{seis} is the appropriate seismic wavelength. The problem only becomes more complicated for P waves reflected into S-wave energy, or S waves reflected into P-wave energy within the solid. In this case, referring again to the geometry of Fig. 1, it can be seen that forward-scattered diffraction lobes are formed at angles

$$\sin(-\gamma_n)=\frac{n\lambda_{seis}^{out}}{\Delta x}\cos(\theta)-\frac{v_{seis}^{out}}{v_{seis}^{in}}\sin(\theta), \quad n=0,1,2,..., \tag{10}$$

where v_{seis}^{in} refers to the velocity of the vertically propagating wave incident on the interface and v_{seis}^{out} and λ_{seis}^{out} are the velocity and wavelength of the outgoing seismic phase, respectively. Again, the fundamental lobe solution $(n=0)$ is the only physically realistic one. Thus, the required stairstep spacing is

$$\Delta x<\frac{\lambda_{seis}^{out}\cos(\theta)}{1+(v_{seis}^{out}/v_{seis}^{in})\sin(\theta)}. \tag{11}$$

Compressional velocities are always greater than shear velocities within an elastic solid, and in water-saturated sediments the ratio may be as high as 13 (Hamilton, 1979). Thus, for S- to P conversions, Eq. (11) predicts that the required stairstep spacing is very small. For a V_p/V_s ratio of 2, the required stairstep spacing is $\lambda_p/3$ for a 40° slope; for a V_p/V_s ratio of 10, a 40° stairstep slope must be sampled at intervals of $\lambda_p/10$. Corresponding discretization values for P- to S conversions are predicted to be even smaller. For $V_p/V_s=2$, Δx must be less than or equal to $0.55\lambda_s$ $(\approx\lambda_p/3.5)$ for a 40° slope; for $V_p/V_s=10$, Δx must be less

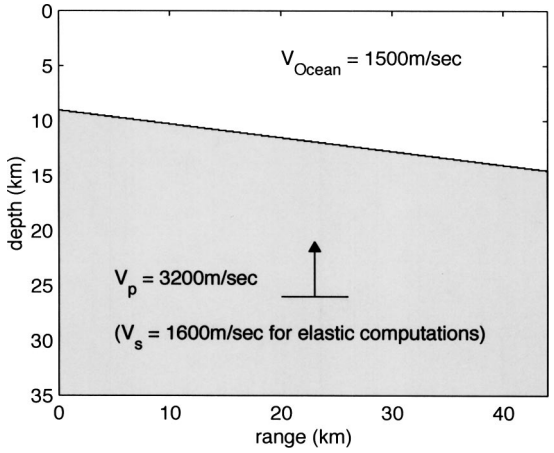

FIG. 5. Environmental model for numerical computations, with varying stairstep spacings. A cosine beam of width 6 km, at 26-km depth, is incident from below on a boundary with a 1:8 gradient. The compressional velocity is 3200 m/s in the lower medium and 1500 m/s in the upper medium. For the acoustic computations, the shear velocity is 0 throughout; for the elastic computations, the shear velocity is 1600 m/s in the lower medium.

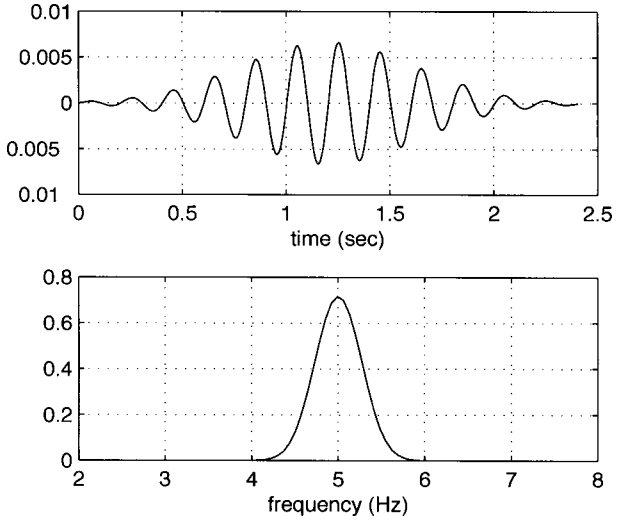

FIG. 6. The source function for the computations. (a) Time series for the central element within the source beam. (b) The source spectrum.

than or equal to $0.7\lambda_s(\approx\lambda_p/14)$ for the same slope.

Similarly, the general formula for diffraction angles of backscattered reflections is given by

$$\sin(\gamma_n)=\frac{n\lambda_{\text{seis}}^{\text{out}}}{\Delta x}\cos(\theta)+\frac{v_{\text{seis}}^{\text{out}}}{v_{\text{seis}}^{\text{in}}}\sin(\theta),\quad n=0,1,2,..., \tag{12}$$

and the appropriate discretization is

$$\Delta x<\frac{\lambda_{\text{seis}}^{\text{out}}\cos(\theta)}{1-(v_{\text{seis}}^{\text{out}}/v_{\text{seis}}^{\text{in}})\sin(\theta)}. \tag{13}$$

The stairstep spacing required for accurately modeling backscattered reflections is larger than for the forward-scattered reflections. Thus, the limiting stairstep spacing required to simulate a smooth boundary when modeling seismic to acoustic interactions for sources within the elastic ocean crust is given by Eq. (11), for an incident *P* wave and a reflected *S* wave.

III. NUMERICAL SOLUTIONS

A. Results for a fluid–fluid boundary

The test problem, shown in Fig. 5, features an interface that angles downward to the right at a gradient of 1/8 ($\approx$7.1°). The compressional velocity is 1.5 km/s in the upper medium and 3.2 km/s in the lower medium; the density contrast between the lower and upper medium is 2.3. The densities and compressional velocities of the lower medium are representative of solidified marine sediments at the ocean floor. Acoustic field solutions are sought for a compressional cosine source beam directed upward. Each element in the source array is a 5-Hz sinusoid with exponential growth and decay as shown in Fig. 6(a); the bandwidth of the source is as shown in Fig. 6(b).

The criteria developed in the previous section are valid for monochromatic plane waves incident on a stairstep boundary from directly below; however, the cosine beam source used here is neither perfectly planar nor monochromatic. Given that the source beam has a finite width and is located a finite distance from the stairstep boundary, it may be mathematically represented as a superposition of plane waves using the Cagnaird–de Hoop method (Aki and Richards, 1980), with wave vectors pointing in all directions. The presence of energy with wave vectors in a direction that departs from that of the main beam affects the stepsize criterion; the geometry for forward scattering from a beam incident at an arbitrary angle i with respect to the normal to a stairstep boundary is shown in Fig. 7. As before, the path lengths d and b may be written in terms of the fractional number of wavelengths, i.e., $d=\alpha\lambda_{\text{seis}}$ and $b=\beta\lambda_{\text{oc}}$. Constructive interference occurs at angles such that $\alpha+\beta=n$. After some algebraic manipulation, one derives

$$\sin(\gamma_n)=\frac{n\lambda_{\text{oc}}}{\Delta x}\cos(\theta)-\frac{v_{\text{oc}}}{v_{\text{seis}}}\sin(i),\quad n=0,1,2,..., \tag{14}$$

as the angles at which constructive interference occurs. Again, only the $n=0$ solution is physically realistic, so the stairstep discretization criterion for a plane wave incident at

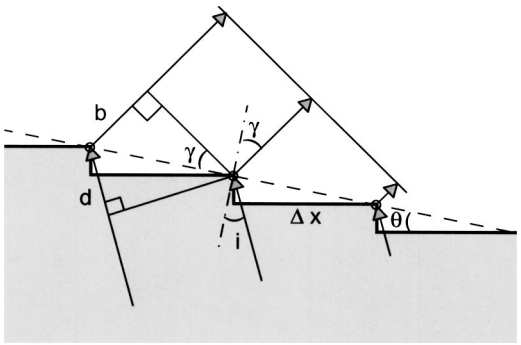

FIG. 7. Geometry for computing the propagation angle of diffractions transmitted into the ocean column in the downslope direction for a plane source at an incidence angle of i with respect to the boundary. Coherent reflections occur when the path length difference $(d+b)$ is an integral number of wavelengths.

an arbitrary angle i with respect to the normal to the interface becomes

$$\Delta x < \frac{\lambda_{oc}\cos(\theta)}{1+(v_{oc}/v_{seis})\sin(i)}. \tag{15}$$

It may be similarly shown that the $\sin(\theta)$ term in the denominator of each of the discretization criteria listed in Eqs. (2), (4), (9), (11), and (13) is replaced by $\sin(i)$. Thus, given that the discretization criteria depend on both the angle of incidence and the frequency (through the wavelength), it should be emphasized that they do not represent a sharp cutoff, but rather, the onset of scattering is gradual. A broader discussion on the use of beams to approximate a plane wave source may be found in Stephen (2000).

Finally, interface waves, like head waves or Stoneley waves, which are excited by the interaction of a spherical wave with a plane boundary, could be excited by the source beam since it includes spherical wave components. Furthermore, since the stairsteps act as secondary point scatterers, they could also play a role in exciting interface waves. A full treatment of interface waves is beyond the scope of this paper; however, in the examples shown here, the solutions are dominated by the diffraction effects discussed in the previous section.

A two-dimensional (2D) acoustic finite difference time-domain (FDTD) modeling method is applied to the test problem. To eliminate reflections from outgoing waves at the edges of the computational domain, and thereby model an unbounded region, the perfectly matched layer absorbing boundary condition (Berenger, 1994), modified for use in acoustics, is used to absorb energy at the bottom and sides of the grid over a wide range of angles. For each computation, a grid spacing of 20 m in both the horizontal and vertical directions is used, i.e., over 15 points per compressional wavelength—greater than the minimum of 10–12 nodes per wavelength required to minimize numerical dispersion in the FDTD approach (Taflove and Hagness, 2000). In the following, acoustic field solutions are computed for a series of stairstep spacings in increments of 160 m. These spacings were chosen so that the grid size could be uniform within each model. Thus, for a stairstep spacing of 160 m, a vertical step of 1 gridpoint occurs every 8 horizontal gridpoints; for a stairstep spacing of 320 m, a vertical step of 2 gridpoints occurs every 16 horizontal gridpoints, etc., given that the slope has an average gradient of 1/8. Thus, differences in the solutions are due to variations in both the stairstep spacing and the step rise. Larger rises between steps mainly affect the amplitude of the sidelobes; however, an examination of the sidelobe amplitudes is beyond the scope of this paper.

Equation (7) predicts that the maximum allowable spacing required for modeling physically realistic transmissions at the seafloor boundary is 281 m for a 5-Hz source. The acoustic field solution for a model with a stairstep spacing of 160 m, shown in Fig. 8 at $t=11.25$ s, thus corresponds to the result for a smooth slope. By this time, the upgoing acoustic phase has been partly reflected from the interface at an angle of 2θ with respect to the incident phase, and partly transmitted into the upper medium in a direction nearly perpendicular to the interface, as predicted by Snell's law.

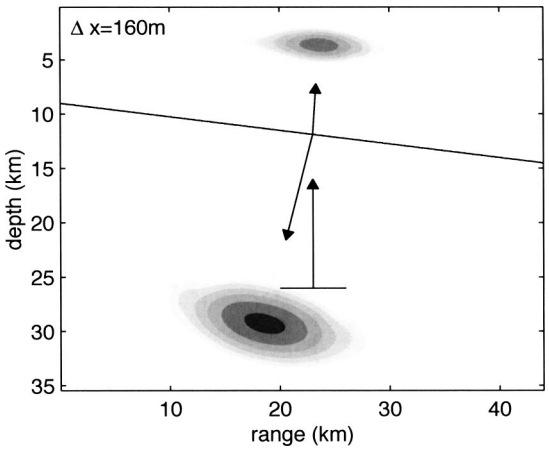

FIG. 8. Envelope of the acoustic field solution for a stairstep spacing of 160 m. The result corresponds to that of a smooth sloping boundary. Arrows show the direction of the incoming phase and the predicted angles of specular transmission and reflection for $f=5$ Hz. The length of each arrow is proportional to the velocity of the phase. Contour intervals are from 24 to 60 dB (from white to black), in steps of 6 dB.

Figure 9 shows acoustic field solutions at $t=11.25$ s, computed at stairstep spacings of 320 m and more. Equations (7) and (9) predict that diffraction sidelobes are transmitted in both the upslope and downslope directions for $\Delta x = 320$ m, but that no sidelobes should be excited in the lower medium at this spacing. This is confirmed by Fig. 9(a); diffraction sidelobes excited in the ocean propagate at angles of approximately 61° with respect to the normal in the downslope direction and 81° in the upslope direction, as predicted by Eqs. (6) and (8), respectively. As shown in the lower panels, the angle of propagation of these numerical artifacts steepens with increasing stairstep spacing. This is in agreement with the predicted propagation angles, which are shown by the arrows in each panel.

With stairstep spacings greater than 540 m, sidelobes corresponding to both the $n=1$ and $n=2$ solutions of Eqs. (6) and (8) are transmitted into the ocean column. Although a full analysis of the diffraction amplitudes is beyond the scope of this paper, note that Fig. 9 indicates that the amplitude of the sidelobes decreases with increasing order number, similar to the behavior of a diffraction grating. As the stairstep spacing increases beyond 565 m, Eq. (2) predicts that forward-reflected sidelobes are generated in the lower medium, as shown in Fig. 9(c). For stairstep spacings greater than 725 m, sidelobes are also reflected in the upslope direction, as shown in Fig. 9(d), and as predicted by Eq. (4). Figure 9(d) also shows a third-order diffraction node in the ocean that, from Eq. (6) should not exist for $f=5$ Hz. The existence of this sidelobe is likely due to the source bandwidth; third-order sidelobes can be generated in the downslope direction for $f>5.3$ Hz, which is within the source bandwidth as shown in Fig. 6(b).

B. Results for a fluid–solid boundary

The test problem is similar to that described above for a fluid–fluid boundary, with the exception that the lower medium in this case is an elastic solid with a shear velocity of 1.6 km/s. A 2D FDTD method suitable for elastic media

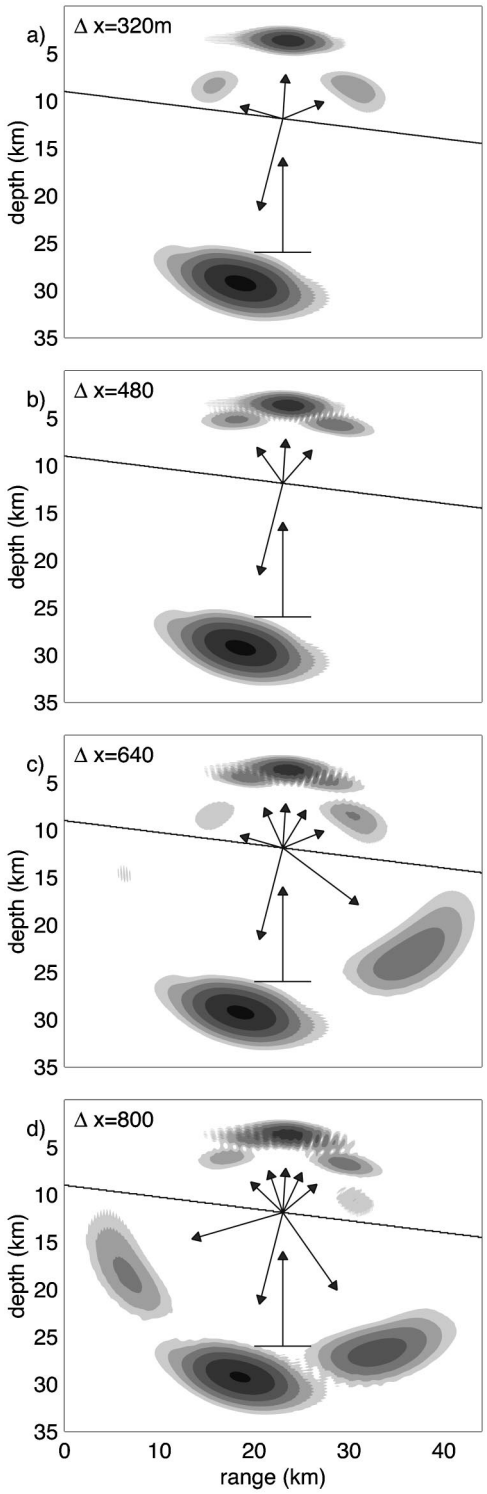

FIG. 9. Acoustic field solutions for stairstep spacings of (a) 320 m; (b) 480 m; (c) 640 m; and (d) 800 m. Arrows show the predicted propagation directions of both the specular and diffracted phases.

(Virieux, 1986), is applied to the test problem. A first-order absorbing boundary condition is used to terminate the sides and bottom of the grid to simulate an infinite half-space (e.g., Taflove and Hagness, 2000). As before, a grid spacing of 20 m in both the x and z directions is used. Again, a pressure source beam with a center frequency of 5 Hz is applied. However, because the source lies within the elastic medium, it is impossible to introduce an entirely compressional source beam. Instead, the differential pressure at the edges of the beam yields a small shear source component with a velocity equal to that of the compressional beam. The derived solutions are thus a superposition of the results for both a compressional source and a shear source.

For this problem, the maximum allowable spacing for avoiding physically unrealistic diffractions is identical to that of the acoustic problem above, i.e., 281 m. The elastic solution for a model with a stairstep spacing of 160 m is shown in Fig. 10, at 11.25 s. The pressure field, shown in Fig. 10(a), is nearly identical to the acoustic field solution shown in Fig. 8. The shear field solution, shown in Fig. 10(b), features two reflected waves. The faster one is an artifact arising from the fact that the source beam includes both shear and compressional components, which propagate at equal velocity. The incident shear component gives rise to the faster, specularly reflected shear phase. The slower reflected phase is associated with the partial reflection of the incident P wave into an S wave.

Figure 11 shows the pressure field solution and the shear stress field for a stairstep spacing of 320 m. The pressure field is nearly identical to the acoustic field solution of Fig. 9(a). However, as shown in Fig. 11(b), shear diffractions are excited in the lower medium by the incident P phase. The sidelobe to the right propagates at the angle predicted by Eq. (10) for an incident P wave and outgoing shear diffracted phase, at 5 Hz. Equation (12) predicted that the shear sidelobe to the left should only exist at frequencies greater than 5.3 Hz; thus, its presence is likely due to the finite source bandwidth.

IV. MODELING T-PHASE EXCITATION

The examples of the previous section illustrate not only the limits that must be placed on the stairstep spacing in order to obtain a physically realistic solution but also, incidentally, the effectiveness of scattering from an array of point sources in transforming an upgoing seismic phase into a nearly horizontally propagating acoustic phase in the ocean column. Therefore, in a modeling study designed to distinguish between the two competing hypotheses of T-phase excitation, i.e., downslope propagation vs seafloor scattering, it is vital to limit the stairstep size in order to avoid introducing acoustic scattering artifacts that result only from an overly coarse discretization of the seafloor, and not from actual roughness in the model.

In computing T-phases, one must consider the multiple interactions of the ocean acoustic phase with the seafloor, as well as the upgoing seismic phase. In downslope propagation at a slope with angle θ, it can be shown that the propagation angle steepens by 2θ with each bottom interaction. For a plane wave with incident angle i with respect to the stairstep boundary, the spacing required to maintain accuracy in the downward reflected acoustic waves within the ocean column is

$$\Delta x < \frac{\lambda_{oc}\cos(\theta)}{1-\sin(i)}, \tag{16}$$

where we have substituted λ_{oc} for λ_{seis} in Eq. (4)—because the geometry for propagation within the ocean is similar to

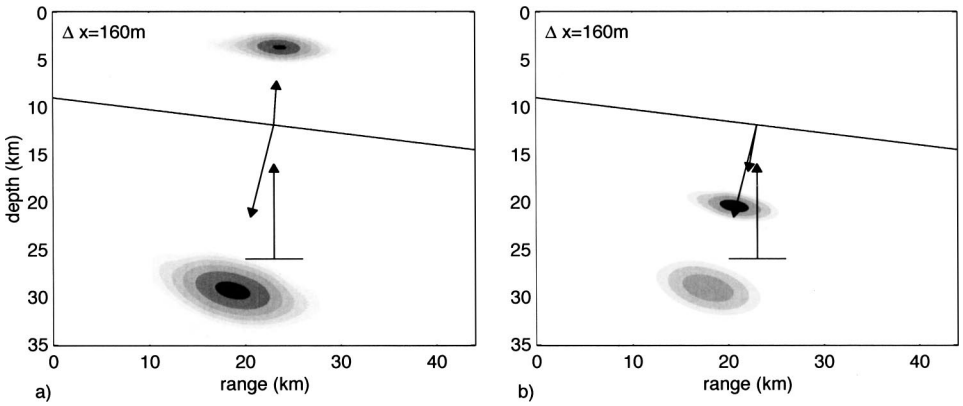

FIG. 10. Solution for a stairstep spacing of 160 m. The pressure field is shown in (a). The shear field, represented by the stress tensor component τ_{xz}, is shown in (b). The result corresponds to the result for a smooth sloping boundary. The faster shear component excited in the lower medium is a source artifact arising from the fact that the compressional source beam generates a small shear component with equal velocity.

the geometry in Fig. 2, with the ocean and seafloor reversed—and sin(i) for sin(θ)—because, as outlined in Sec. III, the sin(θ) term in the denominator of each discretization criterion in Sec. II is replaced by sin(i) for an arbitrary angle of incidence i. Thus, the criterion for simulating a smooth interface becomes less stringent with repeated seafloor reflections, that is, Δx increases as the propagation angle inclines to the horizontal.

In this section, T-phase excitation is computed for several versions of a 2D model with a simple triangular ridge, as shown in Fig. 12. In each one, the water velocity profile corresponds to the annual average sound-speed profile at (42N,130W), as derived from the Levitus database (Levitus and Boyer, 1994). The seafloor velocity profile consists of two layers representing the upper and middle oceanic crust, with velocities and thicknesses obtained from the CRUST2 model at 43N, 129W. (The CRUST2 model is available at http://mahi.ucsd.edu/Gabi/rem.html) The model features a ridge with sides sloping at angles of 6.8°, with a peak at 1.5-km depth, well below the sound-speed minimum at 575 m but above the reciprocal depth at 2.8 km. The source is a point source located at 7-km total depth, directly below the peak of the ridge. The source time function and spectrum are as shown in Fig. 6. Responses are synthesized for a vertical array of hydrophones at depths from 50 to 2950 m at a 50-m spacing, at a lateral distance of 100 km from the source, and also for a horizontal ''array'' at the depth of the sound-speed minimum, 600 m, at ranges from 20 to 110 km from the ridge peak, with a lateral spacing of 10 km.

T-phases are calculated for four variants of the model using the time-domain finite difference methods described in the previous section. The object is to determine the role that small-scale seafloor roughness plays in exciting T-phases, and also to examine the importance of treating the oceanic crust and sediments as elastic materials. The first variation is an acoustic model, that is, the shear velocities are identically zero, and the seafloor and sides of the ridge are modeled as flat surfaces. The stairstep spacing for the sides of the ridge ranges from 200 to 225 m, below the minimum spacing of 240 m needed to simulate a smooth, sloping interface, as derived by Eq. (7) for a source with a maximum frequency of 6 Hz. Note that seafloor roughness has not been entirely eliminated as the ridge peak serves as a large scale scatterer. For the second set of computations, the top of each layer is replaced by a rough surface, as indicated by the heavy lines shown in Fig. 12. The scale of the seafloor roughness is within the limits imposed for small-scale scattering, i.e., the amplitude of the scatterers is smaller than the source wavelength, and the gradient is much less than 1 (Ogilvy, 1987). For the third model, the seafloor is an elastic medium with velocities as given in Fig. 12, with smooth sides. For this model, the minimum stairstep spacing required to simulate smooth sides is 231 m, as given by Eq. (7) for an incident 6-Hz S wave with velocity 2.5 km/s. The final model is an elastic model with the top oceanic crustal boundaries replaced by a rough surface.

The models differ from realistic ocean models in several important respects. First, the real seafloor is generally characterized by roughness over a wide range of scale lengths (Herzfeld *et al.*, 1995). Here, the treatment of seafloor roughness is limited to small-scale scattering. In most regions where submarine earthquakes occur, the seafloor is rougher

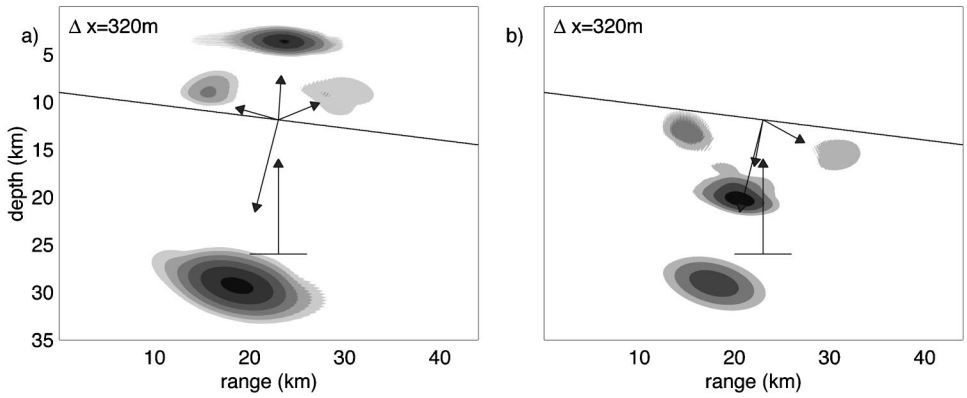

FIG. 11. Elastic field solutions. (a) pressure field for $\Delta x = 320$ m; (b) shear field for $\Delta x = 320$ m.

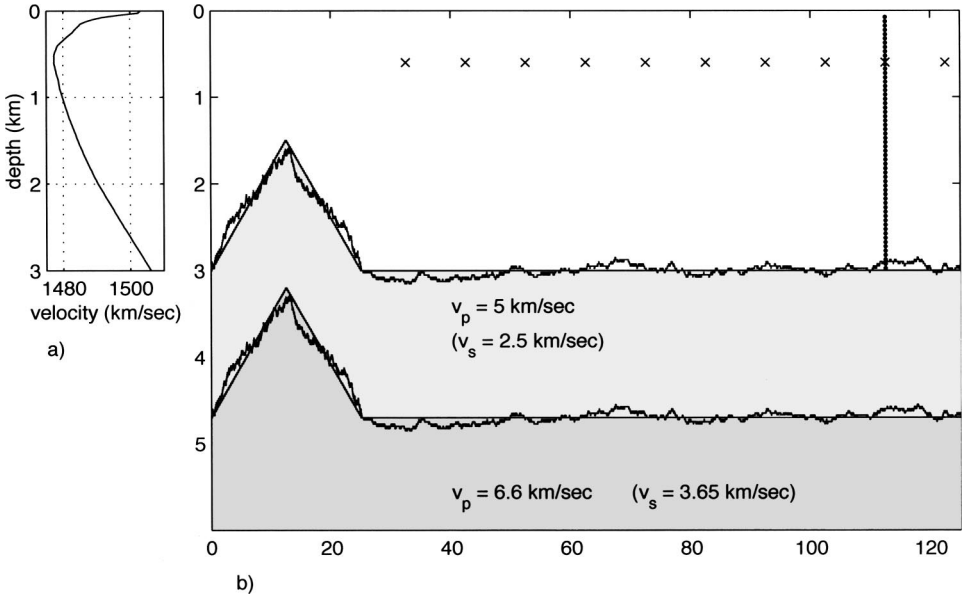

FIG. 12. Environmental model for numerical computation of T-phases. The model consists of 5000×360 elements, each 25 m on a side. Slopes are modeled using a stairstep approximation. A vertical hydrophone array consisting of 59 elements at depths ranging from 50 m to 1 km is located 100 km from the ridge. The locations of hydrophones at the sound-speed minimum are marked by x's. The ocean sound-speed profile is shown to the left. The seafloor velocities are typical for seafloor crust.

than the models. Second, low-velocity marine sediments are not included in any of the models, although they may play an important part in T-phase excitation and propagation (de Groot-Hedlin and Orcutt, 2001). Soft sediments are neglected here due to numerical constraints; the very fine discretization required to include a layer with very low shear velocities would make the problem too computationally intensive. Finally, attenuation within the seafloor is neglected in these models.

A. Acoustic solution

The critical angle for ocean/crust reflection is only 17.5° with respect to the normal to the seafloor boundary for the acoustic models. Given that the slope angle of the ridge is 6.8°, only one or two downslope reflections of the acoustic phase at the sloping seafloor are needed to trap the acoustic phase within the ocean layer. By contrast, an acoustic phase would have to propagate at an angle of 79° with respect to the vertical to be completely trapped within the sound channel for the given ocean velocity profile. That would require six downslope reflections at the sloping boundary. A phase propagating at the critical angle would be multiply reflected from both the sea surface and seafloor and have a horizontal velocity of 450 m/s. This would be the slowest velocity at which one could expect to see any arrivals. Oceanic phases with a greater number of reflections at the sloping ridge would yield a phase propagating at an angle inclined further to the horizontal, with earlier arrivals. More steeply propagating phases would have a slower phase velocity and would be eventually transmitted into the seafloor.

Figure 13 shows smoothed envelopes of the pressure responses for the acoustic model along the line of hydrophones at 600 m. Envelopes are plotted since phase information at this distance is inaccurate due to the numerical dispersion inherent in the FDTD method (Taflove and Hagness, 2000). The dash-dotted line corresponds to arrivals with a group velocity of 1.5 km/s, i.e., a T-phase. The dashed line corresponds to arrival times for a phase propagating at the critical angle to the interface. The large-amplitude arrivals for the model with smooth seafloor planes, shown in Fig. 13(a), propagate at about 1.1 km/s across the array. The lack of energy at T-phase velocities indicates that little energy is

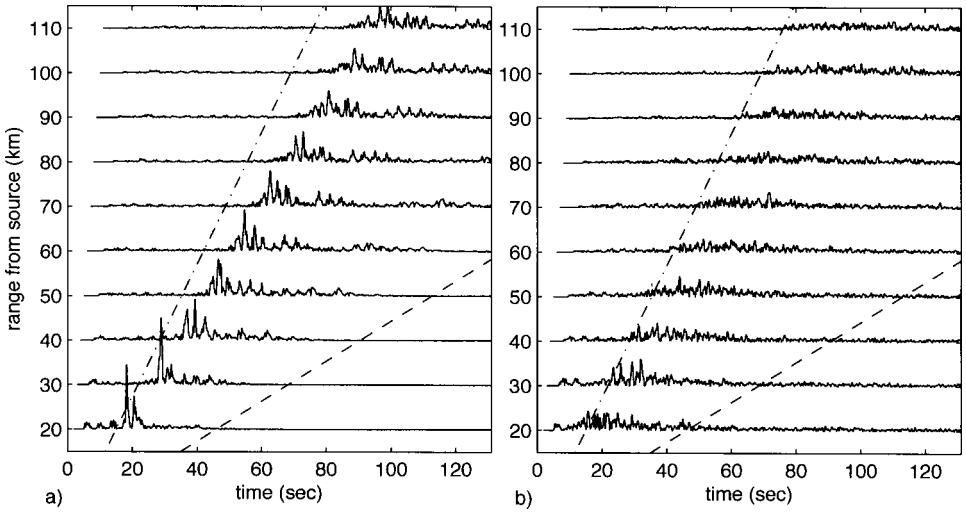

FIG. 13. Envelopes of the pressure responses at the horizontal hydrophone array for the acoustic seafloor models. The dotted line corresponds to the expected T-phase arrival; the dashed line corresponds to an arrival for an acoustic phase propagating at the critical angle to the seafloor. (a) Acoustic field solution for the smooth seafloor model. (b) Acoustic field solution for the rough seafloor. Amplitudes scales are uniform for (a) and (b).

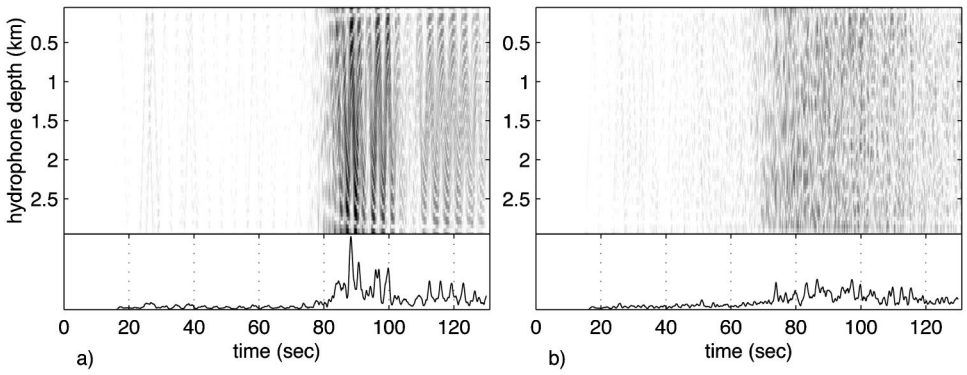

FIG. 14. Envelopes of the pressure response at the vertical hydrophone array for the acoustic seafloor models. Envelopes for the element at the sound-speed minimum, smoothed over 0.75 s, are shown below the array response for each example. (a) Acoustic field solution for smooth seafloor model. (b) Acoustic field solution for the rough seafloor.

scattered directly into the sound channel by the ridge peak. Corresponding results for the model with the rough seafloor, in Fig. 13(b), show that the earliest arriving ocean-borne acoustic phases propagate at the T-phase velocity. These would correspond to energy scattered directly into the sound channel nearest the ridge peak. The length of the wavetrain indicates that acoustic energy is scattered into the sound channel at several subsequent seafloor reflections. Although the maximum amplitude of the arrivals for the smooth seafloor model are 2–3 times greater than for the rough model, they decrease more rapidly with increasing range from the ridge.

Figure 14 shows pressure envelopes for the vertical hydrophone array at a range of 100 km from the ridge peak for each of the acoustic models, along with the smoothed envelope for the element at 600 m, near the sound-speed minimum. The results for the smooth seafloor model (left) clearly indicate that the arrivals are reflections between the ocean surface and seafloor, whereas distinct reflections are not observed in the corresponding acoustic phases for the rough seafloor model (right). Pressure amplitudes are significant below the reciprocal depths for both models.

B. Elastic solutions

The critical angle for ocean/crust reflection increases when shear velocities are introduced. For the model of Fig. 12, it is 36.9°; thus, at least three downslope reflections are required to trap acoustic energy within the ocean. Since there is bottom loss at each downslope reflection before the critical angle is reached, the amplitude of the trapped acoustic phase is expected to be lower than for the corresponding acoustic model. Acoustic phases propagating at the critical angle would have a horizontal velocity of 1.125 km/s.

The pressure responses along the horizontal hydrophone array are shown in Fig. 15 for the model with the elastic seafloor. The dashed line corresponds to arrivals with the horizontal velocity of a phase propagating at the critical angle for shear waves. The later arrivals for the smooth seafloor, shown in Fig. 15(a), propagate more steeply than the critical angle and so should eventually be transmitted into the seafloor at greater ranges. As expected, the amplitude of the trapped acoustic phase is much smaller than for the corresponding model with the fluid seafloor—note that the initial *P* waves can be seen at this scale. Overall, the waveforms are shorter in duration but more complex than for the corresponding acoustic models.

Envelopes of the pressure responses at the vertical hydrophone array are shown in Fig. 16. Again, distinct reflections are observed in the results for the smooth seafloor but not for the rough seafloor. A faint reflection at about 60 s for the smooth seafloor model corresponds to an arrival that is trapped between the ocean surface and lower crust layer. The peak amplitudes for the rough model arrive nearly 20 s before those of the corresponding smooth seafloor model, indicating that the trapped acoustic phases propagate more horizontally for the rough seafloor model. Again, this implies

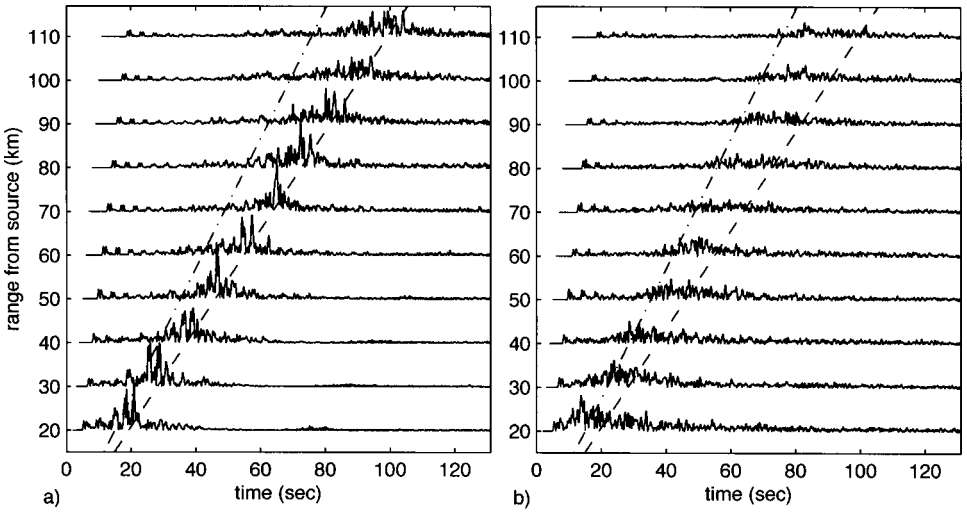

FIG. 15. Similar to Fig. 13, but for the elastic seafloor models. Amplitude scales are uniform for (a) and (b).

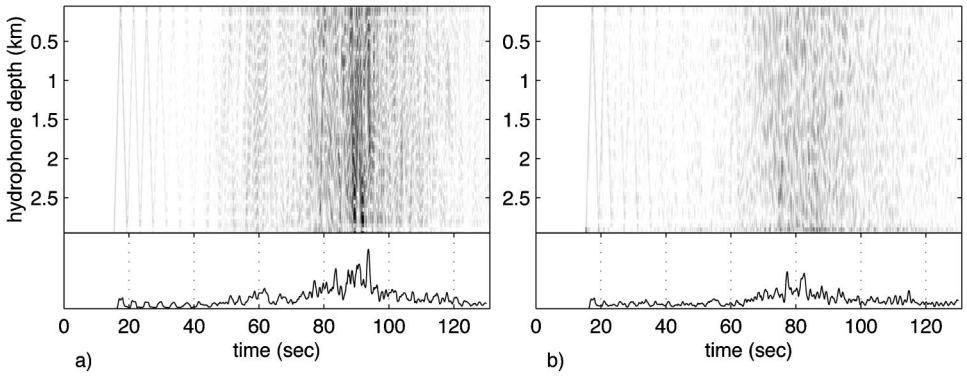

FIG. 16. Similar to Fig. 14, but for the elastic seafloor models.

that small-scale roughness at the seafloor is an effective mechanism for converting vertically propagating seismic energy into a nearly horizontally propagating T-phase.

V. DISCUSSION

The discretization criteria developed in Sec. II indicate that the stairstep spacing required to simulate a smooth slope decreases with increasing slope angle. However, numerical computation of T-phases generated at low slope angles may be equally problematic since, for any numerical method in which sloping boundaries are represented by stairsteps, the distance between steps increases with decreasing slope angle. Given that downward propagation at a shallow slope is relatively inefficient at converting a vertically propagating acoustic phase to a nearly horizontally propagating phase (since bottom loss is high at near-vertical incidence), the energy contributed by sidelobe diffractions may actually dominate the computed acoustic arrivals at large distances.

Reliable synthesis of T-phases requires accuracy over a wide range of directions, from upgoing seismic phases to horizontally propagating ocean acoustic phases. This is in contrast to the case for a source within the ocean column, where one may usually neglect vertical propagation for long-range propagation problems. Thus, a more efficient and accurate method of computing T-phases would be to employ a two-stage process. In the vicinity of the source region, a computational method that is accurate over all propagation directions would be applied, using small step sizes. As the ocean acoustic phase inclines to the horizontal at greater ranges from the source, a more efficient computational method that is accurate at larger step sizes could be used.

VI. CONCLUSIONS

Discretization levels necessary to simulate a smooth interface using a stairstep boundary were derived using a model of an incident plane wave on a sloping boundary with point scatterers arrayed along its length. The stairstep spacings needed to accurately compute both forward (downslope) and backward (upslope) sidelobe reflections and transmissions for both fluid–fluid and solid–fluid boundaries were found to be proportional to the smallest wavelength in the model. The results also indicate that the criterion for eliminating either forward-reflected or backward-transmitted sidelobes is the most stringent.

A modeling study was conducted to distinguish between the two competing hypotheses of T-phase excitation—downslope propagation and seafloor scattering—and to determine the importance of modeling the seafloor as an elastic medium. The models were discretized in accordance with the stairstep spacings derived earlier to ensure that any scattered energy in the acoustic field solutions resulted from real model roughness and was not a numerical modeling artifact. The results indicate that the acoustic phases trapped in the ocean column for the smooth models had higher amplitudes but lower velocities than for the corresponding rough models for ranges up to 110 km from the epicentral location. Given that the velocity of the trapped acoustic phase for the rough model is closer to that of observed T-phases (Tolstoy and Ewing, 1950) and that the roughness of the seafloor in the vicinity of most submarine earthquakes is actually greater than that of the rough models in this study (so that scattering would be even stronger), I conclude that scattering is the dominant mechanism for T-phase excitation, even in regions of high impedance contrast. If downslope propagation was the dominant mechanism, one would expect to observe much slower T-phase velocities. A much steeper feature would be required to generate downslope-generated acoustic phases with greater horizontal velocities. However, most observed T-phases are generated at bathymetric features no steeper than the ridge modeled here. The computed amplitudes for the smooth models may be unrealistically large because seafloor attenuation was neglected in each model.

The relatively long wavetrains of the trapped acoustic phases for both the rough acoustic and elastic models suggests that energy is scattered into the sound channel both as it transits the ocean/crust boundary, and at several subsequent seafloor reflections. This is in contrast to the model of T-phase excitation proposed by de Groot-Hedlin and Orcutt (2001), in which only primary scattering was considered and energy contributions by the ensuing seafloor reflections were neglected. That model proved adequate in regions with thick layers of gently sloping marine sediments. For a model with low-velocity marine sediments, much of the energy would be transmitted into the seafloor at each bottom reflection, so there would be little energy remaining to be scattered into the sound channel after the first reflection. This implies that T-phases should be longer for models with high impedance contrasts. This hypothesis is supported by the models considered in this paper; the effective impedance contrast between the ocean column and seafloor is greater for the model with

the acoustic seafloor than with the elastic seafloor (Brekhovskikh and Lysanov, 1991), and the computed wavetrains have greater durations for the acoustic than for the elastic seafloor model.

ACKNOWLEDGMENTS

I am grateful to Emile Okal, and two anonymous reviewers for their useful comments and recommendations. This work was funded by NOPP Grant N00014-01-1-1076.

Aki, K., and Richards, P. G. (**1980**). *Quantitative Seismology: Theory and Methods* (Freeman, San Francisco).

Berenger, J.-P. (**1994**). ''A perfectly matched layer for the absorption of electromagnetics waves,'' J. Comput. Phys. **114**, 185–200.

Brekhovskikh, L. M., and Lysanov, Y. P. (**1991**). *Fundamentals of Ocean Acoustics* (Springer, Berlin).

de Groot-Hedlin, C. D., and Orcutt, J. A. (**1999**). ''Synthesis of earthquake-generated T-waves,'' Geophys. Res. Lett. **26**, 1227–1230.

de Groot-Hedlin, C. D., and Orcutt, J. A. (**2001**). ''Excitation of T-phases by seafloor scattering,'' J. Acoust. Soc. Am. **109**, 1944–1954.

Halliday, D., and Resnick, R. (**1974**). *Fundamentals of Physics* (Wiley, Toronto).

Hamilton, E. L. (**1979**). ''V_p/V_s and Poisson's ratios in marine sediments and rocks,'' J. Acoust. Soc. Am. **66**, 1093–1101.

Herzfeld, U. C., Kim, I. I., and Orcutt, J. A. (**1995**). ''Is the ocean floor a fractal?,'' Math. Geol. **27**, 421–462.

Jensen, F. B. (**1998**). ''On the use of stair steps to approximate bathymetry changes in ocean acoustic models,'' J. Acoust. Soc. Am. **104**, 1310–1315.

Levitus, and Boyer (**1994**). *World Ocean Atlas 1994* (NOAA Atlas NESDIS 4, Washington D.C.).

Ogilvy, J. A. (**1987**). ''Wave scattering from rough surfaces,'' Rep. Prog. Phys. **50**, 1553–1608.

Park, M., Odom, R. I., and Soukup, D. J. (**2001**). ''Modal scattering: A key to understanding oceanic T-waves,'' Geophys. Res. Lett. **28**, 3401–3404.

Stephen, R. A. (**2000**). ''Optimum and standard beam widths for numerical modeling of interface scattering problems,'' J. Acoust. Soc. Am. **107**, 1095–1102.

Taflove, A., and Hagness, S. C. (**2000**). *Computational Electrodynamics: The Finite Difference Time-Domain Method* (Artech House, Boston).

Talandier, J., and Okal, E. A. (**1998**). ''On the mechanism of conversion of seismic waves to and from T waves in the vicinity of Island Shores,'' Bull. Seismol. Soc. Am. **88**, 621–632.

Tolstoy, I., and Ewing, M. W. (**1950**). ''The T phase of shallow focus earthquakes,'' Bull. Seismol. Soc. Am. **40**, 25–51.

Virieux, J. (**1986**). ''P-SV wave propagation in heterogeneous media; Velocity-stress finite-difference method,'' Geophysics **51**, 889–901.

Acoustic diagnosis for porous medium with circular cylindrical pores

Heui-Seol Roh and Suk Wang Yoon[a)]
Acoustics Research Laboratory and BK21 Physics Research Division, Department of Physics, SungKyunKwan University, Suwon 440-746, Republic of Korea

(Received 22 May 2002; accepted for publication 1 December 2003)

Acoustic transmission coefficient and phase velocity of a Lucite slab with circular cylindrical pores with a nonrigid pore frame were experimentally and theoretically investigated. For theoretical investigation a new phenomenological model, the modified Biot-Attenborough (MBA) model, was proposed. The MBA model takes into account both the first kind and the second kind of waves introduced by Biot. It also separately considers viscous and thermal effects with three new phenomenological parameters: boundary, phase velocity, and impedance parameters. The theoretical estimation with three phenomenological parameters shows reasonably good agreement with the experimental data. The physical characteristics of porous medium such as porosity and pore size can be inversely analyzed in terms of the acoustic data such as the transmission coefficient and phase velocity as the functions of porosity and frequency. This makes acoustic diagnosis possible for noninvasively investigating physical characteristics of porous media such as bones and ocean sediments. © *2004 Acoustical Society of America.* [DOI: 10.1121/1.1645247]

PACS numbers: 43.35.Bf [RAR] Pages: 1114–1124

I. INTRODUCTION

Applications of sound to medical diagnosis have recently attracted more attention.[1–3] Comparison between the acoustic method and other methods like X ray, magnetic resonance imager (MRI), and positron emission tomography (PET) shows the strength of acoustic diagnosis. The acoustic method offers a low-cost, noninvasive, nonionizing, portable alternative to the other methods for the assessment of bone characteristics. Although bone sonometry has been established as a useful modality for the prediction of osteoporotic fracture risk, the physical mechanisms underlying the interaction between sound and bone are not yet completely understood. Sound propagation models in porous media such as Biot theory[4] and Attenborough's approach[5] are only applicable to some limited cases. Although the Biot theory is a relatively comprehensive approach with the viscous effect consideration for elastic material, it does not consider the thermal effect. The thermal effect is indispensable in investigating sound propagation in porous media, as Biot's later paper described.[6] Furthermore, the Biot theory needs many uncertain input parameters and does not provide analytic solutions. Separate treatment of viscous effect and thermal effect was introduced in porous media by Attenborough,[5] but the pore frame was considered as rigid material. The first kind of wave in the Biot theory is not included in Attenborough's approach.

Physical characteristics of a porous medium can be inversely analyzed from its acoustic properties. Acoustic wave propagation in porous medium like human bone may be modeled by that in solid material containing circular capillary pores with fluid, since human bone is regarded as a locally reacting medium. Acoustic wave propagation in porous media for more complex situations, including such a nonrigid pore frame, has been a valuable topic.[7,8] In this study, the Lucite slab with circular cylindrical tube-shaped pore is selected as a preliminary test sample instead of the real bone specimen because of easy manipulation and nonrigid pore frame. Attenborough's approach to the porous material[5] is adopted and then modified for the Lucite slab with nonrigid pore frame and cylindrical pores, where the first kind (fast) of wave and the second kind (slow) of wave identified by Biot[4] exist. This will be called the modified Biot-Attenborough (MBA) model hereafter. Phase velocity and transmission coefficient of the porous Lucite slab were experimentally measured in water, and compared with the theoretical estimation by the MBA model.

II. MODIFIED BIOT-ATTENBOROUGH MODEL FOR POROUS MEDIUM

Attenborough's separate treatment of viscous effect and thermal effect to the porous material[5] is modified for the Lucite slab with nonrigid pore frame and cylindrical pores. The reason for modifying Attenborough's approach rather than Biot theory is that the modification in the separate treatment of viscous effect and thermal effect is more straightforward. This further suggests that the modified treatment is a phenomenologically mixed approach based on the strengths of Attenborough's approach and the Biot theory. In the MBA model, the fast wave is taken into account in addition to the slow wave in a solid and fluid mixed medium.

The separate treatment of viscous effect and thermal effect is justified, at least in the limiting cases of low and high frequencies.[5,9,10] It assumes that the pore frame is rigid except for the pore fluid of porous material. However, a material such as Lucite used in this experiment is not rigid. It is required to modify the Attenborough's approach by substituting the rigid material frame for the nonrigid one. In the MBA

[a)]Electronic mail: swyoon@skku.ac.kr

 0001-4966/2004/115(3)/1114/11/$20.00

model, modification from rigid frame to nonrigid frame with bulk cylindrical pores is suggested phenomenologically; three phenomenological parameters s_1, s_2, and s_3 are introduced. The elastic properties of pore frame should be more rigorously taken into account, but they are not considered here to avoid complication in this paper.

A. Propagation in a single cylindrical pore

Wave propagation in a single cylindrical pore is restricted to one-dimensional description for simplicity, and the propagation direction is normal to the surface of porous medium. Since the boundary condition at nonrigid frame should be different from that at rigid frame, the MBA model is focused on the boundary condition at nonrigid frame.

The continuity equation is given by

$$-\rho_0 \frac{\partial \langle v \rangle}{\partial x} = \frac{\partial \rho}{\partial t}, \tag{1}$$

where ρ_0 is the equilibrium fluid density and $\langle v \rangle$ is the average particle velocity over the pore cross section.

The equation of motion is in terms of the complex density $\rho_c(\omega)$, given by

$$\frac{\partial p}{\partial x} = \rho_c(\omega) \frac{\partial \langle v \rangle}{\partial t}, \tag{2}$$

where p is the acoustic pressure. The complex density may be written by

$$\rho_c(\omega) = \rho_0 [1 - 2(\lambda \sqrt{i})^{-1} T(\lambda \sqrt{i})]^{-1}, \tag{3}$$

where

$$T(\lambda \sqrt{i}) = J_1(\lambda \sqrt{i}) / J_0(\lambda \sqrt{i}), \tag{4}$$

with J_0 and J_1 the zeroth- and first-order cylindrical Bessel functions, respectively. A dimensionless parameter λ, which is related to the size of the viscous boundary layer at the pore wall, is introduced by

$$\lambda = a s_1 (\omega / \nu)^{1/2}, \tag{5}$$

where a is the pore radius and ν is the kinematic viscosity of fluid.

The boundary parameter s_1 in (5) is introduced to represent the rigidity of pore frame, which is roughly estimated by the density ratio of rigid frame material to nonrigid frame material: $s_1 \to 1$ for very rigid frame material and $s_1 > 1$ for general nonrigid frame material. In this approach, s_1 is fixed by looking at the experimental data for the phase velocity and transmission coefficient as a function of frequency. The effective radius of a pore r_{eff} is given as $a s_1$. This scheme may be justified since the relative particle velocity at the boundary $r = a$ becomes zero for rigid wall but nonzero at the boundary $r = a$ for nonrigid wall. It suggests that the relative particle velocity for nonrigid frame material becomes zero at the effective radius $r_{\text{eff}} = a s_1$.

It is assumed that the fluid is a nonviscous conducting fluid, the heat flow within a circular capillary pore is only transported in transverse directions, and acoustic pressure is uniform over the pore cross section. The thermal equation produces the complex compressibility of fluid $C_c(\omega)$

$$C_c(\omega) = \frac{1}{\rho_0} \frac{d\rho}{dp} = (\gamma p_0)^{-1} [1 + 2(\gamma - 1) \times (N_{\text{Pr}}^{1/2} \lambda \sqrt{i})^{-1} T(N_{\text{Pr}}^{1/2} \lambda \sqrt{i})], \tag{6}$$

where N_{Pr} is the Prandtl number.

B. Phenomenological extension to bulk cylindrical pores for nonrigid medium

The modification considered from the propagation of single pore is extended to bulk cylindrical pores for nonrigid medium. When all the pores are identical, the average particle velocity $\langle v \rangle$ of a single pore is related to the average velocity u over the unit cross section of the porous medium

$$\langle v \rangle \simeq q \left[\frac{C_c(w) z_b \omega}{k_b} \right] u, \tag{7}$$

where q is the tortuosity of the pore, z_b is the characteristic impedance of the bulk medium, and k_b is the propagation constant of the bulk medium. Note that $\langle v \rangle = qu/\Omega$ for the case of rigid medium. The effective density for the bulk medium ρ_b is phenomenologically proposed by

$$\rho_b(\omega) = \frac{z_b k_b}{\omega q}. \tag{8}$$

In this case, the equation of continuity becomes

$$-q \left[\frac{C_c(w) z_b \omega}{k_b} \right] \frac{\partial u}{\partial x} = \frac{1}{\rho_0} \frac{d\rho}{dp} \frac{\partial p}{\partial t}. \tag{9}$$

The equation of motion leads to

$$-\frac{\partial p}{\partial x} = \rho_b(\omega) \frac{\partial u}{\partial t}. \tag{10}$$

From Eqs. (9) and (10), the wave equation becomes

$$\frac{\partial^2 p}{\partial x^2} = \frac{1}{c_b^2} \frac{\partial^2 p}{\partial t^2}, \tag{11}$$

where $c_b = \omega / k_b$.

The complex propagation constant k_b in the case of nonrigid pore frame is parametrized from the wave equation (11) with help from (3), (6), and (8)

$$k_b^2 = q^2 [k_m^2 k_c^2 / ((1 - \Omega)^{s_2} k_c^2 + \Omega^{s_2} k_m^2)], \tag{12}$$

where Ω is the porosity and

$$k_c^2 = \omega^2 C_c(\omega) \rho_c(\omega). \tag{13}$$

The form of the propagation constant (12) is based on a specific parametrization of the phase velocity, since $\text{Re}[k_b] = \omega / c_b$

$$c_b^2 = [(1 - \Omega)^{s_2} c_m^2 + \Omega^{s_2} c_c^2] / q^2, \tag{14}$$

where c_m is the longitudinal sound velocity for pure frame material and c_c is the sound velocity for pore fluid. In fact, the fast and slow waves generally propagate in the mixed state of solid and fluid,[4,11] but the sound velocity is estimated by only the dominant wave contribution. This can be justified since the fast and slow waves normally appear mixed without distinct separation in time. Nevertheless, different param-

etrizations for the mixed, fast, and slow waves may be used in the case of well-separated waves, respectively.

The measurement data for the phase velocity of porous medium determine the phase velocity parameter s_2 in (14). It is fixed by looking at the sound velocity profile as a function of porosity. s_2 is less than 1 for the convex profile, is larger than 1 for the concave profile, and is equal to 1 for the linear profile of the phase velocity as the function of porosity. This specific parametrization is set so that the phase velocity at porosity zero asymptotically becomes the pore frame velocity, and the phase velocity at porosity 1 becomes the pore fluid velocity.

The characteristic impedance of the medium is given by

$$z_b = R + iX = q^2 \omega \rho_b(\omega)/k_b . \tag{15}$$

The effective impedance of bulk porous medium is parametrized by

$$z_b = q^2[-s_3\Omega^2 + (\rho_c c_c - \rho_m c_m + s_3)\Omega + \rho_m c_m], \tag{16}$$

where ρ_m and c_m are the pure matter density and sound velocity of pore frame, respectively, and ρ_c and c_c are the pure fluid density and sound velocity of pore fluid, respectively. The effective impedance asymptotically becomes the impedance of frame material at the porosity 0 and the impedance of pore at the porosity 1. It effectively represents increasing impedance in pore frame in the low-porosity region; the specimen becomes more rigid as the porosity increases in the low-porosity region, where the fast wave is dominant. It also represents decreasing impedance due to pores of porous medium in the high-porosity region, where the slow wave is dominant. The impedance parametrization for the mixed wave is likewise used, but different parametrizations for the mixed, fast, and slow waves may be used in the case of well-separated waves.

The impedance parameter s_3 synthetically depends on acoustic characteristics of porous medium: the rigidity, porosity, pore size, frequency, etc. The impedance parameter s_3 is small for large pore size and large for small pore size. It is also small for high frequency and large for low frequency. Phenomenologically, the parameter s_3 can be determined by fitting the theoretical calculation to the measurement data for the transmission coefficient or reflection coefficient.

The effective density for the bulk medium ρ_b in (8) is thus obtained from Eqs. (12) and (16)

$$\rho_b(\omega) = [(-s_3\Omega^2 + (\rho_c c_c - \rho_m c_m + s_3)\Omega + \rho_m c_m)] \times [k_m^2 k_c^2/((1-\Omega)^{s_2} k_c^2 + \Omega^{s_2} k_m^2)]^{1/2} q/\omega. \tag{17}$$

The parameters s_2 and s_3 represent slopes for the phase velocity and impedance of porous medium as a function of the porosity, respectively. Note that the effective density is much different from the physical density, $\rho_p = (1-\Omega)\rho_m + \Omega\rho_0$, which is determined by the simple mixing of pore frame density and fluid density.

C. Transmission and reflection coefficients

The previous result can be applied to the case in which a plane acoustic wave encounters porous medium delimited by a plane normal to the incident wave. In the one-dimensional case, a pore medium is occupied by the region $0 \leqslant x \leqslant d$. In the region $x < 0$, there exists an incident wave of amplitude A_1 and a reflected wave of amplitude B_1

$$p_1 = A_1 \exp i(\omega t - k_1 x) + B_1 \exp i(\omega t + k_1 x). \tag{18}$$

In the region $x > d$, there exists a transmitted wave of amplitude A_3

$$p_3 = A_3' \exp i(\omega t - k_3 x) = A_3 \exp i(\omega t - k_3(x-d)), \tag{19}$$

where $x = d$ is taken as the origin for the transmitted wave in this region $x > d$. In the pore medium, $0 \leqslant x \leqslant d$, there exist a left-moving wave of amplitude A_b and a right-moving wave of amplitude B_b

$$p_b = A_b \exp(i\omega t - ik_b x) + B_b \exp(i\omega t + ik_b x). \tag{20}$$

The continuity conditions of pressure and particle velocity at the boundary $x = 0$ give

$$\begin{aligned} &A_1 + B_1 = A_b + B_b , \\ &(A_1 - B_1)/\rho_1 c_1 = (A_b - B_b)/\rho_b c_b , \end{aligned} \tag{21}$$

and the same boundary conditions at $x = d$ lead to

$$A_b \exp(-ik_b d) + B_b \exp(ik_b d) = A_3 , \tag{22}$$

$$(A_b \exp(-ik_b d) - B_b \exp(ik_b d))/\rho_b c_b = A_3/\rho_3 c_3 . \tag{23}$$

From the boundary conditions, the transmission coefficient T and reflection coefficient R are

$$T = A_3/A_1 = \frac{2}{(1+z_1/z_3)\cos(k_b d) + i(z_b/z_3 + z_1/z_b)\sin(k_b d)}, \tag{24}$$

$$R = B_1/A_1 = \frac{(1-z_1/z_3)\cos(k_b d) + i(z_b/z_3 - z_1/z_b)\sin(k_b d)}{(1+z_1/z_3)\cos(k_b d) + i(z_b/z_3 + z_1/z_b)\sin(k_b d)}, \tag{25}$$

with the characteristic impedances $z_1 = \rho_1 c_1$, $z_b = \rho_b c_b$, and $z_3 = \rho_3 c_3$. The effective density ρ_b and effective propagation constant k_b for porous nonrigid medium are given by Eqs. (8) and (12).

III. THEORETICAL AND EXPERIMENTAL COMPARISON OF PHASE VELOCITY AND TRANSMISSION COEFFICIENT

Phase velocity and transmission coefficient of the porous Lucite slab were experimentally measured in water.[12] And, they are compared with the theoretical estimation by the MBA model. The first and second waves were observed in the experimental measurement of the Lucite slab with circular cylindrical pores. Their acoustic characteristics are analyzed as the functions of porosity and frequency. The reason for choosing the phase velocity and transmission coefficient in this measurement is that they are much easier to measure practically than the other experimental characteristics such as attenuation constant, reflection coefficient, and scattering cross section.[2] Comparison between the experimental and

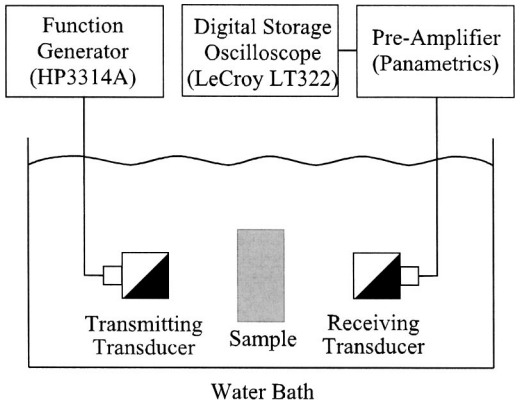

FIG. 1. Block diagram of experimental apparatus for acoustic measurements of the Lucite slab in water bath.

theoretical data suggests usefulness of the MBA model in diagnosing the characteristics of human bones or ocean sediments.

The experiment was performed in water, since the pore of real bone is mostly filled with water-like fluid. Figure 1 shows the block diagram of transmission coefficient and phase velocity measurements. The distance between the transmitter and the receiver was 135 mm. The characteristics of Lucite samples are given in Table I. The pore direction is normal to the Lucite slab surface (tortuosity $q=1$) and the Lucite slab has the size $100\times100\times4.8$ mm as shown in Fig. 2. There were two types of pores of radius 1 mm and 2 mm, and six types of porosity 0, 0.056, 0.099, 0.155, 0.223, 0.304 were used. The transmission coefficient and phase velocity of the Lucite slab were measured by the pulse technique with one-half wavelength in the frequencies 2.0, 2.3, 2.6, 2.9, and 3.2 MHz.

The experimental data for the transmission coefficient and phase velocity represent average values of those measured five times. Their standard deviations are within 3 percent.

The transmission coefficient and phase velocity for the Lucite slab with water-filled cylindrical pores were theoretically estimated with the MBA model. Since the dimensionless parameter λ in Eq. (5) is the order of 10^3, the theoretical estimations lie in the high-frequency limit, which is suitable to apply the MBA model. The input data for theoretical calculation are given in Table II. The ratio of specific heat for theoretical calculation, 1.004, was used for water. The other required input data for the MBA model are the three parameters, boundary, phase velocity, and impedance parameters, introduced in this paper. The tortuosity factor, porosity, frequency, pore size, and slab thickness are the measurable input data described above.

TABLE I. Characteristics of test specimen materials.

Material	Porosity	Pore radius (mm)	Pore fluid
Lucite 1	0.0	1 or 2	Water
Lucite 2	0.056	1 or 2	Water
Lucite 3	0.099	1 or 2	Water
Lucite 4	0.155	1 or 2	Water
Lucite 5	0.223	1 or 2	Water
Lucite 6	0.304	1 or 2	Water

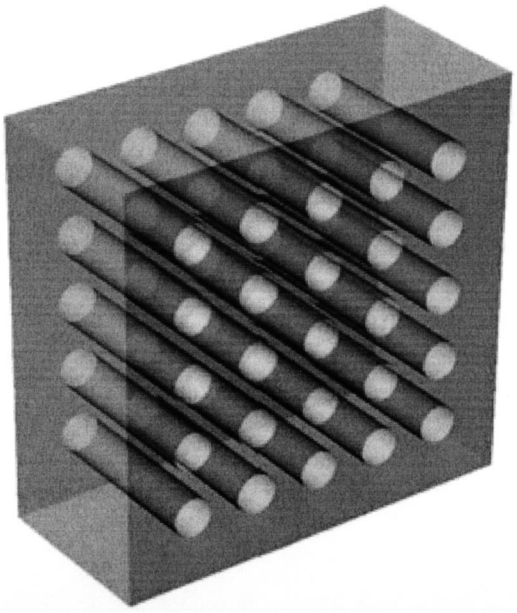

FIG. 2. Lucite slab with water-filled cylindrical pores. The Lucite slab specimen has the size $100\times100\times4.8$ mm.

A. Fast and slow waves

Figure 3 is the 3.2-MHz transmitted signal through pure water. Figure 4 shows the transmitted signals through the Lucite slab with water-filled cylindrical pores of the 1-mm radius and 2-mm radius as a function of time, respectively. The first part of a received signal mainly corresponds to the signal through the frame of Lucite, and the second part corresponds to the signal through circular cylindrical pores, even though they do not independently propagate. Two signals are overlapped if the travel time difference is not large compared with the pulse length in time. Two signals are separated due to the difference of travel time in Lucite and water. They can be recognized by the fast wave, which corresponds to the first kind of wave in the solid and fluid in phase, and the slow wave, which corresponds to the second kind of wave in the motion out of phase.[4,11] Particularly, the fast wave is dominant in the low-porosity region, while the slow wave is dominant in the high-porosity region.

B. Phase velocity

The time difference of transmitted signals between through Lucite slab and through pure water is used to calculate the experimental signal velocity of the Lucite slab. The

TABLE II. Input data for theoretical calculation.

Material	Lucite	Water
Density (kg/m^3)	1200	998
Sound velocity (m/s)	2700	1481
Kinematic viscosity (m^2/s)		10^{-6}
Impedance ($Pa\cdot s/m$)	3.24×10^6	1.48×10^6
Attenuation coefficient	$0.016\times f^{0.5}$	

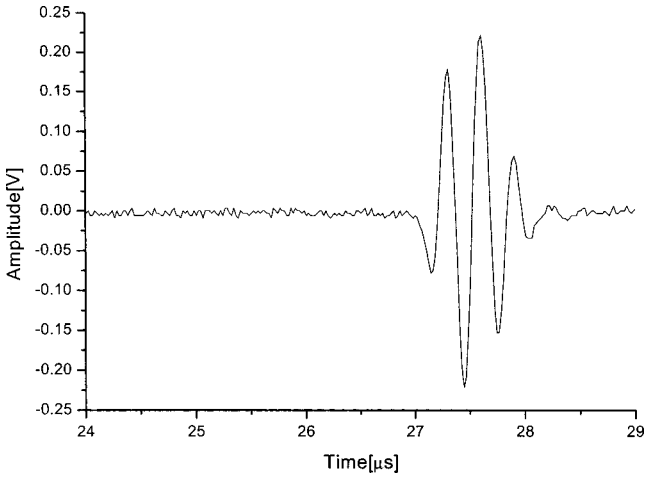

FIG. 3. Transmitted signal of the center frequency 3.2 MHz as a function of time through water.

signal velocity can be estimated from $C=C_w/(1-C_w\delta t/d)$, where d is the thickness of the Lucite slab, C_w is the sound speed in water, and δt is the difference in arrival times. The highest peaks are used to compare the time difference. Strictly speaking, the measured velocity is the signal velocity. However, it is almost the same with the phase velocity, which can be estimated by $C=C_w/(1-C_w\delta\phi/\omega d)$

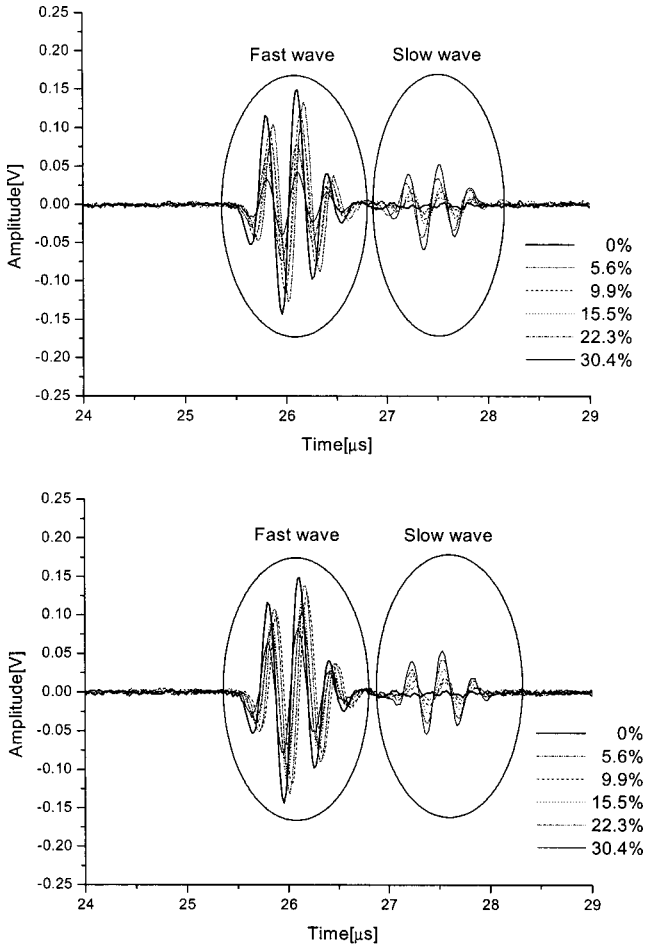

FIG. 4. A 3.2-MHz transmitted signal as a function of time through Lucite with water-filled pores of the radius 1 mm (upper) and 2 mm (lower). The fast and slow waves propagate through the porous Lucite.

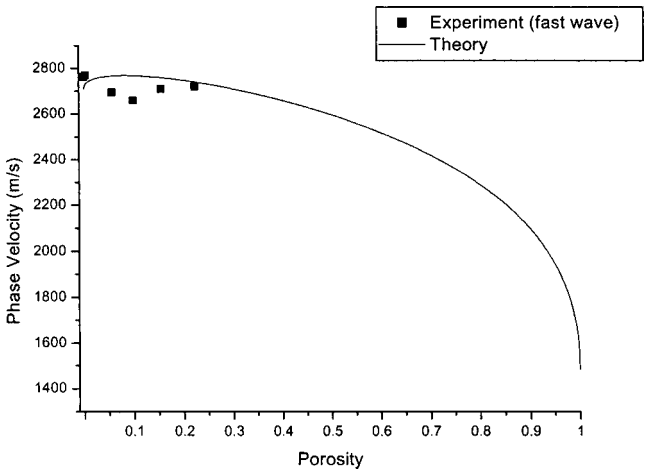

FIG. 5. Theoretical and experimental phase velocities as a function of porosity at the frequency 2 MHz for the water-filled Lucite slab with the pore radius 2 mm. The phase velocity parameter $s_2=0.5$ was used in the theoretical estimation of the phase velocity for the mixed wave of the fast and slow waves. The experimental data are phase velocities for the fast waves in the low-porosity region.

with the phase difference $\delta\phi$ and the angular frequency ω, since the signal used in experiment has a single frequency component. In this context, the measured velocity is referred to the phase velocity in the following. Experimental phase velocities are obtained separately for the fast wave and slow wave, while the theoretical ones are obtained only for the dominant wave.

In Fig. 5, comparison between theoretical and experimental phase velocities for the fast wave is shown as a function of porosity at the frequency 2 MHz for the water-filled Lucite slab with the pore radius 2 mm. The theoretical calculation uses the phase velocity parameter $s_2=0.5$. This figure represents the theoretical data for the mixed wave of the fast and slow waves.

The boundary parameter $s_1\sim1.5$ can be chosen by looking at the comparison data between the theoretical and experimental phase velocities. The estimation of the value $s_1\sim1.5$ in this way is relatively simple since the theoretical phase velocity is calculated with a fixed phase velocity parameter s_2 regardless of the impedance parameter s_3.

Experimental and theoretical phase velocities of Lucite slabs with pore radius 1 mm and 2 mm are given as a function of porosity in Figs. 6 and 7, respectively. The transmitted temporal signal through the Lucite slab with pores is used to calculate the experimental phase velocities. The experimental phase velocities of the fast and slow waves are almost constant as a function of porosity in the experimental, low-porosity region, respectively, even though it is expected that the phase velocity of the fast wave decreases as the porosity increases in the high-porosity region. The theoretical fitting results of the phase velocity for the parameters $s_2\simeq0.55$ and $s_2\simeq0.5$ in Eq. (14) show reasonable agreement with the experimental results as shown in Figs. 6 and 7. The dependence of the phase velocity on the porosity is not significant compared with the transmission coefficient. The result described above implies that the fast and slow waves propagate with almost constant sound speeds without porosity dependence, respectively, in the low-porosity region of

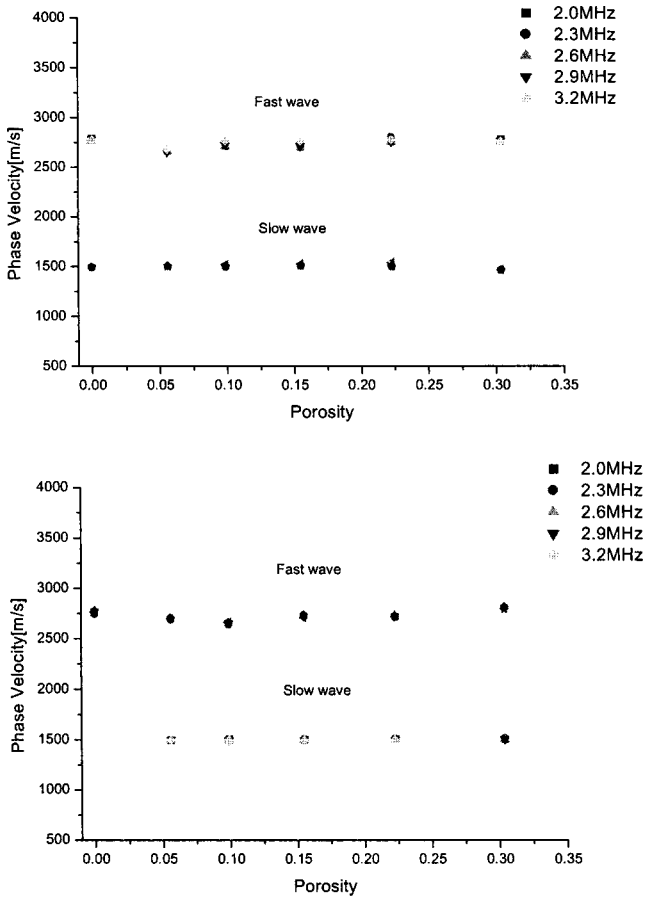

FIG. 6. Experimental phase velocities as a function of porosity for the water-filled Lucite slab with the pore radius 1 mm (upper) and 2 mm (lower). The experimental data represent average values of those measured five times and their standard deviations are within 3 percent.

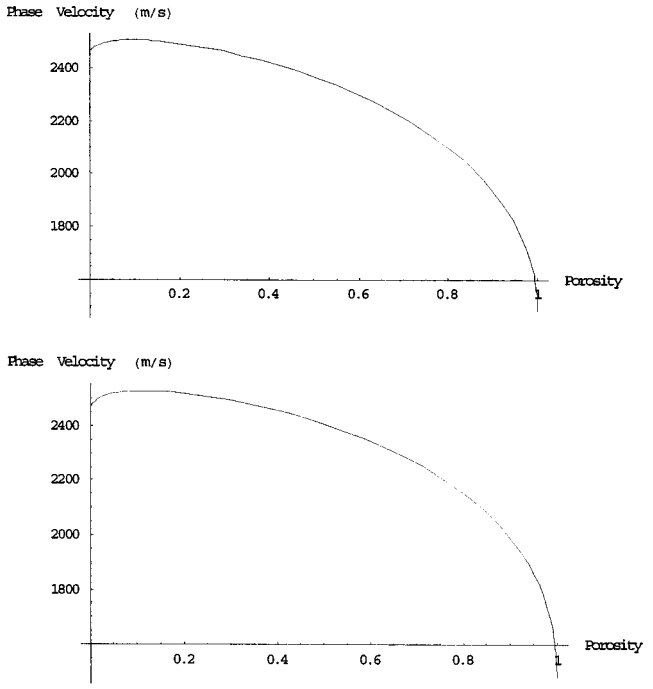

FIG. 7. Theoretical phase velocities as a function of porosity at the frequency 2 MHz for the water-filled Lucite slab with the pore radius 1 mm (upper) and 2 mm (lower). The phase velocity parameters $s_2=0.55$ and $s_2=0.5$ were used in the theoretical estimation of phase velocities for the mixed wave of the fast and slow waves, respectively.

Lucite
slabs with circular cylindrical pores. Interactions of solid and fluid particles in the sound speeds are relatively weak in the simple structure of specimens used in these measurements. However, they may become strong in the other shape of porous media such as sediment and bone. In fact, sound speeds in such porous media strongly depend on their porosities, as observed in many references.[11,13]

For the same porosity and frequency, the phase velocity of the fast wave slightly increases as the pore size increases. In this case, the phase velocity of the slow wave slightly decreases as the pore size increases. The theoretical estimations agree well with the experimental results as noticing the comparison of Figs. 6 and 7 if the phase velocity parameter changes from $s_2=0.55$ to $s_2=0.5$ when the pore radius changes from $a=1$ mm to $a=2$ mm. This suggests the close relation between the parameter s_2 and the pore radius a.

For the same porosity and pore size, the overall phase velocity is constant up to 3 MHz as shown in Fig. 8. For the constant porosity, frequency, and pore size, the phase velocity of the fast wave does not vary much as the slab thickness increases.

Figure 9 represents the 3D plot of the theoretical phase velocity as the functions of porosity and frequency for the pore radius 1 and 2 mm in the case of the total wave. Figure 10 shows the 3D plot of theoretical phase velocity as the functions of porosity and pore size in the case of the total wave. The phase velocity depends more strongly on porosity than on frequency or pore size. It is illustrated that these two 3D plots may be applicable to diagnose physical properties of specimens from the data of phase velocities.

C. Acoustic pressure transmission coefficient

The Fourier-transformed amplitude of transmitted temporal signal through the Lucite slab with pores is used to calculate the experimental transmission coefficient. The pressure transmission coefficient is estimated by the pressure ratio of two received signals. Experimental transmission coefficients are obtained separately for the fast wave, slow wave, and total wave, while theoretical ones are obtained only for the total wave.

In Fig. 11, comparison between theoretical and experimental transmission coefficients for the total wave is given

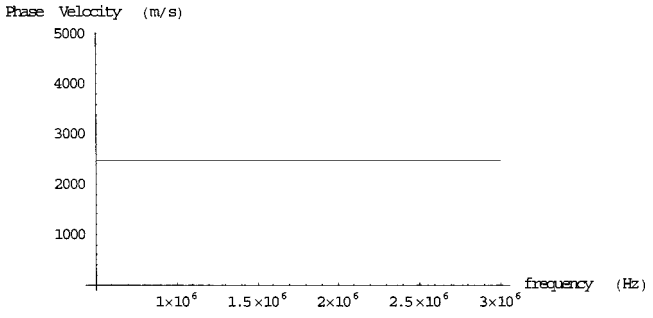

FIG. 8. Theoretical phase velocity as a function of frequency at the porosity 0.3 for the water-filled Lucite slab with the pore radius 1 mm. The phase velocity parameter $s_2=0.55$ was used in the theoretical estimation of the phase velocity for the mixed wave of the fast and slow waves.

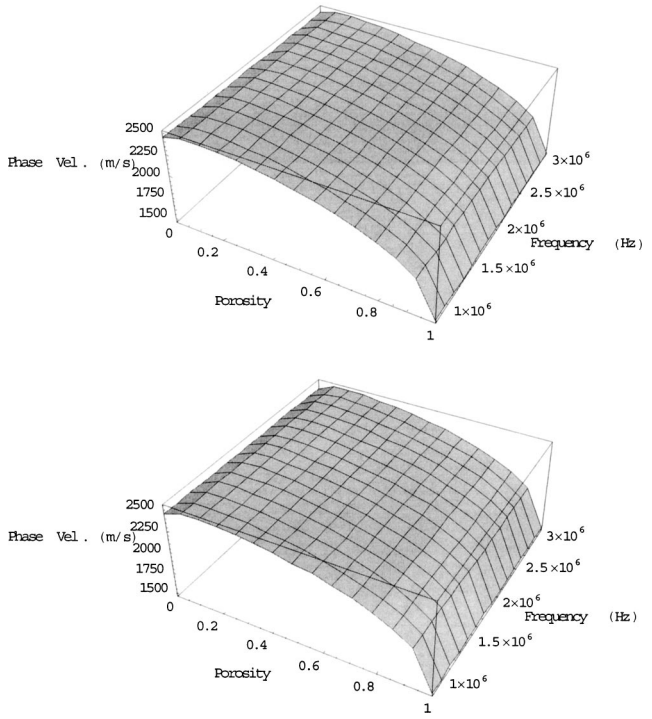

FIG. 9. Theoretical 3D plot of the phase velocity as the functions of porosity and frequency for the water-filled Lucite slab with the pore radius 1 mm (upper) and 2 mm (lower). The phase velocity parameters $s_2=0.55$ and $s_2=0.5$ were used in the theoretical estimation of phase velocities for the mixed wave of the fast and slow waves, respectively.

as a function of porosity at the frequency 2 MHz for the water-filled Lucite slab with the pore radius 2 mm. The theoretical calculation uses the impedance parameter $s_3=1.0\times10^8$ Pa·s/m.

The parameter $s_1=1.5$ can be obtained as well by looking at the experimental and theoretical data of transmission coefficients. The value $s_1\sim1.5$ obtained by the data of transmission coefficients, whose theoretical values are estimated with a fixed impedance parameter s_3 regardless of the phase velocity parameter s_2, agrees with the one obtained by the data of phase velocities.

Experimental transmission coefficients of Lucite slabs with pore radius 1 and 2 mm are shown as a function of porosity in Figs. 12–14, respectively, for the fast wave, slow wave, and total wave. Theoretical transmission coefficients of Lucite slabs with pore radius 1 mm for the total wave are

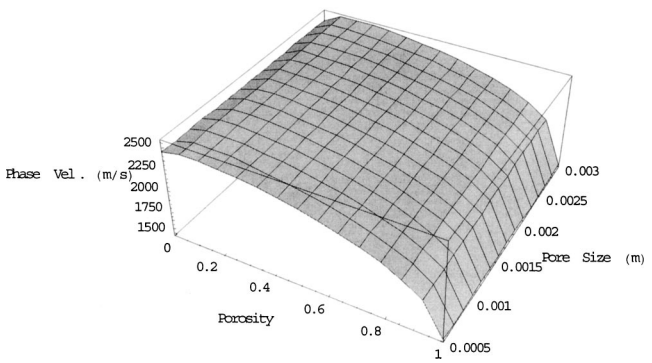

FIG. 10. Theoretical 3D plot of the phase velocity as the functions of porosity and pore size for 2 MHz.

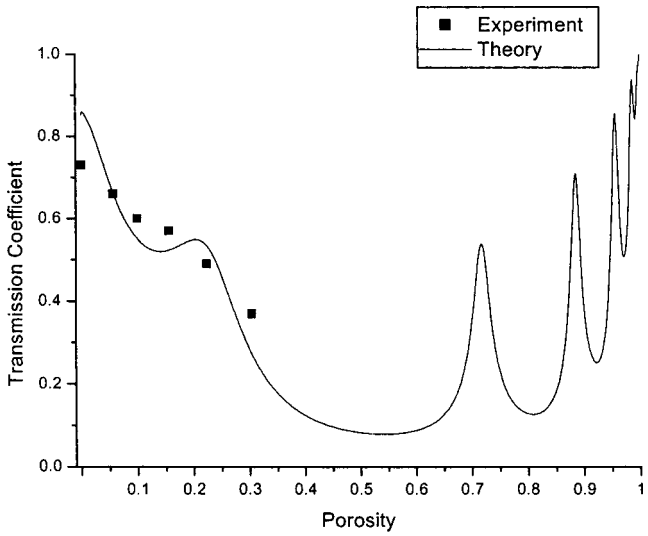

FIG. 11. Theoretical and experimental transmission coefficients as a function of porosity at the frequency 2 MHz for the water-filled Lucite slab with the pore radius 2 mm. The impedance parameter $s_3=1.0\times10^8$ Pa·s/m was used in the theoretical estimation of the transmission coefficient for the mixed wave of the fast and slow waves. The experimental data are also transmission coefficients for the mixed wave of the fast and slow waves.

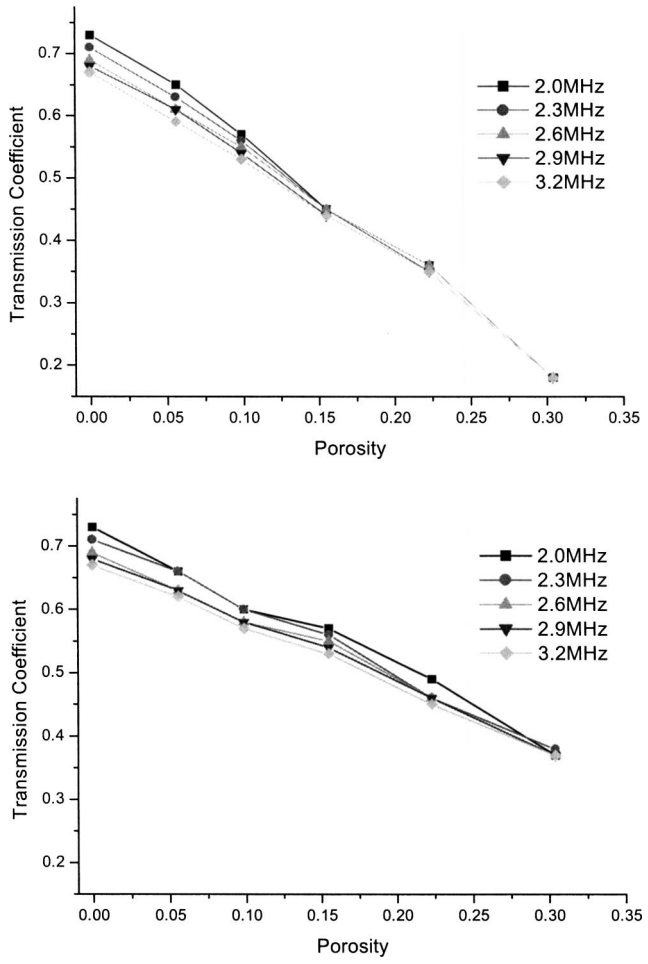

FIG. 12. Experimental transmission coefficients as a function of porosity for the fast wave of the water-filled Lucite slab with the pore radius 1 mm (upper) and 2 mm (lower).

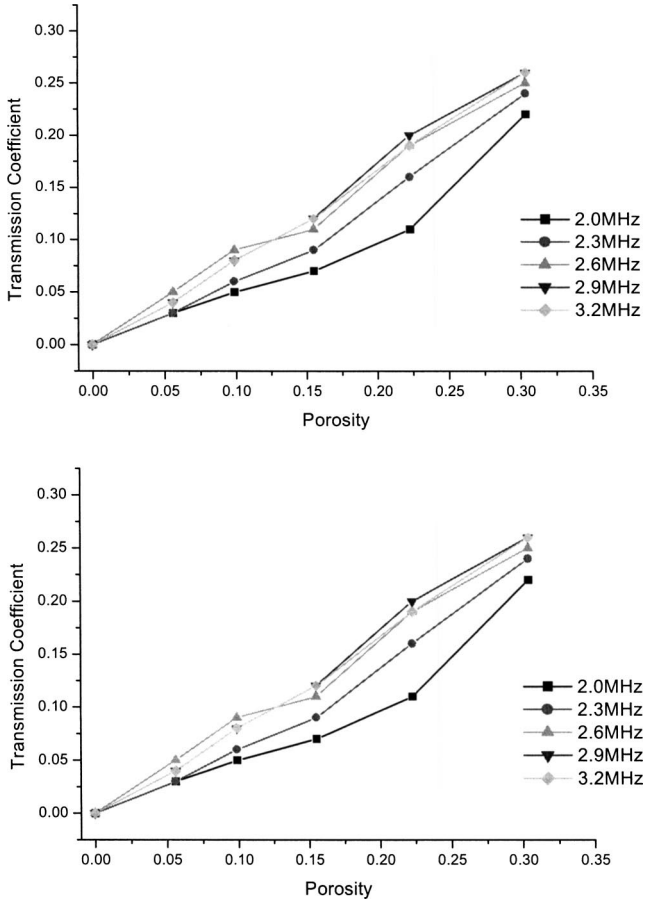

FIG. 13. Experimental transmission coefficients as a function of porosity for the slow wave of the water-filled Lucite slab with the pore radius 1 mm (upper) and 2 mm (lower).

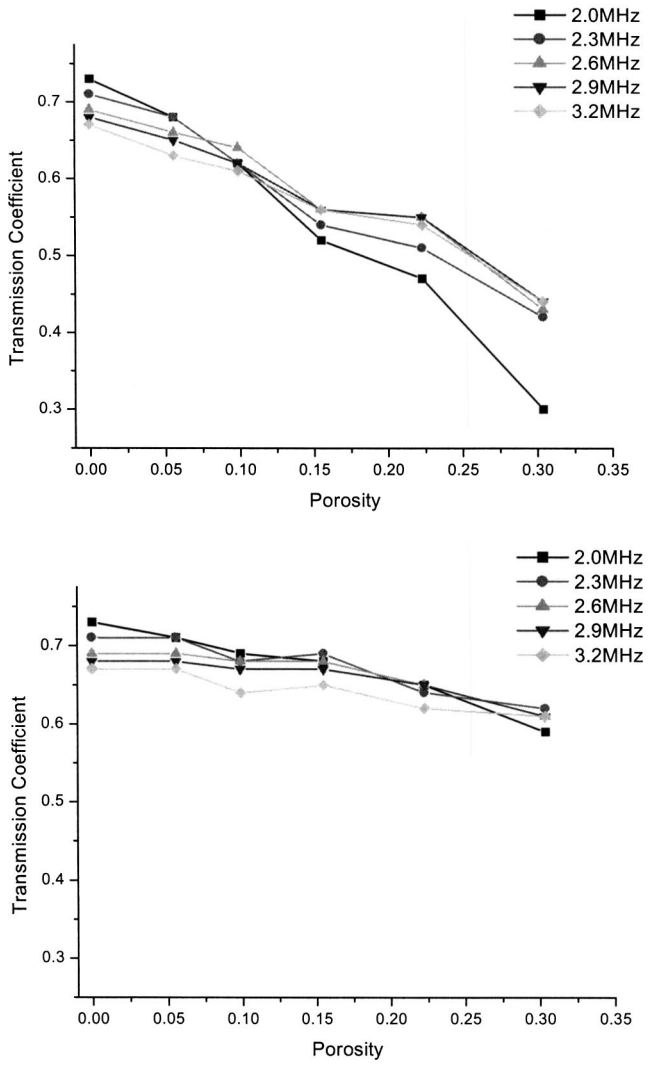

FIG. 14. Experimental transmission coefficients as a function of porosity for the total wave of the water-filled Lucite slab with the pore radius 1 mm (upper) and 2 mm (lower).

given as a function of porosity at the frequencies 2 and 1 MHz in Fig. 15. Those with pore radius 2 mm for the total wave are given as a function of porosity at the lower frequencies 0.2 and 0.1 MHz in Fig. 16. Theoretical calculations with the impedance parameter $s_3 \simeq 1.5\times 10^8$ Pa·s/m in Eq. (16) show reasonable agreement with experimental results at the low-porosity region when noticing the comparison of Figs. 13 and 15. The transmission coefficient of the fast wave decreases as the porosity increases. However, the transmission coefficient of the slow wave increases as the porosity increases. The overall transmission coefficient in the region of low porosity is roughly dominated by the fast wave, while the overall transmission coefficient in the region of high porosity is dominated by the slow wave. It implies that the effective impedance for Lucite slab increases as the porosity increases in the low-porosity region, while it might decrease in the high-porosity region. The transmission coefficient decreases and then increases as the porosity increases for the total, mixed wave of the fast and slow waves. The attenuation during the acoustic wave passage through pure Lucite material is very important: in this calculation, the attenuation coefficient for pure Lucite material, $\alpha=\alpha_0 f^n = 0.016 f^{0.5}$ with the frequency f in Hz, is used following the behavior of attenuation coefficient proportional to $f^{0.5}$ at high frequencies.[4] It is emphasized that the overall transmission coefficient does not monotonically increase from that for pure Lucite to that for pure water as the porosity increases from 0 to 1. The conventional equation (24) with the consideration of porosity dependence only calculates transmission coefficients at two extreme states, homogeneous pure Lucite and water. If only the slow wave is considered in Eq. (24), the monotonic increase of the transmission coefficient is possible.

For the same porosity and frequency, the transmission coefficient of the fast wave increases as the pore size increases. In this case, the transmission coefficient of the slow wave increases as the pore size increases. For the same porosity and frequency, the overall transmission coefficient increases as the pore size increases.

Figures 15 and 16 show the theoretical results for different frequencies and pore radii. They use the different impedance parameters $s_3=1.5\times 10^8$ Pa·s/m and $s_3=1.0\times 10^8$ Pa·s/m, respectively. This suggests the close relation between impedance parameter with pore radius and frequency. As shown in Figs. 15 and 16, the overall transmission coefficient can fluctuate due to the values of $\sin(k_b d)$ and $\cos(k_b d)$ in Eq. (24): there is more fluctuation as the

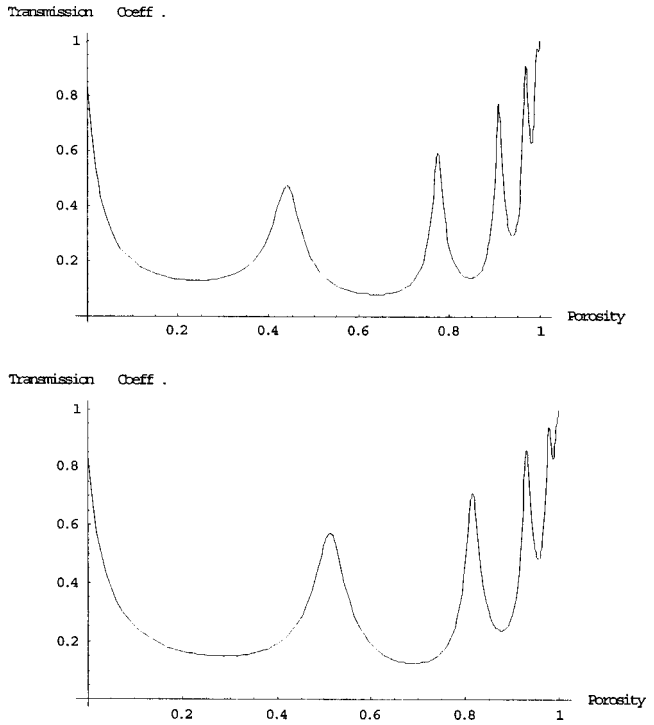

FIG. 15. Theoretical transmission coefficients as a function of porosity at the frequency 2 MHz (upper) and 1 MHz (lower) for the water-filled Lucite slab with the pore radius 1 mm. The impedance parameter $s_3=1.5\times10^8$ Pa·s/m was used in the theoretical estimation of the transmission coefficient for the mixed wave of the fast and slow waves.

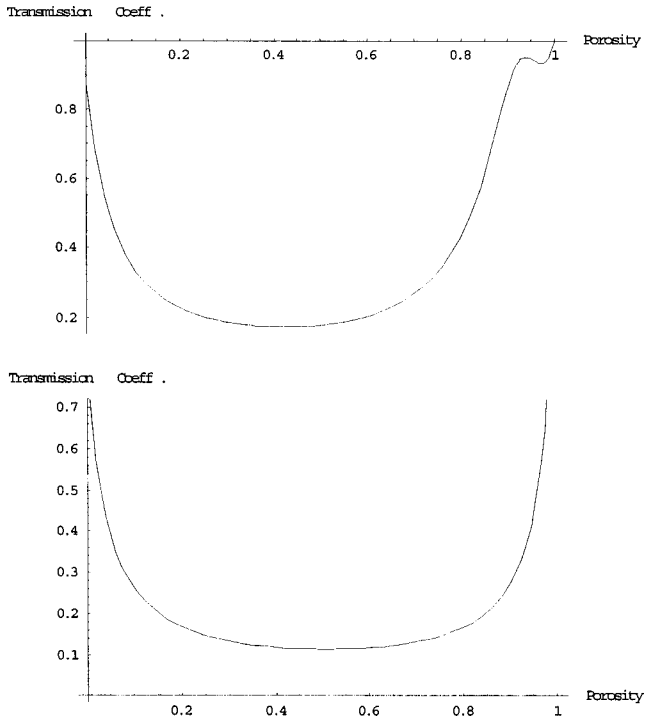

FIG. 16. Theoretical transmission coefficients as a function of porosity at the frequency 0.2 MHz (upper) and 0.1 MHz (lower) for the water-filled Lucite slab with the pore radius 2 mm. The impedance parameter $s_3=1.0\times10^8$ Pa·s/m was used in the theoretical estimation of the transmission coefficient for the mixed wave of the fast and slow waves.

function of porosity in the higher frequency in the figures. Therefore, the information on frequency, pore size, and porosity of porous medium is contained in the effective density equation (8), the propagation constant equation (12), and the impedance equation (16).

For the same porosity and pore size, the overall transmission coefficient oscillates as the frequency increases if the frequency ranges are wide enough. The overall transmission coefficients oscillate at the porosity 0 and 0.3, but they are different in magnitude, as shown in Fig. 17. The oscillation occurs due to the complex value $k_b d$ in Eq. (24). The total transmission $|T|=1$ in the case of the pure Lucite with no attenuation takes place at the multiple frequencies of 260 kHz for the given sample thickness, 4.8 mm. Around the frequency 2 MHz, the overall transmission coefficient increases as the frequency increases in the case of water-filled pores for the radius 1 mm. The relation between pore size and frequency is introduced in Eq. (5). The oscillating phenomena as the functions of frequency and slab thickness may be clearly observed by using broadband frequency measurements rather than single-frequency measurements used here. For the constant porosity, frequency, and pore size, the transmission coefficient of the fast wave oscillates as the slab thickness increases.

Figure 18 represents the 3D plot of the theoretical transmission coefficient as the functions of porosity and frequency in the case of the total wave. Figure 19 shows the 3D plot of the theoretical transmission coefficient as the functions of porosity and pore size in the case of the total wave. The transmission coefficient more significantly depends on porosity, frequency, and pore size than the phase velocity. It is illustrated that these two 3D plots may be applicable to diagnose physical properties of specimens from the data of transmission coefficients.

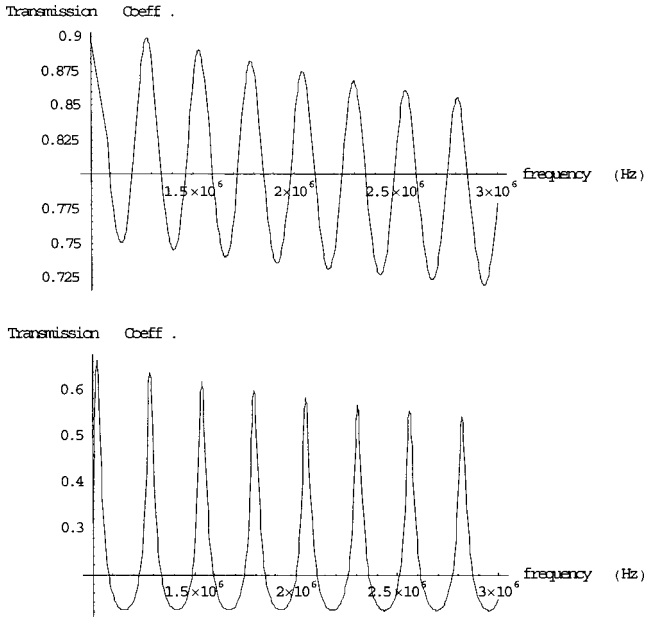

FIG. 17. Theoretical transmission coefficients as a function of frequency for the water-filled Lucite slab with the pore radius 1 mm at the porosity 0 (upper) and 0.3 (lower). The impedance parameter $s_3=1.5\times10^8$ Pa·s/m was used in the theoretical estimation of the transmission coefficient for the mixed wave of the fast and slow waves.

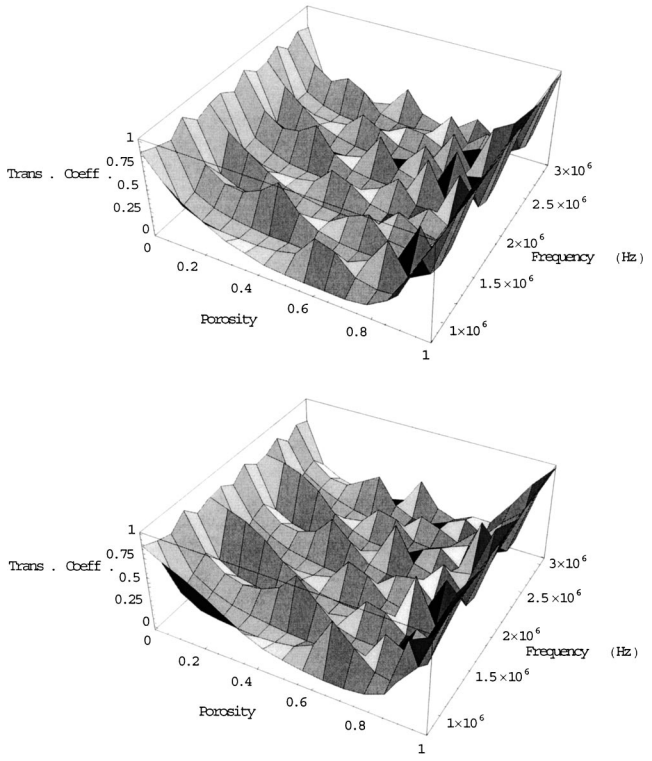

FIG. 18. Theoretical 3D plot of the transmission coefficient as the functions of porosity and frequency for water-filled Lucite slab with the pore radius 1 mm (upper) and 2 mm (lower). The impedance parameters $s_3=1.5\times10^8$ Pa·s/m and $s_3=1.0\times10^8$ Pa·s/m were in the theoretical estimation of transmission coefficients for the mixed wave of the fast and slow waves, respectively.

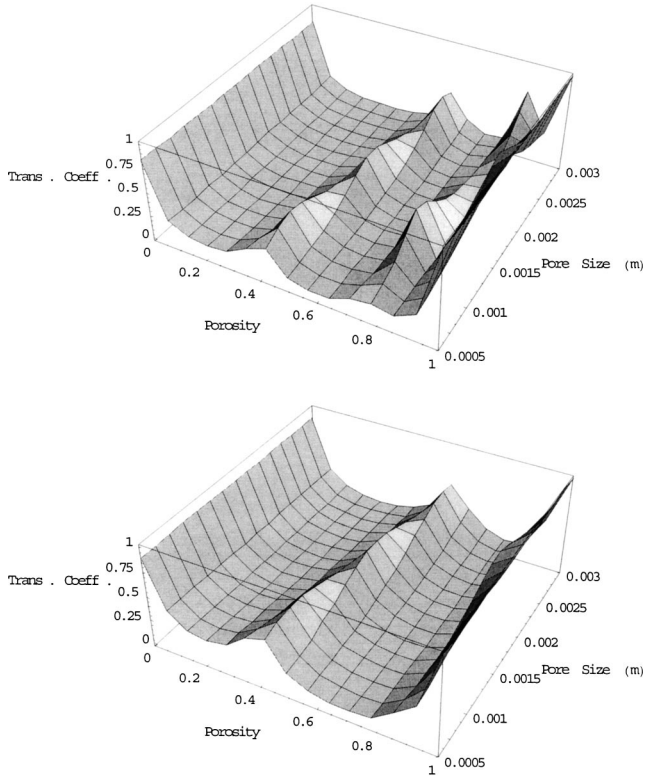

FIG. 19. Theoretical 3D plot of the transmission coefficient as the functions of porosity and pore size for 2 MHz (upper) and 1 MHz (lower).

D. Summary on phenomenological parameters

In the MBA model, three phenomenological boundary, phase velocity, and impedance parameters, s_1, s_2 and s_3, are introduced for taking account of nonrigid boundary condition, phase velocity slope, and impedance slope, respectively. For the Lucite slab with 1-mm-radius cylindrical pores, three parameters $s_1=1.5$, $s_2=0.55$, and $s_3=1.5\times10^8$ Pa·s/m are empirically obtained and for the Lucite slab with 2-mm radius cylindrical pores, $s_1=1.5$, $s_2=0.5$, and $s_3=1.0\times10^8$ Pa·s/m are phenomenologically obtained. The parametrized effective density, phase velocity, propagation constant, and impedance are proposed based on the measurements for nonrigid medium slab with circular cylindrical pores as follows:

$$\rho_b=[(-s_3\Omega^2+(\rho_c c_c-\rho_m c_m+s_3)\Omega+\rho_m c_m)]\times[k_m^2k_c^2/((1-\Omega)^{s_2}k_c^2+\Omega^{s_2}k_m^2)]^{1/2}q/\omega,$$

$$c_b=((1-\Omega)^{s_2}c_m^2+\Omega^{s_2}c_c^2)^{1/2},$$

$$k_b=(q^2[k_m^2k_c^2/((1-\Omega)^{s_2}k_c^2+\Omega^{s_2}k_m^2)])^{1/2},$$

$$z_b=q^2[-s_3\Omega^2+(\rho_c c_c-\rho_m c_m+s_3)\Omega+\rho_m c_m],$$

where ρ_m is the pure material density, ρ_c the single pore fluid density, q the tortuosity factor, and c_m the pure material sound velocity. The physical density different from the effective density ρ_p is given by $\rho_p=(1-\Omega)\rho_m+\Omega\rho_0$ with the pure fluid density ρ_0.

E. Acoustic diagnosis for porous medium

For acoustic diagnosis, the phase velocity and transmission coefficient (or attenuation) of a Lucite slab are first experimentally obtained and then physical parameters such as porosity and pore size are extracted from the experimental data with the MBA model. To achieve this aim, both the relation between phase velocity and porosity (or frequency) and the relation between transmission coefficient and porosity (or frequency) should be phenomenologically obtained before applying the theory developed in this paper. This means that the prediction of pore size and porosity is possible for the diagnosis of porous medium with unknown physical characteristics if the phase velocity and transmission coefficient are data based as a function of porosity or frequency. Therefore, it is required to parametrize the phase velocity and transmission coefficient as a function of porosity based on experiments for various types of porous media such as bones and sediments.

In the previous subsections, the theoretical and experimental phase velocity and transmission coefficient of the Lucite slab were compared in the low-porosity regime. Where the diagnosis of bone is concerned, the experimental data are more comparable to the application of the cortical (compact) bone, which has the high volume fraction of solid (above 0.7). The theoretical data from the MBA model are also available for the cancellous (sponge) bone, which has the low volume fraction of solid (less than 0.7). The MBA model is thus applicable to the entire region of porosity. As discussed in the measurement data, it is suggested that the fast (or first kind) wave is more significant in the cortical bone-type Lucite, while the slow (or second kind) wave may be

significant in the cancellous bone-type Lucite. For example, the conventional separate treatment of viscous effect and thermal effect[5] is available for cancellous bone in which the slow wave is dominant, while the MBA model introduced here is useful for both cortical and cancellous bones since the fast wave should be considered in general as well as the slow wave.

IV. CONCLUSIONS

Acoustic transmission coefficient and phase velocity for a Lucite slab with circular cylindrical pores were experimentally measured as functions of porosity, frequency, and pore size. The first kind (fast) of wave and the second kind (slow) of wave are experimentally observed. The transmission coefficient and phase velocity were also compared with those theoretically estimated with the modified Biot-Attenborough (MBA) model with three phenomenological parameters: boundary, phase velocity, impedance parameters. They showed reasonably good agreement for the porous Lucite slab. In the theoretical aspect, the separate treatment of viscous effect and thermal effect to rigid material with circular cylindrical pores is modified for nonrigid material with circular cylindrical pores, and is applied for the theoretical calculation of the transmission coefficient and phase velocity through porous medium. The MBA model incorporates phenomenological improvement for the separate treatment of viscous effect and thermal effect by Attenborough and the simultaneous consideration of the fast wave and the slow wave by Biot in the mixed state of solid and fluid. The MBA model is thus formulated by taking into account the fast wave in the mixed state of solid and fluid as the extension of the conventional, separate treatment of viscous effect and thermal effect considering only the slow wave. This implies that relations among frequency, porosity, and pore size of porous medium can be inversely analyzed in terms of the transmission coefficient and phase velocity data as the functions of porosity and frequency. This illustrates that acoustic methods may therefore be useful for osteoporosis diagnosis as a prescreening method or for sediment diagnosis in underwater exploration.

ACKNOWLEDGMENTS

This work is supported in part by BK21 Program from the Ministry of Education. One of the authors (S.W.Y.) is also supported in part by Korea Research Foundation Grant No. 2000-015-DP0178. The authors would like to thank J. Y. Baik for his help in obtaining the measurement data.

[1] C. M. Langton, S. B. Palmer, and R. W. Porter, ''The measurement of broadband ultrasonic attenuation in cancellous bone,'' Eng. Med. **13**, 89–91 (1984).

[2] K. Wear, ''Frequency dependence of ultrasonic backscatter from human trabecular bone: Theory and experiment,'' J. Acoust. Soc. Am. **106**, 3659–3664 (1999).

[3] S. Chaffai, F. Padilla, G. Berger, and P. Laugier, ''*In vitro* measurement of the frequency-dependent attenuation in cancellous bone between 0.2 and 2 MHz,'' J. Acoust. Soc. Am. **108**, 1281–1289 (2000), and references therein.

[4] M. A. Biot, ''Theory of propagation of elastic waves in a fluid-saturated porous solid. I. Low-frequency range,'' J. Acoust. Soc. Am. **28**, 168–178 (1956); ''Theory of propagation of elastic waves in a fluid-saturated porous solid. II. Higher frequency range,'' *ibid.* **28**, 179–191 (1956); ''Generalized theory of acoustic propagation in porous dissipative media,'' *ibid.* **34**, 1254–1264 (1962).

[5] K. Attenborough, ''Acoustic characteristics of rigid fibrous absorbents and granular materials,'' J. Acoust. Soc. Am. **73**, 785–799 (1983), and references therein.

[6] M. A. Biot, ''Variational irreversible thermodynamics of heat and mass transfer in porous solids: New concepts and methods,'' Q. Appl. Math. **36**, 19–38 (1978).

[7] A. Bedford, R. D. Costley, and M. Stern, ''On the drag and virtual mass coefficients in Biot's equation,'' J. Acoust. Soc. Am. **76**, 1804–1809 (1984).

[8] R. Burridge and J. B. Keller, ''Poroelasticity equations derived from microstructure,'' J. Acoust. Soc. Am. **70**, 1140–1146 (1981).

[9] C. Zwikker and C. W. Kosten, *Sound Absorbing Materials* (Elsevier, Amsterdam, 1949).

[10] H. S. Roh, W. P. Arnott, J. M. Sabatier, and R. Raspet, ''Measurement and calculation of acoustic propagation constants in arrays of small air-filled rectangular tubes,'' J. Acoust. Soc. Am. **89**, 2617–2624 (1991).

[11] A. Hosokawa and T. Otani, ''Ultrasonic wave propagation in bovine cancellous bone,'' J. Acoust. Soc. Am. **101**, 558–562 (1997); ''Acoustic anisotropy in bovine cancellous bone,'' *ibid.* **103**, 2718–2722 (1998).

[12] J. Y. Baik, H. S. Roh, and S. W. Yoon, ''Acoustic characteristics of Lucite slab with circular cylindrical pores,'' J. Acoust. Soc. Korea **19**(2s), 299–302 (2000).

[13] E. L. Hamilton, ''Compressional-wave attenuation in marine sediments,'' Geophysics **37**, 620–646 (1972).

Finite element predictions for the dynamic response of thermo-viscoelastic material structures

M. Castaings,[a] C. Bacon, and B. Hosten
Laboratoire de Mécanique Physique, Université Bordeaux 1, UMR CNRS 5469 351, Cours de la Libération, 33405 Talence Cedex, France

M. V. Predoi
Catedra de Mecanica, Universitatea Politehnica Bucuresti, Splaiul Independentei 313, Bucuresti, Romania

(Received 9 May 2002; revised 31 October 2003; accepted 4 November 2003)

In this paper, constitutive relations are solved in the Fourier domain using a finite-element-based commercial software. The dynamic responses of viscoelastic bars or plates to either thermal or mechanical loads are predicted by considering complex moduli (Young, Poisson, stiffness moduli) as input data. These moduli are measured in the same frequency domain as that which is chosen for modeling the wave propagation. This approach is simpler since it suppresses the necessity of establishing a rheological model. Specific output processing then allows the numerical predictions to be compared to analytical solutions, in the absence of scatterers. The performances of this technique and its potential for simulating more complicated problems like diffraction of waves or for solving inverse problems are finally discussed. © *2004 Acoustical Society of America.*
[DOI: 10.1121/1.1639332]

PACS numbers: 43.35.Mr [YHB] Pages: 1125–1133

I. INTRODUCTION

The study of elastic wave propagation in materials has been a subject of extensive investigation in the literature. It is of great importance in a variety of applications ranging from seismology to nondestructive testing of composite structures used in aircraft, spacecraft, or other engineering industries. Polymers or polymer-based matrix composites are widely used in these industrial environments. These materials possess isotropic or anisotropic viscoelastic properties that can strongly affect the propagation of waves. Constitutive relations developed in the Fourier domain and using complex moduli that represent the viscoelastic material properties allow the dynamic behavior of these media to be properly described.[1–3] For example, the case of waves generated in rods by thermal excitation has been investigated.[4] Several other cases of waves propagating in plates made of dissipative materials have also been modeled.[5–9] However, these models are limited to predicting the propagation in structures of simple geometries (plates, pipes, flawless media, ...). For instance, when the diffraction of waves by a localized inhomogeneity (hole, edge, notch, crack, ...) is considered, numerical or hybrid techniques based, for example, on the finite element (FE), finite difference (FD), or boundary element (BE) methods are commonly used.[10–19] However, the wide range of publications found on this subject is restricted to modeling elastic materials only, except in a few cases where temporal functions of relaxation are introduced.[20–22] The use of a numerical technique combining a spatial Fourier transform with the method of characteristics is also an alternative.[23] Finally, in most of the commercial FE softwares, the viscoelastic behavior can be taken into account by using multi spring-dashpot elements having different coefficients. The problem with all these various techniques is that data concerning the material behavior are usually measured in quasi-static regime, and used for establishing rheologic laws required, in the FE model, which may not be representative of the dynamic behavior of the material, i.e., at high frequency regime that concerns wave propagation. An alternative to avoid this consists in using the concept of complex moduli representing the viscoelastic material properties, these moduli being directly measured in the same frequency domain as that used for modeling the propagation of waves. This requires solving the FE problem in the frequency domain, due to the Boltzmann's principle of superposition.[2,3] Although this option is available in other commercial codes than that used here, no work has been published so far on its investigation for modeling wave propagation problems in viscoelastic, isotropic, or anisotropic solids.

In this paper, a commercially available finite element software[24] is used to simulate the dynamic response of thermo-viscoelastic material structures to thermal or mechanical loads. Propagation in isotropic or anisotropic bars or plates is considered by introducing complex moduli representing the viscoelastic material properties. These moduli are measured using an immersion ultrasonic technique[25] and, according to previous experimental studies[26,27] on the attenuation of bulk waves in polymer-based materials, they are supposed to be non-frequency-dependent in the frequency range of investigation and for the materials considered in this paper. The constitutive relations are solved in the Fourier domain for each node of the meshed structure. A great advantage of this method is that the finite element code supplies stationary solutions for a small number of frequency components representing a given temporal excitation. This approach considerably speeds up the computation by avoiding the numerical temporal differentiation and decreasing the number of variables used for each calculation step. In com-

[a]Electronic mail: m.castaings@lmp.u-bordeaux1.fr

TABLE I. Thickness (mm), density, and viscoelastic modulus (GPa) for the Perspex and glass-epoxy plates.

Material	Thickness	Density	C_{11}^*	C_{22}^*	C_{12}^*	C_{66}^*
Perspex	4	1.2	$8.5+i0.4$	$8.5+i0.4$	$4.3+i0.2$	$2.1+i0.1$
Glass epoxy	5	1.9	$20+i0.7$	$50+i2.5$	$9+i0.4$	$6+i0.2$

parison to classical FE solutions that use numerical routines for producing time marching solutions, thus requiring hundreds or thousands of iterative calculations, the method proposed here is much less time consuming since it consists in solving the dynamic equations of equilibrium for a limited number of frequencies (usually less than 50) that constitutes the frequency spectrum of a temporal excitation. Moreover, the use of measured complex moduli[25] as input data has more physical meaning than employing temporal functions of relaxation for modeling the wave attenuation. Results supply both displacements and stresses at any node of the mesh and for each frequency of the input. Then, data processing such as the temporal inverse Fourier transform can be used for obtaining the corresponding temporal waveforms. Direct spatial Fourier transform is also used for quantifying the phase velocity or attenuation of waves, which are compared in turn with solutions obtained from an analytical model.[9] Section II states the various problems investigated in this paper, i.e., the propagation of waves along a viscoelastic bar, launched by a thermal or mechanical excitation applied at one edge, and the propagation of Lamb modes guided along a viscoelastic plate, excited at one edge by a mechanical single- or multi-modal though-thickness shape. Section III describes the software-required formulation of the dynamic equations of equilibrium, for one- and two-dimensional thermo-viscoelastic material problems. Section IV briefly deals with FE specifications, like defining the mesh, imposing specific boundary conditions, or applying dynamic excitations. Finally, Sec. V presents numerical predictions, which are compared to analytical solutions. Specific processing of the output data produced by the software is also described in this section.

II. PROBLEM STATEMENT

A. Viscoelastic bar

The 1-D cases consist in modeling a PVC bar of 200-mm length (direction x). Its density and complex Young modulus are $\rho=1380$ kg/m^3 and $E^*=(3.8+i0.13)$ GPa, respectively. The complex value of E has been measured on a PVC bar sample using the technique described in Ref. 4. Its coefficient of linear thermal expansion is chosen equal to $\alpha=80\times10^{-6}$/C, according to Ref. 28.

B. Viscoelastic plate

The 2-D cases consist in modeling two different plates of length $L=200$ mm (direction x_2). The first plate is 4 mm thick (direction x_1) and made of Perspex. The second plate is a 5-mm-thick composite sample made of unidirectional glass fibers impregnated in an epoxy matrix. Both plates are considered as infinite in direction x_3, which is normal to the plane of propagation formed by directions x_1 and x_2. For the composite plate, the fibers are aligned to direction x_2. Plane strain conditions will then be assumed in the model. The viscoelastic properties of these material plates have been previously estimated using an immersion ultrasonic technique.[25] The measured complex moduli, given in Table I, show the Perspex to be an isotropic and viscoelastic material, and the glass epoxy to be an anisotropic and viscoelastic material, as expected. In Sec. V B, these two sets of values will be used as input data for the FE model and also for the analytical model.

For either the PVC bar or the plates, it is interesting to note that the measured complex moduli are not frequency dependent. This assumption has been shown to be valid for polymer-based materials, in a much larger frequency domain ($\approx$0.3 to 5 MHz) than that investigated for the numerical applications presented in this paper. It comes from the fact that measured attenuations of longitudinal and shear bulk waves in this type of material vary linearly with respect to frequency.[26,27]

III. FORMALISM

The software[24] used here is a numerical tool for solving partial differential equations (PDEs) by a finite element method. In the field of mechanics, some models are implemented in the libraries provided with the software. However, no mechanical model is implemented in the case of a thermo-viscoelastic material. In order to consider this kind of material, the corresponding PDE problem must be written in the specific following form:

$$\begin{aligned} &d_a\frac{\partial u}{\partial t}+\nabla\cdot(-c\nabla u-\alpha u+\gamma)+\beta\cdot\nabla u+au=f \quad \text{in } \Omega,\\ &\mathbf{n}\cdot(c\nabla u+\alpha u-\gamma)+qu=g-h^T\mu \quad \text{on } \partial\Omega,\\ &hu=r \quad \text{on } \partial\Omega, \end{aligned} \tag{1}$$

where u is a time-dependent variable to be determined in the domain called Ω of boundary $\partial\Omega$, or a vector of dependent variables, and t is the time for nonstationary problems. The outward unit vector on $\partial\Omega$ is denoted by $\mathbf{n}$. The first equation is the PDE that must be satisfied inside the domain Ω. The second and third ones are the Neumann and Dirichlet conditions, respectively, defined at the boundary $\partial\Omega$. The symbol ∇ is the vector differential operator defined as

$$\nabla=\left(\frac{\partial}{\partial x_1},\ldots,\frac{\partial}{\partial x_n}\right), \tag{2}$$

where n is the number of space dimensions. The other parameters are coefficients that depend on the considered problem. If u is a single variable, all these coefficients are scalars except α, β, and γ, which are vectors with n components and c, which may be a n-by-n matrix.

As explained before, the aim of our work is to take the thermo-viscoelastic effects into account by considering the equations in the frequency domain and by using complex coefficients. By this way, it will be shown for the two cases treated in this paper that Eq. (1) can be simplified as follows:

$$\begin{aligned} &\nabla\cdot(c\nabla\tilde{u}-\gamma)-a\tilde{u}=0 \quad \text{in } \Omega,\\ &\mathbf{n}\cdot(c\nabla\tilde{u}-\gamma)=g \quad \text{on } \partial\Omega,\\ &h\tilde{u}=r \quad \text{on } \partial\Omega, \end{aligned} \tag{3}$$

where $\tilde{u}$ is a frequency-dependent variable to be determined.

The second and third equations represent the stress boundary condition and the displacement boundary condition, respectively, where g is the stress vector at the boundary and r is the amplitude of the forced displacements. Here h is a 2×2 matrix, the elements of which are either 0 or 1 depending on the direction of the forced displacements and also on the orientation of each considered boundary. In fact, a graphic interface allows various boundary conditions to be easily defined without requiring entering explicit values for the elements of the various coefficients g, r, or h. The coefficients c, γ, and a depend on the number n of space dimensions of the problem considered. They are related to the stiffness of the material, the thermal stress, and the inertia effect, respectively. They will be given in the following sections for different cases: (A) the one-dimensional case of a bar and (B) the two-dimensional cases of a plate in a plane stress or a plane strain states. In all cases, the materials are thermo-viscoelastic and can be submitted to a temperature rise and/or to a mechanical load.

A. Viscoelastic bar

Let us consider a bar, which is straight, cylindrical, slender, and made of a linearly viscoelastic material submitted to a rapid temperature rise. Its density is ρ. If the lateral dimensions of the bar are much shorter than the wavelength, the radial inertia can be neglected. Then, the Fourier transform $\tilde{\sigma}(x,\omega)$ of the normal stress $\sigma(x,t)$ is related to the Fourier transform $\tilde{u}(x,\omega)$ of the axial displacement $u(x,t)$ at axial coordinate x and at time t by

$$\frac{\partial\tilde{\sigma}}{\partial x}=-\rho\omega^2\tilde{u}, \tag{4}$$

where the angular frequency ω is related to the frequency ν by $\omega=2\pi\nu$. In the frequency domain, the linear viscoelastic behavior of the material can be expressed as

$$\tilde{\sigma}=E^*\tilde{\varepsilon}-E^*\alpha\tilde{\theta}, \tag{5}$$

where E^* is the complex Young modulus of the material, α is its coefficient of linear thermal expansion, and $\tilde{\varepsilon}(x,\omega)$ and $\tilde{\theta}(x,\omega)$ are the Fourier transforms of the longitudinal strain and the temperature rise above the initial temperature, respectively. Note that this formalism would allow E^* to be frequency dependent if required. But, as explained in Sec. II, the material properties will be chosen as non-frequency-dependent in the present models. To facilitate the analysis, it will be assumed that the temperature increase is small enough so that it has negligible effect on the mechanical behavior of the material. In the hypothesis of small strains, the longitudinal strain is related to the axial displacement by $\tilde{\varepsilon}=\partial\tilde{u}/\partial x$. Then, from the above equations, a differential equation is found:

$$E^*\frac{\partial^2\tilde{u}}{\partial x^2}+iE^*\frac{\alpha}{\omega}\frac{\partial\tilde{\theta}}{\partial x}+\rho\omega^2\tilde{u}=0, \tag{6}$$

where $\tilde{\theta}(x,\omega)$ is the Fourier transform of the time derivative of the temperature rise. It is convenient to use this time derivative because this function is generally time limited. This is often not the case for the temperature rise $\theta(x,t)$.

By comparing (3) and (6), the coefficients c, γ, and a are shown to be in the following form:

$$c=E^*, \quad \gamma=-iE^*\alpha\frac{\tilde{\theta}}{\omega}, \quad \text{and } a=-\rho\omega^2. \tag{7}$$

B. Viscoelastic plate

For an orthotropic linearly viscoelastic material of density ρ, the displacement two-dimensional general equation is written as follows in the frequency domain:

$$\begin{aligned} &Q_{11}^*\frac{\partial^2\tilde{u}_1}{\partial x_1^2}+Q_{66}^*\frac{\partial^2\tilde{u}_1}{\partial x_2^2}+(Q_{12}^*+Q_{66}^*)\frac{\partial^2\tilde{u}_2}{\partial x_1\partial x_2}+i\frac{B_1}{\omega}\frac{\partial\tilde{\theta}}{\partial x_1}\\ &\quad+\rho\omega^2\tilde{u}_1=0,\\ &Q_{22}^*\frac{\partial^2\tilde{u}_2}{\partial x_2^2}+Q_{66}^*\frac{\partial^2\tilde{u}_2}{\partial x_1^2}+(Q_{21}^*+Q_{66}^*)\frac{\partial^2\tilde{u}_1}{\partial x_1\partial x_2}+i\frac{B_2}{\omega}\frac{\partial\tilde{\theta}}{\partial x_2}\\ &\quad+\rho\omega^2\tilde{u}_2=0, \end{aligned} \tag{8}$$

where $(\tilde{u}_1,\tilde{u}_2)$ is the Fourier transform of the displacement vector, and x_1 and x_2 are the coordinates of the orthotropic directions. The function $\tilde{\theta}$ is the Fourier transform of the time derivative of the temperature rise. The expressions of the complex coefficients Q_{ij}^* and B_i are different whether plane strain or plane stress state is considered. If a plane strain state is considered ($\varepsilon_{13}=\varepsilon_{23}=\varepsilon_{33}=0$), theses values are related to the components C_{ij}^* of the complex stiffness matrix and to the coefficients of linear thermal expansion α_i by

$$Q_{ij}^*=C_{ij}^* \quad \text{and } B_i=C_{i1}^*\alpha_1+C_{i2}^*\alpha_2+C_{i3}^*\alpha_3. \tag{9}$$

For a plane stress state ($\sigma_{13}=\sigma_{23}=\sigma_{33}=0$), these values become

$$Q_{ij}^*=C_{ij}^*-\frac{C_{i3}^*C_{j3}^*}{C_{33}^*} \quad \text{for } i,j=1,2, \quad Q_{66}^*=C_{66}^*, \tag{10}$$

and

$$\begin{aligned} B_i=&C_{i1}^*\alpha_1+C_{i2}^*\alpha_2+C_{i3}^*\alpha_3\\ &-\frac{C_{i3}^*(C_{31}^*\alpha_1+C_{32}^*\alpha_2+C_{33}^*\alpha_3)}{C_{33}^*} \quad \text{for } i=1,2. \end{aligned} \tag{11}$$

Again, this formalism allows the complex stiffness moduli C_{ij}^* to be considered as frequency dependent if required. But,

as explained in Sec. II, they will be chosen frequency independent here.

After some calculations, the above differential equation must be written in the form of the first equation of (3), where the variable $\tilde{u}$ to be determined corresponds to the vector $(\tilde{u}_1, \tilde{u}_2)$. Then, the coefficient c is a 2×2 matrix where the components are 2×2 matrices:

$$c_{11}=\begin{pmatrix} Q_{11}^* & 0 \\ 0 & Q_{66}^* \end{pmatrix}, \quad c_{12}=\begin{pmatrix} 0 & Q_{12}^* \\ Q_{66}^* & 0 \end{pmatrix},$$

$$c_{21}=\begin{pmatrix} 0 & Q_{66}^* \\ Q_{21}^* & 0 \end{pmatrix}, \quad c_{22}=\begin{pmatrix} Q_{66}^* & 0 \\ 0 & Q_{22}^* \end{pmatrix}. \tag{12}$$

The coefficient a is a 2×2 matrix:

$$a=\begin{pmatrix} -\rho\omega^2 & 0 \\ 0 & -\rho\omega^2 \end{pmatrix}. \tag{13}$$

The coefficient γ is a vector, the two components of which are the following vectors:

$$\gamma_1=\begin{pmatrix} -i\dfrac{B_1\tilde{\theta}}{\omega} \\ 0 \end{pmatrix}, \quad \gamma_2=\begin{pmatrix} 0 \\ -i\dfrac{B_2\tilde{\theta}}{\omega} \end{pmatrix}. \tag{14}$$

IV. FINITE ELEMENT MODEL

A. Software

Numerical solution of the partial differential equations can be supplied by the finite element method (FEM). The versatility and ease-of-use are the principal characteristics of the software.[24] Two possibilities exist to determine the dynamic response of thermo-viscoelastic structures to time-varying loads (temperature, displacements, forces, ...). Time marching solutions are commonly used, but this option was very time consuming and inaccurate solutions were obtained. Working in the frequency domain was then the alternative. The frequency spectrum of a time-dependent excitation is defined using a direct Fourier transform. Then, the structure response (complex displacements and stresses at any location) is calculated at each frequency of this load, i.e., the finite element code supplies stationary solutions for each frequency component of the temporal excitation. Since a small number of frequencies (less than 50) are sufficient to achieve a correct representation of a wide variety of temporal excitations, this approach considerably speeds up the computation by avoiding the numerical temporal differentiation and by decreasing the number of calculation steps. The other advantage of this method is that the viscoelastic behavior is taken into account by considering complex moduli as input data to the constitutive relations, since these are expressed in the frequency domain. This has more physical meaning than using temporal functions of relaxation for modeling the dissipation in materials, especially if the complex moduli are previously measured.[25] If needed, temporal waveforms corresponding to the local response of the structure can be reconstructed by inverse Fourier transforms.

B. Mesh

Automatic meshing is a major advantage of the software. The choice of the element size, along the bar (1-D cases) or in the plane of propagation of the plate (2-D cases), is made such that the shortest wavelength is sampled by at least five elements. Elements with nth-order behavior are available. Series of tests showed the code to systematically converge towards the same consistent solutions when the order was greater than or equal to 3. Therefore, elements with cubic Lagrange polynomials behavior have been used for most of the simulations considered in this paper. Several mesh sizes can be used for defining different regions of complex structures. Also, if small details exist in a given region, the mesh can easily be locally refined.[29] Different boundary conditions can be imposed at the output borders of the mesh: free displacements or free stresses, but also continuity of specific displacement or stress components if regions are connected together.

C. Excitation—Response—Processing

Stresses, displacements, changes in temperature, or many other types of excitation can be defined as functions of the spatial coordinates. These functions can be input either as closed form solutions or set from data files containing their numerical values. In the current study, two types of excitation have been used: temperature rise or displacement loads. These will be detailed further in sections corresponding to each specific case.

Complex displacements and stresses at every node of the mesh are predicted, as the response of a structure to a given excitation. These output data can directly be plotted in different forms using a graphic interface. They also can be stored in specific files for further processing. In the current study, the responses of bars or plates to series of frequencies are modeled and analyzed. Temporal inverse Fourier transform is used for obtaining the temporal waveforms at specific locations in the structure. Direct spatial Fourier transform is used, too, for quantifying the phase velocity or attenuation of waves. This is explained in Sec. V B 2.

V. RESULTS

A. Viscoelastic bar

In order to validate the finite element predictions for a viscoelastic material submitted to either a mechanical load or a temperature rise, it is necessary to perform calculations in cases where the exact solutions are known. This is possible for one-dimensional problems when the excitation and boundary conditions are quite simple.

1. Mechanical excitation

Let us consider the bar which is described in Sec. II A. It is submitted to a mechanical harmonic excitation at one end ($x=0$ mm), the other end ($x=200$ mm) being either free or rigidly clamped. The differential equation of motion for the bar is

$$\rho\frac{\partial^2 u}{\partial t^2}=(E'+iE'')\frac{\partial^2 u}{\partial x^2}. \tag{15}$$

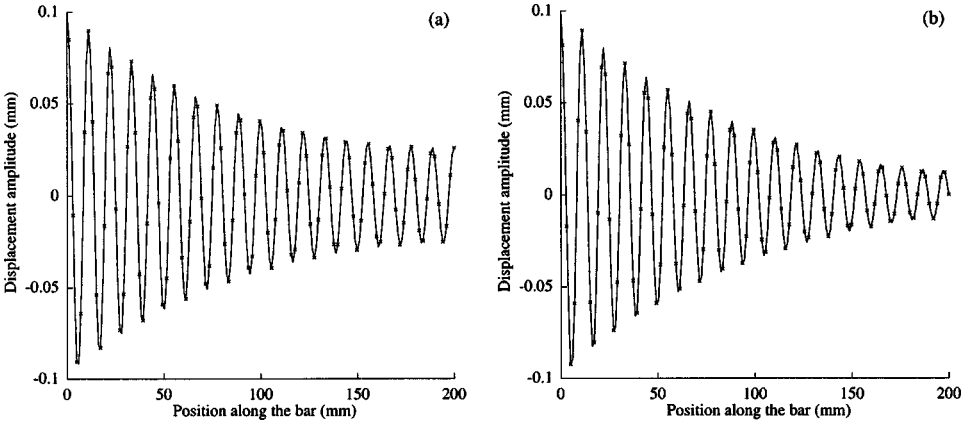

FIG. 1. Displacement amplitudes along the (a) free-end bar and (b) fixed-end bar; solutions from analytical model (———) and finite element predictions (×××).

For harmonic displacement, the solution is

$$u(x,t)=U(x)e^{i\omega t}, \tag{16}$$

so that the bar-wave equation becomes

$$-\omega^2\rho U=(E'+iE'')\frac{\partial^2 U}{\partial x^2}. \tag{17}$$

The square of the complex wave-number $k^*=k'+ik''$ associated to the bar wave is

$$(k^*)^2=\frac{\rho\omega^2}{E'}\left(\frac{1-i\varepsilon}{1+\varepsilon^2}\right), \tag{18}$$

where $\varepsilon=E''/E'$. Then, the analytical solution for wave propagation towards the positive x values in an infinite bar is

$$U(x)=Ae^{(-k''+ik')x}. \tag{19}$$

Since the bar considered in this study is of finite length, the solution must include both forwards and backwards traveling waves, i.e.,

$$U(x)=A_1e^{(-k''+ik')x}+A_2e^{(k''-ik')x}. \tag{20}$$

The frequency of the harmonic excitation is 150 kHz and its amplitude is equal to 0.1 mm. A number of 240 Lagrange quadratic elements have been used for meshing the bar. As shown in Fig. 1, excellent agreements are obtained between the finite element predictions and the analytical solutions of the displacement $U(x)$ along the bar, both for the free-end and fixed-end cases.

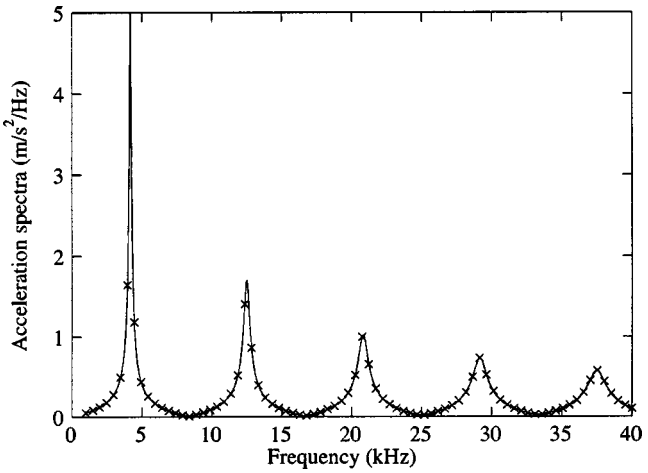

FIG. 2. Acceleration spectra for PVC bar submitted to a rapid temperature rise; solutions from analytical model (———) and finite element predictions (×××).

2. Thermal excitation

The same bar as that used in the previous case is now submitted to a thermal load, and both of its ends are free. It is assumed that the material is uniformly heated during a time τ and that the heat conduction is neglected. In this case, the exact solution is known.[4] Then, the temperature rise is

$$\theta(x,t)=\begin{cases}0 & \text{for } t<0,\\ \theta_{\max}\times\dfrac{t}{\tau} & \text{for } 0<t<\tau,\\ \theta_{\max} & \text{for } t>\tau.\end{cases} \tag{21}$$

This function is not time-limited contrary to its derivative. The Fourier transform of the time derivative of $\theta(x,t)$ is given by

$$\tilde{\theta}(x,\omega)=\begin{cases}\theta_{\max}\times\dfrac{1}{i\omega\tau}(1-e^{-i\omega\tau}) & \text{for } \omega\ 0,\\ \theta_{\max} & \text{for } \omega=0.\end{cases} \tag{22}$$

It is assumed that the maximum temperature rise is $\theta_{\max}=1\,^{\circ}\mathrm{C}$ and $\tau=1\ \mu\mathrm{s}$. According to the frequency range of the excitation, the mesh consists of 31 nodes and 30 one-dimensional elements. The numerical and exact solutions are presented in Fig. 2. In order to compare with Ref. 4, the FE predicted and exact spectra of the acceleration, i.e., $|\omega^2U|$, at the end of the heated bar are plotted. Both solutions are very close in the chosen frequency range.

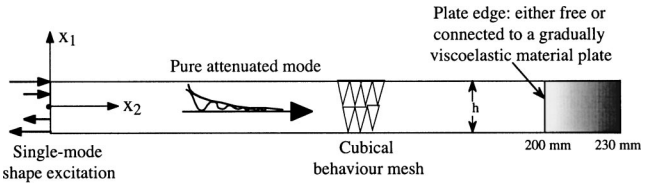

FIG. 3. Schematic of pure mode excitation along a viscoelastic material plate connected to a gradually absorbing extra plate.

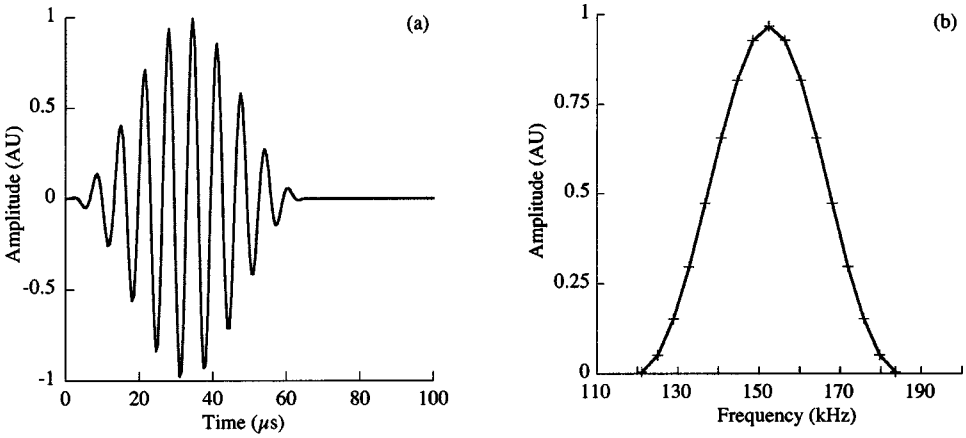

FIG. 4. Excitation used for launching the pure s_0 mode along the Perspex plate; (a) temporal waveform and (b) frequency spectrum (crosses indicate discrete frequency components).

B. Viscoelastic plates

The Perspex and composite plates described in Sec. II are now considered. Two kinds of excitation have been applied to the left-hand side ($x_2=0$) of these viscoelastic plates: (1) a specific through-thickness displacement field suitable for launching a single Lamb mode along the Perspex plate and (2) a uniform through-thickness displacement field suitable for launching several guided modes along either the Perspex or the composite plate. In all the cases, the two surfaces of the plates were free of stress. The end opposite to that which is excited is either a free or absorbing like boundary, as explained further.

1. Single-mode excitation

The 4-mm-thick, 200-mm-long Perspex plate is considered (Fig. 3). A Hanning-windowed, ten-cycle signal centered at 150 kHz [Fig. 4(a)] is suitable for exciting a pure s_0 Lamb mode along this plate. The frequency spectrum of such temporal waveform is quite narrow, and 17 frequencies are sufficient to represent the excitation [Fig. 4(b)].

The first FE calculation of the response of the plate was made considering its right-hand side as a stress-free edge. According to the smallest wavelength of the s_0 mode ($\approx$10 mm), in the frequency range of the excitation, the plate was meshed by 280 triangular elements (two elements through the plate thickness). Complex displacements were predicted in both directions x_1 and x_2 for the whole set of nodes. This run lasted less than 1 min on a 1.45 GHz, bi-processors, G4 Macintosh. Temporal waveforms were then reconstructed for several node positions, by applying an inverse FFT to the set of harmonic displacements predicted for the 17 frequency components of the input. As an example, Fig. 5(a) shows the signal corresponding to normal displacement predicted at position $x_2=135$ mm. This temporal response shows that the viscoelastic material properties have a strong effect on the wave propagation since the s_0 mode reflected by the free edge of the plate has an amplitude of about 25% that of the incident mode. These two amplitudes should be equal if the material was purely elastic.

A second FE run was made attempting to eliminate the reflection from the right-hand side of the plate, i.e., by modeling the plate as semi-infinite in the positive x_2 direction. Totally nonreflecting boundary conditions or specialized finite elements are unavailable for waves propagating along guides, at least according to the investigated literature. However, a solution has recently been proposed for eliminating the reflections of guided modes from plate-edges.[30] This consists in adding several absorbing regions contiguously to the end of the plate. The stiffness matrix (that in the equation of dynamic equilibrium) for each of these regions is rendered complex by adding to its initial real part an artificial imaginary part that gets bigger as the region is far from the edge of the plate. The absorber presented in this paper uses this principle of adding extra absorbing regions to one end of the plate, although some improvements are made: (1) only one region was added to the end of the plate instead of ten like in Ref. 30, thus simplifying the model, and (2) instead of rendering complex the stiffness matrix which appears in the equation of dynamic equilibrium, and which is not always easily accessible in commercialized software, the imaginary parts of the material viscoelastic moduli, which are required input data, were defined as exponentially increasing with the

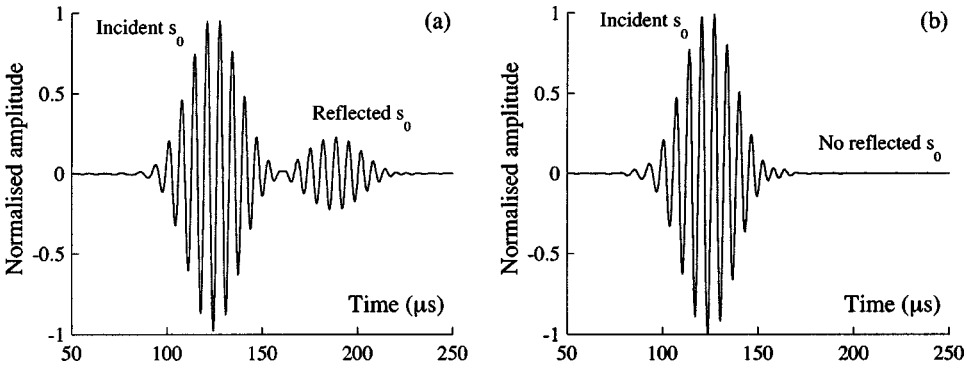

FIG. 5. Temporal waveforms corresponding to the normal-displacement at position $x_2=135$ mm at one surface of the Perspex plate for s_0 mode propagation; (a) free plate edge and (b) with extra absorbing region.

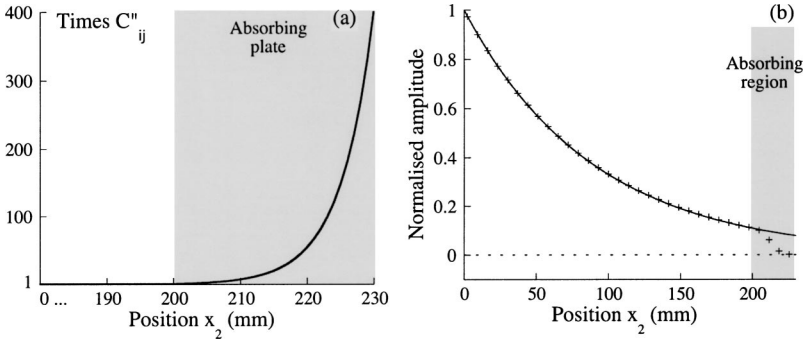

FIG. 6. Gradually absorbing extra-plate; (a) relative changes in viscoelastic properties and (b) amplitude of the surface displacement at 150 kHz, FE predictions (+++) and (———) analytical solution.

position x_2 along the absorber, using the following closed-form solution:

$$(C_{ij})_{\text{Absorber}} = (C'_{ij})_{\text{Main plate}} + \underbrace{i(C''_{ij})_{\text{Main plate}} e^{(x_2-L)/a}}_{(C''_{ij})_{\text{Absorber}}} \tag{23}$$

where $L=0.2$ m is the length of the principal plate and a is coefficient chosen so that each imaginary part C''_{ij}, at the end of the absorbing region, is around 400 times larger than its value in the principal plate ($a=0.005$ in this model), as shown in Fig. 6(a). Note that this exponential law implies absolute continuity of the two material's properties at the boundary between both regions (at $x_2=200$ mm). In this way, there is no brutal acoustic impedance mismatch between them, and so no more reflections at the end of the main plate. The absorbing region added to the end of the plate was 4 mm thick (like the plate), and 30 mm long only, as shown in Fig. 3. In this case, a number of the 328 triangular elements are defining the total mesh, and the run was 10% longer than that with no absorbing region. The predicted amplitude of the surface normal-displacement is shown in Fig. 6(b). As expected, it exponentially decreases from positions $x_2=0$ to 200 mm according to the simple law $e^{-k'x_2}$, where k'' is the attenuation of the s_0 pure mode at 150 kHz ($k''=0.011\,\text{mm}^{-1}$) propagating along an infinitely long plate. Then, in the absorbing region, i.e., from $x_2=200$ to 230 mm, this amplitude drastically diminishes and tends towards zero. Consequently, no s_0 mode propagates backwards along the main plate, as it is confirmed by the temporal waveform shown in Fig. 5(b).

2. Multi-mode excitation

Both Perspex and composite plates described in Sec. II are now acted by a harmonic, uniform displacement along the x_1 direction, at position $x_2=0$ (Fig. 7). By opposition to the single mode shape excitation used in Sec. V B 1, this piston like input is suitable for launching several guided modes along the plates. The temporal excitation and the mesh are different depending on the plate that is considered, and will be described further. For each case, the complex normal displacements are predicted for a series of positions along the x_2 direction, at one plate surface. As before, this process is repeated for each frequency component of the input, thus supplying a set of output data, noted $\tilde{u}_1(x_2,f)$ as in (8). A specific signal processing is then applied to these FE data to recover the wave numbers and attenuations of the various guided modes propagating along the plates. First, a standard spatial FFT is applied to transform the $\tilde{u}_1(x_2,f)$ output data into a *wave-number−frequency* diagram, noted $\tilde{u}_1(k,f)$. Then, it is straightforward to plot the wave-number, k_m, versus frequency, for each mode m propagating along the plate. Finally, the spatial FFT process is applied to two sets of output data, $\{\tilde{u}_1(x_2,f)\}^I$ and $\{\tilde{u}_1(x_2,f)\}^{II}$, obtained for two series of points centred at positions x_2^I and x_2^{II}, respectively (Fig. 7). The two *wave-number−frequency* diagrams thus obtained, $\{\tilde{u}_1(k,f)\}^I$ and $\{\tilde{u}_1(k,f)\}^{II}$, allow the attenuation of each mode m to be easily quantified, using the following relation:

$$k''_m = \frac{2}{(x_2^I - x_2^{II})} \text{Ln}\left|\frac{\{\tilde{u}_1(k_m,f)\}^{II}}{\{\tilde{u}_1(k_m,f)\}^I}\right|. \tag{24}$$

This technique is very convenient for processing displacement data corresponding to the coexistence of several modes.

a. Perspex plate. The temporal excitation is a Gaussian-windowed, three-cycle toneburst having a frequency spectrum centred at 150 kHz with −15-dB points at 50 and 250 kHz. This spectrum is decomposed into 58 spectral components by Fourier transforming the temporal excitation. Each of these components will then be a harmonic excitation for the FE model. According to the smallest wavelength ($\lambda_{\min} \approx 5$ mm) in the frequency range of interest, a number of 1120 triangular third-order elements are forming the mesh (four elements through the plate thickness). The whole FE run supplying complex displacements at each node of the mesh lasted 6 min on the bi-processors G4 machine. A selection of these output data, corresponding to positions $x_2=0$ to 150 mm along the plate surface, every 1 mm, was then used to quantify the wave-numbers and attenuations of the various modes, according to the signal processing described above. As shown in Fig. 8, very good agreement is obtained between the FE predictions and the analytical solutions, for both the wave-number and the attenuation results.

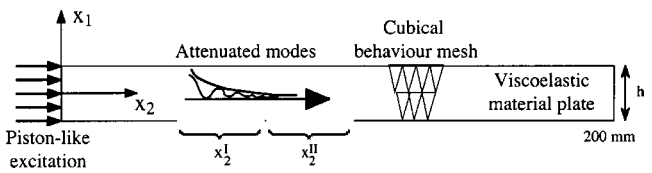

FIG. 7. Schematic of multi-mode excitation along a viscoelastic material plate.

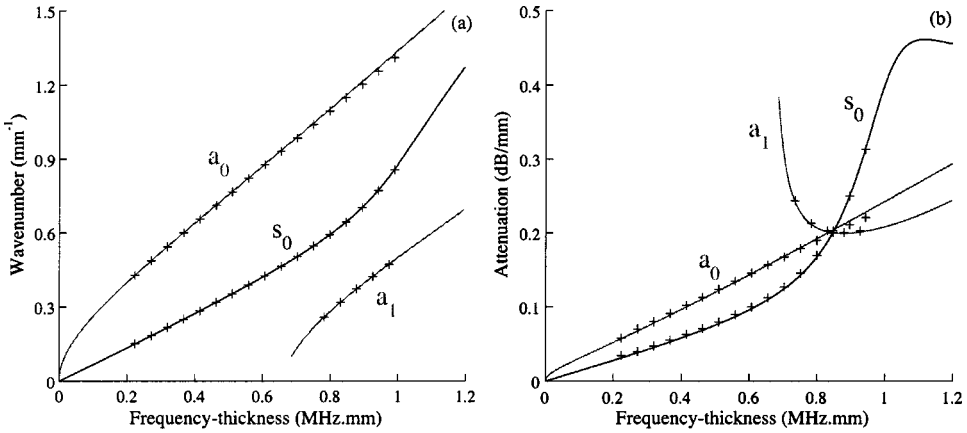

FIG. 8. Lamb waves dispersion curves for Perspex plate; (a) real wavenumber and (b) attenuation; solutions from analytical model (———) and finite element predictions and processing (+++).

b. Glass epoxy plate. The temporal excitation is a Gaussian-windowed, six-cycle toneburst having a frequency spectrum centred at 300 kHz with −20-dB points at 200 and 400 kHz. This spectrum is decomposed into 53 spectral components by Fourier transforming the temporal excitation. Each of its components is then a harmonic excitation for the FE model. According to the smallest wavelength ($\lambda_{\min} \approx 4$ mm) in the frequency range of interest, a number of 2267 triangular third-order elements are forming the mesh (eight elements through the plate thickness). The whole FE run supplying complex normal displacements at each node of the mesh lasted 7.5 min. A selection of these output data, corresponding to positions $x_2 = 0$ to 150 mm along the plate surface, every 0.8 mm, was then used to quantify the wavenumbers and attenuations of the various modes, according to the signal processing previously described. As shown in Fig. 9, the simultaneous propagation of five Lamb modes has been successfully modeled. Even if the plate response is made of symmetric modes, s_0, s_1 and s_2, and antisymmetric modes, a_0 and a_1, the processed wave-numbers and attenuations agree remarkably well with the analytical solutions. The complexity of this example proves the robustness of the output data processing, as well as the efficiency of the FE software to model wave propagation in anisotropic, viscoelastic materials.

VI. CONCLUSION

The numerous technical applications involving thermo-viscoelastic materials require robust numerical tools for simulating the dynamic behavior of such media. In this paper, a commercially available finite element (FE) software[24] has been used for modeling the propagation of waves guided along viscoelastic bars or plates, in stationary mode, which is suitable for modeling structures' responses to harmonic excitations. First, the constitutive relations for thermal, anisotropic, viscoelastic materials have been implemented in a specific format of partial differential equations (PDEs). In the Fourier domain, these equations involve complex moduli that represent the viscoelastic material properties. Then, the frequency spectra of various temporal excitations have been calculated using the standard Fourier transform $\int_{-\infty}^{\infty} f(t) e^{-i\omega t}\, dt$. Specific frequency loops have then been defined for solving the PDE for each frequency component of either mechanical or thermal excitations. This use of the FE method constitutes a fast and efficient way to predict the dynamic behavior of thermal, anisotropic, viscoelastic materials. Both complex displacements and stresses at any location in the structures can be predicted.

The 1-D and 2-D cases have been investigated for modeling the propagation of waves along bars or plates. Specific signal processing was applied to the output displacement data to quantify the characteristics of the wave modes propagating along these elements. The responses of a PVC bar to either a temperature rise or a displacement load at one end were modeled and successfully compared to analytical solutions. The responses of an isotropic Perspex plate and of an anisotropic glass-epoxy plate to displacement loads have also been modeled and successfully compared to analytical solu-

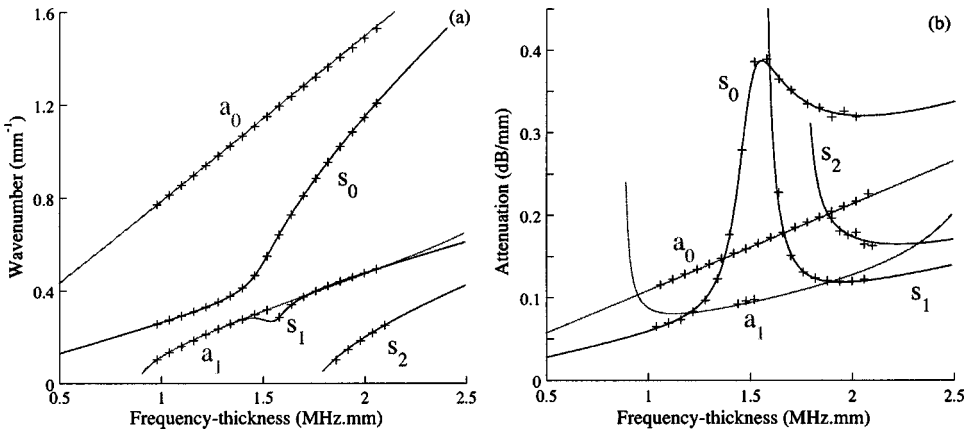

FIG. 9. Lamb waves dispersion curves for composite plate made of unidirectional glass fibers and epoxy matrix; (a) real wave-number and (b) attenuation; solutions from analytical model (lines) and finite element predictions and processing (+++).

tions. In all cases, the material viscoelasticity was shown to be properly taken into account in these FE models, whether a single mode propagates or several modes coexist. An efficient way to eliminate reflections from plate edges that can sometimes be unwanted has also been proposed. This consists in simulating a short media connected at the edge of the main structure, and having viscoelastic properties that exponentially increase with the distance away from this edge. No brutal acoustic impedance mismatch exists between the two connected media, and the amplitude of waves incoming into the absorber quickly dropped down to zero. Working in the Fourier domain rather than in the more conventional temporal domain leads to FE calculations shorter than 10 min on a 1.45-GHz, bi-processor, G4 Macintosh, for all the cases considered in this study. In addition to the physical interest, which consists in using measured viscoelastic material properties as input data, the FE computations run in the frequency domain are much faster than if they were run in the temporal domain since fewer iterations are involved.

The efficiency of the graduated, highly absorbing region shows the potentiality of this technique to simulate large structures using small numbers of elements, like for example infinitely long plates. Isolated regions with defects could also be modeled without the necessity of meshing large domains for avoiding reflections from edges. Introducing properly the anisotropic and viscoelastic material properties will allow FE modeling polymer-based composite structures, and especially the simultaneous propagation of several wave modes having different attenuations. Predicting the diffraction of waves by defects in such composite structures is therefore one of the objectives.[29] Finally, the high-speed performances of the FE code offers the possibility of automatically changing the geometry (size, position, shape) of the flaws, thus opening the way to solve inverse problems.

[1] W. Flüge, *Viscoelasticity*, 2nd ed. (Springer-Verlag, Berlin, 1975).
[2] J. D. Ferry, *Viscoelastic Properties of Polymers* (Wiley, New York, 1980).
[3] R. M. Christensen, *Theory of Viscoelasticity: An Introduction* (Academic, New York, 1971).
[4] C. Bacon, B. Hosten, and P. A. Bernard, ''Acoustic wave generation in viscoelastic rods by time-gated microwaves,'' J. Acoust. Soc. Am. **106**, 195–201 (1999).
[5] J. P. Charlier and F. Crowet, ''Wave equations in linear viscoelastic materials,'' J. Acoust. Soc. Am. **79**, 895–900 (1986).
[6] R. T. Weaver, W. Sachse, and L. Niu, ''Transient ultrasonic waves in a viscoelastic plate: Theory,'' J. Acoust. Soc. Am. **85**, 2255–2261 (1989).
[7] C. W. Chan and P. Cawley, ''Lamb waves in highly attenuative plastic plates,'' J. Acoust. Soc. Am. **104**, 874–881 (1998).
[8] A. Bernard, M. J. S. Lowe, and M. Deschamps, ''Guided waves energy velocity in absorbing and nonabsorbing plates,'' J. Acoust. Soc. Am. **110**, 186–196 (2001).
[9] M. Castaings and B. Hosten, ''Guided waves propagating in sandwich structures made of anisotropic, viscoelastic, composite materials,'' J. Acoust. Soc. Am. **113**, 2622–2634 (2003).
[10] M. Lowe, P. Cawley, J. Y. Kao, and O. Diligent, ''The low frequency reflection characteristics of the fundamental antisymmetric Lamb wave a_0 from a rectangular notch in a plate,'' J. Acoust. Soc. Am. **112**, 2612–2622 (2002).
[11] A. H. Harker, ''Numerical modeling of the scattering of elastic waves in plates,'' J. Nondestruct. Eval. **4**(2), 89–106 (1984).
[12] M. Koshiba, S. Karakida, and M. Suzuki, ''Finite-element analysis of Lamb wave scattering in an elastic plate waveguide,'' IEEE Trans. Sonics Ultrason. **SU-31**(1), 18–25 (1984).
[13] S. W. Liu and S. K. Datta, ''Scattering of ultrasonic wave by cracks in plate,'' ASME J. Appl. Mech. **60**(3), 352–357 (1993).
[14] J. Paffenholz, J. W. Fox, X. Gu, G. S. Jewett, S. K. Datta, and H. A. Spetzler, ''Experimental and theoretical study of Rayleigh-Lamb waves in a plate containing a surface-breaking crack,'' Res. Nondestruct. Eval. **1**, 197–217 (1990).
[15] S. W. Liu, S. K. Datta, and T. H. Ju, ''Transient scattering of Rayleigh-Lamb waves by a surface-breaking crack: comparison of numerical simulation and experiment,'' J. Nondestruct. Eval. **10**(3), 111–126 (1991).
[16] L. Wang and J. Shen, ''Scattering of elastic waves by a crack in an isotropic plate,'' Ultrasonics **35**(6), 451–457 (1997).
[17] W. M. Karunasena, A. H. Shah, and S. K. Datta, ''Plane-strain-wave scattering by cracks in laminated composite plates,'' ASCE J. Eng. Mech. **117**(8), 1738–1754 (1991).
[18] Y. Cho and J. L. Rose, ''An elastodynamic hybrid boundary element study for elastic guided wave interactions with a surface-breaking defect,'' Int. J. Solids Struct. **37**(30), 4103–4124 (2000).
[19] J. L. Rose, W. Zhu, and Y. Cho, ''Boundary element modeling for guided wave reflection and transmission factor analyses in defect classification,'' Proc. IEEE Ultrason. Symp. **1**, 885–888 (1998).
[20] L. Jiang and J. B. Haddow, ''A finite element solution of plane wave propagation in inhomogeneous linear viscoelastic solids,'' J. Sound Vib. **184**(3), 429–438 (1995).
[21] Z. You, M. Lusk, R. Ludwig, and W. Lord, ''Numerical simulation of ultrasonic wave propagation in anisotropic and attenuative solid materials,'' IEEE Trans. Ultrason. Ferroelectr. Freq. Control **38**(5), 436–445 (1991).
[22] P. Stucky and W. Lord, ''Finite element modeling of ultrasonic waves in viscoelastic media,'' Rev. Prog. QNDE, edited by D. O. Thompson and D. E. Chimenti (Plenum, New York), **16A**, 113–120 (1997).
[23] A. Alshaikh, D. Turhan, and Y. Mengi, ''Propagation of transient out-of-plane shear waves in viscoelastic layered media,'' Int. J. Mech. Sci. **43**, 2911–2928 (2001).
[24] FEMLAB—Comsol AB. Reference Manual, 2002.
[25] M. Castaings, B. Hosten, and T. Kundu, ''Inversion of ultrasonic, plane-wave transmission data in composite plates to infer viscoelastic material properties,'' NDT & E Int. **33**(6), 377–392 (2000).
[26] B. Hosten and M. Castaings, ''Transfer matrix of multilayered absorbing and anisotropic media. Measurements and simulations of ultrasonic wave propagation through composite materials,'' J. Acoust. Soc. Am. **94**, 1488–1495 (1993).
[27] S. Baudoin and B. Hosten, ''Immersion ultrasonic method to measure elastic constants and anisotropic attenuation in polymer-matrix and fiber-reinforced composite materials,'' Ultrasonics **34**, 379–382 (1996).
[28] http://www.matls.com/
[29] B. Hosten, M. Castaings, ''FE modeling of the S_0 Lamb mode diffraction by a notch in a viscoelastic material plate,'' *Emerging Technolgies in NDT*, edited by D. Van Hemelrijck, A. Anastasopoulos and N. E. Melanitis, p. 3–7, 2004.
[30] G. R. Liu and S. S. Quek Jerry, ''A non-reflecting boundary for analysing wave propagation using the finite element method,'' Finite Elem. Anal. Design **39**, 403–417 (2003).

Experimental studies of a thermoacoustic Stirling prime mover and its application to a cooler

Y. Ueda,[a] T. Biwa, and U. Mizutani
Department of Crystalline Materials Science, Nagoya University, Nagoya 464-8603, Japan

T. Yazaki
Department of Physics, Aichi University, Kariya 448, Japan

(Received 15 August 2003; revised 19 December 2003; accepted 28 December 2003)

An acoustic field spontaneously induced in a thermoacoustic prime mover consisting of a looped tube and resonator is determined through simultaneously measurements of pressure P and velocity U. A thermal efficiency of the thermoacoustic prime mover of this type has been reported to reach 30%. The measurements of the acoustic field in the present system revealed that a phase lead of U relative to P takes a negative value of about $-20°$ in the regenerator where the output power of the prime mover is generated. It was concluded that the possession of a negative phase lead at this position is taken as a clue in a significant increase in the output power. Moreover, the analysis in the thermoacoustic mechanism shows that a precise position for the location of a second regenerator acting as a heat pump exists in the looped tube. Indeed, by locating the second regenerator at the position, a thermoacoustic cooler was constructed. The thermoacoustic cooler could generate a low temperature of $-25\,°C$ without involving any moving parts. © *2004 Acoustical Society of America.* [DOI: 10.1121/1.1649333]

PACS numbers: 43.35.Ud [RR] Pages: 1134–1141

I. INTRODUCTION

A conventional internal-combustion prime mover such as a car engine has many mechanical parts like pistons, valves, etc. An efficient energy conversion can be achieved, only if these mechanical parts are properly tuned. This requires high maintenance- and production costs. On the other hand, a thermoacoustic prime mover can perform an efficient energy conversion without nuisance mechanical parts.

A thermoacoustic prime mover is composed of a regenerator, two heat exchangers, and a tube. Here, the regenerator is sandwiched by the heat exchangers in the tube. When a steep temperature gradient is set up along the regenerator by the heat exchangers, an acoustic wave accompanying pressure

$$P = pe^{i\omega t}, \tag{1}$$

and cross-sectional mean velocity

$$U = u^{i(\omega t+\Phi)}, \tag{2}$$

is spontaneously generated in the tube, where ω is an angular frequency and Φ is a phase lead of U relative to P. The spontaneously generated acoustic wave forces a gas parcel in the regenerator to experience a thermodynamic cycle consisting of the compression, heating, expansion, and cooling. As a result, the energy conversion of heat flow Q into work flow I occurs without involving moving parts.[1–4]

Thermoacoustic prime movers are classified into two types depending on the value of the phase lead Φ; one is a standing wave thermoacoustic prime mover and the other is a traveling wave one. In a standing wave prime mover, a gas parcel with Φ nearly equal to $\pi/2$ contributes to the energy conversion through irreversible thermal contacts with wall in a regenerator. We call this phase lead ($\Phi=\pi/2$) the *standing wave phase*. Many prime movers of this type have been constructed[5,6] and used for operating a refrigerator to liquefy natural gas.[7] However, their thermal efficiencies are at best[8] 20% because their energy conversion is based on the irreversibility.[1]

A traveling wave thermoacoustic prime mover was originally proposed by Ceperley in 1979.[9] In this prime mover, a gas parcel with Φ nearly equal to zero contributes to the energy conversion through reversible thermal contacts with wall in a regenerator. This phase lead ($\Phi=0$) is called the *traveling wave phase*. In order to gain a deeper insight into details of a thermodynamic cycle performed in the traveling wave prime mover, we attempt to elucidate the relation between pressure P and cross-sectional mean displacement ζ under the condition $\Phi=0$. This is illustrated in Fig. 1(a). Since ζ is always out of phase with the velocity U by $\pi/2$, it is also out of phase with P by $\pi/2$. When a gas parcel with $\Phi=0$ locally makes isothermal contacts with wall in a regenerator, where a finite temperature gradient exists as shown in Fig. 1(b), it would undergo the thermodynamic cycle of four stages: (1) the gas parcel is pressurized around the cold end (compression); (2) moves to the hot end (heating); (3) is depressurized around the hot end (expansion); and (4) moves back to the cold end (cooling). Ceperley pointed out that this thermodynamic cycle is essentially the same as that performed in a conventional Stirling prime mover. Since a conventional Stirling prime mover has a thermal efficiency of 20%–38%,[10] he considered that a traveling wave thermoacoustic prime mover can in principle have a high efficiency without any moving parts. However, it had not been realized until 1998, when Yazaki *et al.* succeeded for the first time in constructing a traveling wave thermoacoustic prime mover by using a looped tube.[11] Yazaki *et al.*

[a]Electronic mail: ueda@mizu.xtal.nagoya-u.ac.jp

 0001-4966/2004/115(3)/1134/8/$20.00

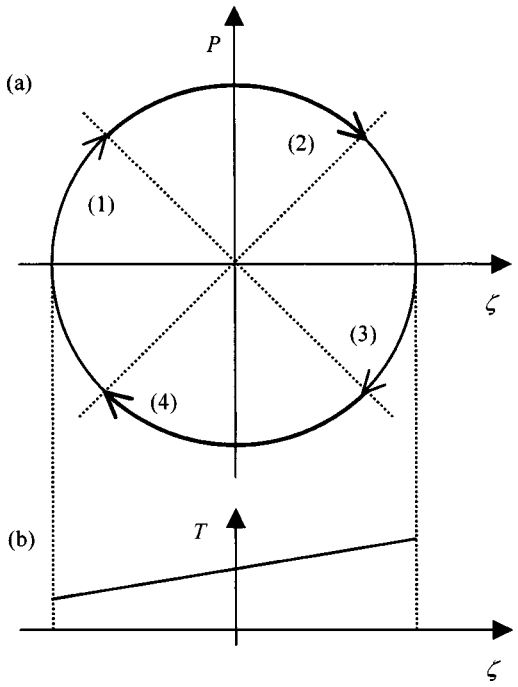

FIG. 1. (a) Relation between pressure P and displacement ζ with the traveling wave phase. (b) Temperature gradient in a regenerator.

simultaneously measured both P and U in the acoustic field induced in the looped tube prime mover, and found that its phase lead Φ was close to a traveling wave phase ($\Phi=0$) in the regenerator.

In 1999, Backhaus and Swift upgraded a thermal efficiency up to 30% by introducing a resonator in a looped tube.[8] The efficiency has reached a level comparable to that of a car engine.[10] They attribute such a high efficiency to the fulfillment of the two conditions. One is the possession of the traveling wave phase and the other is that of a high value of a dimensionless acoustic impedance z defined as

$$z=\frac{P/P_m}{U/c}, \tag{3}$$

where P_m is a mean pressure and c is the adiabatic sound speed. If a free-traveling acoustic wave, whose Φ is always zero, is generated in a thermoacoustic prime mover, the acoustic impedance z would be fixed at the specific heat ratio $\gamma=c_p/c_v$, where c_p and c_v are specific heat of the gas at constant pressure and volume, respectively. The low value of z ($=\gamma$) would lead to significant viscous losses in a regenerator because of the motion of the gas with a high velocity. In order to reduce the viscous losses, z should be increased far beyond the value of γ. Though they stressed the importance of these two conditions above to achieve a high efficiency, the values of Φ and z in their prime mover have not been experimentally determined.

This paper describes an attempt in the optimization of the feature size of the Backhaus and Swift-style thermoacoustic prime mover so as to generate an intense acoustic wave, and presents the values of Φ and z determined by simultaneous measurements of P and U in the prime mover. Their preliminary data were already reported.[12] We show from the present data that the energy conversion from heat flow Q into work flow I is performed in the regenerator by a gas parcel having an acoustic impedance large enough to suppress viscous losses. Its phase lead Φ, however, turns out to be negative rather than zero corresponding to a pure traveling wave phase. We demonstrate below that the possession of a negative value of the phase lead in a regenerator plays a key role in producing the output power of the present prime mover.

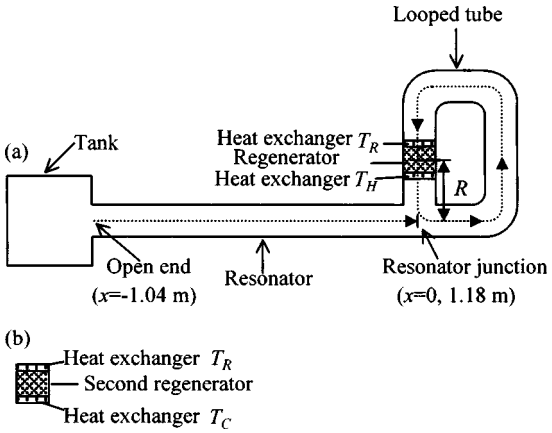

FIG. 2. (a) Thermoacoustic Stirling prime mover consisting of a looped tube and a resonator. A regenerator sandwiched by two heat exchangers is located in the looped tube. (b) Regenerator working as a thermoacoustic heat pump. Two heat exchangers are located on its both ends.

In the second part of the present work, a construction of a thermoacoustic Stirling cooler driven by the present prime mover is reported. The experimental results obtained from the simultaneous measurements of P and U allow us to pinpoint the position where the reversed Stirling cycle can be executed. Indeed, by locating a second regenerator acting as a heat pump at this particular position, we could construct the cooler without involving any moving parts. It could generate $-25\,^{\circ}\mathrm{C}$ and have a cooling power of 11 W at $0\,^{\circ}\mathrm{C}$ when an input heat power was 210 W.

II. THERMOACOUSTIC STIRLING PRIME MOVER

A. Apparatus

The present thermoacoustic prime mover, as schematically illustrated in Fig. 2(a), is composed of a looped tube and resonator made of Pyrex glass tubes. They are 40 mm in inner diameter and are filled with atmospheric air. One end of the resonator, which is hereafter referred to as the resonator junction, is joined with the looped tube. The other end, called the open end of the resonator, is connected to a 2.0×10^{-2}-m^3 tank. Pressure transducers are installed on the wall of both looped tube and resonator. The direction of gravity is headed from upper to lower sides in Fig. 2(a).

A regenerator of 35 mm in length is made of a stack of 60-mesh stainless-steel screens with a wire diameter of 0.12 mm and is located in the looped tube, as shown in Fig. 2(a). From the measurement of porosity of the regenerator, we estimated its hydraulic radius[13] to be 0.13 mm. This is much smaller than the thermal penetration depth[14] δ_t formed at the wall and, thus, we consider that a good thermal contact between a gas parcel and wall of the screens is ensured throughout the present work. The two heat exchangers,

where brass plates 0.5 mm in thickness and 10 mm in height are placed at 0.5-mm intervals, are located on both sides of the regenerator. One is water-cooled and kept at room temperature T_R. The other is heated by an electrical resistance heater wound around it, and its temperature T_H is controlled by the heater power Q_H up to 210 W.

B. Optimization to generate an intense acoustic wave

The performance of the present apparatus was tested by varying the total length of the looped tube L_l, the length of the resonator L_r, and the distance R from the resonator junction to the center of the regenerator [see Fig. 2(a)]. When Q_H exceeded some critical value Q_{cri}, a gas oscillation spontaneously generated in the setup with all combinations of L_l, L_r, and R we tested. The wavelength λ of the acoustic wave thus generated was estimated from its frequency, and it was found that λ is essentially four times as long as the sum of L_l and L_r. Hence, we call the acoustic oscillation the quarter-wavelength mode, which is the same as that induced in the Backhaus and Swift prime mover.[8] As Q_H was increased beyond Q_{cri}, the amplitude of the acoustic oscillation was also increased. We measured the position dependence of the pressure amplitude when $Q_H = 210$ W. It was found that the pressure node and antinode always appear near the open end of the resonator and the cold end of the regenerator, respectively, regardless of the combinations of L_l, L_r, and R. However, the magnitude of the pressure amplitude p_{an} at the antinode turns out to depend on the combination. Backhaus and Swift have carefully shaped a diameter of their looped tube to generate the acoustic wave having the pressure amplitude of 10% of a mean pressure based on an idealized lumped element equivalent.[8] In the present work, an intense acoustic wave is obtained by using the tube with a uniform inner diameter and experimentally optimizing the combination of L_l, L_r, and R.

We measured p_{an} at the pressure antinode under the condition such that R and L_r were varied while $L_l = 1.74$ m. The results are shown in Fig. 3(a). The value of p_{an} as a function of L_r shows a peak at a given R. The peak value is found to increase with decreasing R. Therefore, R was fixed at the smallest attainable value of 0.27 m. In other words, the hot end of the regenerator was located at the position as close to the resonator junction as possible.

The value of L_l was then optimized under the condition $R = 0.27$ m. In Fig. 3(b), the measured p_{an} is plotted as a function of L_r under different values of L_l. Note that the data shown in Fig. 3(b) with closed circles are the same as those in Fig. 3(a) with the same symbol. As can be seen in Fig. 3(b), p_{an} at the peak can be further enhanced as L_l decreases. The largest value of p_{an} reached was 8.6 kPa, corresponding to 8.5% of the mean pressure, when $L_l = 1.18$ m and $L_r = 1.35$ m were chosen.

As indicated by two arrows in Fig. 3(b), the magnitude of p_{an} sharply decreases when $L_l = 1.18$ m and $L_r = 1.4$–1.5 m, and $L_l = 1.34$ m and $L_r = 1.6$–1.8 m. We experimentally found that two acoustic modes were simultaneously excited in the present prime mover with these two combinations. They are the quarter-wavelength and one-wavelength modes,[15] in the latter of which the acoustic wave having $\lambda = L_l$ is excited. Hence, the sharp decreases of p_{an} are attributed to the competition[16] between these two modes. In order to avoid an excitation of the one-wavelength mode, we finally adopted L_l, L_r, and R of 1.18, 1.04, and 0.27 m, respectively. The present prime mover thus optimized generates the spontaneous acoustic oscillation with the frequency $f = 41$ Hz when Q_H is increased beyond 56 W ($T_H > 210\,^{\circ}$C). The pressure amplitude p_{an} becomes 8.3 kPa when Q_H reaches 210 W.

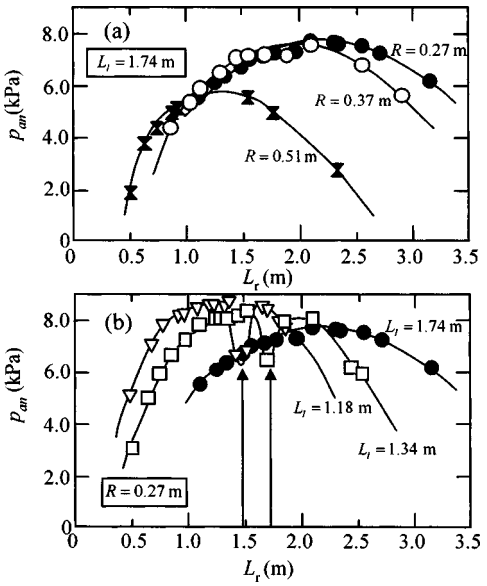

FIG. 3. The pressure amplitude p_{an} at the pressure antinode as a function of the resonator length L_r with (a) given distances R and (b) given looped tube lengths L_l. Curves are drawn to guide for the eye.

C. Simultaneous measurements of pressure and velocity

In order to reveal the mechanism of the thermoacoustic energy conversion between I and Q, we measured both velocity and pressure[17,18] in the present prime mover. The axial velocity was measured with a laser Doppler velocimeter (LDV). In the LDV, two beams generated from a single laser source are crossed at the center of the tubes. The tracer particles (cigarette smoke) running together with an oscillating gas scatter light at the cross point of the beams. The light is detected by a photomultiplier as a burst signal. A frequency of the signal is converted to the voltage proportional to the velocity of the oscillating gas by a tracker-type processor. It should be noted that the tracker-type processor causes time delay in signal. We measured the time delay,[18] and found it to be 2.7×10^{-5} s in the present experiments.

The pressure $P = pe^{i\omega t}$ was measured with a series of the pressure transducers attached on the tube wall. We experimentally found that a time delay in the pressure measurements is 0.9×10^{-6} s, which can be neglected in this experiment compared with that involved in the velocity measurement. The pressure is independent of the radial direction of the tube, because their radius (=20 mm) is much smaller than the wavelength λ of the acoustic wave in the present prime mover (≃8 m).

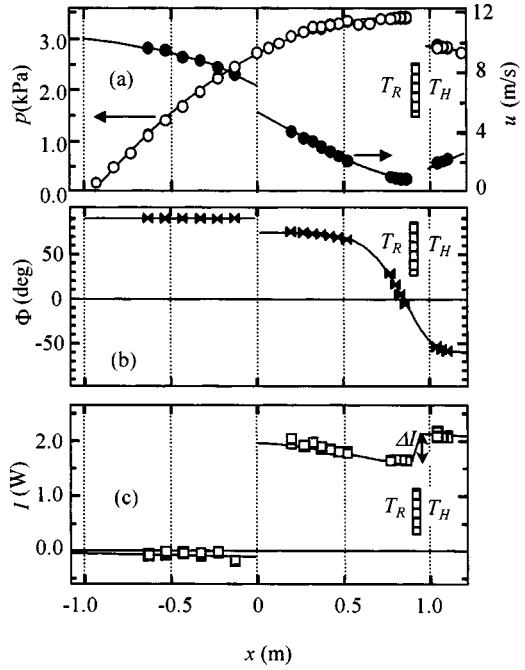

FIG. 4. Acoustic field in the thermoacoustic Stirling prime mover. The axial distribution of (a) p and u; (b) Φ; and (c) I. A hatched area represents the position of the regenerator and the lines are guides for the eye.

By taking the time delay in velocity measurements into account, we simultaneously measured pressure $P=pe^{i\omega t}$ and velocity $U_C=u_Ce^{i(\omega t+\Phi_C)}$ along a central axis of the tube, when a heat input Q_H was 83 W. The velocity changes in a radial direction in the tube because of the presence of viscosity. Hence, the cross-sectional mean velocity $U=ue^{i(\omega t+\Phi)}$ was determined from the measured U_C by applying a laminar flow theory, which provides the relations $\Phi-\Phi_C=0.99°$ and $u/u_C=1.02$ for the present experiment.[17]

D. Analysis of the measured acoustic field

The values of p, u, and Φ determined by the simultaneous measurements are plotted in Figs. 4(a) and (b) as a function of position x in the present prime mover. The resonator junction is set to be $x=0$, i.e., an origin of the coordinate shown in Fig. 2(a) and a positive direction of x is taken anticlockwise in the looped tube while it is done towards the right in the resonator.

As can be seen in Fig. 4(a), the pressure amplitude p increases whereas velocity amplitude u decreases, as x increases from -1.04 to 0.90 m. This clearly indicates that a quarter-wavelength mode was excited in the present prime mover. The phase lead Φ shown in Fig. 4(b) takes nearly 90° in the resonator ($-1.04\leqslant x\leqslant 0$), and decreases from 85° to $-60°$ with increasing x in the looped tube ($0\leqslant x\leqslant 1.18$). Both values of u and Φ show discontinuities at $x=0$, where the waveguide is separated into two, so as to satisfy the laws of conservation of energy and mass.

Figure 4(c) shows the distribution of work flow I, which is calculated by inserting the data shown in Figs. 4(a) and (b) into the following equation:

$$I=A\tfrac{1}{2}pu\cos\Phi, \tag{4}$$

where A is the cross-sectional area of a tube. A slope of I is always negative outside the regenerator, indicating the presence of energy dissipations in the looped tube (0.34 W/m) and resonator (0.1 W/m). Note that a sign of I represents its direction. The work flow I emitted from the hot end of the regenerator ($x=0.94$) is directed toward the resonator junction ($x=1.18$) and is divided into two at the resonator junction. One is delivered to the resonator to compensate for the dissipation in it. The other runs into the looped tube in the counterclockwise direction, and is fed back into the cold end of the regenerator ($x=0.90$). The work flow reaching the cold end is amplified from 1.7 to 2.2 W in the regenerator, and the amplified work flow is output from the hot end again. The amplification of I demonstrates that the energy conversion from Q into I takes place in the regenerator. The difference of the work flow between the hot and cold ends ($\Delta I=0.5$ W) represents the output power of the present prime mover sustaining the spontaneously induced acoustic field.

Now, we focus on the acoustic field near the regenerator. The phase lead Φ takes a pure traveling wave phase ($=0$) at $x=0.85$ m, i.e., the position close to the cold end of the regenerator. At this particular position, p and u take a maximum (3.4 kPa) and minimum (0.78 m/s), respectively. Hence, the dimensionless specific acoustic impedance z reaches the value 10 times as large as γ and is much larger than that observed by Yazaki[15] in the looped tube prime mover ($z\simeq 3\gamma$). The high acoustic impedance can significantly suppress viscous losses in the regenerator. The value of Φ at the center of the present regenerator is found to be about $-20°$, as obtained by interpolating the values at its both ends. This can be taken as evidence that the present prime mover generates the output power ΔI through the Stirling cycle because this value of Φ is near the traveling wave phase ($\Phi=0°$) rather than the standing wave one ($\Phi=-90°$ and 90°).

We should note two facts: (1) Φ is near the traveling wave phase and (2) its value is negative in the present regenerator. We consider that both of them are critically important in producing the output power ΔI as was discussed previously.[12] The first fact is needed to execute the Stirling cycle as mentioned above. The importance of the second one is described below. Briefly, Eq. (4) leads to the expression

$$\frac{\Delta I}{I}\simeq\frac{\Delta p}{p}+\frac{\Delta u}{u}-\tan\Phi\cdot\Delta\Phi, \tag{5}$$

where Δp, Δu, and $\Delta\Phi$ represent differences in p, u, and Φ at the hot end relative to the cold one, respectively. By inserting the experimental data shown in Fig. 4 into the three terms in the right-hand side of Eq. (5), we find that $\Delta p/p\sim-0.2$, $\Delta u/u\sim 0.7$, $-\tan\Phi\cdot\Delta\Phi\sim-0.2$ across the regenerator. This means that $\Delta I/I$ is largely gained from the second term. Its positive and large value arises from the fact that the velocity node is positioned near the cold end of the regenerator because this makes its denominator a small value but the numerator large. If the velocity node with $\Phi=0$ were positioned in the regenerator, the numerator of the second term would have also become small and, thus, the second term would have been reduced as small as the first and third terms, resulting in a much smaller ΔI. Therefore, we con-

sider that the possession of a negative Φ in a regenerator is essential for producing a large ΔI while suppressing viscous losses in a thermoacoustic Stirling prime mover equipped with a looped tube and resonator.

E. Thermal efficiency of the thermoacoustic prime mover

The present thermoacoustic Stirling prime mover turns out to have the output power ΔI of 0.5 W when $Q_H = 86$ W. Its thermal efficiency is about 0.6%. This is much smaller than that reported by Backhaus and Swift (30%). The low efficiency may be attributed to the use of atmospheric air as a working gas in the present prime mover. The use of atmospheric air is required in the present work to measure the acoustic field with LDV. On the other hand, Backhaus and Swift used helium gas with a mean pressure P_m of 3 MPa. Based on the performance of the present prime mover, we consider below what efficiency a thermoacoustic Stirling prime mover of this type will gain when such a highly pressurized gas is employed.

The work flow at the pressure antinode, where $\Phi = 0$, is obviously given from Eq. (4) as

$$I = \frac{AP_m c}{2z}\left(\frac{p}{P_m}\right)^2, \tag{6}$$

where $\cos\Phi = 1$ and $z = (p/P_m)/(u/c)$ are used. In the case of the Backhaus and Swift thermoacoustic prime mover, for example, A is 6.2×10^{-3} m^2, P_m is 3 MPa, and c is 1.0 km/s. They obtain $p/P_m = 0.1$ when the input heat power is 4.0 kW, and estimate z at 15–30 γ ($\gamma \sim 1.66$ for helium).[8] Hence, the work flow at the pressure antinode would become 3.8–1.9 kW. Assuming that this amount of the work flow running into the regenerator is amplified by the ratio $\Delta I/I = 0.3$ in the same way as that in the present prime mover, we can evaluate the output power to be 1.1–0.6 kW. Hence, the thermal efficiency of their prime mover would become 25%–15%. The efficiency thus estimated would refer to only a possible minimum value for their prime mover, because the temperature ratio $\eta = (T_H - T_C)/T_C$ of 2.3 in their prime mover is higher than that in the present one ($\eta = 0.8$). All the analysis above indicates that an extremely high efficiency achieved by the Backhaus and Swift is reasonably understood from the extension of the present results.

F. Visualization of an acoustic streaming

We discuss in this subsection a visualization of the gas motions from the Lagrangian point of view, which allows us to measure a secondary flow induced in the present prime mover. The motivation for this measurement is that it has been pointed out that the net of the secondary flow carries heat away from the hot heat exchanger on the regenerator and generates an unwanted heat leak, resulting in a decrease in an efficiency.[8,19] A sheet-like plane light of a 400-mW argon-ion laser was passed through the axis of the looped tube. Tracer particles of 20 μm in diameter were introduced within the tube, where spontaneous gas oscillations were excited with $Q_H = 86$ W, i.e., the same condition as that employed in the pressure and velocity measurements.

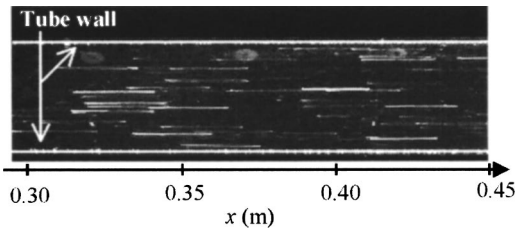

FIG. 5. Visualization of the streaming. Bright lines represent traces of the moving tracer particles.

Figure 5 shows a typical photograph taken in the region over $x = 0.30$ to 0.45 m. The traces of the particles are seen as horizontal bright lines in Fig. 5. This is because the shutter speed was slower than the inverse of the oscillating frequency (1/41 s) and the velocity in the tube is uniaxial. The length of the line, therefore, represents the peak-to-peak displacement of the tracer particle, and is found to be 26 mm at $x = 0.35$ m. This agrees well with the peak-to-peak displacement estimated from the velocity measurements shown in Fig. 4(a).

We found that bright lines moved slowly with the dc velocity U_0 along the tube axis. This indicates the existence of a secondary flow in the present prime mover. It turned out that U_0 depends on the radial coordinate. At the center of the tube, U_0 was about 34 mm/s and its flow was always directed from right to left. This is opposite to the direction of I. Near the tube wall, U_0 was faster than that at the center. Its direction was reversed and became the same as that of I. However, the net flow rate of the secondary flow and its direction could not be experimentally observed in the present prime mover. Therefore, it was experimentally unclear whether the secondary flow significantly reduced the efficiency of the present prime mover or not.

III. CONSTRUCTION OF A COOLER DRIVEN BY THE THERMOACOUSTIC STIRLING PRIME MOVER

A. Thermoacoustic cooling effect

This section describes the construction and performance of a cooler driven by the present thermoacoustic Stirling prime mover. The present prime mover generates the output power ΔI through the Stirling cycle. By using this ΔI as a source of power, we produce a thermoacoustic cooling effect[15] without moving parts. A second regenerator, which acts as a thermoacoustic heat pump, was inserted into the present thermoacoustic prime mover.

The measured acoustic field allowed us to locate precisely a right position for the installation of the second regenerator. The position is $x = 0.85$ m, because the acoustic impedance z becomes the maximum (10 γ) and Φ takes exactly zero there. The maximum acoustic impedance can significantly reduce viscous losses in the second regenerator to a minimum level. The traveling wave phase can cause a thermoacoustic cooling effect through the reversed Stirling cycle as explained below. As can be seen Fig. 1(a), a gas parcel having $\Phi = 0$ in the second regenerator will experience the following cycle: (1) pressure of the gas parcel is increased near one end of its travel and then, the gas parcel releases heat to the wall of the second regenerator, since the tempera-

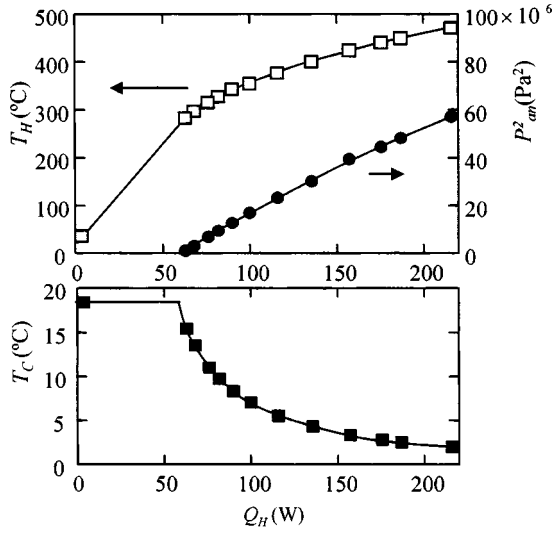

FIG. 6. Performance of the thermoacoustic Stirling cooler with the use of atmospheric air. Temperatures T_H at the hot end of the regenerator, in which the output power is generated, and T_C at the cold end of the second regenerator, in which the heat pump effect is operated, and square of pressure amplitude $p_{an}^2$are plotted as a function of input power Q_H. The lines are guides for the eye.

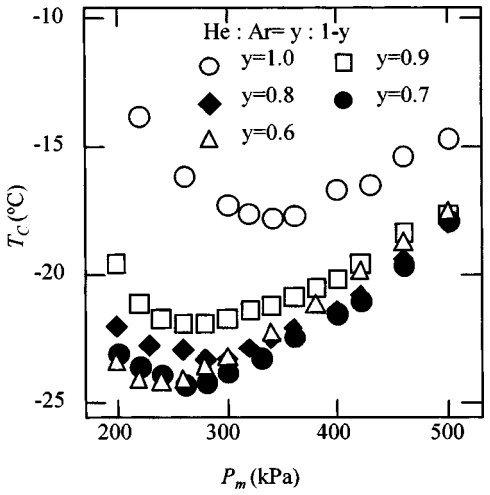

FIG. 7. Temperature T_C of the cold end of the second regenerator as a function of P_m, for input power $Q_H=210$ W.

ture of the gas parcel is kept equal to that of the wall through the thermal contact between them; (2) the gas parcel moves toward the other end; (3) where its pressure is decreased and then, it receives heat from the wall, and (4) it moves back to the first position. By repeating this cycle, a heat flow can be pumped from one end to the other of the second regenerator in the opposite direction to *I*, resulting in the generation of a temperature gradient along it.

B. Construction of a thermoacoustic Stirling cooler

Figure 2(b) shows the schematic illustration of a ceramic honeycomb used as the second regenerator. The regenerator of 80 mm in length has many square pores with the cross section 0.6×0.6 mm^2. Two heat exchangers are placed on both sides of the regenerator. One is cooled by water to keep it at T_R. The other is exposed to surrounding air and its temperature T_C is measured by a thermocouple. The second regenerator is located in the position over $x=0.77$ to 0.85 m in the present prime mover.

We tested the performance of the cooler by gradually increasing Q_H. Figures 6(a) and (b) shows the measured T_H, T_C, and p_{an}^2 as a function of Q_H. The temperature T_H monotonically increases with increasing Q_H, but p_{an}^2 and T_C remain unchanged at 0 and room temperature of 18 °C as long as $Q_H \leqslant 63$ W, respectively, because of the absence of gas oscillations. When Q_H exceeds Q_{cri} of 63 W, the gas parcels begin to oscillate. Now, p_{an}^2 becomes finite and T_C begins to decrease from room temperature. This proves that the heat flow was indeed pumped across the second regenerator from its cold heat exchanger (T_C) to the room-temperature one (T_R) by thermoacoustically generated gas oscillations. We measured the pressure along the tube and found that the position of the pressure antinode, where $\Phi=0$, remained unchanged upon the installation of the second regenerator. Therefore, the reversed Stirling cycle to pump heat is executed in the second regenerator. With increasing Q_H, p_{an}^2 increases and T_C decreases. When Q_H is increased to 210 W, p_{an} reaches 7.5 kPa and T_C drops to the lowest temperature of 2 °C.

C. Cooler filled with pressurized gas

In order to further enhance the cooling performance, we modified the cooler in the way discussed below. The glass looped tube and resonator are replaced by stainless-steel tubes with 40 mm inner diameter. Pressurized helium gas with mean pressure of $P_m=220-500$ kPa is employed as working gas in place of atmospheric air. The values of L_l, L_r, and R are adjusted to be 1.04, 1.40, and 0.20 m, respectively. In the high-pressure cooler thus constructed, the frequency f of the spontaneous gas oscillations turned out to be 118 Hz.

Under the condition $Q_H=210$ W, we measured T_C in the high-pressure thermoacoustic cooler as a function of P_m. The measured T_C, as shown in Fig. 7 by open circles, reaches -13.8 °C at $P_m=220$ kPa and is further decreased with increasing P_m up to 350 kPa. The value of T_C reaches the lowest value of -17.8 °C at $P_m=350$ kPa but is increased with further increase in P_m beyond 350 kPa.

The existence of the minimum on the T_C-P_m curve can be explained by using the relations

$$\delta_v \propto (P_m\omega)^{-1/2}, \tag{7}$$

and

$$\delta_v = \delta_t \sigma^{1/2}, \tag{8}$$

where σ is Prandtl number, and δ_v and δ_t are the viscous and thermal penetration depths,[14] respectively. The viscous penetration depth δ_v can be decreased by increasing P_m through Eq. (7), resulting in the suppression of viscous losses generated in the two regenerators. However, δ_t is also decreased by increasing P_m through Eq. (8). A decreasing δ_t will cause the loss of a good thermal contact between a gas parcel and the wall in the regenerators. Since a good thermal contact is indispensable for the Stirling prime mover and cooler, an increase in P_m beyond some critical value will reduce the

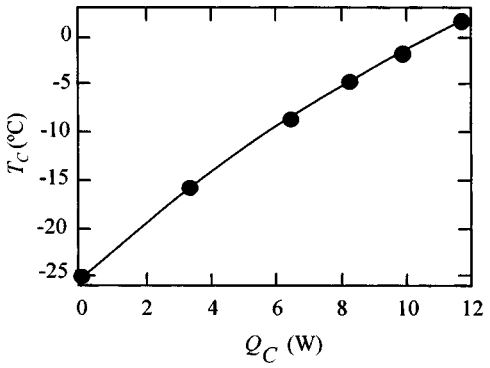

FIG. 8. Cooling power of the thermoacoustic Stirling cooler. Temperature T_C of the cold end of the second regenerator is plotted as a function of the load Q_C, when an input power $Q_H=210$ W. The line is a guide for the eye.

performance of the cooler as shown in Fig. 7.

We tried to decrease T_C further. Equation (8) indicates that, if σ can be decreased, δ_v is decreased, resulting in a decrease of viscous losses. Since σ can be decreased by using a mixture of helium and argon,[20] we employed it as a working gas. While adding argon to helium, we measured the temperature T_C with $Q_H=210$ W.

The value of T_C is shown in Fig. 7 as a function of P_m at a given ratio of helium to argon. The ratio was estimated from the measured frequency f_{mix} of the spontaneous gas oscillation for the mixture and the equation,

$$\frac{f_{\mathrm{He}}}{f_{\mathrm{mix}}}=\sqrt{\frac{(1-y)N_{\mathrm{Ar}}+yN_{\mathrm{He}}}{N_{\mathrm{He}}}}, \tag{9}$$

where f_{He} ($=118$ Hz) is the frequency for pure helium in the present cooler and N_{He} and N_{Ar} are the molar mass of helium and argon, respectively, and y is a mole fraction of helium. The T_C-P_m curves with the mixture fall consistently lower than that with pure helium in the region $200\leqslant P_m \leqslant 500$ kPa. The mixture at a given ratio also takes an optimum value of P_m in the same reason as that with pure helium. The optimum P_m of the mixture is lower than that of pure helium. This is attributed to the fact that the mixture can reduce viscous losses while keeping a good thermal contact at low P_m compared with helium. As can be seen in Fig. 7, when y was 0.7 and P_m was the optimum value of 260 kPa, we obtained the lowest temperature T_C of -25 °C, which was lower by 47 °C than room temperature T_R ($\simeq$22 °C).

Finally, we demonstrate the cooling power of the present cooler with the choice of the optimized mixture gas, where $y=0.7$ and $P_m=260$ kPa. A resistance heater was wound around the cold heat exchanger on the second regenerator and the cooling power was measured under the condition $Q_H=210$ W. In Fig. 8, T_C is plotted as a function of the heat load Q_C supplied to the heater. As Q_C increases to 12 W, T_C raises from -25 to 2 °C. The thermal efficiency of the cooler defined as Q_C/Q_H turns out to be 5% at 0 °C.

IV. SUMMARY

We have measured the acoustic field in the thermoacoustic prime mover having the looped tube and resonator by simultaneous measurements of pressure P and cross-sectional mean velocity U. The acoustic field thus observed enabled us to prove that the thermoacoustic Stirling prime mover executes the thermodynamic cycle by using an acoustic wave having a high acoustic impedance and a negative phase lead Φ. We consider that a negative Φ plays a key role to increase the efficiency of a thermoacoustic prime mover having a looped tube and resonator. Moreover, based on these experimental results, we succeeded in constructing a Stirling cooler driven by the present thermoacoustic prime mover. The cooler generated a temperature of -25 °C and had a cooling power Q_C of 11 W at 0 °C with an input power Q_H of 210 W.

The thermoacoustic prime mover and cooler have a potential to become an efficient device, because the mutual conversions between Q and I are executed through the Stirling cycle which has an inherent reversibility. They are very inexpensive to maintain and to construct it, and produce neither waste gas nor require chlorofluorocarbon. We consider that a thermoacoustic prime mover and cooler will become a new technology to use a waste and solar heat with a high efficiency and low cost.

[1] G. W. Swift, "Thermoacoustic engines and refrigerators," Phys. Today **48**, 22–28 (1995); "Thermoacoustic engines" J. Acoust. Soc. Am. **84**, 1145–1180 (1988).

[2] A. Tominaga, "Thermodynamic aspects of thermoacoustic theory," Cryogenics **35**, 427–440 (1995).

[3] J. C. Wheatley, T. Hofler, G. W. Swift, and A. Migliore, "Experiments with an intrinsically irreversible acoustic heat engine," Phys. Rev. Lett. **50**, 499–502 (1983); "An intrinsically irreversible thermoacoustic heat engine," J. Acoust. Soc. Am. **74**, 153–170 (1983); "Understanding some simple phenomena in thermoacoustics with applications to acoustical heat engines," Am. J. Phys. **53**, 147–162 (1985).

[4] Work flow I is defined as $I=A\cdot\langle PU_r\rangle$ and heat flow Q is defined as $Q=A\cdot\rho_m\cdot T_m\cdot\langle SU_r\rangle$, where the bars and angular brackets indicates the time and radial averages, and A is cross-sectional area, ρ_m, T_m, S, and U_r are mean mass density, mean temperature, entropy per unit mass, and axial velocity, respectively.

[5] A. A. Atchley and F. Kuo, "Stability curves for a thermoacoustic prime mover," J. Acoust. Soc. Am. **95**, 1401–1404 (1994).

[6] A. A. Atchley, "Analysis of the initial buildup of oscillations in a thermoacoustic prime mover," J. Acoust. Soc. Am. **95**, 1661–1664 (1994).

[7] R. Radebaugh, K. M. McDermott, G. W. Swift, and R. A. Martin, "Development of a thermoacoustically driven orifice pulse tube refrigerator," in Proceedings of the Interagency Meeting on Cryocoolers, p. 205. 24, October 1990, Plymouth MA.

[8] S. Backhaus and G. W. Swift, "A thermoacoustic Stirling heat engine," Nature (London) **399**, 335–338 (1999); "A thermoacoustic-Stirling heat engine: Detailed study," J. Acoust. Soc. Am. **107**, 3148–3166 (2000).

[9] P. H. Ceperley, "A pistonless Stirling engine—traveling wave heat engine," J. Acoust. Soc. Am. **66**, 1508–1513 (1979).

[10] S. Garrett, "Reinventing the engine," Nature (London) **399**, 303–305 (1999).

[11] T. Yazaki, A. Iwata, T. Maekawa, and A. Tominaga, "Traveling wave thermoacoustic engine in a looped tube," Phys. Rev. Lett. **81**, 3128–3131 (1998).

[12] Y. Ueda, T. Biwa, T. Yazaki, and U. Mizutani, "Acoustic field in a thermoacoustic Stirling engine having a looped tube and resonator," Appl. Phys. Lett. **81**, 5252–5254 (2002).

[13] The hydraulic radius is the ratio of gas volume to gas–solid contact area.

[14] The thermal penetration depth δ_t is defined as $\sqrt{2\alpha/\omega}$, where α is a thermal diffusivity defined by using thermal conductivity κ, isobaric heat capacity c_p, and mean density ρ_m as $\kappa/(c_p\rho_m)$.

[15] T. Yazaki, T. Biwa, and A. Tominaga, "A pistonless Stirling cooler," Appl. Phys. Lett. **80**, 157–159 (2002).

[16] T. Biwa, Y. Ueda, T. Yazaki, and U. Mizutani, ''Thermodynamical mode selection rule observed in thermoacoustic oscillations,'' Europhys. Lett. **60**, 363–368 (2002).
[17] T. Yazaki and A. Tominaga, ''Measurement of sound generation in thermoacoustic oscillations,'' Proc. R. Soc. London, Ser. A **454**, 2113–2122 (1998).
[18] T. Biwa, Y. Ueda, T. Yazaki, and U. Mizutani, ''Work flow measurements in a thermoacoustic engine,'' Cryogenics **41**, 305–310 (2001).
[19] S. Backhaus and G. W. Swift, ''An acoustic streaming instability in thermoacoustic devices utilizing jet pumps,'' J. Acoust. Soc. Am. **113**, 1317–1324 (2003).
[20] J. R. Belcher, W. V. Slaton, R. Raspet, H. E. Bass, and J. Lightfoot, ''Working gases in thermoacoustic engines,'' J. Acoust. Soc. Am. **105**, 2677–2684 (1999).

Optoacoustic generation of a helicoidal ultrasonic beam

Stefan Gspan, Alex Meyer, Stefan Bernet, and Monika Ritsch-Marte
Institute for Medical Physics, University of Innsbruck, Müllerstr. 44, A-6020 Innsbruck, Austria

(Received 25 June 2003; revised 22 November 2003; accepted 1 December 2003)

The optoacoustic generation of a helicoidal ultrasonic beam is demonstrated. Such an ultrasonic ''doughnut'' beam has a pressure amplitude minimum in the center along its entire longitudinal extension, and it carries orbital angular momentum. It is produced by illuminating a specially structured absorbing surface in a water tank with pulsed laser light. The absorbing surface has a profile with a screw dislocation, similar to the transverse cross-sectional surface of a helix. Upon illumination with modulated light, a correspondingly prepared absorber generates an ultrasonic wave with the desired phase discontinuity in its wave front, which propagates through the water tank and is detected with spatial resolution using a scanning needle hydrophone. This situation can be viewed as the optoacoustic realization of a diffractive acoustical element. The method can be extended to tailor optoacoustically generated ultrasonic waves in a customized way. © *2004 Acoustical Society of America.* [DOI: 10.1121/1.1643367]

PACS numbers: 43.35.Yb, 43.20.El [YHB] Pages: 1142–1146

I. INTRODUCTION

During the past years laser-induced generation of ultrasound[1] has become an active field of research with respect to applications in medicine[2–6] and in material sciences.[7–9] A major advantage, which is inherent to this approach but not often utilized, is the possibility to generate ultrasound waves with predetermined spatial intensity patterns. On the other hand, in optics as well as in acoustics helicoidal beams and vortices are currently being studied for new areas of application.

In optics, for instance, higher order Laguerre–Gaussian beams, which are sometimes called ''doughnut beams'' for their dark hollow in the center along the propagation axis, have been applied to trap particles. The dark central spot of a doughnut mode can confine absorptive or reflective particles[10] as well as dielectric low-index particles such as hollow glass spheres,[11] due to the scattering force or the gradient force, respectively. Since such a light field carries ''orbital'' angular momentum,[12,13] it may even be used to induce a rotation of the trapped particles.[10,14] In the context of laser cooling optical doughnut modes have found a successful application in trapping and guiding of neutral atoms in ''atomic funnels.'' [15,16]

On the acoustics side, there have recently been some experiments on levitation of heavy particles by ultrasonic beams. Tungsten particles, for instance, have been suspended in the air in a standing (kHz frequency) sound wave.[17,18] This raises the question, whether some of the above mentioned optical applications of helicoidal beams might, at least partly, be adaptable to acoustics. Helicoidal ultrasonic beams could have particularly promising applications, since (like their optical counterparts) they carry orbital angular momentum that can be transferred to particles and induce rotation. It should also be possible to trap or guide particles or gas bubbles inside an acoustical doughnut beam. The combination of an acoustical trap (levitator) with a hollow beam carrying orbital angular momentum might serve as a particularly useful tool for contact-free spatial control over particles. Acoustical doughnut beams have also been suggested for underwater alignment purposes,[19] since the pressure minimum in the center of the beam is always exactly localized on the beam axis, and for remote sensing of the symmetry of ultrasound scattering objects or vortices.

The work presented in this paper is to be understood as a first step on the way to our ultimate goal, which is to employ computer-generated holography on a LCD screen to steer optoacoustically generated ultrasound waves.[20]

II. OPTOACOUSTIC GENERATION OF ULTRASOUND

Considerations involving the torque applicable to particles in a helicoidal sound wave have recently led to new attempts for efficient and custom-designed generation of helicoidal ultrasonic beams. Some years ago, Hefner and Marston[19] suggested a four-panel piezo-composite transducer to generate the desired helicoidal ultrasound beams. In this system it was possible to choose the output frequency within a range from several kHz to several hundred kHz.

In the present paper we describe a method that utilizes the optoacoustic effect to create the ultrasonic counterpart of an optical doughnut beam. To our knowledge, helicoidal ultrasonic beams have not been generated optoacoustically to date. The optoacoustic effect is based on absorption of modulated light, resulting in thermal expansion, which produces a propagating pressure wave, if certain conditions are satisfied (stress confinement and thermal confinement).[21] The conversion efficiency between optical intensity and pressure amplitude depends on the so-called Grueneisen parameter.[22,23] Since this efficiency is low for solids or liquids, typically short laser pulses (in the nanosecond range or shorter) with a correspondingly high peak power are used, which produce a short ultrasonic pulse with a broad frequency bandwidth.

Our deliberate choice of a μs-pulse laser system (pulse width 10 μs), however, has the advantage that the pulse duration is on the one hand short enough to provide the high peak intensity necessary for efficient ultrasound generation,

 0001-4966/2004/115(3)/1142/5/$20.00

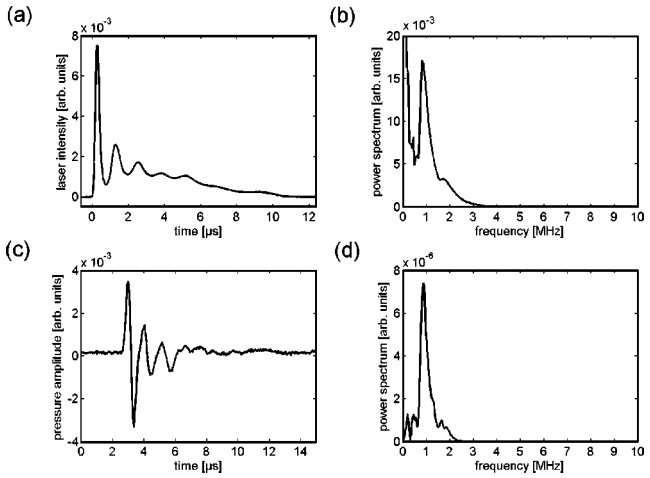

FIG. 1. Laser and pressure pulse and respective power spectra. (a) Laser pulse intensity distribution produced by the titanium sapphire laser. (b) Corresponding power spectrum of the laser pulse. (c) Pressure pulse that is generated by the laser pulse shown in (a) via the optoacoustic effect. (d) Corresponding power spectrum of the ultrasonic wave.

but on the other hand long enough to allow external modulation for generating a defined ultrasound frequency in the MHz range, which is important for medical diagnostics. For harmonic modulation in the MHz range several modulation cycles can be employed within one laser pulse. For example, the spectral width of frequently used ns pulses would be too broad to produce doughnut beams in the way outlined in this paper.

In our experiments we used a flashlamp-pumped titanium sapphire laser tuned to a wavelength of 780 nm, which delivers 10-μs pulses with a maximum pulse energy of 550 mJ at a maximum repetition rate of 20 Hz. Actually, for the experiment reported here, no external modulation was applied, since the laser pulses are already intensity modulated ''internally'' due to the presence of relaxation oscillations which are typical for pulsed titanium sapphire lasers. Figure 1 shows the temporal course of the laser intensity within one pulse of the titanium sapphire laser (upper left graph), measured with a fast photo diode. The temporal oscillations are modulated with a center frequency of about 750 kHz, as demonstrated by the corresponding power spectrum (upper right graph). Behind the absorber, the pressure amplitude of the emitted ultrasonic wave was recorded with a hydrophone needle in the water tank. The detected pressure pulse is plotted in the lower left graph, and its corresponding power spectrum on the right side. The emerging ultrasonic wave has a center frequency of 750 kHz, corresponding to a wavelength of about 2 mm in water (the speed of sound in water c being roughly 1540 m/s). In previous experiments we also generated other intensity modulation frequencies of the emitted pulses by using a fast electro-optic modulator.

The absorbing material used in our experiment is silicon gasket material (speed of sound roughly 1130 m/s). The optical penetration depth of the laser pulse into this material is about 300 μm. Due to the large area of the absorber that is illuminated (about 10 wavelength diameter, the wavelength in silicon being roughly 1.5 mm) the stress confinement condition is sufficiently satisfied. Thus the boundary conditions for the generation of an ultrasonic wave are quasi-two-dimensional.

III. GENERATION OF DOUGHNUT MODES

Helicoidal beams have zero intensity along the beam axis. Their transverse cross section resembles a doughnut, and thus they are sometimes called ''doughnut modes.'' In optics doughnut modes emerge as mode solutions in cylindrically symmetric laser cavities. Since the wave equation for pressure waves (d'Alembert equation) is of the same form as that for scalar light fields[24] the mathematics for paraxial scalar light fields can be repeated for acoustical fields. Within the paraxial approximation, propagating fields can be expressed as a superposition of $e^{i\omega t-ikz}u_p^m(r,\phi,z)$, and complex conjugate terms (with k and ω being the wave-vector eigenvalues and corresponding oscillation frequencies $\omega=ck$). The so-called Laguerre–Gauss (LG) modes $u_p^m(r,\phi,z)$ are solutions of the (scalar) paraxial wave equation $\partial^2u/\partial x^2+\partial^2u/\partial y^2-2ik(\partial u/\partial z)=0$. In cylindrical coordinates (r,ϕ,z) the LG modes are of the general form[25,26]

$$u_p^m(r,\phi,z)=f_{pm}(r,z)e^{-r^2/w(z)^2}q^{|m|/2}L_p^{|m|}(q)e^{-im\phi} \quad (1)$$

with $L_p^{|m|}$ denoting the generalized Laguerre polynomials evaluated at $q=2r^2/w(z)^2$ with

$$w(z)=w_0\sqrt{1+(z/z_R)^2}. \quad (2)$$

Here w_0 represents the beam waist [i.e., the radial distance from the axis where the Gaussian in Eq. (1) has decreased to $1/e$ of its on-axis value in the focus located at $z=0$] and $z_R=\pi w_0/\lambda$ the Rayleigh range (i.e., the distance from the beam focus, where the beam area doubles). The function

$$f_{pm}(r,z)=\frac{c_{pm}w_0}{w(z)}e^{-i[kr^2/2R(z)-\Psi(z)]}, \quad (3)$$

apart from a constant c_{pm}, contains a phase factor describing the wave front curvature, with $R(z)=z(1+(z_R/z)^2)$ denoting the radius of curvature, and the Gouy phase $\Psi(z)=(2p+|m|+1)\arctan(z/z_R)$. For paraxial beams this phase factor represents a small distortion of the wave front and can be neglected.

Note that the *only* dependence on the azimuthal angle ϕ is contained in the factor $e^{im\phi}$, and that it is intricately connected to the azimuthal mode index m. Clearly this term leads to a ''chirality'' in the phase front of the field for $m\neq0$. Therefore m is sometimes called ''topological charge.''[27] It can be shown that m relates to the orbital angular momentum of the higher-order LG fields.[12] The simplest such case is a doughnut mode with $m=\pm1$ and $p=0$. In a LG mode with a radial index p the number of concentric rings around the axis is given by $p+1$, thus for $p=0$ only one ring is present.

Within the paraxial equation the wave front of a propagating solution $e^{-ikz}u_p^m(r,\phi,z)\propto e^{-ikz-im\phi}$ is approximately given by $k\,z+m\phi=\text{const}$. For the doughnut case $m=\pm1$, this leads to a ''spiral stairs'' wave front with a chirality depending on the sign of m. Within a fixed plane perpendicular to the beam propagation direction the maximum of the pressure amplitude moves on a circle.

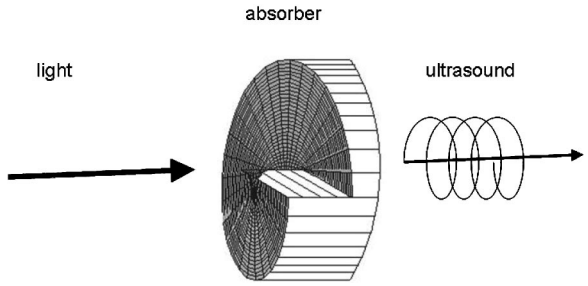

FIG. 2. Sketch of the helicoidal surface and the illumination geometry for creating an acoustic helicoidal beam. The surface of an absorbing material which is illuminated by the laser light has a profile which corresponds to the cross sectional area of a helix. The acoustic wave is detected behind the other (not illuminated) side of the absorber, which is plane.

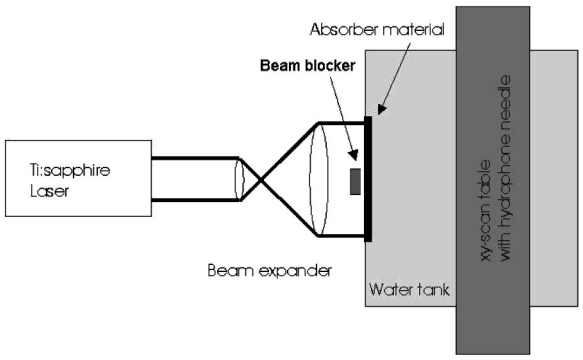

FIG. 3. Schematic drawing of the experimental setup. The intensity modulated laser beam is expanded and illuminates a structured absorbing surface in a water tank. A circular area with a diameter of 6 mm at the center of the expanded laser beam is blocked by a disk just in front of the absorber in order to avoid artifacts at the strong phase gradient in this area. At the absorbing layer inside the water tank an ultrasonic wave is produced via the optoacoustic effect. At a certain distance behind the absorber within a plane perpendicular to the propagation direction of the sound wave the ultrasonic field is recorded using a spatially scanning PVDF needle hydrophone.

This form of the wave front can straightforwardly be taken as a starting point to experimentally create an *ultrasonic* doughnut mode: To realize such an ultrasonic beam one has to ''imprint'' a wave front that looks like the spiral staircase. This can be achieved by embossing a screw dislocation directly into the sound emitting optoacoustic absorber surface, where the ultrasonic wave is generated, i.e., at the side of the absorber which is illuminated. Thus the absorber surface looks like the top view of a transversely cut helix. A sketch of such an absorber, the direction of illumination and the direction of the emitted ultrasonic wave is plotted in Fig. 2. Of course the pitch of the screw dislocation must suit the wavelength of the ultrasound (satisfying $|z|/\lambda = \phi/2\pi$), i.e., the surface height of the absorber has to be of the form $z = \pm\lambda\phi/2\pi$, which yields a pitch of λ for one full turn of the screw of either chirality. There, λ is the ultrasound wavelength in the absorber material, i.e., $\lambda = 2\pi\, c_{\text{absorber}}/\omega$.

Besides this straightforward method to create a doughnut mode, in optics phase holograms are often used.[10] However, this has the disadvantage that only the first diffraction order has the desired beam shape. Finally we would like to remark that another approach in optics to generate a helicoidal beam is the use of diffractive optical elements (DOE).[28] They directly imprint the phase distribution necessary to achieve a hollow beam to an incoming plane wave. Recently the generation of an optical doughnut beam with a conversion efficiency near 100% has been realized by the use of a liquid-crystal display (LCD).[29] In analogy to a DOE, our optoacoustic generation of sound emitted from a surface with a screw dislocation could also be viewed as a DAE (Ref. 30) to generate an acoustic ''doughnut mode.''

IV. EXPERIMENTAL RESULTS

To create the desired helicoidal surface, in our first-step experiments we simply ''stamped'' an appropriately manufactured object made of PVC plastic directly into the light absorber, i.e., black silicone gasket material, and let it dry afterwards. According to Huygens' principle, the surface relief $z = z(\phi)$ of the dried light absorber directly embosses the desired phase relief on the wave front of the emitted ultrasonic field: the screw dislocation on the absorber leads to a helicoidal ultrasonic wave propagating through a water tank. The typical dark hollow in the middle of this ''acoustical doughnut'' is formed by means of destructive interference on the beam axis.

For the formation of an acceptable doughnut it is necessary to shape the surface with an accuracy and smoothness on the order of a tenth of the ultrasound wavelength (with $\lambda \approx 2$ mm). Especially the singularity at the center of the absorbing layer has to be very sharp. Since it turned out that this posed the main problem in the production of such a phase embossing layer, we decided to block the middle of the laser beam, and thus the area with the most critical inaccuracies. This may seem like an ''unintended'' way to produce a hollow beam, however, diffraction theory (and experimental evidence) tell us that blocking the middle of a beam, optical or acoustical, does *not* lead to an intensity minimum in the center over long distances.

Figure 3 sketches our experimental setup. The stamped light absorber was illuminated with a laser beam expanded to 16 mm with a region of 6 mm diameter in its center being blocked due to the reasons mentioned above. The ultrasonic field distribution was measured by scanning a PVDF hydrophone needle with an active element of 0.4 mm diameter, controlled by a two-dimensional scanning stage, inside the water tank in a plane parallel to the absorbing layer. The increment in both scan directions was 2 mm and the measured values were averaged 20 times.

The ultrasonic field distributions shown in Fig. 4 (upper graphics) was recorded in four different planes which were perpendicular to the propagation direction of the acoustic wave and located at four different distances behind the absorbing layer (30, 60, 90, 120 mm). The estimated extension of the near field is about 50 mm. Thus our measurements cover the whole wave propagation regimes between Krichhoff (near field), Fresnel (mid field) and Frauenhofer (far field). In all of the four planes we found a minimum of the amplitude in the center of the ultrasonic beam. Since the propagation of the optical vortex in a doughnut beam is similar to the propagation of a TEM_{00} beam,[25,27] the diameter of the dark spot increases linearly with increasing distance from

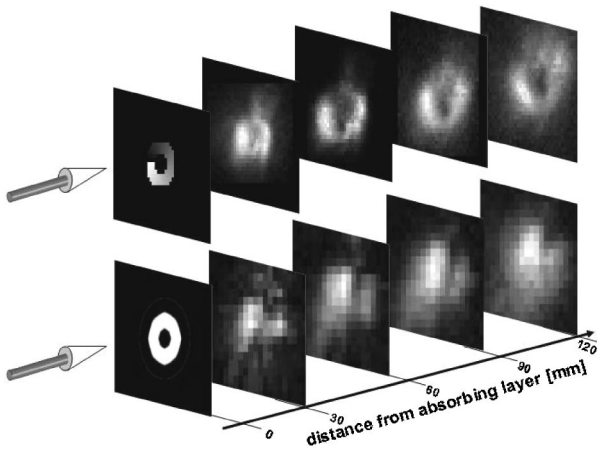

FIG. 4. Spatial development of the ultrasonic pressure field in the water tank. The upper part of the figure shows the field distribution created at different distances behind the absorber with the imprinted screw dislocation. The direction of illumination is indicated by arrows. Scans were taken in planes 30, 60, 90, and 120 mm behind the absorbing layer. The gray levels are proportional to the measured pressure amplitude (note that the ultrasonic *intensity contrast* would be more pronounced). The maximum pressure amplitude is about 10 kPa. The first planes of the graph sketches the surface profile of the corresponding absorbing layer. The doughnut mode measured at the shortest distance from the absorber (first data plane) has an extremely sharp localized minimum in its center, which is only poorly resolved, since it corresponds only to one single central pixel of the measured data. The lower part of the figure shows the results of a control experiment, where the laser beam illuminated a plane absorber (without screw dislocation), again with an area of 6 mm blocked at its center. Data were recorded under the same conditions and at the same locations as in the previous experiment. Clearly, there is no pressure minimum in the center.

the absorbing layer. The deviation from the ideal circular shape is due to inaccuracies of the silicone surface which are on the order of 0.2 mm, and to small inhomogeneities in the profile of the expanded laser beam (''top hat'' profile with small inhomogeneities). For comparison, in Fig. 4 we also show measurements of the ultrasonic field produced by a *plane* absorbing layer (*without* a screw dislocation) illuminated by the same laser beam with its center blocked as before. Clearly, no central dark spot in the middle is formed in this case. In Fig. 5 the measured width of the pressure amplitude minima (full width at half maximum) is plotted as

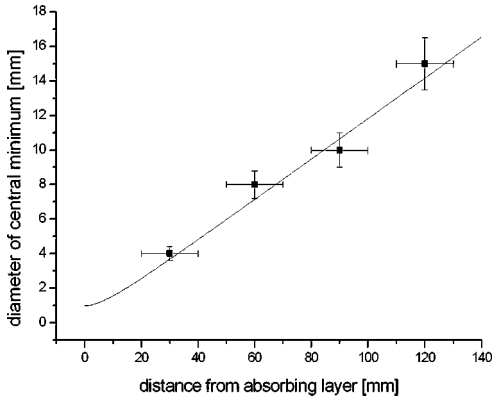

FIG. 5. Width of the central pressure minima of the acoustic doughnut beam (full width at half maximum) measured at different distances from the absorber. The straight line sketches the behavior expected from Eq. (2). The experimental results are in good agreement with the theoretical behavior for a LG mode with $m=1$.

a function of the beam propagation length. The linear increase of the beam width is in full accordance with the behavior expected from Eq. (2), i.e., with the assumption that the width of the pressure minimum increases at the same rate as the width of a TEM_{00} Gaussian beam.

V. SUMMARY AND OUTLOOK

We have presented a new way of generating helicoidal acoustical fields using the optoacoustic effect. This method of creating an ''ultrasonic doughnut'' combines the advantages of contact-free ultrasound generation with all the options present in an acoustic field that carries orbital angular momentum, and could thus turn into a versatile tool to manipulate small particles.

For future work we hope to further develop the optoacoustic generation of helicoidal acoustic beams. Adopting the ''hardware approach,'' the production of silicone absorbers can doubtlessly be improved; we are still investigating various materials and relief-shaping processes.

Alternatively, in the ''software approach,'' we are currently developing a procedure using holographic methods including a LCD spatial light modulator to generate preselectable ultrasonic patterns including doughnut beams.[19] For instance, one can feed so-called ''kinoform''[31] phase holograms into the LCD and project the light transmitted by the LCD (carrying the phase information for the optoacoustic sound wave generation) to an *entirely flat* absorbing layer inside a water tank. Thereby the desired acoustic phase distribution is directly generated at the absorber surface and a 100% diffraction efficiency should be possible. The central key point to achieve this is to use *polarization* modulated light for illumination of the LCD (without entrance polarizer), rather than intensity modulated light as before. In preliminary work we have already proven the feasibility of such a procedure by creating phase gratings with a programmed grating constant by means of computer-generated phase holograms on the LCD. In such a setup the ultrasound frequency can be adjusted by the choice of the polarization modulation frequency, and the spatial pattern displayed on the LCD screen determines the spatial phase pattern of the sound wave. This allows one to choose the parameters for the generated acoustic intensity distribution in a wide range. Using an LCD also offers the possibility of changing the emitted sound wave properties at video rate, e.g., it is possible to scan the ultrasonic beam, or to quickly switch from doughnut to ''normal'' beam profiles. Thus it might be possible to guide particles with sound by sweeping the field parameters (e.g., frequency or spatial mode) of the trapping ultrasonic field.

ACKNOWLEDGMENTS

We wish to gratefully acknowledge the financial support of the Austrian Science Fund (FWF-Project No. P14813-PHY). A. Meyer was supported by the Ministère de la Culture, de l'Enseignement Supérieur et de la Recherche, Luxembourg (BFR/01/009).

[1] V. P. Zarov and V. S. Letokhov, *Laser Opto-Acoustic Spectroscopy* (Springer-Verlag, New York, 1984).
[2] K. P. Köstli, M. Frenz, H. P. Weber, G. Paltauf, and H. Schmidt-Kloiber, ''Optoacoustic tomography: time gated measurement of pressure distributions and image reconstruction,'' Appl. Opt. **40**, 3800–3809 (2001).
[3] T. W. Murray, S. Krishnaswamy, and J. D. Achenbach, ''Laser generation of ultrasound in films and coatings,'' Appl. Phys. Lett. **74**, 3561–3563 (1999).
[4] A. A. Oraevsky, S. L. Jacques, and F. K. Tittel, ''Measurement of tissue optical properties by time-resolved detection of laser-induced transient stress,'' Appl. Opt. **36**, 402–416 (1997).
[5] G. Paltauf and H. Schmidt-Kloiber, Laser-Tissue Interaction, Tissue Optics and Laser Welding III, San Remo, pp. 70–79, (1997), edited by G. P. Delacretaz *et al.*, SPIE proceeding, Bellingham, 1998.
[6] P. Beard, Biomedical Optoacoustics III, San Jose, pp. 54–63, (2002), edited by A. A. Oraevsky, SPIE proceeding, Bellingham, 2002.
[7] Y. Shen, Z. Lu, S. Spiers, H. A. MacKenzie, H. S. Ashton, J. Hannigan, S. S. Freeborn, and J. Lindberg, ''Measurement of the optical absorption coefficient of a liquid by use of a time-resolved photoacoustic technique,'' Appl. Opt. **39**, 4007–4012 (2000).
[8] L. Wu, J. Cheng, and S. Zhang, ''Mechanisms of laser-generated ultrasound in plates,'' J. Phys. D **28**, 957–964 (1995).
[9] M. W. Sigrist, ''Laser generation of acoustic waves in liquids and gases,'' J. Appl. Phys. **60**, R83–R121 (1986).
[10] H. He, M. E. J. Friese, N. R. Heckenberg, and H. Rubinsztein-Dunlop, ''Direct observation of transfer of angular momentum to absorptive particles from a laser beam with a phase singularity,'' Phys. Rev. Lett. **75**, 826–829 (1995).
[11] K. T. Gahagan and G. A. Swartzlander, ''Optical vortex trapping of particles,'' Opt. Lett. **21**, 827–829 (1996).
[12] L. Allen, M. W. Beijersbergen, R. J. C. Spreeuw, and J. P. Woerdman, ''Orbital angular momentum of light and the transformation of Laguerre-Gaussian laser modes,'' Phys. Rev. A **45**, 8185–8189 (1992).
[13] S. M. Barnett and L. Allen, ''Orbital angular momentum and nonparaxial light beams,'' Opt. Commun. **110**, 670–678 (1994).
[14] L. Paterson, M. P. MacDonald, J. Arlt, W. Dultz, H. Schmitzer, W. Sibbett, and K. Dholakia, ''Controlled simultaneous rotation of multiple optically trapped particles,'' J. Mod. Opt. **50**, 1591–1599 (2003).
[15] S. Kuppens, M. Rauner, M. Schiffer, K. Sengstock, W. Ertmer, F. E. van Dorsselaer, and G. Nienhuis, ''Polarization-gradient cooling in a strong doughnut-mode dipole potential,'' Phys. Rev. A **58**, 3068–3079 (1998).
[16] M. Schiffer, M. Rauner, S. Kuppens, M. Zinner, K. Sengstock, and W. Ertmer, ''Guiding, focusing, and cooling of atoms in a strong dipole potential,'' Appl. Phys. B: Lasers Opt. **67**, 705–708 (1998).
[17] W. J. Xie and B. Wei, ''Parametric study of single-axis acoustic levitation,'' Appl. Phys. Lett. **79**, 881–883 (2001).
[18] E. H. Brandt, ''Acoustic Physics: Suspended by sound,'' Nature (London) **413**, 474–475 (2001).
[19] B. T. Hefner and P. L. Marston, ''An acoustical helicoidal wave transducer with applications for the alignment of ultrasonic and underwater systems,'' J. Acoust. Soc. Am. **106**, 3313–3316 (1999).
[20] A. Meyer, S. Gspan, S. Bernet, and M. Ritsch-Marte, ''Tailoring ultrasonic beams with optoacoustic holography,'' Laser Resonators and Beam Control VI, San Jose, 2003, edited by V. Kudryashov, SPIE proceeding, Bellingham, 2003.
[21] M. Frenz, G. Paltauf, and H. Schmidt-Kloiber, ''Laser-generated cavitation in absorbing liquid induced by acoustic diffraction,'' Phys. Rev. Lett. **76**, 3546–3549 (1996).
[22] R. S. Dingus and R. J. Scammon, ''Grueneisen-stress-induced ablation of biological tissue,'' Laser-Tissue Interaction II, 1427, pp. 45–54, 1991, edited by S. L. Jacques, SPIE Proceeding, Bellingham, 1991.
[23] G. Paltauf and H. Schmidt-Kloiber, ''Measurement of laser-induced acoustic waves with a calibrated optical transducer,'' J. Appl. Phys. **82**, 1525–1531 (1997).
[24] H. Kuttruff, *Ultrasonics—Fundamentals and Applications* (Elsevier Applied Science, New York, 1991).
[25] A. E. Siegman, *Lasers* (University Science-Books, Sausalito, 1986).
[26] J. Arlt and M. J. Padgett, ''Generation of a beam with a dark focus surrounded by regions of higher intensity: the optical bottle beam,'' Opt. Lett. **25**, 191–193 (2000).
[27] D. Rozas, C. T. Law, and A. Swartzlander, ''Propagation dynamics of optical vortices,'' J. Opt. Soc. Am. B **14**, 3054–3065 (1997).
[28] M. W. Beijersbergen, R. P. C. Coerwinkel, M. Kristensen, and J. P. Woerdman, ''Helical-wavefront laser beams produced with a spiral phaseplate,'' Opt. Commun. **112**, 321–327 (1994).
[29] D. Ganic, X. Gan, M. Gu, M. Hain, S. Somalingam, S. Stankovic, and T. Tschudi, ''Generation of doughnut laser beams by use of a liquid-crystal cell with a conversion efficiency near 100%,'' Opt. Lett. **27**, 1351–1353 (2001).
[30] M. Clark, S. D. Sharples, and M. G. Somekh, ''Diffractive acoustic elements for laser ultrasonics,'' J. Acoust. Soc. Am. **107**, 3179–3185 (2000).
[31] L. B. Lesem, P. M. Hirsch, and J. A. Jordan, Jr., ''The Kinoform: A new wavefront reconstruction device,'' IBM J. Res. Dev. **13**, 150–155 (1969).

Effect of handset proximity on hearing aid feedback

Michael R. Stinson[a] and Gilles A. Daigle
Institute for Microstructural Sciences, National Research Council, Ottawa, Ontario K1A 0R6, Canada

(Received 30 March 2003; revised 9 August 2003; accepted 2 December 2003)

The increased sensitivity of hearing aids to feedback as a telephone handset is brought near has been studied experimentally and numerically. For the measurements, three different hearing aids were modified so that the open-loop transfer function could be measured. They were mounted in the pinna of a mannikin and the change in open-loop transfer function determined as a function of handset proximity. Increases of over 20 dB were observed, most of this change occurring within the first 10 mm of separation between pinna and handset. Numerical calculations performed using a boundary element technique were in good agreement with the measurements. [DOI: 10.1121/1.1643358]

PACS numbers: 43.38.Ar, 43.38.Si, 43.66.Ts [AJZ] Pages: 1147–1156

I. INTRODUCTION

Acoustical feedback in hearing aids can limit their performance and utility.[1,2] Typically, there is sound leakage mainly through a vent in the hearing aid mold, back to the microphone port—this feedback signal, if too large, can result in a howling or squeal of the aid when the Nyquist stability criterion is violated at one or more frequencies. The vent is generally necessary to reduce the occlusion effect.[3] However, the possibility of feedback howl can limit the amount of gain that can be put into the hearing aid.[4–7] Gain margins of 3–6 dB are typical in practice.[8,9]

The acoustical feedback can be characterized by the ''open-loop transfer function,'' the gain of an acoustical signal in its round trip through the hearing aid and back to the microphone.[10,11] This function will be discussed more thoroughly later in this article.

Even with a carefully maximized gain setting, a hearing aid can still exhibit feedback howl. The presence of an exterior object, such as a telephone handset, can increase the feedback signal at the microphone port through reflection or diffraction of sound, what we will refer to as the proximity effect. Hellgren *et al.*[12] have investigated this increase in the open-loop transfer function in the case of several exterior objects and for three hearing aid categories: behind the ear (BTE), in the ear (ITE), and in the canal (ITC). A nearby wall, the hearing aid user's hand, hats, and another nearby person were all found to induce a proximity effect. It was found, though, that a telephone handset typically yielded the most dramatic increase in hearing aid feedback. For a BTE-type hearing aid, the presence of a handset led to a maximum increase in open-loop transfer function in the 2–5-kHz frequency range of 14 dB on human subjects and 11 dB on a mannikin. Similarly, increases of 17 dB were observed for an ITE-type hearing aid. Hearing aid dispensers need to be aware of the magnitude of the proximity effect when they prescribe gain targets.

One thing missing from the Hellgren *et al.* studies is a quantification of the proximity effect, the dependence of the effect on the physical distance between pinna and reflecting object. The objective of the present study was to fill in this missing information, through both measurements and numerical simulation.

Feedback cancellation methods are often employed in hearing aids to reduce the acoustical feedback.[13] Knowledge of the open-loop transfer function and how it varies with proximity of a telephone handset is important if a robust and effective cancellation is to be achieved. A comprehensive study of all the factors that might affect the proximity effect is beyond the scope of this report. We will present results for three different types of hearing aids, making use of representative pinnae, a single telephone handset, and a typical orientation and trajectory for the handset. A limited number of additional measurements will be presented to discuss the effect of vent diameter and sensitivity to orientation of the handset.

In Sec. II, acoustical feedback will be discussed and the key descriptor, the open-loop transfer function, described. Section III will present the experimental approach used for determining the open-loop transfer function and Sec. IV will report the measured results. A numerical approach for the calculation of open-loop transfer functions will be discussed in Sec. V. Numerical results for an ITC aid and a comparison to experiment will follow in Sec. VI.

II. FEEDBACK IN HEARING AIDS

The sketch in Fig. 1 illustrates some of the mechanisms by which acoustical feedback can occur in hearing aids. An incident sound pressure p_i is received at the microphone port. The electrical signal produced by the microphone, in response, is passed on to the receiver (intermediate electronics ignored, for now) which produces an acoustical signal p_{ec} at the receiver point in the ear canal. Some of this signal can get back to the inlet port of the microphone. One of the main routes, and the one considered in detail in this article, is through the hearing aid vent. This opening is necessary to reduce the sensations of a static pressure and the presence of the occlusion effect.[3] Other feedback paths exist, however. There can be leakage between the hearing aid mold and the wearer's ear canal or leakage through the shell of the hearing

[a]Electronic mail: mike.stinson@nrc-cnrc.gc.ca

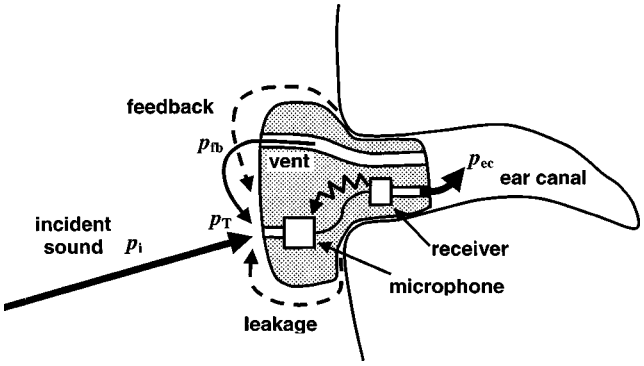

FIG. 1. Sketch of a hearing aid showing some of the paths of feedback by which an acoustical signal can get back to the microphone. The main path considered here is through the vent but the leakage path (dashed lines), between hearing aid and wall of the ear canal, can be important also. Vibrational and electromagnetic coupling from receiver to microphone is possible (jagged line) but was not observed.

aid back to the microphone port. Electrical or mechanical coupling between receiver and microphone can lead to responses being generated by the microphone without an actual sound pressure being generated at the microphone port: we can treat these feedback paths as producing *effective* sound pressures at the microphone port. If we consider all feedback contributions collectively as giving a sound pressure p_{fb} at the microphone port, then we have a total sound pressure

$$p_T = p_i + p_{\mathrm{fb}} \tag{1}$$

at the microphone.

The overall gain G of the feedback system relates the feedback signal to the signal at the microphone port: this ''open-loop transfer function'' is defined through

$$p_{\mathrm{fb}} = G p_T, \tag{2}$$

assuming a linear system. This gain function depends on the overall amplification of the hearing aid, the acoustics of the ear canal, the nature of the acoustical leakage (including, in particular, the vent diameter and length), and the diffractive and reflective behavior of the handset and pinna. Combining Eqs. (1) and (2), we can write

$$p_T = p_i/(1-G). \tag{3}$$

For relatively small gain, the total pressure is not much different than the initial, incident pressure. However, for gains that approach unity, the total pressure can become very much larger. The signal delivered to the ear canal is correspondingly large. The behavior of the system, for gains that approach or exceed unity, is more properly assessed within the context of stability analysis. According to Nyquist,[14] feedback howl can occur at frequencies for which the magnitude and phase of the gain function G satisfy the following criteria:

$$|G| \geqslant 1, \tag{4a}$$

$$\angle G = 0. \tag{4b}$$

Under these conditions, the input signal p_i can be zero and howling can still occur spontaneously. As will be seen later, it is possible for these criteria to be met at more than one frequency.

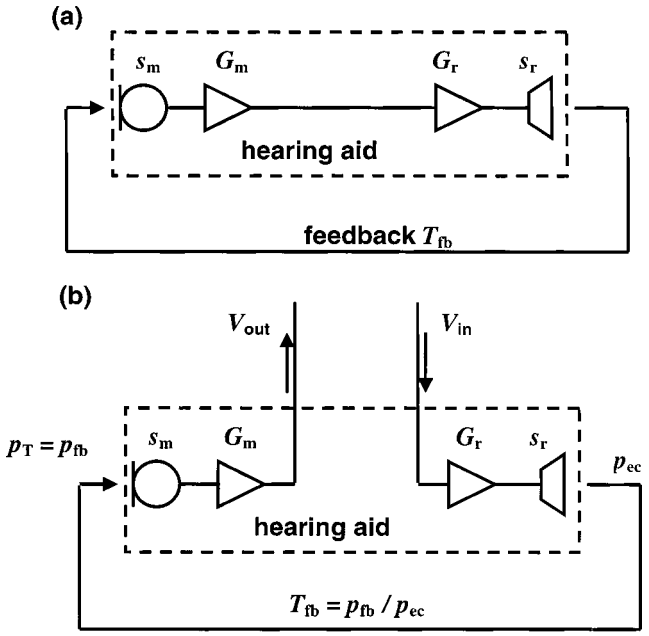

FIG. 2. Schematic representation of a linear hearing aid, showing (a) the closed-loop condition and (b) the open-loop condition. For measurement of the open-loop transfer function, a voltage V_{in} is input into the receiver stage of the aid and the resulting voltage V_{out} after the microphone stage determined.

III. MEASUREMENT PROCEDURE

Figure 2(a) shows the basic electrical/acoustical circuit representation of the linear hearing aid of Fig. 1, with no input signal. This is the closed-loop condition. The electronics of these hearing aids can be simply represented as two stages of amplification, G_m associated with the microphone and G_r associated with the receiver. The total feedback gain G is

$$G = s_m G_m G_r s_r T_{\mathrm{fb}}, \tag{5}$$

where s_m and s_r are the sensitivities of the microphone and receiver (in units of V/Pa and Pa/V, respectively). T_{fb} is the acoustical transfer function that describes the propagation of sound from the ear canal through vent to microphone port, according to

$$T_{\mathrm{fb}} = p_{\mathrm{fb}}/p_{\mathrm{ec}}. \tag{6}$$

It will be affected by any change in the acoustical environment in which the hearing aid is situated. Of particular interest here is the change in T_{fb}, and hence G, that results from a change in the separation between hearing aid and a telephone handset. We refer to this change as the *proximity effect*.

To determine G directly, the feedback path needs to be broken. The hearing aids under study were modified: the inner circuit path was split and leads brought out, as indicated in Fig. 2(b). Then, applying an electrical signal V_{in} to the lead on the receiver side of the split, a voltage V_{out} can be measured on the microphone lead. These voltages are related by

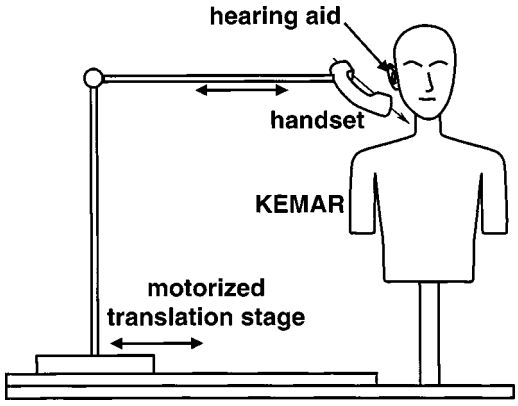

FIG. 3. The experimental approach to measure the proximity effect. The hearing aid is mounted in the pinna of a mannikin, with leads available for determination of the open-loop transfer function. The telephone handset is attached to a rigid boom, its position controlled by a translation stage under computer control. The proximity effect is the change in open-loop transfer function as the handset approaches the pinna. The arrow running along the face of the handset is used in the text to describe the orientation of the handset.

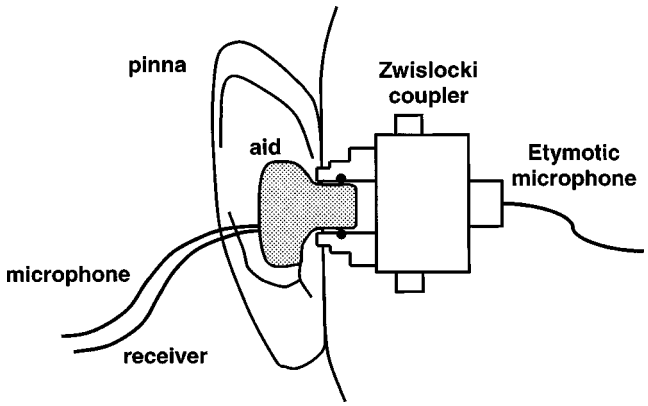

FIG. 4. Detailed sketch of the mounting of the hearing aid. The hearing aid mold has been cast to fit the pinna supplied with the mannikin. An O-ring provides the acoustical seal. Inside, a Zwislocki coupler provides an acoustical load representative of that in the human ear canal. A microphone at the inner end of the coupler measures the ear canal sound pressure.

$$V_{\text{out}} = G_r s_r T_{\text{fb}} s_m G_m V_{\text{in}}, \tag{7}$$

and therefore the open-loop transfer function is simply the ratio of voltages, i.e.,

$$G = V_{\text{out}} / V_{\text{in}}. \tag{8}$$

The measurements of open-loop transfer function were made using a Knowles Ear Manikin (KEMAR) mounted on a rigid post, as shown in Fig. 3. The hearing aid was installed in the artificial pinna of the mannikin, with the leads brought out to the electrical measurement apparatus. A Stanford Research SRT 785 analyzer provided the electrical input to the receivers and accepted the output from the hearing aid microphones. Stepped tones (1024 points), logarithmically spaced between 200 Hz and 10 kHz, were used in the measurements. The telephone handset could be accurately and repeatably positioned near the hearing aid to better than 0.5 mm using a motorized translation stage. The motion was perpendicular to the midplane of the mannikin. The use of narrow, rigid booms to connect handset to translation stage reduced the effects of scattering. Measurements were done in an Eckel anechoic chamber having tip-to-tip dimensions of $3.4 \times 3.8 \times 5.8$ m. The chamber wedges were designed to have a low-frequency cutoff of no more than 80 Hz and measurements to commission the chamber confirmed that it is anechoic down to frequencies of about 100 Hz.

The hearing aids were fit individually to artificial pinnae. The shell of the BTE aid was fit to a Knowles DE-065 pinna. These were mounted on a DB-100 occluded ear simulator (Zwislocki style) via a DB-050 ''canal extension.'' The shells of the ITE and ITC aids were each fit to a DB-090 pinna (a DB-056 canal extension was in place during the casting, then removed afterward). They were mounted on the occluded ear simulator via the DB-055 canal extension, as sketched in Fig. 4. This adapter has an internal O-ring to provide an acoustical seal. Although this arrangement of pinna and ear simulator gives a good approximation to the human external ear, it is noted that the properties of skin and flesh are not accommodated. An Etymotic ER-11 microphone, at the inner end of the simulator, is available to give a measurement of the internal, ''ear canal'' pressure. The quoted sensitivity of -42 dB (re 1 V/microbar) was used to convert the microphone output voltage to sound pressure; the phase component of the sensitivity was assumed to be zero.

A positioning jig was constructed so that the handset could be placed near the pinna in a repeatable fashion. Before a measurement run, the pinna was removed and this jig screwed into the mannikin in its place. The handset was placed in this guide and the bolts holding it onto the boom locked in place. This handset position is defined as the 0-mm position. After then translating the handset back away from the mannikin, the positioning jig was removed and the pinna with hearing aid put back in place. In this way, the handset could be oriented next to the pinna consistently, to better than 0.5° and 0.5 mm. The orientation was our best approximation to what seemed like a typical use. In Fig. 3, a reference arrow has been included across the face of the handset. For the measurements, this arrow makes an angle of 12° with the horizontal plane and 32° with the sagittal plane; the handset has a roll of 10° about the arrow. When the handset was translated back to the 0-mm position, it just touched or compressed slightly the posterior aspect of the pinna, midway up its vertical extent, and the mouthpiece was approximately 10 mm from the lips of the mannikin.

For the following measurements of proximity effect, handset positions are the distances moved laterally away from the pinna. This movement provides a good approximation to a typical orientation and trajectory for a handset and is easily implemented by the motorized translation stage. Measurements were made at various fixed handset positions between 0 and 130 mm. Measurements were also made with the handset not present. Although the lateral movement is expected to provide a good characterization of the proximity effect, a few additional measurements and calculations were performed in the case of the ITC aid to get a sense of the sensitivity to the orientation of the handset.

Both the vent diameter and length will affect the open-loop response of the hearing aid. However, the intention in this work was not to study how this function changed with

TABLE I. Details of the three hearing aids used in the experiments. The hearing aids (obtained from and modified by Unitron Hearing) contain Knowles microphones and receivers.

Model	Type	Microphone	Receiver	Vent diameter (mm)	Vent length (mm)
Vista canal, class D linear	ITC	EM-4346cx	BK-1615	2.4	11
Vista full-shell, power B linear	ITE	EM-4346cx	EP-4107	2.4	20.5
ICON AoHP	BTE	EK-3032	CK-3122	2	21.5

vent diameter, length or other parameters—the interest is in the proximity effect, i.e., the *change* in the open-loop transfer function as a telephone handset is moved near the pinna. A reasonable change in vent diameter or length is not expected to significantly affect the reported proximity effect results. Nonetheless, a limited number of measurements were made with different vent diameters in the case of the ITC aid.

IV. MEASUREMENTS

Measurements were made using three different hearing aids, obtained from and modified for these experiments by Unitron Hearing. The aids provide a representative sampling, one being a BTE aid, another, an ITE aid, and the third, an ITC aid. A summary is provided in Table I. For those aids with a gain control, a setting of maximum gain was used. Preliminary tests were performed, with the aids in the open-loop condition, to determine the linear range of operation of receivers and microphones. For the receiver, different input voltages were applied and the resulting ear canal pressures observed using the coupler microphone; for the microphone, a mouth simulator was used to produce different incident sound pressures at the front of the hearing aid and the microphone output voltages observed. In the measurements of open-loop transfer function, an input voltage of 14 mV rms to the receiver was used, low enough that clipping by the receivers and microphones was generally avoided. Acoustical leakage was a major concern. It was found that measurements could be corrupted by leakage of sound through the O-ring seal through which the hearing aid mold passed with just relatively slight adjustments of the position of the aid. A test procedure was adopted to ensure that there was no leakage immediately prior to and after a test run: the response of the hearing aid microphone to a signal input at the receiver was compared with the vent first open and then sealed with plasticene. It was required that the response in the sealed case be 15–20 dB less at all frequencies up to 6 kHz. The face of the handset was sealed as well, to minimize acoustical absorption at the earpiece.

A. ITC hearing aid

In Fig. 5, the measured open-loop transfer function is shown for the ITC hearing aid. Both magnitude and phase are shown as functions of frequency for several handset positions. Below 3 kHz, the magnitude is greatest for the curve labeled 0 mm, i.e., the handset is immediately adjacent to the pinna. As the handset is moved laterally away from the pinna and head, the open-loop transfer function drops. Most of this drop occurs in the first 10 mm of displacement away from the pinna; indeed, the curves determined at handset positions 20, 50, and 100 mm are quite similar. Measurements made at 130 mm and with the handset not present (not shown) are indistinguishable from the 100-mm measurements.

The proximity effect can be observed more clearly if difference curves are plotted. Since the measurements show that the 100 mm is about the minimum distance from the pinna at which the open-loop transfer function no longer decreases, we use the results obtained for the 100-mm position as a reference and compute the difference between this and the results for the other handset positions. Using this procedure, the structure in the curves of Fig. 5 due to the frequency responses of microphone, receiver, and feedback path is removed, leaving the effect due to handset proximity. For this ITC aid, the proximity effect is shown in Fig. 6. It is clear that the presence of the telephone handset increases the feedback signal by nearly 20 dB at 2.5 kHz. At higher frequencies, a more complicated effect is observed, due to interference between the acoustic signals reaching the microphone port directly from the vent and by reflection off the surface of the handset.

The Nyquist criterion was investigated for this hearing aid. The two electrical leads were shorted, with the handset

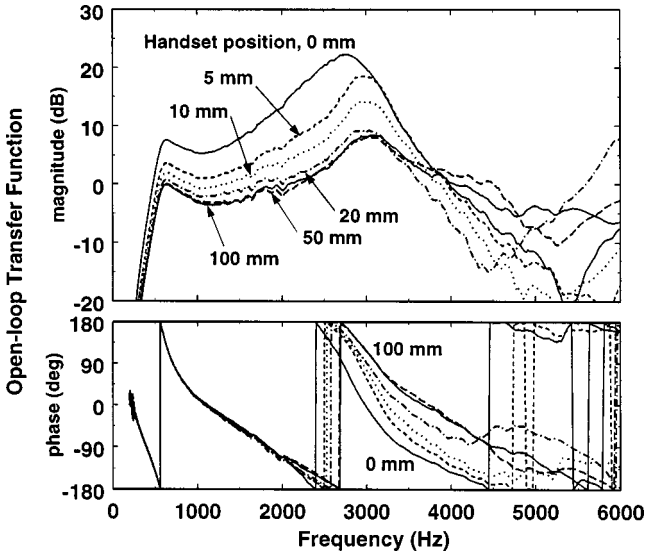

FIG. 5. Measured open-loop transfer function for an ITC hearing aid. Magnitude is shown in the upper panel, phase in the lower panel. The different curves correspond to different positions of the telephone handset. For the 0-mm curve, the handset is just touching or slightly compressing the pinna. For the other curves, the label gives the distance through which the handset is moved laterally away from the pinna. Significant differences between the curves are evident, particularly in the 0–10-mm range. After a 50-mm separation has been reached, little subsequent change is observed below 4 kHz.

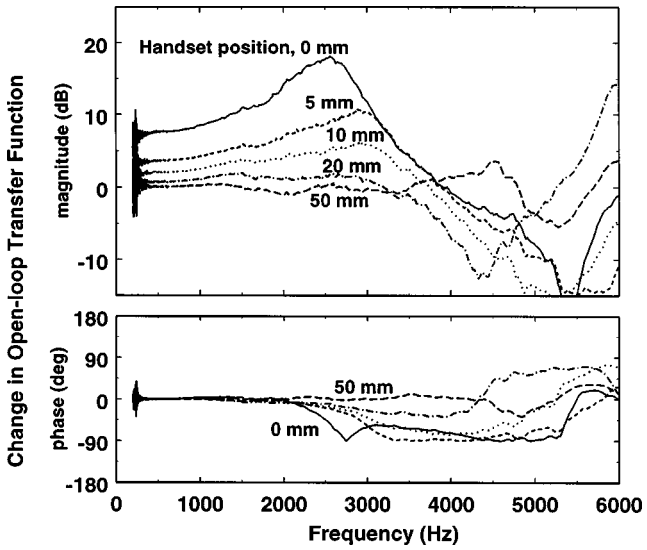

FIG. 6. The proximity effect for the ITC hearing aid. The change in open-loop transfer function, using the 100-mm curve of Fig. 5 as a reference, is plotted. An increase of 20 dB is evident as the handset approaches the pinna. This increase represents the additional burden placed on any feedback reduction technique built into the aid.

in the 0-mm position, and feedback howl occurred. The measured response at the ear canal microphone is shown in the bottom panel of Fig. 7. A very large peak is seen just below 3 kHz (as well as a harmonic just below 6 kHz). The upper two panels of this figure show the corresponding open-loop transfer function, magnitude and phase, for this handset

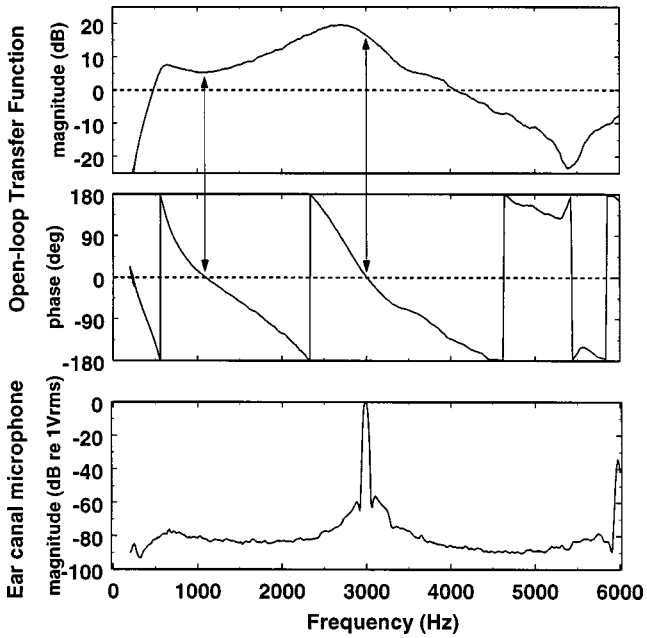

FIG. 7. Examination of the Nyquist criterion for feedback howl. The top two panels show the measured open-loop transfer function for the ITC hearing aid with the handset in the 0-mm position. According to the criterion, feedback howl can occur when the magnitude of the open-loop transfer function exceeds unity (0 dB) and its phase is zero. There are two possible frequencies of feedback howl, indicated by the vertical arrows. When the measurement leads are reconnected, see Fig. 2(a), howl occurs as evidenced by the sound pressure measured by the ear canal microphone shown in the bottom panel. The sharp peak near 3 kHz corresponds to the possible frequency of howl having the greatest magnitude.

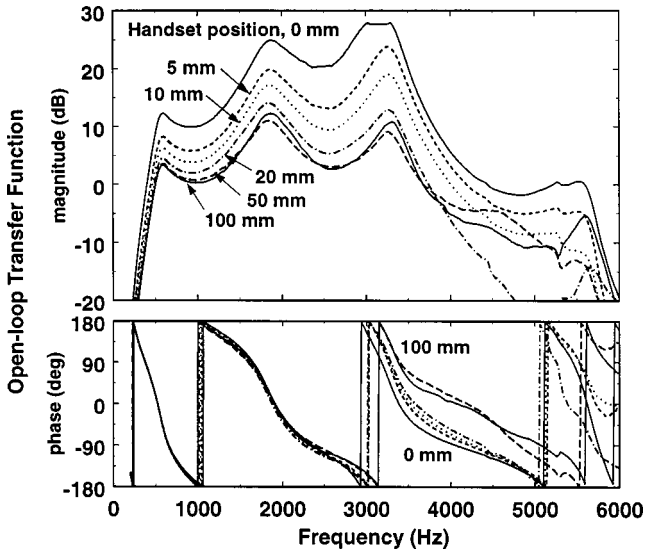

FIG. 8. Measured open-loop transfer function for the ITE hearing aid. The different curves correspond to the different handset positions.

position—these are the 0-mm results already shown in Fig. 5. The magnitude exceeds 0 dB for frequencies between 500 Hz and 4 kHz. Within this range, there are two zero crossings of the phase function, one at 1.1 kHz, the other at 3 kHz. These are, then, the possible frequencies of feedback howl according to the Nyquist criterion. In this example, the system oscillates at the zero-crossing frequency for which the magnitude is greater. To avoid feedback oscillation, the system gain would have to be reduced by 18 dB. It was also verified that feedback oscillation occurred at the lower zero-crossing frequency when the open-loop response was low-pass filtered to remove the frequencies above 2500 Hz.

For this hearing aid, the gain is sufficiently high that, even when no handset is present, acoustical feedback howl occurred spontaneously. These tests and others have confirmed the appropriateness of the Nyquist criterion. Strictly, the amplication by the microphone and receiver (G_m and G_r) may change at high voltage levels, when one or both enter a nonlinear regime of operation during howling. As well, there could be impedance loading effects with the measurement apparatus.

The open-loop response of this hearing aid was also measured with vent diameters of 1.6, 1.14, and 0.51 mm. The vent diameter was reduced by using Unitron's Selectavent D insert kit. In the case of the 1.6- and 1.14-mm vent diameters, the magnitude of the open-loop response decreases slightly, but the overall shape of the curves, and hence also the difference curves (the proximity effect), remain essentially unchanged. In the case of the 0.51-mm vent diameter, though, the measured response curve is noticeably altered at frequencies below 2 kHz. A detailed study of the effect of very small vent diameters on the proximity effect is beyond the scope of this work and was not pursued further.

B. ITE hearing aid

The measured open-loop transfer functions for the ITE hearing aid are shown in Fig. 8. The general behavior is similar to that observed for the ITC aid. The effect of the

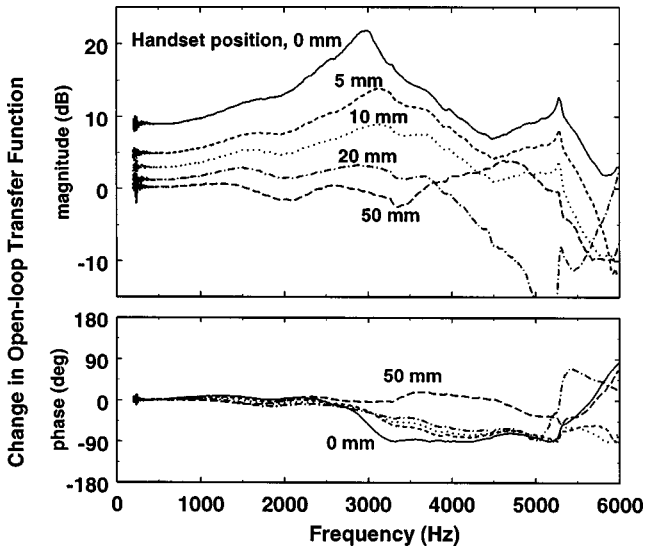

FIG. 9. Proximity effect for the ITE hearing aid. The change in open-loop transfer function, using the 100-mm curve of Fig. 8 as a reference, is plotted. The effect exceeds 20 dB at 3 kHz.

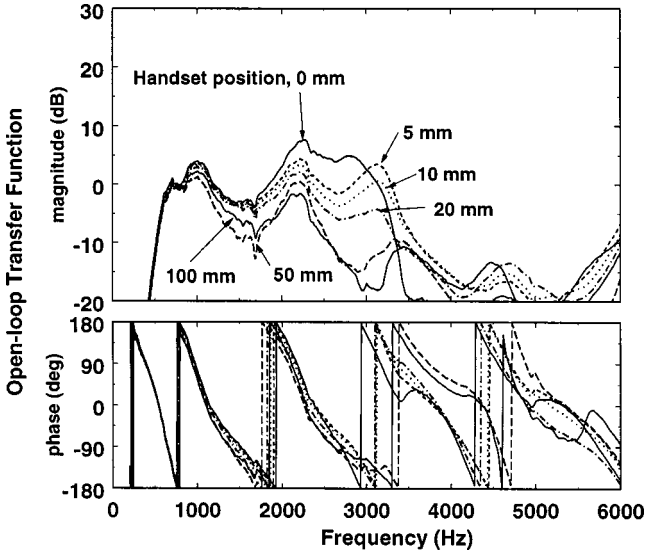

FIG. 10. Measured open-loop transfer function for the BTE hearing aid.

handset is most apparent when it is within 10 mm of the pinna. With a separation of 20 mm or more, the change in open-loop transfer function is small. We note that the measurement for the 0-mm position shows a peak between 3 and 3.3 kHz that is somewhat flattened: the acoustical feedback is sufficiently large that clipping is beginning to occur in the microphone.

The magnitude of the open-loop transfer function exceeds 0 dB for all curves between 400 Hz and 3.7 kHz, so the first part of the Nyquist criterion, Eq. 4(a), is satisfied. Within this range of frequencies, the phase component of each open-loop transfer function is seen to cross zero more than once, each crossing satisfying Eq. 4(b), the second part of the Nyquist criterion. For each handset position, there are actually three frequencies at which feedback howl can occur. One frequency is near 500 Hz, another is just below 2 kHz, and the third lies somewhere between 3.2 and 4.3 kHz (and depends on the handset position).

The proximity effect, with differences calculated relative to the 100-mm result, is shown more clearly in Fig. 9. The maximum value of the effect is 22 dB, somewhat larger than for the ITC aid. Although the vent length of this aid is about twice that of the ITC aid (see Table I), the overall shape of the curves is quite similar to the curves shown in Fig. 6. Measurements made at 130 mm and with the handset not present were indistinguishable from the 100-mm measurements.

C. BTE hearing aid

We show in Fig. 10 the measured open-loop transfer functions for the BTE hearing aid. These functions are quite different than those shown in Figs. 5 and 8: with the microphone located near the top of the pinna, the direct and reflected acoustical paths from vent to microphone port are different than for the ITC and ITE aids. Still, there is a similar progression as the separation between pinna and handset is varied.

The magnitude of the open-loop transfer function, for this hearing aid, is considerably less than for the other two hearing aids. For some handset positions the Nyquist criterion is not met; for others it is only met marginally.

The proximity effect is more clearly seen by computing differences, relative to the 100-mm curve. The magnitude of the proximity effect, shown in Fig. 11, reaches 20 dB and is comparable to that of the other two hearing aids. For this BTE aid, there are significant changes in open-loop transfer function as the handset moves between the 20- and 100-mm positions. Measurements made at 130 mm and with the handset not present (not shown here) were essentially the same as the 100-mm measurements, up to 1.5 kHz. At higher frequencies, though, there were differences of up to 2 or 3 dB: the effect of the handset is not confined to a limited range of motion as for the ITC and ITE hearing aids.

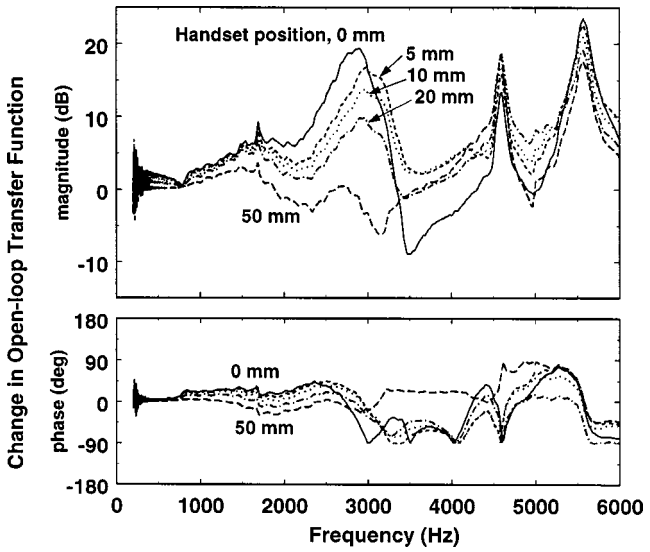

FIG. 11. Proximity effect for the BTE hearing aid. The change in open-loop transfer function, using the 100-mm curve of Fig. 10 as a reference, is plotted. The effect reaches 20 dB at 3 kHz.

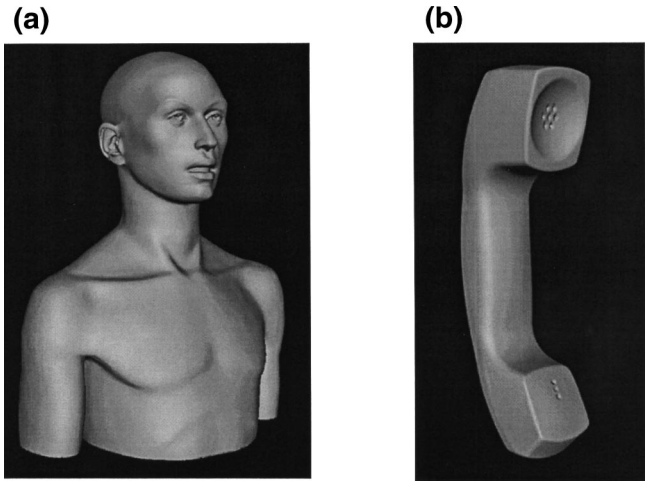

FIG. 12. The three-dimensional visualization obtained from the laser scans made of (a) mannikin with ITC hearing aid mounted in pinna and (b) handset used in the proximity experiments. The data for the mannikin correspond to approximately 350 000 triangular elements. The data for the handset correspond to approximately 260 000 elements. These meshes were the starting point for the boundary element calculation of the proximity effect.

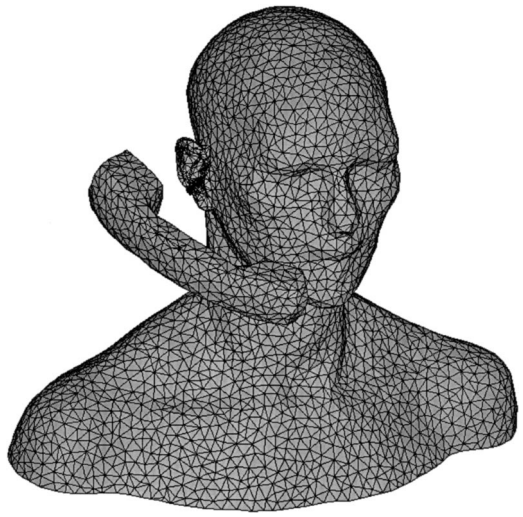

FIG. 13. The mesh actually used for the boundary element calculations. A ''mesh coarsening'' of the data shown in Fig. 12 reduced the number of elements to 9690 elements, for the mannikin part, and to 944, for the handset portion. The triangular elements generally did not exceed 14 mm in any dimension.

V. NUMERICAL MODELING PROCEDURE

In parallel with the measurements, numerical computation of the proximity effect was performed. A boundary element calculation was used to obtain the sound field radiated from the vent. The calculated change in sound pressure at the microphone position for different positions of the handset yields the numerical prediction for the proximity effect. Three-dimensional images of the system (mannikin with hearing aid and handset, separately) were used to construct a mesh suitable for a boundary element calculation. The ITC aid was chosen for the modeling since it was expected to be the most challenging numerically of the three aids, because of the close proximity of vent, microphone port, and handset.

Figure 12(a) shows the three-dimensional image of the mannikin, with the ITC hearing aid installed, obtained using an in-house laser scanning system.[15] Nearly 350 000 triangular surface elements comprise this mesh. For a boundary element calculation, the computation time would be enormous. This number of elements is unnecessarily large: a common guideline is to use elements with linear dimension $\lambda/8$, where λ is the wavelength corresponding to the highest frequency of interest. Several stages of simplication were implemented. First, we made use of the editing capabilities of the InnovMetric software used for the laser imaging. The left pinna and the lower half of the torso were removed and the mesh resolution decreased. The total number of elements was reduced to about 30 000. However, there was considerable variability in the size of the elements, flat areas having quite large elements—this is appropriate for visualization purposes, but not suitable for an acoustical boundary element calculation. At this point, the vent is imaged down several mm into the hearing aid. HyperMesh, a finite element pre- and post-processing application, was used to remove these inner elements and patch over the outlet plane. The next stage was a mesh coarsening procedure to reform the mesh into a smaller number of larger elements. In this procedure, similar to that used by Kahana,[16] small elements having sides less than 7 mm are removed by an ''edge collapse'' process: The two nodes defining the edge between a target element and the adjacent element are moved together to become a single node—both elements disappear. The formed node is not necessarily at the midpoint between the two original nodes. We select a position normal to the edge, either out from the surface or into the surface, such that the volume change incurred by the edge collapse is identically zero. Checks are in place to ensure that no edge collapses are made if the orientation of the remaining elements is changed by more than 10°. The mesh coarsening procedure is applied systematically to all the elements of the mesh. In the process, some considerably larger elements are formed. Elements having sides greater than 14 mm are then split. Elements that are too obtuse, defined as having an angle greater than or equal to 152°, are also split. Several passes through the data set were made, collapsing and splitting, until no further changes were observed. The final mesh contains 9690 triangular elements (4847 nodes). The average element side is about 10 mm. Reliable sound field calculations are obtained for frequencies up to and including 5 kHz.

The handset was treated in a similar fashion. The three-dimensional laser-scanned image is shown in Fig. 12(b). It contains approximately 260 000 elements. The small holes at the earpiece and mouthpiece were first removed. Then, the mesh coarsening procedure applied to obtain a final mesh with 944 elements (474 nodes).

The handset mesh is moved and oriented next to the mannikin mesh, using HyperMesh, to match the experimental configurations. In Fig. 13, we show the total mesh for the handset in the 50-mm position. Most elements are seen to be approximately equilateral. A close-up view of the pinna is shown in Fig. 14. The detailed shape of the pinna and the hearing aid, with leads exiting, is evident. These elements tend to be quite a bit smaller than those forming the other sections of the mannikin. Our restriction that element orientation not change by more than 10° led to many small ele-

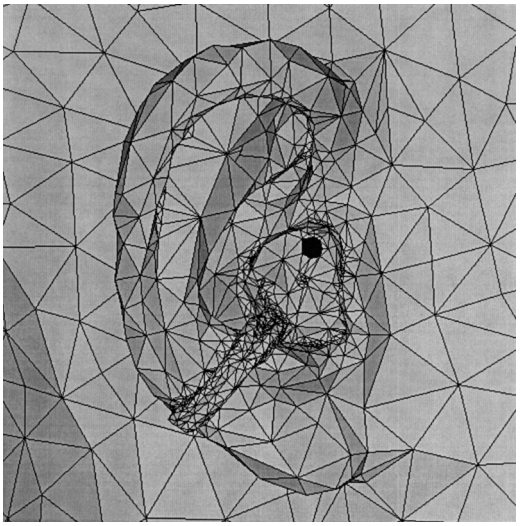

FIG. 14. Close-up view of the boundary element mesh representing the pinna and hearing aid. Much smaller elements were retained so that the detailed geometry near the hearing aid would be preserved. The vent of the hearing aid is shown as the darker elements in the upper quadrant of the aid.

ments being preserved. This result turns out to be useful. There will be rapid changes of the sound field in the vicinity of the vent, so small elements having sides comparable in size or smaller than the vent are necessary locally. Shaw and Teranishi[17] and, more recently, Nelson and Kahana[18] have shown that the small details of pinna structure can have a significant effect on the local sound fields, so the use of elements considerably smaller than the usual $\lambda/8$ specification was accepted. The vent is highlighted in Fig. 14 as the darker area in the upper-right quadrant of the aid. The microphone position is near the bottom of the aid, as viewed, about 2 mm below and to the right of the leads.

Sound field calculations were made using the SYSNOISE computational package, selecting the BEM Direct module. The seven elements forming the vent (total surface area of 7.4 mm^2) were assigned a nominal velocity of 1 m/s and the radiated sound field computed. The sound pressure at the position of the microphone port was picked out of the data.

To enable comparison of the calculations to the measurements, the assumed vent velocity must be related to the output of the receiver. As shown in the Appendix, the actual volume velocity u_v at the exit side of the vent is given by

$$u_v = \frac{p_{\mathrm{ec}}}{W_{11} Z_{\mathrm{rad}} + W_{12}},$$

where $Z_{\mathrm{rad}} = p_v / u_v$ is the radiation impedance at the vent exit (obtained from the boundary element calculation), and W_{11} and W_{12} are elements of a transfer matrix, defined in Eq. (A1), that describes the acoustical propagation through the vent. The boundary element calculations, obtained using $u_v = 1$, are scaled to match this volume velocity computed using the measured p_{ec}.

VI. NUMERICAL RESULTS

The calculated sound pressure at the microphone position is shown in Fig. 15. Both magnitude and phase components are shown, as the open circles, for frequencies between

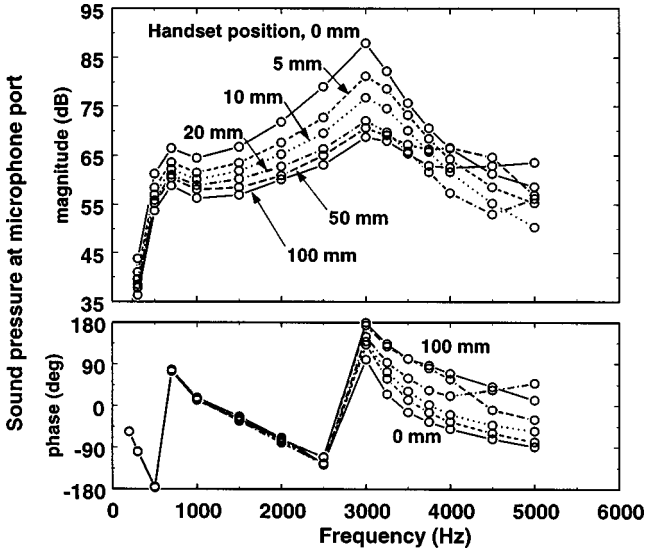

FIG. 15. Calculated sound pressures at the microphone position of the ITC hearing aid, for constant velocity of the elements representing the outlet of the vent. Magnitude and phase of the pressure are shown in the upper and lower panels, respectively. The labeled positions of the handset correspond as nearly as possible to positions used in the experiments.

200 Hz and 5 kHz. The same qualitative behavior is evident here as was observed for the measured open-loop transfer function shown in Fig. 5 for the ITC hearing aid. The microphone pressure varies as the handset position changes. Most of the change occurs as the handset moves between the 0- and 10-mm positions. The changes are more evident if we plot difference curves. The 100-mm calculation is used as a reference and is subtracted from the responses obtained for the other handset locations. This is shown in Fig. 16. The effect of handset proximity reaches 20 dB.

The calculated pressures in Fig. 15 cannot be compared directly to the open-loop transfer functions in Fig. 5. We would need to include in the calculations the sensitivity of

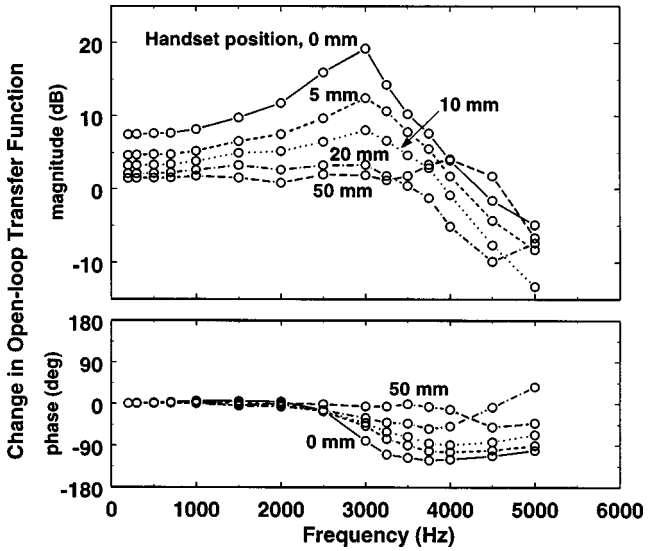

FIG. 16. Calculated proximity effect for the ITC hearing aid. The 100-mm curve of Fig. 15 is used as a reference to determine the change in sound pressure as handset approaches the pinna. This change corresponds directly to the measured change in open-loop transfer function. The proximity effect reaches 20 dB at about 3 kHz.

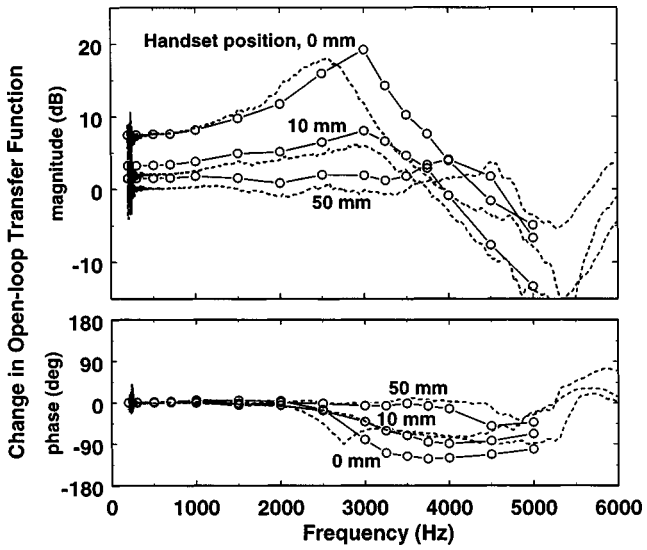

FIG. 17. Comparison between measured and calculated proximity effects, for the ITC hearing aid, choosing handset positions of 0, 10, and 50 mm.

the microphone and the amplification associated with the microphone (the s_m and G_m of Fig. 2) as well as a calibration of the ear canal microphone. Measurement of these functions, including both magnitude and phase, is nontrivial. Our goal in this report is to study the *changes* in response as a handset moves, i.e., difference curves are the desired result. The difference curves shown in Fig. 16 *can* be compared directly to the difference curves shown in Fig. 6. Both show the proximity effect. In Fig. 17, this comparison is made explicitly for three handset positions: the open circles show the calculated proximity effect, the dashed line, the measured effect. Agreement is quite good. The discrepancies are believed to be due to handset orientation and position not being exactly the same in simulations and measurements. The curves of Fig. 5 demonstrate the importance of getting the same 0-mm position for experiment and calculations—a 1-mm difference leads to a frequency-dependent difference in response of up to 2 dB. Additional measurements and calculations were performed to get a sense of the sensitivity to orientation. A downward translation of the handset resulted in a nearly linear drop in the open-loop transfer function over most of the frequencies of interest, with a 3-dB drop after a downward translation of 10 mm. Changes in angular position of 5°, e.g., a roll about the long axis of the handset, led to frequency-dependent changes of up to 1 dB. These sensitivities to position and orientation would be expected to be most important when the handset is immediately adjacent to the pinna containing the hearing aid, i.e., the 0-mm position.

VII. CONCLUSIONS

The presence of a telephone handset increases the acoustical feedback signal reaching the microphone of a hearing aid, increasing the possibility of feedback howl. This effect has been determined experimentally by measurement of the open-loop transfer function for hearing aids mounted in a mannikin. The increase in open-loop transfer function due to the presence of the handset, what we have termed the proximity effect, can be more than 20 dB. Three types of hearing aids were investigated (behind the ear, in the ear, and in the canal) and all three were susceptible to a proximity effect of this magnitude. These results are consistent with the findings of Hellgren *et al.*[12] The orientation of the handset was ensured through use of a positioning jig at the start of each experiment. The dependence of the proximity effect on separation between handset and pinna was quantified. The biggest effects were observed as the handset moved between the 0-mm position (just touching the pinna) and a position 20 mm lateral. Further increases in separation caused the open-loop transfer function to change by only a couple decibels.

There are several other factors not, or only partially, investigated in this report that could affect the proximity effect, including the diameter of the vent, the shape of the handset, pinna size and shape, and the trajectory followed by the handset. Also, our measurements were performed using a mannikin, not human subjects. These factors will all affect the open-loop transfer function to a greater or lesser extent. For the proximity effect, though, we are looking at *changes* in open-loop transfer function as a handset moves, so their effects should be less important.

We have focused our effort on the telephone as a source of increased sensitivity to feedback. In some applications, particularly for BTE-type aids, a user can benefit from a telecoil built into the aid. However, as pointed out by Hellgren *et al.*, the telephone handset is only one of several objects that typically cause feedback howl.

Our results define the additional feedback-handling requirement for a feedback suppression technique in a hearing aid. Such techniques are often built into the signal processing of a hearing aid, to enable the use of higher gain settings or larger vents. Most such techniques would not be able to handle the 20 dB of increased sensitivity to feedback howl that we have demonstrated.

The feedback problem was also addressed theoretically, through a boundary element calculation. The mannikin, with ITC hearing aid installed, was imaged using a laser scanning system and a boundary element mesh obtained. Numerical calculations of the sound field resulting from a volume velocity source at the vent were used to compute the proximity effect. The results obtained, for the ITC hearing aid, agreed quite well with the measurements. We have, then, both theoretical and experimental approaches that can be used to study the acoustical feedback problem in hearing aids. Considerable detail was included in the modeling effort. It may be possible to reduce the amount of detail, e.g., the use of larger mesh elements for the pinna and hearing aid, without sacrificing accuracy.

ACKNOWLEDGMENTS

We acknowledge with gratitude the efforts of Michel Picard and Luc Cournoyer from NRC's Institute of Information Technology in producing the three-dimensional laser images of mannikin and handset. Dr. Horst Arndt of Unitron Hearing provided the modified hearing aids. We appreciate the advice of Dr. James Ryan of Gennum and the ongoing technical assistance of René St. Denis.

APPENDIX

The boundary element calculations were made assuming a nominal velocity for the elements comprising the vent outlet. To relate the radiated sound field to the actual output of the hearing aid receiver, the propagation of sound through the vent of the hearing aid needs to be considered. For tubes of small diameter, Egolf[19] has shown that viscous and thermal boundary layer effects must be included. We make use of his modeling here.

At the inner end of the vent, we have a sound pressure p_{ec} and volume velocity u_{ec} entering the vent. At the vent outlet, we have sound pressure p_v and volume velocity u_v. For a vent of radius a and length L, these quantities are related[19] through a transfer matrix $\mathbf{W}$:

$$\begin{pmatrix} p_{ec} \\ u_{ec} \end{pmatrix} = \mathbf{W} \begin{pmatrix} p_v \\ u_v \end{pmatrix} = \begin{pmatrix} \cosh(\Gamma L) & Z\sinh(\Gamma L) \\ \sinh(\Gamma L)/Z & \cosh(\Gamma L) \end{pmatrix} \begin{pmatrix} p_v \\ u_v \end{pmatrix}. \tag{A1}$$

The propagation constant Γ and characteristic impedance Z are

$$\Gamma = i\frac{\omega}{c}\left[\frac{1+(\gamma-1)T(\alpha a)}{1-T(\beta a)}\right]^{1/2}, \tag{A2a}$$

$$Z = \frac{\rho c}{\pi a^2}[1-T(\beta a)]^{-1/2}[1+(\gamma-1)T(\alpha a)]^{-1/2}, \tag{A2b}$$

where

$$T(\xi) \equiv 2J_1(\xi)/\xi J_0(\xi), \tag{A3}$$

$$\alpha = (-i\omega\rho N_{pr}/\mu)^{1/2}, \tag{A4}$$

and

$$\beta = (-i\omega\rho/\mu)^{1/2}. \tag{A5}$$

Here, μ is the coefficient of viscosity, ρ is the density of air, c is the free space sound speed, γ is the ratio of specific heats in air (1.4), N_{pr} is the Prandtl number (0.702), ω is the angular frequency, and J_0 and J_1 are Bessel functions of the first kind of orders 0 and 1.

From Eq. (A1), we can write

$$u_v = \frac{p_{ec}}{W_{11}Z_{rad} + W_{12}}, \tag{A6}$$

where the radiation impedance is $Z_{rad} = p_v/u_v$. In the boundary element calculations, the sound pressure p_v was determined for specified u_v, so the radiation impedance was available. Using the measured ear canal sound pressure p_{ec}, the calculated transfer matrix term $\mathbf{W}$, and the radiation impedance, we can calculate the actual vent volume velocity u_v that would have existed for the measurements. The boundary element calculations, made using $u_v = 1$, can be scaled accordingly to make them consistent with the measurements.

Although Eq. (A6) was used because of its generality, a simpler approximation would have sufficed for the present configuration. It was determined numerically that

$$|W_{11}Z_{rad}| \ll |W_{12}| \tag{A7}$$

for all of our measurement conditions. (The same result can be obtained by treating the vent simply as an orifice in an infinite baffle; then, for vents of diameter less than 3 mm and with $a \ll L$, the relation is found to hold up to 6 kHz.) With the approximation of Eq. (A7), the volume velocity at the vent is simply

$$u_v \approx p_{ec}/W_{12}. \tag{A8}$$

[1] F. N. Erickson and D. J. Van Tasell, "Maximum real-ear gain or in-the-ear hearing aids," J. Speech Hear. Res. **34**, 351–359 (1991).
[2] S. Lybarger, "Acoustic feedback control," in *The Vanderbilt Hearing-Aid Report*, edited by G. A. Studebaker and F. H. Bess (Monographs in Contemporary Audiology, Upper Darby, PA, 1982), pp. 87–90.
[3] M. Ø. Hansen, "Occlusion effects, Part I, Hearing aid users experiences of the occlusion effect compared to the real ear sound level," Report No. 71 (Dept. of Technical Audiology, Technical University of Denmark).
[4] F. K. Kuk, "Maximum usable real-ear insertion gains with ten earmold designs," J. Am. Acad. Audiol **5**, 44–51 (1994).
[5] B. C. Grover and M. C. Martin, "On the practical gain limit for post-aural hearing aids," Br. J. Audiol. **8**, 121–124 (1974).
[6] S. Gatehouse, "Limitations on insertion gains with vented earmoulds imposed by oscillatory feedback," Br. J. Audiol. **23**, 133–136 (1989).
[7] O. Dyrlund and P. Lundh, "Gain and feedback problems when fitting behind-the-ear hearing aids to profoundly hearing-impaired children," Scand. Audiol. **19**, 89–95 (1990).
[8] O. Dyrlund, "Acoustical feedback associated with the use of post aural hearing aids for profoundly deaf children," Scand. Audiol. **18**, 237–241 (1989).
[9] J. Hellgren, T. Lunner, and S. Arlinger, "System identification of feedback in hearing aids," J. Acoust. Soc. Am. **105**, 3481–3496 (1999).
[10] D. P. Egolf, H. C. Howell, K. A. Weaver, and D. S. Barker, "The hearing aid feedback path: Mathematical simulations and experimental verification," J. Acoust. Soc. Am. **78**, 1578–1587 (1985).
[11] D. P. Egolf, B. T. Haley, H. C. Howell, S. Legowski, and V. D. Larson, "Simulating the open-loop transfer function as a means for understanding the acoustic feedback in hearing aids," J. Acoust. Soc. Am. **85**, 454–467 (1989).
[12] J. Hellgren, T. Lunner, and S. Arlinger, "Variations in the feedback of hearing aids," J. Acoust. Soc. Am. **106**, 2821–2833 (1999).
[13] J. M. Kates, "Constrained adaptation for feedback cancellation in hearing aids," J. Acoust. Soc. Am. **106**, 1010–1019 (1999).
[14] H. Nyquist, "Regeneration theory," Bell Syst. Tech. J. **11**, 126–147 (1932).
[15] M. Rioux, "Digital 3-D imaging: Theory and applications," SPIE Vol. 2350 Videometrics III (1994).
[16] Y. Kahana, "Numerical modelling of the head-related transfer function," Ph.D. thesis, University of Southampton, Faculty of Engineering and Applied Science, Institute of Sound and Vibration Research, 2000.
[17] E. A. G. Shaw and R. Teranishi, "Sound pressure generated in an external-ear replica and real human ears by a nearby point source," J. Acoust. Soc. Am. **44**, 240–249 (1968).
[18] P. A. Nelson and Y. Kahana, "Spherical harmonics, singular-value decomposition and the head-related transfer function," J. Sound Vib. **239**, 607–637 (2001).
[19] D. P. Egolf, "Techniques for modeling the hearing aid receiver and associated tubing," in *Acoustical Factors Affecting Hearing Aid Performance*, edited by G. A. Studebaker and I. Hochberg (University Park Press, Baltimore, 1980).

Power transmission in L-shaped plates including flexural and in-plane vibration

Nicole J. Kessissoglou
Mechanical Engineering, James Cook University, Townsville Qld 4811, Australia

(Received 15 February 2002; revised 2 August 2003; accepted 30 October 2003)

In this paper, power flow propagation in plates connected in an L-joint is investigated in both the low and high frequency ranges. An exact solution is derived to describe the flexural, in-plane longitudinal and in-plane shear wave motion in the plates. The coupled plates are simply supported along two parallel sides, and free at the other two ends. A point force is used to generate flexural wave motion only. The flexural wave coefficients are determined from the boundary conditions, continuity equations at the driving force locations, and continuity equations at the corner junction of the plates. Structural intensity expressions are used to examine the structural noise transmission in the low and high frequency ranges. The contributions from the individual wave types are also examined. © *2004 Acoustical Society of America.* [DOI: 10.1121/1.1635415]

PACS numbers: 43.40.Dx [JGM] Pages: 1157–1169

I. INTRODUCTION

When examining the vibration of plates in built-up structures such as ship hulls, generally only the flexural waves are considered. However, a pure bending wave impinging at a corner junction will induce in-plane longitudinal and in-plane shear waves, as well as other flexural waves in the connected plates. In addition, the in-plane waves are partly transformed into flexural waves at further structural junctions. In the last couple of decades, energy transmission in right-angled joints including flexural and in-plane wave motion has been given considerable attention.[1–13] In one of the earliest works, Budrin and Nikiforov[1] examined the transmission of flexural and extension waves through a semi-infinite cross-shaped joint. Craven and Gibbs[2] examined flexural plane wave incidence at any arbitrary angle at the junction of an L, T, or cross-shaped plate. Their analysis was extended to include in-plane incidence at the plate junctions.

It has recently been shown that the inclusion of in-plane waves becomes significant in both high frequency region, and at distances far from the vibrating source.[3–7] When examining vibrating structures in the high frequency range, both statistical energy analysis (SEA) and finite element analysis (FEA) are popular methods. SEA is an energy balance method, and considers the flow of energy into a system, the energy flow between subsystems, and the time and space averaged energy contained within each subsystem. Rather than giving detailed knowledge of the modal behavior of a structure, SEA results as presented by Tratch[3] and Lyon[4] are given in terms of mean energy levels, which are obtained by energy levels averaged over broad frequency bands. The inclusion of in-plane modes using SEA models of plate structures has been investigated by several researchers.[3–5] Bercin and Langley[6] extended the dynamic stiffness method to include in-plane vibrations, and the technique is applied to a built-up plate structure. Results were presented in terms of bending energy transmission ratios of each plate component, where the energy levels were averaged over one-third octave frequency bands. Energy transmission ratios were calculated for bending waves only (by restricting the in-plane degrees of freedom), and for bending energy in which the in-plane terms were included in the analysis. In their results, Bercin and Langley discuss that there is a reduction in the bending energy level (in-plane inclusive) of the neighboring plate to the driven plate. This is attributed to the fact that some of the incident flexural wave energy impinging on a junction will be converted into in-plane energy in the second plate, which is not accounted for in the ''bending only'' energy transmission ratios. However, at greater distances from the driven plate, the energy levels including the in-plane waves are significantly greater than those for bending waves only. This is attributed to the fact that the in-plane modes are transformed back into flexural modes as they travel through junctions. In a further study, Bercin[7] compared the results obtained from the dynamic stiffness method to those obtained using FEM and SEA. While the finite element method (FEM) technique is a very popular method to model in-plane vibrations, it becomes very difficult to apply FEM successfully in the higher frequency range.[7] This is because at higher frequencies, the number of modes contributing the structural response increases and become more closely spaced together. Hence, the system must be discretized into elements of smaller size, resulting in a large number of simultaneous equations and excessive degrees of freedom. In addition, mesh refinement at higher frequencies results in a decrease in the computational feasibility.

In addition to the problem of wave transmission through right angled joints, several authors have studied the flexural and longitudinal wave motion through beams and plates joined at an angle.[14–17] Park *et al.*[14] developed power flow models for longitudinal and in-plane shear waves for thin plates. The derived energy equations were applied to a finite coupled structure connected at a certain angle. They found that the in-plane energy levels are greater than those of the flexural waves at higher frequencies and for higher damping.

In this paper, the effect of in-plane waves on the power flow in coupled plate structures is examined. The results presented provide detailed information of the modal response of a structure for narrow-band frequency ranges, instead of

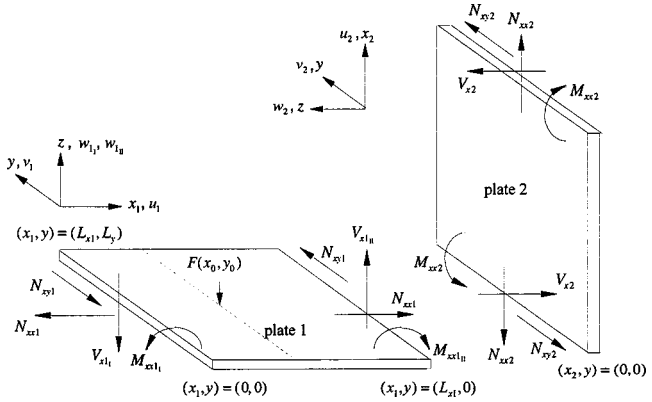

FIG. 1. Free body diagram of the L-shaped plate showing the sign convention, displacements, forces, and moments for flexural and in-plane motion.

broadband statistical energy estimates. A combination of the modal method and the traveling wave method resulting in an exact solution to describe the structural response is used. The results generated using this method are exact, and do not require mesh refinement as the frequency increases, as finite element models do. The traveling wave approach for flexural vibration has been extended to include both in-plane longitudinal and in-plane shear waves, and is applied to an L-shaped plate under point force excitation. Results are presented using the structural intensity expression, and are compared with those obtained ignoring the in-plane contributions. Using the power flow approach, the contributions from the various wave types propagating through the structure can be quantitatively compared in both the low and high frequency regions.

II. THEORY

A. Flexural and in-plane vibration of thin coupled plates

Figure 1 shows the displacements and coordinate system for an L-shaped plate. The L-shaped plate is simply supported along two parallel edges corresponding to $y=0$ and $y=L_y$, and free at the other two edges corresponding to $x_1=0$ and $x_2=L_{x2}$. The junction of the two plates corresponds to $x_1=L_{x1}$ and $x_2=0$. For mathematical simplicity, the two plates are of the same material and thickness. Since vibrating machinery such as engines are generally mounted vertically over a supporting plate, only excitation in the out-of-plane direction is considered. This is modeled as point force excitation of force amplitude F_0 at a location of (x_0,y_0) in plate 1, and is described by a Dirac delta function. Figure 1 also shows the forces and moments acting on the edges of the two plates, where M_{xx} is the bending moment, N_{xx} is the in-plane longitudinal force, and N_{xy} is the in-plane shear force. V_x is the net vertical shear force, and is given by $V_x=Q_x+\partial M_{xy}/\partial y$. Note that V_x and M_{xx} are different in the two sections (I and II) in plate 1 due to the external forcing function. For the sign convention used in Fig. 1, the force and moment equations are given by

$$Q_{xx}=-D\left(\frac{\partial^3 w}{\partial x^3}+\frac{\partial^3 w}{\partial x\partial y^2}\right), \tag{1}$$

$$M_{xx}=-D\left(\frac{\partial^2 w}{\partial x^2}+\upsilon\frac{\partial^2 w}{\partial y^2}\right), \tag{2}$$

$$M_{xy}=-D(1-\upsilon)\frac{\partial^2 w}{\partial x\partial y}, \tag{3}$$

$$N_{xx}=\frac{Eh}{1-\upsilon^2}\left(\frac{\partial u}{\partial x}+\upsilon\frac{\partial v}{\partial y}\right), \tag{4}$$

$$N_{xy}=\frac{Eh}{2(1+\upsilon)}\left(\frac{\partial u}{\partial y}+\frac{\partial v}{\partial x}\right), \tag{5}$$

where w, u, and v represent the flexural, in-plane longitudinal and in-plane shear plate displacements, respectively. $D=Eh^3/12(1-\upsilon^2)$ is the plate flexural rigidity, and E, h, and υ are respectively the Young's modulus, thickness, and Poisson's ratio of the two connected plates. The differential equations of motion for the flexural, in-plane longitudinal, and in-plane shear wave motions are respectively given by[6]

$$D\nabla^4 w+\rho h\frac{\partial^2 w}{\partial t^2}=F(x,y,t), \tag{6}$$

$$\frac{\partial^2 u}{\partial x^2}+\frac{(1-\upsilon)}{2}\frac{\partial^2 u}{\partial y^2}+\frac{(1+\upsilon)}{2}\frac{\partial^2 v}{\partial x\partial y}-\frac{(1-\upsilon^2)\rho}{E}\frac{\partial^2 u}{\partial t^2}=0, \tag{7}$$

$$\frac{\partial^2 v}{\partial x^2}+\frac{(1-\upsilon)}{2}\frac{\partial^2 v}{\partial y^2}+\frac{(1+\upsilon)}{2}\frac{\partial^2 u}{\partial x\partial y}-\frac{(1-\upsilon^2)\rho}{E}\frac{\partial^2 v}{\partial t^2}=0. \tag{8}$$

Due to the simply supported boundary edges, general solutions for the flexural and in-plane displacements in the three sections of the plates can be described in terms of a modal and traveling wave solution. The general solutions for the in-plane displacements were developed in Ref. 6, where the "$\cos k_y y$" term for v allows for the decoupling of the in-plane differential equations:

$$w_{1_I}(x_1,y)=\sum_{m=1}^{\infty}(A_1e^{-jk_xx_1}+A_2e^{jk_xx_1}+A_3e^{-k_nx_1}+A_4e^{k_nx_1})\sin k_y y,\quad 0\leqslant x_1\leqslant x_0, \tag{9}$$

$$w_{1_{II}}(x_1,y)=\sum_{m=1}^{\infty}(A_5e^{-jk_xx_1}+A_6e^{jk_xx_1}+A_7e^{-k_nx_1}+A_8e^{k_nx_1})\sin k_y y,\quad x_0\leqslant x_1\leqslant L_{X1}, \tag{10}$$

$$w_2(x_2,y)=\sum_{m=1}^{\infty}(A_9e^{-jk_xx_2}+A_{10}e^{jk_xx_2}+A_{11}e^{-k_nx_2}+A_{12}e^{k_nx_2})\sin k_yy,\quad 0\leqslant x_2\leqslant L_{x2},\tag{11}$$

$$u_1(x_1,y)=\sum_{m=1}^{\infty}(\lambda_1B_1e^{\lambda_1x_1}+\lambda_2B_2e^{\lambda_2x_1}+k_yB_3e^{\lambda_3x_1}+k_yB_4e^{\lambda_4x_1})\sin k_yy,\quad 0\leqslant x_1\leqslant L_{x1},\tag{12}$$

$$u_2(x_2,y)=\sum_{m=1}^{\infty}(\lambda_1B_5e^{\lambda_1x_2}+\lambda_2B_6e^{\lambda_2x_2}+k_yB_7e^{\lambda_3x_2}+k_yB_8e^{\lambda_4x_2})\sin k_yy,\quad 0\leqslant x_2\leqslant L_{x2},\tag{13}$$

$$v_1(x_1,y)=\sum_{m=1}^{\infty}(k_yB_1e^{\lambda_1x_1}+k_yB_2e^{\lambda_2x_1}+\lambda_3B_3e^{\lambda_3x_1}+\lambda_4B_4e^{\lambda_4x_1})\cos k_yy,\quad 0\leqslant x_1\leqslant L_{x1},\tag{14}$$

$$v_2(x_2,y)=\sum_{m=1}^{\infty}(k_yB_5e^{\lambda_1x_2}+k_yB_6e^{\lambda_2x_2}+\lambda_3B_7e^{\lambda_3x_2}+\lambda_4B_8e^{\lambda_4x_2})\cos k_yy,\quad 0\leqslant x_2\leqslant L_{x2}.\tag{15}$$

$k_y=m\pi/L_y$ is the modal wave number along the y direction, where m is the mode number. $k_p=\sqrt{\omega}(\rho h/D)^{1/4}$ is the *in vacuo* plate flexural wave number. $k_x=\sqrt{k_p^2-k_y^2}$ and $k_n=\sqrt{k_p^2+k_y^2}$ are respectively the wave numbers along the x direction for the propagating and evanescent waves. $\lambda_{1,2}=\pm\sqrt{k_y^2-k_L^2}$ and $\lambda_{3,4}=\pm\sqrt{k_y^2-k_S^2}$ are eigenvalues for the in-plane general solutions, where $k_L=\omega\sqrt{\rho(1-\upsilon^2)/E}$ and $k_s=\omega\sqrt{2\rho(1+\upsilon)/E}$ are the in-plane longitudinal and in-plane shear wave numbers, respectively.[6]

There are 20 unknown coefficients corresponding to A_i for $i=1-12$ and B_j for $j=1-8$. Twenty equations can be developed from (i) the boundary conditions at the free edges, (ii) continuity equations at the driving force location, and (iii) coupling equations at the junction of the two plates. There are eight boundary conditions at the free edges corresponding to $x_1=0$ and $x_2=L_{x2}$, resulting in[15,18]

$$V_{x1_I}=V_{x2}=0,\tag{16}$$

$$M_{xx1_I}=M_{xx2}=0,\tag{17}$$

$$N_{xx1}=N_{xx2}=0,\tag{18}$$

$$N_{xy1}=N_{xy2}=0.\tag{19}$$

The external disturbance is due to a force applied normally to the surface of the plate, resulting in power injected into the flexural modes only. There are four continuity equations at the driving force location (x_0,y_0) which are described in Ref. 18. Finally, there are eight continuity equations at the coupling junction of the two plates corresponding to $x_1=L_{x1}$ and $x_2=0$. These continuity equations have previously been developed for thick plate theory,[19] but are modified for the classical thin plate theory. For the sign notation defined in Fig. 1, the eight coupling equations can be written as

$$w_{1_{II}}=u_2,\tag{20}$$

$$w_2=-u_1,\tag{21}$$

$$V_{x1_{II}}=N_{xx2},\tag{22}$$

$$V_{x2}=-N_{xx1},\tag{23}$$

$$M_{xx1_{II}}=M_{xx2},\tag{24}$$

$$\frac{\partial w_{1_{II}}}{\partial x_1}=\frac{\partial w_2}{\partial x_2},\tag{25}$$

$$v_1=v_2,\tag{26}$$

$$N_{xy1}=N_{xy2}.\tag{27}$$

Using the 20 developed equations, a matrix expression can be obtained as $[\alpha][\mathbf{X}]=[\mathbf{F}]$, where $[\alpha]$ is a 20×20 matrix and is given in Appendix A. $[\mathbf{X}]$ and $[\mathbf{F}]$ are the coefficient and force matrices, respectively, and are given by

$$[\mathbf{X}]=[A_1\ A_2\ A_3\ A_4\ A_5\ A_6\ A_7\ A_8\ A_9\ A_{10}\ A_{11}\ A_{12}\ B_1\ B_2\ B_3\ B_4\ B_5\ B_6\ B_7\ B_8]^T,\tag{28}$$

$$[\mathbf{F}]=\left[0\ 0\ 0\ 0\ 0\ 0\ 0\ 0\ 0\ 0\ 0\ 0\ \frac{2F_0}{L_yD}\sin k_yy_0\ 0\ 0\ 0\ 0\ 0\ 0\ 0\ 0\right]^T.\tag{29}$$

Solutions to the unknown coefficients in Eqs. (9)–(15) can be obtained by $[\mathbf{X}]=[\alpha]^{-1}[\mathbf{F}]$.

B. Flexural vibration only of thin coupled plates

In order to examine the effect of the in-plane longitudinal and in-plane shear vibration on the structural power transmission, results were also obtained when the in-plane vibration was neglected in the plates. However, the in-plane force and displacement are considered at the coupling junction of the two plates, when equating the displacements and forces at the junction. The analysis is reduced to a one-dimensional problem in the x direction to consider flexural vibration only in the plates, as described by Eqs. (9)–(11). There are now only 12 unknown coefficients A_i for i

$=1-12$. At the free edges corresponding to $x_1=0$ and $x_2=L_{x2}$, there are now only four boundary conditions as described by Eqs. (16) and (17). The continuity equations at the driving force location in plate 1 remain unchanged. At the junction of the two plates, there are now only four continuity equations. The first two correspond to continuity of moment and slope from plate 1 to 2, as described by Eqs. (24) and (25). The third and fourth continuity equations are developed by equating the displacements and forces of the flexural and in-plane longitudinal waves at the corner junction. In this case, the effect of the in-plane shear force and displacement is considered negligible, that is, the longitudinal force simplifies to $N_{xx}=[Eh/(1-\nu^2)]\partial u/\partial x$. Since the analysis is reduced to a one-dimensional problem to consider the flexural wave transmission along the x-direction only, the expression for the bending shear force is simplified to $V_x=-D\partial^3 w/\partial x^3$. General expressions for the longitudinal in-plane waves for the two plates become $u_1(x_1)=C_1e^{jk_Lx_1}$ and $u_2(x_2)=C_2e^{-jk_Lx_2}$, where u_1 corresponds to a reflected in-plane wave in plate 1 due to the flexural waves in plate 2, and, similarly, u_2 corresponds to a transmitted wave in plate 2 due to the flexural waves in plate 1 impinging on the corner junction. Using Eqs. (20)–(23) with the simplified force and displacement expressions, the remaining two boundary equations can be obtained:

$$D\frac{\partial^3 w_{1_{\mathrm{II}}}}{\partial x_1^3}=\frac{jk_LEh}{1-\nu^2}w_{1_{\mathrm{II}}}, \tag{30}$$

$$-D\frac{\partial^3 w_2}{\partial x_2^3}=\frac{jk_LEh}{1-\nu^2}w_2. \tag{31}$$

The 12 unknown coefficients can also be determined using a similar matrix expression $[\alpha][\mathbf{X}]=[\mathbf{F}]$ as shown in Sec. II A. In this case, however, $[\alpha]$ is a 12×12 matrix and is given in Appendix B, and the coefficient and force matrices are reduced to

$$[\mathbf{X}]=[A_1\ A_2\ A_3\ A_4\ A_5\ A_6\ A_7\ A_8\ A_9\ A_{10}\ A_{11}\ A_{12}]^T, \tag{32}$$

$$[\mathbf{F}]=\left[0\ \ 0\ \ 0\ \ 0\ \ 0\ \ 0\ \ 0\ \ \frac{2F_0}{L_yD}\sin k_yy_0\ \ 0\ \ 0\ \ 0\ \ 0\right]^T. \tag{33}$$

C. Structural intensity in the plates

An expression for the structural intensity corresponding to the power flow per unit width of the plate including both flexural and in-plane components is given by[20]

$$P_x=-\left[\dot{w}Q_x-\frac{\partial\dot{w}}{\partial x}M_{xx}-\frac{\partial\dot{w}}{\partial y}M_{xy}+\dot{u}N_{xx}+\dot{v}N_{xy}\right]. \tag{34}$$

The time averaged vibration intensity at a given x location for flexural and in-plane vibration can be written as[14,18]

$$P_x=-\int_0^{L_y}\mathrm{Re}\left((j\omega w)^*Q_x-\left(j\omega\frac{\partial w}{\partial x}\right)^*M_{xx}-\left(j\omega\frac{\partial w}{\partial y}\right)^*M_{xy}+(j\omega u)^*N_{xx}+(j\omega v)^*N_{xy}\right)dy, \tag{35}$$

where the asterisk (*) denotes the complex conjugate. When the in-plane terms are neglected in the analysis as described in Sec. II B, the above expression simply reduces to

$$P_x=-\int_0^{L_y}\mathrm{Re}\left((j\omega w)^*Q_x-\left(j\omega\frac{\partial w}{\partial x}\right)^*M_{xx}-\left(j\omega\frac{\partial w}{\partial y}\right)^*M_{xy}\right)dy. \tag{36}$$

III. COMPUTATIONAL RESULTS

For the L-shaped plate, both plates were given the same material properties corresponding to aluminum, and were of the same thickness and width corresponding to $h=0.002$ m and $L_y=0.5$ m. The length of plate 1 is $L_{x1}=1.2$ m. The length of plate 2 is $L_{x2}=0.6$ m. The material parameters for aluminum are $\rho=2800$ kg/m^3, $E=7.1\times10^{10}$ N/m^2, and $\nu=0.3$. The internal loss factor was included in the analysis by using the complex Young's modulus $E(1+j\eta)$, where $\eta=0.001$ is the structural loss factor. The point force excitation was located at $(x_0,y_0)=(0.74,0.31)$, where the force and response positions are given in meters.

In order to ensure that a sufficient number of modes were chosen to accurately describe the response in the frequency ranges of interest, the modal density was investigated for the various frequency ranges. The modal density of the assembled structure can be estimated as the sum of the modal densities for the individual plates.[9] The number of modes N in a plate with resonance frequencies below the radian frequency ω is given by[17]

$$N=\frac{k^2S}{4\pi}, \tag{37}$$

where k is the wave number and S is the surface area of the plate. Using the flexural and in-plane wave numbers of a plate, the number of modes corresponding to the three wave types in each plate can be determined using $N_B=(L_xL_y/2h)\sqrt{12\rho(1-\nu^2)/E}f$ (number of bending modes), $N_L=[\pi L_xL_y\rho(1-\nu^2)/E]f^2$ (number of in-plane longitudinal modes), and $N_S=[\pi L_xL_y2\rho(1+\upsilon)/E]f^2$ (number of in-plane shear modes), where f is the excitation frequency in Hz. In the computational modelling, the number of modes used in each frequency range was held constant. A significantly greater number of modes were chosen for each frequency band than the minimum number using Eq. (37) to ensure that all results converged.

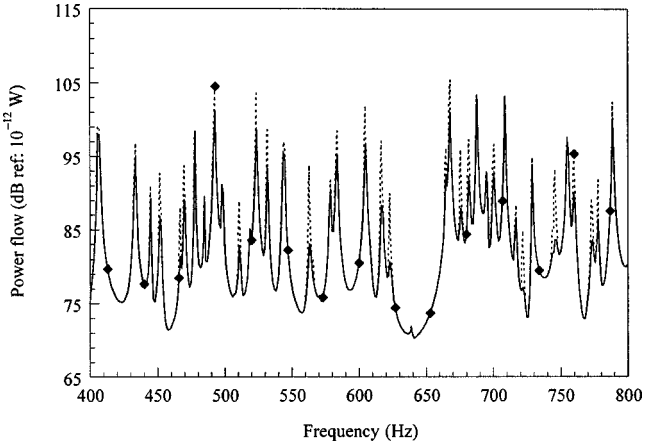

FIG. 2. Comparison of the structural power in plate 1 with (---◆---) and without (———) the inclusion of the in-plane vibration.

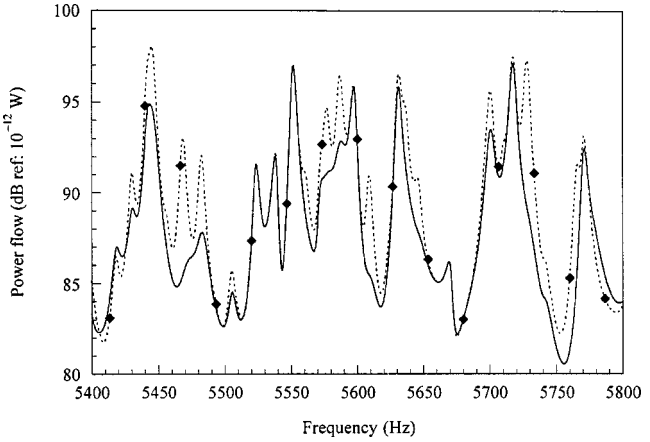

FIG. 4. Comparison of the structural power in plate 1 with (---◆---) and without (———) the inclusion of the in-plane vibration.

Results are presented in terms of structural intensity (power flow per unit width of plate) and comparing the power flow with and without the inclusion of the in-plane analysis as described by Eqs. (35) and (36), respectively. In order to investigate the effect of the in-plane wave motion on the structural transmission, results are presented for both plates in the low and high frequency ranges. Figures 2 and 3 show the structural power flow in plates 1 and 2, respectively, for a narrow frequency span of 400 Hz in a low frequency range. The response locations (in meters) are $(x_1,y)=(0.8,0.31)$ and $(x_2,y)=(0.35,0.31)$. At low frequencies, it is observed that the in-plane waves have the effect of increasing the total power at the structural resonances. This effect is more obvious when examining the power transmission in plate 2, as shown in Fig. 3. Figures 4 and 5 show the structural power at the same location in both plates, for a narrow frequency span in a higher frequency range. These figures show that the difference between the total power when the in-plane analysis is included compared with the power obtained using the flexural analysis only increases as the frequency increases. The increase in the power when the in-plane analysis is included is more evident when examining the structural power transmission through an L-joint, as shown in Fig. 5.

It is also of interest to investigate the effect of the in-plane terms on the power transmission in more complex built-up structures. It is expected that as the location from the vibrating source increases in more complex plate structures such as a ship hull, the difference between the structure-borne noise levels with and without the inclusion of the in-plane waves will increase.[3–6] This is due to the fact that flexural waves are partly transformed into in-plane waves upon transmission through a structural junction, and are then partly transformed back into flexural waves upon transmission through subsequent junctions. In addition, in-plane waves can also travel significant distances and through several intervening junctions before being partly transformed into flexural waves in the adjacent plates. The structural power transmission was investigated for a built-up structure consisting of five connected plates. All plates have the same thickness and width. The length of plate 1 is 1.2 m, and the remaining lengths are 0.6 m. For consistency with the continuity equations presented in this paper, only plates connected at right angles in an L-joint were considered, as shown in Fig. 6. At each corner junction corresponding to (x_i,x_{i+1})

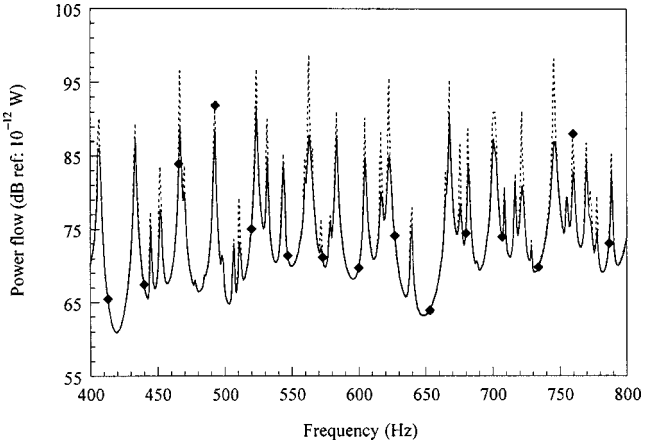

FIG. 3. Comparison of the power transmission in plate 2 with (---◆---) and without (———) the inclusion of the in-plane vibration.

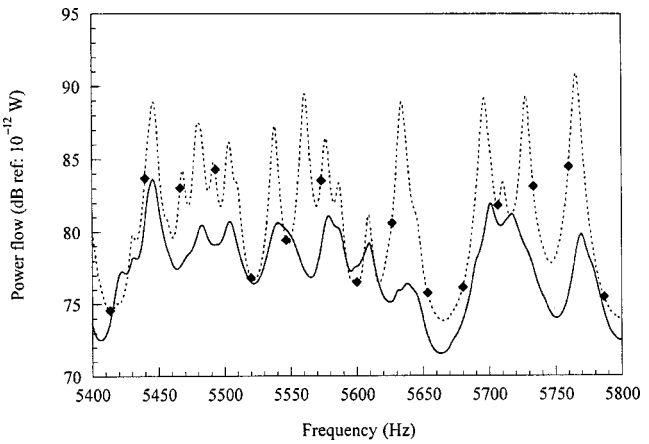

FIG. 5. Comparison of the power transmission in plate 2 with (---◆---) and without (———) the inclusion of the in-plane vibration.

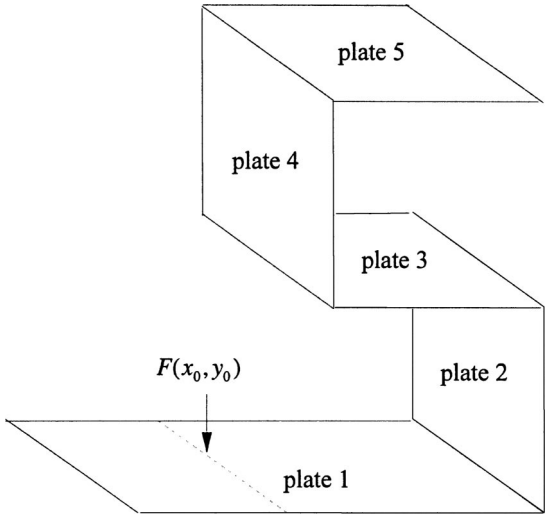

FIG. 6. Schematic of the built-up structure consisting of five connected plates.

$=(L_{xi},0)$, there are eight continuity equations. These continuity equations follow the same right-hand rule sign convention as those presented for plates 1 and 2, and described by Eqs. (20)–(27). With the addition of three more plates, the analytical modeling when the in-plane analysis is included results in 44 unknown coefficients, corresponding to A_i for $i=1-24$ and B_j for $j=1-20$. These are determined using the boundary conditions, continuity equations at the driving force location in plate 1, and the continuity equations at each L-joint. When only the plate flexural displacement is considered in the analysis as described in Sec. II B, there are only 24 unknown coefficients to determine (A_i for $i=1-24$). Figures 7 and 8 respectively show the structural power in plates 1 and 5 at response locations of $(x_1,y)=(0.8,0.31)$ and $(x_5,y)=(0.35,0.31)$. Each figure shows the total power obtained when the in-plane analysis is both included and omitted from the analysis. As expected, when comparing Figs. 7 and 8, the total power in plate 5 is significantly less than that in plate 1. However, in plate 5, the effect of the in-plane analysis significantly increases the total power at all resonance frequencies, even in a low frequency range (Fig. 8).

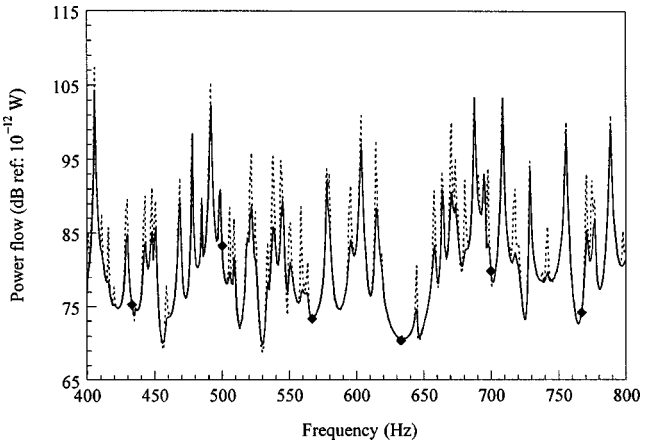

FIG. 7. Comparison of the structural power in plate 1 with (---◆---) and without (———) the inclusion of the in-plane vibration.

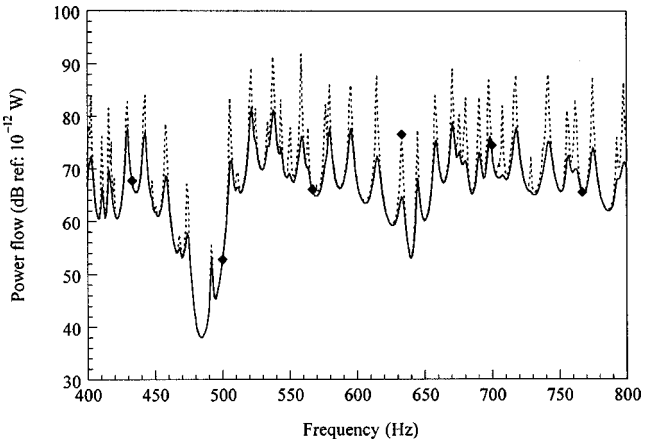

FIG. 8. Comparison of the power transmission in plate 5 with (---◆---) and without (———) the inclusion of the in-plane vibration.

Figure 9 shows the power in both plates 1 and 5 for the same response locations and at a higher frequency range. In this figure it is evident that the effect of including the in-plane wave motion in the analysis is to dramatically increase the total transmitted power as both the frequency and the distance between the source and receiver increases. The total power transmission when the in-plane analysis is included is globally higher than the power transmission obtained using the flexural analysis only. When the in-plane vibration is not included in the calculation of the power, the transmitted structural power levels can be underestimated by as much as 15 dB at the structural resonances in the 5-kHz frequency range. As the frequency increases, the difference between the transmitted power levels when the in-plane vibration is included and omitted from the analysis will dramatically increase. Hence, it is obvious that the in-plane vibration needs to be included in the analysis for the transmitted power, otherwise sizeable errors will result when predicting the structural noise transmission in built-up structures.

To obtain more insight into the increase in the structural noise transmission when the in-plane vibration is included, the contributions from the individual wave types were ob-

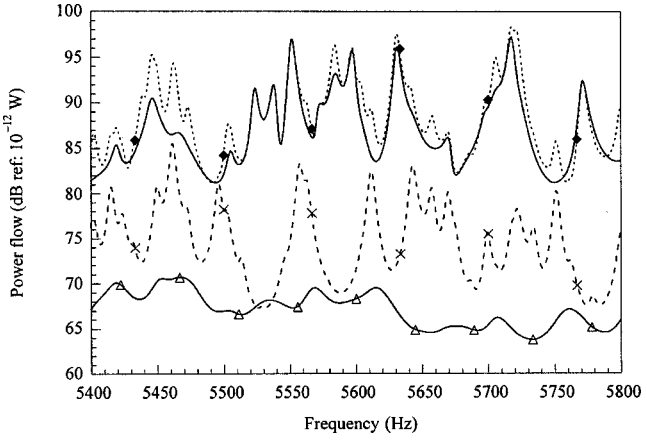

FIG. 9. Comparison of the structural power in plate 1 with (---◆---) and without (———) the inclusion of the in-plane vibration. Comparison of the structural power transmission in plate 5 with (--×--) and without (—△—) the inclusion of the in-plane vibration.

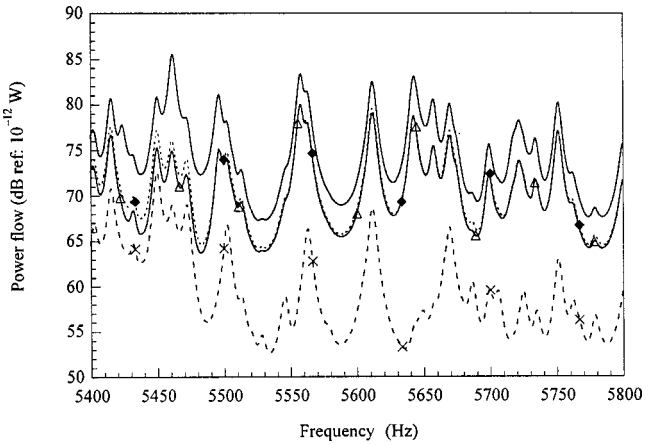

FIG. 10. Power flow transmission in plate 5 including the in-plane vibration (———), and the contributions from the first three structural intensity terms in Eq. (35) corresponding to the shear force (---◆---), bending moment (—△—) and twisting moment (--×--).

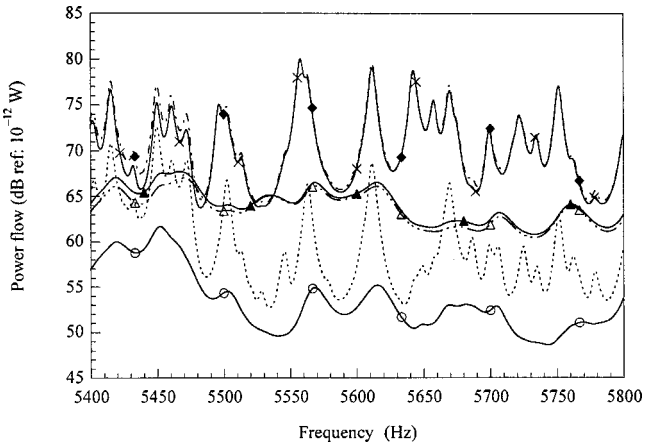

FIG. 12. Comparison of the first three terms in the structural intensity expressions described by Eqs. (35) and (36). Shear force term with (--◆--) and without (—▲—) in-plane vibration. Bending moment term with (—×—) and without (—△--) in-plane vibration. Twisting moment term with (---) and without (—○—) in-plane vibration.

served. Figures 10 and 11 show the total power flow at $(x_5, y) = (0.35, 0.31)$ in plate 5 in the high frequency range and the contributions by the individual terms in Eq. (35). Figure 10 shows the contribution from the first three terms in the structural intensity expression which include the shear force, bending moment and twisting moment. It is shown that the shear force and bending moment have similar contributions to the total response. Figure 11 shows the total power transmission in plate 5, and the last two terms in the structural intensity expression which describe the in-plane longitudinal and in-plane shear waves. Comparing Figs. 10 and 11 reveals that increases in the total power flow at discrete resonance frequencies of around 5460, 5560, and 5650 Hz can be directly attributed to the in-plane modes. As the frequency increases, the contribution from the individual in-plane terms is expected to increase. Figure 12 compares the shear force, bending moment, and twisting moment terms in plate 5, when the in-plane analysis is both included and omitted in the development of the total power flow. Increases in the transmitted power can be attributed to not only an increase in the total power due to the contribution from the in-plane terms, but also to the increase in the individual flexural terms. This is due to the fact that the in-plane modes act as an additional path for the flexural wave energy, and can be partly transformed back into flexural modes upon transmission through a structural junction.

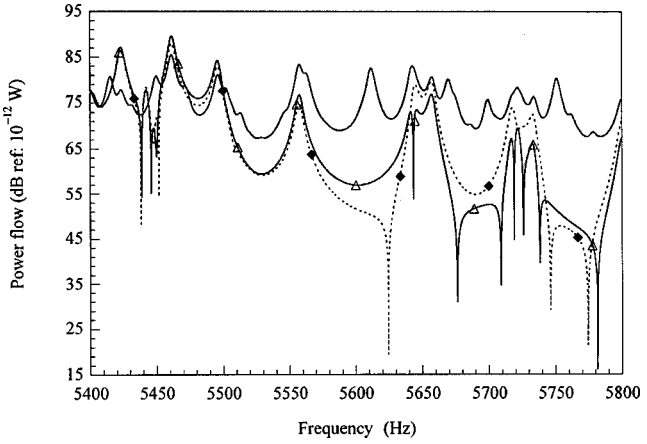

FIG. 11. Power flow transmission in plate 5 including the in-plane vibration (———), and the contributions from the last two structural intensity terms in Eq. (35) corresponding to the in-plane longitudinal force (---◆---) and in-plane shear force (—△—).

IV. CONCLUSIONS

In-plane waves can act as efficient transmitters of flexural energy through structural junctions. For a built-up structure consisting of thin plates connected at right angles, the total energy transmission is significantly increased as the frequency and distance from the source to the receiver increases. This is attributed to the fact that the in-plane modes act as flanking paths for the flexural wave energy. The mathematical analysis is an exact solution using a combination of a traveling wave and modal solution to describe the flexural, in-plane longitudinal, and in-plane shear displacements. The results presented in this paper examined the structural power transmission in the low and high frequency ranges, instead of averaged energy levels in one-third octave frequency bands. Further insight is given by examining the contribution from the individual terms in the structural intensity expression. Although only out-of-plane excitation was considered in this paper, it could be expected that if the external force was inclined at an angle, thereby generating both flexural and in-plane vibration in plate 1, the effect of the in-plane vibration on the total noise transmission would be significantly increased.

ACKNOWLEDGMENT

The author would like to acknowledge Dr. James Forrest for his assistance with the in-plane modeling.

Appendix A

$$
[\alpha]=\begin{bmatrix}
\left(-k_x^2-\upsilon k_y^2\right)e^{-jk_xL_{x1}} & \left(-k_x^2-\upsilon k_y^2\right)e^{jk_xL_{x1}} & \left(k_n^2-\upsilon k_y^2\right)e^{-k_nL_{x1}} & \left(k_n^2-\upsilon k_y^2\right)e^{k_nL_{x1}} & 0\\
jk_x\left(k_x^2+(2-\upsilon)k_y^2\right)e^{-jk_xL_{x1}} & -jk_x\left(k_x^2+(2-\upsilon)k_y^2\right)e^{jk_xL_{x1}} & -k_n\left(k_n^2-(2-\upsilon)k_y^2\right)e^{-k_nL_{x1}} & k_n\left(k_n^2-(2-\upsilon)k_y^2\right)e^{k_nL_{x1}} & 0\\
0 & 0 & 0 & 0 & 0\\
0 & 0 & 0 & 0 & 0\\
0 & 0 & 0 & 0 & 0\\
0 & 0 & 0 & 0 & 0\\
0 & 0 & 0 & 0 & 0\\
0 & 0 & 0 & 0 & 0\\
e^{-jk_xx_0} & e^{jk_xx_0} & e^{-k_nx_0} & e^{k_nx_0} & -e^{-jk_xx_0}\\
-jk_xe^{-jk_xx_0} & jk_xe^{jk_xx_0} & -k_ne^{-k_nx_0} & k_ne^{k_nx_0} & jk_xe^{-jk_xx_0}\\
-k_x^2e^{-jk_xx_0} & -k_x^2e^{jk_xx_0} & k_n^2e^{-k_nx_0} & k_n^2e^{k_nx_0} & k_x^2e^{-jk_xx_0}\\
jk_x^3e^{-jk_xx_0} & -jk_x^3e^{jk_xx_0} & -k_n^3e^{-k_nx_0} & k_n^3e^{k_nx_0} & -jk_x^3e^{-jk_xx_0}\\
0 & 0 & 0 & 0 & 1\\
0 & 0 & 0 & 0 & 0\\
0 & 0 & 0 & 0 & 0\\
0 & 0 & 0 & 0 & -jk_x\\
0 & 0 & 0 & 0 & jk_x\left(k_x^2+(2-\upsilon)k_y^2\right)D\\
0 & 0 & 0 & 0 & 0\\
0 & 0 & 0 & 0 & 0\\
0 & 0 & 0 & 0 & -k_x^2-\upsilon k_y^2
\end{bmatrix}
$$

Appendix A (*Cont.*)

$$
\begin{bmatrix}
0 & 0 & 0 & 0 & 0 & 0 \\
0 & 0 & 0 & 0 & 0 & 0 \\
0 & 0 & 0 & 0 & 0 & 0 \\
0 & 0 & 0 & 0 & 0 & 0 \\
0 & 0 & 0 & \left(-k_x^2-\upsilon k_y^2\right)e^{-jk_xL_{x2}} & \left(-k_x^2-\upsilon k_y^2\right)e^{jk_xL_{x2}} & 0 \\
0 & 0 & 0 & jk_x\left(k_x^2+(2-\upsilon)k_y^2\right)e^{-jk_xL_{x2}} & -jk_x\left(k_x^2+(2-\upsilon)k_y^2\right)e^{jk_xL_{x2}} & 0 \\
0 & 0 & 0 & 0 & 0 & 0 \\
0 & 0 & 0 & 0 & 0 & 0 \\
-e^{jk_xx_0} & -e^{-k_nx_0} & -e^{k_nx_0} & 0 & 0 & 0 \\
-jk_xe^{jk_xx_0} & k_ne^{-k_nx_0} & -k_ne^{k_nx_0} & 0 & 0 & 0 \\
k_x^2e^{jk_xx_0} & -k_n^2e^{-k_nx_0} & -k_n^2e^{k_nx_0} & 0 & 0 & 0 \\
jk_x^3e^{jk_xx_0} & k_n^3e^{-k_nx_0} & -k_n^3e^{k_nx_0} & 0 & 0 & 0 \\
1 & 1 & 1 & 0 & 0 & 0 \\
0 & 0 & 0 & 1 & 1 & 1 \\
0 & 0 & 0 & 0 & 0 & 0 \\
jk_x & -k_n & k_n & jk_x & -jk_x & 0 \\
-jk_x\left(k_x^2+(2-\upsilon)k_y^2\right)D & -k_n\left(k_n^2-(2-\upsilon)k_y^2\right)D & k_n\left(k_n^2-(2-\upsilon)k_y^2\right)D & 0 & 0 & 0 \\
0 & 0 & 0 & 0 & 0 & 0 \\
0 & 0 & 0 & -jk_x\left(k_x^2+(2-\upsilon)k_y^2\right)D & jk_x\left(k_x^2+(2-\upsilon)k_y^2\right)D & 0 \\
-k_x^2-\upsilon k_y^2 & k_n^2-\upsilon k_y^2 & k_n^2-\upsilon k_y^2 & k_x^2+\upsilon k_y^2 & k_x^2+\upsilon k_y^2 & 0
\end{bmatrix}
$$

Appendix A (*Cont.*)

$$
\begin{bmatrix}
0 & 0 & 0 & 0 & 0 & 0 \\
0 & 0 & 0 & 0 & 0 & 0 \\
0 & 0 & 0 & \left(\lambda_1^2-\upsilon k_y^2\right)e^{\lambda_1 L_{x1}} & \left(\lambda_2^2-\upsilon k_y^2\right)e^{\lambda_2 L_{x1}} & \lambda_3 k_y\left(1-\upsilon\right)e^{\lambda_3 L_{x1}} \\
0 & 0 & 0 & 2\lambda_1 k_y e^{\lambda_1 L_{x1}} & 2\lambda_2 k_y e^{\lambda_2 L_{x1}} & \left(\lambda_3^2+k_y^2\right)e^{\lambda_3 L_{x1}} \\
\left(k_n^2-\upsilon k_y^2\right)e^{-k_n L_{x2}} & \left(k_n^2-\upsilon k_y^2\right)e^{k_n L_{x2}} & 0 & 0 & 0 & 0 \\
-k_n\left(k_n^2-(2-\upsilon)k_y^2\right)e^{-k_n L_{x2}} & k_n\left(k_n^2-(2-\upsilon)k_y^2\right)e^{k_n L_{x2}} & 0 & 0 & 0 & 0 \\
0 & 0 & 0 & 0 & 0 & 0 \\
0 & 0 & 0 & 0 & 0 & 0 \\
0 & 0 & 0 & 0 & 0 & 0 \\
0 & 0 & 0 & 0 & 0 & 0 \\
0 & 0 & 0 & 0 & 0 & 0 \\
0 & 0 & 0 & 0 & 0 & 0 \\
1 & 1 & \lambda_1 & \lambda_2 & k_y & k_y \\
0 & 0 & k_y & k_y & \lambda_3 & \lambda_3 \\
k_n & -k_n & 0 & 0 & 0 & 0 \\
0 & 0 & 0 & 0 & 0 & 0 \\
0 & 0 & 2\lambda_1 k_y & 2\lambda_2 k_y & \lambda_3^2+k_y^2 & \lambda_3^2+k_y^2 \\
k_n\left(k_n^2-(2-\upsilon)k_y^2\right)D & -k_n\left(k_n^2-(2-\upsilon)k_y^2\right)D & \left(\lambda_1^2-\upsilon k_y^2\right)Eh/(1-\upsilon^2) & \left(\lambda_2^2-\upsilon k_y^2\right)Eh/(1-\upsilon^2) & \lambda_3 k_y Eh/(1+\upsilon) & -\lambda_3 k_y Eh/(1+\upsilon) \\
-\left(k_n^2-\upsilon k_y^2\right) & -\left(k_n^2-\upsilon k_y^2\right) & 0 & 0 & 0 & 0
\end{bmatrix}
$$

Appendix A (*Cont.*)

$$
\begin{bmatrix}
0 & 0 & 0 & 0 & 0 & 0 \\
0 & 0 & 0 & 0 & 0 & 0 \\
\lambda_4 k_y (1-\upsilon) e^{\lambda_4 L_{x1}} & 0 & 0 & 0 & 0 & 0 \\
\left(\lambda_4^2 + k_y^2\right) e^{\lambda_4 L_{x1}} & 0 & 0 & 0 & 0 & 0 \\
0 & 0 & 0 & 0 & 0 & 0 \\
0 & 0 & 0 & 0 & 0 & 0 \\
0 & \left(\lambda_1^2 - \upsilon k_y^2\right) e^{\lambda_1 L_{x2}} & \left(\lambda_2^2 - \upsilon k_y^2\right) e^{\lambda_2 L_{x2}} & \lambda_3 k_y (1-\upsilon) e^{\lambda_3 L_{x2}} & \lambda_4 k_y (1-\upsilon) e^{\lambda_4 L_{x2}} \\
0 & 2\lambda_1 k_y e^{\lambda_1 L_{x2}} & 2\lambda_2 k_y e^{\lambda_2 L_{x2}} & \left(\lambda_3^2 + k_y^2\right) e^{\lambda_3 L_{x2}} & \left(\lambda_4^2 + k_y^2\right) e^{\lambda_4 L_{x2}} \\
0 & 0 & 0 & 0 & 0 \\
0 & 0 & 0 & 0 & 0 \\
0 & 0 & 0 & 0 & 0 \\
0 & 0 & 0 & 0 & 0 \\
0 & -\lambda_1 & -\lambda_2 & -k_y & -k_y \\
k_y & 0 & 0 & 0 & 0 \\
\lambda_4 & -k_y & -k_y & -\lambda_3 & -\lambda_4 \\
0 & 0 & 0 & 0 & 0 \\
0 & \left(\lambda_1^2 - \upsilon k_y^2\right) Eh/(1-\upsilon^2) & \left(\lambda_2^2 - \upsilon k_y^2\right) Eh/(1-\upsilon^2) & \lambda_3 k_y Eh/(1+\upsilon) & \lambda_4 k_y Eh/(1+\upsilon) \\
\lambda_4^2 + k_y^2 & -2\lambda_1 k_y & -2\lambda_2 k_y & -\left(\lambda_3^2 + k_y^2\right) & -\left(\lambda_4^2 + k_y^2\right) \\
\lambda_4 k_y Eh/(1+\upsilon) & 0 & 0 & 0 & 0 \\
0 & 0 & 0 & 0 & 0
\end{bmatrix}
$$

Appendix B

$$
[\alpha]=\begin{bmatrix}
\left(-k_{x1}^2-\upsilon k_y^2\right)e^{-jk_{x1}L_{x1}} & \left(-k_{x1}^2-\upsilon k_y^2\right)e^{jk_{x1}L_{x1}} & \left(k_{n1}^2-\upsilon k_y^2\right)e^{-k_{n1}L_{x1}} & \left(k_{n1}^2-\upsilon k_y^2\right)e^{k_{n1}L_{x1}} & 0 & 0 \\
jk_{x1}\left(k_{x1}^2+(2-\upsilon)k_y^2\right)e^{-jk_{x1}L_{x1}} & -jk_{x1}\left(k_{x1}^2+(2-\upsilon)k_y^2\right)e^{jk_{x1}L_{x1}} & -k_{n1}\left(k_{n1}^2-(2-\upsilon)k_y^2\right)e^{-k_{n1}L_{x1}} & k_{n1}\left(k_{n1}^2-(2-\upsilon)k_y^2\right)e^{k_{n1}L_{x1}} & 0 & 0 \\
0 & 0 & 0 & 0 & 0 & 0 \\
0 & 0 & 0 & 0 & 0 & 0 \\
e^{-jk_{x1}x_o} & e^{jk_{x1}x_o} & e^{-k_{n1}x_o} & e^{k_{n1}x_o} & -e^{-jk_{x1}x_o} & -e^{jk_{x1}x_o} \\
-jk_{x1}e^{-jk_{x1}x_o} & jk_{x1}e^{jk_{x1}x_o} & -k_{n1}e^{-k_{n1}x_o} & k_{n1}e^{k_{n1}x_o} & jk_{x1}e^{-jk_{x1}x_o} & -jk_{x1}e^{jk_{x1}x_o} \\
-k_{x1}^2e^{-jk_{x1}x_o} & -k_{x1}^2e^{jk_{x1}x_o} & k_{n1}^2e^{-k_{n1}x_o} & k_{n1}^2e^{k_{n1}x_o} & k_{x1}^2e^{-jk_{x1}x_o} & k_{x1}^2e^{jk_{x1}x_o} \\
jk_{x1}^3e^{-jk_{x1}x_o} & -jk_{x1}^3e^{jk_{x1}x_o} & -k_{n1}^3e^{-k_{n1}x_o} & k_{n1}^3e^{k_{n1}x_o} & -jk_{x1}^3e^{-jk_{x1}x_o} & jk_{x1}^3e^{jk_{x1}x_o} \\
0 & 0 & 0 & 0 & -k_{x1}^2 & -k_{x1}^2 \\
0 & 0 & 0 & 0 & -jk_{x1} & jk_{x1} \\
0 & 0 & 0 & 0 & j\left(k_{x1}^3-k_p^4/k_L\right) & -j\left(k_{x1}^3+k_p^4/k_L\right) \\
0 & 0 & 0 & 0 & 0 & 0
\end{bmatrix}
$$

$$
\begin{bmatrix}
0 & 0 & 0 & 0 & 0 & 0 \\
0 & 0 & 0 & 0 & 0 & 0 \\
0 & 0 & \left(-k_{x2}^2-\upsilon k_y^2\right)e^{-jk_{x2}L_{x2}} & \left(-k_{x2}^2-\upsilon k_y^2\right)e^{jk_{x2}L_{x2}} & \left(k_{n2}^2-\upsilon k_y^2\right)e^{-k_{n2}L_{x2}} & \left(k_{n2}^2-\upsilon k_y^2\right)e^{k_{n2}L_{x2}} \\
0 & 0 & jk_{x2}\left(k_{x2}^2+(2-\upsilon)k_y^2\right)e^{-jk_{x2}L_{x2}} & -jk_{x2}\left(k_{x2}^2+(2-\upsilon)k_y^2\right)e^{jk_{x2}L_{x2}} & -k_{n2}\left(k_{n2}^2-(2-\upsilon)k_y^2\right)e^{-k_{n2}L_{x2}} & k_{n2}\left(k_{n2}^2-(2-\upsilon)k_y^2\right)e^{k_{n2}L_{x2}} \\
-e^{-k_{n1}x_o} & -e^{k_{n1}x_o} & 0 & 0 & 0 & 0 \\
k_{n1}e^{-k_{n1}x_o} & -k_{n1}e^{k_{n1}x_o} & 0 & 0 & 0 & 0 \\
-k_{n1}^2e^{-k_{n1}x_o} & -k_{n1}^2e^{k_{n1}x_o} & 0 & 0 & 0 & 0 \\
k_{n1}^3e^{-k_{n1}x_o} & -k_{n1}^3e^{k_{n1}x_o} & 0 & 0 & 0 & 0 \\
k_{n1}^2 & k_{n1}^2 & k_{x2}^2 & k_{x2}^2 & -k_{n2}^2 & -k_{n2}^2 \\
-k_{n1} & k_{n1} & jk_{x2} & -jk_{x2} & k_{n2} & -k_{n2} \\
-\left(k_{n1}^3+jk_p^4/k_L\right) & \left(k_{n1}^3-jk_p^4/k_L\right) & 0 & 0 & 0 & 0 \\
0 & 0 & j\left(k_{x2}^3+k_p^4/k_L\right) & -j\left(k_{x2}^3-k_p^4/k_L\right) & -\left(k_{n2}^3-jk_p^4/k_L\right) & \left(k_{n2}^3+jk_p^4/k_L\right)
\end{bmatrix}
$$

[1] S. V. Budrin and A. S. Nikiforov, ''Wave transmission through assorted plate joints,'' Sov. Phys. Acoust. **9**, 333–336 (1964).
[2] P. G. Craven and B. M. Gibbs, ''Sound transmission and mode coupling at junctions of thin plates, Part I: Representation of the problem,'' J. Sound Vib. **77**, 417–427 (1981).
[3] J. Tratch, Jr., ''Vibration transmission through machinery foundation and ship bottom structures,'' M.S. thesis, MIT, 1985.
[4] R. H. Lyon, ''In-plane contribution to structural noise transmission,'' Noise Control Eng. J. **26**, 22–27 (1986).
[5] J. S. Kim, H. S. Kim, H. J. Kang, and S. R. Kim, ''Effects of inplane modes in SEA on structure-borne noise transmission in ship structures,'' in Proceedings of the 4th International Congress on Sound and Vibration, St. Petersburg, Russia (1996), pp. 217–222.
[6] A. N. Bercin and R. S. Langley, ''Application of the dynamic stiffness technique to the inplane vibrations of plate structures,'' Comput. Struct. **59**, 869–875 (1996).
[7] A. N. Bercin, ''An assessment of the effects of in-plane vibrations on the energy flow between coupled plates,'' J. Sound Vib. **191**, 661–680 (1996).
[8] J. M. Cuschieri, ''Structural power-flow analysis using a mobility approach of an L-shaped plate,'' J. Acoust. Soc. Am. **87**, 1159–1165 (1990).
[9] C. Boisson, J. L. Guyader, P. Millot, and C. Lesueur, ''Energy transmission in finite coupled plates, Part II: Application to an L shaped structure,'' J. Sound Vib. **81**, 93–105 (1982).
[10] J. M. Cuschieri and M. D. McCollum, ''In-plane and out-of-plane waves' power transmission through an L-plate junction using the mobility power flow approach,'' J. Acoust. Soc. Am. **100**, 857–870 (1996).
[11] J. L. Guyader, C. Boisson, and C. Lesueur, ''Energy transmission in finite coupled plates, Part I: Theory,'' J. Sound Vib. **81**, 81–92 (1982).
[12] Y. Shen and B. M. Gibbs, ''An approximate solution for the bending vibrations of a combination of rectangular thin plates,'' J. Sound Vib. **105**, 73–90 (1986).
[13] P. Mees and G. Vermier, ''Structure-borne sound transmission at elastically connected plates,'' J. Sound Vib. **166**, 55–76 (1993).
[14] D.-H. Park, S.-Y. Hong, F.-G. Kil, and J.-J. Jeon, ''Power flow models and analysis of in-plane waves in finite coupled thin plates,'' J. Sound Vib. **244**, 651–668 (2001).
[15] N. H. Farag and J. Pan, ''On the free and forced vibration of single and coupled rectangular plates,'' J. Acoust. Soc. Am. **104**, 204–216 (1998).
[16] J. L. Horner and R. G. White, ''Prediction of vibrational power transmission through bends and joints in beam-like structures,'' J. Sound Vib. **147**, 87–103 (1991).
[17] L. Cremer, M. Heckl, and E. E. Ungar, *Structure-Borne Sound*, 2nd ed. (Springer-Verlag, Berlin, 1988), p. 489.
[18] X. Pan and C. H. Hansen, ''Active control of vibratory power transmission along a semi-infinite plate,'' J. Sound Vib. **184**, 585–610 (1995).
[19] M. D. McCollum and J. M. Cuschieri, ''Bending and in-plane wave transmission in thick connected plates using statistical energy analysis,'' J. Acoust. Soc. Am. **88**, 1480–1485 (1990).
[20] A. J. Romano, P. B. Abraham, and E. G. Williams, ''A Poynting vector formulation for thin shells and plates, and its application to structural intensity analysis and source localization. Part I. Theory,'' J. Acoust. Soc. Am. **87**, 1166–1175 (1990).

A pole-zero representation for the admittance matrix of elastic beam and plate systems

Douglas M. Photiadis[a] and Martin H. Marcus
Naval Research Laboratory, 4555 Overlook Avenue SW, Washington, DC 20375-5320

(Received 14 March 2003; revised 11 October 2003; accepted 30 December 2003)

The behavior of coupled elastic systems is often analyzed in terms of the admittances or impedances of the component systems. In many applications, the admittances are approximated by a small number of simple oscillators; i.e., a low-order truncation of the normal-mode expansion. Such an approach is reasonable in the neighborhood of system resonances, but is much less convenient and accurate in the neighborhood of antiresonances. Pole-zero product expansions of the sort employed in circuit analysis offer a potential means of improving the accuracy of low-order approximations. The validity of such representations of the admittance matrix is explored here, and it is noted that in general the off-diagonal components cannot be written in this fashion. Nevertheless, it is shown below that the entire admittance matrix of beam and plate strip systems can always be represented in the pole-zero product form. Further, the representation is shown to be valid even when the beam or plate is coupled to an arbitrary conservative elastic structure. © *2004 Acoustical Society of America.* [DOI: 10.1121/1.1649331]

PACS numbers: 43.40.Hq [ANN] Pages: 1170–1178

I. INTRODUCTION

The admittance $Y_{ij}(x,\omega)$, the response of a system at position x to a general harmonic point excitation at the same position x, is a basic quantity of interest in the characterization of linear systems. The admittance is of direct physical significance because it characterizes the local density of states of the system and reveals information regarding the spatial character of the modes.[1,2] Further, the admittance also determines the coupling between elastic structures effectively attached to one another at a point. The admittance is therefore needed to make predictions of dynamic behavior ranging from simple transduction processes to the acoustic response of complex structures with many components. As such, much effort has been invested in the study of the properties of the admittance and its inverse, the impedance.[3–7]

A basic outstanding problem in this area, particularly in the area of elastic structures, lies in obtaining accurate mathematical models of the admittance in particular situations. In many contexts,[8–13] simple and inadequate models have been employed, reducing subsequent predictions or analyses to a qualitative level. We have explored an approach for the modeling of admittances which can overcome these difficulties, namely, the pole-zero product expansion often employed in the context of circuit analysis.[4–7] This approach yields approximations which are more accurate than corresponding modal expansions, particularly in the neighborhood of antiresonances, using equal numbers of unknowns and equally simple mathematical expressions.

A number of general results regarding the properties of the response functions of scalar systems are known, both from the physical point of view of linear response theory[4–7,14] and from the mathematical point of view of Sturm–Liouville theory.[15] Of particular interest to us here, it is known that the admittance and impedance of scalar systems can always be represented in a pole-zero product form with real poles and real zeros, and further, that the poles and zeros alternate. This result is applicable to any linear system and enables algebraic simplifications in system modeling. Further, the mathematical properties of the poles and zeros strongly impact the functional behavior of the response functions; admittance functions always exhibit a characteristic interleaving of poles and zeros, and are always monotonic in frequency indicative of progressive phase behavior. These mathematical properties of the admittance functions have been exploited in various contexts.

A complication one encounters in attempting to apply the known results to the typical problems of elastic structures is the vector nature of the vibrational problem; i.e., the response and excitation of the system in the elastic case are typically vectors. The admittance in the elastic case is therefore a matrix of functions as opposed to the single function one encounters in the scalar circuit analysis case. In general, this difference is indeed quite significant.

The problem in the vector case has to do with evaluating the cross admittance, the response of a particular component to a force applied to a different component at the same point. General problems of this sort have been investigated in the context of matrix Sturm–Liouville theory.[15] The body of knowledge which seems to be most applicable concerns the oscillatory behavior of the eigenfunctions and forced solutions. While related, these results unfortunately do not directly apply to the problem at hand.

Circuit analysis applies only to the scalar case, and results concerning off-diagonal elements can be obtained from this body of research only by viewing such elements as general transfer functions. In this case, while the poles are still real, and of course identical for all components, the zeros may be complex, though they must occur in complex conjugate pairs.[5,6] Further, the results in the literature provide little

[a]Electronic mail: douglas.photiadis@nrl.navy.mil

 0001-4966/2004/115(3)/1170/9/$20.00

guidance as to the nature of the solution in a particular case; the zeros may be real, and then again, they may be complex, depending on the details of the problem at hand. The poles and zeros may alternate and guarantee progressive phase behavior, or they may not, a significant difference in the mathematical behavior of the response function of interest. The primary focus of this paper is to determine whether more definite statements can be made in the case of the cross-admittance matrix of some problems of interest in the context of the vibration of elastic structures.

We have shown under fairly general conditions that the admittance matrices of beams and plate strips coupled to arbitrary conservative structures through a force or moment at the edge of the system admit a pole-zero product expansion with real poles and zeros. In these situations, any component of the admittance matrix may be written as

$$g_\alpha(\omega)=C_\alpha(\omega)\frac{\Pi_n(1-\omega^2/\omega_{n,\alpha}^2)}{\Pi_n(1-\omega^2/\omega_n^2)}. \tag{1}$$

Here, $C_\alpha(\omega)=c_\alpha\omega^{k_\alpha}$ is a simple overall factor and the poles ω_n and zeros $\omega_{n,\alpha}$ of the expansion will always be real. Further, the poles and zeros alternate and the full body of knowledge concerning the admittance functions of scalar systems may immediately be applied to any component of the full admittance matrix of these systems. Note that both $C_\alpha(\omega)$ and $\omega_{n,\alpha}$ depend on the particular component α of the admittance matrix.

Our result, though limited in scope, does address elastic systems of a fairly basic nature, and does advance our theoretical knowledge in this area. One may now, with no reservations, represent any of the components of the admittance matrix of a beam coupled to a general oscillatory system as a pole-zero product expansion with the only errors being related to the accuracy with which the resonance and antiresonance frequencies are determined. Thus, such representations can now be employed in many modeling situations, and further, the mathematical properties of these functions can be exploited.

An outline of the body of the paper is as follows. In Sec. II, we briefly recall some of the basic facts regarding the admittance matrix of general linear systems, primarily results from circuit theory. The validity of the pole-zero representation with real poles and zeros for the diagonal components of the admittance matrix of any linear system is noted, and the difficulties with regard to the off-diagonal case, the cross admittances, are described. In the interest of brevity, we will often refer to the validity of a pole-zero expansion with real poles and zeros as the validity of a pole-zero expansion. This should lead to no confusion because the existence of a pole-zero expansion with complex poles and zeros is *always assured*, merely being a statement that the response functions are rational functions of frequency for a discrete system.

In Sec. III, the admittance matrix of a beam in flexure is examined. The validity of the pole-zero expansion for the entire admittance matrix is proved first for a beam with ordinary impedance boundary conditions. The proof is then extended to the case of a beam coupled to an arbitrary conservative system. This extension is quite important because it enables one to employ the pole-zero expansion in situations in which the admittance matrix is not known explicitly, and perhaps can only be partially inferred from experimental or numerical data.

In Sec. IV, the results are extended to a two-dimensional example, a plate strip. The plate strip is assumed to be uniform along the strip axis and is effectively one-dimensional, but the wave number along the axis of the strip is taken to be nonzero. This example is similar to evaluating the input admittance of the modes of an annular ring, without the additional complications of the membrane stresses. The approach employed to demonstrate the pole-zero expansion for the beam is also successful in this case, though some difficulties are encountered, and we have only been able to show that almost all of the zeros are real in this case. The lowest-frequency zero may be complex in this case. This plate analysis shows some of the complexity that can appear in a two-dimensional system.

In Sec. V, we examine the representative example of a free–free beam. Within this context, we show how the zeros and poles can be obtained in practice. The pole-zero expansion is obtained explicitly and compared to both the exact solution and the modal solution. Intuitively, just as the Padé approximation is an improvement over simple Taylor series or Laurent series, the pole-zero representation is expected to be more accurate than the modal representation in regions of low modal density. We explore this aspect and also discuss the relationship of these results to improved modal expansions.[16–19] The increased accuracy that can be obtained by employing a truncated pole-zero expansion as opposed to a truncated modal solution with an equal number of unknowns is evident from the results.

II. ADMITTANCE OF A GENERAL LINEAR SYSTEM

We first consider the system to consist of N identical degrees of freedom, each of mass m, linearly coupled to one another. Within this context, the system may be equally well considered to be a general N-port linear circuit and the general results from circuit theory can be immediately applied.[4–6] Our approach is however more in the spirit of the description of physical systems. The Lagrangian of the system is taken to be

$$L_0=\frac{1}{2}m\sum_\alpha |\dot{q}_\alpha|^2-\frac{1}{2}\sum_{\alpha\beta} q_\alpha K_{\alpha\beta}q_\beta, \tag{2}$$

where the q_α are the generalized coordinates of the system and the geometry is contained in the coupling matrix K, which we take to be symmetric and positive definite. The N equations of motion of the system in response to a steady-state excitation $\exp(-i\omega t)$ applied to a particular coordinate q_σ are

$$\mathcal{L}_{\alpha\beta}(\omega)G_{\beta\sigma}=(K_{\alpha\beta}-m\omega^2\delta_{\alpha\beta})G_{\beta\sigma}=\delta_{\alpha\sigma}, \tag{3}$$

where $G_{\alpha\beta}$ is the discrete version of the Green's function.

The solution of Eq. (3) may be written using Cramer's rule as

$$G_{\alpha\beta}=C_{\beta\alpha}/\det(\mathcal{L}), \tag{4}$$

where $C_{\alpha\beta}(\omega)$ is the cofactor of $\mathcal{L}(\omega)$. Every component of $G_{\alpha\beta}$ is thus a ratio of polynomials in ω^2 with the denominator a polynomial of order N, and the numerator a polynomial of order $(N-1)$ or $(N-2)$ for diagonal or off-diagonal components, respectively.

We are assured of N real resonance frequencies,[20] zeros of the denominator of Eq. (4), because of the symmetric, positive definiteness of K. Similarly, it has been demonstrated[6] for the diagonal case, $G_{\sigma\sigma}$ for any σ, that the $(N-1)$ zeros of the numerator of Eq. (4) are real and correspond to resonance frequencies of the constrained boundary value problem with the coordinate $q_\sigma=0$. No such statement can be made regarding the zeros of the numerator in the off-diagonal case, however, because the minors of $\mathcal{L}_{\alpha\beta}(\omega)$ are not necessarily symmetric. Instead, one can show only that the zeros of the general components of the Green's function must occur in complex conjugate pairs.[6] The pole-zero representation is therefore valid for the diagonal components of the Green's function matrix of any linear system, while such a representation for the off-diagonal components must be examined in a case-by-case fashion.

III. ADMITTANCE MATRIX OF A BEAM OR ROD IN FLEXURE

A. Equations of motion

One of the simplest elastic systems with more than one degree of freedom per point is a transversely vibrating rod or beam. The steady-state equation of motion of a beam subjected to a delta function transverse force at $x=0^+$ is[21]

$$D\frac{\partial^4 u}{\partial x^4}-m\omega^2 u=\delta(x-\epsilon), \tag{5}$$

where D is the flexural rigidity and m is the mass per unit length of the beam. The beam has two degrees of freedom at each point x, the transverse displacement $u(x)$ and the rotation $u'(x)$. Let us assume the beam has length a and satisfies a free-boundary condition at $x=0$

$$\frac{\partial^3 u}{\partial x^3}(0)=\frac{\partial^2 u}{\partial x^2}(0)=0, \tag{6}$$

corresponding to the vanishing of the shear force and moment, respectively. Let us consider any general impedance condition at $x=a$ which yields a self-adjoint boundary value problem. The boundary condition at a must be physically realizable, energy conserving, and frequency independent.

The admittance matrix consists of the following four response functions: Y_{11}, the displacement u in response to a unit force f, Y_{21}, the rotation u' in response to a unit force f, Y_{12}, the displacement u in response to a local unit torque τ, and Y_{22}, the rotation u' in response to a local unit torque τ. In terms of the Green's function $G(x,x')$, we have

$$Y_{11}(\omega)=G(x=0,\ x'=0),$$

$$Y_{21}(\omega)=Y_{12}(\omega)=\frac{\partial G}{\partial x}(x=0,\ x'=0),$$

$$Y_{22}(\omega)=\frac{\partial^2 G}{\partial x\partial x'}(x=0,\ x'=0). \tag{7}$$

The diagonal components Y_{11} and Y_{22} admit a pole-zero representation by virtue of the general result for any linear system discussed in the Introduction, but we shall demonstrate this result directly to motivate the proof for the off-diagonal components Y_{12} and Y_{21}.

B. The diagonal case for an isolated beam

Consider the classical eigenfunction solution for the Green's function

$$G(x,x')=\frac{1}{m}\sum_n \frac{\psi_n(x)\psi_n(x')}{\omega_n^2-\omega^2}, \tag{8}$$

where $\psi_n(x)$ and ω_n are the eigenfunctions and eigenfrequencies of the system with the specified boundary conditions. We are assured of the orthogonality of the eigenfunctions and real eigenfrequencies by the self-adjointness of the boundary value problem.[15]

Examining the expression for the admittance

$$Y_{11}(\omega)=G(0,0)=\frac{1}{m}\sum_n \frac{\omega_n^2(0)}{\omega_n^2-\omega^2}, \tag{9}$$

we note that every term in the expansion has a positive coefficient $\psi_n^2(0)$. For frequencies slightly greater than ω_n, $Y_{11}\to-\infty$, while for frequencies slightly less than ω_{n+1}, $Y_{11}\to+\infty$. There are no singularities in the interval (ω_n,ω_{n+1}) and therefore Y_{11} is continuous in this interval. In addition, Y_{11} is easily seen to be monotonic by examining the derivative $Y_{11}'(\omega)$. Thus, Y_{11} must have exactly one zero in the interval (ω_n,ω_{n+1}). Denote this set of zeros as $\{\omega_{n,11}\}$.

We wish to emphasize that the mathematical fact shown above has been proven many times in various contexts. Our purpose here is not to provide yet another proof of this fact; rather, we have presented our version of a classical proof to illustrate the basic mathematical technique we employ later in the paper in the case of the cross admittance.

Simply counting the zeros in the case of the discrete limit indicates that the zeros thus obtained are the only zeros of $Y_{11}(\omega)$ in the complex plane, but one may also substitute a trial solution $\omega=\tilde{\omega}+i\zeta$ into Eq. (9) and quickly obtain $\zeta=0$ as the only solution to the imaginary part of Eq. (9).

Consider the function

$$g(\omega)=C(\omega)\frac{\Pi_n(1-\omega^2/\omega_{n,11}^2)}{\Pi_n(1-\omega^2/\omega_n^2)}, \tag{10}$$

where we choose $C(\omega)$ so that the $\omega\to0$ behavior of $g(\omega)$ is the same as that of $Y_{11}(\omega)$. The ratio of $g(\omega)$ to $Y_{11}(\omega)$ is analytic everywhere, including the point at infinity, and by Liouville's theorem[22] must therefore be a constant. We have thus directly demonstrated the validity of the pole-zero expansion in this case.

The pole-zero representation can be shown to be valid for the Y_{22} component in an identical fashion, since we have

$$Y_{22}(\omega)=\frac{\partial^2 G}{\partial x\partial x'}(0,0)=\frac{1}{m}\sum_n \frac{(\psi_n'(0))^2}{\omega_n^2-\omega^2}. \tag{11}$$

This expression is identical to Eq. (9) with the substitution $\psi_n(0) \rightarrow \psi_n'(0)$, a modification which makes no difference because the details of the coefficients $\psi_n(0)$ are irrelevant—only the fact that the coefficient of each resonance denominator is positive is needed. Thus, we wish to emphasize the following general statement we shall use often in the remainder of this paper: *If the constant coefficients of a resonant expansion such as Eq. (9) are all of the same sign, then the zeros of the expansion are all real and alternate with the poles*.

Finally, we note that it is apparent that the details of the boundary conditions, the location of the source point, and the details of the differential equation are not important provided the various Green's functions exist at the excitation point. In two and three dimensions, the Green's functions will usually be singular for wave-bearing systems and thus only the discrete limit discussed in the previous section, or some other regularization, is relevant.

C. The off-diagonal case for an isolated beam

In this section, we shall prove that the zeros of the off-diagonal components of the admittance matrix of an isolated beam are real and therefore can be represented as a pole-zero product expansion with real poles and zeros.

Proceeding as above, we expand $Y_{12}(\omega)$ as

$$Y_{12}(\omega) = \frac{\partial G}{\partial x}(0,0) = \frac{1}{m}\sum_n \frac{\psi_n(0)\psi_n'(0)}{\omega_n^2 - \omega^2}. \tag{12}$$

The expression in Eq. (12) is clearly closely related to that of Eq. (9), the difference being the appearance of the quantity $\psi_n(0)\psi_n'(0)$ in the numerator rather than $\psi_n^2(0)$. The real character of the zeros is related directly to the signs of this product. In particular, as noted above, if we show that the signs of the product $\psi_n(0)\psi_n'(0)$ are all the same, the validity of the pole-zero expansion is established. Our approach then will be to demonstrate this fact.

With this end in mind, consider the Taylor expansion of a particular eigenfunction. We have

$$\begin{aligned}
\psi_n(x) &= \psi_n(0) + \psi_n^{(1)}(0)x + \psi_n^{(4)}(0)\frac{x^4}{4!} \\
&\quad + \psi_n^{(5)}(0)\frac{x^5}{5!} + \cdots \\
&= \psi_n(0) + \psi_n^{(1)}(0)x + \left(\frac{m\omega_n^2}{D}\right)\psi_n(0)\frac{x^4}{4!} \\
&\quad + \left(\frac{m\omega_n^2}{D}\right)\psi_n^{(1)}(0)\frac{x^5}{5!} + \cdots \\
&= \psi_n(0)\left(1 + \frac{m\omega_n^2}{D}\frac{x^4}{4!} + \left(\frac{m\omega_n^2}{D}\right)^2\frac{x^8}{8!} + \cdots\right) \\
&\quad + \psi_n'(0)\left(1 + \frac{m\omega_n^2}{D}\frac{x^5}{5!} + \left(\frac{m\omega_n^2}{D}\right)^2\frac{x^9}{9!} + \cdots\right),
\end{aligned} \tag{13}$$

where we have denoted the derivatives $d^m\psi/dx^m$ as $\psi^{(m)}$. In the first step of Eq. (13) we have exploited the boundary condition $\psi_n^{(2)}(0) = \psi_n^{(3)}(0) = 0$, while in the second step the governing differential equation has been used to reduce higher derivatives to lower ones.

We now demonstrate by contradiction that $\psi_n(0)$ and $\psi_n'(0)$ have opposite signs, and thus the signs of the products $\psi_n(0)\psi_n'(0)$ are the same for all n. Suppose for a particular n that $\psi_n(0)$ and $\psi_n'(0)$ have the same sign. Then, every term in the Taylor series expansion given in Eq. (13) is positive and $\psi_n(x)$ can have no zeros in the interval $[0,a]$. This can only be the case for the lowest-order eigenfunction, a rigid translation mode if it exists, since all other eigenfunctions must have nodes.[20] And, the rigid-body mode is irrelevant because $\psi_n'(0) = 0$ for this case. Hence, $\psi_n(0)$ and $\psi_n'(0)$ must have opposite signs for all n. The coefficient of every term in the expansion, Eq. (12), is therefore negative, and we have proven (recall the general discussion in Sec. II B) that the zeros of the off-diagonal components $Y_{12}(Y_{21})$ are real in this case.

A few observations regarding the generality of this result are the following: The boundary conditions on the opposite end of the beam are clearly allowed to be arbitrary provided the resulting boundary value problem for the eigenfunctions is self-adjoint. The excitation point, however, is restricted to be at the end of the beam, and the boundary condition at this point must be free. Further, the details of the differential operator are clearly relevant insofar as the proof relies upon details of the specific fourth-order operator for a beam in flexure.

D. A beam attached to an arbitrary elastic structure

We examine here the important generalization of a beam or rod attached to a general conservative elastic structure. This modification makes no difference with respect to the diagonal components since if one considers the system as a whole, the general results from Sec. II guarantee the validity of the pole-zero expansion. The off-diagonal case, however, must be reexamined.

The coupling of the beam to the structure is assumed to occur at the end of the beam via an admittance relationship of the type

$$q_i = \tilde{Y}_{ij}(\omega)F_j, \tag{14}$$

relating the generalized forces to the generalized coordinates at frequency ω via the input admittance of the attached structure $\tilde{Y}_{ij}(\omega)$. The indices $i = 1,2$ refer to the displacement $q_1 = u(a)$ and the rotation $q_2 = u'(a)$ with corresponding shear force and torque. Recalling that the shear force is given by $F_1 = Du^{(3)}(a)$ and the applied moment by $F_2 = -Du^{(2)}(a)$, the impedance coupling to a general elastic system yields a traditional boundary value problem for the beam apart from the frequency dependence of the admittance $\tilde{Y}_{ij}(\omega)$. As a result of this complication, the eigenfunctions of the beam alone are no longer orthogonal and the approach of the previous section, which relied upon the orthogonality of the eigenfunctions of the beam, is not immediately applicable. The normal modes of the entire system are in fact

orthogonal, but because the orthogonality results from an integral over the entire system, this fact does not help us show that the product $\psi_n(0)\psi_n'(0)$ has a particular sign.

Our goal is once again to demonstrate that the zeros of the various admittance functions are real. We proceed using frequency-dependent eigenfunctions, a technique employed by Morse and Feshbach[3] in related non-self-adjoint problems. We proceed in two steps. In step one, we use the frequency-dependent expansion to show that the products $\psi_n(0,\omega)\psi_n'(0,\omega)$ in the frequency-dependent eigenfunction expansion all have the same sign. The singularity structure of the admittance is thus shown to alternate. In step two, we show that there is exactly one zero between each pair of poles. To demonstrate this aspect, we return to the modal expansion. The details are as follows.

Treat the frequency ω as a parameter and seek the solution of Eq. (5) in terms of the eigenfunctions of the operator

$$\mathcal{L}(\omega)=D\frac{\partial^4}{\partial x^4}-m\omega^2, \tag{15}$$

subject to free-boundary conditions at $x=0$ and the frequency-dependent impedance boundary conditions at $x=a$. The eigenfunctions of $\mathcal{L}(\omega)$ are identical in form with the usual eigenfunctions, $\exp(\pm ik_n(\omega)x)$ and $\exp(\pm k_n(\omega)x)$, but the wave number $k_n(\omega)$ is not given directly from the dispersion relation; instead, $k_n(\omega)$ is determined by the boundary conditions. The set of eigenfunctions so obtained will be orthogonal since ω is merely a parameter and the above boundary value problem is self-adjoint.[3] The eigenvalues of $\mathcal{L}(\omega)$ are $Dk_n^4(\omega)-m\omega^2$, as opposed to simply Dk^4, and the resulting eigenfunction expansion for the Green's function is

$$G(x,x')=\frac{1}{m}\sum_n \frac{\phi_n(x,\omega)\phi_n(x',\omega)}{(D/m)k_n^4(\omega)-\omega^2}. \tag{16}$$

The expansion given in Eq. (16) is quite similar in form to the traditional expansion but is subtly different. The eigenvalues $k_n(\omega)$ and eigenfunctions $\phi_n(x,\omega)$ are frequency dependent, and are not the resonance frequencies and normal modes of the system. The expansion is, however, closely related to the modal expansion.

We establish a few facts concerning the properties of expansion before proceeding. This discussion is in part similar to considerations in Morse and Feshbach.[3] The poles of the Green's function as a function of ω are given by the zeros of the denominators of Eq. (16). At a resonance frequency ω_n, the denominator $(D/m)k_n^4(\omega_n)-\omega_n^2=0$, since the solution then coincides with the usual normal-mode solution. Thus, the frequency dependence of $k_n(\omega)$ is such that each denominator has only a single simple zero at the resonance frequency ω_n, in order that the analytic structure of $G(x,x')$ coincides with that of the normal-mode solution. Further, the residues of each pole of $(k_n^4(\omega)-\omega^2)^{-1}$ must have the same sign; otherwise, the alternating pole-zero result for the diagonal case would be violated since $\phi_n^2(x,\omega)\geqslant 0$. We note in passing that the eigenfunctions $\phi_n(x,\omega)$ must be analytic in the complex ω plane, so that spurious singularities are not introduced in the Green's function.

We now use the same technique as that employed in Sec. III C to show that the signs of the products $\phi_n(0,\omega)\phi_n'(0,\omega)$ are all the same. Taylor expanding the frequency-dependent eigenfunctions $\phi_n(x,\omega)$ in x, we find identical results to those given in Eq. (13) if we replace the quantities $(m\omega_n^4/D)$ with the corresponding quantities $k_n^4(\omega)$. Thus, the coefficients of the Taylor series expansion of the quantity $\phi_n(x,\omega)$ are all positive, and the arguments concerning the relative signs of $\phi_n(0,\omega)$ and $\phi_n'(0,\omega)$ go through with no modification. Thus, $\phi_n(x,\omega)$ will be strictly positive if $\phi_n(0,\omega)$ and $\phi_n'(0,\omega)$ have the same sign, and in order to be mutually orthogonal, only a single frequency-dependent eigenfunction, the rigid-body translational mode, may have this characteristic. Recalling that the rigid-body translational mode does not contribute to the off-diagonal component of the Green's function, the product $\phi_n(0,\omega)\phi_n'(0,\omega)$ must be strictly less than zero, and every term in the expansion must have the same sign.

This fact is not enough to fully determine the characteristics of the zeros since, unlike a standard eigenfunction expansion, the coefficients of the frequency-dependent expansion, Eq. (16), are not constants. Nevertheless, the statement $\phi_n(0,\omega)\phi_n'(0,\omega)<0\ \forall n$ implies that for frequencies just above each resonance ω_n, $Y_{12}\to-\infty$, while for frequencies just below the following resonance ω_{n+1}, $Y_{12}\to+\infty$. Continuity thus assures the existence of at least one zero between each pair of poles. The statement that there is exactly one zero between each pair of poles requires us to show in addition that $Y_{12}(\omega)$ is monotonic away from the singularities. This is more difficult to show in the frequency-dependent expansion than in the modal expansion because of the frequency dependence of the functions $\phi_n(x,\omega)$. We therefore proceed as follows.

Consider then the corresponding normal-mode expansion for Y_{12}. The coefficients of every term in this expansion must *also* have the same sign in order that $Y_{12}(\omega_n^+)\to-\infty$ and $Y_{12}(\omega_{n+1}^-)\to+\infty$ in agreement with the above analysis. And therefore, based on the general discussion in Sec. III B, we can immediately assert that the zeros of $Y_{12}(\omega)$ must all be real and alternate with the poles of the system. The pole-zero product expansion is thus a generally valid representation for the admittance matrix of a beam or rod in flexure coupled to any conservative elastic system.

IV. A TWO-DIMENSIONAL SYSTEM: A PLATE STRIP

The two-dimensional character of the plate strip introduces some interesting complications and our claims in this case are not quite as strong; here, we can show in general that there is at most one complex zero of the cross-admittance function. The steady-state flexural motion of a vibrating plate is governed by the two-dimensional analog of Eq. (5)

$$D\left(\frac{\partial^2}{\partial x^2}+\frac{\partial^2}{\partial y^2}\right)^2 u-m\omega^2 u=f\delta(r). \tag{17}$$

We assume the system to be a strip finite in the x direction and impose periodic boundary conditions in the y direction. The boundary value problem hence approximately models

the flexural motion of an annular plate at frequencies above the ring frequency. The Green's function can be expanded in Fourier components in the y direction, resulting in the effectively one-dimensional system for each value of k_y

$$D\left(\frac{\partial^2}{\partial x^2}-k_y^2\right)^2 u - m\omega^2 u = f\delta(x^+). \tag{18}$$

The plate is taken to be free on the edge $x=0$ subjected to excitation and hence satisfies the Kirchhoff boundary conditions[20]

$$u^{(3)}(0)=(2-\nu)k_y^2 u^{(1)}(0), \quad u^{(2)}(0)=\nu k_y^2 u(0). \tag{19}$$

The two degrees of freedom in this case are again the displacement u and the angular displacement $\partial u/\partial x$. We first examine the case in which the edge at $x=a$ satisfies a general self-adjoint boundary condition.

The four eigenfunctions of the homogeneous plate operator with eigenvalue Dk_f^4 are of the form $\exp(ik_x x)$, with $k_x=\{\pm(k_f^2-k_y^2)^{1/2}, \pm i(k_f^2+k_y^2)^{1/2}\}$. Imposition of the boundary conditions yields the resonance frequencies $\omega_n(k_y)$ and associated eigenfunctions $\psi_n(x,k_y)$. Thus, we have the normal-mode expansion for the Green's function for each k_y

$$G(x,x',k_y)=\frac{1}{m}\sum_n \frac{\psi_n(x,k_y)\psi_n(x',k_y)}{\omega_n^2(k_y)-\omega^2}. \tag{20}$$

The off-diagonal components of the Green's function are given by the analog to Eq. (7)

$$Y_{12}=Y_{21}=\frac{\partial G(0,0,k_y)}{\partial x}=\frac{1}{m}\sum_n \frac{\psi_n'(0,k_y)\psi_n(0,k_y)}{\omega_n^2(k_y)-\omega^2}. \tag{21}$$

We continue in analogy with the beam case; our goal is to demonstrate that the signs of the products $\psi_n'(0,k_y)\psi_n(0,k_y)$ are all the same, with the immediate conclusion that the zeros are real. Consider the Taylor series for $\psi_n(x,k_y)$. We seek to eliminate the higher derivatives in this expansion recursively using the equations of motion, Eq. (18), in the form

$$\frac{\partial^m \psi_n(x,k_y)}{\partial x^m}=2k_y^2\frac{\partial^{m-2}\psi_n(x,k_y)}{\partial x^{m-2}}+\left(\frac{m\omega_n^2}{D}-k_y^4\right)\times\frac{\partial^{m-4}\psi_n(x,k_y)}{\partial x^{m-4}}, \tag{22}$$

where $m\geqslant 4$. Here, unlike in the plate case, the coefficients in this recursion are not necessarily positive.

To proceed, we assert that there is at most a single eigenvalue, the lowest eigenvalue, which can violate the condition $((m\omega_n^2/D)-k_y^4)>0$. This fact can be shown as follows. Consider the governing equation, Eq. (18), for free–free boundary conditions. In this case, it has been shown by Fletcher *et al.*[23,24] that there is a single eigenvalue such that $((m\omega_n^2/D)-k_y^4)<0$, and that all other eigenvalues satisfy $((m\omega_n^2/D)-k_y^4)>0$. The Rayleigh–Courant–Fisher theorem[20,25] then implies that the effect of any additional constraints, the imposition of boundary conditions for example, shifts each eigenvalue upwards from these values. Thus, in general, we have the result that there is *at most* a single eigenfrequency, the lowest mode, for which $((m\omega_n^2/D)-k_y^4)<0$.

Let us restrict our attention then to any of the higher modes $\psi_n(x,k_y)$ for which we have $((m\omega_n^2/D)-k_y^4)>0$. For any of these modes, the Taylor series expansion may be recursively reduced to contain at most third derivatives using the expression Eq. (22), and the coefficients resulting from this procedure will all be positive. The Taylor series for $\psi_n(x,k_y)$ may then be further reduced using the Kirchhoff boundary conditions, Eq. (19), to eliminate the second and third derivatives; note that the coefficients encountered in this step are also positive. This results in the expansion

$$\psi_n(x,k_y)=\psi_n(0,k_y)\sum_{m=0}^{\infty} a_m(k_y)x^{2m} + \psi_n'(0,k_y)\sum_{m=0}^{\infty} b_m(k_y)x^{2m+1}, \tag{23}$$

where the coefficient functions $a_m(k_y)$ and $b_m(k_y)$ are therefore positive. The requirement that the $\{\psi_n(x,k_y)\}$ be an orthogonal set implies that $\psi_n(0,k_y)$ and $\psi_n'(0,k_y)$ must have opposite signs, and the zeros of Y_{12} are hence real and alternate with the poles, with the possible exception of the lowest zero.

The generalization of this result to the case of a plate strip attached to an arbitrary system with translational symmetry in the y direction closely follows the analysis of the beam case, and we omit the details in the interest of brevity. No difficulties are encountered in the extension, however, and the corresponding results concerning the zeros are valid in the case of a plate strip attached to a general, energy-conserving, elastic structure.

V. AN EXPLICIT EXAMPLE: THE ADMITTANCE MATRIX OF A FREE–FREE BEAM

The free–free beam is a simple example for which the pole-zero representation for the admittance may be explicitly worked out. We employ a direct solution technique which illustrates one method by which the zeros may be obtained and discuss other solution techniques. The admittance may be evaluated exactly, approximated by a truncated pole-zero expansion, and approximated by a traditional truncated modal expansion. The results from the truncated expansions are compared to exact analytical results. Of course, the solution of this boundary value problem employing traditional methods is well known.[21] Nevertheless, we give some explicit formulas to enable the reader to quickly reproduce the detailed results of this section.

The equations of motion and the boundary conditions are given in Eqs. (5) and (6). The exact solution is obtained by interpreting the external force or moment as a boundary condition. This leads to the boundary conditions at $x=0$

$$\frac{\partial^2 u}{\partial x^2}(0)=0, \quad \frac{\partial^3 u}{\partial x^3}(0)=1/D \quad (\text{source} \quad \delta(x)),$$

$$\frac{\partial^2 u}{\partial x^2}(0)=-1/D, \quad \frac{\partial^3 u}{\partial x^3}(0)=0 \quad (\text{source}-\delta'(x)), \tag{24}$$

for an applied force or moment, respectively. A closed-form expression for the Green's function, the delta function force case, may be obtained without difficulty

$$G(x,0)=\frac{g(x)}{2k^3D(\cos(ka)\cosh(ka)-1)}, \tag{25}$$

where

$$\begin{aligned} g(x)=&\cosh k(a-x)\sin(ka)+\cosh(ka)\sin k(a-x)\\ &+\cos k(a-x)\sinh(ka)-\cos(ka)\sinh k(a-x)\\ &+\sin(kx)-\sinh(kx). \end{aligned}$$

A similar expression results in the case of a moment excitation. The various components of the admittance matrix are then evaluated according to Eq. (7); in particular $Y_{11}=G(0,0)$ and $Y_{12}=Y_{21}=G'(0,0)$.

The classical modal solution for the Green's function is

$$G(x,x')=\frac{1}{m}\sum_n \frac{\psi_n(x)\psi_n(x')}{\omega_n^2-\omega^2}, \tag{26}$$

where the ω_n and $\psi_n(x)$ are the eigenfrequencies and eigenfunctions of the beam equation with free–free boundary conditions. The first two eigenfunctions are rigid-body modes with zero resonance frequency, $\psi_0(x)=(1/a)^{1/2}$ and $\psi_1(x)=(3/a)^{1/2}(1-2x/a)$, corresponding to rigid translation and rotation, respectively. The remaining modes must be calculated numerically. Our results are in agreement with the literature.[26]

The pole-zero solution employs the eigenvalues obtained in the normal-mode solution. In addition, we must evaluate the appropriate antiresonance frequencies. In the case of Y_{11}, we seek the frequencies at which the displacement at the excitation point vanishes when the beam is subjected to a shear force at the end. We note that the solution at these frequencies will satisfy the boundary conditions of a simply supported beam

$$\frac{\partial^2 u}{\partial x^2}(0)=0, \quad u(0)=0. \tag{27}$$

These are the complementary boundary conditions to those of the forced problem. The set of eigenfrequencies so obtained by solving this related boundary value problem yields the antiresonance frequencies of Y_{11}.

In the off-diagonal case, Y_{12}, the manipulations are identical. We seek the frequencies at which the angular displacement at the excitation point vanishes when the beam is subjected to a shear force at the end, and note that the solution at these frequencies will satisfy the boundary conditions

$$\frac{\partial^3 u}{\partial x^3}(0)=0, \quad u(0)=0. \tag{28}$$

In this case, the boundary conditions do *not* specify a physically realizable boundary value problem; that is, the boundary value problem is not self-adjoint. Thus, the eigenfrequencies obtained by solving this homogeneous set of equations are *not* the resonance frequencies of another physically realizable system, and are in general complex. Nevertheless, we are guaranteed by the results of the preceding sections that the solutions of the boundary value problem specified by Eq. (28) will have real eigenfrequencies $\{\omega_{n,12}\}$.

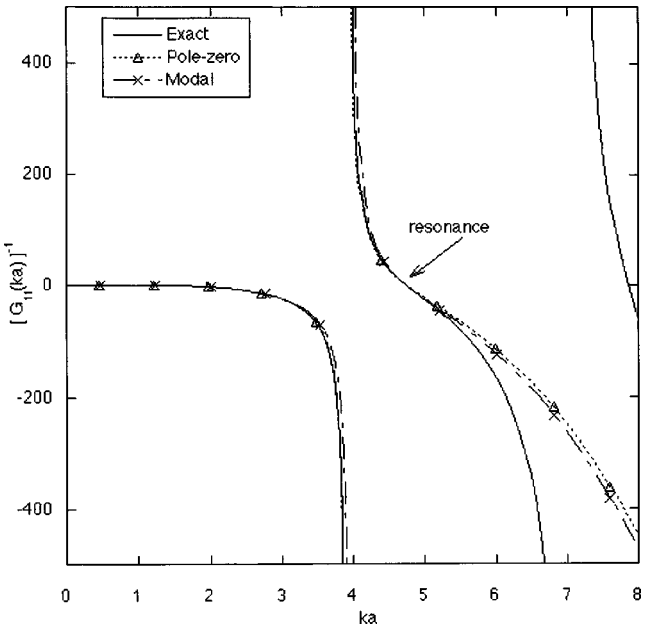

FIG. 1. The reciprocal of the Green's function G_{11} for a free–free beam calculated exactly(solid line), with a pole-zero product expansion truncated to a single pole and zero(dotted line) and a modal expansion truncated to a single term(dashed-dotted line).

The pole-zero solution for $Y_{ij}(\omega)$ is hence

$$Y_{ij}(\omega)=C_{ij}(\omega)\frac{\Pi_n(1-\omega^2/\omega_{n,ij}^2)}{\Pi_{n>2}(1-\omega^2/\omega_n^2)}, \tag{29}$$

where $C_{ij}(\omega)$ is determined by evaluating the $\omega\to 0$ response of the Green's function. It is straightforward to show that

$$C_{ij}(\omega)=\frac{1}{m\omega^2 a}\begin{cases} -4 & (\text{for } Y_{11})\\ 6/a & (\text{for } Y_{21} \text{ and } Y_{12})\\ -12/a^2 & (\text{for } Y_{22}) \end{cases}. \tag{30}$$

The exact modal and pole-zero solutions are shown in Figs. 1–3 for the three distinct components of the admittance matrix. The truncated expansions are required to have equal numbers of unknowns. In the modal expansion, each term contains two unknowns, the resonance frequency and mode amplitude. This corresponds to the ratio of a single zero and pole of the pole-zero expansion. Both approximate solutions are truncated to the first term in the expansion and can be expected to be valid only for frequencies below or of order the first resonance frequency. Both expansions in this example contain two numerically determined constants; the first resonance frequency and associated modal amplitude in the case of the modal expansion, and the first resonance frequency and first antiresonance frequency in the pole-zero expansion. The reciprocals of the admittance are displayed so that the accuracy of the solutions near the antiresonances, the range of most difficulty for the truncated modal expansions, can be most easily seen. Note that resonances will therefore appear in the plots as zeros and antiresonances as singularities.

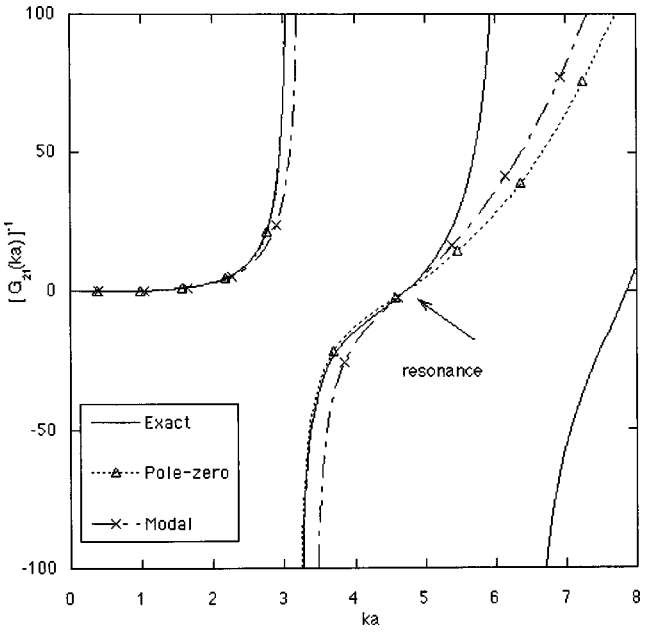

FIG. 2. The reciprocal of the Green's function G_{21} for a free–free beam calculated exactly(solid line), with a pole-zero product expansion truncated to a single pole and zero(dotted line) and a modal expansion truncated to a single term(dashed-dotted line).

A single term in the pole-zero expansion is seen to provide an excellent approximation for all frequencies below the first resonance, while the modal expansion works well for the (11) component but not nearly so well for the (21) and (22) components. It would seem from this example that the accuracy of the truncated modal expansion is decreased if the poles and zeros are farther apart from one another. We have, however, made no attempt to quantify the accuracy of the truncated pole-zero expansion relative to the truncated modal expansion in a general way.

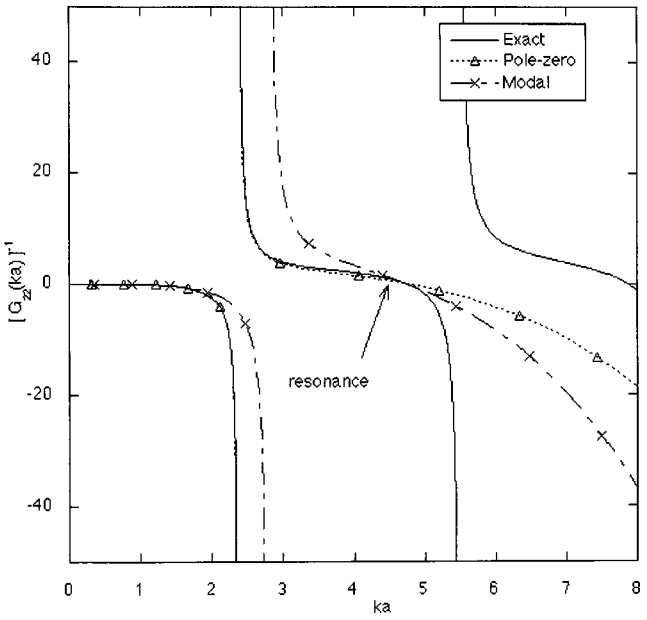

FIG. 3. The reciprocal of the Green's function G_{22} for a free–free beam calculated exactly(solid line), with a pole-zero product expansion truncated to a single pole and zero(dotted line) and a modal expansion truncated to a single term(dashed-dotted line).

It is worth noting that this failure of the truncated modal expansion is known in the literature, and various steps can be taken to improve the expansion.[16–19] Generally, these steps involve adding modal information not contained in the truncated expansion. We have found, for example, that the modal truncation augmentation method, which involves adding a single term resembling the load, performs quite well. These methods may or may not be preferable to the pole-zero expansion depending on the demands of a particular application. We merely note that these approaches do involve adding additional information, and by necessity will be somewhat more algebraically complicated than their pole-zero counterparts; on the other hand, they have been fairly well tested.[19]

VI. CONCLUSIONS

We have investigated the properties of the admittance matrix of two of the simplest multidegree of freedom, wave-bearing systems, namely beams and plate strips in flexure. In both types of systems, at each point x, the displacement $u(x)$ and the angular displacement $u'(x)$ are independent and the admittance of the system at any point is therefore a 2×2 matrix.

We have shown that all the components of the admittance matrix for edge-excited beam and plate strip systems can be represented as pole-zero product expansions such that all the poles and almost all the zeros are real. The results we have obtained here are valid for a fairly wide class of systems because the beam, or plate strip, may be attached to an arbitrary conservative system. This statement must be qualified somewhat in that the attached system is assumed not to induce coupling to the previously uncoupled degrees of freedom; for example, the attached structure is not allowed to couple flexural motion to longitudinal motion in the beam. The pole-zero representation may be valid in this context, but we have not demonstrated that it is.

The main new mathematical statement we have obtained concerns the zeros of the off-diagonal elements of the admittance matrix. We have shown that for beams, the zeros are always real and alternate with the poles. In the plate case with nonzero transverse wave number, we have shown that this is almost always true. The exceptional case concerns the lowest zero which can in principle be complex depending on the boundary conditions. We note, however, that we have not observed this anomalous behavior in any example, and that it is possible that the ''theorem'' holds even in this case.

The pole-zero expansion assures the accuracy of truncated approximations near both the resonance and antiresonance frequencies, and is therefore better behaved than corresponding truncated modal expansions. Thus, this approach offers improved accuracy and simpler expressions than traditional elementary coupled oscillator representations.

Our results have several implications. First, we have increased the general theoretical knowledge in this area. For systems in which beams or long plates effectively couple vibrating subsystems to one another, we are now assured that a pole-zero product representation can be used to represent the entire admittance matrix. This implies not only that pole-zero product expansions with real poles and zeros can be

used in an algebraic modeling context, but in addition implies that the cross-admittance functions have the same mathematical properties as the diagonal elements.

An application of particular interest to the authors concerns the vibration of ribbed plates and shells. Quantitative predictions of the propagation modes of ribbed shells have been difficult to obtain for many years,[9,27,28] and only finite-element models have been successful. The fundamental problem encountered by researchers has been simple; the modeling of the impedance matrix of the ribs in the various models has typically been inadequate. Modal expansions of the rib impedance matrices have not been seriously attempted, no doubt in part because of the complexity expansions of this sort are known to add to an already complicated problem in order to obtain accurate results, even at relatively low frequencies.[29] A pole-zero approximation of lowest order would resolve this problem; it would be fairly accurate and nearly as simple as a single oscillator representation. Thus, for example, we expect researchers to be able to obtain accurate analytical predictions of the dispersion curves of framed shells using this method.

Finally, it does not seem unreasonable to the authors to expect that extensions of the theorem can be made. Various extensions would seem to be fairly straightforward. One aspect which seems almost certain to be unnecessarily restrictive concerns the fact that the attachment and excitation points must be at the ends of the structure. Another aspect concerns the coupling of flexure to other components. We have established in a number of examples that the theorem continues to be valid for this generalization, but have not yet pursued a general mathematical proof. Finally, our results do seem to indicate that the theorem or some variant may in fact be true for almost all linear vector systems, a result which would have far-reaching significance.

ACKNOWLEDGMENTS

One of the authors (D.M.P.) acknowledges many useful conservations with E. Williams. The authors gratefully acknowledge the Office of Naval Research for support of this work.

[1] I. M. Lifshitz, S. A. Gredeskul, and L. A. Pastur, *Introduction to the Theory of Disordered Systems* (Wiley, New York, 1988).
[2] D. J. Thouless, *Ill-Condensed Matter* (North Holland, Amsterdam, 1979), Chap. Percolation and Localization, pp. 5–60.
[3] P. M. Morse and H. Feshbach, *Methods of Theoretical Physics* (McGraw-Hill, New York, 1953).
[4] C. M. Close, *The Analysis of Linear Circuits* (Harcourt, Brace and World, New York, 1966).
[5] E. A. Guillemin, *The Mathematics of Circuit Analysis* (Wiley, New York, 1949).
[6] E. A. Guillemin, *Synthesis of Passive Networks* (Wiley, New York, 1957).
[7] *Aspects of Network Theory*, edited by R. E. Kalman and N. Declaris (Holt, Rinehart and Winston, New York, 1971).
[8] G. Maidanik and A. J. Tucker, J. Sound Vib. **34**, 519 (1974).
[9] C. B. Burroughs, J. Acoust. Soc. Am. **75**, 715 (1984).
[10] D. M. Photiadis, J. A. Bucaro, and B. H. Houston, J. Acoust. Soc. Am. **101**, 87 (1997).
[11] M. Strasburg and D. Feit, J. Acoust. Soc. Am. **99**, 335 (1996).
[12] J. A. Bucaro, A. Romano, A. Sarkissian, D. M. Photiadis, and B. H. Houston, J. Acoust. Soc. Am. **103**, 1867 (1998).
[13] A. Harari, J. Acoust. Soc. Am. **62**, 1196 (1977).
[14] E. A. Guillemin, *Theory of Linear Physical Systems; Theory of Physical Systems from the View-point of Classical Dynamics, Including Fourier Methods* (Wiley, New York, 1963).
[15] E. A. Coddington and N. Levinson, *Theory of Ordinary Differential Equations* (Krieger, Malabar, FL, 1984).
[16] R. L. Bisplinghoff, *Principles of Aeroelasticity* (Wiley, New York, NY, 1962).
[17] A. F. Seybert, T. W. Wu, and W. L. Li, J. Sound Vib. **115**, 152 (1993).
[18] J. M. Dickens and K. V. Pool, Comput. Struct. **45**, 685 (1992).
[19] J. M. Dickens, J. M. Nakagawa, and M. J. Wittbrodt, Comput. Struct. **62**, 985 (1997).
[20] R. Courant and D. Hilbert, *Methods of Mathematical Physics* (Wiley, New York, 1962).
[21] P. M. Morse and K. U. Ingard, *Theoretical Acoustics* (McGraw-Hill, New York, 1968).
[22] G. F. Carrier, M. Krook, and C. E. Pearson, *Functions of a Complex Variable* (McGraw-Hill, New York, 1966).
[23] H. Fletcher, N. Woodfield, and K. Larsen, Technical Report CFSTI AD-107-224, Brigham Young University, Provo, Utah (1956).
[24] A. W. Leissa, *Vibration of Plates* (NASA SP-160, Washington, D.C., 1969).
[25] V. Arnold, *Mathematical Methods of Classical Mechanics*, 2nd ed. (Springer, New York, 1989).
[26] W. T. Thomson, *Theory of Vibration with Applications* (Prentice-Hall, Englewood Cliffs, NJ, 1972).
[27] D. M. Photiadis, J. A. Bucaro, and B. H. Houston, J. Acoust. Soc. Am. **96**, Part 1, 2785 (1994).
[28] M. H. Marcus, B. H. Houston, and D. M. Photiadis, J. Acoust. Soc. Am. **109**, 865 (2001).
[29] C. H. Hodges and J. Woodhouse, J. Acoust. Soc. Am. **74**, 894 (1983).

Statistical errors in the estimation of time-averaged acoustic energy density using the two-microphone method

Justin Ghan,[a] Ben Cazzolato, and Scott Snyder
Department of Mechanical Engineering, University of Adelaide, SA 5005, Australia

(Received 31 August 2002; revised 31 October 2003; accepted 31 October 2003)

Time-averaged acoustic energy density can be estimated using the auto- and cross-spectral densities between two closely spaced microphones. In this paper, an analysis of the random errors that arise using two microphone measurements is undertaken. An expression for the normalized random error of the time-averaged acoustic energy density spectral density estimate is derived. This expression is verified numerically. The lower and upper bounds of the normalized random error are derived. It is shown that the normalized random error of the estimate is not a strong function of the sound field properties, and is chiefly dependent on the number of records averaged. © *2004 Acoustical Society of America.* [DOI: 10.1121/1.1639334]

PACS numbers: 43.58.-e, 43.60.Qv [JCB]

Pages: 1179–1184

I. INTRODUCTION

Acoustic energy density is defined as the sum of the acoustic potential energy density and the acoustic kinetic energy density at a point. It has been shown[1] that energy density provides a significantly better estimate of the total acoustic energy within an enclosure than does the acoustic potential energy (estimated by microphones). Subsequently, several authors have found energy density to be an effective sensor for active noise control applications, as it measures the total energy at a point, and generally outperforms microphones.[2–6]

The bias errors arising from the inherent and instrumentation errors in energy density sensing have been thoroughly investigated.[7–9] Additionally, the estimation of potential energy density and kinetic energy density in the frequency domain and the associated statistical errors have been discussed by Elko.[10] In this paper, the statistical errors associated with the estimation of total acoustic energy density are analyzed.

An expression for the estimation of time-averaged total acoustic energy density in the frequency domain has been previously derived.[11] In this paper, an expression for the normalized random error of this estimate is derived. The method here is similar to that used to derive the normalized random error in the estimation of sound intensity.[12]

A Simulink model will be used to simulate the estimation of the time-averaged acoustic energy density. The resulting measurements will be analyzed to verify the derived expression for the normalized random error.

It will be shown that the normalized random error does not depend heavily upon the nature of the sound field being measured. In fact, it is bounded between two functions dependent only on n_d, the number of records averaged to produce the ''smooth'' spectral density estimates used in the expression for the time-averaged acoustic energy density spectral density estimate. As a result, the averaging time required to attain a desired level of accuracy can be chosen without knowledge of any of the specifics of the experiment.

II. ANALYTICAL DERIVATION OF THE RANDOM ERROR

The instantaneous acoustic energy density, $E_D(t)$, at a point is defined as the sum of the acoustic potential energy density, $U(t)$, and the acoustic kinetic energy density, $T(t)$, at that point, given by[13]

$$U(t)=\frac{p^2(t)}{2\rho c^2}, \tag{1}$$

$$T(t)=\frac{\rho v^2(t)}{2}, \tag{2}$$

$$E_D(t)=U(t)+T(t)=\frac{p^2(t)}{2\rho c^2}+\frac{\rho v^2(t)}{2}, \tag{3}$$

where $p(t)$ and $v(t)$ are the instantaneous pressure and particle velocity magnitude, respectively, at that point, c is the speed of sound, and ρ is the mean density of the fluid.

It has been shown[11] that, using the two-microphone measurement method with a microphone separation distance of $2h$, the single-sided time-averaged acoustic energy density spectral density is approximated by

$$\overline{E_D}(\omega)\approx\left(\frac{1}{8\rho c^2}+\frac{1}{8\rho\omega^2h^2}\right)(G_{11}(\omega)+G_{22}(\omega)) + \left(\frac{1}{8\rho c^2}-\frac{1}{8\rho\omega^2h^2}\right)(2\,\mathrm{Re}[G_{12}(\omega)]), \tag{4}$$

where $G_{11}(\omega)$ and $G_{22}(\omega)$ are the single-sided auto-spectral densities, and $G_{12}(\omega)$ is the single-sided cross-spectral density, of the two microphone pressure signals. If the cross-

[a]Author to whom all correspondence should be addressed; electronic mail: justin.ghan@adelaide.edu.au

spectral density is separated into real and imaginary components, $G_{12}(\omega)=C_{12}(\omega)+\mathrm{j}Q_{12}(\omega)$, Eq. (4) can be rewritten as

$$\overline{E_D}(\omega)\approx\left(\frac{1}{8\rho c^2}+\frac{1}{8\rho\omega^2h^2}\right)(G_{11}(\omega)+G_{22}(\omega))+\left(\frac{1}{8\rho c^2}-\frac{1}{8\rho\omega^2h^2}\right)(2C_{12}(\omega)). \tag{5}$$

An estimate of the time-averaged acoustic energy density spectral density is given by

$$\overline{\hat{E}_D(\omega)}\approx\left(\frac{1}{8\rho c^2}+\frac{1}{8\rho\omega^2h^2}\right)(\hat{G}_{11}(\omega)+\hat{G}_{22}(\omega))+\left(\frac{1}{8\rho c^2}-\frac{1}{8\rho\omega^2h^2}\right)(2\hat{C}_{12}(\omega)), \tag{6}$$

where $\hat{G}_{11}(\omega)$, $\hat{G}_{22}(\omega)$, and $\hat{C}_{12}(\omega)$ are "smooth" estimates of the auto-spectral densities and the real part of the cross-spectral density, obtained by averaging n_d statistically independent "raw" estimates.

Estimates of time-averaged potential energy density and time-averaged kinetic energy density are given by

$$\hat{\overline{U}}(\omega)\approx\frac{1}{8\rho c^2}(\hat{G}_{11}(\omega)+\hat{G}_{22}(\omega)+2\hat{C}_{12}(\omega)), \tag{7}$$

$$\hat{\overline{T}}(\omega)\approx\frac{1}{8\rho\omega^2h^2}(\hat{G}_{11}(\omega)+\hat{G}_{22}(\omega)-2\hat{C}_{12}(\omega)). \tag{8}$$

Elko[10] derived the normalized random error of these estimates. While the derivations were based upon incorrect expressions for the estimates, the method and results remain valid:

$$\epsilon(\hat{\overline{U}}(\omega))\approx\frac{1}{\sqrt{n_d}}, \tag{9}$$

$$\epsilon(\hat{\overline{T}}(\omega))\approx\frac{1}{\sqrt{n_d}}. \tag{10}$$

It can be shown that the variance of the estimate in Eq. (6) is, to a first-order approximation,

$$\begin{aligned}\mathrm{var}\{\overline{\hat{E}_D(\omega)}\}\approx&\left(\frac{\partial\overline{\hat{E}_D}}{\partial\hat{G}_{11}}\right)^2\mathrm{var}\{\hat{G}_{11}(\omega)\}+\left(\frac{\partial\overline{\hat{E}_D}}{\partial\hat{G}_{22}}\right)^2\mathrm{var}\{\hat{G}_{22}(\omega)\}+\left(\frac{\partial\overline{\hat{E}_D}}{\partial\hat{G}_{12}}\right)^2\mathrm{var}\{\hat{C}_{12}(\omega)\}\\&+2\left(\frac{\partial\overline{\hat{E}_D}}{\partial\hat{G}_{11}}\right)\left(\frac{\partial\overline{\hat{E}_D}}{\partial\hat{G}_{22}}\right)\mathrm{cov}\{\hat{G}_{11}(\omega),\hat{G}_{22}(\omega)\}+2\left(\frac{\partial\overline{\hat{E}_D}}{\partial\hat{G}_{11}}\right)\left(\frac{\partial\overline{\hat{E}_D}}{\partial\hat{G}_{12}}\right)\mathrm{cov}\{\hat{G}_{11}(\omega),\hat{C}_{12}(\omega)\}\\&+2\left(\frac{\partial\overline{\hat{E}_D}}{\partial\hat{G}_{22}}\right)\left(\frac{\partial\overline{\hat{E}_D}}{\partial\hat{G}_{12}}\right)\mathrm{cov}\{\hat{G}_{22}(\omega),\hat{C}_{12}(\omega)\},\end{aligned} \tag{11}$$

where the derivatives are evaluated at the true values $\hat{G}_{11}(\omega)=G_{11}(\omega)$, $\hat{G}_{22}(\omega)=G_{22}(\omega)$, and $\hat{C}_{12}(\omega)=C_{12}(\omega)$.

Assuming stationary Gaussian random signals, the relevant variances and covariances are[14]

$$\mathrm{var}\{\hat{G}_{11}(\omega)\}=\frac{G_{11}^2(\omega)}{n_d}, \tag{12}$$

$$\mathrm{var}\{\hat{G}_{22}(\omega)\}=\frac{G_{22}^2(\omega)}{n_d}, \tag{13}$$

$$\mathrm{var}\{\hat{C}_{12}(\omega)\}=\frac{G_{11}(\omega)G_{22}(\omega)+C_{12}^2(\omega)-Q_{12}^2(\omega)}{2n_d}, \tag{14}$$

$$\mathrm{cov}\{\hat{G}_{11}(\omega),\hat{G}_{22}(\omega)\}=\frac{|G_{12}(\omega)|^2}{n_d}, \tag{15}$$

$$\mathrm{cov}\{\hat{G}_{11}(\omega),\hat{C}_{12}(\omega)\}=\frac{G_{11}(\omega)C_{12}(\omega)}{n_d}, \tag{16}$$

$$\mathrm{cov}\{\hat{G}_{22}(\omega),\hat{C}_{12}(\omega)\}=\frac{G_{22}(\omega)C_{12}(\omega)}{n_d}. \tag{17}$$

Therefore,

$$\mathrm{var}\{\hat{\overline{E_D(\omega)}}\}\approx\left(\frac{1}{8\rho c^2}+\frac{1}{8\rho\omega^2h^2}\right)^2\frac{G_{11}^2(\omega)}{n_d}+\left(\frac{1}{8\rho c^2}+\frac{1}{8\rho\omega^2h^2}\right)^2\frac{G_{22}^2(\omega)}{n_d}+4\left(\frac{1}{8\rho c^2}-\frac{1}{8\rho\omega^2h^2}\right)^2$$
$$\times\frac{G_{11}(\omega)G_{22}(\omega)+C_{12}^2(\omega)-Q_{12}^2(\omega)}{2n_d}+2\left(\frac{1}{8\rho c^2}+\frac{1}{8\rho\omega^2h^2}\right)^2\frac{|G_{12}(\omega)|^2}{n_d}+4\left(\frac{1}{8\rho c^2}+\frac{1}{8\rho\omega^2h^2}\right)$$
$$\times\left(\frac{1}{8\rho c^2}-\frac{1}{8\rho\omega^2h^2}\right)\frac{G_{11}(\omega)C_{12}(\omega)}{n_d}+4\left(\frac{1}{8\rho c^2}+\frac{1}{8\rho\omega^2h^2}\right)\left(\frac{1}{8\rho c^2}-\frac{1}{8\rho\omega^2h^2}\right)\frac{G_{22}(\omega)C_{12}(\omega)}{n_d}. \tag{18}$$

Noting that

$$[\overline{E_D}(\omega)]^2\approx\left(\frac{1}{8\rho c^2}+\frac{1}{8\rho\omega^2h^2}\right)^2(G_{11}^2(\omega)+G_{22}^2(\omega)+2G_{11}(\omega)G_{22}(\omega))$$
$$+\left(\frac{1}{8\rho c^2}-\frac{1}{8\rho\omega^2h^2}\right)^2(4C_{12}^2(\omega))+2\left(\frac{1}{8\rho c^2}+\frac{1}{8\rho\omega^2h^2}\right)\left(\frac{1}{8\rho c^2}-\frac{1}{8\rho\omega^2h^2}\right)(G_{11}(\omega)+G_{22}(\omega))(2C_{12}(\omega)), \tag{19}$$

it can be seen that

$$\mathrm{var}\{\hat{\overline{E_D(\omega)}}\}\approx\frac{1}{n_d}\left[[\overline{E_D}(\omega)]^2+2\left(\frac{1}{8\rho c^2}-\frac{1}{8\rho\omega^2h^2}\right)^2(G_{11}(\omega)G_{22}(\omega)-C_{12}^2(\omega)-Q_{12}^2(\omega))\right.$$
$$\left.+2\left(\frac{1}{8\rho c^2}+\frac{1}{8\rho\omega^2h^2}\right)^2(|G_{12}(\omega)|^2-G_{11}(\omega)G_{22}(\omega))\right]. \tag{20}$$

Since $C_{12}^2(\omega)+Q_{12}^2(\omega)=|G_{12}(\omega)|^2=\gamma_{12}^2(\omega)G_{11}(\omega)G_{22}(\omega)$, where $\gamma_{12}^2(\omega)$ is the coherence between the two microphone pressure signals,

$$\mathrm{var}\{\hat{\overline{E_D(\omega)}}\}\approx\frac{1}{n_d}\left[[\overline{E_D}(\omega)]^2-8\left(\frac{1}{8\rho c^2}\right)\left(\frac{1}{8\rho\omega^2h^2}\right)(1-\gamma_{12}^2(\omega))G_{11}(\omega)G_{22}(\omega)\right]. \tag{21}$$

Therefore, the normalized random error of the estimate $\hat{\overline{E_D(\omega)}}$, defined as

$$\epsilon(\hat{\overline{E_D(\omega)}})=\frac{\sqrt{\mathrm{var}\{\hat{\overline{E_D(\omega)}}\}}}{\overline{E_D}(\omega)}, \tag{22}$$

is

$$\epsilon(\hat{\overline{E_D(\omega)}})\approx\frac{1}{\sqrt{n_d}}\left[1-\frac{8\left(\frac{1}{8\rho c^2}\right)\left(\frac{1}{8\rho\omega^2h^2}\right)(1-\gamma_{12}^2(\omega))G_{11}(\omega)G_{22}(\omega)}{[\overline{E_D}(\omega)]^2}\right]^{1/2}. \tag{23}$$

Since $\mathrm{Re}[G_{12}(\omega)]=|G_{12}(\omega)|\cos\phi_{12}(\omega)=\gamma_{12}(\omega)\sqrt{G_{11}(\omega)G_{22}(\omega)}\cos\phi_{12}(\omega)$, where $\phi_{12}(\omega)$ is the phase angle between the two microphone pressure signals and $\gamma_{12}(\omega)$ is the positive square root of $\gamma_{12}^2(\omega)$, Eq. (4) can be rewritten as

$$\overline{E_D}(\omega)\approx\left(\frac{1}{8\rho c^2}+\frac{1}{8\rho\omega^2h^2}\right)(G_{11}(\omega)+G_{22}(\omega))+\left(\frac{1}{8\rho c^2}-\frac{1}{8\rho\omega^2h^2}\right)(2\gamma_{12}(\omega)\sqrt{G_{11}(\omega)G_{22}(\omega)}\cos\phi_{12}(\omega)). \tag{24}$$

Substituting Eq. (24) into Eq. (23) and multiplying the numerator and denominator of the fraction by $(8\rho\omega^2h^2)^2/[4G_{11}(\omega)G_{22}(\omega)]$ yields

$$\epsilon(\hat{\overline{E_D(\omega)}})\approx\frac{1}{\sqrt{n_d}}\left[1-\frac{2(kh)^2(1-\gamma_{12}^2(\omega))}{[((kh)^2+1)X+((kh)^2-1)\gamma_{12}(\omega)\cos\phi_{12}(\omega)]^2}\right]^{1/2}, \tag{25}$$

where the wave number is given by $k=\omega/c$, and

$$X=\frac{1}{2}\left(\sqrt{\frac{G_{11}(\omega)}{G_{22}(\omega)}}+\sqrt{\frac{G_{22}(\omega)}{G_{11}(\omega)}}\right). \tag{26}$$

If the auto-spectral densities of the two microphone pressure signals are approximately equal, $G_{11}(\omega) \approx G_{22}(\omega)$, then $X \approx 1$, so

$$\epsilon(\hat{\overline{E_D(\omega)}}) \approx \frac{1}{\sqrt{n_d}} \left[1 - \frac{2(kh)^2(1-\gamma_{12}^2(\omega))}{[((kh)^2+1)+((kh)^2-1)\gamma_{12}(\omega)\cos\phi_{12}(\omega)]^2} \right]^{1/2}. \tag{27}$$

The normalized random error for this case is plotted in Fig. 1, assuming that the phase between the two signals is solely due to the propagation delay so that $\phi_{12}=2kh$. It is important to note that while the bias errors that occur when using the two-microphone method are affected by spatial aliasing, the random errors are not.

III. SIMULINK SIMULATION

A Simulink model (see Fig. 2) was created to simulate the two-microphone method for estimating acoustic energy density.

The two microphone pressure signals were calculated by simulating two points in a free space pressure field generated by a white noise point source. The transfer function from a monopole point source to a sensor at distance r is

$$G(s) = \frac{1}{r} e^{-(r/c)s}, \tag{28}$$

where c is the speed of sound. These transfer functions were implemented using a second-order Padé approximation in series with a gain. In order to vary the coherence between the two pressure readings, an amount of incoherent noise was introduced to one of the signals.

To compute a single estimate, a frequency spectrum of each of the microphone pressure readings was obtained by performing a 512 point fast Fourier transform (FFT) (see Fig. 3). The auto- and the cross-spectral densities were then calculated, and Eq. (4) was applied to produce an acoustic energy density spectral density estimate with $n_d=1$ (see Fig. 3). A number, N, of acoustic energy density spectral density estimates were calculated, and the standard deviation of each spectral line was divided by the mean value to produce an estimate of the normalized random error.

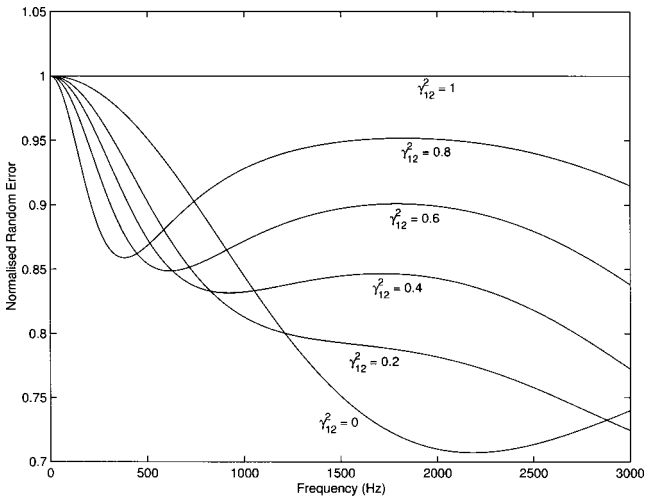

FIG. 1. Normalized random error of the acoustic energy density estimate ($n_d=1$), for $2h=50$ mm, $c=343\ \mathrm{m\,s^{-1}}$. It is assumed that $G_{11}(\omega) \approx G_{22}(\omega)$ and $\phi_{12}=2kh$. When the microphone separation distance exceeds $\lambda/2$, half the wavelength, the bias errors become very large, so the random error is unimportant. In this case, this occurs at frequencies above 3430 Hz.

The microphone pressure readings, p_1 and p_2, were also sampled in the time domain. Each time signal was divided into overlapping 512 point sections, each of which was windowed. The FFTs of these windowed sections were averaged to obtain spectra estimates, which were then used to calculate the auto- and cross-spectral densities, coherence and phase angle. Equation (25) was applied to calculate the normalized random error.

Comparisons of the results between the two methods for estimating the normalized random error for various values of N are shown in Fig. 4. As the number, N, of acoustic energy density estimates used in the average increases, the estimate of the normalized random error converges to that predicted by the derived equation (25). This would seem to confirm the validity of the expression for the normalized random error of the acoustic energy density spectral density estimate.

IV. BOUNDS OF THE RANDOM ERROR

Since the fraction in Eq. (25) is always non-negative, the normalized random error is bounded above by

$$\epsilon(\hat{\overline{E_D(\omega)}}) \leqslant \frac{1}{\sqrt{n_d}}, \tag{29}$$

and equality occurs when $\gamma_{12}^2(\omega)=1$.

The denominator of the fraction in Eq. (25) can be rearranged as

$$\begin{aligned}[((kh)^2+1)X+((kh)^2-1)\gamma_{12}(\omega)\cos\phi_{12}(\omega)]^2 \\ =[(X+\gamma_{12}(\omega)\cos\phi_{12}(\omega))(kh)^2 \\ +(X-\gamma_{12}(\omega)\cos\phi_{12}(\omega))]^2.\end{aligned} \tag{30}$$

Since the arithmetic mean of

$$(X+\gamma_{12}(\omega)\cos\phi_{12}(\omega))(kh)^2$$

and

$$(X-\gamma_{12}(\omega)\cos\phi_{12}(\omega))$$

is greater than or equal to their geometric mean,

$$\begin{aligned}[(X+\gamma_{12}(\omega)\cos\phi_{12}(\omega))(kh)^2+(X-\gamma_{12}(\omega)\cos\phi_{12}(\omega))]^2 \\ \geqslant 4(X^2-\gamma_{12}^2(\omega)\cos^2\phi_{12}(\omega))(kh)^2.\end{aligned} \tag{31}$$

Since $\cos^2\phi_{12}(\omega) \leqslant 1$,

$$4(X^2-\gamma_{12}^2(\omega)\cos^2\phi_{12}(\omega))(kh)^2 \geqslant 4(X^2-\gamma_{12}^2(\omega))(kh)^2. \tag{32}$$

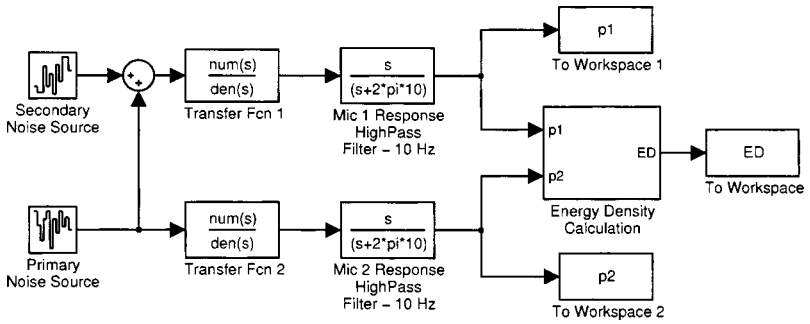

FIG. 2. The simulated sound field. The microphones (separation distance, $2h=50$ mm) are placed at distances $r_1=5.00$ m and $r_2=5.05$ m from the noise sources. The primary noise source produces continuous white noise of 1.0 Pa at 1 m (94 dB *re* 20 μPa). The secondary (contaminating) noise source produces continuous white noise of 0.010 Pa at 1 m (54 dB *re* 20 μPa). Speed of sound, $c=343$ m s^{-1}, and density of air, $\rho=1.21$ kg m^{-3}. The "energy density calculation" submodel is shown in Fig. 3.

Equation (30) and inequalities (31) and (32) yield

$$[((kh)^2+1)X+((kh)^2-1)\gamma_{12}(\omega)\cos\phi_{12}(\omega)]^2 \geqslant 4(X^2-\gamma_{12}^2(\omega))(kh)^2. \tag{33}$$

Therefore,

$$\frac{1-\gamma_{12}^2(\omega)}{2(X^2-\gamma_{12}^2(\omega))} \geqslant \frac{2(kh)^2(1-\gamma_{12}^2(\omega))}{[((kh)^2+1)X+((kh)^2-1)\gamma_{12}(\omega)\cos\phi_{12}(\omega)]^2}, \tag{34}$$

so that the normalized random error is bounded below by

$$\epsilon(\hat{\overline{E_D(\omega)}}) \geqslant \frac{1}{\sqrt{n_d}}\left[1-\frac{1-\gamma_{12}^2(\omega)}{2(X^2-\gamma_{12}^2(\omega))}\right]^{1/2}. \tag{35}$$

Equality occurs in inequality (31) when $(X+\gamma_{12}(\omega)\cos\phi_{12}(\omega))(kh)^2=(X-\gamma_{12}(\omega)\cos\phi_{12}(\omega))$, and equality occurs in inequality (32) when $\cos^2\phi_{12}(\omega)=1$. Therefore, equality occurs in inequality (35) either when $\phi_{12}(\omega)=0$ and $(X+\gamma_{12}(\omega))(kh)^2=(X-\gamma_{12}(\omega))$, or when $\phi_{12}(\omega)=\pi$ and $(X-\gamma_{12}(\omega))(kh)^2=(X+\gamma_{12}(\omega))$.

Inequalities (29) and (35) together yield

$$\frac{1}{\sqrt{n_d}}\left[\frac{2X^2-1-\gamma_{12}^2(\omega)}{2X^2-2\gamma_{12}^2(\omega)}\right]^{1/2} \leqslant \epsilon(\hat{\overline{E_D(\omega)}}) \leqslant \frac{1}{\sqrt{n_d}}. \tag{36}$$

When $G_{11}(\omega)=G_{22}(\omega)$, $X=1$ so that the lower bound in Eq. (36) becomes $1/\sqrt{2n_d}$. The definition of X (26) shows that $X\geqslant 1$ always, since the arithmetic mean of $\sqrt{G_{11}(\omega)/G_{22}(\omega)}$ and $\sqrt{G_{22}(\omega)/G_{11}(\omega)}$ is greater than or equal to their geometric mean. Therefore,

$$\frac{2X^2-1-\gamma_{12}^2(\omega)}{2X^2-2\gamma_{12}^2(\omega)} = 1-\frac{1-\gamma_{12}^2(\omega)}{2(X^2-\gamma_{12}^2(\omega))} \geqslant 1-\frac{1-\gamma_{12}^2(\omega)}{2(1-\gamma_{12}^2(\omega))} = \frac{1}{2}. \tag{37}$$

This shows that the lower bound for the normalized random error is minimum at $1/\sqrt{2n_d}$ when $G_{11}(\omega)=G_{22}(\omega)$. Indeed,

$$\frac{1}{\sqrt{2n_d}} \leqslant \epsilon(\hat{\overline{E_D(\omega)}}) \leqslant \frac{1}{\sqrt{n_d}}. \tag{38}$$

V. DISCUSSION

The expression (36) shows that the normalized random error of time-averaged acoustic energy density spectral density estimates is always bounded within a narrow tolerance. As the upper bound in Eq. (29) is dependent only on $\sqrt{n_d}$, the number of records averaged, it can be ensured that the normalized random error is no greater than a specified tolerance by an appropriate choice of n_d, without the need to know any other information about the measurement. Thus it is not in fact necessary to first estimate the coherence or phase angle.

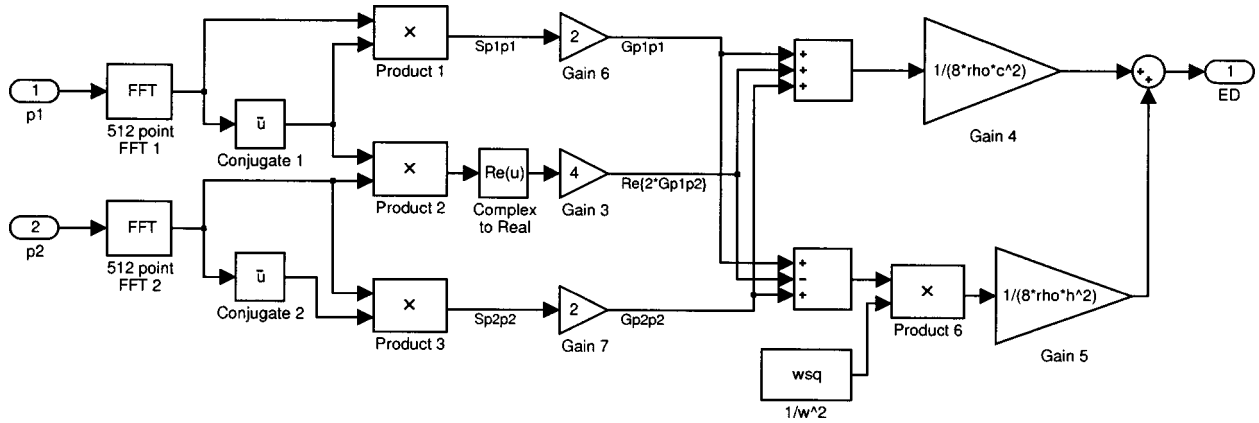

FIG. 3. Model for the calculation of the time-averaged acoustic energy density estimate using the frequency domain expression in terms of the auto- and cross-spectral densities of the two pressure readings.

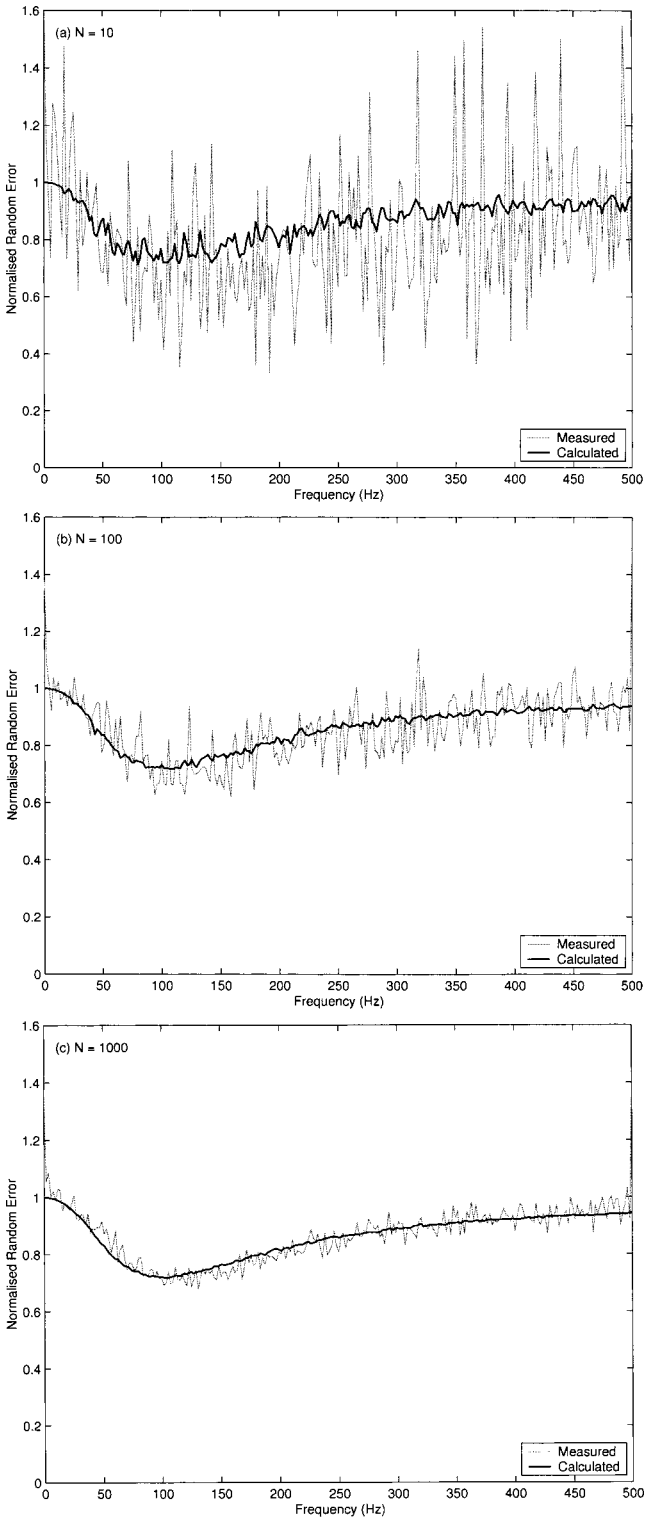

FIG. 4. Estimates of the normalized random error of the acoustic energy density spectral density estimates, obtained from the standard deviation of measurements, compared with the calculated normalized random error as predicted by the derived theoretical expression. Results are shown for (a) 10, (b) 100, and (c) 1000 acoustic energy density spectral density estimates.

The lower bound in Eq. (38) shows that the averaging time resulting from this approach will exceed the minimum necessary averaging time at most by a factor of $\sqrt{2}$.

VI. CONCLUSIONS

An expression for the normalized random error of the time-averaged acoustic energy density spectral density estimates has been derived. A simulation in Simulink was used to validate the expression numerically. The estimates of the normalized random error resulting from the simulated measurements agree with the error predicted by the expression.

Because the normalized random error is only heavily dependent on n_d, an experiment can be designed to achieve a desired normalized random error without measuring the local properties of the sound field first.

[1] R. K. Cook and P. A. Schade, "New method for the measurement of the total energy density of sound waves," in Proceedings of Inter-Noise 74, 1974, pp. 101–106.
[2] P. J. Nashif and S. D. Sommerfeldt, "An active control strategy for minimising the energy density in enclosures," in Proceedings of Inter Noise 92, 1992, pp. 357–361.
[3] W. Shen and J. Q. Sun, "A study of shell interior noise control," Proc. SPIE **3041**, 812–818 (1997).
[4] Y. C. Park and S. D. Sommerfeldt, "Global attenuation of broadband noise fields using energy density control," J. Acoust. Soc. Am. **101**, 350–359 (1997).
[5] S. D. Sommerfeldt and P. J. Nashif, "A comparision of control strategies for minimising the sound field in enclosures," in Proceedings of Noise-Con 91, 1991, pp. 299–306.
[6] S. D. Sommerfeldt and J. Parkins, "Active control of energy density in three dimensional enclosures," J. Acoust. Soc. Am. **95**, 2989 (1994).
[7] B. S. Cazzolato and C. H. Hansen, "Errors arising from three-dimensional energy density sensing in one-dimensional sound fields," J. Sound Vib. **236**, 375–400 (2000).
[8] J. W. Parkins, S. D. Sommerfeldt, and J. Tichy, "Error analysis of a practical energy density sensor," J. Acoust. Soc. Am. **108**, 211–222 (2000).
[9] B. S. Cazzolato and C. H. Hansen, "Errors in the measurement of acoustic energy density in one-dimensional sound fields," J. Sound Vib. **236**, 800–831 (2000).
[10] G. W. Elko, "Frequency domain estimation of the complex acoustic intensity and acoustic energy density," PhD thesis, The Pennsylvania State University, 1984.
[11] J. Ghan, B. S. Cazzolato, and S. D. Snyder, "Expression for the estimation of time-averaged acoustic energy density using the two-microphone method," J. Acoust. Soc. Am. **113**, 2404–2407 (2003).
[12] A. F. Seybert, "Statistical errors in acoustic intensity measurements," J. Sound Vib. **75**, 519–526 (1981).
[13] F. Fahy, *Sound Intensity*, 2nd ed. (E&FN Spon, London, 1995).
[14] J. S. Bendat and A. G. Piersol, *Random Data—Analysis and Measurement Procedures*, 2nd ed. (Wiley, New York, 1986).

Classification of distant targets situated near channel bottoms

Hongwei Liu, Paul Runkle, and Lawrence Carin[a)]
Department of Electrical and Computer Engineering, Duke University, Durham, North Carolina 27708-0291

Timothy Yoder
SFA Inc., Largo, Maryland 20774

Thomas Giddings
Metron, Inc., Reston, Virginia 20190

Luise Couchman and Joseph Bucaro
Naval Research Laboratory, Physical Acoustics, Code 7130, Washington, DC 20375-5000

(Received 20 May 2002; revised 7 November 2003; accepted 19 November 2003)

Identification algorithms are considered for a class of targets situated near the bottom of a water channel. It is assumed that the target-sensor distance relative to the channel depth is such that a ray-based representation of the scattered fields is appropriate (*vis-à-vis* a modal representation). Two approaches are considered for processing the scattered fields. In one algorithm a deconvolution is performed to remove the channel response, and thereby recover the free-field target scattered signature. In this case the classifier is trained based on free-field data. In the second approach the array receiver is employed to point the sensor in particular directions, and the beam-formed signal is used directly in the subsequent classifier. In this case the classifier must be trained based on in-channel data. Multiple scattered signals are measured, from a sequence of target-sensor orientations, with the waveforms classified via a hidden Markov model. Example results are presented for scattering data simulated via the finite-element method and coupled to a normal-mode waveguide modal, for elastic targets situated in a water channel. © *2004 Acoustical Society of America.* [DOI: 10.1121/1.1643363]

PACS numbers: 43.60.Lq, 43.60.Pt, 43.60.Bf [JCB] Pages: 1185–1197

I. INTRODUCTION

The use of scattered fields to infer the identification of a distant or concealed target constitutes a problem of long-standing interest. It is well known that scattered fields are a strong function of the target sensor-orientation[1] motivating research on classification algorithms based on fusing the information in multiple scattered signatures.[2–6] Although these methods have realized good results, they have generally been applied to the free-field case. In this paper, elastic targets are situated in a water channel. For this situation the target scattered signature is often significantly distorted by multipath propagation, with such dependent on the sensing parameters, such as target and receiver location, water depth, seabed geoacoustic parameters, etc. A ray-based representation is applied to characterize channel effects. The ray model is appropriate for a subset of channel depths and target-sensor distances. In particular, when the target-sensor distance is large relative to the channel depth, a modal representation is required.

The target-in-channel problem may be addressed in two ways. One may attempt to deconvolve the channel effects from the target-scattered signal, to recover an approximation of the scattered signal in the absence of the channel. The subsequent classifier may be based on monostatic free-field scattering data. In this sense one may directly apply existing free-field classifiers.[2–5] The channel effects are typically represented by using a Green's function, and the received acoustical pressure may be modeled as the convolution of the target scattered signatures with the Green's function. One direct method to recover the target's scattered signatures is referred to as deterministic deconvolution.[7,8] This method is sensitive to the Green's-function mismatch. A more generalized method was developed recently by using the minimum entropy deconvolution (MED) method[9] to estimate the channel response function, which requires that the channel's Green's function be sufficiently ''sparse.'' For the case of a shallow water channel, and for long observation distances (the concern of this paper), the channel's Green's function is not sparse enough for MED. Angle[10] used an array of sources to approximately generate a low-order mode, and an array of receivers is used to isolate from the received echo a low-order mode, and thus extract the approximately free-field target response in shallow water. In general, this procedure requires a large number of sources, especially for wide-band implementation, for which many modes will be excited. Chevret[11] developed a new in-channel sonar target classification approach based on a time-frequency filter, using the target's free-field response as a reference signal. If the target response is highly dependent on the target-receiver orientation, the computational complexity of this algorithm increases significantly, and the classification performance decreases as well. In this paper, a new procedure is developed to approximately recover the free-field scattered signal from the near-grazing (to the bottom) rays. No *a priori* knowledge is assumed with regard to the channel properties, other than

[a)]Electronic mail: lcarin@ee.duke.edu

that near-grazing rays are considered, with this generally appropriate for targets on or near the sea bottom.

The deconvolution procedure is demonstrated to work well when the noise/clutter level is relatively low (less than 1% error). However, as the signal-to-noise (or clutter) ratio diminishes, the performance of such deconvolution techniques deteriorates. In this case better classification performance is achieved if training is performed on the in-channel scattered waveform directly (i.e., no channel deconvolution is attempted). The advantage of this procedure is that it is more robust to noise/clutter, although it requires training on data for the target in a channel. This procedure is limited by possible mismatches between the true channel and that used to train the classifier. Moreover, the in-channel scattered signal is a strong function of the target-sensor distance. This implies that one may require multiple classifiers, applicable for multiple target-sensor distances. Both of these processing strategies are considered and compared, for realistic targets and false targets in a channel. Moreover, the Cramer–Rao bound[12] is employed to place performance bounds on the feasibility of channel deconvolution, as a function of target and sensor parameters. Such studies are particularly important for addressing the viability of channel deconvolution in various settings.

The multiaspect scattered waveforms, with or without the channel deconvolved, are processed via a hidden Markov model (HMM).[13] The HMM classifier has received significant attention for targets in free field,[2–6] and therefore minimal additional details are presented here. Two feature-extraction tools are addressed, as well as the concept of designing what is termed a class-based classifier. Concerning the latter, rather than designing individual HMM's for each target of interest, a single HMM is designed for multiple targets that constitute a target class.[5] While training, one may not have available data for all targets that may be observed during testing. However, in the training phase, by linking several targets together, to constitute a target class, ideally the classifier should be able to identify a target within the same class, even if that particular target was not seen during training. The various issues discussed above are addressed by considering scattering data for a target placed in a channel. The wideband, free-field bistatic scattered fields from several targets are obtained from finite-element method (FEM) (Ref. 14) simulations. These scattered fields are then coupled with a separate model applied to simulate the channel,[15] with such yielding the overall target-in-channel signatures.

Before proceeding, it is worthwhile to indicate the aspects of the paper that are new. To our knowledge, this is one of the first papers to address the *classification* of a target in a simulated water channel based on backscattered waveforms; this involves distinguishing targets of interest—for example, sea mines—from false targets, e.g., rocks. Most previous classification research has focused principally on the free-field problem.[2–6,16–19] There has also been significant research performed on processing sonar imagery for targets in a channel, although no attempt has been made to deconvolve the channel.[20,21] There has also been much published work on the analysis of targets in a water channel using, for example, matched-field processing.[14] However, that work has been directed principally toward source localization (or detection), and has not addressed the classification problem. Therefore the principal new aspect of this paper is that we have demonstrated how the HMM classifier (used previously for free-field target classification) can be extended to the case of a target in a water channel (waveguide). This has been done two ways: (i) by trying to extract the ray paths (multipath) and (ii) by processing the multipath directly (via beam steering). We have also computed Cramer–Rao bounds for the accuracy with which one can perform (i), in noisy data.

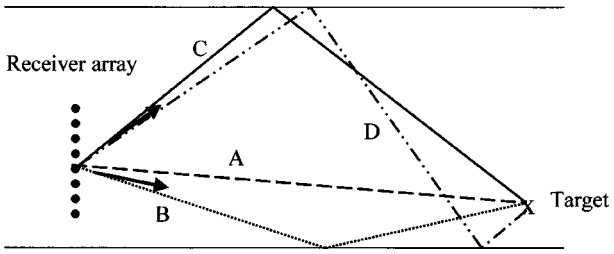

FIG. 1. Illustration of channel propagation, using a ray model. The bold arrows emanating from the array indicate the two pointing directions, when beam forming is performed.

The remainder of the text is organized as follows. The deconvolution technique is discussed in Sec. II, as applied for the near-grazing target signature. In Sec. III array beamforming is discussed briefly, and employed to process the in-channel target signature, without attempting to perform channel deconvolution. In Sec. IV the time- and frequency-domain feature parsing techniques are discussed. The HMM classifier is summarized briefly in Sec. V, wherein issues of concern to a class-based classifier are addressed. Example processing results are presented in Sec. VI, where Cramer–Rao performance bounds are discussed, with regard to the potential of channel deconvolution. The work is summarized in Sec. VII.

II. NEAR-GRAZING SCATTERING MODEL AND SIGNAL DECONVOLUTION

A. Signal model

Wide-band propagation is considered in a water channel, as illustrated in Fig. 1. It is assumed that the target-sensor distance and channel depth are such that only a relatively small number of ray paths are important (Fig. 1). When the target-sensor distance is large relative to the channel depth, a modal interpretation is required, *vis-à-vis* the rays depicted in Fig. 1. A wide-band pulse is transmitted into the channel from a point source situated at the center of a vertical receiver array. The received signal consists of a convolution with the transfer function of the channel and of the target. The bandwidth of the time-domain excitation is assumed to be large enough (relative to the channel parameters, such as water depth and target-receiver distance) such that many of the ray paths indicated in Fig. 1 may be separated via temporal windowing (discussed further below). The focus is on rays that propagate near the bottom (the target is at or near the bottom). This near-grazing component is composed of multiple terms, and these are typically not separated easily

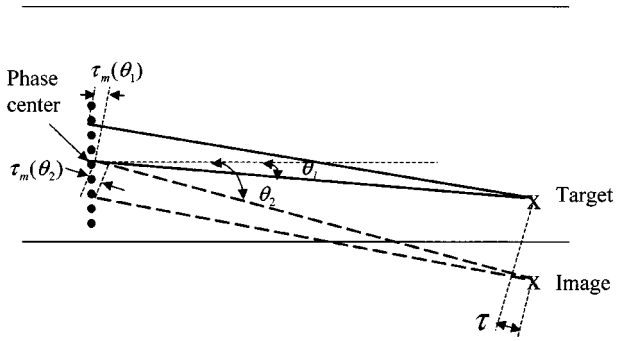

FIG. 2. Time-delay illustration for the near-grazing paths.

by simple temporal windowing. Four near-grazing propagation paths are considered (see Fig. 1): A-A, A-B, B-A, and B-B. Additional paths are considered in subsequent discussions. Generally the sound-speed profile is a function of water depth for ocean-channel propagation. However, since the near-grazing paths propagate mainly near the sea bottom, it is assumed that the sound speed is constant for this case. Under these assumptions, the time-dependent scattered waveform received at array element m is expressed as (ordered A-A, B-A, A-B, and B-B, respectively)

$$x_m(t)=s(t-\tau_m(\theta_1))+\gamma s(t-\tau_m(\theta_1)-\tau)+\gamma s \times(t-\tau_m(\theta_2)-\tau)+\gamma^2 s(t-\tau_m(\theta_2)-2\tau)+n_m(t), \tag{1}$$

where $s(t)$ is the free-field target-scattered signal (for this near-grazing incidence angle). The center of the receiver array is chosen as the time reference (phase center), and $\tau_m(\theta_i)$ is the propagation delay associated with the mth array element and incident angel θ_i to the array [$\tau_m(\theta_i)=0$ for the center array element]. The angle θ_1 corresponds to propagation from the target center directly back to the array (path A in Fig. 1), while θ_2 corresponds to signal arrival at the array after reflecting off the bottom (path B in Fig. 1). As indicated in Fig. 2, τ is the temporal difference between paths B and A, and γ is a complex factor representing attenuation from reflection at the bottom (γ is assumed constant over the frequency range of interest). Note that it is assumed that the target scattered signal $s(t)$ is the same (except for attenuation and time delay) for each ray in Eq. (1), this dictated by the assumption of near-grazing incidence (i.e., the target-sensor distance is large relative to the target/sensor height above the bottom, such that the angle from the target is approximately the same for paths A and B). The signal $n_m(t)$ represents additive noise/clutter observed on array element m.

After applying a Fourier transform to the observed signal, the frequency-domain version of Eq. (1) is

$$X(f_i)=A_{\theta_1}(f_i)S(f_i)+\gamma\cdot A_{\theta_1}(f_i)S(f_i)e^{-j2\pi f_i\tau}+\gamma\cdot A_{\theta_2}(f_i)S(f_i)e^{-j2\pi f_i\tau}+\gamma^2 A_{\theta_2}(f_i)S(f_i)e^{-j2\pi f_i 2\tau}+N(f_i), \tag{2}$$

where $X(f_i)=[X_1(f_i),X_2(f_i),\ldots X_M(f_i)]^T$, $N(f_i)=[N_1(f_i),N_2(f_i),\ldots N_M(f_i)]^T$, and $A_{\theta_j}(f_i)=[e^{-j2\pi f_i\tau_1(\theta_j)},e^{-j2\pi f_i\tau_2(\theta_j)},\ldots,e^{-j2\pi f_i\tau_M(\theta_j)}]^T$. Here $X_m(f_i),N_m(f_i),S(f_i)$ are the Fourier coefficients of $x_m(t)$, $n_m(t)$ and $s(t)$, respectively, at frequency f_i, where $i=1,2,\ldots,I$. Let $\overline{S_1}(f_i)=S(f_i)+\gamma S(f_i)e^{-j2\pi f_i\tau}$, $\overline{S_2}(f_i)=\gamma\overline{S_1}(f_i)e^{-j2\pi f_i\tau}$, and Eq. (2) may be rewritten as

$$X(f_i)=\overline{A}_\theta(f_i)\overline{S}(f_i)+N(f_i), \tag{3}$$

where $\overline{A}_\theta(f_i)=[A_{\theta_1}(f_i),A_{\theta_2}(f_i)]$ and $\overline{S}(f_i)=[\overline{S_1}(f_i),\overline{S_2}(f_i)]^T$.

The objective is to extract the signal $s(t)$ from this near-grazing scattered waveform, and to subsequently perform classification based on $s(t)$. In this process the effects of the channel are removed, and therefore the classifier is designed based on the free-field scattered waveforms $s(t)$. Since the target response $s(t)$ is a strong function of the target position relative to the sensor, with this unknown, no *a priori* knowledge of $s(t)$ is assumed; this is particularly relevant for false targets, e.g., a rock, for which $s(t)$ is entirely unknown. The reflection coefficient γ is also assumed unknown. Note from Fig. 2 that $\tau_m(\theta_i)$ and τ may be recovered with knowledge of θ_1 and θ_2, assuming that the target-sensor distance is known. Summarizing, the unknown parameters to be recovered are $s(t)$, γ, θ_1, and θ_2. Note that *a priori* knowledge of the relative target-sensor position approximately yields the angles θ_1 and θ_2, and knowledge of the bottom properties may be used to approximate (or constrain) γ; these values may be used as the initial values in the deconvolution algorithm.

B. Target-response recovery

If the random process $n(t)$ is assumed to be white Gaussian noise, then maximum-likelihood (ML) parameter estimation reduces to

$$\langle\hat{\theta}_1,\hat{\theta}_2,\overline{S}\rangle=\arg\min_{\theta_1,\theta_2,\overline{S}}\sum_{i=1}^{I}\|X(f_i)-\overline{A}_\theta(f_i)\overline{S}(f_i)\|^2, \tag{4}$$

where $\|\cdot\|$ is the Euclidean norm. This is a multidimensional nonlinear search problem, the computational complexity of which is typically intractable. The problem is first simplified by performing estimation one frequency at a time,

$$\langle\hat{\theta}_1,\hat{\theta}_2,\overline{S}(f_i)\rangle=\arg\min_{\theta_1,\theta_2,\overline{S}(f_i)}\|X(f_i)-\overline{A}_\theta(f_i)\overline{S}(f_i)\|^2. \tag{5}$$

Since the angles θ_1 and θ_2 are frequency independent, they may be taken as the average across all frequencies in the sensor bandwidth. With regard to the assumption of white Gaussian noise, it is important to emphasize that this assumption is largely driven by the goal of yielding a mathematically tractable solution. This noise assumption is likely to be vitiated by ''real-world'' natural and man-made clutter sources.

An iterative solution has been developed, in which the solution for $\{\theta_1,\overline{S_1}(f_i)\}$ and $\{\theta_2,\overline{S_2}(f_i)\}$ are considered sequentially. In particular, $\{\theta_1,\overline{S_1}(f_i)\}$ is initialized and

$$X'(f_i)=X(f_i)-A_{\theta_1}(f_i)\overline{S_1}(f_i). \tag{6}$$

Then, Eq. (5) becomes

$$\langle \hat{\theta}_2, \overline{S_2}(f_i) \rangle = \arg \min_{\theta_1, \overline{S_2}(f_i)} \|X'(f_i) - A_{\theta_2}(f_i)\overline{S_2}(f_i)\|^2. \quad (7)$$

The estimates of $\{\theta_2, \overline{S_2}(f_i)\}$ may be obtained as

$$\hat{\theta}_2 = \arg \max_{\theta} \|A_\theta(f_i)^H X'(f_i)\|^2, \quad (8)$$

$$\overline{S_2}(f_i) = \left. \frac{A_\theta(f_i)^H X'(f_i)}{A_\theta(f_i)^H A_\theta(f_i)} \right|_{\theta = \hat{\theta}_2}. \quad (9)$$

Using the estimated $\{\theta_2, \overline{S_2}(f_i)\}$ as known parameters, $X'(f_i)$ is now defined in Eq. (6) in terms of $\{\theta_2, \overline{S_2}(f_i)\}$ [rather than $\{\theta_1, \overline{S_1}(f_i)\}$], and the parameters $\{\theta_1, \overline{S_1}(f_i)\}$ are estimated by using Eqs. (8) and (9). This process is iterated until convergence is achieved for $\{\theta_1, \overline{S_1}(f_i)\}$ and $\{\theta_2, \overline{S_2}(f_i)\}$.

With regard to initializing the direction-of-arrival (DOA) parameters $\hat{\theta}_i$, for a uniform array the peaks in the Fourier transform of the received array amplitudes (at a given frequency) correspond to directions of arrival. High-resolution spectral algorithms may be applied. Note also that the above algorithm estimates the DOA parameters one frequency at a time. Generally, the target signature does not have a flat spectrum, and therefore the signal-to-noise ratio (SNR) is typically frequency dependent. A Fourier transform is applied first to the received signal, and frequency bins are selected with high energy and high frequency (the latter important for resolution), with the DOA estimation performed in high-SNR frequency bins. The average of these estimated DOA parameters may be used as the final estimate, and therefore $\overline{S_1}(f_i)$ and $\overline{S_2}(f_i)$ need only be estimated at the remaining (high noise) frequencies f_i.

Having estimated $\overline{S_1}(f_i)$ and $\overline{S_2}(f_i)$, the channel parameters τ and γ are estimated by solving

$$\langle \hat{\tau}, \hat{\gamma} \rangle = \arg \min_{\tau, \gamma} \sum_{i=1}^{I} \|\overline{S_2}(f_i) - \gamma \overline{S_1}(f_i) e^{-j2\pi f_i \tau}\|. \quad (10)$$

The solutions of the above equation are

$$\hat{\tau} = \arg \max_{\tau} \|a(\tau)^H (\overline{S_1^*} \cdot \overline{S_2})\|, \quad (11)$$

$$\hat{\gamma} = \frac{a(\hat{\tau})^H (\overline{S_1^*} \cdot \overline{S_2})}{\overline{S_1}^H \overline{S_1}}, \quad (12)$$

where H is conjugate transpose operator, $*$ is conjugate operator, and $\cdot$ denotes the Hadamard product. In Eqs. (11) and (12) $\overline{S_1} = [\overline{S_1}(f_1), \overline{S_1}(f_2), \ldots \overline{S_1}(f_I)]^T$, $\overline{S_2} = [\overline{S_2}(f_1), \overline{S_2}(f_2), \ldots \overline{S_2}(f_I)]^T$, and $a(\tau) = [e^{-j2\pi f_1 \tau}, e^{-j2\pi f_2 \tau}, \ldots, e^{-j2\pi f_N \tau}]^T$.

The estimated target signature is now recovered as

$$\hat{S}(f_i) = \frac{\overline{S_1}(f_i)}{1 + \hat{\gamma} \cdot \exp(-j2\pi f_i \hat{\tau})} \quad (13)$$

or

$$\hat{S}(f_i) = \frac{\overline{S_2}(f_i)}{(1 + \hat{\gamma} \cdot \exp(-j2\pi f_i \hat{\tau}))^2}. \quad (14)$$

The alternative representations in Eqs. (13) and (14) may be averaged.

III. SIGNAL EXTRACTION VIA BEAM FORMING

The technique developed in Sec. II works well for low-clutter data (quantified in Sec. IV), but its performance deteriorates as the signal-to-clutter ratio decreases. For this case an alternative approach is considered, in which the classifier is trained based on in-channel data (*vis-à-vis* free-field data). This scenario is discussed below.

Classical beam forming[22] is employed to "point" the array in particular directions. As indicated in Fig. 1, two such directions are considered: (i) toward the rays reflected at the air-water interface, and (ii) toward rays arriving from the near-grazing direction (these array-pointing directions considered separately). Considering (i) first, note that fields scattered off the air-water interface have several components. For example, referring to Fig. 1, there is a monostatic component coming from the C-C ray path, as well as bistatic components produced by such rays as A-C, A-D, and C-D (and several others of this type). Many of these components may be separated via temporal windowing, although finite bandwidth makes signal overlap unavoidable for some of the rays. Simple deconvolution techniques, like those considered in Sec. II, are far more complicated for such overlaped waveforms, since both monostatic and bistatic signals are considered [it may not be assumed that $s(t)$ is the same for all rays, as was applicable in Eq. (1), for the near-grazing components]. This issue is compounded by the fact that the relevant monostatic and bistatic rays are a strong function of the channel parameters and of the target-sensor distance. For example, in Fig. 1 the angles of rays C and D with respect to the target are a function of the target-sensor distance. Consequently, the classifier is retrained as such parameters are varied—this underscores the motivation of Sec. II, in which the channel parameters are deconvolved.

For the array-focused scattering data, temporal windowing is employed where appropriate to remove nonoverlapping rays (e.g., for focusing in the near-grazing direction, ray paths A-A, A-B, B-A, and B-B are typically well separated from such paths as C-A and D-A). Where such overlapping may not be removed via simple temporal windowing, the classification algorithm is based on the total (overlapped) scattered waveform. The training is based on in-channel data, and therefore a channel model is important. However, when performing algorithm testing, additive clutter will also be considered, and therefore the testing and training data are distinct. Further details of the beam-formed data are discussed in Sec. VI, when presenting results.

IV. FEATURE EXTRACTION

The classification algorithm discussed in Sec. V is based on processing a sequence of time-domain waveforms, as the sensor moves relative to the target. For the near-grazing term discussed in Sec. II, these time-domain waveforms corre-

spond to $s(t)$. Concerning the beam-formed data summarized in Sec. III, a beam-formed time-domain waveform is obtained with which classification is performed (two beam-formed waveforms are obtained, from two array ''look'' directions, these offering the potential for fusion).

Rather than performing classification based on the time-domain scattering data directly, features are first extracted. The particular feature-extraction technique employed plays an important role in subsequent target-classification performance. The objective in feature extraction is to obtain a set of parameters that represent the scattering data compactly, while being robust to possible mismatches between training and testing data. For example, for the near-grazing waveform $s(t)$ deconvolved as in Sec. II, the presence of clutter yields errors in the extracted $s(t)$. The corresponding features should ideally be robust to such variations. Two feature-extraction algorithms are examined below.

A. Matching pursuits

Matching pursuits (MP) is a well-known feature-extraction technique,[2,3,23] in which a dictionary of canonical features is pre-defined. The MP dictionary is matched to transient wave scattering, composed of general wavefronts and resonances.[15] Wavefronts are scattered from local target scattering centers, and have localized temporal support, while resonances capture global properties and are typically characterized by less localized temporal support. For an MP dictionary parametrized by $\gamma_n=\{\alpha_n,\omega_n,\tau_n,\phi_n\}$, the dictionary elements are

$$e_{\gamma_n}(t)=K_{\gamma_n}\cos[\omega_n(t-\tau_n)+\phi_n]e^{-\alpha_n(t-\tau_n)}U(t-\tau_n), \tag{15}$$

where $U(t)$ is the Heaviside step function [$U(t)=0$ *for* $t<0$ and $U(t)=1$ *for* $t>0$], and K_{γ_n} is a normalization constant. This dictionary is capable of modeling both wavefronts (small temporal support, characterized by large damping, α_n) and resonances (large temporal support, characterized by small damping, α_n). The temporal position τ_n between consecutively extracted dictionary elements yields the time delays between target scattering centers. In this paper, three MP iterations are sufficient to extract all necessary information from the target response (based on the results discussed in a previous paper).[23] The set of MP features calculated as mentioned are therefore $\{\omega_1,\alpha_1,\omega_2,\alpha_2,\tau_2-\tau_1,\omega_3,\alpha_3,\tau_3-\tau_1\}$. Note the use of the *relative* time delay between consecutive wavefronts, rather than the absolute time of arrival. The former is a characteristic of target geometry, while the latter has a strong correlation with target-sensor distance. Hence the absolute time of arrival is not considered as a potential feature for target classification.

B. Subband-energy principal component coefficients

As implemented in the above section, the MP features are based on time-domain scattering characteristics. Alternatively features may be extracted based on the frequency-domain characteristics of the scattered fields. A feature vector is therefore developed that exploits the spectral character of the time-domain scattered waveform, in several frequency subbands. In particular, a fast Fourier transform (FFT) is applied to the time-domain signals discussed in Secs. II and III, and data are divided into N uniform subbands. The power is calculated in each subband, yielding the N-dimensional vector $\mathbf{P}=\{P_1,P_2,\ldots,P_N\}^T$, where $P_n=1/K\Sigma_{k=1}^{K}\|X(f_{(n-1)K+k})\|^2$ is the power in subband n, composed of K frequencies ($K=I/N$, where I represents the total number of discrete frequencies). Recall that the scattered waveform is in general a strong function of the target-sensor orientation (pose), and therefore the feature vector is as well. Using available training data, all (normalized) feature vectors $\mathbf{P}_m$ are considered from targets of interest, and compute an $N\times N$ correlation matrix $\mathbf{R}=(1/M)\Sigma_{m=1}^{M}\mathbf{P}_m\mathbf{P}_m^T$ (assume M such normalized feature vectors are available for training). The eigenvectors of this matrix span the space defined by the vectors $\mathbf{P}_m$, and those eigenvectors with relatively large associated eigenvalues are retained. These ''principal'' eigenvectors are represented by $\mathbf{q}_1,\mathbf{q}_2,\ldots,\mathbf{q}_L$, where $L<N$ (ideally $L\ll N$). As applied in a traditional principal components analysis (PCA),[24] a given N-dimensional feature vector $\mathbf{P}_m$ is mapped to a corresponding L-dimensional vector $\mathbf{P}'_m$, with the lth component of $\mathbf{P}'_m$ representative of the inner product of $\mathbf{P}_m$ and $\mathbf{q}_l$.

V. CLASS-BASED MULTIASPECT CLASSIFICATION

For a fixed target-sensor orientation, assume a scattered waveform $g(t)$, determined via channel deconvolution (Sec. II) or via beam forming (Sec. III). Further, assume that the signal $g(t)$ is expressed as

$$g(t)=\begin{cases} h_1(t)+c(t), & g\in H_1 \\ h_2(t)+c(t), & g\in H_2 \end{cases}, \tag{16}$$

where hypothesis H_1 corresponds to targets of interest being present, while hypothesis H_2 corresponds to the presence of a false target. In both cases $c(t)$ represents additive clutter (typically *not* white). It is important to emphasize that classification is being performed, and hypothesis H_1 and H_2 both correspond to the presence of a scatterer [represented by $h_1(t)$ and $h_2(t)$, respectively]. The distinction is that $h_1(t)$ correspond to targets of interest. By contrast, $h_2(t)$ correspond to scattering from the infinite class of ''false targets,'' that may confuse a classifier, e.g., $h_2(t)$ could correspond to a rock. It is assumed that *a priori* knowledge is available with regard to $h_1(t)$; no knowledge is assumed for the false targets represented by $h_2(t)$, since in the ''real'' problem there are an infinite number of false targets.

It is often difficult to discriminate between targets based on a measurement from a single target-sensor orientation, which motivates multi-aspect sensing.[2–6] In particular, assuming a fixed target-sensor distance, the multiple scattered waveforms are measured by changing the relative angle (orientation) between the target and sensor. Although the multiple scattered waveforms have enhanced information, *vis-à-vis* a single measurement, the processing of this sequence of scattered signatures is complicated by the fact that the waveforms scattered from a given target are often highly nonstationary, as a function of target-sensor orientation.[1] However, one may typically divide the target-sensor orientations into a

set of states, each state a generally contiguous set of target-sensor orientation over which the backscattered waveforms are approximately stationary. The sequence of sampled states may be modeled approximately as a Markov process, since the explicit target-sensor orientation is unknown. This statistical characterization reduces to a hidden Markov model (HMM).[13] Let an HMM be represented by $M_i=(S_i,\pi_i,A_i,B_i)$, trained by using the scattering data from target T_i, where $S_i=\{s_1,s_2,\ldots,s_{N_s}\}$ are the N_s states of the targets, π_i is an N_s-dimensional vector representing the probability that the initial observation is in each of the states, A_i is a $N_s\times N_s$ matrix representing the state-transition probability, and B_i is the observation probability matrix for state i (representing the likelihood of observing a given feature vector in state i). Assume that the feature vectors associated with the nth scattered waveform from a given target are denoted by $\mathbf{y}_n$. Assuming N multiaspect measurements, the classification of target class T_i is declared if

$$p(\mathbf{y}_1,\mathbf{y}_2,\ldots\mathbf{y}_N|T_i)\geqslant\alpha, \tag{17}$$

where α is a chosen threshold. In this paper, a continuous HMM (Refs. 2–6, 13) is used to evaluate $p(\mathbf{y}_1,\mathbf{y}_2,\ldots\mathbf{y}_N|T_i)$.

An HMM is not designed for *each* target of interest. Rather, a *single* HMM is designed for each *class* of targets.[5] A target class is composed of *multiple* targets having similar geometrical and elastic properties, such that their associated scattered fields are closely related. In practice there may be a large number of targets of interest, although each of these may be similar acoustically and elastically (e.g., the same general shape and size). To train an HMM for each target may yield an unnecessarily large number of specific classifiers. Moreover, while training one may only have access to a subset of the targets in a given class, although while testing new, previously unseen targets in the same class may be observed. A classifier designed to sense a given class, rather than specific targets, will ideally be able to recognize these new (but similar) targets. In the class-based classifier, all scattering data from all targets within the same class are used while training.[5] Other than being based on data from multiple similar targets, the class-based HMM is of the same form as in previous individual-target-dependent HMM's.[2–6]

The Fisher discriminant function[25] is often used to select those features that yield optimal separation between targets and false targets (nontargets). However, in this work no *a priori* knowledge is assumed for the false targets. Nevertheless, for the features discussed in Sec. IV, feature pruning has been found useful, for class-based classification. Assume there are J targets within a given class. Feature selection is performed using the cost function

$$D(i)=\sum_{j=1}^{J}\sum_{n=1}^{N_s}\frac{|\mu_{\text{noise}}(i,n,j)-\mu(i,n,j)|^2}{\sigma^2_{\text{noise}}(i,n,j)+\sigma^2(i,n,j)}, \tag{18}$$

where $\mu(i,n,j)$ is the mean value of feature i, target j, in HMM state n, for the noise-free case. The parameters $\mu_{\text{noise}}(i,n,j)$ are defined similarly for the case of additive noise. The symbol $\sigma(i,n,j)$ represents the variance of feature i, target j, state n for the noise-free case, with $\sigma_{\text{noise}}(i,n,j)$ similarly defined for the case of additive noise.

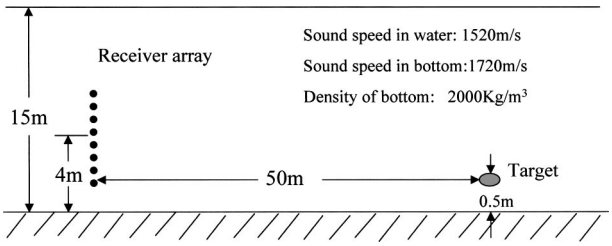

FIG. 3. Summary of the two-layers geoacoustic model used in most computations.

The features with relatively small D are selected. The cost function in Eq. (18) may select those features that are robust to additive noise/clutter. For a class-based processor, it is of particular importance to also select those features that make the multiple targets within a given target class appear most similar. To obtain this, the cost function in Eq. (18) is readily modified as

$$D(i)=\sum_{j=1}^{J}\sum_{k=1}^{J}\sum_{n=1}^{N_s}\frac{|\mu(i,n,j)-\mu(i,n,k)|^2}{\sigma^2(i,n,j)+\sigma^2(i,n,k)}. \tag{19}$$

VI. EXAMPLE RESULTS

A. Problem description

Five distinct scatterers are considered in the channel. Two of the targets are deemed "targets of interest," constituting hypothesis H_1 in Eq. (16), and the other three are deemed false targets (hypothesis H_2, with the associated targets not seen by the classifier during the training phase). The wideband bistatic scattered fields are computed for all targets via a free-field finite-element method (FEM) (Ref. 14) simulation. The incident fields on the target correspond to the fields of a point source situated at the center of the sensor array, and the scattered fields are computed by the FEM for observation in a plane, this plane situated within the channel, at a fixed distance from the target center. The fields within this plane are then coupled to a modal channel model,[15] with which they are propagated away from the target through the channel to the sensor. The large number of wave guide modes employed in these simulations underscores the appropriateness of the ray picture summarized in Fig. 1. The modal simulation is used because this channel code is well known and widely applied.[15] The water depth is 15 m, and the target-receiver distance (parallel to the bottom) is 50 m. A 28-element linear array receiver is employed perpendicular to the bottom. The array is 2 m long and its center is situated 3 m above the sea bottom. The center of each target is located 0.5 m above the sea bottom. A two-layer geoacoustic model is considered (see Fig. 3).

The two targets in H_1 are minelike targets (a steel and fiberclass cylinder) that are noted by $T1$ and $T2$. The three false targets are a 55-gallon drum, an oxygen tank, and a rock. The data covers the frequency band 50 Hz–10 KHz, and the scattered waveforms are considered in the time domain (after Fourier synthesis), as propagated through the channel to the array receiver. Each of the five targets is rotated about its axis over 360°, with 1° angular sampling. Therefore, for the classification algorithm, sensor rotation is

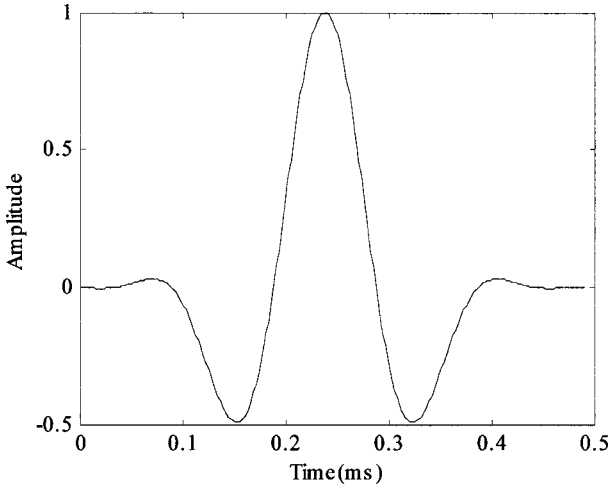

FIG. 4. Wave form used for the transmitted pulse.

considered about the target, with a minimum angular sampling rate of 1°. The shape of the pulse driving the point-source transmitter is shown in Fig. 4.

B. Channel deconvolution

For the channel considered in Fig. 3, the bottom reflection coefficient of the "near-grazing" path[14] is $\gamma = -0.7683 - j0.4139$. In Fig. 5 the channel impulse response is plotted as a function of frequency for the near-grazing paths, based on the model described in Eq. (2). Note that the channel has a frequency null centered at about 2 KHz. Therefore the deconvolution discussed in Sec. II is initially performed at relatively high frequencies (>5 KHz). At lower frequencies only the frequency-dependent $\overline{S_1}(f)$ and $\overline{S_2}(f)$ need be estimated, where we employ the angles of arrival θ_1 and θ_2 estimated as above at high frequencies.

For the geometry and targets considered, it has been found that the deconvolution procedure in Sec. II works essentially perfectly for the case of no additive noise or clutter. Results are therefore only presented here for the case of additive clutter. In particular, using the model in Eq. (1), for the parameters discussed above, a clutter signal $c(t)$ is added. The clutter $c(t)$ is computed[26] by convolving the incident

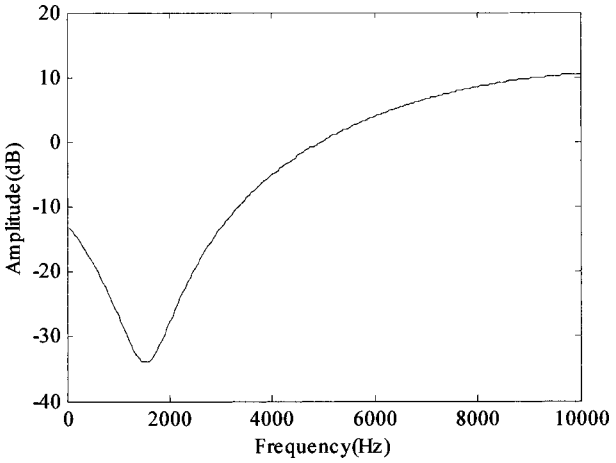

FIG. 5. Channel impulse response for the near-grazing paths, based on the model in Eq. (1).

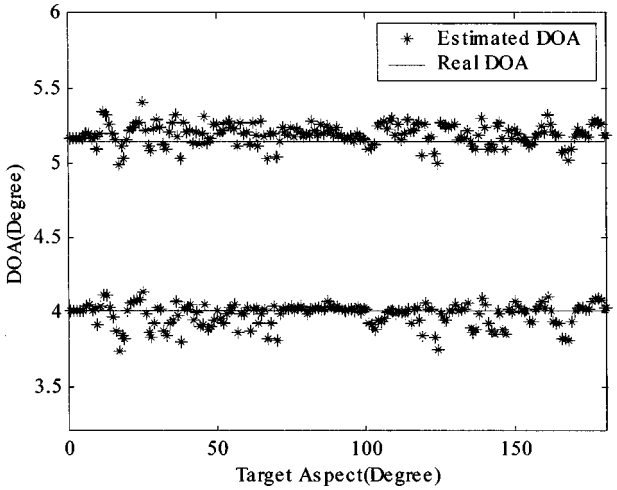

FIG. 6. Estimation results of two incident angles of the near-grazing paths, SNR=20 dB.

pulse shape (Fig. 4) with white Gaussian noise, and therefore $c(t)$ approximately represents the incident field scattered from a random environment (e.g., the sea bottom). The signal-to-clutter ratio is defined as the signal energy divided by the clutter energy, computed over the nominal support of the scattered waveform $s(t)$. A signal-to-clutter ratio of 20 dB is considered for each sensor element's received signal. For target $T1$, in Fig. 6 is plotted the estimated angles of arrival θ_1 and θ_2, as the target is rotated through 180° with respect to the sensor [each azimuthal angle corresponds to a distinct $s(t)$]. These results are shown for one clutter realization, for each target-sensor angle, and therefore the results in Fig. 6 represent random-variable instantiations. The optimal variance of such estimates is considered in the next section.

For example target orientations, in Fig. 7 is presented the original scattered waveform $s(t)$, the waveform as present after propagating through the channel with 20 dB clutter, and the deconvolved waveforms. The deconvolution is effective, although there is clearly clutter- and channel-induced distortion. Such distortion plays an important role in the subsequent HMM classifier. In particular, note that the MP feature extractor discussed in Sec. IV A matches the data to wavefront and resonance dictionary elements. The distortions demonstrated in Fig. 7, between the deconvolved data and the original free-field $s(t)$, undermine the effectiveness of an MP-based classifier. It is therefore anticipated that the simpler, spectral feature parser discussed in Sec. IV B will be more useful for such data.

C. Bounds on deconvolution performance

In Eq. (3) the signals received on the sensor array are expressed as $X(f_i) = \overline{A}_\theta(f_i)\overline{S}(f_i) + N(f_i)$, for a given frequency f_i. Recall that the 2×1-dimensional vector $\overline{S}(f_i)$ represents the frequency-domain signals received at the two near-grazing angles θ_1 and θ_2 discussed above, and the $M \times 2$ dimensional vector $\overline{A}_\theta(f_i)$ represents the associated received signals of these waveforms, on the M-element vertical sensor array. The $X(f_i)$ is expressed in a form readily com-

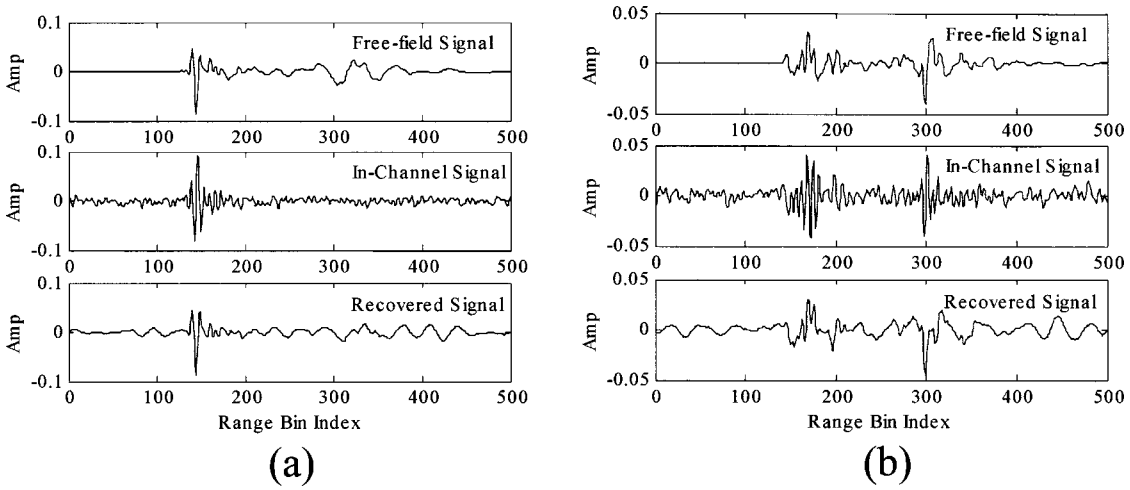

FIG. 7. Examples of signal recovery results for target T1 using the deconvolution algorithm. Top: target free-field response signal; middle: noisy "near-grazing" in-channel received signal; bottom: recovered signal. The SNR = 20 dB. (a) Target orientation 10°. (b) Target orientation 30°.

patible with digital signal processing, in particular, at a particular frequency f_i, the signal on array element m is expressed as

$$X_m = \sum_{n=1}^{2} A_n z_n^m + N_m, \tag{20}$$

where $z_n = \exp(-jk \sin \theta_n d)$, with k representing the wave number in the water and d the spacing between elements in the linear array. The complex amplitudes A_n represent the strengths of the two near-grazing rays, determined by the scattered values for a given target-receiver orientation. The objective is to employ the M-dimensional vector (for M array elements) composed of X_m to estimate the direction of arrivals θ_1 and θ_2, and the complex amplitudes A_n. The vector $\mathbf{X} = \{X_1, X_2, \ldots, X_M\}^T$ is a random process (due to the additive random N_m) and therefore the *estimated* parameters θ_n and A_n are random variables. Ideally the mean values of the estimated θ_n and A_n are correct (constituting an unbiased estimator). Of significant importance is the estimator variance, since the anticipated accuracy of any particular estimate is of interest.

The Cramer–Rao bound (CRB) (Ref. 12) provides a well-known metric on the accuracy of such a parameter-estimation problem. There are many previous papers that detail the computation of the CRB,[27,28] and therefore that is not the focus. Rather, the CRB is employed to quantify the optimal variance that one may achieve for an unbiased estimator, and ask the fundamental question of whether such a variance is sufficient for the particular deconvolution task in this paper. In particular, if the variance of the *optimal* estimator is too large from a systems perspective, one must consider an alternative processing strategy (i.e., one should not attempt such deconvolution). This motivated the alternative, beamforming approach discussed in Sec. III.

For the near-grazing example discussed above, a variance threshold $t = (\theta_2 - \theta_1)/2$ is defined (in this example $\theta_2 - \theta_1 = 0.57°$). If the CRB is greater than this threshold it is argued that even the optimal estimator is inadequate for the deconvolution task (one may wish to impose an even tighter constraint). In the CRB studies it is assumed that the real and imaginary parts of the complex additive random signal N_m are representative of white Gaussian noise of variance $\sigma^2/2$. In Fig. 8 are plotted the CRB's as a function of frequency, at various values of SNR (here SNR is defined as the signal power for a given frequency divided by the noise power). In Fig. 9 the DOA estimation results using the algorithm described in Sec. II are compared with the CRB at a frequency of 10 KHz. These results underscore that the deconvolution procedure works best at higher frequencies, at which higher resolution is available. Moreover, the performance is a strong function of the SNR. These results demonstrate the complexity of the deconvolution procedure. In fact, the problem is more difficult than that considered in the above CRB study, since the additive random process is correlated [representative of clutter $c(t)$], *vis-à-vis* the white Gaussian noise considered in the CRB computations.

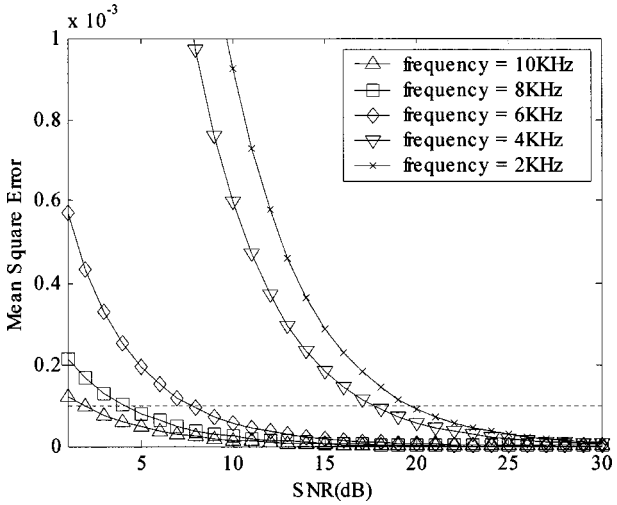

FIG. 8. Cramer–Rao bound (CRB) as a function of frequency and SNR. The dotted line indicates the separate threshold of the two incident angles, defined as half of the angular separation between two incident angles. Results are shown for different operating frequencies.

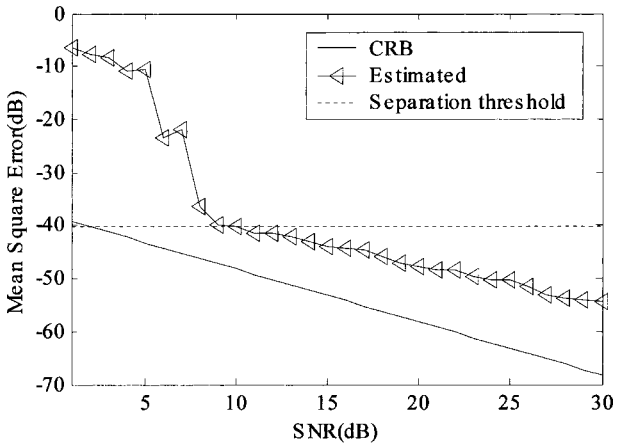

FIG. 9. Comparison of Cramer–Rao bound and direction-of-arrival estimation results, at a given frequency of 10 KHz.

D. Classification performance using near-grazing deconvolution

Classification performance is considered based on deconvolving the near-grazing rays, in the manner discussed in Sec. II. Two similar targets are used to constitute the H_1 hypothesis (targets of interest), and three false targets are considered. The HMM classifier[2–6] is designed to process a sequence of multiaspect, deconvolved $s(t)$. A single HMM is designed for the two targets in H_1, and the H_2 targets were not seen during training. The HMM is trained on noise-free data from H_1, and the testing is done on targets from H_1 and H_2, with additive clutter $c(t)$, as indicated in Eq. (16). Consequently, the training and testing data are distinct. During the testing phase, the classifier is initially unaware of both the target identity and pose (orientation with respect to the sensor).

In Fig. 10 the receiver-operating characteristic (ROC) is plotted for the HMM classifier, as a function of the multiaspect sequence length. Results are shown for 5° azimuthal angular sampling between consecutive measurements. In Fig. 10(a) results are presented based on the MP time-domain features discussed in Sec. IV A, while the results in Fig. 10(b) correspond to the frequency-based PCA-based features discussed in Sec. IV B. Results are shown for the 20-dB signal-to-clutter ratio (SCR) considered in Sec. VI B. With regard to the SCR, the *average* signal energy is computed for both targets in H_1, for all target-sensor orientations. It is important to emphasize that the SCR is actually target and orientation dependent, since the strength of $s(t)$ depends on these parameters. When computing the ROC curves, every possible initial angle of observation is considered for each target (all possible sequences), and five instantiations of clutter $c(t)$ are considered per scattered wave-form.

As anticipated, in Fig. 10 the ROC performance improves with increasing sequence length. An increasing sequence length corresponds to an increased sensor aperture (e.g., for 5° angular sampling, a sequence length of nine corresponds to a 40° cumulative aperture). The performance of the MP features, as extracted from the deconvolved $s(t)$, is inferior to that of the PCA features. This is attributed to the fact that the MP wave-front-resonance decomposition extracts features that capture the detailed time-domain character of the signal $s(t)$. Errors in the deconvolution process are magnified by the MP features. By contrast, the PCA-based approach employs the *magnitude* of the frequency-domain response, in a finite number of spectral subbands. The magnitude of the frequency spectrum is less likely to be perturbed by distortions in the wave-form shape, which are of significant importance for the phase. These results underscore the importance of appropriate feature extraction. In all subsequent examples frequency-domain PCA features are employed.

E. Classification via beam forming

In the next set of results the processing is performed based on simple beam forming. In particular, to point the array in the direction θ with respect to the array normal, array element n is weighted in the frequency domain by $a_n = w_n \exp[-j\beta \sin \theta n \Delta z]$, where Δz represents the array spacing and $\beta = \omega/c$ represents the wave number for sound speed

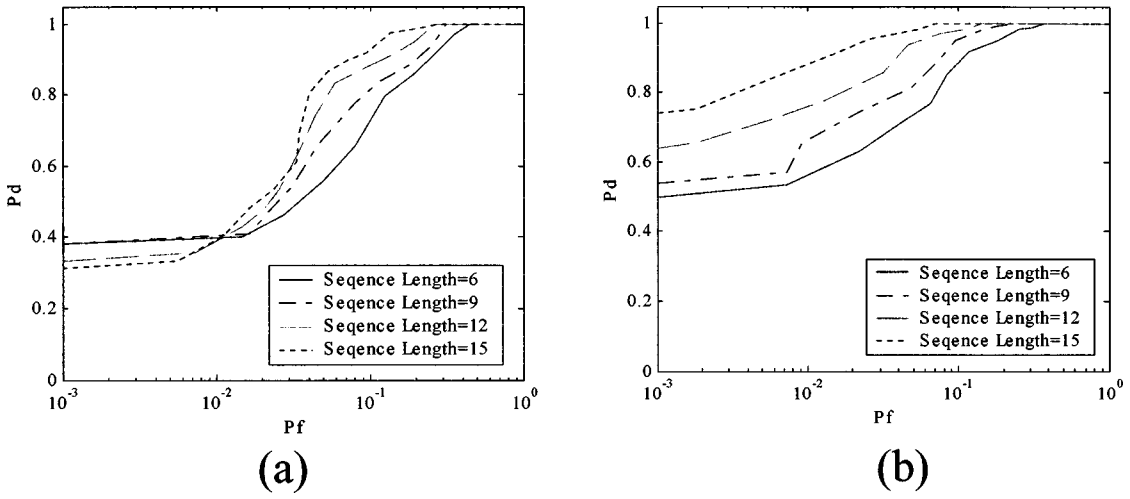

FIG. 10. Classification results based on the deconvolved signal using the matching-pursuits (MP) features and using principal-component-analysis (PCA)-based features. The angular sampling between consecutive measurements in the sequence is 5°. Results are shown for different sequence lengths. (a) MP features, (b) PCA-based features.

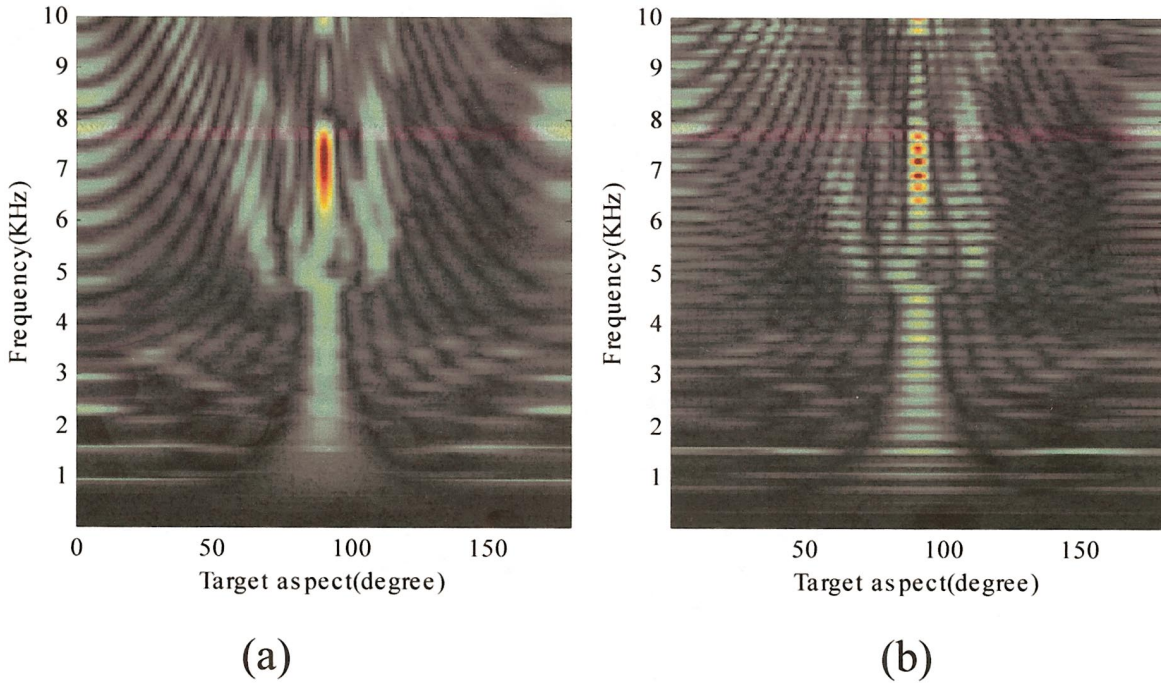

FIG. 11. Frequency response of the oxygen-tank. (a) Free-field response, (b) in-channel response, after beam forming and temporal windowing (for the array pointing toward the air-water paths).

c. As indicated above, the array considered here has $M=28$ elements and $\Delta z=7.4$ cm. This array spacing is designed to avoid grating lobes at the 10-KHz upper frequency (and below). The weighting w_n corresponds to a 30-dB Chebyshev window, designed to mitigate array end effects. The array processing yields a single time-domain scattered waveform, corresponding to the array directed toward the angle θ. Since the classification is always performed after the target detection, the beam-forming angles may be estimated based on prior information of channel parameter and target location; as indicated below, these parameters need not to be known exactly.

As an example, in Fig. 11 the frequency- and orientation-dependent scattered fields are determined after beam forming, for the array directed toward the air-water surface bounce (see Fig. 1). The results are presented for the oxygen-tank target, for the free-field and in-channel problems (the latter after beam forming). Considering Fig. 1, recall that the array pointed toward the surface extracts round-trip rays of the type C-C, C-D, D-C, and D-D, these all arriving nearly coincident in time, for the target position (near the bottom) considered. Based on ray path lengths, it is clear that such rays arrive *after* those that travel along the paths A-C, B-C, A-D, etc. Therefore the results in Fig. 11 represent the spectrum of the time-windowed beam-formed data, using the second arrival of scattered fields. Concerning the windowed rays, C-C represents monostatic scattered fields, while C-D, D-C, and D-D represent bistatic scattering. As indicated above, due to the limitations in processing these rays separately, via deconvolution, they are treated together as a composite signal. This underscores the limitation of the approach, for the classifier training must be performed with in-channel data, and such is a function of the target-sensor distance (even with all other parameters fixed).

Considering Fig. 11 in detail, note that the free-field monostatic scattered fields are similar to those determined via the beam forming. However, there appears to be interference in the signal, as a function of frequency. This is attributed to the interference caused by the multiple overlapping rays.

In the classification results presented next, for the same two "true" H_1 targets and three "false targets" H_2, the frequency-domain PCA-based features are considered (Sec. III B). A single HMM is again designed matched to the two targets in H_1, and the three false targets are not seen prior to testing. Additive clutter $c(t)$ is again considered, as considered in the previous examples, and therefore the testing and training data are distinct (training is performed on noise-free data).

In Fig. 12(a) are presented example classification results using the beam-formed data, with the sensor directed toward the air-water interface. Results are shown for a signal-to-clutter ratio (SCR) of 5 dB for each sensor's received signal (before beam forming). Note that by avoiding the deconvolution technique of Sec. II A, the classifier may now operate at lower SCR. In Fig. 12(a) results are again presented as a function of the number of multiaspect measurements in the sequence, using angular sampling between consecutive measurements of 5°. Note that these results are considerably better than those based on the deconvolved near-grazing waveform $s(t)$.

In the example of Fig. 12(a), the classification is based on beam forming toward the air-surface interface. One could also beam form toward the near-grazing rays, using temporal windowing to separate rays A-A, A-B, B-A, and B-B from C-A, D-A, etc., as in the previous example. In this case the rays of interest arrive earliest in time. In the case of beam forming, however, the cumulative near-grazing rays A-A,

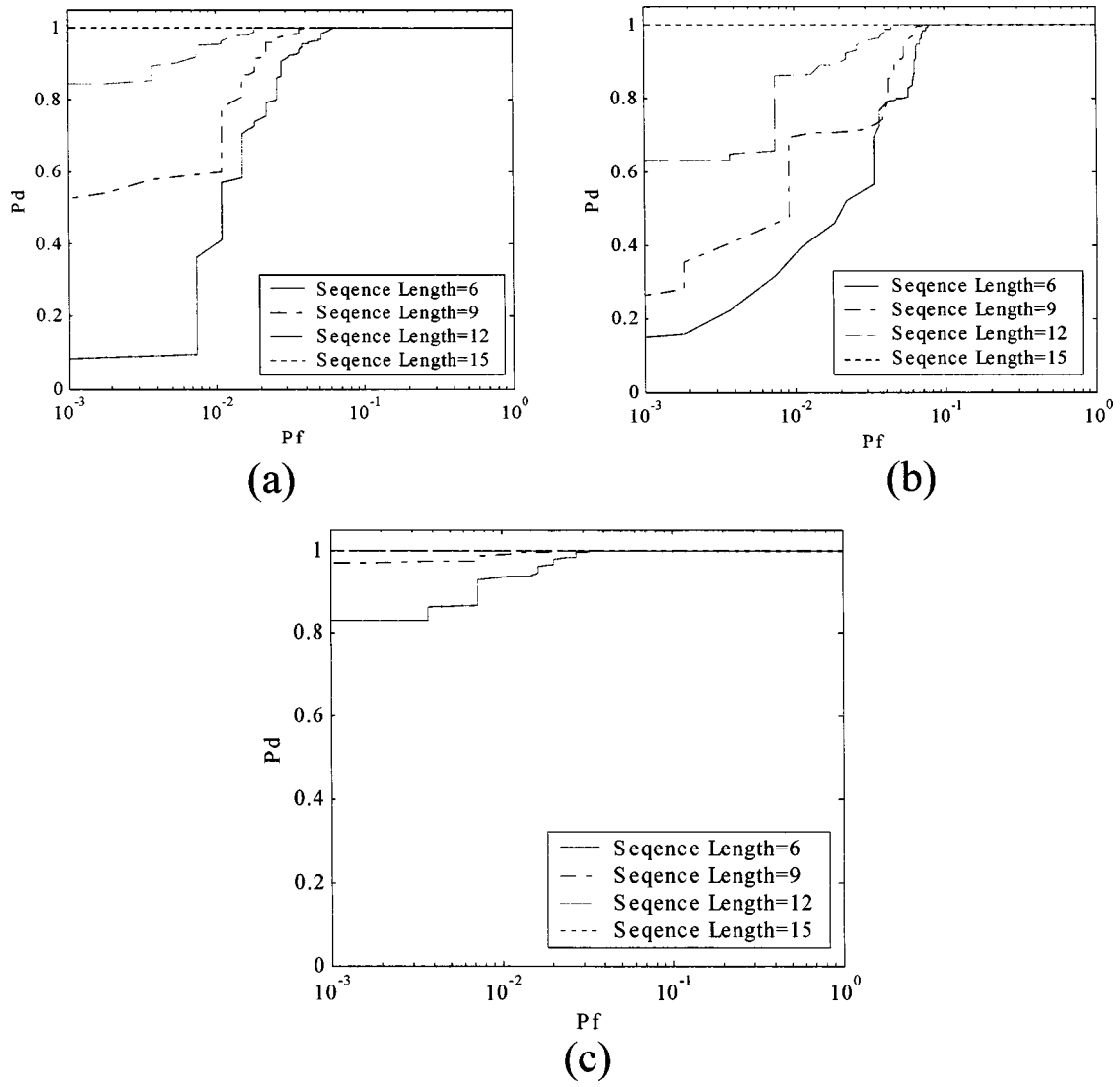

FIG. 12. Classification results based on the beam-formed and temporal windowed signal, training by using the noise-free in-channel data, and testing by using the noisy (cluttered) in-channel data. The SNR at each sensor element is 5 dB (before beam forming). (a) Air-water paths alone, (b) near-grazing paths alone, (c) fusion of both paths.

A-B, B-A, and B-B are processed as a single composite waveform, rather than attempting deconvolution. Recognizing the opportunity of exploiting two array-pointing directions (see Fig. 1), the processed waveforms from each array direction may be fused, to further enhance classification performance. In particular, classification may be performed based on the beam formed waveforms extracted by pointing toward the surface *and* in the near-grazing direction. The HMM design has been augmented, now characterizing the target states by two beam-formed waveforms, as extracted by beamsteering in these two directions. This constitutes a modest change in the HMM design (the features from the two ''look'' directions are simply concatenated). The HMM performance is shown in Figs. 12(b) and (c), based on pointing in the near-grazing direction alone, and based on fusing these two beam-formed waveforms. This simple fusion construct yields markedly improved classification performance. The results in Fig. 12 are based on a SCR of 5 dB.

TABLE I. Channel parameters used for training and testing, when the channel parameters are varied during testing (to examine channel-parameter mismatch).

	Sound speed in water (m/s)	Sound speed in sediment (m/s)	Bottom attenuation factor (dB/kmHz)	Bottom density (g/cm^3)
Training case	1520	1800	0.5	1.5
Testing case 1	1517	1783	0.51	1.52
Testing case 2	1551	1868	0.49	1.54
Testing case 3	1523	1820	0.52	1.51
Testing case 4	1512	1793	0.51	1.43
Testing case 5	1535	1812	0.48	1.46

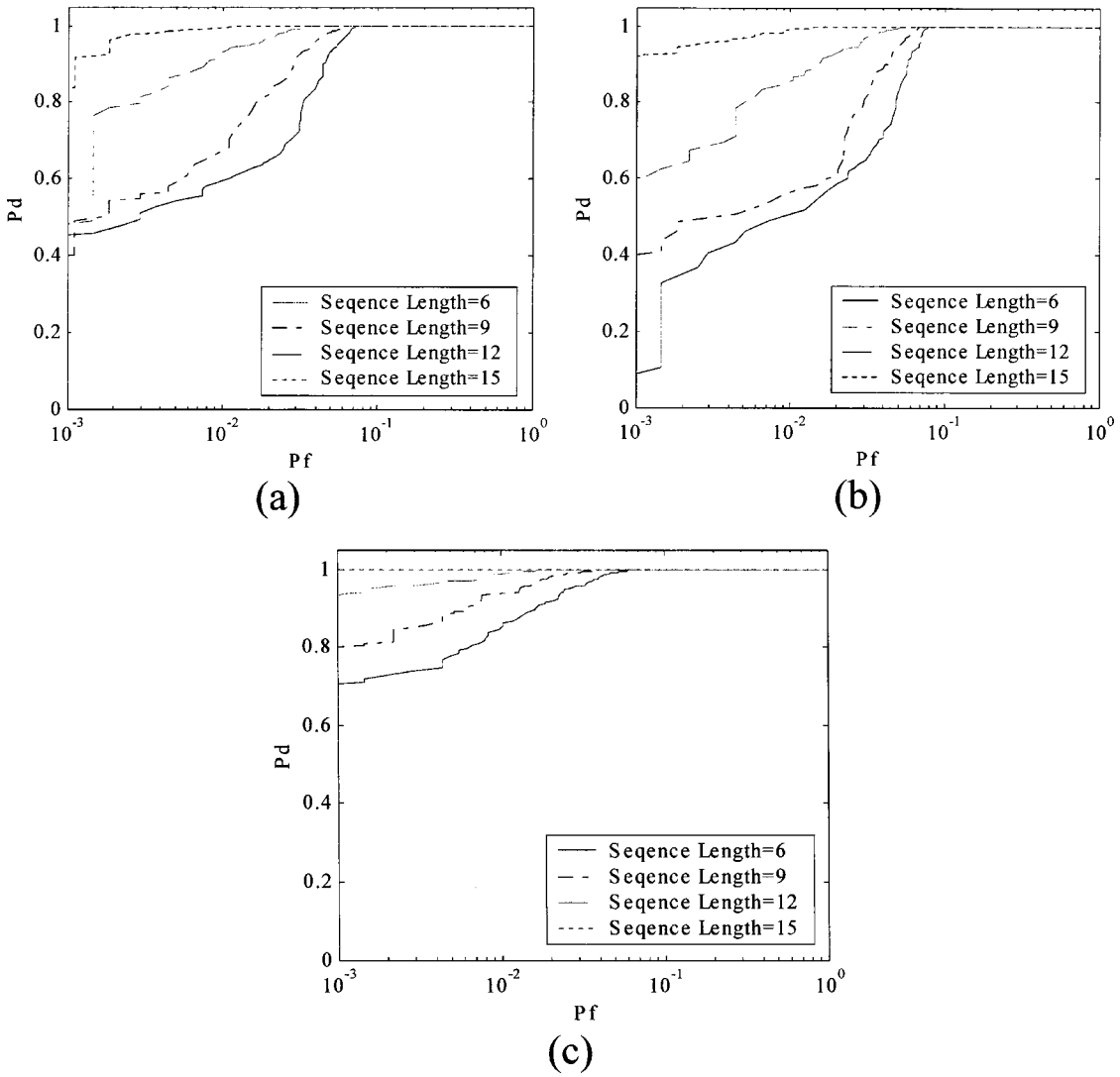

FIG. 13. Classification results based on the beam-formed and temporal-windowed signal, training by using the noise free in-channel data, and tested by using the noisy in-channel data with channel parameters mismatched. The SNR at each sensor element is 5 dB (before beam forming). (a) Air-water paths alone, (b) near-grazing paths alone, and (c) fusion of both.

F. Stability to channel variation

In the example of Fig. 12, classification results are presented when training is performed on noise-free in-channel data, and testing is performed using noisy in-channel data. There is no channel-parameter mismatch between the training and testing data sets. Actually, the channel parameters are always not known exactly in practice. It is of interest to evaluate the stability of the beam-forming-based classification approach to channel uncertainty. Four channel parameters are considered as random variables: the speed in water, the sound speed in the sediment, the bottom attenuation factor, and the sediment density. The channel parameters for training data and testing data are illustrated in Table I. The classification results given below are average from the five testing cases (representing five realizations of the channel random variables). The principal limitation in this study is found in the time required to compute the forward-scattering data, thereby limiting the number of random-variable instantiations considered. The beam forming for each testing cases is performed based on the channel parameters used for the training case, implying that there is steering error when beam forming for the testing case (i.e., there is a mismatch between the assumed and actual channel parameters, while beam forming, and between the training and testing). In Fig. 13 the HMM performance is presented for the case of parameter mismatch, based on pointing toward the air-water interface alone, based on pointing in the near-grazing direction alone, and based on fusing these two beam-formed waveforms. Comparing with Fig. 12, the performance decrease is not significant, indicating that the classification approach is relatively stable to the channel parameters variation (for the parameters considered).

VII. CONCLUSION

Classification of elastic targets situated in a water channel has been considered. The multiaspect classification has been performed using a hidden Markov model (HMM), and multiple targets have been used to constitute a target class. In particular, rather than designing a classifier for each individual target, a classifier is designed for a set (class) of

targets.[5] There are two distinct approaches to performing such classification, for a target in a channel. One may (i) attempt to deconvolve the perturbations introduced by the channel, and perform classification based on the targets' free-field signature (after deconvolution); or (ii) one may process the in-channel signature directly, through beamforming, for example, without attempting deconvolution. While approach (i) is attractive, in that it ideally removes the effects of the channel, it has been have demonstrated that this approach is sensitive to additive noise/clutter. While approach (ii) has the disadvantage of requiring in-channel data for training, it has demonstrated superior classification performance, *vis-à-vis* (i). The sensitivity of (ii) to uncertainty in the channel parameters has also been examined, and for the examples studied robust performance was observed.

While the results presented here appear encouraging, it should be emphasized that a limited problem class has been considered. In particular, the range of channel parameters considered (relative to bandwidth) support the ray-based model. As the target-sensor distance increases, for the same set of channel parameters, the number of overlapping rays increases to the point that a modal model is required. This is a particularly challenging problem, and it will constitute the subject of future research. Directions of interest in this context include matched-field processing[14] (here not simply for source localization, but also for classification), as well as the related technique of reverse-time migration.[29]

ACKNOWLEDGMENTS

This work was supported, in part, by ONR Code 32MIW.

[1] D. M. Photiadis, J. A. Bucaro, and B. H. Houston, "Scattering from flexural waves on a ribbed cylindrical shell," J. Acoust. Soc. Am. **96**, 2785–2790 (1994).
[2] P. R. Runkle, P. K. Bharadwaj, L. Couchman, and L. Carin, "Hidden Markov models for multi-aspect target classification," IEEE Trans. Signal Process. **47**, 2035–2040 (1999).
[3] P. K. Bharadwaj, P. R. Runkle, and L. Carin, "Target Identification with wave-based matched pursuits and hidden Markov models," IEEE Trans. Antennas Propag. **47**, 1543–1554 (1999).
[4] N. Dasgupta, P. K. Bharadwaj, L. Couchman, and L. Carin, "Dual hidden Markov model for characterizing wavelet coefficients from multi-aspect scattering data," Signal Process. **81**, 1303–1316 (2001).
[5] N. Dasgupta, P. Runkle, L. Carin, L. Couchman, T. Yoder, J. Bucaro, and G. J. Dobeck, "Class-based target identification with multiaspect scattering data," IEEE J. Ocean. Eng. **28**, 271–282 (2003).
[6] X. Liao, P. R. Runkle, Y. Jiao, and L. Carin, "Identification of ground targets from sequential HRR radar signatures," *Proceeding of ICASSP2001*, Vol. V, May, 2001, Salt Lake City.
[7] M. K. Broadhead, "Broadband source signature extraction from underwater acoustics data with sparse environment information," J. Acoust. Soc. Am. **97**, 1322–1325 (1995).
[8] M. K. Broadhead, R. L. Field, and J. H. Leclere, "Sensitivity of the deconvolution of acoustic transients to Green's function mismatch," J. Acoust. Soc. Am. **94**, 994–1002 (1993).
[9] M. K. Broadhead, L. A. Pflug, and R. L. Field, "Use of high order statistics in source signature estimation," J. Acoust. Soc. Am. **107**, 2576–2585 (2000).
[10] S. Angle, "Extraction of a target scattering response from measurements made over long ranges in shallows water," J. Acoust. Soc. Am. **102**, 825–832 (1997).
[11] P. Chevret, N. Gache, and V. Zimpfer, "Time-frequency filters for target classification," J. Acoust. Soc. Am. **106**, 1829–1837 (1999).
[12] T. Cover and J. Thomas, *Elements of Information Theory* (John Wiley & Sons, New York, 1991).
[13] L. R. Rabiner, "A tutorial on hidden markov models and selected applications in speech recognition," Proc. IEEE **77**, 257–285 (1989).
[14] F. B. Jensen, W. A. Kuperman, M. B. Porter, and H. Schmidt, "*Computational Ocean Acoustics*" (AIP, Woodbury, NY, 1993).
[15] M. B. Porter, "Acoustical models and sonar systems," IEEE J. Ocean. Eng. **18**, 425–437 (1993).
[16] M. R. Azimi-Sadjadi, D. Yao, Q. Huang, and G. J. Dobeck, "Underwater target classification using wavelet packets and neural networks," IEEE Trans. Neural Netw. **11**, 784–794 (2000).
[17] C. Yuan, M. R. Azimi-Sadjadi, J. Wilbur, and G. J. Dobeck, "Underwater target detection using multi-channel subband filtering and high-order correlation schemes," IEEE J. Ocean. Eng. **25**, 192–205 (2000).
[18] M. R. Azimi-Sadjadi, S. Charleston, J. Wilbur, and G. J. Dobeck, "A new time delay estimation in subbands for resolving multiple specular reflections," IEEE Trans. Signal Process. **46**, 3398–3403 (1998).
[19] G. Cauwenberghs, R. T. Edwards, D. Yunbin, R. Genov, and D. Lemonds, "Neuromorphic processor for real-time biosonar object detection," *2002 IEEE Int. Conf. Acoustics, Speech and Sig. Proc.*, Vol. 4, pp. 3984–3987 (2002).
[20] M. Montanari and H. Schmidt, "Buried mine classification by means of high-order spectral analysis," J. Acoust. Soc. Am. **112**, 2222 (2002).
[21] G. J. Dobeck and J. T. Cobb, "Advances in algorithm fusion for automated sea mine detection and classification," J. Acoust. Soc. Am. **112**, 2307 (2002).
[22] R. Monzingo and T. Miller, *Introduction to Adaptive Arrays* (Wiley, New York, 1980).
[23] M. McClure, L. Carin, "Matching pursuits with time-frequency dictionaries," IEEE Trans. Signal Process. **45**, 2912–2927 (1997).
[24] N. S. Jayant and P. Noll, *Digital Coding of Waveforms* (Prentice-Hall, Englewood Cliffs, NJ, 1984).
[25] R. O. Duda and P. E. Hart, *Pattern Classification and Scene Analysis* (Wiley, New York, 1973).
[26] W. S. Burdic, *Underwater Acoustic System Analysis*, 2nd ed. (Prentice Hall, Englewood Cliffs, NJ, 1991).
[27] A. Weiss and B. Friedlander, "On the Cramer-Rao bound for direction finding of correlated signals," IEEE Trans. Signal Process. **41**, 495–499 (1993).
[28] B. Friedlander and A. Weiss, "Direction finding using noise covariance modeling," IEEE Trans. Signal Process. **43**, 1557–1567 (1995).
[29] H. C. Song, W. A. Kuperman, and W. S. Hodgkiss, "A time-reversal mirror with variable range focusing," J. Acoust. Soc. Am. **103**, 3234–3240 (1998).

Tracking target in cluttered environment using multilateral time-delay measurements

Dragana Carevic[a)]
Maritime Operations Division, Defence Science and Technology Organisation, Bldg A-51, HMAS Stirling, Rockingham, WA 6958, Australia

(Received 25 August 2003; revised 25 November 2003; accepted 17 December 2003)

The problem considered here is that of tracking a single underwater target in clutter using multilateral time-delay measurements derived from short-duration acoustic emissions, or transients, radiated by the target. The target is moving linearly with constant velocity and depth. To account for the effects on the time-delay estimates due to acoustic propagation in uncertain environments, the time-delay measurement errors between pairs of sensors are modeled using Gaussian mixture distributions. An approach is proposed that utilizes an iterative maximum likelihood optimization technique based on the expectation-maximization algorithm. In each iteration a nonlinear least-squares procedure is used to compute the target model parameters. A detection mechanism is also formulated that can validate the correctness of the estimated track parameters and verify the existence of a target. The proposed method is tested using simulated time-delay measurements from a linear array of three equally spaced sensors mounted onboard an observer platform. Extensive tests are performed for several scenarios with different tracking geometry. [DOI: 10.1121/1.1647491]

PACS numbers: 43.60.Jn, 43.60.Gk, 43.30.Wi [EJS] Pages: 1198–1206

I. INTRODUCTION

This paper addresses the problem of estimating trajectory (i.e., location and velocity) of an underwater target using multilateral time-delay measurements derived from passive wideband acoustic emissions. Considered is a particular class of acoustic emissions characterized by relatively short time durations and arbitrary waveform shapes, also known as transients. Typically, the duration of these signals ranges from few tens of milliseconds to several seconds, and they are used to detect, identify, and localize very low noise targets.

Passive localization can be accomplished by measuring simultaneous differences in the arrival times of an emitted signal on a number of spatially separated receiving sensors (hydrophones). The sensors can be mounted onboard a ship, towed, or deployed in the water, and their position is assumed to be known. A minimum of two differences in the arrival times, or relative time delays, is required for the localization (Ferguson and Cleary, 2001; Hassab *et al.*, 1981).

Standard approach to estimating the time delays based on transients is to use second- or higher-order correlation between the outputs from given pairs of sensors (see Carter, 1981; Ferguson and Cleary, 2001; Pflug *et al.*, 1993). The accuracy of the estimation depends on the transient signal spectrum and is sensitive to a decrease in the received signal-to-noise ratio (SNR) (Ianniello, 1982; Carter and Robinson, 1993). Pflug *et al.* (1993) point out that signals may also be distorted as a result of acoustic propagation in spatially varying and multipath environments. These effects are sometimes alleviated by using only the leading edges of the received transients to compute time delays (Stotts *et al.*, 1997). This approach is suboptimal, since an optimal computation requires using the correlation with sufficiently long integration time in order to reduce noise influence (Ferguson and Cleary, 2001; Carter, 1981; Hahn, 1975). Ferguson (1989) proposes that low received SNRs can be improved by replacing each sensor with an array of receivers and by beamforming the array outputs, whereas Ching *et al.* (1999) apply wavelet-based denoising techniques to increase the accuracy of time-delay estimates. However, these techniques cannot completely eliminate the effect of noise, and, in some situations, large errors in time-delay estimation are possible. As a consequence, the time-delay error distribution may have wide tails and may thus deviate from the commonly used Gaussian model. In Carevic (2003) a two-component Gaussian mixture probability density function (pdf) is proposed as a more general model for this error distribution.

Recently, it was demonstrated that considerable improvement in target tracking accuracy can be achieved from the addition of transient signal time difference of arrival information to the set of bearings-only target measurements (Barsanti, 2002). Also, in situations where it is required to detect and track targets characterized by very low-level continuous broadband noise, these tasks can sometimes be accomplished solely by using transients. However, transients radiated by the target are typically observed in the presence of clutter that can originate from a variety of sources, such as nearby shipping traffic, biological noise, etc., so a number of false alarms is possible. Although some clutter measurements produced by sensors can be excluded by utilizing transient classifiers, due to error inherent to the classifier not all clutter can be eliminated. Since it is not known which measurements in the batch originate from the target and which are clutter, the estimation of the target motion parameters

a)Electronic mail: dragana.carevic@dsto.defense.gov.au

using such measurements presents a comparatively difficult problem.

Several techniques for tracking single and multiple targets using measurements of uncertain origin have been proposed. One approach uses probabilistic association of measurements with the target to define a joint likelihood function, which is then directly maximized to obtain the target motion parameters (Bar-Shalom and Fortman, 1988). This technique, known as the probabilistic data association (PDA), is successfully applied to tracking underwater acoustic sources in Shertukde and Bar-Shalom (1990), Jauffret and Bar-Shalom (1990), and Kirubarajan and Bar-Shalom (1995). As applied in these references, the PDA requires that all combinations of feasible data associations are taken into account. This may impede the convergence of the algorithm, particularly when applied in conjunction with highly nonlinear measurements such as time delays.

An alternative approach considers tracking of (multiple) targets using measurements of uncertain origin from the viewpoint of parameter estimation from finite mixture densities (Gauvrit *et al.*, 1997; Avitzour, 1992). This approach does not enumerate all possible combinations of feasible data associations. Rather, it performs a search for the measurement to target association that maximizes a likelihood of the observed measurements. The multitarget tracking is formulated as an incomplete data problem where the measurement to target assignment is taken to be the missing information. A maximum likelihood (ML) estimator based on the expectation-maximization (EM) algorithm (Dempster *et al.*, 1977) is used to compute in an optimal manner measurement-to-target association probabilities. Gauvrit *et al.* (1997) extend this approach by the inclusion of a state vector composed of target states and assignment probabilities; as a result a maximum *a posteriori* (MAP) estimator is obtained. They show that this method is equivalent to the probabilistic multihypothesis tracking (PMHT) technique proposed by Streit and Luginbuhl (1994) (see also Streit and Luginbuhl, 1995). Gauvrit *et al.* (1997) and Hutchins and Dunham (1997) apply the EM-based methods to tracking underwater targets in clutter. Other approaches to detecting, localizing, and tracking of a moving source in an underwater environment include using matched-field processing (Tantum and Nolte, 1998; Wilmut and Ozard, 1998), and tracking targets based on measurements obtained from a linear array of sensors (Hassab *et al.*, 1981; Xerri *et al.*, 2002; Carevic, 2003).

Most of the above methods are developed under the assumption that the measurement errors have Gaussian distributions. Both the PDA and the methods based on the EM algorithm can, in principle, handle the errors distributed according to Gaussian mixture pdf's by using appropriate optimization techniques. This paper describes an extension to these methods which enables that the optimization is done using nonlinear least squares (LS). In particular, an approach to tracking a target in cluttered environments using multilateral time-delay measurements is proposed. It utilizes an iterative ML estimation based on the EM algorithm and jointly solves two different problems: (1) measurement data association, and (2) target model estimation where the measurement errors are modeled as having Gaussian mixture pdf's. In each iteration the algorithm applies a nonlinear LS technique to find the target model parameter estimates. A detection mechanism is also proposed that can validate the correctness of the estimated track parameters and/or verify the existence of target. The algorithm is tested using simulated measurements obtained from a linear array of sensors mounted onboard an observer platform. The derivation of this tracking method is presented in Sec. II. Numerical simulations using several scenarios with different tracking geometries are described in Sec. III.

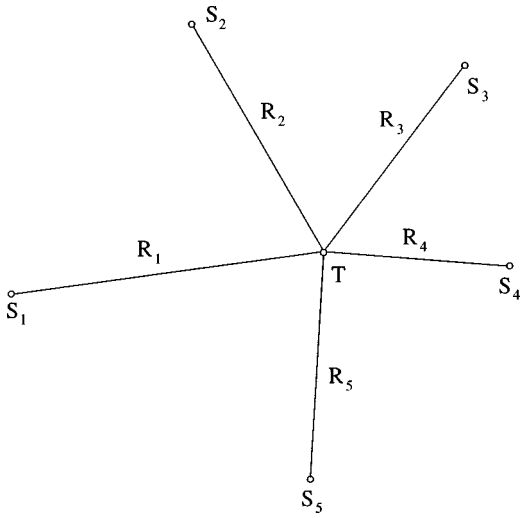

FIG. 1. General geometry used for passive localization.

II. ALGORITHM DERIVATION

A general geometry utilized in the time-delay analysis is shown in Fig. 1. Denoted by S_i are sensors and by R_i the signal paths from the target to each of the sensors. Sensors can be fixed or moving and their positions are assumed to be known. The target is moving in two dimensions with constant velocity $[v_x, v_y]'$. Its dynamics is described by the following linear equation:

$$X_t = X_{t^*} + (t - t^*)v_x, \tag{1}$$

$$Y_t = Y_{t^*} + (t - t^*)v_y, \tag{2}$$

where t^* is a reference time at which the source position is estimated and $[X_t, Y_t]'$ denotes the target position at time t. The parameter vector of the target is defined by

$$V = [X_{t^*}, Y_{t^*}, v_x, v_y]'. \tag{3}$$

Let there be N (different) transient signals detected during an observation time which includes both target-originated signals and clutter. Associated with this set is a sequence of time instants $\{t_i\}_{i=1}^{N}$ determined by the arrival times of the signals at a reference sensor[1] (these time instants are generally not evenly spaced). Related to the signal received at the time instant t_i there are n_{t_i} time-delay measurements

$$Z_{t_i} = \{Z_{t_i}^{(1)}, \ldots, Z_{t_i}^{(n_{t_i})}\}, \tag{4}$$

obtained by crosscorrelating the outputs from different pairs of sensors as discussed above. Under the target assumption, the measurements $\{Z_{t_i}^{(r)}\}_{r=1}^{n_{t_i}}$ are described by the following observation model:

$$Z_{t_i}^{(r)} = \tau_{t_i}^{(r)} + e_{t_i}^{(r)}, \tag{5}$$

where $\tau_{t_i}^{(r)}$ is the exact time delay

$$\tau_{t_i}^{(r)} = f_{t_i}^{(r)}(X_{t_i}, Y_{t_i}), \tag{6}$$

and the functions $f_{t_i}^{(r)}(X_{t_i}, Y_{t_i})$ depend on the sensor geometry at time t_i. The errors $e_{t_i}^{(r)}$ in Eq. (5) are modeled as independent random variables that are distributed according to a two-component Gaussian mixture model

$$p(e_{t_i}^{(r)}) = (1-\epsilon_{t_i}^{(r)})\mathcal{N}(e_{t_i}^{(r)}; 0, \sigma_{t_i}^{(r,1)^2}) + \epsilon_{t_i}^{(r)}\mathcal{N}(e_{t_i}^{(r)}; 0, \sigma_{t_i}^{(r,2)^2}), \tag{7}$$

where $\mathcal{N}(x; \mu, \sigma^2)$ is a Gaussian (normal) pdf in variable x with mean μ and variance σ^2, and $0 < \epsilon_{t_i}^{(r)} < 1$ defines the proportion of the two Gaussian pdf's in the mixture. The Gaussian mixture pdf is an important concept that has found many applications in the areas such as underwater acoustic signal detection (Kassam, 1988; Bouvet and Schwartz, 1988) and pattern classification (Gong, 2002). Also note that by setting $\epsilon_{t_i}^{(r)} = 0$ the distribution in Eq. (7) becomes a standard Gaussian pdf.

Denote the batch measurements by $\mathcal{Z} = \{Z_{t_i}\}_{i=1}^{N}$. Following the approaches presented in Gauvrit *et al.* (1997) and Streit and Luginbuhl (1995), $\mathcal{Z}$ represents incomplete data. The complete data are given by $\{\mathcal{Z}, \mathcal{K}\}$, where $\mathcal{K} = \{k_{t_i}^{(1)}, \ldots, k_{t_i}^{(n_{t_i})}\}_{i=1}^{N}$ is a set of discrete valued measurement assignment indices associated with the batch $\mathcal{Z}$, and $k_{t_i}^{(r)} \in \{1,2\}$, $r = 1, \ldots, n_{t_i}$; each index $k_{t_i}^{(r)}$ assigns the corresponding measurement, $Z_{t_i}^{(r)}$, to either the target model (track) (when $k_{t_i}^{(r)} = 1$) or to clutter ($k_{t_i}^{(r)} = 2$). Also denote by $\pi_{t_i} = \{\pi_{t_i}^{(1)}, \pi_{t_i}^{(2)}\}$ the probability vector related to the assignment indices $\{k_{t_i}^{(r)}\}_{r=1}^{n_{t_i}}$, where $\pi_{t_i}^{(n)} = \text{Prob}[k_{t_i}^{(r)} = n]$, and by $\Pi = \{\pi_{t_i}\}_{i=1}^{N}$ the assignment probabilities for the batch $\mathcal{Z}$. The assignment probabilities are not known and need to be estimated along with the target motion parameter vector V.

The complete data probability, conditioned on the vector V and the batch assignment probabilities Π, is given by

$$P(\mathcal{Z}, \mathcal{K} | V, \Pi) = \prod_{i=1}^{N} \prod_{r=1}^{n_{t_i}} \pi_{t_i}^{(m)} p_{t_i}^{(r,m)}|_{m = k_{t_i}^{(r)}}. \tag{8}$$

Here, $p_{t_i}^{(r,1)}$ denotes the measurement model pdf corresponding to the target assignment, $k_{t_i}^{(r)} = 1$, which

$$p_{t_i}^{(r,1)} = p(Z_{t_i}^{(r)}; \tau_{t_i}^{(r)}) = (1-\epsilon_{t_i}^{(r)})\mathcal{N}(Z_{t_i}^{(r)}; \tau_{t_i}^{(r)}, \sigma_{t_i}^{(r,1)^2}) + \epsilon_{t_i}^{(r)}\mathcal{N}(Z_{t_i}^{(r)}; \tau_{t_i}^{(r)}, \sigma_{t_i}^{(r,2)^2}). \tag{9}$$

For the clutter assignment, $k_{t_i}^{(r)} = 2$, $p_{t_i}^{(r,2)} = \rho$, where ρ is a constant (an adjustable parameter).

Alternatively, the Gaussian mixture model for the measurement error under the target assumption implies that $e_{t_i}^{(r)}$ can be generated either from the normal pdf $\mathcal{N}(e_{t_i}^{(r)}; 0, \sigma_{t_i}^{(r,1)^2})$ or from the pdf $\mathcal{N}(e_{t_i}^{(r)}; 0, \sigma_{t_i}^{(r,2)^2})$, where $(1-\epsilon_{t_i}^{(r)})$ and $\epsilon_{t_i}^{(r)}$ are the respective prior probabilities. An auxiliary set of batch assignment indices $\mathcal{L} = \{l_{t_i}^{(1)}, \ldots, l_{t_i}^{(n_{t_i})}\}_{i=1}^{N}$ is introduced, where $l_{t_i}^{(r)} \in \{1,2,3\}$. The joint probability of the batch measurements $P(\mathcal{Z}, \mathcal{L} | V, \Xi)$ for the given batch assignment indices $\mathcal{L}$ is then defined by

$$P(\mathcal{Z}, \mathcal{L} | V, \Xi) = \prod_{i=1}^{N} \prod_{r=1}^{n_{t_i}} \xi_{t_i}^{(r,n)} q_{t_i}^{(r,n)}|_{n = l_{t_i}^{(r)}}, \tag{10}$$

where

$$q_{t_i}^{(r,n)} = \begin{cases} \mathcal{N}(Z_{t_i}^{(r)}; \tau_{t_i}^{(r)}, \sigma_{t_i}^{(r,n)^2}) & n = 1,2, \\ \rho & n = 3, \end{cases} \tag{11}$$

and $\xi_{t_i}^{(r,1)} = \pi_{t_i}^{(1)}(1-\epsilon_{t_i}^{(r)})$, $\xi_{t_i}^{(r,2)} = \pi_{t_i}^{(1)}\epsilon_{t_i}^{(r)}$, and $\xi_{t_i}^{(r,3)} = \pi_{t_i}^{(2)}$. The assignment $l_{t_i}^{(r)} = n$, $n \in \{1,2\}$, assigns the measurement $Z_{t_i}^{(r)}$ to the target and chooses the measurement model based on the Gaussian pdf $\mathcal{N}(Z_{t_i}^{(r)}; \tau_{t_i}^{(r)}, \sigma_{t_i}^{(r,n)^2})$. The case where $l_{t_i}^{(r)} = 3$ denotes the assignment to clutter. The probabilities $\xi_{t_i} = \{\xi_{t_i}^{(r,1)}, \xi_{t_i}^{(r,2)}, \xi_{t_i}^{(r,3)}\}_{r=1}^{n_{t_i}}$ are the associated assignment probabilities, where $\xi_{t_i}^{(r,n)} = \text{Prob}[l_{t_i}^{(r)} = n]$, $n = 1,2,3$, and $\Xi = \{\xi_{t_i}\}_{i=1}^{N}$ denotes the corresponding batch assignment probabilities.

The marginal distribution of $P(\mathcal{Z}, \mathcal{K} | V, \Pi)$ over (all possible measurement to target/clutter assignments) $\mathcal{K}$, $P(\mathcal{Z} | V, \Pi)$, is defined by

$$P(\mathcal{Z} | V, \Pi) = \sum_{\mathcal{K}} P(\mathcal{Z}, \mathcal{K} | V, \Pi) = \prod_{i=1}^{N} \prod_{r=1}^{n_{t_i}} \sum_{m=1}^{2} \pi_{t_i}^{(m)} p_{t_i}^{(r,m)}. \tag{12}$$

Similarly, the marginal pdf $P(\mathcal{Z} | V, \Xi)$ over $\mathcal{L}$ is defined by

$$P(\mathcal{Z} | V, \Xi) = \sum_{\mathcal{L}} P(\mathcal{Z}, \mathcal{L} | V, \Xi) = \prod_{i=1}^{N} \prod_{r=1}^{n_{t_i}} \sum_{n=1}^{3} \xi_{t_i}^{(r,n)} q_{t_i}^{(r,n)}. \tag{13}$$

Under the above assumptions about the relationship between the assignment probabilities, π_{t_i} and ξ_{t_i}

$$P(\mathcal{Z} | V, \Pi) = P(\mathcal{Z} | V, \Xi). \tag{14}$$

The proposed algorithm computes an ML estimate of the parameter vector V and the batch assignment probabilities $\Xi=\{\xi_{t_i}\}_{i=1}^{N}$ from the marginal pdf $P(\mathcal{Z}|V,\Xi)$. It uses the EM method and follows in its derivation the general approach outlined in Gauvrit *et al.* (1997) (see also Streit and Luginbuhl, 1995). Denote the parameter vector by $\phi=\{V,\Xi\}$. Also denote by ϕ^j the parameter vector estimated during the jth iteration obtained via the EM method, and by ϕ^{j+1} the updated parameter vector at the $(j+1)$-th iteration. From the Bayes theorem, define the conditional pdf on $\mathcal{L}$, $P(\mathcal{L}|\mathcal{Z},\phi)$, by

$$P(\mathcal{L}|\mathcal{Z},\phi)=\frac{P(\mathcal{Z},\mathcal{L}|\phi)}{P(\mathcal{Z}|\phi)}. \tag{15}$$

Substitution of Eqs. (10) and (13) into Eq. (15) produces

$$P(\mathcal{L}|\mathcal{Z},\phi)=\prod_{i=1}^{N}\prod_{r=1}^{n_{t_i}} w_{t_i}^{(r,n)}|_{n=l_{t_i}^{(r)}}, \tag{16}$$

where

$$w_{t_i}^{(r,n)}=\frac{\xi_{t_i}^{(r,n)}q_{t_i}^{(r,n)}}{\Sigma_m \xi_{t_i}^{(r,m)}q_{t_i}^{(r,m)}}. \tag{17}$$

Each iteration of the EM algorithm comprises an expectation step (E step) and a maximization step (M step). The E step of the EM algorithm is concerned with finding expectation $Q(\phi|\phi^j)$ as a function of ϕ^j, i.e., as

$$Q(\phi|\phi^j)=\log[P(\mathcal{Z}|\phi)] + \sum_{\mathcal{L}} \log[\mathcal{P}(\mathcal{L}|\mathcal{Z},\phi)]P(\mathcal{L}|\mathcal{Z},\phi^j). \tag{18}$$

The M step finds the parameter vector ϕ which maximizes $Q(\phi|\phi^j)$ as

$$\phi^{j+1}=\arg\max_{\phi} Q(\phi|\phi^j). \tag{19}$$

The log-likelihood $\log[P(\mathcal{Z}|\phi)]$ is increased in each iteration and the algorithm assures the convergence to at least a local maximum (Dempster *et al.*, 1977).

Gauvrit *et al.* (1997) show that the expectation function $Q(\phi|\phi^j)$ can be broken into several independent subfunctions by separating the variables in the parameter vector ϕ. For the problem considered in this paper

$$Q(\phi|\phi^j)=\sum_{i=1}^{N} Q'(\xi_{t_i}|\phi^j)+Q''(V|\phi^j), \tag{20}$$

where

$$Q'(\xi_{t_i}|\phi^j)=\sum_{r=1}^{n_{t_i}}\sum_{n=1}^{3}(w_{t_i}^{(r,n)})^j \log \xi_{t_i}^{(r,n)} \quad i=1,...,N, \tag{21}$$

$$Q''(V|\phi^j)=\sum_{i=1}^{N}\sum_{r=1}^{n_{t_i}}\sum_{n=1}^{2}(w_{t_i}^{(r,n)})^j \log q_{t_i}^{(r,n)}. \tag{22}$$

Each weight $(w_{t_i}^{(r,n)})^j$ in Eqs. (21) and (22) represents the posterior probability that the corresponding measurement $Z_{t_i}^{(r)}$ originates from either of the Gaussian target models (for $n\in\{1,2\}$) or from clutter (for $n=3$).

In this way the M step of the EM method is decoupled into a maximization problem for each of the N assignment probabilities ξ_{t_i} and for the target parameter vector V. The maximization for the assignment probabilities $\xi_{t_i}^{(r,n)}$, $n=1,2,3$, at time t_i and for a given $r\in\{1,...,n_{t_i}\}$, is constrained by the requirement that $\Sigma_n \xi_{t_i}^{(r,n)}=1$, i.e., these probabilities must sum to unity, as each represents the fraction of the measurement produced by a particular model. An additional constraint follows from the definition of the joint probability of batch measurements $P(\mathcal{Z},\mathcal{L}|V,\Xi)$ in Eq. (10), $\xi_{t_i}^{(r,1)}=(1-\epsilon_{t_i}^{(r)})(\xi_{t_i}^{(r,1)}+\xi_{t_i}^{(r,2)})$. The two constraints are combined and rewritten as

$$\xi_{t_i}^{(r,1)}+(1-\epsilon_{t_i}^{(r)})\xi_{t_i}^{(r,3)}=1-\epsilon_{t_i}^{(r)}, \tag{23}$$

$$\xi_{t_i}^{(r,2)}+\epsilon_{t_i}^{(r)}\xi_{t_i}^{(r,3)}=\epsilon_{t_i}^{(r)}. \tag{24}$$

For $r=1,...,n_{t_i}$, there are $2n_{t_i}$ constraints and the Lagrangian for this problem is formulated as

$$\begin{aligned} L_{t_i}=Q'(\xi_{t_i}|\phi^j)&+\sum_{r=1}^{n_{t_i}}\lambda_{t_i}^{(r,1)}[1-\epsilon_{t_i}^{(r)}-\xi_{t_i}^{(r,1)} \\ &-(1-\epsilon_{t_i}^{(r)})\xi_{t_i}^{(r,3)}]+\sum_{r=1}^{n_{t_i}}\lambda_{t_i}^{(r,2)}[\epsilon_{t_i}^{(r)}-\xi_{t_i}^{(r,2)} \\ &-\epsilon_{t_i}^{(r)}\xi_{t_i}^{(r,3)}], \end{aligned} \tag{25}$$

where $\lambda_{t_i}^{(r,k)}$, $k=1,2$ are Lagrange multipliers. Differentiating the Lagrangian with respect to $\xi_{t_i}^{(r,n)}$ and setting the result to zero yields

$$\xi_{t_i}^{(r,n)}=\begin{cases} \dfrac{1}{\lambda_{t_i}^{(r,n)}}(w_{t_i}^{(r,n)})^j & n=1,2, \\ \dfrac{1}{\Sigma_{p=1}^{n_{t_i}}[\lambda_{t_i}^{(p,1)}(1-\epsilon_{t_i}^{(p)})+\lambda_{t_i}^{(p,2)}\epsilon_{t_i}^{(p)}]}\displaystyle\sum_{p=1}^{n_{t_i}}(w_{t_i}^{(p,n)})^j & n=3, \end{cases} \tag{26}$$

where $r=1,...,n_{t_i}$. The expression for $n=3$ in Eq. (26) is derived by taking into account that $\xi_{t_i}^{(r,3)}=\pi_{t_i}^{(2)}$, that is, that $\xi_{t_i}^{(r,3)}$ are equal for all $r=1,...,n_{t_i}$. Combining Eqs. (23), (24), and (26), and noting that $\Sigma_{r=1}^{n_{t_i}}\Sigma_{m=1}^{3}(w_{t_i}^{(r,m)})^j=n_{t_i}$, it follows that

$$\sum_{r=1}^{n_{t_i}}[\lambda_{t_i}^{(r,1)}(1-\epsilon_{t_i}^{(r)})+\lambda_{t_i}^{(r,2)}\epsilon_{t_i}^{(r)}]=n_{t_i}. \tag{27}$$

By substituting this expression back into Eq. (26) for $n=3$, and using again Eqs. (23) and (24), the update for ξ_{t_i} is obtained as

$$(\xi_{t_i}^{(r,1)})^{j+1}=\frac{1-\epsilon_{t_i}^{(r)}}{n_{t_i}}\sum_{p=1}^{n_{t_i}}\sum_{n=1}^{2}(w_{t_i}^{(p,n)})^j, \tag{28}$$

$$(\xi_{t_i}^{(r,2)})^{j+1}=\frac{\epsilon_{t_i}^{(r)}}{n_{t_i}}\sum_{p=1}^{n_{t_i}}\sum_{n=1}^{2}(w_{t_i}^{(p,n)})^j, \tag{29}$$

$$(\xi_{t_i}^{(r,3)})^{j+1}=\frac{1}{n_{t_i}}\sum_{p=1}^{n_{t_i}}(w_{t_i}^{(p,3)})^j. \tag{30}$$

Similarly, the update for the target parameter vector is defined by

$$(V)^{j+1}=\arg\max_{V} Q''(V|\phi^j). \tag{31}$$

Rearranging Eq. (22) yields

$$Q''(V|\phi^j)\propto\sum_{i=1}^{N}\sum_{r=1}^{n_{t_i}}\log\mathcal{N}(Z_{t_i}^{(r)};\tau_{t_i}^{(r)},(\sigma_{t_i}^{(r)^2})^j), \tag{32}$$

where $\mathcal{N}(Z_{t_i}^{(r)};\tau_{t_i}^{(r)},(\sigma_{t_i}^{(r)^2})^j)$ is a Gaussian with the effective variance

$$(\sigma_{t_i}^{(r)^2})^j=\left(\frac{(w_{t_i}^{(r,1)})^j}{\sigma_{t_i}^{(r,1)^2}}+\frac{(w_{t_i}^{(r,2)})^j}{\sigma_{t_i}^{(r,2)^2}}\right)^{-1}. \tag{33}$$

The target parameter vector update $(V)^{j+1}$ can be obtained by using a standard weighted nonlinear LS procedure such as the Levenberg–Marquardt algorithm (see, for example, Press *et al.*, 1995).

Detection of local ML solutions

Depending on the configuration of clutter measurements in the batch, in some cases the proposed algorithm may converge to one of suboptimal (or local) ML solutions. The intention is to detect and discard such solutions. Denote by ϕ^* the parameter vector estimated by the algorithm, and by $P(\mathcal{Z}|\phi^*)$ the corresponding likelihood defined by Eq. (13). The likelihood $P(\mathcal{Z}|\phi^*)$ of a local ML solution is usually significantly lower than the likelihood of the global solution (Streit and Luginbuhl, 1995).

The detection statistic can be formulated as

$$\Lambda(\mathcal{Z},\phi^*)=\log\frac{P(\mathcal{Z}|\phi^*)}{P(\mathcal{Z}|\phi^c)}=\sum_{k=1}^{N}\Lambda^{(k)}(Z_{t_k},\phi^*), \tag{34}$$

where $\Lambda^{(k)}(Z_{t_k},\phi^*)$ is defined by

$$\Lambda^{(k)}(Z_{t_k},\phi^*)=\log\frac{P(Z_{t_k}|\phi^*)}{P(Z_{t_k}|\phi^c)}, \tag{35}$$

$$P(Z_{t_k}|\phi)=\prod_{r=1}^{n_{t_k}}\sum_{n=1}^{3}\xi_{t_k}^{(r,n)}q_{t_k}^{(r,n)}, \tag{36}$$

and ϕ^c denotes the parameter vector that corresponds to the case where all measurements in the batch $\mathcal{Z}$ are false (clutter). Here, it is taken that the number of target-originated time-delay measurements n_{t_k} at each time t_k is the same, i.e., $n_{t_k}=C$.

Equation (34) ensures that $\Lambda(\mathcal{Z},\phi^*)$ is normalized with respect to the (variable) number of clutter measurements in the measurement batch $\mathcal{Z}$. However, the number of target-originated measurements also varies. Besides, in the cases where the global ML solution is attained there is always a relatively small number of the target-originated measurements $Z_{t_k}=\{Z_{t_k}^{(1)},...,Z_{t_k}^{(C)}\}$ in the batch to which the estimated track is close in the sense that the corresponding likelihood ratios $\Lambda^{(k)}(Z_{t_k},\phi^*)$ are relatively large. Because of the Gaussian mixture pdf for the time-delay measurement errors, other measurements may have larger errors, and their corresponding likelihood ratios are then relatively small. As a consequence, the detection statistic in Eq. (34) that uses all measurements may be unsuitable for robust and accurate detection of optimal ML solutions.

An alternative detection statistic is proposed that uses only the measurements to which the estimated solution ϕ^* is well fitted. The number of such measurements $\tilde{K}$ is taken to be the smallest number of the target-originated measurements $\mathcal{Z}_{t_k}$ sufficient to convey the information about the target parameter vector V (e.g., $\tilde{K}=4$ or 5). Then, $\tilde{K}$ maximal values of $\Lambda^{(k)}(Z_{t_k},\phi^*)$ over all $k\in\{1,...,N\}$ are selected and used to compute the test statistic. This is done by placing the ratios $\{\Lambda^{(k)}(Z_{t_k},\phi^*)\}_{k=1}^{N}$ in decreasing order of their values (where the corresponding ordering is denoted by $\tilde{k}$) and by summing the first $\tilde{K}$ ordered values, i.e., as

$$\tilde{\Lambda}(\mathcal{Z},\tilde{K},\phi^*)=\sum_{\tilde{k}=1}^{\tilde{K}}\Lambda^{(\tilde{k})}(Z_{t_{\tilde{k}}},\phi^*). \tag{37}$$

The test is constructed such that under the hypothesis H_0 the algorithm converges to the global ML solution and the estimated parameter vector ϕ^* is accepted. Under the hypothesis H_1 the solution is assumed to correspond to a local maximum in which case ϕ^* is discarded. Hence, the test at level of significance α is defined as

$$\begin{aligned}&\text{if } \tilde{\Lambda}(\mathcal{Z},\tilde{K},\phi^*)\leqslant T_\alpha \quad \text{then } H_0 \text{ is rejected}\\ &\qquad\qquad\qquad\quad (H_1 \text{ is accepted})\\ &\qquad\text{else} \qquad H_0 \text{ is accepted.}\end{aligned} \tag{38}$$

In a situation where the presence of the target is not known, a similar test can be used to validate the existence of a target corresponding to the estimated track. The decision mechanism now distinguishes between two hypothesis: (1) that the track exists and the estimated parameter vector ϕ^* is the

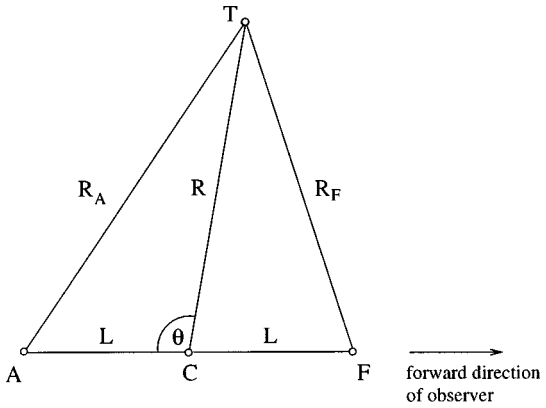

FIG. 2. The geometry used in the simulations for passive localization.

global solution (hypothesis H_0), and (2) that there is no track or that ϕ^* is a local maximum (hypothesis H_1). The testing H_0 against H_1 in this case is the same as in Eq. (38). The global maximum detected when H_0 is true leads to the acceptance of the target hypothesis, whereas suboptimal ML solution in this case represents a missed detection.

The estimation of the pdf of the detection statistics $\tilde{\Lambda}(\mathcal{Z},\tilde{K},\phi^*)$ is discussed in Sec. III.

III. SIMULATION RESULTS AND DISCUSSION

The sensor geometry applied in the time delay analysis in the simulations is shown in Fig. 2. "F," "C," and "A" denote collinear equally spaced sensors with intersensor separation L. The sensors are assumed to be mounted onboard an observer platform, and the intersensor distance L is limited by the physical dimensions of the platform. The observer is moving with a constant velocity $[v_x^p, v_y^p]'$ and its position at time t is denoted by $[X_t^p, Y_t^p]'$.

Three scenarios with different target geometry are used to test the ML estimator discussed in Sec. II. The starting positions (at time $t^s=0$) and velocities of the target for these scenarios are given in Table I. The starting position of the observer is $[0\,\text{km}, 0\,\text{km}]'$ and the velocity is $[4.5\,\text{m/s}, 0\,\text{m/s}]'$.

For each scenario, $\Omega=100$ sets of target-originated simulated measurements are generated. The transients are observed at the time instants defined by $t_1=t^s$, $t_k=t_{k-1}+\Delta t_k$, $k=2,...,N^T$, where Δt_k is uniformly distributed in the interval $[\Delta t_{\min}, \Delta t_{\max}]$, with $\Delta t_{\min}=10$ s, $\Delta t_{\max}=4$ min. The time delays of arrival are measured between pairs of sensors C and A, and F and C (see Fig. 2), so that the number of measurements for a transient at time t_k is $n_{t_k}=2$. The exact time delay between sensors C and A is denoted by $\tau_{t_k}^{(1)}$, and between sensors F and C by $\tau_{t_k}^{(2)}$. Given range R_{t_k} and bearing angle θ_{t_k} to the transient source, these time delays are computed as

$$\tau_{t_k}^{(1)} = \frac{1}{c}\left(R_{t_k} - \sqrt{R_{t_k}^2 + L^2 - 2LR_{t_k}\cos\theta_{t_k}}\right), \tag{39}$$

$$\tau_{t_k}^{(2)} = \frac{1}{c}\left(\sqrt{R_{t_k}^2 + L^2 + 2LR_{t_k}\cos\theta_{t_k}} - R_{t_k}\right), \tag{40}$$

where c denotes the velocity of sound in the medium (water), which is assumed to be homogeneous. Similarly, range R_{t_k} and bearing angle θ_{t_k} are computed, respectively, as

$$R_{t_k} = \sqrt{(X_{t_k} - X_{t_k}^p)^2 + (Y_{t_k} - Y_{t_k}^p)^2}, \tag{41}$$

$$\theta_{t_k} = \pi/2 + \tan^{-1}\left[\frac{X_{t_k} - X_{t_k}^p}{Y_{t_k} - Y_{t_k}^p}\right] + C_{t_k}^p, \tag{42}$$

where $C_{t_k}^p$ is the sensor array orientation which is assumed to be equivalent to the observer heading, so that $C_{t_k}^p = \tan^{-1}[v_y^p/v_x^p]$ for $v_x^p > 0$.

The time-delay error distribution is taken to be equivalent for both time delays, and for all t_k, so that $\epsilon_{t_k}^{(r)} = \epsilon$ and $\sigma_{t_k}^{(r,n)} = \sigma^{(n)}$ for $n=1,2$, and $r=1,2$. The values used in the simulations are: $\sigma^{(1)}=20\ \mu$s, $\sigma^{(2)}=100\ \mu$s, and $\epsilon=0.25$. The intersensor separation is $L=50$ m and the velocity of sound in water is $c=1500$ m/s. The observation area is limited to have a maximum range of 12 km and bearings between θ_0 and $\pi-\theta_0$, where $\theta_0=\pi/6$. All (noisy) measurements that fall outside this area are discarded so that the effective number of target-originated transients in a simulation is between $N^T=12$ and $N^T=17$.

Each target-originated measurement set is combined with a set of clutter measurements. The number of clutter measurements per km^2 per hour has a Poisson distribution with mean m, and the measurements occur at the time instants randomly chosen from the time interval that starts 8 min before and finishes 8 min after the observation time for the target-originated measurement set.

The ML and MAP estimators based on the EM algorithm are sensitive to the choice of the initial values of the parameters (Gauvrit *et al.*, 1997; Streit and Luginbuhl, 1995). Poor initialization of the algorithm may result in convergence to suboptimal solutions, i.e., the algorithm may converge only to a local ML solution and not to a global solution. The technique commonly applied to improve the convergence rates of these algorithms is to initially inflate the measurement variance (covariance) inside the E step in the EM process (Willett *et al.*, 2002). The initial iteration of the EM algorithm is performed with a large variance and the variance is decreased (or *deflated*) in the subsequent iterations.

In this application, to find the value of the target parameter vector V to initialize the ML estimator, an annealing M-estimator (AM-estimator) (Carevic, 2003) is used. This technique is statistically less efficient than the proposed ML estimator as it does not explicitly utilize the knowledge of the measurement model. However, it is very robust and is

TABLE I. Starting target positions $[X_{t^s}, Y_{t^s}]'$ at time $t^s=0$ and velocities $[v_x, v_y]'$ for the three tracking scenarios.

Tracking scenario	X_{t^s} (km)	Y_{t^s} (km)	v_x (m/s)	v_y (m/s)
1	−4.0	4.5	6.0	2.2
2	−3.5	10.0	7.0	−2.5
3	−1.5	7.0	5.5	−0.2

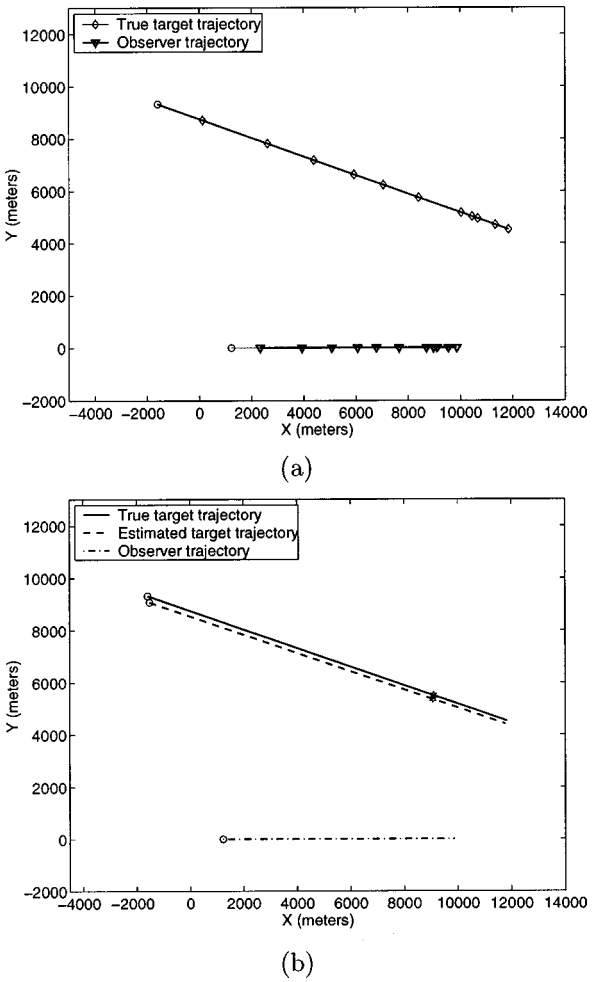

FIG. 3. A simulation corresponding to tracking scenario 2: (a) true target trajectory and observer trajectory; (b) true and estimated target trajectories. True and estimated positions of the target at the reference time t^* are denoted by the star symbols.

usually capable of finding an estimate of the target parameter vector in the vicinity of the global ML solution. The variance deflation method is also applied, whereby both variances in the Gaussian mixture model $\sigma_{t_i}^{(r,n)^2}$, $n=1,2$, are deflated by the factors {4,3,2.5,2,1.5} in the first several iterations of the EM process. On initialization both target and clutter are considered to be equally probable.

A simulation corresponding to tracking scenario 2 is shown in Fig. 3(a). The true target trajectory and the trajectory estimated using the proposed method are shown in Fig. 3(b). The noisy measurements $\{Z_{t_k}^{(1)}\}_{k=1}^{N}$ used in the simulation in Fig. 3 are shown in Fig. 4. True and estimated positions of the target at the reference time t^* in Fig. 3 are denoted by the star symbols. Also, symbols ''o'' denote starting positions of the observer and target.

The pdf of the detection statistic in Eq. (37), $\tilde{\Lambda}(\mathcal{Z},\tilde{K},\phi^*)$, under H_0 is estimated empirically using the following approximation:

$$P[\tilde{\Lambda}(\mathcal{Z},\tilde{K},\phi^*)|H_0]\approx P[\tilde{\Lambda}(\mathcal{Z},\tilde{K},\phi^{\text{true}})]. \tag{43}$$

ϕ^{true} denotes true model parameters where $\xi_{t_k}^{(r,1)}=(1-\epsilon)$, $\xi_{t_k}^{(r,2)}=\epsilon$, and $\xi_{t_k}^{(r,3)}=0$ for the target-originated measurements, $\xi_{t_k}^{(r,1)}=\xi_{t_k}^{(r,2)}=0$ and $\xi_{t_k}^{(r,3)}=1$ for clutter measurements, and V^{true} is the true target motion parameter vector. For the pdf estimation, the length of the target model $\tilde{N}^T$ in ϕ^{true} is taken to be equal to the mean number of the target-originated measurements over $\Omega=100$ sets that correspond to different tracking scenarios (see Table I).

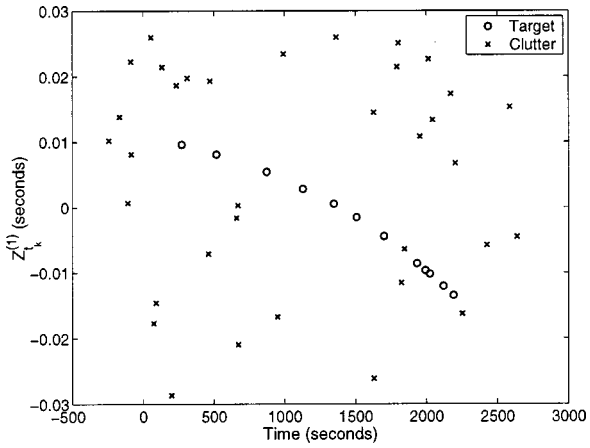

FIG. 4. Noisy time-delay measurements used in tracking simulation in Fig. 3.

The pdf's of the detection statistic estimated using the ML solutions from the tracking simulations, $P[\tilde{\Lambda}(\mathcal{Z},\tilde{K},\phi^*)|H_0]$, and using the approximation $P[\tilde{\Lambda}(\mathcal{Z},\tilde{K},\phi^{\text{true}})]$, for $\tilde{K}=5$ and $\tilde{N}^T=15$, are shown in Fig. 5. It can be seen that the approximation in Eq. (43), $P[\tilde{\Lambda}(\mathcal{Z},\tilde{K},\phi^{\text{true}})]$, well models the true distribution of the detection statistics, and is much easier to compute. Using the estimated pdf $P[\tilde{\Lambda}(\mathcal{Z},\tilde{K},\phi^{\text{true}})]$ the threshold T_α in Eq. (25) is determined for the significance level $\alpha=0.15\%$.

Performance of the proposed ML estimator

The performance of the ML estimator is measured using the mean absolute distance between the true target trajectory (X_t,Y_t) and the trajectory that corresponds to the estimated parameters (X_t^*,Y_t^*). For each simulation l, $l=1,...,\Omega$

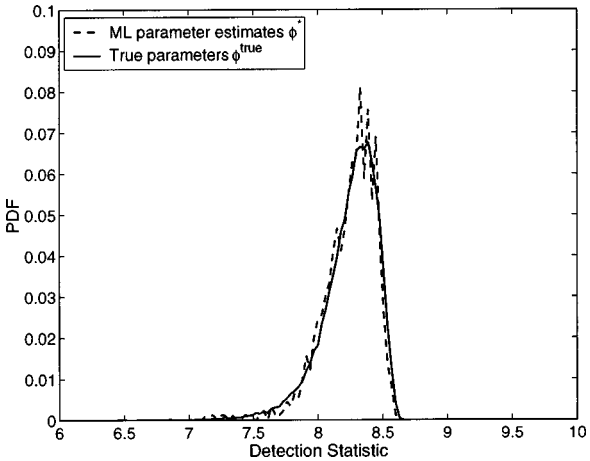

FIG. 5. Pdf's of the detection statistic estimated using global ML solutions obtained from the algorithm, ϕ^*, and using true parameters ϕ^{true} for $\tilde{K}=5$ and $\tilde{N}^T=15$.

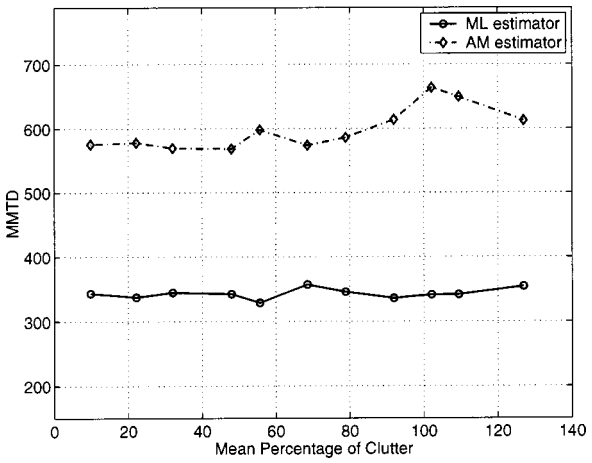

FIG. 6. The results of testing the ML estimator and comparison with the AM-estimator for tracking scenario 1.

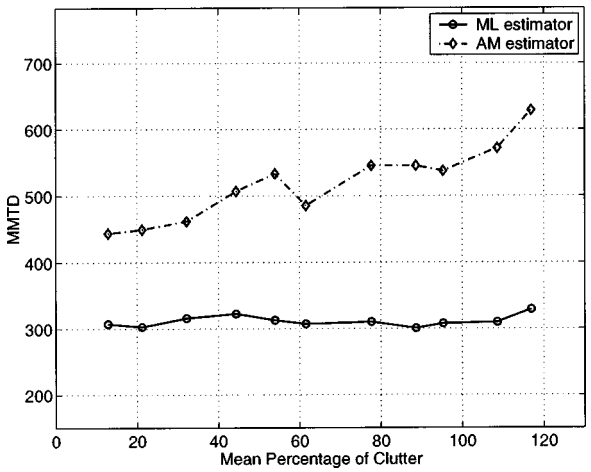

FIG. 7. The results of testing the ML estimator and comparison with the AM-estimator for tracking scenario 2.

$=100$, the detection test is performed as described above. If ϕ_l^* is accepted as the global solution, the mean trajectory distance (MTD) is computed as

$$\mathrm{MTD}_l=\frac{1}{N_l^T}\sum_{k=1}^{N_l^T}\sqrt{\Delta X_{t_{l,k}}^2+\Delta Y_{t_{l,k}}^2}, \tag{44}$$

with

$$\Delta X_{t_{l,k}}=X_{t_{l,k}}-X_{t_l^*,k}^*, \tag{45}$$

$$\Delta Y_{t_{l,k}}=Y_{t_{l,k}}-Y_{t_{l,k}}^*. \tag{46}$$

$X_{t_{l,k}}^*$ and $Y_{t_{l,k}}^*$ are obtained using the estimated target parameter vector V_l^*, where $t_{l,k}$, $k=1,...,N_l^T$ denote the time instants of the target-originated measurements in the measurement batch. The mean of the MTD over all accepted simulations Ω', denoted by MMTD, is then computed as

$$\mathrm{MMTD}=\frac{1}{\Omega'}\sum_{\Omega'}\mathrm{MTD}_l. \tag{47}$$

The tests are done for a range of values of the parameter of the Poisson distribution m. For each m, the mean percentage of clutter measurements (MPC) is computed as the mean of the number of clutter measurements relative to the number of the target-originated measurements over all accepted simulations Ω', i.e., as

$$\mathrm{MPC}=\frac{100}{\Omega'}\sum_{\Omega'}\frac{N_l^C}{N_l^T}(\%). \tag{48}$$

The MMTD values as a function of the mean percentage of clutter for the three tracking scenarios under consideration are shown in Figs. 6–8 where the MMTD values are measured in meters. The results are presented for the proposed ML estimator and the AM-estimator. The estimates obtained using the ML procedure are, on average, much more accurate than those obtained using the AM-estimator.

The experiment is repeated using $\Omega=200$ sets of target-originated measurements corresponding to each of the three tracking scenarios, where the mean percentage of clutter measurements in a batch [defined by Eq. (48)] varies over a range of values as discussed above. The results obtained using the 6600 simulated batches are utilized to estimate the probability of track detection P_{td}. This probability is $P_{\mathrm{td}}=0.96$. Similarly, 1000 batches that contain only clutter measurements are used to estimate the probability of false alarm P_{fa}. This probability is $P_{\mathrm{fa}}=0$.

IV. CONCLUSION

An approach to tracking a single target in cluttered environments using multilateral time-delay measurements has been presented. The measurement errors are modeled as having (possibly different) Gaussian mixture pdf's. The method utilizes an ML optimization approach based on the EM algorithm, and it is shown that the ML estimates of the target model parameters can be obtained using a nonlinear LS method. A detection mechanism that can validate the correctness of the estimated track parameters and verify the existence of target has also been formulated.

Under consideration has been the problem of tracking underwater targets based on measurements derived from passively sensed transient signals. The proposed method is applied to the time-delay measurements derived using a linear array of sensors mounted on board an observer platform.

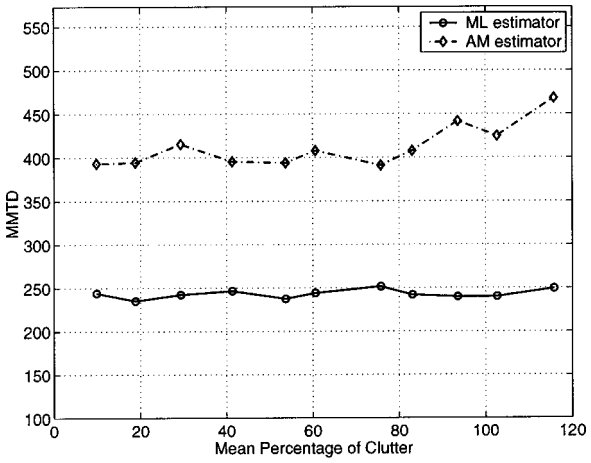

FIG. 8. The results of testing the ML estimator and comparison with the AM-estimator for tracking scenario 3.

Extensive tests are carried out on simulated data for several scenarios with different tracking geometry, and it is shown that the proposed method performs better when compared to an annealing M-estimator.

ACKNOWLEDGMENT

The author thanks Dr. P. Willett for his comments on the paper.

[1]Here, exact target times are approximated by observer times, as is a common practice in underwater target tracking. The main effect of using observer instead of target times for passive tracking of relatively slow targets (compared to the velocity of sound propagation in water) is the introduction of a near-constant time offset into target location. For very slow targets, such as submarines, this effect can be assumed to be negligible.

Avitzour, D. (**1992**). ''A maximum likelihood approach to data association,'' IEEE Trans. Aerosp. Electron. Syst. **28**, 560–566.

Bar-Shalom, Y., and Fortman, T. E. (**1988**). *Tracking and Data Association* (Academic, New York).

Barsanti, R. J. (**2002**). ''Improved acoustic target tracking using wavelet based time difference of arrival information,'' in Proc. IEEE SoutheastCon 2002 (Columbia, SC), pp. 451–456.

Bouvet, M., and Schwartz, S. C. (**1988**). ''Underwater noises: Statistical modeling, detection, and normalization,'' J. Acoust. Soc. Am. **83**, 1023–1033.

Carevic, D. (**2003**). ''Robust estimation techniques for target-motion analysis using passively sensed transient signals,'' IEEE J. Ocean. Eng. **28**, 262–270.

Carter, G. C. (**1981**). ''Time delay estimation for passive sonar signal processing,'' IEEE Trans. Acoust., Speech, Signal Process. **29**, 463–470.

Carter, G. C., and Robinson, E. R. (**1993**). ''Ocean effects on time delay estimation requiring adaptation,'' IEEE J. Ocean. Eng. **18**, 367–377.

Ching, P. C., So, H. C., and Wu, S. Q. (**1999**). ''On wavelet denoising and its application to time delay estimation,'' IEEE Trans. Signal Process. **47**(10), 2879–2882.

Dempster, A. P., Liard, N. M., and Rubin, D. B. (**1977**). ''Maximum likelihood from incomplete data via EM algorithm,'' J. R. Stat. Soc. Ser. B. Methodol. **39**, 1–38.

Ferguson, B. G. (**1989**). ''Improved time-delay estimates of underwater acoustic signals using beamforming and prefiltering techniques,'' IEEE J. Ocean. Eng. **14**, 238–244.

Ferguson, B. G., and Cleary, J. L. (**2001**). ''*In situ* source level and source position estimates of biological transient signals produced by snapping shrimp in an underwater environment,'' J. Acoust. Soc. Am. **109**, 3031–3037.

Gauvrit, H., Le Cadre, J. P., and Jauffret, C. (**1997**). ''A formulation of multitarget tracking as an incomplete data problem,'' IEEE Trans. Aerosp. Electron. Syst. **33**, 1242–1257.

Gong, Y. (**2002**). ''Noise-dependent Gaussian mixture classifiers for robust rejection decision,'' IEEE Trans. Speech Audio Process. **10**, 57–64.

Hahn, W. R. (**1975**). ''Optimum signal processing for passive sonar range and bearing estimation,'' J. Acoust. Soc. Am. **58**, 201–207.

Hassab, J. C., Guimond, B. W., and Nardone, S. C. (**1981**). ''Estimation of location and motion parameters of a moving source observed from a linear array,'' J. Acoust. Soc. Am. **70**, 1054–1061.

Hutchins, R. G., and Dunham, D. T. (**1997**). ''Evaluation of a probabilistic multihypothesis tracking algorithm in cluttered environment,'' in Proc. Thirtieth Asilomar Conf. on Signals, Systems and Computers, Vol. 2 (Los Alamitos, CA), pp. 1260–1264.

Ianniello, J. P. (**1982**). ''Time delay estimation via cross-correlation in the presence of large estimation errors,'' IEEE Trans. Acoust., Speech, Signal Process. **30**, 998–1003.

Jauffret, C., and Bar-Shalom, Y. (**1990**). ''Track formation with bearing and frequency measurements in clutter,'' IEEE Trans. Aerosp. Electron. Syst. **26**, 999–1010.

Kassam, S. A. (**1988**). *Signal Detection in Non-Gaussian Noise* (Springer, New York).

Kirubarajan, T., and Bar-Shalom, Y. (**1995**). ''Low observable target motion analysis using amplitude information,'' IEEE Trans. Aerosp. Electron. Syst. **32**, 1367–1384.

Pflug, L. A., Ioup, G. E., Ioup, J. W., Field, R. L., and Leclere, J. H. (**1993**). ''Time-delay estimation for deterministic transients using second- and higher-order correlations,'' J. Acoust. Soc. Am. **94**, 1385–1399.

Press, W. H., Teukolsky, S. A., Vetterling, W. T., and Flannery, B. P. (**1995**). *Numerical Recipes in C*, 2nd ed. (Cambridge University Press, Cambridge).

Shertukde, H. M., and Bar-Shalom, Y. (**1990**). ''Detection and estimation for multiple targets with two omnidirectional sensors in the presence of false measurements,'' IEEE Trans. Acoust., Speech, Signal Process. **38**, 749–763.

Stotts, S. A., James, L. M., and Bedford, N. (**1997**). ''Multiple-source localization using GPS technology and received arrival time structure analysis in an air deployed system,'' IEEE J. Ocean. Eng. **22**, 576–582.

Streit, R. L., and Luginbuhl, T. E. (**1994**). ''Maximum likelihood method for probabilistic multi-hypothesis tracking,'' Proc. SPIE **2235**, 394–405.

Streit, R. L., and Luginbuhl, T. E. (**1995**). ''Probabilistic multi-hypothesis tracking,'' in *Studies in Probabilistic Multi-Hypohesis Tracking and Related Topics*, edited by R. L. Streit (NUWC, Newport, RI), pp. 5–50.

Tantum, S. L., and Nolte, L. W. (**1998**). ''Tracking and localizing a moving source in an uncertain shallow water environment,'' J. Acoust. Soc. Am. **103**, 362–372.

Willett, P., Ruan, Y., and Streit, R. (**2002**). ''PMHT: Problems and some solutions,'' IEEE Trans. Aerosp. Electron. Syst. **38**, 738–754.

Wilmut, M. J., and Ozard, J. M. (**1998**). ''Detection performance of two efficient source tracking algorithms for matched-field processing,'' J. Acoust. Soc. Am. **104**, 3351–3355.

Xerri, B., Cavassilas, J.-F., and Borloz, B. (**2002**). ''Passive tracking in underwater acoustic,'' Signal Process. **82**, 1067–1085.

The representation of periodic sounds in simulated sustained chopper units of the ventral cochlear nucleus

Lutz Wiegrebe[a)]
Dept. Biologie II, Universität München, Luisenstrasse 14, 80333 München, Germany

Ray Meddis[b)]
Psychology Department, University of Essex, Wivenhoe Park, Colchester, CO4 3SQ, United Kingdom

(Received 11 July 2003; accepted for publication 1 December 2003)

The nature of the neural processing underlying the extraction of pitch information from harmonic complex sounds is still unclear. Electrophysiological studies in the auditory nerve and many psychophysical and modeling studies suggest that pitch might be extracted successfully by applying a mechanism like autocorrelation to the temporal discharge patterns of auditory-nerve fibers. The current modeling study investigates the possible role of populations of sustained chopper (Chop-S) units located in the mammalian ventral cochlear nucleus (VCN) in this process. First, it is shown that computer simulations can predict responses to periodic and quasiperiodic sounds of individual Chop-S units recorded in the guinea-pig VCN. Second, it is shown that the fundamental period of a periodic or quasiperiodic sound is represented in the first-order, interspike interval statistics of a population of simulated Chop-S units. This is true across a wide range of characteristic frequencies when the chopping rate is equal to the $f0$ of the sound. The model was able to simulate the results of psychophysical studies involving the pitch height and pitch strength of iterated ripple noise, the dominance region of pitch, the effect of phase on pitch height and pitch strength, pitch of inharmonic stimuli, and of sinusoidally amplitude modulated noise. Simulation results indicate that changes in the interspike interval statistics of populations of Chop-S units compare well with changes in the pitch perceived by humans. It is proposed that Chop-S units in the ventral cochlear nucleus may play an important role in pitch extraction: They can convert a purely temporal pitch code as observed in the auditory nerve into a temporal *place* code of pitch in populations of cochlear-nucleus, Chop-S with different characteristic frequencies, and chopping rates. Thus, populations of cochlear-nucleus Chop-S units, together with their target units presumably located in the inferior colliculus, may serve to establish a stable rate-place code of pitch at the level of the auditory cortex. [DOI: 10.1121/1.1643359]

PACS numbers: 43.64.Bt, 43.64.Qh, 43.66.Ba [WPS] Pages: 1207–1218

I. INTRODUCTION

Tracking the pitch of periodic sounds is one of the fundamental tasks of the auditory system. Periodic sounds in nature are normally harmonically structured. The perceived pitch of the stimulus can typically be matched to a sinusoid whose frequency is the same as the fundamental of the harmonic series ($F0$). This perception persists even when there is no auditory excitation in the $F0$ frequency region, indicating that pitch perception is a synthetic process. The pitch percept is also particularly strong when the harmonic components are well separated relative to the frequency resolving power of the cochlea, suggesting that pitch often involves the combination of information taken across a range of frequency-selective channels. Any model of the physiological basis of pitch processing must take these basic facts into account.

Historically, models of pitch perception have championed either spectral (e.g., Terhardt, 1979; Goldstein, 1973) or temporal (e.g., Schouten, 1970; Licklider, 1951) explanations. Spectral explanations focus on the frequency-resolving properties of the basilar membrane, while temporal explanations seek to show that the temporal resolution of the auditory-nerve (AN) response is an adequate basis for pitch extraction. Models using an autocorrelation analysis of auditory-nerve response patterns (Licklider, 1959; Lyon, 1984; Meddis and Hewitt, 1991a,b) have suggested that pitch could, in principle, be extracted from the temporal pattern of activity in the peripheral input. More direct evidence in favor of a temporal code for pitch comes from electrophysiological recordings from the cat auditory nerve (Horst *et al.*, 1986; Cariani and Delgutte, 1996a,b): They showed that temporal analyses such as autocorrelation, when applied to the auditory-nerve temporal discharge pattern, results in a reliable estimate of the stimulus pitch for a comprehensive set of test conditions.

The study to be described below takes this analysis as its starting point, but asks how this temporal information is extracted physiologically and made available for later processing. Physiological mechanisms that might serve the process that extracts pitch information from the temporal pattern of activity in the AN have not yet been discovered but may be located at least partly in the cochlear nucleus (CN), the only nucleus to receive direct AN input. de Cheveigne (1998) adopted a temporal approach and proposed that pitch percep-

[a)]Electronic mail: lutzw@lmu.de
[b)]Electronic mail: rmeddis@essex.ac.uk

tion may involve ''an array of delay lines and inhibitory gating.'' Shamma and Klein (2000) have suggested a template approach based on across-frequency coincidence detection. They treat the cochlear nucleus as a second stage containing ''a matrix of coincidence detectors that compute the average pairwise instantaneous correlation (or product) between responses from all characteristic frequencies (CFs) across the channels.'' Both these approaches are functionally plausible but await direct physiological confirmation. Below it will be suggested that the intrinsic membrane properties of sustained-chopper cells (Chop-S) provide a possible basis for the transformation of an auditory-nerve, temporal pitch code into a temporal *place* code of pitch at the level of the CN. This approach is based on the measured physiological responses of Chop-S units to pitch sounds, and the model has the advantage that it can be tuned to match the physiological responses. Of course, it remains the case that the autocorrelation analysis that has proved successful at the level of the AN would also work at the level of the cochlear nucleus, given that many units preserve the fine-structure information that is present in the AN. However, this would still leave the question as to how this autocorrelation is performed and at what level in the nervous system.

The cochlear nucleus contains different cell types that can be separated both anatomically and in terms of their electrophysiological response characteristics (Blackburn and Sachs, 1989). Shofner (1991, 1999) showed that primarylike units in the chinchilla ventral cochlear nucleus were well able to represent the period of rippled noise and iterated rippled noise in their temporal discharge patterns. Wiegrebe and Winter (2001) and Winter *et al.* (2001) have suggested that Chop-S units in the ventral cochlear nucleus (VCN) may play a role in pitch perception: Chop-S units are characterized by a regular response pattern in response to pure tones at their CF (Young *et al.*, 1988). More recently, it has been shown that the temporal discharge pattern becomes more regular when a Chop-S unit is stimulated with a periodic stimulus whose $f0$ is near the unit's intrinsic chopping rate (CR, Winter *et al.*, 2001; Wiegrebe and Winter, 2001). This selective enhancement of regularity is the focus of the model to be described.

The model consists of a large number of simulated Chop-S units organized according to their CF and CR. An ensemble of units with the same CR, but spread across CFs, is called a ''Chop-S population.'' Each Chop-S population will synchronize its activity to the $f0$ of the input stimulus if the $f0$ is close to the CR of the Chop-S population. The important feature of Chop-S units is that this synchronization to $f0$ does not only occur in Chop-S units that are spectrally tuned to $f0$ but also in Chop-S units that are spectrally tuned to integer multiples (harmonics) of $f0$. Information about the $f0$ of the input is therefore distributed across all chopping units in terms of the amount of synchronization present in each, i.e., a synchronization/place code. This synchronization is quantified in the model as its normalized CR-locked rate; its computation is described below. A global estimate of the amount of synchronization to a particular fundamental frequency can be found by averaging the normalized CR-locked rate across a Chop-S population, i.e., across the Chop-S units with the same CR but different CFs. This is used as the model's estimate of the strength of a pitch equivalent to the CR. If pitch strength is estimated at a number of values of CR, the CR yielding the highest value can be used to predict the pitch most likely to be selected in a psychophysical pitch-matching experiment.

Clearly, this model can only represent the first stage of a much longer process whereby the synchronization observed in individual Chop-S units is further processed and combined to give a pitch percept. Given that the chopper units are thought to project to the inferior colliculus, it is possible that the next processing step is located there. It may involve coincidence units that are driven when populations of units with similar CF and CR fire in synchrony but not otherwise. Hewitt and Meddis (1994) have already shown how such circuits can convert a change in synchrony into a rate change. However, the present modeling study is only concerned with the processing observed at the level of the cochlear nucleus. The model is intended to demonstrate that the activity of the chopper units provides an adequate basis for later stages of pitch processing. It is already clear that auditory-nerve activity supplies an adequate basis for predicting psychophysical pitch judgments (Horst *et al.*, 1986; Cariani and Delgutte, 1996a,b). The aim of this study is to move forward to the next stage by identifying Chop-S units as the most likely carrier of pitch information by virtue of their ability to synchronize *selectively* to particular pitches. This selectivity converts the temporal code found in the auditory nerve to a temporal *place* code in the cochlear nucleus. As such, it makes a unique and important contribution to pitch processing in the auditory brainstem.

II. SIMULATIONS

A. Simulations of electrophysiological recordings

1. Model structure

The computer model incorporated the Chop-S model of Hewitt *et al.* (1992). Other models (Ghoshal *et al.*, 1992; Lai *et al.*, 1994) could have been used, and it is not expected that they would yield fundamentally different results. The input to the Chop-S model used recently updated models of the auditory periphery. Two different peripheral models were used: one for the guinea pig when modeling physiological observations and one for humans when modeling psychophysical data. The models consisted of (a) a system of bandpass filters designed to simulate the effect of the outer- and middle ear; (b) a dual-resonance, nonlinear filterbank with parameters set to match properties of the guinea pig (Meddis *et al.*, 2001); (c) mechanical to electrical transduction in the IHC; (d) IHC-auditory-nerve (AN) synapse (Sumner *et al.*, 2002); (e) AN spike generation sufficient to give 15 independent fibers with the same CF to each Chop-S unit; (f) the application of a 0.75-ms refractory time; and (g) Chop-S unit dendritic filtering using a first-order low-pass filter with a cutoff frequency of 300 Hz.

The Chop-S units were modeled using the algorithm suggested by MacGregor (1987). Fifteen input fibers were used because recent physiological investigations have revealed that the 60 fibers suggested in Hewitt *et al.* (1992)

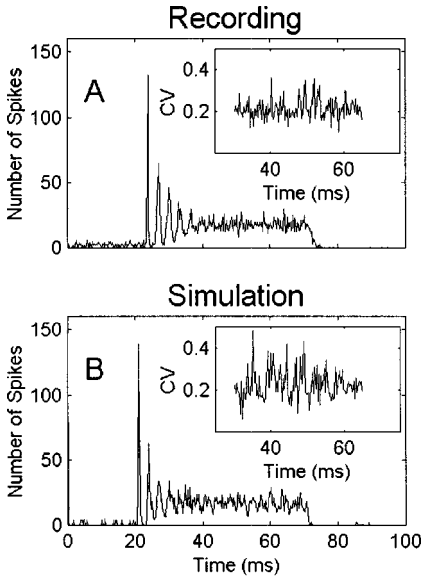

FIG. 1. Comparison of responses of a recorded Chop-S unit with a CF of 3 kHz and a chopping rate (CR) of 250 Hz (A) and its simulation (B) in response to 250 repetitions of 50-ms CF tones at 50 dB above threshold. Peristimulus time histograms are shown in (A) and (B); the coefficients of variation (CV) based on a regularity analysis are shown in the figure insets. Note that the simulation captures the main features of both the PSTH and the regularity analysis.

may be too many. Ferragamo *et al.* (1998), using *in vitro* techniques, estimated that at least five AN fibers converge on the dendrites of VCN stellate cells. We found that five input fibers were too few to generate realistic simulations of our animal data. The CF of the simulated Chop-S unit is determined by the center frequency of the cochlear filter driving its input AN fibers; the CR of the unit was manipulated by changing the potassium recovery time constant (Hewitt *et al.*, 1992).

All model parameters can be obtained from ⟨http://www.essex.ac.uk/psychology/hearinglab/models⟩. The model was implemented using publicly available computer coded modules in the Development System for Auditory Modelling (DSAM) library (footnote 1). The DSAM modules were called from MATLAB programs that generated the stimuli and analyzed the response of the modeled Chop-S units.

The electrophysiological recordings shown here are taken from the study by Winter *et al.* (2001).

2. Response to best-frequency pure tones

The parameters of the model were tuned so that the model generated pure-tone responses as similar as possible to those recorded in guinea pig in an earlier study (Winter *et al.*, 2001; Wiegrebe and Winter, 2001). Figure 1(A) shows the peristimulus, time-histogram (PSTH) of a Chop-S unit with a CF of 3 kHz to 250 repetitions of 50-ms CF tones presented at 50 dB above unit threshold. Figure 1(B) shows the PSTH response of the model to the same stimulus. The figure insets show the coefficient of variation (CV) of the responses. The CV is computed by dividing the standard deviation of the interspike intervals by its mean (Blackburn and Sachs, 1989). Both animal and model data have an average CV close to 0.2.

3. Responses to complex tones

Hewitt *et al.* (1992) showed that simulated Chop-S units were able to predict the response characteristics of recorded Chop-S units when stimulated by sinusoidally amplitude modulated (SAM) tones. In our study, the refined Chop-S model was tested with an extended set of stimuli including iterated rippled noise (IRN) and harmonic complexes. The individual tone components of the harmonic complexes were added in either cosine phase (CPH) or random phase (RPH). The IRN stimuli were generated in an add-same configuration (Yost, 1996a). They are designated "IRNS(d,g,n)" where "d" is the delay in ms, "g" is the linear gain in the delay loop, and "n" is the number of iterations. Both RPH complexes and IRN stimuli were refreshed for every presentation for both recording and simulation. The $f0$ (equivalent to the IRN delay reciprocal) ranged from 31.25 to 1000 Hz.

Responses were typically obtained using 25 repetitions of 409.6-ms stimuli generated with 20-ms, raised-cosine ramps at a sampling rate of 20 kHz. The presentation level was set so that neural rate responses were always well above threshold. First-order interspike interval histograms (ISIHs) in response to periodic sounds are shown in Fig. 2. Abeles (1982) introduced a method to quantify interspike interval distributions independent of binwidth and overall firing rate. The method is easily implemented by dividing the number of intervals in a bin of an interspike interval histogram by the product of binwidth and the overall number of interspike intervals. All ISIHs presented here are expressed in terms of firing rate as suggested by Abeles (1982). The recorded unit has a CR of 250 Hz and is the same unit as shown in Fig. 1. The figure is arranged with animal ISIHs in the left three columns and the model ISIHs in the right three columns. The three columns represent the response to IRN, RPH, and CPH, respectively. $F0$ increases from bottom to top (see the central column). For all stimuli except the CPH with lower $f0$'s, the ISIHs of both animal data and model response show a pronounced mode around 4 ms, regardless of the $f0$ of the signal. This reflects the intrinsic chopping of the unit. However, this mode becomes taller and thinner when the $f0$ of the signal is the same as the CR of the unit (250 Hz; equivalent to a chopping period of 4 ms).

Note that simulated responses to CPH tones show some deviations from the physiological data. Specifically, the ISIH shows some temporal fine structure which is absent in the recorded data. The lack of fine structure in the recorded data may result from the influence of temporally random inhibition, as suggested by Lai *et al.* (1994).

Overall firing rate responses for the same recordings and simulations are shown in Fig. 3. For IRNS and RPH stimuli, rate responses are largely independent of the $f0$ (fine and strong continuous lines). This result agrees with previous observations on modulation tuning in chopper units (Frisina *et al.*, 1990a,b). However, with CPH stimulation alone (dashed lines), both the recordings and simulations show a pronounced increase in the rate response with increasing $f0$. CPH closely resemble click trains. At very low $f0$'s, the Chop-S unit responds with a single spike per click. As these become fewer with decreasing $F0$, the rate response decreases.

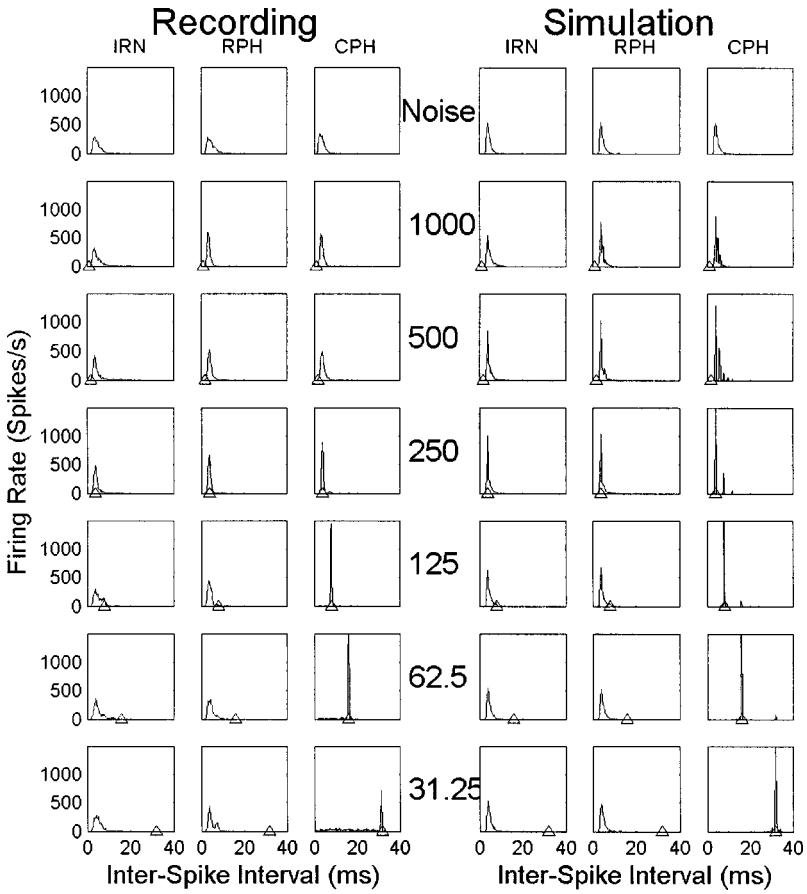

FIG. 2. Interspike interval histograms (ISIHs) of the 3-kHz Chop-S unit and its simulation as shown in Fig. 1 in response to harmonic complex tones and iterated rippled noise. The stimulus $F0$ (=1000/delay for IRNS) is given in the middle column. Stimuli were either IRNS(d,1,16), random-phase harmonic complexes (RPH), or cosine-phase complexes (CPH). The ordinate of the ISIHs is scaled in terms of firing rate after Abeles (1982) to make the ISIHs independent of binwidth and overall firing rate. Note that when the stimulus $F0$ matches the chopping rate (250 Hz), intervals are redistributed in favor of the interval corresponding to $F0$ (upward triangles).

Frisina *et al.* (1990a,b) used amplitude modulated pure tones to demonstrate bandpass modulation tuning functions in VCN chop-S units. This shows that the Chop-S unit synchronized its discharges with the stimulus modulation frequency for only a narrow range of modulation frequencies. A similar phenomenon can be demonstrated with IRN stimuli but a different method of analysis is required to show it, because IRN and RPH stimuli are not amenable to synchronization analysis. This is because their phase spectrum is random and, for IRN stimulation, the phase spectrum is also time variant. Thus, any analysis of regularity or synchrony with this kind of stimulation must be primarily based on interspike interval statistics.

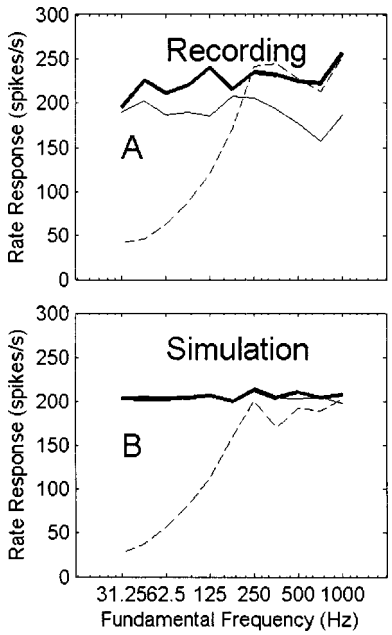

FIG. 3. Overall firing rate responses of the recording shown in Fig. 2. Note that both in the recording (A) and the simulation (B) the rate response is independent of the stimulus $F0$ when the stimuli were IRNS or RPH (fine and strong continuous lines). With CPH stimulation (dashed lines), however, the rate response increases with increasing $F0$ because of the transient periodic envelope fluctuation of the CPH.

Shofner (1999) quantified changes in the height of the first peak in the neural autocorrelogram (equivalent to an all-order, interspike interval analysis) using the formula

$$\text{Normalized, CR-locked rate} = \frac{R_\tau - R_{\text{ave}}}{R_{\text{ave}}},$$

where R_τ equals the ISIH firing rate at an interspike interval corresponding to the CR of the unit and R_{ave} equals the ISIH firing rate averaged across all interspike intervals. As the ISIH firing rates are independent of binwidth and overall firing rate (Abeles, 1982), also the normalized, CR-locked firing rate is independent of these parameters. We use the same measure of peak height here. Note, however, that, unlike in Shofner (1999), peak heights were calculated based on a first-order ISIH analysis, not on an all-order ISIH analysis. A first-order ISIH analysis was preferred because Winter *et al.* (2001) showed that the bandpass tuning to a specific range of $f0$'s is demonstrated only with a first-order ISIH analysis. Binwidths of 250 μs are used throughout the whole body of this paper.

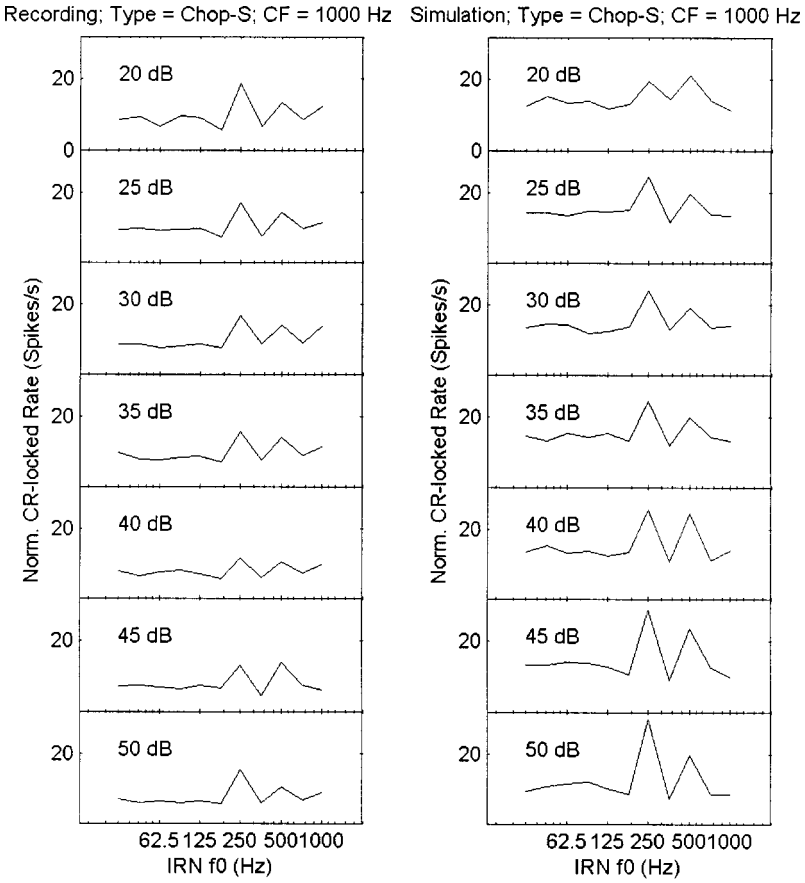

FIG. 4. Normalized CR-locked rate as a function of stimulus $f0$. The stimuli were IRNS(d,1,16), where d equals the $f0$ reciprocal. Recorded responses are shown in the left column; simulated responses are shown in the right column. The attenuation of the sound-pressure level of the stimulus is given in the individual panels. Note that when the IRNS $f0$ matches the chopping rate of the unit (250 Hz), there is a clear peak in the normalized CR-locked rate. Moreover, the position of this peak is not affected by the sound-pressure level of stimulation. Thus, this measure is quite stable against changes in sound-pressure level. A secondary peak is observed when the IRNS $f0$ is 500 Hz, i.e., twice the chopping rate. This feature of Chop-S units is discussed in Sec. III.

The normalized, CR-locked rate is shown as a function of $f0$ in Fig. 4. The stimuli were IRNS(d,1.16). Again, analyses of the guinea-pig recordings are shown in the left column; analyses of the simulated responses are shown in the right column. The recorded and the simulated unit was a Chop-S unit with a CF of 1000 Hz and a CR of 250 Hz. Different rows represent different stimulus attenuations as shown in the panels. Note that the normalized, CR-locked rate always shows a pronounced peak when the IRNS $f0$ matches the CR. Moreover, this peak is stable over the 30-dB range of sound levels tested and it is similar in the recording and the simulation. These data reflect the previous finding that Chop-S units provide a selectivity for $f0$ which is independent of sound level when the unit is in saturation (Wiegrebe and Winter, 2001). A secondary peak is seen at an $f0$ of 500 Hz, i.e., when the IRNS $f0$ is twice the CR. This secondary peak reflects the fact that a Chop-S unit is capable to lock onto an integer multiple of its input period. This is a possible neurophysiological foundation of octave confusions observed psychophysically. This topic is discussed in Sec. III.

B. Simulations of pitch phenomena in populations of Chop-S units

1. Model structure

Psychophysical studies of pitch perception have employed many different kinds of stimuli. The response of the model will now be evaluated using some of these stimuli. It was necessary to make two major changes to the model in order to make it suitable for evaluation against human, psychophysical data. First, the peripheral model was changed to match that of human listeners. Second, the model was expanded to included populations of Chop-S units with a wide range of CRs (about 100 to 550 Hz). The outer- and middle-ear transfer function was modified to fit the human outer- and middle-ear transfer function (Glasberg and Moore, 2002). Cochlear processing was implemented with a filterbank consisting of dual-resonance, nonlinear, bandpass filters fitted to explain human forward-masking measurements (Lopez-Poveda and Meddis, 2001). The filterbank consisted of 20 nonlinear filters with CFs equally spaced on a logarithmic frequency axis between 200 and 6000 Hz. The simulated Chop-S units form populations of Chop-S units where each population is determined by its common CR. A population consists of 20 Chop-S units (i.e., one per filter) with a common CR and CFs determined by the center frequencies of the auditory filters. In other respects, the model is identical to that used to simulate the physiological recordings.

2. Simulation paradigm

Unless otherwise stated, simulated responses are based on 25 repetitions of 409.6-ms stimuli presented at 40 dB above rate threshold. Stimuli are always windowed with 20-ms raised-cosine gates. Again, data are analyzed in terms of the Chop-S first-order ISIH scaled as suggested by Abeles (1982). Binwidth was always 250 μs. The dependent variable is the normalized CR-locked rate produced by a stimulus. The model implies that the normalized CR-locked rate reflects the perceived pitch strength, while the pitch itself is

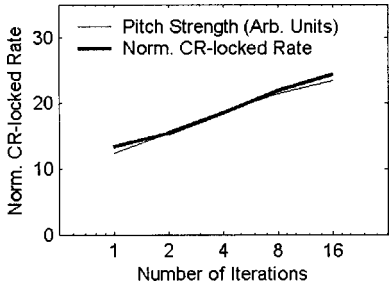

FIG. 5. The change of pitch strength (fine line; after Yost, 1996b) and normalized CR-locked rate (strong line) as a function of the number of iterations of IRNS(5,1,n). The normalized CR-locked rate was averaged over an array of 20 Chop-S units with CFs between 200 and 6000 Hz and a CR of 250 Hz. The data indicate the linear relationship between normalized CR-locked rate and the perceived pitch strength.

reflected in a distributed manner in terms of which population of Chop-S units shows the strongest normalized CR-locked rate.

3. Simulation 1: The representation of the pitch strength of IRN

Yost (1996b) showed that the pitch strength of IRN can be predicted using the height of the first major peak in the autocorrelation function of the stimulus waveform ($h1$). Specifically, the perceived pitch strength is proportional to 10 raised to the power of $h1$. The Chop-S model is evaluated by measuring the normalized CR-locked rate to IRN stimuli with different pitch strengths. The growth of the normalized CR-locked rate (averaged over a population of Chop-S units) is plotted against the number of iterations for both Yost's function and the model (Fig. 5). For this demonstration, the Chop-S units are spread over a wide range of CFs (200 to 6000 Hz) but CRs were fixed at 200 Hz, equal to the IRN delay reciprocal. Thus, the stimuli were IRNS(5,1,n), where n, the number of iterations, was 1, 2, 4, 8, and 16. The fine line in Fig. 5 represents Yost's estimate of pitch strength of the stimulus, based on $h1$, as a function of the number of iterations. The strong line show the normalized CR-locked rate averaged across an array of simulated Chop-S units. It can be seen that the normalized CR-locked rate for a population of simulated Chop-S units grows in proportion with Yost's estimate of perceived pitch strength. This is an important feature of the normalized CR-locked rate because it implies that the measure can be used additively when it is investigated how different units contribute to overall pitch strength. The feature is exploited in the subsequent simulations.

4. Simulation 2: The dominance region of harmonic sounds

For simple harmonic complexes, Ritsma (1967) showed that it is the low harmonics that contribute most to pitch strength. He asked listeners to match the pitch of a reference stimulus to that of a test stimulus. The test stimulus was a harmonic complex manipulated so that harmonics 1 to n were shifted down to be based on a lower $f0$ ($F0\_\text{low} = 0.9*F0$) and harmonics $n+1$ to 12 were shifted up to be based on a higher $f0$ ($F0\_\text{high} = 1.1*\text{F0}$). The reference

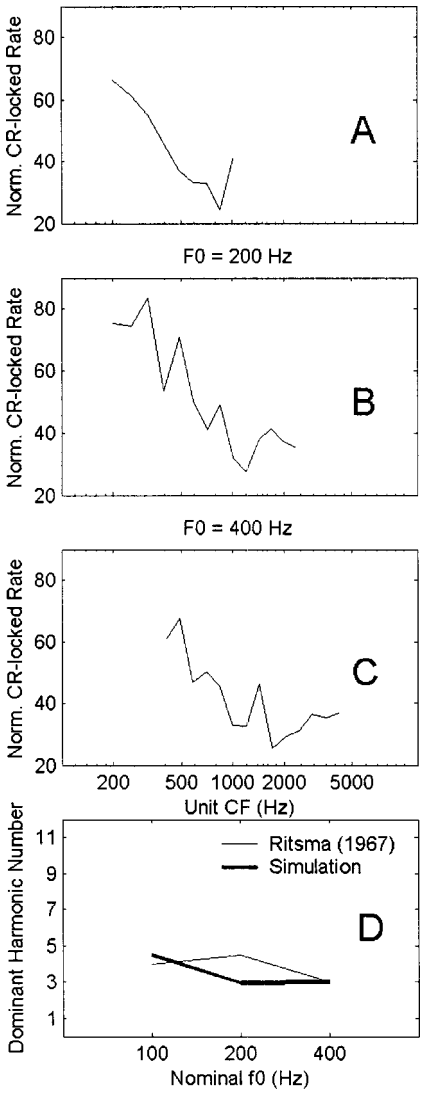

FIG. 6. Simulated neural correlates of the dominance region of pitch: Normalized CR-locked rate of a Chop-S population tuned to the stimulus $F0$ is shown as a function of unit CF in (A) to (C) for $F0$'s of 100, 200, and 400 Hz, respectively. Note that the low harmonics always produce the strongest normalized CR-locked rate. From these data, the center of dominance is calculated as described in the text. The predicted dominant harmonic number is shown along with the data of Ritsma (1967) in (D).

stimulus was a harmonic complex consisting of all 12 unmodified harmonics. Listeners were asked to judge whether the test stimulus was higher or lower in pitch compared with the reference stimulus. The center of dominance corresponds to that harmonic, n, which, when assigned either to the lower $F0$ or to the higher $F0$ in the test stimulus, results in a change in the listener's decision. However, this does not mean that n is the strongest harmonic; it means that the aggregated pitch strength of harmonics 1 to n is equal to the aggregated pitch strength of harmonics $n+1$ to 12 (Plomp, 1976).

The same stimuli were used in an evaluation of the current model. Normalized CR-locked rate in a Chop-S population with a CR equal to $F0$ is shown as a function of unit CF for 12 harmonics of $F0$'s of 100, 200, and 400 Hz in Figs. 6(A) to (C), respectively. The center of dominance is determined by that specific CF where the integrated, normalized

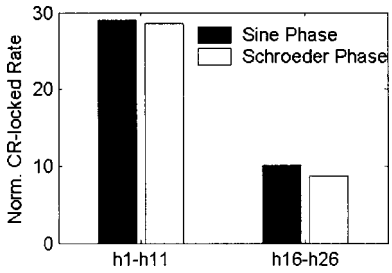

FIG. 7. Normalized CR-locked rate averaged across a population of Chop-S units with 20 CFs between 200 and 6000 Hz and a CR of 200 Hz in response to harmonic complexes with an $F0$ of 200 Hz. Harmonics are added either in sine phase (solid bars) or in Schroeder phase (open bars). The left two bars show the normalized CR-locked rate averaged across a series of low harmonics ($h1-h11$); the right two bars show normalized CR-locked rate averaged across high harmonics ($h16-h26$). In agreement with the perception of pitch strength, the normalized CR-locked rate is strong and phase independent for the resolved harmonic complexes ($h1-h11$), and it is generally weaker for high complexes ($h16-h26$). Moreover, as in the perception, the normalized CR-locked rate for high Schroeder-phase complexes is slightly weaker than for high sine-phase complexes.

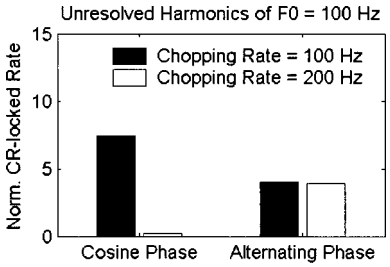

FIG. 8. Normalized CR-locked rate averaged across two Chop-S populations (one with a CR of 100 Hz, solid bars, and one with a CR of 200 Hz, open bars) in response to spectrally unresolved harmonics 16 to 26 of an $F0$ of 100 Hz. Harmonics were added in either cosine phase or alternating phase. The unresolved cosine-phase harmonics produce a strong, normalized CR-locked rate in the Chop-S population tuned to 100 Hz and almost no normalized CR-locked rate in the Chop-S population tuned to 200 Hz. The unresolved alternating-phase harmonics produce normalized CR-locked rate of similar amount in both the 100-Hz Chop-S population and in the 200-Hz population.

CR-locked rate below this CF equals the integrated, normalized CR-locked rate above this CF. The resulting CF is converted to harmonic number and plotted in Fig. 6(D) as a function of the stimulus $F0$ (strong line). The data show that the simulated center of dominance matches the data by Ritsma (1967) reasonably well.

5. Simulation 3: The influence of phase on pitch strength

Houtsma and Smurzynski (1990) investigated the extent to which the pitch strength of harmonic complexes depends on the phase relations between the harmonics. They measured frequency difference limens to obtain a quantitative measure of pitch strength. The influence of phase was measured for a set of low harmonics (1–11) as well as for a set of high harmonics (16–26). Houtsma and Smurzynski (1990) found that for a set of low harmonics pitch strength was high, and the phase relation between the harmonics did not influence pitch strength. For a set of high harmonics, pitch strength was generally much lower, and the pitch strength of harmonics added in sine phase was slightly stronger than when the harmonics were added in Schroeder phase. Adding harmonics in Schroeder phase minimizes the amplitude modulation of the waveform envelope, whereas sine-phase harmonics result in a ''peaky'' waveform. When simulating their experiment, harmonic complexes consisted of either 11 low harmonics ($h1$ to $h11$) or 11 high harmonics ($h16$ to $h26$). $F0$ was set to 200 Hz as used by Houtsma and Smurzynski (1990). Simulated neural output was obtained from 25 repetitions of 409.6-ms stimuli. The simulated Chop-S population had a CR of 200 Hz (corresponding to the $F0$ of 200 Hz).

The normalized CR-locked rate averaged across unit CFs is shown for low harmonics ($h1-h11$) and high harmonics ($h16-h26$) added in either sine phase (filled bars) or Schroeder phase (open bars) in Fig. 7. As expected from the previous simulation, the normalized CR-locked rate caused by low harmonics is considerably larger than the normalized CR-locked rate caused by high harmonics. This finding is in agreement with Houtsma and Smurzynski (1990), who showed that $F0$ difference limens (a psychophysical measure of pitch strength) are better for low harmonics than for high harmonics.

Moreover, for high harmonics, the simulations show a smaller normalized CR-locked rate for Schroeder-phase complexes than for sine-phase complexes. Several repetitions of the simulations showed that this difference is highly significant. Again, this is in agreement with Houtsma and Smurzynski (1990) because they showed that pitch strength (quantified as $F0$ difference limens) was slightly stronger when high harmonics were added in sine phase than when high harmonics were added in Schroeder phase.

6. Simulation 4: The influence of phase on the pitch of harmonic complexes

Patterson (1987) and Shackleton and Carlyon (1994) investigated the pitch of harmonic complexes where the harmonics were added either in cosine phase or in alternating phase (odd-order harmonics have a phase of 0°; even-order harmonics have a phase of 90°) as a function of whether their listeners could resolve the individual spectral components. They found that when harmonics were added in cosine phase, the perceived pitch corresponds to $F0$ regardless of whether the harmonics were spectrally resolved or unresolved. However, when the harmonics were added in alternating phase, the perceived pitch corresponds to $F0$ only for spectrally resolved harmonics. Spectrally unresolved harmonics added in alternating phase produce a pitch that matches to $2F0$.

For the simulation, stimuli consisted of harmonics 16 to 26 of a harmonic complex with an $F0$ of 100 Hz and added in either cosine phase or alternating phase. Neural responses were obtained for two Chop-S populations, one with a CR equal to $F0$ and one with a CR equal to $2F0$.

Normalized CR-locked rate averaged across each Chop-S population is shown in Fig. 8. In the Chop-S population tuned to $F0 = 100$ Hz (solid bars), the normalized CR-locked rate is stronger for the unresolved cosine-phase harmonics than for the unresolved alternating-phase harmonics.

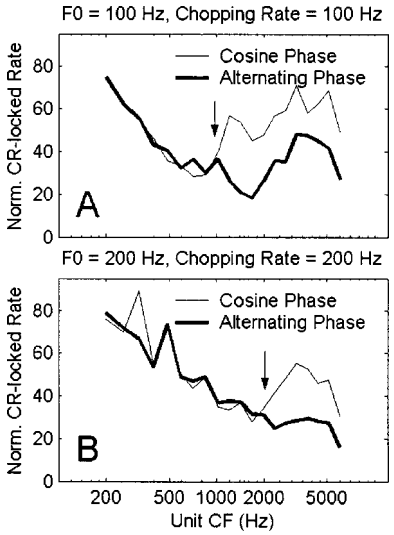

FIG. 9. Normalized CR-locked rate as a function of unit CF for harmonic complexes added in either cosine phase (fine lines) or alternating phase (strong lines). The stimulus $F0$ and the population CR were either 100 Hz (A) or 200 Hz (B). Note that the normalized CR-locked rate to spectrally resolved harmonics is phase independent. The CF at which neural responses start to become phase sensitive (arrows) is at a fixed harmonic number (about 10), and not at a fixed frequency.

In the Chop-S population tuned to $F0=200$ Hz (open bars), the unresolved cosine-phase harmonics generate no normalized CR-locked rate, whereas the alternating-phase stimuli generate a normalized CR-locked rate that almost equals that for the Chop-S population tuned to 100 Hz.

Shackleton and Carlyon (1994) also showed that the perceived pitch does not depend on the absolute frequency region (low vs high frequency) but on the harmonic number (low vs high harmonics). To verify, if this was the case for the Chop-S model we calculated the normalized CR-locked rate for cosine-phase complexes and alternating-phase complexes with $F0$'s of 100 and 200 Hz with both resolved and unresolved harmonics. The normalized CR-locked rate of a Chop-S population tuned to 100 Hz in response to a 100-Hz harmonic complex as a function of unit CF is shown in Fig. 9(A). Chop-S responses are phase independent up to about 1000 Hz (arrow). The same plot is shown for an $F0$ of 200 Hz and a Chop-S population tuned to 200 Hz in Fig. 9(B). With this $F0$, the phase sensitivity starts at about 2000 Hz, i.e., at about the same harmonic number (10), not at the same frequency.

These simulations show that the Chop-S model is insensitive to the phase of spectrally resolved harmonics and it is sensitive to the phase of unresolved harmonics. Thus, it produces predictions of pitch in qualitative agreement with the psychophysical data of Shackleton and Carlyon (1994).

7. Simulation 5: Inharmonic pitch shifts and pitch ambiguity

The pitch shifts and pitch ambiguity resulting from inharmonic complexes (consisting of equally spaced but inharmonic components) have strongly influenced modern theories of pitch perception. Chop-S units have classically been regarded as sensitive to the waveform envelope (modulation sensitivity: Frisina *et al.* 1990a,b). However, the envelope of the waveform of a harmonic complex is not affected by inharmonic shifts. Thus, the pitches evoked by inharmonic complexes appear to represent a special challenge for a model of pitch based exclusively on Chop-S units.

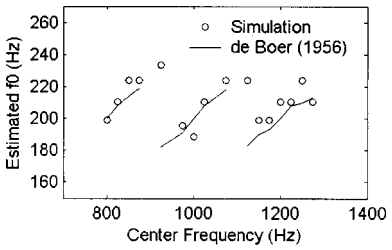

FIG. 10. Simulation of pitch shifts produced by inharmonically shifted complexes. The spacing of the five harmonics was always 200 Hz. The lines shows the pitches matched after de Boer (1956) as a function of the frequency of the central component (the carrier). The open circles indicate the CR of that Chop-S population which produces the strongest, normalized CR-locked rate in response to the complex.

The first simulation is an attempt to reproduce the data obtained by de Boer (1956). He asked listeners to match the pitch of a carrier tone amplitude modulated with the sum of a 200- and 400-Hz tone. This results in a harmonic complex with five harmonics and a harmonic spacing of 200 Hz. The overall position of the five harmonics depends exclusively on the frequency of the carrier tone. When the frequency is an integer multiple of 200 Hz, the resulting complex is harmonic; otherwise, it is inharmonically shifted by the signed difference of the carrier frequency and the nearest multiple of 200 Hz. The matching results by de Boer (1956) indicated that when a shift of -80 Hz was applied, listeners matched a pitch of about 173 Hz. With increasing shift, the pitch match increased and reached a value of about 214 Hz for an inharmonic shift of $+80$ Hz. Moreover, the pitch matches were circular in that a further increase of pitch shift to $+100$ Hz and beyond resulted in a jump of the perceived pitch from about 230 Hz back down to 170 Hz. The magnitude of the pitch shifts tends to decrease with increasing harmonic number of the carrier frequency (see also Moore and Moore, 2003).

The simulation paradigm investigates the representation of such an inharmonic, five-component complex in 11 discrete Chop-S populations with CRs between 170 and 235 Hz. Inharmonic shifts matched those produced by de Boer (1956). The $F0$ was 200 Hz. The normalized CR-locked rate was calculated for each Chop-S population in response to an inharmonic complex with each of the inharmonic shifts. Figure 10 shows the CR of that Chop-S population which produced the strongest normalized CR-locked rate for each inharmonic shift. Simulation results (open circles) are plotted together with the results of de Boer (1956).

Yost (1997) investigated the pitch of IRN when the IRN gain is negative (corresponding to a delay-and-subtract algorithm instead of delay-and-add). A negative gain results in a shift of all spectral peaks in the IRN stimulus by a frequency corresponding to half the delay reciprocal, $0.5/d$. This results in a stimulus spectrum similar to an inharmonic complex with a frequency shift equal to half the $f0$. Yost (1997) showed that the pitch of IRN with negative gain depends not

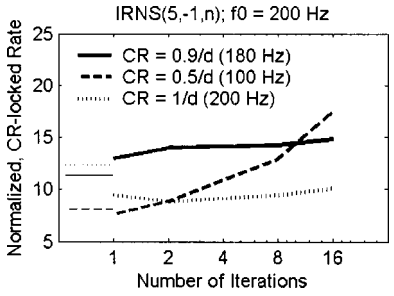

FIG. 11. Simulated neural correlate of inharmonic pitch shifts with IRN stimuli: The stimulus is IRNS$(5,-1,n)$, with n ranging from 1 to 16 iterations in doublings. Normalized CR-locked rate averaged over a population of Chop-S units is shown with a population CR of $0.9/d$ (180 Hz), $0.5/d$ (100 Hz), and $1/d$ (200 Hz). IRNS with negative gain produces a pitch of $0.9/d$ or $1.1/d$ for a low number of iterations and a pitch equal to $0.5/d$ for a high number of iterations. In qualitative agreement with this perception, normalized CR-locked rate for a Chop-S population tuned to $0.9/d$ is strongest for a low number of iterations but, with increasing number of iterations, the Chop-S population tuned to $0.5/d$ starts to produce the strongest, normalized CR-locked rate. Note, however, that the change in perceived pitch occurs typically between 2 and 4 iterations, whereas the crossover of the rate functions occurs between 8 and 16 iterations. The reason for the deviation between the experimental data and the simulations probably lies in the different values of the normalized CR-locked rate in response to white-noise stimuli (horizontal lines on the left). Compensation of these different offsets would result in an improved fit to the experimental data.

only on the IRN gain but also on the number of iterations. With one or two iterations, listeners matched pitches corresponding to $1.1/d$ or $0.9/d$, whereas with a high number of iterations, listeners tended to match a pitch equal to $0.5/d$. Simulations were performed using IRNS$(5,-1,n)$ where n, the number of iterations, is variable. These stimuli would produce a pitch corresponding to 200 Hz if a positive gain were used. Populations of Chop-S units with three different CRs were used. These CRs were equal to $0.9/d$, $0.5/d$, and $1/d$. Figure 11 shows the normalized CR-locked rate averaged across each population for the three populations as a function of the number of iterations.

For a low number of iterations, the Chop-S population with a CR at $0.9/d$ shows the strongest normalized CR-locked rate (solid line). With increasing number of iterations, the normalized CR-locked rate of the Chop-S population with a CR of $0.5/d$ grows fastest. For 16 iterations, the Chop-S population with a CR of $0.5/d$ shows the strongest normalized CR-locked rate. The Chop-S population with a CR of $1/d$ shows only a weak, normalized CR-locked rate. This latter population produces the strongest normalized CR-locked rate when the gain is positive (cf. Fig. 5). Note that for this population, the normalized CR-locked rate is below that obtained for white-noise (aperiodic) stimulation (short horizontal lines on the left).

8. Simulation 6: The segregation of concurrent pitches

Assmann and Paschall (1998) investigated the extent to which listeners can match the pitch of each of two vowel-shaped harmonic complexes as a function of the separation of the $f0$'s of the two complexes. They found that when the $f0$ difference of the vowels was below four semitones (24%), listeners matched a single pitch to the complex consisting of two $f0$'s. When the $f0$ difference was four semitones, the listeners provided bimodal pitch matches, i.e., sometimes they matched the lower pitch and sometimes they matched the higher pitch. This performance indicates the listeners' ability to "hear out" each of the two $f0$'s. The following simulation investigates the extent to which the Chop-S model is capable to segregate two simultaneously presented harmonic complexes. The stimuli consisted of CPH with either a lower $f0$ or a higher $f0$ or the sum of the two CPHs. Averaged, normalized CR-locked rates were obtained for populations of Chop-S units with closely spaced CRs in the range surrounding the two $f0$'s. Simulation results are shown in Fig. 12. For an $f0$ difference of 50% or 24% (A) and (B), the simulations reveal a clear peak in response to each single complex and a bimodal distribution in response to the sum of the two CPHs. With an $f0$ difference of 12% [Fig. 12(C)], there is no clear bimodal distribution despite the fact that the spacing of the CRs was halved compared to Figs. 12(A) and (B).

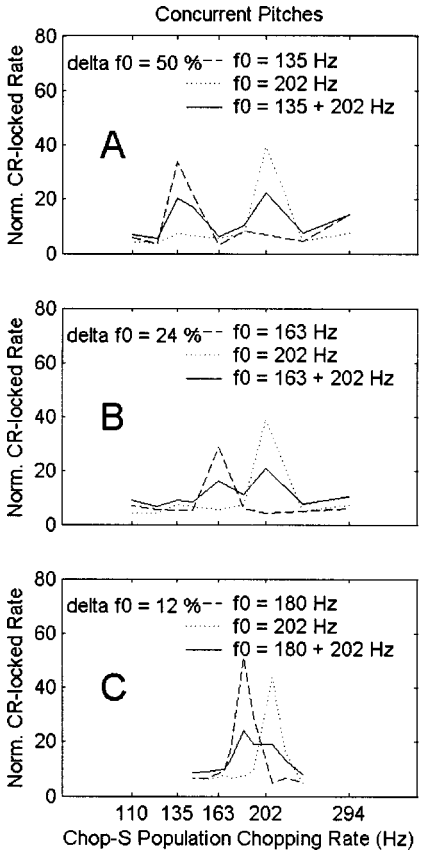

FIG. 12. Segregation of concurrent pitches in Chop-S populations: Normalized CR-locked rate responses are shown as a function of the population CR when stimulated with either of two harmonic complexes or their sum. The dashed lines show responses to the lower of the two $f0$'s; dotted lines show responses to the higher of the two $f0$'s. Solid lines show the responses to the sum of the two complexes. Note that when the $f0$ deviation is 50% (A) or 24% (B) the two pitches are well resolved (solid lines). With a 12% $f0$ deviation (C) a bimodal distribution of the estimated pitches is not found, although the spacing of the population CRs was halved compared to (A) and (B).

III. DISCUSSION

The simulations demonstrate that the normalized CR-locked rate measure applied to a model of VCN Chop-S units

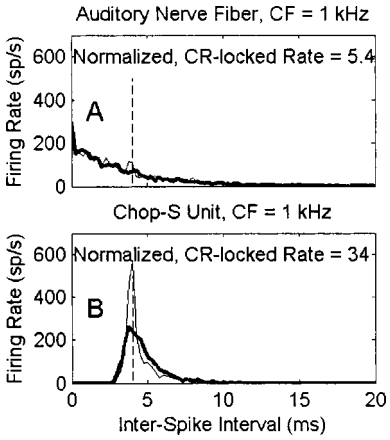

FIG. 13. Comparison of the interspike interval histograms of a simulated auditory-nerve fiber (A) and a Chop-S unit (B). Stimuli were either white noise (strong lines) or a random-phase harmonic complex (RPH) with an $F0$ of 250 Hz (fine lines). Note that both in the simulated auditory-nerve fiber and in the simulated Chop-S unit, the RPH leads to a redistribution if interspike intervals in favor of the intervals equal to the stimulus period (vertical dashed lines), compared to white-noise stimulation. However, the degree of this redistribution, quantified as normalized CR-locked rate, is much higher in the Chop-S unit compared to the auditory-nerve fiber.

can reflect the strength of pitch percepts observed in a wide range of psychophysical studies. The demonstrations present a *prima facie* case that Chop-S units may play a role in transmitting pitch-related information to higher stations in the nervous system. The model can simulate responses to a variety of pitch phenomena. It is able to predict changes of the IRN pitch strength with increasing number of iterations, the dominance region of pitch, changes of pitch strength which depend on the phase relations between the harmonics, changes of the pitch when harmonics are added in cosine phase compared to alternating phase, the pitches of inharmonic complexes and the pitches of IRN with negative gain (which also produces inharmonic shifts), and the pitches of concurrent harmonic complexes, and the pitch and pitch strength of SAM noise.

Chop-S units have traditionally been characterized as followers of signal envelope. This modeling study suggests that they may have an important role to play in transmitting information concerning stimulus fine structure as well. Most physiological experiments have used high-frequency (CF) carrier stimuli subject to low-frequency modulation. Few if any studies have looked at synchronization to unmodulated pure tones other than CF tones. However, psychophysical pitch studies have shown that it is the resolved (and therefore only weakly modulated or unmodulated) sinusoidal components of harmonic complexes that contribute most to the strength of the pitch percept. The model predicts that a strong normalized CR-locked rate is observed in response to resolved harmonics when the frequency of the harmonic is equal to the intrinsic CR or equal to an integer multiple of the CR of the unit.

The latter is a crucial features of Chop-S units: Imagine a Chop-S unit with a CF of 750 Hz and a CR of 250 Hz being stimulated by a harmonic complex with an $f0$ of 250 Hz. Spectrally, this unit is tuned to the third harmonic of the complex. As this harmonic is spectrally well resolved, the auditory-nerve representation of this third harmonic will show very little amplitude modulation corresponding to $f0$. Instead, the Chop-S unit will receive an auditory-nerve input with a dominant period (summed across all auditory-nerve fibers converging on the Chop-S unit) of 1.33 ms, the reciprocal of 750 Hz. The important function of the Chop-S unit is that it is capable to skip input spikes and lock onto an integer multiple of the 1.33-ms period. It will choose a period which is most suitable for its CR. Thus, the Chop-S unit will fire with a highly regular interspike interval of 4 ms, which means firing on every third input maximum. Thus, a Chop-S unit is capable to ''interpret'' the 750-Hz not as a 750-Hz pure tone but as being the third harmonic of an $f0$ of 250 Hz even if the unit has no indication that the 250-Hz component is actually present.

The simulations described above indicate that assemblies of Chop-S units may supply a useful neural representation of pitch information. However, Chop-S units are just one of a variety of cell types found in the CN. Primarylike units have been shown to transmit the highest temporal precision of neural discharge. Their firing characteristics are very similar to those of auditory-nerve fibers, which have been shown to represent a reliable pitch code in their all-order interspike intervals (Horst *et al.*, 1986; Cariani and Delgutte, 1996a,b). The special advantage of Chop-S units is that they are narrowly tuned in terms of which fundamental frequencies produce a strong, normalized CR-locked rate. Other unit types are typically broadly tuned to $f0$, if at all (Winter *et al.*, 2001). This is illustrated in Fig. 13, where ISIHs and normalized CR-locked rate of a simulated Chop-S unit (B) is compared to its auditory-nerve input (A). As outlined above, this input consists of the aggregated firing activity of 15 auditory-nerve fibers. Responses are shown to white noise (strong lines) and an RPH with $F0=250\,\mathrm{Hz}$ (fine lines). Note the redistribution of ISI in favor of the 4-ms period (vertical dashed line) in both unit types. However, as a consequence of its bandpass temporal tuning, the Chop-S unit provides a much higher normalized CR-locked rate compared to the auditory nerve. Thus, the temporal tuning of a Chop-S unit to a narrow range of ISIs results in a twofold benefit for the system: first, it increases its sensitivity to changes in the ISI distribution when the ISI is in this tuning range. Second, the temporal tuning of Chop-S units may serve as a physiological basis for the identification of common harmonicity across the many components of a harmonic complex, even though they are spread across a range of frequencies.

Chop-S units show less modulation gain in response to envelope-modulated stimuli than other unit types like onset units (Kim *et al.*, 1990). However, considering the fact that the low, weakly modulated harmonics of a harmonic complex contribute most to pitch strength, it is questionable whether sensitivity to envelope modulation is the most important physiological parameter for neural pitch extraction. The current study shows that Chop-S units reveal a good sensitivity to the period of the low, weakly modulated harmonics. As such, they may represent the first stage of sensitivity to pitch.

Shortcomings of the model

The current model depends on the assumption that there is a population of Chop-S units for each $f0$ encountered. The existence region of the $f0$ related pitch of harmonic complexes spans from about 30 Hz to about 1400 Hz. However, Chop-S units are not frequently seen with CRs greater than 500 Hz or smaller than 100 Hz. Thus, at present, the Chop-S model cannot account for these pitches. Concerning higher $f0$'s, it is possible that Chop-S units show synchronization to a subharmonic of $f0$ when this subharmonic fits the CR of the unit. This is reflected in Fig. 2, where an increased normalized CR-locked rate at the natural CR will be seen in response to these $f0$ multiples. This model behavior might be interpreted as a neural correlate of octave confusions, as they are often encountered in pitch judgments.

This study has not considered pitches based upon the many different types of dichotic signals that generate a pitch sensation (Culling, 2000; Culling *et al.*, 1998a,b). At the level of the CN, the neural representation of these stimuli will be no different than for an aperiod stimulus because of the monaural nature of the CN. Thus, the pitch sensation evoked by dichotic-pitch stimuli cannot be mediated by the processing of Chop-S units. However, at the next prospective stage of the model under development, the Chop-S units project to coincidence detector units in the inferior colliculus. At this stage, there is pronounced binaural interaction and it is possible that binaural properties of coincidence detector units may be involved in the perception of dichotic pitches. The behavior of a model fully developed to the level of the inferior colliculus remains to be tested.

Another potential problem for the model concerns the firing rates of sustained chopper units at very low signal levels. The model assumes that chop-S units have low thresholds and low saturation thresholds. Above saturation levels, the firing rate is roughly constant (regardless of level) and will synchronize to acoustic events at that frequency. At low signal levels, the rate/constancy assumption clearly does not hold and the pitch percept should be affected by reductions in rate. Unfortunately, it is difficult to estimate from the animal data the levels at which this would become an issue. We also know relatively little about how low pitch percepts behave close to absolute threshold. Nevertheless, this issue is potentially problematic and will need to be kept in view in the future.

May *et al.* (1998) described responses of chopper units to vowel sounds where the position of the vowel formants was varied systematically. They showed that a variation in formant position resulted in a change of the units' rate responses regardless of the overall sound-pressure level of the presented vowel. This finding represents an interesting challenge for the current suggestion that temporal response characteristics of Chop-S units play an important role in pitch perception.

First, however, it must be pointed out that the suggested role in pitch perception applies to relatively low pitches with fundamental frequencies below about 500 Hz. The role of Chop-S units in the encoding of spectral envelope features applies to formants that are typically located at frequencies of 1 kHz and above. Thus, the encoding of the low harmonics numbers (which are the most important for pitch perception) is not likely to be affected by the unit's sensitivity to spectral envelope features. For higher harmonic numbers, however, it must be assumed that there will be interference between a Chop-S unit's rate-response changes in response to changes in the spectral envelope and the unit's sensitivity to the fundamental frequency of these high harmonics. Such interference, however, is also observed perceptually: It is difficult for listeners to estimate the low pitch of higher-order harmonics independently of spectral envelope and overall sound level. One example is the study by Walliser (1969), where it was shown that the pitch of a 300-Hz harmonic complex octave band filtered around 4000 Hz depends significantly on sound-pressure level. Another example is the occurrence of edge pitches.

An extensive study of Chop-S units with iterated rippled noise, where the spectral envelope in the spectrally unresolved frequency region is flat, has shown that (for these ''nonvowel'' sounds) Chop-S units reach their rate saturation at relatively low sound-pressure levels and they preserve their sensitivity to periodic sounds in rate saturation (Wiegrebe and Winter, 2001).

In summary, the temporal tuning of a Chop-S unit to a narrow range of ISIs results in a twofold benefit for the system: first, it increases its sensitivity to changes in the ISI distribution when the ISI is in this tuning range. Second, the temporal tuning of Chop-S units may serve as a physiological basis for the identification of common harmonicity across the many components of a harmonic complex, even though they are spread across a range of frequencies.

ACKNOWLEDGMENTS

We would like to thank Ian Winter, Alain de Cheveigne, and an unknown reviewer for very helpful comments on earlier versions of this manuscript. We would also like to thank Roy Patterson and Ian Winter for many fruitful discussions on pitch processing and the cochlear-nucleus physiology.

Abeles, M. (**1982**). ''Quantification, smoothing, and confidence limits for single-units' histograms,'' J. Neurosci. Methods **5**, 317–325.

Assmann, P. F., and Paschall, D. D. (**1998**). ''Pitches of concurrent vowels,'' J. Acoust. Soc. Am. **103**, 1150–1160.

Blackburn, C. C., and Sachs, M. B. (**1989**). ''Classification of unit types in the anteroventral cochlear nucleus: PST histograms and regularity analysis,'' J. Neurophysiol. **62**, 1303–1329.

Burns, E. M., and Viemeister, N. F. (**1981**). ''Played-again Sam: Further observation on the pitch of amplitude- modulated noise,'' J. Acoust. Soc. Am. **70**, 1655–1660.

Cariani, P. A., and Delgutte, B. (**1996a**). ''Neural correlates of the pitch of complex tones. I. Pitch and pitch salience,'' J. Neurophysiol. **76**, 1698–1716.

Cariani, P. A., and Delgutte, B. (**1996b**). ''Neural correlates of the pitch of complex tones. II. Pitch shift, pitch ambiguity, phase invariance, pitch circularity, rate pitch, and the dominance region for pitch,'' J. Neurophysiol. **76**, 1717–1734.

Culling, J. F. (**2000**). ''Dichotic pitches as illusions of binaural unmasking. III. The existence region of the Fourcin pitch,'' J. Acoust. Soc. Am. **107**, 2201–2208.

Culling, J. F., Marshall, D. H., and Summerfield, A. Q. (**1998a**). ''Dichotic pitches as illusions of binaural unmasking. II. The Fourcin pitch and the dichotic repetition pitch,'' J. Acoust. Soc. Am. **103**, 3527–3539.

Culling, J. F., Summerfield, A. Q., and Marshall, D. H. (**1998b**). ''Dichotic pitches as illusions of binaural unmasking. I. Huggins' pitch and the binaural edge pitch,'' J. Acoust. Soc. Am. **103**, 3509–3526.

de Boer, E. (**1956**). ''On the 'residue' in hearing,'' Doctoral dissertation, University of Amsterdam.
de Cheveigne, A. (**1998**). ''Cancellation model of pitch perception,'' J. Acoust. Soc. Am. **103**, 1261–1271.
Ferragamo, M. J., Golding, N. L., and Oertel, D. (**1998**). ''Synaptic inputs to stellate cells in the ventral cochlear nucleus,'' J. Neurophysiol. **79**, 51–63.
Frisina, R. D., Smith, R. L., and Chamberlain, S. C. (**1990a**). ''Encoding of amplitude modulation in the gerbil cochlear nucleus. I. A hierarchy of enhancement,'' Hear. Res. **44**, 99–122.
Frisina, R. D., Smith, R. L., and Chamberlain, S. C. (**1990b**). ''Encoding of amplitude modulation in the gerbil cochlear nucleus. II. Possible neural mechanisms,'' Hear. Res. **44**, 123–141.
Ghoshal, S., Kim, D. O., and Northrop, R. B. (**1992**). ''Amplitude-modulated tone encoding behavior of cochlear nucleus neurons: Modeling study,'' Hear. Res. **58**, 153–165.
Glasberg, B. R., and Moore, B. C. J. (**2002**). ''A model of loudness applicable to time-varying sounds,'' J. Audio Eng. Soc. **50**, 331–342.
Goldstein, J. L. (**1973**). ''An optimum processor theory for the central formation of the pitch of complex tones,'' J. Acoust. Soc. Am. **54**, 1496–1516.
Hewitt, M. J., and Meddis, R. (**1994**). ''A computer model of amplitude-modulation sensitivity of single units in the inferior colliculus,'' J. Acoust. Soc. Am. **95**, 2145–2159.
Hewitt, M. J., Meddis, R., and Shackleton, T. M. (**1992**). ''A computer model of a cochlear-nucleus stellate cell: Responses to amplitude-modulated and pure-tone stimuli,'' J. Acoust. Soc. Am. **91**, 2096–2109.
Horst, J. W., Javel, E., and Farley, G. R. (**1986**). ''Coding of spectral fine structure in the auditory nerve. I. Fourier analysis of period and interspike interval histograms,'' J. Acoust. Soc. Am. **79**, 398–416.
Houtsma, A. J. M., and Smurzynski, J. (**1990**). ''Pitch identification and discrimination for complex tones with many harmonics,'' J. Acoust. Soc. Am. **87**, 304–310.
Kim, D. O., Sirianni, J. G., and Chang, S. O. (**1990**). ''Responses of DCN-PVCN neurons and auditory nerve fibers in unanesthetized decerebrate cats to AM and pure tones: Analysis with autocorrelation/power-spectrum,'' Hear. Res. **45**, 95–113.
Lai, Y. C., Winslow, R. L., and Sachs, M. B. (**1994**). ''A model of selective processing of auditory-nerve inputs by stellate cells of the antero-ventral cochlear nucleus,'' J. Comput. Neurosci. **1**, 167–194.
Licklider, J. C. R. (**1951**). ''A duplex theory of pitch perception,'' Experientia **7**, 128–133.
Licklider, J. C. R. (**1959**). ''Three auditory theories,'' in *Psychology, A Study of A Science*, edited by S. Koch (McGraw-Hill, New York).
Lopez-Poveda, E. A., and Meddis, R. (**2001**). ''A human nonlinear cochlear filterbank,'' J. Acoust. Soc. Am. **110**, 3107–3118.
Lyon, R. F. (**1984**). ''Computational models of neural auditory processing,'' in Proc IEEE ICASSP 84.3.
MacGregor, R. J. (**1987**). *Neural and Brain Modeling* (Academic, San Diego).
May, B. J., Prell, G. S., and Sachs, M. B. (**1998**). ''Vowel representations in the ventral cochlear nucleus of the cat: Effects of level, background noise, and behavioral state,'' J. Neurophysiol. **79**, 1755–1767.
Meddis, R., and Hewitt, M. J. (**1991a**). ''Virtual pitch and phase sensitivity of a computer model of the auditory periphery. I. Pitch identification,'' J. Acoust. Soc. Am. **89**, 2866–2882.
Meddis, R., and Hewitt, M. J. (**1991b**). ''Virtual pitch and phase sensitivity of a computer model of the auditory periphery. II. Phase sensitivity,'' J. Acoust. Soc. Am. **89**, 2883–2894.
Meddis, R., O'Mard, L. P., and Lopez-Poveda, E. A. (**2001**). ''A computational algorithm for computing nonlinear auditory frequency selectivity,'' J. Acoust. Soc. Am. **109**, 2852–2861.
Moore, G. A., and Moore, B. C. (**2003**). ''Perception of the low pitch of frequency-shifted complexes,'' J. Acoust. Soc. Am. **113**, 977–985.
Patterson, R. D. (**1987**). ''A pulse ribbon model of monaural phase perception,'' J. Acoust. Soc. Am. **82**, 1560–1586.
Plomp, R. (**1976**). *Aspects of Tone Sensation: A Psychophysical Study* (Academic, London, New York, San Francisco).
Ritsma, R. J. (**1967**). ''Frequencies dominant in the perception of the pitch of complex sounds,'' J. Acoust. Soc. Am. **42**, 191–198.
Schouten, J. F. (**1970**). ''The residue revisited,'' in *Frequency Analysis and Periodicity Detection in Hearing*, edited by R. Plomp and G. F. Smoorenburg (Sijthoff, Leiden), pp. 39–58.
Shackleton, T. M., and Carlyon, R. P. (**1994**). ''The role of resolved and unresolved harmonics in pitch perception and frequency modulation discrimination,'' J. Acoust. Soc. Am. **95**, 3529–3540.
Shamma, S., and Klein, D. (**2000**). ''The case of the missing pitch templates: How harmonic templates emerge in the early auditory system,'' J. Acoust. Soc. Am. **107**, 2631–2644.
Shofner, W. P. (**1991**). ''Temporal representation of rippled noise in the anteroventral cochlear nucleus of the chinchilla,'' J. Acoust. Soc. Am. **90**, 2450–2466.
Shofner, W. P. (**1999**). ''Responses of cochlear nucleus units in the chinchilla to iterated rippled noises: Analysis of neural autocorrelograms,'' J. Neurophysiol. **81**, 2662–2674.
Sumner, C. J., Lopez-Poveda, E. A., O'Mard, L. P., and Meddis, R. (**2002**). ''A revised model of the inner-hair cell and auditory-nerve complex,'' J. Acoust. Soc. Am. **111**, 2178–2188.
Terhardt, E. (**1979**). ''Calculating virtual pitch,'' Hear. Res. **1**, 155–182.
Walliser, K. (**1969**). ''Zusammenhänge zwischen dem Schallreiz und der Periodentonhöhe,'' Acustica **21**, 319–329.
Wiegrebe, L., and Winter, I. M. (**2001**). ''Temporal representation of iterated rippled noise as a function of delay and sound level in the ventral cochlear nucleus,'' J. Neurophysiol. **85**, 1206–1219.
Winter, I. M., Wiegrebe, L., and Patterson, R. D. (**2001**). ''The temporal representation of the delay of iterated rippled noise in the ventral cochlear nucleus of the guinea-pig,'' J. Physiol. (London) **537**, 553–566.
Yost, W. A. (**1996a**). ''Pitch of iterated rippled noise,'' J. Acoust. Soc. Am. **100**, 511–518.
Yost, W. A. (**1996b**). ''Pitch strength of iterated rippled noise,'' J. Acoust. Soc. Am. **100**, 3329–3335.
Yost, W. A. (**1997**). ''Pitch strength of iterated rippled noise when the pitch is ambiguous,'' J. Acoust. Soc. Am. **101**, 1644–1648.
Young, E. D., Robert, J. M., and Shofner, W. P. (**1988**). ''Regularity and latency of units in ventral cochlear nucleus: Implications for unit classification and generation of response properties,'' J. Neurophysiol. **60**, 1–29.

The influence of transducer operating point on distortion generation in the cochlea

Davud B. Sirjani, Alec N. Salt,[a] Ruth M. Gill, and Shane A. Hale
Department of Otolaryngology, Washington University School of Medicine, St. Louis, Missouri, 63110

(Received 18 September 2003; revised 19 November 2003; accepted 15 December 2003)

Distortion generated by the cochlea can provide a valuable indicator of its functional state. In the present study, the dependence of distortion on the operating point of the cochlear transducer and its relevance to endolymph volume disturbances has been investigated. Calculations have suggested that as the operating point moves away from zero, second harmonic distortion would increase. Cochlear microphonic waveforms were analyzed to derive the cochlear transducer operating point and to quantify harmonic distortions. Changes in operating point and distortion were measured during endolymph manipulations that included 200-Hz tone exposures at 115-dB SPL, injections of artificial endolymph into scala media at 80, 200, or 400 nl/min, and treatment with furosemide given intravenously or locally into the cochlea. Results were compared with other functional changes that included action potential thresholds at 2.8 or 8 kHz, summating potential, endocochlear potential, and the $2f1-f2$ and $f2-f1$ acoustic emissions. The results demonstrated that volume disturbances caused changes in the operating point that resulted in predictable changes in distortion. Understanding the factors influencing operating point is important in the interpretation of distortion measurements and may lead to tests that can detect abnormal endolymph volume states. © *2004 Acoustical Society of America.* [DOI: 10.1121/1.1647479]

PACS numbers: 43.64.Jb, 43.64.Nf [BLM] Pages: 1219–1229

I. INTRODUCTION

These studies investigate the possibility that physiological response changes associated with changes in cochlear transducer operating point may be of value in the characterization of endolymph volume disturbances, such as endolymphatic hydrops. If the relationship between mechanical input and electrical output of the cochlear transducer can be described by a response curve, then the operating point represents the location on this curve in the absence of stimulation. It has been suggested that endolymph volume disturbances can mechanically disturb transduction in the ear through changes in static position and thus operating point of the organ of Corti (Kirk *et al.*, 1997). Changes in emitted distortion products consistent with operating point shifts have been demonstrated during low-frequency biasing experiments (Frank and Kössl, 1996; 1997) with both the $f2-f1$ and $2f1-f2$ emissions being modulated by a bias tone. Low-frequency biasing of the $2f1-f2$ emission has also been used to derive the cochlear transducer function (Bian *et al.*, 2002). Detailed studies of the relationships between operating point and acoustic emissions were reported by Kirk and Patuzzi (1997) and Kirk *et al.* (1997). In these studies it was found that exposure to a high-level, low-frequency tone produced marked changes of both the operating point and the $f2-f1$ emission. Subsequent studies have demonstrated that low-frequency tone exposures can produce a transient endolymphatic hydrops (Flock and Flock, 2000; Salt *et al.*, 2002; 2003). The study by Salt (2003) utilized chemical volume markers that were monitored in the endolymphatic space by ion-selective microelectrodes. Exposure to 200 Hz tones at 115 dB produced marker concentration changes indicating an endolymph volume increase of approximately 30% in the second turn of guinea pigs. A similar degree of hydrops was reported during stimulation with a 140-Hz tone at 109 dB SPL by Flock and Flock (2000). They used confocal microscopy to view Reissner's membrane in the apical turn of the guinea pig cochlea and found substantial bowing of Reissner's membrane towards scala vestibuli.

The purpose of the present study was to quantify changes in operating point, distortion, and other functional measures during manipulations intended to disturb endolymph volume or endolymph homeostasis. We used three types of interventions: (1) Tone exposures at 200 Hz, 115 dB SPL that have been shown to cause transient endolymphatic hydrops (Salt, 2003; Flock and Flock, 2000); (2) Direct injections of artificial endolymph into scala media of the second cochlear turn (Salt and DeMott, 1997); (3) Treatment with furosemide, a blocker of ion transport in the lateral wall of the cochlea that results in substantial reduction of the endolymphatic potential and ionic changes of endolymph (Brusilow, 1976; Rybak and Morizono, 1982; Rybak and Whitworth, 1986).

In order to determine the cochlear transducer operating point, we have adopted an approach similar to that used by Kirk *et al.* (1997), in which operating point was derived from an analysis of the cochlear microphonic waveform. Operating point changes were compared with a number of measures of cochlear distortion, including harmonic distortions of the microphonic and acoustic two-tone distortion products $2f1-f2$ and $f2-f1$. Operating point was also compared with a number of other functional measures including cochlear sensitivity as assessed by action potential thresholds and summating potentials.

[a]Electronic mail: salta@wustl.edu

II. METHODS

A. Animal preparation

Pigmented NIH-strain guinea pigs weighing 350–500 g were used in this study. Animals were anesthetized with intraperitoneal sodium thiobutabarbital (Inactin, Sigma, St. Louis, 100–125 mg/kg) and placed on a thermistor-controlled heating pad to maintain core temperature at 38 °C. A central line was placed in the left external jugular vein for supplementary anesthetic and other drugs. The trachea was cannulated and the animal was ventilated. End tidal CO_2 was monitored and the tidal volume of the respirator was adjusted to maintain an end tidal CO_2 level of 38 mm Hg (5%). Heart rate was monitored. Prior to recordings, pancuronium bromide (Pavulon, Baxter, Irvine, approximately 0.05 mg, to effect) was given intravenously to minimize myogenic artifacts and to aid mechanical ventilation.

The caudal portion of the right jaw was removed and the auditory bulla was exposed by a ventral approach. The bulla was opened, leaving middle-ear structures intact. A longitudinal incision was made along the external auditory canal and a hollow earbar was inserted until it sealed to the canal wall.

The instrumentation for stimulus generation and data acquisition was Tucker-Davis System 3 hardware controlled by a custom-written VISUAL BASIC (Microsoft) program. An acoustic emissions system (Etymotic ER-10C, microphone and 2 speakers) and a high-intensity speaker (Sennheiser HD580) were incorporated into the hollow earbar so that each sound channel terminated near the tip of the earbar. Sound stimuli in the ear canal were calibrated at the beginning of each experiment using the ER10C microphone with an automated procedure that tracked a criterion sound level of 70 dB SPL across a range of frequencies (1 to 16 kHz for Etymotic speakers, 125 Hz to 16 kHz for the Sennheiser speaker) in 1/4–octave steps.

B. Cochlear evoked potentials

Cochlear responses were recorded from an Ag/AgCl ball electrode positioned at the junction between the round-window membrane and the bony otic capsule. The signal was amplified 1000× and high-pass filtered at 5 Hz. Signals were digitized at 48.8 kHz and averaged using Tucker-Davis RP-2 modules.

C. Responses to biphasic tone bursts

Cochlear potentials [cochlear microphonic (CM), summating potential (SP), and action potential (AP)] were recorded in response to phase-locked tone bursts of two opposing polarities. Typically ten responses to positive onset stimuli and ten responses to negative onset stimuli were averaged. Tone bursts were 12 ms in duration with 0.5-ms cosine-shaped onset. Waveforms containing the AP and SP were obtained by summing the responses to both polarities, and the CM was obtained by subtracting the responses to opposite polarities. Cochlear responses were typically recorded in response to 4-kHz stimulus at 90 dB SPL. In addition, the same collection paradigm was incorporated into an automated routine by which the AP threshold was established using a 10-μV criterion. The criterion magnitude was approximately 4 times greater than the background noise level in the averaged response. Stimuli were increased in 5-dB steps until an AP greater than 10 μV was detected and then stimuli were reduced in 5-dB steps until the AP was below the 10-μV criterion. The threshold was determined by interpolation between the above- and below-threshold amplitude values. Thresholds were monitored during experimental manipulations with stimuli at 2.8 and 8 kHz. In addition, prior to manipulations a frequency/threshold curve (AP audiogram) was measured in 1/4-octave steps from 1 to 16 kHz.

D. Single-phase CM analysis

The CM obtained as detailed above, by subtracting responses to opposite polarity stimuli, is not appropriate for operating point analysis because polarity-sensitive components are canceled in the waveform subtraction procedure. Instead, CM was averaged in response to a sustained 500-Hz tone, presented at high level to saturate the cochlear transducer. Data sampling was initiated 5 s after the tone commenced, phase-locked to positive-going zero crossings of the tone. Twenty epochs of a 2048-point waveform (42-ms window) were averaged. The waveform was Hamming windowed and the power spectrum was calculated. The peaks representing the primary, second harmonic, and third harmonic were measured. Harmonics were expressed in dB relative to the amplitude of the primary. Half of the waveform (1024 points) was then subjected to an analysis to determine operating point, as detailed below.

E. Acoustic emissions

Acoustic emissions were recorded in response to 4- and 4.8-kHz primaries, presented at 75 or 80 dB SPL. Frequencies of the primaries were optimized to ensure an exact number of cycles in the sample buffer. An 8192-point (168-ms) buffer was averaged, with phase based on synchronous positive zero crossings of both primaries. Stimuli were turned on for 5 s before data collection started. The spectrum of the buffer was then calculated and a number of spectra were averaged to produce the final spectrum. Typically, three spectra were averaged with each spectrum derived from an average of five time buffers. Spectral peaks were derived as the local maximum within an 11-point cursor centered at the expected frequency. The noise floor was established by averaging 6 points of the cursor distant from the peak, i.e., 3 points from each end of the 11-point cursor. At the stimulus levels used, $2f1-f2$ amplitude was an average of 34.1 dB above the noise floor and $f2-f2$ was an average of 24.8 dB above the noise floor.

F. Endolymphatic manipulations

1. Exposure to 200 Hz, 115 dB SPL

A 200-Hz tone was delivered to the ear from the Sennheiser speaker at a level of 115 dB for 3 min. This exposure has previously been shown to induce transient endolym-

phatic hydrops (Flock and Flock, 2000; Salt, 2003). During exposure to the tone, no sound-evoked potentials or acoustic emissions were collected.

2. Injection of artificial endolymph

The bone overlying stria vascularis in the second turn was thinned with a flap knife (Mueller AU13400) and a small, approximately 30-μm, fenestra was made with an angled pick (Storz N1705-80). Injections were performed from double-barreled glass pipettes, with their tips beveled to a diameter of 15–20 μm. The injection barrel was filled with an artificial endolymph consisting of 140-mM KCl and 25-mM $KHCO_3$ and was mounted on a Nanoliter 2000 microinjection pump [World Precision Instuments (WPI), Sarasota]. The second barrel of the pipette was filled with 500-mM KCl and was used to record endocochlear potential. The pipettes were inserted into endolymph through the access fenestra using registration of a stable positive voltage as verification the pipette tip was located in the endolymphatic space.

3. Treatment with furosemide

Animals were given furosemide (Vetus Furoject, 50 mg/ml, Burns, New York) intravenously at a dose of 100 or 50 mg/kg. Drug delivery was followed by 0.3 ml of lactated Ringer's to ensure the entire dose was expelled from the cannula.

In experiments where furosemide was injected locally in the cochlea, an injection pipette containing 10 mg/ml of furosemide was sealed into the basal turn of scala tympani. The stock 50-mg/ml furosemide was diluted 1:4 in artificial perilymph containing (in mM) NaCl (125), KCl (3.5), $CaCl_2$ (1.3), $NaHCO_3$ (25), $MgCl_2$ (1.2), NaH_2PO_4 (0.75), and glucose (5). The injection pipette was mounted on a WPI Ultrapump. The otic capsule was thinned and the dry bone coated with thin cyanoacrylate adhesive. The thinned area was surrounded by a ring of two-part silicone adhesive (Kwik-Cast, WPI, Sarasota) and a small fenestra made in the middle with an angled pick. The injection pipette was inserted and droplet of cyanoacrylate was applied while wicking fluid away from the site. When a seal had been achieved the entire field was covered with more two-part silicone adhesive. Injections into scala tympani were performed at a rate of 100 nl/min for a period of 10 min.

G. Experimental design

Immediately after the cochlea was exposed, animals were evaluated with an AP threshold audiogram and the measurement and analysis of CM to low-frequency tones. Animals showing hearing loss, specifically with an AP threshold more than 2 standard deviations above the laboratory mean, were excluded from the study, as were any animals in which the cochlear microphonic to a 500-Hz, 90-dB SPL tone was less than 200 μV. This latter exclusion criterion was set arbitrarily to ensure that the signal-to-noise ratio was adequate to resolve low-level spectral peaks in the CM analysis. We also excluded some animals in which we observed tissue in the external canal contacting the tympanic membrane. This could be seen through the tympanic membrane from the middle-ear side and occurred when sectioning the ear canal compromised venous drainage from the structure. These animals typically showed elevated AP thresholds to low frequencies, low CM amplitude, and a notably distorted CM to low frequencies. Congestion of the tissue was subsequently avoided by making the incision for the earbar parallel to the long axis of the ear canal. The baseline data obtained from the above measurements were summarized as representing the premanipulation state of the animals. Experimental procedures on the cochlea, such as perforating the otic capsule and placing injection pipettes, were performed after baseline data were collected.

The experimental study consisted of measuring cochlear potentials to biphasic and single phase stimuli, AP thresholds to 8- and 2.8-kHz tones, and acoustic emissions repeatedly. In endolymph injection experiments the endocochlear potential was also measured. It required approximately 35 s to collect a complete set of measurements, so the sampling interval was set to 40 s. Data collection was performed as a fully automated procedure. Measured parameters were graphed and stored as they were collected. When repeated measurements made over at least a 5-min period were judged by the experimenter to be stable (i.e., not drifting in one direction), the animal was subjected to one of the interventions listed above, during which the collection of responses continued.

The Animal Studies Committee of Washington University approved the experimental procedures used in this study under protocol numbers 19 990 029 and 20 020 010.

H. Calculated dependence of distortion on cochlear transducer operating point

The output signal (V) generated by the cochlear transducer responding to a sine wave input (P) was calculated using a first-order Boltzmann function to describe the transducer [Eq. (1)], an approach that has previously been used by Kirk *et al.* (1997)

$$V = -P_{\mathrm{sat}} + (2\ \ P_{\mathrm{sat}})/(1+\exp(z(P+P_{\mathrm{o}}))), \tag{1}$$

where P_{sat} is the saturation voltage of the transducer, z is the sensitivity of the transducer, and P_{o} is the operating point.

Based on this equation, the slope of the calculated transducer curve varies when the saturation voltage (P_{sat}) is changed. To avoid this problem, we therefore defined z in terms of a slope parameter (S) and P_{sat} [Eq. (2)]. When z was defined by this relationship, changing P_{sat} did not change the slope of the transducer curve

$$z = -2\ \ S/P_{\mathrm{sat}}. \tag{2}$$

Output waveforms were calculated for a sinusoidal input as operating point was systematically varied. Waveforms were subjected to the same methods of spectral analysis and determination of operating point as were the recorded cochlear microphonic data. This analysis of calculated waveforms was used both to validate the operating point analysis method and to aid in the interpretation of experimental data.

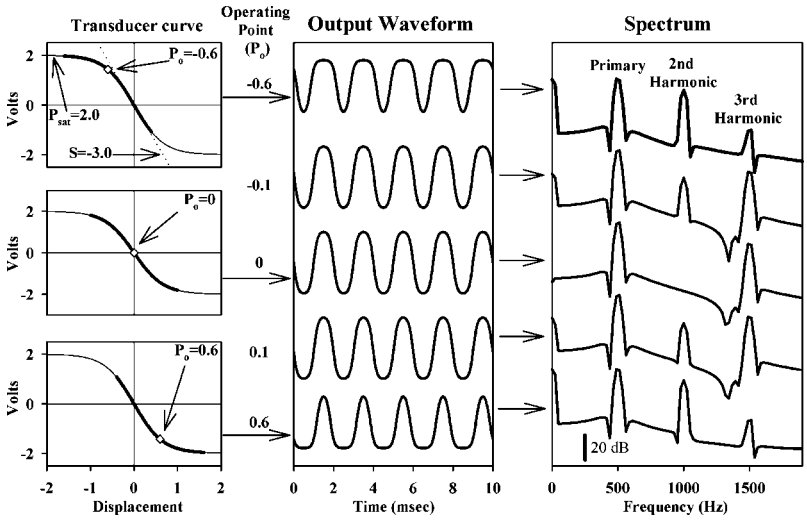

FIG. 1. Output waveforms (middle panel) calculated for transducers with varying operating points (P_o) as indicated. The three panels at the left show the transducer curves for operating point values of 0.6 (upper), 0 (middle), and −0.6 (lower). In each plot, the heavy line indicates the region of the transducer curve over which the stimulus is applied. Spectral analysis of each output waveform is shown in the right panel. For operating point set to zero, the output waveform is symmetric and shows low second harmonic distortion. Even small deviations in operating point (0.1) cause second harmonic distortion increases, even though distortion is not apparent in the time waveform. With operating point values further from zero (0.6) the time waveform is highly asymmetric and a prominent second harmonic distortion peak is apparent in the spectrum.

I. Operating point analysis of cochlear microphonic

A simulated microphonic waveform was calculated as described above and based on the Boltzmann parameters P_{sat}, S, and P_o together with parameters for frequency (f), phase (p), and dc offset (V_o). A curve-fitting procedure was then used in which the six parameters were simultaneously varied to best fit the calculated waveform to the experimentally recorded cochlear microphonic waveform. Fit was optimized by minimizing the sum of squares of differences between calculated and experimental curves. The fitting procedure was performed in real time during data collection, and the derived Boltzmann parameters were recorded. The amplitude of the cochlear microphonic determined the parameters S and P_{sat}. Under this analysis, the scale of operating point is such that a value of 1 is equal to the displacement of the transducer at the peak of the applied sinusoidal stimulus.

III. RESULTS

A. Simulations

The cochlear transducer has nonlinear, saturating characteristics and can be approximated by a Boltzmann function. With such a transducer, the output signal depends on where the input signal is ''centered'' with respect to the transducer, the so-called ''operating point.'' This concept and its consequences are shown in Fig. 1, where output waveforms were calculated for a sinusoidal input at 500 Hz with different values of operating point. The transducer curve, based on the Boltzmann function and its parameters, is shown in the left column. With the transducer operating point at zero (left center panel), a sinusoidal input gives a symmetric output voltage. Spectral analysis of this output shows an absence of second harmonic distortion. Positive or negative values of operating point produce an asymmetry of the time waveform which is detected in the spectrum as a second harmonic distortion. For small values of operating point (e.g., 0.1), little change in the time waveform is apparent, while the spectrum shows a prominent second harmonic. The polarity of operating point shown here is intended to represent displacement of structures in a similar manner to an applied pressure in the ear canal. Positive displacement indicates positive pressure in the ear canal and displacement of the organ of Corti towards scala tympani. Since organ of Corti displacements towards scala tympani cause a negative voltage shift in that scala, the slope of the transducer (left column) is negative.

The calculated relationships between distortion and operating point are shown in Fig. 2. These curves show the magnitude of the second and third harmonics from spectra similar to those in Fig. 1, relative to the magnitude of the primary. This demonstrates graphically that second harmonic distortion is extremely sensitive to deviations of the operating point away from zero, with distortion increasing by almost 50 dB as operating point increases over the range shown. In contrast, the third harmonic distortion peak, which is dominated by the saturating characteristic of the transducer, is relatively unchanged for small operating point changes but decreases when operating point becomes large. These data suggest that measures of second harmonic distortion may be a potentially useful indicator of small changes of cochlear transducer operating point.

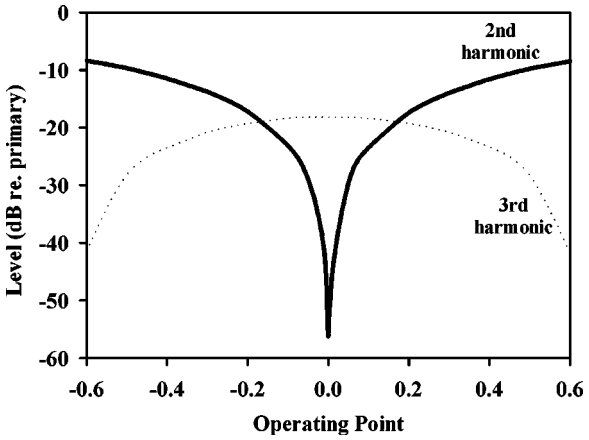

FIG. 2. Dependence of harmonic distortion amplitude on transducer operating point. Second harmonic distortion is extremely sensitive to small operating point changes and increases rapidly as operating point moves away from zero. Third harmonic distortion is less sensitive to small operating point changes but decreases for higher operating point values.

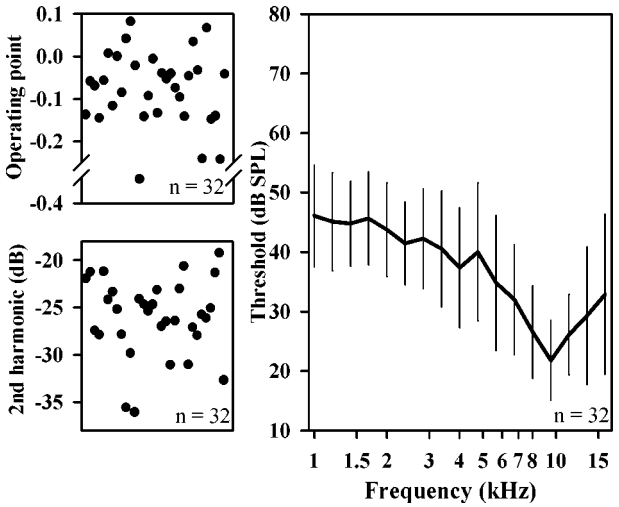

FIG. 3. Baseline measurements of operating point (upper left), second harmonic distortion (lower left), and of cochlear sensitivity as indicated by AP thresholds (right). Each data point in the plots at the left represent an individual animal. Bars on the AP threshold plot indicate standard deviation. Baseline measurements were made prior to any manipulations of the cochlea.

B. Baseline measurements

The variation of operating point, second harmonic distortion, and cochlear sensitivity prior to any experimental manipulations is given in Fig. 3. Both operating point and second harmonic distortion were highly variable across individual animals. Although the mean value of operating point was -0.08 (s.d. 0.09, $n=32$), there were a number of animals with positive operating point values. Second harmonic distortion, measured in dB relative to the primary peak, varied from -36 dB to over -20 dB. All animals showed normal cochlear function as assessed by AP thresholds, even the animal with an outlying large negative operating point (-0.35).

C. 200-Hz tone exposure

Figure 4 shows the simultaneously measured operating point and second harmonic distortion changes resulting from exposure to 200 Hz for 3 min at 115 dB SPL in two experiments. Both examples showed a movement of operating point in the positive direction following sound exposure, although the time courses differ slightly. In contrast, the behavior of the second harmonic differs markedly in the two experiments. In example 1, second harmonic distortion increased after the exposure, while in example 2 it showed a marked decrease. The difference between the two animals can be appreciated by plotting each pair of operating point and second harmonic distortion values against each other, as shown in the correlation plots in the right column of the figure. For example 1, the pre-exposure operating point was slightly positive. In this case, moving further positive, away from zero, would be expected to increase distortion, which is what was observed. In contrast, the animal in example 2 showed a negative operating point before exposure. In this case, a movement of operating point in the positive direction brings operating point closer to zero, with an expected reduction of second harmonic distortion. In this example, the relationship between measured operating point and second harmonic distortion closely follows the calculated curve.

Interpretation of harmonic distortion changes during experimental manipulations is therefore extremely difficult unless the baseline operating point of the individual animal is considered. Since distortion may differ in both magnitude and direction in different animals, calculating the deviation of responses across animals has little value. In the figures that follow, we have therefore shown individual response curves together with the mean value to interpret distortion changes.

The response changes resulting from 200-Hz, 115-dB SPL exposure are summarized in Fig. 5. This exposure condition has been shown to induce a transient endolymphatic hydrops that recovers back to normal over a 10–20-min period with a recovery half-time of 3.2 min (Salt, 2003). In the present study, the treatment produced a transient positive shift in operating point by approximately 0.1, consistent with a hydrops-induced displacement of the organ of Corti towards scala tympani. The operating point shift was transient, however, and showed a recovery back to baseline within 3–4

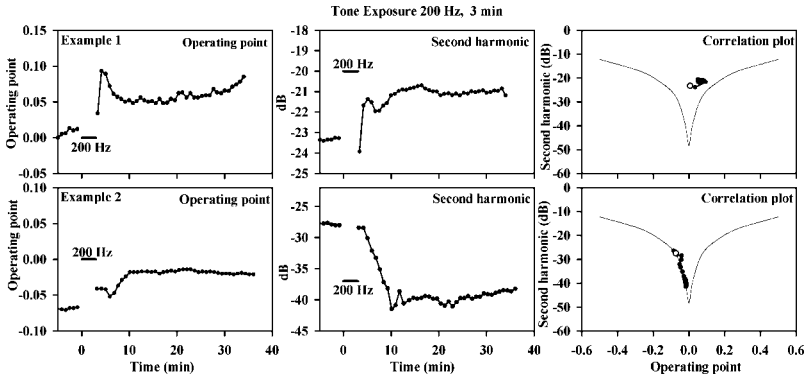

FIG. 4. Two examples in which changes of operating point and second harmonic distortion were recorded simultaneously before and after exposure to a 200-Hz tone for 3 min at 115 dB SPL. The exposure increases operating point in both examples. Second harmonic is increased in example 1 (upper row) and is decreased in example 2 (lower row). This difference is accounted for by consideration of the pre-exposure operating points for the two animals. The positive deflection moves operating point further from zero in example 1 (causing distortion to increase) and closer to zero in example 2 (causing distortion to decrease). The correlation plots (right column) show second harmonic distortion plotted as a function of operating point. The open symbol shows the pretreatment value and the thin line shows the calculated dependence from Fig. 2.

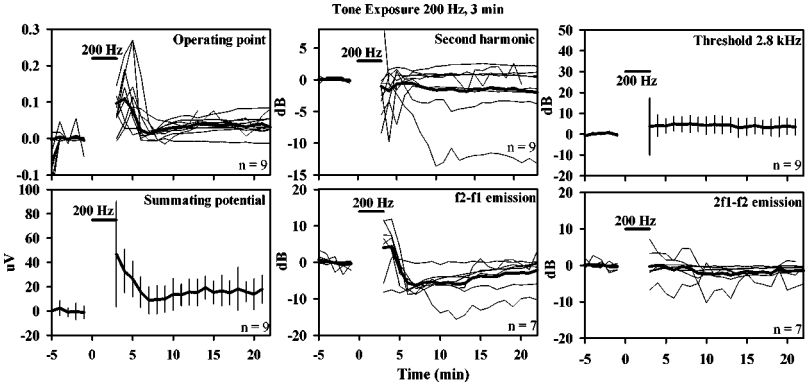

FIG. 5. Response changes elicited by exposure to a 200-Hz tone for 3 min at 115 dB SPL. In each panel, the mean curve is shown as a thicker line. Thin lines represent individual experiments. Bars indicate standard deviation. Operating point and SP are transiently increased due the 200-Hz-induced endolymph volume increase. Second harmonic distortion and the $f2-f1$ emission show substantial changes that vary in direction, magnitude, and time course due to the complex dependence on operating point. Cochlear sensitivity, as assessed by thresholds at 8 and 2.8 kHz and by the $2\,f1-f2$ emission, is not markedly changed by the exposure.

min of the tone exposure ending. The SP similarly increased transiently and recovered back to baseline within a few minutes. The cochlear microphonic measured with single-phase 500-Hz stimuli or 4-kHz biphasic stimuli showed only small amplitude fluctuations relative to the mean baseline amplitudes of 1478 μV (s.d.$=$243, $n=9$) and 538 μV (s.d. $=$137, $n=9$), respectively (data not shown). Second harmonic distortion showed substantial changes in all animals, but the timing, magnitude, and polarity of the change were highly variable due to the reasons discussed above. The $f2-f1$ emission similarly showed substantial changes in all animals, typically larger than 10 dB. Both increases and decreases of $f2-f1$ were apparent, comparable to changes in the second harmonic. Measures of cochlear sensitivity [AP thresholds at 8 kHz (not shown), 2.8 kHz, and the $2\,f1-f2$ emission] indicated only minor changes during the tone-induced endolymph volume disturbance.

D. Artificial endolymph injection at 80 nl/min

Injection of artificial endolymph has previously been used to induce endolymph volume disturbances. In a prior study, 15-min injections at rates higher than 25 nl/min caused endolymphatic hydrops and a basally directed endolymph flow in the cochlea (Salt and DeMott, 1997). Figure 6 summarizes the effect of injections at 80 nl/min for 15 min (total 1.2 μL injected) on the measured responses. Rather than operating point increasing due to the endolymph volume increase, in most cases we found that large oscillations of operating point occurred. The initial deflection, though large and positive in one animal, was negative in others. The mean curve showed a decrease during the injection, followed by a slow increase some time after the injections finished. The second harmonic also showed oscillations in amplitude with occasional larger deflections. In each experiment, the second harmonic distortion changes were accounted for by the operating point changes, as shown in the example correlation plot at the upper right. In this case, distortion decreased and passed through a minimum as operating point moved through zero, then increased as operating point became more positive. The observation of a minimum close to the measured zero operating point validates the accuracy of the operating point estimate. Two of the experiments showed distortion going through a minimum as the operating point of the animal passed through zero. The SP and $f2-f1$ emission similarly showed increased variation throughout the injection with stabilization afterwards. The injection produced only minor changes in EP, $2\,f1-f2$ emission, and thresholds at 8 kHz. In contrast, thresholds at 2.8 kHz showed a systematic increase during injection (average 15 dB) and a slow recovery afterwards, consistent with the injection-induced endolymph volume disturbance.

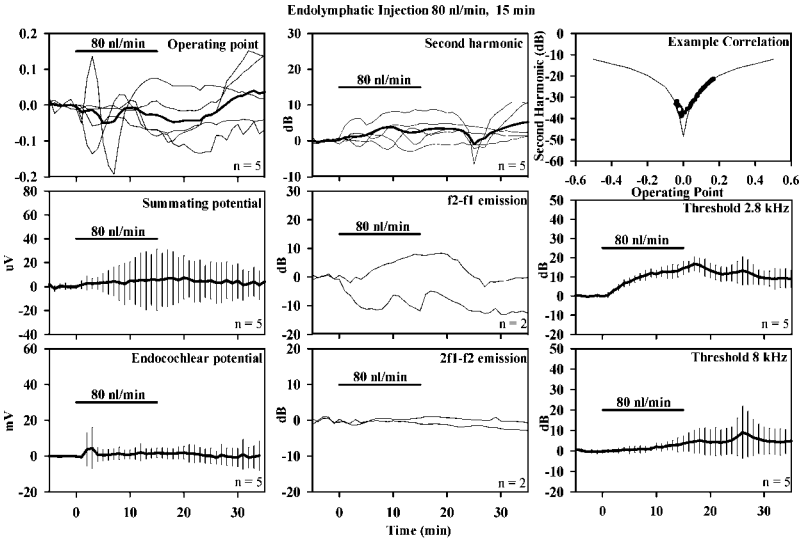

FIG. 6. Response changes elicited by artificial endolymph injection into the second turn of scala media at 80 nl/min for 15 min. Mean curves are shown as thicker lines. Thin lines represent individual experiments. Bars indicate standard deviation. Operating point shows injection-induced fluctuations but no overall increase indicating endolymphatic hydrops. Summating potential similarly shows changes that are not consistent. Second harmonic distortion and the $f2-f1$ emission show variations that depend on operating point. An example of the correlation between second harmonic distortion and operating point is shown at the upper right.

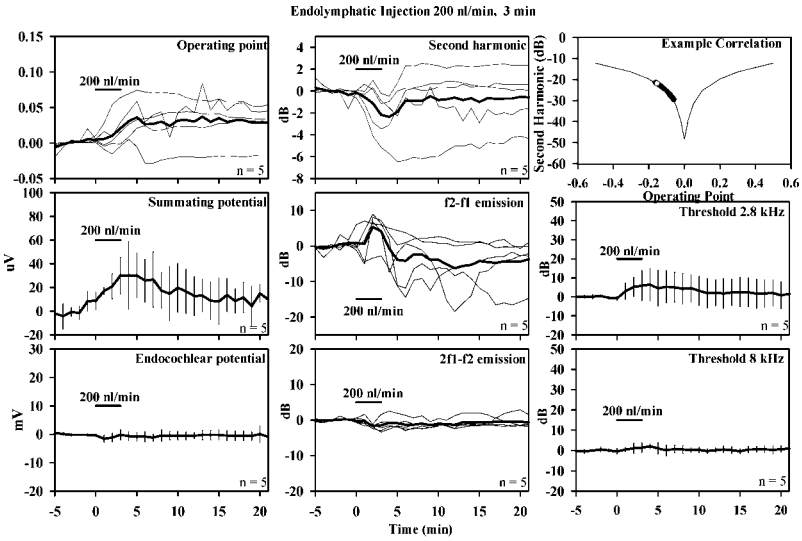

FIG. 7. Response changes elicited by artificial endolymph injection into the second turn of scala media at 200 nl/min for 3 min. Mean curves are shown as thicker lines. Thin lines represent individual experiments. Bars indicate standard deviation. In the majority of animals, operating point is increased by the injection, although cyclical fluctuations are also apparent and are reflected in second harmonic distortion and $f2-f1$ emission changes. An example of the correlation between second harmonic distortion and operating point is shown at the upper right.

E. Artificial endolymph injection at 200 nl/min

In view of the rapid recovery of operating point following hydrops induced by 200 Hz, and the absence of a major operating point increase with 80-nl/min injection, it appeared likely that operating point could adapt quickly to abnormal endolymph volume states. We therefore performed injections at higher rates to induce larger endolymph volume changes more rapidly. Figure 7 summarizes the response changes resulting from 200-nl/min injection of artificial endolymph into the second turn of the cochlea for 3 min, for a total of 0.6 μL injected. In four of five animals, operating point showed an increase consistent with endolymphatic hydrops. The fifth showed operating point oscillations, similar to those observed with lower injection rates, but no overall increase. The second harmonic showed transient changes during injection, as did the $f2-f1$ emission. Second harmonic distortion changes were more consistent in this group as all five animals had negative baseline operating points. In the example correlation plot, second harmonic distortion showed a sizable decrease, consistent with the movement of operating point towards zero and in a manner close to that predicted by the simulations. The SP showed an injection-induced increase. Injection at this rate again had little influence on EP, thresholds at 8 kHz, and the $2f1-f2$ emission. Thresholds at 2.8 kHz were slightly elevated, with a mean increase of 6 dB. The smaller threshold increase at 2.8 kHz compared with the 80-nl/min injection group is accounted for by the smaller total volume injected.

F. Artificial endolymph injection at rate of 400 nl/min

The physiologic changes induced by artificial endolymph injection at the higher rate of 400 nl/min for 3 min are summarized in Fig. 8. The total volume delivered in this procedure was 1.2 μL, the same as the injections shown in subsection D at 80 nl/min. Although four out of five animals showed a transient operating point increase during injection, almost all showed a subsequent operating point decrease to below the preinjection value. The decline in operating point appears to be associated with the larger total volume injected. The second harmonic typically showed transient decreases, followed by an increase as expected from the operating point changes, as shown by the example correlation plot. The SP also showed a prominent increase during injection but did not fall below baseline afterwards. The $f2-f1$

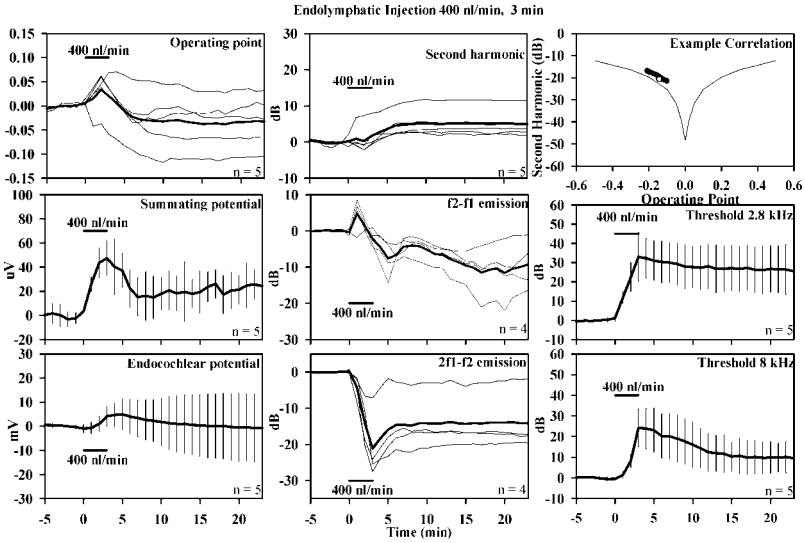

FIG. 8. Response changes elicited by artificial endolymph injection into the second turn at 400 nl/min for 3 min. Mean curves are shown as thicker lines. Thin lines represent individual experiments. Bars indicate standard deviation. In most animals, operating point was transiently increased by the injection and subsequently declined. The summating potential showed a similar time course of change. Second harmonic distortion increased, consistent with the operating point change as indicated in the correlation example. The $f2-f1$ emission decreased. Endocochlear potential and cochlear microphonic amplitude increased, while all measures of cochlear sensitivity (thresholds at 8 kHz, 2.8 kHz, and $2f1-f2$ emission) suggest sensitivity declines.

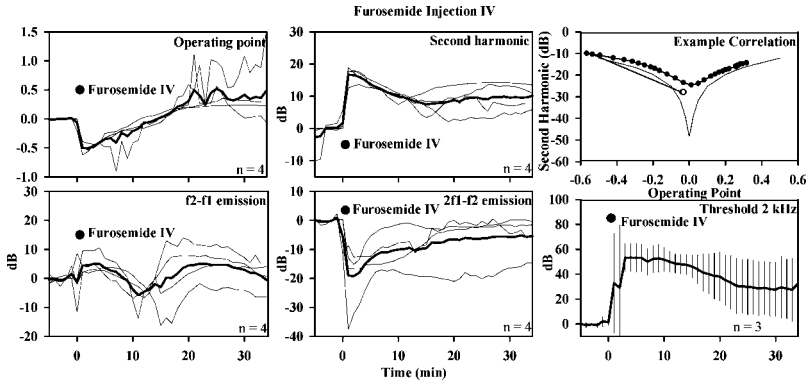

FIG. 9. Response changes elicited by intravenous administration of furosemide. Mean curves are shown as thicker lines. Thin lines represent individual experiments. Bars indicate standard deviation. Operating point transiently decreases, before increasing above the baseline value. Both second harmonic and the $f2-f1$ emission show an increase, followed by a decrease to a minimum caused by the transducer operating point passing through zero. An example of the relationship between second harmonic distortion and operating point is given. Cochlear sensitivity declines, as indicated by the reduction in $2\,f1-f2$ emission, elevation of threshold at 2 kHz, and decline in cochlear microphonic.

emission showed a transient increase during injection and a subsequent decline. Although the endocochlear potential and CM were both increased by injection, measures of cochlear sensitivity (thresholds at 8 kHz, 2.8 kHz, and the $2\,f1-f2$ emission) all indicated a substantial decrease in cochlear sensitivity from injection at this rate with little indication of recovery afterwards.

G. Intravenous furosemide injection

Administration of furosemide was found to produce substantial changes of operating point that allowed the dependence of cochlear distortion on operating point to be demonstrated. The changes induced by intravenous furosemide are summarized in Fig. 9. In all animals, furosemide caused an operating point decrease followed by a slow increase. This resulted in a rapid increase in second harmonic distortion, followed by a decrease reaching a minimum after approximately 10 min, before increasing again. The example correlation plot shows the dependence of distortion on the operating point movements. Of great interest is the observation that with this treatment, the $f2-f1$ emission showed changes comparable to those of the second harmonic. Specifically, $f2-f1$ showed an increase followed by a decline passing through a minimum before increasing again. This complex time course would not be interpretable without some understanding of the effects of operating point on distortion in the cochlea. The reduction in the $f2-f1$ emission to a minimum varies in time from animal to animal but undoubtedly represents the time when the cochlear transducer operating point passed through zero as it moves positive in the recovery phase. Intravenous furosemide caused a large reduction in cochlear microphonic amplitude (not shown) and decreased cochlear sensitivity, as indicated by reduction of $2\,f1-f2$ emission and the elevation of thresholds at 2 kHz.

H. Furosemide injected locally into the cochlea

Locally applied furosemide had markedly different effects on operating point than when given intravenously, as summarized in Fig. 10. The operating point shows a substantial increase followed by a decline. Second harmonic distortion showed a substantial decline, in some cases becoming 40 dB lower than the primary as zero operating point was passed. The example correlation shows the clear dependence of distortion level on the cochlear transducer operating point. The magnitude of reduction of second harmonic distortion varied in different experiments, depending on the baseline operating point of each animal. With this treatment, the $f2-f1$ emission did not show changes similar to the second harmonic, as was noted previously with intravenous furosemide. This is accounted for by the fact that local furosemide may rapidly affect the basal cochlear turn but will only slowly influence higher cochlear turns. The slow reduction in $f2-f1$ emission, $2\,f1-f2$ emission, and slow elevation of threshold at 2 kHz are consistent with all of these responses originating from higher cochlear turns that are less influenced by furosemide. This supports the view that the operating point associated with the 500-Hz cochlear microphonic differs from the operating point associated with the $f2-f1$ emission, presumably because operating point can vary between different cochlear locations.

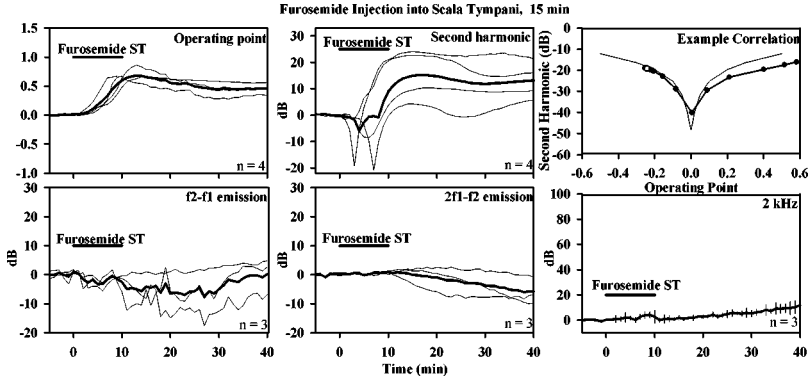

FIG. 10. Response changes elicited by local administration of furosemide into the basal turn of scala tympani. Mean curves are shown as thicker lines. Thin lines represent individual experiments. Bars indicate standard deviation. Operating point increases, causing a complex change in the second harmonic as expected, based on the correlation shown at the upper right. The $f2-f1$ emission, $2\,f1-f2$ emission, and 2-kHz threshold all show slow, minor changes, consistent with their generation at more apical sites that are less influenced by the applied furosemide.

IV. DISCUSSION

Our findings support the views of Frank and Kossl (1996) and Kirk and Patuzzi (1997) that the operating point of the cochlear transducer plays a critical role governing the levels of distortion in the ear. While the prior studies focused on $f2-f1$, the present study also shows a strong dependence of second harmonic distortion of the cochlear microphonic on operating point. In addition, we found that baseline operating points measured prior to experimental manipulations varied over a considerable range, with animals showing positive or negative values. This distribution accounted for the variable levels of second harmonic distortion in the cochlear microphonic and explained sometimes oppositely directed distortion changes with endolymph manipulations. The baseline variation of operating points appears to have only minor influence on cochlear sensitivity measured by AP thresholds, with all animals in the study showing normal threshold curves across the frequency range.

The calculated relationship between second harmonic distortion and operating point shown in Fig. 2 provides a conceptual framework for the interpretation of distortion changes during experimental manipulations. The fact that an experimental treatment may cause distortion increases in some animals and distortion decreases in others, or may show complex patterns with minima, as in Figs. 9 and 10, would be difficult to interpret without taking into account their underlying dependence on transducer operating point. The observation that in some experiments the second harmonic distortion goes through a minimum as the measured operating point passes through zero (e.g., Figs. 6, 9, and 10) also validates the methodology used to derive operating point. It is notable that the pretreatment level of second harmonic distortion is not always low and in many cases the distortion level seen in the initial normal state was reduced by the experimental treatment (e.g., Figs. 4, 5, 6, 7, and 10). The average operating point measured with a 500-Hz, 90-dB stimulus was -0.08, suggesting a bias of the cochlear transducer equivalent to a movement of the organ of Corti towards scala media. This observation agrees with the findings of Kirk *et al.* (1997) in which the examples they presented showed negative pretreatment operating points. However, the range of operating points and the possibility that some animals may have positive values have not previously been documented. The variation of operating point also explains some of the variations in prior studies. In the study of Frank and Kössl (1996), low-frequency bias tones were found to modulate the $f2-f1$ emission either at the frequency of the bias tone or in some animals at twice the frequency of the bias tone. We interpret this as showing that if the operating point is nonzero, and the bias amplitude is not sufficient to drive the transducer to reach zero, then the modulation by the bias would occur at the frequency of the bias tone. On the other hand, if operating point is near zero and the bias tone is large enough to drive the transducer through zero, then the distortion will show increases twice per bias cycle and the modulation will occur at twice the frequency of the applied stimulus. Operating point thus plays a key role in generating distortion and is central to our understanding and interpretation of second harmonic and $f2-f1$ distortion.

Disturbances of the endolymphatic system are shown to cause transient changes of operating point in the cochlea. Two hundred-Hz tones and injections into endolymph at high rates (200 nl/min and higher) cause a positive movement of operating point, consistent with an endolymph volume enlargement and displacement of the organ of Corti towards scala tympani. Comparison of the time courses of endolymph volume change induced by 200-Hz tone exposure (Salt, 2003) or by artificial endolymph injections (Salt and DeMott, 1997) with operating point data from the present study shows that operating point recovers substantially faster than does the endolymph volume disturbance. This is consistent with the observation that slowly occurring endolymph volume increases (80-nl/min injection rate) appear to produce instability or slow oscillations of operating point, rather than a sustained operating point change. These observations suggest that some form of compensation for the induced endolymph volume disturbance occurs at the level of the organ of Corti. Thus, operating point, while sensitive to some volume disturbances, is not a direct measure of endolymph enlargement but is influenced by compensation processes. Kirk *et al.* (1997) calculated that the recovery kinetics of operating point could be explained by two exponential processes with time constants of 30 and 220 s. Our data are consistent with this analysis.

An important finding of the study is that acute endolymph volume disturbances can be detected by noninvasive means and are seen as substantial changes of the $f2-f1$ emission. Although the $f2-f1$ changes temporally corresponded with the endolymph volume change, the magnitude, direction, and time course of change were not indicative of the magnitude or duration of endolymph volume change. It is apparent that The observation that $f2-f1$ changes can be large (greater than 10 dB) while $2f1-f2$ emission and AP threshold changes are minor (a few dB). Kirk *et al.* (1997) and Frank and Kössl (1996) interpreted this difference as suggesting that a fundamental change in distortion generation was occurring, rather than an alteration to the mechanical drive to a constant distortion generator. It is our interpretation that the large magnitude of the $f2-f1$ and second harmonic distortion changes is a reflection of the high sensitivity of distortion to small operating point changes, as shown in Fig. 3, especially when operating point approaches zero. The mechanism of generation is not fundamentally different but the dependence on operating point is highly nonlinear. At present, a quantitative interpretation of $f2-f1$ changes is not possible. Correlations of $f2-f1$ magnitude with operating point derived from CM recordings are poor, since both responses are collected with different stimulus conditions and involve different cochlear regions. It is likely that the operating points of different cochlear regions will vary according to the properties of the local hair-cell population. At present, we cannot determine the operating point at the specific sites involved in $f2-f1$ generation, at the frequencies and levels of stimulation used to elicit the emission. The theoretical foundation provided by our study may permit a more quantitative approach to the analysis of $f2-f1$ changes in the future.

Our findings with 200-Hz exposure replicate to a con-

siderable degree the findings of Kirk and Patuzzi (1997), although slightly different conditions were used in our study. We delivered the 200-Hz tone at a level of 115 dB SPL, which is higher than that used by Kirk and Patuzzi. It is a level that we have shown consistently produces endolymphatic hydrops in the second turn of the cochlea (Salt, 2003). In addition, our probe tone was delivered at 500 Hz and at 90 dB SPL, compared to Kirk and Patuzzi (1997), who used a 200-Hz tone at 95 dB SPL to obtain CM from the basal turn. We similarly found an increase in operating point with the exposure, consistent with an induced endolymphatic hydrops. Due to the higher level of tone exposure, we find the bounce in AP thresholds after the exposure to be less apparent, which has been reported previously (Salt, 2003).

We initially expected that endolymphatic injections would increase endolymph volume with minimal secondary effects and could possibly provide a well-controlled manipulation of operating point. Instead, we found that injections at rates that are known to produce hydrops caused fluctuations and oscillation of the operating point. Only with the higher injection rates was an increase in operating point apparent. However, after the injection of 1200 nl of artificial endolymph, either in 3 min (400 nl/min) or in 15 min (80 nl/min) the operating point in many animals decreased to a level below the starting value. The cause of this overcompensation is not known. In comparison, for those animals that received a total of 600 nl of artificial endolymph at 200 nl/min, operating point change remained positive in all except one. Operating point changes with injection thus seem to be affected by both the rate and the total volume of artificial endolymph injected.

Furosemide treatment produced large changes of operating point. Given intravenously, operating point showed a consistent decrease, followed by an increase and overshoot. With a local injection of a dose that caused a similar cochlear microphonic decrease, a consistent, but opposite, result was obtained. Operating point increased markedly, then recovered but remained elevated. Furosemide inhibits the Na/K/2Cl cotransporter (NKCC1) found in the marginal cells of stria vascularis and other cell types. This action would be expected to suppress K^+ currents circulating through the endolymph. Given intravenously, furosemide has been shown to reduce the endocochlear potential and to reduce endolymph K^+ and Cl^- (Brusilow, 1976; Rybak and Morizono, 1982; Rybak and Whitworth, 1986). It is likely the ion reductions would be accompanied by water movement out of endolymph and possibly an endolymph volume reduction, which would be consistent with the operating point decrease. However, we cannot conclude that the operating point change reflects an endolymph volume change as other mechanisms may predominate. As there are likely both current and voltage changes at the level of the hair cells, operating point changes may arise by a number of other mechanisms.

It is interesting that locally applied furosemide gave an oppositely directed operating point change. This is likely explained by different cochlear locations being affected by the drug. The first possibility is that different regions along the length of the cochlea may be involved, with intravenous furosemide affecting the entire length and local injection affecting primarily the base (Schmiedt *et al.*, 2002). It has also been shown that the cell types involved in ion transport processes vary from base to apex (Spicer *et al.*, 2003), so a variation of sensitivity to furosemide with location is possible. Alternatively, it is possible that within any segment of the cochlea furosemide may have access to different cell types when given intravenously compared to when it is given locally. Intravenous drug will have ready access to the vascularized intrastrial space and from there influence the marginal cells. In contrast, when given into scala tympani furosemide must first cross the basal and intermediate cell layer, with associated extremely tight junctions (Jahnke, 1975), in order to reach the marginal cells. Other cell types that contain the NKCC1 cotransporter would likely be exposed to relatively higher doses and may disturb radial ionic movements in a manner different from the suppression of ion transport in the marginal cells. The specific other cell types expressing the NKCC1 cotransporter are spiral ligament fibrocytes of type II, IV, and V, especially in the suprastrial region and in the vicinity of the outer sulcus, and spiral limbus fibrocytes (Crouch *et al.*, 1997; Sakaguchi *et al.*, 1998). If these cell types regulate ion currents in a manner different from the marginal cells, it may account for the different direction of operating point movement.

The acoustic emissions changes we observed with furosemide ($2f1-f2$ and $f2-f1$) were comparable to those observed by Mills *et al.* (1993). They found the $f2-f1$ to exhibit changes completely different from $2f1-f2$, characterized by sharp minima as we also observed. Based on phase measurements they interpreted the minima as representing zero crossings, an interpretation that our present study supports.

Under some conditions operating point, second harmonic, $f2-f1$, and SP changes occurred with minimal changes of AP thresholds or of the $2f1-f2$ emission. Prior studies have noted that the $f2-f1$ emission and operating point are variable and influenced by a variety of factors that are not normally associated with cochlear sensitivity change. Psychophysical experiments in humans initially showed that the magnitude of the difference tone ($f2-f1$) was highly variable across subjects (Plomp, 1965; Humes, 1979). Modeling studies by Hall (1974) concluded that $f2-f1$ was dependent on the inclusion of asymmetric nonlinearities. With the advent of acoustic emissions, Brown (1988) characterized the $f2-f1$ response, showing that the magnitude decreased as stimulation was prolonged, during which time $2f1-f2$ remained stable. Brown also found the $f2-f1$ emission to be susceptible to anesthesia and suggested that the sensitivity change could be an efferent effect. Mountain (1980) found $f2-f1$ emission magnitude to be sensitive to electrical stimulation of the efferent system. Pharmacological manipulation studies by Kirk and Johnstone (1993) also gave support for efferent involvement. In contrast, similar studies of $f2-f1$ variation in rabbits were found to be inconsistent with an efferent involvement (Whitehead *et al.*, 1991). A subsequent study by Kujawa *et al.* (1995) documented changes in $f2-f1$ with the duration of stimulation, but pharmacologic treatments of the cochlea failed to support the

concept that $f2-f1$ was controlled by the efferent system. Based on an analysis of cochlear microphonic during electrical efferent stimulation, Patuzzi and Rajan (1990) also concluded that the stimulation-induced increase in microphonic amplitude occurred with little or no change in operating point. The possibility that distortion was linked to operating point was implied by Mills *et al.* (1993), in their interpretation of $f2-f1$ changes that ''went through another apparent zero'' during furosemide treatment. This concept was further developed by Frank and Kossl (1996) and Kirk and Patuzzi (1997), in which operating point changes induced distortion changes in a predictable manner based on the known characteristics of cochlear transduction, as discussed above. Combined with our present study, there is good evidence that second harmonic and $f2-f1$ distortion are highly dependent on operating point, but operating point appears to be insensitive to efferent effects.

V. CONCLUSIONS

A dependence of second harmonic distortion and $f2-f1$ emissions on transducer operating point has been demonstrated. The operating points shown by different animals varied prior to treatments, a difference which markedly influences the observed responses to experimental manipulations. Second harmonic and $f2-f1$ distortion are sensitive to manipulations of the endolymphatic system and may provide a means to monitor endolymph volume disturbances.

ACKNOWLEDGMENTS

This work was supported by research grants RO1 DC01368 (A.N.S.) and T32 DC00022 (D.S.) from the National Institutes on Deafness and Other Communication Disorders (NIDCD), National Institutes of Health.

Bian, L., Chertoff, M. E., and Miller, E. (**2002**). ''Deriving a cochlear transducer function from low-frequency modulation of distortion product otoacoustic emissions,'' J. Acoust. Soc. Am. **112**, 198–210.

Brown, A. M. (**1988**). ''Continuous low level sound alters cochlear mechanics: An efferent effect?'' Hear. Res. **34**, 27–38.

Brusilow, S. W. (**1976**). ''Propanalol antagonism to the effect of furosemide on the composition of endolymph in guinea pigs,'' Can. J. Physiol. Pharmacol. **54**, 42–48.

Crouch, J. J., Sakaguchi, N., Lytle, C., and Schulte, B. A. (**1997**). ''Immunohistochemical localization of the Na–K–Cl co-transporter (NKCCl) in the gerbil inner ear,'' J. Histochem. Cytochem. **45**, 773–778.

Flock, A., and Flock, B. (**2000**). ''Hydrops in the cochlea can be induced by sound as well as by static pressure,'' Hear. Res. **150**, 175–188.

Frank, G., and Kössl, M. (**1996**). ''The acoustic two-tone distortions $2f1-f2$ and $f2-f1$ and their possible relation to changes in the operating point of the cochlear amplifier,'' Hear. Res. **98**, 104–115.

Frank, G., and Kössl, M. (**1997**). ''Acoustical and electrical biasing of the cochlea partition. Effects on the acoustic two tone distortions $f2-f1$ and $2f1-f2$,'' Hear. Res. **113**, 57–68.

Hall, J. L. (**1974**). ''Two tone distortion products in a nonlinear model of the basilar membrane,'' J. Acoust. Soc. Am. **56**, 1818–1828.

Humes, L. E. (**1979**). ''Perception of the simple difference tone $(f2-f1)$,'' J. Acoust. Soc. Am. **66**, 1064–1074.

Jahnke, K. (**1975**). ''The fine structure of freeze-fractured intracellular junctions in the guinea pig inner ear,'' Acta Oto-Laryngol., Suppl. **336**, 5–40.

Kirk, D. L., and Johnstone, B. M. (**1993**). ''Modulation of $f2-f1$: Evidence for a GABA-ergic efferent system in apical cochlea of guinea pig,'' Hear. Res. **67**, 20–34.

Kirk, D. L., and Patuzzi, R. B. (**1997**). ''Transient changes in cochlear potentials and DPOAEs after low-frequency tones: The 'two-minute bounce' revisited,'' Hear. Res. **112**, 49–68.

Kirk, D. L., Moleirinho, A., and Patuzzi, R. B. (**1997**). ''Microphonic and DPOAE measurements suggest a micromechanical mechanism for the 'bounce' phenomenon following low-frequency tones,'' Hear. Res. **112**, 69–86.

Kujawa, S. G., Fallon, M., and Bobbin, R. P. (**1995**). ''Time-varying alterations in the $f2-f1$ DPOAE response to continuous primary stimulation. I. Response characterization and contribution of the olivocochlear efferents.'' Hear. Res. **85**, 142–154.

Mills, D. M., Norton, S. J., and Rubel, E. W. (**1993**). ''Vulnerability and adaptation of distortion product otoacoustic emissions to endocochlear potential variation,'' J. Acoust. Soc. Am. **94**, 2108–2122.

Mountain, D. C. (**1980**). ''Changes in endolymphatic potential and crossed olivocochlear bundle stimulation alter cochlear mechanics,'' Science **210**, 71–72.

Patuzzi, R., and Rajan, R. (**1990**). ''Does electrical stimulation of the crossed olivo-cochlear bundle produce movement of the organ of Corti,'' Hear. Res. **45**, 15–32.

Plomp, R. (**1965**). ''Detectability threshold for combination tones,'' J. Acoust. Soc. Am. **37**, 1110–1123.

Rybak, L. P., and Morizono, T. (**1982**). ''Effect of furosemide upon endolymph potassium concentration,'' Hear. Res. **7**, 223–231.

Rybak, L. P., and Whitworth, C. (**1986**). ''Changes in endolymph chloride concentration following furosemide injection,'' Hear. Res. **24**, 133–136.

Salt, A. N. (**in press**). ''Acute endolymphatic hydrops generated by exposure of the ear to nontraumatic low-frequency tones,'' J.A.R.O. (submitted).

Salt, A. N., and DeMott, J. E. (**1997**). ''Longitudinal endolymph flow associated with acute volume increase in the guinea pig cochlea,'' Hear. Res. **107**, 29–40.

Salt, A. N., DeMott, J. E., and Hale, S. A. (**2002**). ''Acute endolymphatic hydrops is induced by non-traumatizing low frequency stimulation,'' 25th Midwinter Research Meeting of the ARO (abstract) 105.

Sakaguchi, N., Crouch, J. J., Lytle, C., and Schulte, B. A. (**1998**). ''Na–K–Cl cotransporter expression in the developing and senescient cochlea,'' Hear. Res. **118**, 114–122.

Schmiedt, R. A., Lang, H., Okamura, H., and Schulte, B. A. (**2002**). ''Effects of furosemide applied chronically to the round window: A model of metabolic presbycusis,'' J. Neurosci. **22**, 9643–9650.

Spicer, S. S., Smythe, N., and Schulte, B. A. (**2003**). ''Ultrastructure indicative of ion transport in tectal, deiters, and tunnel cells: Differences between gerbil and chinchilla basal and apical cochlea,'' Anat. Rec. **271A**, 342–359.

Whitehead, M. L., Lonsbury-Martin, B. L., and Martin, G. K. (**1991**). ''Slow variation of the amplitude of acoustic distortion at $f2-f1$ in awake rabbits,'' Hear. Res. **51**, 293–300.

Harmonic distortion in intracochlear pressure and its analysis to explore the cochlear amplifier[a)]

Elizabeth S. Olson[b)]
Department of Otolaryngology, Head and Neck Surgery, Columbia University, P & S 11-452, 630 W. 168th Street, New York, New York 10032

(Received 3 September 2003; revised 1 December 2003; accepted 15 December 2003)

Intracochlear pressure was measured close to the basal basilar membrane in gerbil with pure-tone stimulation. This report describes harmonic distortion in the pressure. The harmonic components were tuned in frequency and physiologically vulnerable, implying that they were related to the cell-derived force that sharpens tuning at low levels in healthy cochleae. For stimulus frequencies in the vicinity of the best frequency the harmonic distortion appeared to be produced locally, at the place of measurement. Therefore, it could be explored with a local nonlinear model. The combined model and observations demonstrate two specific points: First, the harmonics in the cell-based force were likely similar in size to the harmonics in pressure (multiplied by area) close to the basilar membrane. This is distinctly different than the situation for the fundamental component, where the cell-based force is apparently much smaller than the pressure (times area). Second, although the fundamental component of the measured pressure was much larger than its harmonic components, the harmonic and fundamental components of the active force were likely much more similar in size. This allows the harmonic components in the pressure to be used as an indirect measure of the active force. © *2004 Acoustical Society of America.* [DOI: 10.1121/1.1645611]

PACS numbers: 43.64.Kc, 43.64.Bt [WPS] Pages: 1230–1241

I. INTRODUCTION

The cochlea is a fluid-filled hose divided along its long axis by a ribbon of sensory tissue and coiled into the shape of a snail. Upon acoustic stimulation, a traveling wave of motion ripples down the ribbon and peaks at a place that depends on the frequency of the stimulus. High frequencies peak in the cochlear base, low frequencies closer to the apex. Observing one position and varying the stimulus frequency, one finds that at frequencies close to the best frequency (b.f.) the phase of the motion shows a rapid accumulation. This phase accumulation is the signature of the slowing of the cochlear traveling wave that accompanies its peaking. An outer hair cell (OHC)-generated force exists in the cochlea that enhances the sensory tissue motion and thus cochlear sensitivity. In the base of the cochlea, with stimulus frequencies close to the b.f., low-stimulus-level motion responses can be enhanced by 40 dB or more relative to high-stimulus-level responses (Robles and Ruggero, 2001). As to be expected, this large degree of compressive nonlinearity is accompanied by harmonic distortion. However, the degree of harmonic distortion in basal displacement is small, at the several percent level for stimulus frequencies close to the b.f. (Cooper, 1998) at a stimulus level of 60 dB SPL. Harmonic distortion has also been measured in the cochlear apex at relatively high stimulus levels (Khanna and Hao, 1999).

This report describes harmonic distortion in the intracochlear pressure in the base of the gerbil cochlea. Close to the sensory tissue's basilar membrane (b.m.) the pressure shared the interesting features of b.m. motion described above: frequency tuning, compressive nonlinearity at frequencies close to the b.f., a phase-vs-frequency response that indicates the presence of the traveling wave, and a low level of harmonic distortion. The harmonics were tuned in frequency, peaking at stimulus frequencies around the b.f. and with sharper tuning at low stimulus levels. The low-stim-level harmonics disappeared into the noise postmortem, just as the low-stim-level enhancement of tuning of the fundamental disappears. High-stim-level harmonics (80 dB SPL and above) changed postmortem, but did not always disappear, although when followed over 2 h they decreased substantially or disappeared. The tuning and physiological vulnerability of the harmonic distortion in pressure link it to the cochlea's nonlinear tuning. The basis for the nonlinear tuning is outer hair cells (e.g., Kiang *et al.*, 1986).

At stimulus frequencies within the best frequency peak the phase-vs-frequency relationship of the harmonics was very similar to that of the fundamental. That means that the harmonics arrived at the place of measurement with the same delay as the fundamental, strongly suggesting that the harmonics were locally generated at the place of measurement. This observation allows the pressure harmonics to be interpreted and analyzed as components of the local cell-derived force (as opposed to having been produced by cellular forces elsewhere in the cochlea and traveling independently to the place of measurement) and used to explore the character of that force.

This exploration is made quantitative with a local nonlinear model of one longitudinal segment of the cochlea. The model is a spring–mass system, with a resistive force that is

[a)]A preliminary version of this work was presented at the Mechanics of Hearing Meeting in Titisee, Germany in July, 2002, and was published in the meeting proceedings: Olson, E.S. (**2003**). ''Harmonic distortion in intracochlear pressure: Observations and interpretation,'' in: *Biophysics of the Cochlea: From Molecules to Models*, edited by A.W. Gummer (World Scientific, Singapore), pp. 228–236.

[b)]Electronic mail: eao2004@columbia.edu

proportional to and opposed to velocity and a nonlinear force that is proportional to a fractional power of velocity. By being proportional to velocity, the nonlinear force adds energy to the system and is an ''active force.'' The spring is the stiffness of the OCC. The mass is composed of both the fluid mass and the mass of the organ of Corti complex (OCC, the organ of Corti and basilar and tectorial membranes). Because of the fluid mass the pressure close to the OCC is a force within the spring–mass system. In this contribution, the model will be fitted to one set of pressure data in order to draw general conclusions about the size and possible shape of the active force.

This paper has to do with using intracochlear pressure to explore the active cochlear force, and some relevant background on intracochlear pressure and the active force is provided here. The cochlear pressure is composed of two components. The compressive pressure is timed to the in–out compression-rarefaction motion of the stapes and is also known as the ''fast-wave'' pressure. The pressure that is tied to the motion of the OCC and the adjacent fluid is known as the ''slow-wave'' pressure (Peterson and Bogart, 1950). The slow and fast waves obtain these designations because the fast wave propagates at the speed of sound in water, about 1500 m/s, whereas the slow wave's propagation speed is about 9 m/s in the region of the b.f. where the cochlear traveling wave is moving slowly (Rhode, 1971), and was found to be as small as 3.2 m/s in very localized measurements (Ren, 2002). The slow-wave pressure is largest close to the OCC and varies rapidly in space in this region, where the fluid acceleration is greatest (Olson, 1999). It produces a pressure difference across the OCC. In contrast, the fast-wave pressure is nearly equal in space throughout the cochlea and, because it creates no pressure difference across the OCC, it is thought not to cause motion of the OCC.

When making pressure measurements in the fluid the fast wave is of course measured along with the slow wave. Cancellation between the slow and fast waves occurs in the region of the b.f. peak because the slow wave is large in the peak region, goes through rapid phase variations there, and is sometimes out of phase with the fast wave. The cancellation results in pressure notches, discussed in Olson (1998, 2001) and visible in the data below. At frequencies well above the peak the slow-wave pressure is small and the fast-wave pressure dominates it, giving rise to a plateau in pressure phase (see Fig. 3). Even further above the peak there is a plateau in OCC motion as well (e.g., Robles and Ruggero, 2001; Rhode, 1971). This is likely due to nontraveling pressure modes that are present in the vicinity of a cochlear window, natural or unnatural (Steele and Taber, 1979; Cooper and Rhode, 1996). These pressure modes are like the fast wave in that they are timed to the motion of the stapes, but like the slow wave in that they are associated with fluid motion (as opposed to compression).

Moving on to background for the active force: the physiological basis for the active force is outer hair cells (e.g., Robles and Ruggero, 2001; Kiang *et al.*, 1986). How exactly the outer hair cells exert forces that give rise to enhanced tuning is a rich research question. The possibilities for this force have been bounded by several studies. These were used to guide the characteristics for the active force in the model of the current study. The effect of the active force on b.m. motion was largest at low levels (Rhode, 1971) and therefore the active force is assumed to be compressive. The modeling/experimental studies of deBoer and Nuttall (e.g., 2000) indicated that the active force had the character, in terms of impedance, of a negative resistance. This means the active force is in phase with velocity—like a damping force, but instead of resisting the velocity, the active force assists it. Shera (2001) also concluded that the active force had the character of a negative resistance, based on the lack of level dependence in the timing of the zero crossings in the b.m. motion response to a click. Finally, an approximately direct measurement of OCC impedance, and how it changed with stimulus level in a healthy cochlea, showed that the active force was small compared with the passive cochlear forces (Olson, 2001). This was also found in the study of deBoer and Nuttall (2000).

This report grew out of a contribution to the Mechanics of Hearing Meeting in Titisse, Germany in July, 2002 (Olson, 2003).

II. METHODS

A brief description of methods is given here; details have been published (Olson, 1998). The measurements were made in deeply anesthetized gerbils stimulated with tones via a speaker coupled to the ear canal. Stimuli were pure tones, 32 ms in duration. Stimulation levels refer to the sound-pressure level in the ear canal. Intracochlear pressure was measured by inserting specialized pressure sensors through small holes that were hand-drilled in the cochlear bone. Pressure measurements in the scala tympani (s.t.) were made in the first turn of the cochlea where the best frequency (b.f.) was approximately 20 kHz. In s.t. the pressure was measured at a series of distances from the b.m.; this report emphasizes the close measurements within 10 μm of the b.m. The pressure in the scala vestibuli (s.v.) just next to the stapes was measured within seconds of each measurement in the s.t. The pressure responses were averaged ($\sim$100 times) and the averaged responses stored and later analyzed via Fourier transform to find the magnitude and phase at the stimulus frequency (fundamental) and the second and third harmonic frequencies. An antialiasing filter cut off the measured response above 60 kHz; therefore, the third harmonic data are only available up to a 20-kHz stimulus frequency. When referencing phases of the harmonics to those of the fundamental, a small phase adjustment was made to account for the frequency dependence of the phase of the antialiasing filter.

An electrode at the round window measured the compound action potential (CAP) response of the auditory nerve to tone pips, as a monitor of cochlear health.

The pressure sensor consists of a glass capillary with inner and outer diameters 100 and 170 μm, tipped with a gold-coated polymer diaphragm. Light from an LED is delivered via a fiber optic threaded into the capillary, and reflects from the diaphragm. The amount of light returning to the fiber optic for transmission to a photodetector varies linearly with the pressure-induced motion of the diaphragm (Hu *et al.*, 1992). As described previously, the sensors are cali-

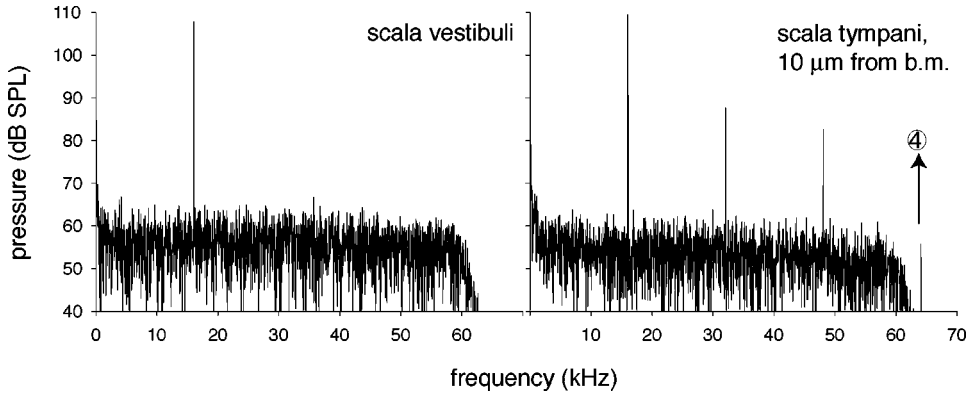

FIG. 1. Pressure spectra, animal 8-28-01. The stimulus was a 16-kHz, 80-dB SPL tone. The s.t. sensor was close to the b.m. (10 μm from it), the s.v. sensor was near the stapes. If the harmonics were associated with the nonlinear mechanics of the organ of Corti, they are expected to be larger in the s.t. pressure close to the basilar membrane than in the s.v. pressure measured near the stapes. This is apparent in the figure, where second, third, and fourth harmonics are visible in the s.t. data but do not emerge from the noise in the s.v. data. The frequency of the fourth harmonic is high enough that it falls above the cutoff frequency of the antialiasing filter. The circled "4" indicates the size of the fourth harmonic after accounting for the attenuation of the filter.

brated by submerging them a known distance beneath the surface of a vial of water which is then shaken with a known acceleration (Bruel & Kjaer model 4290). This produces a known pressure at the position of the sensor. The sensitivity of the sensors is approximately flat (within 3 or 4 dB) up to at least 40 kHz. At a frequency above 40 kHz, the precise value of which varies between sensors, the sensitivity decreases. This is probably due to viscous resistance in the sensor's membrane material. The variation between sensors is likely due to variations in membrane thickness. The drop-off in sensitivity is at high enough frequencies that it does not affect the fundamental response much, but it can affect the harmonics. The sensors are calibrated through 58 kHz, although a resonance in the shaker reduces its reliability above 50 kHz. The primary data set for analysis of this report, the s.t. measurement of Fig. 1, was recorded with a sensor whose cutoff frequency was above 50 kHz, so the sensitivity had decreased very little at the harmonic frequencies and is considered to be flat.

III. OBSERVATIONS

A. Physiological basis for the distortion

The first observations we report tie the distortion to forces within the organ of Corti. When delivering tones into a cavity, the digital-analog/analog-digital (DA/AD) system used in these studies produced harmonic distortion at levels 50 dB below the fundamental. This is not terrifically low (the system has since been upgraded), and several aspects of the data can be used to check that the measured distortion is physiologically based. Because the s.t. pressure was measured close to the OCC, whereas the s.v. pressure was measured near the stapes, if the distortion were generated in the OCC it was expected to be larger in the s.t. measurement than in the s.v. measurement. This is shown in Fig. 1, spectra from animal 8-28-01. This cochlea was mildly nonlinear, with CAP thresholds that were healthy following the initial surgery but elevated by ~15 dB at frequencies around 20 kHz after making the holes to the cochlea. The stimulus was a 16-kHz, 80-dB SPL tone, and the s.t. sensor was close to the b.m. (10 μm from it). Second, third, and fourth harmonics were clearly seen in s.t. but do not emerge out of the noise in s.v.

Changes due to an aging preparation and then postmortem are shown in the spectra of Fig. 2, from animal 4-18-01, a mildly nonlinear cochlea. The measurements were made 10 μm from the basilar membrane with a 17-kHz, 80-dB SPL tone stimulus. A spectrum from data gathered early in the experiment is shown in the left panel (1). The middle panel (2) shows results several hours later, pre-mortem, and the

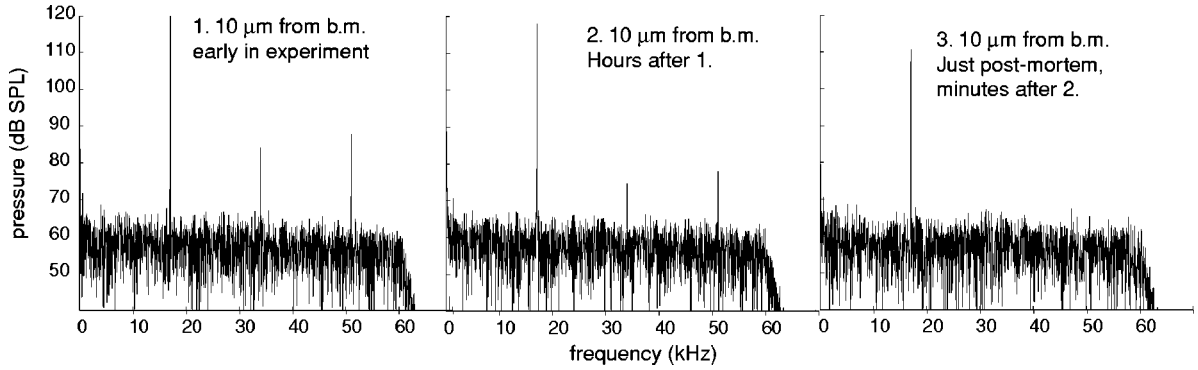

FIG. 2. Pressure spectra, animal 4-18-01. Changes due to an aging preparation and then postmortem. The pressure was measured in scala tympani, 10 μm from the basilar membrane, with a 17-kHz, 80-dB SPL stimulus. A spectrum from data gathered early in the experiment is shown in the left panel. The middle panel shows data gathered several hours later, pre-mortem, and the right panel shows data gathered just minutes later, postmortem.

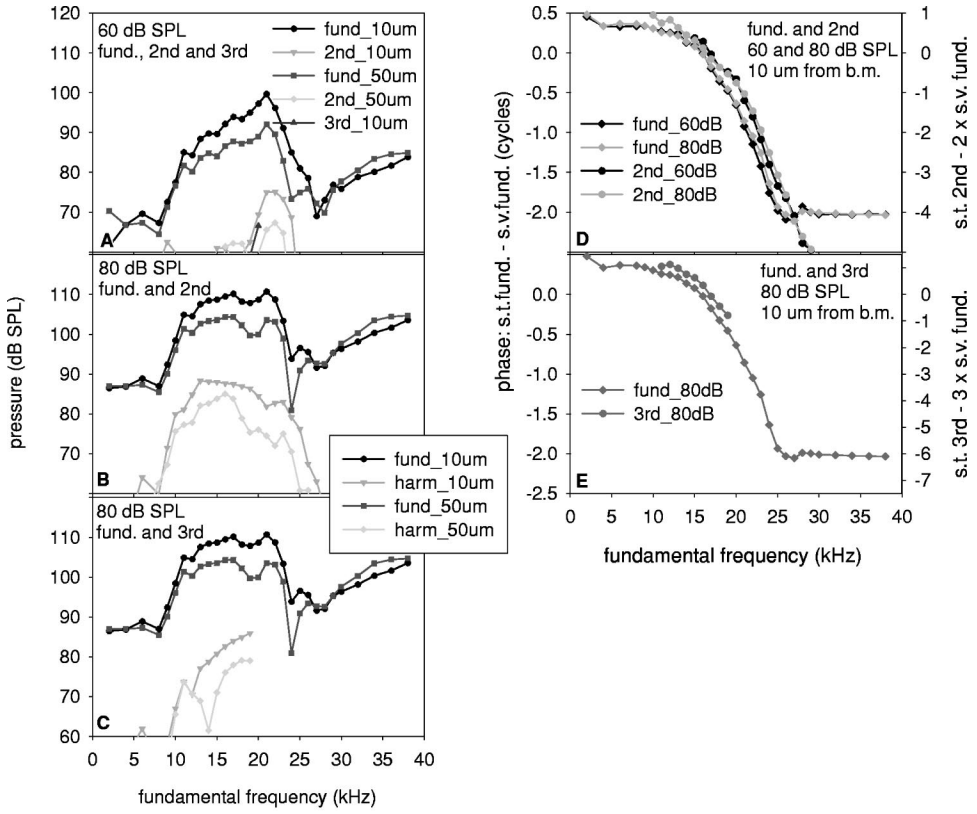

FIG. 3. Scala tympani pressure frequency responses, animal 8-28-01. The magnitude plots [panels (A), (B), and (C)] show the responses at distances 10 and 50 μm from the basilar membrane; the phase plots [panels (D) and (E)] show the response phase at the 10-μm position. Panel (A) shows the fundamental, second, and third harmonic components with 60-dB SPL stimuli. Panel (B) shows the fundamental and second harmonic components with 80-dB SPL stimuli. Panel (C) is similar to panel (B) except the third harmonic is shown. Panel (D) shows the fundamental and second harmonic phases with 60- and 80-dB stimuli. Panel (E) shows the fundamental and third harmonic phases with 80-dB stimuli. The reference for all the phase data was the s.v. pressure fundamental. The s.v. fundamental phase was multiplied by 2 in order to use it for the reference for the s.t. second harmonic, and by 3 in order to use it for the reference for the s.t. third harmonic.

right panel (3) directly (minutes) after the panel (2) data, postmortem. The distortion became smaller with time, and disappeared postmortem.

Another quality of the distortion that speaks for its physiological basis is that the distortion drops off with distance from the b.m. This is seen in Figs. 3 and 5.

B. Frequency sweeps

Frequency sweeps showing the fundamental, second, and third harmonics are shown from three animals. The *x* axis is the frequency of the fundamental, so the frequencies of the harmonics are 2 and 3 times this frequency.

In Fig. 3 s.t. pressure responses from cochlea 8-28-01, the same cochlea as in Fig. 1, are shown. The magnitude plots (A), (B), and (C) show the pressure at distances 10 and 50 μm from the basilar membrane; the phase plots [(D) and (E)] show the pressure phase at the 10-μm position. In (B) and (C) the sound-pressure level was 80 dB SPL, in (A) it was 60 dB. When the stimulus level was 60 dB the fundamental component showed about 10 dB of compressive nonlinearity compared to the response with the 80-dB stimulus. When the stimulus was reduced to 50 dB SPL there was little additional compression due to the nonoptimal condition of the cochlea. Nevertheless, the compression between 60 and 80 dB SPL produced the characteristic sharpening of the response at the lower stimulus level and thus the OHC force was at work in this preparation. With stimulus levels of 50 (not shown) and 60 dB SPL the second harmonic was a peak positioned in frequency at 20–24 kHz, the frequencies where the fundamental peaked in a broader fashion. When the stimulus level was 80 dB SPL the second harmonic formed a broad plateau between 10 and 25 kHz, with a shape that was similar to the broad tuning of the fundamental. The third harmonic was in the noise when the stimulus level was 50 dB SPL and at 60 dB SPL just emerged from the noise. At 80 dB SPL the third harmonic was broadened in a fashion similar but not identical to that of the second harmonic.

The fundamental and harmonics both decreased with distance from the basilar membrane. The spatial pressure variations reflect fluid motion. ($\nabla p \approx -\rho \mathbf{a}$, where p is pressure, ∇ is the gradient operator, symbolizing spatial differences, ρ is fluid density, and $\mathbf{a}$ is the fluid acceleration. See Olson, 1998, 2001.) One characteristic of note is that the notch that appeared in the fundamental with the 80-dB, 24-kHz stimulus at the 50-μm position did not appear in the harmonic [Fig. 3(B)]. The notch is due to cancellation between the fast-and slow-wave pressures of the fundamental. At the harmonic frequencies, the pressure fell off with distance without a fast-wave–slow-wave cancellation. The observation that the harmonic does not itself notch in the region of the fundamental notch rules out the possibility that the

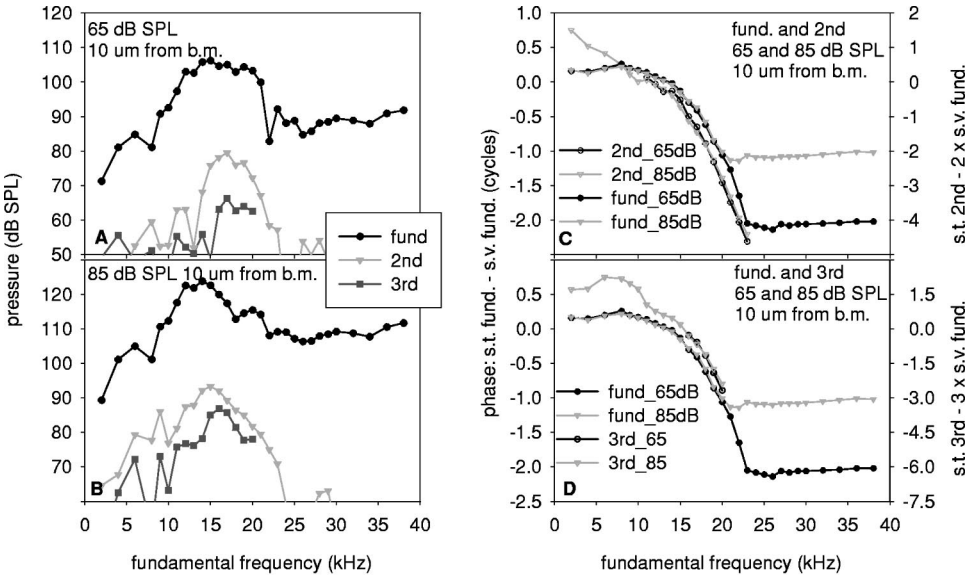

FIG. 4. Scala tympani pressure frequency responses, animal 4-25-00. Responses at 65 and 85 dB SPL, at a position close to the b.m. (10 μm away) are shown. Panel (A) shows the magnitude of the fundamental, second, and third harmonics with 65-dB stimuli, Panel (B) the same with 85 dB stimuli. Panels (C) and (D) show the response phases with 65- and 85-dB stimuli. Panel (C) shows the fundamental and second harmonic, (D) the fundamental and third harmonic.

distortion is an artifact due to nonlinearity in the pressure-sensing membrane.

Figures 3(D)–(E), the phase responses that go along with the 10-μm s.t. pressure magnitudes of Figs. 3(A)–(C), contain one of the principal observations of this study. Figure 3(D) shows the s.t. second harmonic and fundamental phases; Fig. 3(E) shows the s.t. third harmonic and fundamental phases. The phase of each component of the s.t. pressure was referenced to the fundamental component of the s.v. pressure. The s.v. fundamental phase was multiplied by 2 in order to use it for the reference for the s.t. second harmonic, and was multiplied by 3 in order to use it to for the reference for the third harmonic. (That this multiplication of phase is appropriate can be appreciated by thinking of the phase reference as representing an offset in time from the zero phase time of the fundamental s.v. pressure. That time corresponds to a phase that increases linearly with frequency.) The fundamental frequency was plotted on the *x* axis, so that, for example, the 10-kHz fundamental and its harmonics at 20 and 30 kHz are all plotted at the same *x* position. The fundamental phase uses the left *y* axis and the harmonic phase uses the right *y* axis. The axes of the second and third harmonic phases were expanded by factors of 2 or 3 relative to the *y* axis of the fundamental phase. The phase plots have the notable characteristic that the phase-vs-frequency slope was nearly the same for the fundamental, the second and the third harmonic. This means that all three components arrived at the point of measurement with the same delay. This strongly suggests that the harmonics were locally generated. In this picture, the fundamental propagates down the cochlea, producing harmonic distortion as it goes. The harmonic distortion does not propagate and therefore the delays of the harmonics measured at a given position are the same as the delay of the fundamental response.

Figure 4 shows frequency sweep data from animal 4-25-00. This was also a mildly nonlinear cochlea. Responses at 65 and 85 dB SPL, at a position close to the b.m. (10 μm away) are shown. The purpose of the figure is to show the repeatability of the results from Fig. 3, namely, tuned harmonics, whose tuning was sharper than the fundamental at the lower stimulus level but became as broad as the fundamental at the higher stimulus level; and harmonic phase-vs-frequency curves that nearly paralleled that of the fundamental. In this cochlea the harmonic phase-vs-frequency slopes deviated from that of the fundamental at low frequencies, 5–10 kHz. The low-frequency deviation might be due to harmonics that were produced basal to the measurement position and traveled to the probe position independently of the fundamental, and with different delays. (However, the third harmonic were nearly in the noise at low frequencies, reducing the reliability of those data.)

The frequency sweeps shown in Fig. 5 were from the healthiest cochlea of this study, (9-8-98), with CAP thresholds that were increased by only about 10 dB following making the holes to the cochlea. In this cochlea at 85 dB SPL [panel (D)] there were two peaks in the second harmonic response, with the upper frequency peak occurring at stimulus frequencies close to the b.f. at the probe position (the usual peak) and a second peak appearing at stimulus frequencies~one-half the b.f. The lower peak might be the result of distortion generated basal to the measurement position and traveling to the measurement position, its own b.f. place, where it peaked. This would be the ''amplified distortion'' reported by Cooper (1998) in measurements of harmonic distortion in b.m. displacement.

The phase data from this cochlea are in Figs. 5(F) and (G). In this cochlea the harmonic phase-vs-frequency curves paralleled that of the fundamental over a relatively restricted frequency range in the region of the b.f. peak. At frequencies below the b.f. peak the lack of similarity means that the distortion was not so closely tied to the fundamental, and might have arrived from other parts of the cochlea. This jibes with the magnitude data described above. The apparent enhanced ability for distortion to propagate in this cochlea might be related to the relative health of the preparation. (Data now emerging from our lab support this view and will be reported in a future publication.) The independently traveling distortion bears further investigation, but not here. In the analysis that follows, the distortion that is generated with stimulus frequencies in the region of the b.f. is explored. As

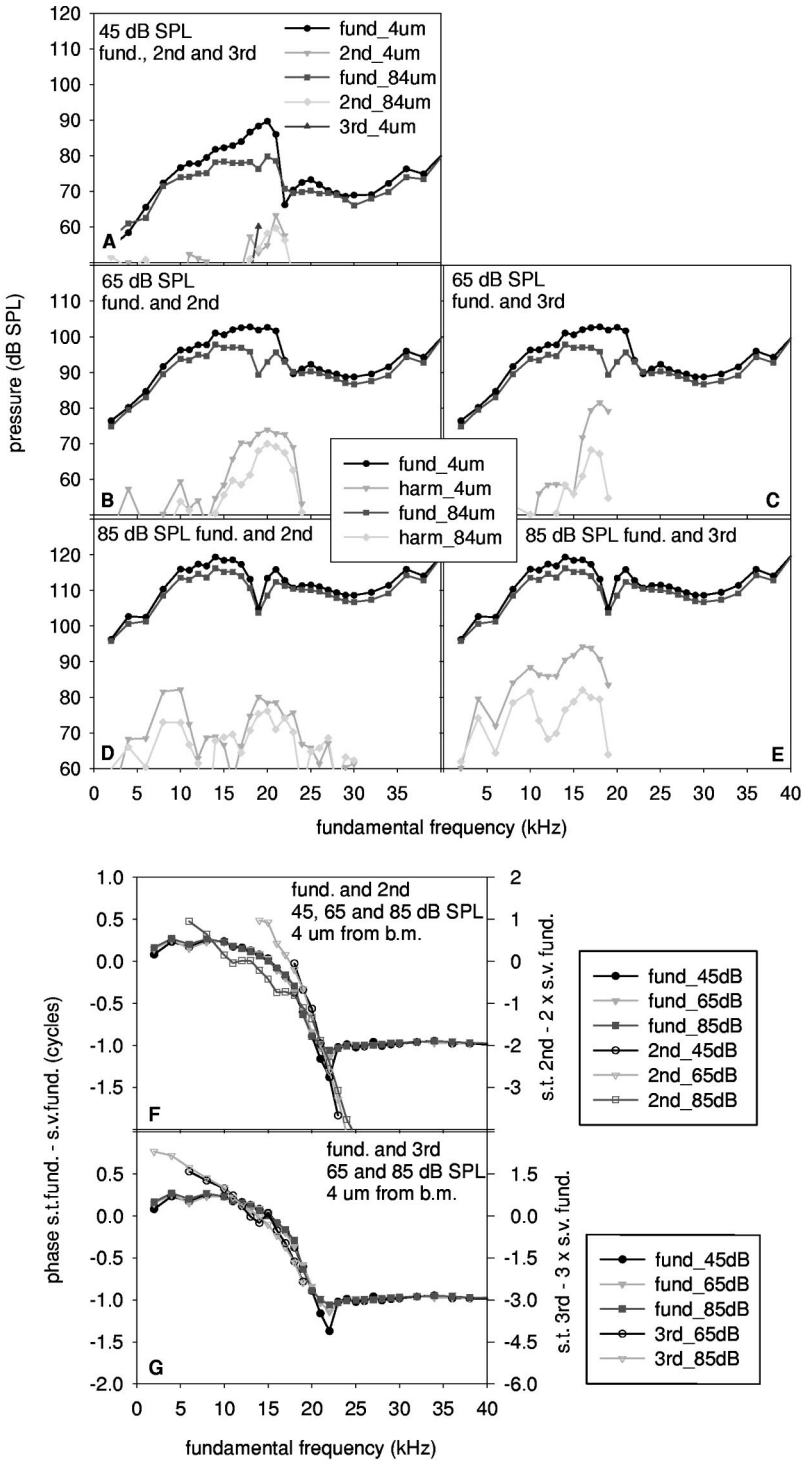

FIG. 5. Scala tympani pressure frequency responses, animal 9-8-98. This was the healthiest animal in this study and had slightly more complicated harmonic behavior seemingly due to an enhanced ability for harmonic distortion, once established, to travel independently of the fundamental traveling wave. The magnitude plots [panels (A)–(E)] show the responses at distances 4 and 84 μm from the basilar membrane; the phase plots [panels (F)–(G)] show the response phases at the 4-μm position. Panel (A) shows the fundamental, second, and third harmonic components with 45-dB SPL stimuli. Panel (B) shows the fundamental and second harmonic components with 65-dB SPL stimuli. Panel (C) is similar to panel (B) except the third harmonic is shown. Panel (D) shows the fundamental and second harmonic components with 85-dB SPL stimuli. Panel (E) is similar to panel (D) except the third harmonic is shown. Panel (F) shows the fundamental and second harmonic phases with 45-, 65-, and 85-dB stimuli. Panel (G) shows the fundamental and third harmonic phases with 65- and 85-dB SPL stimuli.

described above, the phase-vs-frequency behavior of the distortion in this region indicates that it is locally generated—it is a distortion of the fundamental response that has arrived at the place of measurement. This is a requirement of the simple local nonlinear model that is used.

IV. ANALYSIS/MODEL

Consider the cross section sketched in Fig. 6. The forces on the organ of Corti upon acoustic stimulation can be determined by considering this section of the OCC as the mass in the equation expressing Newton's second law, $\Sigma F_{\text{ext}} = m_{\text{oc}} a$. The external forces are exerted on the OCC by the fluid and structures that surround it: The attachment points of the lamina and ligament provide restoring and resistive forces. The fluid pressure of the adjacent fluid, multiplied by the surface area, provides a force that is directed perpendicular to that surface area. The active force is envisioned as arising from the outer hair cells pushing (via the tectorial membrane) between the wall of the inner sulcus, an external structure, and the OCC (Steele and Lim, 1999; deBoer, 1993). We are not concerned with predicting frequency tuning; the response at just one stimulus frequency is examined

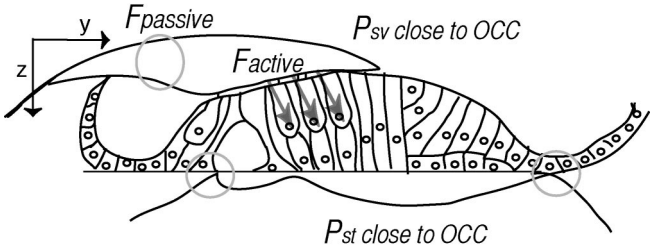

FIG. 6. Cross-sectional sketch of the organ of Corti complex and the forces that govern its motion.

in the model. The strategy is to write force balance for the segment, including a nonlinear active force, and solve the equation in the time domain for the harmonic response in the motion. The distortion in each contributing force is then found and examined. One objective of the model is to demonstrate that although only a small degree of distortion was observed in the pressure close to the b.m., the active force itself probably has a large degree of distortion. The analysis and observations together are used to estimate the size and possible shape of the active force.

The model is based on a 10-μm-long section of OCC, with a width of 200 μm. [Note that 200 μm is approximately the width of the b.m. in turn one of the gerbil cochlea (Plassman *et al.*, 1987) and 10 μm was chosen for the length of a segment, based on the width of hair cells.]
The symbols used in this analysis are as follows:

P_{sv} = scala vestibuli pressure close to the OCC
P_{st} = scala tympani pressure close to the basilar membrane
m_{oc} = mass of the OCC
m_f = effective mass of the cochlear fluid
$m = m_{oc} + m_f$
$a = \ddot{z}$ = acceleration of the OCC in the z direction
$\dot{z}$ = velocity of the OCC in the z direction
z = displacement of the OCC in the z direction
d = radial width of the OCC
b = longitudinal width of segment of the OCC
$\Lambda = b \cdot d$ = area of segment of the OCC
F_{active} = force exerted by outer hair cells
$F_{passive}$ = passive forces on the OCC
s = stiffness associated with restoring force
R = viscous forces resisting motion of the OCC
$\omega = 2\pi f$, where f is the driving frequency in Hz
F_{drive} = drive force arriving from adjacent basal segment
P_{sv_drive} = associated drive pressure in scala vestibuli
P_{st_drive} = associated drive pressure in scala tympani
F_0 = amplitude of drive force arriving from adjacent basal segment
λ = wavelength of the cochlear traveling wave
A, v_0, v_w, and ex = parameters that describe the size, range, and offset of the active force.

Force balance in the z direction for the segment is expressed as

$$m_{oc}a = (P_{sv} - P_{st})\Lambda + F_{passive} + F_{active}. \quad (1)$$

$F_{passive}$ consists of reactive and resistive components, and the force balance equation is written more specifically as

$$m_{oc}\ddot{z} = (P_{sv} - P_{st})\Lambda - sz - R\dot{z} + F_{active}. \quad (2)$$

The local pressure difference across the OCC, $P_{sv} - P_{st}$, is related to the local fluid motion. In a symmetric cochlear model, $P_{st} = -P_{sv}$ and, for an inviscid fluid and small fluid velocities

$$P_{st}\Lambda = \frac{m_f}{2}\ddot{z}, \quad (3)$$

where m_f is the effective fluid mass per unit length (Steele and Taber, 1979). (The pressure at the OCC both drives the motion of the OCC and the motion of the fluid adjacent to the OCC.) So, the force balance equation becomes

$$m_{oc}\ddot{z} = -m_f\ddot{z} - sz - R\dot{z} + F_{active}. \quad (4)$$

Thus, pressure has been replaced by acceleration, which brings the equation closer to a form that can be solved. m_f depends on the local curvature of the traveling wave (curvature$\propto$1/wavelength), the width of the OCC, and the size and shape of the cochlear fluid space (Steele, 1987). The curvature of the wave depends on its frequency. For a lightly damped cochlea stimulated at a frequency ω, equating the local kinetic and potential energies of the traveling wave leads to the relationship between the local mass, stiffness, and frequency

$$(m_{oc} + m_f) = \frac{s}{\omega^2}. \quad (5)$$

(Lighthill, 1983). (While this relationship is for a linear system, for which $|\dot{z}| = \omega|z|$, it is approximately true for the cochlea because of the relatively small size of the distortion. The relationship essentially prescribes the size of the fluid mass so that the traveling wave will exist at the frequency ω.) m_{oc} does not change with frequency; m_f decreases with frequency via changes in the curvature. [Two quick asides about effective fluid mass that are not used here, but are discussed in for example, Lighthill (1981): (i) As an example of effective fluid mass, for a simple 2D wave $m_f \propto \lambda \propto \text{curvature}^{-1}$. Substituting this into Eq. (5) results in a relationship between curvature and frequency that can be used to find the wave's propagation speed. Such a step, followed by an accounting for longitudinal variations in stiffness, is the beginning of a 2D cochlear model. (ii) When the frequency becomes so large that $m_{oc} \gg m_f$, the wavelength plunges to zero and there is no longer a cochlear traveling wave; in models where m_{oc} is assumed zero, this ''cutoff'' or ''resonant'' frequency does not exist.]

The simple analysis of this report models one longitudinal segment and one stimulus frequency. Equation (5) is used to eliminate the mass terms from the force balance equation and get the stimulation frequency into it

$$\ddot{z} = -\omega^2 z - \frac{\omega^2}{s}R\dot{z} + \frac{\omega^2}{s}F_{active}. \quad (6)$$

Because the model is only of one longitudinal segment, there is no ''input.'' The nonactive model works without an input as long as there is no energy dissipation. Then, the oscillatory motion of the segment goes on and on at fre-

quency ω, just as if a stimulus at that frequency were continuously on, with a size that depends on initial conditions. However, when resistance is present there is energy loss within the segment and, when Eq. (6) is solved with zero active force the result is a damped oscillation. Further insight into how to include an input from the segment basal to our model segment is provided by full cochlear models. Mathematically, when resistance is present in the OCC, the effective fluid mass becomes complex. This can be understood by looking at Eq. (4) in the passive, linear case. The stiffness and mass terms are out of phase and can cancel, but there is not a term to balance the resistive force. Such a term must be present and it arises by m_f becoming complex. Physically, this means that in the damped system the fluid pressure at the OCC is not solely in phase with acceleration, but has a component that is in phase with velocity. This was observed experimentally in Olson (2001). (This component will also arise due to resistance within the fluid (Steele and Taber, 1979), but fluid viscosity is not included here.) In order to include this component of the pressure in our model, a small input force at stimulus frequency ω was added, $F_{\text{drive}} = F_0 \cos(\omega t)$. This can be thought of as a fluid pressure arriving from the adjacent basal segment: $F_{\text{drive}} = (P_{\text{sv\_drive}} - P_{\text{st\_drive}})\Lambda = -2P_{\text{st\_drive}}\Lambda$. This last equation will be used after solving the model equation in order to find $P_{\text{st\_drive}}$. $P_{\text{st\_drive}}$ will be added to the P_{st} found from Eq. (3) in order to predict the measured pressure in scala tympani close to the basilar membrane.

We assume a form for the active force of $A[(\dot{z} - v_0)/v_w]^{(ex)}$. The active force is (nonlinearly) proportional to velocity by design, in order that it add energy to the system. This choice was based on cochlear models and experimental analyses (Neely and Kim, 1986; deBoer and Nuttall, 2000; Shera, 2001) in which the mechanism that sharpens the cochlear response at low stimulus levels works by adding energy to the cochlear traveling wave. It is important to note that by making the nonlinear force proportional to velocity, the possibilities for its waveform are restricted—it will be maximum when the velocity is maximum. The free parameters of the model, F_0, A, ex, v_0, and v_w were chosen to provide agreement with the *magnitude* of the spectral components at one stimulus frequency in the region of the b.f. peak, like the data shown in Fig. 1. The phase of the spectral components was not considered. In order to match both the magnitude and phase of the data's spectral components, the form of the active force will need to be relaxed. This is a future study. Finally, the equation that describes the motion of the segment is

$$\ddot{z} = \omega^2 \left\{ -z - \frac{R}{s}\dot{z} + \frac{A}{s}[(\dot{z} - v_0)/v_w]^{(ex)} + \frac{F_0}{s}\cos(\omega t) \right\}. \tag{7}$$

When this equation is solved, harmonics of the stimulus frequency are generated.

At this point the observation that the phase-vs-frequency curves of the harmonics paralleled that of the fundamental comes into play. The observation means that the harmonics arrived at the place of measurement with the same delay as the fundamental, strongly suggesting that the harmonics were locally generated at the place of measurement. The harmonics were not themselves part of traveling waves at their own frequencies, with their own wavelengths and their own effective fluid masses. Rather, the fluid mass corresponding to the fundamental frequency is envisioned as moving with a distorted time waveform. Then, Eq. (7), whose effective fluid mass corresponds to the fundamental (stimulus) frequency via Eq. (5), applies even though the response contains harmonic frequencies.

To enlarge upon the applicability of the model: It was noted when the data were presented that in the healthiest cochleae (Fig. 5), in addition to the local distortion we can analyze with Eq. (7), propagating distortion components appeared to be present. These components were largest at stimulus frequencies about one-half of the local b.f., where the frequencies of the harmonic components themselves were close to the b.f. In contrast, for stimulus frequencies close to the local b.f. the harmonic frequencies are well above the b.f., and propagating distortion components are not expected to be present. In support of this expectation, at stimulus frequencies close to the local b.f. the phase-vs-frequency data in Fig. 5 are similar to those from Figs. 3 and 4, and indicated that the distortion was local. Therefore, the analysis here is applicable to a healthy cochlea for stimulus frequencies close to the b.f. and is still applicable at frequencies quite a bit smaller than the b.f. when the cochlea is in moderate condition.

The parameter values listed below were based on a 10-μm-long section of OCC, with a width of 200 μm. The analysis models the s.t. pressure data of Fig. 1. Therefore, the stimulus frequency was set at 16 kHz, $\omega = 100\,000$ radians/s.

The stiffness was found using the OCC specific acoustic impedance data from Olson (2001). In those results the imaginary part of the impedance had a value that was $\sim$10 Pa/(mm/s) at 10 kHz. At this frequency, somewhat below the $\sim$20-kHz peak, the imaginary part of the impedance is expected to be primarily determined by stiffness, so we chose to determine its value there. (At frequencies at and above the peak, the imaginary part of the impedance might be reduced from that of stiffness due to proximity to a spring–mass resonance of the OCC stiffness and mass.) To go from this specific acoustic impedance (in units of pressure/velocity) to stiffness (in units of force/displacement) requires multiplying by the area (10×200 μm) and by 2π times 10 000 Hz. The resulting stiffness value is $s = 1.2$ N/m$= 1.2$ μN/μm. (The last change is made in order to work in units that are more natural for the cochlea.) This value is quite consistent (within about a factor of 2) with the turn one stiffness measured with a blunt, 10-μm-wide stiffness probe (Naidu and Mountain, 1998).

The resistance was found in reference to the impedance data from Olson (2001) and those of deBoer and Nuttall (2000). The high-stim-level impedance data of Olson showed real and imaginary parts of the impedance that were similar in size, although the imaginary part was usually a little bit bigger, sometimes about twice the size of the real part. [See Figs. 15 and 22 of Olson (2001).] If the real part were really

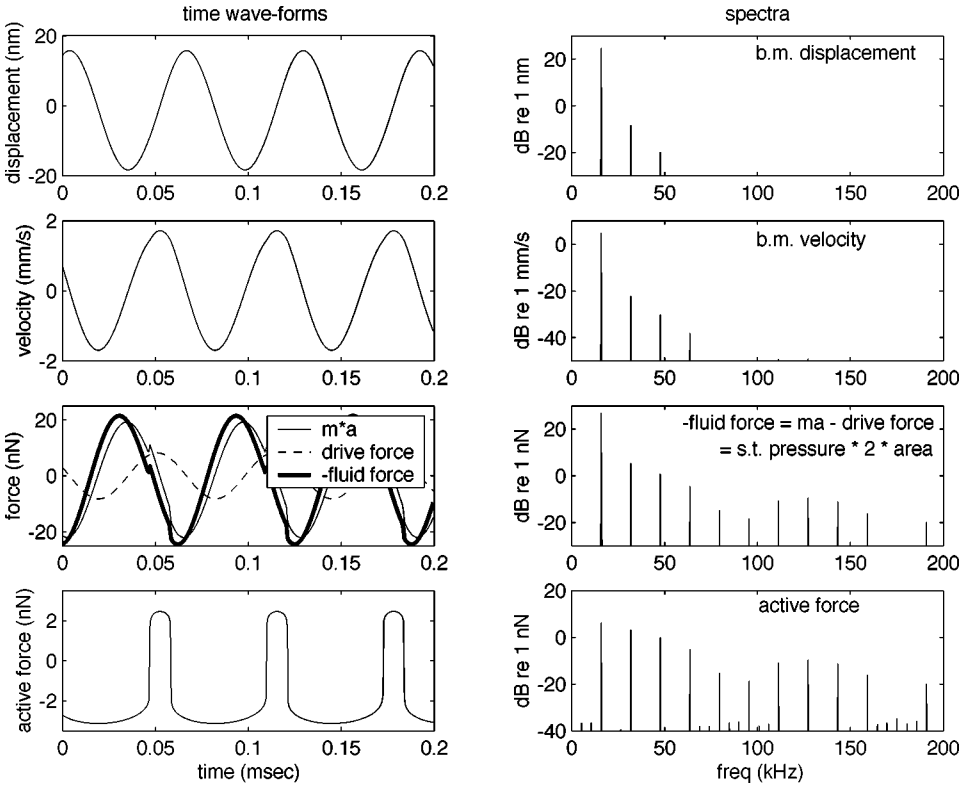

FIG. 7. Model results. The first two rows show the displacement and velocity of the OCC. The left panels show the time waveforms, the right panels show the associated spectra. The dashed line in the third row's left panel shows the drive force. The thin solid line in the third row's left panel shows the acceleration multiplied by m, the mass of both the OCC and fluid. Because the fluid mass is expected to dominate that of the OCC at frequencies below the peak, this is approximately equal to the acceleration multiplied by the fluid mass alone. Following Eq. (3) and the discussion relating the drive force to fluid pressure above Eq. (7), the fluid force on the OCC$=(P_{sv}-P_{st})\Lambda=(F_{drive}-m_f a)\approx(F_{drive}-ma)$. $ma-F_{drive}$ is the negative of the fluid force, plotted as the heavy solid line. The negative of the fluid force is plotted in order to begin to relate the modeling results to the experimental observations: $(P_{sv}-P_{st})\Lambda=-2\Lambda P_{st}$, and P_{st} is measured. The fluid force's spectrum is plotted in the right panel. The fourth row shows the active force, time waveform on the left, associated spectrum on the right.

as big as the imaginary part the passive cochlea would be rather heavily damped, which is not the view of most cochlear mechanics theory. The results of deBoer and Nuttall, in the high-stim-level case, showed an imaginary impedance that was about twice the size of the real part. (In both studies, both the real and imaginary parts tended to come down with frequency.) For the purposes of the model here the resistance value was chosen so that the resistive impedance was half the size of the stiffness-based impedance at the stimulus frequency. So, $R\omega=s/2, R=6\cdot 10^{-6}$ μN-s/μm.

The size of F_0 was chosen to give typical response magnitudes in the passive case and to match the data set of Fig. 1. Its value is $F_0=0.0082$ μN.

A, v_0, v_w, and ex determine the size and shape of the active force. Measurements of OCC impedance showed that at moderate levels of stimulus (50–60 dB SPL), even though the active force was causing substantial enhancement in tuning, the fundamental component of the active force was small compared to the restoring force of stiffness (Olson, 2001; deBoer and Nuttall, 2000), and this observation guided the values of the active force parameters. Beyond that, these parameters were chosen in order that the model results matched the observed scala tympani pressure close to the b.m. in Fig. 1—the magnitude of the spectral components. $A=0.0014$ μN, $v_w=1$ μm/s, $v_0=1435$ μm/s, and $ex=\frac{1}{10}$. The individual values of the active force parameters are not likely to be of general significance because their choice was highly dependent on the specific amplitude of the velocity. What is significant and of general interest is the resultant size and obvious distortion of the active force's time waveform.

Equation (7) was solved using MATLAB's ODE45 differential equation solver. (The MATLAB program is available from the author of this paper).

V. MODEL RESULTS

The model results are presented in Figs. 7, 8, and 9. The passive case partner ($A=0$) for Fig. 7 is in Fig. 10.

The four rows of Fig. 7 show displacement, velocity, acceleration recast as fluid force, and active force. The left panels show the time waveforms; the right panels show the associated spectra. The displacement harmonics are at least 30 dB smaller than the fundamental, which compares favorably with Cooper's (1998) result. The velocity harmonics are relatively bigger than the displacement harmonics because velocity scales with displacement times frequency. For the same reason, the acceleration harmonics are relatively bigger than the velocity harmonics. The acceleration in row 3 was recast as force by showing not $\ddot{z}$ but $\ddot{z}(m_{oc}+m_f)=\ddot{z}\cdot(s/\omega^2)$. If $m_{oc}\ll m_f$, as it is expected to be except possibly right at and above the peak [some cochlear models argue that m_{oc} is effectively zero (Steele, 1987)], then

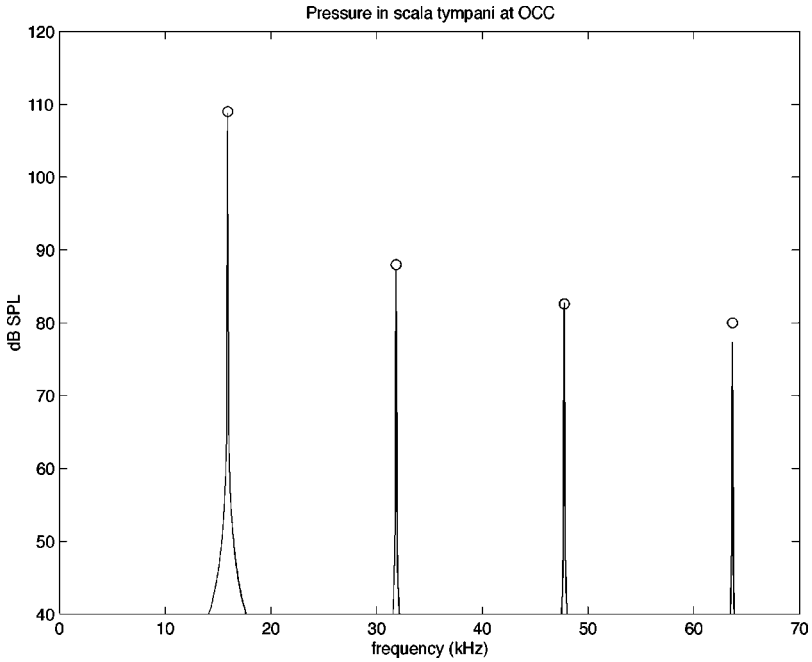

FIG. 8. Model results. The fluid force from the third row of Fig. 7 is divided by 2 times the area of the model segment to find the pressure in scala tympani at the OCC. This can be compared with the experimental measurements of pressure close to the b.m., for example from Fig. 1. The circles show the position of the spectral peaks in the Fig. 1 data, where the fourth harmonic component includes the adjustment for the filter attenuation.

$\ddot{z}\cdot(s/\omega^2)$ is the force that accelerates the effective mass of the fluid. The drive force is also plotted in this panel, as a dashed line. From the discussion leading to Eq. (3) and the discussion on the drive force above Eq. (7), the fluid force on the OCC, $(P_{sv}-P_{st})\Lambda$, is composed of two parts. One of the components, $-m_f\ddot{z}\approx-\ddot{z}\cdot(s/\omega^2)$, is in phase with negative acceleration. The second component is the drive force, which was introduced to balance resistive forces. Their sum, $-\ddot{z}\cdot(s/\omega^2)+F_{\text{drive}}=(P_{sv}-P_{st})\Lambda=$the fluid force on the OCC, and the symmetry relationship $(P_{sv}-P_{st})\Lambda=-2P_{st}\Lambda$ relates the fluid force to the measured pressure. The negative of the fluid force is plotted as the bold curve in the same panel. The right-hand panel shows the corresponding spectrum. In Fig. 8 the fluid force is divided by 2Λ, to find the magnitude of P_{st}, the fluid pressure in s.t. close to the OCC, which can be compared with the measured pressure. The circles show the positions of the spectral peaks in the Fig. 1 s.t. pressure data. The agreement is quite good, by design. [As a clarifying note, the fast-wave pressure has not been taken into account in the model because in the frequency region close to the b.f. the slow-wave pressure at the b.m. is bigger than the fast wave pressure (Olson, 2001). Including the fast wave in the model would increase the size of the model's fundamental peak by a few dB, but would not change the harmonics.]

The fourth row of Fig. 7 shows the active force, the time waveform on the left and the associated spectrum on the right. In time it has the shape of a brief impulse that occurs when the velocity is a maximum. The spectral components are large, with the second harmonic just a few dB smaller than the fundamental, and the third and fourth harmonics only decreasing by a few more dB.

Figure 9 shows the dc, fundamental, and second and third harmonic components of all the forces represented in Eq. (7). The time courses of the forces were found using the displacement and velocity solutions shown in Fig. 7. Recall that Fs, the force due to stiffness, $=-s\cdot z$. Fr, the force due to resistance, $=-R\cdot\dot{z}$. FD, the drive force, $=F_0\cos(\omega t)$. FA, the active force, $=A[(\dot{z}-v_0)/v_w]^{(ex)}$. Fm is the mass times acceleration, $\ddot{z}(m_{oc}+m_f)=\ddot{z}\cdot(s/\omega^2)$. Figure 9 makes clear something that is probably obvious—for each harmonic component of the force–balance equation, force balance must occur. For example, the dc force introduced by the offset in the active force is balanced by a small offset in the position of the OCC, which produces a dc component of Fs.

Looking at the fundamental, Fs is twice the size of Fr; this was by design. Fm balances Fs, and FA and FD both contribute to balancing Fr. Note that FA, the active force, is small compared with Fs, the stiffness force. This is also by design, to be consistent with results of Olson (2001) and deBoer and Nuttall (2000).

Moving on to the harmonics, the phase relationship between Fs, Fm, and Fr is the same as for the fundamental—Fs and Fm are 180° out of phase, Fr is 90° between them. However, Fs and Fm are no longer of equal size. That is because the fluid mass is such that Fm balances Fs at the *fundamental* frequency; therefore, at the second harmonic frequency Fm is four times bigger than Fs. The discrepancy gets bigger as the harmonics gets higher in frequency. The active force must provide force balance for Fm at the harmonic frequencies; i.e., the active force bears most of the responsibility for accelerating the fluid and OCC mass at harmonic frequencies. Therefore, in contrast to the fundamental frequency, where the active force is relatively small, at the harmonic frequencies the active force is relatively large, about the same size as Fm. With the assumption that the fluid mass is much larger than the OCC mass, Fm is approximately equal to the fluid pressure times area. So, the harmonics in the fluid pressure give a good measure of the harmonics in the active force/area. This is clear in the right-hand panels of Fig. 7, in which the harmonics in active force are nearly the same size as the harmonics in the fluid force plotted above it. From the lower panel of Fig. 7, the active

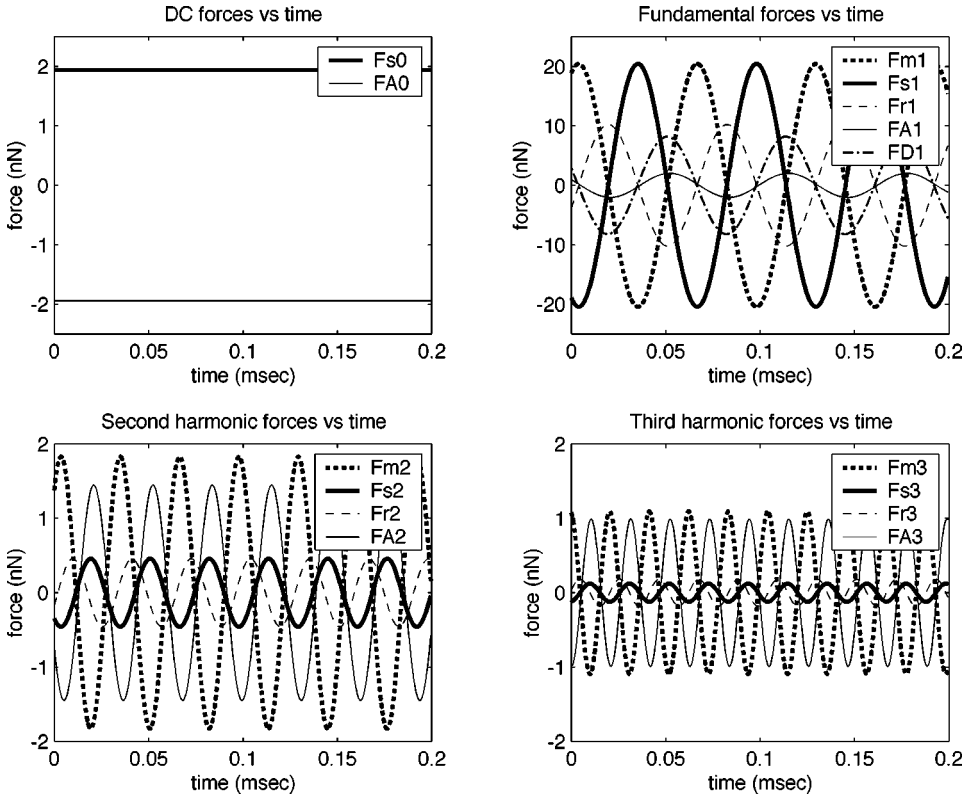

FIG. 9. Model results. The dc, fundamental, and second and third harmonic components of all the forces represented in Eq. (7).

force has a value at the fundamental frequency just over 2 nN, and the second harmonic is just a few dB less; 2 nN corresponds to 660 pN in each of the three outer hair cells in the section. This value can be related to the force that a constrained outer hair cell has delivered *in vitro*: ~100 pN/mV, with a dc whole-cell voltage clamp stimulus (Iwasa and Adachi, 1997), and ~30 pN/mV at frequencies up to at least 50 kHz, with a micro-chamber voltage stimulus (Frank *et al.*, 1999).

Figure 10 shows the displacement, velocity, and fluid forces when the active force is set to zero. Without the nonlinear force no harmonics are generated. The active force did not produce much increase in the fundamental response; a full cochlear model is needed to see its effect (e.g., deBoer and Nuttall, 2000).

The shape of the active force in Fig. 7 brings to mind the image of a child pumping a swing with a swift motion—a brief pulse occurring as the swing (or OCC) passes through its resting position. (Except here it looks more like a parent pushing the swing, as the force occurs at only one point in the cycle, not both coming and going as a swing-pumper would usually do.) Some features of the active force's waveform (e.g., its timing) were produced by model choices that are not settled (e.g., that the active force is proportional to velocity) and might need to be revisited. What is generally illustrated by the model is that to get the series of high-level

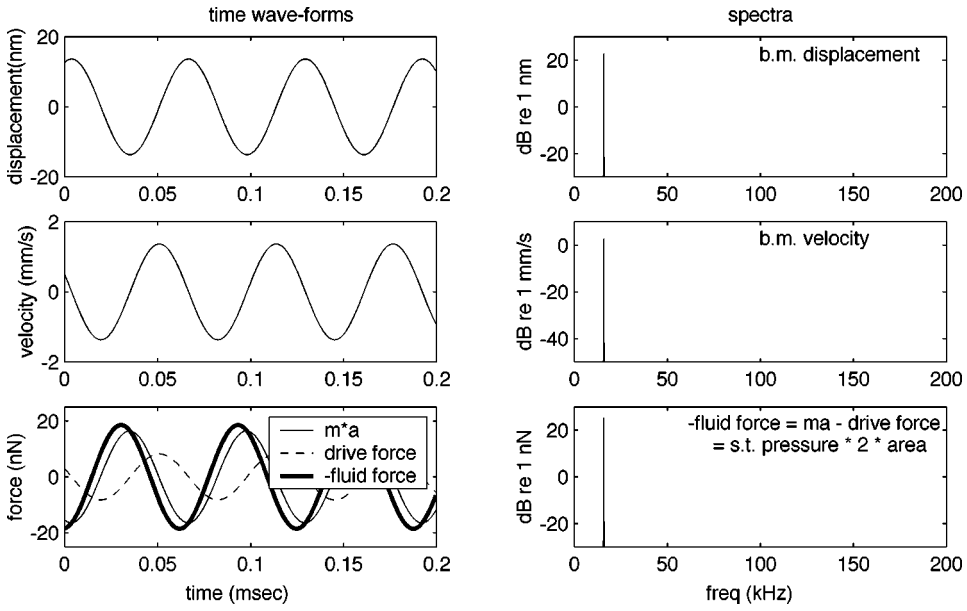

FIG. 10. Model results. This figure is like Fig. 7 except that the active force has been set to zero and therefore no harmonic distortion is produced.

harmonics that is observed (second, third, fourth, ...?), the active force is likely a brief impulse. [A similar point was made by Kemp and Brown (1983) in a study of two-tone emissions.] The impulse-like active force might indicate material decoupling (stereocilia from the tectorial membrane?) cyclically, at high levels of stimulation. Or, it might be intrinsic to the cellular mechanism that produces the active force. In conclusion, the harmonic content of the pressure response close to the b.m. is a measure of the harmonic content of the active force and can be used to predict its size and shape. This knowledge can help guide our understanding of the cellular and structural mechanics of the active force.

ACKNOWLEDGMENTS

This work was supported by NIH DC03130. Thanks to the JASA reviewers and to W. Dong and O. de La Rochefoucauld for helpful comments on the manuscript and to S. Khanna for fruitful discussions.

Cooper, N.P., and Rhode, W.S. (**1996**). ''Fast traveling waves, slow traveling waves and their interactions in experimental studies of apical cochlear mechanics,'' Aud. Neurosci. **2**, 207–212.

Cooper, N.P. (**1998**). ''Harmonic distortion on the basilar membrane in the basal turn of the guinea pig cochlea,'' J. Physiol. (London) **509**, 277–288.

deBoer, E. (**1993**). ''The sulcus connection. On a mode of participation of outer hair cells in cochlear mechanics,'' J. Acoust. Soc. Am. **93**, 2845–2859.

deBoer, E., and Nuttall, A.L. (**2000**). ''The mechanical waveform of the basilar membrane. III. Intensity effects,'' J. Acoust. Soc. Am. **107**, 1497–1507.

Frank, G., Hemmert, W., and Gummer, A.W. (**1999**). ''Limiting dynamics of high-frequency electromechanical transduction of outer hair cells,'' Proc. Natl. Acad. Sci. U.S.A. **96**, 4420–4425.

Hu, A., Cuomo, F., and Zuckerwar, A.J. (**1992**). ''Theoretical and experimental study of a fiber optic microphone,'' J. Acoust. Soc. Am. **91**, 3049–3056.

Iwasa, K.H., and Adachi, M. (**1997**). ''Force generation in the outer hair cell of the cochlea,'' Biophys. J. **73**, 546–555.

Kemp, D.T., and Brown, A.M. (**1983**). ''An integrated view of cochlear mechanical nonlinearities observable from the ear canal,'' in *Mechanics of Hearing*, edited by E. deBoer and M.A. Viergever (Martinus Nijhoff, Delft), pp. 75–82.

Khanna, S.M., and Hao, L. (**1999**). ''Nonlinearity in the apical turn of living guinea pig cochlea,'' Hear. Res. **135**, 89–104.

Kiang, N.Y.S., Liberman, M.C., Sewell, W.F., and Guinan, J.J. (**1986**). ''Single unit clues to cochlear mechanisms,'' Hear. Res. **22**, 171–182.

Lighthill, J. (**1981**). ''Energy flow in the cochlea,'' J. Fluid Mech. **106**, 149–213.

Lighthill, J. (**1983**). ''Advantages from describing cochlear mechanics in terms of energy flow,'' in *Mechanics of Hearing*, edited by E. deBoer and M.A. Viergever (Martinus Nijhoff, Delft), pp. 63–71.

Naidu, R.C., and Mountain, D.C. (**1998**). ''Measurements of the stiffness map challenge a basic tenet of cochlear theories,'' Hear. Res. **124**, 124–131.

Neely, S.T., and Kim, D.O. (**1986**). ''A model for active elements in cochlear biomechanics,'' J. Acoust. Soc. Am. **79**, 1472–1480.

Olson, E.S. (**1998**). ''Observing middle and inner ear mechanics with novel intracochlear pressure sensors,'' J. Acoust. Soc. Am. **103**, 3445–3463.

Olson, E.S. (**1999**). ''Direct measurements of intracochlear pressure waves,'' Nature (London) **402**, 526–529.

Olson, E.S. (**2001**). ''Intracochlear pressure measurements related to cochlear tuning,'' J. Acoust. Soc. Am. **110**, 349–367.

Olson, E.S. (**2003**). ''Harmonic distortion in intracochlear pressure: Observations and interpretation,'' in: *Biophysics of the Cochlea: From Molecules to Models*, edited by A.W. Gummer (World Scientific, Singapore), pp. 228–236.

Peterson, L.C., and Bogart, B.P. (**1950**). ''A dynamical theory of the cochlea,'' J. Acoust. Soc. Am. **22**, 369–381.

Plassman, W., Peetz, W., and Schmidt, M. (**1987**). ''The cochlea in gerbilline rodents,'' Brain Behav. Evol. **30**, 82–101.

Ren, T. (**2002**). ''Longitudinal pattern of basilar membrane vibration in the sensitive cochlea,'' Proc. Natl. Acad. Sci. U.S.A. **99**, 17101–17106.

Rhode, W.S. (**1971**). ''Observations of the vibration of the basilar membrane in squirrel monkeys using the Mossbauer Technique,'' J. Acoust. Soc. Am. **49**, 1218–1231.

Robles, L., and Ruggero, M.A. (**2001**). ''Mechanics of the mammalian cochlea,'' Physiol. Rev. **81**, 1305–1352.

Shera, C.A. (**2001**). ''Intensity-invariance of fine time structure in basilar-membrane click responses: Implications for cochlear mechanics,'' J. Acoust. Soc. Am. **110**, 332–348.

Steele, C.R. (**1987**). ''Cochlear mechanics,'' in *Handbook of Bioengineering*, edited by R. Skalak and S. Chien (McGraw-Hill, New York), pp. 30.1–30.22.

Steele, C.R., and Taber, L.A. (**1979**). ''Comparison of WKB calculations and experimental results for three-dimensional cochlear models,'' J. Acoust. Soc. Am. **65**, 1007–1018.

Steele, C.R., and Lim, K.M. (**1999**). ''Cochlear model with 3-dimensional fluid, inner sulcus and feed-forward mechanism,'' Audiol. Neuro-Otol. **4**, 197–203.

Deconvolution of evoked responses obtained at high stimulus rates

Rafael E. Delgado[a)]
Intelligent Hearing Systems Corp., 7356 S.W. 48th Street, Miami, Florida 33155

Ozcan Ozdamar
University of Miami, Department of Biomedical Engineering, PO Box 248294, Coral Gables, Florida 33124

(Received 1 July 2003; accepted for publication 6 November 2003)

Continuous loop averaging deconvolution (CLAD) is a new general mathematical theory and method developed to deconvolve overlapping auditory evoked responses obtained at high stimulation rates. Using CLAD, arbitrary stimulus sequences are generated and averaged responses deconvolved. Until now, only a few special stimulus series such as maximum length sequences (MLS) and Legendre sequences (LGS) were capable of performing this task. A CLAD computer algorithm is developed and implemented in an evoked potential averaging system. Computer simulations are used to verify the theory and methodology. Auditory brainstem responses (ABR) and middle latency responses (MLR) are acquired from subjects with normal hearing at high stimulation rates to validate and show the feasibility of the CLAD technique. [DOI: 10.1121/1.1639327]

PACS numbers: 43.64.Ri, 43.64.Yp [WPS] Pages: 1242–1251

I. INTRODUCTION

Widespread use of evoked potential (EP) methodology has made the functional testing of many sensory and motor neural pathways possible in both normal and diseased states. With rare exceptions, EPs require the use of time-domain conventional averaging to improve the poor signal-to-noise ratio (SNR) encountered in many practical situations. Over the years, conventional averaging has proven to be a very reliable acquisition technique for EPs. Its performance is only diminished when artifacts contaminate the responses under which longer acquisition periods are required (e.g., Ozdamar and Delgado, 1996). In spite of its advantages, conventional averaging has one severe limitation. If the response to each stimulus is not complete prior to the presentation of the next stimulus, overlapping responses are acquired which may never be separated into their corresponding components. As a consequence of this limitation, the rate of stimulation for transient EP recordings is limited by the duration of the recorded physiological response. In the case of auditory brainstem response (ABR), which typically lasts 12–15 ms, the maximum stimulation rate that can be used is limited to between 83.3 and 66.7 Hz. As shown in Fig. 1(A), a stimulus train is presented at a specific rate and data are acquired over a window immediately following the stimulus. Responses are added to provide the final averaged response. An interstimulus interval (ISI) is used to delay the presentation of each stimulus until the next acquisition window. The ISI can be shortened to increase the stimulation rate, with a maximum stimulation rate corresponding to an ISI of one sampling interval.

The SNR improvement property of conventional averaging is primarily dependent on the number of stimuli averaged. Under some poor SNR conditions, such as ABR acquisition, thousands of responses may need to be averaged to obtain reliable responses. Thus, minutes may be needed for the acquisition of one response. This limitation has severely curtailed the applications of EPs for various potential clinical uses such as audiogram determination, newborn screening, and interoperative monitoring. Adaptation characteristics of the auditory pathway also cannot be studied due to short refractory periods observed in auditory neurons. An important clinical application for measuring adaptation effects is in demyelinating diseases, but this has never been thoroughly realized due to this rate limitation.

Faster stimulation rates can be used in the acquisition of steady-state responses (SSRs). Under these conditions the responses overlap each other, resulting in a complex waveform that is typically analyzed in the frequency domain as shown in Fig. 1(B). In a steady-state condition, the characteristics of the overlapping responses depend on the sensitivity of the responses at the stimulation rate (Picton *et al.*, 1992, Azzena *et al.*, 1995). Although SSRs can be used for certain applications, such as hearing screening, where the only requirement is to determine if a response is present or not, critical information provided by the waveform morphology and components are mostly lost due to the overlapping responses.

In 1982, Eysholdt and Schreiner (1982) introduced a revolutionary procedure to circumvent the limitations imposed by conventional averaging. By using specially designed stimulus sequences called maximum length sequences (MLS), they were able to separate the individual response from overlapping responses. Subsequent investigations showed the validity and reliability of the MLS method and the existence of other similar sequences such as the Legendre sequences (LGS) to accomplish the same goal (Li *et al.*, 1988; Burkard *et al.* 1990; Picton *et al.*, 1992). These studies also showed that the response generation was likely to be the

[a)]Electronic mail: redelgado@ihsys.com

 0001-4966/2004/115(3)/1242/10/$20.00

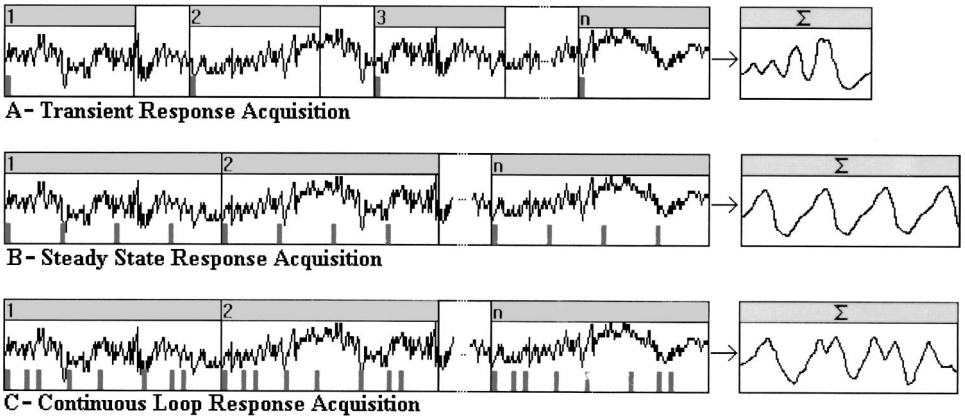

FIG. 1. Comparison between standard, steady state, and continuous loop averaging. In each graph, the bars represent the stimulus presentation. In standard averaging (top), a stimulus is presented and data are acquired over a prespecified window interval. An interstimulus interval (ISI) where no data are acquired between windows is typically present. The acquired data are analyzed directly in the time domain. In steady-state averaging (center), a stimulus is presented at a constant rate and data are acquired over multiple windows. The resulting data consisting of multiple responses are typically analyzed in the frequency domain to determine the presence of a response. In continuous loop averaging (bottom) a stimulus is presented in a nonperiodic manner in order to allow deconvolution. After deconvolution, the data are analyzed in the time domain.

same as in conventional averaging. Later studies by other investigators expanded the application and improved the acquisition methods (Chan *et al.*, 1992; Lasky *et al.*, 1992; Marsh, 1992; Burkard, 1994; Picton *et al.*, 1992; Thornton, 1993; Thornton and Slaven, 1993; Weber and Roush, 1995).

One major limitation of the MLS method has been its limited choice of sequences. Researchers designate MLS sequences by their minimum pulse interval (MPI) rather than mean rate. For example, an MLS sequence of $L=127$ contains 64 pulses. If presented with an MPI of 2 ms, the mean rate for this sequence would be 251.97 Hz, with a minimum of 15.748 Hz and a maximum of 503.94 Hz. These sequences cover a wide range of rates with a high degree of jitter (Burkard *et al.*, 1990). Since EP adaptation effects differ widely in different neurosensory systems, the interpretation of MLS-generated responses could sometimes be difficult (Picton *et al.*, 1992).

Until recently there have been no pseudorandom sequences with low stimulus jitters that would overcome this limitation. Very recently, however, Jewett and colleagues presented a novel method to overcome this limitation. They have devised a frequency-domain method called WAAD (wrap around average deconvolution) to solve a specially designed sequence for temporally overlapping responses (Jewett *et al.*, 2001). The method, however, is not generalized and works only with a few specially designed sequences. For a given stimulus sequence, the solution may not exist due to the instability of the transfer function. The specified sequences are generated by trial and error after long and tedious calculations and iterations.

In this study we present a generalized time-domain method for generating and deconvolving the output of nearly any given stimulation sequence. The problem is first presented in terms of a stimulation sequence. From the stimulation sequence, a set of simultaneous linear equations with many unknowns is automatically formulated using matrix equations. The number of unknowns corresponds to the number of data points to be acquired. If the conditions for a unique solution are presented, the equations are solved and a deconvolution matrix generated for use during data acquisition. The proposed technique and algorithms allow researchers to easily generate their own unique sequences.

II. THEORY AND METHODS

A. Principles of response acquisition

Transient response (TR) acquisition using conventional averaging [Fig. 1(A)] is the oldest and the most well-known method of all, where a stimulus is presented at a constant rate with little or no time jitter. The response acquisition time is always less than or equal to the interstimulus interval. The transient response is assumed to disappear before the next stimulus appears so no overlap of responses occurs within the acquisition time. The responses are analyzed mostly in the time domain using techniques such as latency and amplitude measurements.

Steady-state response (SSR) acquisition [Fig. 1(B)] uses the same averaging techniques with a constant stimulus rate and no jitter. The interstimulus interval, however, is shorter than the natural response time so considerable overlap of transient responses or other possible resonance effects occurs. The steady-state responses are typically analyzed in the frequency domain by measuring spectral peaks. Response acquisition time generally includes at least a few stimuli so that a meaningful spectral analysis can be done. The steady-state responses obtained in this way can never be decomposed into their original individual components due to the periodic nature of the stimulus sequence. The mathematical reasons for this will become apparent in the following sections.

As described above, the TR method cannot be used for fast stimulus rates due to overlap of responses, and the SSR method cannot be used for analyzing the characteristics of the individual responses due to overlap. The MLS and other similar methods mentioned above solve the problem of component decomposition only for a few special stimulus sequences. These special sequences have a wide range of jitter, which limits the usefulness of the method in different appli-

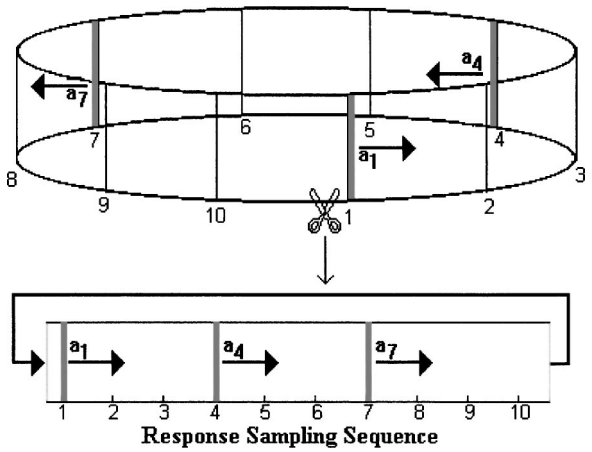

FIG. 2. Representation of loop averaging technique. Data are continuously acquired during presentation of triggering events for the sequence {1 0 0 1 0 0 1 0 0 0} until the cycle is repeated again. The resulting vector $[v(t)]$ is deconvolved to obtain the individual responses to each triggering event.

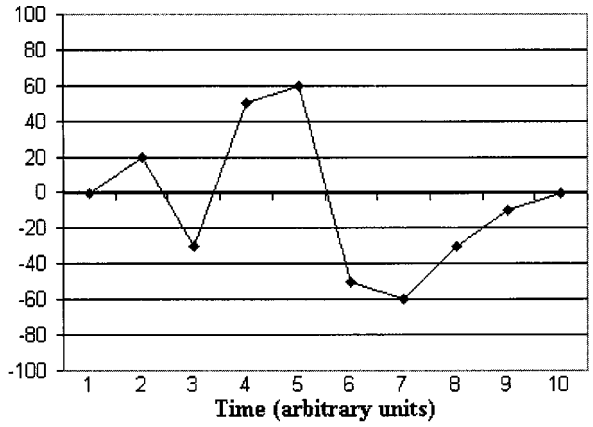

a[t]	0	20	-30	50	60	-50	-60	-30	-10	0
Time:	1	2	3	4	5	6	7	8	9	10

FIG. 3. Arbitrary 10-data point signal $\mathbf{a}[t]$ generated by triggering event.

cations. The new method, CLAD (continuous loop averaging deconvolution) proposed in this study presents the brain with a nonisochronic sequence of stimuli in a rapid manner such that the responses overlap each other, resulting in a complex convoluted response [Fig. 1(C)]. The CLAD algorithm deconvolves the resulting complex signal to obtain a measure of the response to each individual stimulus. The primary assumption and requirement is that the individual responses to each stimuli are independent of each other, and that the measured complex response is the arithmetic sum of the individual overlapping responses. Given these constraints, the proposed technique can deconvolve the resulting complex response acquired to provide the actual response to each stimulus (or triggering event). Although this assumption has proven adequate for the implementation of CLAD, the literature also suggests the existence of high-order interactions and contributions (Shi and Hecox, 1991) and should be explored in further studies.

B. Data acquisition

The CLAD method requires data to be acquired using a continuous acquisition loop buffer. A continuous acquisition loop is required because components arising from each of the responses (triggered events) in the sequence would not be properly represented in the linear equations if the acquisition contained gaps (i.e., equations would be missing from the set of linear equations required to obtain a solution). After a desired stimulus presentation sequence has been determined (see Sec. III A for details), data are continuously acquired throughout the sequence until the sequence starts again. The time duration of the acquisition loop determines the total duration of the deconvolved response.

For simplicity, the following example shown in Fig. 2 is based on a 10-point data acquisition sequence with a stimulus or triggering signal occurring at the first, fourth, and seventh point of the sequence. The actual technique was implemented using a 256-point sequence for data acquisition. The algorithm was developed to be implemented using any number of data acquisition points, the only limitation being memory and the computational speed of the computer.

Data are acquired in a discrete continuous loop vector, $\mathbf{v}[t]$, containing the arithmetic sum of all the individual responses starting at their respective triggering positions. Given a discrete arbitrary triggered response signal $\mathbf{a}[t]$, as shown in Fig. 3, the resulting convoluted response for the 10-point example with stimulus presentations at first, fourth, and seventh data points is shown in Fig. 4.

In order to obtain the desired standard transient response $\mathbf{a}[t]$, the technique developed deconvolves the measured response $\mathbf{v}[t]$ using the following matrix manipulation technique. For this example, $\mathbf{v}[t]$ represents the sum of the individual responses to three stimuli (triggering events) as follows:

$v[1]=a_1[1]+a_4[8]+a_7[5]$	Start of response a_1 with
$v[2]=a_1[2]+a_4[9]+a_7[6]$	overlapping components
$v[3]=a_1[3]+a_4[10]+a_7[7]$	of a_4 and a_7
$v[4]=a_1[4]+a_4[1]+a_7[8]$	Start of response a_4 with
$v[5]=a_1[5]+a_4[2]+a_7[9]$	overlapping components
$v[6]=a_1[6]+a_4[3]+a_7[10]$	of a_1 and a_7
$v[7]=a_1[7]+a_4[4]+a_7[1]$	Start of response a_7 with
$v[8]=a_1[8]+a_4[5]+a_7[2]$	overlapping components
$v[9]=a_1[9]+a_4[6]+a_7[3]$	of a_1 and a_4
$v[10]=a_1[10]+a_4[7]+a_7[4]$	

where $\mathbf{v}[t]$ is the overall measured response, $a_1[t]$ represents the response generated by the first stimulus, $a_4[t]$ represents the response generated by the second stimulus occurring at time 4, and $a_7[t]$ represents the response generated by the third stimulus occurring at time 7. It should be noted that although the $a_4[t]$ response sequence starts at the time corresponding to $v[4]$, the sequence does not end at the last point of the acquisition buffer, but wraps around such that the time corresponding to $v[1]$ also corresponds to $a_4[8]$. The same wrapping effect occurs for the $a_7[t]$ response sequence. Hence, each one of the responses completely wraps

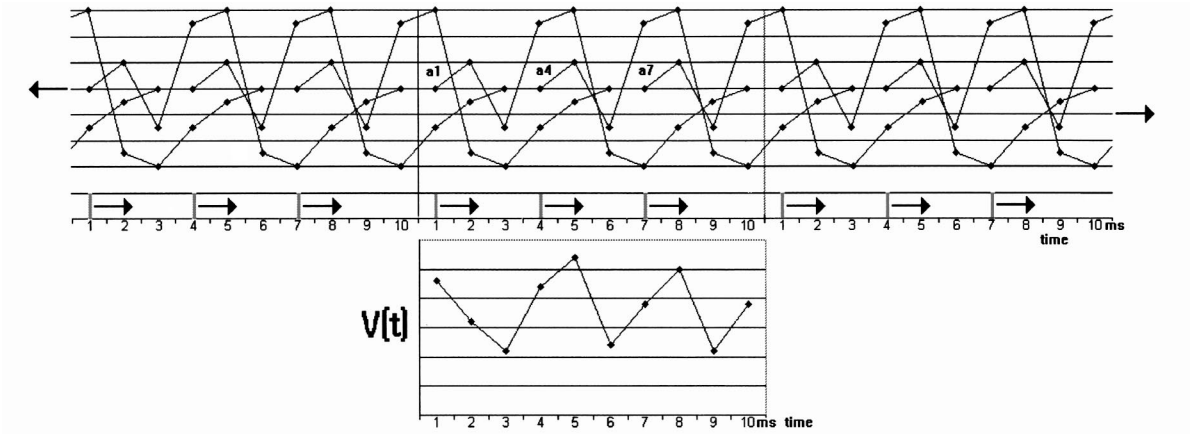

Trigger:	1			4			7			
$a_1[t]$	0	20	-30	50	60	-50	-60	-30	-10	0
$a_4[t]$	-30	-10	0	0	20	-30	50	60	-50	-60
$a_7[t]$	60	-50	-60	-30	-10	0	0	20	-30	50
$\mathbf{v}[t]$	30	-40	-90	20	70	-80	-10	50	-90	-10
time:	1	2	3	4	5	6	7	8	9	10

FIG. 4. Top graph shows the overlapping arbitrary signal depicted in Fig. 2 originating from the stimulus (triggering event) occurring at the specified presentation sequence 1, 4, and 7 depicted by the shaded boxes in the table. The bottom graph shows the resulting convoluted response acquired in the acquisition loop buffer $\mathbf{v}[t]$.

around the acquisition buffer until the next corresponding stimulus is presented.

Because the individual unit responses are assumed to be equivalent, $a_1[t]=a_4[t]=a_7[t]=\mathbf{a}[t]$, the above equations can be rewritten as follows:

$$
\begin{aligned}
v[1] &= a[1]+a[8]+a[5]\\
v[2] &= a[2]+a[9]+a[6]\\
v[3] &= a[3]+a[10]+a[7]\\
v[4] &= a[4]+a[1]+a[8]\\
v[5] &= a[5]+a[2]+a[9]\\
v[6] &= a[6]+a[3]+a[10]\\
v[7] &= a[7]+a[4]+a[1]\\
v[8] &= a[8]+a[5]+a[2]\\
v[9] &= a[9]+a[6]+a[3]\\
v[10] &= a[10]+a[7]+a[4]
\end{aligned}
$$

These equations can be written in a simple matrix equation [Eq. (1)], where $\mathbf{v}[t]$ and $\mathbf{a}[t]$ are time vectors representing the measured convoluted response values and deconvoluted response values to individual stimuli, respectively. $\mathbf{M}$ is a matrix representing the equation coefficients. The resulting matrix $\mathbf{M}$ contains a sequence of ''1''s and ''0''s representing the presence or absence of any specific term. It is in a multidiagonal matrix form where the ''1''s and ''0''s are mapped diagonally across the entire matrix. The diagonal mapping is caused by the time sequence relationship of the variables in the equations.

$$\mathbf{v}[t]=\mathbf{M}\mathbf{a}[t]. \tag{1}$$

$$
\begin{bmatrix} v[1]\\ v[2]\\ v[3]\\ v[4]\\ v[5]\\ v[6]\\ v[7]\\ v[8]\\ v[9]\\ v[10] \end{bmatrix}
=
\begin{bmatrix}
1 & 0 & 0 & 0 & 1 & 0 & 0 & 1 & 0 & 0\\
0 & 1 & 0 & 0 & 0 & 1 & 0 & 0 & 1 & 0\\
0 & 0 & 1 & 0 & 0 & 0 & 1 & 0 & 0 & 1\\
1 & 0 & 0 & 1 & 0 & 0 & 0 & 1 & 0 & 0\\
0 & 1 & 0 & 0 & 1 & 0 & 0 & 0 & 1 & 0\\
0 & 0 & 1 & 0 & 0 & 1 & 0 & 0 & 0 & 1\\
1 & 0 & 0 & 1 & 0 & 0 & 1 & 0 & 0 & 0\\
0 & 1 & 0 & 0 & 1 & 0 & 0 & 1 & 0 & 0\\
0 & 0 & 1 & 0 & 0 & 1 & 0 & 0 & 1 & 0\\
0 & 0 & 0 & 1 & 0 & 0 & 1 & 0 & 0 & 1
\end{bmatrix}
\times
\begin{bmatrix} a[1]\\ a[2]\\ a[3]\\ a[4]\\ a[5]\\ a[6]\\ a[7]\\ a[8]\\ a[9]\\ a[10] \end{bmatrix}.
$$

Deconvoluted response to individual stimuli can be obtained simply by solving for $\mathbf{a}[t]$. For any given stimulation sequence, the software developed generates the matrix $\mathbf{M}$ and attempts to solve Eq. (1) for $\mathbf{a}[t]$. Solving Eq. (1) for $\mathbf{a}[t]$ requires inverting the $\mathbf{M}$ matrix as follows:

$$\mathbf{a}[t]=\mathbf{M}^{-1}\mathbf{v}[t]. \tag{2}$$

The resulting inverted matrix $\mathbf{M}^{-1}$ for the above example is shown below

$$\begin{bmatrix} 0.33 & 0.33 & 0.33 & 0.33 & 0.33 & 0.33 & 0.33 & -0.67 & -0.67 & -0.67 \\ -0.67 & 0.33 & 0.33 & 0.33 & 0.33 & 0.33 & 0.33 & 0.33 & -0.67 & -0.67 \\ -0.67 & -0.67 & 0.33 & 0.33 & 0.33 & 0.33 & 0.33 & 0.33 & 0.33 & -0.67 \\ -0.67 & -0.67 & -0.67 & 0.33 & 0.33 & 0.33 & 0.33 & 0.33 & 0.33 & 0.33 \\ 0.33 & -0.67 & -0.67 & -0.67 & 0.33 & 0.33 & 0.33 & 0.33 & 0.33 & 0.33 \\ 0.33 & 0.33 & -0.67 & -0.67 & -0.67 & 0.33 & 0.33 & 0.33 & 0.33 & 0.33 \\ 0.33 & 0.33 & 0.33 & -0.67 & -0.67 & -0.67 & 0.33 & 0.33 & 0.33 & 0.33 \\ 0.33 & 0.33 & 0.33 & 0.33 & -0.67 & -0.67 & -0.67 & 0.33 & 0.33 & 0.33 \\ 0.33 & 0.33 & 0.33 & 0.33 & 0.33 & -0.67 & -0.67 & -0.67 & 0.33 & 0.33 \\ 0.33 & 0.33 & 0.33 & 0.33 & 0.33 & 0.33 & -0.67 & -0.67 & -0.67 & 0.33 \end{bmatrix}.$$

Not all stimulation sequences will result in equations that generate unique solutions. The stimulus sequence generation software determines if the desired sequence is valid by attempting to solve the system of equations.

One very important property of the inverse matrix is that it retains its multidiagonal property. All the coefficients repeat diagonally across the entire matrix. This allows the developed system to store only the first row of the matrix $[\mathbf{M}^{-1}]_{\mathbf{r}}$ as a row vector $\mathbf{m}^{-1}[t]$ for use during deconvolution resulting in a considerable data storage savings. The actual array $[\mathbf{M}^{-1}]_{\mathbf{r}} = \mathbf{m}^{-1}[t]$ that is stored for this example is shown below

$$[0.33 \quad 0.33 \quad 0.33 \quad 0.33 \quad 0.33 \quad 0.33 \quad 0.33 \quad -0.67 \quad -0.67 \quad -0.67].$$

C. Deconvolution calculations

The deconvolution process requires the use of $[\mathbf{M}^{-1}]_{\mathbf{r}}$ for a given sequence. The convoluted measured response vector $\mathbf{v}(t)$ is multiplied by the $[\mathbf{M}^{-1}]_{\mathbf{r}}$ matrix. Before the next value of the $\mathbf{a}[t]$ is calculated, the $[\mathbf{M}^{-1}]_{\mathbf{r}}$ vector is time shifted in order to position the coefficients correctly as follows:

$$\begin{aligned}
\mathbf{a}[1] &= [0.33 \quad 0.33 \quad 0.33 \quad 0.33 \quad 0.33 \quad 0.33 \quad 0.33 \quad -0.67 \quad -0.67 \quad -0.67]\ \mathbf{v}[t] \\
\mathbf{a}[2] &= [-0.67 \quad 0.33 \quad 0.33 \quad 0.33 \quad 0.33 \quad 0.33 \quad 0.33 \quad 0.33 \quad -0.67 \quad -0.67]\ \mathbf{v}[t] \\
\mathbf{a}[3] &= [-0.67 \quad -0.67 \quad 0.33 \quad 0.33 \quad 0.33 \quad 0.33 \quad 0.33 \quad 0.33 \quad 0.33 \quad -0.67]\ \mathbf{v}[t] \\
\mathbf{a}[4] &= [-0.67 \quad -0.67 \quad -0.67 \quad 0.33 \quad 0.33 \quad 0.33 \quad 0.33 \quad 0.33 \quad 0.33 \quad 0.33]\ \mathbf{v}[t] \\
\mathbf{a}[5] &= [0.33 \quad -0.67 \quad -0.67 \quad -0.67 \quad 0.33 \quad 0.33 \quad 0.33 \quad 0.33 \quad 0.33 \quad 0.33]\ \mathbf{v}[t].
\end{aligned}$$

Table I shows the calculations to deconvolve $\mathbf{v}[t]$ for the previous example shown in Fig. 3 and Fig. 4. The product of each $\mathbf{v}[t]$ and the appropriate $[\mathbf{M}^{-1}]_{\mathbf{r}}$ coefficient, after time shifting, are shown. These products are added across columns to obtain the individual $\mathbf{a}[t]$ values. As shown, the calculations reproduce the original $\mathbf{a}[t]$ vector that was overlapped by the triggering sequence.

III. IMPLEMENTATION AND PROCEDURES

For this study, modules are developed for implementing the CLAD procedures in a commercial EP system, SmartEP from Intelligent Hearing Systems Corporation, Miami, FL. The CLAD procedures are organized in two modules: (a) CLAD sequence generator and simulator; (b) CLAD acquisition and real-time deconvolution. The function and implementation of these modules and the procedures for testing them are described below.

A. CLAD sequence generator and deconvolution simulator

This module allows the user to generate any desired stimulation sequence for use in data collection and deconvolution. The user can either enter an average stimulation rate and the program then generates the appropriate sequence, or the user can enter individual data point positions where the stimulation is to occur. The sequence base can be expanded to any number of points and the sampling rate between acquisition points is totally arbitrary and can be selected to suit the desired application. The module then determines if the desired stimulation sequence is valid by attempting to solve the generated simultaneous equations. An augmented matrix is generated and the algorithm inverts the matrix by putting the matrix into a reduced echelon form. The reduction calculations are carried into the augmented portion of the matrix, resulting in an inverted matrix.

TABLE I. Deconvolution process. First two rows display the convoluted response vector $\mathbf{v}[t]$ showing the overlapped responses and the reduced inverse matrix $[\mathbf{M}^{-1}]_\mathbf{r}$ as a row vector. Deconvoluted response $\mathbf{a}[t]$ is computed by the circular correlation formula shown in the third row.

$\mathbf{v}[t]=$		30	−40	−90	20	70	−80	−10	50	−90	−10	
$[\mathbf{M}^{-1}]_\mathbf{r}=$		0.33	0.33	0.33	0.33	0.33	0.33	0.33	−0.67	−0.67	−0.67	
					$\mathbf{v}[t]*[\mathbf{M}^{-1}]_r=\mathbf{a}[t]$							$\mathbf{a}[t]$
$a[1]$	$=\Sigma$	10.0	−13.33	−30.0	6.66	23.33	−26.66	−3.33	−33.33	60.0	6.66	0
$a[2]$	$=\Sigma$	−20.0	−13.33	−30.0	6.66	23.33	−26.66	−3.33	16.66	60.0	6.66	20
$a[3]$	$=\Sigma$	−20.0	26.66	−30.0	6.66	23.33	−26.66	−3.33	16.66	−30.0	6.66	−30
$a[4]$	$=\Sigma$	−20.0	26.66	59.99	6.66	23.33	−26.66	−3.33	16.66	−30.0	−3.33	50
$a[5]$	$=\Sigma$	10.0	26.66	59.99	−13.33	23.31	−26.66	−3.33	16.66	−30.0	−3.33	60
$a[6]$	$=\Sigma$	10.0	−13.33	59.99	−13.33	−46.66	−26.66	−3.33	16.66	−30.0	−3.33	−50
$a[7]$	$=\Sigma$	10.0	−13.33	−30.0	−13.33	−46.66	53.33	−3.33	16.66	−30.0	−3.33	−60
$a[8]$	$=\Sigma$	10.0	−13.33	−30.0	6.66	−46.66	53.33	6.67	16.66	−30.0	−3.33	−30
$a[9]$	$=\Sigma$	10.0	−13.33	−30.0	6.66	23.33	53.33	6.67	−33.33	−30.0	−3.33	−10
$a[10]$	$=\Sigma$	10.0	−13.33	−30.0	6.66	23.33	−26.66	6.67	−33.33	60.0	−3.33	0

If the simultaneous equations are solvable, the software generates the inverse matrix $\mathbf{M}^{-1}$ and saves the stimulation sequence along with the $[\mathbf{M}^{-1}]_\mathbf{r}$ vector for use by the CLAD acquisition and real-time deconvolution module. Although a large number of sequences can easily be generated, some sequences cannot be solved. Isochronous sequences, i.e., sequences where the triggering events are equidistant from each other, have no solution. Even though isochronous sequences cannot be generated, sequences having near-isochronous properties can be achieved by varying the position of the final trigger. If a solution is not possible for a specific sequence (i.e., $\mathbf{M}^{-1}$ cannot be generated), the system notifies the user that the selected sequence cannot be solved. The user can then modify the sequence and try again. Even in cases when a solution cannot be obtained, a similar one can readily be achieved by slightly changing the position of one or more of the triggering points.

In addition, this software module allows the user to simulate data acquisition and deconvolution using a test EP response, $\mathbf{a}[t]$, and provides information as to triggering rate distributions. The purpose of the simulation is to make sure that the deconvolution procedure is working properly. A separate testing routine convolves the test EP by simulating the onset of the response at each of the stimulation points and wrapping it around the entire acquisition buffer as would occur during actual data acquisition. The solution that is generated by solving the set of linear equations is then applied to the convolved test EP signal by a separate routine in the algorithm. The output of the deconvolution routine is then compared to the original test EP.

B. CLAD real-time data acquisition and deconvolution

The CLAD real-time application can be implemented in any data acquisition system by implementing a continuous acquisition loop with event triggering occurring at the specified time periods. The data can then be deconvolved using the inverted $\mathbf{M}$ matrix as described above. During data acquisition, a menu is used to allow the user to select any pregenerated stimulation sequence stored in files. When the stimulation sequence is selected, the corresponding $[\mathbf{M}^{-1}]_\mathbf{r}$ vector is also loaded allowing for real-time deconvolution.

1. Averaging

Depending on the SNR of the application, averaging may or may not be required. In cases where averaging is required, the triggering cycle is repeated as needed and data are added into the acquisition buffer in a time-synchronous manner. As in standard synchronized time averaging, the SNR of the acquired signal increases with each acquired cycle. Nonsynchronous events are averaged out as data are collected.

2. Split-sweep dual-buffer data acquisition

Data can be collected using one or two acquisition buffers. In the split-sweep dual-buffer acquisition technique, depicted in Fig. 5, data are collected using two loop buffers. Each acquisition cycle is considered a sweep. The even-numbered sweeps are averaged in the first buffer and the odd-numbered sweeps are averaged in the second buffer. The split-sweep technique allows for the following capabilities: (1) The SNR of the signal being averaged can be estimated in real time using a cross-correlation technique. (2) Artifact rejection is accomplished by rejecting sweeps, as in conventional averaging. In this case, however, each sweep represents an entire acquisition loop composed of multiple stimulus presentations. Since stimulus signals occur within the acquisition window, care must be taken not to reject sweeps due to stimulus artifacts alone. This issue was resolved by implementing an artifact rejection technique with a selectable time window that can be set to any time interval within the acquisition loop. It is also very important not to saturate the input of the A/D converters at any point, since this will result in the elimination of components required to solve the simultaneous equations.

C. Experimental procedures

1. Simulations and system testing

Simulations were conducted to ascertain whether the original signal convolved according to the generated stimulus sequence could be reconstructed. After entering the desired stimulus sequence and determining if a solution was possible, a convolved response was constructed using a standard test EP response as described in Sec. II. The simulated

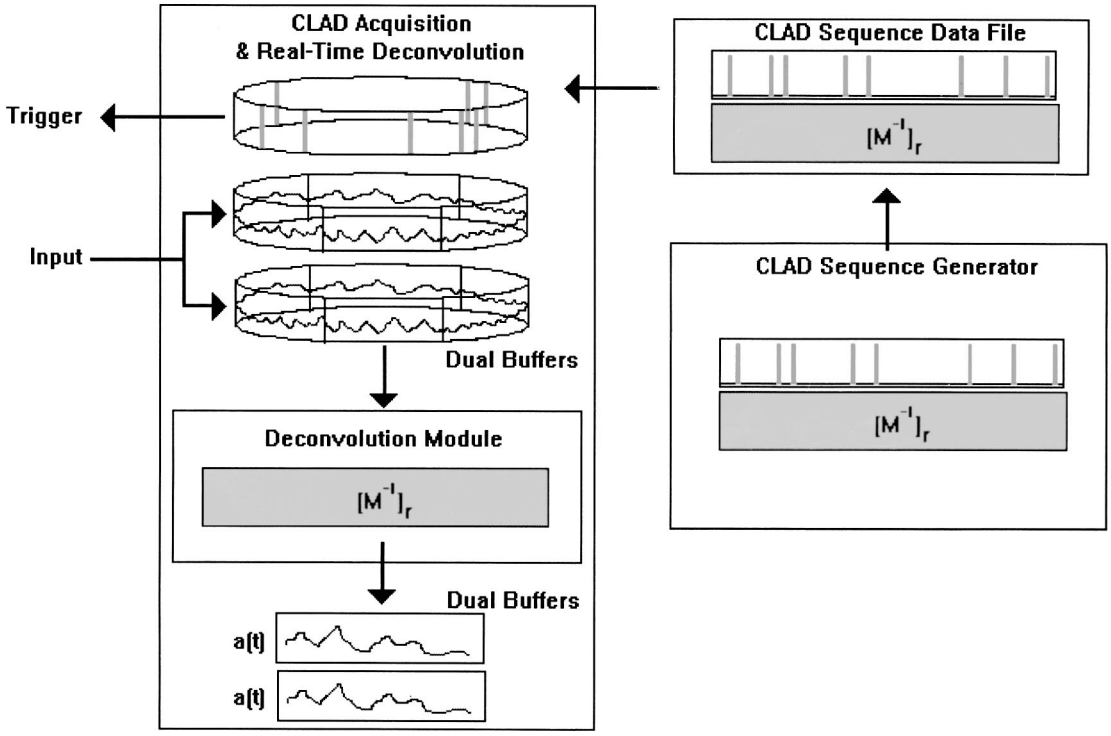

FIG. 5. Representation of CLAD system modules. The CLAD sequence generator outputs a data file containing the triggering sequence and deconvolution inverse matrix solution. The data file is used by the real-time acquisition and deconvolution module to generate the trigger signals and to read and deconvolve incoming data.

convolved response for each sequence was then deconvolved using the CLAD procedure and compared to the original signal.

System testing was also conducted by using a loop-back cable from the stimulus sound output of the EP device to the amplifier input. The recorded signals, consisting of the stimulus sequence, were deconvolved. Proper deconvolution would yield only one stimulus at time zero.

2. Human ABR and MLR recordings using CLAD

Auditory brainstem response (ABR) and middle latency response (MLR) recordings at 60-dB nHL were acquired from four ears using CLAD at six stimulation rates ranging from 58.6 to 507.8 Hz. Similar recordings were obtained at two lower rates (11.1 and 19.1 per second) using conventional averaging methods for comparison (Ozdamar and Kraus, 1983). Scalp recordings were obtained using standard procedures (gain 100 000, +forehead, −ipsi mastoid, ground contra mastoid) using monaural rarefaction clicks. Bandpass filter settings were 100–1500 Hz for ABR and 10–1500 Hz for joint ABR–MLR recordings. The continuous loop buffer contained 2048 data points collected at a 25-μs sampling time. This sampling time provided a recording period of 51.2 ms. A total of 512 sweeps was averaged for each recording. Each sweep consisted of an entire stimulus sequence. Response deconvolution was calculated in real time as the data were acquired. Both convolved and deconvolved recordings were stored for analysis.

IV. RESULTS

A. Simulations and system testing

Different simulation experiments were conducted using different individual response functions. The results of a simulation using an arbitrary EP as a transient response are depicted in Fig. 6. In this simulation a typical newborn ABR [shown in panel (A)] was used as the transient response. The convolution process is depicted in the bottom panel, and the resulting convoluted response is shown in panel (B). The deconvolution process by CLAD produced the response in panel (C), which is identical to the response in panel (A). All

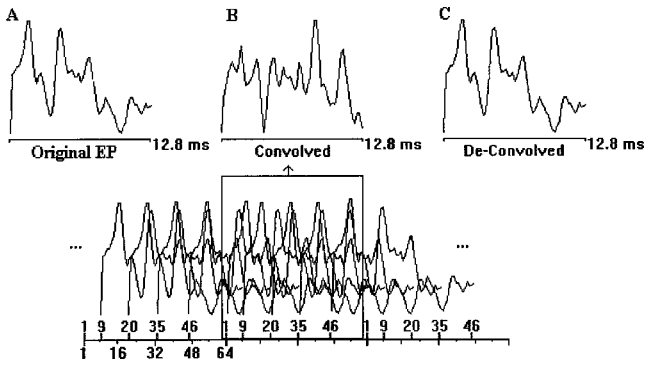

FIG. 6. Example of simulation conducted for testing of CLAD algorithm. If a mathematical solution was found for a given stimulation sequence, a test EP signal (A) was convolved by simulating the overlapping responses occurring at each stimulation point (B). In this example, a 64-point EP with stimuli occurring at the 1st, 9th, 20th, 35th, and 46th data points was used. The deconvolution matrix was then applied to the convoluted signal to verify that the original signal could be reconstructed (C).

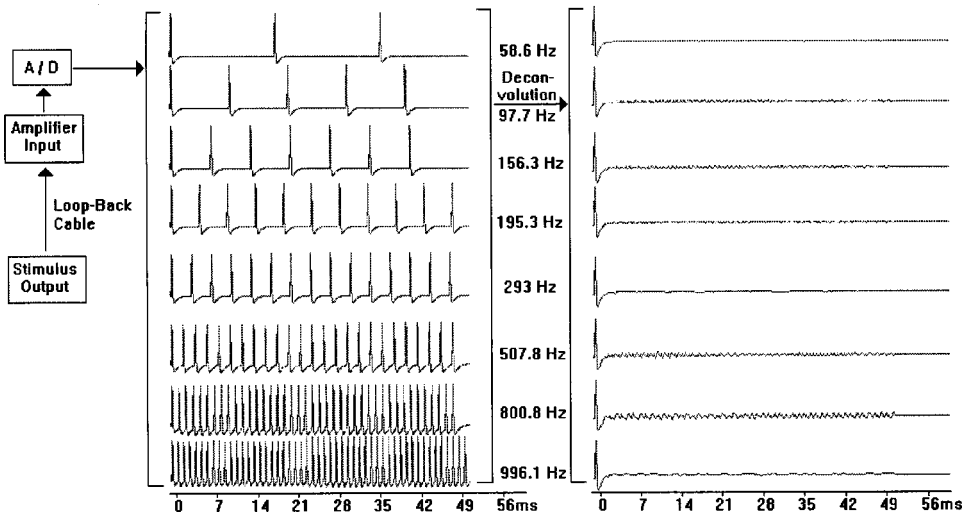

FIG. 7. System testing using a loop-back cable, shown on the left side, to record the stimulus output for each sequence. The results of the deconvolution process for each sequence are shown on the right side. After deconvolution, the stimulus sequence collapses to the origin showing that the process is working properly. Some deconvolved recordings show small oscillations due to amplifier noise and saturation.

the simulation experiments produced the same results. In all cases where a solution was obtained to a given sequence, the deconvolution algorithm was able to reconstruct the original signal.

The loop-back testing of the various stimulation sequences yielded the results shown in Fig. 7. As expected, the deconvolution of the recorded stimulus sequences yielded one stimulus pulse at the origin for each sequence. These results showed that the algorithms and their implementations in the recording system were working properly and that actual data recording could proceed.

B. ABR and MLR acquisition

ABR–MLR recordings obtained produced identifiable wave V and P_a components at all six rates. Examples of two conventional ABR–MLR recordings and three nondeconvolved and deconvolved ABR–MLR recordings obtained using 60-dB nHL clicks at different rates are shown in Fig. 8. All recordings were obtained with wide bandpass (10–1500 Hz) filters for simultaneous acquisition of ABR and MLR (Ozdamar and Kraus, 1983). Conventional recordings obtained at 11.1 and 19.1 Hz show the typical ABR complex within the first 10 ms and the P_a component of the MLR in the 30-ms range, as expected. For higher rates, averaging produced overlapping and sometimes undecipherable tracings shown on the left-hand side. Only at somewhat lower stimulation rates (58.6 and 97.7 Hz) could the ABR waveform be discerned without the MLR. Deconvolution using the CLAD procedure produced the readily identifiable ABR–MLR recordings seen in the right column. These recordings compare favorably with the conventional recordings.

ABR recordings obtained with 100–1500-Hz filter settings produced readily identifiable wave V component in all rates. Examples of convolved and deconvolved recordings using 60-dB nHL clicks at six different rates are shown in Fig. 9. As can be observed, waves I, III, and V are readily discernible in both convolved and deconvolved recordings obtained at rates of less than 100 s. For higher rates, ABR components start overlapping with each other, producing complex tracings. Deconvolved responses obtained with CLAD clearly show the observed wave V component even at 507.8/s. As expected, at high rates wave V starts diminishing in amplitude and increasing in latency. Earlier components I and III are less discernible at such rates.

V. DISCUSSION

In this study, a theory and methodology are developed to deconvolve evoked responses obtained at high acquisition rates with overlapping responses. The device developed is intended for the acquisition of any signal requiring the presentation of an excitatory triggering event followed by time-synchronized averaging data acquisition. The device uses a newly developed technique, continuous loop averaging deconvolution (CLAD) that allows the presentation of excitatory triggering events at very high speeds using almost any presentation sequence. An example application is auditory evoked potentials (AEPs), where a short-duration sound stimulus signal is presented to the ear and the elicited electrical impulses that travel from the cochlea to the brain are recorded using surface electrodes placed on the scalp. Because of the low signal-to-noise ratio (SNR) of these electrical responses compared to the overall electroencephalographic (EEG) activity, many stimulus presentations are averaged to increase the SNR. Previously developed devices present the excitatory signals at specific and constant intervals with interstimulus intervals (ISI) large enough to allow the system response to decay before the next excitatory signal is presented. For example, the early portion of AEPs, called auditory brainstem responses (ABR), corresponds to the first 10 ms after stimulation. During ABR acquisition, the sound stimulus signal is presented at rates ranging from 1 to 100 Hz. In the standard acquisition technique, stimulation rates faster than 100 Hz would result in a truncation and distortion of the desired ABR response due to overlapping. The CLAD technique overcomes this limitation by using a real-time deconvolution algorithm that allows the stimulus signals to be presented in a rapid manner before the response decays, thereby providing information as to the response characteristics at very high stimulation rates not possible with conventional techniques.

It is also important to remember that CLAD assumes that the responses terminate or are substantially diminished

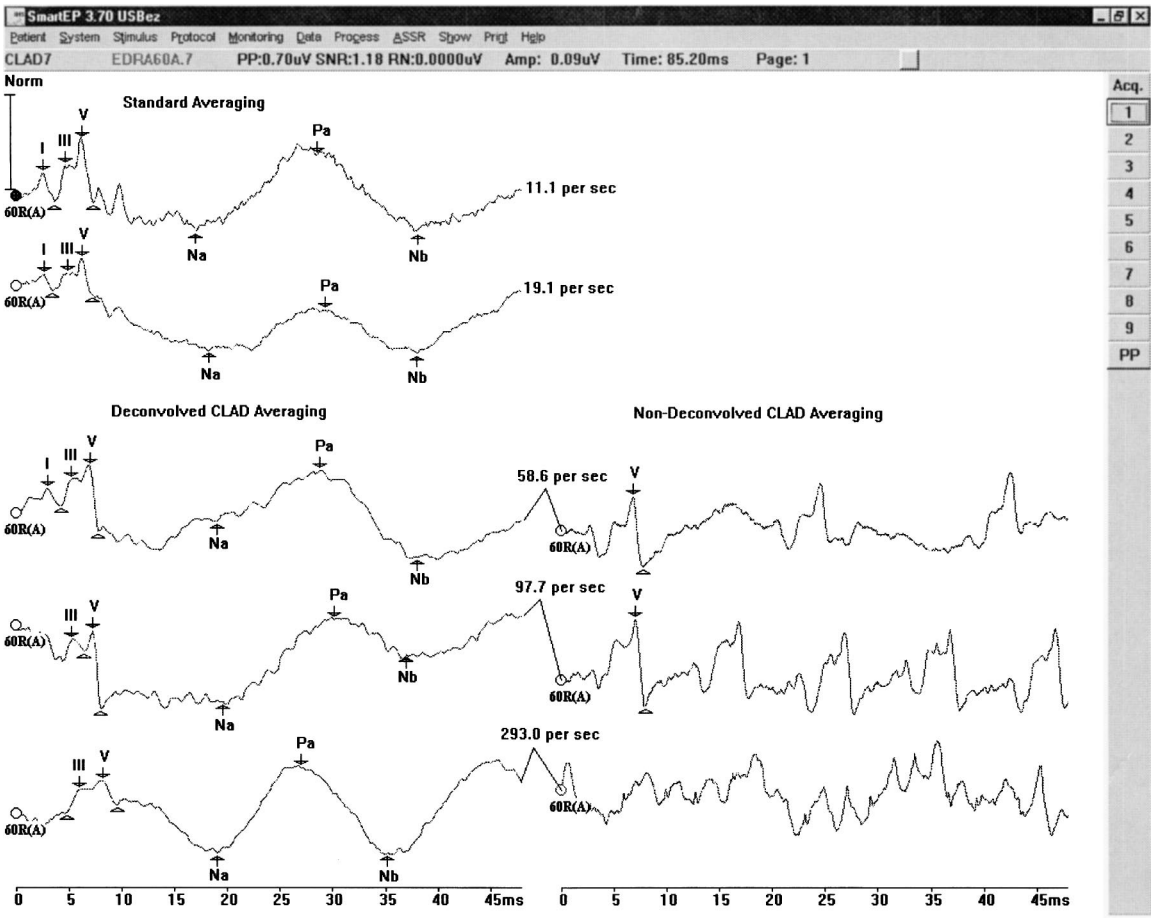

FIG. 8. MLR recordings: Implementation of real-time CLAD data acquisition and deconvolution for auditory evoked potentials in the SmartEP system (Intelligent Hearing Systems Corp.). The recordings were acquired using CLAD stimulation sequences with mean stimulation rates of 58.6, 97.7, and 293.0 Hz with the instantaneous stimulation rate varying from 55.6 to 64.9, 87.7 to 102.0, and 192.0 to 454.6 Hz, respectively. The top left side of the graph shows recordings acquired using a standard averaging technique at rates of 11.1 and 19.1 Hz. Below and to the right are the original nondeconvolved recordings. Below and to the left are the deconvolved recordings using the CLAD stimulation sequences. The latencies and amplitudes of the primary peaks for each mean stimulation rate are as follows: 11.1 Hz: I: 2.5 ms 0.21 μV, III: 4.7 ms 0.26 μV, V: 6.3 ms 0.46 μV, Na: 17.6 ms, Pa: 28.6 ms 0.63 μV, Nb: 38.1 ms; 19.1 Hz: I: 2.7 ms 0.24 μV, III: 4.90 ms 0.25 μV, V: 6.3 ms 0.54 μV, Na: 18.4 ms, Pa: 29.1 ms 0.66 μV, Nb: 38 ms; 58.6 Hz: I: 3.0 ms 0.14 μV, III: 5.2 ms 0.22 μV, V: 7.0 ms 0.54 μV, Na: 19.2 ms Pa: 28.8 ms 0.72 μV, Nb: 38.0 ms; 97.7 Hz, III: 5.20 ms 0.06 μV, V: 7.2 ms 0.43 μV, Na: 19.6 ms, Pa: 30.3 ms 0.21 μV, Nb: 37.0 ms; and 293.0 Hz. III: 6.0 ms 0.17 μV, V: 8.20 ms 0.18 μV, Na: 19.2 ms, Pa: 26.8 ms 0.69 μV, Nb: 35.3 ms:.

within the continuous loop averaging buffer time period. Residual response components that continue to wrap around the acquisition buffer will not be represented by the current CLAD technique and will also be averaged into the deconvolved responses as in conventional averaging. CLAD, however, does allow for the acquisition time base to be increased in order to expand the time duration of the loop buffer, be it at a lower sampling rate. This provides the potential to examine components that might wrap around the smaller loop acquisition buffers.

The issue of SNR improvement, as a function of stimulus presentation count, needs to be studied further. In standard averaging, SNR increases as function of presentations that are averaged. In CLAD, however, the fact that stimuli are being presented at a fast rate does not translate to a reduced acquisition time, especially with low SNR signals such as ABRs. The results indicate that the SNR improvement is primarily a function of the total number of loops averaged. During averaging in CLAD, the entire loop can be thought of as a single event. Activity that is not synchronized to the loop is averaged out. This is consistent with the manner in which averaging eliminates random noise. The amount of noise cancellation attributed to the deconvolution process depends on the spectral composition of the residual noise and the interaction of the individual data points during the deconvolution process. Each CLAD sequence results in a unique SNR transfer function that may enhance or decrease signal quality at specific frequency components. A complete analysis of the developed CLAD sequences will be the focus of further study.

VI. SUMMARY AND CONCLUSIONS

The ABR and MLR examples shown in this paper demonstrate CLAD can be successfully implemented in a real-time data acquisition system. The recordings obtained were comparable to those obtained at the lower stimulation rates demonstrating that the deconvolution technique was working properly. As expected, the ABR and MLR recordings showed the typical increase in peak latency as a function of increasing stimulation rate. All major ABR and MLR peaks were

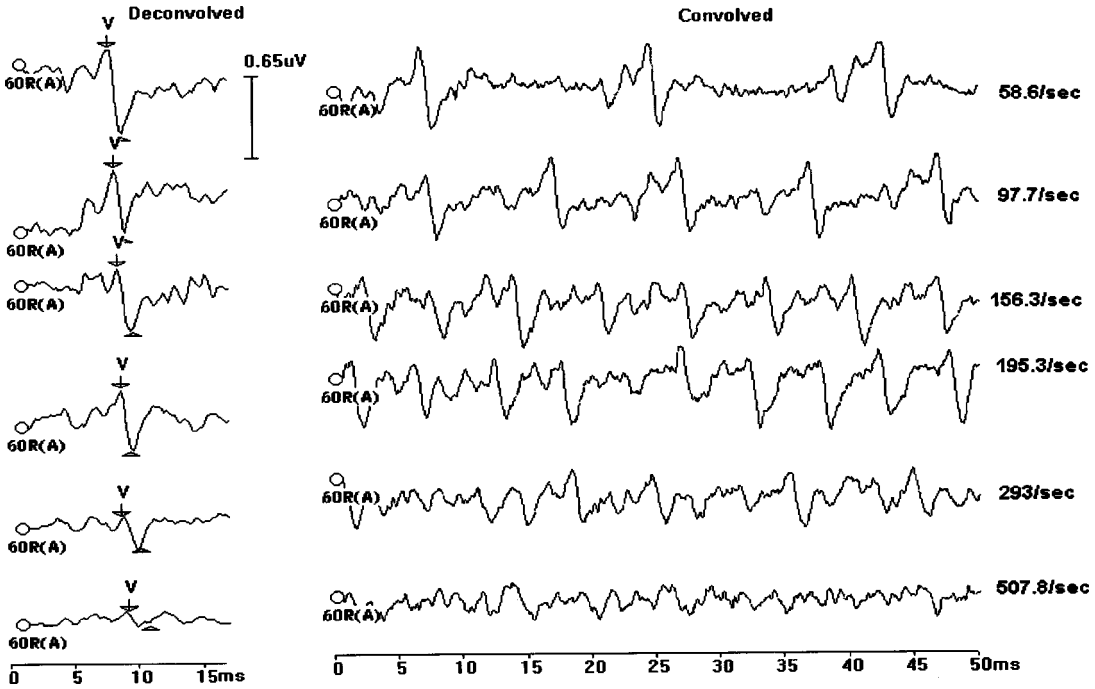

FIG. 9. ABR recordings: Implementation of real-time CLAD data acquisition and deconvolution for auditory evoked potentials in the SmartEP system. Examples of the ABR component of AEPs recorded using the CLAD method using average stimulation rates (instantaneous rate range in parentheses) of 58.6 (55.6 to 64.9), 97.7 (87.7 to 102.0), 156.3 (151.5 to 192.3), 195.3 (106.4 to 714.3), 293 (192.0 to 454.6) and 507.8 (312.5 to 1666.7) Hz. The right side represents the raw data (v[t]) prior to deconvolution and the left side represents the data after deconvolution (a[t]). The peak latencies and recording morphology are consistent with data recorded using a conventional averaging technique. The peak V latency and amplitude for each mean stimulation rate are as follows: 58.6 Hz: 7.94 ms 0.68 μV; 97.7 Hz: 8.38 ms 0.50 μV; 156.3 Hz: 8.53 ms 0.49 μV; 195.3 Hz: 8.82 ms 0.47 μV; 293 Hz: 9.12 ms 0.27 μV; and 507.8 Hz: 9.41 ms 0.15 μV.

clearly detectable. The variability in the P_a MLR component can be attributed to changes in subject arousal state.

The CLAD technique provides the user with the flexibility to design almost any stimulation sequence desired. Due to the large selection of possible stimulation sequences, CLAD provides a great tool for studying adaptation effects at very high stimulation rates. Unlike previously developed sequences, CLAD also provides the ability to generate near-isochronous sequences that provide results that can be better compared to previous studies using standard averaging methods. This ability will enable researchers to expand their work and look at responses to stimuli not possible before.

Although the CLAD technique does not reduce testing time, it provides a very important tool in the analysis of system responses to fast stimulation rates. The applications go beyond the auditory evoked response examples supplied in this paper. CLAD provides a general nonsynchronous excitation and deconvolution technique that can be applied to any technique requiring excitation and time averaging of acquired signals such as magnetic resonance imaging (MRI), nuclear magnetic resonance (NMR) for chemical analysis, acoustical systems, sonar, radar, electrical systems, mechanical systems, and hydraulic systems.

Azzena, G. B., Conti, G., Santarelli, R., Ottoviani, F., Paludetti, G., and Maurizi, M. (**1995**). ''Generation of human auditory steady-state responses (SSRs). I. Stimulus rate effects,'' Hear. Res. **83**, 1–8.

Burkard, R., Shi, Y., and Hecox, K. E. (**1990**). ''A comparison of maximum length sequences and Legendre sequences for the derivation of brainstem auditory evoked responses at rapid rates of stimulation,'' J. Acoust. Soc. Am. **87**, 1656–1664.

Burkard, R. (**1994**). ''Gerbil brain-stem auditory-evoked responses to maximum length sequences,'' J. Acoust. Soc. Am. **95**, 2126–2135.

Chan, F. H. Y., Lam, F. K., Poon, P. W. F., and Du, M. H. (**1992**). ''Measurement of human BAERs by the maximum length sequence technique,'' Med. Biol. Eng. Comput. **30**, 32–40.

Eysholdt, U., and Schreiner, C. (**1982**). ''Maximum length sequences—a fast method for measuring brainstem evoked responses,'' Audiology **21**, 242–250.

Jewett, D. L., Larson-Prior, L. S. and Baird, W. (**2001**). ''A novel techniques for analysis of temporally-overlapped neural responses,'' Evoked Response Audiometry XVII Biennial Symposium IERASG, p. 31. (2001).

Lasky, R. (**1992**). ''Maximum length sequence auditory evoked brainstem responses in human newborns and adults,'' J. Am. Acad. Audiol **3**, 383–389.

Li, H. F., Chan, F. H. Y., Poon, P. W. F., Hwang, J. C., and Chan, W. S. (**1988**). ''Maximum length sequence applied to the measurement of brainstem auditory evoked responses,'' J. Biomed. Eng. **10**, 14–24.

Marsh, R. (**1992**). ''Signal to noise constraints on maximum length sequence auditory brain stem responses,'' Ear Hear. **13**, 396–400.

Picton, T. W., Champagne, S. C., and Kellet, A. J. C. (**1992**). ''Human auditory evoked potentials using maximum length sequences,'' Electroencephalogr. Clin. Neurophysiol. **84**, 90–100.

Ozdamar, O., and Kraus, N. (**1983**). ''Auditory middle-latency responses in humans,'' Audiology **22**, 34–49.

Ozdamar, O., and Delgado, R. E. (**1996**). ''Measurement of signal and noise characteristics in ongoing auditory brainstem response averaging,'' Ann. Biomed. Eng. **4**, 702–715.

Shi, Y., and Hecox, K. E. (**1991**). ''Nonlinear system identification by m-pulse sequences: Application to brainstem auditory evoked responses,'' IEEE Trans. Biomed. Eng. **38**, 834–845.

Thornton, A. R. D. (**1993**). ''High rate otoacoustic emissions,'' J. Acoust. Soc. Am. **94**, 132–136.

Thornton, A. R. D., and Slaven, A. (**1993**). ''Auditory brainstem responses recorded at fast stimulation rates using maximum length sentences,'' Br. J. Audiol. **27**, 205–210.

Weber, B. A. and Roush, P. A. (**1995**). ''Use of maximim length sequence analysis in new born testing,'' J. Am. Acad. Audiol. **6**, 187–190.

Spectral-temporal factors in the identification of environmental sounds

Brian Gygi,[a] Gary R. Kidd, and Charles S. Watson
Department of Speech and Hearing Sciences, Indiana University Bloomington, Indiana 47405

(Received 25 February 2003; revised 28 October 2003; accepted 3 November 2003)

Three experiments tested listeners' ability to identify 70 diverse environmental sounds using limited spectral information. Experiment 1 employed low- and high-pass filtered sounds with filter cutoffs ranging from 300 to 8000 Hz. Listeners were quite good (>50% correct) at identifying the sounds even when severely filtered; for the high-pass filters, performance was never below 70%. Experiment 2 used octave-wide bandpass filtered sounds with center frequencies from 212 to 6788 Hz and found that performance with the higher bandpass filters was from 70%–80% correct, whereas with the lower filters listeners achieved 30%–50% correct. To examine the contribution of temporal factors, in experiment 3 vocoder methods were used to create event-modulated noises (EMN) which had extremely limited spectral information. About half of the 70 EMN were identifiable on the basis of the temporal patterning. Multiple regression analysis suggested that some acoustic features listeners may use to identify EMN include envelope shape, periodicity, and the consistency of temporal changes across frequency channels. Identification performance with high- and low-pass filtered environmental sounds varied in a manner similar to that of speech sounds, except that there seemed to be somewhat more information in the higher frequencies for the environmental sounds used in this experiment.
[DOI: 10.1121/1.1635840]

PACS numbers: 43.66.Lj, 43.66.Mk, 43.66.Ba [NFV] Pages: 1252–1265

I. INTRODUCTION

The study of the perception of environmental sounds has lagged behind that of the three classes of stimuli that have been the subject of the great majority of auditory research: speech, music, and laboratory-generated test sounds. Nevertheless, research has shown that humans have a remarkable ability to easily and quickly identify a large range of naturally occurring sounds (Lass *et al.*, 1982; Ballas, 1993) representing a wide range of objects and interactions in the world (Gaver, 1993a). Because of the variety of sources, the range of spectral and temporal variation among nonspeech environmental sounds greatly exceeds that of speech (see Attias and Scheiner, 1997), for which the source, either actual or simulated (in the case of synthesized speech), is the human vocal tract.

Their tremendous variety makes it difficult to arrive at generalizations that apply to the entire class of environmental sounds. Several studies have instead focused on the perception of particular classes of sounds (e.g., bouncing and breaking bottles, Warren and Verbrugge, 1984; hands clapping, Repp, 1987; mallets striking metal pans, Freed, 1990; footsteps, Li *et al.*, 1991). Many of these investigations have examined the associations between the acoustic properties and the identifiability of specific sounds. Some have looked at how specific physical features of objects are specified by acoustics, such as the amount of liquid in a cylinder (Cabe *et al.*, 2000) and the dimensions and shapes of objects (Carello *et al.*, 1998; Kunkler-Peck and Turvey, 2000; Lakatos *et al.*, 1997). Others have focused on subjective (or cognitive) judgments of sound qualities or properties in an attempt to relate these judgments to acoustic properties of the sounds (Halpern *et al.*, 1986; Ballas and Howard, 1987; Ballas, 1993, Gaver, 1993b).

Many identification studies have examined recognition accuracy of a moderately sized corpus (20–40 sounds) in quiet at suprathreshold levels (Lass *et al.*, 1982; Vanderveer, 1979), often with an emphasis on the effect of cognitive factors on listeners' performance (Ballas, 1993). Gaver (1993a) developed a preliminary taxonomy of environmental sounds, based on dimensions of the type of interacting material (gas, liquid, solid) and the type of interaction (e.g., collision, explosion, splash). These varied approaches have demonstrated the ready identifiability of a diverse body of environmental sounds, and provided some evidence of the acoustic properties listeners use to identify specific sounds, such as damping of the envelope for bouncing and breaking bottles (Warren and Verbrugge, 1984) and centroid (spectrum mean) for footsteps (Li *et al.* 1991). In contrast, Lutfi and colleagues (Lutfi and Oh, 1997; Lutfi, 2001) have shown that under certain conditions, listeners do not attend to the appropriate acoustic features, giving undue weight to frequency at the expense of other, more informative features.

In the present series of experiments, an approach used in early studies of the perception of speech is applied to a catalog of environmental sounds. Research by telephone scientists and engineers devoted a considerable effort to determining the importance of various frequency regions for the identification of speech. One method was to measure the identifiability of low-, high-, and bandpass filtered speech, which eventually led to the development of the Articulation

[a]Current affiliation: East Bay Institute for Research and Education, Martinez, CA. Electronic mail: bgygi@ebire.org

TABLE I. List of sounds used in the environmental sound identification study.

Sound	Code	Dur (ms)	Sound	Code	Dur (ms)
Airplane flying	AIR	3426	Harp being strummed	HAR	2839
Baby crying	BAB	3119	Helicopter flying	HCP	3100
Basketball bouncing	BBA	3184	Horse neighing	HRN	1464
Beer can opening	BER	431	Horse running	HRR	2046
Bells chiming	BLS	3100	Ice dropping into glass	ICE	738
Billiard balls colliding	BIL	1684	Laughing	LAF	1836
Bird calling	BRD	1283	Match being lit	MAT	1366
Bowling	BOW	3062	Paper being crumpled	PAP	1697
Bubbling	BUB	2212	Phone ringing	PHN	3100
Buzzer sounding	BZZ	2523	Ping-pong ball bouncing	PNG	3945
Camera shutter clicking	CAM	1398	Printing paper	PRN	3154
Car accelerating	CRA	3209	Projector running	PRJ	2909
Car starting	CRS	3551	Rain	RAI	3362
Cars crashing	CRC	3110	Rocking chair	RCK	3234
Cars honking	CRH	3367	Rooster crowing	ROO	2004
Cash register closing	REG	2841	Scissors cutting paper	SCI	2807
Cat meowing	CAT	1054	Screen door closing	SCR	3292
Chimp calling	CHP	2315	Sheep baaing	SHP	1365
Chopping wood	AXE	2624	Shoveling	SHV	1585
Clapping	CLP	1035	Siren blaring	SIR	1534
Clock ticking	CLK	2882	Sneezing	SNZ	844
Coughing	COF	1043	Splash	SPL	2338
Cow mooing	COW	1290	Stapling	STA	822
Cymbals being hit	CYM	1204	Tennis ball being hit	TEN	2761
Dog barking	DOG	1007	Thunder rolling	THU	2895
Door opening and closing	DOR	1802	Toilet flushing	TOI	2494
Drumming	DRM	2747	Train moving	TRN	3333
Electric guitar (strum)	GTR	2087	Tree falling	TRE	3424
Electric saw cutting	ESW	2600	Typing on keyboard	TYK	1033
Flute playing	FLU	2566	Typing on typewriter	TYT	2755
Footsteps	FST	2700	Water pouring	POU	3302
Gargling	GRG	2523	Waves crashing	WAV	2876
Glass breaking	GLS	1018	Whistle blowing	WHI	2047
Gun shot	GUN	902	Windshield wipers	WWP	3023
Hammering a nail	HAM	1833	Zipper	ZIP	1733

Index (AI) (French and Steinberg, 1947). The primary goal was to determine the overall bandwidth required to communicate human conversations, and the frequency content of individual speech sounds was not of concern.

In the first two experiments described below, the identifiability of 70 environmental sounds was measured under conditions of low-, high-, and bandpass filtering. Although the methodology is similar to those of early speech studies, the primary goal was not to determine the overall bandwidth needed to recognize the majority of environmental sounds, because, as with vowels and consonants, it is clear that many environmental sounds occupy small portions of the audible range. Instead, the purpose was to identify the spectral regions that include the most useful identifying information for a wide range of environmental sounds by measuring changes in identification performance under different filtering conditions. Listeners will not necessarily attend to the same frequency band under all listening conditions (depending on context), and the attended-to spectral regions may be narrower, wider, or may vary over time. However, the results provide an indication of where the most useful information is located, as well as a measure of listeners' abilities to utilize information in different spectral regions (including regions that may provide little identifying information). This information may aid in the assessment of listening strategies observed in other contexts.

Many environmental sounds are really a collection of repeated brief sounds, such as a ping-pong ball bouncing, chopping wood, or a clock ticking. These sounds usually have fairly broad spectra, being akin to noise bursts, and it is likely their temporal patterning that allows identification. Consequently, they may be recognizable even with extremely limited spectral information. This hypothesis was tested by creating what are termed here event-modulated noises (EMNs). An EMN is a broadband noise whose temporal envelope is modulated by the envelope of a particular environmental sound; the resulting sound preserves the temporal structure of the environmental sound, but has a uniform spectrum. This is similar to the noise-band vocoder techniques used to create vocoder speech (e.g., Shannon *et al.*, 1995). Together, the two types of stimulus manipulations (filtering and EMN) demonstrate the spectral and temporal information listeners use to identify familiar environmental sounds.

II. THE CATALOG OF ENVIRONMENTAL SOUNDS

The 70 environmental sounds used in the experiments reported here are listed in Table I. They were taken from high-quality sound effects CDs (Hollywood Leading Edge and Sound FX The General) sampled at 44.1 kHz. The sounds were selected on the basis of familiarity, pairwise discriminability, and ready identifiability in the quiet based on pilot studies. An effort was made to select a fairly representative sampling of the classes of meaningful sounds encountered in everyday listening: nonverbal human sounds, animal vocalizations, machine sounds, the sounds of various weather conditions, and sounds generated by human activities. The sounds were equated for overall rms, with a correction for pauses of greater than 50 ms (the pause-corrected rms for these sounds is discussed in Appendix A) and stored as binary files. While no formal study of the recognition of the stimuli in their unfiltered forms was conducted, all but a few of the 70 unfiltered sounds were correctly identified on the first trial in the training phase of experiment 1. All were identified with greater than 95% accuracy by the fourth presentation. This, as well as performance in the widest filter condition reported below, demonstrates that all sounds are easily identified in their unfiltered form. The mean duration of the sounds was 2.3 s, with the shortest sound being beer can opening (431 ms) and the longest being ping-pong ball bouncing (3945 ms).

III. EXPERIMENT 1. IDENTIFICATION WITH LOW- AND HIGH-PASS FILTERING

A. Methods

1. Stimuli

The set of 70 environmental sounds was filtered with third-order Chebyshev type I filters, with slopes of 48 dB/octave and a level of -60 dB in the stopbands. The high-pass filter cutoffs (f_c, measured at the 3-dB down point) were 300, 600, 1200, 2400, 4800, and 8000 Hz. Low-pass f_c were 300, 600, 1200, 2400, and 4800 Hz. The 8000-Hz high-pass filter was added after pilot testing, which indicated an f_c higher than 4800 Hz would be necessary to properly estimate the full range of performance. The filter coefficients were generated by MATLAB's signal-processing module (sptool).

2. Listeners

The listeners were four females between the ages of 18–30, all with normal hearing as measured by pure-tone audiograms (thresholds $<$15 dB HL). All were undergraduates at Indiana University, and were paid for their participation.

3. Procedure

The listeners were seated in listening booths, facing VT100 terminals and keyboards. The stimuli were played over Sennheiser HD 250 Linear headphones. The headphones' frequency response (measured using pure tones and an acoustic coupler) varied by no more than 3 dB from 10–25 000 Hz.[1] The stimuli were generated from the stored raw files by TDT 16-bit D/A converters and amplified by a Crown headphone amplifier. The presentation level was set so that the unfiltered, equated stimuli were presented at 80 dB SPL at the headphones.

It should be noted that there was no attempt to equate the rms of the filtered stimuli. A result was that in some cases, usually with the highest or lowest bandpass filter, an extremely small amount of energy was output by the filter. While this meant that a few stimuli were barely audible, this approach was preferred to equating levels of the filtered sounds, because of the greater ecological validity in preserving the relative levels of all frequency components across the filter conditions.

The listeners were given a sheet listing the sounds to be presented and three-letter codes with which to respond (shown in Table I). The labels for the sounds were intended to give a sense of the source objects and the events involved. The response codes were selected to be as distinctive as possible; with a few exceptions, codes differed by two or three letters (one exception was TYT and TYK for typing on a typewriter and typing on a keyboard, respectively).

Listeners were instructed to identify the sound they heard by typing the appropriate code on the keyboard. The list of codes was always within view in front of each subject. If the listener did not respond within 7 s, a prompt would flash on the screen, encouraging them to respond. If the listener responded with a code that was not valid, they were prompted to reenter the code. Throughout the training stages of all experiments reported here, right–wrong feedback was provided, but not in the testing stages.

The experiment proceeded in four sequential phases.

(a) *Pretraining:* Listeners were told that their ability to identify various common environmental sounds was going to be tested, and that they were to respond using three-letter codes. Each listener was then encouraged to look over the sheet containing the list of sounds to be used and the associated codes with which to respond to each. Then, five practice trials were given in which listeners were played an unfiltered sound and asked to identify it. These practice sounds were alternative examples of ones that were used in later testing (e.g., a different cat sound).

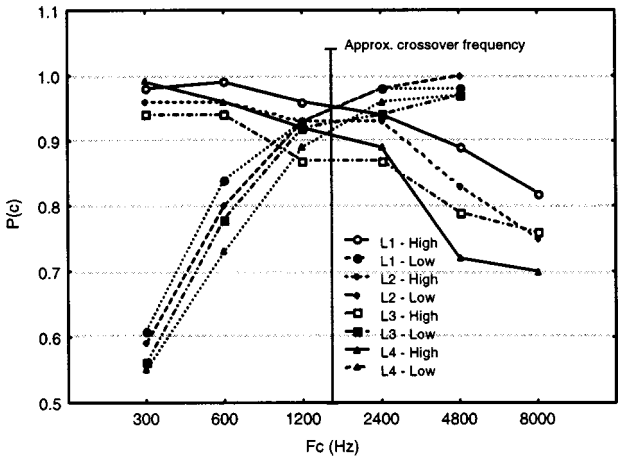

FIG. 1. Performance by four listeners (designated L1–L4) under low- and high-pass filtering conditions. The approximate crossover frequency is the isointelligibility point for the low- and high-pass functions (see the text).

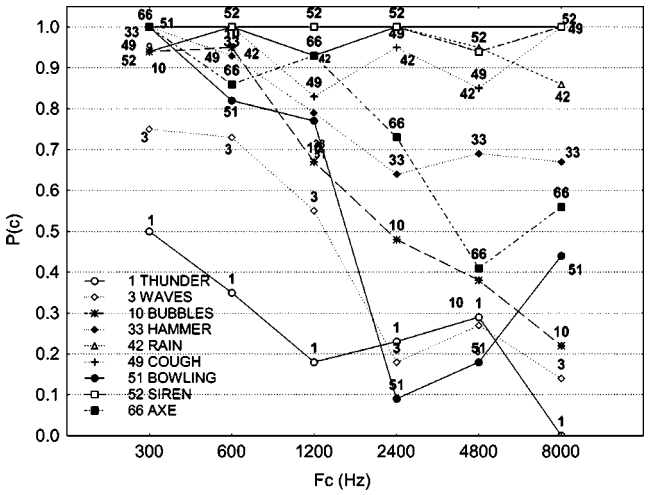

FIG. 2. Identifiability of selected sounds under high-pass filtering.

(b) *Familiarization:* The set of 70 unfiltered sounds was next presented in the order that it appeared on the response sheet, and the listeners identified each. The listeners were told that in this phase they should attempt to learn the sounds and the associated codes.

(c) *Training:* The unfiltered sounds were presented in random order. The complete list was presented a sufficient number of times for listeners to reach >95% accuracy with relatively short latencies for entering the three-letter codes. This required four iterations of the whole list, about 1.5 h of testing time. Although no systematic effort was made to distinguish between sounds which were recognized perfectly and those for which an error or two was made, on the fourth iteration of the list only nine sounds were recognized with less than 100% accuracy, and those all had only one error among the four subjects. Listeners were given a 1-min break after every block of 35 trials, which averaged about 8 min to complete, and a 5-min break after every four blocks.

(d) *Testing:* The listeners were told that they were going to be tested with filtered sounds, and they then heard examples of high- and low-pass filtering of a sound that was not used in the later tests. The filtered stimuli were then presented in random order, and the listeners identified them using the three-letter codes. Over 9 days of testing, the complete list of 770 stimuli (70 sounds×11 filter types) was presented five times. Breaks were given as in the training phases.

B. Result and analysis

Figure 1 shows the probability of correct responses for each listener across all f_c for both the high- and low-pass conditions. For both high- and low-pass filter conditions performance was nearly perfect (95%–100% correct) in the least severe filter conditions, but recognition gradually declined as more information was filtered out. However, performance at the most extreme filter cutoffs was still fairly good, especially in the high-cutoff conditions, where performance never dropped below 70% correct. This is consistent with some results from the voice identification literature, such as Compton (1963) in which identifiability was not affected by high-pass filtering but was substantially impaired by low-pass filtering. The proportion correct for all sounds is listed in Appendix B, along with the mean and s.d. for each filter condition. In general, the s.d. of the sounds is inversely related to the filter width. However, in the widest filter conditions the low variance is due to a ceiling effect, as listeners achieved near-perfect recognition scores in these conditions.

One measure speech scientists have used to characterize the importance of various frequency regions for speech perception is the crossover point, a single frequency that divides the speech spectrum into equally intelligible halves. Various values have been found for the crossover point, from 1900 Hz for nonsense syllables (French and Steinberg, 1947) to 1189 Hz for continuous discourse (Studebaker *et al.* 1987). In general, according to Bell *et al.* (1992), the crossover point tends to decrease as the redundancy of the speech material increases. When defined as the isoperformance point the crossover frequency for low- and high-pass environmental sounds is about 1300 Hz (noted in Fig. 1), which is in the lower end of the range for speech sounds. However, since the high-pass function has more area below it (due to the much shallower slope than the low-pass function) the frequency dividing the spectrum into equally intelligible halves would likely be somewhat higher than 1300 Hz.

Despite the overall tendency for high-pass filtered sounds to be better recognized than lowpass, there was considerable variation in the identifiability of individual sounds in both conditions. Figures 2 and 3 show the range of identification performance for a group of specific sounds in the low- and high-pass conditions. The selected sounds were either easily identifiable, not identifiable at all, or showed a graded loss in identifiability as more and more high or low frequencies were eliminated. As might be expected, under high-pass filtering, sounds such as thunder and waves are more difficult to identify, while most of the other sounds are easily recognized. The differences in identifiability are not due to audibility; both thunder and waves are audible even at the most severe high-pass f_c. Overall, for both filter condi-

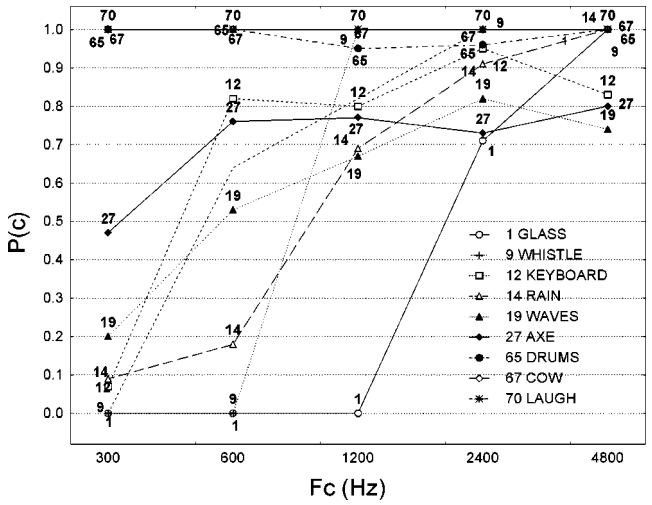

FIG. 3. Identifiability of selected sounds under low-pass filtering.

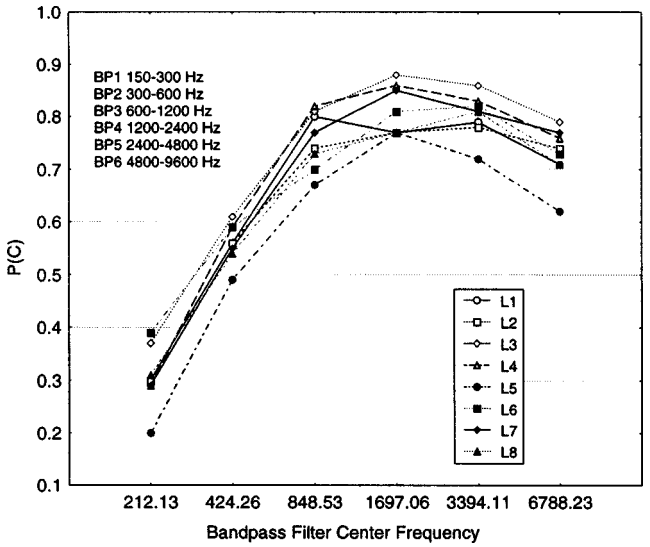

FIG. 4. Listener performance by bandpass filter type.

tions (low- and high-pass), the correlation between the rms output by the filter and $p(c)$ was close to zero. Under low-pass filtering there are sounds such as glass breaking for which the essential information is almost totally removed by moderate filtering. And, in both conditions there are sounds that retain their identifiability as long as any portion of their spectrum is audible.

However, high- and low-pass filtering only indicate general regions that are necessary for identification. It is also possible that specific frequency bands within their overall spectrum are particularly informative for certain sounds. The second experiment, therefore, examined the identification of bandpass filtered environmental sounds.

IV. EXPERIMENT 2. IDENTIFICATION WITH BANDPASS FILTERING

A. Methods

1. Stimuli

The sounds used were those in experiment 1. They were filtered with third-order Chebyshev type I filters, with slopes of 48 dB/octave and a level of −60 dB in the stopbands. Six different passbands (f_c measured at the 3-dB down point) were used, listed in Table II. The procedure for creating the stimuli was the same as in experiment 1.

TABLE II. Bandpass filter specifications.

	f_c Low (Hz)	f_c High (Hz)	Log midpoint (Hz)
BP1	150	300	212.13
BP2	300	600	424.26
BP3	600	1200	848.53
BP4	1200	2400	1697.06
BP5	2400	4800	3394.11
BP6	4800	9600	6788.23

2. Listeners

Six women and two men were recruited who had not participated in experiment 1. The criteria for age range and hearing thresholds were the same as in experiment 1. With one exception, they were all undergraduates at Indiana University.

3. Procedure

The procedure was the same as in experiment 1.

B. Result and analysis

Figure 4 shows the mean probability of correct responses to all of the sounds for each listener in each filter condition. The eight subjects all performed quite similarly, although there are noticeable and consistent individual differences: the best listener's scores were 10%–20% better than those of the worst listener at every filter setting. The most difficult filter settings were the two lowest, BP1 and BP2 (31% and 51% correct, respectively), whereas mean performance in the four highest bandpass settings was between 70%–80%. Scheffé's *post hoc* test showed that performance differed significantly under each filter setting ($p < 0.05$) from every other filter setting, except for BP4 vs BP5, and BP3 vs BP6. If the overall function were symmetrical, a level of performance comparable to BP1, based on the log axis shown in Fig. 4, would be achieved with a high-bandpass filter spanning the frequency region 19.2–38.4 kHz. Since this is above the range of human hearing, it is clear that the function is not symmetrical. An empirical question for a later date is whether the decline in performance at filter settings higher than 9600 Hz is gradual or shows a sharp drop-off.

Not all of the 70 sounds, however, followed the group pattern. Some sounds were much better recognized on the basis of the lower frequencies (e.g., bubbles), some were recognized well only at one specific filter setting (bowling) and several were identified perfectly across almost the whole range of bandpass filter settings. Across filters there were

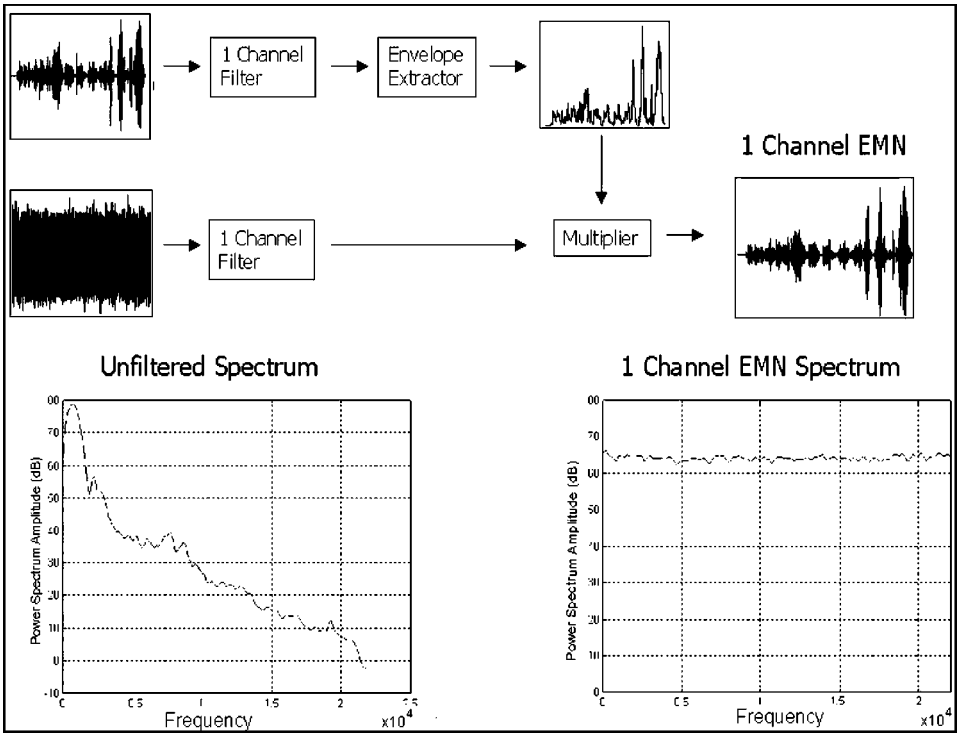

FIG. 5. Single-channel event-modulated noise (EMN) created using the bubbles sound and broadband noise.

quite large differences in identifiability between sounds: in general, the between-sound performance was only significantly correlated in contiguous filters (e.g., BP3 and BP4).

The preceding experiments focused on the informative value of different spectral regions for identifying environmental sounds. However, it may be that in many cases the temporal information is more important than the spectral patterning for identifying these sounds. Certainly, there are several sounds with strong characteristic periodicity (drums, gallop, helicopter), and others with distinctive, nonperiodic temporal structure (baby crying, laugh, bowling). It may be that such sounds could be identified by the energy in any spectral region as long as the temporal information is preserved. In the next experiment the importance of the temporal patterning was tested with environmental sounds that had most of the fine-grained frequency information removed.

V. EXPERIMENT 3. IDENTIFICATION OF EVENT-MODULATED NOISES

There has been a good deal of research using speech that has had most of the temporal information removed using vocoder methods (see, e.g., Dudley, 1940, 1958; Carrat, 1984; Eremenko and Ermakov, 1985). One of the most striking findings is that a relatively small number of channels (sometimes as few as three or four) is needed for almost perfect speech recognition, if the envelopes of each channel are low-pass filtered at a cutoff frequency of at least 50 Hz (Shannon *et al.*, 1995). This implies that temporal cues are sufficient to identify speech with a very coarse grain of spectral information. Given the results in the previous section, which suggested that the same might be true of environmental sounds, it was decided to test this with a methodology similar to Shannon's, using environmental sounds processed with vocoder techniques.

There are many ways of implementing vocoder principles; one recently used by Shannon *et al.* (e.g., 1995, 1998) is a simplification of the original design. Called a noise-band vocoder, it uses multiple noise-band carriers to represent the speech envelope signals from broad spectral bands without implementing the voicing detector and pitch estimator employed by Dudley. Figure 5 is a schematic showing how this was used with the envelope of an environmental sound to create an example of what will be termed here event-modulated noise (EMN). In the simplest case, there was only one broadband filter applied to the original sound, so there is little or no spectral information remaining. This is referred to as a single-channel EMN, and as Fig. 5 shows, the temporal envelope of the original waveform (bubbles) is preserved, while the spectrum is almost flat.

Frequency information can be reintroduced by partitioning the signal with several bandpass filters, and then using the envelope obtained from each filter to modulate a noise, the bandwidth of which is that of the corresponding filter. The several noises are summed and the resulting spectrum is closer to that of the original sound, although it is perceptibly "noisy."

The primary goal of the following experiments was to determine the identifiability of the set of environmental sounds used in the previous studies when all or nearly all of the spectral information was removed, leaving only temporal information. Three experiments were conducted using EMN. Experiments 3a and 3b used single-channel EMN. However, because the various studies by Shannon and others have

shown remarkably accurate identification of speech when only modest spectral information was reintroduced, it was of interest to learn whether environmental sounds showed a similar pattern. In a third study, 3c, listeners were tested on the identification of six-channel EMN.

A. Methods

1. Stimuli

The same 70 environmental sounds were used as in the previous experiments. Single-channel event-modulated noises were created by

(a) Extracting the envelope by half-wave rectifying the waveform and passing through a four-pole Butterworth LP ($f_c = 20$ Hz) filter; and
(b) Multiplying the envelope by a broadband noise of the same bandwidth (0–22.5 kHz).

Six-channel event-modulated noises were created by

(a) Extracting the envelope of all six bandpass filtered versions of each sound used in the previous experiment, by the method described above;
(b) Multiplying each envelope by a bandpass noise of the same bandwidth; and
(c) Adding the resulting six waveforms back together.

All manipulations were carried out in MATLAB. The EMN were then equated for rms minus silences of more than 50 ms, as was done previously for the original sounds.

2. Listeners

Three different studies were carried out, each using different sets of eight listeners with the same age and hearing threshold criteria as experiments 1 and 2. Listeners were 18 women and six men, all undergraduates at Indiana University. One group had participated in experiment 2. All were paid for their participation.

3. Procedure

The setting, apparatus, and presentation level were the same as in experiments 1 and 2. Three EMN identification studies using different listeners were conducted.

Experiment 3a. Single-channel EMN identified by experienced listeners. The listeners were those who took part in the bandpass filter studies. This study was run immediately after the bandpass filter trials, so the listeners were extremely familiar with the original sounds. They were told that in this study, the sounds would be altered in a manner similar to that of some electronic musical instruments, and were played two examples of EMN with a sound that was not used in the subsequent testing. The 70 EMN were then presented as in experiment 2. In one 1-1/2-h session, the complete list of 70 stimuli was presented five times.

Experiment 3b. Single-channel EMN identified by naive listeners. A new set of eight listeners was recruited, consisting of four males and four females. None of them had taken part in any of the previous studies. Two of the listeners, both males, dropped out after the first day of testing, so their data were not included in any of the subsequent analysis. The listeners were given instructions and pretraining as in the first phase of the bandpass filter experiment. The 70 EMN were then presented as in experiment 3a. This experiment took place over two 1-1/2-h sessions on subsequent days. On the first day, the listeners did not have a familiarization phase, so they had no knowledge of the original sounds before they identified the EMN. At the start of the second day, before further testing, they heard the original unprocessed 70 sounds and had to respond as in the familiarization phase of experiment 2. Then, they were tested again as on the first day. On the first day, the set of 70 EMN was presented four times; on the second day, five times.

Experiment 3c. Six-channel EMN identified by naive listeners. The participants were eight new listeners, three men and five women, none of whom had taken part in any of the previous studies. The stimuli were six-channel EMN rather than single-channel EMN. The procedure was the same as in experiment 3b. On the first day, the set of 70 EMN was presented four times; on the second day, five times. Familiarization with the original set of unprocessed sounds took place on the start of the second day only.

TABLE III. $P(c)$ by day for each listener group in the EMN experiments.

	Experienced (3a) single-channel	Naive (3b) single-channel	Naive (3c) six-channel
Day 1	0.46	0.13	0.36
Day 2		0.23	0.66

B. Results

Table III shows the $p(c)$ for each group of listeners in experiment 3a, b, and c on each day. There was a substantial improvement for both groups of naive listeners on day 2 after they heard the original waveforms, even though they heard each one only once. Because the day 1 single-channel EMN performance for the naive group was so poor, all further discussion of the EMN results will refer to the day 2 findings for both groups of naive listeners. It should be noted, however, that 15 sounds, among them helicopter, gallop, and ping-pong, were identified with better than 50% accuracy even on day 1 by naive listeners, who at that point had no experience with the original sounds.

There was a strong effect of experience with the sounds. Experienced listeners, who were trained to criterion on the original unprocessed sounds, identified the single-channel EMN significantly better than the naive listeners who had only heard the original sounds once, on day 2, $t(12) = 6.74$, $p < 0.000\,02$. The sounds with a strong temporal patterning (scissors, axe, footsteps) tended to show the greatest improvement in identifiability due to learning of the sounds.

Comparing the results from the single-channel and six-channel EMN conditions, there was significant improvement as spectral information was added, $t(12) = 12.61$, $p < 0.000\,001$. The identification of harmonic sounds, such as bubble, bird, and dog, showed the greatest improvement between the two conditions. There were some sounds that were not affected by experience or by the amount of spectral in-

TABLE IV. Most and least identifiable sounds for all groups of listeners, along with their $p(c)$ in each condition. The italicized sounds were recognized either nearly perfectly or not at all across the three groups. The boldfaced sound was not identified at all in the Single Channel EMN conditions, and nearly perfectly in the Six-Channel condition.

		Most identifiable sounds			
Single-channel EMN experienced listeners		Single-channel EMN naive listeners		Six-channel EMN naive listeners	
FOOTSTEPS	1.00	HELICOPTER	0.93	BABY CRY	0.98
GALLOP	1.00	RAIN	0.69	**BIRD**	0.98
HELICOPTER	1.00	CLOCK	0.64	CLOCK	0.98
MATCH	1.00	GALLOP	0.63	*PING PONG*	0.98
PING PONG	1.00	*PING PONG*	0.63	GALLOP	0.94
		Least identifiable			
Single-channel EMN experienced listeners		Single-channel EMN naive listeners		Six-channel EMN naive listeners	
BIRD	0.00	**BIRD**	0.00	FLUTE	0.16
FLUTE	0.00	CAR ACCEL.	0.00	CARS HONK	0.18
CRASH	0.00	CRASH	0.00	*ELECTRIC SAW*	0.18
ELECTRIC SAW	0.00	*ELECTRIC SAW*	0.00	PHONE	0.18
GUITAR	0.00	GUITAR	0.00	BUZZER	0.20

formation: helicopter and gallop were among the most easily recognized sounds in each condition (helicopter was identified correctly at least 90% of the time), whereas electric saw and flute were never identified more than 18% of the time by any of the groups. A listing of the five most identifiable and five least identifiable sounds for each group is in Table IV.

Overall, the EMN identification studies showed that, as with speech, in the absence of frequency information temporal information is sufficient to identify many environmental sounds (35 out of 70) with at least 50% accuracy (chance being 1.4% correct). The sounds that tend to be best identified under these conditions are those with more salient temporal patterning. There was also a strong effect of experience with the sounds, presumably because listeners with the more extensive training from experiment 2 became more attuned to the temporal features important for identification.

VI. ACOUSTIC FACTORS IN EMN IDENTIFICATION

A. Factors considered

In an attempt to quantify temporal structure, several measurements of the original waveforms (preprocessing) were made. These variables reflected different spectral-temporal aspects of the sounds including statistics of the envelope, autocorrelation statistics, and moments of the long-term spectrum. The measures and a brief description are below.

1. Envelope measures: Long-term rms/pause-corrected rms, number of peaks, number of bursts, burst duration/total duration

The first measure roughly corresponds to the amount of silence in a waveform. Peaks are quick transients, bursts are more sustained rises in amplitude, consisting of a 4-dB gain sustained for at least 20 ms [based on an algorithm developed by Ballas (1993)]. Burst duration/total duration yields a measure of the ''roughness'' of the envelope.

2. Autocorrelation statistics: Number of peaks, maximum, mean, s.d.

The autocorrelation matrix reveals periodicities in the waveform, and the statistics measure different features of these periodicities, such as the intensity and consistency of the periodicities.

3. Correlogram-based pitch measures (from Slaney, 1995): Mean pitch, median pitch, s.d. pitch, max pitch, mean pitch salience, max pitch salience

The correlogram measures the pitch and pitch salience by autocorrelating in sliding 16 ms time windows, and so is a combined spectral and temporal variable.

4. Moments of the spectrum: Mean (centroid), s.d., skew, kurtosis

These were included to see if some spectral characteristics were preserved when the spectral information was drastically reduced.

5. Spectral shift in time measures: Centroid mean, centroid s.d., mean centroid velocity, s.d. centroid velocity, max centroid velocity

The centroid mean and s.d. are based on consecutive 50-ms time windows throughout the waveform. The spectral centroid velocity was calculated by measuring the spectral centroid in sliding 50-ms rectangular time windows. As with the correlogram, the spectral shift in time is a spectral-

TABLE V. Single channel EMN, experienced listeners' partial *r*.

Spectrum s.d.	0.485
Burst duration/total duration	0.445
Cross-channel correlation	0.367
Maximum spectral centroid velocity	0.319
# of autocorrelation peaks	0.298
Pause-corrected rms/total rms	−0.196
Spectral centroid velocity s.d.	−0.155
Multiple regression solution, $R=0.79$, $R^2=0.63$	

temporal feature which may be represented as temporal discontinuities in an EMN, since in the real world changes in the spectrum of a sound are usually accompanied by temporal discontinuities.

6. Cross-channel correlation

This measures the consistency of the envelope across channels.

B. Modeling results

Each of these measures was correlated with the EMN identification results for each group (for the single-channel and six-channel conditions with naive listeners, only the day 2 data were used). The magnitude of the correlation may suggest the degree to which each measure captures a temporal feature that listeners use to identify sounds in the absence of spectral information, or alternatively, the perceptual ''weight'' given to that measure. Multiple regression analysis of the experienced listeners' results using forward stepwise regression retained seven variables which were largely independent: the highest correlation between any two of the variables was $r=0.39$. The partial correlations of all retained variables (ordered by decreasing magnitude) are shown in Table V. The variable with the largest *r*, spectrum s.d., suggests that sounds that have broader spectra are better recognized as EMN than sounds with narrower spectra. As mentioned, several of the rhythmic sounds, such as scissors and gallop, have long-term spectra similar to a broadband noise, and so they are not changed appreciably as EMN. Alternatively, the spectrum s.d. may reflect a spectral attribute of the original sound that is correctly inferred from the EMN by listeners familiar with the original sounds. The next three variables more directly represent temporal aspects of the waveform such as the amount of silence, the ''roughness'' of the envelope, the periodicity, and the presence of amplitude bursts. Together, the seven variables accounted for 63% of the variance in the identification thresholds.

TABLE VI. Single channel EMN, naive listeners' partial *r*.

# of autocorrelation peaks	0.360
Cross-channel correlation	0.359
Burst duration/total duration	0.340
Spectrum s.d.	0.139
Pause-corrected rms/total rms	−0.019
Multiple regression solution, $R=0.62$, $R^2=0.39$	

TABLE VII. Six-channel EMN, naive listeners' partial *r*.

# of autocorrelation peaks	0.381*
Maximum autocorrelation peak	0.319
Burst duration/total duration	0.303*
s.d. autocorrelation peak	−0.293
Cross-channel correlation	−0.230*
Spectrum mean	−0.230
Mean salience	−0.171
Mean spectral centroid velocity	0.170
Mean autocorrelation peak	0.170
Multiple regression solution, $R=0.70$, $R^2=0.5$	

Multiple regressions on the naive listeners' single-channel EMN results accounted for less variance (39%), although there was a problem of restricted range since the naive listeners' performance was overall not very good. The solution yielded five independent variables, all of which had been included in the solution for experienced listeners (see Table VI).

The multiple regression solutions for the six-channel EMN data with naive listeners retained nine independent variables and accounted for half of the variance. Table VII shows the partial correlations for the variables with the six-channel EMN. The starred variables in Table VII were the same as for the experienced listeners single-channel EMN.

Three variables which occurred in all three solutions were the number of autocorrelation peaks, the ratio of burst duration to total duration, and cross-channel correlation. These are all temporal features, reflecting periodicity, amount of silence, and coherence of envelope across channels. There are two notable differences between the solutions for the single- and six-channel EMN for the naive listeners. All the statistics of the autocorrelation peak (number, maximum, mean, and s.d.) were significant predictors of the identification of six-channel EMN, but not single-channel EMN. In addition, the spectrum mean (also called the centroid) was a significant predictor only in the six-channel condition, reflecting the presence of more spectral information in six-channel EMN.

In general, the amount of variance accounted for and the relatively few outliers (points outside the 95%-confidence limits of the regression line) in the various multiple regression solutions suggest that in each case these variables likely represent acoustic features to which listeners pay some attention. The different variables retained in each solution point to the different features listeners were attending to in each condition. Most of the variables used are fairly low order, so it is possible there are higher-order variables incorporating the lower-order ones that would do a better job of capturing the temporal structure of these sounds.

VII. DISCUSSION AND CONCLUSIONS

These studies illustrate that some methods borrowed from speech research can contribute to our understanding of the recognition of environmental sounds. Although determining importance functions and something akin to an Articula-

tion Index for all environmental sounds is probably not feasible, given the diversity of environmental sounds, the findings do suggest some frequency regions that are, on average, more informative than others for identification. The most important frequencies are in the 1200–2400-Hz region, comparable to those found for speech. Like speech, a wide variety of environmental sounds can be either severely high- or low-pass filtered and still be identifiable. Even at the most extreme low- and high-pass filter settings, 300 and 8000 Hz, the percent of correct identification was never less than 50%. For speech, by comparison, the important frequency bands for calculating the AI span a more restricted range, from 300 to 6400 Hz.

The crossover point for environmental sounds, 1300 Hz (see Fig. 1), is approximately the same as that for continuous discourse. As mentioned earlier, several studies have found that the crossover frequency for speech materials is thought to decrease as the redundancy of the speech materials increases (Studebaker *et al.*, 1987; Bell *et al.*, 1992). This may be because the redundancy increases the intelligibility of the high-frequency end of the speech signal, by reducing the effective size of the possible catalog of speech sounds which may be present. The high-frequency region of the speech spectrum has less energy than the low-frequency end, and typically would yield lower $p(c)$ under low redundancy listening.

The crossover point might indicate that environmental sounds, too, have a high redundancy. However, for speech materials redundancy is generally defined as linguistic context, in which the possibilities for a given speech sound (phoneme, morpheme, word) are highly constrained by the preceding or subsequent speech sounds. It is not clear what units, if any, within a sound might act as phonemes or words with sequential dependencies that a listener can detect. Although meaningful sequences of environmental sounds surely exist, Ballas and Mullins (1991) have shown that the ''grammar'' for such sequences is much less constraining than it is for speech, especially in experiments such as those described here. This is also likely to be the case in the present experiments, in which single environmental sounds selected at random are presented outside of any relevant context. It is certainly possible that the experimental setting could lead to underestimation of the identifiability of sounds that would be much more recognizable in an appropriate setting.

A concern with the closed-set format (even though it was 70 AFC) is that it could lead to overestimation of the identifiability of some sounds, due to response biases for certain sounds. Although there may have been some response biases, they were greatly reduced by the training on the unprocessed forms of the 70 sounds. One consequence of continuing that training until the listeners could respond accurately with short latencies was that they certainly came to have far more homogeneous expectations for all the sounds than they did before the training. In fact, an analysis of the confusion matrices for each of the experiments showed no large or consistent response biases for any particular sounds.

The greater recognizability of high-pass filtered environmental sounds as compared to speech may be due to the presence of relatively more high-frequency information in the environmental sounds. Figure 6 plots the summed spectra of the environmental sounds used in these studies versus the summed long-term spectra of multiple talkers, equated for overall level. The slope for the environmental sounds is lower than that for speech, suggesting that there is relatively more high-frequency energy, at least for the set of sounds used in this study. Clearly, a wide variety of spectra is possible with environmental sounds, because of the greater variety of objects and events that produce these sounds. Almost all speech is created by the movement of air through cavities of various sizes. With very rare exceptions, impacts of solid bodies are not involved. However, of the 70 environmental sounds used in these studies, 25 of them were created at least in part by the impact of two solid bodies. Since brief impacts, by definition, create broadband transients (the brevity being proportional to the rigidity of the bodies involved), it would be expected that environmental sounds would have a flatter spectrum (thus more high-frequency energy) than speech.

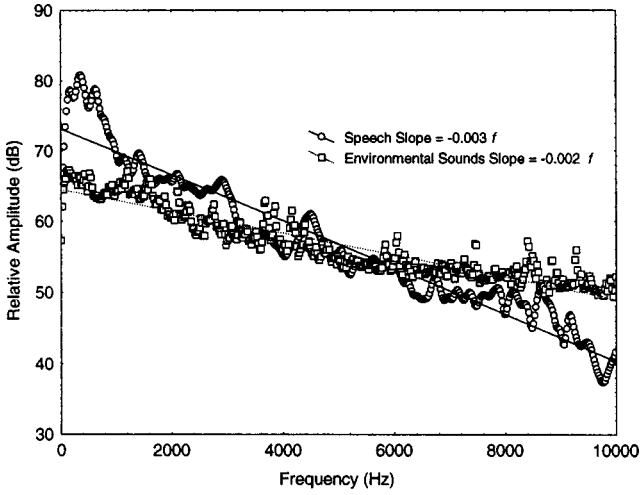

FIG. 6. Long-term spectra of 70 summed environmental sounds and 6 summed talkers, equated for overall level.

The ability to recognize many environmental sounds is robust despite removal of fine-grained spectral information. When listeners' decisions were based on temporal information and limited spectral information, half of the environmental sounds in this sample set were still recognized at better than 50% correct by experienced listeners. It may be that somewhat more spectral information is necessary for near-perfect identification of a wide range of environmental sounds than for near-perfect identification of speech; Shannon *et al.* (1995) showed that speech was recognized nearly perfectly with four channels, whereas identification of environmental sounds was approximately 66% with six channels. A listener who was extremely familiar with the sounds (the first author) had 90% or better recognition on only two-thirds of the six-channel EMN, and some EMN, like phone, electric saw, and harp, were almost unidentifiable. Like speech, environmental sounds have a multiplicity of acoustic cues available to listeners, due to their complex spectral-temporal composition. For both classes of sounds this redundancy enables identification with a degraded signal.

The speech studies which motivated this paper, such as vocoder studies and the development of the AI, have greatly assisted the development of voice communication devices. Recently there has been quite a bit of work involving computer use of natural sounds, such as ''auralization,'' auditory warning devices, and work with virtual environments. The results reported here may be useful to investigators and applications developers in these areas.

As these filtered-sound and EMN studies have shown, the differences between individual sounds make it difficult to draw generalizations about all environmental sounds. The spectral-temporal variation in environmental sounds is immense, from steady-state inharmonic sounds (buzzers) to rapidly varying harmonic sounds (birds singing). Even within types of sounds there can be a great deal of variation, depending on the particular token used. So, they may in fact not all be listened to in the same way. Lewicki (2002) suggested a separation between ''animal vocalizations'' and ''other environmental sounds'' in terms of coding by the auditory system, and Gaver's (1993a) taxonomy may relate to listening strategies, as well as to source distinctions.

A more productive approach to understanding the perception of environmental sounds may be to consider subclasses of those sounds. Some possible bases for such classification are

Acoustic features, such as the harmonic/inharmonic continuum; the frequency region which allows the best identifiability; or, perhaps the salience of temporal structure.

The sources and events which produced the sound, as proposed by Gaver (1993a). Thus acoustic commonalities might be specified that differentiate between ''impact,'' ''water-based,'' ''air-based,'' and ''simple,'' ''hybrid,'' and ''complex'' environmental sounds.

Higher-order semantic features, such as causal ambiguity, ecological frequency, or importance to the listener. Examples: ''alerting sounds,'' ''rewarding sounds,'' ''ignorable sounds.''

Future research with environmental sounds will almost certainly reveal a combination of bottom-up and top-down processing, as has been observed with many other categories of familiar stimuli. As in the case of speech, the listeners' knowledge of likely sequences of sounds will greatly aid both detection and recognition. While there may be no formal grammar constraining the sequences of such sounds, nature clearly imposes a great many limitations on the spectral-temporal structure of environmental sounds and the probabilities of various sequences of environmental sounds. These constraints operate on many different levels, from the moment-to-moment details of a single event (such as a door closing) to constraints on the types of acoustic events that are likely to occur in a given context. The extent to which listeners are sensitive to these different constraints remains to be determined.

ACKNOWLEDGMENTS

This research was supported by Grant No. RO1 DC00250 from National Institute on Deafness and other Communicative Disorders and by Grant No. MH12436-01

TABLE VIII. RMS when omitting pauses of different lengths, shown below for 16 of the sounds used in these studies.

	Pause length						
Sound	15 ms	25 ms	35 ms	50 ms	65 ms	100 ms	Full sound
Door opening	2176.21	2158.5	2129.79	2090.01	2090.01	2030.68	1637.1
Baby	1490.27	1483.97	1483.97	1483.97	1483.97	1483.97	1446.77
Horse gallop	2769.68	2769.68	2769.68	2769.68	2769.68	2769.68	2705.82
Drums	4448.92	4448.92	4448.92	4448.92	4448.92	4448.92	4368.8
Electric saw	2354.36	2354.36	2354.36	2354.36	2354.36	2354.36	2318.66
Clock	2883.74	2883.74	2818.6	2818.6	2818.6	2818.6	1344.05
Helicopter	3153.31	3153.31	3153.31	3153.31	3153.31	3153.31	3092.27
Cough	2223.79	2223.79	2223.79	2223.79	2223.79	2223.79	2115.63
Cow	1513.16	1513.16	1513.16	1513.16	1513.16	1513.16	1453.13
Cymbal	2698.41	2698.41	2698.41	2698.41	2698.41	2698.41	2617.35
Bird	2508.29	2508.29	2508.29	2508.29	2508.29	2508.29	2496.75
Bubbles	2600.22	2600.22	2600.22	2600.22	2600.22	2600.22	2543.52
Dog	2412.54	2340.24	2340.24	2286.93	2286.93	2286.93	2287.63
Car starting	1656.27	1656.27	1656.27	1656.27	1656.27	1656.27	1638.92
Rooster	4161.07	4161.07	4161.07	4161.07	4161.07	4161.07	4057.9
Water pouring	765.64	765.64	765.64	765.64	765.64	765.64	797.68
Mean rms	2643.66	2637.64	2633.88	2630.16	2628.85	2621.48	2481.25

APPENDIX B: PROPORTION CORRECT FOR ALL SOUNDS IN EXPERIMENT 1 BY FILTER TYPE

	High-pass filter cutoff (Hz)						Low-pass filter cutoff (Hz)				
Sound	300	600	1200	2400	4800	8000	300	600	1200	2400	4800
AIRPLANE	0.50	0.76	0.71	0.73	0.65	0.78	0.87	0.95	0.91	0.94	1.00
AXE	1.00	0.86	0.93	0.73	0.41	0.56	0.47	0.76	0.77	0.73	0.80
B-BALL	0.83	0.73	0.71	0.73	0.58	0.78	1.00	0.89	0.89	1.00	0.93
BABY	1.00	1.00	1.00	1.00	1.00	1.00	0.95	1.00	1.00	1.00	1.00
BEER	1.00	1.00	1.00	1.00	0.96	1.00	0.12	0.87	1.00	1.00	1.00
BELLS	1.00	1.00	1.00	1.00	1.00	1.00	0.86	1.00	1.00	1.00	1.00
BILLIARDS	1.00	0.96	0.92	1.00	0.73	0.11	0.53	0.87	1.00	1.00	1.00
BIRD	1.00	1.00	1.00	1.00	1.00	1.00	0.00	0.00	0.73	1.00	1.00
BOWLING	1.00	0.82	0.77	0.09	0.18	0.44	0.47	0.81	0.94	0.94	1.00
BUBBLES	0.94	0.95	0.67	0.48	0.38	0.22	1.00	1.00	1.00	0.94	1.00
BUZZER	0.75	1.00	1.00	1.00	0.94	1.00	0.31	0.73	1.00	0.90	1.00
CAMERA	1.00	1.00	1.00	0.94	1.00	0.86	0.00	0.71	0.93	1.00	1.00
CAR START	1.00	0.95	1.00	0.90	0.95	1.00	0.82	0.75	1.00	1.00	0.91
CAT	1.00	0.91	1.00	1.00	1.00	0.78	0.00	0.78	1.00	1.00	1.00
CHIMP	1.00	1.00	1.00	1.00	1.00	1.00	0.00	1.00	1.00	1.00	0.95
CLAPS	1.00	1.00	0.67	0.60	0.42	0.29	0.13	0.35	0.92	1.00	1.00
CLOCK	1.00	1.00	1.00	1.00	1.00	1.00	0.69	0.76	0.93	1.00	1.00
COPTER	1.00	1.00	0.91	0.93	0.74	0.89	0.80	0.95	0.85	1.00	1.00
COUGH	1.00	1.00	0.83	0.95	0.85	1.00	0.80	1.00	1.00	1.00	1.00
COW	1.00	1.00	1.00	1.00	0.82	0.29	1.00	1.00	1.00	1.00	1.00
CRASH	1.00	0.94	0.73	0.81	0.80	0.57	0.47	0.71	0.87	1.00	0.91
CYMBAL	1.00	1.00	1.00	1.00	1.00	1.00	0.94	0.88	0.95	0.86	1.00
DOG	1.00	1.00	1.00	0.80	0.65	0.67	0.36	0.80	1.00	1.00	1.00
DOOR	1.00	0.73	0.60	0.71	0.59	1.00	0.40	0.92	0.89	1.00	1.00
DRUMS	0.88	0.92	0.93	1.00	1.00	0.89	1.00	1.00	0.95	0.96	1.00
FLUTE	1.00	1.00	1.00	1.00	1.00	0.71	1.00	1.00	1.00	1.00	1.00
FOOTSTEP	1.00	1.00	1.00	1.00	0.82	0.86	1.00	1.00	1.00	1.00	1.00
GALLOP	1.00	1.00	1.00	1.00	1.00	1.00	0.94	1.00	1.00	1.00	1.00
GARGLE	1.00	1.00	1.00	0.88	0.43	0.44	0.82	1.00	0.95	1.00	0.93
GLASS	1.00	1.00	1.00	1.00	1.00	1.00	0.00	0.00	0.00	0.71	1.00
GUITAR	1.00	1.00	1.00	0.95	1.00	0.29	1.00	1.00	1.00	1.00	1.00
GUN	1.00	1.00	1.00	0.77	0.47	0.33	0.67	0.88	1.00	1.00	1.00
HAMMER	1.00	0.93	0.79	0.64	0.69	0.67	0.62	0.87	1.00	0.95	1.00
HARP	1.00	1.00	1.00	1.00	1.00	0.57	1.00	1.00	1.00	1.00	1.00
ICE DROP	1.00	1.00	1.00	1.00	1.00	0.56	0.13	0.85	1.00	1.00	1.00
KEYBOARD	1.00	1.00	0.74	0.64	0.54	0.29	0.07	0.82	0.80	0.95	0.83
LAUGH	1.00	1.00	1.00	1.00	1.00	1.00	1.00	1.00	1.00	1.00	1.00
MATCH	1.00	1.00	1.00	0.94	1.00	0.89	0.40	0.65	0.73	0.94	1.00
NEIGH	1.00	1.00	1.00	1.00	0.93	1.00	0.96	0.88	1.00	1.00	1.00
PAPER	0.92	1.00	0.90	0.93	0.81	0.71	0.05	0.05	0.47	0.80	0.94
PEELOUT	1.00	0.91	0.76	0.80	0.05	0.14	0.82	0.94	1.00	1.00	1.00
PHONE	1.00	1.00	1.00	1.00	1.00	1.00	0.00	0.67	1.00	1.00	0.95
PINGPONG	1.00	1.00	1.00	1.00	1.00	1.00	1.00	1.00	0.94	0.80	1.00
POUR	1.00	1.00	1.00	1.00	0.95	1.00	0.80	0.87	0.93	1.00	1.00
PRINTER	1.00	0.95	1.00	1.00	1.00	0.89	0.93	0.91	1.00	1.00	1.00
PROJECTOR	0.94	1.00	0.93	1.00	1.00	1.00	0.64	0.77	1.00	1.00	1.00
RAIN	1.00	1.00	1.00	1.00	0.95	0.86	0.09	0.18	0.69	0.91	1.00
REGISTER	1.00	1.00	1.00	1.00	1.00	1.00	0.82	0.86	1.00	1.00	1.00
ROCKING	1.00	1.00	1.00	1.00	1.00	1.00	0.64	0.68	1.00	1.00	1.00
ROOSTER	1.00	1.00	1.00	1.00	0.96	1.00	0.67	0.95	1.00	1.00	1.00
SAW	0.92	1.00	0.93	1.00	1.00	0.57	0.00	0.87	0.93	0.94	0.80
SCISSOR	1.00	1.00	1.00	1.00	1.00	0.86	0.47	0.73	0.92	0.93	1.00
SCREEN	1.00	0.94	1.00	1.00	0.88	1.00	0.08	0.79	1.00	0.96	0.93
SHEEP	0.92	1.00	0.94	0.80	0.64	0.57	0.05	0.73	0.76	0.89	1.00
SHOVEL	1.00	0.94	0.93	0.93	0.79	1.00	0.88	0.91	1.00	1.00	1.00
SIREN	1.00	1.00	1.00	1.00	0.94	1.00	0.95	1.00	1.00	1.00	1.00
SNEEZE	1.00	1.00	1.00	0.80	0.56	0.67	0.84	0.93	1.00	0.96	1.00
SPLASH	1.00	1.00	0.68	0.75	0.41	0.43	0.15	0.53	0.76	1.00	1.00
STAPLER	1.00	1.00	0.93	1.00	0.94	1.00	0.88	0.82	0.92	1.00	1.00
TENNIS	1.00	1.00	1.00	0.95	0.79	0.86	0.24	0.74	1.00	1.00	1.00
THUNDER	0.50	0.35	0.18	0.23	0.29	0.00	0.93	1.00	0.73	0.91	1.00
TOILET	1.00	1.00	1.00	0.88	0.76	0.43	0.86	1.00	1.00	1.00	1.00
TRAFFIC	1.00	1.00	1.00	1.00	0.93	1.00	0.94	1.00	1.00	1.00	1.00
TRAIN	1.00	1.00	0.86	1.00	0.64	0.89	0.00	0.64	0.82	1.00	1.00
TREE FALL	1.00	1.00	1.00	1.00	0.67	0.44	0.26	0.73	0.95	1.00	1.00
TYPEWRITER	1.00	1.00	0.87	0.89	0.89	1.00	0.35	0.69	0.91	0.95	0.95
WAVES	0.75	0.73	0.55	0.18	0.27	0.14	0.20	0.53	0.67	0.82	0.74
WHISTLE	1.00	1.00	1.00	1.00	1.00	1.00	0.00	0.00	1.00	1.00	1.00
WIPERS	1.00	1.00	0.93	1.00	0.89	0.78	1.00	1.00	1.00	1.00	1.00
ZIPPER	1.00	1.00	1.00	1.00	1.00	1.00	0.53	0.53	1.00	1.00	1.00
Mean	0.97	0.96	0.92	0.89	0.81	0.76	0.57	0.79	0.92	0.97	0.98
s.d.	0.10	0.10	0.15	0.20	0.24	0.29	0.37	0.25	0.15	0.06	0.05

APPENDIX C: PROPORTION CORRECT FOR ALL SOUNDS IN EXPERIMENT 2 BY FILTER TYPE

	Bandpass cutoffs (Hz)					
SOUND	150–300	300–600	600–1200	1200–2400	2400–4800	4800–9600
AIRPLANE	1.00	0.89	0.85	0.73	0.60	0.72
AXE	0.42	0.63	0.60	0.48	0.55	0.63
BABY	0.33	1.00	1.00	1.00	1.00	1.00
B-BALL	0.72	0.75	0.81	0.63	0.56	0.53
BEER	0.15	0.33	0.75	0.44	0.60	0.63
BELLS	0.06	0.95	1.00	1.00	1.00	0.93
BILLIARDS	0.00	0.10	0.47	0.85	0.98	0.55
BIRD	0.00	0.03	0.14	0.97	1.00	0.95
BOWLING	0.08	0.50	0.78	0.23	0.10	0.00
BUBBLES	0.93	1.00	0.98	0.93	0.53	0.18
BUZZER	0.03	0.19	0.98	0.90	0.88	0.78
CAMERA	0.00	0.48	1.00	1.00	1.00	0.93
CAR START	0.10	0.72	0.78	0.98	0.98	0.98
CAT	0.03	0.70	0.83	1.00	1.00	1.00
CHIMP	0.00	0.38	1.00	1.00	0.98	1.00
CLAPS	0.45	0.50	0.58	0.31	0.58	0.58
CLOCK	0.45	0.93	0.98	1.00	1.00	1.00
COPTER	0.43	0.83	0.95	0.90	0.90	0.80
COUGH	0.10	0.78	0.93	0.98	0.83	0.58
COW	0.48	1.00	0.98	0.95	0.93	0.88
CRASH	0.08	0.05	0.03	0.05	0.20	0.25
CYMBAL	0.23	0.68	0.80	0.98	0.92	1.00
DOG	0.00	0.98	0.98	0.98	0.75	0.43
DOOR	0.50	0.23	0.33	0.40	0.38	0.35
DRUMS	0.91	0.83	0.85	0.93	1.00	0.90
FLUTE	0.58	0.97	1.00	1.00	1.00	0.83
FOOTSTEP	0.63	0.78	0.61	0.93	0.89	0.80
GALLOP	0.95	0.83	1.00	0.95	0.97	1.00
GARGLE	0.28	0.97	0.95	0.95	0.95	0.45
GLASS	0.00	0.00	0.00	0.75	0.98	0.98
GUITAR	0.83	0.97	0.97	1.00	1.00	0.65
GUN	0.78	0.85	0.75	0.78	0.60	0.53
HAMMER	0.70	0.88	0.88	0.90	0.75	0.55
HARP	1.00	1.00	0.98	0.98	1.00	0.98
ICE DROP	0.00	0.28	0.90	0.98	1.00	0.98
KEYBOARD	0.05	0.65	0.68	0.58	0.63	0.80
LAUGH	0.98	1.00	1.00	1.00	1.00	1.00
MATCH	0.35	0.42	0.70	0.83	0.83	0.88
NEIGH	0.00	0.25	1.00	1.00	0.98	0.93
PAPER	0.03	0.05	0.18	0.88	0.80	0.42
PEELOUT	0.80	0.94	0.69	0.55	0.69	0.00
PHONE	0.00	0.03	1.00	1.00	1.00	1.00
PINGPONG	0.85	1.00	1.00	1.00	1.00	1.00
POUR	0.00	0.60	0.68	1.00	0.83	0.65
PRINTER	0.03	1.00	0.98	0.89	1.00	0.83
PROJECTOR	0.33	0.14	0.53	1.00	0.97	0.93
RAIN	0.00	0.25	0.28	0.53	0.88	0.93
REGISTER	0.00	0.18	0.90	0.90	1.00	1.00
ROCKING	0.33	0.65	0.93	0.95	0.98	0.98
ROOSTER	0.03	0.83	1.00	1.00	0.98	0.93
SAW	0.03	0.65	0.80	0.93	0.92	0.97
SCISSOR	0.06	0.45	0.93	1.00	0.95	1.00
SCREEN	0.15	0.69	1.00	0.98	0.98	0.89
SHEEP	0.20	0.38	0.78	0.67	0.90	0.83
SHOVEL	0.35	0.41	0.58	0.70	0.73	0.83
SIREN	0.00	1.00	1.00	1.00	1.00	1.00
SNEEZE	0.65	0.67	0.98	0.94	0.85	0.58
SPLASH	0.08	0.08	0.28	0.30	0.58	0.43
STAPLER	0.58	0.64	0.60	0.70	0.63	0.50
TENNIS	0.13	0.08	0.75	0.68	0.70	0.65
THUNDER	0.73	0.43	0.08	0.03	0.00	0.00
TOILET	0.28	0.48	0.66	0.45	0.18	0.15
TRAFFIC	0.43	0.92	1.00	1.00	1.00	1.00
TRAIN	0.00	0.15	0.85	0.97	0.93	0.83
TREE FALL	0.00	0.03	0.55	0.63	0.65	0.47
TYPEWRITER	0.10	0.08	0.58	0.81	0.93	0.88
WAVES	0.23	0.48	0.55	0.58	0.22	0.22
WHISTLE	0.00	0.00	0.93	1.00	0.98	0.97
WIPERS	0.30	0.95	0.78	0.65	0.58	0.63
ZIPPER	0.13	0.00	0.05	0.48	0.73	0.73
Mean	0.31	0.57	0.75	0.81	0.81	0.73
s.d.	0.32	0.35	0.28	0.25	0.25	0.28

from the National Institute of Mental Health. The bandpass filter and EMN conditions were conducted as part of the doctoral dissertation at Indiana University of the first author. Numerous conversations with Diane Kewley-Port and Donald Robinson contributed materially to this research, and Eric Healey supplied the MATLAB code for the bandpass filters. Pierre Divenyi reviewed the finished product and made several helpful suggestions and comments.

APPENDIX A: EQUATING THE RMS OF ENVIRONMENTAL SOUNDS

Obtaining SPL measurements for spectrally complex, time-varying sounds such as the sounds used in this study is problematic. Various measures have been used in the speech literature for measuring speech level, such as ''fast,'' ''slow'' and ''impulse'' detector–indicator characteristics, as well as long-term rms. Ludvigsen (1992), comparing these various measures of speech level, concluded that long-term rms integration was the preferred method, except when the signal consisted of a series of words with pauses between them, in which case the long-term rms with a correction for the known pauses, what he termed ''pause-corrected'' rms, more accurately represented the energy in the signal.

For the identification studies reported in this paper, the rms was computed with gaps of silence longer than 50 ms omitted from the calculation. The 50-ms value was arrived at partially through intuition and partially through comparing the rms when omitting pauses of different lengths, shown in Table VIII for 16 of the sounds used.

[1]The use of headphones clearly limits the ecological validity of these studies to some degree. However, it was decided that headphones would probably yield stimuli with spectral characteristics closer to those of the recorded sounds, than would loudspeakers in the multisubject facility available for this research.

Attias, H., and Schreiner, C. E. (**1997**). ''Temporal low-order statistics of natural sounds,'' in *Advances in Neural Info Processing Systems*, edited by M. Mozer (MIT Press, Cambridge, MA), Vol. 9, pp. 27–33.

Ballas, J. A. (**1993**). ''Common factors in the identification of an assortment of brief everyday sounds,'' J. Exp. Psychol. Hum. Percept. Perform. **19**(2), 250–267.

Ballas, J. A., and Howard, J. H. (**1987**). ''Interpreting the language of environmental sounds,'' Environ. Behav. **19**(1), 91–114.

Ballas, J. A., and Mullins, T. (**1991**). ''Effects of context on the identification of everyday sounds,'' Hum. Perform. **4**(3), 199–219.

Bell, T. S., Dirks, D. D., and Trine, T. D. (**1992**). ''Frequency-importance functions for words in high- and low-context sentences,'' J. Speech Hear. Res. **35**, 950–959.

Cabe, P. A., and Pittenger, J. B. (**2000**). ''Human sensitivity to acoustic information from vessel filling,'' J. Exp. Psychol. Hum. Percept. Perform. **26**(1), 313–324.

Carello, C., Anderson, K. L., and Kunkler-Peck, A. J. (**1998**). ''Perception of object length by sound,'' Psychol. Sci. **9**(3), 211–214.

Carrat, R. (**1984**). ''Analysis and synthesis of speech regarding cochlear implant,'' Acta Oto-Laryngol., Suppl. **411**, 85–94.

Compton, A. J. (**1963**). ''Effects of filtering and vocal duration on the identification of speakers, aurally,'' J. Acoust. Soc. Am. **35**(11), 1748–1752.

Dudley, H. (**1940**). ''Remaking speech,'' J. Acoust. Soc. Am. **11**, 169–177.

Dudley, H. (**1958**). ''Phonetic pattern recognition vocoder for narrow-band speech transmission,'' J. Acoust. Soc. Am. **30**, 733–739.

Eremenko, Y. I., and Ermakov, V. P. (**1985**). ''Theoretical aspects of the construction of reading devices for the blind using vocoder techniques,'' Defektologiya **1**, 81–86.

Freed, D. (**1990**). ''Auditory correlates of perceived mallet hardness for a set of recorded percussive sound events,'' J. Acoust. Soc. Am. **87**(1), 311–322.

French, N. R., and Steinberg, J. C. (**1947**). ''Factors governing the intelligibility of speech sounds,'' J. Acoust. Soc. Am. **19**, 90–119.

Gaver, W. W. (**1993a**). ''What in the world do we hear?: An ecological approach to auditory event perception,'' Ecological Psychol. **5**, 1–29.

Gaver, W. W. (**1993b**). ''How do we hear in the world?: An ecological approach to auditory event perception,'' Ecological Psychol. **5**, 285–313.

Halpern, D., Blake, R., and Hillenbrand, B. (**1986**). ''Psychoacoustics of a chilling sound,'' Percept. Psychophys. **39**(2), 77–80.

Kunkler-Peck, A. J., and Turvey, M. T. (**2000**). ''Hearing shape,'' J. Exp. Psychol. Hum. Percept. Perform. **26**(1), 279–294.

Lakatos, S., McAdams, S., and Caussé, R. (**1997**). ''The representation of auditory source characteristics: Simple geometric form,'' Percept. Psychophys. **59**(8), 1180–1190.

Lass, N. J., Eastman, S. K., Parrish, W. C., Scherbick, K. A., and Ralph, D. (**1982**). ''Listeners' identification of environmental sounds,'' Percept. Mot. Skills **55**, 75–78.

Lewicki, M. S. (**2002**). ''Efficient coding of natural sounds,'' Nat. Neurosci. **5**(4), 356–363.

Li, X., Logan, R., and Pastore, R. (**1991**). ''Perception of acoustic source characteristics: Walking sounds,'' J. Acoust. Soc. Am. **90**(6), 3036–3049.

Ludvigsen, C. (**1992**). ''Comparison of certain measures of speech and noise level,'' Scand. Audiol. **21**, 23–29.

Lutfi, R. A., and Oh, E. (**1997**). ''Auditory discrimination of material changes in a struck clamped bar,'' J. Acoust. Soc. Am. **102**(6), 3647–3656.

Lutfi, R. A. (**2001**). ''Auditory detection of hollowness,'' J. Acoust. Soc. Am. **110**(2), 1010–1019.

Repp, B. (**1987**). ''The sound of two hands clapping: An exploratory study,'' J. Acoust. Soc. Am. **81**, 1100–1109.

Shannon, R. V., Zeng, F. G., Wygonski, J., Kamath, V., and Ekelid, M. (**1995**). ''Speech recognition with primarily temporal cues,'' Science **270**, 303–304.

Shannon, R. V., Zeng, F. G., and Wygonski, J. (**1998**). ''Speech recognition with altered spectral distribution of envelope cues,'' J. Acoust. Soc. Am. **104**(4), 2467–2476.

Slaney, M. (**1995**). ''Auditory Toolbox: A MATLAB toolbox for auditory modeling work,'' Apple Computer Technical Report #45.

Studebaker, G. A., Pavlovic, C. V., and Sherbecoe, R. L. (**1987**). ''A frequency importance function for continuous discourse,'' J. Acoust. Soc. Am. **81**, 1130–1138.

Vanderveer, N. J. (**1979**). ''Ecological acoustics: Human perception of environmental sounds,'' Dissertation Abstracts International **40**: 4543B (University Microfilms No. 8004002).

Warren, W. H., and Verbrugge, R. R. (**1984**). ''Auditory perception of breaking and bouncing events: A case study in ecological acoustics,'' J. Exp. Psychol. Hum. Percept. Perform. **10**, 704–712.

Chaotic vibrations of a vocal fold model with a unilateral polyp

Yu Zhang[a] and Jack J. Jiang[b]
Department of Surgery, Division of Otolaryngology Head and Neck Surgery, University of Wisconsin Medical School, Madison, Wisconsin 53792-7375

(Received 2 September 2003; revised 16 December 2003; accepted 29 December 2003)

A nonlinear model was proposed to study chaotic vibrations of vocal folds with a unilateral vocal polyp. The model study found that the vocal polyp affected glottal closure and caused aperiodic vocal fold vibrations. Using nonlinear dynamic methods, aperiodic vibrations of the vocal fold model with a polyp were attributed to low-dimensional chaos. Bifurcation diagrams showed that vocal polyp size, stiffness, and damping had important effects on vocal fold vibrations. An increase in polyp size tended to induce subharmonic patterns and chaos. This study provides a theoretical basis to model aperiodic vibrations of vocal folds with a laryngeal mass. © *2004 Acoustical Society of America.* [DOI: maximum]

PACS numbers: 43.70.Aj, 43.70.Bk, 05.45.Pg [AL] Pages: 1266–1269

I. INTRODUCTION

Vocal polyps resulting from vocal misuse and overuse represent one of the most common benign laryngeal lesions.[1] Vocal polyps may disrupt glottal closure and cause an increased direct current (dc) offset of the glottal waveform.[2] Furthermore, aperiodic and subharmonic patterns are observed in voices from individuals with this lesion.[2,3] Using linear theory, it is difficult to explain why small polyps can qualitatively change the vibratory characteristics of vocal folds and cause aperiodic behaviors. Nonlinearity is inherently involved in laryngeal systems. Qualitative state changes of vocal folds are associated with bifurcations.[4] Subharmonics and chaos have been observed in human voices,[5] nonlinear models,[6–8] and excised larynx experiments.[9,10] Applying chaos theory and nonlinear dynamic methods to the study of aperiodic activities of vocal folds with a polyp is important and has the potential to increase our understanding of abnormal vocal dynamics and lead to improved diagnostic methods. Recent studies have used model simulations to investigate the vibratory characteristics of vocal folds with vocal polyps.[11,12] However, chaotic dynamics of vocal folds with a polyp has not been studied using a model simulation. In this article, we propose a nonlinear model of the vocal folds with a vocal polyp and employ nonlinear dynamic methods to study vibrations. Bifurcation diagrams are used to investigate the effects of polyp size, stiffness, and damping. The results demonstrate the deterministic chaos mechanism of aperiodic vibrations of the vocal fold model with a vocal polyp.

II. THE VIBRATORY MODEL OF VOCAL FOLDS WITH A VOCAL POLYP

We added a unilateral mass representing a vocal polyp to the two-mass model of Steinecke and Herzel.[7] To deduce the equations, we made the following assumptions:

(1) The assumptions by Steinecke and Herzel[7] about the biomechanical and aerodynamic properties of the vocal folds were used.
(2) A unilateral vocal polyp was connected with the lower mass m_{1r} of the right vocal fold by the spring k_{3r} and the damper r_{3r} [see Fig. 1(a)]. The right lower mass m_{1r} has length l, depth D, and height d_1, and the vocal polyp has mass m_{3r}, length l_3, depth D_3, and height d_3 [see Fig. 1(b)]. The polyp and vocal folds have the same density. Collisions can occur between m_{1l} and m_{1r}, m_{1l} and m_{3r}, and m_{2l} and m_{2r}. The cubic nonlinearities of the vocal polyp were considered[11] because of the strong coupling and colliding interactions between the vocal polyp and the vocal folds.

The dynamic equations of the vibratory system are described as the vocal folds,

$$m_{i\alpha}\ddot{x}_{i\alpha}+r_{i\alpha}\dot{x}_{i\alpha}+k_{i\alpha}x_{i\alpha}+\Theta(-a_i)c_{i\alpha}\frac{a_i}{2l}+k_{c\alpha}(x_{i\alpha}-x_{j\alpha})+T_{i\alpha}=F_{i\alpha}, \tag{1a}$$

and the right vocal polyp,

$$m_{3r}\ddot{x}_{3r}-T_{1r}+T_{1l}=F_3, \tag{1b}$$

where the indices i, $j=1,2$ denote the upper and lower masses, and $\alpha=l$, r denotes the left and right vocal fold. x_{1r}, x_{2r}, x_{1l}, x_{2l} are the displacements of the masses $m_{i\alpha}$ with the length d_i. x_{3r} is the displacement of the right vocal polyp m_{3r}. $r_{i\alpha}$ is the damping constant. $k_{i\alpha}$ is the stiffness constant and $k_{c\alpha}$ is the coupling stiffness between $m_{1\alpha}$ and $m_{2\alpha}$. $c_{i\alpha}$ is the spring constant during vocal fold collisions.

$$\Theta(x)=\begin{cases}\tanh(50x/x_0), & x>0\\ 0, & x\leqslant 0\end{cases},$$

gives the collision function. The right polyp m_{3r} and the right lower mass m_{1r} are coupled by the damping and nonlinear spring forces,

$$T_{1r}=r_{3r}(\dot{x}_{1r}-\dot{x}_{3r})+k_{3r}[x_{1r}-x_{3r}+\eta_{k3}(x_{1r}-x_{3r})^3]. \tag{2}$$

[a]Electronic mail: zhang@surgery.wisc.edu
[b]Author to whom correspondence should be addressed. Electronic mail: jiang@surgery.wisc.edu

 0001-4966/2004/115(3)/1266/4/$20.00

When the right polyp m_{3r} collides with the left lower mass m_{1l}, the compressed vocal polyp produces the nonlinear collision force,

$$T_{1l}=\Theta(-a_3)c_{3r}\left[\frac{a_3}{2l_3}+\eta_{h3}\left(\frac{a_3}{2l_3}\right)^3\right], \tag{3}$$

where c_{3r} is the spring constant during the collision between m_{3r} and m_{1l}. η_{k3} and η_{h3} are 100 and 500, respectively.[13] In Eq. (1), $T_{2l}=0$ and $T_{2r}=0$ show that the right vocal polyp m_{3r} has no coupling and collision actions with m_{2l} and m_{2r}.

The glottal areas of the lower-mass pair $m_{1\alpha}$ and the upper-mass pair $m_{2\alpha}$ satisfy $a_i=a_{0i}+l(x_{il}+x_{ir})=a_{il}+a_{ir}$. $a_{i\alpha}$ is the area formed from the midline to $m_{i\alpha}$. a_3 formed from m_{3r} to m_{1l} and a'_{3r} formed from the midline to m_{1r} satisfy [see the infraglottic view of the vocal folds in Fig. 1(c)]

$$a_3=a_{03}+l_3(x_{1l}+x_{3r}),$$

$$a'_{3r}=\frac{a_{01}}{2}-l_3D_3+(l-l_3)x_{1r}+l_3x_{3r}, \tag{4}$$

where $a_{03}=l_3(a_{01}/l-D_3)$. The minimal glottal area is given by

$$a_{\min}=\min(a_{1l},a_{2l})+\min(a_{1r},a_{2r},a'_{3r}). \tag{5}$$

The glottal airflow at any point below the narrowest part of the glottis is described by the Bernoulli equation, i.e., $P(a)=P_s-(\rho/2)(U/a)^2$, where P_s is the subglottal pressure and $P(a)$ denotes the pressure at the point with the glottal area a. Then the volume flow velocity U, P_1 acting on $m_{1\alpha}$, P_2 acting on $m_{2\alpha}$, and P_3 acting on m_{3r} are

$$\begin{aligned}
&U=\sqrt{\frac{2P_s}{\rho}}a_{\min}\Theta(a_{\min}),\\
&P_1=P_s\left[1-\Theta(a_{\min})\left(\frac{a_{\min}}{a_1}\right)^2\right]\Theta(a_1),\\
&P_2=0,\quad P_3=P_s\left[1-\Theta(a_{\min})\left(\frac{a_{\min}}{a'_3}\right)^2\right]\Theta(a'_3),
\end{aligned} \tag{6}$$

where $a'_3=a_{01}/2+lx_{1l}+a'_{3r}$. From Fig. 1(a), the driving forces $F_{i\alpha}$ acting on $m_{i\alpha}$ and F_3 acting on m_{3r} are deduced to be

$$\begin{aligned}
&F_{1l}=P_1l(d_1-d_3)+P_3ld_3,\quad F_{2l}=0,\\
&F_{1r}=P_1l(d_1-d_3)+P_3(l-l_3)d_3,\quad F_{2r}=0,\\
&F_3=P_3l_3d_3\Theta(a_3).
\end{aligned} \tag{7}$$

Equations (1)–(7) give the vibratory equations of the vocal folds coupled with a right vocal polyp. When $T_{i\alpha}=0$, $l_3=0$, $d_3=0$, and $D_3=0$, this vocal fold model with a vocal polyp is reducible to the two-mass model of Steinecke and Herzel.[7]

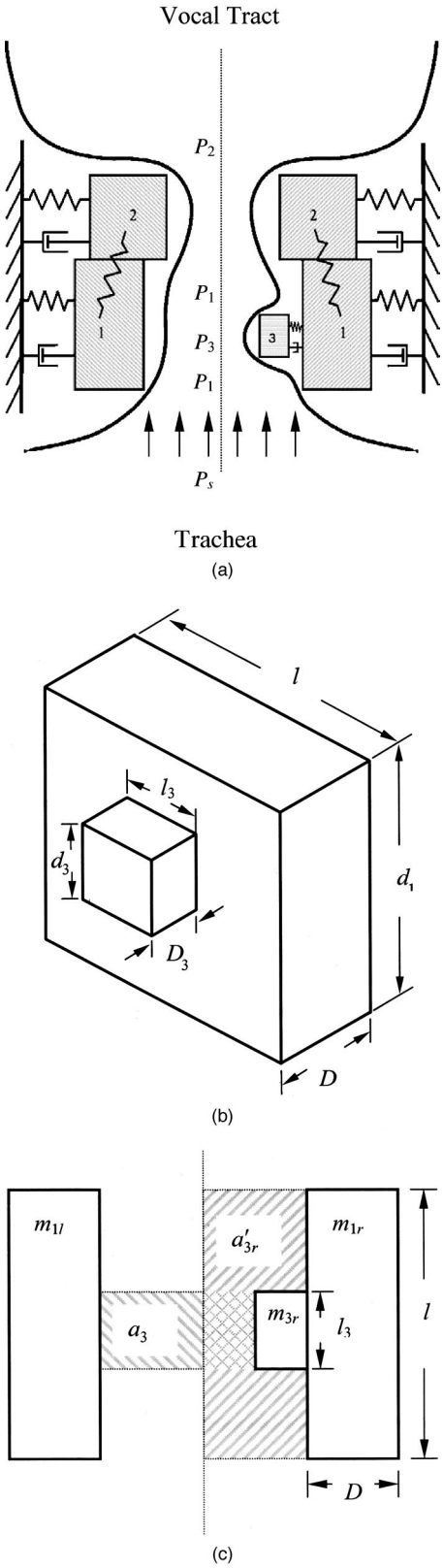

FIG. 1. (a) The schematic diagram of the vocal fold model with a right vocal polyp. (b) The geometric sizes of the right lower mass m_{1r} and the vocal polyp m_{3r}. (c) The infraglottic view of the vocal folds at the point of the vocal polyp m_{3r}.

III. NUMERICAL CALCULATIONS AND DISCUSSIONS

Figure 2 shows the volume flow velocity U of the model where the default parameter values[7,13] of the vocal folds are used: $m_{1\alpha}=0.125$, $m_{2\alpha}=0.025$, $r_{i\alpha}=0.02$, $k_{1\alpha}=0.08$, $k_{2\alpha}=0.008$, $c_{i\alpha}=3k_{i\alpha}$, $k_{c\alpha}=0.025$, $d_1=0.25$, $d_2=0.05$, $a_{01}=a_{02}=0.05$, $D=0.3$, $P_s=0.006$ ($\approx$6 cm H_2O), $l=1.4$, and $\rho=0.00113$. Based on previous studies,[11–13] we used the vo-

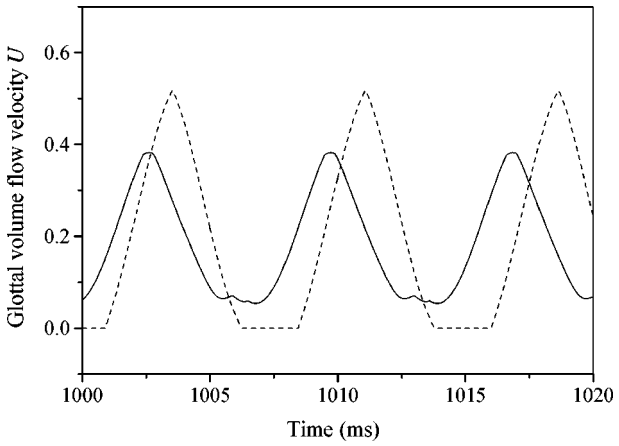

FIG. 2. The glottal volume flow velocity U of the models without a vocal polyp (dashed line) and with a vocal polyp [solid line, where $P_s=0.006$, $k_{3r}=0.014$, $l_3=l/3$, $D_3=0.1D$, and $d_3=(d_1+d_2)/3$].

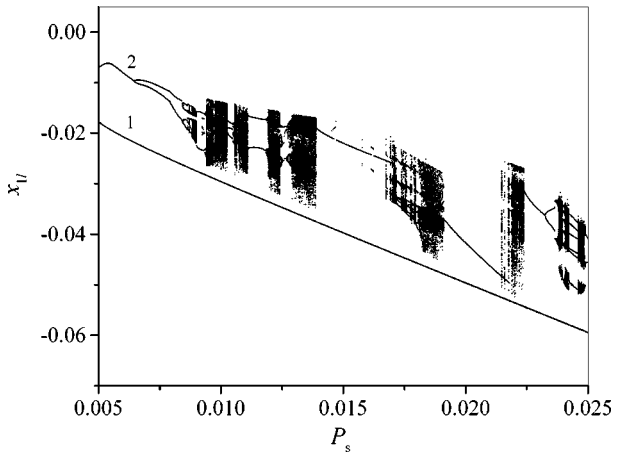

FIG. 3. The bifurcation diagram (for $v_{1l}=0$, the Poincare section of x_{1l} versus P_s) of the models (1) without a vocal polyp and (2) with a vocal polyp ($k_{3r}=0.002$ and $D_3=0.05D$).

cal polyp parameters: $m_{3r}=m_{1r}l_3D_3d_3/lDd_1$, $r_{3r}=r_{1r}\sqrt{m_{3r}k_{3r}/m_{1r}k_{1r}}$, $k_{3r}=0.014$, $c_{3r}=3k_{3r}$, $l_3=l/3$, $D_3=0.1D$, and $d_3=(d_1+d_2)/3$. All parameters are given in units of cm, g, ms, and their corresponding combinations. When there is no vocal polyp, the dashed line in Fig. 2 shows that the glottal airflow U has the valley-cut sinusoid shape. During the closing stage of the glottal cycle, the vocal fold collision cuts off the airflow and leads to zero dc flow. However, when the vocal polyp is included, the amplitude of U decreases (see the solid line in Fig. 2). During the closing stage of the glottal cycle, the vocal folds cannot close. Thus, the vocal polyp interferes with vocal closure and causes nonzero dc flow, which shows consistency with clinical study.[2]

Furthermore, the unilateral polyp may induce bifurcations and chaos. Figure 3 shows the bifurcation diagrams (the Poincare section of x_{1l} versus the subglottal pressure P_s), where for each value of P_s, the continuous signal $x_{1l}(t)$ with the length of $2s$ is projected to discrete points by using a Poincare map at $v_{1l}=0$.[8,14] For the vocal folds without a vocal polyp, periodic vibrations appear within $0.005<P_s<0.025$ (see the curve 1 in Fig. 3). However, for the vocal folds with a vocal polyp, the curve 2 in Fig. 3 displays the route from period-doubling bifurcation to chaos where $k_{3r}=0.002$ and $D_3=0.05D$. In a Poincare section, a single, a pair of, and a group of points illustrate periodic, period-doubling, and aperiodic vibrations, respectively. Period-doubling vibrations with alternate amplitudes are associated with diplophonia or subharmonic vibrations. Aperiodic vibrations in this model can be quantitatively described by calculating the Lyapunov exponents and Kaplan–Yorke dimension.[8] The Lyapunov exponents of the aperiodic vibration at $P_s=0.01$ asymptotically converge to $\lambda_1\approx0.083$, $\lambda_2\approx0$, $\lambda_3\approx-0.155$, $\lambda_4\approx-0.17$, $\lambda_5\approx-0.191$, $\lambda_6\approx-0.308$, $\lambda_7\approx-0.309$, $\lambda_8\approx-0.327$, $\lambda_9\approx-0.388$, and $\lambda_{10}\approx-0.468$, and the Kaplan–Yorke dimension is $D_L\approx2.54$. The positive Lyapunov exponent and finite Kaplan–Yorke dimension demonstrate the chaos mechanism of the aperiodic vibrations.

Polyp size, stiffness, and damping influence the vibratory characteristics of the vocal folds. The bifurcation diagram (the Poincare section of x_{1l} versus S_0) in Fig. 4(a) shows the effects of polyp size, where $P_s=0.01$ and S_0 is a dimensionless parameter of the polyp size. We uniformly changed polyp length, depth, and height by $l_3=S_0l/3$, $D_3=0.05S_0D$, and $d_3=(d_1+d_2)S_0/3$. However, we found that independently changing l_3, D_3, and d_3 produced qualitatively similar results. When $S_0\ll1$, the solution of our model with the vocal polyp approaches the two-mass model of Steinecke and Herzel.[7] A very small polyp does not qualitatively change the periodic state of the vocal folds. However, when the polyp size S_0 is sufficiently increased, vocal fold asymmetry increases and chaos appears. This suggests that an increase in polyp size would produce a progressive decline in voice quality; however, a significant reduction in polyp size, e.g., resulting from a polyp excision, might prevent voice irregularity. Clinically, microlaryngeal surgical removal of mass lesions can reduce voice roughness and dc leakage.[15] The proposed model may provide a theoretical approach to study the effects of clinical treatment of laryngeal mass lesions.

Figures 4(b) and (c) show the effects of polyp stiffness k_{3r} and damping r_{3r} where $P_s=0.01$. When k_{3r} and r_{3r} are sufficiently large, the polyp m_{3r} is firmly fastened to m_{1r} so that the relative motions between m_{3r} and m_{1r} are prevented, and the vibrations are periodic. However, when k_{3r} and r_{3r} are decreased, the polyp becomes loosely attached to m_{1r} and vibrates asynchronously with m_{1r}, and chaos may be induced. The exact relationship of polyp stiffness and damping to the biomechanical properties of polyp tissue is unclear in the proposed model, which is also the case in the relationship of vocal fold stiffness and damping to the biomechanical properties of vocal fold tissue in two-mass models.[7,8,13] Finite element models allow us to consider the biomechanical properties of vocal fold tissue.[12] However, modeling chaotic activities of vocal folds with a polyp using finite element models is a difficult task at present. The mass-spring models are important for the study of chaotic dynamics of vocal folds with a vocal polyp.

Nonlinearity is fundamental for chaotic vibration of the vocal folds. Chaos has been observed in the nonlinear models of both symmetric[6,8] and asymmetric vocal folds.[7] In the proposed nonlinear model with a polyp, the vocal polyp in-

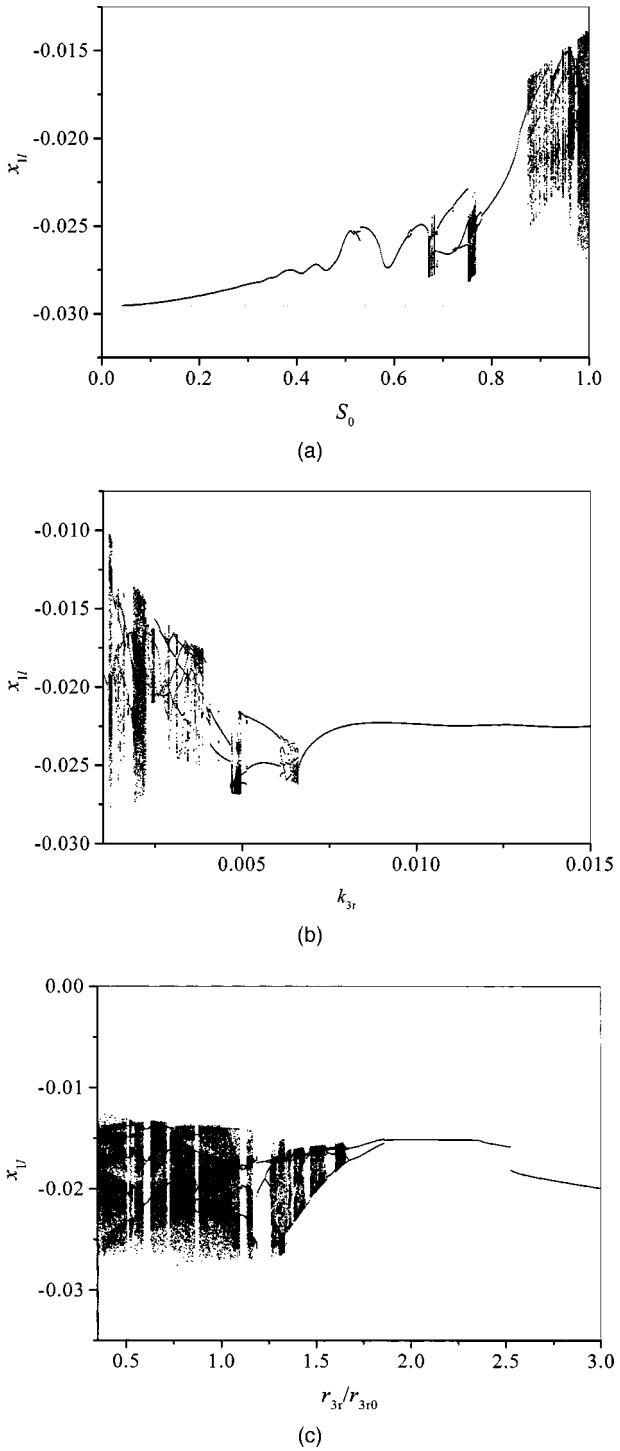

FIG. 4. The effects of the polyp size, stiffness, and damping are shown in the bifurcation diagrams, where $P_s=0.01$. (a) x_{1l} versus S_0, where the dotted line represents the result of the two-mass model, $D_3=0.05S_0D$, $l_3=S_0l/3$, and $d_3=(d_1+d_2)S_0/3$; (b) x_{1l} versus k_{3r}; (c) x_{1l} versus r_{3r}, where $r_{3r0}=r_{1r}\sqrt{m_{3r}k_{3r}/m_{1r}k_{1r}}$.

troduces extra nonlinear stiffness and collision to the vocal folds, produces disturbances of the glottal closure and glottal airflow, and leads to vocal fold asymmetry. Bifurcation and chaos can be induced by the presence of a vocal polyp. High subglottal pressure may produce chaos in symmetric vocal folds.[8–10] In the proposed model with a vocal polyp and the asymmetric model associated with laryngeal paralysis,[7] chaotic vibrations occur even under normal values of subglottal pressure, e.g., 10 cm H_2O.

IV. CONCLUSIONS

We proposed a nonlinear model to study chaotic vibrations of vocal folds with a unilateral polyp. The vocal polyp affected vocal closure, and aperiodic vibrations were produced even when subglottal pressure was within the normal pressure range. Aperiodic vibrations of the vocal fold model with a vocal polyp were attributed to low-dimensional chaos. Polyp size, stiffness, and damping have important effects on inducing chaotic vibrations. Removal of a vocal polyp may lead to periodic vibrations. Clinically, many other mass lesions, such as nodules, cysts, Reinke's edema, etc., also impart extra mass and might produce abnormal vocal fold movements. We suggest that the proposed model may be valuable for understanding abnormal vocal activities and predicting the effects of treatment on patients with these laryngeal mass lesions.

ACKNOWLEDGMENTS

We thank Clancy McGilligan for his assistance and Dennis Connaughton for his editorial comments. This study was supported by NIH Grant No. 1-RO1DC006019-01 from the National Institute of Deafness and other Communication Disorders.

[1] F. Chagnon and R. E. Stone, "Nodules and Polyps," in *Organic Voice Disorders Assessment and Treatment*, edited by W. S. Brown, B. P. Vinson, and M. A. Crary (Singular, San Diego, 2000), p. 219.
[2] M. Hirano, W. J. Gould, A. Lambiase, and Y. Kakita, "Vibratory behavior of the vocal folds in a case with a unilateral polyp," Folia Phoniatr. **33**, 275–284 (1981).
[3] K. Omori, H. Kojima, R. Kakani, D. H. Slavit, and S. M. Blaugrund, "Acoustic characteristics of rough voices: subharmonics," J. Voice **11**, 40–47 (1997).
[4] I. R. Titze, R. Baken, and H. Herzel, "Evidence of chaos in vocal fold vibration," in *Vocal Fold Physiology: New Frontier in Basic Science*, edited by I. R. Titze (Singular, San Diego, 1993), pp. 143–188.
[5] Y. Zhang and J. J. Jiang, "Nonlinear dynamic analysis of signal typing of pathological human voices," Electron. Lett. **39**, 1021–1023 (2003).
[6] D. A. Berry, H. Herzel, I. R. Titze, and K. Krischer, "Interpretation of biomechanical simulations of normal and chaotic vocal fold oscillations with empirical eigenfunctions," J. Acoust. Soc. Am. **95**, 3595–3604 (1994).
[7] I. Steinecke and H. Herzel, "Bifurcation in an asymmetric vocal-fold model," J. Acoust. Soc. Am. **97**, 1874–1884 (1995).
[8] J. J. Jiang, Y. Zhang, and J. Stern, "Modeling of chaotic vibrations in symmetric vocal folds," J. Acoust. Soc. Am. **110**, 2120–2128 (2001).
[9] D. A. Berry, H. Herzel, I. R. Titze, and B. H. Story, "Bifurcation in excised larynx experiments," J. Voice **10**, 129–138 (1996).
[10] J. J. Jiang, Y. Zhang, and C. N. Ford, "Nonlinear dynamics of phonations in excised larynx experiments," J. Acoust. Soc. Am. **114**, 2198–2205 (2003).
[11] T. Koizumi, S. Taniguchi, and F. Itakura, "An analysis-by-synthesis approach to the estimation of vocal cord polyp features," Laryngoscope **103**, 1035–1042 (1993).
[12] J. J. Jiang, C. E. Diaz, and D. G. Hanson, "Finite element modeling of vocal fold vibration in normal phonation and hyperfunctional dysphonia: implication for the pathogenesis of vocal nodules," Ann. Otol. Rhinol. Laryngol. **107**, 603–609 (1998).
[13] K. Ishizaka and J. L. Flanagan, "Synthesis of voiced sounds from a two-mass model of the vocal cords," Bell Syst. Tech. J. **51**, 1233–1268 (1972).
[14] M. Henon, "On the numerical computation of Poincare maps," Physica D **5**, 412 (1982).
[15] S. M. Zeitels, R. E. Hillman, R. Desloge, M. Mauri, and P. B. Doyle, "Phonomicrosurgery in singers and performing artists: treatment outcomes, management theories, and future directions," Ann. Otol. Rhinol. Laryngol. **111**, 21–40 (2002).

Spectrum effects of subglottal pressure variation in professional baritone singers

Peta Sjölander and Johan Sundberg
KTH Voice Research Centre, Speech Music Hearing, KTH, 100 44 Stockholm, Sweden

(Received 26 January 2001; revised 17 June 2003; accepted 30 October 2003)

The audio signal from five professional baritones was analyzed by means of spectrum analysis. Each subject sang syllables [pæ] and [pa] from loudest to softest phonation at fundamental frequencies representing 25%, 50%, and 75% of his total range. Ten subglottal pressures, equidistantly spaced between highest and lowest, were selected for analysis along with the corresponding production of the vowels. The levels of the first formant and singer's formant were measured as a function of subglottal pressure. Averaged across subjects, vowels, and F_0, a 10-dB increase at 600 Hz was accompanied by a 16-dB increase at 3 kHz. © *2004 Acoustical Society of America.*
[DOI: 10.1121/1.1646403]

PACS numbers: 43.70.Aj, 43.70.Bk, 43.75.Rs [AL]

Pages: 1270–1273

I. INTRODUCTION

The spectral slope of voiced sounds is an important parameter in voice analysis. This slope is influenced by vocal loudness. Fant (1959) observed that, as the overall sound level rises, the gain is greater for higher than for lower partials. Analyzing spectra of sung vowels produced by professional singers, Cleveland and Sundberg (1985) observed that an increase of the overall SPL caused the relative level of the singer's formant, a high-spectrum envelope peak characteristic of western male operatic singers, to increase. Bloothooft and Plomp (1986) found that a 10-dB rise of SPL caused the relative level of the singer's formant to increase by between 15.4 and 2.1 dB, depending on singer classification, vowel, and register. Sundberg (2001) reported values in the range of 14 and 24 dB for a 10-dB increase of the overall SPL.

An increase of vocal loudness is produced by means of an increase of subglottal pressure (Ladefoged, 1961; Schutte, 1980). Such increases affect the waveform of the glottal voice source (Gauffin and Sundberg, 1989). The relationship between such waveform characteristics and the spectrum slope was analyzed by Monsen and Engebretson (1977), who observed that changes of one were accompanied by changes in the other. Holmberg *et al.* (1995) observed that shifting vocal loudness from comfortable to loud caused a significant reduction of the level difference between formants 1 and 3. Sundberg *et al.* (1999) analyzed the relationship between subglottal pressure and maximum flow declination rate (MFDR), i.e., the negative peak amplitude of the differentiated flow glottogram in professional baritone singers, and found that the logarithm of this amplitude was strongly correlated with overall SPL.

The waveform–spectrum relationship was analyzed theoretically by Fant and co-workers (Fant *et al.*, 1985), who demonstrated that the spectrum tilt is determined by the abruptness of the return phase of the flow glottogram, i.e., the speed at which the differentiated flow glottogram curve returns to zero at the end of the flow pulse. This abruptness, in turn, is therefore controlled by subglottal pressure.

On the other hand, it is difficult to analyze the relationship between spectrum slope and flow glottograms derived from inverse filtering, since the filtering tends to reduce the speed of the return phase. More reliable information on spectrum levels should be available from long-term average spectra (LTAS). Ternström (1993) analyzed LTAS of choral singing in rooms with different reverberation times. For a youth choir he found that a 10-dB increase in overall sound level produced an increase of 10 dB at around 800 Hz and 20 dB at 3 kHz. For an adult choir the increase at 3 kHz was slightly less. White (1998) used the same method in an analysis of children, who sang a song at low, middle, and high degrees of vocal loudness. She found that an increase of 10 dB near 600 Hz was accompanied by an increase of about 16 dB in the frequency range around 3.25 kHz.

Earlier findings thus demonstrate the need to take into account vocal loudness in spectral voice analysis. However, although previous studies are fairly consistent, they have compared utterances produced at only a few levels of vocal loudness. For reliable comparisons of voice spectra, an analysis is needed of how systematic loudness variation affects the spectrum slope. For an accurate description of this relationship, it is obviously advantageous to analyze many different degrees of vocal loudness.

The effect of subglottal pressure variation on various glottal voice source parameters was studied in five professional baritone singers in a previous investigation (Sundberg *et al.*, 1999). They based their results on observations collected at ten different subglottal pressures. A highly systematic variation with subglottal pressure was found for maximum flow declination rate MFDR, closed quotient, peak-to-peak flow amplitude, and the level difference between the fundamental and the second partial of the voice source spectrum. Glottal dc flow, i.e., glottal leakage, on the other hand, failed to show any systematic variation with subglottal pressure. The aim of the present study was to use the same material to describe concomitant effects on the overall spectrum slope measured in terms of the level difference between the first formant and the singer's formant.

II. SUBJECTS

In untrained voices, increased loudness typically results in an increase of pitch (Gramming *et al.*, 1988). Singers, on the other hand, possess the ability to control loudness independently of pitch. Hence, it is advantageous to use professional singers as subjects in investigations of the effects of loudness variation on the voice. The material recorded for the investigation mentioned above (Sundberg *et al.*, 1999) was therefore reanalyzed for the present investigation. It consisted of the recorded audio channel for five professional baritone singers aged from 29 to 65 years.

III. METHOD

Each singer sang a diminuendo at a constant pitch, continuously repeating the syllable [pa:] and then repeating the syllable [pæ:]. Three test pitches were used, C#3, G3, and C#4 (for one of the singers B2, F3, and C4) corresponding to 25%, 50%, and 75% of the singer's professional pitch range as measured in semitones. Three productions, or *takes*, of each pitch condition were recorded.

The audio signal, picked up by a B&K condenser microphone, at a distance of 30 cm from the subject's mouth, was recorded onto a multichannel recorder (TEAC PCM). Subglottal pressure was estimated from the oral pressure during the [p]-occlusion. This pressure was captured by a pressure transducer (Glottal Enterprises) attached to a thin plastic tube that the subject held in the corner of his mouth. Simultaneous recordings were made of the glottal flow by means of a Rothenberg-type flow mask (Rothenberg, 1973). Calibration signals for pressure as measured by means of a manometer, and for sound-pressure level (SPL) as determined by a sound-level meter, were recorded on the tape.

The earlier paper (Sundberg *et al.*, 1999) reported that the singers tended to reproduce quite accurately glottal parameter values when repeatedly singing at identical pitch and subglottal pressures. This supports the assumption that, for each subject, vowels produced at the same subglottal pressure had similar characteristics and, thus, we have reasons to assume, like the earlier paper, that the data obtained were reliable.

IV. ANALYSIS

The subglottal pressures were recorded on a strip chart recorder. For each vowel and pitch condition, ten subglottal pressures, equidistantly spaced between the extreme values, were selected across the three productions of syllable repetitions. This procedure produced 60 measurement points per subject (2 vowels×3 pitches×10 values), making a total of 300 values. The syllables following these pressure signals, as recorded on the audio channel, were subjected to spectrum analysis (frequency range 0–5 kHz, bandwidth 150 Hz) using a commercially available signal editing system (SOUNDSWELL). Two measures were made of each spectrum: the level of the first formant, L_1; and the level difference between the first formant and the singer's formant, L_1-L_{SF}. These measures were combined with the corresponding subglottal pressure values. SPL was measured by a B&K sound-level recorder (2307) analysis of the audio track.

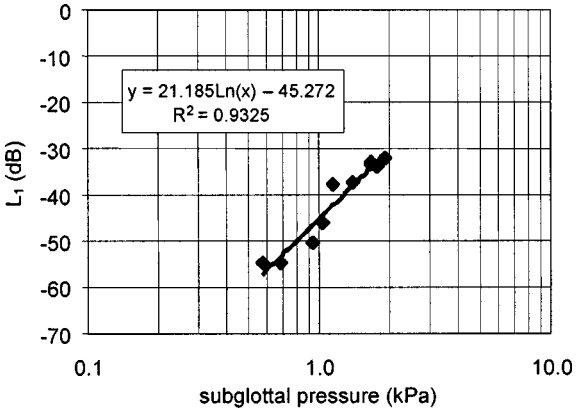

FIG. 1. Example of the relationship between subglottal pressure and the level of the first formant, L_1, in one subject. The subject sang the vowel [æ:] at 25% of his vocal pitch range.

Three spectra were eliminated, as subglottal pressure was not measurable. During softest phonation, a further 36 spectra revealed an absence of harmonic energy in the singer's formant region and so were excluded from the L_1-L_{SF} part of the data analysis but were included for the L_1 measurements. The 280 SPL values obtained at the time of recording (see Sundberg *et al.*, 1999) were also used in the experiment.

V. RESULTS

Figures 1 and 2 show examples from one individual of the relationship between $Ln(P_S)$ and L_1, and between $Ln(P_S)$ and L_1-L_{SF}, respectively. In most cases these data could be approximated by a straight line, with r^2 varying between 0.69 and 0.99 (mean=0.93). These figures show that an increase of P_S was accompanied by an increase of L_1 and a decrease of the L_1-L_{SF} difference. In other words, the spectral tilt decreased with increasing loudness.

Table I shows the means and standard deviations for the slope of the best linear fit of the five singers' values, as plotted in the example shown in Fig. 1. The slope values reflect the growth of L_1 observed for a doubling of P_S for [æ] and [a] as sung by the subjects at low, middle, and high pitches. The correlation shows high values, while the s.d.

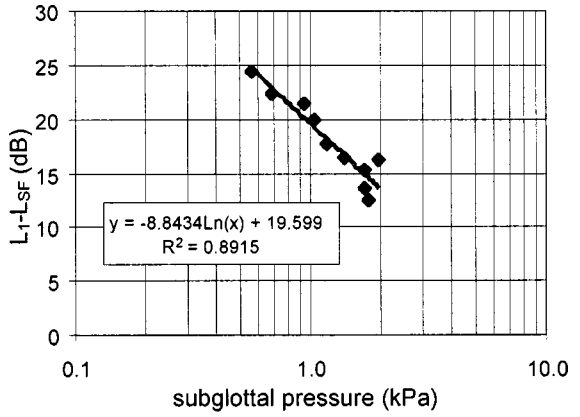

FIG. 2. Example of the relationship between subglottal pressure and L_1-L_{SF} difference (same subject as in Fig. 1). Vowel [æ:] produced at 25% of the subject's vocal pitch range.

TABLE I. Increase of L_1 ($n=297$) for a doubling of P_S, averaged across singers. The r shows the correlation.

% Pitch range/vowel	ΔL1 /(2*P_S) dB	s.d. dB	r Means
25 æ	11.1	2.4	0.858
25 a	11.9	1.7	0.936
50 æ	12.2	3.2	0.932
50 a	13.4	1.7	0.933
75 æ	13.4	1.7	0.971
75 a	11.4	2.8	0.947
Mean	12.24	2.258	0.930
s.d.	1.006	0.630	0.038

varied between 1.7 and 3.2 dB. A doubling of P_S caused an increase of L_1 that varied between 11.1 and 13.4 dB (mean $=12.2$ dB). The values varied among singers. A general linear model analysis of variance revealed that these intersubject differences were not significant.

Table II shows the corresponding values of the best linear fit of the five singers' L_1-L_{SF} data versus $Ln(P_S)$, as plotted in the example given in Fig. 2. The values reflect the decrease of L_1-L_{SF} observed for a doubling of P_S for [æ] and [a] at low, middle, and high pitch. The correlation shows reasonably high values and the s.d. varied between 2.1 and 3.2 dB. A doubling of P_S caused a decrease of L_1-L_3 that varied between 5.9 and 8.1 dB, mean 7.2 dB. A general linear model analysis of the variance between singers revealed that these differences were not significant. The relationship implies that L_{SF} will increase by $12.2+7.2=19.4$ dB for a doubling of P_S, or for a 10-dB increase of L_1 by $19.4/1.22=15.9$ dB. In other words, the gain in L_{SF} will be 1.6 times the gain in L_1.

The relationship between SPL and $Ln(P_S)$ is another interesting aspect of our data. Table III lists the mean slopes and intercepts observed for the SPL increase associated with a doubling of P_S. These values also varied between singers and a general linear model analysis of variance showed that the intersubject differences were significant for pitch for both slope [$F(2,8)=5.697$, $p=0.029$] and intercept [$F(2,8)=5.578$, $p=0.030$]. The significant effect of pitch on the intercept values was that the lowest pitch revealed an elevated estimated marginal mean compared to the mean for mid pitch, which in turn was higher than the mean for high pitch. The opposite effect was observed for the effect of pitch on slope values in that the estimated marginal means were highest for high pitch and lowest for low pitch. The average across singers, vowels, and pitches showed that

$$\mathrm{SPL}=10.1\times Ln(P_S)+76.1 \text{ dB}.$$

This implies that P_S values of 1 and 2 kPa yielded, on average, SPL values at 0.3 m of 76.1 and 83.1 dB, respectively.

TABLE II. Decrease of L_1-L_{SF} ($n=261$) for a doubling of P_S averaged across singers. The r shows the correlation.

% Pitch range/vowel	ΔL_1-L_{SF} /(2*P_S) dB	s.d. dB	r Means
25 æ	−6.7	2.1	−0.863
25 a	−7.4	2.6	−0.919
50 æ	−5.9	3.2	−0.791
50 a	−7.5	2.3	−0.840
75 æ	−7.2	2.4	−0.854
75 a	−8.1	2.6	−0.834
Mean	−7.15	2.55	−0.850
s.d.	0.76	0.38	0.042

TABLE III. Mean relationship ($n=280$) between P_S and SPL at 0.3 m expressed as the slope and intercept for the best linear fit of SPL values versus $Ln(P_S)$. The values represent the shifts associated with a doubling of P_S. The r shows the correlation.

Pitch/vowel	Slope SPL means	s.d.	Icpt SPL means	s.d.	r Means
25 æ	8.3	3.0	78.2	1.7	0.907
25 a	9.2	1.1	77.7	1.5	0.964
50 æ	10.0	3.1	76.1	2.3	0.970
50 a	10.5	2.6	76.6	1.7	0.969
75 æ	11.3	1.8	74.3	1.7	0.991
75 a	11.3	2.7	73.7	2.6	0.967
Mean	10.1		76.1		0.961
s.d.	1.2		1.8		0.028

VI. DISCUSSION

We found that, for our singer subjects, SPL increased by an average of 12 dB per doubling of P_S. This is similar to measurements reported earlier by Schutte (1980), who analyzed P_S and SPL, among other things, in singers and untrained voices as well as dysphonic patients. On the basis of theoretical considerations, Fant (1982) predicted an SPL increase of 9.5 dB for a doubling of P_S. This prediction assumed an increase of F_0, which typically accompanies an increase of vocal loudness in speech. This condition was not met by the singers who kept pitch constant. The effect of the pitch change assumed by Fant is small, however, and the discrepancy between our data and the prediction may very well emanate from the voice source. For example, the effect of an increased P_S on the closed phase may be larger than that assumed by Fant.

The data presented above refer to the level of the first formant. At soft phonation the fundamental rather than the first formant is strongest in the spectrum, so the overall SPL is determined mainly by the fundamental under such conditions. The results above thus concern the relationship between L_1 and L_{SF} as opposed to the overall sound level and L_{SF}.

A Rothenberg flow mask records the airflow in terms of the pressure gradient across an acoustic resistance represented by a fine mesh. This resistance adds to the formant bandwidths and thus reduces the levels of the spectrum peaks. This effect is not relevant to our results, however, since they concern the effect of subglottal pressure on relative spectrum levels rather than on absolute spectrum levels. Also, our spectrum data refer to the audio rather than to the flow signal. On the other hand, the relationship between P_S and SPL is influenced by this effect and SPL also varies depending on formant frequencies and F_0. This would explain why our results showed rather low SPL values as compared to data previously published (e.g., Titze and Sundberg, 1992).

Our results can be assumed to be applicable also to data obtained using long-term average spectrum (LTAS) analysis. Ternström (1993) made LTAS analyses of choirs who sang the same piece of music at low, middle, and high degrees of vocal effort. For an adult choir he found that the gain of an LTAS peak near 3 kHz was 1.7 times as great as the gain near 800 Hz, and the gain at 3 kHz for a youth choir was twice as great as the gain near 800 Hz. White (1998) made a corresponding analysis of 15 11-year-old school children who sang a song at three degrees of vocal loudness. She found the gain of an LTAS peak near 3.2 kHz was 1.9 times as great as the gain near 600 Hz for girls, and the corresponding values for boys were 1.6 as great. These values are similar to those observed in the present study, which supports the assumption that our observations are applicable also to LTAS data. These differences in the gain between boys and girls and between a youth choir and an adult choir suggest that the gain varies depending on glottal factors.

The highest spectrum envelope peak between 2 and 4 kHz as produced by baritone singers typically is the singer's formant, generated by a clustering of formants 3, 4, and 5 (Sundberg, 1987). The gain in the level of the singer's formant should be similar to the gain of L_3 for voices lacking a singer's formant. Support for this assumption can be found in Gauffin and Sundberg (1989), who analyzed the levels in different frequency bands when subjects varied vocal loudness. They observed an L_3 increase from 47 to 65 dB when their untrained subject raised his L_1 by 11 dB; this corresponds to a gain factor of 1.6. They found a marginally smaller gain for their singer subject. Similar results were recently observed in an LTAS investigation of untrained voices reading a standard text at different degrees of vocal loudness (Nordenberg, 2003).

In comparing voices as analyzed in terms of LTAS or of the spectra of sustained vowels, the level in various spectrum bands is sometimes compared. Such comparisons would be more informative if concomitant changes of L_1 were taken into account. On the basis of our findings, the correction needed can be estimated analytically. Thus, on average, a change in the level of the first formant (ΔL_1) will be associated with a change of the level of the singer's formant, which can be approximated by the following equation:

$$\Delta \mathrm{L}_3 = 1.6 \times \Delta \mathrm{L}_1 .$$

The equation is based on the average of professional singers' productions of the vowels /æ/ and /a/. As the effect would originate from voice source rather than from formant frequency characteristics, the same expression should be applicable also to other vowels. As mentioned above, a level gain of a similar magnitude has been observed for the third formant (ΔL_3) in untrained voices. Hence, the equation can be assumed to be applicable also to nonsinger voices.

VII. CONCLUSION

The relationship between the logarithm of subglottal pressure and the level of the F_1 in baritone singers can be approximated by a linear function, such that a doubling of subglottal pressure causes a 12-dB increase of L_1. Likewise, the level increase of partials near 3 kHz approximates a linear function of the logarithm of subglottal pressure. However, the level of these partials increases 1.6 times as much as L_1.

ACKNOWLEDGMENTS

This study used data originally recorded for the masters dissertations of Maria Andersson and Clara Hultqvist. The statistical advice given by Joakim Westerlund is gratefully acknowledged, as are the comments provided by the reviewers on earlier drafts of this paper. This research is funded by the European Commission (ERBFMBI-CT98-3542), and by the Swedish Research Council, *Vetenskapsrådet* (621-2002-3863).

Bloothooft, G., and Plomp, R. (**1986**). ''The sound level of the singer's formant in professional singing,'' J. Acoust. Soc. Am. **79**, 2028–2033.

Cleveland, T., and Sundberg, J. (**1985**). ''Acoustic analyses of three male voices of different quality,'' in *SMAC 83: Proceedings of the Stockholm International Music Acoustics Conference* (Roy. Sw. Acad. Music, Stockholm), Vol. 1, No. 46:1, 143–156.

Fant, G. (**1959**). ''Acoustic Analysis and Synthesis of Speech with Applications to Swedish'' (Ericsson Technics No. 1, Stockholm).

Fant, G. (**1982**). ''Preliminaries to analysis of the human voice source,'' KTH Speech Music Hearing Quart. Prog. and Stat. Report **4/1982**, 1–27.

Fant, G., Liljencrants, J., and Lin, Q. (**1985**). ''A four-parameter model of glottal flow,'' KTH Speech Music Hearing Quart. Prog. and Stat. Report **4/1985**, 1–13.

Gauffin, J., and Sundberg, J. (**1989**). ''Spectral correlates of glottal voice source waveform characteristics,'' J. Speech Hear. Res. **32**, 556–565.

Gramming, P., Sundberg, J., Ternström, S., Leanderson, R., and Perkins, W. (**1988**). ''Relationships between changes in voice pitch and loudness,'' J. Voice **2**, 118–126.

Holmberg, E., Hillman, R., Perkell, J., Guiod, P., and Goldman, S. (**1995**). ''Comparisons among aerodynamic, electroglottographic, and acoustic spectral measures of female voice,'' J. Speech Hear. Res. **38**, 1212–1223.

Ladefoged, P. (**1961**). ''Subglottal activity during speech,'' in Proceedings of the 4th International Congress of Phonetic Sciences, Helsingfors, 73–91.

Monsen, R. B., and Engebretson, A. M. (**1977**). ''Study of variations in the male and female glottal wave,'' J. Acoust. Soc. Am. **62**, 981–993.

Nordenberg, M. (**2003**). ''How does vocal intensity affect LTAS?'' [Hur förändras LTAS vid variation av röststyrkan?), Masters thesis (in Swedish), February 2003, Department of Phoniatrics and Logopedics, Lund University Hospital, Sweden.

Rothenberg, M. (**1973**). ''A new inverse-filtering technique for deriving the glottal airflow waveform during voicing,'' J. Acoust. Soc. Am. **53**, 1632–1645.

Schutte, H. (**1980**). ''The Efficiency of Voice Production,'' doctoral dissertation, Groningen University.

Sundberg, J. (**1987**). *The Science of the Singing Voice* (Northern Illinois University Press, DeKalb, IL).

Sundberg, J. (**2001**). ''Level and center frequency of the singer's formant,'' J. Voice **15**, 176–186.

Sundberg, J., Andersson, M., and Hultqvist, C. (**1999**). ''Effects of subglottal pressure variation on professional baritone singers' voice sources,'' J. Acoust. Soc. Am. **105**, 1965–1971.

Ternström, S. (**1993**). ''Long-time average spectrum characteristics of different choirs in different rooms,'' J. Voice **2**, 55–77.

Titze, I., and Sundberg, J. (**1992**). ''Vocal intensity in speakers and singers,'' J. Acoust. Soc. Am. **91**, 2936–2946.

White, P. (**1998**). ''The effect of vocal intensity variation on children's voices using long-term average spectrum (LTAS) analysis,'' Log. Phon. Voc. **23**, 111–120.

A vocal-tract model of American English /l/

Zhaoyan Zhang[a] and Carol Y. Espy-Wilson[b]
Department of Electrical and Computer Engineering, University of Maryland, College Park, Maryland 20742

(Received 29 May 2003; revised 22 November 2003; accepted 1 December 2003)

The production of the lateral sounds involves airflow paths around the tongue produced by the laterally inward movement of the tongue toward the midsagittal plane. If contact is made with the palate, a closure is formed in the flow path along the midsagittal line. The effects of the lateral channels on the sound spectrum are not clear. In this study, a vocal-tract model with parallel lateral channels and a supralingual cavity was developed. Analysis shows that the lateral channels with dimensions derived from magnetic resonance images of an American English /l/ are able to produce a pole–zero pair in the frequency range of 2–5 kHz. This pole–zero pair, together with an additional pole–zero pair due to the supralingual cavity, results in a low-amplitude and relatively flat spectral shape in the $F3-F5$ frequency region of the /l/ sound spectrum. © *2004 Acoustical Society of America.* [DOI: 10.1121/1.1645248]

PACS numbers: 43.70.Bk, 43.70.Fq [AL] Pages: 1274–1280

I. INTRODUCTION

Research on vocal-tract acoustics requires accurate models of sound propagation through complex geometries formed by the articulators. The production of /l/ sounds involves one or two lateral channels which are airflow paths around the tongue produced by laterally inward movement of the tongue toward the midsagittal plane (Stevens, 1998). In cases where the tongue makes contact with the palate, the airflow above the tongue terminates at the contact point along the midsagittal line, giving rise to a ''cul-de-sac'' supralingual side branch to the main airflow pathways of the lateral channels (Fig. 1). When two lateral channels are formed, they split at a point determined by the approach of the tongue dorsum to the teeth, and join again anterior to the lingual–alveolar contact.

The effects of these geometric features on the acoustics of the vocal tract are not clear. In particular, the lateral liquid /l/ is generally characterized by pole–zero clusters around 2–5 kHz in its spectrum. Figure 2 shows a spectrogram of the word ''bell'' produced by a male speaker and Fig. 3 compares spectra during the vowel /ɛ/ and the following /l/. The resonances around 2200 and 3200 Hz during the vowel ($F3$ and $F4$) are absent during the /l/ due to zeros. In fact, the /l/ spectrum is fairly flat between 1600 and 3400 Hz. Although details differ, this scenario holds true for both ''dark'' and ''light'' allophones of /l/ (Lehman and Swartz, 2000). Due to the existence of reported data, this paper will concentrate primarily on accounting for /l/'s as produced in American English. However, the issue of accounting for the acoustics of lateral channels is general to the class of lateral sounds.

There are several possible source(s) of the zeros during /l/ sounds, and their relative contribution to the acoustic spectrum for /l/ remains unclear. One possible source is the midsagittal supralingual side branch (Fant, 1970; Stevens, 1998; Bangayan *et al.*, 1999; Narayanan and Kaun, 1999). An additional source of zeros may be produced when there are two lateral channels and they are of different lengths. Prahler (1998) has shown that uniform lateral channels that have the same length produce a pole–zero pair at the same frequency location so that they cancel each other. Thus, the net result is an all-pole spectrum. If, on the other hand, the lateral channels are of different lengths, then the poles and zeros will be at different frequencies. Specifically, Prahler has shown that when the lateral channels are uniform, but of different lengths, the combined length of the lateral channels needs to be around 16 cm long to produce zeros in the region around 2 kHz. This required length of the lateral channels, however, is much higher than that measured from MRI data (Narayanan *et al.*, 1997; Zhang *et al.*, 2003) or speculated by Fant (1970). As we discuss below, such long lateral channels may not be needed to produce a zero in the $F3-F5$ region if we assume more realistic lateral channels with nonuniform areas.

In this paper, we develop a simple tube vocal-tract model for /l/ that includes both a supralingual side branch and one or two lateral channels. Even though MRI data obtained from a male speaker are used to determine dimensions, the purpose of this study is not to explore the specific vocal-tract shape of a particular individual. Instead, our purpose is to investigate the possible sources of the pole–zero clusters in American English /l/ and the frequency ranges in which they are likely to occur.

II. THEORETICAL BACKGROUND

A. Vocal-tract acoustic response

There have been considerable efforts in the development of computer vocal-tract models. Maeda (1982) developed a time-domain method to calculate the vocal-tract acoustic response function for the vowels and nasal sounds, in which the nasal tract is modeled as a side branch to the vocal tract. This method was modified by Jackson *et al.* (2001) to accommodate an additional side branch needed to model the sublingual cavity of American English /r/'s. To understand better the production of American English /l/, Prahler (1998) developed a vocal-tract model that included uniform lossless

[a]Electronic mail: zhaoyan@glue.umd.edu
[b]Electronic mail: espy@glue.umd.edu

 0001-4966/2004/115(3)/1274/7/$20.00

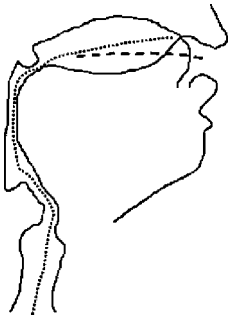

FIG. 1. Schematic of airflow paths above (dotted line) and around the tongue (dashed line) during /l/ sound production. Tracing is from MRI data collected during the sustained /l/ sound produced by the subject used for this study.

lateral channels, but no side branches. Until this study, there was no vocal-tract model that included both side branches and lateral channels, as in the case of /l/ sounds.

In this study, a new frequency-domain model for the vocal-tract acoustic response (VTAR) was developed. The vocal tract is decomposed into various modules such as single tubes, branching, and lateral channels. For a single-tube module the input and output pressures and volume velocities are related by a transfer matrix

$$\begin{bmatrix} p_{\text{in}} \\ U_{\text{in}} \end{bmatrix} = K \begin{bmatrix} p_{\text{out}} \\ U_{\text{out}} \end{bmatrix} = \begin{bmatrix} A & B \\ C & D \end{bmatrix} \begin{bmatrix} p_{\text{out}} \\ U_{\text{out}} \end{bmatrix}, \tag{1}$$

where A, B, C, and D are the coefficients of the transfer matrix K, and depend on the properties of the air and the vocal-tract wall.

The transfer matrix can be calculated using the transmission-line model. The single tube is simulated as a concatenation of cylindrical sections with lengths far less than the acoustic wavelength. Assuming plane-wave propagation, each cylindrical section is represented by an analog circuit as shown in Fig. 4. The transmission-line model has been discussed extensively in many studies (cf. Flanagan, 1972). The exact expressions for each circuit element used in this study are given as follows:

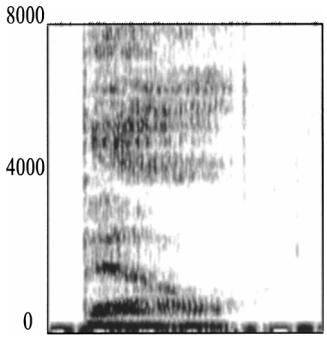

FIG. 2. Spectrogram of word "bell."

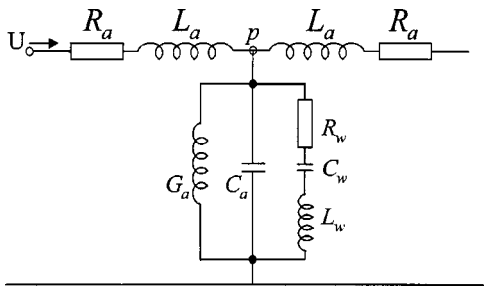

FIG. 4. Transmission line representation of the vocal tract.

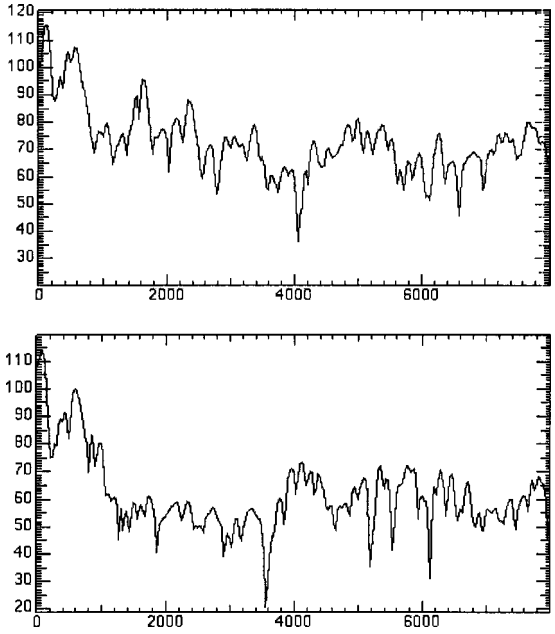

FIG. 3. Spectra during the vowel /ε/ (top figure) and the following /l/ (bottom figure).

$$R_a = \frac{lP}{2S^2}\sqrt{\frac{\omega\rho\mu}{2}}, \quad L_a = \frac{\rho l}{2S}\omega,$$

$$C_a = \frac{lS}{\rho c^2}\omega, \quad G_a = Pl\frac{\eta-1}{\rho c^2}\sqrt{\frac{\lambda\omega}{2C_p\rho}}, \tag{2}$$

$$L_w = \frac{m}{lP}\omega, \quad R_w = \frac{b}{lP}, \quad C_w = \frac{lP}{k}\omega,$$

where ω is the angular frequency of interest, l is the length of the cylindrical section, S is the tube area, P is the cylindrical circumference, ρ is the air density, c is the speed of sound, μ is the viscosity, λ is the coefficient of heat conduction, η is the adiabatic constant, C_p is the specific heat of air at constant pressure, and m, b, and k are the mass, mechanical resistance, and the stiffness of the wall per unit area of the tube, respectively. This model includes the losses due to the flow viscosity, heat conduction, and vocal-tract wall vibration. The overall transfer matrix of the single tube is simply the product of the transfer matrix of each cylindrical section.

If a branching configuration is present in the vocal tract [Fig. 5(a)], such as the coupling of the nasal tract, a sublingual cavity, or supralingual cavity to the vocal tract, an extra

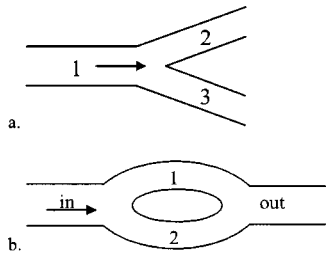

FIG. 5. Models for (a) tube branching and (b) lateral channels.

branch-coupling matrix is used to relate the state variables across the branching point (Sondhi and Schroeter, 1987)

$$\begin{bmatrix} p_1 \\ U_1 \end{bmatrix} = \begin{bmatrix} 1 & 0 \\ 1/Z_3 & 1 \end{bmatrix} \begin{bmatrix} p_2 \\ U_2 \end{bmatrix}, \quad \text{or} \quad \begin{bmatrix} p_1 \\ U_1 \end{bmatrix} = \begin{bmatrix} 1 & 0 \\ 1/Z_2 & 1 \end{bmatrix} \begin{bmatrix} p_3 \\ U_3 \end{bmatrix}, \tag{3}$$

where Z_2 and Z_3 are the input impedances of the side branches 2 and 3, respectively.

The lateral channels are modeled as two single channels joined together at both ends. Therefore, the two lateral channels have the same input and output pressures [Fig. 5(b)]. Assume for each lateral channel that the input and output state variables are related by

$$\begin{bmatrix} p_{\text{in},i} \\ U_{\text{in},i} \end{bmatrix} = K_i \begin{bmatrix} p_{\text{out},i} \\ U_{\text{out},i} \end{bmatrix}. \tag{4}$$

Applying boundary conditions and flow continuity, simple algebraic manipulation leads to a relationship between the input and output of the lateral channels

$$\begin{bmatrix} p_{\text{in}} \\ U_{\text{in}} \end{bmatrix} = \begin{bmatrix} \dfrac{A_1B_2+A_2B_1}{B_1+B_2} & \dfrac{B_1B_2}{B_1+B_2} \\ C_1+C_2-\dfrac{(D_1-D_2)(A_1-A_2)}{B_1+B_2} & \dfrac{D_1B_2+D_2B_1}{B_1+B_2} \end{bmatrix} \times \begin{bmatrix} p_{\text{out}} \\ U_{\text{out}} \end{bmatrix}. \tag{5}$$

The entire vocal tract is modeled by combining the appropriate modules and multiplying the individual transfer matrices in an order corresponding to their geometric location. This modeling results in a single equation relating the pressures and volume velocities at the glottis and the lips

$$\begin{bmatrix} p_g \\ U_g \end{bmatrix} = K \begin{bmatrix} p_l \\ U_l \end{bmatrix} = \begin{bmatrix} A & B \\ C & D \end{bmatrix} \begin{bmatrix} p_l \\ U_l \end{bmatrix}. \tag{6}$$

The acoustic response function can be calculated as

$$20 \log_{10} |U_l / U_g| = 20 \log_{10} (1/(CZ_l + D)), \tag{7}$$

where Z_l is the radiation impedance at the lips.

B. Code validation

The VTAR model was first validated against Maeda's model (1982) for the simplest case of vowel production. Maeda's model was chosen because it is publicly available and widely accepted. A comparison of the calculated formants for the high front vowel /i/ as in "heed" using Maeda's model and VTAR, with and without radiation load, shows close agreement, within 4 percent. The side branch module was validated against Jackson *et al.*'s (2001) model and complete agreement was obtained.

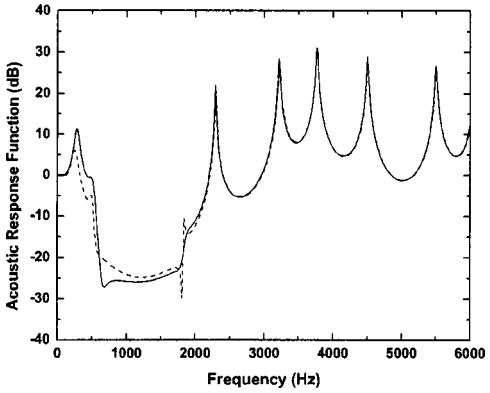

FIG. 6. Comparison between the vocal-tract acoustic response function predicted from Maeda's code (solid line) and VTAR (dashed line), for nasalized vowel /i/, with zero radiation impedance.

Since there are no direct data or models for the lateral channels, data for nasalized vowels were used in this study to validate the lateral channel module. Like /l/'s that are produced with two lateral channels, nasalized vowels are produced with two airflow paths, the oral tract and the nasal tract. In addition, the posterior end of the two paths has the same pressure, assuming plane-wave propagation. The difference between the production of nasalized vowels and /l/ sounds is that, for the nasal sounds, the two paths generally have different radiation impedances and therefore different termination pressures, while the two lateral channels of /l/ have the same termination pressure. Therefore, if the radiation impedance is neglected, nasalized vowels can be modeled using the lateral channel model. Data for a nasalized vowel /i/ and Maeda's simulation code were used in the validation. Figure 6 shows the comparison between the vocal-tract acoustic response functions predicted using Maeda's code and that obtained from the VTAR program. Zero radiation was imposed at both the nose and mouth. The agreement is very good, although there is some mismatch in the spectral amplitude around the first zero frequency (around 600 Hz). These errors are expected in regions around resonances and antiresonances where losses are important. The possible source of error is the different loss formulations used in the time-domain method (Maeda's model) and the frequency domain method VTAR.

C. Uniform lateral channels

For lateral channels consisting of uniform lossless tubes, the input and output pressure and volume velocity of each tube are related by (Kinsler *et al.*, 2000)

$$\begin{bmatrix} p_{\text{in},i} \\ U_{\text{in},i} \end{bmatrix} = \begin{bmatrix} \cos(-kl_i) & -\dfrac{j\rho c}{S_i} \sin(-kl_i) \\ \dfrac{S_i}{j\rho c} \sin(-kl_i) & \cos(-kl_i) \end{bmatrix} \begin{bmatrix} p_{\text{out},i} \\ U_{\text{out},i} \end{bmatrix}, \tag{8}$$

where k is the wave number, and S_i and l_i are the area and length of the ith tube, respectively. Neglecting the radiation at the lateral channels outlet, substitution of Eq. (8) into Eq. (5) yields

$$\frac{U_{\text{out}}}{U_{\text{in}}}=\frac{S_1 \sin kl_2+S_2 \sin kl_1}{S_1 \cos kl_1 \sin kl_2+S_2 \sin kl_1 \cos kl_2}. \tag{9}$$

The terms in the right-hand side of Eq. (9) have specific physical meanings. The two terms in the numerator represent the volume velocity at the outlets of the two channels. Similarly, the two terms in the denominator represent the inlet volume velocity of the two channels. Assuming $S_2>S_1$ allows Eq. (9) to be rewritten as

$$\frac{U_{\text{out}}}{U_{\text{in}}}=\frac{2 \sin k\dfrac{l_1+l_{2,z}}{2}\cos k\dfrac{l_1-l_{2,z}}{2}}{\sin k(l_1+l_{2,p})}, \tag{10}$$

where $l_{2,z}$ and $l_{2,p}$ are the effective zero and pole length of the second lateral channel, respectively, and are defined as,

$$\sin kl_{2,z}=(s_1/s_2)\sin kl_2$$
$$\sin k(l_1+l_{2,p})=\sin kl_1 \cos kl_2+(s_1/s_2)\sin kl_2 \cos kl_1. \tag{11}$$

They represent the effective lengths the second channel needs to be to have volume velocities canceling out with the volume velocity from the first channel at the outlet (therefore a zero) and inlet (therefore a pole), respectively.

Two types of zeros in the acoustic response function of the lateral channels can be identified from Eq. (10). The first set of zeros is at multiples of the frequencies $c/(l_1+l_{2,z})$. This frequency corresponds to the total-length resonance, at which most of the input airflow circulates in between the two channels. The second set of zeros is at odd multiples of the frequencies $c/[2(l_1-l_{2,z})]$. This set of frequencies corresponds to the half-wavelength antiresonance frequency of approximately the difference in the lengths of the lateral channels, in which sound waves at the outlet of the lateral channels are 180° out of phase with each other. The second type of zeros normally occurs at high frequencies since they are related to the length differences. However, in the case of two nonuniform lateral channels, the effective length of $l_{2,z}$ can be very different from l_1, yielding zeros that may appear in the low-frequency range of human speech.

In general, the two effective lengths are functions of both the area ratio and length ratio of the two channels. Consider two special cases in which the two channels have the same lengths and the same areas, respectively. For both cases, the two effective lengths are the same and equal to the length of the wider lateral channels. Equation (10) reduces to

$$\frac{U_{\text{out}}}{U_{\text{in}}}=\begin{cases}1/\cos kl & l=l_1=l_2\\ \dfrac{\cos k\dfrac{l_1-l_2}{2}}{\cos k\dfrac{l_1+l_2}{2}} & S_1=S_2.\end{cases} \tag{12}$$

When the lateral channels have the same length but different areas, the second set of zeros does not exist and the first set of zeros is canceled by poles so that the vocal-tract acoustic response function consists only of poles. In this case, the lateral channels do not contribute any zero to the sound spectra, as shown in Prahler (1998). When the lateral channels have the same areas but different lengths, the first set of zeros is also canceled out by poles. However, the second set of zeros remains, and the lateral channels will contribute zeros to the sound spectra.

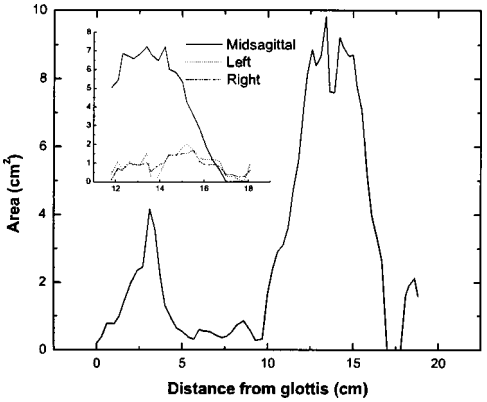

FIG. 7. MRI-derived area functions of the vocal tract, lateral channels (left and right), and supralingual cavity (midsagittal).

It should be noted that lateral channels are usually asymmetric in real speech production. The changes in the acoustic impedance due to the area variation will modify the sound field, and change the phase of the sound waves arriving at the outlets, thereby changing the effective length. The effective lengths of the two channels, due to the area variation, are different even if the two channels have the same lengths [Eq. (11)]. Therefore, the lateral channels always produce pole–zero pairs in real speech production.

III. DATA

Two sets of data were used in the study to illustrate the individual contributions from the supralingual cavity and the lateral channels with reasonable dimensions. The first set of data, which is referred to as the real data or real area functions, is cross-sectional area functions obtained from MRI images of the vocal tract during a sustained /l/ production (Zhang *et al.*, 2003) by the same speaker producing the ''bell'' word shown earlier. The MRI-derived area function is shown in Fig. 7. Notice that the real area function is nonuniform along the length.

The axial length of the midsagittal closure is generally very small, about 1–2 cm long (Narayanan *et al.*, 1997). However, the flow split, therefore the starting point of the lateral channels and the supralingual cavity, may occur at a position posterior to the midsagittal closure. The velocity and the pressure may show different amplitudes and phases, and therefore needs to be modeled acoustically as separate channels. The lateral inward bracing of the tongue may also help the early flow split into two or three channels. In the data processing (Zhang *et al.*, 2003), the vocal-tract cross sections in the region immediately posterior to the midsagittal closure were divided into three regions (the supralingual cavity and

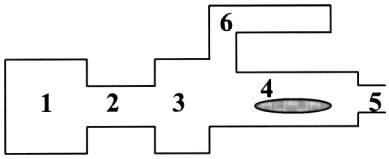

FIG. 8. Simple-tube model of the vocal tract for /l/ sound production.

two lateral channels), and their area functions are also shown in Fig. 7. The supralingual cavity and the lateral channels therefore start posterior at the same location.

The second set of data is the simple-tube data derived from the real MRI-derived area functions. The simple-tube model, as manifested by its name, simplifies the geometry of the vocal tract and its acoustic complexity, and therefore enables us to easily identify the articulatory affiliation of the formants. The simple-tube data were obtained by first dividing the whole vocal tract into several sections. As shown in Fig. 8, the model consists of a back cavity, a pharyngeal constriction, a middle cavity, two lateral channels, a front cavity, and a supralingual cavity modeling the space between the tongue and the palate posterior to the oral closure in the midsagittal line. If the pharyngeal constriction is weak, the first three tubes may be combined into one long back cavity with area perturbations in the middle range (see Stevens, 1998). The area of each section is obtained by averaging the area function over its length. The dimensions of the simple tube model used in this study are shown in Table I. Note that the two lateral channels have the same length in Table I.

Acoustic recordings of a sustained /l/ were also obtained from the same speaker while in supine position at a different time from the MRI recordings. The speaker was attempting to duplicate the sustained /l/ produced during the MRI session.

IV. SIMULATIONS

We consider three simulation cases to help us understand the contributions of the supralingual cavity and the lateral channels in the production of /l/. In the first two simulations, the whole vocal-tract model except the supralingual cavity was used to investigate the possible contributions of the lateral channels alone to the /l/ spectrum. The supralingual cavity was then included in the vocal-tract model in the third simulation and its effects on the spectrum were studied. Simple-tube data were used unless otherwise mentioned.

TABLE I. Dimensions of simple-tube model of /l/ sounds used in simulations. Values in parentheses are used in simulation A for lateral channels of different lengths.

	Length	Area
Back cavity	5.7	1.4734
Pharyngeal constriction	4.3	0.5098
Middle cavity	3.9	5.7064
Lateral channel 1	4.2(5.0)	1.011
Lateral channel 2	4.2(3.4)	0.963
Front cavity	0.7	1.9290
Supralingual cavity	3.1	3.9807

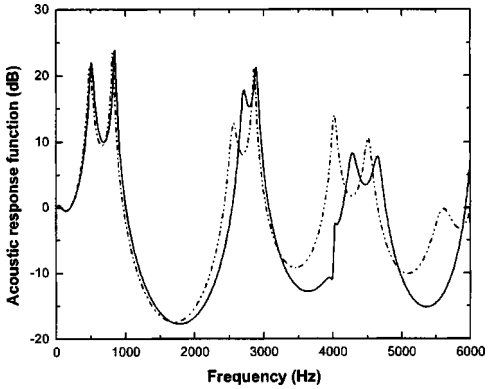

FIG. 9. Vocal-tract acoustic response function for simple-tube model with two uniform lateral channels of different lengths, modeled using lateral channel model (solid line) and with two lateral channels combined into one single tube with an area equal to the combined areas of the two lateral channels (dash-dotted line). Without supralingual cavity.

A. Lateral channels of different lengths

The first simulation considers the case of uniform lateral channels with different lengths (the values in parentheses in Table I). The supralingual cavity was excluded to isolate the effects of the lateral channels on the acoustic response function. Figure 9 shows the calculated vocal-tract acoustic response function. Also shown in the figure is the acoustic response function obtained when the two lateral channels are combined into one single tube with area equal to the sum of the area of the two separate lateral channels. The presence of two lateral channels gives rise to zeros in the acoustic response function, as compared with the all-pole spectrum if the lateral channels are modeled as a single tube. A zero at around 4 kHz is present in Fig. 9, which corresponds to the first type of zero for the total length of 8.4 cm for the lateral channels.

B. Lateral channels of equal length

Figure 10 shows the acoustic response function calculated for the case of uniform lateral channels of equal length. As discussed earlier, uniform channels of equal length do not produce zeros in the spectrum. However, this is not true if the real area functions of the lateral channels are used, as shown in Fig. 10 with the dash-dotted line. Note that a pole–

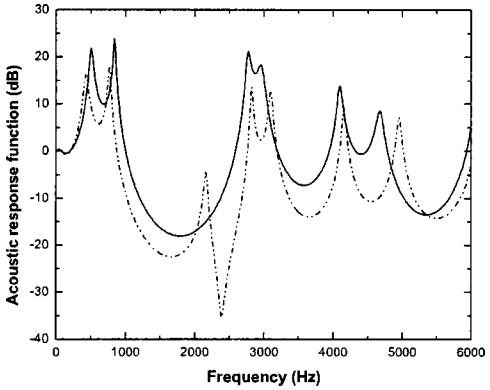

FIG. 10. Vocal-tract acoustic response functions for simple-tube model with two lateral channels of same lengths and uniform (solid line) and nonuniform (dash-dotted line) real area function. Without supralingual cavity.

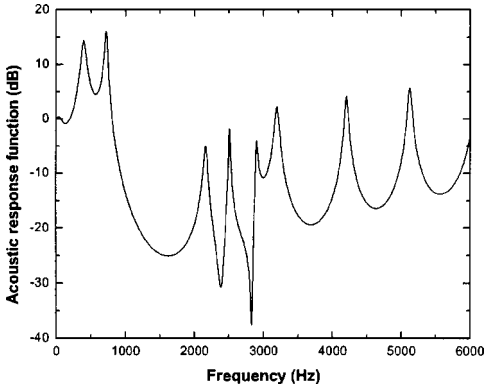

FIG. 11. Vocal-tract acoustic response function for simple-tube model with two nonuniform lateral channels of equal length and a uniform supralingual cavity.

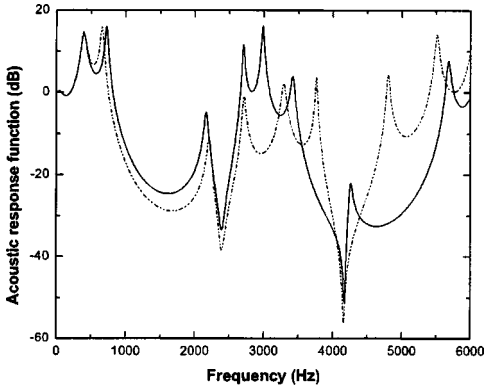

FIG. 12. Vocal-tract acoustic response function for the simple-tube model with two nonuniform real lateral channels and a nonuniform supralingual cavity (solid line), and vocal-tract acoustic response function when the real area function for the entire vocal tract (dash-dotted line) was used.

zero pair appears around 2.4 kHz in the resulting spectrum. The pole–zero pair occurs because the effective lengths of the two channels are unequal due to the nonuniform area functions, according to Eqs. (10) and (11). The nonuniform lateral channels of equal length in this case are essentially the same as uniform lateral channels of different length, as in simulation A. Therefore, zeros are produced even when the two nonuniform lateral channels are of the same length.

Note that the two lateral channels in both simulations A and B have the same combined length (8.4 cm). However, the zero frequency in simulation B (around 2.4 kHz seen in Fig. 10) is much lower than that in simulation A (around 4 kHz seen in Fig. 9) where the lateral channels were also of unequal length but uniform area. The nonuniformity of the area function effectively increases the combined length, resulting in a lower frequency for the zero. This implies that, in real speech production, the lateral channels do not need to be as long as 8 cm to produce zeros in the 2–3-kHz range. It is interesting to note that the zero at 2.4 kHz corresponds roughly to a first type of zeros of a combined length of 14.6 cm if the lateral channels are of uniform area. This length is close to that required in Prahler's work (16 cm) to produce zeros in the range of 2–3 kHz.

C. Supralingual cavity

The addition of the supralingual cavity to the model results in the acoustic response function shown in Fig. 11. Uniform simple-tube data were used for the whole vocal tract except the lateral channels, for which real area data was used. The supralingual cavity, as a side branch, gives rise to an additional zero around 2.8 kHz. The frequency of the zero corresponds to the first quarter-wavelength resonance of a supralingual cavity of length 3.1 cm. The two pole–zero pairs cluster in the range of 2–3 kHz, which coincides with the range of $F3-F4$ for vowels. The prominence of the nearby formants ($F3$ and $F4$) is weakened by the presence of the zeros.

In the production of the lateral sounds, the supralingual cavity is, of course, not uniform in area. In most cases, the supralingual cavity has a tapering area function towards the lingual–alveolar constriction. This tapering actually decreases the effective length of the supralingual cavity, thereby increasing its corresponding zero frequencies, as shown by the solid line in Fig. 12. In this case, the real area function of the supralingual cavity was used.

Also shown in Fig. 12 is the acoustic response function calculated when the real area function was used for the whole vocal tract. The pole values are slightly changed as the real area function reflects more fine features which the simple-tube data fail to include. These changes in the locations of the poles and zeros, although small, significantly change the spectral shape, especially the relative prominence of the pole–zero cluster in the range of 2–4 kHz.

V. DISCUSSION

The simple tube model of American English /l/ presented in this paper shows that both the supralingual cavity and the presence of two lateral channels result in pole–zero clusters around $F3$ and above. In the spectrum of the word-final /l/ in ''bell'' shown in Fig. 3, the pole–zero clusters weakened $F3$ and $F4$, thereby resulting in a fairly flat spectrum between 1600 and 3400 Hz. In Fig. 13, we show the long-term average power spectrum of the acoustic data of the sustained /l/ produced from the same speaker. In the sustained /l/ spectrum, $F3$ and $F5$ have been weakened considerably by zeros and $F4$ is still evident around 3700 Hz. One possible source of the variability in the /l/ spectral shape is

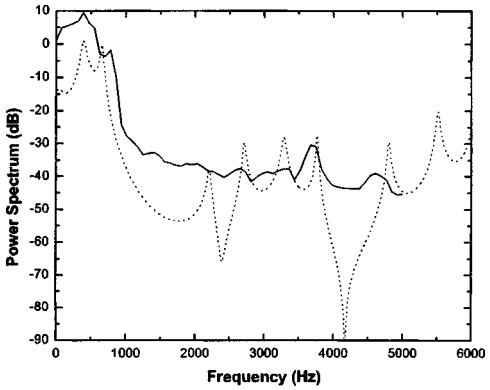

FIG. 13. Measured spectrum of sustained /el/ sound (solid line), and predictions from measured vocal-tract area function with corrections for effects of the source and the radiation (dash-dotted line).

the relative movement of the poles and zeros. Figure 12 has shown that the movement of the poles significantly affects the overall spectral shape. In the simulations, we have shown that the asymmetry of the lateral channels can contribute zeros to the spectrum. The zero frequencies depend on the whole area functions of the lateral channels, and therefore are very sensitive to the changes in either the channel length or the area at one point. This sensitivity will lead to a large variability in the zero location and therefore in the overall /l/ spectral shape.

To compare the simulations with the real power spectrum, the sound spectrum is estimated by adding the effects of the source and radiation as discussed in Stevens (1998) to the acoustic response function calculated by VTAR (dash-dotted line in Fig. 12). The resulting spectrum is shown in Fig. 13 in comparison with the measured power spectrum of the sustained /l/. The two spectra compare well in their spectral shape, especially in the frequency locations of the resonances and the zeros. The first and second formants and the peaks around 3700 and 4600 Hz in the sound power spectrum are accurately predicted by VTAR. The pole–zero cluster in the predicted spectrum that is due to the lateral channels coincide with the ripples in the same range (2000 to 3500 Hz) in the real power spectrum. The predicted zero due to the supralingual cavity occurs during the relatively flat part of the spectrum in the region between 3700 and 4600 Hz. This agreement is not surprising given that the acoustic modeling is based on the same speaker's MRI data. In fact, the agreement between the power spectrum and the model prediction is quite good considering that the acoustic and MRI data were recorded at different times. The main difference is the prominence of resonances and antiresonances above $F2$. The predicted bandwidths of these poles and zeros are much narrower than those observed in the power spectrum. It is possible that some losses related to the air passage through the narrow lateral channels are either not modeled or are underestimated in Eq. (2). In addition, there were some errors involved in estimating the lengths and areas of the lateral channels and supralingual cavity, as discussed in Sec. III. Particularly, since the speaker's teeth have not been superimposed on the MRI slices, the cross-sectional areas of the lateral channels may be overestimated. Smaller areas of the lateral channels will result in more loss, which could reduce further the prominence of the poles and zeros in the cluster region.

VI. CONCLUSION

A vocal-tract model with parallel lateral channels and a supralingual cavity has been developed in this study. Theoretical analysis based on uniform lateral channels shows that lateral channels may produce two types of zeros. The first type of zeros occurs at frequencies at which most of the input airflow circulates around the lateral channel loop. The second type of zeros occurs at frequencies at which the sound waves at the outlet of the two channels are 180° out of phase with each other. Simulations based on both simple-tube data and real data (for the lateral channels only) show that lateral channels of small length (less than 4 cm) can produce zeros in the range of 2–3 kHz, if they have nonuniform areas. The addition of the supralingual cavity introduces another pole–zero pair in the 2–5 kHz range. Thus, this model shows that both the lateral channels and the supralingual cavity are possible causes of the pole–zero clusters in the $F3-F5$ region during /l/ sound production.

ACKNOWLEDGMENTS

This work was supported by NIH Grant 1 R01 DC05250-01 and 1 K02 DC00149-01A1. The authors are grateful to Mark Tiede for the MRI data and for his helpful comments during this project. We also thank Suzanne Boyce for helpful comments on an earlier version of this manuscript and Ken Stevens for a helpful discussion in the beginning of this work.

Bangayan, P., Alwan, A., and Narayanan, S. (**1999**). ''From MRI and acoustic data to articulatory synthesis: A case study of the lateral approximants in American English,'' Proceedings of International Congress of Spoken Language Processes, Philadelphia, PA.

Fant, G. (**1970**). *Acoustic Theory of Speech Production* (Mouton, The Hague, Netherlands).

Flanagan, J. L. (**1972**). *Speech Analysis, Synthesis, and Perception* (Academic, New York).

Jackson, M. T., Espy-Wilson, C., and Boyce, S. (**2001**). ''Verifying a vocal tract model with a closed side-branch,'' J. Acoust. Soc. Am. **109**, 2983–2987.

Kinsler, L. E., Frey, A. R., Coppens, A. B., and Sanders, J. V. (**2000**). *Fundamentals of Acoustics* (Wiley, New York).

Lehman, M. E., and Swartz, B. (**2000**). ''Electropalatographic and spectrographic descriptions of allophonic variants of /l/,'' Percept. Mot. Skills **90**, 47–61.

Maeda, S. (**1982**). ''A digital simulation method of the vocal-tract system,'' Speech Commun. **1**, 199–229.

Narayanan, S., Alwan, A., and Haker, K. (**1997**). ''Toward articulatory-acoustic models for liquid approximants based on MRI and EPG data. I. The laterals,'' J. Acoust. Soc. Am. **101**, 1064–1077.

Narayanan, S., and Kaun, A. (**1999**). ''Acoustic modeling of tamil retroflex liquids,'' Proceedings of International Congress of Phonetic Society, San Francisco.

Prahler, A. (**1998**). ''Analysis and Synthesis of the American English Lateral Consonant,'' MIT thesis, Cambridge, Massachusetts.

Sondhi, M. M., and Schroeter, J. (**1987**). ''A hybrid time-frequency domain articulatory speech synthesizer,'' IEEE Trans. Acoust., Speech, Signal Process. **35**, 955–967.

Stevens, K. N. (**1998**). *Acoustic Phonetics* (The MIT Press, Cambridge, MA).

Zhang, Z., Espy-Wilson, C. Y., and Tiede, M. (**2003**). ''Acoustic modeling of American English lateral approximants,'' Proceedings of the Eighth Eurospeech Conference.

Using the Speech Transmission Index for predicting non-native speech intelligibility

Sander J. van Wijngaarden,[a] Adelbert W. Bronkhorst, Tammo Houtgast, and Herman J. M. Steeneken
TNO Human Factors, PO Box 23, 3769 ZG Soesterberg, The Netherlands

(Received 5 March 2003; revised 10 February 2003; accepted 15 December 2003)

While the Speech Transmission Index (STI) is widely applied for prediction of speech intelligibility in room acoustics and telecommunication engineering, it is unclear how to interpret STI values when non-native talkers or listeners are involved. Based on subjectively measured psychometric functions for sentence intelligibility in noise, for populations of native and non-native communicators, a correction function for the interpretation of the STI is derived. This function is applied to determine the appropriate STI ranges with qualification labels (''bad''–''excellent''), for specific populations of non-natives. The correction function is derived by relating the non-native psychometric function to the native psychometric function by a single parameter (ν). For listeners, the ν parameter is found to be highly correlated with linguistic entropy. It is shown that the proposed correction function is also valid for conditions featuring bandwidth limiting and reverberation.
 [DOI: 10.1121/1.1647145]

PACS numbers: 43.70.Kv, 43.71.Hw, 43.71.Gv [KWG] Pages: 1281–1291

I. INTRODUCTION

The intelligibility of speech is generally considered to depend on the characteristics of the talker and the listener, the complexity of the spoken messages, and the characteristics of the communication channel. Objective speech intelligibility predictions models have been shown to accurately predict the influence of the communication channel characteristics on speech intelligibility. An example of such a model is the Articulation Index (AI) model (French and Steinberg, 1947; Kryter, 1962), and more advanced models based on the AI, such as the Speech Intelligibility Index (SII; ANSI, 1997) and the Speech Transmission Index (STI; IEC, 1998; Steeneken and Houtgast, 1980; Steeneken and Houtgast, 1999).

In some cases, the overall speech intelligibility that is experienced is clearly affected by factors other than the physical characteristics of the channel. Individual talker differences (Bradlow *et al.* 1996; Hood and Poole, 1980) and message complexity (Pollack, 1964) were already mentioned. Other examples are individual differences in speaking style (Picheny *et al.* 1985) and hearing loss (Plomp, 1978).

An important determining factor for speech intelligibility is language proficiency, of talkers (van Wijngaarden *et al.*, 2002a) as well as listeners (van Wijngaarden *et al.*, 2002b). Learning a language at a later age results in a certain degree of limitation to language proficiency (Flege, 1995). So-called non-native speech communication is practically always less effective than native communication. The intelligibility effects of non-native speech production and non-native perception show an interaction with speech transmission quality (the quality of the channel). Speech degrading influences such as noise (Buus *et al.*, 1986; Florentine *et al.*, 1984; Florentine, 1985) and reverberation (Nábelek and Donahue, 1984) aggravate the intelligibility effects of non-native speech communication.

For various applications, it would be very useful to have an objective, quantitative intelligibility prediction method that is capable of dealing with non-native speech. In Sec. II of this article, the suitability of existing objective speech intelligibility prediction models for non-native applications is discussed.

Section III continues by proposing a way in which the Speech Transmission Index (STI) can be used in various non-native scenarios. Section IV contains a validation of this approach for speech in noise, bandwidth limiting, and reverberation.

II. SUITABILITY OF OBJECTIVE INTELLIGIBILITY PREDICTION MODELS FOR NON-NATIVE SPEECH

A. Speech transmission quality versus speech intelligibility

Speech intelligibility can be thought of as the success that a source and a receiver (talker and listener) have in transmitting information over a channel. Each unique talker–listener pair has a certain potential for transmitting messages of a given complexity. The quality of the transmission channel determines how much of this potential is realized. A typical transmission channel could be a phone line, a public address system, or the acoustic environment of a specific room.

Objective prediction models are especially good in quantifying speech transmission quality. The influence of factors determining speech intelligibility related to talkers and listeners, rather than the channel, has been incorporated to a lesser degree. A proficiency factor has been proposed (Pavlovic and Studebaker, 1984) for incorporating talker- and listener-specific factors into the framework of the articulation index, but this has not been developed to a level where practically useful predictions can be obtained.

[a]Electronic mail: vanwijngaarden@tm.tno.nl

TABLE I. Relation between STI and qualification labels.

Label	STI lower boundary	STI upper boundary
Bad	···	0.30
Poor	0.30	0.45
Fair	0.45	0.60
Good	0.60	0.75
Excellent	0.75	···

To predict the intelligibility of non-native speech, the interaction between speech transmission quality and language proficiency (quantified, for instance, by a linguistic entropy measure) of talkers and listeners needs to be studied.

B. Features of the SII, STI, and SRS models

At least three speech intelligibility prediction models presented in open literature show promise for predicting the effects of non-native factors: the Speech Intelligibility Index (SII; ANSI, 1997), the Speech Transmission Index (STI; IEC, 1998), and the Speech Recognition Sensitivity (SRS; Müsch and Buus, 2001a) models. Features of each separate model that are related to suitability for non-native applications are summarized in this section.

1. The Speech Transmission Index (STI)

The Speech Transmission Index combines the general concept of the articulation index with the observation that speech intelligibility is related to the preservation of the envelope spectrum of speech. The transmission quality of a channel is characterized by its modulation transfer function (MTF), which quantifies distortions in both the time and frequency domain (Houtgast *et al.*, 1980). The MTF is expressed as a matrix, giving a modulation index m as a function of 7 octave bands (125–8000 Hz) and 14 modulation frequencies (0.63–12.5 Hz). For conversational speech, using a wider range of modulation frequencies (up to 31.5 Hz) gives more accurate STI results in the presence of reverberation (van Wijngaarden and Houtgast, 2003).

The STI is purely a measure of speech transmission quality: it indicates to which degree the channel allows talkers and listeners to fulfill their potential for speech communication. Individual properties of talkers and listeners are not taken into account. The relation between STI and speech intelligibility has been verified and documented using various speech intelligibility measures (e.g., Houtgast and Steeneken, 1984).

To facilitate the use of the STI as an acceptability criterion, qualification labels (''bad''–''excellent'') have been attached to ranges of STI values (Table I). The ranges of Table I are based on the relation between STI and intelligibility for normal hearing, native subject populations, pragmatically taking ''round'' STI values as the category boundaries (ISO, 2002).

Commercially available measuring devices and measuring software can be used for *in situ* STI measures, or the STI can be calculated from theoretical knowledge of the channel (such as the output of room acoustics simulation software).

2. The Speech Intelligibility Index (SII)

The SII is an extension of a widely used version of the articulation index (Kryter, 1962) by incorporation the findings of Pavlovic, Studebaker, and others (e.g., Pavlovic, 1987; Pavlovic and Studebaker, 1984; Studebaker *et al.*, 1987). Instead of the MTF, the SII uses a band audibility function (based on the speech-to-noise ratio as a function of frequency) to quantify the contributions of different frequency bands to speech intelligibility.

The contribution of different frequencies to the SII is given by a frequency importance function. The ANSI standard associates different frequency importance functions with different measures of speech intelligibility. This means that the SII is not just a measure of speech transmission quality: it is designed to predict intelligibility according to different evaluation methods. Different SII values may be calculated for the same channel, depending on the chosen frequency importance function.

Poor communication is associated with SII below 0.45; good communication yields an SII in excess of 0.75.

3. The Speech Recognition Sensitivity (SRS) model

The SRS model, which uses statistical decision theory to explain how information is used across frequency, has quite recently been proposed, and has been shown to accurately predict intelligibility in a number of cases (Müsch and Buus, 2001a; 2001b). The SRS model explicitly includes listener-related factors that determine intelligibility, such as the power of ''cognitive noise'' that can be adjusted to fit the listener population. The predictability of the speech material (number of response alternatives in a recognition task) is also included in the model. The model can be applied to (qualitatively) explain the relation between linguistic entropy and speech intelligibility (see also Bronkhorst *et al.* 2002; van Rooij, 1991; van Wijngaarden *et al.*, 2002b). This is an attractive feature in the context of non-native speech communication, where linguistic entropy tends to be an important variable.

4. STI, SII, and SRS in relation to non-native speech

Of the prediction models described above, the SRS model is theoretically best equipped for dealing with non-native speech. Effects of non-native speech communication can be integrated directly through the model parameters. Despite the elegance of such a solution, the choice was made to base the approach proposed in this paper on the STI (in a manner to allow easy adaptation to the SII), not the SRS. The main reason is that, in order to make the results of our study as readily applicable as possible, a prediction method is sought that can be integrated seamlessly with tools already widely used to predict speech intelligibility, by researchers as well as engineers. The fact that the SRS method has (yet) to prove its validity and applicability as an operational tool outweighs, for the purposes of the current study, its theoretical appeal.

III. PROPOSED CORRECTION OF THE STI QUALIFICATION SCALE FOR NON-NATIVE SPEECH COMMUNICATION

A. Rationale for correcting the qualification scale

Modifying the STI method by including a proficiency factor (Pavlovic *et al.*, 1984) may seem attractive at first. It would change the index from a measure of speech transmission quality into more of an overall intelligibility predictor. However, the STI is commonly used to characterize communication channels (rooms or equipment), often for verification against certain minimum criteria (ISO, 2002). A talker-, listener-, or message-dependent STI may correlate better with intelligibility, but may also create confusion: the same channel can be characterized by various STI values, depending on factors other than the channel.[1]

We therefore propose to leave the STI calculation and measurement procedures unchanged. Instead, our approach is to make the *interpretation* of the STI dependent on language proficiency. This is done by correcting the qualification scale (Table I) for non-native speech communication. For each population of talkers and listeners, a specific correction applies, which makes sure that the qualification labels (''bad''–''excellent'') correspond to the same speech intelligibility as they normally do for native speech.

B. Method for correcting the qualification scale

1. Principles of the correction function

The key to relating the STI to non-native intelligibility lies in the difference between the psychometric functions for native and non-native speech recognition. The psychometric function $\pi(r)$ gives the percentage of correctly recognized test units (phonemes, words, or sentences), as a function of an independent variable r, which is a physical measure of speech degradation (such as speech-to-noise ratio, SNR). In cases where the independent parameter has a monotonic relationship with the STI, a correction function can be derived that relates a calculated or measured (''native'') STI, to a ''non-native STI'' that is required to obtain the same intelligibility in case of non-native communication. This correction function can then be applied to the qualification scale boundaries, relating the standard STI to the proper qualification labels for non-native communication. Please note that the correction function is used to calculate the *required* STI to achieve a certain level of intelligibility, not to change the STI value itself.

Figure 1 is a visual representation of a correction function, where the independent variable r is the speech-to-noise ratio. The noise spectrum is presumed to be equal to the long-term average speech spectrum, and no speech degrading influences other than noise are present. This results in a simple relation between STI and SNR, represented by the double horizontal axis labeling. The L1 and L2 psychometric curves in Fig. 1 are fictitious. Intelligibility qualifications (Table I) represent different levels of intelligibility (the vertical axis in Fig. 1). By following the arrows, the required native STI to reach a certain level of intelligibility is translated into a required non-native STI, that corresponds to the same intelligibility.

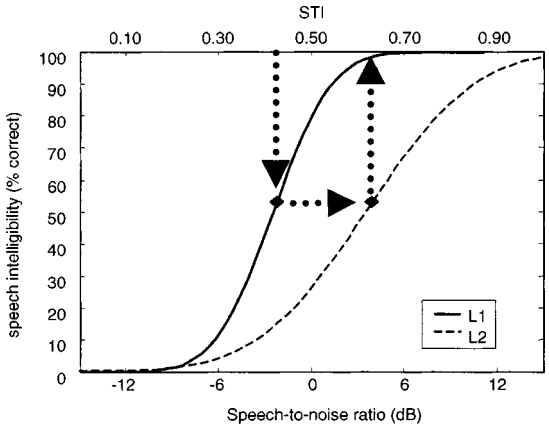

FIG. 1. Schematic representation of the procedure for deriving a correction function for non-native interpretation of the STI. The psychometric curves are fictitious, but representative of those found when measuring native and non-native sentence intelligibility.

Functions $f(r)$ to calculate the STI for different choices of physical parameter r, such as bandwidth, speech-to-noise ratio (SNR), and reverberation times, are known. The operations visualized by Fig. 1 can only be carried out mathematically if the relation $f(r)$ is reversible, meaning that Eq. (1) must be a unique function

$$r = f^{-1}(\mathrm{STI}). \tag{1}$$

This is, for instance, the case for additive noise that has the same long-term spectrum as speech, provided that no other speech degrading factors are present (the case of Fig. 1). The SNR then fully determines the STI, so each value of the STI corresponds to a single SNR.[2] All that is needed to calculate a correction function is a model of the psychometric functions shown in Fig. 1. Of the possible choices for independent variable r, the SNR is the easiest and most directly accessible option, and will be used throughout this paper.

After mathematically deriving (or numerically implementing) the correction of Fig. 1, it can be applied to the STI boundaries of Table I. For each population of L2 talkers and listeners, the correction function will be different, leading to specific versions of Table I.

2. Deriving the correction function from psychometric function models

Assuming that the psychometric function for native (L1) speech may be approximated by a cumulative normal distribution (e.g., Versfeld *et al.*, 2000), it is best described by

$$\pi_{L1}(r) = \Phi\left(\frac{r-\mu_{L1}}{\sigma_{L1}}\right), \tag{2}$$

where $\Phi(z)$ is the standardized cumulative normal distribution, μ_{L1} and σ_{L1} are the mean and standard deviation of the distribution for fully native speech, respectively. A straightforward way to derive a correction function is to assume that Eq. (2) also holds for non-native speech, in which case μ_{L2} and σ_{L2} will depend on the average proficiency level of the population. By solving $\pi_{L1} = \pi_{L2}$, substituting Eq. (1), a correction function as given in Eq. (3) is obtained

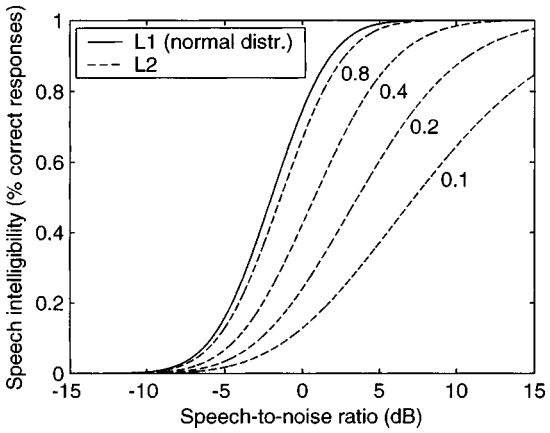

FIG. 2. Examples of L2 psychometric functions derived from a cumulative normal L1 psychometric function ($\mu=-2,\sigma=3$), according to Eq. (4), for $\nu=0.8$, $\nu=0.4$, $\nu=0.2$, and $\nu=0.1$.

$$\mathrm{STI}_{L2}=f\left(\sigma_{L2}\left(\frac{f^{-1}(\mathrm{STI}_{L1})-\mu_{L1}}{\sigma_{L1}}\right)+\mu_{L2}\right). \tag{3}$$

Thus, assuming that, for a certain type of test that measures intelligibility as a function of r, μ_{L1}, and σ_{L1} are known, the information needed to correct a required STI_{L1} into an equivalent required STI_{L2} is a specification of the L2 population in terms of μ_{L2} and σ_{L2}.

Earlier results show that μ_{L2} and σ_{L2}, when estimated as two separate parameters, are not independent. They tend to be highly correlated: when the mean of the psychometric function shifts, the slope also changes. This is related to the behavior of L1 and L2 psychometric functions near 0% intelligibility. In all cases, intelligibility starts to ''build up'' from 0% around the same SNR, for listeners (van Wijngaarden *et al.*, 2002b: Fig. 11) as well as talkers (van Wijngaarden *et al.*, 2002a: Fig. 6). In other words, L1 and L2 psychometric curves share a common origin (in Fig. 1 around -12 dB). The most likely reason is that the detection threshold for L1 and L2 speech is the same; hence, contributions to intelligibility are expected from the same SNR (the detection threshold) upward. However, as the SNR increases, intelligibility rises more quickly for L1 than L2 subjects, causing the psychometric functions to diverge. This suggests that, instead of estimating the two parameters μ_{L2} and σ_{L2}, the L2 psychometric function can be derived from the L1 psychometric function using a single parameter ν, according to Eq. (4)

$$\pi_{L2}(r)=1-(1-\pi_{L1}(r))^{\nu}. \tag{4}$$

The parameter ν (cf. Boothroyd and Nittrouer, 1988) can assume any value between 0 (no speech recognition at all) and 1 (native speech communication), and quantifies the degree to which non-native intelligibility is able to keep up with native intelligibility as the SNR increases, from the detection threshold upward. A family of psychometric functions according to Eq. (4), derived from a L1 psychometric function that follows a normal distribution, is shown in Fig. 2.

It appears that Eq. (4) describes earlier experimental data very well, with only one parameter (ν) instead of two (μ_{L2} and σ_{L2}), while allowing a very intuitive interpretation. Another advantage has to do with artifacts at low SNRs when calculating the STI correction function. Small errors in estimates of μ and σ may lead to an L2 psychometric function that is locally higher than the L1 function. Although the difference in intelligibility at these SNRs is very small, the effect on the correction function according to Eq. (3) can be noticeable.

A disadvantage of Eq. (4) is that a correction equation cannot be obtained in mathematically closed form by simply solving $\pi_{L1}=\pi_{L2}$, if the L1 psychometric curve is modeled as a cumulative normal distribution [Eq. (1)]. Sometimes the logistic function is used as an approximation of the cumulative normal distribution (e.g., Versfeld *et al.*, 2000). In that case, the correction function in closed form can be calculated (see the Appendix). However, due to differences around the tails of the distribution, small but noticeable deviations in the calculated correction function are observed compared to a correction function based on the cumulative normal distribution.

A numerical implementation of the correction function as a function of ν was easily realized, based on Eqs. (1), (2), and (4), following the procedure visualized in Fig. 1. This numerical implementation was used to calculate the correction functions used in this study.

3. Complexity of test material to use for measuring psychometric functions

Message complexity and context effects are always key factors for speech intelligibility (Pollack, 1964), but especially when non-native listeners are involved. Context effects influence speech intelligibility differently for non-natives than for natives (e.g., Mayo *et al.*, 1997; van Wijngaarden *et al.*, 2002b). This means that a correction function as visualized in Fig. 1 depends on the amount of contextual information in the test material.

Our aim for the correction function is to allow interpretations of the STI for non-natives in the same way as for natives, in practical situations where non-native talkers or listeners are involved. This means that the test material used to obtain correction functions must contain the same sources of contextual information that are also expected in practice (telephone conversations, public address messages, etc.). Correction functions based on, for instance, psychometric curves for phoneme recognition would have little practical meaning; differences in use of contextual information would simply not be included in the correction. A suitable choice of test material, representative of common situations involving non-natives, seems to be a corpus of everyday sentences, carrying a representative amount of semantic, syntactic, and lexical redundancy.

The corrections used in this paper are all based on psychometric functions obtained using an implementation of the Speech Reception Threshold (SRT) procedure (Plomp and Mimpen, 1979). The SRT is the SNR at which the intelligibility of short, redundant sentences is 50%. Additional measurements, at fixed SNRs around the SRT, were used to estimate the slope of the psychometric function (van

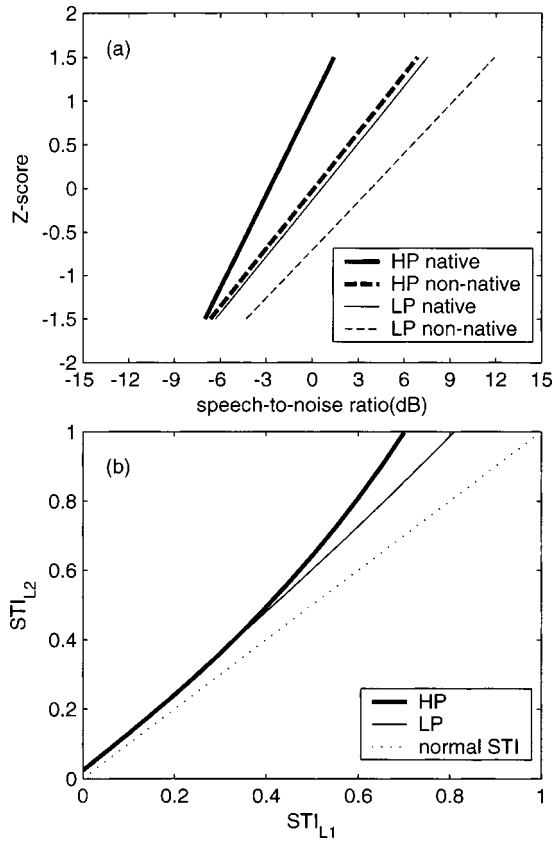

FIG. 3. (a) Psychometric functions, in terms of Z-score as a function of SNR, for high-predictability (HP; $\nu=0.36$, $\mu_{L1}=-2.8$ dB, and $\sigma_{L1}=2.8$ dB) and low-predictability (LP; $\nu=0.50$, $\mu_{L1}=0.6$ dB, and $\sigma_{L1}=4.6$ dB) sentences (after Florentine, 1985); (b) the STI correction functions derived from these psychometric functions.

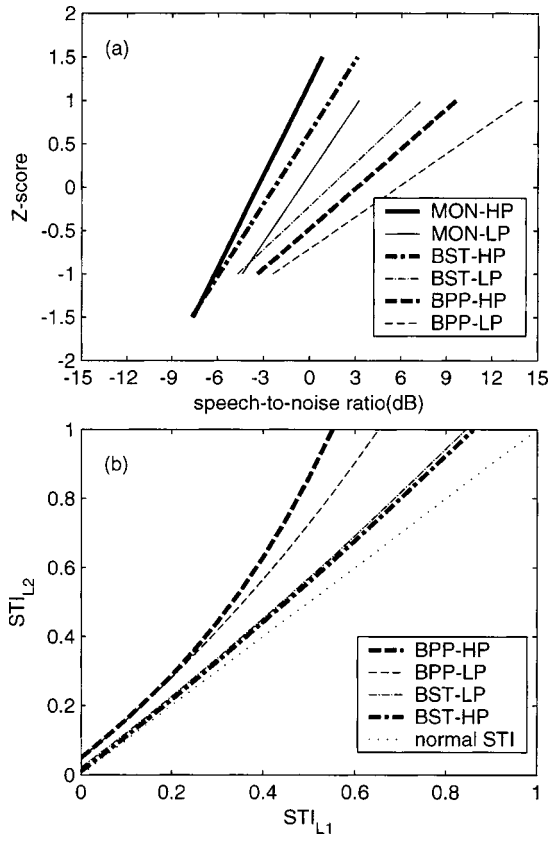

FIG. 4. (a) Psychometric functions, in terms of Z-score as a function of SNR, for high-predictability (HP; $\mu_{L1}=-3.4$ dB and $\sigma_{L1}=2.8$ dB) and low-predictability (LP; $\mu_{L1}=-0.5$ dB and $\sigma_{L1}=3.8$ dB) sentences, for three groups of nine subjects: monolinguals (MON), early bilinguals (bilingual since toddler, BST), and late bilinguals (bilingual post puberty, BPP; after Mayo *et al.*, 1997); (b) the STI correction functions derived from these psychometric functions.

Wijngaarden *et al.*, 2001). The speech recordings that were used were part of the VU corpus (male talker) of SRT sentences (Versfeld *et al.*, 2000).

C. Qualification labels for non-native listeners

1. Correction functions for different populations of listeners

To summarize the previous section: a correction of the qualification scale can be derived from any study that results in native and non-native intelligibility of everyday sentences, as a function of SNR. Several studies yielding such results for non-native listeners have been reported.

Florentine (1985) used the Speech Perception in Noise (SPIN) test (Kalikow and Stevens, 1977) to measure intelligibility of high-predictability (HP) and low-predictability (LP) sentences, with a mixed population of 16 non-native subjects. Results were compared to similar results for 13 native (U.S. English) listeners. The final word in HP sentences was semantically predictable, the final word in LP sentences was not. Scoring was based only on recognition of the final word. This makes the HP sentences a more suitable candidate for deriving a correction function; since semantic redundancy is important for practical non-native scenarios, it should be reflected by the correction function.

The original data taken from Florentine (1985) are shown in Fig. 3(a). From the reported psychometric functions (given as Z-scores as a function of SNR), separate values of μ_{L1} and σ_{L1} were taken for HP and LP sentences, and values of ν were obtained using a Gauss–Newton nonlinear fitting procedure. The correction functions for HP ($\nu=0.36$) and LP ($\nu=0.50$) sentences are given in Fig. 3(b).

The difference between correction functions for high-predictability and low-predictability sentences is clear. The difference in ν can be seen as a quantification of Florentine's finding that non-natives are not as able as natives to make use of semantic redundancy.

Following an approach similar to Florentine's, Mayo *et al.* (1997) investigated speech perception of Mexican–Spanish-speaking listeners in English. Groups of early bilinguals (bilingual-since-toddler, BST) and late bilinguals (bilingual-post-puberty, BPP) were compared to native English subjects using the SPIN test.[3] All groups consisted of nine subjects. The original data are given in Fig. 4(a), the derived correction functions in Fig. 4(b).

The correction functions differ between early bilinguals ($\nu=0.64$ for HP, $\nu=0.57$ for LP) and late bilinguals ($\nu=0.15$ for HP, $\nu=0.22$ for LP). The proficiency differences are reflected by differences in ν, and in relation to that, by the slope of the correction function.

Earlier data from trilingual non-native listeners (van Wijngaarden *et al.*, 2002b) yield similar results for ν values

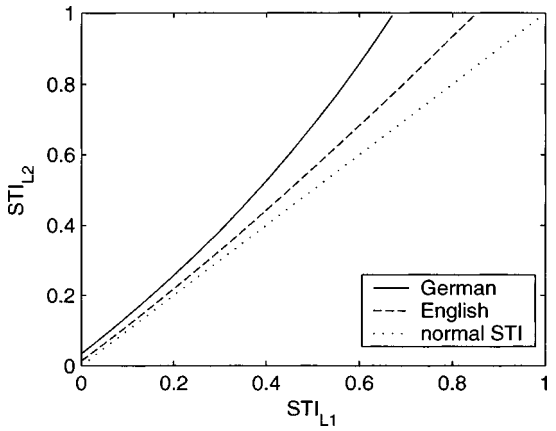

FIG. 5. STI correction functions for trilingual Dutch listeners of German (low proficiency, $\nu=0.21$) and English (high proficiency, $\nu=0.52$); $\mu_{L1}=-0.50$ dB and $\sigma_{L1}=3.21$ dB (after van Wijngaarden *et al.*, 2002b).

and correction functions as the data by Mayo *et al.* The trilingual subjects were highly proficient in English, and showed poor to moderate proficiency in German. The SRT sentence material used to obtain these results is closest to the HP sentences of the SPIN test. Calculated mean ν values are 0.21 (German speech) and 0.52 (English speech). The corresponding STI correction functions are given in Fig. 5.

2. Relation between STI and qualification labels for non-native listeners

By applying the correction functions of Figs. 3, 4, and 5 to Table I, the STI qualification label boundaries of Table II are obtained. From Figs. 3 and 4, the functions for HP sentences are used.

Table II shows how qualitative descriptions of populations of listeners, such as early versus late bilinguals, or low-proficiency versus high-proficiency listeners, can be used for the interpretation of the STI. The same speech transmission quality (STI) leads to different qualifications of intelligibility, depending on the population of listeners.

The SRT data behind Fig. 5 can also be related to L2 listeners' proficiency in a quantitative way (van Wijngaarden *et al.*, 2002b). Along with SRT results, estimates of linguistic entropy were obtained using the letter guessing procedure (LGP; Shannon and Weaver, 1949; van Rooij, 1991). This orthographic procedure, which measures the extent to which subjects are able to make use of linguistic redundancy, can be seen as a measure of proficiency, which correlates well with non-native speech intelligibility. A strong relation between linguistic entropy and the ν parameter is expected. Linguistic entropy and psychometric function estimates were obtained separately, using different subject groups (which where matched for L2 proficiency, age, and gender). Unfortunately, this means that LGP results from that study cannot be related to the ν parameter on an individual level. However, the mean linguistic entropy L can be compared to the mean value of ν for three different languages: native Dutch ($L=0.53$, $\nu=1$ by definition), English ($L=0.70$, $\nu=0.57$), and German ($L=0.87$, $\nu=0.23$). The explained variance by correlating these data ($R^2=0.995$), if only on the basis of three observations, seems promising.

To further investigate this relation, new experiments were carried out with eight native and eight non-native listeners. The non-native group consisted of L2 learners of the Dutch language, with different language backgrounds (American English, Amharic, German, Greek, Hungarian, Indonesian, Polish, and Tigrinya) and different levels of proficiency. All were late bilinguals, differing mainly in L2 experience. Six of the listeners could be classified as relatively low-proficiency subjects, with average of 4 years of experience with the Dutch language, and a mean self-reported proficiency (on a five-point scale) of 3.2. The other two subjects were classified as high proficiency, with an average of 13 years of experience, and a self-reported proficiency of 4.5. The native group was matched to the non-native group in terms of age, gender, and level of education. All subjects were between 19 and 33 years of age, and were taking part in (or had recently completed) higher education in the Netherlands.

In order to be able to estimate the ν parameter for the non-native subjects, individual psychometric functions were measured for all 16 listeners. Sentences in noise were presented at five fixed SNRs, centered around the SRT with 2-dB intervals. The mean percentage of correctly recognized sentences was measured using 13 sentences per SNR, after which the psychometric function was fitted. This procedure was repeated three times with each listener; the mean of these three fits was taken to obtain a more accurate estimate.

For the native subjects, the psychometric function was assumed to be a cumulative normal distribution. The mean native psychometric function in this experiment is described by $\mu_{L1}=-4.38$ dB and $\sigma_{L1}=2.20$ dB. For each individual non-native listener, the psychometric function was related to the mean native psychometric function according to Eq. (4), by fitting the ν parameter.

A significant correlation was found between linguistic

TABLE II. Relation between STI and qualification labels for non-native listeners, after correction according to Figs. 4 and 6 (HP sentences), and Fig. 7. The text ">1" indicates that an STI greater than 1 would be required, meaning that this qualification cannot be reached.

STI label category boundary	Standard	Florentine (1985)	Mayo *et al.* (1997) BST (early)	Mayo *et al.* (1997) BPP (late)	van Wijngaarden *et al.* (2002) English	van Wijngaarden *et al.* (2002) German
Bad–poor	0.30	0.36	0.33	0.44	0.33	0.38
Poor–fair	0.45	0.57	0.50	0.74	0.50	0.60
Fair–good	0.60	0.79	0.68	>1	0.68	0.86
Good–excellent	0.75	>1	0.86	>1	0.87	>1

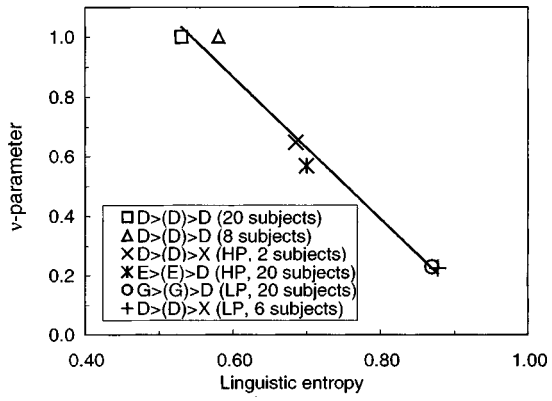

FIG. 6. Relation between mean linguistic entropy and the ν parameter, for Dutch learners of German and English (20 subjects) and learners of Dutch from various language backgrounds (two high-proficiency listeners, six low-proficiency listeners; $R^2=0.98$).

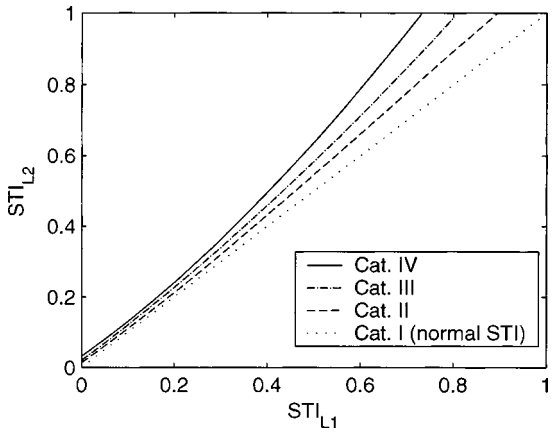

FIG. 7. STI correction functions for L2 talkers of the Dutch language, for different degrees of foreign accent strength (cat. I–cat. IV; van Wijngaarden *et al.*, 2002a). Category I means that the talker has (virtually) no foreign accent, category IV means that the accent is severe (see Table III for the corresponding values of ν, μ_{L1}, and σ_{L1}).

entropy and the ν parameter on an individual level ($R^2=0.74$). The means of the native, high-proficiency, and low-proficiency subjects in this experiment are given in Fig. 6, along with the means from the earlier experiments in German (low proficiency) and English (high proficiency).

As seen in Fig. 6, linguistic entropy estimates are found in the 0.50–0.60 range for native subjects; linguistic entropy is higher for non-natives. Despite the differences in test languages and language backgrounds of the listeners, the data from the two experiments seem to fit the same relation between linguistic entropy and the ν parameter. The importance of this relation lies in the fact that the experimental procedures to determine a subject's linguistic entropy requires only a fraction of the time needed to assess the ν parameter on an individual basis. Through the ν parameter, the interpretation of the STI for non-natives can be derived from linguistic entropy estimates.

D. Qualification labels for non-native talkers

Psychometric functions describing the intelligibility of foreign-accented speech are similar to the ones observed for non-native listeners, although non-native speech production tends to have a smaller overall impact on speech intelligibility than non-native perception.[4] Previously reported data on talkers from four different categories of accent strength (numbered I–IV, ranging from "native" to "severe accent") were used to calculate STI correction functions (Fig. 7). The resulting STI label categories are given in Table III.

Figure 7 and Table III are based on data obtained with native listeners. Translation of the STI to objective qualification labels when non-native talkers *and* non-native listeners are involved is not possible using Tables II and III, due to interaction effects. The overall intelligibility may be higher than expected when simply adding up the individual effects of non-native talking and non-native listening. This so-called interlanguage speech intelligibility benefit may occur when the native language of talker and listener is the same, but also if their language background is different (Bent and Bradlow, 2003).

IV. VALIDATION OF THE QUALIFICATION SCALE CORRECTION

A. Validation issues

If speech is degraded by additive, steady-state noise only, there is little reason to question the validity of the correction functions described above. With the already-mentioned limitations regarding the amount of contextual information in the intelligibility test material, the approach of correcting the required STI for a certain level of intelligibility (by finding the STI value that leads to equal intelligibility for non-native communication) should work by definition. However, in the presence of speech degrading influences other than steady-state noise, the validity of this approach remains to be proven. Two important sources of speech degradation are bandwidth limiting and reverberation.

Using the STI correction functions for non-native speech communication in cases where the SNR depends on frequency implies the assumption that the relative importance of all frequency bands is the same as for native speech. The validity of this assumption is verified by measuring speech intelligibility of bandwidth-limited speech in noise for non-native and native listeners.

In case of reverberation, the STI model expressed the degree of speech degradation in terms of an "equivalent speech-to-noise ratio," which is calculated through the modulation transfer function (MTF). Again, the correction function approach is only valid under the assumption that

TABLE III. Relation between STI and qualification labels for non-native talkers differing in degree of foreign accent, after correction according to Fig. 7. The text ">1" indicates that an STI greater than 1 would be required, meaning that this qualification cannot be reached. The mean ν value for each category is also given ($\mu_{L1}=-0.50$ dB, $\sigma_{L1}=3.21$ dB).

STI label boundary	Category: Standard STI (Cat. I)	Cat. II (ν=0.67)	Cat. III (ν=0.48)	Cat. IV (ν=0.32)
Bad–poor	0.30	0.32	0.34	0.36
Poor–fair	0.45	0.49	0.52	0.56
Fair–good	0.60	0.66	0.71	0.79
Good–excellent	0.75	0.85	0.91	>1

this MTF-based operation is equally valid for non-native as for native communicators. To investigate this, speech intelligibility is measured under reverberant conditions, with native and non-native listeners.

Once intelligibility measurements in bandwidth-limited and reverberant conditions have been carried out, there is a straightforward procedure to investigate whether the validity of the proposed correction functions extends to these conditions. The correction functions are based on measures of speech intelligibility as a function of STI (Fig. 1). However, the only independent parameter [r in Eq. (1)] that was varied to obtain different values of the STI was the speech-to-noise ratio. When bandwidth limiting and reverberation come into play, the relation between intelligibility and STI (native and non-native) must remain the same as the noise-only case for the correction functions to remain valid.

In other words: regardless of the type of degradation, a certain level of intelligibility (such as 50% intelligibility of sentences) must always correspond to the same STI. This was one of the design objectives for the STI method, and normally found to be true for native speech (Steeneken and Houtgast, 1980). For the proposed correction functions to be valid, the same must be true for non-native speech. Maintaining the same, consistent relation between (corrected) STI and speech intelligibility (the same for bandwidth limiting and reverberation as for noise-only) is a necessary and sufficient condition for validity.

B. Effects of bandwidth limiting

The same 16 listeners who participated in the SRT and LGP experiments reported above and shown in Fig. 6 took part in an experiment consisting of SRT measurements in bandwidth-limited conditions. The experiments were carried out in Dutch, using the eight Dutch subjects to obtain a native baseline. The eight non-native listeners were treated as a single group, and were all presented with the same conditions as the native listeners. SRT sentences pronounced by a single male Dutch speaker were used, in a wideband condition as well as three bandwidth-limited conditions. The bandwidth-limited conditions offered a bandwidth of 4 octaves (500-Hz–4-kHz bands), 3 octaves (500-Hz–2-kHz bands) and 2 octaves (1-kHz and 2-kHz bands). Complementary stop-band noise was added to the bandlimited speech, to prevent spreading of information into adjacent bands through nonlinear auditory phenomena.

In each of the conditions, the SRT was measured (the SNR corresponding to 50% sentence intelligibility). The corresponding STI was calculated, based on the available bandwidth and the SNR resulting from the SRT measurement. Because the SRT is the SNR corresponding to a fixed level of intelligibility (namely 50%), the ''STI at the SRT'' should be a constant value for the proposed correction function approach to be valid; as indicated in the previous section, this is a necessary and sufficient condition for validity. Results are given in Fig. 8.

For non-native as well as native listeners, the STI at the SRT is fairly constant. With the exception of the difference between the wideband and the three-octave condition for the native group, none of the within-group differences in Fig. 8 is statistically significant ($p<0.05$). The average across all bandwidth-limited conditions (native and non-native considered separately) does not differ significantly from the wideband condition. This means that the proposed approach is also valid for bandwidth-limited conditions. To further illustrate this, Table IV compares corrected native STI values to the non-native STI values as shown in Fig. 8. The close correspondence between corrected native STI and measured non-native STI demonstrates that the correction function can indeed be used in conditions featuring noise as well as bandwidth limiting.

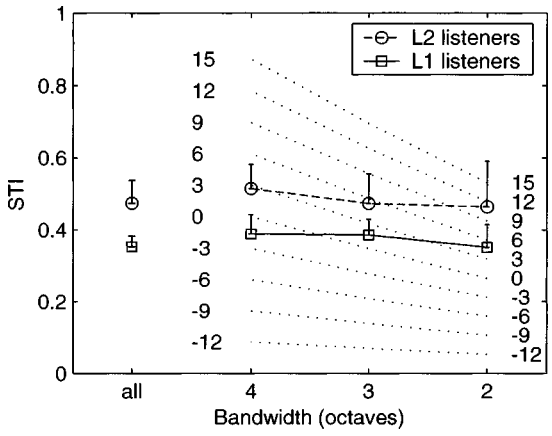

FIG. 8. STI at the SRT, for conditions with and without bandwidth limiting. The dotted lines indicate the maximum STI at each bandwidth, as a function of the SNR. The errorbars indicate the standard deviation ($N=24$; 8 listeners, each 3 SRT measurements per condition).

The mean native STI results fall in the range between 0.30 and 0.45, leading to a classification of ''poor'' according to the standard table (Table I). The mean non-native results for each condition would be (incorrectly) categorized as ''fair.''

The ν value for each non-native listener was determined in a separate experiment, following the procedure described above in relation to Fig. 6. Using the mean value of the ν parameter across all L2 listeners ($\nu=0.33$), a correction function for this population of non-native listeners was obtained. After applying this correction function, the L2 results correctly fall into the ''poor'' category (the corresponding STI range after correction is $0.37<\mathrm{STI}<0.59$).

C. Effects of reverberation

In addition to bandwidth-limiting conditions, SRT experiments were carried out in conditions featuring reverberation. The same subjects participated, and speech material by the same talker was used.

TABLE IV. ''STI at the SRT'' results with and without bandwidth limiting, for non-native and native subjects. STI means and s.d.'s are calculated across 8 subjects, 3 observations per condition.

	L1 STI		L1 STI after correction		L2 STI	
Condition	Mean	s.d.	Mean	s.d.	Mean	s.d.
Wideband	0.35	0.03	0.44	0.05	0.47	0.07
4 octaves	0.39	0.05	0.50	0.07	0.51	0.07
3 octaves	0.39	0.04	0.50	0.06	0.47	0.08
2 octaves	0.35	0.06	0.44	0.09	0.46	0.13

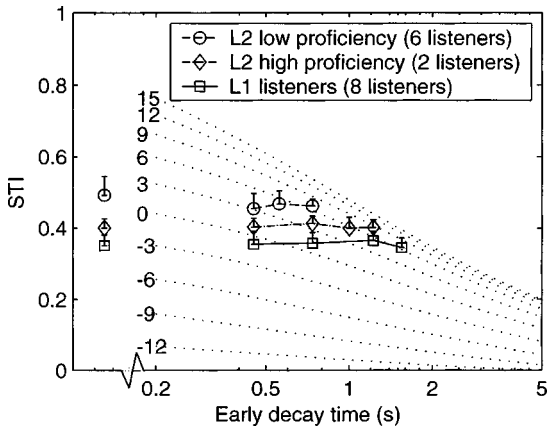

FIG. 9. STI at the SRT, for conditions with and without reverberation. The dotted lines indicate the maximum STI at each EDT, as a function of the SNR. The errorbars indicate the standard deviation (2 to 8 listeners, each 3 SRT measurements per condition). The EDT in this plot is the mean EDT in the octave bands 125 Hz–8 kHz. The STI calculation is nonstandard, and includes modulation frequencies up to 31.5 Hz.

To obtain conditions differing in early decay time (EDT), but with as little other differences as possible, the same highly reverberant room was used for all conditions. The only difference between conditions was the amount of acoustic absorption material in the room. Impulse responses with a length of approx. 1.5 s were recorded in each condition, and stored digitally. From these impulse responses, the EDT was measured in each octave band.

In order to be able to present reverberant speech to the subjects without physically having to change the acoustic properties of the reverberant room between conditions, the prerecorded impulse responses were used for the stimulus presentations. The SRT test sentences were convolved with the impulse responses in real time, using an overlap-add procedure. All stimuli were presented diotically, excluding binaural effects (for which the STI has not been validated) from the experiment. For the experiment, conditions with EDTs between approx. 0.5 and 2 s were used. The eight native subjects all participated in the same conditions. The differences in proficiency between the L2 subjects were such that some were able to carry out the test at longer EDTs than others. For this reason, the same distinction between ''high proficiency'' (two subjects) and ''low proficiency'' (six subjects) used in Fig. 6, was again applied. Results of STI calculations at the SRT as a function of EDT, similar to Fig. 8, are given in Fig. 9.

The STI calculations underlying Fig. 9 are based on a modulation frequency range of 0.63–31.5 Hz instead of the standardized range (0.63–12.5 Hz), for reasons related to speaking style and envelope spectrum of the talker (van Wijngaarden and Houtgast, 2003). In earlier, similar experiments concerned with the effects of reverberation, the ''STI at the SRT'' was found to be independent of early decay time for normal hearing as well as hearing impaired listeners (Duquesnoy and Plomp, 1980).

For all three groups in Fig. 9, the STI at the SRT appears to be independent of EDT, and (nearly) the same as for the condition without reverberation. The mean values for the reverberant conditions do not differ significantly from the condition without reverberation. This indicates that the same STI always represents the same level of intelligibility, in noise as well as reverberation, meaning that the proposed correction function approach is valid for reverberant conditions as well. This is illustrated by Table V, which shows that only a small difference remains between the measured non-native STI and the native STI after correction.

V. DISCUSSION AND CONCLUSIONS

A. The ν parameter

The approach for non-native interpretation of the STI, as proposed in this article, is based on a few novel concepts. Perhaps the most important of these is modeling the non-native psychometric function by relating it to the native psychometric function, through a single parameter ν. This has several advantages, such as its intuitive interpretation, and the fact that this parameter can be related to linguistic entropy (which can be measured with relative ease). Among the disadvantages of this approach is the fact that the non-native psychometric function, even when derived from a native function that *is* modeled as a cumulative normal distribution, does not exactly follow such a normal distribution itself. This causes mathematical complications, and may take away some of its theoretical appeal. However, measurements of the non-native psychometric function appear to be in support of this psychometric function model. The particular way in which differences in proficiency result in a family of psycho-

TABLE V. ''STI at the SRT'' results with and without reverberation, for non-native and native subjects. STI means and s.d.'s are calculated across 8 subjects, 3 observations per condition. The early decay time given in this table is the mean EDT across octave bands 125 Hz–8 kHz.

Early decay time (s)	L1 STI		High proficiency				Low proficiency			
			L1 STI after correction		L2 STI		L1 STI after correction		L2 STI	
	Mean	s.d.	Mean	s.d.	Mean	s.d.	Mean	s.d.	Mean	s.d.
(no rev.)	0.35	0.03	0.38	0.03	0.40	0.03	0.48	0.05	0.49	0.05
0.59	0.35	0.04	0.39	0.04	0.40	0.03	0.49	0.05	0.45	0.05
0.75	⋯	⋯	⋯	⋯	⋯	⋯	⋯	⋯	0.47	0.04
1.00	0.36	0.03	0.39	0.03	0.41	0.02	0.49	0.04	0.46	0.02
1.22	⋯	⋯	⋯	⋯	0.40	0.02	⋯	⋯	0.44	0.02
1.76	0.36	0.03	0.40	0.04	0.40	0.02	0.51	0.04	⋯	⋯
2.62	0.35	0.03	0.37	0.03	⋯	⋯	0.47	0.03	⋯	⋯

metric curves (e.g., van Wijngaarden *et al.*, 2002a: Fig. 6) closely matches expectations based on differences in the ν parameter. This leads us to conclude that this non-native psychometric function model is the most appropriate choice for our current purposes.

B. Effects of linguistic message content

Our correction function approach yields, by definition, representative results if the only speech degrading factor is steady-state noise, and if the messages have the approximate linguistic characteristics of SRT sentences. This indicates two specific concerns for the validity of the approach: differences in complexity of the speech material, and speech degrading conditions other than additive noise. Section IV dealt with the concerns regarding other types of speech degradation. Message complexity is an issue that perhaps needs closer consideration; differences were found between correction functions for high-predictability (HP) and low-predictability (LP) sentences, indicating that differences in semantic redundancy can result in different correction functions (Figs. 3 and 4). However, the STI is most commonly applied to situations where little variation in semantic redundancy is expected. Moreover, deviations between the HP and LP curves only appear to occur for subjects of quite low proficiency, and then only on the high end of the STI scale. In conclusion, if reasonably representative sentence material is chosen for measurement of the psychometric curves, than the specific details of linguistic content are considered to be of minor importance. In Figs. 3 and 4, the HP curves are expected to be most representative of the STI application domain.

C. Application of the proposed approach

Any prediction of speech intelligibility for a population of non-native talkers or listeners must always be based on some description of this population. Preferably, this should be a description in terms of easily observed or accessible characteristics (such as a general categorization of L2 proficiency, or severity of foreign accent). The approach outlined in this article is based on the use of systematically measured psychometric functions, matched with some of these observations and characteristics (specifically accent ratings and linguistic entropy).

As an efficient procedure for obtaining a correction function for non-native listeners, one could estimate the linguistic entropy distribution for the target population using the letter guessing procedure (Shannon and Weaver, 1949). This is a time-efficient procedure; it is feasible to collect distributions of individual linguistic entropy for larger populations of non-native listeners, for instance, by setting up a booth at an international airport, or even through the Internet. Once a distribution of linguistic entropy for the target population is known, the next step is an external choice: how do we wish to represent this population? The mean of the distribution will be appropriate for many applications, while for some, one may want to choose a more conservative threshold (for instance, the 25th percentile, in which case 75% of the population shows equal or better proficiency than the threshold). Using the relation shown in Fig. 6, the chosen entropy threshold can be converted into the equivalent value of the ν parameter, from which the corresponding correction function can be calculated.

For talkers, a similar approach can be adopted, but based on a distribution of proficiency self-ratings rather than linguistic entropy. Combined with a categorization scheme such as the one used in Fig. 7, self-ratings can also be translated into equivalent values of the ν parameter.

In conclusion, the proposed correction function approach broadens the scope of applicability of the STI method to include various applications involving non-natives. Obvious applications include public address systems at airports, and auditoria used for international conferences.

APPENDIX: DERIVATION OF AN STI CORRECTION FUNCTION BASED ON A LOGISTIC FUNCTION

Deriving a correction function based on the psychometric functions described by Eqs. (2) and (4) involves solving $\pi_{L1}=\pi_{L2}$, as represented by Eq. (A1)

$$\Phi\left(\frac{r_{L1}-\mu_{L1}}{\sigma_{L1}}\right)=1-\left[1-\Phi\left(\frac{r_{L2}-\mu_{L1}}{\sigma_{L1}}\right)\right]^{\nu}. \tag{A1}$$

The cumulative normal distribution $\Phi([r-\mu]/\sigma)$ may be approximated by a logistic function (e.g., Versfeld *et al.*, 2000), such as Eq. (A5)

$$\Lambda(\rho)=\frac{e^{\rho}}{1+e^{\rho}}, \tag{A2}$$

where

$$\rho=\frac{r-\mu}{\sigma\sqrt{\pi/8}}. \tag{A3}$$

By substituting $\Lambda(\rho)$ for $\Phi([r-\mu]/\sigma)$ in Eq. (A1) and solving, Eq. (A4) is obtained

$$\rho_{L2}=\ln[(e^{\rho_{L1}}+1)^{(1/\nu)}-1]. \tag{A4}$$

By substituting Eqs. (1) and (A3) in Eq. (4), the correction function Eq. (A5) is obtained

$$\mathrm{STI}_{L2}=f(\mu_{L1}+\sigma_{L1}\sqrt{\pi/8}\ln[(e^{[f^{-1}(\mathrm{STI}_{L1})-\mu_{L1}]/(\sigma_{L1}\sqrt{\pi/8})}+1)^{(1/\nu)}-1]). \tag{A5}$$

[1]Something similar *always* applies (even without using the proficiency factor) for the SII, since the SII depends on the type of intelligibility test it aims to predict.

[2]This is only true if the SNR is between −15 and +15 dB. Outside this range, the STI is (respectively) always 0 or 1, meaning that STI=1 corresponds to any SNR greater or equal than +15. This topic is addressed later on in this section.

[3]Mayo *et al.* (1997) also tested a separate bilingual-since-infancy (BSI) group. Because of the limited number of subjects in this group (3), Mayo *et al.* chose to combine their BST and BSI groups for statistical analysis. The BSI group data are not used in this article.

[4]This statement is based on comparisons of SRT results between cases where only the talker is non-native, and only the listener is non-native (talkers and listeners of comparable proficiency). In both cases, the speech material is fixed; this means that the non-native talkers do not rely on their own linguistic resources (vocabulary, syntactical knowledge, etc.), but simply use the language that is handed to them. If the dynamics of free conversation are taken into consideration, the situation will be much more

complex, and the comparison between the magnitudes of perception and production effects may have a different outcome.

ANSI (**1997**). ANSI S3.5-1997, ''Methods for calculation of the speech intelligibility index'' (American National Standards Institute, New York).

Bent, T., and Bradlow, A. R. (**2003**). ''The interlanguage speech intelligibility benefit,'' J. Acoust. Soc. Am. **114**, 1600–1610.

Boothroyd, A., and Nittrouer, S. (**1988**). ''Mathematical treatment of context effects in phoneme and word recognition,'' J. Acoust. Soc. Am. **84**, 101–104.

Bradlow, A. R., Toretta, G. M., and Pisoni, D. B. (**1996**). ''Intelligibility of normal speech. I. Global and fine-grained acoustic-phonetic talker characteristics,'' Speech Commun. **20**, 255–272.

Bronkhorst, A. W., Brand, T., and Wagener, K. (**2002**). ''Evaluation of context effects in sentence recognition,'' J. Acoust. Soc. Am. **111**(6), 2874–2896.

Buus, S., Florentine, M., Scharf, B., and Canevet, G. (**1986**). ''Native, French listeners' perception of American-English in noise,'' in Proc. Internoise 86, pp. 895–898.

Duquesnoy, A. J. H. M., and Plomp, R. (**1980**). ''Effect of reverberation and noise on the intelligibility of sentences in cases of presbyacusis,'' J. Acoust. Soc. Am. **68**, 537–544.

Flege, J. E. (**1995**). ''Second-language speech learning: Theory, findings, and problems,'' in *Speech Perception and Linguistic Experience*, edited by W. Strange (York, Baltimore).

Florentine, M. (**1985**). ''Non-native listeners' perception of American-English in noise,'' in Proc. Internoise 85, pp. 1021–1024.

Florentine, M., Buus, S., Scharf, B., and Canevet, G. (**1984**). ''Speech reception thresholds in noise for native and non-native listeners,'' J. Acoust. Soc. Am. **75**, S84–S84.

French, N. R., and Steinberg, J. C. (**1947**). ''Factors governing the intelligibility of speech sounds,'' J. Acoust. Soc. Am. **19**, 90–119.

Hood, J. D., and Poole, J. P. (**1980**). ''Influence of the speaker and other factors influencing speech intelligibility,'' Audiology **19**, 434–455.

Houtgast, T., and Steeneken, H. J. M. (**1984**). ''A multi-lingual evaluation of the Rastimethod for estimating speech intelligibility in auditoria,'' Acustica **54**, 185–199.

Houtgast, T., Steeneken, H. J. M., and Plomp, R. (**1980**). ''Predicting speech intelligibility in rooms from the modulation transfer function. I. General room acoustics,'' Acustica **46**, 60–72.

IEC (**1998**). IEC 60268-16 2nd ed. ''Sound system equipment. Part 16: Objective rating of speech intelligibility by speech transmission index'' (International Electrotechnical Commission, Geneva, Switzerland).

ISO (**2002**). ISO/FDIS 9921 ''Ergonomics—Assessment of speech communication'' (International Organization for Standardization, Geneva, Switzerland).

Kalikow, D. N., and Stevens, K. N. (**1977**). ''Development of a test of speech intelligibility in noise using sentence materials with controlled word predictability,'' J. Acoust. Soc. Am. **61**, 1337–1351.

Kryter, K. D. (**1962**). ''Methods for the calculation and use of the articulation index,'' J. Acoust. Soc. Am. **34**, 1689–1697.

Mayo, L. H., Florentine, M., and Buus, S. (**1997**). ''Age of second-language acquisition and perception of speech in noise,'' J. Speech Lang. Hear. Res. **40**, 686–693.

Müsch, H., and Buus, S. (**2001a**). ''Using statistical decision theory to predict speech intelligibility. I. Model structure,'' J. Acoust. Soc. Am. **109**, 2896–2909.

Müsch, H., and Buus, S. (**2001b**). ''Using statistical decision theory to predict speech intelligibility. II. Measurement and prediction of consonant-discrimination performance,'' J. Acoust. Soc. Am. **109**(6), 2910–2920.

Nábelek, A. K., and Donahue, A. M. (**1984**). ''Perception of consonants in reverberation by native and non-native listeners,'' J. Acoust. Soc. Am. **75**, 632–634.

Pavlovic, C. V. (**1987**). ''Derivation of primary parameters and procedures for use in speech intelligibility predictions,'' J. Acoust. Soc. Am. **82**, 413–422.

Pavlovic, C. V., and Studebaker, G. A. (**1984**). ''An evaluation of some assumptions underlying the articulation index,'' J. Acoust. Soc. Am. **75**, 1606–1612.

Picheny, M. A., Durlach, N. I., and Braida, L. D. (**1985**). ''Speaking clearly for the hard of hearing I. Intelligibility differences between clear and conversational speech,'' J. Speech Hear. Res. **28**, 96–103.

Plomp, R. (**1978**). ''Auditory handicap of hearing impairment and the limited benefit of hearing aids,'' J. Acoust. Soc. Am. **63**(2), 533–549.

Plomp, R., and Mimpen, A. M. (**1979**). ''Improving the reliability of testing the speech reception threshold for sentences,'' Audiology **18**, 43–52.

Pollack, I. (**1964**). ''Message probability and message reception,'' J. Acoust. Soc. Am. **36**, 937–945.

Shannon, C. E., and Weaver, W. (**1949**). *The Mathematical Theory of Communication* (University of Illinois Press, Urbana).

Steeneken, H. J. M., and Houtgast, T. (**1980**). ''A physical method for measuring speech transmission quality,'' J. Acoust. Soc. Am. **67**, 318–326.

Steeneken, H. J. M., and Houtgast, T. (**1999**). ''Mutual dependence of the octave-band weights in predicting speech intelligibility,'' Speech Commun. **28**, 109–123.

Studebaker, G. A., Pavlovic, C. V., and Sherbecoe, R. L. (**1987**). ''A frequency importance function for continuous discourse,'' J. Acoust. Soc. Am. **81**, 1130–1138.

van Rooij, J. C. G. M. (**1991**). ''Aging and the perception of speech; auditive and cognitive aspects,'' Free University of Amsterdam.

van Wijngaarden, S. J., and Houtgast, T. (**2004**). ''Effect of talker and speaking style on the Speech Transmission Index,'' J. Acoust. Soc. Am. **115**(1), 38–41.

van Wijngaarden, S. J., Steeneken, H. J. M., and Houtgast, T. (**2001**). ''Methods and models for quantitative assessment of speech intelligibility in cross-language communication,'' in *Proceedings of the RTO Workshop on Multi-lingual Speech and Language Processing* (Aalborg, Denmark).

van Wijngaarden, S. J., Steeneken, H. J. M., and Houtgast, T. (**2002a**). ''Quantifying the intelligibility of speech in noise for non-native talkers,'' J. Acoust. Soc. Am. **112**(6), 3004–3013.

van Wijngaarden, S. J., Steeneken, H. J. M., and Houtgast, T. (**2002b**). ''Quantifying the intelligibility of speech in noise for non-native listeners,'' J. Acoust. Soc. Am. **111**(4), 1906–1916.

Versfeld, N. J., Daalder, J., Festen, J. M., and Houtgast, T. (**2000**). ''Method for the selection of sentence materials for efficient measurement of the speech reception threshold,'' J. Acoust. Soc. Am. **107**, 1671–1684.

Intelligibility of bandpass filtered speech: Steepness of slopes required to eliminate transition band contributions

Richard M. Warren,[a] James A. Bashford, Jr., and Peter W. Lenz
Department of Psychology, University of Wisconsin-Milwaukee, Post Office Box 413, Milwaukee, Wisconsin 53201-0413

(Received 14 January 2003; revised 10 December 2003; accepted 15 December 2003)

Despite the recognition that the steepness of filter slopes can play an important role in the intelligibility of bandpass speech, there has been no systematic examination of its importance. The present study used high orders of finite impulse response (FIR) filtering to produce slopes ranging from 150 to 10 000 dB/octave. The slopes flanked 1/3-octave passbands of everyday sentences having a center frequency of 1500 Hz (the region of highest intelligibility for the male speaker's voice). Presentation levels were approximately 75 and 45 dB. No significant differences were found for the two presentation levels. Average intelligibility scores ranged from 77% at 150 dB/octave down to the asymptotic intelligibility score of 12% at 4800 dB/octave. These results indicate that slopes of several thousand dB/octave may be required for accurate and unambiguous specification of the range of frequencies contributing to intelligibility of filtered speech. In addition, the extremely steep slopes are needed to ensure that none of the spectral components contributing to intelligibility has its relative importance diminished by spectral tilt.
[DOI: 10.1121/1.1646404]

PACS numbers: 43.71.Es [PFA]

Pages: 1292–1295

I. INTRODUCTION

When speech is filtered, sloped transition bands always accompany the passbands. Although it is recognized that flanking transition bands contribute to speech intelligibility (e.g., Kryter, 1960; Müsch and Buus, 2001; Stickney and Assmann, 2001; Studebaker and Sherbecoe, 1993), there has been no systematic study of the effect of the steepness of transition band slopes upon the intelligibility of bandpass speech, nor has there been a determination of the slopes required to permit the measurement of passband intelligibility without the confound of contributions from transition bands.

A recent series of studies has indicated that even steep filter slopes can play a major role in determining the intelligibility of narrow-band speech. When a single band of speech consists entirely of filter slopes, it can still be highly intelligible despite the lack of a conventional passband. Thus, when everyday sentences were reduced to high-pass and low-pass slopes of 48 dB/octave intersecting at 1.5 kHz, the average intelligibility was over 95% (Bashford, Riener, and Warren, 1992; see p. 213). When these slopes were increased to approximately 100 dB/octave in a subsequent study, the intelligibility of the triangular band was still quite high at 77% (Warren *et al.*, 1995). These observations suggested that the intelligibility of bandpass speech could be due largely to frequencies lying outside the nominal bandwidth as conventionally defined by the frequencies encompassed by the passband. To test this hypothesis, Warren and Bashford (1999) separated the passbands and transition bands of 1/3-octave everyday sentences that had slopes of approximately 100 dB/octave and a center frequency of 1.5 kHz. When intact, the bands had an intelligibility of over 95%, in keeping with the 1995 study by Warren *et al.* When the passband and its pair of flanking transition bands were separated using slopes of approximately 1000 dB/octave produced by 2000-order digital FIR filtering, it was found that the near-ceiling intelligibility of the intact band was due chiefly to the transition bands: the isolated 100-dB/octave transition bands separated by a 1/3-octave gap had a much higher intelligibility (82%) than the isolated passband (24%). However, there was no assurance that slopes of 1000 dB/octave were adequate to eliminate all contributions to intelligibility (as we shall see, the same sentences were used in the present study, and it was determined that the 1000-dB/octave slopes of the ''isolated'' passbands were responsible for about half of the intelligibility score of 24%). When sentential context was eliminated by substituting monosyllabic word lists for the sentences, intelligibility dropped as would be expected. But once more, the intelligibility of the transition bands was more than three times greater than that of the passband (Bashford, Warren, and Lenz, 2000).

The present study was undertaken to determine: (1) how intelligibility of a nominal 1/3-octave band of everyday sentences (center frequency 1.5 kHz) changes as the slopes are varied from 150 to 10 000 dB/octave; (2) the steepness of slopes required to ensure that transition bands do not contribute appreciably to intelligibility; and (3) the intelligibility of the 1/3-octave passband when contributions from transition bands are absent. Separate groups of subjects received the stimuli at passband levels of 75 and 45 dB (these levels were chosen to span the range of moderate speech intensities). As will be shown, the scores obtained at the two levels were not statistically different. The averaged scores decreased exponentially with increasing slopes, reaching an asymptotic value at 4800 dB/octave. Passbands accompanied by transition bands with 2400-dB/octave slopes had an average score that was significantly greater than the asymptote.

[a]Electronic mail: rmwarren@csd.uwm.edu

 0001-4966/2004/115(3)/1292/4/$20.00

II. METHOD

A. Subjects

The 70 listeners were randomly assigned to one of two groups of 35 members each. All were native English speakers who reported having no known hearing problems. They were recruited from introductory Psychology courses at the University of Wisconsin-Milwaukee and were paid for their participation.

B. Stimuli

The test sentences employed in this study were 98 of the 100 Central Institute for the Deaf (CID) "everyday" sentences published by Silverman and Hirsh (1955). They were produced by a male speaker having a voicing frequency of about 100 Hz and no evident regional accent, and were recorded digitally (44.1-kHz sampling, 16-bit quantization). The same recording had been used in several of our previous studies that examined the effect of slopes upon the intelligibility of narrow-band speech (Bashford, Warren, and Lenz, 2000; Warren and Bashford, 1999; Warren, Bashford, and Lenz, 2000, 2003). An additional 21 sentences, which served as practice stimuli, were drawn from the high-predictability sublist of the revised Speech Perception in Noise (SPIN) test (Bilger *et al.*, 1984; Kalikow, Stevens, and Elliot, 1977). They were produced by the same speaker and were recorded and presented in the same manner as the test sentences.

Prior to filtering, sentences were transduced by a Sennheiser HD 250 Linear II headphone and their slow-rms peak levels were matched to within 0.2 dB using a flat-plate coupler in conjunction with a Brüel & Kjaer model 2230 digital sound-level meter set at A-scale weighting (as were all measurements reported in this study). Seven different bandpass-filtered versions of the sentences were then prepared using function *fir*1 in MATLAB. The bandpass versions of the sentences all had nominal 1/3-octave passbands centered on 1.5 kHz (1336- to 1684-Hz cutoffs), but varied in the steepness of their transition bands, which had slopes of 150, 300, 600, 1200, 2400, 4800, and 10 000 dB/octave, respectively. Transition bands having these slopes were produced by FIR filtering that used varying numbers of taps (ranging from 171 to 21 200) as determined by an iterative procedure of successive approximation.[1] This procedure yielded high-pass and low-pass slopes that each deviated less than 1% from the desired value, as measured from the cutoff frequencies to the 50-dB downpoints along the low-pass and high-pass transition bands [a previous study had demonstrated that truncation of slopes at this downpoint had no effect upon intelligibility (Warren, Bashford, and Lenz, 2000]. The stimuli were subsequently filtered a second time with 20 000-order low-pass and high-pass filtering at the 55-dB downpoints along the transition bands; this final filtering stage ensured a stop-band attenuation greater than 75 dB for all conditions. Table I presents the actual filter slopes for each of the seven conditions, along with the filter orders (number of taps) of stage 1 FIR filtering required to produce them.[2] Figure 1 shows the long-term averaged spectrum for the 1/3-octave band having the steepest slopes (10 000 dB/octave).

TABLE I. Filter slopes and orders of FIR filtering. The dB/octave values were extrapolated from the attenuation measured from the cutoff frequencies to the 50-dB downpoints along the filter skirts.

	Nominal slope (dB/octave)						
	150	300	600	1200	2400	4800	10 000
Actual high-pass slope dB/octave	150	300	604	1194	2409	4 780	9 937
Actual low-pass slope dB/octave	150	301	599	1206	2402	4 785	9 983
High-pass filter order	268	502	985	1952	3902	10 260	21 200
Low-pass filter order	171	360	741	1547	3300	7 080	16 520

C. Procedure

Listeners in each of two groups received 98 of the 100 "everyday" (CID) sentences, with separate 14-sentence sets assigned to the 7 filter-slope conditions in a pseudorandom order; each slope condition was assigned 5 times to each sentence set and appeared 5 times in each serial position across listeners in each group. Prior to the presentation of a given slope condition, subjects were familiarized with the effects of filtering by listening to a practice set of three high-predictability SPIN sentences. Each practice sentence was first presented broadband and then filtered in the same manner as the test sentences that followed. Stimuli were presented diotically to listeners through Sennheiser HD 250 Linear II headphones. For one group of listeners, the bandpass sentences were presented at a slow-rms peak level that averaged 75 dB for the shallowest slope (150 dB/octave) and decreased down to 74.3 dB for the steepest slope (10 000 dB/octave). For the second group of listeners, who heard the same stimuli at a lower amplitude, slow-rms peak levels averaged 45 dB for the shallowest slope and 44.3 dB for the steepest slope. Listeners were tested individually while seated with the experimenter in an audiometric chamber. They were asked to repeat each sentence as best they could, and were told to guess if unsure. The experimenter recorded

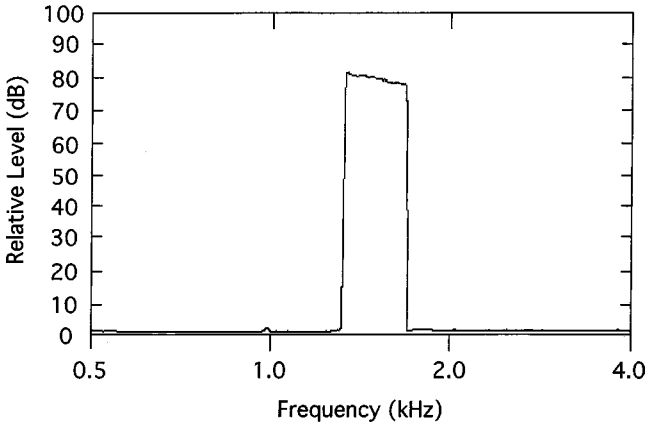

FIG. 1. Long-term averaged spectrum based upon the 98 1/3-octave CID sentences having transition bands minimized through steep FIR filtering (10 000-dB/octave slopes). The plot was generated offline via discrete Fourier transform (DFT) with linear averaging of spectra obtained using a 64 000-point (1.45-s, 0.7-Hz resolution) Blackman window across the entire set of digitally recorded sentences.

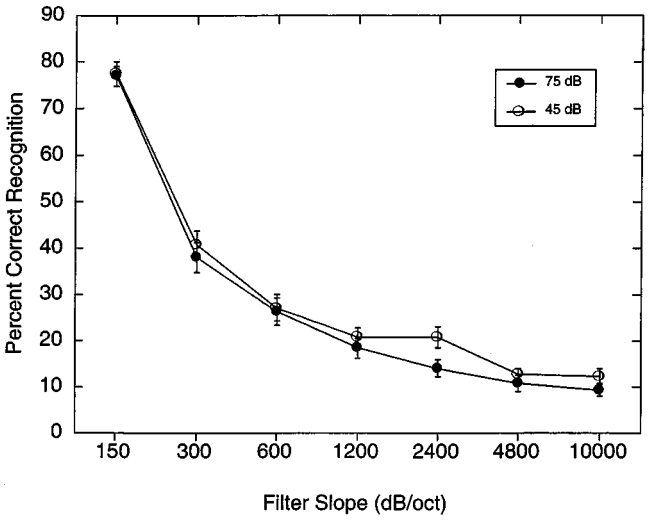

FIG. 2. Mean intelligibility scores and standard error confidence intervals for the 98 1/3-octave CID sentences having transition band slopes ranging from 150 to 10 000 dB/octave. Sentences were presented to separate groups of listeners ($N=35$ in each case) at slow-rms peak levels of 45 or 75 dB.

the number of keywords reported correctly for each sentence. Testing was accomplished in a single session lasting approximately 30 min.

III. RESULTS

The average intelligibility scores for the 75- and 45-dB slow-rms peak level conditions are plotted as a function of filter slope in Fig. 2.

Intelligibility scores were subjected to a two-factor mixed (presentation level×filter slope) analysis of variance, which yielded a significant effect of filter slope [$F(6,408)=269.02, p<0.0001$], a nonsignificant effect of presentation level [$F(1,68)=1.88, p>0.17$], and a nonsignificant interaction of slope and level [$F(6,408)=0.50, p>0.80$].[3] Subsequent analysis of the data using Helmhert single-df contrasts (Hays, 1988) revealed that intelligibility decreased monotonically with increasing filter slope down to an asymptote reached at 4800 dB/octave [$F\geqslant 12.50, p<0.001$].

IV. DISCUSSION

This study demonstrates that if the *nominal* bandwidth (based upon the passband) of narrow-band speech is to correspond to the *effective* bandwidth (based upon all frequencies contributing to intelligibility), then extremely steep slopes are required. When nominal and effective bandwidths differ, then the term ''effective bandwidth'' can be used to denote all frequencies responsible for intelligibility. However, the use of effective bandwidth rather than ''nominal bandwidth'' as a descriptor for bandlimited speech can also introduce problems. When both passbands and transition bands are present, the integrity of the normal spectral profile within the effective bandwidth is compromised; the contribution to intelligibility by transition bands is diminished appreciably by their spectral tilt, while that of the passband remains intact (see Warren, Bashford, and Lenz, 2000). Elimination of transition bands using FIR filtering avoids these problems and permits an accurate and unambiguous description of frequencies responsible for the intelligibility of bandlimited speech.[4,5]

As shown in Fig. 1, the filter slopes continue down to the stopband lying more than 75 dB below the level of the passband. For those conditions in which the transition bands affect intelligibility (150 to 2400 dB/octave), it might be expected that the increase in amplitude from 45 to 75 dB would produce an appreciable increase in intelligibility, since a greater range of supraliminal frequencies would become available along the slopes. However, it is only the upper portion of the slopes that contribute. Kryter (1960) had estimated that information more than 30 dB down the slopes does not influence intelligibility. This estimate is consistent with the results obtained by Warren, Bashford, and Lenz (2000), who truncated 100-dB/octave slopes of everyday sentences at graded downpoints using 2000-order FIR filtering, and found that truncation beyond the 30- or 40-dB downpoints (depending upon location of the transition bands) did not affect intelligibility. This range corresponds to the range of amplitude fluctuations that normally contribute to intelligibility (see Studebaker and Sherbecoe, 2002, for discussion of this effective dynamic range of speech). However, the limiting attenuation range for integrating information present at different frequencies may apply only to components present within a single band. A limit did not apply when two 1/3-octave bands of everyday sentences with nearly vertical slopes were separated by an appreciable spectral gap; when one band had a fixed level of 75 dB, all supraliminal levels of the second band contributed to intelligibility (Warren, Bashford, and Lenz, 2003).

ACKNOWLEDGMENT

This work was supported by NIH Grant DC00208.

[1]FIR slopes are approximately constant in dB/Hz rather than dB/octave; therefore, lower slopes are shallower than higher slopes for a given bandpass filter order. In order to obtain slopes that are matched in dB/octave, considerably higher filter orders were used for the lower transition band as shown in Table I.

[2]Healy (1998) employed the same 1/3-octave speech used by Warren *et al.* (1995) and in the present study. He reported that FIR filtering using 82, 275, and 2000 orders resulted in scores of 98%, 56%, and 16%, respectively. However, he used a single filter order for both lower and higher slopes, resulting in considerable asymmetry. In keeping with footnote 1, his upper transition bands were much steeper than his lower transition bands (the ratio of higher to lower slopes was 2.8 for the 82 FIR order, 1.53 for the 275 FIR order, and 1.25 for the 2000 FIR order). Because of this asymmetry in slope values, Healy's intelligibility scores cannot be compared with those of the present study that employed the same dB/octave values for both transition bands.

[3]A reviewer noted that an apparent effect of presentation level is noticeable in Fig. 1 for the 2400-dB/octave slope condition. Repetition accuracy at that slope was 6.7% higher at 45 dB than at 75 dB, whereas the average (nonsignificant) difference across all slopes favors the 45-dB condition by the smaller value of 2.6%. We performed an ANOVA using data only from the 2400-dB/octave slope condition, and obtained an uncorrected *F*-ratio that was significant [$F(1,68)=5.06, p<0.03$]. However, since there was no *a priori* reason for performing this individual comparison, a Bonferroni correction is required, imposing a p level of $0.05/7=0.007$ for significance. Therefore, the apparent difference at 2400 dB/octave slope is considered spurious.

[4]While it is computationally expensive, high-order FIR filtering can allow us to separate contributions made by passbands and transition bands. The ad-

dition of noise to filtered speech can reduce (but not eliminate) contributions made by transition bands by masking their outlying lower-amplitude components. However, noise produces a risk of selectively masking lower-amplitude components within passbands, such as fricatives and plosives, while leaving strongly voiced vowels relatively unaffected (see Steeneken and Houtgast, 2002).

[5]It should be noted that the relation between slope steepness and intelligibility found in the present study would most likely vary with different center frequencies, as would the relative contributions made by the high-pass and low-pass slopes. An earlier study (Warren and Bashford, 1999) found that for 1/3-octave everyday sentences having a center frequency of 1.5 kHz, and high-pass and low-pass slopes of 100 dB/octave, the lower frequency slopes contributed more to intelligibility than the higher frequency slopes, probably due at least in part to the upward spread of masking by the passband.

Bashford, Jr. J. A., Riener, K. R., and Warren, R. M. (**1992**). ''Increasing the intelligibility of speech through multiple phonemic restorations,'' Percept. Psychophys. **51**, 211–217.

Bashford, Jr., J.A. Warren, R. M., and Lenz, P. W. (**2000**). ''Relative contributions of passband and filter skirts to intelligibility of bandpass speech: Some effects of amplitude and context,'' ARLO **1**, 31–36.

Bilger, R. C., Nuetzel, J. M., Rabinowitz, W. M., and Rzeczkowski, C. (**1984**). ''Standardization of a test of speech perception in noise,'' J. Speech Hear. Res. **27**, 32–48.

Hays, W. L. (**1988**). *Statistics* (Holt, Rinehart, and Winston, Chicago).

Healy, E. H. (**1998**). ''A minimum spectral contrast rule for speech recognition: Intelligibility based upon contrasting pairs of narrow-band amplitude patterns,'' Ph.D. dissertation, University of Wisconsin-Milwaukee, Milwaukee, WI.

Kalikow, D. N., Stevens, K. N., and Elliott, L. L. (**1977**). ''Development of a test of speech intelligibility in noise using sentence materials with controlled word predictability,'' J. Acoust. Soc. Am. **61**, 1337–1351.

Kryter, K. D. (**1960**). ''Speech bandwidth compression through spectrum selection,'' J. Acoust. Soc. Am. **32**, 547–556.

Müsch, H., and Buus, S. (**2001**). ''Using statistical decision theory to predict speech intelligibility. I. Model structure,'' J. Acoust. Soc. Am. **109**, 2896–2909.

Silverman, S. R., and Hirsh, I. J. (**1955**). ''Problems related to the use of speech in clinical audiometry,'' Ann. Otol. Rhinol. Laryngol. **64**, 1234–1245.

Steeneken, H. J. M., and Houtgast, T. (**2002**). ''Phoneme-group specific octave-band weights in predicting speech intelligibility,'' Speech Commun. **38**, 399–411.

Stickney, G. S., and Assmann, P. F. (**2001**). ''Acoustic and linguistic factors in the perception of bandpass-filtered speech,'' J. Acoust. Soc. Am. **109**, 1157–1165.

Studebaker, G. A., and Sherbecoe, R. L. (**1993**). ''Frequency-importance functions for speech recognition,'' in *Acoustical Factors Affecting Hearing Aid Performance*, edited by G. A. Studebaker and I. Hochberg (Allyn and Bacon, Needham, MA), pp. 185–204.

Studebaker, G. A., and Sherbecoe, R. L. (**2002**). ''Intensity-importance functions for bandlimited monosyllabic words,'' J. Acoust. Soc. Am. **111**, 1422–1436.

Warren, R. M., and Bashford, Jr. J. A. (**1999**). ''Intelligibility of 1/3-octave speech: Greater contribution of frequencies outside than inside the nominal passband,'' J. Acoust. Soc. Am. **106**, L47–L52.

Warren, R. M., Bashford, Jr. J. A., and Lenz, P. W. (**2000**). ''Intelligibility of bandpass speech: Effects of truncation or removal of transition bands,'' J. Acoust. Soc. Am. **108**, 1264–1268.

Warren, R. M., Bashford, Jr. J. A., and Lenz, P. W. (**2003**). ''Intelligibility of dual rectangular speech bands: Implications of observations concerning amplitude mismatch and asynchrony,'' Speech Commun. **40**, 551–558.

Warren, R. M., Riener, K. R., Bashford, Jr. J. A., and Brubaker, B. S. (**1995**). ''Spectral redundancy: Intelligibility of sentences heard through narrow spectral slits,'' Percept. Psychophys. **57**, 175–182.

Detection of speech landmarks: Use of temporal information

Ariel Salomon,[a] Carol Y. Espy-Wilson, and Om Deshmukh
Electrical and Computer Engineering Department, University of Maryland, A.V. Williams Building, College Park, Maryland 20742

(Received 26 July 2001; accepted for publication 11 December 2003)

Studies by Shannon *et al.* [Science, **270**, 303–304 (1995)], Van Tasell *et al.* [J. Acoust. Soc. Am. **82**, 1152–1161 (1987)], and others show that human listeners can understand important aspects of the speech signal when spectral shape has been significantly degraded. These experiments suggest that temporal information is particularly important in human speech perception when the speech signal is heavily degraded. In this study, a system is developed that extracts linguistically relevant temporal information that can be used in the front end of an automatic speech recognition system. The parameters targeted include energy onset and offsets (computed using an adaptive algorithm) and measures of periodic and aperiodic content; together these are used to find abrupt acoustic events which signify landmarks. Overall detection rates for strongly robust events, robust events, and weak events in a portion of the TIMIT test database are 98.9%, 94.7%, and 52.1%, respectively. Error rates increase by less than 5% when the speech signals are spectrally impoverished. Use of the four temporal parameters as the front end of a hidden Markov model (HMM)-based system for the automatic recognition of the manner classes ''sonorant,'' ''fricative,'' ''stop,'' and ''silence'' results in the same recognition accuracy achieved when the standard 39 cepstral-based parameters are used, 70.1%. The combination of the temporal parameters and cepstral parameters results in an accuracy of 74.8%. © *2004 Acoustical Society of America.* [DOI: 10.1121/1.1646400]

PACS numbers: 43.72.Ar, 43.72.Ne [DOS] Pages: 1296–1305

I. INTRODUCTION

This paper investigates the use of temporal information for extraction of linguistically relevant details from a speech signal. This study has been considered in the context of a longer-term program on lexical access from features (LAFF) (Stevens, 1986; 2002) and event-based speech recognition (EBS) (Espy-Wilson, 1994; Juneja and Espy-Wilson, 2003), which is a furthering of the lexical access from spectra (LAFS) proposed by Klatt (1979). LAFF and EBS are paradigms for (human or machine) speech recognition in which landmarks in a speech signal are first located, and then features are attached to those landmarks. In this paper, motivated by studies of speech perception under certain types of degradation, we have concentrated on access to temporal information. The goal of this work is to develop a system that automatically extracts temporal cues that can be used in the front end of an automated speech recognition system.

A. Background

The motivations for this work come most importantly from studies of speech perception. A major problem in the development of speech recognition systems is the detection of speech from noise (cf. Viikki, 2001) or otherwise reduced spectral information. Recent studies show that human listeners can understand some aspects of the speech signal even when spectral shape has been significantly degraded. A source of information that may be of use, particularly under heavily degraded conditions, is that of temporal cues—information derived from the temporal structure of the speech signal. These cues are not targeted by traditional speech recognition systems, which generally focus on spectral features using data-derived spectral templates. Temporal processing is a significant factor in the auditory system, as observed by effects such as the phase locking of auditory-nerve firing to periodic signals (Moore, 1997). As such, this information should be available for use in human speech recognition.

The ability of human listeners to understand spectrally degraded speech has been examined in several studies (Shannon *et al.*, 1995; Van Tasell *et al.*, 1987; Turner *et al.*, 1995, among others) which demonstrate the ability of human listeners to recognize speech—particularly manner, nasality, and voicing—from primarily temporal cues. The general result has been that spectrally degraded speech still contains limited information about manner, nasality, and voicing. In light of these results, it is proposed that it should be possible to build a detector for acoustic events (prototypical landmarks) that is both largely independent of detailed spectral information and resistant to noise. Further, addition of temporal parameters should also improve performance and increase noise resistance for a system based on spectral information. Note, however, that improved performance may not occur if the noise has speech-like temporal characteristics. Turner *et al.* (1995) have shown that the use of temporal information is prevented when the speech signal is corrupted by modulated babble noise.

B. Temporal information

For the purpose of this study, it is helpful to specify exactly what is considered to be the ''temporal information''

[a]Currently at MIT, Research Lab of Electronics, Speech Communication Group, 77 Massachusetts Avenue, Rm. 36-511, Cambridge, MA 02142. Electronic mail: ariel@speech.mit.edu

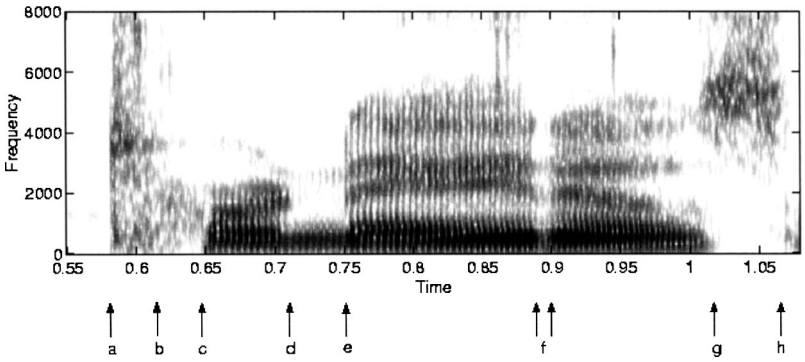

FIG. 1. Sample landmarks in the word ''tornadoes.'' (a) Release of stop consonant; (b) frication/aspiration boundary (nonrequired event); (c) onset of vowel; (d) closure for nasal consonant; (e) release of nasal consonant; (f) closure and release of stop consonant produced as a flap; (g) closure for fricative consonant; (h) release of fricative consonant.

in the signal. Temporal information is defined here in terms of bandpass components of the speech signal. Rosen (1992) proposes three categories of temporal information in speech: (1) ''envelope information'' (with fluctuations at rates from 2 to 50 Hz) which contains amplitude and duration cues to manner of articulation and voicing, as well as information about vowel identity (for example vowel length) and prosodic cues; (2) ''periodicity information'' (fluctuations at rates from approximately 50 to 500 Hz) which provides cues to voicing which can aid in manner identification, as well as marking stress locations by changes in pitch; and (3) ''fine structure'' (fluctuations at higher rates) which largely provides information also available from spectral shape. Note that normal-hearing subjects cannot detect amplitude fluctuations above about 1000 Hz; and response to modulation degrades rapidly above 100 Hz (Viemeister, 1979). This suggests that, at most, human listeners can only derive first-formant information from the temporal fine structure, if any information regarding fluctuations above the rate of pitch modulations is perceptually significant. Only the first two categories of temporal information are considered in this study.

Our goal in using temporal information is to aid in the analysis of the speech signal. In the human speech production system, a sequence of discrete elements (phonemes, words, etc.) is translated into an analog, continuous acoustic signal by the vocal apparatus. The process of understanding speech can be considered to be a reconstruction of the discrete stream of symbols from the speech signal. However, not all regions of a signal have the same information content: steady-state portions can be sampled slowly to determine overall properties, while abrupt points such as the critical point of a transition for a consonantal closure can contain a significant number of linguistically important cues in a concentrated region. These transition regions can contain information about the adjacent segments, most importantly in the type of transitions in and out of the target position. In this paper, we are concerned with landmarks involving abrupt acoustical changes, a set of which is illustrated for an utterance in Fig. 1.

C. System goals

The goal of event detection is to generate a set of landmarks referred to as *events* that will direct further analysis of the speech signal. To ensure the success of further levels of processing (outside the scope of this paper), this set should be essentially complete with respect to the perceptually sharpest events, for example events corresponding to stop-consonant bursts, strident fricatives, and stressed vowels. Note that insertions are somewhat less critical as they can be discarded by further analysis. On the other hand, it is likely that some weaker events are going to be captured less often: semivowels (particularly the glides /w/ and /y/), for which the primary cues consist of formant movement (Espy-Wilson, 1992); weak fricatives which have become sonorant, such as a common pronunciation of the /v/ in ''everyday'' (Catford, 1977; Espy-Wilson, 1994; Deshmukh and Espy-Wilson, 2003) and other cases of events that do not involve a significant degree of energy fluctuation. In cases of heavily coarticulated segments, it is expected that the output of the system will reflect the type of events that actually occurred rather than the canonical events expected from segment-based labels (e.g., sonorant events rather than onset and offset of frication for the /v/ in ''everyday'' when it is manifest as a sonorant consonant).

The parameters used to locate landmarks in the speech signal are changes in spectral energy or in the periodicity content of the signal, corresponding to the two relevant types of temporal information discussed above. This work relies on the assumption that abrupt landmarks are initially located based on only amplitude changes in the signal (Stevens, 2002). It is at later stages of processing that spectral information is integrated, and then higher-level information such as phonotactics and lexical constraints is applied. The question in this study is how much information can be detected regarding manner information in speech from strictly temporal information. It is certain that additional use of spectral information, wider context, and high-level constraints will be able to improve the results.

This work builds on work by Espy-Wilson (1992), where the degree of abruptness in an energy difference measure was used to distinguish the glides /w,y,r/ from the consonantal sonorant consonants /m,n,l/, and by Bitar (1997), where energy differences were used to find stop bursts and to perform segmentation. The methodology is similar to research by Liu (1994), who used energy differences computed from specific frequency bands to find certain types of landmarks in the speech signal. In addition, it bears similarity to the processing used by Browne and Cooke (1994), who used onsets and offsets and pitch information as cues in a system for auditory scene analysis. In this study, event detection is based on general processing of all frequency bands and the

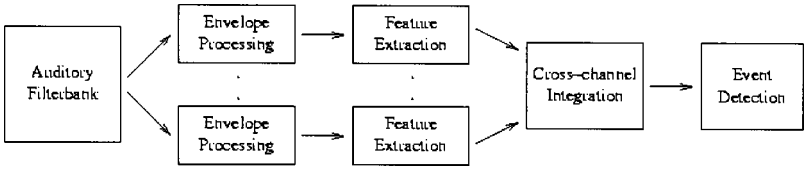

FIG. 2. Overall structure of analysis algorithm. Several stages of computation are performed within each channel, followed by integration into summary measures for use in event detection.

signal processing is adaptive. Energy change is combined with information about periodicity and aperiodicity to detect events; and analysis is performed for both clean and spectrally impoverished speech signals. In addition, we compare the performance of these temporal parameters with the traditional cepstral-based parameters in the manner classification of speech using an HMM-based recognition system (Young, 1995).

II. METHOD FOR LANDMARK DETECTION EXPERIMENTS

A. Database

The TIMIT database (Seneff and Zue, 1988) was used as a corpus of labeled speech data. This is a widely available database of speech recorded in quiet and labeled at the level of words and phonetic strings. Although it would have been more useful to use a database labeled at the landmark level (e.g., a database currently under development at the Massachusetts Institute of Technology; see Choi *et al.*, 1997), a large enough database of this type was not yet available. The TIMIT database consists of 6300 utterances spoken by 630 speakers, of which 4620 utterances make up the suggested training set and 1680 are in the test set. In particular, we used the phonetically compact (**sx**) sentences. Training was performed using a set of 20 **sx** sentences (spoken by 10 males, 10 females) randomly drawn from the TIMIT training set. Testing was performed using all 120 **sx** sentences from the TIMIT core test set (spoken by 8 female speakers and 16 male speakers, evenly distributed over all 8 dialect regions).

For the purpose of comparing with the detected landmarks, a set of expected (posited) landmarks was generated from the phonetically labeled transcriptions available in the TIMIT database using a simple rule-based algorithm based on the manner class of adjacent segments at each boundary. The posited landmarks are expected to have some inherent error as the mapping is underspecified. Some of the underspecification in the TIMIT labels is accounted for by inserting events that are labeled as ''nonrequired'' because they are possible, and may be caught by the matching algorithm, but not necessarily strongly expected. An example of a nonrequired event is the frication/aspiration boundary (event b) in Fig. 1. [Note from part (e) of Fig. 4 that this boundary is detected as a −C event by our algorithm.] The 20 utterances in the training database were also hand labeled for more reliable system development and training. For analysis of the effect of using generated landmark labels, the trained system was evaluated on both the generated labels and the hand labels of the training set. The overall error rate was 18.5% for the training set with the generated labels and 14.8% for the training set with the hand labels. Focusing on only the robust set of landmarks, the error rate was 6.54% for the training set with the generated labels and 6.06% for the training set with the hand labels. Note that the robust set contained approximately 70% of the total set of landmarks under analysis.

In addition to using this clean version of TIMIT to test our algorithm, we also spectrally impoverished the TIMIT database to see how well the temporal parameters perform with degraded spectral information. The spectral impoverishment was performed using a bank of four filters in a technique developed by Shannon *et al.* (1995).

B. Signal analysis

Signal analysis consisted of a series of stages per channel, as shown in Fig. 2. The signal was first filtered into a set of bandpass frequency channels, and each narrow-band signal was examined independently. In each channel, the signal underwent envelope analysis and feature extraction, which consisted of periodicity measurements and an energy onset/offset measure. This was followed by combination into a number of cross-channel summary measures as functions of time: summary levels of aperiodicity and periodicity, pitch, and energy onset and offset measures. The resulting waveforms were analyzed to locate events in the speech signal.

The filter bank used was a 60-channel auditory gammatone filter bank with characteristic frequencies (CFs) based on the ERB scale (Patterson, 1992). An auditory filter bank was chosen for spectral analysis in order to provide an accurate weighting of frequency components, most importantly in terms of the strength of events corresponding to voiced excitation of speech relative to their unvoiced counterparts.

In order to avoid excessive smoothing in the time domain, an envelope operator based on the Hilbert information (Rabiner and Gold, 1975) was used. The envelopes $e_i(t)$ of the individual channels are obtained by the function

$$e_i(t) = |x_i(t) + j \cdot H\{x_i(t)\}|,$$

where $x_i(t)$ is the input signal, and $H\{x_i(t)\}$ is the Hilbert transform of the input signal. Given a real narrow-band signal as input, the Hilbert transform produces a version of its input signal that is precisely 90° out of phase, such that the amplitude of the complex sum of these two signals is an estimate of the low-frequency amplitude modulation applied to the signal. This transform is an improvement over a simple smoothing operation because abrupt changes are preserved, at the maximum rate that can be captured by a particular channel given its CF.

1. Periodicity and aperiodicity feature extraction

The first feature extraction algorithm applied to the temporal envelopes makes a three-way classification between silence, periodic, and aperiodic in each channel every 2.5 ms.

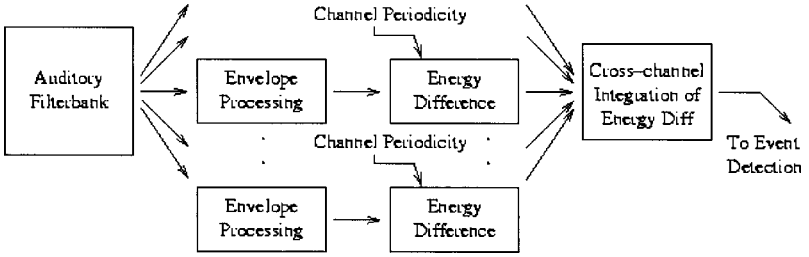

FIG. 3. Structure of energy analysis component of feature extraction. Note that the first difference operators used as the energy difference measure are adapted based on periodicity information within each channel. Following this, summary onset and offset measures are computed across all channels.

A periodic signal is defined to be one that contains regular temporal fluctuations at rates from roughly 55–500 Hz (Deshmukh and Espy-Wilson, 2003).

2. Energy operator feature extraction

The other major feature extraction algorithm used is an energy onset/offset detector based on a first-difference measure, originally derived from the onset/offset parameters designed by Espy-Wilson (1992) to capture rate of spectral change for distinguishing between sonorant consonants. These parameters were later used by Bitar (1997) to detect the abrupt onset of stop consonants. The onset/offset measure in this study is constructed from first differences in each channel output from the temporal envelope analysis stage described above [see parts (d) and (e) of Fig. 4]. The first difference is computed as a log difference between the sum amplitude of two adjacent nonoverlapping windows of the signal in a particular channel, as per the formula

$$D_{i,k} = 20 \log \sum_{m=-\infty}^{\infty} x_i(n+m)w(m) - 20 \log \sum_{m=-\infty}^{\infty} x_i(n+m-k)w(m-k),$$

where $x_i(n)$ is an individual channel input signal, k is the time difference between the two windows, and the windows $w(n)$ are rectangular windows of length k. The computed difference is scaled in decibels (dB). This first difference operation is essentially the same as the rate-of-rise (ROR) detector used by Liu (1994), but the two windows are adjacent in time to minimize error in location of the detected peaks.

It was observed that by increasing the window sizes (and correspondingly increasing k, referred to as the difference time) for the first difference computation, noise in the measurement over the utterance is reduced, particularly in fricative regions. However, an unfortunate side effect of lengthening the window sizes was a decrease in the strength of peaks and temporal accuracy in the onset signal associated with stop bursts. In order to obtain the advantages of a long window size, a method of dynamically adapting the difference time based on features of the signal measured by the periodicity detector was developed. Under this method, the energy difference detector is adapted in each channel independently, with difference length targets based on the existence of silence or periodic/aperiodic excitation, and according to the pitch estimate in periodic regions, as follows: (1) the difference time is shortened (5 ms) for silence to sharpen the response to onsets that are preceded by silence (as expected for stop bursts); (2) the difference time is lengthened (30 ms) in aperiodic regions, to maximally smooth the first difference output in fricated segments; and (3) the difference time is tuned to exactly twice the pitch period in periodic regions, to prevent detection of spurious energy fluctuation due to misalignment with the pitch period. There is also a slew rate control of 0.5 ms per millisecond (the difference operator is sampled every ms) to prevent discontinuities.

3. Summary measures

The measurements made in individual channels are combined to produce summary measures. The silence/periodic/aperiodic decisions are combined across channels to produce two measurements called P_{eng} and AP_{eng}, which are the proportions of periodic energy and aperiodic energy in the signal, respectively.

From the per-channel differences, two measures are computed: the positive differences (increasing levels) are summed to produce an ''onset'' signal, and the negative differences (decreasing levels) are summed to produce an ''offset'' signal. The offset parameter is usually inverted for analysis to make it positive, allowing generalization of all further computations; note, however, that the noninverted negative version of the parameter is the one shown in all figures. A scaling by $1/N$, where N is the total number of channels, produces an average energy change per channel on a dB scale

$$\text{on}(n) = \frac{1}{N} \sum_{i:D_{i,k}(n)>0} D_{i,k}(n),$$

$$\text{off}(n) = \frac{1}{N} \sum_{i:D_{i,k}(n)<0} D_{i,k}(n).$$

This set of parameters in combination over a speech signal visibly provides useful information about the content of the signal, as can be seen in Fig. 4 for the same utterance used in Fig. 1. Note that the periodicity and aperiodicity proportion measures in (b) provide a decomposition of the signal into periodic (roughly, voiced) and aperiodic elements. Also note that the onset and offset measures in (d) have peaks at most of the important events in the signal.

C. Event detection

The manner classes of speech segments are listed in Table I, along with corresponding source types. Derived from these classes for the purpose of detection, a set of event types based on acoustic parameters was defined, and is listed in Table II. The categories correspond to the polarity (onset or offset of energy) of the event, and their correlation with periodic and/or aperiodic excitation. Events are labeled

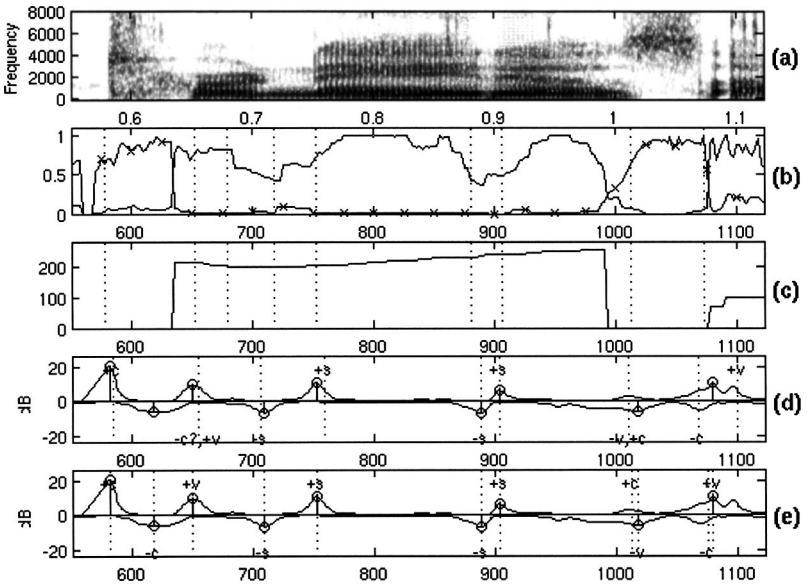

FIG. 4. Parameter extraction results for the word "tornadoes." (a) Spectrogram; (b) proportion of periodic (solid line) and aperiodic (solid line with "×" overlaid) energy; (c) smoothed pitch estimate in periodic regions; (d) onset and offset parameters, chosen peaks (stems), posited events (nonrequired marked with ?); (e) detected events.

based on their occurrence either at a boundary where periodic content begins or ends (±V, correlated with voicing onset or offset), or when surrounded by periodic excitation (±S, correlated with sonorant consonant boundaries), or their occurrence at a boundary of aperiodic excitation or at least occurring outside of periodic excitation (±C, correlated with obstruent consonants). The output of the event detector consists of this set of event labels. Part (d) of Fig. 4 shows a posited set of these events generated from TIMIT labels; part (e) shows detected events from the speech signal.

The normalized summary periodic and aperiodic energy measures, P_{eng} and AP_{eng}, are analyzed (after median smoothing) to locate potential confident regions and their boundaries. The set of confidently periodic/aperiodic regions is determined by applying a minimum threshold for a required maximum value of P_{eng} or AP_{eng} for a region. Following this, lower thresholds are used to find the boundaries of each region. Aperiodic regions are discarded unless at least one end of the region is associated with an onset/offset event, i.e., the beginning of the region near an onset event or the end of the region near an offset event. They are also discarded if the aperiodic region is shorter than 10 ms.

The onset and offset parameters are converted into a sequence of potential events by use of a convex hull-based peak-picking algorithm. There are thresholds for minimum peak height, and a required minimum dip between two adjacent peaks. Onset and offset peaks are associated with boundaries of periodic/aperiodic regions in order to classify event types. Onset/offset peaks located near the beginning/end of a periodic region are labeled as ±V. Correspondingly, onset/offset peaks located near the beginning/end of an aperiodic region are labeled as ±C. The locality criteria are determined from trained thresholds. Remaining boundaries of confidently periodic/aperiodic regions are labeled as landmarks of the corresponding types, but note that the times are less accurate.[1] Remaining onset/offset peaks are labeled as ±S if they are within a periodic region, or ±C if they are outside of any periodic region. The full set of trained parameters used in this process is listed in detail in Table III.

TABLE I. Modes of speech production (manner classes).

Manner	Oral tract	Primary source
Vowel	Open	Periodic
Semivowel	Slightly constricted	Periodic
Nasal	Closed (with nasal coupling)	Periodic
Fricative	Narrow constriction	Aperiodic
Stop	Completely closed	Aperiodic

D. Training procedure

Some adjustment was performed on a number of the time, energy, and confidence-level thresholds involved in event extraction. These included the pairs of thresholds used for determining confident regions of periodicity or aperiodicity as discussed above. The training procedure adjusted a set of 12 parameters, listed in Table III. The procedure was a sequence of Nelder–Mead simplex optimization stages on three subsets of the parameters (as defined in Table III), performed over the score $S = N_{\text{matches}} - N_{\text{insertions}}$ (Nelder and Mead, 1965). This cost is equivalent to minimizing the total error rate, as the base number of posited required events will not change (and as such a decrease in the number of matches corresponds to an increase in the number of deletions). The

TABLE II. Event types.

Label	Name	Description
+V	Voicing onset	Onset corresponding to beginning of periodicity (beginning of a vowel or sonorant consonant)
−V	Voicing offset	Offset corresponding to end of periodicity (end of a vowel or sonorant consonant)
+S	Sonorant onset	Onset within periodic region (onset at release of nasal or semivowel)
−S	Sonorant offset	Offset within periodic region (offset at release of nasal or semivowel
+C	Obstruent onset	Onset corresponding to beginning of aperiodicity (stop consonant burst, affricate or fricative onset)
−C	Obstruent offset	Offset corresponding to end of aperiodicity (stop, affricate or fricative offset)

TABLE III. Parameters with trained values. P_{on} and P_{off} refer to the boundaries of a periodic region; AP_{on} and AP_{off} are the corresponding locations for an aperiodic region.

Parameter	Description	Value
	Periodicity parameters	
$t_{before}:P_{on}$	Max. time from P_{on} to corresp. onset peak (peak *precedes* P_{on})	59.8 ms
$t_{after}:P_{on}$	Max. time from P_{on} to corresp. onset peak (peak *follows* P_{on})	4.48 ms
T_{per_RGN}	"Peak threshold" on P_{eng} to consider a region as periodic	58.7%
T_{per}	"Boundary threshold" on P_{eng} to located ends of a periodic region	31.1%
$t:P_{off}$	Maximum time between P_{off} and corresponding offset peak	61.7 ms
	Aperiodicity parameters	
$t:AP$	Max. time between AP_{on}/AP_{off} and corresponding on/off peak	31.1 ms
T_{aper_RGN}	"Peak threshold" on AP_{eng} to consider a region as aperiodic	84.2%
T_{aper}	"Boundary thresh." on AP_{eng} to located ends of aperiodic region	66.0%
	Onset/offset parameters	
T_{on_peak}	Minimum peak height in onset measure	4.70
T_{on_dip}	Minimum dip between peaks in onset measure	4.70
T_{off_peak}	Minimum peak height in offset measure	5.15
T_{off_dip}	Minimum dip between peaks in offset measure	5.15

procedure was dependent on initial conditions, which were set by trial and error and knowledge of front-end behavior. The training process was iterated twice to ensure some degree of convergence.

E. Scoring algorithm

A standard algorithm used for scoring speech recognizer performance at the phonetic level was modified to support scoring landmark results. The algorithm was derived from the DARPA speech recognizer performance evaluation tools (Pallett, 1989). This code aligns a recognized token string with reference labels using a dynamic programming algorithm. The original code supported scoring costs for insertions, deletions, and substitutions in a stream of labels. Modifications were made to perform the task of landmark scoring: (a) a cost was added for the difference in time (in ms) from the posited label to the detected label, to ensure that label matches and substitutions were close in time (insertion/deletion costs are equivalent to the cost of matching a label 50 ms from its posited location); (b) support for nonrequired events with zero deletion cost was added; (c) support for pairs of co-occurring events which could be found in either order was added, for example the onset of a fricative at the same point as the offset of the preceding vowel; and (d) substitution cost was doubled in the case that the polarity was incorrect, such that +C for −C was a more costly substitution than −V for −C, as it was more likely in the polarity mismatch cases that there was actually both an insertion and a deletion, rather than just a substitution.[2] Additional adjustments in the final score were made to ignore insertions before the beginning and after the end of the labeled speech, under the assumption that integrating an endpoint detector in the system would prevent positing events at these locations.

A set of summary statistics was defined to analyze matching results. All are defined in terms of the base rate N, the number of posited tokens not counting neutral deletions (of tokens marked as non-required). Defining N_P as the total number of posited tokens (including those marked nonrequired), D as the number of error deletions (of required tokens), D_N as the number of neutral deletions, S as the number of substitutions, and I as the number of insertions, the metrics are computed according to the following formulas:

$$N = N_P - D_N \quad \text{(base rate of matched tokens)},$$

$$\text{detection rate } R_M = \frac{N - D - S}{N},$$

$$\text{deletion rate } R_D = \frac{D}{N},$$

$$\text{substitution rate: } R_S = \frac{S}{N},$$

$$\text{insertion rate: } R_I = \frac{I}{N}.$$

III. METHOD FOR BROAD-CLASS RECOGNITION EXPERIMENTS

A. Database

The TIMIT database was used for the recognition experiments. The training data consisted of 2710 utterances from the suggested training section of the TIMIT database. The performance of the recognizers was based on 504 utterances from the suggested test set.

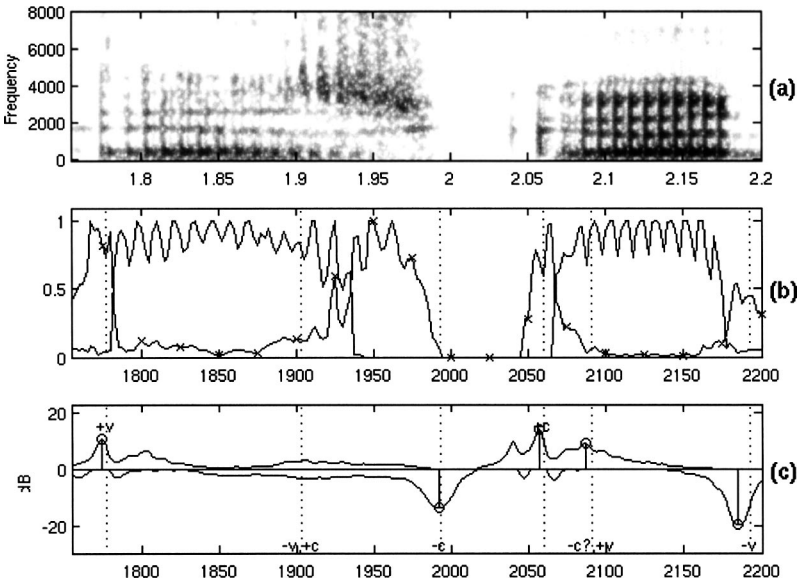

FIG. 5. Parameter extraction results for the fragment ''is going,'' displaying the difficulty of locating the boundary between a vowel and an adjacent voiced fricative /z/. (a) Spectrogram; (b) proportion of periodic (solid line) and aperiodic (solid line with ''×'' overlaid) energy; (c) onset and offset parameters, chosen peaks (stems), posited events.

B. Models

Acoustic models were built for four manner classes: sonorant (includes vowels and sonorant consonants), stop, fricative, and affricate. In addition, a model was built for silence. The back-end processing was done using an HMM-based recognition system (Young, 1995). Each model consisted of a three-state (plus 2 terminal states) HMM with eight Gaussian mixtures in each state. Each mixture was initialized as zero mean and unit diagonal covariance. Each mixture had diagonal variance and all the mixtures weights in all the states were initialized at the same value. Left-to-right state transition with one skip was incorporated with the additional constraint that each model had to start at the first state. All of the allowable transitions were initialized as equiprobable.

Three different front ends were used in the recognition experiments. The first front end consisted of 12 mel-frequency cepstral coefficients (MFCCs) and energy with their delta and acceleration coefficients. The second front end consisted of the four temporal-based parameters: aperiodic energy measure, periodic energy measure, onset waveform, and offset waveform. The third front end consisted of both the cepstral-based parameters and the temporal-based parameters. All of the parameters were computed at a rate of 5 ms and the window size was 20 ms. The mean of each parameter was normalized to zero.

C. Scoring

For scoring, the phonetic transcriptions provided with the TIMIT database were mapped into the four manner classes and silence. Although separate models were built for affricates and stops, they were recognized as the same class. Flaps were allowed to score as either a stop or a sonorant consonant. Glottal stops were allowed to score as either a vowel or a stop.

IV. RESULTS

A. Detection of events in clean and spectrally impoverished speech

Results for the event detection in clean and spectrally impoverished speech are plotted separately for the categories ''strongly robust,'' ''robust,'' and ''weak'' event types in Fig. 5. Weak events were a set of events that were expected to be less abrupt, including releases and closures for nasals, voiced nonstrident fricatives, and voiced stops labeled as flaps. The rest of the events were considered robust, and a subset of these that were detected with an error rate (includes deletions and substitutions) less than 2% in clean speech was labeled as strongly robust. Details of the detection rates for different events are given in the Appendix. Events were detected[3] with an overall detection rate of 80.2% on the clean test data set with an insertion rate of 8.7%, and 76% on the impoverished test set with an insertion rate of 36.6%. Note that for each category, the difference between the detection results for the clean speech and the impoverished speech is within 5%. Thus, the temporal parameters are quite robust to spectral degradation.

Nearly half of the error rate is due to missed landmarks at the boundary between a nasal consonant and a vowel, an event type that was detected with only 45.6% accuracy. Another major error source was from landmarks for voiced nonstrident fricatives; initial onsets preceding the fricative were located only 48.1% of the time, and landmarks for a voiced weak fricative adjacent to a vowel were detected with 49.0% accuracy. A third difficult case involved locating landmarks for stop consonants labeled as flaps, of which only 42.6% were detected correctly. These three cases combined account for 69.5% of all errors made. Discounting these classes of landmarks, the detection rate was 91.8%; and the detection rate for a subset consisting of the most strongly robust event types was 98.5%.

Landmark types that were detected well included stop consonants and unvoiced fricatives: 90.9% of stop closures following a vowel were detected, and 96.0% of stop bursts

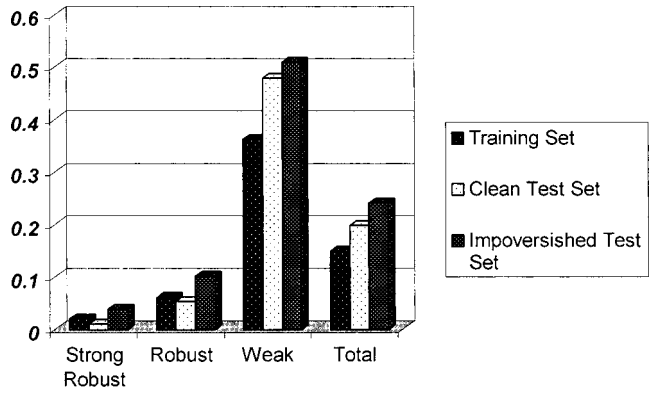

FIG. 6. Landmark detection results for clean and impoverished speech.

were detected (including 99.0% of unvoiced stop releases). Landmarks for unvoiced fricative closures and releases adjacent to a vowel were detected with 99.0% accuracy (and 92.4% for voiced stridents). Note that affricate consonants were grouped with strident fricatives for this count. The voiced /z/ and /zh/ fricatives can have a difficulty to locate boundary due to overlap with neighboring segments; see, for instance, the utterance shown in Fig. 6. More results for robust event types are given in the Appendix.

The results from this study are somewhat different in organization than those of Liu (1994), but a gross comparison of some of the results is possible. When tested across the full TIMIT test set using automatically generated labels, the landmark detector developed by Liu had an error rate of 15% for deletions, 6% for substitutions, and 25% for insertions. Our overall error rate on a subset of the TIMIT test data is 19% for deletions when laterals are included (15% when laterals are not included in the events expected to be detected, 4.8% for substitutions, and 8.7% for insertions). Note that these numbers may not be directly comparable since there are differences in the way the results were tallied. One possible conclusion from this comparison is that a selection of broader frequency bands such as those used by Liu may be more appropriate for the detection of nasals and laterals, whereas summary measures across all frequency channels may be better for obstruents.[4]

B. Temporal parameters vs cepstral parameters for manner-class recognition

The manner class recognition results are given in Table IV. As can be seen, the four temporal parameters result in performance that is comparable to that obtained with the 39 cepstral-based parameters. Adding the temporal-based parameters to the cepstral-based parameters results in close to a 5% improvement in accuracy. This increase in performance is due largely to improved detection of landmarks, particularly for the stop and fricative consonants. Note that the performance of the recognizers may in fact be considerably better than the numbers in Table IV suggest. In an analysis of manner–class recognition experiments performed by Bitar and Espy-Wilson (1995) using some of the same TIMIT test sentences, Bitar and Espy-Wilson found that presumed misclassifications of voiced obstruents as sonorant consonants was not incorrect. Many of the voiced obstruents were in fact realized as sonorant consonants, even though this change in the surface realizations of the voiced obstruents is not reflected in the TIMIT transcriptions. More recent results evaluating the proportion of periodic vs aperiodic energy in speech signals by Deshmukh and Espy-Wilson (2003) show that about 33% of voiced obstruents have a strong periodic component with little or no aperiodic component, and about half of all voiced obstruents show strong periodicity.

TABLE IV. Recognition results (in percent) for the broad classes: Sonorant (includes vowels and sonorant consonants), fricative, stop and silence.

	Correct	Accuracy
MFCCs (39 parameters)	73.9	70.1
Temporal measures (4 parameters)	78.0	70.1
MFCCs+temporal measures (43 parameters)	81.1	74.8

V. DISCUSSION

There are a number of key areas where accuracy could be improved, particularly in use of prediction and longer-term integration of information. In the front end, silence detection may be improved by addition of masking constraints; this will result in improved contextual reliability as a function of signal level. Of primary interest are spectral masking effects of tones on noise with respect to thresholds for detection of aperiodicity in the presence of a primarily periodic signal. The onset/offset detector could benefit from improved adaptation of the temporal sensitivity parameter; one possibility may be to examine separately adapting versions tuned to periodic excitation and aperiodic events for optimal detection of fricative events. Finally, it may be possible to modify the event extraction stage of the system to dynamically adapt thresholds as necessary. This could be done using temporal constraints (expected events or segments per unit time, adapted for speaking rate) rather than explicit required levels for peaks.

An important area for further research will be improving the extraction of temporal cues from noisy inputs. The present system is subject to errors (likely to be primarily insertions, which may be filterable based on spectral characteristics) given a signal mixed with rapidly fluctuating noise. The use of a large number of narrow bands allows for adaptation to noise if methods are developed to identify which bands to ignore; such methods could include correlation methods, or scene analysis techniques such as those used in missing-data approaches to speech recognition (Cooke *et al.*, 1997).

The next stage of this work will be to combine cues derived from temporal information with a recognition system based on spectral features, as both types of features will be important for a complete system. It is clear that temporal information is used by the human speech recognition system, and so should be critical to achieving high-quality performance in a computer speech recognition system; spectral cues are also of significant importance, for example formant frequencies and other spectral cues to place. This merging

could involve spectral weighting of temporal components, or a merger at the event output stage, increasing confidence in existence of an event if it is posited from multiple types of information. Later stages of the recognizer will be able to take into account a broader range of temporal and spectral cues.

VI. CONCLUSION

This work has shown that use of temporal information for landmark detection is feasible, particularly for a subset of robust abrupt events such as stop bursts. Although previous studies have investigated the use of temporal information in particular cases or as an additional measure, this work extends this body of work by using temporal information everywhere as the primary information source. As noted by use of a tunable onset/offset detector, it was determined that some locations require different degrees of sensitivity to temporal information. It has also pointed to certain landmark types where spectral features and perhaps more subtle temporal features (on a longer time scale) are important, particularly for landmarks related to sonorant consonants. It would be expected that the optimal system would integrate both temporal and spectral information.

ACKNOWLEDGMENTS

This work was supported in part by NSF Grant No. SBR-9729688 and NIH Grant No. 1K02 DC00149-01A1. Thanks to the three anonymous reviewers and the associate editor for useful comments on this manuscript.

APPENDIX A: ERROR RATES IN THE DETECTION OF ROBUST EVENTS IN THE CLEAN TEST SET

Landmark type	% Deletion and substitution errors	% Deletion error	# of tokens
	Consonantal landmarks adjacent to vowels		
Stop closure	9.14	1.57	383
Unvoiced stop release	1.03	0.34	291
Voiced stop release	8.51	0.00	188
Unvoiced fricative	1.01	1.01	397
Voiced fricative	7.05	7.05	156
	Interconsonantal landmarks		
Stop/strident fricative boundary	1.23	0.00	81
Strident fricative/stop boundary	5.49	4.40	91
Fricative/nasal and nasal/fricative boundary	5.00	5.00	40
	Initial and final events		
Glottal onset/offset	10.50	5.88	238
Strident fricative (initial or final)	1.11	1.11	90
Unvoiced weak fricative (initial or final)	11.11	11.11	9

APPENDIX B: ERROR DETECTION RATE OF WEAK EVENTS IN CLEAN TEST SET

Landmark type	% Substitution and deletion errors	% Deletion errors	# of tokens
	Consonantal landmarks adjacent to a vowel		
Stop (labeled as a flap)	57.45	31.91	94
Stop release (labeled without a burst)	46.67	13.33	15
Voiced weak fricative	51.03	51.03	194
Nasal	54.45	43.64	472
Aspiration (h)	31.82	31.82	44
	Interconsonantal landmarks		
Stop/nonstrident fricative or nonstrident fricative/stop boundary	19.05	14.29	42
Non-strident fricative/nasal or nasal/nonstrident fricative boundary	33.33	33.33	27
Stop/nasal or nasal/stop boundary	21.18	20.00	85
	Initial and final events		
Initial voiced nonstrident fricative	51.85	51.85	27
Aspiration (initial or final)	36.36	36.36	11

[1]The periodicity results are compiled only every 2.5 ms, whereas onset/offset parameters are computed with a 1-ms frame rate. Also, the energy change measurement is inherently more accurate in time as the periodicity computation is dependent on even longer time scales corresponding to pitch periods.

[2]Due to inclusion of a cost for the distance in time between the posited and generated events, this type of substitution would never be chosen by the scoring algorithm, as the cost structure makes it cheaper for the system to count it as an insertion plus a deletion.

[3]Events for flaps (labeled ''dx'') were considered correct whether they were detected as ±V or ±S.

[4]Note that Liu provides detailed data similar to those listed in the Appendix, but it is for the LAFF database which was hand labeled. Although a direct comparison is difficult given the differences in the databases and the differences in the generation of the reference labels, Liu's detector may perform better on nasal consonants than our detector (29% error on closures and 44% error on releases, vs 54.5% error), but it does not reach our level of performance for unvoiced stop releases (8% error vs 1.0% error).

Bitar, N. (**1997**). ''Acoustic analysis and modeling of speech based on phonetic features,'' Ph.D. dissertation, Boston University, Boston, Mass.

Bitar, N., and Espy-Wilson, C. Y. (**1995**). ''A signal representation of speech based on phonetic features,'' Proceedings of the IEEE Dual-Use Technologies and Applications Conference, SUNY Inst. of Tech., Utica, Rome, pp. 310–315.

Browne, G. J., and Cooke, M. (**1994**). ''Computational auditory scene analysis,'' Comput. Speech Lang. **8**, 297–336.

Catford, J. C. (**1977**). *Fundamental Problems in Phonetics* (Indiana University Press, Bloomington, IN).

Choi, J. Y., Chuang, E., Gow, D., Kwong, K., Shattuck-Hufnagel, S., Stevens, K. N., and Zhang, Y. (**1997**). ''Labeling a speech database with landmarks and features,'' 134th Meeting of the Acoustical Society of America, S3163.

Cooke, M., Morris, A., and Green, P. (**1997**). ''Missing data techniques for robust speech recognition,'' Proceedings of the ICASSP, pp. 863–866.

Deshmukh, O., and Espy-Wilson, C. (**2003**). ''Detection of the periodicity and aperiodicity profile of speech,'' Proceedings of the ICASSP, pp. 448–451.

Espy-Wilson, C. Y. (**1992**). ''Acoustic measures for linguistic features distinguishing the semivowels /wjrl/ in American English,'' J. Acoust. Soc. Am. **92**, 736–757.

Espy-Wilson, C. Y. (**1994**). ''A feature-based semivowel recognition system,'' J. Acoust. Soc. Am. **96**, 65–72.

Glasberg. B. R. and Moore, B. C. J. (**1990**). ''Derivation of auditory filter shapes from notched-noise data,'' Hear. Res. **47**, pp. 103–138.

Juneja, A., and Espy-Wilson, C. Y. (**2003**). ''An Event-based Acoustic Phonetic Approach for Speech Segmentation and E-Set Recognition,'' Proceedings of the International Congress of Phonetic Sciences, pp. 1333–1336

Klatt, D. (**1979**). ''Speech perception: A model of acoustic-phonetic analysis and lexical access,'' J. Phonetics **7**, 279–312.

Liu, S. (**1994**). ''Landmark detection for distinctive feature based speech recognition,'' Ph.D. thesis, Massachusetts Institute of Techology, Cambridge, MA.

Moore, B. C. J. (**1997**). *An Introduction to the Psychology of Hearing*, 4th ed. (Academic, London).

Nelder, J. A., and Mead, R. (**1965**). ''A simplex method for function minimization,'' Comput. J. (UK) **7**, 308–313.

Pallett, D. S. (**1989**). ''Benchmark tests for DARPA resource management database performance evaluations,'' in Proceedings of the 1989 International Conference on Acoustics, Speech and Signal Processing, pp. 536–539.

Rabiner, L. R., and Gold, B. (**1975**). *Theory and Application of Digital Signal Processing* (Prentice Hall, Englewood Cliffs, NJ).

Rosen, S. (**1992**). ''Temporal information in speech: Acoustic, auditory, and linguistic aspects,'' Philos. Trans. R. Soc. Lond. B Biol. Sci. **336**, 367–373.

Seneff, S., and Zue, V. (**1988**). ''Transcription and alignment of the TIMIT database,'' included with TIMIT database.

Shamma, S., and Hermansky, H. (**2000**). ''Speech recognition from temporal patterns,'' Proceedings of the ICSLP.

Shannon, R. V., Zeng, F., Kamath, V., Wygonski, J., and Ekelid, M. (**1995**). ''Speech recognition with primarily temporal cues,'' Science **270**, 303–304.

Stevens, K. N. (**1986**). ''Models of phonetic recognition. II. A feature-based model of speech recognition,'' in Proceedings of the Montreal Satellite Symposium on Speech Recognition, Twelfth International Conference on Acoustics, edited by P. Mermelstein, pp. 67–68.

Stevens, K. N. (**2002**). ''Toward a model for lexical access based on acoustic landmarks and distinctive features,'' J. Acoust. Soc. Am. **111**, 1872–1891.

Turner, C. W., Souza, P. E., and Forget, L. N. (**1995**). ''Use of temporal envelope cues in speech recognition by normal and hearing impaired listeners,'' J. Acoust. Soc. Am. **97**, 2568–2576.

Van Tasell, D. J., Soli, S. D., Kirby, V. M., and Widin, G. P. (**1987**). ''Speech waveform envelope cues for consonant recognition,'' J. Acoust. Soc. Am. **82**, 1152–1161.

Viemeister, N. F. (**1979**). ''Temporal modulation transfer functions based upon modulation thresholds,'' J. Acoust. Soc. Am. **66**, 1364–1380.

Viikki, O. (**2001**). ''Noise robust ASR,'' Speech Commun. **34**, 1–2.

Young, S. (**1995**). *The HTK Book* (Cambridge Research Lab, Entropic, Cambridge, England), http://htk.eng.cam.ac.uk

The psychomechanics of simulated sound sources: Material properties of impacted bars[a)]

Stephen McAdams[b)]
Institut de Recherche et Coordination Acoustique/Musique (SMTS-Ircam-CNRS), 1 place Igor Stravinsky, F-75004 Paris, France and Département d'Etudes Cognitives, Ecole Normale Supérieure (DEC/ENS), 45 rue d'Ulm, F-75230 Paris, France

Antoine Chaigne[c)]
Département TSI, Ecole Nationale Supérieure des Télécommunications (ENST/TSI), 46 rue Barrault, F-75013 Paris, France

Vincent Roussarie[d)]
SMTS-Ircam-CNRS, 1 place Igor Stravinsky, F-75004 Paris, France and ENST/TSI, 46 rue Barrault, F-75013 Paris, France

(Received 25 March 2003; accepted for publication 15 December 2003)

Sound can convey information about the materials composing an object that are often not directly available to the visual system. Material and geometric properties of synthesized impacted bars with a tube resonator were varied, their perceptual structure was inferred from multidimensional scaling of dissimilarity judgments, and the psychophysical relations between the two were quantified. Constant cross-section bars varying in mass density and viscoelastic damping coefficient were synthesized with a physical model in experiment 1. A two-dimensional perceptual space resulted, and the dimensions were correlated with the mechanical parameters after applying a power-law transformation. Variable cross-section bars varying in length and viscoelastic damping coefficient were synthesized in experiment 2 with two sets of lengths creating high- and low-pitched bars. In the low-pitched bars, there was a coupling between the bar and the resonator that modified the decay characteristics. Perceptual dimensions again corresponded to the mechanical parameters. A set of potential temporal, spectral, and spectrotemporal correlates of the auditory representation were derived from the signal. The dimensions related to mass density and bar length were correlated with the frequency of the lowest partial and are related to pitch perception. The correlate most likely to represent the viscoelastic damping coefficient across all three stimulus sets is a linear combination of a decay constant derived from the temporal envelope and the spectral center of gravity derived from a cochlear representation of the signal. These results attest to the perceptual salience of energy-loss phenomena in sound source behavior.
[DOI: 10.1121/1.1645855]

PACS numbers: 43.75.Cd, 43.66.Jh, 43.75.Kk [NHF] Pages: 1306–1320

I. INTRODUCTION

The perception of the properties of sound sources is important for their categorization and identification as well as for our own interactions with them in the environment (McAdams, 1993). Recent research has begun to study listeners' sensitivities to auditory cues that communicate aspects of the geometry and material properties of vibrating objects as well as changes in the state of objects (e.g., breaking) or the activity of organisms (e.g., walking). Listeners' auditory sensitivity to the geometry of vibrating objects has been demonstrated for clapping hands (Repp, 1987), impacted bars (Houix *et al.*, 1999; Lakatos *et al.*, 1997; Lutfi, 2001), impacted plates (Kunkler-Peck and Turvey, 2000), falling and bouncing balls (Guski, 2000), rods that fall and bounce on the floor (Carello *et al.*, 1998), vessels being filled with liquid (Cabe and Pittenger, 2000), the size and velocity of rolling balls (Houben, 2002), or to the geometric integrity or loss thereof in falling jars that bounce or shatter (Warren and Verbrugge, 1984). A similar sensitivity to properties such as density and elasticity that vary with the materials of which an object is composed has also been shown (Avanzini and Rocchesso, 2001; Klatzky *et al.*, 2000; Lutfi and Oh, 1997).

Such studies have used a variety of approaches such as recognition, identification, classification, or categorization of the object (Avanzini and Rocchesso, 2001; Cabe and Pittenger, 2000; Houix *et al.*, 1999; Krotkov *et al.*, 1996; Repp, 1987; Warren and Verbrugge, 1984), discrimination among sounds (Lakatos *et al.*, 1997; Lutfi, 2001; Lutfi and Oh, 1997), scaling sounds according to prespecified properties such as hardness, length, mass, or speed (Carello *et al.*,

[a)]Preliminary results leading to the present study were first reported at the combined 16th International Congress on Acoustics and 135th Meeting of the Acoustical Society of America, Seattle, WA and at the 139th Meeting of the Acoustical Society of America, Atlanta, GA.

[b)]Address correspondence to S. McAdams at DEC/ENS. Electronic mail: mcadams@dec.ens.fr

[c)]Current address: ENSTA-UME, chemin de la Hunière, F-91761 Palaiseau, France. Electronic mail: chaigne@ensta.fr

[d)]Current address: PSA Peugeot-Citroën, DRIA/SARA/PEFH, route de Gizy, F-78140 Vélizy-Villacoublay, France. Electronic mail: vincent.roussarie@mpsa.com

1998; Freed, 1990; Kunkler-Peck and Turvey, 2000), or estimating relative similarity of sound pairs (Klatzky *et al.*, 2000). The last technique is of particular interest as it lends itself to an exploratory data analysis approach that imposes few *a priori* hypotheses on the nature of the underlying perceptual structure that results from variation in a set of mechanical properties of the objects of interest or the acoustical properties resulting from setting them into vibration.

In most of the studies cited above, the sounds used were either natural (objects set into vibration in the presence of the listeners or digitally recorded) or synthetic (most often by Fourier synthesis). The former have the advantage of representing the richness of the everyday acoustic environment and the disadvantage of clearly establishing what it is in the sound that listeners are using to make their judgments. The latter have the advantage of being deterministic and simple, but often suffer from not truly representing real-life vibrating objects. A judicious compromise is the use of physical models that simulate the vibratory behavior of objects. One can control precisely the mechanical parameters of the synthesis model, all the while obtaining the complex relations among analytic signal parameters that specify the mechanical nature of the object. The perceptual study of such sounds also has the advantage of leading to an understanding of which mechanical properties are the most relevant for simulation in virtual environments.

To study the perceptual representation of material properties of impacted bars, a physical model was used to create the sounds. The model has been presented elsewhere (Chaigne and Doutaut, 1997; Doutaut *et al.*, 1998) and only the aspects that are relevant to the present psychophysical quantification of the relation between some of the model parameters and their corresponding perceptual dimension will be presented here. Listeners performed dissimilarity ratings on pairs of sounds. A multidimensional scaling technique was used to recover a mathematical model that represents the dissimilarities as distances (McAdams *et al.*, 1995). Indeed, multidimensional scaling has been a technique of predilection for the study of musical timbre (Gray, 1977; Hajda *et al.*, 1997; Iverson and Krumhansl, 1993; Lakatos, 2000; McAdams, 1999; McAdams *et al.*, 1995; Plomp, 1970; Wessel, 1979). One then uses the distance model to compare the dimensionality of the ''perceptual space'' with that of the physical stimulus space and to quantify the relations among mechanical properties, analytic parameters derived from the resulting signals, and the perceptual dimensions. Of particular interest are the nature of timbral and pitch cues that underlie the perceptual representation.

II. PHYSICAL MODELING SYNTHESIS

The software used to build the sound palette for the psychoacoustic experiments is a time-domain sound synthesis program based on a physical model. The program digitally simulates mallet percussion instruments (Chaigne and Doutaut, 1997; Doutaut *et al.*, 1998). The physical equations of the complete model are thus reproduced and solved numerically, providing control of the different mechanical and geometrical parameters of the equations. We will briefly present in order the physical model of the vibrating bar. The mechanical equations are taken from Chaigne and Doutaut (1997). They are presented only briefly here to underscore the choices of physical parameters that were made for the synthesis of the test stimuli. For a fuller development of the theory and implementation, in particular the interaction between mallet and bar and the acoustic radiation, see Chaigne and Doutaut (1997) and Doutaut *et al.* (1998). All parameters related to these parts of the model were held constant in our sound stimuli. Experiment 1 used parameter settings of the model for rectangular bars of constant cross-sectional geometry, whereas experiment 2 used parameters for tuned bars of variable cross section as are found in the xylophone and marimba. The notations used to represent the physical parameters in the equations for the bars are shown in Table I.

TABLE I. Variables used in the bar model.

Symbols	Definitions (units)
$w(x,t)$	Vertical displacement (m)
E	Young's modulus (N/m^2)
ρ	Density (kg/m^3)
$S(x)$	Cross section (variable) (m^2)
$I(x)$	Moment of inertia of cross-section (m^4)
L	Length (m)
b	Width (m)
$h(x)$	Thickness (variable) (m)
γ_B	Fluid damping coefficient (s^{-1})
η	Viscoelastic damping coefficient (s)
α	Damping factor (s^{-1})
$f(x,x_0,t)$	Force per unit mass (m/s^2)

In this section the mechanical equations are presented, notably taking into account energy loss phenomena that are crucial to our study. Energy loss processes are ubiquitous in physical phenomena. In particular, any excited physical system will dissipate the received energy over the course of time in the form of internal or external exchanges. When a mallet excites a bar, part of the incident energy is dissipated into the air in the form of an acoustic wave, i.e., a sound. This external wave whose acoustic radiation is caused by the vibrating structure is one of the external exchanges. However, this loss is most often negligible compared with the losses due to viscosity within the material (except for metal bars of particular size, around and above the critical frequency). Chaigne and Lambourg (2001), for example, have shown that the fine-grained modeling of damping is complex, but that in the case of bars, an approximate description of damping with two constants (fluid and viscoelasticity) already gives good results for sound synthesis. The energy losses are reflected in the sound's temporal evolution and are consequently perceived by the listener as a progressive attenuation of the sound level and at times as a modification of the timbre of the sound. One of the aims of sound synthesis with physical models is to reproduce as closely as possible the signals arising from mechanically produced events. It is thus imperative for high fidelity synthesis to introduce energy loss phenomena. However, the physical justification and the mathematical formulation of these phenomena can be very complex. It is thus necessary to start with simple, general models. The validity of these models derives from both experimental physical measures and perceptual validation by

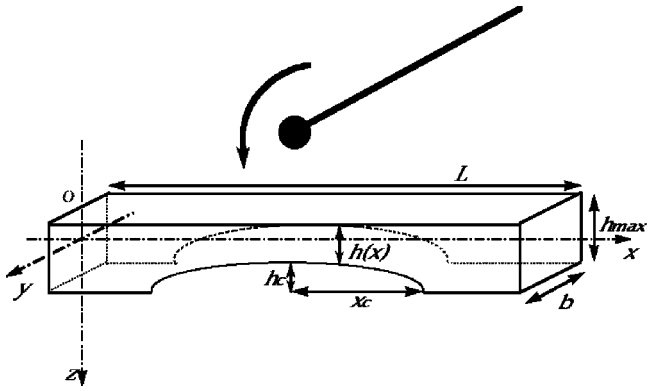

FIG. 1. Geometry of the xylophone bar.

listeners. The present study focuses on the latter aspect.

The physical system under consideration is composed of a bar of constant (or variable) cross section with free edges, of a mallet with a spherical head, and of a resonator. The diagram of the bar is presented in Fig. 1.

The bars are simulated with elastic supports as in a xylophone. One-dimensional Euler–Bernoulli bar equations are used to describe wave propagation in the material, which is presumed to be homogeneous and isotropic. This model is refined by taking into account the damping of the transverse bending waves with a model of viscoelastic loss. The vertical component $w(x,t)$ of the displacement of the bar is governed by the following equation:

$$\frac{\partial^2 w}{\partial t^2}(x,t)=\frac{E}{\rho S(x)}\left(1+\eta\frac{\partial}{\partial t}\right)\frac{\partial^2}{\partial t^2}\left(I(x)\frac{\partial^2 w}{\partial x^2}\right)-\gamma_B\frac{\partial w}{\partial t}+f(x,x_0,t), \tag{1}$$

where E is Young's modulus, ρ is the density, $S(x)$ is the rectangular cross section, which varies as a function of the position x along the longitudinal axis of the bar, η is the viscoelastic damping coefficient, $I(x)$ is the moment of inertia of the cross section, γ_B is the fluid damping coefficient, and $f(x,x_0,t)$ is the force per unit mass. As discussed in Chaigne and Doutaut (1997), γ_B determines (asymptotically) the losses in the lowest partials and η determines (asymptotically) the losses in the higher ranking partials. Their combination results in a decay envelope that can be characterized with two decay constants (see Sec. III).

For a rectangular cross section, we have

$$S(x)=bh(x) \quad \text{and} \quad I(x)=\frac{bh^3(x)}{12}. \tag{2}$$

Under the assumption of free-free boundary conditions, one obtains

$$\frac{\partial^2 w}{\partial x^2}(x,t)=0, \quad \frac{\partial^3 w}{\partial x^3}(x,t)=0\Big|_{x=0,L}, \tag{3}$$

which means that force and moment vanish at both ends of the bar. We assume that the sound of an impacted bar is due to the flexural motion of the bar in the vertical x-z plane. This amounts to neglecting the contribution of torsional and longitudinal waves, as well as of flexural waves in the x-y plane. An additional assumption is that this motion can be adequately described by the one-dimensional Euler–Bernoulli equations. Previous measures on xylophone bars show this assumption to be valid in the low-frequency range to a first degree of approximation (Rossing and Russell, 1990), the model leading to a tuning error of less than 2% for fundamental frequencies below 1.2 kHz (Doutaut, 1996).

Although for wood this is an approximation, the material is assumed to be homogeneous and isotropic. Since bars are usually cut in the direction of the fibers, Eq. (1) is acceptable if Young's modulus, E in the equation, is taken equal to the longitudinal modulus of elasticity (Bucur, 1995).

The damping of the flexural waves is represented in Eq. (1) by two terms. The first one represents viscoelastic losses and is proportional to the coefficient η (in s). The relation between stress σ and strain ε in the material is expressed by

$$\sigma(x,t)=E\left(\varepsilon(x,t)+\eta\frac{\partial\varepsilon}{\partial t}(x,t)\right). \tag{4}$$

The second term is equivalent to a fluid damping. Its magnitude is represented by the coefficient $\gamma_B(\mathrm{s}^{-1})$. Chaigne and Doutaut (1997) showed that the introduction of these damping terms in Eq. (1) yields a good representation of losses in wooden bars. The coefficients η and γ_B are estimated from the decay times of partials. The solutions of Eq. (1), decomposed on the basis of plane waves, allow us to write the solutions in the form of the product of a spatial function and a temporal function. In order to characterize damping, we define the damping factor α as the inverse of the time it takes for the amplitude to decay by a factor of $1/e$. Assuming damped sinusoidal waves as solutions to Eq. (1) imposes the following relation between damping and frequency:

$$\alpha(f)=\frac{\gamma_B}{2}+2\pi^2\eta f^2. \tag{5}$$

This relation allows us to compute the coefficients of the damping model by measuring the value of α for each partial in real bars.

III. DERIVATION OF ANALYTIC SIGNAL PARAMETERS

All sounds were synthesized in 16-bit mono format at a 48-kHz sampling rate. Three classes of analytic signal parameters were derived: temporal, spectral, and spectrotemporal. The temporal parameters were derived from the temporal envelope $[A_{HT}(t)]$, which was determined by taking the imaginary part of the Hilbert transform of the signal and filtering the absolute value of this imaginary part using a third-order Butterworth filter with a low-pass cutoff frequency of 50 Hz.

The spectral and spectrotemporal parameters were derived from one of two time-frequency representations. In the raw signal representation, a 4096-point fast Fourier transform (FFT) with a Hamming window was performed. To estimate the frequencies of the partials composing each sound, the beginning of this time window was positioned just after the attack of the sounds at 23 ms.

The second time-frequency representation simulates the output of the human cochlea. In this representation, the sig-

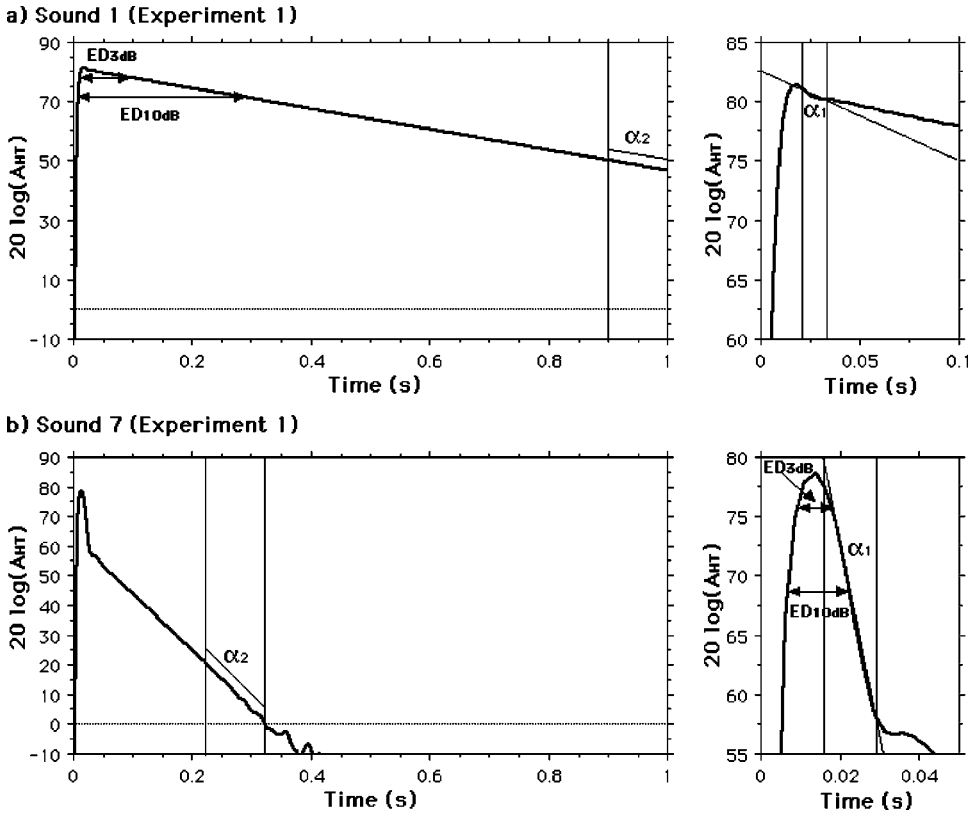

FIG. 2. Temporal envelopes for sounds 1 (a) and 7 (b) from experiment 1, representing the lowest and highest degrees of damping, respectively (see Table III). The derivation of decay constants α_1, α_2 (slopes of lines fitted to portions of the curve) and equivalent durations $ED_{3\mathrm{dB}}$, and $ED_{10\mathrm{dB}}$ from these functions is shown. The full envelope over the 1-s duration is shown on the left and a blowup of the initial portion of each envelope is shown on the right.

nal is first processed in a way that simulates the outer and middle ear filtering. The magnitude transfer function is deduced from behavioral measures of the minimum audible field (absolute auditory threshold; Killion, 1978). It is implemented as a cascade of an IIR high-pass filter to account for the sharp loss of sensitivity at low frequencies and a FIR equalizer (two second-order filters in cascade) to account for the peak of sensitivity around 2 kHz and the loss of sensitivity in the high frequencies. The filtered signal is then processed in several steps to obtain an approximation of the excitation pattern along the basilar membrane, function of the frequency locus (or characteristic frequency, CF) along the membrane and of time. In a first step, the waveform is multiplied by a window shaped as the time-reversed envelope of a gammatone impulse response (Patterson *et al.*, 1995) with an equivalent rectangular duration of about 20 ms. The windowed slices are Fourier transformed to obtain a power spectrum. The frequency resolution of this power spectrum is similar to that of the characteristic frequency with the narrowest cochlear filter. The power spectrum is remapped to get a resolution similar to the cochlea and channels evenly spaced on an equal-resolution scale (Moore and Glasberg, 1983). This scale is derived from psychophysical measures of auditory filter bandwidth (in equivalent rectangular bandwidth, or ERB, units) along the cochlear partition (the ERB-rate scale). Each channel of the new spectrum is the weighted sum of power spectrum coefficients, with weights designed to approximate the shape of a cochlear filter. This new power spectrogram has a frequency resolution and scale similar to that of the cochlea. Its temporal resolution is commensurable with that measured psychophysically (equivalent rectangular duration $=8-13$ ms) (Plack and Moore, 1990). All channels have the same temporal resolution. In this respect, it differs from the gammatone filter-bank which allows better temporal resolution at higher frequencies, but not at the lowest. Different temporal resolution in different channels makes the calculation of parameters such as the instantaneous spectral centroid unstable, so uniform temporal resolution is preferable. As a final step, the power in each channel is raised to the power 0.25 to approximate excitation or partial loudness (Hartmann, 1997).

A. Decay constants (α_1, α_2)

The temporal envelope of percussive sounds is often assimilated to a decaying exponential function of the form $A\exp(-\alpha t)$. Damping can thus be practically characterized by the decay constant α. This parameter can be estimated as the slope of the linear regression equation on $\ln[A_{HT}(t)]$. However, as Fig. 2 shows, the form of this envelope has two slopes, related to γ_B and η as discussed previously: one just after the maximum and another anywhere from several tens to several hundreds of ms later, respectively. The first, α_1, was estimated over a time frame of 15 ms starting 2.5 ms after the envelope maximum. The second, α_2, was estimated over a 100-ms time frame ending either at the end of the sound for those sounds that were artificially cut off at 1 s, or at the moment at which $\ln[A_{HT}(t)]=0$. The envelope generally becomes erratic below this value.

B. Equivalent durations ($ED_{3\mathrm{dB}}, ED_{10\mathrm{dB}}$)

Since the damping strongly affects the perceived duration of the sounds, an additional analytic parameter related to the decay constant was computed. This parameter represents

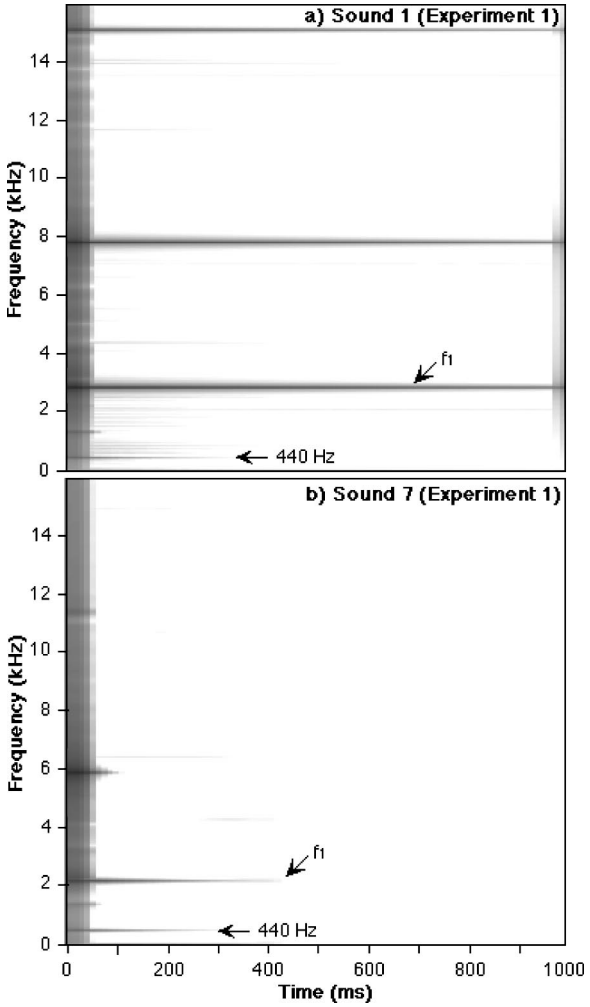

FIG. 3. Spectrograms of sounds 1 and 7 from experiment 1. The 440-Hz component due to the resonator and the lowest partial due to the bar (f_1) are shown.

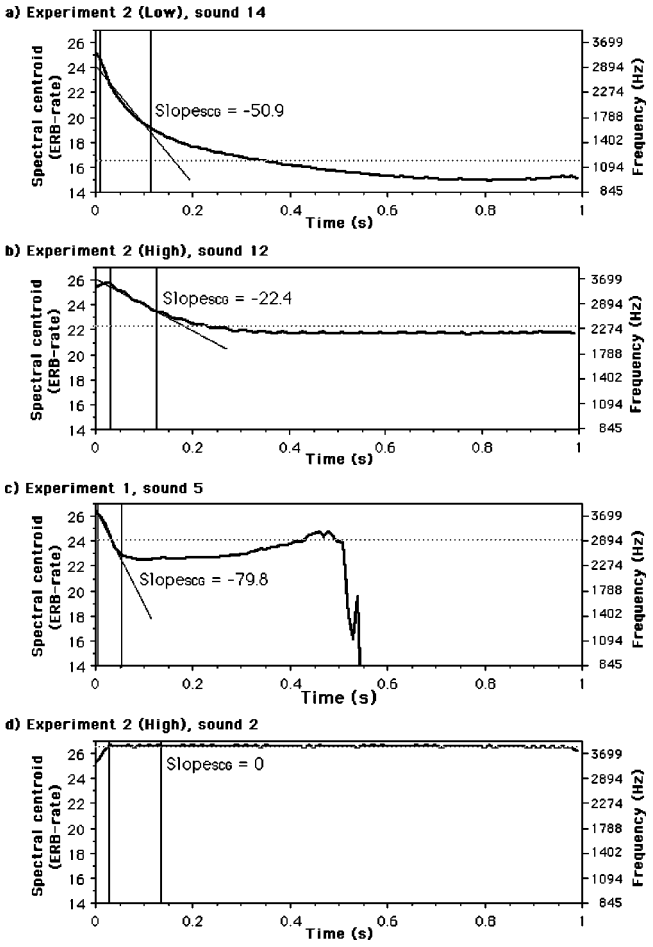

FIG. 4. Variation over time of the spectral center of gravity (SCG). The spectral centroid values are expressed in physiological units (ERB-rate) on the left and physical units (Hz) on the right. $\text{Slope}_{\text{SCG}}$ is determined from the regression of SCG(t) onto a straight line over the time window between the two vertical lines. The mean SCG for each curve is shown by the horizontal dotted line.

the amount of time a sound event has a rms amplitude that exceeds a critical value that is expressed in decibels below the maximum (Fig. 2). It has been shown to be strongly correlated with the perceptual dimension that distinguishes continuously and impulsively excited sounds (McAdams *et al.*, 1995). Two critical values were tested here: 3 and 10 dB.

C. Frequency of the first partial (f_1)

The frequency of the first partial, f_1, was estimated from the lowest prominent component in the FFT, the amplitude of which exceeded that of a constant 440-Hz component present in all stimuli due to excitation of the fixed-length resonator (see Fig. 3). Quite often, f_1 corresponded to the primary pitch heard in the bar sounds.

D. Spectral center of gravity (SCG)

The instantaneous spectral center of gravity is computed on the cochlear representation. For each time frame, the specific loudness-weighted average frequency on the ERB-rate scale is computed. The variation of this quantity over time gives the SCG(t) function (Fig. 4). The mean SCG is computed on this array of values over that portion of the signal for which $\ln[A_{HT}(t)]>0$ to avoid including less reliably determined SCG values in low-level parts of the signal essentially represented by fluctuation in the lowest bit.

E. Slope of SCG(t) ($\text{Slope}_{\text{SCG}}$)

One feature of bar sounds is that damping depends on frequency. Given that the damping increases as the square of the frequency, for a given value of η, the instantaneous SCG of the bar without the resonator decreases monotonically over time and eventually asymptotes, in many cases near the fundamental frequency. The rate of decrease in instantaneous SCG is thus always greater at the beginning of its temporal evolution [Fig. 4(a)]. The SCG(t) curve characterizes this rate of decrease over an initial 100-ms time frame. Due to the short-duration presence at the beginning of all the sounds of the low-amplitude 440-Hz component resulting from the presence of the fixed-length resonator, the SCG(t) curve sometimes rises briefly before beginning its descent, particularly for sounds with higher-frequency partials such as those in experiment 1 and the high sounds in experiment 2 [Figs.

4(b) and (d)]. Since the behavior of this component is not related to the material of the bar, this part of the curve was ignored. The slope was thus measured starting 2.5 ms after the initial maximum or initial plateau. In a few cases, the curve asymptotes before the 100-ms time frame has passed. In such cases, the window over which the slope was estimated was reduced so as to end at the bend in the curve [Fig. 4(c)]. [The fact that the SCG(t) curve increases beyond 0.35s in Fig. 4(c) should be ignored because the amplitude of the signal is close to zero beyond this point.] Finally, in three stimuli in experiment 1, the curves were flat after the initial rise and their slopes were thus set to 0 [Fig. 4(d)].

IV. GENERAL METHOD

A. Procedure

The listener's task was to rate the perceived dissimilarity between two stimuli according to any criteria that seemed perceptually salient. The aim is to discover what listeners hear as being salient, not to impose a particular judgment criterion. This rating was to be performed on all pairs of different sounds within the stimulus set for a given experiment. In order to give the listener a sense of the range of variation to be encountered and thus to make the best use of the rating scale, all of the sounds were presented in random order at the beginning of each experiment. Then ten training trials, chosen at random from the experimental set, were presented to provide practice with the rating scale. On each trial, two sounds were presented, separated by a 1-s silence. In the experimental block, each pair of different sounds was presented once. The order of presentation of the two sounds was randomly chosen for each listener. The dissimilarity rating was indicated by moving a cursor on the computer screen along a horizontal scale labeled ''very similar'' at the left and ''very dissimilar'' at the right. The end points of this continuous scale were coded as 0 and 100, respectively. The cursor was moved by clicking on it and dragging it with a mouse. There were also two buttons available on the computer screen that could be activated by clicking on them: one for replaying the sound pair as many times as necessary to reach a satisfactory rating, the other for recording the position of the cursor and moving to the next trial. The ratings were compiled into a triangular matrix without diagonal, which constituted the data set for each listener.

B. Multidimensional scaling of dissimilarity ratings

The analysis of the dissimilarity data was performed with multidimensional scaling, using an extension of the CLASCAL program (McAdams *et al.*, 1995; Winsberg and De Soete, 1993). This analysis represents the relations among sounds with a distance model.

CLASCAL uses an extended Euclidean distance model that includes positions in a Euclidean space shared by all of the sounds, specific dimensions for individual sounds (called ''specificities''), and weights on each of the dimensions and on the set of specificities for each latent class of listeners. The distance between sounds i and j for class t is written

$$d_{ijt}=\left[\sum_{r=1}^{R} w_{tr}(x_{ir}-x_{jr})^2+\nu_t(s_i+s_j)\right]^{1/2}, \tag{6}$$

where x_{ir} is the coordinate for stimulus i along dimension r, w_{tr} is the weight on dimension r for class t, s_i is the specificity of stimulus i, and ν_t is the weight on the whole set of specificities for class t.

We do not know the number of latent classes in advance. We use a Monte Carlo significance testing procedure proposed by Hope (1968) and first applied in the context of latent class analysis by Aitken *et al.* (1981). [See McAdams *et al.* (1995) for a more detailed description of the procedure as applied to timbre perception.]

For highly nonlinear models such as those used in multidimensional scaling, information-based statistics cannot be used reliably to determine the appropriate spatial model, i.e., the appropriate dimensionality of the Euclidean common space, and the absence or presence of specificities. To choose the model, the following procedure was used:

Step 1: Choose the appropriate number of latent classes, using the Hope procedure on the fully saturated or null model (i.e., the matrix of mean dissimilarities between all pairs of stimuli).

Step 2: Choose two competing spatial models by selecting the two models with lowest BIC statistics from models with generally from about one to five or six dimensions with and without specificities. BIC (Schwarz, 1978) is an information-based criteria for model selection. BIC $=-2\log \mathrm{L}+\log(n_o)n_p$, (where $\log \mathrm{L}=$ log likelihood, n_o = the number of observations, and n_p = the number of model parameters).

Step 3: Using the number of latent classes selected in step 1 above, choose the appropriate spatial model from the top two or three competing models, perhaps also including an additional model that is of interest on theoretical grounds, using the Hope procedure.

Step 4: Verify the appropriate number of latent classes using the Hope procedure as in step 1, but using the spatial model selected in step 3.

Step 5: If the number of latent classes selected in step 4 is identical to the number selected in step 1, STOP; otherwise repeat steps 2 and 3 with the number of classes selected in step 4, and repeat step 4 with the newly selected model.

Since one-class solutions are rotationally invariant, they are subsequently rotated to an extended, weighted Euclidean model (EXSCAL: Winsberg and Carroll, 1988, 1989) in which weights are computed for each subject. This has the effect of orienting the axes along psychologically meaningful dimensions as represented by the directions of maximum variation across subject weights. Note that BIC cannot reliably choose between an N-class model and a one-class model since the degrees of freedom of the former model increase with the number of subjects. So in the one-class case, steps 2, 3, and 4 are reduced to spatial model selection and rotation to the fully weighted model solution.

TABLE II. Parameters held constant in the bar model in experiment 1. The columns represent the name of the parameter, its symbol, its value, and the physical units.

Parameter	Symbol	Value	Units
	Bars		
Young's modulus	E	9.29×10^{9}	N/m^2
Moment of inertia	I	2.67×10^{-5}	m^4
Fluid damping	γ_B	8.0	s^{-1}
Thickness	h	0.02	m
Width	B	0.04	m
Length	L	0.20	m
Cross-section	S	8×10^{-4}	m^2
	Mallet		
Mass	m_m	0.012	kg
Radius	R_m	0.012	m
Stiffness	K	4.2×10^{8}	$Nm^{-3/2}$

V. EXPERIMENT 1: BARS OF CONSTANT CROSS-SECTION

A. Method

1. Subjects

A group of 19 subjects (9 women and 10 men) participated in the experiment. Their ages ranged from 21 to 40 years. No subject was a professional musician. All reported having normal hearing. They were paid for their participation.

2. Stimuli

Sixteen sounds were synthesized with a bar model with constant cross-section. All sounds were equalized in loudness by an adjustment procedure performed with five listeners. The final levels corresponded to the mean of the adjusted levels.

The geometric and elastic parameters of the bar (E,I,ρ,h,b,L,S) affect the frequencies of the spectral components of the sound and thus the perceived pitch. We varied density (ρ) and held all the other parameters constant (Table II). The mallet and resonator parameters were also held constant. Density varied linearly in the interval [300, 900 kg/m^3]. The values were chosen so that at least a quarter-tone interval (3% difference in frequency) existed between the lowest partial of adjacent sounds on this continuum, ensuring their discriminability in terms of pitch.

The damping parameters (γ_B, η) affect the spectral distribution and the temporal envelope of the sound. As previously shown in Eq. (5), the effect of the fluid damping coefficient γ_B is to limit the decay time in the low-frequency range (the lowest partial of the bars), whereas the effect of the viscoelastic coefficient η is to reproduce the decrease of the decay time with increasing frequency observed in real bars. We thus chose to vary η as a second parameter, which directly affects the temporal decay as a function of frequency. The damping factor was varied exponentially in the interval [0.1, 200.0 ns]. This interval of damping coefficients covers a large range of materials from glass to wood, including carbon and some plastic materials. It would not include metals for which the laws of variation of damping as a function of frequency are much more complex. It was determined in a pilot study that this distribution gave a reasonably homogeneous spread of perceived differences between adjacent values. Beyond this range, the sounds created with the constant cross-section model become perceptually indistinguishable: too highly damped sounds are perceived as clicks, and too lowly damped sounds are perceived as being constant over the duration used in our stimuli.

In order to have 16 different values for each of the physical parameters with only 16 sounds, we chose a homogeneous pseudo-random distribution within a 16×16 matrix in the physical space defined by density and damping (the latter being on a log scale). The distribution allows us to have 16 values on each parameter and ensures that all pairs of sounds are distinguishable while covering the desired physical space. The exact values of the model parameters are listed in Table III as are the corresponding analytic parameters.

3. Procedure

All distinct pairs of the 16 stimuli were presented for a total of 120 experimental trials. The experiment lasted approximately 40–50 min per subject.

4. Apparatus

The experiment took place at Ircam. Listeners were seated in a Soluna S1 double-walled sound-isolation chamber. The sounds were reproduced with a NeXT computer equipped with an ISPW sound-processing card and the Max sound-synthesis software (Lindemann *et al.*, 1991). The digital output was converted to an analog signal with a ProPort DAC equipped with anti-aliasing filters. The signal was then amplified with a Canford stereo amplifier and presented diotically over AKG-1000 open-air headphones. The experimental program, sound presentation, subject interface, and data collection were programmed with the PsiExp (Smith, 1995) software environment.

B. Results

1. CLASCAL analyses

The CLASCAL analysis yielded a model with two dimensions, no specificities, and a single latent class. This model is invariant under rotation and was thus rotated to the *N*-class model. The distances between the sounds in the model explain 92% of the variance in the mean dissimilarity ratings.

Four main points emerge from this analysis. First, the dimensionality of the perceptual space is identical to that of the physical space. Second, listening to the experimental stimuli in order as projected onto each of the perceptual dimensions reveals a variation in timbre along dimension 1 and in pitch along dimension 2. The timbre variation appears to have a temporal component and a spectral component. At one end of this dimension, sounds ring longer and are brighter. At the other end, they are quickly deadened and duller sounding. Third, since the fit of distances to dissimilarities is performed with a linear metric, we can compare the relative extent of variation along the two dimensions. The range of variation along dimension 1 is 1.75 times larger

TABLE III. Experiment 1: Summary of mechanical parameters used in the physical model (η, ρ) for a constant-section rectangular bar, of descriptors derived from the resulting signals (α_1, α_2, ED_{3dB}, ED_{10dB}, SCG, Slope_{SCG}), and of perceptual coordinates derived from the CLASCAL analysis of dissimilarity ratings (Dim1, Dim2).

	Mechanical		Signal descriptors							Perceptual	
Sound	η (ns)	ρ (kg/m^3)	α_1 (s^{-1})	α_2 (s^{-1})	ED_{3dB} (ms)	ED_{10dB} (ms)	SCG (ERB-rate)	Slope_{SCG} (ERB-rate/s)	f_1 (Hz)	Dim1	Dim2
1	0.1	300	8.6	4.0	72	277	26.7	0.0[a]	2857	−50.9	32.2
2	70.0	340	35.4	15.8	14	67	24.3	−24.0	2685	22.8	22.9
3	4.0	380	15.5	4.5	41	157	26.2	−1.8	2543	−44.9	19.4
4	40.0	420	50.1	9.8	12	35	25.1	−28.5	2419	0.8	25.1
5	150.0	460	97.3	21.5	9	17	24.1	−79.8	2313	35.5	11.3
6	6.0	500	13.1	4.6	388	140	26.6	−3.3	2220	−41.6	5.8
7	200.0	540	184.0	23.0	9	12	24.5	−109.0	2138	45.9	4.1
8	50.0	580	47.0	9.2	13	37	25.0	−29.3	2062	14.1	−2.0
9	20.0	620	24.7	5.8	21	75	26.0	−7.9	1992	−13.3	−4.5
10	2.0	660	9.7	5.0	58	222	27.9	0.0[a]	1922	−44.1	−10.5
11	120.0	700	71.4	12.6	12	25	24.5	−45.5	1874	28.3	−11.2
12	1.0	740	9.1	4.4	39	250	27.8	0.0[a]	1816	−45.8	−14.6
13	30.0	780	27.4	6.2	19	67	25.5	−8.9	1781	−3.3	−23.3
14	100.0	820	62.6	11.6	12	27	24.3	−41.6	1734	26.6	−19.1
15	90.0	860	55.0	10.5	13	32	24.2	−35.7	1693	29.6	−21.5
16	180.0	900	108.3	17.3	10	17	23.8	−78.6	1658	40.2	−14.6

[a]There was some difficulty measuring accurately the value of Slope_{SCG} for some sounds in which SCG(t) was flat or very slightly increasing.

than that along dimension 2, suggesting a perceptual dominance of dimension 1. For this set of sounds, listeners are thus collectively more sensitive to timbral variation than to pitch variation.

2. Correlational analyses

The mechanical and analytic signal parameters as well as the coordinates in the perceptual space are listed in Table III. The acoustic information related to the mechanical parameters is presumed to be carried by the analytic signal parameters (i.e., derivable from the sensory representation of the acoustic signal). Note that in many cases the relation between the parameters is not linear. For example, f_1 is inversely proportional to the square-root of ρ. Over the range of variation of f_1 in this stimulus set, linear and logarithmic relations between f_1 and dimension 2 give the same correlation coefficient. For this reason, only the linear relation is used throughout the paper. The transformation of the objective parameters to achieve a good fit to the perceptual coordinates can be a logarithmic (α,ED) or a power function (ρ, η,Slope_{SCG}). In the case of the latter, a function of the form $\Psi = a + b\varphi^c$ was used to fit the physical parameters (φ) to the perceptual dimensions (Ψ), leaving a, b, and c as free parameters. In this way, exponents of 0.33 and 0.39 were found for the relation of dimension 1 to η and to Slope_{SCG}, respectively.

The correlations among $\eta^{0.33}$, $\log(\alpha_1)$, $\log(\alpha_2)$, SCG, ED_{3dB}, ED_{10dB}, $\text{Slope}_{SCG}^{0.39}$, and dimension 1, on the one hand, and among $\rho^{-1/2}$, f_1, and dimension 2, on the other, are in most cases very high [$0.87 \leqslant |r(14)| \leqslant 1.00$, $p \leqslant 0.0001$, in all cases], whereas those between these two groups of parameters are generally low [$0.05 \leqslant |r(14)| \leqslant 0.35$, $p > 0.19$ in all cases], attesting to the perceptual and acoustic independence of the two groups.

Several analytic parameters (SCG, α_1, α_2, ED_{3dB}, ED_{10dB}, Slope_{SCG}) are partially correlated with dimension 1 and η. Therefore, a stepwise multiple regression with dimension 1 as dependent variable and the appropriate power or log transforms of these parameters as independent variables was performed. The aim was to evaluate the relative contribution of each analytic parameter to a possible combined perceptual effect represented as dimension 1. The statistic of interest is the coefficient of determination, adjusted for the inclusion of several regressors (R^2_{adj}), which is considered to represent the variance in the dependent variable explained by the linear combination of independent variables. Forward and backward selection procedures were used to verify whether they converged on the same set of regressors. The forward selection starts with no independent variables in the model and adds them in order of their ability to predict the dependent variable based on the partial F-ratio. It stops when the addition of a new parameter is not statistically significant. The backward selection starts with all independent variables in the model and removes the one that is least useful in predicting the dependent variable. It stops when the least useful independent variable still makes a significant contribution to predicting the dependent variable.

For forward selection, once Slope_{SCG} was entered into the regression, no other parameter made a significant enough contribution to enter subsequently ($R^2_{adj} = 0.92$). This parameter is also very highly correlated with $\eta^{0.33}$ ($R^2_{adj} = 0.96$). Scatter plots of these regessions are shown in Fig. 5(a). The backward selection only removes two of the six analytic parameters leaving Slope_{SCG}, SCG, α_2, and ED_{10dB} ($R^2_{adj} = 0.97$). Note, however, that the increase in explained variance with the addition of the last three parameters is only 5%, due primarily to the fact that the correlations among the predictor variables are quite high, as mentioned previously. This perceptual dimension would thus seem to be primarily explained by a spectrotemporal component that is closely correlated both with the mechanical parameter being varied and the corresponding perceptual dimension, confirming the

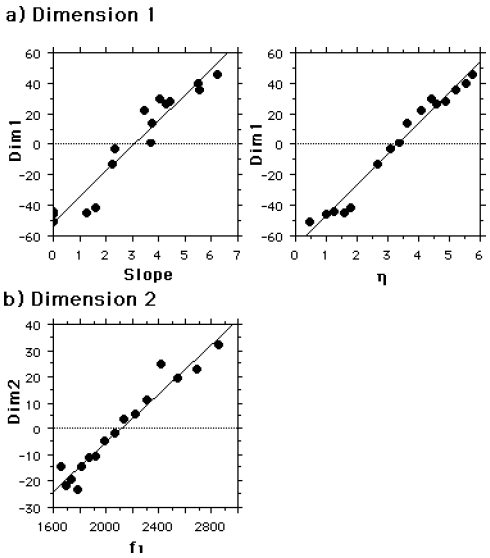

FIG. 5. Experiment 1. Linear regressions of coordinates along one dimension of the perceptual space onto signal descriptors of mechanical parameters. (a) Dimension 1 compared to $\text{Slope}_{\text{SCG}}^{0.39}$ and $\eta^{0.33}$. (b) Dimension 2 compared to f_1.

triangular relation between mechanical processes, acoustic information, and perceptual result.

For the second perceptual dimension, closely related to the density parameter of the model, and thus to the frequency composition of the bar sounds, a highly significant correlation between f_1 and the coordinates along dimension 2 is found, confirming the impression that this dimension is related to pitch [Fig. 5(b)]. As mentioned previously, pitch variation was rated as occupying a smaller range of perceptual variation than the timbral variation related to the damping parameter. The range of pitches represented by f_1 is situated between 1658 and 2857 Hz (about 9.5 semitones), and adjacent pitches in the stimulus set were separated by intervals ranging from slightly more than a semitone (sounds 1 and 2:107 cents) to slightly less than a quarter-tone (sound 15 and 16:36 cents). It should be noted that no difference in correlation coefficient was found for the comparisons between dimension 2 coordinates and either linear or log frequency scales for f_1. Indeed, due to the small range of variation of f_1, its log and linear versions are highly correlated in a linear regression ($R^2 = 0.99$).

C. Discussion

The multidimensional scaling analysis of dissimilarity ratings, made by listeners on a set of sounds synthesized by a physical model, revealed a perceptual space that had the same dimensionality as the original mechanical space. Transformations of the mechanical parameters were related to potential signal parameters that could be extracted by the auditory system and perceived as perceptual dimensions of the stimuli. Strong correlations were found among all three domains. The nature of the transforms provides important information about the nature of the sensory or perceptual representation of these complex, naturalistic stimuli. This representation would then be the basis upon which stimuli could be compared and perhaps analyzed in order to recognize the material properties of the vibrating objects. One of the surprising results of this experiment is that simultaneous variation in pitch did not annihilate the contribution of timbre to a global impression of dissimilarity among sounds. On the contrary, the timbral variation was much stronger in the resulting perceptual space than was the pitch variation. To pursue further this latter point, a second experiment was conducted on tuned bars in which the range of variation of the damping parameter was reduced and that of the perceived pitch was increased.

VI. EXPERIMENT 2: BARS OF VARIABLE CROSS-SECTION

To achieve the necessary range of f_1 variation in experiment 2, a model of tuned xylophone bars was used. The tuning of the partial structure was achieved by varying the cross-sectional geometry as shown in Fig. 1, and f_1 variation was created by modifying the length (L) of the bar. All of the other geometrical and mechanical properties affecting the frequency content were held constant. Two sets of bars were tested. One set (referred to as high) had modal frequencies in the same range as those of experiment 1. In these sounds, the lowest partial's frequency was at least a major sixth (a ratio of 1.68) above the resonance frequency of the fixed-length tube resonator (440 Hz). The other set (referred to as low) was created by using bar lengths that were four times those of the first set, giving lowest partials in a range near that of the resonator. The aim with this set was to study the effects of bar-resonator coupling on material perception, particularly since such coupling affects the decay characteristics of the sound which were shown in experiment 1 to play a possible role in the perception of sound properties related to the materials.

A. Method

1. Subjects

The experiment was performed in two separate sessions corresponding to the two sets of bar sounds by 21 subjects (13 men, 8 women) aged from 22 to 40 years. None of them had participated in experiment 1. No subject reported having hearing problems and none was a professional musician. All were paid for their participation.

2. Stimuli

Fourteen sounds were synthesized in each set using the same set of viscoelastic damping coefficients (η), but different sets of bar lengths. In light of the results from experiment 1, η was varied in experiment 2 according to a power function in order to obtain a relatively constant perceptual difference between adjacent values along this continuum. The range of variation of η on a log scale is slightly smaller in experiment 2. On the scale of the power function from experiment 1 with an exponent for η of 0.33, the perceptual range for experiment 2 is 66% of that for experiment 1. All other material properties were held constant and took the values specified in experiment 1 except ρ, which was held constant at a value of 782 kg/m^3.

TABLE IV. Experiment 2: Summary of mechanical parameters used in the physical model (η, L) for a variable-section tuned bar, of descriptors derived from the resulting signals (α_1, α_2, ED_{3dB}, ED_{10dB}, SCG, $Slope_{SCG}$), and of perceptual coordinates derived from the CLASCAL analysis of dissimilarity ratings (Dim1, Dim2) for both High (a) and Low (b) sound sets.

	Mechanical		Signal descriptors							Perceptual	
Sound	η (ns)	L (cm)	α_1 (s^{-1})	α_2 (s^{-1})	ED_{3dB} (ms)	ED_{10dB} (ms)	SCG (ERB-rate)	$Slope_{SCG}$ (ERB-rate/s)	f_1 (Hz) [musical pitch]	Dim1	Dim2
(a) High sound set											
1	0.03	14.68	8.7	3.9	73	280	27.5	−0.1	1659 [G#5]	−8.2	−31.2
2	0.06	13.46	8.0	4.0	74	280	26.5	0.0[a]	1973 [B5]	−29.3	−13.3
3	0.18	12.34	9.0	4.1	70	270	25.9	−0.3	2347 [D6]	−34.4	2.2
4	0.32	14.26	8.8	4.2	96	263	26.9	−0.5	1757 [A5]	−12.2	−24.5
5	0.56	13.08	9.3	4.6	63	240	26.8	−1.1	2090 [C6]	−24.1	−6.3
6	1.00	9.79	9.6	4.2	63	250	27.5	−1.9	3730 [A#6]	−11.7	43.8
7	1.78	15.55	9.9	4.8	58	220	25.9	−3.0	1478 [F#5]	−14.2	−35.5
8	3.16	10.68	10.5	4.6	56	230	25.9	−6.5	3135 [G6]	−17.1	33.2
9	5.62	11.64	10.5	4.7	56	228	24.5	−7.6	2635 [E6]	0.7	21.7
10	10.00	12.70	25.4	4.9	21	108	23.4	−15.2	2215 [C#6]	17.9	−8.3
11	17.78	13.85	30.9	5.2	17	70	22.2	−22.4	1862 [A#5]	21.7	−19.3
12	23.70	11.31	12.4	6.8	43	168	24.7	−6.5	2792 [F6]	16.2	25.6
13	31.62	11.00	33.9	11.0	13	88	24.9	−7.5	2958 [F#6]	46.7	11.8
14	56.23	12.00	27.2	12.6	16	93	23.8	−11.7	2486 [D#6]	48.1	0.1
(b) Low sound set											
1	0.03	29.36	8.9	4.0	75	285	25.6	−11.2	415 [G#3]	−33.6	−14.9
2	0.06	26.92	8.1	4.0	80	288	24.7	−12.7	493 [B3]	−28.2	−21.3
3	0.18	24.68	7.3	4.1	83	288	24.5	−9.6	587 [D4]	−27.2	7.6
4	0.32	28.52	7.1	4.2	75	273	25.1	−11.1	440 [A3]	−36.9	−11.8
5	0.56	26.16	8.7	4.3	75	265	24.3	−9.2	523 [C4]	−18.9	−9.1
6	1.00	19.02	16.6	4.1	66	255	24.1	−3.0	987 [B4]	−18.5	35.5
7	1.78	31.10	10.2	4.6	53	203	24.3	−15.4	370 [F#3]	−25.0	−31.0
8	3.16	21.36	14.7	4.3	52	213	22.7	−7.2	784 [G4]	4.9	29.0
9	5.62	23.28	12.3	4.1	52	173	21.6	−17.0	659 [E4]	8.8	12.9
10	10.00	25.40	19.0	3.9	35	150	20.3	−24.4	554 [C#4]	20.0	−9.1
11	17.78	27.70	26.7	3.9	19	88	18.5	−36.0	466 [A#3]	29.1	−19.9
12	23.70	22.62	23.8	4.2	23	113	19.5	−25.4	698 [F4]	33.1	12.2
13	31.62	22.00	29.7	4.3	19	108	18.4	−32.5	740 [F#4]	43.6	19.1
14	56.23	24.00	36.1	4.4	15	133	16.5	−50.9	622 [D#4]	48.8	1.0

[a]There was some difficulty measuring accurately the value of $Slope_{SCG}$ for one sound in which SCG(t) was flat.

The width (b) and maximum thickness (h_{max}) were set to the values from experiment 1:4 cm and 2 cm, respectively. The other geometrical parameters specified a variable cross section to account for the tuning of the bar's partials to a harmonic frequency spectrum (Fig. 1). To change the pitch of the bar sounds, the length of the bar was varied. The lengths (L), corresponding frequencies (f_1), and resulting musical pitches are listed in Table IV. Note that the range of variation of f_1 on a semitone scale is 158% of that in experiment 1 (15 vs 9.5 semitones). Thus, in this experiment the range of pitch variation is greater and the range of variation in the damping factor is less. The height (h_c) and radius (x_c) of curvature (see Fig. 1) vary with L, but the ratios x_c/L and h_c/h_{max} are held constant. This ensures that the tuning of the first three partials of the bar is constant. Their frequencies were in a ratio of 1:4:9 and therefore formed a harmonic series (in contrast to the stimuli of experiment 1 which were inharmonic). These parameters are similar to those used by instrument makers in the manufacture of mallet percussion instruments. The resonator geometry was also held constant. The tube length was $L_T = 0.179$ m. The tube radius was $a_T = 0.02$ m. The bar-tube distance was $d = 0.015$ m.

3. Procedure

For each sound set, all distinct pairs of the 14 stimuli were presented for a total of 105 experimental trials. Each session lasted approximately 30–40 min per subject. The two sessions were performed on the same day in counterbalanced order, separated by a break.

4. Apparatus

The experiment took place at the ENST. Listeners were seated in a sound-isolated room. The sounds were reproduced with a Sun computer equipped with an integrated sound card and DAC. The signal was then amplified with a Rotel stereo amplifier and presented diotically over Sennheiser headphones connected directly to the output of the DACs. The experimental program, sound presentation, subject interface, and data collection were programmed with the Matlab software environment.

B. Results

1. CLASCAL analyses

a. High sound set. The CLASCAL analysis yielded two dimensions without specificities and three latent classes.

Since the orientation is fixed in this model due to the class weights, no rotation was necessary. The perceptual coordinates of each sound are listed in Table IV(a). The model distances explain 85% of the variance in the mean dissimilarity ratings. Five subjects were in class 1, six in class 2, and nine in class 3. Class belongingness as tested by *a posteriori* probabilities with Bayesian statistics was very clear. Posterior probabilities were greater than 0.89 in all cases except one for which classification was ambiguous with respect to classes 2 and 3. The weights were very strong (1.75) on dimension 1 and very weak (0.40) on dimension 2 for class 1, very weak (0.38) on dimension 1 and moderate (1.15) on dimension 2 for class 2, and moderately weak (0.87) on dimension 1 and strong (1.45) on dimension 2 for class 3. The weightings of the two dimensions are thus quite different across classes.

b. Low sound set. The CLASCAL analysis yielded two dimensions without specificities and two latent classes. The model distances explain 86% of the variance in the mean dissimilarity ratings. Class 1 contained 14 of the 21 subjects, the other 7 being in class 2. Class belongingness was very clear, all posterior probabilities being greater than 0.99. The weights on dimensions 1 and 2 were 0.55 and 1.70 for class 1, and 1.45 and 0.30 for class 2, respectively. Listeners in class 1 thus weight dimension 2 much more heavily, while those in class 2 weight dimension 1 more heavily. The perceptual coordinates of each sound are listed in Table IV(b). In spite of the differences in bar length and bar-resonator coupling, the perceptual spaces are very similar for high and low sounds (Dim1 high vs Dim2 low, $R^2=0.90$; Dim2 high vs. Dim1 low, $R^2=0.80$, $df=12$ in both cases).

2. Correlational analyses

The fitting of η and $\text{Slope}_{\text{SCG}}$ to the appropriate perceptual dimensions according to a power function gave exponents of 0.28 for η in both sound sets and of 0.46 and 0.63 for $\text{Slope}_{\text{SCG}}$ in high and low sets, respectively.

a. High sound set. The correlations among $\eta^{0.28}$, $\log(\alpha_1)$, $\log(\alpha_2)$, SCG, $\log(ED_{3\text{dB}})$, $\log(ED_{10\text{dB}})$, $\text{Slope}_{\text{SCG}}^{0.46}$, and dimension 1, on the one hand, and among $\rho^{-1/2}$, f_1, and dimension 2, on the other, are moderate to high [$0.50 \leqslant |r(12)| \leqslant 1.00$, $p \leqslant 0.07$, in all cases]. The lower correlations are due to $\log(\alpha_2)$ in comparison with SCG ($r=-0.50$, $p=0.07$) and $\text{Slope}_{\text{SCG}}$ ($r=0.53$, $p=0.05$), all others being greater than 0.68 ($p \leqslant 0.0055$). Correlations across these two groups of parameters are generally low [$0.01 \leqslant |r(12)| \leqslant 0.31$, $p>0.28$ in all cases]. Stepwise regression of the analytic parameters related to damping onto dimension 1 with forward selection yielded a linear combination of $\log(ED_{3\text{dB}})$ and $\log(\alpha_2)$ ($R^2_{\text{adj}}=0.86$), whereas the backward selection yielded a combination of $\log(\alpha_1)$ and $\log(\alpha_2)$ ($R^2_{\text{adj}}=0.88$) [Fig. 6(a)]. Stepwise regression of the parameters on $\eta^{0.28}$ yielded a combination of $\log(\alpha_2)$ and $\text{Slope}_{\text{SCG}}$ ($R^2_{\text{adj}}=0.97$) for both forward and backward selection. Nearly 94% of the variance along dimension 2 is predicted by f_1 [Fig. 6(b)].

b. Low sound set. The correlations among damping-related parameters and dimension 1, on the one hand, and among length-related parameters and dimension 2, on the other, are quite high [$0.83 \leqslant |r(12)| \leqslant 1.00$, $p \leqslant 0.0001$, in all cases], if $\log(\alpha_2)$ is excluded. Due to the prolonged resonance of these sounds, this parameter does not vary much across the sound set. The correlations between the two groups of parameters are generally low [$0.03 \leqslant |r(12)| \leqslant 0.42$, $p>0.13$ in all cases]. Stepwise regression of damping-related analytic parameters on dimension 1 gave the same result with forward and backward selection: a combination of SCG and $\text{Slope}_{\text{SCG}}$ ($R^2_{\text{adj}}=0.98$). Stepwise regression of these parameters on $\eta^{0.28}$ yielded a combination of SCG and $\log(\alpha_2)$ ($R^2_{\text{adj}}=0.98$) for both selection procedures [Fig. 7(a)]. As with the other sound set, the pitch dimension (Dim2) is highly correlated with f_1 ($R^2=0.91$) [Fig. 7(b)].

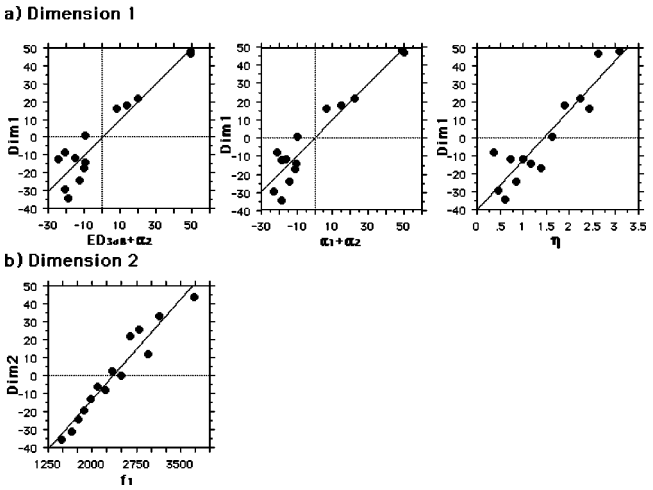

FIG. 6. Experiment 2 (high bars). Linear regressions of coordinates along one dimension of the perceptual space onto signal descriptors of mechanical parameters. (a) Dimension 1 compared to linear combinations of $ED_{3\text{dB}}$ and $\log \alpha_2$ and of $\log \alpha_1$ and $\log \alpha_2$, and to $\eta^{0.28}$. (b) Dimension 2 compared to f_1.

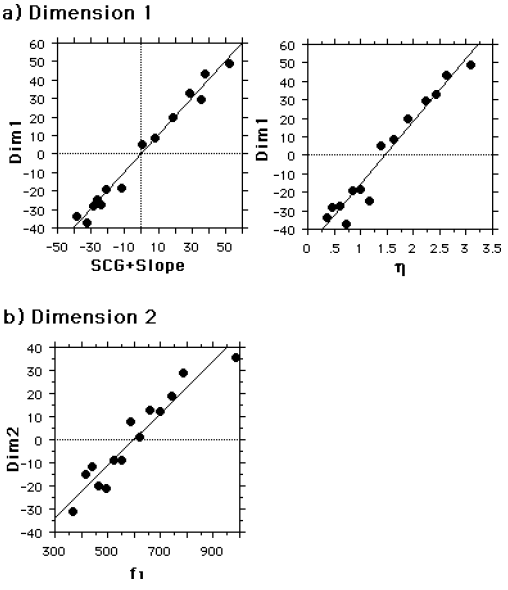

FIG. 7. Experiment 2 (low bars). Linear regressions of coordinates along one dimension of the perceptual space onto signal descriptors of mechanical parameters. (a) Dimension 1 compared to a linear combination of SCG and $\text{Slope}_{\text{SCG}}^{0.63}$, and to $\eta^{0.28}$. (b) Dimension 2 compared to f_1.

C. Discussion

As in experiment 1, the dimensionality of the perceptual spaces corresponds to that of the physical spaces. A variation in timbre occurs along dimension 1 related to damping and a variation in pitch along dimension 2 related here to bar length. In spite of the smaller variation of the damping parameter and the larger variation of the frequency parameter in the stimulus set, with each sound separated from its neighbor by at least a semitone, the range of values occupied by the pitch dimension in the perceptual space is still less than that occupied by the timbre dimension. The factor has nonetheless increased to 78% for the low sounds and 96% for the high sounds, compared to 57% in experiment 1. In the present experiment, the bars were tuned to a harmonic series by using a variable cross-section model. Further, the sensation of damping was lessened by the fact that the fundamental had a much lower damping than in experiment 1. This effect is even more prominent for the low sounds in which the sound is prolonged by a coupling between the bar and the resonator. Note that the range of the α_2 decay constant was 4.0–23.0 s^{-1} in experiment 1 compared to 3.9–12.6 s^{-1} (high) and 3.9–4.6 s^{-1} (low) in experiment 2, or 60%–75% of the range on a log scale.

A word about the perceptual effects of resonator-bar coupling which affects decay rate are in order here. The mechanical origins of this coupling have been discussed in detail in Chaigne and Doutaut (1997). The same values of η were used for both high and low sound sets. As can be seen in Table IV, α_1 has a similar range of variation for the high and low sound sets, whereas α_2 is nearly constant for the low set and varies only for the five sounds with the highest values of η in the high set. What is of import for the present study is the fact that in spite of the much longer decay times in the low sound set compared to the high set, the main result is essentially the same for the two: the perceptual dimensions related to the damping parameter in the two sets are highly correlated ($R^2=0.80$, $p<0.0001$). It may be, however, that different cues are being used since the correlations between the perceptual dimension and spectral cues (SCG) are higher for the low set, and those with temporal descriptors ($ED_{3\mathrm{dB}}, \alpha_1$) are higher for the high set. We will return to the issue of common or multiple cues in Sec. VII.

VII. GENERAL DISCUSSION

The dimensionality of the three perceptual spaces from both experiments is identical to that of the physical parameter space in which the stimuli were created. Further, there are strong correlations among mechanical and analytic parameters and perceptual dimensions, demonstrating a close relation between mechanical properties and putative parameters derived from the signals that represent the physical stimuli perceptually. Note, however, that many of these signal-derived parameters undergo a monotonic transformation in the perceptual representation that is either a logarithmic or a power function.

Many physical parameters are perceived according to power functions (luminosity, loudness, weight, electric shock, etc.) (Stevens, 1975). The damping factor used in the bar model, as well as one of its possible signal correlates ($\mathrm{Slope}_{\mathrm{SCG}}$), would seem to be additions to this set. This relation is all the more interesting in that a similar exponent for η was found in three different sets of comparable stimuli that nonetheless had many differences in terms of the range of variation of damping factor and either bar length or density, as well as in the spectral content of the sounds (inharmonic in experiment 1, harmonic in experiment 2). We will now consider in turn the relation between mechanical parameters, signal descriptors, and perceptual dimensions across the three sound sets.

A. Damping-related dimension

One dimension in each of the perceptual spaces was related to the shape-invariant damping factor and is clearly related to the sound's timbre. Very strong correlations between a power function of the damping factor and the perceptual dimension were found. The signal characteristics, or combinations of them, that were hypothesized to specify the damping factor seem to vary somewhat according to the stimulus set. A comparison was performed among the eight signal descriptors that were the most highly correlated with the perceptual coordinates and η in the three sound sets. The chosen descriptors include $\mathrm{Slope}_{\mathrm{SCG}}$, $\alpha_1+\alpha_2$, $\alpha_2+ED_{3\mathrm{dB}}$, $\alpha_2+ED_{10\mathrm{dB}}$, $\alpha_2+\mathrm{Slope}_{\mathrm{SCG}}$, $\mathrm{SCG}+\mathrm{Slope}_{\mathrm{SCG}}$, and $\alpha_2+\mathrm{SCG}$ $\mathrm{Slope}_{\mathrm{SCG}}+\mathrm{SCG}+\alpha_2+ED_{10\mathrm{dB}}$. All eight of these signal descriptors (using the appropriate logarithmic or power functions of each) were fitted by multiple regression to both the damping-related perceptual dimension and η for each of the three spaces. The correlation coefficients and their 95% confidence intervals were determined for each comparison. Two descriptors were considered of equivalent predictive power if the correlation coefficient of one fell within the 95% confidence interval of the other.

For experiment 1, all of the descriptors have equivalent predictive power for both the perceptual dimension and η ($0.93\leqslant R^2\leqslant 0.99$). For experiment 2 (High bars), most of the predictors have equivalent predictive power for both the perceptual dimension ($0.85\leqslant R^2\leqslant 0.91$) and η($0.86\leqslant R^2\leqslant 0.99$). The exceptions are $\mathrm{Slope}_{\mathrm{SCG}}$ and $\mathrm{SCG}+\mathrm{Slope}_{\mathrm{SCG}}$ for which R^2 is significantly lower at about 0.55 in relation to the perceptual dimension and 0.72 in relation to η. The correlations of the parameters with η are significantly higher than with the perceptual dimension for this stimulus set. For experiment 2 (low bars), the correlation coefficients of the descriptors are quite dispersed, but the same three descriptors are found at the top, and have equivalent predictive power, for both the perceptual dimension and its mechanical origin. Aside from the four-factor descriptor, the other two include $\alpha_2+\mathrm{SCG}$ and $\mathrm{SCG}+\mathrm{Slope}_{\mathrm{SCG}}$. There is one descriptor that is common to all three spaces ($\alpha_2+\mathrm{SCG}$). Further, the second descriptor for the high bars in experiment 2 is not a good descriptor for the low bars, and vice versa. As mentioned in the discussion on experiment 2, this might lead one to conclude that separate acoustic cues were used by listeners for each sound set, according to what was the most useful for that set, e.g., $\alpha_2+\mathrm{Slope}_{\mathrm{SCG}}$ for the high bars and $\mathrm{SCG}+\mathrm{Slope}_{\mathrm{SCG}}$ for the low bars, either being a good candidate for the constant cross-section bars of experiment 1. A more

parsimonious approach, and the one that led to this analysis, is to attempt to find a single descriptor that works optimally for all three sound sets. A linear combination of a temporal factor (long-term decay constant, α_2) and a spectral factor (spectral centroid, SCG) is a reasonable candidate as the signal vehicle of the mechanical parameter: it explains 92%–98% of the variance in the perceptual coordinates and 97%–99% of the variance in η.

B. Frequency-related dimension

Dimension 2 in all three spaces was clearly related to pitch perception. Variations in both material density (ρ) and bar length (L) create changes in the component frequencies that vary as $\rho^{-1/2}$ and L^{-2}, respectively. Each perceptual dimension was strongly correlated with the frequency of the first partial, f_1, which explains 91%–94% of the variance along this dimension. This result is similar to that of Miller and Carterette (1975) (experiment 1) in which both pitch (fundamental frequency) and timbral characteristics (envelope shape, spectral envelope) were varied. Miller and Carterette varied the pitch over a two-octave range. A multidimensional scaling analysis revealed a three-dimensional space with pitch along one dimension, decay rate along another, and a third dimension that seemed to be related to the impulsivity of the beginning of the sound (rapid attack followed by an initial rapid decay that either continued to decay for one sound or attained a sustain level at 40% of the maximum amplitude for another sound). The relative perceptual variation for the three dimensions was equivalent. However, stimulus variation in the spectral envelope (perhaps related to SCG) was not reflected in their perceptual space.

C. Relative perceptual salience of the two dimensions

In the present study, an attempt to increase the pitch variation by 170% (on a log scale) and decrease the variation in damping by 66% (on a scale defined by a power function with an exponent of 0.3) in experiment 2, only created a slight decrease in the dominance of the timbral dimension over the pitch dimension: the range of variation on the second dimension in the perceptual space was 57% of that of the first dimension in experiment 1 and was 78%–96% in experiment 2. This result should be qualified by the relative weights assigned to the two dimensions by the latent subject classes in experiment 2. A quarter of the listeners for the high bars had greater variation on the timbre dimension by a factor of 4.4 compared to the pitch dimension, whereas the other three-fourths had 1.7–3.0 times as much variation on the pitch dimension compared to the timbre dimension. For the low bars, a third of the listeners privileged the timbre dimension by a factor of 4.8, whereas the other two-thirds gave greater weight to the pitch dimension by a factor of 3.0. There would thus seem to be differences among listeners concerning the relative dominance of pitch and timbre when they vary simultaneously.

Lutfi and Oh (1997) found a predominance of frequency over intensity and decay constant in a study in which listeners were to identify which of two sounds came from an object of a particular material (iron versus silver, steel or copper, and glass versus crystal, quartz or aluminum). Their sounds were synthesized sums of damped sinusoids designed to replicate the frequencies, amplitudes, and radiation decay constants of materials with particular elasticity, dimensions, and density. The differences among sets of sounds representing each material were chosen to be around threshold identification performance. It may be that the relative variation of frequency at these small differences was more salient. Closer to the results of the present study, Klatzky *et al.* (2000) presented synthesized sums of sinusoids to represent different materials and asked listeners to judge the proximity of the sounds in terms of the materials they evoked. They varied the sounds according to fundamental frequency and to a frequency-invariant damping parameter. They performed multidimensional scaling and forced the solution to two dimensions (apparently no attempt was made to determine the dimensionality of the perceptual space as was done in the present study). Their two dimensions corresponded clearly to frequency and decay correlates with a predominance being found for the latter, as here. What the present studies add to this result is a statistical verification of the dimensionality, the use of synthesized sounds that more closely resemble those produced by physical impact processes, and the quantification of the signal descriptors that potentially carry information concerning the mechanical properties.

D. Predicting dissimilarities from signal descriptors

The combinations of appropriately transformed analytic parameters can be used to derive an objective distance measure among the sounds, which can in turn be compared with the mean dissimilarities given by the listeners. For the three sound sets used, the resulting distance models combining $\log \alpha_2$ and SCG between sounds i and j are the following:
Experiment 1:

$$d_{ij}=\{[0.047(f_{1i}-f_{1j})]^2+[76.028(\log \alpha_{2i}-\log \alpha_{2j}) - 12.015(\mathrm{SCG}_i-\mathrm{SCG}_j)]^2\}^{1/2}, \quad (7)$$

Experiment 2 (high):

$$d_{ij}=\{[0.037(f_{1i}-f_{1j})]^2+[118.517(\log \alpha_{2i}-\log \alpha_{2j}) - 5.389(\mathrm{SCG}_i-\mathrm{SCG}_j)]^2\}^{1/2}, \quad (8)$$

Experiment 2 (low):

$$d_{ij}=\{[0.113(f_{1i}-f_{1j})]^2+[36.68(\log \alpha_{2i}-\log \alpha_{2j}) - 9.973(\mathrm{SCG}_i-\mathrm{SCG}_j)]^2\}^{1/2}. \quad (9)$$

These distances explain 80%, 64%, and 73% of the variance in the mean dissimilarity ratings, respectively. These coefficients of determination are to be compared with those of the distance model derived from the CLASCAL solutions which explain 92%, 85%, and 86% of the variance in the mean dissimilarity ratings. Using the four-factor analytic model does not result in a statistically significant improvement over the two-factor model. It would seem then that while covering a major proportion of the variance in the perceptual data, our signal parameters, adjusted to the individual dimensions, leave a certain proportion of the variance in the data unexplained.

VIII. CONCLUSIONS

Listeners were asked to judge the dissimilarity among synthesized sounds produced with a physical model of a bar. The sounds were varied according to the mass density or the length of the bar and to a viscoelastic damping parameter. Both constant cross-section bars and tuned variable cross-section bars were tested. A multidimensional scaling analysis of the dissimilarity data revealed perceptual spaces with the same dimensionality as that of the original physical parameter space using statistical criteria for the model selection. The results thus validate two aspects of the synthesis model and quantify psychophysically the relations between the mechanical parameters, the potential signal characteristics that carry them, and the perceptual representation. The modal frequencies vary with mass density and length and the likely perceptual correlate is pitch. Variation in the damping coefficient creates spectral and temporal variations in the signal, and thus has several potential signal characteristics that could serve as the acoustic vehicle for the mechanical origin. The most parsimonious signal descriptor that explains a significant amount of variance in the data sets for all stimuli is a linear combination of long-term decay constant and spectral center of gravity. The latter descriptor was derived from a model of the peripheral representation of the sounds in the human auditory system. This is one of the first demonstrations of a perceptual dimension being explained by a combination of temporal and spectral signal descriptors. Further, the perceptual representation of the damping coefficient would seem to have a power function relation to the mechanical parameter. These results demonstrate the perceptual salience of energy-loss phenomena in sound source behavior.

This study has examined only two of the many parameters that characterize the physical model of the impacted bar. It has demonstrated the importance of energy-loss phenomena in the perceptual representation of bar sounds, in coherence with the results of Klatzky *et al.* (2000). The understanding of such phenomena in the perceptual domain are important for the development of high-quality audio synthesis and may be applicable to the creation of sound simulations in virtual reality environments, for example. Future research will need to explore the perception of the other parameters of the synthesis model to quantify further its psychophysical underpinnings.

ACKNOWLEDGMENTS

Portions of this work were funded by a grant from the French Ministry of the Environment to Stephen McAdams and Antoine Chaigne and a doctoral fellowship from the French Ministry of Higher Education and Research to Vincent Roussarie. The cochlear representation and the extraction of SCG(t) and SCG were obtained with a Matlab routine (ERBspect) developed by Alain de Cheveigné and are used with the permission of the author. The authors thank two anonymous reviewers and Alain de Cheveigné for helpful comments on an earlier version of this paper.

Aitken, M., Andersen, D., and Hinde, J. (**1981**). ''Statistical model of data on teaching styles,'' J. R. Stat. Soc., Ser. A **144**, 419–461.

Avanzini, F., and Rocchesso, D. (**2001**). ''Controlling material properties in physical models of sounding objects,'' in *Proceedings of the International Computer Music Conference 2001*, La Habana, Cuba, (ICMA, La Habana, Cuba), pp. 91–94.

Bucur, V. (**1995**). *Acoustics of Wood* (CRC, Boca Raton, FL).

Cabe, P. A., and Pittenger, J. B. (**2000**). ''Human sensitivity to acoustic information from vessel filling,'' J. Exp. Psychol. Hum. Percept. Perform. **26**, 313–324.

Carello, C., Anderson, K. A., and Kunkler-Peck, A. J. (**1998**). ''Perception of object length by sound,'' Psychol. Sci. **9**, 211–214.

Chaigne, A., and Doutaut, V. (**1997**). ''Numerical simulations of xylophones. I. Time-domain modeling of the vibrating bars,'' J. Acoust. Soc. Am. **101**, 539–557.

Chaigne, A., and Lambourg, C. (**2001**). ''Time-domain simulation of damped impacted plates. I. Theory and experiments,'' J. Acoust. Soc. Am. **109**, 1422–1432.

Doutaut, V. (**1996**). ''Etude expérimentale et simulation numérique d'instruments de percussion à clavier,'' Ph.D. thesis, Ecole Nationale Supérieure des Télécommunications, Paris.

Doutaut, V., Matignon, D., and Chaigne, A. (**1998**). ''Numerical simulations of xylophones. II: Time-domain modeling of the resonator and of the radiated sound pressure,'' J. Acoust. Soc. Am. **104**, 1633–1647.

Freed, D. J. (**1990**). ''Auditory correlates of perceived mallet hardness for a set of recorded percussive sound events,'' J. Acoust. Soc. Am. **87**, 311–322.

Grey, J. M. (**1977**). ''Multidimensional perceptual scaling of musical timbres,'' J. Acoust. Soc. Am. **61**, 1270–1277.

Guski, R. (**2000**). ''Studies in auditive kinetics,'' in *Contributions to Psychological Acoustics: Results of the 8th Oldenburg Symposium on Psychological Acoustics*, edited by A. Schick, M. Meis, and C. Reckhardt (Bis, Oldenburg), pp. 383–401.

Hajda, J. M., Kendall, R. A., Carterette, E. C., and Harshberger, M. L. (**1997**). ''Methodological issues in timbre research,'' in *Perception and Cognition of Music*, edited by I. Deliège and J. Sloboda (Psychology, Hove), pp. 253–306.

Hartmann, W. M. (**1997**). *Signals, Sound, and Sensation* (AIP, Woodbury, NY).

Hope, A. C. (**1968**). ''A simplified Monte Carlo significance test procedure,'' J. R. Stat. Soc. Ser. B. Methodol. **30**, 582–598.

Houben, M. (**2002**). ''The sound of rolling objects: Perception of size and speed,'' Technische Universiteit Eindhoven, Eindhoven, The Netherlands.

Houix, O., McAdams, S., and Caussé, R. (**1999**). ''Auditory categorization of sound sources,'' in *Studies in Perception and Action*, edited by M. A. Grealy and J. A. Thomson (Lawrence Erlbaum Associates, Mahwah, NJ), Vol. V, pp. 47–51.

Iverson, P., and Krumhansl, C. L. (**1993**). ''Isolating the dynamic attributes of musical timbre,'' J. Acoust. Soc. Am. **94**, 2595–2603.

Killion, M. C. (**1978**). ''Revised estimate of minimum audible pressure: Where is the 'missing 6 dB'?'' J. Acoust. Soc. Am. **63**, 1501–1508.

Klatzky, R. L., Pai, D. K., and Krotkov, E. P. (**2000**). ''Perception of material from contact sounds,'' Presence: Teleoperators and Virtual Environments **9**, 399–410.

Krotkov, E, Klatzky, R., and Zumel, N. (**1996**). ''Robotic perception of material: Experiments with shape-invariant acoustic measures of material type,'' in *Experimental robotics IV: Lecture notes in control and information science*, edited by O. Khatib and X. Salisbury (New York, Springer Verlag) Vol. 223, pp. 204–211

Kunkler-Peck, A. J., and Turvey, M. T. (**2000**). ''Hearing shape,'' J. Exp. Psychol. Hum. Percept. Perform. **26**, 279–294.

Lakatos, S. (**2000**). ''A common perceptual space for harmonic and percussive timbres,'' Percept. Psychophys. **62**, 1426–1439.

Lakatos, S., McAdams, S., and Caussé, R. (**1997**). ''The representation of auditory source characteristics: Simple geometric form,'' Percept. Psychophys. **59**, 1180–1190.

Lindemann, E., Dechelle, F., Smith, B., and Starkier, M. (**1991**). ''The architecture of the IRCAM Musical Workstation,'' Comput. Music J. **15**(3), 41–19.

Lutfi, R. A. (**2001**). ''Auditory detection of hollowness,'' J. Acoust. Soc. Am. **110**, 1010–1019.

Lutfi, R. A., and Oh, E. L. (**1997**). ''Auditory discrimination of material changes in a struck-clamped bar,'' J. Acoust. Soc. Am. **102**, 3647–3656.

McAdams, S. (**1993**). ''Recognition of sound sources and events,'' in *Thinking in Sound: The Cognitive Psychology of Human Audition*, edited by S. McAdams and E. Bigand (Oxford U.P., Oxford), pp. 146–198.

McAdams, S. (**1999**). ''Perspectives on the contribution of timbre to musical structure,'' Comput. Music J. **23**(2), 96–113.
McAdams, S., Winsberg, S., Donnadieu, S., De Soete, G., and Krimphoff, J. (**1995**). ''Perceptual scaling of synthesized musical timbres: Common dimensions, specificities, and latent subject classes,'' Psychol. Res. **58**, 177–192.
Miller, J. R., and Carterette, E. C. (**1975**). ''Perceptual space for musical structures,'' J. Acoust. Soc. Am. **58**, 711–720.
Moore, B. C. J., and Glasberg, B. R. (**1983**). ''Suggested formulae for calculating auditory-filter bandwidths and excitation patterns,'' J. Acoust. Soc. Am. **74**, 750–753.
Patterson, R. D., Allerhand, M., and Giguère, C. (**1995**). ''Time-domain modeling of peripheral auditory processing: a modular architecture and a software platform,'' J. Acoust. Soc. Am. **98**, 1890–1894.
Plack, C. J., and Moore, B. C. J. (**1990**). ''Temporal window shape as a function of frequency and level,'' J. Acoust. Soc. Am. **87**, 2178–2187.
Plomp, R. (**1970**). ''Timbre as a multidimensional attribute of complex tones,'' in *Frequency Analysis and Periodicity Detection in Hearing*, edited by R. Plomp and G. F. Smoorenburg (Sijthoff, Leiden), pp. 397–414.
Repp, B. H. (**1987**). ''The sound of two hands clapping: An exploratory study,'' J. Acoust. Soc. Am. **81**, 1100–1109.
Rossing, T. D., and Russell, D. (**1990**). ''Laboratory observation of elastic waves in solids,'' Am. J. Phys. **58**, 1153–1162.
Schwarz, G. (**1978**). ''Estimating the dimensions of a model,'' Ann. Stat. **6**, 461–464.
Smith, B. K. (**1995**). ''PsiExp: An environment for psychoacoustic experimentation using the IRCAM Musical Workstation,'' SMPC95: Society for Music Perception and Cognition, Berkeley, CA (University of California, Berkeley, Berkeley, CA).
Stevens, S. S. (**1975**). *Psychophysics: Introduction to its Perceptual, Neural and Social Prospects* (Wiley, New York).
Warren, W. H., and Verbrugge, R. R. (**1984**). ''Auditory perception of breaking and bouncing events: A case study in ecological acoustics,'' J. Exp. Psychol. Hum. Percept. Perform. **10**, 704–712.
Wessel, D. L. (**1979**). ''Timbre space as a musical control structure,'' Comput. Music J. **3**(2), 45–52.
Winsberg, S., and Carroll, J. D. (**1988**). ''A quasi-nonmetric method for multidimensional scaling via an extended Euclidean model,'' Psychometrika **53**, 217–229.
Winsberg, S., and Carroll, J. D. (**1989**). ''A quasi-nonmetric method for multidimensional scaling of multiway data via a restricted case of an extended INDSCAL model,'' in *Multi-way Data Analysis*, edited by R. Coppi and S. Bolasco (North-Holland, Amsterdam), pp. 405–414.
Winsberg, S., and De Soete, G. (**1993**). ''A latent class approach to fitting the weighted Euclidean model. CLASCAL,'' Psychometrika **58**, 315–330.

On the use of the derivative of electroglottographic signals for characterization of nonpathological phonation

Nathalie Henrich[a)]
LAM (UPMC, CNRS, Ministère de la culture), 11 rue de Lourmel, 75015 Paris, France and LIMSI-CNRS, BP 133, F91403 Orsay, France

Christophe d'Alessandro and Boris Doval
LIMSI-CNRS, BP 133, F91403 Orsay, France

Michèle Castellengo
LAM (UPMC, CNRS, Ministère de la culture), 11 rue de Lourmel, 75015 Paris, France

(Received 26 March 2003; revised 28 October 2003; accepted 8 December 2003)

Electroglottography is a common method for providing noninvasive measurements of glottal activity. The derivative of the electroglottographic signal, however, has not attracted much attention, although it yields reliable indicators of glottal closing instants. The purpose of this paper is to provide a guide to the usefulness of this signal. The main features that are to be found in this signal are presented on the basis of an extensive analysis of a database of items sung by 18 trained singers. Glottal opening and closing instants are related to peaks in the signal; the latter can be used to measure glottal parameters such as fundamental frequency and open quotient. In some cases, peaks are doubled or imprecise, which points to special (but by no means uncommon) glottal configurations. A correlation-based algorithm for the automatic measurement of fundamental frequency and open quotient using the derivative of electroglottographic signals is proposed. It is compared to three other electroglottographic-based methods with regard to the measurement of open quotient in inverse-filtered derived glottal flow. It is shown that agreement with the glottal-flow measurements is much better than most threshold-based measurements in the case of sustained sounds. © *2004 Acoustical Society of America.* [DOI: 10.1121/1.1646401]

PACS numbers: 43.75.Yy, 43.70.Jt, 43.75.Rs [SM] Pages: 1321–1332

I. INTRODUCTION

Electroglottography (EGG), invented by Fabre in 1956 (Fabre, 1957, 1958, 1959, 1961), is a common, widespread technique that enables the investigation of vocal-fold contact area in phonation in an easy and noninvasive way. A high-frequency modulated current ($F \simeq 1$ MHz) is sent through the neck of the subject, as shown in Fig. 1. Between the electrodes, electrical admittance varies with the vibratory movements of the vocal folds, increasing as the vocal folds increase in contact. For a more detailed review, we refer the reader to Childers and Krishnamurthy (1985), Colton and Conture (1990), and Orlikoff (1998).

In order to analyze the EGG signal, several comparative studies have been conducted using stroboscopic photography (Fourcin, 1974; Lecluse *et al.*, 1975; Pedersen, 1977; Teaney and Fourcin, 1980), videostroboscopy (Anastaplo and Karnell, 1988; Karnell, 1989), high-speed cinematography (Baer *et al.*, 1983a; Childers *et al.*, 1990; Childers and Krishnamurthy, 1985; Childers and Larar, 1984; Childers *et al.*, 1983b, 1984), photoglottography (Baer *et al.*, 1983a,b; Berke *et al.*, 1987; Dejonckere, 1981; Gerrat *et al.*, 1988; Kitzing, 1977, 1983; Kitzing *et al.*, 1982; Titze *et al.*, 1984), subglottal pressure measurements (Kitzing *et al.*, 1982) and inverse filtering (Childers *et al.*, 1983b; Fourcin, 1981; Rothenberg, 1981; Rothenberg and Mahshie, 1988). All of these studies confirm that the EGG signal is related to the vocal-fold contact area: the larger the contact surface, the larger the measured admittance. Lecluse and Brocaar (1977) and Childers and Krishnamurthy (1985) have proposed a schematic description of the EGG signal during one glottal period produced by laryngeal mechanism 1 on the basis of comparisons with glottal visualization (we refer the reader to the Appendix for details concerning laryngeal mechanisms and the terminology used in this paper). We can draw on their observations to provide a schematic description of the EGG signal in the case of laryngeal mechanisms 1 and 2, as shown in Fig. 2.

During a vocal-fold vibratory cycle, the corresponding EGG signal can be described by four main phases.

①–③: Closing phase. Contact is initiated along the lower margins of the vocal folds (① to ②), then propagating to the upper margins (② to ③). As closing is generally faster than opening, this phase is characterized by a steep slope in the EGG signal. The instant of maximum slope can be found at ②, which corresponds to a strong positive peak in the derivative of the EGG signal (DEGG signal).

③–④: Closed phase. The vocal folds are in full contact, preventing air from passing through the glottis. The slight increase and decrease observed in the signal could be due to the elastic collision of tissue (Childers and Krishnamurthy, 1985).

[a)]Electronic mail: henrich@lam.jussieu.fr

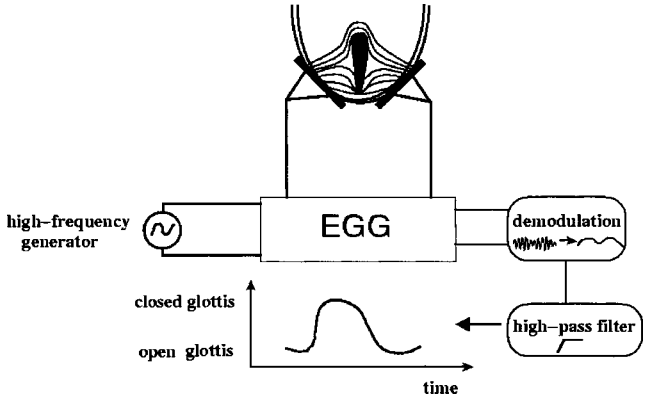

FIG. 1. Principle of an electroglottograph (EGG), using the ''vocal fold contact area'' (VFCA) convention in which the EGG signal is represented as a function of vocal-fold contact.

④–⑥: Opening phase. The lower margins of the vocal folds begin to separate gradually (④ to ⑤), followed by separation along the upper margins (⑤ to ⑥). The instant of maximum slope can be found at ⑤, which corresponds to the negative peak in the DEGG signal.

⑥–①: Open phase. The vocal folds are apart. A relatively flat signal is observed, as there is little variation in the admittance.

The closing and opening phases are illustrated in Fig. 3 by simultaneous visualization of high-speed images,[1] the corresponding electroglottographic signal, and its derivative during nonpathological male phonation (mechanism 1, $f_0 = 110\,\mathrm{Hz}$). The physiological correlates of the peaks observed on the DEGG signal in ② (''closing peak'') and ⑤ (''opening peak'') were mainly studied by Childers *et al.*, using simultaneous and synchronized measurements of EGG and DEGG signals, inverse-filtered derived glottal flow and glottal area measured from ultrahigh-speed cinematography (Childers *et al.*, 1990; Childers and Krishnamurthy, 1985; Childers and Larar, 1984; Childers *et al.*, 1983a,b), along with a theoretical study of the relation between the EGG/DEGG signals and the glottal contact area calculated from a physical model (Childers *et al.*, 1986). In the case of nonpathological productions, they showed that these peaks are related to the instants of glottal opening and closing, defined as the instants of initialization and termination of glottal area

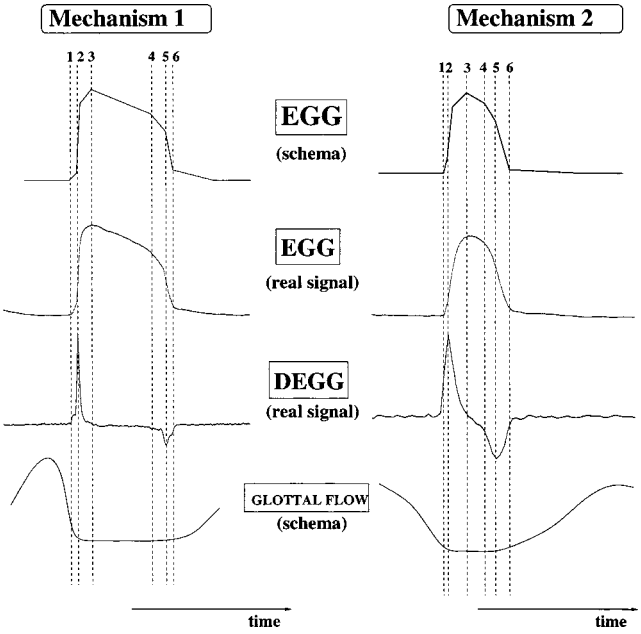

FIG. 2. Illustration of a glottal duty cycle as seen on an EGG and a DEGG signal. (1)–(3) closing phase; (3)–(4) closed phase; (4)–(6) opening phase; (6)–(1): open phase. As a comparison, one glottal flow period is presented.

variation. But, this is only valid for a normal male voice in mechanism 1. A special case was brought to light by these authors: in the case of a mucus strand bridging the glottis during the opening phase, the opening peak occurs at the instant when the mucus strand breaks, rather than at the instant of glottal opening. Colton and Conture (1990) showed that the presence of a mucus bridge affected the EGG signal but also the inverse-filtered glottal flow. The glottal flow does not increase much until the mucus strand breaks, and thus the opening peak occurs when glottal flow starts to increase greatly.

Other studies confirmed these results. Berke *et al.* (1987) made simultaneous measurements of EGG, photoglottography, subglottal pressure, and stroboscopic photography ''*in vivo*'' in dogs, and they observed that slope variations in the EGG signal were correlated with the opening of the vocal folds along their upper margin and with the complete closure of the lower margin. Anastaplo and Karnell (1988) obtained similar results concerning the glottal open-

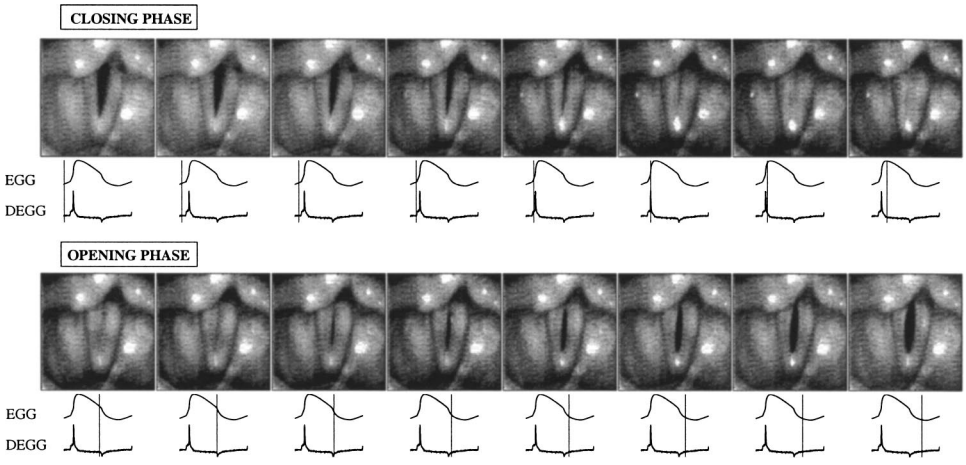

FIG. 3. Visualization of the closing and opening phases by simultaneous high-speed and electroglottographic recordings. Vertical bars indicate the moment in time at which the visual image occurs with respect to the EGG and DEGG signals. This example corresponds to a nonpathological male phonation in mechanism 1, with $f_0 = 110\,\mathrm{Hz}$. The EGG sampling frequency is 44 444 Hz and the high-speed camera sampling frequency is 3704 frames/s.

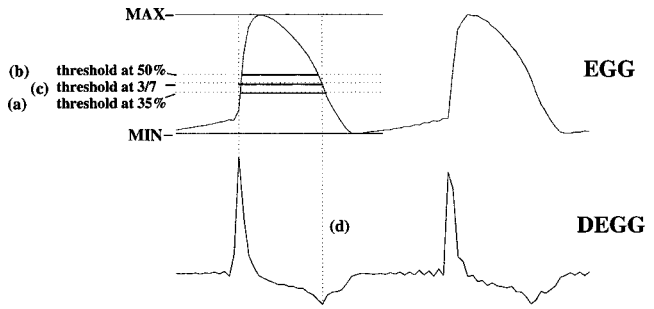

FIG. 4. Illustration of four methods for measuring the open quotient (or its equivalent, the closed quotient) on an EGG signal and its derivative: (a) on the EGG signal using a threshold detection (35% of the difference between the minimum and maximum value of the signal over a glottal period); (b) same method as (a) with a threshold of 50%; (c) in combining an EGG-based threshold method (3/7) with a detection of glottal closing instants on the DEGG signal; (d) on the DEGG signal by the detection of opening and closing peaks.

ing instant, using EGG and synchronized videostroboscopy in 4 subjects (2 males, 2 females). By comparing EGG, photoglottographic, and inverse-filtered derived glottal flow in V–C–V samples, Cranen (1991) showed that DEGG peaks were related to the peaks observed in the derivative of photoglottographic signals and to the opening and closing instants measured on the glottal flow and its derivative.

On the substantial basis of these studies, DEGG peaks may be considered as reliable indicators of glottal opening and closing instants, the latter being defined by reference to the glottal flow, as the instants when the flow starts to increase greatly from the baseline (opening) and decrease greatly to the baseline (closing). As glottal closing is usually abrupt, the closing peak is often very strong and precise. The opening can be less precise, which is reflected in a weaker opening peak. This may explain the reservations expressed by Baken (1992) on the use of these peaks as a measure of glottal opening instant.

The first part of the present study offers a characterization of DEGG signals from an extensive database of 18 trained singers. The recording procedure is briefly presented in Sec. II A; its main features are brought out in Sec. II B and discussed in Sec. II C.

The second part of this study concerns the use of DEGG signals for the measurement of fundamental frequency and open quotient. This is one major application of the detection of glottal closing and opening instants. The duration between two consecutive glottal closing instants corresponds to a fundamental period; its inverse gives the fundamental frequency of the voice. In the same manner, the duration between the glottal opening instant and the consecutive glottal closing instant corresponds to the open time. The open quotient can then be derived from these two measures as the ratio between open time and fundamental period.

In the literature, the main electroglottographic-based methods for detecting the glottal closing and opening instants use the EGG signal and not its derivative. As illustrated by cases (a) and (b) in Fig. 4, a threshold method is generally applied (Rothenberg and Mahshie, 1988): a level line is chosen either as a percentage of the amplitude between the minimum and maximum of the signal over a glottal period (50% for a normal to pressed voice and 35% for a relaxed voice). The crossing points between the level line and the EGG signal are approximated as the instants of glottal closing and opening, and these are used for the open quotient measurement. These methods are very convenient for medical purposes, as they are robust and can be applied even on noisy or weak signals. Nevertheless, the results of such methods are by their nature imprecise and can be inaccurate, as compared to what would be measured on a glottal area signal or on a glottal flow signal (Rothenberg and Mahshie, 1988).

An improvement over such a method has recently been proposed by Howard [Howard (1995); Howard *et al.* (1990)]: using the DEGG closing peak for detecting the glottal closing instant, and an EGG-based threshold method for detecting the glottal opening instant. This is illustrated by case (c) in Fig. 4. This method should give more accurate results, because of reliable detection of the glottal closing instants. In the present study, we propose a method based on the DEGG signals only, in the case of precise opening and closing peaks. This correlation-based method is described in Sec. III. The measurements of open quotient made on EGG, DEGG, and glottal-flow signals are compared and discussed in Sec. III D.

II. DESCRIPTION OF THE DEGG SIGNALS EXTRACTED FROM A SINGING DATABASE

A. Material

A corpus of sung items designed for the purpose of open quotient measurements was recorded by 18 trained singers. The singers were classically trained and most of them were professional singers, insofar as they earn their living from singing. Seven were baritones (subjects B1 to B7), 2 were tenors (T1 and T2), 3 were countertenors (CT1 to CT3), 3 were mezzosopranos (MS1 to MS3), and 3 were sopranos (S1 to S3). The database comprises several parts; the present study only draws on the part where the singers were asked to produce glissandos, crescendos, and sustained vowels for different pitches and at different loudness levels. Three vowels were used: (French) [a], [e], and [u]. When necessary, the singers were asked to indicate in which mechanism (M1 or M2) they were singing.

The singers were placed in a soundproof booth. The acoustic and electroglottographic signals were recorded simultaneously on the two channels of a DAT recorder (PORTADAT PDR1000), with a sampling frequency of 44.1 or 48 kHz. A two-channel electroglottograph [EG2, Rothenberg (1992)] was used for the electroglottographic recordings. The low-frequency cutoff was set to 20 Hz and no high-frequency limit was applied. The technical computing environment MATLAB was used for digital signal processing.

More details about the recording procedure, the subjects, and the tasks which are not relevant for the understanding of this study are presented in a subsequent paper concerning the results of open quotient measurements in singing (Henrich *et al.*, submitted).

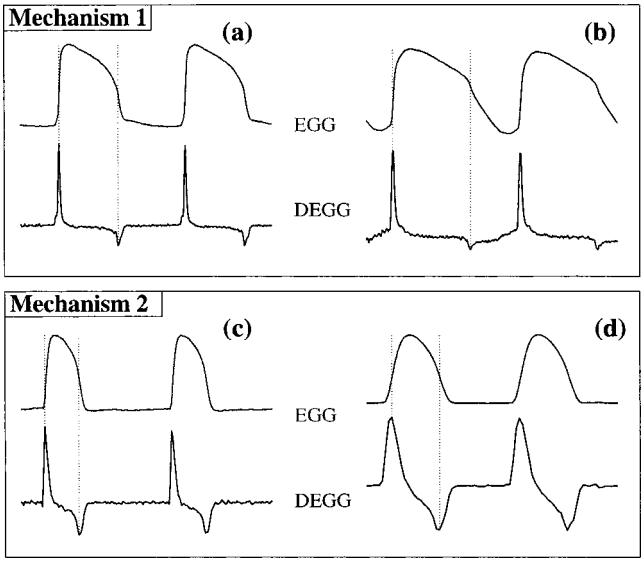

FIG. 5. Typical examples of two-period EGG and DEGG signals, extracted from the singing voice database. In these cases, the opening and closing peaks are precisely defined. Case (a): subject B2, vowel [u], C4 (260 Hz); Case (b): subject B4, vowel [e], E4 (330 Hz); Case (c): subject S2, vowel [a], A4 (440 Hz); Case (d): subject S3, vowel [a], C6 (1040 Hz).

B. Main features

Visual exploration of the database revealed that a DEGG signal presents recurrent features that can easily be categorized. These categories will now be defined and illustrated through typical examples. A major distinction is made between the cases where both opening and closing peaks are well defined and the cases where one (or both) is not well defined.

1. Well-defined peaks

Typical cases when the opening and closing peaks are precisely defined are shown in Fig. 5.

Cases (a) and (b) correspond to voiced productions in mechanism 1. They are taken from crescendos sung by two baritones (subjects B2 and B4). A long closed phase is noticeable (relative to the fundamental period), represented by the distance between two successive vertical broken lines. Cases (c) and (d) correspond to voiced production in mechanism 2. They are extracted from crescendos sung by two sopranos (subjects S2 and S3). The closed phase is shortened as compared to the previous examples.

The laryngeal mechanism differences can be seen in the shape of both the EGG and DEGG signals. The EGG signal is usually more rounded and symmetrical in mechanism 2. The corresponding DEGG signal presents less abrupt peaks. The amplitude of the closing peak is comparable to that of the opening peak, whereas in mechanism 1, the closing peak is much stronger than the opening peak.

2. Double or imprecise peaks

Typical cases where the opening or closing peaks are double or imprecise are presented in Fig. 6. The observed features can be divided into three main categories: imprecise opening peaks, double closing peaks, and double opening peaks.

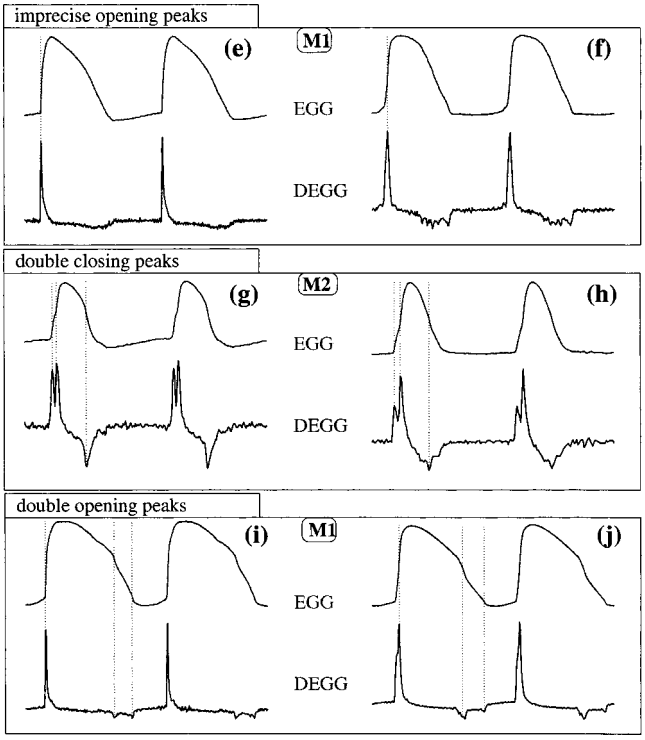

FIG. 6. Typical examples of two-period EGG and DEGG signals, where the opening or closing peaks are double or imprecise. Case (e): subject MS2, vowel [a], F3# (185 Hz); Case (f): subject B2, vowel [u], C4 (260 Hz); Case (g): subject CT3, vowel [a], E4 (330 Hz); Case (h): subject S2, vowel [a], A4 (440 Hz); Case (i): subject B4, vowel [a], G3 (196 Hz); Case (j): subject B6, vowel [a], B3 (245 Hz).

The first typical case is the absence or imprecision of the opening peak, as illustrated at the top of Fig. 6. In case (e), no opening peak is detected. In case (f), numerous peaks can be observed, none of them standing out clearly. Such lack of precision, which was often observed with regard to the opening peaks, was not found in the case of closing peaks in the present material.

Either the closing peak is extremely precise and unique, as we have seen previously, or there are two visible peaks, as illustrated in Fig. 6 for cases (g) and (h). The latter phenomenon, hereafter called ''double closing peak,'' can also be found at opening, as illustrated in cases (i) and (j), although ''double opening peaks'' are less strong and less close to each other than ''double closing peaks.'' In cases (g) and (i), both peaks have the same amplitude, whereas the peak amplitude differs greatly in cases (h) and (j). It should be noted that the opening or closing peaks are seldom tripled or quadrupled.

3. Occurrences

What is the proportion of precise single peaks as compared to imprecise or double peaks? Occurrences of single opening peaks and single closing peaks were measured by applying an automatic method for single peak detection (see further description in Sec. III). Table I presents the results as a percentage of the voiced measures, 100% meaning that only precise peaks were detected during the voicing part and 0% meaning that not a single precise peak was found.

TABLE I. Detection of single closing peaks ($N_c=1$) and single opening peaks ($N_o=1$), expressed as a percentage of the voiced measures. The third row gives the percentage of the voiced measures for which the closing and the opening peaks were detected as single.

Singer	B1	B2	B3	B4	B5	B6	B7	T1	T2	CT1	CT2	CT3	MS1	MS2	MS3	S1	S2	S3
$N_c=1$	51	85	66	75	76	68	16	81	65	81	82	35	86	59	61	68	89	90
$N_o=1$	34	49	21	56	41	50	19	64	31	49	53	64	63	44	46	52	82	80
$N_c=1$ and $N_o=1$	31	48	19	56	40	43	8	61	25	46	46	30	62	44	45	35	81	78

These results indicate that the double-peak feature is not uncommon, for opening as well as for closing. The rate of single closing peaks ranges from 16% (baritone B7) to 90% (soprano S3) and the rate of single opening peaks from 19% (baritone B7) to 82% (soprano S2). Except for two singers (B7 and CT3), there are more single closing peaks than single opening peaks. As an extreme example, only 8% of the peaks detected for baritone B7 were single at both opening and closing.

It appears that for a given singer, peak doubling may be consistently associated with either soft or loud production, and with either low or high pitches. As an example, case (f) in Fig. 6 and case (a) in Fig. 5 are extracted from the same crescendo sung by baritone B2. The onset of the crescendo is characterized by imprecise opening peaks; this imprecision disappears when the singer sings loudly. Another example is given by case (c) in Fig. 5 and case (h) in Fig. 6, which are extracted from a crescendo sung by soprano S2. In this case, the increase in vocal intensity is accompanied by a doubling of closing peaks. No evidence was found, however, relating the double-peak feature in any general way to a change in fundamental frequency or vocal intensity. Variability across singers was found to be rather large, e.g., opening peak doubling is related to an increase of vocal intensity for singers B3, B4, and T2 and to a decrease of vocal intensity for singers B2, CT2, and S1.

C. Discussion

These results highlight the difficulty of using the DEGG signal to detect the closing and opening instants. This may be part of the reason why this signal is not more widely used in the literature. Nevertheless, these difficulties should not prevent its use, as the DEGG signal provides an accurate detection of glottal opening and closing instants, at least in the case of single peaks. Moreover, these peaks may offer visual clues to some characteristic features of the vocal folds' vibratory movement. This hypothesis will be illustrated below by the analysis of the transition between laryngeal mechanisms.

1. Visualization of the laryngeal mechanism transition on the DEGG signal

The studies conducted by Askenfelt *et al.* (1980); Kitzing (1982); Lecluse (1977); Lecluse and Brocaar (1977); Roubeau (1993); Roubeau and Castellengo (1993); Roubeau *et al.* (1987) have shown that a transition between laryngeal mechanisms affects the amplitude and shape of an EGG signal. A rapid change in shape occurs within two voiced periods (Roubeau *et al.*, 1987; Svec *et al.*, 1999), whereas amplitude changes more slowly within about 130–150 ms (Roubeau *et al.*, 1987). A loss of pitch control is often observed (Miller, 2000; Roubeau *et al.*, 1987; Svec *et al.*, 1999). These amplitude variations can also be seen on the DEGG signals, as illustrated in Fig. 7. Thus, observation of a DEGG signal can complement that of an EGG signal for the detection of laryngeal mechanism transitions. Moreover, the slight changes in shape can be seen more easily on the DEGG than on the EGG signal. Figure 7(b) shows the transition from mechanism 1 to mechanism 2 and the bottom panels (c) zoom in on two periods before the transition

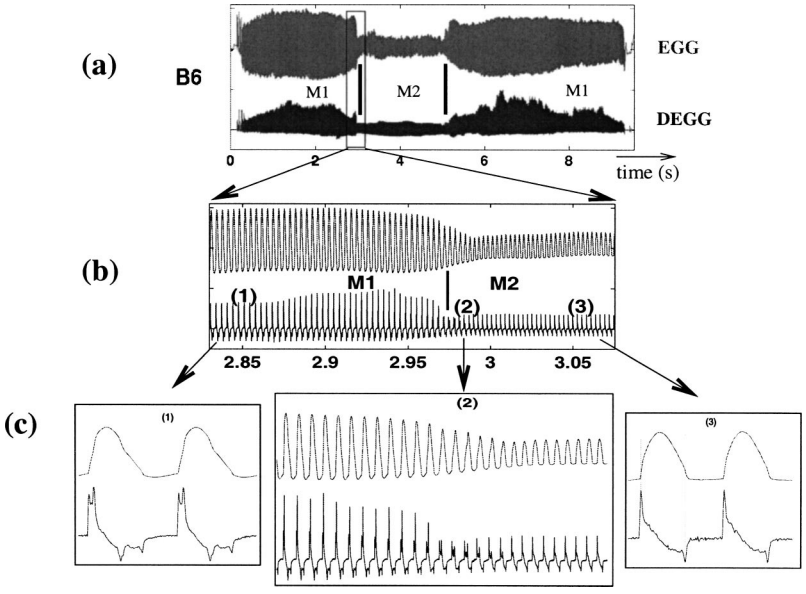

FIG. 7. EGG and DEGG signals, in the case of a glissando sung by the baritone B6. The top panel (a) presents the shape of both signals over the whole glissando. The transitions between mechanism 1 (M1) and mechanism 2 (M2) correspond to the instants of major amplitude change (around 3 s for M1 to M2 transition and 5 s for M2 to M1 transition). The middle panel (b) highlights the first transition (M1–M2) and the bottom panels (c) present several EGG and DEGG periods just before (1), during (2), and just after (3) the transition.

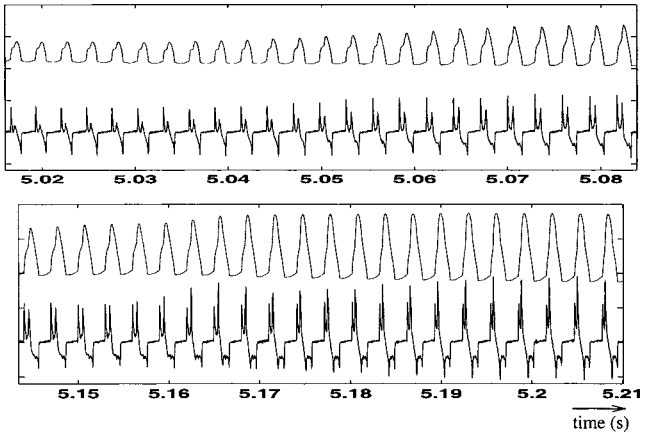

FIG. 8. The second transition (M2–M1) located around 5 s corresponding to the case of the glissando sung by the baritone B6 presented in Fig. 7.

[panel c(1)], on a few periods during the transition [panel c(2)], and on two periods after the transition [panel c(3)]. Right before the transition [panel c(1)], both the closing and opening peaks are doubled. During the transition [panel c(2)], the amplitude of one peak decreases, whereas the amplitude of the other increases. This can be observed for the closing peaks as well as for the opening peaks. After the transition [panel c(3)], both closing and opening peaks are single and the characteristic shape of a DEGG signal in mechanism 2 is observed.

The transition from mechanism 2 to mechanism 1 presents the same features in reverse succession, as shown in Fig. 8: single peaks in mechanism 2, doubling and amplitude change during the transition, and double peaks in mechanism 1. The analysis of the glissandos in the whole database reveals that these features are neither ''singer-specific'' (specific to this individual) nor a common characteristic found at any transition between laryngeal mechanisms.

It is clear from this example that a DEGG signal can highlight tiny changes in shape that would have gone unnoticed in the EGG signal. For instance, if the transition between laryngeal mechanisms appears to be very sudden (a couple of periods) when looking at the amplitude of the EGG and DEGG signals, the peak changes over several periods indicate that there may be some slower adjustments in the vocal-fold contact process. These observations call for research combining electroglottography with some kind of visualization. A characterization of DEGG features using high-speed cinematography is currently under way. At present, the following preliminary hypothesis to explain the double-peak feature is proposed.

2. Hypothesis for explaining double peaks

It is speculated that the double-peak feature observed on a DEGG signal is related to either a difference in how opening (or closing) takes place over the thickness of the vocal folds or to a time-lag opening (or closing) at two different parts of the glottis. A time-lag opening over the length of the glottis was observed by Karnell (1989), who compared synchronized videostroboscopy and electroglottography. For one subject, glottis-anterior opening occurred before posterior opening; for another, posterior opening occurred first. These

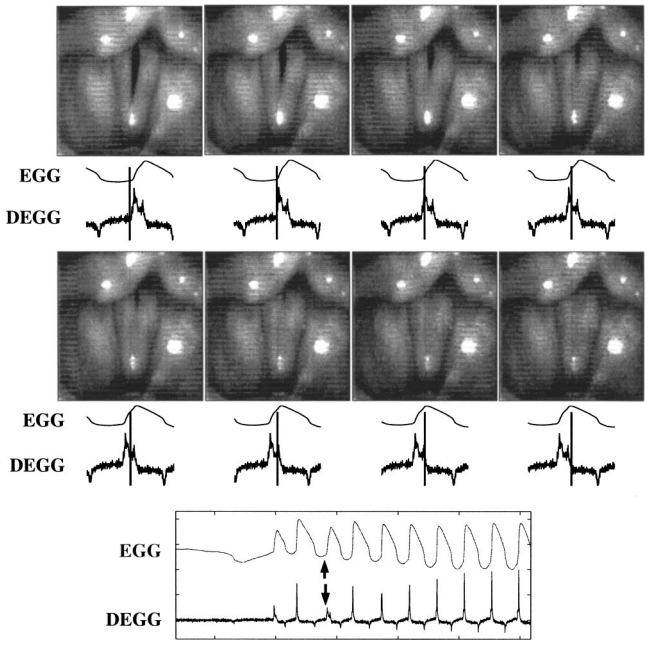

FIG. 9. Visualization of a double peak by simultaneous high-speed and electroglottographic recordings. Vertical bars indicate the moment in time at which the visual image occurs with respect to the EGG and DEGG signals. This example corresponds to the voice onset (bottom panel) of a nonpathological male phonation in mechanism 1, with $f_0 = 110$ Hz. The EGG sampling frequency is 44 444 Hz and the high-speed camera sampling frequency is 3704 frames/s.

glottal opening behaviors are not uncommon, having also been observed by Anastaplo and Karnell (1988) and recently by Hess and Ludwigs (2000). They could be related to voice quality: according to Hess and Ludwigs (2000), a relaxed voice would be produced with a posterior-to-anterior opening, whereas a pressed voice would rather be produced with an anterior-to-posterior opening. This corresponds to expectations, as arytenoid tension is greater in the case of pressed phonation, preventing the air from passing through the posterior part, whereas the posterior part of the glottis is not firmly closed during relaxed phonation (it can even be slightly open, as in the case of a glottal chink).

The double-peak feature is illustrated in Fig. 9, by simultaneous visualization of high-speed images and electroglottographic signal at voice onset. The data come from the same male phonation previously used to describe the closing and opening phases. The first closing peak corresponds to vocal-fold contact over two-thirds of the glottis length, as shown on the four top images. A glottal chink remains in the posterior part of the glottis. The second closing peak seems to be related to the closing of this glottal chink, as shown on the four bottom images.

D. Conclusion

These data warrant the assertion that DEGG signals provide information on glottal opening and closing for M1 and M2. These features may be related to some properties of vocal-fold contact that call for an extensive study that would combine this signal with other means of exploration such as high-speed visualization and glottal-flow estimation. When the peaks observed on the DEGG signal are single, they can

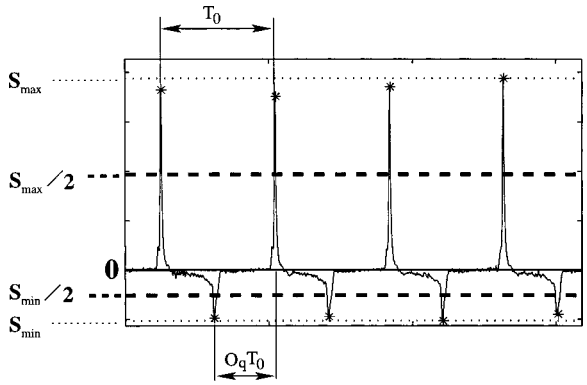

FIG. 10. Direct detection of closing and opening peaks by using a threshold. The values of the fundamental period T_0 and the open quotient O_q can be derived directly from the peak detection.

be related to the instants of glottal opening and closing. In that case, they can be used to measure fundamental frequency and open quotient. A method for such measurement is described in the following section.

III. MEASUREMENTS OF FUNDAMENTAL FREQUENCY AND OPEN QUOTIENT ON A DEGG SIGNAL

A. Introduction

In the previous section, it has been shown that the DEGG signal can present precise single peaks at glottal opening instants. In such a case, it can be assumed that a method which would take these peaks into account should give more accurate open quotient measurements than any threshold-based method. In Sec. III B, a new DEGG-based method (DECOM method) is proposed that can be applied to the case of quasisteady voiced sounds. The performance is compared to the above-mentioned methods in Sec. III D.

B. A DEGG-based method: DECOM

As illustrated in Fig. 10, the easiest way to measure the fundamental period and the open quotient using a DEGG signal consists of detecting the maxima located above a given positive threshold and the minima located below a given negative threshold. This threshold can be chosen as a percentage of the maximum (respectively, minimum) amplitude of the windowed signal.

This method yields good results when the closing and opening peaks are very precise. When the opening peaks are less precise, it can no longer be applied. Thus, a more general and robust method which is based on the determination of peak distance by correlation was developed: the DECOM method. The designation DECOM comes from "DEgg Correlation-based method for Open quotient Measurement." This method is rooted in the standard methods for fundamental frequency estimation of a voiced signal.

The principle of the DECOM method is to measure fundamental frequency and open quotient using a correlation-based method to estimate the distance between two consecutive closing peaks and the distance between an opening peak

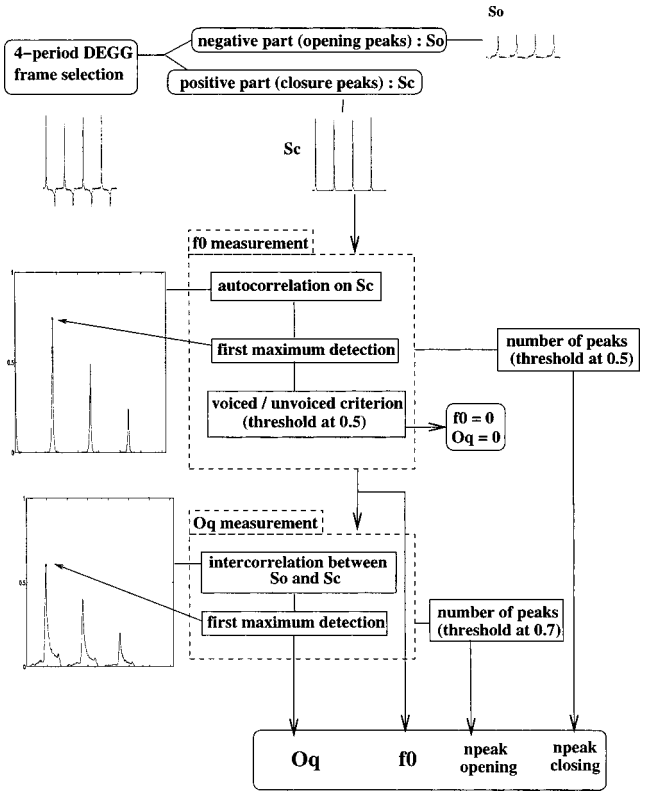

FIG. 11. Schematic description of the algorithm for the measurement of fundamental frequency (f_0) and open quotient (O_q). In addition, an automatic detection of the number of peaks at closing ($npeak$ closing) and at opening ($npeak$ opening) is performed.

and the consecutive closing peak. The corresponding algorithm is presented in Fig. 11. A step-by-step description follows.

1. Frame selection

The selected frames are four periods long, assuming that the fundamental period is already known. During the analysis process, an approximate value of the fundamental period can be deduced from the preceding frame. If not, as in the case of voicing onset or absence of voicing, the rectangular window has a fixed length of 40 ms for male voice and 20 ms for female voice. The analysis step is two fundamental periods or 5 ms if the fundamental period is unknown.

2. Division of the signal into positive and negative parts

The signal is separated into two parts: a positive part S_c, which contains information concerning glottal closing peaks, and a negative part S_o, which contains information concerning glottal opening peaks. The signal S_c is derived from the original signal by replacing any negative value by zero. In the same way, the signal S_o is derived from the original signal by replacing positive values by zero. Moreover, it is inverted, resulting in a positive signal. The original signal can then be reconstructed as the difference between the two signals: $S_{\text{original}} = S_c - S_o$.

3. Fundamental frequency measurement

A normalized biased autocorrelation function is calculated on signal S_c. The fundamental period is given by the position of the first maximum, which corresponds to the time between two consecutive closing peaks. The maxima of the autocorrelation function are detected as the inflection points for which the first derivative's sign inverts from positive to negative. Only the inflection points whose amplitude is above a given threshold of 50% of the maximal inflection points amplitude are selected, and the first of these points is kept as the first maximum of the autocorrelation function. It should be noted that no subharmonic error is likely to occur, i.e., a false selection of higher-order maxima, because of the quasi-impulsive form of signal S_c, which implies that the first maximum always has the maximal amplitude.

A criterion for discrimination between voiced and unvoiced parts is applied. The amplitude of the detected maximum of the normalized autocorrelation function is compared to a threshold value, empirically set at 0.5. If the amplitude value is less than the threshold value, the frame is considered to correspond to an unvoiced part, f_0 and O_q are set to zero, and the algorithm stops. If the amplitude is greater than the threshold value, the frame is considered to correspond to a voiced part. The measurement of the fundamental period is refined by applying a cubic-spline interpolation between five samples chosen around the first maximum of the autocorrelation function. The interpolation step is related to the uncertainty ΔT_0 of T_0 measurement. The uncertainty Δf_0 of f_0 depends on the uncertainty of T_0 by: $\Delta f_0/f_0=\Delta T_0/T_0$. Thus, a given uncertainty Δf_0 of f_0 measurement requires the uncertainty of T_0 to be $\Delta T_0=\Delta f_0/f_0^2$. The interpolation step is chosen so that the uncertainty of f_0 is 0.5 Hz and is calculated using an approximated value of f_0.

4. Open quotient measurement

A normalized biased intercorrelation function is calculated between signals S_o and S_c. The first maximum of this function corresponds to the time between an opening peak and the consecutive closing peak. It is detected in the same way as in the case of the autocorrelation function, but only the inflection points whose amplitudes are above a given threshold of 80% of the maximal inflection points amplitude are now selected. If we note T_1, the corresponding time, the open quotient O_q can be deduced from this time and the previous measure of fundamental period T_0 by: $O_q=T_1/T_0$. The uncertainty of O_q depends on the uncertainty of T_1 and T_0 by: $\Delta O_q/O_q=(\Delta T_1/T_1)+(\Delta T_0/T_0)$. As previously done for the f_0 measurement, the measurement is refined by applying a cubic-spline interpolation between five samples chosen around the first maximum of the intercorrelation function. The interpolation step is chosen to be equal to the one calculated for f_0 measurement, which implies that $\Delta T_1=\Delta T_0$. As $T_1=O_qT_0$, $\Delta O_q=(\Delta T_0/T_0)(1+O_q)<2(\Delta T_0/T_0)=2(\Delta f_0/f_0)$. For the considered frequency range ($f_0\geqslant 100$ Hz), the uncertainty of O_q is less than 0.01.

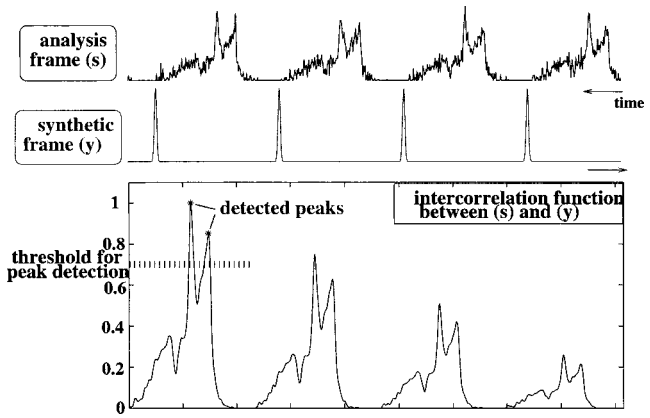

FIG. 12. Method for the detection of double- or imprecise peaks in the DEGG signal by intercorrelation between the signal to be analyzed and a Gaussian comb.

5. Automatic detection of peak doubling

The final part of the algorithm is dedicated to the automatic detection of double or undefined peaks. As illustrated in Fig. 12, a biased intercorrelation function is calculated between the signal to be analyzed (either S_c or S_o) and a synthetic signal of identical length and period, composed of Gaussian-modulated sinusoidal pulses. The pulses are given by the following equation:

$$y(t)=e^{-(\pi^2t^2)/[2\ln(2)*(1/BWf_0)]}\cos(2\pi f_0t).$$

The fractional bandwidth BW is chosen to be equal to 40 Hz, so that the Gaussian pulses are very narrow as compared to the fundamental period. Thus, this synthetic signal is similar to an S_c signal for which the peaks would be very precise. The detection is made over a window of length T_0, centered on the first maximum. Only the maxima which are located above a given threshold are taken into account, to allow for peak detection even when there is a great difference in amplitude between peaks. The threshold is set to 50% of the maximum in the case of closing and 70% in the case of opening.

6. Result of the algorithm

The algorithm returns the values of the fundamental frequency and open quotient measured for the given frame, as well as the estimated number of peaks ($npeak$) at closing and opening ($npeak=1$ for a single peak, $npeak=2$ for a double peak; if $npeak>2$, the peak is undefined). This last information will be taken into account in the experimental results, as the measure of open quotient is only valid if the opening and closing peaks are precise and single.

C. Illustration

This correlation-based method is applied to the study of open quotient in singing in a companion paper (Henrich *et al.*, submitted). Figure 13 illustrates the analysis of a sustained vowel sung by a mezzosoprano in mechanism 1. A doubling of the opening peak is detected between $t=0.2$ and $t=0.65$ s and between $t=1.65$ and $t=2$ s ("o" marks). The second opening peaks, which have the greatest amplitude, have been chosen for open quotient estimation in this case.

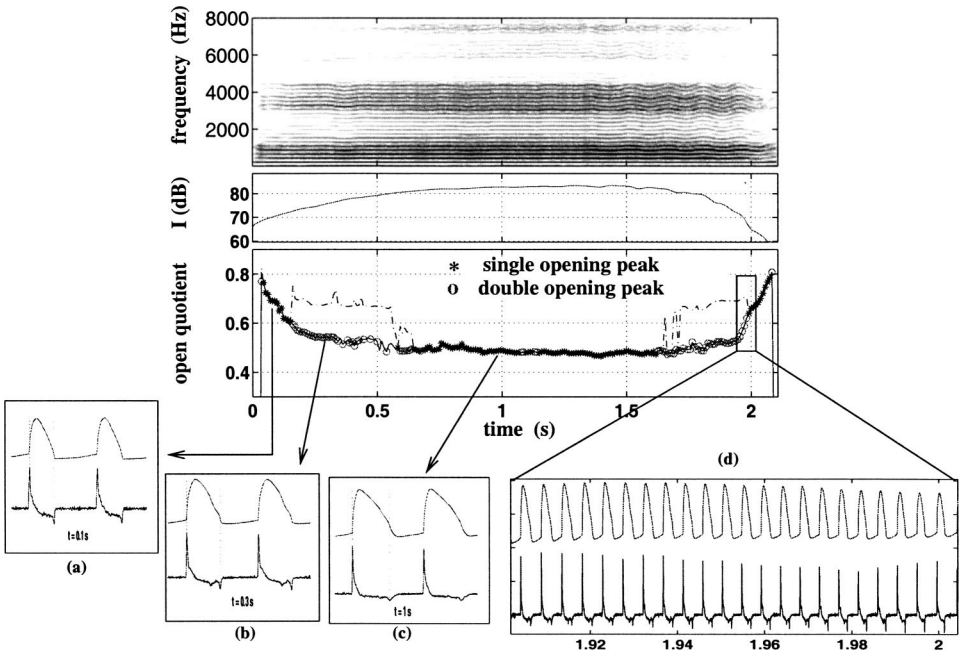

FIG. 13. Analysis of a sustained vowel sung by the mezzosoprano MS2 in mechanism 1, with $f_0 = 220$ Hz (A3). The top panel presents the sound spectrogram, the vocal intensity (I) curve, and the open quotient measures plotted against time. The measures related to single-peak detection are marked with "∗" and the ones related to double-peak detection are marked with "o". In the latter case, the second opening peak which has the maximum amplitude has been chosen for the measure of open quotient. The dash-dot lines show the measures that would have resulted if the first opening peaks had been chosen (between 0.2 and 0.65 s and between 1.65 and 2 s). The bottom panels (a), (b), (c), and (d) present the EGG and DEGG signals on several periods at a given time.

The open quotient values resulting from the choice of the first opening peaks are also plotted (broken lines). In the case of a double peak, the choice of one peak or another leads to markedly different values of the open quotient, the difference ranging between 0.1 and 0.2 in this case. It is clear from this example that the open quotient cannot be accurately measured on a DEGG signal unless the closing and opening peaks are single and precise.

D. EGG, DEGG, and glottal-flow measurements comparison

A comparison of the different methods for open quotient measurement mentioned in Sec. III A has been conducted on a database of five male speakers provided by Childers (2000) (subjects M01 to M05). The open quotient was measured on the EGG or DEGG signal using the following four methods: EGG thresholds at 50% and 35%, Howard's method with a threshold at 3/7, and the DECOM method. The open quotient was also estimated on the acoustic signal by a pitch-synchronous covariant linear prediction method proposed by Ljungqvist (1986). The error criterion was minimized with regard to the KLGLOTT88 glottal flow model (Klatt and Klatt, 1990).

Table II presents the results of the acoustic and electroglottographic measurements for vowels [a], [i], and [u]. The table on the left gives the mean open quotient values mea-

TABLE II. Comparison of five different methods for open quotient measurement, for 5 speakers (M01 to M05, Childers, 2000) and for the 3 vowels [a], [i], and [u]: threshold methods based on the EGG signal (50% and 35%), on a combination of EGG and DEGG signals (3/7), on the DEGG signal (DECOM), and on the inverse-filtered glottal flow (gf). The left table gives the mean value of open quotient in each case and the right table the mean difference in percent between the open quotient measured on the EGG or DEGG signal and the open quotient measured on the inverse-filtered glottal flow. For each case, the minimum difference is in bold.

	Mean open quotient					Mean difference (%) $\lvert Oq_{EGG} - Oq_{GF} \rvert$			
	50%	35%	3/7	DECOM	**gf**	50%	35%	3/7	DECOM
					vowel [a]				
M01	0.62	0.58	0.59	0.60	0.59	2.99	1.25	**0.79**	0.99
M02	0.53	0.47	0.50	0.47	0.46	7.37	2.02	3.75	**1.56**
M03	0.55	0.50	0.51	0.52	0.50	4.71	**1.08**	1.39	2.26
M04	0.54	0.46	0.53	0.55	0.57	3.30	10.89	3.81	**2.39**
M05	0.44	0.36	0.40	0.37	0.37	6.03	1.45	2.44	**1.25**
					vowel [i]				
M01	0.61	0.58	0.59	0.59	0.58	3.26	1.10	1.12	**0.93**
M02	0.53	0.47	0.50	0.51	0.52	1.45	4.86	1.84	**0.96**
M03	0.53	0.46	0.48	0.49	0.47	6.47	**2.08**	3.06	2.98
M04	0.50	0.45	0.49	0.48	0.49	2.00	4.03	1.59	**1.45**
M05	0.43	0.38	0.39	0.40	0.41	4.84	4.70	4.13	**2.47**
					vowel [u]				
M01	0.66	0.62	0.63	0.64	0.63	3.52	1.01	**0.83**	1.29
M02	0.51	0.47	0.49	0.48	0.49	2.37	1.97	**0.97**	1.58
M03	0.51	0.46	0.47	0.48	0.46	5.22	**1.70**	2.39	2.82
M04	0.50	0.43	0.49	0.50	0.52	**2.60**	8.55	3.00	2.60
M05	0.39	0.34	0.35	0.33	0.33	5.39	1.21	1.89	**1.10**

sured with the five different methods; that on the right gives the differences in percent between the measures using electroglottography and the measures conducted on the estimated glottal flow. Threshold methods (either 50% or 35%) show variable differences compared with the ones made on glottal flow, ranging from 1% to 10%. The 35% method seems to yield better results. When the DEGG signal is taken into account, the results are even more similar to the results obtained for the glottal flow. The differences range from 0.79% to 4.13% in the case of Howard's method (3/7) and from 0.93% to 2.98% in the case of the DECOM method presented in this paper. As expected, the open quotient measurements using the DECOM method are, on average, in much better agreement with the glottal-flow measurements than most threshold-based methods for sustained phonation when double pulsing is rejected.

These results confirm that there is a good correspondence between the open quotient measured on a glottal-flow signal and that measured on an electroglottographic signal. The correspondence improves if the derivative of the EGG signal is taken into account. The method developed by Howard gives good results. Yet, in the case of precise opening and closing peaks, the DECOM method seems more appropriate. It is envisioned, as a further improvement of EGG-based open quotient measurement methods, to combine the DECOM method with Howard's method when the peaks are double or imprecise.

IV. CONCLUSION

The use of the differentiated EGG signal to measure the open quotient has been controversial. Yet, little research has been devoted to characterizing this signal in terms of glottal opening and closing instants. One purpose of this paper was to describe the various features which can be observed in this signal by analyzing an extensive corpus of sung items recorded by 18 trained singers.

A DEGG signal presents strong and weak peaks which can accurately be related to the glottal closing and opening instants, respectively, in the case where these peaks are single and precise. A correlation-based algorithm, DECOM, is proposed for measuring fundamental frequency and open quotient using the DEGG signal rather than the EGG signal. The DECOM method is compared to threshold-based methods. It appears that open quotient measurements based on electroglottography are in better agreement with the measurements based on inverse-filtered glottal flow if the DEGG signal is taken into account. The application of the DECOM method to the study of open quotient variations in singing is addressed in a companion paper (Henrich *et al.*, submitted).

Exploration of the database shows that the DEGG can present other typical features, such as a doubling of the opening or of the closing peaks. In these cases, the DEGG signal is not suitable for the purpose of open quotient measurement, but could still complement the EGG signal, as small changes in vocal-fold contact are not easily noticeable on an EGG signal, whereas they appear much more clearly on a DEGG signal. The DEGG signal may provide interesting clues for the detection of peculiar glottal configurations. Yet, the features that can be found on such a signal have to be characterized with regard to vocal-fold physiology and glottal vibratory movement. Comparison with high-speed visualization would significantly advance the understanding of the characteristics of a DEGG signal and is the aim of continuing research. Further research could also be conducted on the possible auditory effect associated with double pulsing.

ACKNOWLEDGMENTS

This work is part of a Ph.D. thesis defended at the Université Pierre & Marie Curie (Paris,France) in November 2001 (Henrich, 2001). The authors would like to thank Jürgen Neubauer and the team from the Department of Phoniatrics and Pediatric Audiology of the University of Erlangen-Nuremberg (Germany) for kindly providing a data file containing the EGG signal and high-speed images of male phonation. They wish to thank Adrian Fourcin and Svante Granqvist for their valuable comments, which resulted in significant improvements of the manuscript. They are grateful to Alexis Michaud, Brian Katz, and Evelyn Abberton for English corrections.

APPENDIX: DEFINITION OF THE LARYNGEAL MECHANISMS

Human vocal production is characterized by the use of four distinctive vocal-fold configurations which differ in respect to the length and thickness of the vocal folds and the muscular laryngeal tensions involved in the vocal process (Roubeau, 1993). Evidence in support of this classification is provided by the noticeable transitions, which can for instance be heard on a glissando and detected on an EGG signal (Henrich *et al.*, 2003b). Many different terms have been used in the literature to describe these laryngeal configurations, which leads to confusing terminology. So as to avoid this confusion, which is related to the notion of register in singing, and to bring out the differences between change in the glottis configuration (laryngeal mechanism) and adjustment of the vocal tract (resonance register), we have chosen to use the term *laryngeal mechanism* instead of *register*, and to number laryngeal mechanisms, following Roubeau (1993).

(1) mechanism 0, or M0, corresponds to the so-called ''vocal fry,'' ''pulse,'' or ''strohbass'' register;
(2) mechanism 1, or M1, corresponds to the so-called ''chest'' or ''modal'' register for male and female and male ''head'' register;
(3) mechanism 2, or M2, corresponds to the so-called ''falsetto'' or ''loft'' male register and to the ''head'' female register;
(4) mechanism 3, or M3, correponds to the so-called ''whistle,'' ''flageolet,'' or ''flute'' register.

A rationale for explaining this terminology and its choice in further detail is formulated in Henrich *et al.* (2003b).

In this paper, we focus on the two main laryngeal mechanisms, M1 and M2, which are commonly used in speech and singing. In mechanism 1, the vocal folds are thick, leading to vertical phase differences in vibration, a

longer closing and opening phase as compared to mechanism 2, where the vocal folds are thin and vibrate without any vertical phase difference (Vennard, 1967).

[1]For the purpose of this illustration, a datafile was kindly provided by a team of the Department of Phoniatrics and Pediatric Audiology of the University of Erlangen-Nuremberg (Germany). It contains a 2-s-long recording of high-speed images and the corresponding EGG signal in the case of a nonpathological male phonation. This recording was made by J. Neubauer, M. Tigges, T. Wittenberg, and U. Eysholdt.

Anastaplo, S., and Karnell, M. P. (**1988**). ''Synchronized videostroboscopic and electroglottographic examination of glottal opening,'' J. Acoust. Soc. Am. **83**, 1883–1890.

Askenfelt, A., Gauffin, J., Sundberg, J., and Kitzing, P. (**1980**). ''A comparison of microphone and electroglottograph for the measurement of vocal fundamental frequency,'' J. Speech Hear. Res. **23**, 250–273.

Baer, T., Löfqvist, A., and McGarr, N. S. (**1983a**). ''Laryngeal vibrations: A comparison between high-speed filming and glottographic techniques,'' J. Acoust. Soc. Am. **73**, 1304–1308.

Baer, T., Titze, I. R., and Yoshioka, H. (**1983b**). ''Multiple simultaneous measures of vocal fold activity,'' in *Vocal Fold Physiology: Contemporary Research and Clinical Issues*, edited by A. Bless (College Hill, San Diego), pp. 229–237.

Baken, R. J. (**1992**). ''Electroglottography,'' J. Voice **6**, 98–110.

Berke, G. S., Moore, D. M., Hantke, D. R., Hanson, D. G., Gerratt, B. R., and Burstein, F. (**1987**). ''Laryngeal modeling: Theoretical, *in vitro*, *in vivo*,'' Laryngoscope **97**, 871–881.

Childers, D. G. (**2000**). *Speech Processing and Synthesis Toolboxes* (Wiley, New York).

Childers, D. G., Hicks, D. M., Moore, G. P., and Alsaka, Y. A. (**1986**). ''A model for vocal fold vibratory motion, contact area, and the electroglottogram,'' J. Acoust. Soc. Am. **80**, 1309–1320.

Childers, D. G., Hicks, D. M., Moore, G. P., Eskenazi, L., and Lalwani, A. L. (**1990**). ''Electroglottography and vocal fold physiology,'' J. Speech Hear. Res. **33**, 245–254.

Childers, D. G., and Krishnamurthy, A. K. (**1985**). ''A critical review of electroglottography,'' CRC Crit. Rev. Biomed. Eng. **12**, 131–161.

Childers, D. G., and Larar, J. N. (**1984**). ''Electroglottography for laryngeal function assessment and speech analysis,'' IEEE Trans. Biomed. Eng. **BME-31**, 807–817.

Childers, D. G., Moore, G. P., Naik, J. M., Larar, J. N., and Krishnamurthy, A. K. (**1983a**). ''Assessment of laryngeal function by simultaneous, synchronized measurement of speech, electroglottography and ultra-high speed film,'' in *Transcripts of the Eleventh Symposium: Care of the Professional Voice.*, edited by V. Lawrence (Voice Foundation, New York), pp. 234–244.

Childers, D. G., Naik, J. M., Larar, J. N., Krishnamurthy, A. K., and Moore, G. P. (**1983b**). ''Electroglottography, speech and ultra-high speed cinematography,'' in *Vocal Fold Physiology and Biophysics of Voice*, edited by I. Titze and R. Scherer (Denver Center for the Performing Arts, Denver), pp. 202–220.

Childers, D. G., Smith, A. M., and Moore, G. P. (**1984**). ''Relationships between electroglottograph, speech, and vocal cord contact,'' Folia Phoniatr. **36**, 105–118.

Colton, R. H., and Conture, E. G. (**1990**). ''Problems and pitfalls of electroglottography,'' J. Voice **4**, 10–24.

Cranen, B. (**1991**). ''Simultaneous modelling of EGG, PGG, and glottal flow,'' in *Vocal Fold Physiology: Acoustic, Perceptual, and Physiological Aspects of Voice Mechanisms*, edited by H. B. Gauffin J. (Singular, San Diego), pp. 57–64.

Dejonckere, P. (**1981**). ''Comparison of two methods of photoglottography in relation to electroglottoraphy,'' Folia Phoniatr. **33**, 338.

Fabre, P. (**1957**). ''Un procédé électrique percutané d'inscription de l'accolement glottique au cours de la phonation: Glottographie de haute fréquence,'' Bulletin de l'Académie Nationale de Médecine, pp. 66–69.

Fabre, P. (**1958**). ''Etude comparée des glottogrammes et des phonogrammes de la voix humaine,'' Ann. Oto. Lar. (Paris) **75**, 767–775.

Fabre, P. (**1959**). ''La glottographie électrique en haute fréquence: Particularités de l'appareillage,'' C. R. Soc. Biol. (Paris) **153**, 1361–1364.

Fabre, P. (**1961**). ''Glottographie respiratoire,'' Ann. Oto. Lar. (Paris) **78**, 814–824.

Fourcin, A. J. (**1974**). ''Laryngographic examination of vocal fold vibration,'' in *Ventilatory and Phonatory Function*, edited by B. Wyke (Oxford University Press, London), pp. 315–326.

Fourcin, A. J. (**1981**). ''Laryngographic assessment of phonatory function,'' ASHA Rep. **11**, 116–124.

Gerrat, B. R., Hanson, D. G., and Berke, G. S. (**1988**). ''Laryngeal configuration associated with glottography,'' Am. J. Otolaryngol. **9**, 173–179.

Henrich, N. (**2001**). ''Etude de la source glottique en voix parlée et chantée (Study of the glottal source in speech and singing),'' Ph.D. thesis, Université Paris 6, France.

Henrich, N., d'Alessandro, C., Castellengo, M., and Doval, B. ''Open quotient measurements in speech and singing,'' J. Acoust. Soc. Am. (submitted).

Henrich, N., Roubeau, B., and Castellengo, M. (**2003b**). ''On the use of electroglottography for characterisation of the laryngeal mechanisms,'' in Stockholm Music Acoustics Conference (Stockholm, Sweden).

Hess, M. H., and Ludwigs, M. (**2000**). ''Strobophotoglottographic transillumination as a method for the analysis of vocal fold vibration patterns,'' J. Voice **14**, 255–271.

Howard, D. M. (**1995**). ''Variation of electrolaryngographically derived closed quotient for trained and untrained adult female singers,'' J. Voice **9**, 163–172.

Howard, D. M., Lindsey, G. A., and Allen, B. (**1990**). ''Toward the quantification of vocal efficiency,'' J. Voice **4**, 205–212.

Karnell, M. P. (**1989**). ''Synchronized videostroboscopy and electroglottography,'' J. Voice **3**, 68–75.

Kitzing, P. (**1977**). ''Methode zur kombierten photo- und elektroglottographischen registrierung von stimmlippenschwingungen,'' Folia Phoniatr. **29**, 249–260.

Kitzing, P. (**1982**). ''Photo- and electroglottographical recording of the laryngeal vibratory pattern during different registers,'' Folia Phoniatr. **34**, 234–241.

Kitzing, P. (**1983**). ''Simultaneous photo- and electroglottographic measurements of voice strain,'' in *Vocal Fold Physiology*, edited by I. R. Totze and R. C. Scherer (The Denver Center for the Performing Arts, Denver), pp. 221–229.

Kitzing, P., Carlborg, B., and Löfqvist, A. (**1982**). ''Aerodynamic and glottographic studies of the laryngeal vibratory cycle,'' Folia Phoniatr. **34**, 216–224.

Klatt, D., and Klatt, L. (**1990**). ''Analysis, synthesis, and perception of voice quality variations among female and male talkers,'' J. Acoust. Soc. Am. **87**, 820–857.

Lecluse, F. (**1977**). ''Elektroglottografie,'' Thesis Rotterdam, Drukkerig Elinkwijk, Utrecht.

Lecluse, F., and Brocaar, M. (**1977**). ''Quantitative measurements in the electroglottogram,'' 17th International Congress of Logopedics and Phoniatrics.

Lecluse, F. L. E., Brocaar, M. P., and Verschuure, J. (**1975**). ''The electroglottography and its relation to glottal activity,'' Folia Phoniatr. **27**, 215–224.

Ljungqvist, M. G. (**1986**). ''Speech analysis-synthesis based on modeling of voice source and vocal-tract characteristics,'' Ph.D. thesis, University of Tokyo.

Miller, D. G. (**2000**). ''Registers in singing,'' Ph.D. thesis, Rijksuniversiteit Groningen, the Netherlands.

Orlikoff, R. F. (**1998**). ''The uses and abuses of electroglottography,'' Phonoscope **1**, 37–53.

Pedersen, M. F. (**1977**). ''Electroglottography compared with synchronized stroboscopy in normal persons,'' Folia Phoniatr. **29**, 191–199.

Rothenberg, M. (**1981**). ''Some relations between glottal air flow and vocal fold contact area,'' ASHA Rep. **11**, 88–96.

Rothenberg, M. (**1992**). ''A multichannel electroglottograph,'' J. Voice **6**, 36–43.

Rothenberg, M., and Mahshie, J. J. (**1988**). ''Monitoring vocal fold abduction through vocal fold contact area,'' J. Speech Hear. Res. **31**, 338–351.

Roubeau, B. (**1993**). ''Mécanismes vibratoires laryngés et contrôle neuromusculaire de la fréquence fondamentale,'' thèse, Université Paris XI, Orsay.

Roubeau, B., and Castellengo, M. (**1993**). ''Revision of the notion of voice register,'' XIXth International CoMeT Congress, Utrecht.

Roubeau, B., Chevrie-Muller, C., and Arabia-Guidet, C. (**1987**). ''Electroglottographic study of the changes of voice registers,'' Folia Phoniatr. **39**, 280–289.

Svec, J. G., Schutte, H. K., and Miller, D. G. (**1999**). ''On pitch jumps

between chest and falsetto registers in voice: Data from living and excised human larynges,'' J. Acoust. Soc. Am. **106**, 1523–1531.
Teaney, D., and Fourcin, A. J. (**1980**). ''The electrolaryngography as a clinical tool for the observation and analysis of vocal fold vibration,'' The Voice Foundation.
Titze, I. R., Baer, T., Cooper, D., and Scherer, R. (**1984**). ''Automatic extraction of glottographic waveform parameters and regression to acoustic and physiologic variables,'' in *Vocal Fold Physiology: Contemporary Research Clinical Issues*, edited by A. J. Bless DM (College Hill, San Diego), pp. 146–154.
Vennard, W. (**1967**). *Singing: The Mechanism and the Technic* (Carl Fischer, New York).

Dynamics of frequency and amplitude modulations in vocalizations produced by eastern towhees, *Pipilo erythrophthalmus*

Brian S. Nelson[a)]
Department of Biology, Indiana University, Bloomington, Indiana, 47405-3700

(Received 26 August 2003; revised 26 December 2003; accepted 29 December 2003)

Eastern towhees, *Pipilo erythrophthalmus* (Emberizidae, Passeriformes), appear to estimate source-SPL using spectral or temporal variables. Nevertheless, vocalizations are dynamic by nature and it remains unclear whether subjects pay attention to correlations between discrete variables or pay attention to the dynamics that these variables summarize. Sine functions are used to describe coarse (slow, <10 Hz) frequency and amplitude modulations in towhee calls and correlations between variables are identified. Towhee calls are also finely (rapidly, >400 Hz) modulated in both amplitude and frequency. Fine amplitude and frequency modulations correlate well (occur in phase) over relatively low fundamental frequencies (<~3.5 kHz) and tend to have greater amplitudes and frequencies over these same frequencies. Modulations and correlations between modulations might exist due to stable dynamic interactions that occur within and between the physical forces that function to produce modulations in vocalizations. Results support the hypothesis that towhees communicate within separate sound frequency channels defined to each side of ~3.5 kHz. [DOI: 10.1121/1.1648976]

PACS numbers: 43.80.Ka [WA] Pages: 1333–1344

I. INTRODUCTION

Vocal production and hearing mechanisms are dynamic by nature and individuals may often exchange information using a currency that is also dynamic in nature. Dynamics in vocalizations are commonly described as modulations, however, some dynamics are commonly distinguished from modulations. For example, songbird vocalizations and syllables within vocalizations are often sequenced and produced with variable repetition rates (e.g., Podos, 2001; Draganoiu *et al.*, 2002). Repetition rates are commonly distinguished from modulations since there often may be no obvious acoustic carrier being modulated between syllables. Thus, repetition and modulation will be treated as separate entities in this paper even though auditory systems might often react similarly in response to both types of periodic signals [Fig. 1(a)].

In contrast with repetition rate, coarse (slow) amplitude modulations (AM) and coarse frequency modulations [FM; Fig. 1(b)] are ubiquitous in songbird vocalizations and have long been defined as modulations (Greenewalt, 1968; Stein, 1968). Gardner *et al.* (2001) demonstrated that relatively coarse changes in subbronchial air pressure and labial tension (elasticity) are often sufficient to produce many of the coarse modulations [Fig. 1(b)] that are evident in bird vocalizations. Nevertheless, few studies have attempted to quantify coarse modulation functions in recorded vocalizations and, as a consequence, little is known about the modulation functions that need to be described by mathematical models of vocal production mechanisms (e.g., Laje *et al.*, 2002; Mindlin *et al.*, 2003; Elemans *et al.*, 2003). More specifically, little is known about the modulation functions that are thought to be derived from relatively slow (>~20 ms) oscillations in subbronchial air pressure or tension on the medial labia (ML) and lateral labia (LL).

Vocalizations and syllables within vocalizations commonly vary in sound frequency, duration, or amplitude [Fig. 1(c)] and correlated measurements between these variables can also often resemble modulating functions (e.g., Nelson, 2000). Functions derived across independently produced vocalizations are not normally defined as modulations but are likely to be produced by the same physical forces (e.g., subbronchial air pressure and labial elasticity). As a consequence, descriptions of the forces that function to produce intrasyllable modulations are likely to also describe the forces that function to produce intersyllable modulations.

Fine (rapid) modulations have also long been recognized in bird vocalizations (Greenewalt, 1968; Stein, 1968). Unlike coarse modulations, however, fine modulations occur, by definition, over relatively short periods of time (typically <10 ms) and may occur due to rapid oscillations in sublabial air pressure or tension on the ML (as opposed to relatively slow oscillations in these same forces). Acoustical interactions between two relatively high frequency carriers (e.g., >1.5 kHz) can also produce fine amplitude modulations in vocalizations (Nowicki and Capranica, 1986a) but are not expected to generate fine frequency modulations. Fine modulations give a vocalization a ''rough'' acoustic quality and are not easily described using discrete acoustic variables [Fig. 1(d)]. Instead, fine modulations are usually quantified in the frequency domain using sidebands in spectra (e.g., Nowicki and Capranica, 1986b; Banta Lavenex, 1999). Sidebands do not, however, differentiate fine amplitude modulations from fine frequency modulations (Beecher, 1988) and, as a consequence, little is known about the fine modulations that occur in songbird vocalizations.

a)Electronic mail: brsnelso@indiana.edu

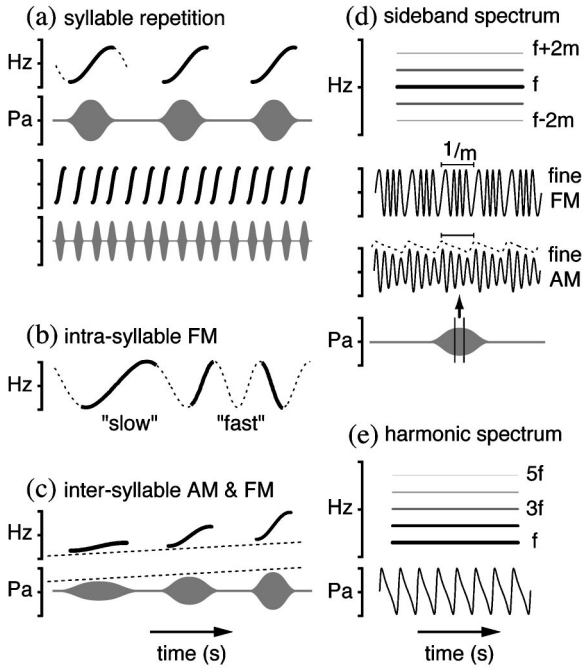

FIG. 1. Schematic illustration of modulations commonly observed in songbird vocalizations. Syllable repetition rate (a) is not often considered to be modulation since there may be no clear signal being modulated between syllables. In contrast, coarse (slow) intrasyllable variation (b) imposed upon a carrier is normally described as modulation. Intersyllable variation (c) is not usually described as modulation, however intersyllable variation can also often resemble a modulating function and such functions may be produced by the same physical forces that function to produce intrasyllable modulations. Fine (rapid) modulations in both frequency and amplitude (d) are also often evident in songbird vocalizations and both fine AM and fine FM can produce spectra that superficially resemble harmonic spectra (e).

Eastern towhee, *Pipilo erythrophthalmus*, "towhee" calls are highly variable in coarse acoustic structure as demonstrated by discrete measurements obtained from calibrated time-amplitude waveforms and time-frequency spectrograms (Nelson, 2000). In this study, coarse amplitude and frequency modulations are quantified using sine functions. In addition, contributions to sidebands in calls are estimated by quantifying the (1) magnitudes of upper and lower sidebands in calls, (2) frequencies (rates) of fine amplitude and frequency modulations, (3) amplitudes of fine amplitude and frequency modulations, and (4) phase relationships between amplitude and frequency modulations.

Sound frequencies below ~3.5 kHz attenuate more reliably than lower sound frequencies (Nelson, 2003) and towhees use different auditory distance cues when played sound frequencies to each side of ~3.5 kHz (Nelson, 2002). These data suggest that towhees communicate within separate sound frequency channels defined to each side of ~3.5 kHz. As a consequence, AM and FM are summarized as a function of sound frequency to determine whether towhees might also impose different modulation patterns upon these same two sound frequency ranges.

II. METHODS

Calls ($N=1067$) were recorded from 36 color-banded subjects (mean±sd=30±30 calls/subject) at Archbold Biological Station, 12 km south of Lake Placid, FL, including calls ($N=315$) that were recorded and analyzed previously (Nelson, 2000). Subjects were captured in a mist net and then placed in a vinyl-coated steel wire (2.4-mm diameter, 1.15×2.25 cm mesh) cage measuring 20×20×20 cm and elevated 1.5–2.5 m above the ground in a small clearing or fire-lane located within each subject's territory. Recordings were obtained with one or two microphones placed parallel to the ground and 100 cm from a perch placed in the center of the cage (Brüel & Kjaer 4188 microphone with a Brüel & Kjaer 2236 sound level meter functioning as a preamplifier, or Brüel & Kjaer 4189 microphone with Brüel & Kjaer 2671 and Radio Design Labs STM-2 preamplifiers). Microphone outputs were recorded using a digital audio tape recorder (Sony TCD-D3 or HHB PortaDAT) or microcomputer (16 bits; 44.1 or 48 kHz sampling rate).

Subjects are not represented equally in this sample. However, no single individual's calls dominated the sample and the trends that are described are not produced by the calls of any single individual. Furthermore, general trends are evident in calls produced by each individual. Subjects could rarely be recaptured, thus differences observed between individuals are not described. Correlations between variables described previously were found to be consistent across individuals (Nelson, 2000) and thus the main goal of this research is to describe modulations in vocalizations produced by individuals throughout this population.

Error in SPL calibration can influence both the correlations and the modulation functions that are described. As a result, 1-kHz, 94-dB (re: 20 μPa) reference calibration tones (Brüel & Kjaer 4231) were recorded before or after calls were recorded and calls were subsequently adjusted to appropriate absolute SPLs before analyses were performed (Nelson, 2000). In most cases, these adjustments were accurate (±0.5 dB) but in some cases slightly larger errors (±2 dB) may have occurred due to various factors. These errors may have introduced noise into measurements but do not produce the correlations nor the modulations that are described.

Time-frequency spectrograms of calls were produced using a 34.8-ms Hanning window, 46.4-ms FFT frame, and 98% overlap between each successive 46.4-ms frame. Frequency modulations were not directly quantified using spectra, however, spectrograms were inspected to ensure that there were no problems with recordings. In addition, spectra extracted from time-frequency spectrograms were used to quantify the magnitudes of sidebands in recorded calls (see below). Each vocalization was next high-pass filtered (30 dB/oct at 200 Hz) and cropped above a 65-dB rms threshold (re: 20 μPa; 0.035 Pa) to minimize background noise (see below). This cropping procedure also functioned to define the times at which calls both started and ended.

Fine modulation in the time domain was measured over the duration of each call using an autocorrelation algorithm (Fig. 2). The autocorrelation algorithm performs best when executed over at least 3 cycles and, as a consequence, frequency estimates were obtained using a sliding 1.5-ms Hanning window so that each window would include at least 3 cycles at 2 kHz. The short-term fundamental frequency within each window was first approximated as the inverse of

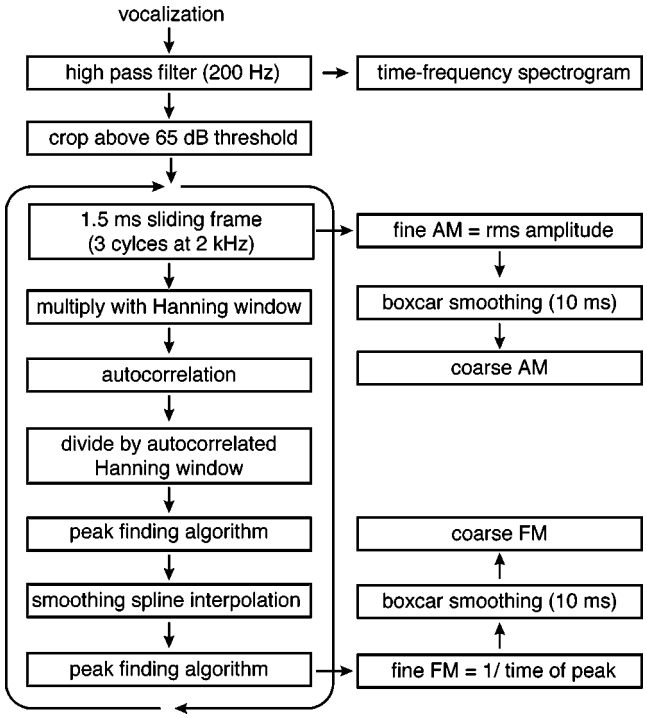

FIG. 2. Schematic illustration of iterative operations used to quantify sound frequency and amplitude over the duration of each call.

the time of the maximum autocorrelation result after dividing results by a second Hanning window of equal length that was first correlated with itself. A smoothing-spline interpolation was next performed over three points to each side of this maximum autocorrelation result and frequency within each window was more accurately calculated as the inverse of the time at which the interpolated waveform reached maximum amplitude. The algorithm has a frequency resolution of ± 2 Hz from 2 to 5 kHz when using a single 1.5-ms window (see Sec. III) and the algorithm is relatively insensitive to AM ($<\pm 1$ Hz). Background noise [$\sim 28 \pm 10$ dB rms, mean$\pm$sd, 2–5 kHz (Nelson, 2003)] may have introduced random errors into measurements, however errors are expected to be small since measurements were obtained only when rms amplitude exceeded 65-dB rms (signal to noise ratio $>\sim 27$ dB; see Sec. III). Fine autocorrelation windows were maximally overlapped (i.e., advanced by only a single point during each iteration) to produce a fine FM waveform with a sampling rate equal to the original waveform. Fine variation in amplitude (AM) was measured within the same algorithm by calculating rms SPL within each overlapped 1.5-ms window.

Estimates of peak frequency that were derived using this relatively simple autocorrelation algorithm were verified by calculating peak frequency over the same maximally overlapped 1.5-ms windows using a second algorithm that first involved a transformation into the frequency domain. In this analysis, each window was first transformed into the frequency domain using a FFT and peak frequency (f) within each window was calculated as

$$f = \frac{\Delta\varphi/2\pi}{S}, \tag{1}$$

where S is the sampling rate of the original waveform and $\Delta\varphi$ is calculated as the change in radial phase within the FFT bin that had the greatest magnitude across each adjacent window (i.e., windows beginning with sample numbers n and $n+1$). Results obtained using this algorithm were nearly identical to results obtained using autocorrelation and are not reported.

Coarse ($<\sim 10$ Hz) and fine ($>\sim 400$ Hz) modulations are likely to be perceived differently and produced by distinct physical forces. As a consequence, coarse AM and FM were quantified by applying a 10-ms sliding average (boxcar) smoothing procedure to fine AM and FM waveforms. This 10-ms window preserves modulation frequencies below 10 Hz (>-0.15 dB) but attenuates (<-40 dB) modulation frequencies lower than 400 Hz.

Coarse FM is sinusoidal and the Levenberg–Marquardt best-fit algorithm was used to fit a sine function to each coarse FM waveform,

$$y_0 = A \cdot \sin(f \cdot 2\pi \cdot t + \varphi), \tag{2}$$

where y_0 is fundamental frequency, A is amplitude (frequency excursion in Hz), t is time, f is coarse FM frequency, and φ is phase. Because fine modulations ($>\sim 400$ Hz) are often strong (see below), modulation frequencies (f) were limited to below 10 Hz.

Coarse AM is difficult to summarize because calls have variable duration. Calls were therefore normalized to one second and coarse AM was approximated using a Gaussian function

$$y_0 = A \cdot e\left(-\frac{t-t_0}{W}\right)^2, \tag{3}$$

where y_0 is call amplitude (Pa), A is the amplitude of the coarse AM function, t is time, t_0 is the time of peak amplitude, and W is the width of the function.

There is no clear rationale for why coarse AM dynamics should be characterized using a single Gaussian function. Thus, onset and offset ramps were also described using best-fit sine functions [Eq. (2), where y_0 is call amplitude, A is modulation amplitude, t is time, f is coarse AM frequency, and φ is phase]. Onset and offset ramps merge together when calls reach maximum amplitude (Fig. 4) and, as a consequence, sine functions were fit to points falling either before or after the center (t_0) of a second Gaussian function that was fit to each original time-amplitude waveform. Offset ramps were referenced to the end of each vocalization and are thus presented using a negative time scale.

First-order sidebands in towhee calls corresponding with $f \pm m$ typically have far greater magnitude (>15 dB) than second-order sidebands corresponding with $f \pm 2m$ (see Sec. III), indicating that fine frequency and amplitude modulations in towhee calls are both coherent and sinusoidal. Preliminary observations of sidebands in time-frequency spectrograms also indicated that fine modulations typically occur with frequencies ranging from between 450 and 550 Hz. I therefore filtered each finely modulated waveform (bandpass FIR filter; 400–600 Hz; -30 dB/oct) and estimated the frequency (rate) of fine AM and FM imposed upon each call's coarse FM carrier (fundamental) by performing a second autocorrelation analysis on each filtered waveform. The

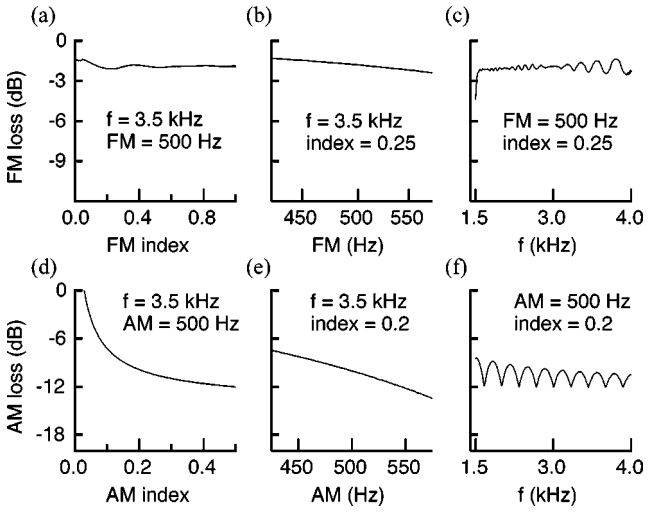

FIG. 3. Methods provide for an accurate estimate of sound frequency and amplitude over a relatively short period of time (1.5 ms) but produce biases in estimates of fine AM and FM amplitude. (a) FM amplitude losses expected as FM index increases (FM index=FM excursion/FM frequency). (b) FM amplitude losses expected as a function of FM frequency. (c) FM amplitude losses expected as a function of fundamental frequency (coarse FM). (d) AM amplitude losses expected as AM index increases (AM index=AM amplitude/carrier amplitude). (e) AM amplitude losses expected as a function of AM frequency. (f) AM amplitude losses expected as a function of fundamental frequency (coarse FM).

autocorrelation algorithm used for this analysis was identical to the algorithm described above with the exception that I used a longer 10-ms time frame so that each frame would encompass at least 4 cycles at 400 Hz.

Fine AM and FM should have a consistent phase relationship if both are produced by a single modulating structure or pair of coupled (integrated) structures. Correlation coefficients were therefore calculated over 8-ms time frames obtained from fine AM and FM waveforms and correlation coefficients were used to describe the phase relationship between fine AM and FM over the duration of each call. An 8-ms time frame was employed so that each frame would encompass at least 4 cycles at 500 Hz.

Calls have variable duration and measurements that vary over the duration of a call are difficult to summarize. As a result, measurements were averaged within 50-Hz sound frequency bins and are summarized as a function of fundamental (coarse FM) frequency as opposed to as a function of time. This analysis allows for comparisons across calls and also allows for an assessment of fine AM and FM as a function of fundamental (carrier) frequency.

Autocorrelation allows for an accurate estimate of sound amplitude and frequency over a relatively short period of time but requires that close attention be paid to window length. For example, while a 1.5-ms window is long enough to allow for an accurate estimate of sound frequency above 2 kHz (see Sec. III), estimates of AM and FM amplitude vary with (1) modulation index, (2) modulation frequency, and (3) fundamental frequency (Fig. 3, FM index=FM excursion/FM frequency; AM index=AM amplitude/carrier amplitude). These methodological biases do not produce the trends or the correlations that occur within and between recorded calls and, in contrast, are likely to weaken these trends and correlations. For example, while modulation amplitude decreases with modulation frequency due to the use of a sliding window [Figs. 3(a) and (d)], the reverse trend occurs in recorded calls. Similarly, estimates of modulation amplitude decrease as modulation index increases [Figs. 3(c) and (f)] and this bias is expected to dampen and not strengthen trends. Relatively clear trends and correlations exist across recorded calls without compensating for these biases and thus measurements of AM and FM amplitude are presented without compensation unless otherwise stated. All measurements were obtained using Igor Pro (Wavemetrics, Inc.).

III. RESULTS

A. Time-series measurements

Eastern towhee calls are highly variable in acoustic structure (Nelson, 2000). For example, call (a) in Fig. 4 has a relatively low bandwidth and low overall amplitude, while calls (b) and (c) have greater amplitude and bandwidth. Calls that span a large bandwidth and include fundamental frequencies above and below ~3.5 kHz are especially interesting since fine amplitude and frequency modulations often have different amplitudes, frequencies, and phase relationships to each side of ~3.5 kHz [Fig. 4(c); see below]. Measurements that vary over time (Fig. 4) are difficult to summarize because calls vary in overall duration (Nelson, 2000). As a consequence, measurements obtained directly from time-amplitude waveforms are not summarized.

B. Coarse AM and FM

Calls are summarized as a function of fundamental frequency (coarse FM) and Fig. 5(a) illustrates how measurements were averaged within 50-Hz bins. Residuals from best-fit operations are small (<~30 Hz) in comparison with the overall bandwidth of coarse FM [~1–2 kHz; Fig. 5(d)]. Small residual values demonstrate that coarse FM is well characterized by a sine function. Nevertheless, residuals from this analysis tend to vary predictably with fundamental frequency [e.g., Fig. 5(a)] and independent sine functions fit to sound frequencies to each side of ~3.5 kHz typically produce far smaller residuals (<5 Hz vs. <30 Hz). In particular, positive residuals near ~3 and ~4 kHz and negative residuals near ~2.5 and ~3.5 kHz decrease substantially when curve fit operations are limited to fundamental frequencies to each side of 3.5 kHz.

Sine equation phase estimates obtained from curve fit operations are summarized in Fig. 5(f) and sine equation frequency estimates are summarized in Fig. 5(g). There is a significant and relatively strong negative correlation between frequency and phase measurements [Fig. 5(e); $r=-0.68$, $F=921$, $N=1067$, $p<0.001$] suggesting that these two variables may either be controlled by the same physical forces or by forces that are coupled during phonation.

Reasonably accurate fits to coarse AM were obtained using a Gaussian function as illustrated by relatively small residuals from best-fit operations [mean±s.d.; $A=0.44\pm0.59$, width$=0.5\pm0.49$, and $t_0=0.59\pm0.22$; Figs. 6(a) and (b)]. Nevertheless, smaller residuals were obtained when call

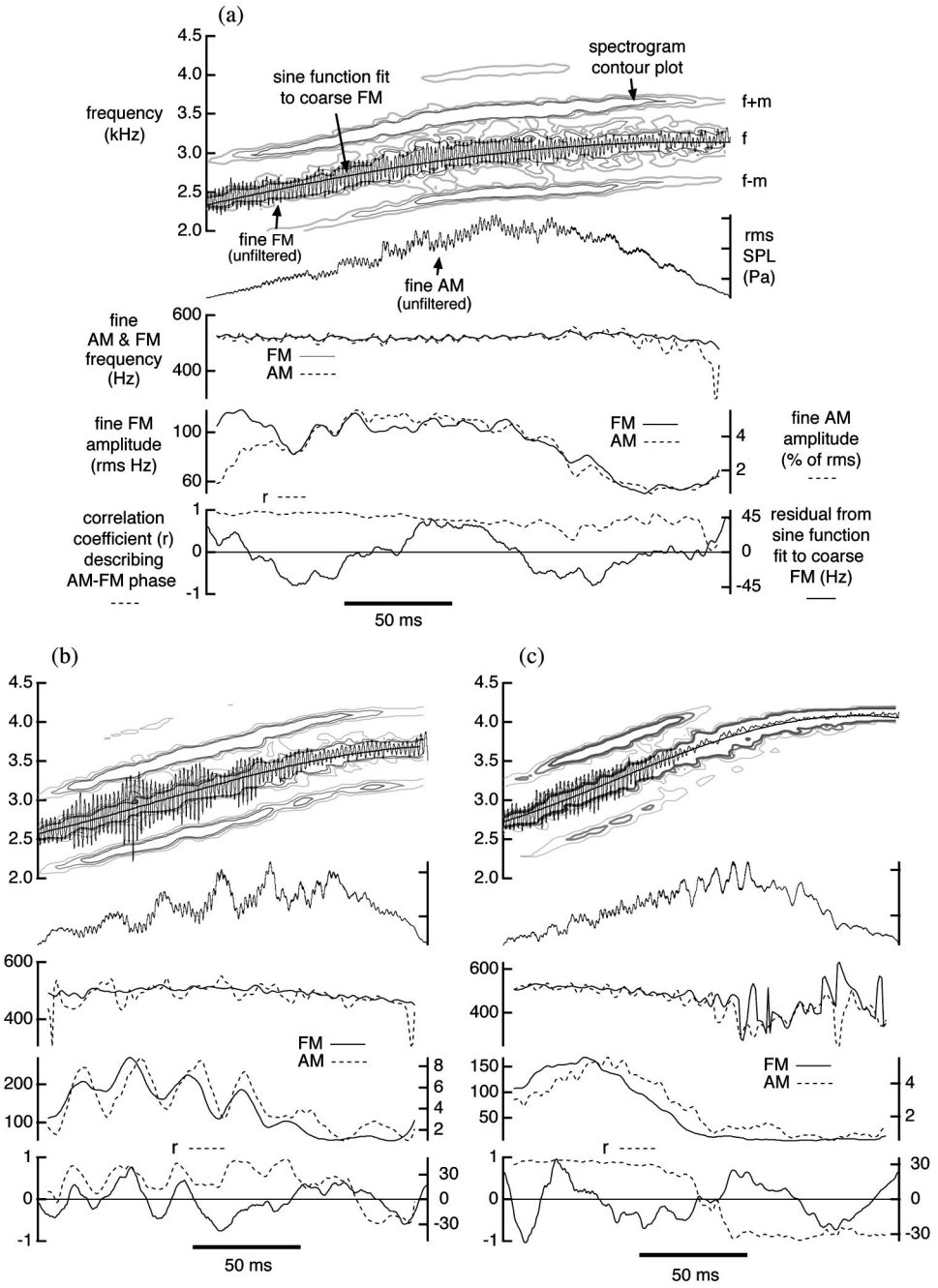

FIG. 4. Time-series data obtained from vocalizations produced by three individuals [(a), (b), and (c)]. The top graph in each panel includes a time-frequency spectrogram, displayed as a contour plot, overlaid with an unfiltered fine FM waveform and sine function fit to coarse FM. The second graph in each panel displays an unfiltered fine AM waveform. The third graph in each panel displays frequency of fine AM and frequency of fine FM as a function of time. The fourth graph displays amplitude of fine FM (Hz) and amplitude of fine AM (calculated as a percent of rms SPL) over the same time period. The last graph in each panel displays residuals that were obtained from the sine function that was fit to coarse FM (solid line; right axis) as well as the strength of the phase relationship (r) between fine AM and fine FM (dashed line; left axis).

onset and offset ramps were fit using independent sine functions [Figs. 6(c) and (e)]. There is a significant and moderately strong negative correlation between onset phase and onset frequency [Fig. 6(d); $r=-0.5$, $F=343$, $N=1067$, $p=0.003$]. Sine equation phase estimates are not summarized for offset ramps because Gaussian functions were used to determine the center (t_0) of each rms SPL waveform and thus the phase of each sinusoidal offset ramp. Onset durations are typically longer than offset durations and AM offset frequencies [Fig. 6(e)] tend to be higher than AM onset frequencies as a result.

Residuals from sine functions fit to both coarse AM and FM onset ramps tend to vary together over time and irregular (nonsinusoidal) changes in both fundamental frequency and rms amplitude often track each other over time. Such changes demonstrate the AM and FM are likely to be produced by the same physical forces. Nevertheless, coarse AM and coarse FM functions do not correlate well across calls because AM and FM functions tend to define different modulation frequencies over different periods of time (AM phase vs. FM phase, $r=0.007$, $n=1067$; AM frequency vs. FM frequency, $r=0.2$, $n=1067$).

C. Fine AM and FM

Fine AM and fine FM should vary together and have a strong positive or negative phase relationship if the physical forces that function to produce these modulations are coupled (integrated) during phonation. The phase relationship between fine AM and fine FM decreases from positive to negative (from in phase to out of phase) rapidly between 3 and 4 kHz and the phase relationship is significantly higher

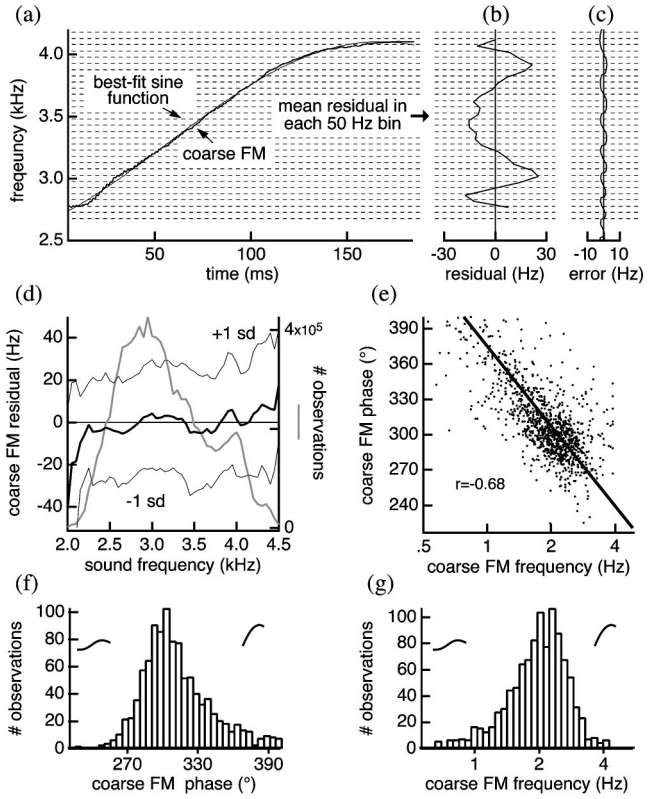

FIG. 5. Coarse frequency modulations are fit well by a sine function. (a) Illustration of how time-series data were averaged within 50-Hz bins. In this example, residuals (b) were calculated as the average difference between coarse FM and the sine function fit to the same waveform. (c) Error that might occur due to the use of a 1.5-ms autocorrelation window (see text). (d) Mean residuals within 50-Hz bins calculated as the difference between each coarse FM waveform the sine function that was fit to each waveform. Error lines depict one standard deviation and the single gray line shows the number of average values obtain within each 50-Hz bin. (e) Scatter plot showing the correlation between sine function frequency [f in Eq. (2)] and phase values [φ in Eq. (2)] derived from best-fit sine functions. (f) Distribution of sine function phase values derived from best-fit sine functions. (g) Distribution of sine function frequency values derived from the same best-fit sine functions. Inset in panels (f) and (g) are coarse FM functions produced with relatively extreme frequency and phase values.

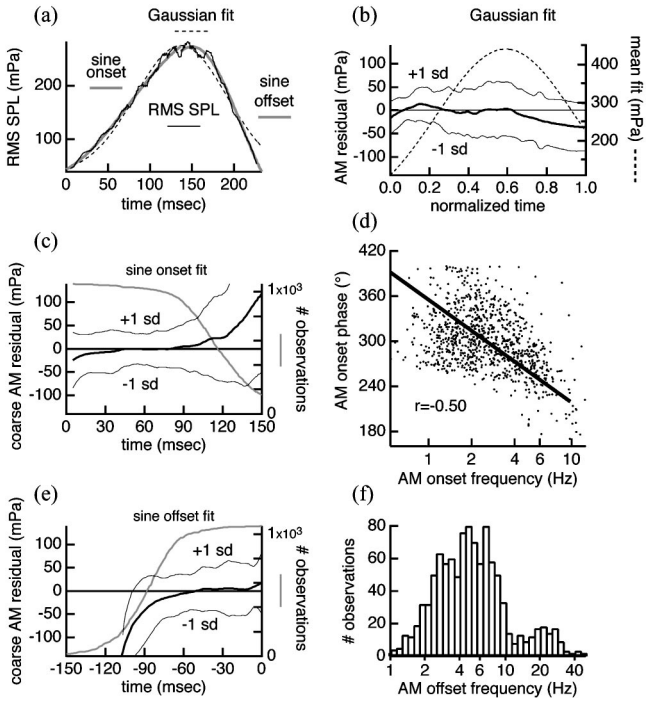

FIG. 6. Coarse amplitude modulations are fit reasonably well by a Gaussian function, however, onset and offset ramps are better fit using sine functions. (a) Schematic illustration of how Gaussian and sinusoidal functions were fit to coarse AM waveforms. (b) Average residuals and Gaussian function obtained in curve fit operations used to describe coarse AM. (c) Mean residuals obtained in best-fit operations used to describe call onsets ramps using a sine function. (d) Relationship between AM onset phase [φ in Eq. (2)] and onset frequency [f in Eq. (2)] estimates obtained across calls. (e) Mean residuals obtained in best-fit sine function operations used to describe call offsets ramps. (f) Distribution of frequency measurements obtained in best-fit sine function operations performed on call offset ramps. The thin lines in (b), (c), and (e) represent one standard deviation and the gray lines in (c) and (e) indicate the number of measurements obtained within each 10-ms window.

at 3.25 kHz than at 3.75 kHz [t-test, $p<0.001$, $n=1270$; Fig. 7(a)]. Measurements are not derived directly from time-series data. Nevertheless, phase estimates may not be independent and thus statistical comparisons drawn as a function of coarse FM frequency need to be viewed with caution.

Sidebands in time-frequency spectra decrease in magnitude above ~3.5 kHz [Figs. 7(b) and (c)] and an especially rapid decrease in sideband magnitude often occurs in the first upper sideband ($f+m$) near ~3.5 kHz [Fig. 7(b)]. The first lower sideband ($f-m$) does not decrease in magnitude as rapidly as the first upper sideband [Fig. 7(c)]. These differences suggest that large changes in upper sideband ($f+m$) magnitude may occur, in part, as a result of phase changes that occur between AM and FM signals as the fundamental frequency in each call (f) approaches and exceeds ~3.5 kHz [Figs. 7(d) and (e)].

Decreases in the phase relationship between AM and FM often occur rapidly in individual calls and this decrease often corresponds with a rapid (~2 ms) decrease in both the frequency and amplitude of AM near ~3.5 kHz [e.g., Fig. 4(c)]. An abrupt change in AM-FM phase might be expected if towhees produce fundamental frequencies to each side of ~3.5 kHz using different sides of their bipartite syrinx or if modulations correlate positively only when calls are increasing in amplitude (see below).

Frequency and amplitude of fine AM and FM vary as a function of fundamental frequency (Fig. 8). For example, fine AM (rms mean=497 Hz) and fine FM (rms mean=456 Hz) both increase in frequency as a function of fundamental frequency (coarse FM) between 2 and 3 kHz. Both frequencies then decrease above ~3 kHz and frequency measurements are significantly higher at 3.25 kHz than at 3.75 kHz [t-test, $p<0.001$, $n=1270$; Figs. 8(a) and (b)]. Fine AM (rms mean=3.1%) and fine FM (frequency excursion; rms mean=59 Hz) also both increase in amplitude as a function of fundamental frequency between 2 and 3 kHz. Both amplitudes then decrease above ~3 kHz and amplitude measurements are significantly higher at 3.25 kHz than at 3.75 kHz [t-test, $p<0.001$, $n=1270$; Figs. 8(c) and (d)]. Modulation measurements may not be independent and thus statistical comparisons that are drawn as a function of fundamental frequency should again be viewed with caution. Nevertheless, decreases in both fine AM and FM amplitude are expected to contribute to the rapid decrease in sideband mag-

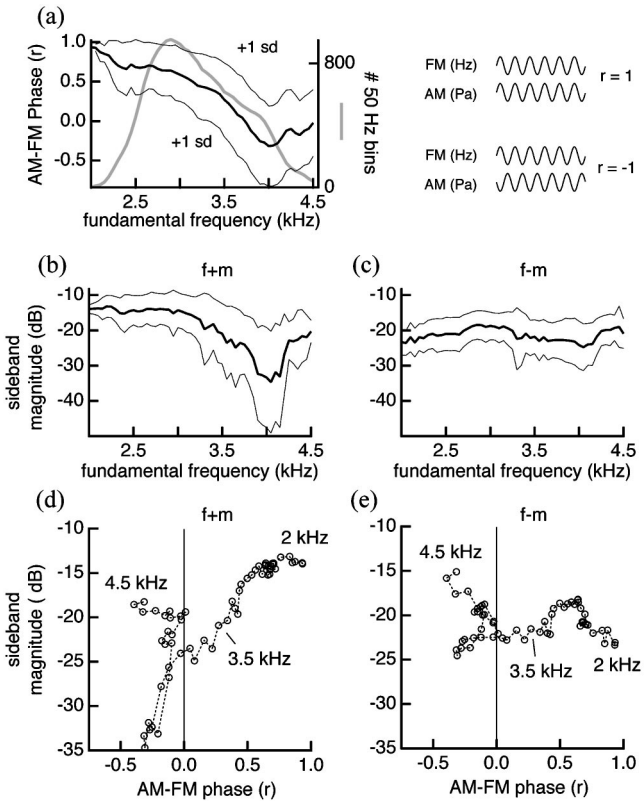

FIG. 7. Upper and lower sideband magnitudes appear to be determined, in part, by the phase relationships that exist between fine amplitude and frequency modulations. (a) Average phase relationship (r) between fine AM and fine FM as a function of fundamental frequency. (b) Average magnitude of the first upper sideband ($f+m$) as a function of fundamental frequency. (c) Average magnitude of the first lower sideband ($f-m$) as a function of fundamental frequency. (d) Relationship between phase measurements presented in (a) and upper sideband magnitudes displayed in (b). (e) Relationship between phase measurements presented in (a) and lower sideband magnitudes displayed in (c). All averages are calculated within 50-Hz bins. Error lines depict one standard deviation and the gray line in (a) illustrates the number of average values obtain within each 50-Hz bin.

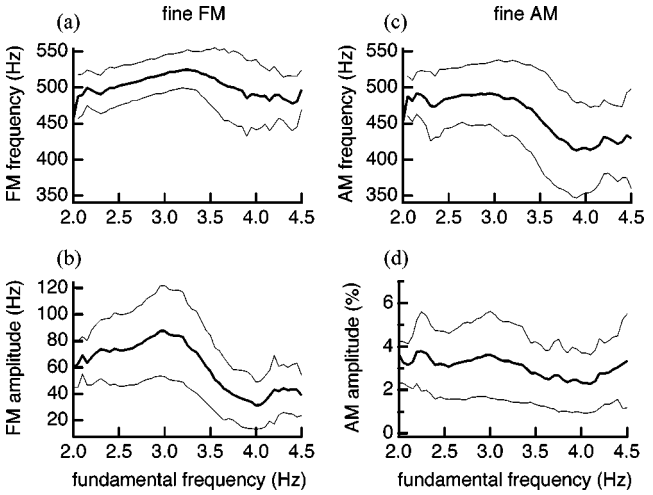

FIG. 8. Fine AM and FM increase in amplitude and frequency as fundamental frequency increases below ~3 kHz but then decrease above ~3.5 kHz. (a) Average frequency of fine FM as a function of fundamental frequency (f, coarse FM). (b) Average amplitude (frequency excursion) of fine FM as a function of f. (c) Average frequency of fine AM as a function of f. (d) Average amplitude of fine AM as a function of f. Averages were calculated within 50-Hz bins derived from coarse FM measurements. Error lines represent one standard deviation. Numbers of measurements obtained within each 50-Hz bin are the same as in Fig. 7(a).

nitude that occurs near ~3.5 kHz [Fig. 7(b)].

Calls increase and then decrease in amplitude (Fig. 6) and positive increases in amplitude tend to occur over relatively low sound frequencies as a result. For example, Gaussian functions fit to amplitude envelopes tend to increase in amplitude over relatively low fundamental frequencies but decrease in amplitude over higher frequencies [Fig. 9(a)]. These factors make it difficult to evaluate whether differences in fine AM and FM (Fig. 8) correlate best with changes in fundamental frequency or amplitude. For example, amplitude of fine FM is not only significantly correlated with fundamental frequency [$r=-0.38$, $N=212\,721$, $p<0.001$, Fig. 8(b)] but is also significantly correlated with the rate to which amplitude is changing within each Gaussian function [ΔdB/5 ms; $r=0.37$, $N=212\,721$, $p<0.001$, Fig. 9(b)]. The same correlation with amplitude (ΔdB/5 ms) is weaker when calculated using coarse amplitude envelopes due to small fluctuations in amplitude that can be attributed to several factors (Fig. 4; $r=0.20$, $N=212\,721$, $p<0.001$). Nevertheless, the forces that regulate amplitude are likely to be the same forces that regulate fundamental frequency (e.g., Laje *et al.*, 2002). As a consequence, it may not be surprising that fundamental frequency and changes in amplitude both correlate with fine modulation amplitude and frequency.

If fine AM and FM are both produced by the same physical forces, or by forces that are coupled (integrated) during phonation, then similar modulation frequencies should be observed whenever there is a strong phase relationship between fine AM and FM (see above). A positive correlation exists between frequency of fine AM and frequency of fine FM [$r=0.31$, $n=212\,721$; Fig. 10(a)]. Similarly, a positive correlation exits between amplitude of fine AM and amplitude (frequency excursion) of fine FM [$r=0.63$, $n=212\,721$; Fig. 10(b)]. All correlations are highly significant ($p<0.01$) and correlations become stronger as the phase relationship between AM and FM increases [Figs. 10(c) and (d)]. For example, the correlation coefficient (r) between frequency of fine AM and frequency of fine FM increased from 0.31 to 0.83 ($n=69\,538$) when measurements were limited to those obtained when the correlation coefficient describing the phase relationship between AM and FM was greater than 0.75. Similarly, the same correlation coefficient between AM and FM decreased from 0.31 to 0.17 (n=54 667) when measurements were limited to those obtained when correlation coefficients (r) describing the same phase relationship were negative [Figs. 10(e) and (f)]. A weak but distinct function (slope) appears to define this correlation when AM and FM are out of phase with one another [$r<0$; Figs. 10(e) and (f)].

Different modulation frequencies and phases are often observed to each side of ~3.5 kHz (Figs. 7 and 8) and thus similar differences in correlation coefficients should occur as a function of fundamental frequency. These results are not illustrated, however, plots produced from measurements obtained over different sound frequency ranges resemble those shown in Fig. 10. For example, figures produced using all

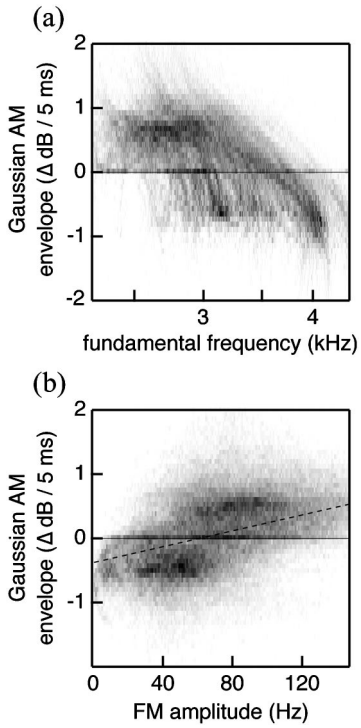

FIG. 9. Differences in modulation amplitude and frequency (Fig. 8) might also be attributed to increases and decreases in call amplitude (Fig. 6). (a) Gaussian functions fit to amplitude envelopes tend to increase in amplitude (ΔdB/5 ms) over relatively low fundamental frequencies ($<\sim 3$ kHz) but decrease in amplitude over higher sound frequencies ($N=212\,721$). (b) Correlation between amplitude of fine FM and the rate with which Gaussian envelopes increase or decrease in amplitude (ΔdB/5 ms; $r=0.37$, $N=212\,721$, $p<0.001$). Individual points are summed within logarithmically or linearly spaced bins and observations within each bin are indicated by level of gray.

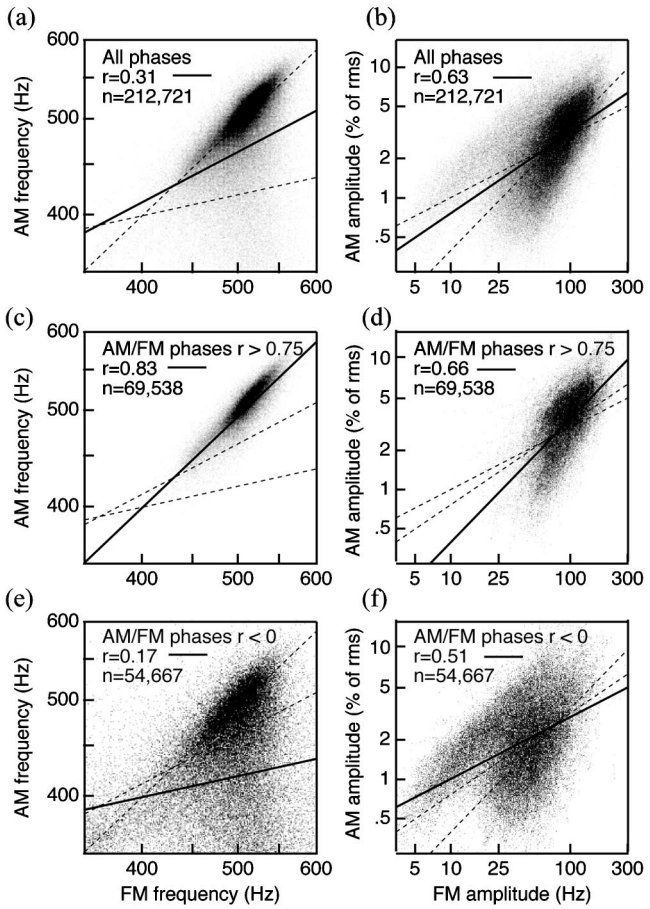

FIG. 10. Fine AM and fine FM amplitude and frequency measurements are most strongly correlated when the phase relationship between fine AM and FM is strong. (a) Frequency of fine AM and frequency of fine FM correlate reasonably well across all calls ($r=0.31$). (b) Similarly, amplitude of fine AM and amplitude of fine FM correlate well across all calls ($r=0.63$). Correlations become strong when fine AM and fine FM waveforms are in phase with each other [phase $r>0.75$; (c) and (d)]. Correlations become weaker when there is either no clear phase relationship between fine AM and fine FM (phase $r\approx 0$) or when these waveforms are out of phase with each other [phase $r<0$; (e) and (f)]. Individual points are summed within 500 logarithmically spaced bins and the number of observations within each bin is indicated by level of gray.

fundamental frequencies resemble plots 10(a) (frequency: $r=0.38$, $n=24\,511$) and 10(b) (amplitude: $r=0.58$, $n=24\,511$), figures produced using fundamental frequencies below 3 kHz resemble plots 10(c) (frequency: $r=0.48$, $n=9204$) and 10(d) (amplitude: $r=0.61$, $n=9204$), and figures produced using fundamental frequencies above 3.5 kHz resemble plots 10(e) (frequency: $r=0.30$, $n=6785$) and 10(f) (amplitude: $r=0.50$, $n=6785$).

Estimates of fine AM and FM amplitude are biased when using a sliding window (Fig. 3) and thus correlations involving measurements of modulation amplitude [Figs. 10(b), (d), and (e)] are expected to be weak in comparison with correlations involving frequency measurements [Figs. 10(a), (c), and (d)]. Regression lines that are fit to measurements of modulation amplitude [Figs. 10(b), (d), and (e)] should also be viewed with caution since the slopes of these lines may be due, in part, to these same biases.

D. Contributions to sidebands from AM and FM

Sidebands in time-frequency spectrograms often increase in width or diverge into distinct spectral peaks whenever fine AM and FM diverge in modulation frequency. These changes demonstrate that AM and FM both contribute to sideband structure but are difficult to quantify due to time-frequency tradeoffs (Beecher, 1988). Modulations in towhee calls are sinusoidal and, as a consequence, contributions to sidebands that are due to both AM and FM can be approximated using estimates of modulation indices derived from time-series data (Fig. 4). An average raw FM index of 0.21 ± 0.06 (mean$\pm$sd; $N=1067$) was obtained over the duration of each call and an adjusted FM index of 0.26 was obtained after compensating for amplitude losses that are due to methodology [i.e., use of a sliding window (Fig. 3) and calculations of rms amplitude versus peak-to-peak amplitude]. Sidebands predicted using an FM index of 0.26 and the Bessel function have a relatively narrow bandwidth (Fig. 11; $f\pm m=-17.8$ dB, $f\pm 2m=-41.5$ dB, $f\pm 3m=-68.8$ dB).

To allow for comparisons with frequency modulations, AM indices were calculated from time intervals in recorded calls where FM indices equaled 0.21 ± 0.005 (mean$\pm$sd; 6320 indices from 878 calls). An average raw AM index of 0.056 ± 0.002 was obtained under these conditions and an adjusted AM index of 0.21 was obtained after compensating for amplitude losses that are due to methodology (see

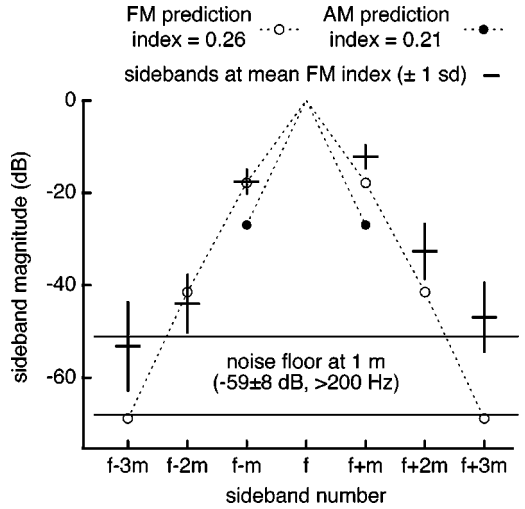

FIG. 11. Upper sideband spectral components produced by fine AM and FM appear to combine in an additive manner over relatively low sound frequencies (<~3.5 kHz) but may not contribute similarly to lower sidebands (see Fig. 7). Horizontal lines with error bars (±1 sd) show mean sideband magnitudes at times in calls where an average adjusted FM index of 0.26±0.005 could be found. Upper sidebands have greater magnitude than predicted using an adjusted FM index of 0.26 (open circles; 0.21 raw FM index) or adjusted AM index of 0.21 (solid circles; 0.056 raw AM index; 6320 indices from 878 calls). Lower sidebands do not have greater magnitude than predicted using an adjusted FM index of 0.26 (open circles).

above). Only two sidebands were predicted using an AM index of 0.21 (Fig. 11; $f \pm m$; −27 dB) since it was assumed that amplitude modulations are sinusoidal.

Sideband magnitude varies as a function of fundamental frequency (Fig. 7) and, on average, each upper sideband has significantly greater magnitude than each corresponding lower sideband (paired *t*-tests, $p \ll 0.001$, N=212 520 from 1067 calls; $f+m=-18.3\pm9.5$ vs. $f-m=-20.7\pm5.3$, $f+2m=-41.0\pm11.7$ vs. $f-2m=-45.1\pm7.2$, $f+3m=-53.1\pm10.6$ vs. $f-3m=-54.7\pm10.4$, mean±sd re: peak magnitude, *f*). To estimate the relative contributions to sidebands from AM and FM, sideband magnitudes were extracted from time-frequency spectrograms where raw FM indices equaled 0.21±0.005 (6320 spectra from 878 calls). Each upper sideband under these conditions again had significantly greater magnitude than each corresponding lower sideband (Fig. 11; paired *t*-tests, $p \ll 0.001$, $N=6320$; $f+m=-12.2\pm2.7$ vs. $f-m=-17.6\pm2.8$, $f+2m=-32.7\pm6.1$ vs. $f-2m=-44.0\pm6.4$, $f+3m=-46.9\pm7.7$ vs. $-3m=-53.2\pm9.8$, mean±sd re: peak amplitude; paired *t*-test, $p \ll 0.001$, $N=6320$). Upper sidebands in spectra extracted from calls under these conditions had greater magnitude than predicted using AM and FM indices (Fig. 11). These differences may exist if modulation indices were underestimated or if spectral components corresponding with upper sidebands in calls, arising from both AM and FM, combine in an additive manner near ~3 kHz where adjusted FM indices of ~0.26 commonly occur (Fig. 7). Lower sidebands in spectra extracted from calls under these same conditions do not have greater magnitude than predicted using an FM index of 0.26 (Fig. 11). Lower sidebands also vary relatively little in magnitude with AM-FM phase (Fig. 7) and thus do not appear to be as sensitive to AM-FM phase as upper sidebands.

IV. DISCUSSION

A. Coarse modulation functions

It is important to understand the control parameters that are required to generate vocalizations (Suthers and Margoliash, 2002) and it is, therefore, interesting that complex birdsong can be modeled using only a few vocal control parameters (Laje *et al.*, 2002; Mindlin *et al.*, 2003; Elemans *et al.*, 2003). Birdsong is often highly stereotyped and, as a result, vocal control parameters are not likely to be described well using continuous functions. Instead, control parameters might best be viewed as discontinuous functions and discontinuities might, in practice, define combinations of parameter values that are rarely observed during phonation. For example, in a relatively extreme case, if a given species only produces upward frequency sweeps in its repertoire, then combinations of parameter values that are required for producing upward frequency sweeps might be physically ''disconnected'' from stable parameter values that are required for producing downward frequency sweeps.

Dynamic systems are rarely stable over a broad range of conditions and thus correlations between modulation functions [Figs. 5(c), 6(d), and 9 (Nelson, 2000)] might be produced by stable interactions that occur between vocal control parameters. Constraints on vocal production mechanisms have been described previously (e.g., Podos, 2001; Zollinger and Suthers, 2001) and constraints are expected to impose limitations on available parameter values. Nevertheless, different combinations of parameter values may not have equal stability within a dynamic system and, thus, relatively unstable combinations of parameter values may have implications similar to those proposed for constraints. The difference is that a constraint defines what subjects cannot physically accomplish while variation in stability describes what subjects normally accomplish as a result of interactions between several dynamic physical forces.

Towhee calls are highly variable in acoustic structure. In addition, several discrete measurements obtained from time-frequency spectrograms correlate well with source-SPL and towhees appear to use at least one of these variables when estimating source-SPL (Nelson, 2000). Nevertheless, vocalizations are dynamic by nature and it remains unclear whether towhees pay attention to these variables (e.g., lowest frequency, bandwidth, etc.) or the dynamics that are summarized by these variables. Coarse modulation frequency decreases with modulation phase (Fig. 5) and thus subjects may, for example, more likely pay attention to modulation frequency or phase when estimating source-SPL. This hypothesis has not yet been tested, however lowest frequency measurements and other variables associated with coarse FM functions correlate well with source-SPL. Towhees reliably estimate source-SPL after hearing only the first, low frequency (<~3.5 kHz) half of synthetic call stimuli (Nelson, 2002) and these results suggest that subjects either (1) assess coarse modulation frequency and phase or (2) somehow resolve discrete variables when estimating source-SPL.

B. Fine modulations

Fine amplitude and frequency modulations in towhee calls are strong, coherent, and sinusoidal. Fine amplitude and frequency modulations in human speech are often described as ''shimmer'' and ''jitter'' and these two measurements are often associated with laryngeal pathologies (e.g., Hansen *et al.*, 1998; Jiang *et al.*, 2003; Vieira *et al.*, 2002). Unlike measurements of shimmer and jitter in speech, however, modulations in towhee calls do not correlate well with fundamental frequency (do not occur on a period by period basis). Instead, modulation frequency remains relatively constant even as fundamental frequency varies between ~2 and 4.5 kHz (i.e., modulation periods are at least three times longer than fundamental periods and are sometimes ten times longer).

AM can be produced whenever there is a direct or indirect (multiplicative) interaction between two signals (e.g., Nowicki and Capranica, 1986b). Unlike AM, however, FM can be produced only when there is a direct integrative interaction between two signals. It is therefore surprising that towhees are able to vary fundamental frequency (~2 to 4.5 kHz) and, at the same time, generate a coherent modulating signal that does not vary directly with fundamental frequency.

Physical models that might account for the modulation patterns that exist in towhee calls have yet to be described. Towhees, like other songbirds, have a duplex syrinx and are able to produce two independent sounds simultaneously in their vocalizations (Greenwalt, 1968; Stein, 1968; Suthers, 1990). Nowicki and Capranica (1986b) proposed that acoustic interactions between these two sounds might sometimes produce AM. Nevertheless, acoustic interactions are not expected to produce FM. Physical mechanisms for producing fine AM have subsequently been proposed for mammals (e.g., Neubauer *et al.*, 2001; Brown *et al.*, 2003) and budgerigars, *Melopsittacus undulates* (Banta Lavenex, 1999). Nevertheless, neither of these models incorporates an explicit mechanism for generating FM and neither model has sought to account for how two independent sinusoidal FM signals might integrate to produce a single vocalization with coherent modulations.

Rapid oscillations (>400 Hz) in subbronchial air pressure (pressure below the medial tympaniform membranes, MTM) might generate the fine frequency and amplitude modulation patterns that are evident in towhee calls (Fletcher, 1988; Laje *et al.*, 2002). However, if the medial labia (ML) and lateral labia (LL) are the primary sound generating structures in the songbird syrinx (Goller and Larsen, 2002, 1997), then rapid changes in sublabial air pressure or labial elasticity might also be responsible for producing modulations in vocalizations (as well as modulations in air pressure measurements obtained below the MTM). The MTM are expected to vibrate in a sinusoidal manner as long as they do not contact the opposite wall of each bronchus (Fletcher, 1988) and are ideally positioned to produce fluctuations in both sublabial air pressure and labial tension (Fee, 2002). Vibrations of the MTM might therefore also potentially generate the frequency and amplitude modulation patterns that are evident in towhee calls. Fee (2002) demonstrated that there is an interaction (integration) between the MTM and ML, however, it remains unclear whether vibrations of the MTM might produce the fine sinusoidal modulations that are evident in towhee calls or whether the MTM might simply vibrate together with the ML to produce a stronger fundamental frequency.

Other songbird species such as Carolina chickadees, *Poecile carolinensis*, and zebra finches, *Taeniopygia guttata*, also produce fine frequency modulations in their vocalizations in addition to fine amplitude modulations (not illustrated). These modulations do not necessarily correlate with fundamental frequencies in these vocalizations and, as a consequence, results presented for the eastern towhee may have relatively broad implications. For example, amplitude modulations in chickadee ''Dee'' syllables are believed to carry important information (e.g., Nowicki, 1989; Freeberg *et al.*, 2003). Furthermore, zebra finches and birds in general appear to resolve fine temporal patterns surprisingly well and may often be able to resolve fine envelope patterns (modulations) with periods as short as 1–2 ms (Dooling *et al.*, 2002).

Pigeons, *Columba liva*, and European starlings, *Sturnus vulgaris*, are able to discriminate low levels of sinusoidal FM (Bräucker and Schwartzkoff, 1986; Langemann and Klump, 1992). High modulation rates are expected to produce spectral cues that span more than one analysis channel (i.e., critical band), and thus spectral cues may help to explain how starlings are able to discriminate low levels (<15 Hz) of high frequency FM (640 Hz, Langemann and Klump, 1992). Similar experiments have yet to be conducted with towhees. Nevertheless, both humans and starlings are able to discriminate smaller frequency limens when frequency changes are imposed upon a low frequency carrier (fundamental). Critical bands generally increase in width as sound frequency increases (e.g., Langemann *et al.*, 1995) and FM discrimination may therefore help to explain why towhees tend to modulate sound frequencies below ~3.5 kHz more strongly than higher sound frequencies.

C. Sound frequency channels

Towhees use SPL as an auditory distance cue when played call stimuli produced with sound frequencies below ~3.5 kHz but use a cue that has yet to be identified when played call frequencies above ~3.5 kHz (Nelson, 2002). Sound frequencies below ~3.5 kHz also attenuate more reliably over distance in comparison with higher sound frequencies, suggesting that towhees might use a duplex sound localization ''strategy'' as a mechanism for improving communication in their natural environment (Nelson, 2003). Given these results, it is interesting that fine AM and FM both decrease in frequency and amplitude above ~3.5 kHz and that the phase relationship between fine AM and FM becomes weak near and above ~3.5 kHz.

Towhees may generate sound frequencies to each side of ~3.5 kHz using separate sides of their bipartite syrinx, as has been observed in other songbird species (e.g., Suthers, 1999), and differences in fine modulation patterns (e.g., phase relationships between fine AM and FM) might exist simply because the left and right sides of the syrinx behave differently.

More specifically, distinct forces operating within the left and right sides of the syrinx might respond differently to a constant driving force (e.g., air pressure), or each side of the syrinx (i.e., each bronchus) might experience a distinct driving force. In fact, residuals from sine functions fit to coarse FM waveforms vary predictably as a function of fundamental frequency and smaller residuals can nearly always be obtained by fitting two separate sine functions to frequencies above or below ~3.5 kHz. As an alternative, the MTM may vibrate more strongly or coherently when amplitude is increasing (i.e., when sublabial air pressure is increasing).

Proximate explanations for these data will require additional investigations into vocal production mechanisms. Nevertheless, sound frequencies to each side of ~3.5 kHz appear to be processed differently by the auditory system (see above) and thus a functional explanation for why subjects often modulate sound frequencies below ~3.5 kHz more strongly than higher sound frequencies in their calls seems to be warranted. Furthermore, it is interesting that towhees should use SPL as a distance cue in the first place since attenuation over distance is often unpredictable (although see Nelson, 2003) and because it has been suggested that some species may vary source-SPL unpredictably (e.g., Brumm and Todt, 2002; Cynx *et al.*, 1998; Manabe *et al.*, 1998), using a compensatory mechanism where subjects are presumably able to counter increases or decreases in subsyringeal air pressure (and thus source-SPL) by decreasing or increasing tension on the ML and LL.

Towhees may vary the physical forces that are required for vocal production by coordinating several distinct neural pathways and individuals may call similarly by generating similar motor control programs (Suthers and Margoliash, 2002). Alternatively, individuals might call similarly if only certain combinations of physical forces are dynamically stable within the syrinx and if extraordinary supplemental forces are required to overcome these stable combinations of forces. These two hypotheses are unlikely to be mutually exclusive and thus it remains interesting that towhees do not normally vary source-SPL unpredictably when calling (Nelson, 2000).

One possible explanation for why towhees do not normally vary source-SPL unpredictably may be that towhees are physically unable to simultaneously produce both fine modulations in vocalizations and the supplementary forces that are required to overcome the stable dynamic forces that normally function to generate highly stereotyped coarse modulation patterns. For example, if rapid changes in sublabial air pressure or labial elasticity function to generate fine modulations, then correlative relationships between source-SPL and spectral and temporal dynamics (fine modulations) might be mediated by interactions between the MTM and the ML. Alternatively, if rapid changes in subbronchial air pressure function to generate fine modulations, then these same relationships might be mediated by the (hypothetical) forces that function to vary subbronchial pressure.

That a close relationship between source-SPL and spectro-temporal patterns might be mediated by stable dynamics within the syrinx remains hypothetical. Nevertheless, a stable dynamic relationship between coarse and fine modulation patterns might help to explain why towhees tend to modulate fundamental frequencies below ~3.5 kHz more strongly than higher fundamental frequencies and pay attention to sound frequencies below ~3.5 kHz when using SPL as a distance cue (Nelson, 2002).

Location is often disassociated from other forms of information that birds might convey when vocalizing (e.g., individual identity, signaler ''quality,'' etc.). Nevertheless, this disassociation likely occurs because researchers often choose to simplify their experiments and does not exclude the possibility that towhees might convey additional information within these same two sound frequency channels. For example, towhees do not simply judge incident-SPL but appear to also estimate source-SPL and thus may perceive a variable comparable to loudness or vocal effort in addition to, or in spite of, distance (e.g., Zahorik and Wightman, 2001). Humans appear to use low frequency cues when judging vocal effort (e.g., Eriksson and Traunmuller, 2002) and thus it may not be surprising that towhees also pay attention to relatively low sound frequencies when judging source-SPL.

ACKNOWLEDGMENTS

I thank Roderick Suthers, Troy Smith, Sumitrajit Dhar, Ellen Ketterson, William Rowland, and Erica Goss for reading earlier versions of the manuscript and Gabriel Beckers for numerous discussions. Support was provided by NSF Grant No. BIR-9413220 to the Center for the Integrative Study of Animal Behavior at Indiana University and by NIH Grant No. NS-29467 to R. Suthers. Archbold Biological Station provided access to research facilities.

Banta Lavenex, P. (**1999**). ''Vocal production mechanisms in the budgerigar (Melopsittacus undulatus): The presence and implications of amplitude modulation,'' J. Acoust. Soc. Am. **106**, 491–505.

Beecher, D. M. (**1988**). ''Spectrographic analysis of animal vocalizations: Implications of the 'uncertainty principle','' Bioacoustics **1**, 187–207.

Bräucker, R., and Schwartzkoff, J. (**1986**). ''Frequency discrimination in the pigeon (Columba liva),'' Naturwissenschaften **73**, 563–564.

Brown, C. H., Alipour, F., Berry, D. A., and Montequin, D. W. (**2003**). ''Laryngeal biomechanics and vocal communication in the squirrel monkey (Saimiri boliviensis),'' J. Acoust. Soc. Am. **113**, 2114–2126.

Brumm, H., and Todt, D. (**2002**). ''Noise-dependent song amplitude regulation in a territorial songbird,'' Anim. Behav. **63**, 891–897.

Cynx, J., Lewis, R., Tavel, B., and Tse, H. (**1998**). ''Amplitude regulation of vocalizations in noise by a songbird, *Taeniopygia guttata*,'' Anim. Behav. **56**, 107–113.

Dooling, R. J., Leek, M. R., Gleich, O., and Dent, M. L. (**2002**). ''Auditory temporal resolution in birds: Discrimination of harmonic complexes,'' J. Acoust. Soc. Am. **112**, 748–759.

Draganoiu, I. T., Nagle, L., and Kreutzer, M. (**2002**). ''Directional female preference for an exaggerated male trait in canary (Serinus canaria) song,'' Proc. R. Soc. London, Ser. B **269**, 2525–2531.

Elemans, C. P. H., Larsen, O. N., Hoffmann, M. R., and Van Leeuwen, J. L. (**2003**). ''Quantitative modelling of the biomechanics of the avian syrinx,'' Anim. Biol. **53**, 183–193.

Eriksson, A., and Traunmuller, H. (**2002**). ''Perception of vocal effort and distance from the speaker on the basis of vowel utterances,'' Percept. Psychophys. **64**, 131–139.

Fee, M. S. (**2002**). ''Measurement of the linear and nonlinear mechanical properties of the oscine syrinx: Implications for function,'' J. Comp. Physiol., A **188**, 829–839.

Fletcher, N. H. (**1988**). ''Bird song—a quantitative acoustic model,'' J. Theor. Biol. **135**, 455–481.

Freeberg, T. M., Lucas, J. R., and Clucas, B. (**2003**). ''Variation in chick-a-dee calls of a Carolina chickadee population, Poecile carolinensis: Identity and redundancy within note types,'' J. Acoust. Soc. Am. **113**, 2127–2136.

Gardner, T., Cecchi, G., Magnasco, M., Laje, R., and Mindlin, G. B. (**2001**). ''Simple motor gestures for birdsong,'' Phys. Rev. Lett. **87**, 208101.
Goller, F., and Larsen, O. N. (**1997**). ''A new mechanism of sound generation in songbirds,'' Proc. Natl. Acad. Sci. U.S.A. **94**, 14787–14791.
Goller, F., and Larsen, O. N. (**2002**). ''New perspectives on mechanisms of sound generation in songbirds,'' J. Comp. Physiol., A **188**, 841–850.
Greenewalt, C. H. (**1968**). *Bird song: Acoustics and Physiology* (Smithsonian Institution, Washington, DC).
Hansen, J. H. L., Gavidia-Ceballos, L., and Kaiser, J. F. (**1998**). ''A Nonlinear Operator-Based Speech Feature Analysis Method with Application to Vocal Fold Pathology Assessment,'' IEEE Trans. Biomed. Eng. **45**, 300–313.
Jiang, J. J., Zhang, Y., and Ford, C. N. (**2003**). ''Nonlinear dynamics of phonations in excised larynx experiments,'' J. Acoust. Soc. Am. **114**, 2198–2205.
Laje, R., Gardner, T. J., and Mindlin, G. B. (**2002**). ''Neuromuscular control of vocalizations in birdsong: A model,'' Phys. Rev. E **65**, 051921.
Langemann, U., and Klump, G. M. (**1992**). ''Frequency discrimination in the European Starling (Sturnis vulgaris): a comparison of different methods,'' Hear. Res. **63**, 43–51.
Langemann, U., Klump, G. M., and Dooling, R. (**1995**). ''Critical bands and critical-ratio bandwidth in the European starling,'' Hear. Res. **84**, 167–176.
Manabe, K., Sadr, E. I., and Dooling, R. J. (**1998**). ''Control of vocal intensity in budgerigars (*Melopsittacus undulatus*): differential reinforcement of vocal intensity and the Lombard effect,'' J. Acoust. Soc. Am. **103**, 1190–1198.
Mindlin, G. B., Gardner, T., Goller, F., and Suthers, R. A. (**2003**). ''Experimental support for a model of birdsong production,'' Phys. Rev. E **68**, 041908.
Nelson, B. S. (**2000**). ''Avian dependence on sound-pressure level as an auditory distance cue,'' Anim. Behav. **59**, 57–67.
Nelson, B. S. (**2002**). ''Duplex auditory distance assessment in a small passerine bird (Pipilo erythrophthalmus),'' Behav. Ecol. Sociobiol. **53**, 42–50.
Nelson, B. S. (**2003**). ''Reliability of sound attenuation in Florida scrub habitat and behavioral implications,'' J. Acoust. Soc. Am. **113**, 2901–2911.
Neubauer, J., Mergell, P., Eysholdt, U., and Herzel, H. (**2001**). ''Spatio-temporal analysis of irregular vocal fold oscillations: Biphonation due to desynchronization of spatial modes,'' J. Acoust. Soc. Am. **110**, 3179–3191.
Nowicki, S. (**1989**). ''Vocal plasticity in captive black-capped chikadees: the acoustic basis and rate of call convergence,'' Anim. Behav. **37**, 64–73.
Nowicki, S., and Capranica, R. R. (**1986a**). ''Bilateral syringeal coupling during phonoation of a songbird,'' J. Neurosci. **6**, 3595–3610.
Nowicki, S., and Capranica, R. R. (**1986b**). ''Bilateral syringeal interaction in vocal production of an oscine bird sound,'' Science **231**, 1297–1299.
Podos, J. (**2001**). ''Correlated evolution of morphology and vocal signal structure in Darwin's finches,'' Nature (London) **409**, 185–188.
Stein, R. C. (**1968**). ''Modulation in bird song,'' Auk **94**, 229–243.
Suthers, R. A. (**1990**). ''Contributions to birdsong from the left and right sides of the intact syrinx,'' Nature (London) **347**, 473–477.
Suthers, R. A. (1999). ''The motor basis of vocal performance in songbirds,'' in *The Design of Animal Communication*, edited by M. D. Hauser and M. Konishi (MIT, Cambridge), pp. 37–62
Suthers, R. A., and Margoliash, D. (**2002**). ''Motor control of birdsong,'' Curr. Opin. Neurobiol. **12**, 684–690.
Vieira, M. N., McInnes, F. R., and Mervyn, J. A. (**2002**). ''On the influence of laryngeal pathologies on acoustic and electroglottographic jitter measures,'' J. Acoust. Soc. Am. **111**, 1045–1055.
Zahorik, P., and Wightman, F. L. (**2001**). ''Loudness constancy with varying sound source distance,'' Nature (London) **4**, 78–83.
Zollinger, S., and Suthers, R. A. (2001). ''Motor strategies of a vocal mimic: Evidence for syringeal and respiratory motor constraints in birdsong production,'' in *Society for Neuroscience Abstracts*, p. 538.17.

Call recognition in the bullfrog, *Rana catesbeiana*: Generalization along the duration continuum[a)]

Andrea Megela Simmons[b)]
Departments of Psychology and Neuroscience, Brown University, Providence, Rhode Island 02912

(Received 1 July 2003; accepted for publication 25 November 2003)

Male bullfrogs emit multicroak, quasiharmonic advertisement calls that function in mate attraction and neighbor recognition. The degree of variability of acoustic features in these calls can influence perceptual decisions by conspecific receivers. Analysis of duration of individual croaks in spontaneous advertisement calls of a sample of males shows considerable intraindividual variability in this feature, even within short chorusing bouts. The influence of this intraindividual variability on behavior was examined in a series of evoked calling experiments. When presented with synthetic calls whose croak durations varied over the range of the natural variability in this feature, males responded similarly to intermediate and long duration croaks, but significantly less to short duration croaks. When presented with playbacks of calls with croak durations outside the natural range of variability, males again responded significantly less to shorter durations. The response gradient for duration is thus asymmetrical, with stimuli at the shorter end of the continuum evoking fewer responses than stimuli at the longer end. This asymmetry may be related to the biological demands of rejecting perception of heterospecific advertisement calls, and of mediating appropriate responses to conspecific aggressive calls. The shape of the response gradient for duration may reflect a process of stimulus generalization. © *2004 Acoustical Society of America.* [DOI: 10.1121/1.1643366]

PACS numbers: 43.80.Lb [WA] Pages: 1345–1355

I. INTRODUCTION

Male anurans of many species use a complex advertisement call to attract females for mating and to maintain territory boundaries against incursions from rival males. Spectral and temporal features of these calls can convey important biological information to receivers, including species identity, individual identity, size, physical condition, genetic fitness, and motivational state (Gerhardt and Huber, 2002). The analysis of physical acoustic features in advertisement calls and the ''meaning'' or salience of these features as derived from receiver response form the basis of much empirical and theoretical work in animal communication systems. Advertisement calls, in their role as conveying species identity, contain distinct, stereotyped species-specific attributes, with little variation between individuals within a species; conversely, other acoustic features in these calls may vary considerably between conspecifics. The variability, rather than stereotypy, of advertisement calls provides room for errors in species identification, leading to mismatings by females and subsequent declines in reproductive success (Wollerman and Wiley, 2002), as well as errors in individual identification, thus potentially disrupting stable male–male territorial interactions and the ability to discriminate neighbors from strangers (Davis, 1987; Bee and Gerhardt, 2001). Understanding the interplay of stereotyped and more variable features of advertisement calls in mediating both female choice and male/male interactions is of considerable interest in deciphering how animals make reproductive decisions in complex acoustic environments.

Gerhardt (1991) examined the variability and repeatability of advertisement calls within males of three different species of North American treefrogs, and categorized specific acoustic parameters of these calls as being either static (stereotyped) or dynamic (more variable), based on the consistency of these parameters in the calls of individuals. Gerhardt and Huber (2002) extended this analysis to a group of 24 species. Their summary shows that carrier frequency, dominant frequency, and pulse rate can be classified as static properties, varying little within individuals, while call rate is a dynamic property, showing considerable intraindividual variability. Interestingly, call duration could not be easily classified, exhibiting different trends across species. Gerhardt and Huber (2002) suggested that short duration signals (<500 ms) are less dynamic and thus may be processed differently than long duration signals (>500 ms). Why call duration cannot be so easily classified as other acoustic features leads to questions about the importance of this particular parameter in mediating call recognition.

Variability in advertisement calls leads to plasticity in response behavior contingent on signaling, and thus can affect communication both ultimately (over evolutionary time) and proximately. In choice experiments, female anurans show different kinds of preference functions for static and dynamic properties of advertisement calls (reviewed in Gerhardt and Huber, 2002). For example, female *Hyla versicolor* prefer pulse rates (a static property) close to that of the mean of calls of males in the population, but prefer call durations (a dynamic property in that species) longer than those observed in the vocalizations of conspecifics (Gerhardt, 1991). These preferences may reflect different degrees of selection (stabilizing or directional) on call properties over evolutionary time (Gerhardt and Huber, 2002). The preference of

[a)]A portion of this work was presented at the 143rd Meeting of the Acoustical Society of America, June 2002.
[b)]Electronic mail: andrea_simmons@brown.edu

some species of female anurans for stimuli with durations outside the range of natural variation in duration has been interpreted as a preference for ''supernormal'' or exaggerated stimuli (Ryan and Keddy-Hector, 1992) that ultimately contributes to the production of complex signals. Preference functions that are not tightly centered on the modal acoustic parameters in conspecific calls may also reflect a process of stimulus generalization in the perceptual representation of individuals (Malott and Malott, 1970), and this may also lead to permissiveness in call recognition (Ryan *et al.*, 2003).

Much of the literature on signal variation in call recognition is concerned with the role of variability of acoustic features in mediating or modifying female choice (reviewed in Gerhardt and Huber, 2002). There is relatively less known about how signal variability influences call recognition in male frogs (Capranica, 1965; Narins and Capranica, 1978; Penna *et al.*, 1997a; Ryan and Rand, 1998; Simmons and Bean, 2000; reviewed in Gerhardt and Huber, 2002). Because males and females derive different ''meanings'' from advertisement calls (for example, neighbor/stranger recognition and/or assessment of rivals by males as opposed to assessment of an appropriate mate by females), they may respond differently to variations in the same acoustic parameter (Searcy and Brenowitz, 1988). The distinction between static and dynamic properties of advertisement calls has typically been interpreted with regards to the influence of these different kinds of features on female perception and mate choice (reviewed in Gerhardt and Huber, 2002). Whether these distinctions also modulate patterns of male calling behavior is not as clear. Male frogs alter such dynamic properties as call rate and call duration in response to changes in playbacks of conspecific advertisement calls, but they can also alter static properties such as dominant frequency (reviewed in Gerhardt and Huber, 2002). It is also unclear whether or not males prefer, or respond more strongly to, so-called supernormal stimuli, in a manner paralleling female responses. The experiments described in this paper explore the range of natural variation in call duration, and male responses to variation in call duration in the bullfrog, *Rana catesbeiana*. The goal is to derive a response function (generalization gradient) for this particular acoustic property, and to test the hypothesis that males identify particular signal durations as species specific. In addition, the hypothesis that males respond preferentially to supernormal stimuli, as might be expected from responses of female frogs, is also addressed.

II. MATERIALS AND METHODS

The Brown University Institutional Animal Care and Use Committee approved the use of animals in this research. Male bullfrogs emit a multicroak (1–12), quasiharmonic, long duration advertisement call, whose spectral and temporal properties have been described from both laboratory and field recordings (Capranica, 1965; Wiewandt, 1969; Megela-Simmons, 1984; Bee and Gerhardt, 2001). I first estimated the range of variability in individual croaks in spontaneous (not evoked by stimulus playback) advertisement calls of individual males, then conducted three playback experiments examining the strength (quantity) of evoked vocal responses to natural and synthetic advertisement calls with durations spanning or exceeding the natural range of variation in this acoustic parameter.

A. Field sites and target animals

Recordings of natural choruses and playback experiments were conducted at two natural ponds, located on private property, in Massachusetts and Rhode Island, in June and July, 2000–2002. Site 1 (Sterling, MA) is approximately 100 m long and 40 m wide, with a maximum depth of 8 m. Chorus density ranged from 7 to 15 vocalizing males over the course of the study. Individual males maintained territories of approximately 1 to 5 m in diameter, and intermale spacing ranged between approximately 5 and 20 m. Site 2 (Barrington, RI) is approximately 80 m long and 35 m wide with a maximum depth of approximately 1.25 m. Chorus density ranged from 6 to 13 males, spaced approximately 2 to 15 m apart. Both for recordings of chorus activity and for playbacks, a different male was chosen as the target, based on his location, subjective judgment of the ''pitch'' and ''timbre'' of his advertisement calls, and any identifying visual features. The fundamental frequency and dominant frequency of bullfrog advertisement calls show little variation within an individual male, and significant between-male variability (Bee and Gerhardt, 2001), suggesting that these features provide a reasonable metric for discriminating individuals. Subjective estimates of the relative fundamental and dominant frequencies of advertisement calls were later verified by digital analysis (see below). I have been conducting experiments at these two ponds yearly since 1989, and it is my experience that, once choruses are formed in late May, males, being territorial, maintain relatively fixed positions within the ponds. In neither pond did the entire chorus relocate during the calling season, as observed by Howard (1978) at a much larger site.

B. Stimuli

1. Recordings of natural choruses

The spontaneous advertisement calls of nine individual male bullfrogs at site 2 were recorded over 6 nights in one season. Each animal was monitored for 30 min. Vocalizations were recorded with a Sennheiser ME66 microphone with K6 power module (50–20 000 Hz, ± 2.5 dB) and SONY DAT Walkman TCD-D8 tape recorder (20–20,000 Hz, ± 1 dB). The microphone was placed on a floating styrofoam platform located 1 m away from and oriented towards the vocal sac of the target animal. Calls from individual frogs were converted to 44.1-kHz, 16-bit WAV format sound files using COOLEDIT 2000 (Syntrillium) running on a Pentium computer. Acoustic analyses of the signals (fast Fourier transforms, stimulus autocorrelations) were computed using MATLAB v. 5.3 scripts (MathWorks, Natick, MA). Durations of individual croaks in multicroak calls and intercroak intervals were analyzed using COOLEDIT software (1-ms resolution) by two assistants unaware of the hypotheses being tested.

2. Experiment 1

The purpose of experiment 1 (conducted in 2000) was to measure evoked vocal responses to a synthetic bullfrog advertisement call with croak duration within the typical range of variability of natural croaks. The synthetic croak stimulus consisted of 21 consecutive harmonics of 100 Hz, summed together with a starting phase of 0°. The dominant frequency (harmonic at a relative amplitude of 0 dB) was 200 Hz. The fundamental frequency of 100 Hz was attenuated by 15 dB, and amplitudes of the other harmonics (300–2100 Hz) were attenuated by 3 to 20 dB relative to the dominant frequency. Stimuli with these parameters have been used previously in evoked calling studies (Simmons and Bean, 2000), and reliably elicit responses from males. Durations of the synthetic croaks used for playbacks were chosen based on the distribution of croak durations in spontaneous advertisement calls, recorded as described above. These were 420 ms (stimulus 1); 560 ms (stimulus 2); 700 ms (stimulus 3), and 840 ms (stimulus 4). All croaks had rise–fall times of 50 ms. Stimuli were recorded into DAT tapes as a series of six croaks of identical duration. Intercroak intervals equaled stimulus duration, so that duty cycle remained constant for all stimuli. Intercall intervals (intervals between each successive group of six croaks) were 30 s, within the range of typical intercall intervals recorded in the field.

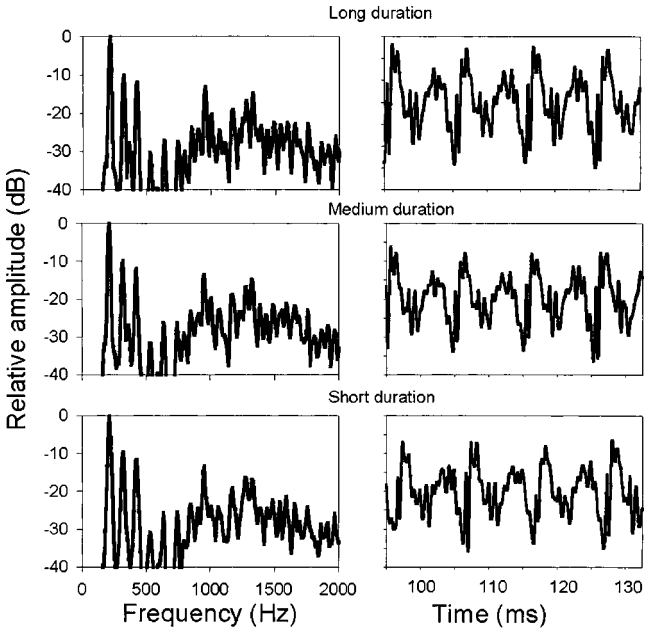

FIG. 1. Power spectral density (left) and segment of the time-domain waveform (right) of exemplar A (experiment 2) after being subjected to the time compression algorithm. Top: long duration stimulus; middle: medium duration stimulus; bottom: short duration stimulus. Power spectral density plots were made using MATLAB v. 5.3 scripts. Time domain waveforms were exported from COOLEDIT 2000.

3. Experiment 2

In experiment 2 (conducted in 2001), I examined evoked vocal responses to natural advertisement calls, some of which were manipulated to be outside the normal range of variability for the species. In order to avoid pseudoreplication problems (Kroodsma, 1989), stimuli for playbacks were derived from recordings of the spontaneous advertisement calls of three individual male frogs (called A, B, and C), made in 1994 at site 2. The natural, multicroak advertisement calls of these three males varied in spectrum and fundamental frequency; the calls were easily discriminated by human listeners. To derive the stimuli used for playbacks, I chose from each male's advertisement call one exemplar croak with a duration at the mean value for that male's calls. Exemplar A had a duration of 626 ms (periodicity 106 Hz, low and high spectral peaks at 214 and 1328 Hz), exemplar B had a duration of 572 ms (periodicity 125 Hz; spectral peaks at 250 and 1500 Hz), and exemplar C had a duration of 518 ms (periodicity 135 Hz; spectral peaks at 405 and 1220 Hz). These exemplar croaks were converted to 44.1-kHz, 16-bit WAV format sound files using COOLEDIT 2000, low-pass filtered below 4000 Hz, and subjected to digital noise reduction through Fourier analysis of intercroak noise samples and statistical reduction of noise frequencies (50% power level). The files were then time compressed or stretched to 50% or 200% based on single croak duration using resampling temporal compression algorithms in COOLEDIT software. These algorithms alter the duration (ratio or absolute duration) of a signal while maintaining its frequency content constant. This is accomplished by splicing isofrequency samples with overlap and splicing frequency determined by the individual signal. For example, to increase the length of an individual croak sample about 0.18 s long to one 0.26 s long with no transposition of frequency content (ratio of 0.67), the algorithm splices isofrequency harmonics with a splicing frequency of 54 Hz with 32% overlap. Higher frequency splicing increases precision of duration change but can enhance artifacts; higher overlap ratios also add to precision but can substantially increase processing time. To produce stimuli for the experiment, the standard exemplar was stretched to 200% (long exemplar), compressed to 50% (short exemplar), and stretched to 200% then compressed back to 100% (medium exemplar), to control for any artifacts introduced by the stretching/compression process. The resulting sounds had durations of 313, 626, 1252 ms (exemplar A), 286, 572, 1144 ms (exemplar B), and 259, 518, 1036 ms (exemplar C). Figure 1 shows the power spectral density and waveform fine structure of the three durations of exemplar A, to illustrate how the time compression algorithm affects the signal.

Stimuli used for playbacks were composed of six croaks of identical duration, with intercroak intervals set at 500 ms. Duty cycles varied from 34% for the short duration exemplar C to 73% for the long duration exemplar A. Stimuli were resaved as 44.1-kHz 16-bit WAV files and recorded onto DAT tapes in groups of 20 six-croak calls of an identical duration, with intercall intervals (intervals between each group of six croaks) ranging randomly from 10 to 120 s to avoid habituation. Stimuli will be referred to subsequently as short duration (313, 286, or 259 ms), medium duration (626, 572, or 518 ms) or long duration (1252, 1144, or 1036 ms).

4. Experiment 3

In experiment 3 (conducted in 2002), the total duration (''on time,'' croak duration plus intercroak intervals) for the

short duration exemplars was set equal to that for the medium duration exemplars, by doubling the number of croaks in the short stimuli from 6 to 12. This manipulation was performed to ascertain whether total stimulus on time rather than croak duration *per se* affected the frogs' responses (the 12 short croak sequence had a total on time equal to that of the six medium croak sequence). In addition, testing with additional exemplars helps rule out problems associated with pseudoreplication (Kroodsma, 1989). Stimuli for playbacks were derived from the spontaneous croaks of three individual male frogs (exemplars D, E, and F), recorded in 1999 at site 1. Sounds were recorded and digitized as described for experiment 2. Exemplar D had a duration of 485 ms (periodicity 113 Hz; spectral peaks at 224 and 1460 Hz); exemplar E had a duration of 596 ms (periodicity 105 Hz; spectral peaks at 206 and 1473 Hz); and exemplar F had a duration of 563 ms (periodicity 108 Hz; spectral peaks at 210 and 950 Hz). These sounds were time compressed and stretched as described above to yield final durations of 242, 485, and 970 ms (exemplar D); 298, 596, and 1192 ms (exemplar E); and 282, 563, and 1126 ms (exemplar F). For the medium and long duration exemplars, stimulus calls used for playbacks were composed of six croaks of identical duration, with intercroak intervals of 500 ms. For the short duration exemplar, stimulus calls used for playbacks were composed of 12 croaks of identical duration, with intercroak intervals of 500 ms. Although stimulus on time for the short duration and medium duration stimuli were similar, duty cycles varied. Signals were presented as described for experiment 2, with intercall intervals ranging randomly from 10 to 120 s to avoid habituation.

C. Procedure

Experiments were conducted between the hours of 2200 and 0100 hours. Air and water temperatures were measured to an accuracy of 1 °C before and after each playback session. Before beginning playbacks, I recorded spontaneous calling for 10–15 min, and identified the positions, relative calling rates, and probable acoustic identity of appropriate target frogs. The amplifier/speaker used for playbacks (Pignose Hog30 model 7-300) was positioned between 6–15 m from a target frog, depending on the geography of the calling site. The recording microphone (Sennheiser) was placed on a floating styrofoam platform, and positioned approximately 1 m away from the target male. Because frogs were not restrained and were free to move, the exact spatial arrangement of target individuals to both the speaker and the microphone could vary within a playback session. To avoid stressing the animals, I did not physically move any other males close to the target male; in any event, since males tend to call preferentially to farther, rather than closer, neighbors (Boatright-Horowitz *et al.*, 2000), such a manipulation would have little effect on the target's calling behavior.

Stimuli were played to the frogs through a Sony DAT TCD-D8 tape recorder and the Pignose amplifier/speaker. The intensity level of each stimulus was calibrated to 80 dB SPL rms (*re*: 20 μPa) at 1 meter, using a Realistic sound-level meter (flat weighting). I measured stimulus levels close to the position of each target frog both before playbacks began and after they ended; these levels varied from about 55 dB SPL at 15 m to about 80 dB SPL at 1 m. The male bullfrog's evoked calling response is relatively insensitive to variations in signal intensity above some threshold level (Boatright-Horowitz *et al.*, 2000; Simmons and Bean, 2000). Spontaneous calling levels were recorded for 5 min before playbacks began, and again for five minutes after the end of playbacks. The males' vocal responses were recorded onto one channel of a Marantz PMD430 (35–14 000 Hz, ± 3 dB) stereo tape recorder. The line output of the DAT recorder was recorded onto the second channel of this tape recorder as a stimulus marker.

In experiment 1, each male was presented with ten repetitions of each stimulus call, at interstimulus intervals of 30 s. In experiments 2 and 3, each male was presented with playbacks of one exemplar, at its three different durations (short, medium, and long). Each duration was presented as a series of 20 six-croak calls, with intercall intervals ranging from 10 to 120 s, with the constraint that stimuli were only played when the target male and his immediate neighbors were not spontaneously vocalizing. The three different durations were presented in a random order. Between one and three individual frogs were tested, with a different exemplar, on a given night.

D. Data analysis

Because the experiment was conducted during active choruses, and because frogs were not moved or displaced from their natural calling positions during playbacks, it is possible that animals may have been responding to each other instead of to the playbacks. I attempted to separate responses from a target male to playbacks from his responses to other frogs, by counting as a response only the vocalizations of that male when he was the first to respond in the silent interval after a particular stimulus. If a neighboring male (within 12 m of the target male) vocalized in response to the stimulus before the target, these trials were excluded from analysis. This is because subsequent responses from the target male could represent responses to his neighbor, rather than responses to the stimulus playback. Responses that occurred during stimulus playbacks (either overlapping or alternating with the stimulus croaks) were treated separately for statistical analyses. Data from the three experiments were analyzed separately.

Data tapes were digitally sampled onto a Gateway Pentium computer at a sampling rate of 22 050 Hz. For each session, total responses (individual croaks) and mean latency to the first response (1-ms accuracy; measured from stimulus offset to response onset) of one individual male over the multiple repetitions of each stimulus were measured. In addition, the duration and the fast Fourier transforms of each answering croak were computed using MATLAB v. 5.3 scripts.

Statistical analysis of results was performed using SPSS v. 11.5 statistical packages. Degrees of freedom for repeated measures analysis of variance (ANOVA) were adjusted, if necessary, using the Greenhouse–Geisser (Greenhouse and Geisser, 1959) corrections to account for any violations of compound symmetry and sphericity. Statistical significance

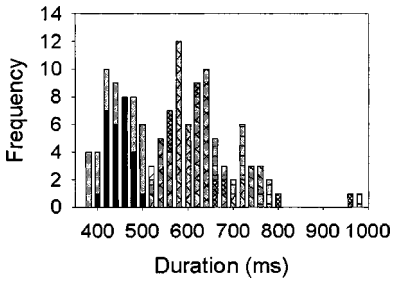

FIG. 2. Frequency distribution of croak duration in the spontaneous advertisement calls of nine individual male bullfrogs. Duration is divided into 20-ms bins. The data for each individual are shown by a different patterned bar; data from some individuals overlap.

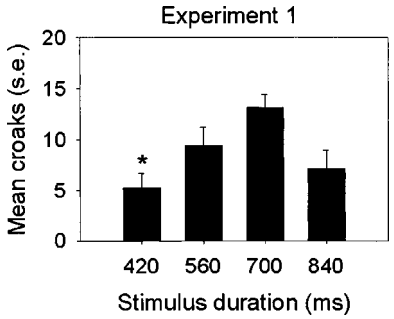

FIG. 3. The relationship between number (mean ±standard error) of answering croaks to stimulus duration. Repeated measures ANOVA showed a significant effect of stimulus duration. Frogs responded most to the stimulus with duration 700 ms, and responded significantly less (*) to the stimulus with duration 420 ms.

of *post hoc* pairwise comparisons was adjusted using the Bonferroni correction for multiple tests.

III. RESULTS

A. Natural variability in croak durations

Spontaneous advertisement calls ($N=297$) of nine individual frogs were analyzed for individual differences and normal range of variability in croak duration. Calls consisting of only one croak were omitted, as were croaks with a signal-to-noise ratio of less than 3:1. The number of croaks analyzed per individual frog varied from 15 to 58. For each male, the durations of each croak in each of his multicroak calls were measured and averaged, and then treated as a repeated measure in ANOVA. The differences in croak duration between individual males were statistically significant [$F_{8,288}=82.8$, $P<0.001$]. Over all nine males, individual croak durations ranged from 370 to 970 ms, and the average croak duration (from each of that male's calls) ranged from 441 to 712 ms (sample mean 551 ms). The frequency distribution of croak duration across all nine males is shown in Fig. 2. An individual could show variability in croak duration over a range as large as 100 ms. The coefficients of variation (100%×standard deviation/mean; Gerhardt and Huber, 2002) calculated from the data for each individual range from 5.54 to 14.7. These data show that the stimulus durations used in experiment 1 extend across the range of variability, and that the short and long duration stimuli used for playbacks in experiments 2 and 3 are outside or at the extremes of the range of variability of spontaneous croak duration for these animals. Intercroak intervals measured from these data ranged from 373 to 772 ms, with a mean across all males of 529 ms. The intercroak intervals used in experiment 1 extend across the range of variability seen in spontaneous advertisement calls, while the standard intercroak interval of 500 ms used in experiments 2 and 3 is near the mean of spontaneous intervals recorded at the study sites.

The croaks of one active caller were analyzed and compared across the three recording sessions (chorus nights) during which this male reliably vocalized. Durations of individual croaks for this male varied from 439 to 918 ms ($N=58$ croaks analyzed per session; coefficients of variation 7 to 10.3). The main effect of recording session was not statistically significant, consistent with the observation that chorus density was similar across the three nights. Air and water temperatures varied between 20–24 °C across recording nights. There was no significant correlation between temperature and croak duration for either individual or the entire sample of frogs.

B. Experiment 1

Data were collected from seven frogs (five at site 1 and two at site 2). Mean (±standard error) number of croaks to the different stimulus durations is shown in Fig. 3. Results of repeated measures ANOVA showed that the within subjects effect of stimulus duration was statistically significant ($F_{3,18}=4.9$, $P<0.05$). Frogs responded more to the stimulus with duration 700 ms than to the other stimuli, but results of pairwise comparisons showed that these differences were significant only when comparing responses evoked by the short duration stimulus (420 ms) and the 700-ms stimulus. Fewer responses were evoked by the 840-ms duration stimulus than by the 700-ms duration stimulus, but this difference was not statistically significant. Five of the seven individual frogs gave the largest number of answering croaks to the 700-ms duration stimulus, while the remaining two gave the largest number of answering croaks to the 560-ms duration stimulus. One frog did not vocalize at all in response to the 420-ms duration stimulus, and another frog did not vocalize at all to the 840-ms duration stimulus.

Duration of responding croaks was analyzed across the different stimulus durations, to determine if frogs matched their response duration with stimulus duration. Across all frogs, there was no significant relationship between response duration and stimulus duration. Individual data were then examined to determine if the lack of a significant relationship in the entire sample was due to averaging across individuals. Data from two individual frogs are shown in Fig. 4. Both of these individuals responded to all four stimuli, and also vocalized spontaneously in baseline (base) trials recorded before playbacks began. Each individual shows a great deal of variability in the durations of his croaks, even to the same stimulus (see responses to the 700-ms duration stimulus by both frogs). Although frog 1 showed a trend of increasing response duration with increasing stimulus duration, this trend was absent in the data for frog 2. Both frogs showed somewhat shorter croak durations in baseline trials compared

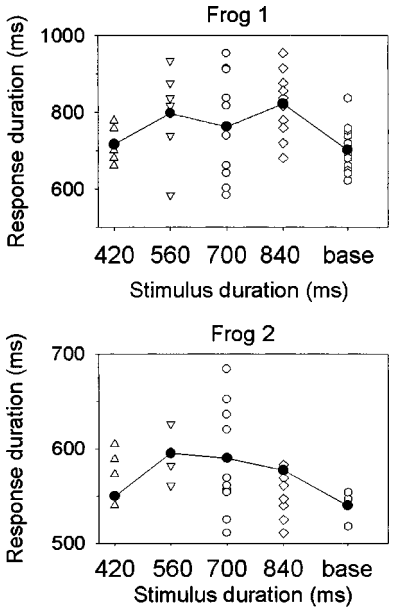

FIG. 4. The duration of answering croaks by two individual frogs in response to different stimulus durations (experiment 1). Base=response duration during baseline (no stimulus) trials. Both of these frogs are included in the data in Fig. 3. For each stimulus duration, the durations of individual responding croaks are shown as a scatter plot (some symbols overlap). The circle/line graph represents the mean response duration for each stimulus duration and baseline period.

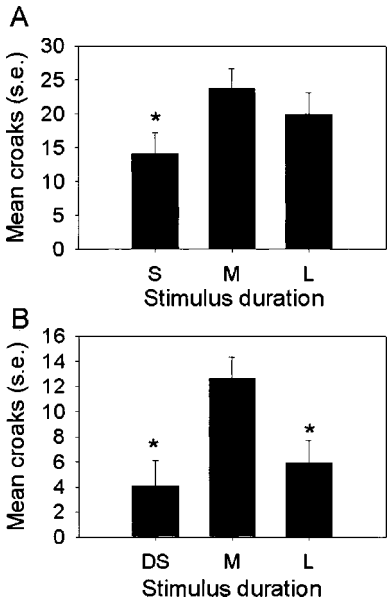

FIG. 5. (A) Number (mean ±standard error, s.e.) answering croaks to stimuli of different durations (S=short duration exemplars; M=medium duration exemplars; L=long duration exemplars) in experiment 2. Frogs responded significantly less (*) to the short duration exemplars. (B) Number (mean ± standard error) answering croaks to stimuli of different durations (DS=short duration exemplars, 12 croaks; M=medium duration exemplars; L=long duration exemplars) in experiment 3. Frogs responded significantly less (*) to the short and long duration exemplars than to the medium duration exemplars.

to playback trials, but this was not observed consistently across the entire sample.

C. Experiment 2

Data were collected from nine individual males (three at site 1 and six at site 2). Data from two additional experiments were eliminated from analysis because the target frog moved away from the speaker during the playback in one, and in another, *post hoc* acoustic analysis revealed that an individual frog had been tested twice. Responses were obtained to four playbacks of exemplar A, three of exemplar B, and two of exemplar C. The total number of answering croaks to the three exemplars, summed across all three durations, did not vary statistically [$X_2^2=2.4$, $P>0.05$], suggesting that the identity of the particular exemplar did not significantly affect responses. The number of playbacks of each exemplar was too small to justify use of a nested ANOVA, and subsequent statistical analyses were thus based on pooling responses from the short, medium, and long duration stimuli across the three exemplars.

Frogs responded differently to playbacks of different croak durations [repeated measures ANOVA: $F_{2,16}=7.7$, $P<0.01$]. These analyses include only those croaks that followed the end of each stimulus presentation (that is, answering croaks which were interspersed between the stimulus croaks were eliminated). Animals vocalized more in response to the medium duration stimulus (mean 23.7 croaks) than to the short duration stimulus (mean 14.1 croaks), with intermediate responses to the long duration stimulus [mean 19.9 croaks; Fig. 5(A)]. Significant *post hoc* differences were obtained between medium and short duration stimuli ($P<0.05$); none of the other comparisons was statistically significant. In terms of individual data, seven of the males showed the absolute greatest number of evoked responses to the medium duration stimulus, one showed the greatest number of responses to the long duration stimulus, and one frog showed equal numbers of responses to the medium and short duration stimulus. Latency of response did not differ significantly across the three durations. For these analyses, no response was given a latency of 30 s. Mean latencies ranged from 9.1 to 11.4 s.

Duration of answering croaks to the three different stimulus durations was analyzed to determine if frogs adjusted their response durations to match stimulus durations. For these analyses, data from four frogs that did not respond at all to the short duration stimulus were excluded. Mean response durations across the five remaining frogs were 538 ms (standard error 5.2) for the medium duration stimulus, 533 ms (standard error 5.8) for the long duration stimulus, and 512 ms (standard error 4.6) for the short duration stimulus. These differences were not statistically significant. Data from individual frogs showed no consistent relationship between stimulus duration and response duration.

D. Experiment 3

Data were collected from 12 individual males (five at site 1 and seven at site 2). Data from three additional experiments were eliminated, because *post hoc* acoustic analyses of vocalizations indicated that individual animals had been tested twice. Responses were obtained from four playbacks of each exemplar. There was no difference in the total number of answering croaks to these three exemplars [$X_2^2=0.7$,

$P > 0.05$], so data were combined across exemplars for subsequent analyses. Again, sample size was too small to use exemplar as a nested factor in an ANOVA.

Results of repeated measures ANOVA indicated that frogs responded differently to playbacks of stimuli of different durations [$F_{1.3,22} = 9.4$, $P < 0.01$]. For these analyses, only those answering croaks that followed the end of each stimulus playback (without being interspersed within the series of six stimuli) were counted. Frogs responded more to the medium duration stimulus (mean croaks 12.6) than to the long (mean 5.9 croaks) or short (mean 4.1 croaks) duration stimuli; these differences were statistically significant [$P < 0.5$ for both comparisons; Fig. 5(B)]. Differences in response between long and short duration stimuli were not significant. Nine individual frogs gave the absolute greatest number of responses to the medium duration stimulus, two gave the greatest number of responses to the long duration stimulus, and one gave equal responses to the long and short duration stimuli. Latency of response also differed significantly [$F_{2,22} = 7.3$, $P < 0.01$]. Latencies were significantly shorter for the medium duration stimulus (mean 4.8 s) than for the short (mean 15.8 s) duration stimulus ($P < 0.01$). Differences in latency of response to the medium or short duration stimuli and to the long duration stimulus (mean 11 s) were not statistically significant.

A major difference between data from experiments 2 and 3 is the smaller number of total answering croaks occurring after the end of each stimulus presentation in experiment 3. Choruses were larger and more active in 2002, and more frogs seemed to vocalize during, rather than after, each stimulus presentation. Croaks occurring during each stimulus presentation were analyzed separately, and divided into two categories, those alternating [Fig. 6(A)] and those not alternating [Fig. 6(B)] with the individual stimulus croaks. In the first case, answering croaks were consistently interspersed in the silent intervals between individual stimulus croaks; in the second case, there was no consistent timing relationship between stimulus and response (the responses sometimes occur coincident with the stimulus). The distribution of alternating and nonalternating croaks varied significantly across the three stimulus durations ($X_2 = 25.6$, $P < 0.001$). There were significantly more instances of nonalternation and significantly fewer instances of alternation in response to the short duration stimulus than to the other stimuli. This suggests that the animals did respond selectively less to the short duration stimulus.

There was no significant relationship between stimulus duration and response duration, either in group data or in the responses of individual frogs.

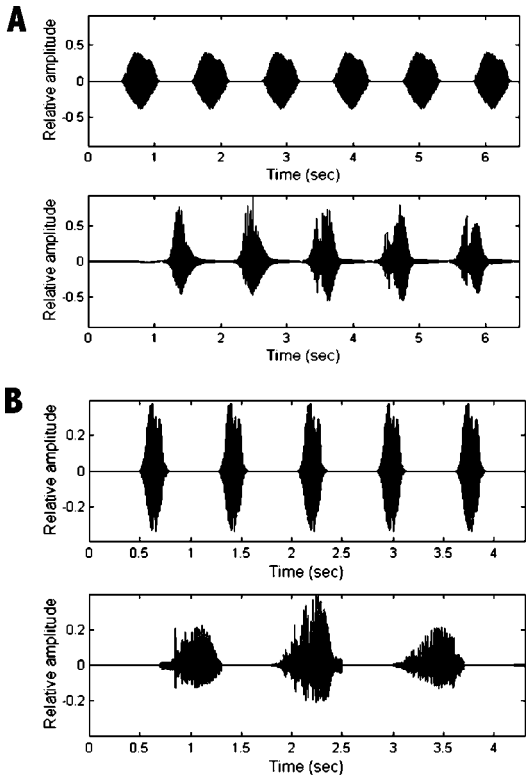

FIG. 6. (A) (top). Time domain waveform of the stimulus (top trace) and the frog's evoked vocal response (bottom trace) to a medium duration exemplar in experiment 3. The onset of each individual croak and the time of peak energy in each croak in the frog's response consistently occur in the time intervals between successive stimulus croaks. This type of pattern was termed alternating. (B) (bottom). Time-domain waveform of the stimulus (top trace) and the frog's evoked vocal response (bottom trace) to a short duration exemplar in experiment 3. The onset of each croak and the time of peak energy in each croak of the frog's response do not consistently occur in the time intervals between successive stimulus croaks. In particular, the peak energy in the second answering croak occurs simultaneously with the third stimulus croak. This type of pattern was termed nonalternating.

IV. DISCUSSION

Analysis of the durations of croaks in spontaneous advertisement calls suggests that croak duration is a dynamic property, as defined by Gerhardt (1991), in bullfrogs. Evoked calling data (experiment 1) show that males vocalize in response to synthetic advertisement calls with durations spanning the natural range of variability, but that calling is less robust to a stimulus duration at the low end of the range. Experiments 2 and 3 show that males vocalize significantly less in response to very short duration stimuli, outside the normal range of variability in croak duration. This was true even under different chorus conditions (experiment 3 was conducted in a larger chorus than experiment 2), suggesting that any differences in calling ''motivation'' arising from overall chorus size do not eliminate differences in response related to stimulus duration. Responses to stimuli longer than spontaneous croaks were inconsistent between experiments 2 and 3, with males showing a steeper drop-off in response in the larger chorus (experiment 3). In any event, neither experiment 2 nor 3 shows any evidence of greater responding to supernormal stimuli. The results of experiments 1–3 suggest that bullfrogs show perceptual generalization across stimulus duration, with a steeper slope of the response gradient on the shorter end compared to the longer end of the continuum. The use of multiple exemplars in these experiments helps control for effects of pseudoreplication (Kroodsma, 1989).

A. Variability in croak duration

Classification of parameters of communication signals as static or dynamic (Gerhardt, 1991; Gerhardt and Huber,

2002) is made on the basis of the degree of variability in that parameter in the calls of individuals. Across different species, call duration can be either, raising questions about the information content of this temporal parameter. From their review of the literature, Gerhardt and Huber (2002) suggested that short duration signals show low variability, while long duration signals show high variability, with the cutoff between these two categories arbitrarily defined as 500 ms (coefficients of variation around 0.5). Individual croaks in bullfrog advertisement calls measured in this study range between 370–970 ms in duration (mean 551 ms), with coefficient of variation ranging from 5.5–14.7. Thus, croak duration fits the definition of a dynamic property. This range of variability is similar to that estimated by Bee and Gerhardt (2001) in a separate, larger sample of bullfrogs (3.0–12.9). The mean croak duration in my sample is shorter than that measured in that study (679 ms); however, my measurements are based on all croaks in a multicroak call, while Bee and Gerhardt's numbers are derived from durations of the first croak only. Capranica (1965) recorded individual croak durations between 600–1500 ms from a group of males housed in the laboratory, but did not provide quantitative data on the range of variability of this parameter either within or between males. In my sample, there were no instances of croak durations over 1000 ms, in either spontaneous or evoked calling. It is possible that the differences in croak duration recorded in these different studies are due to sample (population) differences, differences in chorus density, or to longer croak durations in the field being masked by background noise. This latter is unlikely in the present study, because only croaks with signal-to-noise ratios higher than 3:1 were measured.

The high variability in signal duration within a species raises issues about the importance of this parameter for communication. Gerhardt and Huber (2002) suggested that acoustic features with high variability do not reflect some physiological or mechanistic limit on production, but rather reflect attributes such as physical condition, fitness, or motivation. For example, it is possible that, in bullfrogs, croak duration is related to body size or physical condition. Because I did not individually mark each male in my sample, I could not directly test this hypothesis; however, Bee and Gerhardt (2001) observed no statistically significant correlation between snout-vent length and croak duration in their sample of animals. Similarly, Howard and Young (1998) found no relationship between call duration and body size in a group of male *Bufo americanus*. In terms of fitness, duration might reflect energetics of vocalizations, such that males could produce longer duration stimuli early in the chorus, when they are less tired, for example. This is not supported by the data in Fig. 2, which shows that individual males could vary their croak duration by as much as 100 ms over a time interval as short as 30 min. Similarly, in *B. americanus*, no relationship was found between call duration and body condition, an indirect measure of energetics (Howard and Young, 1998). Wells and Taigen (1986) reported a trade-off between call duration and call rate in *H. versicolor* as a function of chorus density. They also noted a negative relationship between call duration and total calling time, over periods as long as 4 h. In contrast, in the bullfrog, croak duration varied considerably, over short time scales during which chorus size (number of active callers) did not vary. It is possible, however, that overall call duration (number of croaks per advertisement call) might vary over the entire duration of a chorus, but this was not studied here, as measurements were taken only during the first 2–3 h of chorusing on a particular night.

Given the considerable intraindividual variability in croak duration, it is unlikely that this parameter acts like an honest signal in male–male interactions. It is still possible, however, that croak duration is somehow influenced by acoustic interactions within a chorus. One way to test for this would be to measure, for a particular target male, the duration of croaks of other males preceding and following his own. From this hypothesis, one might expect that croak duration in response to playbacks of particular duration would vary consistently with the duration of the playback. In the three experiments here, however, there was no relationship between response duration and croak duration, even for stimulus durations within the normal range of variability in croak duration (experiment 1).

B. Response gradients for croak duration

Even though duration is a dynamic acoustic property, males do not respond equally likely to variations in this parameter. Results of experiment 1 show that males vocalize significantly less often in response to croaks with durations at the lower (shorter) end of the continuum of spontaneous croak durations, than to durations in the middle of the range. Males also responded less to croaks with durations at the upper extreme of the natural duration continuum, although these differences did not reach statistical significance. The results of experiments 2 and 3 again show that males respond more to exemplars with durations near the mean of the duration continuum, with significantly fewer responses to stimuli at the short end of the continuum. Fewer responses were evoked by stimuli with long durations; this was statistically significant only in experiment 3. The different pattern of response to the long duration stimulus in the two experiments might relate to the differences in chorus size during the two experiments, or to the different timing of responses in the two experiments (more responses occurred during the playbacks than in the interstimulus interval following playbacks in experiment 3).

The shape of bullfrog's response function for signal duration suggests a generalization gradient for this signal parameter, with a steeper falloff in response strength at the low end compared to the high end of the continuum. Typical generalization gradients, as defined in theories of learning, are based on changes in conditioned responses to test stimuli at some physical distance from the original stimulus used in acquisition trials (Malott and Malott, 1970). Animals may interpret these test stimuli as similar to (perceptual similarity) or different from (failure of discrimination) the conditioned stimulus. The shape of the generalization function is influenced by factors such as the degree of original learning and prior discrimination training. In the ethological literature (Ghirlanda and Enquist, 1999), ''generalization'' is deter-

mined from changes in unconditioned responses to stimuli varying along some dimension from the original stimulus. The underlying assumption is that the modified stimulus has acquired its relevance, not through explicit laboratory training, but through evolutionary processes (Ghirlanda and Enquist, 1999). For example, in experiments 2 and 3, the medium duration stimulus might represent some ''modal'' value, reinforced through evolutionary time, for which the animal has evolved a particular internal representation. When presented with novel or modified stimuli, the perceptual system may act by estimating the degree of similarity of these stimuli with the internal representation, and a generalization gradient is the behavioral result. Similar assumptions have been made by Ryan *et al.* (2003), who further argue that these types of generalization gradient reflect evolutionary pressures on signal form.

The observation that an asymmetrical generalization gradient for duration exists in the bullfrog is consistent with data from other species of anurans. A steeper drop in response strength (number of evoked vocal responses) across changes in call duration has also been observed by Narins and Capranica (1978) in *Eleutherodactylus coqui*. These asymmetrical preference functions are similar to those observed in the phonotaxis responses of female *H. versicolor* (Gerhardt *et al.*, 2000). In that species, females prefer, in a choice test, calls of average duration over those of short duration, and this preference is stronger than that between calls of average duration and those of long duration. The preference function was thus steeper on the short duration compared to the long duration side. The less vigorous responses to short duration stimuli in both *R. catesbeiana* and *E. coqui* may also reflect a mechanism for discriminating between conspecific and heterospecific advertisement calls. At my study sites, the green frog, *R. clamitans*, is present; the individual notes in the advertisement calls of this species are considerably shorter in duration (105 to 205 ms; Bee *et al.*, 2001) than bullfrog croaks. The shortest signal durations presented to bullfrogs in experiments 2 and 3 (242 ms) are longer than those observed in green frog calls, but even so evoked very little calling. The steep cutoff at the low end of the duration response function for bullfrogs is thus consistent with a mechanism to discriminate against perception of heterospecific calls. The shape of the response gradient in *E. coqui* can also be explained as an adaptation to discriminate against perception of calls of sympatric species (Narins and Capranica, 1978). If this principle is widespread, then the generalization gradient for *R. clamitans* would also be asymmetrical, but with a steeper cutoff on the high, rather than the low, end. The data of Penna *et al.* (1997a), who observed an asymmetrical duration preference function in male *Batrachyla antartandica*, with a steeper slope on the high end, might also be explained by this hypothesis.

Male bullfrogs' lowered responsiveness to short duration stimuli may further represent a mechanism to discriminate between conspecific advertisement and encounter calls. The male bullfrog's encounter call (the ''bonk'' of Wiewandt, 1969) is an aggressive vocalization used in territorial defense. Its spectral composition is similar to that of the advertisement call, but it is considerably shorter in duration ($<$100 ms). A male's typical response to an encounter call is to move or to attack, not to give advertisement calls (Wiewandt, 1969). Stimulus duration may be the parameter allowing the male to discriminate between these two conspecific vocalizations.

C. Lack of preference for supernormal stimuli

Studies in several different anuran species show that females prefer high, over low or intermediate, values of call duration (in those species where duration is a dynamic property; reviewed in Ryan and Keddy-Hector, 1992; Gerhardt and Huber, 2002). Moreover, females can show preferences for stimuli with durations longer than those typically observed in the calls of conspecific males. Ryan and Keddy-Hector (1992) argue that female preferences for these supernormal or exaggerated stimuli reflect a preference for greater sensory stimulation (greater signal-to-noise ratios), and motivate the evolution of complex mating signals.

Preference tests of female bullfrogs for conspecific advertisement croaks or calls varying in duration have not been reported; however, because croak duration is a dynamic acoustic property for this species, preferences for longer duration croaks might be expected. The results of the experiments reported here show that male bullfrogs do not respond more to supernormal croak durations. In experiment 2, there were no significant differences in number of responses evoked by long duration compared to medium duration stimuli; however, in the responses of most individuals, more croaks were evoked by the medium duration stimuli. Results of experiment 3 showed a significant decrease in the number of croaks evoked by long duration compared to medium duration stimuli. However, neither response latency nor the number of evoked responses alternating with individual stimulus croaks varied between long and medium duration stimuli. Experiments 2 and 3 are thus consistent in showing no preference for supernormal durations.

If longer duration signals are preferred by females because they provide more stimulation of the auditory system (Ryan and Keddy-Hector, 1992), why are such signals not preferred by males? Wells and Taigen (1986) suggested that call duration is energetically constrained, and Gerhardt *et al.* (2000) argued that, because of the shape of the female generalization function, for males to increase their call duration beyond a certain limit would not increase their reproductive success. Moreover, if bullfrog croaks are used in neighbor recognition or male–male assessment (Davis, 1987; Bee and Gerhardt, 2001), then males might be expected to be tolerant of variations in the acoustic properties of these signals, in order to provide the maximal individual recognition. Males may not need to increase croak duration beyond some limit because they gain sufficient information about the identity of neighbors from shorter duration signals. Finally, in line with the ''interference risk'' hypothesis presented by Schwartz *et al.* (2001) to explain female choice behavior, tolerance of variability in croak duration would enable males to recognize croaks of neighbors in the midst of fluctuating background noise.

D. Call matching

In experiments 1–3, there was no significant relationship between stimulus duration and response duration in the croaks of individual males. Moreover, males did not consistently add more croaks to their advertisement calls in response to the longer duration stimuli, nor did they decrease the number of croaks to the shortest duration stimuli. These data are not consistent with those of Bee and Perrill (1996), who reported that male *R. clamitans* increased note duration in response to playbacks of conspecific stimuli differing in the number of notes; however, in that study, responses to playbacks of signals differing in the duration of these individual notes were not measured. Wells and Taigen (1986) reported that male *H. versicolor* gave longer calls in response to playbacks of longer calls, but here there was not a precise match between call duration and stimulus duration. These comparisons suggest that the bullfrog call recognition system is more permissive of variability in this specific parameter than that of these other species. This may be related to the relatively longer duration of croaks in bullfrog advertisement calls than notes in the advertisement calls of these other species. It is also possible that bullfrogs may match the number of croaks (and thus overall duration of the entire advertisement call) to the number of croaks in a playback. This possibility was not addressed in the present study.

E. Physiological correlates of duration sensitivity

Responses of neurons in the ascending auditory system to variations in signal duration depend in large part on the classification of neurons as tonic or phasic (fast adapting or slow adapting). The most common response pattern in the auditory nerve and auditory brainstem to stimuli varying in duration is an increase in spike count with increases in duration, described as long-pass functions (Potter, 1965; Narins and Capranica, 1980; reviewed in Gooler and Feng, 1992). In the torus semicircularis of the midbrain of several different frog species, a diversity of response patterns to duration is seen, with some neurons showing bandpass (maximal response to some intermediate duration), short-pass (maximal response to short duration), or all-pass (nonselective) responses (Gooler and Feng, 1992; Penna *et al.*, 1997b). Some of these neurons show selective responses to species-typical stimulus durations (Narins and Capranica, 1980). Potter (1965) reported that neural responses in the bullfrog's midbrain to tones up to 500 ms long reached a plateau at some intermediate duration. These results are consistent with the behavioral data presented here; that shorter stimuli evoke fewer behavioral responses, and fewer neural responses. In the central nucleus of the thalamus of *R. pipiens*, a large proportion of bandpass response functions, with neurons seemingly tuned to particular durations, has been observed (Hall and Feng, 1986). The physiological data do not appear to show, however, a neural mechanism for selective response to supernormal stimulus durations, again consistent with the behavioral data presented here. That is, long-pass response functions with peaks at supernormal durations for that species are not over-represented in midbrain or thalamic responses.

ACKNOWLEDGMENTS

This research was supported by NIH Grant NS28565. I thank Alison Barnstable, Judith Chapman, Seth Horowitz, James Simmons, and Ryan Simmons for assistance.

Bee, M. A., and Perrill, S. A., (**1996**). ''Responses to conspecific advertisement calls in the frog (*Rana clamitans*) and their role in male-male communication,'' Behavior **133**, 283–301.

Bee, M. A., and Gerhardt, H. C. (**2001**). ''Neighbour–stranger discrimination by territorial male bullfrogs (*Rana catesbeiana*). I. Acoustic basis,'' Anim. Behav. **62**, 1129–1140.

Bee, M. A., Kozich, C. E., Blackwell, K. J., and Gerhardt, H. C. (**2001**). ''Individual variation in advertisement calls of territorial male green frogs, *Rana clamitans*: Implications for individual discrimination,'' Ethology **107**, 65–84.

Boatright-Horowitz, S. L., Horowitz, S. S., and Simmons, A. M. (**2000**). ''Patterns of vocal response in a bullfrog (*Rana catesbeiana*) chorus: Preferential responding to far neighbors,'' Ethology **106**, 701–712.

Capranica, R. R. (**1965**). *The Evoked Vocal Response of the Bullfrog: A Study of Communication by Sound* (MIT Press, Cambridge, MA).

Davis, M. S. (**1987**). ''Acoustically mediated neighbor recognition in the North American bullfrog, *Rana catesbeiana*,'' Behav. Ecol. Sociobiol. **21**, 185–190.

Gerhardt, H. C. (**1991**). ''Female mate choice in treefrogs: Static and dynamic acoustic criteria,'' Anim. Behav. **42**, 615–635.

Gerhardt, H. C., and Huber, F. (**2002**). *Acoustic Communication in Insects and Anurans: Common Problems and Diverse Solutions* (University Chicago Press, Chicago, IL).

Gerhardt, H. C., Tanner, S. D., Corrigan, C. M., and Walton, H. C. (**2000**). ''Female preference functions based on call duration in the gray tree frog (*Hyla versicolor*),'' Behav. Ecol. **11**, 663–669.

Ghirlanda, S., and Enquist, M. (**1999**). ''The geometry of stimulus control,'' Anim. Behav. **58**, 695–706.

Gooler, D. M., and Feng, A. S. (**1992**). ''Temporal coding in the frog auditory midbrain: The influence of duration and rise–fall time on the processing of complex amplitude-modulated stimuli,'' J. Neurophysiol. **62**, 1–22.

Greenhouse, S. W., and Geisser, S. (**1959**). ''On methods in the analysis of profile data,'' Psychometrika **24**, 95–112.

Hall, J., and Feng, A. S. (**1986**). ''Neural analysis of temporally patterned sounds in the frog's thalamus: Processing of pulse duration and pulse repetition rate,'' Neurosci. Lett. **63**, 215–220.

Howard, R. D. (**1978**). ''The evolution of mating strategies in bullfrogs, *Rana catesbeiana*,'' Evolution (Lawrence, Kans.) **32**, 850–871.

Howard, R. D., and Young, J. R. (**1998**). ''Individual variation in male vocal traits and female mating preferences in *Bufo americanus*,'' Anim. Behav. **55**, 1165–1179.

Kroodsma, D. E. (**1989**). ''Suggested experimental designs for song playbacks,'' Anim. Behav. **37**, 600–609.

Malott, R. W., and Malott, M. K. (**1970**). ''Perception and stimulus generalization,'' in *Animal Psychophysics*, edited by W. C. Stebbins (Appleton-Century-Crofts, New York), pp. 363–400.

Megela-Simmons, A. (**1984**). ''Behavioral vocal response thresholds to mating calls in the bullfrog, *Rana catesbeiana*,'' J. Acoust. Soc. Am. **76**, 676–681.

Narins, P. M., and Capranica, R. R. (**1978**). ''Communicative significance of the two-note call of the treefrog *Eleutherodactylus coqui*,'' J. Comp. Physiol. **127**, 1–9.

Narins, P. M., and Capranica, R. R. (**1980**). ''Neural adaptations for processing of the two-note call of the Puerto Rican treefrog, *Eleutherodactylus coqui*,'' Brain Behav. Evol. **17**, 48–66.

Penna, M., Feng, A. S., and Narins, P. M. (**1997a**). ''Temporal selectivity of evoked vocal responses of *Batrachyla antartandica* (Amphibia: Leptodactylidae),'' Anim. Behav. **54**, 833–848.

Penna, M., Lin, W-Y., and Feng, A. S. (**1997b**). ''Temporal selectivity for complex signals by single neurons in the torus semicircularis of *Pleurodema thaul* (Amphibia: Leptodactylidae),'' J. Comp. Physiol., A **180**, 313–328.

Potter, H. D. (**1965**). ''Patterns of acoustically evoked discharges of neurons

in the mesencephalon of the bullfrog,'' J. Neurophysiol. **28**, 1155–1184.
Ryan, M. J., and Keddy-Hector, A. (**1992**). ''Directional patterns of female mate choice and the role of sensory biases,'' Am. Nat. **139**, S4–S35.
Ryan, M. J., and Rand, A. S. (**1998**). ''Evoked vocal response in male túngara frogs: Pre-existing biases in male responses?'' Anim. Behav. **56**, 1509–1516.
Ryan, M. J., Rand, W., Hurd, P. L., Phelps, S. M., and Rand, A. S. (**2003**). ''Generalization in response to mate recognition signals,'' Am. Nat. **161**, 380–394.
Schwartz, J. J., Buchanan, B. W., and Gerhardt, H. C. (**2001**). ''Female mate choice in the gray treefrog (*Hyla versicolor*) in three experimental environments,'' Behav. Ecol. Sociobiol. **49**, 443–455.
Searcy, W. A., and Brenowitz, E. A. (**1988**). ''Sexual differences in species recognition of avian song,'' Nature (London) **332**, 152–154.
Simmons, A. M., and Bean, M. E. (**2000**). ''Perception of mistuned harmonics in complex sounds by the bullfrog (*Rana catesbeiana*),'' J. Comp. Psychol. **114**, 167–173.
Wells, K. D., and Taigen, T. (**1986**). ''The effect of social interactions on calling energetics in the gray treefrog (*Hyla versicolor*),'' Behav. Ecol. Sociobiol. **19**, 9–18.
Wiewandt, T. A. (**1969**). ''Vocalization, aggressive behavior, and territoriality in the bullfrog, *Rana catesbeiana*,'' Copeia **1969**, 276–285.
Wollerman, L., and Wiley, R. H. (**2002**). ''Possibilities for error during communication by neotropical frogs in a complex acoustic environment,'' Behav. Ecol. Sociobiol. **52**, 465–473.

Enhanced ultrasound transmission through the human skull using shear mode conversion

G. T. Clement, P. J. White, and K. Hynynen
Department of Radiology, Harvard Medical School, Brigham and Women's Hospital, Boston, Massachusetts 02145

(Received 22 August 2003; revised 2 December 2003; accepted 15 December 2003)

A new transskull propagation technique, which deliberately induces a shear mode in the skull bone, is investigated. Incident waves beyond Snell's critical angle experience a mode conversion from an incident longitudinal wave into a shear wave in the bone layers and then back to a longitudinal wave in the brain. The skull's shear speed provides a better impedance match, less refraction, and less phase alteration than its longitudinal counterpart. Therefore, the idea of utilizing a shear wave for focusing ultrasound in the brain is examined. Demonstrations of the phenomena, and numerical predictions are first studied with plastic phantoms and then using an *ex vivo* human skull. It is shown that at a frequency of 0.74 MHz the transskull shear method produces an amplitude on the order of—and sometimes higher than—longitudinal propagation. Furthermore, since the shear wave experiences a reduced overall phase shift, this indicates that it is plausible for an existing noninvasive transskull focusing method [Clement, Phys. Med. Biol. **47**(8), 1219–1236 (2002)] to be simplified and extended to a larger region in the brain. © *2004 Acoustical Society of America.*
[DOI: 10.1121/1.1645610]

PACS numbers: 43.80.Sh, 43.20.El [FD] Pages: 1356–1364

I. INTRODUCTION

Coherent noninvasive focusing of ultrasound through the human skull has been suggested for a number of therapeutic and diagnostic implications in the brain. For example, ultrasound has been considered as a tool for the transskull treatment of brain tumors,[1–3] targeted drug delivery, improved thrombolytic stroke treatment,[4] blood flow imaging,[5,6] detecting internal bleeding,[7] and tomographic brain imaging.[8–12] Although the human skull has been the barrier to the clinical realization of many of these applications, recent studies have demonstrated both minimally invasive and noninvasive aberration correction methods for transskull focusing. Minimally invasive approaches use receiving probes designed for catheter insertion into the brain[13,14] to measure the amplitude and phase distortion caused by the skull, and then use this information to correct the beam using an array.[15] Alternatively, a completely noninvasive approach uses x-ray computed tomography (CT) images to predict the longitudinal wave distortion caused by the skull.[16] Noninvasive focusing with a therapeutic array has been demonstrated with a longitudinal wave propagation model, but the amplitude of the focus was observed to drop when the focus was directed close to the skull surface.

The assumption that the transcranial propagation is composed of purely longitudinal modes is valid for small incident beam angles,[17] but this assumption rapidly breaks down beyond approximately 25°, as the longitudinal wave approaches its critical angle. This is a plausible explanation for the reduced amplitude observed using the longitudinal model; as the focus was directed toward the periphery of the brain, an increasing number of array elements were oriented at higher incident angles to the skull.

Modeling of shear waves in previous work had been dismissed as being either of insignificant amplitude,[17] or (if significant) as inoperative since the resulting beam would be distorted and hard to predict.[18] The absence of significant information on the skull bone's elastic wave speeds also has prohibited its consideration in modeling. However, a complex conversion from a longitudinal wave (skin) to a shear wave (skull) and back to a longitudinal wave (brain) does not necessarily produce a highly distorted or small-amplitude wave. Our present experimental and theoretical investigations with isotropic phantom materials and an *ex vivo* human skull bone support this hypothesis. In fact, we show that a focused beam traveling as a shear wave in the skull may be less distorted than a longitudinal one. In some instances a focused beam is actually observed to be larger in amplitude than a longitudinal wave propagated through the same skull area. The success of the longitudinal-shear-longitudinal propagation is primarily due to the similarities between the elastic (shear) wave speed ($\sim$1400 m/s) and the sound speeds of water ($\sim$1500 m/s), skin ($\sim$1525 m/s), and the brain ($\sim$1550 m/s). In contrast, the range of longitudinal sound speeds in the skull at relevant frequencies is approximately twice these values.

On the basis of these properties, we examine the possibility of intentionally producing shear modes in the skull bone as a mechanism for producing or enhancing a focus through the skull. We incorporate shear modes into a previously described transskull propagation model, demonstrating a significantly improved ability to predict ultrasound phase and amplitude at high incident angles. To illustrate the approach, we first model the field through a single plastic layer. The approach is then applied to sections of human bone, which are compared to experimental measurements. The approach could be used for more accurate focusing in the brain and could extend the focusing region beyond current methods.

 0001-4966/2004/115(3)/1356/9/$20.00

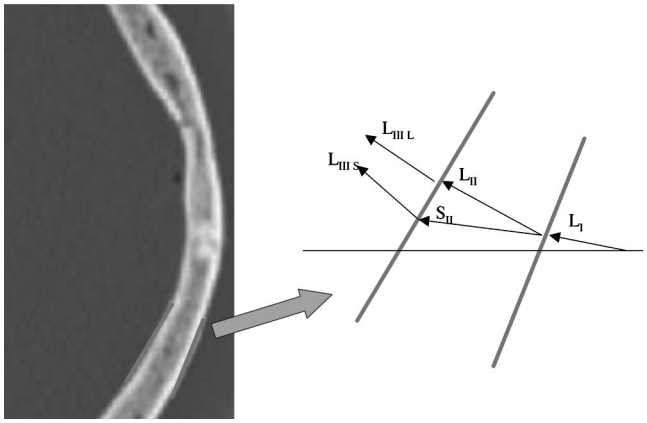

FIG. 1. CT images (left) are segmented in to areas consisting of three-dimensional nonparallel plates. The model then considers isotropic propagation within the bone.

II. TRANSSKULL SHEAR MODE PROPAGATION

Based on the skull's small curvature relative to ultrasound wavelengths,[17,19] the inner and outer surfaces of the skull are sectioned into regions that are each approximated as flat, but not necessarily parallel. A diagram of the problem is given in Fig. 1, showing the one region of the ultrasound field incident upon skull surface. Each region is then modeled as a single-layer isotropic solid with Lamé constants determined as a function of the mean density over the propagation region.

Propagation through an arbitrarily oriented isotropic skull layer is achieved by spectral decomposition of the incident wave, followed by the determination of the ray paths, and attenuation as a function of angular wave number as the field crosses the skull. Each of these initially longitudinal harmonic spectral wave components will be considered below in terms of its velocity potential. Without loss of generalization, a given component may be viewed in a reference frame where the surface normal is oriented along the Cartesian y axis, with the z axis defined by the unit vector of the cross product between the propagation axis and the surface vector. In this frame, the velocity potential is expressed as

$$\phi^I = A_L^I e^{i(\omega t - k_x^I x \sin\theta^I - k_y^I y \cos\theta^I)} + A_{LR}^I e^{i(\omega t - k_x^I x \sin\theta^I + k_y^I y \cos\theta^I)}, \tag{1}$$

where A_L is the amplitude of the longitudinal wave component incident upon the layer surface, A_{LR} is the amplitude of the reflected longitudinal wave, θ is the angle of incidence, and k_x and k_y are the wave vector components in the specified reference frame. The superscripts I to III are used to denote the skin, skull, and brain, respectively, while the subscripts L and S refer to longitudinal or shear waves. Accordingly, the transmitted longitudinal potential in the skull is given by

$$\phi^{II} = A_L^{II} e^{i(\omega t - k_x^{II} x \sin\theta^{II} - k_y^{II} y \cos\theta^{II})}, \tag{2}$$

and the shear vector potential is

$$\boldsymbol{\psi}^{II} = A_S^{II} e^{i(\omega t - k_{S_x}^{II} x \sin\theta_S^{II} - k_{S_y}^{II} y \cos\theta_S^{II})} \hat{z}. \tag{3}$$

Using this description, each spectral wave component must be viewed in its own unique reference frame. At the boundary, the incident wave is split into a reflected wave, a transmitted longitudinal wave, and a transmitted shear wave. The amplitudes of these waves may be determined relative to the incident wave using methods outlined by Kino.[20] Specifically, the normal component of the particle displacement

$$\mathbf{r} = \nabla\phi + \nabla\times\boldsymbol{\psi}, \tag{4}$$

must be continuous at the boundary as well as the normal stress

$$S_{yy} = \lambda \frac{\partial r_x}{\partial x} + (\lambda + 2\mu)\frac{\partial r_y}{\partial y}, \tag{5}$$

and the shear stress

$$S_{xy} = \mu\left(\frac{\partial r_x}{\partial y} + \frac{\partial r_y}{\partial x}\right), \tag{6}$$

with the shear and longitudinal sound speed of a given medium related to the Lamé constants μ and λ by

$$c_S = \sqrt{\frac{\mu}{\rho}}, \quad c_L = \sqrt{\frac{\lambda + 2\mu}{\rho}}. \tag{7}$$

Details of the amplitude calculations are provided in Appendix A. It is stressed that each plane-wave solution describes the behavior of only a single angular wave number. It is necessary to calculate these amplitudes for each component wave vector space. However, this may be readily performed in closed form, as given in Appendix B.

After propagating into the skull, the longitudinal and shear waves are treated separately, with the total wave reaching the brain then equal to

$$\phi^{III} = A_{LL}^{III} e^{i(\omega t - k_x^{III} x \sin\theta^{III} - k_y^{III} y \cos\theta^{III})} + A_{LS}^{III} e^{i(\omega t - k_x^{III} x \sin\theta_S^{III} - k_y^{III} y \cos\theta_S^{III})}, \tag{8}$$

where A_{LL}^{III} and A_{LS}^{III} are the amplitudes of the longitudinal waves due to the incident longitudinal and shear waves in the skull, respectively. The values of the velocity potentials may be found by equating Eqs. (4) through (6) at the skin–bone interfaces after substituting in Eqs. (1) to (3), and solving for A_L^{II} and A_S^{II}. At the skull–brain interface, the incident shear and longitudinal velocity potential amplitudes will be equal to the product of these transmission amplitudes and the absorption loss experienced within the bone. Since each spectral component will have its own independent path length through the skull, its total absorption will generally differ between components. A two-dimensional representation of the problem is given in Fig. 1.

To find the wave amplitudes in the brain, A_{LL}^{III} and A_{LS}^{III}, the problem is once again reduced to two dimensions by rotating the problem into a reference frame where the surface normal is oriented along the Cartesian y axis and the relevant wave vector lies in the $x-y$ plane. Since the soft tissue of the brain is fluid-like, the incident longitudinal wave in the skull bone will be further divided into a reflected shear wave, a reflected longitudinal wave, and a transmitted longitudinal

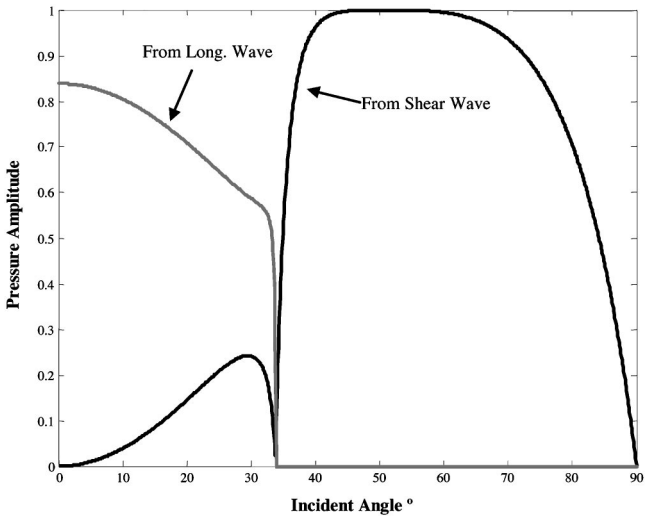

FIG. 2. Calculated pressure amplitude of a planar wave after liquid–solid (Plexiglas)–liquid propagation.

wave. The shear wave in the skull will be similarly divided, but with differing reflection and transmission angles.

The acoustic pressure at a given point in the brain is obtained by separately solving for the amplitude and phase of each spectral component over a planar area. The spectrum is then inverse transformed to give the pressure over the measurement plane. The pressure amplitude is equal to the negative of the normal stress which is related to the amplitude of the scalar velocity potentials in the brain, A_{LL}^{III} and A_{LS}^{III}, by Eq. (4) and Eq. (5). Figure 2 shows the angular dependence of A_{LL}^{III} and A_{LS}^{III} resulting from an infinite plane wave in water after traveling through an ideal acrylic layer. A similar plane-wave methodology was examined by Thompson[21] for examining Doppler beams through plastic.

Based on the skull's high attenuation coefficient,[18] we neglect additional contributions due to multiple reflections within the skull bone.[18,22] The total acoustic pressure at any point in the brain can be determined by calculating the path length and total transmission amplitude for each spectral component. These values then allow the relative acoustic phase and the overall attenuation (including absorption loss) to be estimated. The algorithm for determining the field path lengths from the transducer to the measurement point in the brain is presented in Appendix B. A special case of the method was previously used to trace the longitudinal path length of elements from an array in order to focus ultrasound through human skulls.[16] In that study, sections of the inner and outer surfaces of the skull were assumed to be parallel and shear waves were neglected.

III. PROPAGATION ALGORITHM

We first consider a parallel plastic plate to test the algorithm in order to provide an idealized isotropic case readily verifiable by experiment. The identical plate was previously used in a study involving the propagation of longitudinal waves from a planar source at small incident angles.[23] Relevant values for the plastic are summarized in Table I. The ultrasound source is a 1.5-MHz focused transducer with a diameter of 120 mm and a radius of curvature equal to 160 mm. The source function for the algorithm is acquired by projecting a laboratory-measured pressure field from a plane near the geometric focus backward to the source.[24] This field is measured over a 30×30-mm^2 area with a spatial resolution of 0.5 mm. The source function is then propagated through the plates using an algorithm described numerically in Appendixes A and B. The distance from the source to the measured plane is 121 mm and that from the plastic inner surface to the source is 61 mm.

Similar methodology is used to propagate through *ex vivo* human calvaria (brain cages). Following the laboratory measurements, water is used as the interfacing medium between both the inner and outer skull surface. The ultrasound source for the transskull measurement is a 0.74-MHz focused transducer with a diameter of 8 cm and a radius of curvature equal to 150 mm.

The numeric algorithm is implemented in MATLAB, using matrix-based operations for the layers. Operations were performed on a 1-GHz AMD-based PC. A typical projection of a complex 128×128 matrix through five layers took approximately 30 s to calculate.

IV. EXPERIMENT

A. Skull registration and density

Data for the simulation were obtained from a digitized human-head profile obtained using CT images (Siemens, SOMATOM, AH82 Bone Kernel). Both the coordinates of the skull surfaces as well as the internal density variation were obtained from these images. Scans were taken at 1-mm intervals using a 200×200-mm field of view. A polycarbonate stereotaxic frame was attached around each sample to allow the skulls to be attached to the array and provide a reference for the mechanical positioning system and the CT images. The calculation was performed only in bone lying within the beamwidth of the section being considered. Information about the shape and structure of an individual calvarium was acquired by combining the images, which returned intensities proportional to material density. In the present demon-

TABLE I. Summary of materials and their acoustic properties, including density, longitudinal absorption coefficient, shear absorption coefficient, longitudinal and shear sound speeds, and thickness across the axis of propagation.

Material	Density (kg/m^3)	a_L (Np/m)	a_S (Np/m)	C_L (m/s)	C_S (m/s)	Thickness (mm)
Plastic	1187	45	50	2185	1330	11.8
Skull	2186	85	90	2850	1400	5.29
Water	1000	0	0	1486	NA	Variable

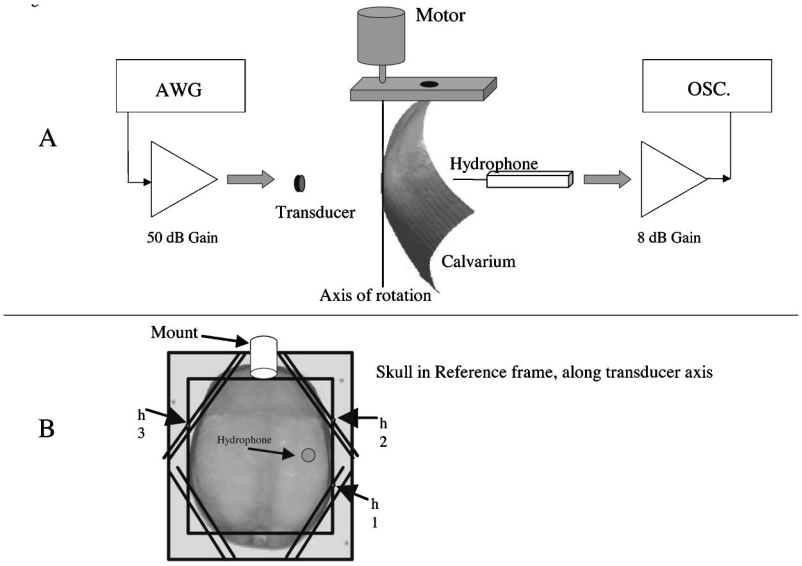

FIG. 3. (A) The experimental setup. (B) An overhead view showing the relative position of the hydrophone within the skull specimen.

stration, the mean density across the layer was used, effectively approximating the skull as an isotropic solid.

Coordinates of points along the inner and outer surfaces of the skull were identified on an image using a threshold filter, which searched for the innermost and outermost densities $>1.4\ \mathrm{gm/cm^3}$ along each line of an image. Points of successive images were combined to give three-dimensional representation of the inner and outer skull surface. Pixel intensities of each image were also combined into a three-dimensional array for later processing.

The projection algorithm relied on precise knowledge of the orientation of the skull relative to individual array elements. To achieve this, the phasing algorithm translated and rotated the skull data from the CT coordinate frame to the transducer coordinate frame as well as translated and rotated the skull from the mechanical positioning system's coordinate frame to the transducer coordinate frame. The program operated using three markers located on the polycarbonate frame affixed to the skull. These locations could be identified mechanically with the positioning system to a precision of approximately 0.1 mm. The algorithm then generated a rotation matrix that mapped between the coordinate systems.

B. Ultrasound measurements

Propagation experiments were set up in a water tank to verify the numeric algorithm. Measurements were performed in degassed and deionized water in a tank padded with rubber to inhibit reflections. Ultrasound signals were generated by a transducer specific to the particular measurement and received with a polyvinylidene difluoride (PVDF) needle hydrophone (Precision Acoustics, Dorchester, UK). To assure a strong reception while maintaining accuracy, a 0.2-mm-diameter hydrophone was used for the 1.5-MHz measurements and a 0.5-mm-diameter hydrophone was used for measurements at 0.74 MHz. The smaller hydrophone at higher frequency was used to minimize hydrophone directivity and prevent phase averaging. A skull (or plastic plate) was placed between the hydrophone and transducer at an angle controlled by a rotational stepping motor (Velmex, New York). A 3D linear positioning system (Velmex, model V P9000) allowed the hydrophone to be scanned over a measurement area centered about the transducer's axis of symmetry. Transducer signals were generated by an arbitrary waveform generator (Wavetek, California, model 305) fed to a power amplifier (ENI, New York, model 2100L). The hydrophone's voltage response was sent though a Precision Acoustics preamp and an amplifier (Preamble Instruments, Oregon, model 1820) before it was recorded by a digital oscilloscope (Tektronix, Oregon, model 380). The voltage waveform was downloaded to a PC by GPIB control and the amplitude and phase at the measurement location were calculated from the FFT of the signal, taking the values at the transducer driving frequency.

The 11.8-mm plastic plate was placed in the test tank and the acoustic transmission was measured on the transducer's axis of symmetry, 121 mm from its face. The acoustic pressure was measured between $-70°$ and $70°$ at an increment of $1°$. Agreement between the measured and simulated waveforms was evaluated by comparing the amplitudes and phases at each angular orientation. The source function for the simulation was a pressure field measurement taken with the transducer in water without a plate present.

For the transskull measurements, two different mounting procedures were performed. The first, shown in Fig. 3(a), was designed to allow measurement through an approximately constant location on the skull at different incident angles. The second configuration, Fig. 3(b), allowed measurement at high incident angles with good registration between the transducer and the skull, but did not facilitate movement of the skull. Initial measurements examined the angular dependence of amplitude on the skull, in order to determine whether amplitude peaks were present beyond the longitudinal Snell's critical angle. A section of skull bone was rotated between $0°$ and $55°$, with the axis of rotation normal to the transducer axis and coincident with a line through the bone. The maximum angle of $55°$ was the highest value obtainable with the current setup.

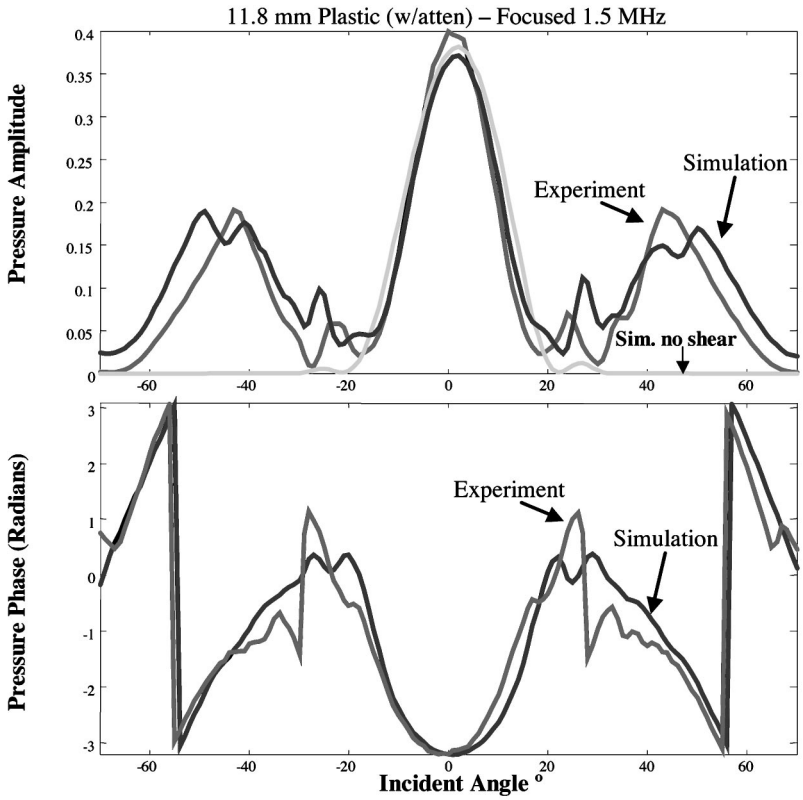

FIG. 4. The on-axis amplitude and phase simulated (dashed), simulated without a shear mode (solid), and measured (dotted) after propagation through an 11.8-mm plastic plate with a focused 1.5-MHz beam.

V. RESULTS

A. Plastic

The correlation between the measured and predicted fields is shown in Fig. 4. For reference, the plot also includes the amplitude of the numeric calculation obtained when shear waves were neglected. The amplitudes and phases of all three curves match closely for incident angles with absolute values below 31°, which is the longitudinal critical angle for the signal's spectral peak. However, beyond this angle, the longitudinal-only simulation is unable to predict the second local maximum in the amplitude, which results from a purely elastic wave within the sample. The major source of discrepancy between the measured data and simulated amplitude possibly results from underestimation of the shear wave absorption coefficient in the simulations. This effect becomes more pronounced at high angles, where the path length is largest. However, very good correlation is found between the simulated and measured ultrasound phase. This agreement extended to nearly all angles, with the exception of the transitional region between 20° and 30°, the region where the wave amplitude is near its minimum. Neglecting this region, 76% of the remaining calculated points deviated from measurements by $\pi/6$—or less—radians.

B. Transskull measurement

By rotating the skull, a local pressure transmission maximum was observed at 32°. This signal is expected to result almost entirely from shear propagation through the bone, based on a longitudinal critical angle of about 30°. Further evidence of the wave's origin as a shear wave at higher incident angles is found in the measured data (Fig. 5), which

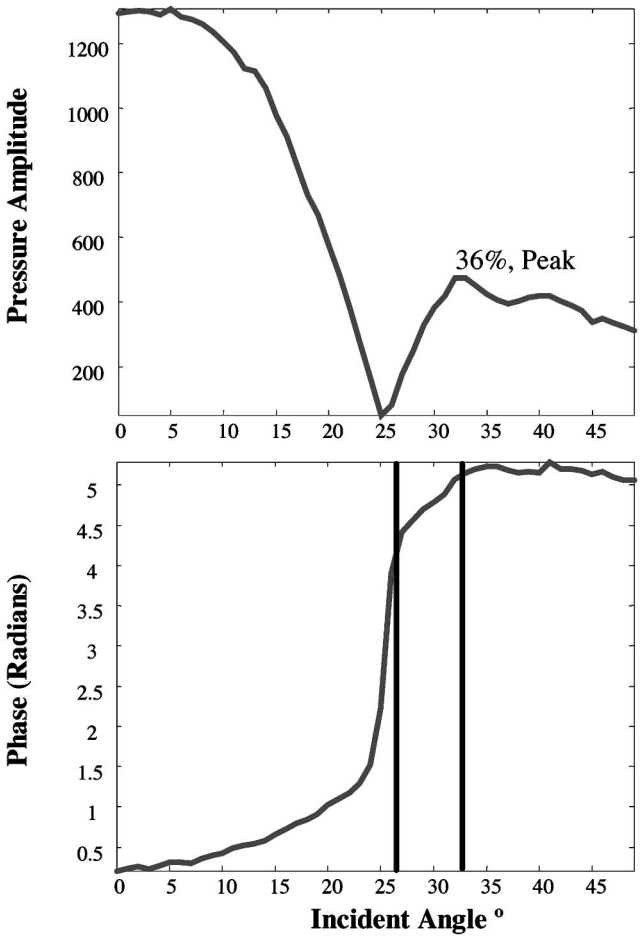

FIG. 5. The on-axis amplitude and phase measured after propagation through a skull bone. The black lines indicate the transition in phase to an entirely shear mode.

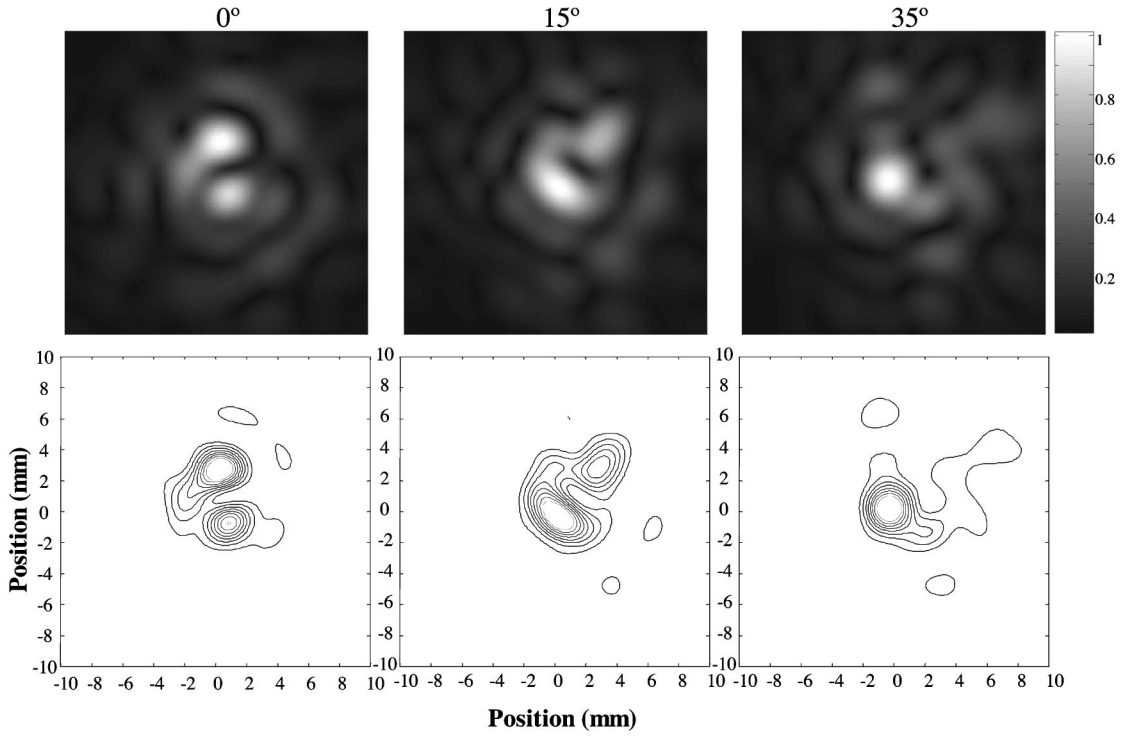

FIG. 6. Transskull ultrasound signal measured at 0°, 15°, and 35° incidence. The measurement indicates reduced distortion beyond Snell's critical angle for the longitudinal mode.

shows the angular dependence of the wave phase. Below 26° the phase closely resembles the behavior of a purely longitudinal wave. Between 26° and 32° there is a deceleration in the slope, indicating a region of superimposed contribution from the shear and longitudinal wave. Beyond 32° the slope is approximately linear and negative, since the shear sound speed is less than the speed of sound in water.

Using the same mounting configuration, field measurements were performed over a 30×30-mm area with 1-mm resolution for different incident angles. Figure 6 shows the field immediately after passing through the skull bone after measurements at 0°, 15°, and 30°, showing less distortion in the signal propagated through the skull as a shear wave than when propagated in a longitudinal mode at both 0° and 15°.

A second set of measurements was performed with skulls placed in reference frames for spatial correlation with CT images. Although only an estimated value of the shear wave speed was used for the study, accurate spatial registration and data for the longitudinal modes allowed the longitudinal critical angle to be identified. Skulls were then aligned to assure that the transmitted signal was from shear propagation in the bone.

Finally, a demonstration was performed with a skull placed in a reference frame, to allow spatial correlation with CT images. Accurate spatial registration and data for the longitudinal modes allowed the longitudinal critical angle to be identified. However, only an estimated value of the shear wave speed was available for the study.[17] Skulls were aligned to assure that the transmitted signal was from shear propagation in the bone. Figure 7 shows a line measurement of the field, with the outer surface of the skull oriented at 32° relative to the axis of symmetry. Although there is discrepancy between the simulation and the measurement, the simulation was nonetheless able to identify the presence of the focused shear wave, with a beam shape resembling that of the measurement.

VI. DISCUSSION

Our preliminary simulations and experimental measurements indicate that transmission of a coherent, focused ultrasound beam through the skull purely as a shear wave is possible. At the presently considered driving frequency near 0.7 MHz, the peak amplitude through the skull due to shear propagation in the bone was found to be between 35% and 55% of the peak longitudinal mode. Although the shear amplitude was lower than longitudinal modes, we found evidence that the overall beam may suffer less distortion when propagated through a localized region of the bone. Furthermore, the shear mode experienced less phase distortion due to the similarity between the shear wave speed and the speed of sound in water. Comparable similarities could be found in soft tissues.

More precise correlation between the simulation and measured data will require accurate measurement of the shear wave speed in the skull bone. The present study used a previously tabulated value of 1400 m/s.[17] It is likely, however, that this value fluctuates as a function of position on the skull and could potentially be correlated either with bone density and/or with bone type (cortical or trabecular).

There are several possible direct implications of the shear transmission method: First, the method may be added to pre-existing noninvasive transskull phasing algorithms for

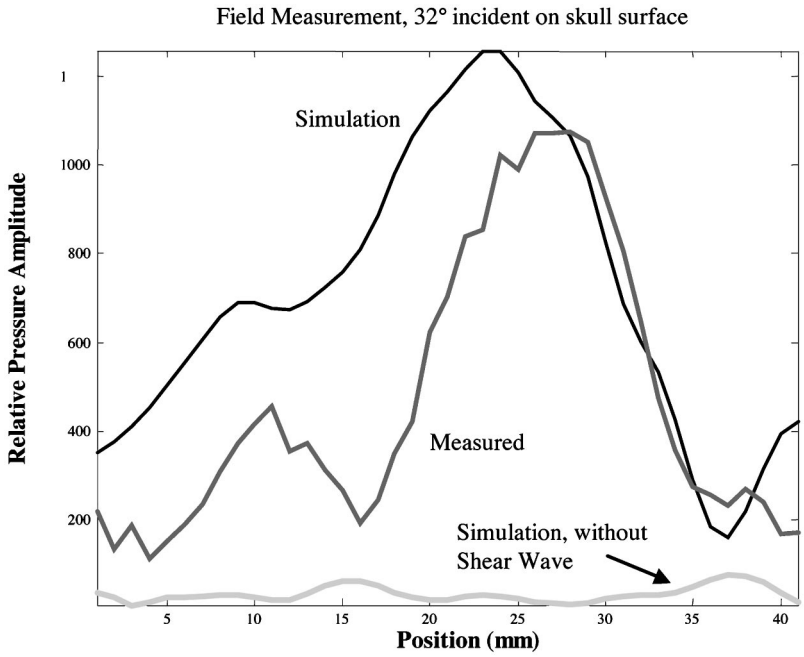

FIG. 7. A linear hydrophone measurement of a transskull ultrasound beam (solid). The measurement is taken parallel to the transducer's propagation axis and passes through the transducer's geometric focus. This scan is compared to a model with (dashed) and without (dotted) consideration of shear propagation in the skull.

improved focusing at high incident angles. This is particularly important when focusing close to the skull surface, where high angular incidence is necessary. Second, the method may have application in transskull imaging, where a narrow ultrasound beam would be directed through the skull and intentionally high incident angles. Finally, the method could potentially be used to detect flow in the brain by means of frequency Doppler shifts. All of these techniques are expected to be feasible in the submegahertz frequency range considered here.

ACKNOWLEDGMENTS

This work was supported by Grants 9R01EB003268 and R21EB00705 from the National Institutes of Health.

APPENDIX A: TRANSMISSION AMPLITUDES

The pressure amplitudes were calculated by solving for the velocity potentials described in Eqs. (1), (2), (3), and (8). After linear algebraic simultaneous solution of the equations, it may be shown that the shear and longitudinal wave amplitudes in the bone are given by

$$A_S^{II}(\theta^I)=\frac{-4A_L^I c^{I^2}k^{I^2}k_L^{II}\rho^I\cos\theta^I\cos\theta_L^{II}\sin\theta_L^{II}/k_S^{II}}{D_{II}(\theta^I)\rho^{II}\cos\theta^I+c_{II}^2k^I\rho^{II}C_{II}(\theta^I)}, \tag{A1}$$

and

$$A_L^{II}(\theta^I)=\frac{2A_L^I c^{II^2}k^{I^2}k_S^{II}\rho^I\cos\theta^I\cos 2\theta_S^{II}/k_L^{II}}{D_{II}(\theta^I)\rho^{II}\cos\theta^I+c^{II^2}k^I\rho^I\cos\theta_L B_{II}(\theta^I)}, \tag{A2}$$

where

$$B_{II}(\theta^I)=k_S^{II}\cos 2\theta_S^{II}+2k_L^{II}\sin\theta_L^{II}\sin\theta_S^{II}, \tag{A3}$$

$$C_{II}(\theta^I)=k_S\cos\theta_L^{II}\cos 2\theta_S^{II}+k_L\sin 2\theta_S^{II}\sin\theta_S^{II}, \tag{A4}$$

$$D_{II}(\theta^I)=k_L^{II}k_S^{II}(c_L^{II^2}\cos 2\theta_S^{II}-2c_S^{II^2}\sin\theta_L^{II}\times\sin(\theta_L^{II}-2\theta_S^{II})), \tag{A5}$$

and the transmitted angles are understood to be functions of θ, related by Snell's law

$$\frac{\sin\theta^I}{c^I}=\frac{\sin\theta_L^{II}}{c_L^{II}}=\frac{\sin\theta_S^{II}}{c_S^{II}}. \tag{A6}$$

The amplitudes of the waves transmitted into the brain from the incident longitudinal and shear waves are equal to

$$A_{LS}^{III}(\theta^I)=\frac{-(2A_S^{II}(\theta^I)c_S^2k_S^2\rho_{sk}\cos\theta_L^{II'}(k_S\cos 2\theta_S^{II'}+2k_L\sin\theta_S^{II'})\sin 2\theta_S^{II'})/k^{III}}{D(\theta^I)\rho^{II}\cos\theta^{III}+c^{III^2}k^{III}\rho^{III}C_{II}(\theta^I)} \tag{A7}$$

and

$$A_{LL}^{III}(\theta^I)=\frac{2A_L^{II}(\theta^I)k_L^{II^2}\rho^{II}\cos\theta_L(c_L^{II^2}-c_S^{II^2}+c_S^{II^2}\cos 2\theta_L^{II})B_{II}(\theta^I)/k^{III}}{\rho^{II}\cos\theta^{III}D_{II}(\theta^I)+c^{III^2}k^{III}\rho^{III}\cos\theta_L^{II}B_{II}(\theta^I)}. \tag{A8}$$

APPENDIX B: PROPAGATION ALGORITHM

Regardless of whether or not the layers are parallel, the transfer function through the layers may still be written in a closed form in terms of the thickness across the z axis, z_n, the sound speed c_n, and density of each layer ($n=I$, II, III). For each interface it is necessary that the unit vectors normal to the layer surfaces $\hat{n}_n$ be calculated. For a given initial wave vector $\mathbf{k}_{0xy}$, the ray path from (0,0, z_0) between any two surface interfaces traverses a distance of

$$|\mathbf{R}_{nxy}| = \frac{(\mathbf{z}_{nxy} - \mathbf{r}_{nxy}) \cdot \hat{n}_{n+1}}{\hat{k}_{nxy} \cdot \hat{n}_{n+1}}, \tag{B1}$$

where, as depicted in Fig. 1, $\mathbf{r}_{nxy}$ is the vector extending along the layer from z axis to the intercept of the layer with the ray. The unit vector along the wave vector's path is given by $\hat{k}_{nxy}$. Again, the frequency dependence on the wave vector orientation is understood. It follows that the ray position vector must be equal to $\mathbf{R}_{nxy} = |\mathbf{R}_{nxy}| \hat{k}_{nxy}$. Although the initial wave vector orientation, $\hat{k}_{0xy}$, is known, the direction of the wave vector in the first and subsequent layers must be calculated using the relation[25]

$$\frac{1}{c_n}(\hat{n}_{n+1} \times \hat{k}_{nxy}) = \frac{1}{c_{n+1}}(\hat{n}_{n+1} \times \hat{k}_{n+1xy}), \tag{B2}$$

which is a consequence of Snell's law in three-dimensional space that requires the incident wave vector, the transmitted wave vector, and the normal vector all be in the same plane. After bifurcation of the wave into a longitudinal and shear mode, the waves are treated separately. The transmitted wave vector on the right-hand side of Eq. (B2) may be obtained by crossing both sides of the equation with $\hat{n}_{n+1}$. Using cross-product relations, it may be shown that

$$\hat{k}_{n+1xy} = \frac{c_{n+1}}{c_n}(\hat{k}_{nxy} - \cos \gamma_{i_{n+1xy}} \hat{n}_{n+1}) + \cos \gamma_{i_{n+1xy}} \hat{n}_{n+1}. \tag{B3}$$

The incident unit wave vector of the nth layer is simply equal to the transmitted wave of the $(n-1)$st layer. With the exception of the 0th layer shown in Fig. 2, it is also necessary to find $\mathbf{r}_{nxy}$ in order to calculate Eq. (B1). Given the thickness across the z axis of each layer, the point of intersection of ray $\mathbf{R}_n$ with the surface of the $n+1$ layer is

$$\mathbf{r}_{n+1} = \mathbf{R}_n + \mathbf{r}_n - \mathbf{z}_n. \tag{B4}$$

Over a series of N layers, the phase of a ray reaching the Nth plane $\phi_R(\mathbf{k}_{Nxy}, \omega)$ is the sum of the phase contributions over each path length given by Eq. (B1). The *spatial* phase at the plane z, is related to the ray phase at N by $\phi_N(\mathbf{k}_{Nxy}, \omega) = \phi_R(\mathbf{k}_{Nxy}, \omega) - 2\pi k_N r_N \sin \gamma_{Nxy}$, as illustrated in Fig. 1. A ray leaving the initial plane with a polar angle $\gamma_{0xy}(\omega)$ will arrive at the plane z with a new orientation $\gamma_{Nxy}(\omega)$ determined by the $N-1$ unit vector $\hat{k}_{N-1}$

$$\phi(\mathbf{k}_{Nxy}, \omega, z) = \phi(\mathbf{k}_{0xy}, \omega, z_0) + \sum_{n=0}^{N-1} k_n \frac{(\mathbf{z}_n - \mathbf{r}_n) \cdot \hat{n}_{n+1}}{\hat{k}_n \cdot \hat{n}_{n+1}} - \sin \gamma_{Nxy}(\omega), \tag{B5}$$

given $\phi(\mathbf{k}_{0xy}, \omega, z_0)$, the phase of $\tilde{p}(k_x, k_y, \omega, z_0)$ at the initial plane.

The pressure over the plane at z can be expressed in terms of the ray phase presented in Eq. (B5) and the transmission coefficient by

$$\tilde{p}(\mathbf{k}_{Nxy}, \omega, z) = \tilde{p}(\mathbf{k}_{0xy}, \omega, z_0) e^{-i \sin \gamma_{Nxy}(\omega)} \times \left[\prod_{n=1}^{N-1} T_{nxy}(\omega) e^{i \phi_N(\mathbf{k}_{Nxy}, \omega, z)} \right], \tag{B6}$$

where the terms in square brackets on the right-hand side of Eq. (B6) can be viewed as an operator that maps the field from k_0 space to a new k_N space. In the present problem, the amplitudes, T, are given by to Eqs. (A7) and (A8) and the component angles, γ_{Nxy}. In practice, this mapping requires interpolation to produce a linearly spaced matrix at z.

[1] F. J. Fry, "Transkull transmission of an intense focused ultrasonic beam," Ultrasound Med. Biol. **3**(2–3), 179–184 (1977).
[2] J. Tobias, K. Hynynen, R. Roemer, A. N. Guthkelch, A. S. Fleischer, and J. Shively, "An ultrasound window to perform scanned, focused ultrasound hyperthermia treatments of brain tumors," Med. Phys. **14**(2), 228–234 (1987).
[3] M. Tanter, J.-L. Thomas, and M. A. Fink, "Focusing and steering through absorbing and aberrating layers: Application to ultrasonic propagation through the skull," J. Acoust. Soc. Am. **103**, 2403–2410 (1998).
[4] S. Behrens, K. Spengos, M. Daffertshofer, H. Schroeck, C. E. Dempfle, and M. Hennerici, "Transcranial-ultrasound-improved thrombolysis: Diagnostic vs therapeutic ultrasound," Ultrasound Med. Biol. **27**(12), 1683–1689 (2001).
[5] F. J. Kirkham, T. S. Padayachee, S. Parsons, L. S. Seargeant, and F. R. House, "Transcranial measurement of blood flow velocities in the basal cerebral arteries using pulsed Doppler ultrasound: Velocity as an index of flow," Ultrasound Med. Biol. **12**(1), 15–21 (1986).
[6] W. Wilkening, S. Helbeck, T. Postert, J. Federlein, J. Rose, P. Hoppe, T. Buttner, and H. Ermert, "Brain perfusion imaging using contrast agent specific imaging modes," 1999 IEEE Ultrasonics Symposium 2, 1721–1725 (1999).
[7] M. A. Moehring, B. P. Wilson, and K. W. Beach, "Intracranial bleed monitor," 1999 IEEE Ultrasonics Symposium 2, 1545–1549 (1999).
[8] F. J. Fry, R. C. Eggleton, and R. F. Heimburger, "Transkull visualization of brain using ultrasound: An experimental model study," Proceedings of the Second World Congress on Ultrasonics in Medicine, Rotterdam, **47** 97–103 (1974).
[9] P. L. Carson, T. V. Oughton, W. R. Hendee, and A. S. Ahuja, "Imaging soft tissue through bone with ultrasound transmission tomography by reconstruction," Med. Phys. **4**, 302 (1977).
[10] S. W. Smith, D. J. Phillips, O. T. von Ramm, and F. L. Thurstone, "Some advances in acoustic imaging through the skull," Ultrasonic Tissue Characterization II, 209–218 (1979).
[11] K. A. Dines, F. J. Fry, J. T. Patrick, and R. L. Gilmor, "Computerized ultrasound tomography of the human head: Experimental results," Ultrason. Imaging **3**(4), 342–351 (1981).
[12] J. Ylitalo, J. Koivukangas, and J. Oksman, "Ultrasonic reflection mode computed tomography through a skull bone," IEEE Trans. Biomed. Eng. **37**(11), 1059–1066 (1990).
[13] M. Tanter, J.-L. Thomas, and M. A. Fink, "Time reversal and the inverse filter," J. Acoust. Soc. Am. **108**(1), 223–234 (2000).
[14] G. T. Clement and K. Hynynen, "Micro-receiver guided transcranial beam steering," IEEE Trans. Ultrason. Ferroelectr. Freq. Control **49**(4), 447–453 (2002).
[15] S. W. Smith, G. E. Trahey, and O. T. von Ramm, "Phased array ultrasound

imaging through planar tissue layers,'' Ultrasound Med. Biol. **12**, 229–243 (1986).
[16] G. T. Clement and K. Hynynen, ''A noninvasive method for focusing ultrasound through the human skull,'' Phys. Med. Biol. **47**, 1219–1236 (2002).
[17] M. Hayner and K. Hynynen, ''Numerical analysis of ultrasonic transmission and absorption of oblique plane waves through the human skull,'' J. Acoust. Soc. Am. **110**(6), 3319–3330 (2001).
[18] G. T. Clement, J. Sun, and K. Hynynen, ''The role of internal reflection in transskull phase distortion,'' Ultrasonics **39**(2), 109–113 (2001).
[19] M. C. Junger and D. Feit, ''Applications of the Elementary Acoustic Solutions,'' in *Sound, Structures, and Their Interaction* (Acoustical Society of America, Woodbury, NY, 1993).
[20] G. S. Kino, *Acoustic Waves: Devices, Imaging, and Analog Signal Processing* (Prentice-Hall, Englewood Cliffs, NJ, 1987).
[21] R. S. Thompson, P. Tortoli, and G. K. Aldis, ''Selective transmission of a focused Doppler ultrasound beam through a plastic layer,'' Ultrasound Med. Biol. **26**(8), 1333–1346 (2000).
[22] J. Sun and K. Hynynen, ''The potential of transskull ultrasound therapy and surgery using the maximum available skull surface area,'' J. Acoust. Soc. Am. **105**(4), 2519–2527 (1999).
[23] G. T. Clement and K. Hynynen, ''Forward planar projection through layered media,'' IEEE Trans. Ultrason. Ferroelectr. Freq. Control **50**(12), 1689–1699 (2003).
[24] G. T. Clement and K. Hynynen, ''Field characterization of therapeutic ultrasound phased arrays through forward and backward planar projection,'' J. Acoust. Soc. Am. **108**(1), 441–446 (2000).
[25] J. E. Marsden and A. J. Tromba, *Vector Calculus* (Freeman, New York, 1988).

Erratum: "Coupled perturbed modes over a sloping penetrable bottom" [J. Acoust. Soc. Am. 114, 3119–3124 (2003)]

C. J. Higham and C. T. Tindle
Department of Physics, University of Auckland, Private Bag 92019, Auckland, New Zealand

(Received 18 December 2003; accepted for publication 28 December 2003)

[DOI: 10.1121/1.1648975]

PACS numbers: 43.30.Bp, 43.10.Vx [ADP]

Typographical errors appear in Eqs. (15) and (16). The equations should read,

$$\Delta k_n = \frac{1}{2k_n}\left[\int_0^\infty \Delta q(\tilde{z};z)X(\tilde{z};z)U_n^2(\tilde{z};z)d\tilde{z} + \int_0^\infty (q(\tilde{z};z)-k_n^2)\Delta X(\tilde{z};z)U_n^2(\tilde{z};z)d\tilde{z}\right], \tag{15}$$

$$a_{nm} = \frac{1}{k_n^2-k_m^2}\left[\int_0^\infty \Delta q(\tilde{z};z)X(\tilde{z};z)U_n(\tilde{z};z)U_m(\tilde{z};z)d\tilde{z} + \int_0^\infty (q(\tilde{z};z)-k_n^2)\Delta X(\tilde{z};z)U_n(\tilde{z};z)U_m(\tilde{z};z)d\tilde{z}\right], \quad (n\neq m). \tag{16}$$

Equations (A4) and (A5) are identical to Eqs. (15) and (16), and should also be corrected.

 0001-4966/2004/115(3)/1365/1/$20.00